ACTA METALLURGICA

Board of Governors

Professor Eric Rudberg

Professor R. Smoluchowski — Professor Maxwell Gensamer

Dr. James B. Austin — Dr. W. A. Baker

Dr. George A. Roberts — Dr. W. Boas

Dr. Oscar Marzke

Dr. J. H. Hollomon, *Secretary-Treasurer*

Editor

Professor Bruce Chalmers, Division of Engineering and Applied Physics,
Harvard University, Cambridge, Massachusetts, U.S.A.

VOL.
4
1956

Associate Editors

M. W. T. Read, Jr. (*North America*) — Professor G. H. H. Wasserman (*Germany*)

Professor Alan Cottrell (*Great Britain*) — Professor E. Rudberg (*Sweden*)

Professor P. Laurent (*France*) — Dr. W. Boas (*Australia*)

Professor P. Coheur (*Belgium*) — Professor Antonio Scortecci (*Italy*)

Professor W. G. Burgers (*Holland*) — Professor Seiji Kaya (*Japan*)

Professor Väinö Hovi (*Finland*) — Professor F. R. N. Nabarro (*South Africa*)

Business Manager: Mr. D. J. Raymond

Business Office: Pergamon Press Inc., *Acta Metallurgica*, 122 East 55th Street, New York 22, N.Y.

VOLUME 4
1956

CONTENTS OF VOLUME FOUR

NUMBER 1

Thermodynamic properties of solid solutions—I. Vapor pressures of cadmium over alpha silver-cadmium alloys — P. Herasymenko — 1

Über die Gitterbindung und die Bänder der Valenzelektronen bei Gallium und Molybdändisilizid — H. Schenk and U. Dehlinger — 7

Thermodynamics of liquid Ag-Au and Au-Cu alloys and the question of strain energy in solid solutions — R. A. Oriani — 15

Kink bands in germanium — Fred D. Rosi — 26

Thermodynamic properties of solid aluminum-silver alloys — Mats Hillert, B. L. Averbach, and Morris Cohen — 31

Calorimetric study of the austenite : pearlite transformation — W. C. Hagel, G. M. Pound, and R. F. Mehl — 37

Fragmentation in tungsten crystals — G. D. Rieck — 47

Vacancies and interstitials in germanium and silicon — Sumner Mayburg — 52

The mechanism of densification during sintering of metallic particles — G. C. Kuczynski — 58

The growth of whiskers by the reduction of metal salts — Sydney S. Brenner — 62

The kinetics of recovery and recrystallization of copper from hardness and thermoelectric-power measurements — T. Ll. Richards, S. F. Pugh, and H. J. Stokes — 75

The internal friction of aluminum single crystals as a function of temperature — H. Birnbaum and M. Levy — 84

Letters to the Editor: — 89

S. S. Brenner and C. R. Morelock; P. Start, B. L. Averbach, and M. Cohen; U. F. Kocks and R. Maddin; J. S. Kirkaldy; E. E. Thomas; Tomio Nagashima and Takaaki Yamamoto; R. E. Hoffman; R. D. Gifkins; Christian de Beaulieu; L. Young

Book reviews — 102

Some current papers in other journals — 107

NUMBER 2

Slip in crystals of the caesium chloride type — W. A. Rachinger and A. H. Cottrell — 109

The influence of hydrogen on the yield point in iron — H. C. Rogers — 114

An isothermal anneal study of quenched and cold-worked copper-palladium alloys — F. E. Jaumot jr and A. Sawatzky — 118

Order-disorder and cold-work phenomena in Cu-Pd alloys — F. E. Jaumot jr. and A. Sawatzky — 127

The rates of oxidation of several faces of a single crystal of copper as determined with elliptically polarized light — Fred W. Young jr., John V. Cathcart, and Allan T. Gwathmey — 145

The structure of oxide films on different faces of a single crystal of copper — Kenneth R. Lawless and Allan T. Gwathmey — 153

The temperature dependence of the elastic constants of gold-cadmium alloys — Stanley Zirinsky — 164

Structural relationships between intermetallic compounds — P. J. Black — 172

Propagation of Lüder's bands in steel wires — J. C. Fisher and H. C. Rogers — 180

Physical evidence of dislocations in chromium — M. J. Fraser, D. Caplan, and A. A. Burr — 186

The critical shear stress in α-brass as a function of zinc concentration and temperature — R. E. Jamison and F. A. Sherrill — 197

Formation de monocristaux de Cu_2O et ZnO par oxydation sélective d'un film de laiton α préparé par évaporation sous vide — N. Takahashi and J. J. Trillat — 201

Cementite morphology in pearlite — F. C. Frank and K. E. Puttick — 206

Letters to the Editor: — 211

Hugh O'Neill; C. W. Berghout; R. Rawlings; R. V. Coleman and G. W. Sears; A. C. Damask; John W. Cahn; D. Hasanovitsh, M. Kaufman, and D. Rosenthal; W. Kaiser and J. A. Kohn; S. Kohara and G. C. Kuczynski; R. D. Misch and E. S. Fisher; H. H. Stadelmaier and R. C. Hock; H. G. Vaughan and M. E. de Morton; E. P. Wohlfarth; J. Païdassi

Book review — 230

Some current papers in other journals — 231

NUMBER 3

Internal friction in solid solutions of tantalum — R. W. Powers and Margaret V. Doyle — 233

The growth of dispersed precipitates in solutions — G. W. Greenwood — 243

Closed miscibility gaps in ternary and quaternary regular alloy solutions — J. L. Meijering and H. K. Hardy — 249

Dislocation arrays and rows of etch-pits — B. A. Bilby and A. R. Entwisle — 257

Low-frequency studies of dislocation interactions with solute atoms — S. Weinig and E. S. Machlin — 262

Mechanism of whisker growth—III. Nature of growth sites — S. S. Brenner and G. W. Sears — 268

An experimental investigation on the mode of slip in α-brass — H. Wilsdorf and J. T. Fourie — 271

Mechanik und Kinetik der diffusionslosen Martensitbildung — H. Knapp und U. Dehlinger — 289

Beiträge zu einer Theorie der plastischen Drahtdehnung — Horst Lippmann — 298

A study of (112) edge dislocations in bent silicon-iron single crystals — W. R. Hibbard jr. and C. G. Dunn — 306

A crystallographic study of mercuric iodide — J. B. Newkirk — 316

Letters to the Editor: — 331

M. R. Achter and R. Smoluchowski; A. J. Goss, K. E. Benson, and W. G. Pfann; J. L. Meijering

Some current papers in other journals — 336

VOL
4
195

NUMBER 4

Single crystal elastic constants of silver and silver alloys — R. Bacon and Charles S. Smith — 337
Structure-dependent chemical reaction and nucleation of fracture in Cu_3Au single crystals — R. Bakish and W. D. Robertson — 342
The Bauschinger effect in super-pure aluminum single crystals and polycrystals — S. N. Buckley and K. M. Entwistle — 352
On the energetics of TlCl-TlBr solid solutions — Väinö Hovi — 362
The delay-time phenomenon in metal single crystals — Tien-Shih Liu, I. R. Kramer, and M. A. Steinberg — 364
Interpenetrating "Bands" in transformed indium-thallium alloys — Z. S. Basinski and J. W. Christian — 371
The shapes of glide planes in bent zinc crystals — B. A. Bilby and E. Smith — 379
The effect of cold work on local order — R. S. Rudman and B. L. Averbach — 382
Plastic deformation of germanium in compression — J. R. Patel and B. H. Alexander — 385
Thermodynamics of iron-carbon melts — E. T. Turkdogan, L. E. Leake, and C. R. Masson — 396
The structure of lithium-magnesium solid solutions—I. Measurements on the Bragg reflections — F. H. Herbstein and B. L. Averbach — 407
The structure of lithium-magnesium solid solutions—II. Measurements of diffuse X-ray scattering — F. H. Herbstein and B. L. Averbach — 414
Magnetically induced grain-boundary motion in bismuth — W. W. Mullins — 421
The evolution of the energy stored by a gold-silver alloy cold-worked at −195°C and at room temperature — Peter Greenfield and M. B. Bever — 433
Letters to the Editor: — 440
C. C. Hsiao; R. W. Christy; S. Marinelli and F. Blaha; D. W. Wakeman and B. B. Argent; W. Bardsley and R. L. Bell
Some current papers in other journals — 447

NUMBER 5

The kinetics of grain boundary nucleated reactions — John W. Cahn — 449
The surface tensions of liquid-metal solutions — J. W. Taylor — 460
A dislocation-attraction model for the first stage of tempering — B. S. Lement and Morris Cohen — 469
X-ray and calorimetric investigations of cold working and annealing of a gold-silver alloy — B. L. Averbach, M. B. Bever, M. F. Comerford, and J. S. Ll. Leach — 477
Easy glide of cubic metal crystals — J. Garstone, R. W. K. Honeycombe, and G. Greetham — 485
Kinetics of precipitation in small lead-tin spheres — W. de Sorbo and D. Turnbull — 495
Fourier analysis of X-ray diffraction profiles obtained from tantalum filings — F. R. L. Schoening — 510
The pinning of dislocations by X-irradiation of alkali halide crystals — R. B. Gordon and A. S. Norwick — 514
Crystal structures of lithium-magnesium alloys at low temperatures — C. S. Barrett — 528
Elastic and plastic behavior of the ferrite lattice in a low-alloy steel — H. C. Vacher, R. Liss, and R. W. Mebs — 532
Initial oxidation rate of metals and the logarithmic equation — Herbert H. Uhlig — 541
Letters to the Editor: — 555
C. Crussard; J. Mackowiak and L. L. Shreir; E. Aerts and W. Dekeyser; A. Münster, K. Sagel, and U. Zwicker; J. D. Eshelby and P. L. Pratt; Hans U. Åström
Some current papers in other journals — 564

NUMBER 6

A quantitative study of the formation of austenite and the solution of cementite at different austenitizing temperatures for a 1.27% carbon steel — Goran Molinder — 565
Transformation kinetics during continuous cooling — John W. Cahn — 572
A theory of surface tension of solids—I. Application to metals — Adam S. Skapski — 576
A next-neighbors theory of maximum undercooling — Adam S. Skapski — 583
Precipitate kinetics and structure in a Cu-2.4% Fe alloy — J. M. Denney — 586
The influence of temperature on pre-yield plastic and anelastic microstrain in low-carbon steel — J. A. Hendrickson, D. S. Wood, and D. S. Clark — 593
The resistivity-temperature-concentration relationships in β-phase titanium-hydrogen alloys — S. L. Ames and A. D. McQuillan — 602
An X-ray investigation of the structure of liquid mercury and liquid mercury-thallium alloys — R. E. Smallman and B. R. T. Frost — 611
The effect of addition elements on the electrical resistivity of α-titanium — S. L. Ames and A. D. McQuillan — 619
Internal friction in alloys of Mg and Cd — J. Lulay and C. Wert — 627
Subgrain and electrical resistivity studies of molybdenum single crystals — K. T. Aust and R. Maddin — 632
The formation of low-energy interfaces during grain growth in alpha and alpha-beta brasses — Hsun Hu and Cyril Stanley Smith — 638
Glide in lead telluride — W. A. Rachinger — 647
Thermal and forced diffusion of oxygen in β-titanium — Fernand Claisse and H. Paul Koenig — 650
Letters to the Editor: — 655
C. W. Chen and E. S. Machlin; H. Lambot; F. van Wijk and J. A. B. van Dijck
Some current papers in other journals — 660

VOL. 4 1956

AUTHOR INDEX

(B) denotes book review

ACHTER, M. R. 331
AERTS, E. 555
ALEXANDER, B. H. 385
AMES, S. L. 602, 619
ARGENT, B. B. 440
ASTRÖM, H. U. 555
AUST, K. T. 632
AVERBACH, B. L. 31, 89, 382, 407, 414, 477
BACON, R. 337
BAKISH, R. 342
BARDSLEY, W. 440
BARRETT, C. S. 528
BASINSKI, Z. S. 371
BEAULIEU, C. DE 89
BELL, R. L. 440
BENSON, K. E. 331
BERGHOUT, C. W. 211
BEVER, M. B. 433, 477
BILBY, B. A. 257, 379
BIRNBAUM, H. 84
BLACK, P. J. 172
BLAHA, F. 440
BRENNER, S. S. 62, 89, 268
BUCKLEY, S. N. 352
BURR, A. A. 186
CAHN, J. W. 211, 449, 572
CAPLAN, D. 186
CATHCART, J. V. 145
CHALMERS, B. 230(B)
CHEN, C. W. 655
CHRISTIAN, J. W. 371
CHRISTY, R. W. 440
CLAISSE, F. 650
CLARK, D. S. 593
COHEN, M. 31, 89, 469
COLEMAN, R. V. 211, 449
COMERFORD, M. F. 477
COTTRELL, A. H. 109
CRUSSARD, C. 555
DAMASK, A. C. 211
DEHLINGER, U. 7, 289
DEKEYSER, W. 555
DENNEY, J. M. 586
DIJCK, J. A. B. VAN 655
DOYLE, M. V. 233
DUNN, C. G. 306
ENTWISLE, A. R. 257
ENTWISTLE, K. M. 352
ESHELBY, J. D. 555
FISHER, E. S. 211
FISHER, J. C. 180
FOURIE, J. T. 271
FRANK, F. C. 206
FRASER, M. J. 186
FROST, B. R. T. 611
GARSTONE, J. 485
GIFKINS, R. D. 89
GORDON, R. B. 514
GOSS, A. J. 331
GREENFIELD, P. 433
GREENWOOD, G. W. 243
GREETHAM, G. 485
GWATHMEY, A. T. 145, 153
HAGEL, W. C. 37
HARDY, H. K. 249
HASANOVITSH, D. 211
HENDRICKSON, J. A. 593
HERASYMENKO, P. 1
HERBSTEIN, F. H. 407, 414
HIBBARD, W. R., JR. 306
HILLERT, M. 31
HOCK, R. C. 211
HOFFMAN, R. E. 89
HONEYCOMBE, R. W. K. 485
HOVI, V. 362
HSIAO, C. C. 440
HU, H. 638
JAMISON, R. E. 197
JAUMOT, F. E., JR. 118, 127
KAISER, W. 211
KAUFMAN, M. 211
KIRKALDY, J. S. 89
KNAPP, H. 364
KOCKS, U. F. 89
KOENIG, H. P. 650
KOHARA, S. 211
KOHN, J. A. 211
KRAMER, I. R. 364
KUCZYNSKI, G. C. 58, 211
LAMBOT, H. 655
LANG, A. R. 102(B)
LAWLESS, K. R. 153
LEACH, J. S. LL. 477
LEAKE, L. E. 396
LEMENT, B. S. 469
LEVY, M. 84
LIPPMAN, H. 298
LISS, R. 532
LIU, TIEN-SHIH 364
LULAY, J. 627
MACHLIN, E. S. 262, 655
MACKOWIAK, J. 555
MADDIN, R. 89, 632
MARINELLI, S. 440
MASSON, C. R. 396
MAYBURG, S. 52
MCQUILLAN, A. D. 602, 619
MEBS, R. W. 532
MEHL, R. F. 37
MEIJERING, J. L. 249, 331
MISCH, R. D. 211
MORELOCK, C. R. 89
MOLINDER, G. 565
MORTON, M. E. DE 211
MULLINS, W. W. 421
MÜNSTER, A. 555
NAGASHIMA, T. 89
NEWKIRK, J. B. 316
NORWICK, A. S. 514
O'NEILL, H. 211
ORIANI, R. A. 15
PAÏDASSI, J. 211
PATEL, J. R. 385
PFANN, W. G. 331
POUND, G. M. 37
POWERS, R. W. 233
PRATT, P. L. 555
PUGH, S. F. 75
PUTTICK, K. E. 206
RACHINGER, W. A. 109, 647
RAWLINGS, R. 211
RICHARDS, T. LL. 75
RIECK, G. D. 47
ROBERTSON, W. D. 342
ROGERS, H. C. 114, 180
ROSENTHAL, D. 211
ROSI, F. D. 26
RUDMAN, P. S. 382
SAGEL, K. 555
SAWATZKY, A. 118, 127
SCHENK, H. 7
SCHOENING, F. R. L. 510
SEARS, G. W. 211, 268
SHERRILL, F. A. 197
SHREIR, L. L. 555
SKAPSKI, A. S. 576, 583
SMALLMAN, R. E. 611
SMITH, C. S. 337, 638
SMITH, E. 379
SMOLUCHOWSKI, R. 331
SORBO, W. DE 495
STADELMAIER, H. H. 211
START, P. 89
STEINBERG, M. A. 364
STOKES, H. J. 75
TAKAHASHI, N. 201
TAYLOR, J. W. 460
THOMAS, E. E. 89
TRILLAT, J. J. 201
TURKDOGAN, E. T. 396
TURNBULL, D. 495
UHLIG, H. H. 541
VAUGHAN, H. G. 211
VACHER, H. C. 532
WAKEMAN, D. W. 440
WEINIG, S. 262
WERT, C. 627
WIJK, F. VAN 655
WILSDORF, H. 271
WOHLFARTH, E. P. 211
WOOD, D. S. 593
YAMAMOTO, T. 89
YOUNG, F. W., JR. 145
YOUNG, L. 89
ZIRINSKY, S. 164
ZWICKER, U. 555

VOL.
4
1956

VOL
4
195

THERMODYNAMIC PROPERTIES OF SOLID SOLUTIONS*—I

VAPOR PRESSURES OF CADMIUM OVER ALPHA SILVER-CADMIUM ALLOYS

P. HERASYMENKO†

A new method of measurement of partial vapor pressures over solid alloys has been developed. Solid alloys are formed at elevated temperatures from pure components—one of them being present in vapor form at constant partial pressure—until equilibrium with vapor is reached. The volatile element is maintained at constant pressure by keeping the pure volatile element in liquid form at constant temperature at the low-temperature end of the reaction vessel.

Partial vapour pressures of cadmium were measured in the whole alpha field for the Ag-Cd system. The partial heats and entropy of solution of cadmium in silver show abrupt changes at about 4.1, 8.33, 25, and 33.3 at. per cent Cd.

These changes are due to changes in ordering.

PROPRIÉTÉS THERMODYNAMIQUES DES SOLUTIONS SOLIDES—I
PRESSIONS DE VAPEUR DU CADMIUM SUR LES ALLIAGES ARGENT-CADMIUM

Il est développé une nouvelle méthode de mesure des pressions de vapeur partielles en présence d'alliages solides. Les alliages solides sont formés à températures élevées à partir des composants purs—l'un existant dans la phase vapeur à la pression partielle constante—jusqu'à ce que l'équilibre avec la vapeur soit atteint. La pression de l'élément volatil est maintenue constante en conservant cet élément à l'état liquide à température constante dans la partie froide de l'enceinte.

Les pressions partielles de vapeur du cadmium ont été mesurées dans tout le domaine α du système Ag-Cd. Les chaleurs et entropie de solution du cadmium dans l'argent changent brusquement vers 4.1, 8.33, 25, et 33.3 at. % Cd.

Ces changements sont dûs à des modifications dans l'ordre.

THERMODYNAMISCHE EIGENSCHAFTEN VON MISCHKRISTALLEN—I
DER DAMPFDRUCK VON CADMIUM ÜBER ALPHA SILBER-CADMIUM LEGIERUNGEN

Es wurde eine neue Methode zur Messung des partiellen Dampfdruckes über festen Legierungen entwickelt. Feste Legierungen werden bei erhöhten Temperaturen aus den reinen Komponenten derart dargestellt, dass man die eine Komponente aus der Gasphase bei konstantem Partialdruck so lange auf die andere einwirken lässt, bis das Gleichgewicht des Systems erreicht ist. Auf der niedrig temperierten Seite des Reaktionsgefässes wird die reine flüchtige Komponente als flüssige Phase auf konstanter Temperatur gehalten, wodurch die Konstanz ihres Druckes gegeben ist.

Die partiellen Dampfdrücke von Cadmium wurden über den gesamten alpha-Bereich des Systems Ag-Cd bestimmt. Bei ungefähr 4.1, 8.33, 25, und 33.3 At% Cd zeigen die partiellen Wärmeinhalte und die Entropie der Lösung von Cadmium in Silber sprunghafte Änderungen.

Diese Änderungen entsprechen Änderungen im Ordnungszustand.

VOL.
4
1956

1. INTRODUCTION

When the energy of bonding between the atoms of a solute and a solvent is greater than that between like atoms, one would expect that the solute atoms would tend to occupy definite positions among the lattice sites of the solvent atoms and tend to be surrounded by unlike atoms. This tendency is opposed by thermal vibrations, and the distribution of atoms on the lattice sites of real solutions often differs substantially from the ideal ordering. Local atomic arrangements may be studied by means of X-ray scattering. In the systems which form superlattices the preference for unlike atoms above the critical temperature has been proved by such measurements, and this type of local arrangement is called a "short-range order". Some indications on the extent of ordering in solid solutions can be obtained by measuring the dependence of partial thermodynamic properties on the concentration of the solute.

An example of a large effect of concentration on partial thermodynamic properties of homogeneous solutions can be found in the gold-cadmium system investigated by A. Ölander[1] by electrochemical methods: e.g., he found that the partial molal heat

* Received August 25, 1954; revised version April 10, 1955.
† Engineering Research Division, New York University, New York 53, New York, U.S.A.

of solution of cadmium in the beta field of this system increases from about —10,000 cal/mol Cd to about —2500 cal/mol Cd, and that the partial entropy increases by 6 entropy units in a narrow interval between 47 and 52 at. per cent cadmium. Examination of other published data on metallic solid solutions led the present author to believe that similar almost discontinuous changes of partial thermodynamic functions (especially of $\overline{\Delta H}$ and $\overline{\Delta S}$) may take place at definite concentrations of solute, and may be due to a change in the mode of ordering with a change in the content of the solute.[2] The accuracy of published data is often not sufficient to prove unequivocally this supposition, and the concentration intervals between alloys of different compositions are usually too large to permit exact determination of the concentrations of the solvent at which abrupt changes in thermodynamic functions occur.

The aim of the present study is to determine accurately the vapor pressures of volatile constituents of solid solutions on a large number of alloys whose alloying content varies by small increments. The results of the measurements serve to evaluate the dependence of thermodynamic properties of alloys on composition.

2. THERMODYNAMIC PROPERTIES ALPHA Ag-Cd ALLOYS

(A) *Experimental Method*

The method developed in this work was initially as follows:

A small alundum boat containing pure cadmium was placed at one end of a quartz tube having a thermocouple well extending almost through the whole length of the tube (see Fig. 1). Starting from the middle of the tube, 20 to 30 specimens of pure silver wire of 0.01 in. diameter were placed in narrow grooves drilled in a flat rectangular piece of alundum

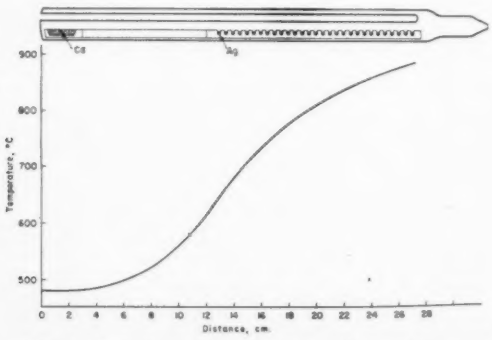

FIG. 1. Reaction tube and its position with respect to temperature distribution in the furnace.

at intervals of 1.5 to 2.5 mm apart. The width and depth of the grooves was 2.5 mm. Silver wire specimens weighing about 80 mg were twisted in short spirals to accommodate them in the grooves. The distance between the boat with the cadmium and the alundum piece with the silver specimens was kept constant by inserting an alundum rod spacer.

After assembling, the tube was thoroughly evacuated, sealed, and placed in a resistance furnace having two separately controlled windings. The quartz vessel was placed in the furnace in a slightly inclined position so that the end with the cadmium was about 1 cm lower than the other end. The temperature distribution along the furnace is schematically indicated in Fig. 1. The end of the quartz tube with the cadmium was placed at the position of the minimum of the temperature curve where the temperature was kept constant to ± 0.5°C over a length of about 3 cm at a certain level above the melting point of cadmium. The other end of the quartz tube lay near the maximum of the temperature curve, so that individual silver specimens were at different positions along the temperature gradient in the furnace. The vapor pressure of cadmium in the whole quartz vessel was constant, and was determined by the temperature of liquid cadmium. The vapor pressure formula used in this study was taken from tables in *Metallurgical Thermochemistry*, by O. Kubaschewski and E. Ll. Evans[3]:

$$\log p_{\text{mmHg}} = -5{,}819T^{-1} - 1.257 \log T + 12.287.$$

Silver wire specimens absorb cadmium from the vapor until they form a silver-cadmium alloy which is in equilibrium with cadmium vapor at the temperature of the alloy. The process of equilibration, which depends on the rate of diffusion, is rather slow. Thus, it was necessary to maintain for more than 100 hours a constant temperature of liquid cadmium and a constant temperature at each point of the temperature gradient where the silver samples were placed. This was achieved by using two electronic temperature controllers for the two separate windings of the furnace. Measurements during runs lasting more than 200 hours have shown that the temperature of liquid cadmium was constant to within ± 0.5°C, and the temperature along the temperature gradient to within ± 1°C. The initial adjustment of the temperature of liquid cadmium in each run was made in the first 24 to 48 hours. In this period the position of the cadmium end of the tube was adjusted in the furnace to coincide with the minimum point of the temperature distribution curve.

It happened in several runs that the cadmium end of the tube was placed initially at a temperature much higher than this minimum, so that a considerable amount of cadmium evaporated. When the position of the liquid cadmium was subsequently shifted to the minimum point of the temperature curve the lost cadmium condensed back, not in the boat but around it, and the liquid pool spread beyond the region of constant temperature. This made the estimation of the vapor pressure of liquid cadmium uncertain, and these runs were discarded.

Since the silver specimens are placed in a temperature gradient, a small shift of position may cause a considerable discrepancy between the actual and assumed temperature of a specimen. Such runs where the position of the silver specimens in the tube was uncertain were also discarded.

In the later stage of this study the design of the vessel was modified to minimize these errors (Fig. 2). The silver wire specimens were formed into rings and fixed on a quartz tube which had a series of quartz beads welded on its surface.

The beads served as spacers for the wire rings, and prevented their displacement during the run. The tube with mounted specimens was shifted on the thermocouple-well tube until it touched a quartz bead welded on the latter. This fixed the position of the thermocouple tube with respect to the thermocouple. Cadmium metal was placed at the low-temperature end, without an alundum boat. The pool of liquid cadmium of about 1 cm length occupied the lowest position in the vessel, since the vessel was held in an inclined position during runs. The whole vessel was made longer, and a longer furnace was used to obtain a less-steep temperature gradient. The accuracy of temperature determinations was substantially improved by these changes.

During the last day of exposure, the temperature distribution in the tube was measured starting from the highest temperature and proceeding in small steps to the temperature of cadmium, and then in the reverse direction.

After the completion of a run the quartz tube was withdrawn from the furnace and rapidly cooled. In most cases the content of cadmium was determined from the weight increase. These results were checked by polarographic analysis of samples. The agreement was quite satisfactory for cadmium contents greater than about 10 at. per cent. At lower concentrations, the contents of cadmium determined by both methods differed in some samples. These erratic deviations were due to errors in the determination of weight increase at small cadmium contents when an ordinary

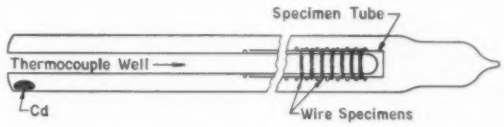

FIG. 2. Modified design of the reaction tube.

analytical balance, which was accurate to about ± 0.1 mg, was used. Therefore, more weight was given to polarographic results at low contents of cadmium.

In the later stage of this work a microbalance sensitive to ± 0.002 mg was used, and this resulted in improved accuracy of cadmium determinations from the weight increase of the specimens, so that time-consuming chemical (polarographic) analyses could be entirely omitted. The reproducibility of cadmium determinations when using the microbalance was about ± 0.05 at. per cent cadmium, and even this spread was caused more by uncertainty in temperature measurements than in weighing.

(B) *Materials Used*

The silver wire used was of 99.99+ per cent purity. Pure cadmium of unknown origin was analyzed polarographically and was found to contain 0.082 per cent Pb and 0.003 per cent Cu. These impurities were entirely eliminated by distilling cadmium *in vacuo*. The content of zinc could not be determined polarographically in the presence of an excesss of cadmium. The presence of even 0.01 per cent Zn in cadmium would seriously affect the results, because the activity coefficient of zinc in liquid cadmium-zinc alloys is greater than unity, so that silver wire would absorb zinc from the vapor phase in larger proportions than it was present in the liquid cadmium-zinc alloy. To eliminate possible traces of zinc, liquid cadmium was heated in shallow boats in a current of steam at 450°C for four hours, whereby zinc was preferentially oxidized. This method was described recently by W. Scheller and W. D. Treadwell[4] who found that this treatment eliminates zinc down to 3×10^{-3} per cent by weight. The oxide film was removed from the surface of the metal by filing.

Polarographic analysis of silver-cadmium alloys obtained by equilibrating silver wires in the vapor of purified cadmium showed no detectable trace of zinc.

(C) *Experimental Results*

More than 250 silver-cadmium alloys were obtained by the described technique in 10 runs at different

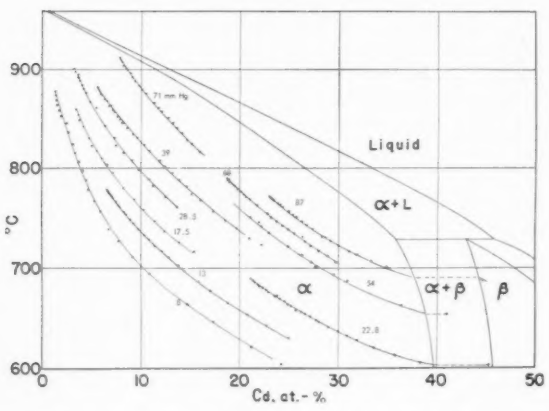

FIG. 3. Isobars of p_{Cd} in the alpha field of the Ag-Cd system.

partial pressures of cadmium. The measurements cover the range from 2 to 45 at. per cent Cd. In most cases the alloys were obtained with pure silver wires as the starting material; in one run the silver-cadmium specimens from a previous run were used again, so that the equilibrium was approached from higher contents of cadmium. Five runs were made with the initial design of the apparatus, and five runs with improved design.

The tabulation of these numerous results is omitted here. Copies of the tables may be obtained on request addressed to the author.

The temperatures of the Ag-Cd alloys obtained in each run are plotted against the observed cadmium contents in Fig. 3, which also shows the solidus and liquidus curves of the corresponding portion of the phase diagram. The curves for each run in Fig. 3 represent separate isobars (curves of constant partial pressure of cadmium) in the phase diagram. These isobars were obtained by graphical interpolation between experimental points on a large-scale plot. They are regarded as representing the average values which are more accurate than the experimental points, and were used as a basis for all subsequent calculations.

The duration of exposure was in all cases more than 100 hours (not counting the time of initial adjustments lasting from 24 to 48 hours). The diameter of silver wire used in most experiments was 0.010 in. It was estimated from published data on the diffusion of cadmium in silver that 100 hours' exposure would be sufficient to saturate wires of this diameter at temperatures above 700°C. Much longer time appeared to be necessary at lower temperatures (e.g., 320 hr at 650°C). However, a direct experiment has shown that silver wire of 0.010 in. diameter reached equilibrium with cadmium vapor in about 100 hr exposure, even at temperatures around 600°C. In the later stage of this work, wires of two diameters (0.010 and 0.005 in.) were used for lower-temperature ranges in the same run. The points for both wires fell smoothly on the same isobar for each run. It is probable that the diffusion coefficients of cadmium increase with cadmium content, so that silver-cadmium alloys with Cd $>$ 10 at. per cent reach equilibrium with cadmium vapor in 100 hours, even in the range from 600 to 700°C, in the case of 0.010-in.-diameter wires.

The logarithms of the partial vapor-pressures were plotted against the reciprocal absolute temperatures in a large-scale graph at 1 at. per cent intervals read from the isobars. Straight lines were obtained for points joining the constant contents of cadmium. The deviations from the straight lines amounted on the average to less than ± 1 degree error in reading the temperature from the isobars smoothed by interpolation.

The plot of the logarithms of the activities against the reciprocal absolute temperature is shown in Fig. 4. The partial heats of solution of cadmium referred to liquid cadmium were calculated from the slopes of the straight lines and are shown in Fig. 5. Partial free energies of solution are also plotted in Fig. 5, and the partial entropies of cadmium in Fig. 6. The smoothed values of various thermodynamic functions are tabulated in Table 1.

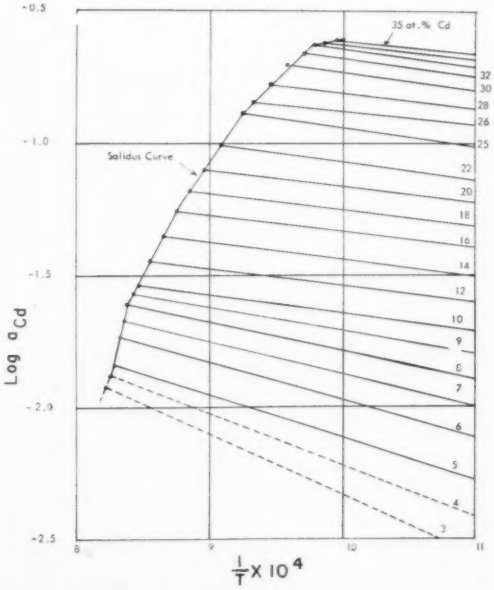

FIG. 4. Plot of log a_{Cd} versus reciprocal absolute temperature.

TABLE 1. Partial thermodynamic functions and molal free energies of formation for the alpha silver-cadmium alloys

Cd at.%	a_{Cd} (1000°K)	γ_{Cd} (1000°K)	$-\bar{F}_{Cd}$ 1000°K cal/at.	$-\bar{H}_{Cd}$ cal/at.	$\bar{S}_{Cd}$ cal/°K	γ_{Ag} 1000°K	$-\Delta F$ 1000°K cal/mole
3	0.0036	0.12	11,250	10,300	0.9	0.995	410
4	0.0058	0.14	10,250	9,100	1.1	0.991	520
5	0.0084	0.167	9,500	7,250	2.2	0.988	615
6	0.0108	0.180	9,000	6,350	3.65	0.985	705
7	0.0129	0.185	8,600	5,750	3.95	0.981	790
8	0.0158	0.197	8,250	5,300	3.95	0.975	865
9	0.0190	0.212	7,870	3,800	4.07	0.973	935
10	0.0222	0.222	7,570	3,200	4.37	0.972	1,000
12	0.0293	0.244	7,020	3,000	4.02	0.971	1,140
14	0.0367	0.262	6,560	2,900	3.66	0.966	1,255
16	0.0465	0.291	6,100	2,800	3.30	0.958	1,365
18	0.0568	0.313	5,720	2,750	2.97	0.942	1,465
20	0.0681	0.340	5,340	2,850	2.49	0.922	1,560
22	0.0838	0.391	4,930	3,130	1.80	0.897	1,650
23	0.0931	0.405	4,720	3,320	1.40	0.885	1,680
24	0.103	0.430	4,520	3,500	1.02	0.871	1,720
25	0.114	0.455	4,320	3,150	1.17	0.858	1,750
26	0.127	0.490	4,100	2,400	1.70	0.846	1,775
28	0.155	0.555	3,700	2,800	0.90	0.814	1,825
30	0.185	0.617	3,400	3,300	0.10	0.774	1,870
32	0.210	0.657	3,100	3,400	−0.30	0.727	1,900
33	0.224	0.680	3,000	3,100	−0.10	0.700	1,905
34	0.234	0.690	2,890	2,350	+0.54	0.675	1,915
35	0.247	0.705	2,780	2,200	+0.58	0.646	1,920

Partial functions for cadmium are with reference to liquid cadmium. The activity coefficients of silver are with reference to solid silver. The molal free energies of formation of silver cadmium alloys are with reference to solid silver and liquid cadmium.

VOL. 4 1956

(D) *Discussion*

The vapor pressure of cadmium in the alpha-field of the Ag-Cd system was studied by C. E. Birchenall and C. H. Cheng[5] with three alloys containing 8.1, 22.7, and 34.1 at. per cent Cd, using Hargreaves's "dew point" method. When plotting the logarithms of activity against reciprocal absolute temperature for three alloys investigated by Birchenall and Cheng, the slopes of the straight lines obtained were practically the same at all three compositions, and corresponded to the partial heat of solution of cadmium of -6000 ± 1000 cal/mol Cd. On the other hand, our experiments have indicated that there was a much larger variation of the partial heat of solution with change of cadmium content. The discrepancy may possibly be due to insufficient time of equilibration of Ag-Cd alloy with cadmium vapor in the dew-point method.

The curves of partial heats of solution of cadmium shown in Figs. 5 and 6 have distinct inflections at 4, 8.3, 25, and 33.3 at. per cent cadmium. These changes indicate changes in local ordering of cadmium atoms in the f.c.c. lattice of silver-cadmium alloys at the following ratios of cadmium atoms to the total number of atoms in the alloys: 1/24, 1/12, 1/4, and 1/3. The values of partial thermodynamic functions at cadmium

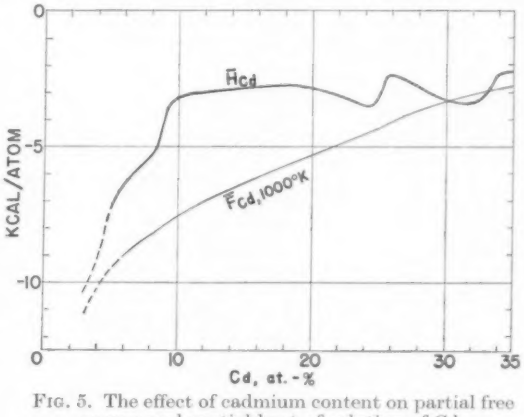

FIG. 5. The effect of cadmium content on partial free energy and partial heat of solution of Cd.

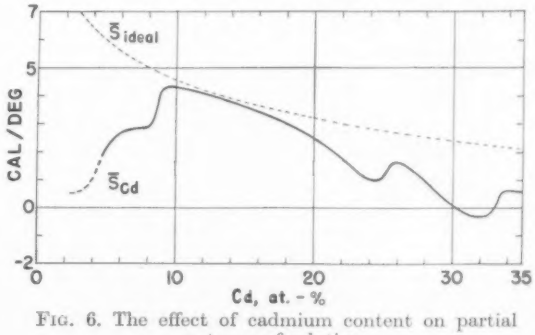

FIG. 6. The effect of cadmium content on partial entropy of solution.

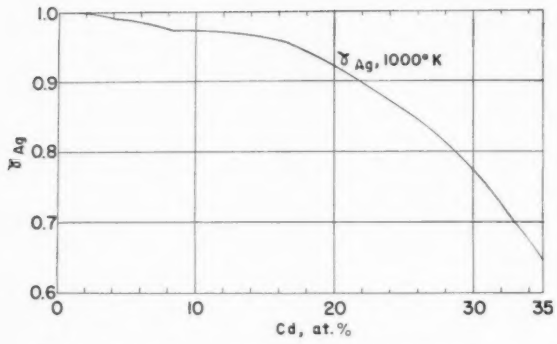

FIG. 7. The effect of cadmium content on the activity coefficient of silver in the Ag-Cd alloys.

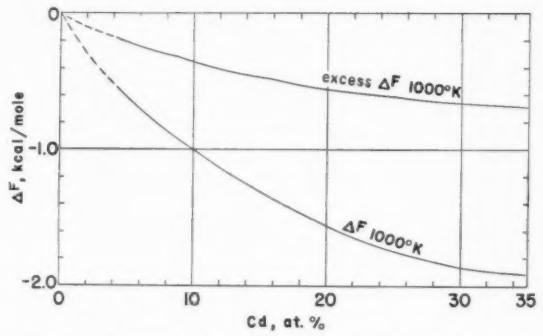

FIG. 8. Concentration dependence of the relative molal free energy and excess free energy of formation of alpha Ag-Cd alloys.

contents below about 4.5 at. per cent are somewhat less accurate than the values at higher concentrations, and are therefore indicated by broken curves. Nevertheless, there is no doubt that the degree of ordering at about 4 at. per cent Cd is quite high, as can be judged from the large difference between the observed entropy and the entropy of a completely disordered (ideal) solution.

It is not excluded that a slight tendency towards ordering is present between 16 and 18 at. per cent Cd, as can be inferred from inflections in the curves of partial heats and entropies in this interval. The changes at 4, 8.3, 25, and 33.3 at. per cent Cd are greater than the range of experimental error, and are considered as real.

Using the Gibbs-Duhem equation, the activity coefficients of silver can be calculated from the observed activity coefficients of cadmium. The results of these calculations are shown in Fig. 7, where the activity coefficients of silver (γ'_{Ag}) are plotted against the cadmium content. This curve shows distinct points of inflection at 4 and 8.3 at. per cent Cd, and less distinct points at 25 and 33.3 at. per cent Cd. The values of the relative molal free energies of formation, and relative excess free energies of formation, for the alpha Ag-Cd alloys (at 1000°K), are shown in Fig. 8.

The results of this work indicate that there are at least four concentration regions in the alpha-field of the silver-cadmium system at which the alloys show a definite tendency towards ordering.

ACKNOWLEDGMENTS

The author wishes to acknowledge the assistance of the Office of Ordnance Research in the sponsorship of this research. He also appreciates the co-operation of Mr. M. Jaworsky in the experimental work, and is indebted to Professor J. P. Nielsen for his interest.

This work was sponsored by the Office of Ordnance Research under Contract No. DA-30-069-ORD-1004.

REFERENCES

1. A. OLANDER, *J. Amer. Chem. Soc.*, **54,** 3819 (1932).
2. P. HERASYMENKO, Discussion of paper by Underwood and Averbach, *Trans. Amer. Inst. Min. Met. Eng.*, **194,** 1220 (1952).
3. O. KUBASCHEWSKI and E. LL. EVANS, *Metallurgical Thermochemistry*, Butterworth-Springer, London (1951).
4. W. SCHELLER and W. D. TREADWELL, *Helv. Chim. Acta*, **35,** 745 (1952).
5. C. E. BIRCHENALL and C. H. CHENG, *Trans. Amer. Inst. Min. Met. Eng.*, **185,** 428 (1949).

ÜBER DIE GITTERBINDUNG UND DIE BÄNDER DER VALENZELEKTRONEN BEI GALLIUM UND MOLYBDÄNDISILIZID *

H. SCHENK und U. DEHLINGER †

Es werden mit einer erweiterten Blochschen Methode Breite und gegenseitige Lage der Bänder, ausgehend von Atomfunktionen die der Punktsymmetrie des Atoms angepasst sind, bestimmt, woraus deren Anteil an der Bindung hervorgeht. In Gallium wird die Bindung innerhalb des im Gitter sichtbaren Paars nahezu durch eine einzige Atomfunktion mit schmalem Band bewirkt. Eine weitere besetzte Atomfunktion sticht ins Leere, während das dritte Elektron des Atoms ein breites Band besetzt und die Bindung zu sechs weiteren Nachbarn besorgt.

Im $MoSi_2$ erzeugen die Atomfunktionen des Si dieselben Bänder wie bei Gallium; sie treten mit den etwas höher liegenden Bändern der d- und s-Funktionen des Molybdäns in Wechselwirkung. Die Si zugeordneten Bänder werden hier stärker besetzt als bei Gallium. Die dort ins Leere gehende Atomfunktion kombiniert mit einer d-Funktion des Mo, das dazugehörige Band senkt sich. Somit ist die bei Gallium nicht abgesättigte Valenz im $MoSi_2$ stark betätigt, was die wesentlich höhere Bindungsfestigkeit des letzteren erklärt. Die hohe Koordinationszahl der Mo- und Si-Atome und die durch die Atomfunktionen gegebene Ladungsverteilung begünstigen eine heteropolare Komponente der Bindung. Ga und $MoSi_2$ ergeben sich als metallisch leitend. Weiterhin folgen Aussagen über Halleffekt und Suszeptibilität. Die effektive Elektronenmasse ist stark anisotrop.

LATTICE BONDING AND BANDS OF VALENCY ELECTRONS IN GALLIUM AND MOLYBDENUM DISILICIDE

Starting from an atom function, accommodated to the point symmetry of the atoms, a determination of breadth and separation of the bands is carried out, using an extension of the Bloch method. This shows the contribution of bands to the bonding. In gallium the bonding between the nearest-neighbor pair is effected significantly by only one atom function with a small band. Another occupied-atom function points in a direction in which there is no neighbor, whereas the third electron of the atom occupies a broad band and is responsible for the bonding to six other neighbors.

In $MoSi_2$ the atom functions of Si produce the same bands as in gallium; there is an interaction between them and the somewhat higher bands of the d- and s-functions of molybdenum. The bands belonging to Si are more occupied than in gallium. The atom function "going into emptiness" in gallium is combined with one d-function of Mo; the band belonging to it is reduced in energy. In this way the unsaturated valency of Ga is strongly active in $MoSi_2$, which explains the significantly higher bond-strength of the latter. The high co-ordination number of the Mo- and Si-atoms and the distribution of charge given by the atom functions favor a heteropolar component of bonding. Ga and $MoSi_2$ are shown to be metallic conductors. There follow predictions regarding the Hall effect and susceptibility. The effective electron mass is highly anisotropic.

SUR LA LIAISON ET LES BANDES DE VALENCE DU GALLIUM ET DU SULFURE DE MOLYBDÈNE

Les largeurs et les positions des bandes sont déterminées par une extension de la méthode de Bloch en partant des fonctions d'ondes de l'atome qui correspondent aux conditions de symétrie. Dans le gallium, la liaison est due sensiblement à une seule fonction d'onde correspondant à une bande étroite à l'intérieur d'un couple d'atomes visible dans le réseau. Une autre fonction d'onde occupée demeure inutilisée, tandis que le troisième électron occupe une bande large et étend la liaison aux six voisins suivants.

Dans $MoSi_2$, les fonctions d'onde de Si produisent les mêmes bandes que pour le gallium. Elles entrent en interaction avec les bandes d et s du molybdène situées à un niveau un peu plus élevé. Les bandes correspondant au silicium sont dans ce cas plus complètement occupées que pour le gallium. La fonction restée inutilisée se combine avec une fonction d du molybdène et abaisse la bande correspondante. Ainsi, la valence non saturée pour le gallium est très active dans $MoSi_2$, ce qui explique l'énergie de liaison nettement plus élevée de ce dernier. Les indices de coordination des atomes de Mo et Si et la répartition de la charge donnée par les fonctions d'ondes favorisent la tendance à l'hétéropolarité de la liaison mais Ga et $MoSi_2$ présentent le caractère métallique. Suit une discussion sur l'effet Hall et la susceptibilité. La masse apparente de l'électron est très fortement anisotrope.

VOL. 4 1956

* Received March 18, 1955.

† Institut für theoretische und angewandte Physik der Technische Hochschule Stuttgart und Max-Planck-Institut für Metallforschung Stuttgart.

1. ÜBERBLICK ÜBER DIE METHODE

Die im folgenden verwandte Methode fußt auf dem Blochschen Theorem,[1] d.h. der Möglichkeit, den Zustand eines Elektrons im Gitter in erster Näherung durch eine Wellenfunktion der Form $\psi_j = e^{2\pi i \boldsymbol{k}\boldsymbol{r}} \cdot u_j(\boldsymbol{r})$, worin $u_j(\boldsymbol{r})$ eine mit dem Gitter periodische Funktion und $\boldsymbol{k}$ der Wellenvektor ist, zu beschreiben. Wir wollen ψ_j von den Zuständen der Valenzelektronen des freien Atoms aus annähern, was durch eine Entwicklung von ψ_j nach Atomeigenfunktionen $\phi_\mu'(\boldsymbol{r} - \boldsymbol{r}_l) = \phi_\mu^{\prime l}$ möglich ist. Die $\phi_\mu'(\boldsymbol{r} - \boldsymbol{r}_l)$ sind Funktionen, die nur in der Umgebung eines Atoms der Zelle, deren Ortsvektor $\boldsymbol{r}_l$ ist von Null wesentlich verschieden sind. Der Index μ kennzeichnet die verschiedenen Funktionen innerhalb einer Zelle. Die Schwierigkeiten, die in der Nichtorthogonalität der an verschiedenen Atomen lokalisierten $\phi_\mu^{\prime l}$ bestehen, lassen sich nach einer von Löwdin[2] angegebenen Methode beseitigen; sie liefert durchweg orthogonale lokalisierte Funktionen: $\phi_\mu^{\,l} = \phi_\mu(\boldsymbol{r} - \boldsymbol{r}_l)$

$$\phi_\mu(\boldsymbol{r} - \boldsymbol{r}_l) = \phi_\mu'(\boldsymbol{r} - \boldsymbol{r}_l) + \sum_{\nu\lambda} a_{\mu\nu\lambda}\phi_\nu'(\boldsymbol{r} - \boldsymbol{r}_\lambda) \quad (1)$$

Eine Funktion $\phi_\mu(\boldsymbol{r} - \boldsymbol{r}_l)$ ist zwar noch in der unmittelbaren Umgebung des Atoms durch $\phi_\mu'(\boldsymbol{r} - \boldsymbol{r}_l)$ bestimmt, im Gebiet seiner Nachbarn überlagern sich ihr alle dort lokalisierten $\phi_\nu'(\boldsymbol{r} - \boldsymbol{r}_\lambda)$ und zwar grademit einem durch die Nichtorthogonalität bestimmten Gewicht $a_{\mu\nu\lambda}$.

Ausserdem soll noch bemerkt werden, dass nur der Winkelanteil von $\phi_\mu^{\prime l}$ mit dem einer entsprechenden Eigenfunktion des freien Atoms identisch ist; der Radialanteil wird zweckmässig nach anderen Näherungsverfahren bestimmt. Für unsere Einelektrongittereigenfunktion ψ_j benützen wir die Entwicklung

$$\psi_j = \sum_{l\nu} e^{2\pi i \boldsymbol{k}\cdot\boldsymbol{r}_l} c_{j\nu}\phi_\nu^{\,l} \qquad j = 1 \cdots n \quad (2)$$

Alle n Funktionen $\phi_\nu^{\,l}$ einer Zelle sind darin mit einem zunächst willkürlichen Koeffizienten $c_{j\nu}$ versehen, ihre Gesamtheit für $r = 1 \cdots n$ stellt einen Eigenvektor ζ_j dar. Die zu ψ_j gehörige Energie E_j berechnet sich nach der Gleichung:

$$E_j = \int \psi_j^* H_0 \psi_j \, d\tau = (\psi_j \,|\, H_0 \,|\, \psi_j) \quad (3)$$

$$\text{mit:} \quad H_0 = -\frac{\hbar^2}{2m}\Delta + V(\boldsymbol{r}); \; V(\boldsymbol{r} + \boldsymbol{r}_{hkl}) = V(\boldsymbol{r})$$

E_j ist somit eine Funktion des Wellenvektors $\boldsymbol{k}$, stellt also ein Energieband dar. Eine Gleichung für die Eigenvektoren ζ_j ergibt sich aus der Forderung eines Minimums für die Energie E_j. Die Variation von E_j nach $C_{j\nu}$ führt auf die Eigenwertgleichung:

$$H\zeta_j = E_j\zeta_j \quad (4)$$

$$H_{\mu\nu} = \tfrac{1}{2}\sum_\lambda e^{2\pi i \boldsymbol{k}\cdot(\boldsymbol{r}_\lambda - \boldsymbol{r}_l)}[(\phi_\mu^{\,l}|H_0|\phi_\nu^{\,\lambda}) + (\phi_\nu^{\,\lambda}|H_0|\phi_\mu^{\,l})^*]$$

In der angeschriebenen Form der Matrixelemente $H_{\mu\nu}$ wird die durch den in H_0 auftretenden Differentialoperator Δ bewirkte Unsymmetrie vermieden. Dabei sind die $(\phi_\mu^{\,l}\,|\,H_0\,|\,\phi_\nu^{\,\lambda})$ dreidimensionale Überlappungsintegrale.

Bei Ga und in anderenFällen kann man ein kompliziertes Gitter durch kleine Verschiebungen seiner Atome in ein einfacheres idealisiertes Gitter überführen, dessen kleinste Zelle nur halb so gross ist wie die des realen Gitters. Der Berechnung der Energiebänder können wir zunächst das idealisierte Gitter zugrunde legen. Der Einfluss der Atomverrückungen lässt sich mit Hilfe eines weiteren Näherungsverfahrens berücksichtigen. Das gesamte Eigenwertproblem $(2n)$-ter Ordnung zerfällt dabei in zwei Eigenwertgleichungen der Ordnung n. Sie lauten, wenn wir die beiden durch die Idealisierung aus der realen Zelle entstehenden Zellen mit den Indizes $k = 1$ und $k = 2$ bezeichnen:

$$\begin{aligned}(H^{11} + H^{12})\zeta_j^{(1)} &= E_j^{(1)}\zeta_j^{(1)} \\ (H^{11} - H^{12})\zeta_j^{(2)} &= E_j^{(2)}\zeta_j^{(2)}\end{aligned} \quad (5)$$

darin ist:

$$H_{\mu\nu}^{\,1k} = \tfrac{1}{2}\sum_{l_k} e^{2\pi i \boldsymbol{k}\cdot(\boldsymbol{r}_{l_k} - \boldsymbol{r}_{\lambda_1})}[(\phi_\mu^{\,\lambda_1}\,|\,H_0\,|\,\phi_\nu^{\,l_k}) + (\phi_\nu^{\,l_k}|\,H_0\,|\,\phi_\mu^{\,\lambda_1})^*]$$

Durch die zweite Gleichung (5) wird gerade die durch das richtige Ga-Gitter geforderte Symmetrie der Energie E_j im $\boldsymbol{k}$-Raum gewährleistet. Die durch den Übergang zum realen Gitter bewirkte Störung der Energie setzt an den Eigenwerten $E_j^{(1)}$ und $E_j^{(2)}$ an. Sie bewirkt eine mit der Verrückung proportionale und daher kleine Verschiebung der Bänder, jedoch keine Aufspaltung derselben.* Im folgenden wird daher nur das idealisierte Gitter des Galliums betrachtet. Bei $MoSi_2$ und WSi_2 verwenden wir das richtige Gitter. Es sei noch bemerkt, dass die Gleichungen (5) auch in einer Mehrelektronentheorie des Kristalls[3] gültig sind, nur treten dort an Stelle eines Satzes von Atomeigenfunktionen, Slaterdeterminanten der verschiedenen Elektronenkonfigurationen, deren Gesamtschwerpunkt in der Umgebung des betreffenden Atomrumpfs liegt.

* Dies soll in einer späteren Mitteilung von H. Schenk im einzelnen gezeigt werden (vergl. (9)).

Die Gewinnung einer Einelektronengittereigenfunktion ψ_j und ihrer Energie soll in drei Schritten erfolgen. Erstens das Aufsuchen der günstigsten Atomfunktionen, auf die dann das Löwdinsche Orthogonalisierungsverfahren angewandt werden kann; zweitens das Aufstellen und Lösen der entsprechenden Eigenwertgleichung, und schliesslich die Diskussion der Ergebnisse.

2. DIE ATOMFUNKTIONEN IN Ga UND $MoSi_2$

Die richtigen Atomfunktionen sind diejenigen, die die Punktsymmetrie des Atoms im Gitter besitzen, und soweit dies möglich ist, zu verschiedenen irreduziblen Darstellungen der Punktsymmetriegruppe gehören. Weiter sollen sie unter sich orthogonal und normiert sein. Um sie abzuleiten, können wir uns auf die von K. Ganzhorn[4] auf die Übergangsmetalle angewandte gruppentheoretische Methode stützen. Ist P ein Symmetrieoperator unserer Punktgruppe des Atoms, so soll für die Funktion $\phi_\mu{}'^l$ gelten:

$$P\phi_\mu{}'^l = e^{i\alpha P}\phi_\nu{}'^l \quad \nu = 1 \cdots n \tag{6}$$

Es lässt sich zeigen, dass dann die entsprechenden Löwdin'schen Funktionen $\phi_\mu{}^l$ derselben Gleichung genügen, also dieselben Transformationseigenschaften wie die $\phi_\mu{}'^l$ haben. Solange bei Rechnungen nur diese Eigenschaften benützt werden, gelten diese auch für die $\phi_\mu{}^l$, erst bei der numerischen Auswertung der Überlappungsintegrale müssen die $\phi_\mu{}^l$ explizit verwandt werden.

Gallium hat ein schwach rhombisches Gitter mit 4 Atomen in der kleinsten Zelle, doch lässt es sich durch kleine Verrückungen der Atome in ein einfacheres, dem $MoSi_2$ verwandtes Gitter überführen.[5] In Fig. 1 sind die wesentlichen Punktlagen dieses idealisierten Gitter angedeutet. Es ist ein Netzwerk aus Sechserringen in zwei aufeinander senkrecht stehenden Ebenen, und zwar hat jeder Ring der einen Ebene 2 Atome mit einem Ring der anderen gemeinsam. Die Sechsecke sind nicht ganz regulär, sondern die Atome A_1 und A_2 haben einen etwas kürzeren Abstand, sie deuten ein Molekül Ga_2 an. (Das richtige Gallium-Gitter entsteht durch eine kleine Drehung der Molekülachse in x-Richtung, dadurch wird die Zahl der nächsten Nachbarn von $1+4$ auf $1+6$ erhöht.) Im $MoSi_2$ nehmen die Si-Atome dieselben Punktlagen ein wie im idealisierten Ga-Gitter. Die Mo-Atome befinden sich in den Mittelpunkten der jetzt regulären Sechsecke. Jedes Mo-Atom hat 10 Si und 4 Mo-Atome als nächste Nachbarn. Beiden beschriebenen Gittern ist die vierzählige Drehachse (z-Achse) gemeinsam. Sie bestimmt weitgehend die Atomfunktionen.

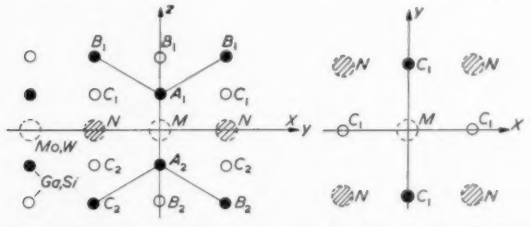

FIG. 1. Punktlagen der Ga-Atome im idealisierten Galliumgitter; sie stimmen mit denen der Si-Atome im $MoSi_2$- und WSi_2-Gitter überein.

Die Aussenelektronen von Gallium und Silizium besetzen mit guter Näherung s- und p-Zustände, in Molybdän und Wolfram dagegen nur s- und d-Zustände. Für Gallium lauten dann die richtigen Atomfunktionen*:

$$\begin{aligned}
\phi_1{}' &= \frac{1}{\sqrt{2}} R_{4p} P_1{}^1 e^{i\varphi} = \tfrac{1}{2}(\varphi_1{}' + i\varphi_2{}' - \varphi_3{}' - i\varphi_4{}') \\
\phi_2{}' &= \frac{1}{\sqrt{2}} R_{4p} P_1{}^1 e^{-i\varphi} = \tfrac{1}{2}(\varphi_1{}' - i\varphi_2{}' - \varphi_3{}' + i\varphi_4{}') \\
\phi_5{}' &= \frac{1}{\sqrt{2}} [R_{4,s}\, P_0{}^0 - R_{4p}\, P_1{}^0] \\
\phi_6{}' &= \frac{1}{\sqrt{2}} [R_{4,s} P_0{}^0 + R_{4p} P_1{}^0]
\end{aligned} \tag{7}$$

darin bedeuten die $\varphi_i{}'$:

$$\varphi_i{}' = \frac{1}{\sqrt{6}} \{\sqrt{2}\, R_{4,s}\, P_0{}^0 + R_{4,p}\, (\delta_{1i}\sqrt{3}\, P_1{}^{1c} + \delta_{2i}\sqrt{3}\, .\, P_1{}^{1s} + P_1{}^0)\} \quad i = 1, 2$$

$$\varphi_i{}' = \frac{1}{\sqrt{6}} \{\sqrt{2}\, R_{4,s}\, P_0{}^0 - R_{4,p}\, (\delta_{3i}\sqrt{3}\, P_1{}^{1c} + \delta_{4i}\sqrt{3}\, P_1{}^{1s} - P_1{}^0)\} \quad i = 3, 4.$$

Die $P_\mu{}^r$ sind die normierten Kugelflächenfunktionen, es gilt z.B. die Beziehung: $P_1{}^1 e^{i\varphi} = P_1{}^{1c} + {}_i P_1{}^{1s} \sim (x + iy)\, R_{4s}$ und R_{4p} sind die Radialanteile der s- und p-Funktionen. Die Funktionen $\phi_1{}'$ und $\phi_2{}'$ sind also in ihren Winkelanteilen Drehimpulseigenfunktionen des freien Atoms; sie beschreiben ein um die vierzählige Drehachse mit dem Impulsmoment $\pm\hbar$ umlaufendes Elektron. In einem um 45° gedrehten Koordinatensystem zeigen die Vorzugsrichtungen

* In U. Dehlinger: *Theoret. Metallkunde*, Berlin 1955, ist eine ausführliche Tabelle enthalten, die anhand der Darstellungstheorie der Gruppen das Aufsuchen der Funktionen ψ_i erleichtert. Diese sind hier nicht linear unabhängig. Man muss daher zu neuen Linearkombinationen mit komplexen Koeffizienten übergehen, die die Eigenschaften der $\psi_i{}'$ erhalten und linear unabhängig sind.

ihres Real und Imaginärteils zu den Nachbarn C. Doch zeigt die Darstellung in den φ_i', deren Maxima gerade zu den Nachbarn B_1 weisen, dass dieser Umlauf auch als ein Durchlaufen der Zustände $\varphi_i' i = 1 \cdots 4$ gedeutet werden kann. Es gilt nämlich für die Wahrscheinlichkeitsdichten die Beziehung:

$$(\phi_1' \,|\, \phi_1') = \tfrac{1}{4}\sum_i (\varphi_i' \,|\, \varphi_i') \tag{8}$$

Somit charakterisieren diese beiden Funktionen hauptsächlich eine gerichtete Bindung eines Atoms A zu seinen Nachbarn B und C. ϕ_5' hat seinen Maximalwert in Richtung zum nächsten Atom A_2, sie charakterisiert also die Molekülbindung, während ϕ_6' mit seiner Vorzugsrichtung auf die unbesetzte Mitte der Sechsecke weist, und an der A_1-A_2-Bindung kaum beteiligt ist. ϕ_3', ϕ_4' und ϕ_7', ϕ_8' sind dieselben Funktionen, nur gehören sie zum 2ten Atom in der Zelle.

Auch in $MoSi_2$ sind die bisher genannten Funktionen $\phi_1' \cdots \phi_8'$ massgebend; sie sind an den Si-Atomen lokalisiert. ϕ_1' und ϕ_2' können hier ausser in den φ_i auch in Funktionen $\bar{\varphi}_i\, i = 1 \cdots 4$ ausgedrückt werden, die Vorzugsrichtungen zu den nächsten Mo-Nachbarn haben. Für die an den Mo-Atomen lokalisierten Atomfunktionen ergibt sich:

$$\begin{aligned}
\phi_9' &= \frac{1}{\sqrt{2}} R_{n,d} P_2^{\,1} e^{i\varphi} = \tfrac{1}{2}(\varphi_5' + i\varphi_6' - \varphi_7' - i\varphi_8') \\
\phi_{10}' &= \phi_9'^{*} \\
\phi_{11}' &= \frac{1}{\sqrt{2}} (R_{n,0} P_0^{\,0} + R_{n,d} P_2^{\,0}) \\
\phi_{12}' &= \frac{1}{\sqrt{2}} (R_{n,0} P_0^{\,0} - R_{n,d} P_2^{\,0}) \\
\phi_{13}' &= R_{n,d} P_2^{\,2s} \\
\phi_{14}' &= R_{n,d} P_2^{\,2c}
\end{aligned} \tag{9}$$

darin bedeuten:

$$\varphi_\nu' = \frac{R_{n,d}}{2\sqrt{6}} \Big\{ (\sqrt{3} - \sqrt{2}) P_2^{\,0} + 2\sqrt{3} \cdot (\delta_{5\nu} P_2^{\,1c} + \delta_{6\nu} P_{21}^{\,s}) + (-1)^\nu (1 + \sqrt{6}) P_2^{\,2c} \Big\} \qquad \nu = 5, 6$$

$$\varphi_\mu' = \frac{R_{n,d}}{2\sqrt{6}} \Big\{ (\sqrt{3} - \sqrt{2}) P_2^{\,0} - 2\sqrt{3} \cdot (\delta_{7\mu} P_2^{\,1c} + \delta_{8\mu} P_2^{\,1s}) + (-1)^\mu (1 + \sqrt{6}) P_2^{\,2c} \Big\} \qquad \mu = 7, 8$$

Die $P_2^{\,m}$ sind die 5 normierten Kugelflächenfunktionen vom d-Typ. $R_{n,d}$ ist der entsprechende Radialanteil, und zwar ist für Mo $n = 5$, für W $n = 6$ zu nehmen.

Die Funktionen ϕ_9' und ϕ_{10}' haben ähnliche Vorzugsrichtungen wie ϕ_1' und ϕ_2'; die Maximalwerte der $\varphi_5'' \cdots \varphi_8'$ weisen auf die nächsten Si-Nachbarn C. ϕ_{11}' hat ausgeprägte Maxima in der $\pm z$-Richtung, charakterisiert also die gerichtete Bindung zu den beiden Si-Atomen (B) auf der z-Achse, während ϕ_{12}' und vor allem ϕ_{13}' mit seinen 4 Extremwerten zu den 4 nächsten Mo-Nachbarn dies für die Mo-Mo-Bindung tut. Schliesslich hat ϕ_{14}' Vorzugsrichtungen zu 4 der übernächsten Mo-Nachbarn.

Die Diskussion dieser Funktionen führt also zu dem Ergebnis, dass wir es sowohl in Gallium als auch in $MoSi_2$ und WSi_2 mit einer gerichteten Bindung der Atome untereinander zu tun haben.

3. BERECHNUNG DER ENERGIEBÄNDER DES GALLIUMS

Im folgenden sei der H-Operator (Gl. 4) und die Lösung des dazugehörigen Eigenwertproblems für Gallium unter Vernachlässigung einer Reihe kleinerer Überlappungsintegrale angegeben. Es können alle Überlappungsintegrale zwischen den die Molekülbindung beschreibenden Funktionen $\phi_5' \cdots \phi_8'$ und den Funktionen $\phi_1' \cdots \phi_4'$ vernachlässigt werden, da ihre Vorzugsrichtungen aufeinander senkrecht stehen. (Diese können später qualitätive berücksichtigt werden[9].) Der so vereinfachte H-Operator hat die Form:

$$H = \begin{pmatrix} \mathscr{B} & 0 \\ 0 & \mathscr{M} \end{pmatrix} \tag{10}$$

Die Matrix $\mathscr{M}$ beschreibt die Molekülbindung, $\mathscr{B}$ die Bindung des Moleküls an die anderen Nachbarn. Im einzelnen lauten die Matrixelemente:

$$\begin{aligned}
\mathscr{B}_{11} &= H_{11} = H_{\mu\mu} = (\phi_1^{A_1} \,|\, H_0 \,|\, \phi_1^{A_1}) \\
&\quad + 4(\phi_1^{A_1} \,|\, H_0 \,|\, \phi_1^{C_1})\gamma_1 + \cdots \quad \mu = 1, 2, 3, 4. \\
H_{12} &= H_{34} = -i(i\phi_1^{A_1} \,|\, H_0 \,|\, \phi_2^{C_1})\gamma_2 + \cdots
\end{aligned} \tag{11a}$$

$$\begin{aligned}
H_{13} &= H_{24} = (\phi_1^{A_1} \,|\, H_0 \,|\, \phi_3^{A_2}) + 4(\phi_1^{A_1} \,|\, H_0 \,|\, \phi_3^{B_1})\gamma_4 \\
&\quad + 4(\phi_1^{A_1} \,|\, H_0 \,|\, \phi_3^{C_1})\gamma_1 + \cdots \\
H_{14} &= H_{23} = 4(\phi_1^{A_1} \,|\, H_0 \,|\, \phi_4^{B_1})\gamma_3 \\
&\quad - 4i(i\phi_1^{A_1} \,|\, H_0 \,|\, \phi_4^{C_1})\gamma_2 + \cdots \\
\mathscr{M}_{11} &= H_{55} = H_{77} = (\phi_5^{A_1} \,|\, H_0 \,|\, \phi_5^{A_1}) \\
&\quad + 4(\phi_5^{A_1} \,|\, H_0 \,|\, \phi_5^{C_1})\gamma_1 + \cdots \\
H_{66} &= H_{88} = (\phi_6^{A_1} \,|\, H_0 \,|\, \phi_6^{A_1}) \\
&\quad + 4(\phi_6^{A_1} \,|\, H_0 \,|\, \phi_6^{C_1})\gamma_1 + \cdots
\end{aligned} \tag{11b}$$

$$H_{57} = (\phi_5^{A_1} \mid H_0 \mid \phi_7^{A_2}) + 4(\phi_5^{A_1} \mid H_0 \mid \phi_7^{C_2})\gamma_1 + \cdots$$

$$H_{56} = H_{78} = (\phi_5^{A_1} \mid H_0 \mid \phi_6^{A_1}) + 4(\phi_5^{A_1} \mid H_0 \mid \phi_6^{C_1})\gamma_1 + \cdots$$

$$H_{58} = H_{67} = (\phi_5^{A_1} \mid H_0 \mid \phi_8^{A_2}) + 4\,(\phi_5^{A_1} \mid H_0 \mid \phi_8^{B_1})\gamma_4 + \cdots$$

$$H_{68} = 4\,(\phi_6^{A_1} \mid H_0 \mid \phi_8^{B_1})\gamma_4 + (\phi_6^{A_1} \mid H_0 \mid \phi_8^{A_2}) + \cdots$$

darin debeuten: $\gamma_1 = \cos \pi \boldsymbol{k}_x \cdot \cos \pi \boldsymbol{k}_y$

$$\gamma_2 = \sin \pi \boldsymbol{k}_x \cdot \sin \pi \boldsymbol{k}_y$$

$$\gamma_3 = \sin \tfrac{1}{2}\pi(\boldsymbol{k}_x + \boldsymbol{k}_y) \cdot \sin \tfrac{1}{2}\pi(\boldsymbol{k}_x - \boldsymbol{k}_y) e^{i\pi \boldsymbol{k}_z}$$

$$\gamma_4 = \cos \tfrac{1}{2}\pi(\boldsymbol{k}_x + \boldsymbol{k}_y) \cdot \cos \tfrac{1}{2}\pi(\boldsymbol{k}_x - \boldsymbol{k}_y) e^{i\pi \boldsymbol{k}_z}$$

In den Überlappungsintegralen kennzeichnen die Indizes $A_i \cdots C_i$ die Lage des Atoms, zu der die betreffende Funktion gehört (Fig. 1). Die Lösung des zugehörigen Eigenwertproblems für $\mathscr{B}$ und $\mathscr{M}$ führt auf folgende Gleichungen für die Energie $E_B = E_j j = 1 \cdots 4$ und $E_M = E_j j = 5 \cdots 8$.

$$E_B = H_{11} + \lambda \sqrt{|H_{12}|^2 + |H_{13}|^2 + |H_{14}|^2} + \varepsilon \sqrt{4\,|H_{12}|^2 \cdot |H_{14}|^2 + (H_{13} \cdot H_{14}^* + H_{13}^* H_{14})^2}$$

$$\lambda = \pm 1 \qquad \varepsilon = \pm 1.$$

$$E_M = \tfrac{1}{2}\{(H_{55} + \varepsilon H_{57})(1 + \varepsilon\lambda) + (H_{66} + \varepsilon H_{68})(1 - \varepsilon\lambda)\} + \frac{\lambda}{2}[H_{56} + \varepsilon H_{58}]\,\rho \cdot R(\rho)$$

mit: $$\rho = 2\,\frac{H_{56} + \varepsilon H_{58}}{[H_{57} - H_{68} + \varepsilon(H_{55} - H_{66})} \qquad (12)$$

$$R(\rho) = 2 \cdot \sum_{n=1}^{\infty} \binom{\frac{1}{2}}{n} \rho^{2(n-1)}, \qquad \varepsilon = \pm 1,\ \lambda = \pm 1.$$

Diese beiden Gleichungen bestimmen je 4 Energiebänder E_B und E_M (Fig. 2), deren Ränder an den Stellen : $\sin \pi \boldsymbol{k}_i = 0$ $i = x, y, z$ liegen.* Ihre Lage lässt sich bei E_B gut übersehen, wenn wir in Gl. (12) $\gamma_2 = 0$ setzen. Es zeigt sich dann, dass zwischen ihnen keine Lücke auftritt und die Breite b dieser 4 Bänder im wesentlichen durch den Ausdruck:

$$b = 4(\phi_1^{A_1} \mid H_0 \mid \phi_1^{C_1}) + 4(\phi_1^{A_1} \mid H_0 \mid \phi_3^{B_1}) \qquad (13)$$

gegeben ist. Wir haben es also mit breiten Energiebändern zu tun. Anders liegen die Dinge bei den

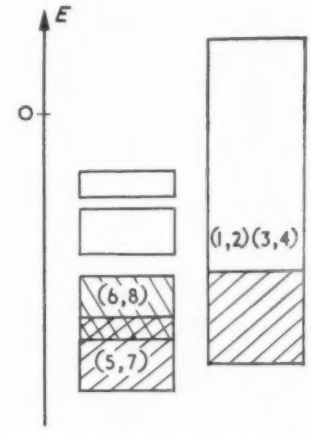

FIG. 2. Bänderschema für das idealisierte Gallium; als Energienullpunkt ist das Atomniveau gewählt.

$4E_M$-Bändern. Ihre Lage wird im wesentlichen durch das Integral $(\phi_5^{A_1} \mid H_0 \mid \phi_7^{A_2})$ in H_{57} bestimmt, alle anderen Integrale sind kleiner als dieses und führen zu verhältnismässig schmalen Bändern, wie sie im Bänderschema der Fig. 2 angedeutet sind. Beim Übergang zum richtigen Galliumgitter werden sie noch verbreitert. Jedes Band in Fig. 2 ist durch die Indizes der Atomfunktionen gekennzeichnet, die mit etwa gleichen Koeffizienten in die Blochfunktion des Bandes eingehen. Alle anderen Funktionen sind ihr nur entsprechend der Wechselwirkung mit den anderen Bändern mit kleineren Koeffizienten beigemischt. Als Beispiel sei je eine Blochfunktion zu einem Band E_B und E_M angeführt:

$$\Psi_{E_B} = \sum_l e^{2\pi i \boldsymbol{k}\cdot\boldsymbol{r}_l}\{[\phi_1^{\,l} + \phi_2^{\,l} + e^{-i\alpha}(\phi_3^{\,l} + \phi_4^{\,l})] + \sum_{v=5}^{8} c_v \phi_v^{\,l}\} \qquad (14a)$$

darin ist α die Phase von $(H_{13} + \varepsilon H_{14})$; ausserdem ist $\gamma_2 = 0$ zu setzen.

Die c_v $v = 5 \cdots 8$ sind der hier vernachlässigten Überlappung mit den $\phi_5 \cdots \phi_8$ proportional und sicher viel kleiner als eins. Entsprechendes gilt bei Ψ_{E_M}, nur mit $v = 1 \cdots 4$:

$$\Psi_{E_M} = \sum_l e^{2\pi i \boldsymbol{k}\cdot\boldsymbol{r}_l}\{[a(\varepsilon)(\phi_5^{\,l} + \varepsilon\phi_7^{\,l}) + b(\varepsilon, \lambda)(\phi_6^{\,l} + \varepsilon\phi_8^{\,l})] + \sum_{v=1}^{4} c_v \phi_v^{\,l}\}$$

darin ist:

$$a(\varepsilon) = -(H_{56} + \varepsilon H_{58})$$

$$b(\varepsilon, \lambda) = \tfrac{1}{2}[H_{55} - H_{66} + \varepsilon(H_{57} - H_{68})][1 - \varepsilon\lambda] + \frac{\lambda}{2}\,a(\varepsilon) \cdot \rho \cdot R(\rho)$$

$$\varepsilon = \pm 1. \qquad \lambda = \pm 1.$$

* Dies gilt im idealisierten Ga-Gitter ganz allgemein bei beliebigem periodischem Potential $V(\boldsymbol{r})$. Beim Übergang zum realen Ga-Gitter verschieben sich diese Bandränder etwas und zwar mindestens quadratisch mit dem Drehwinkel der Molekülachse. Wegen des Beweises sei auf eine weitere Mitteilung von H. Schenk verwiesen.[9]

VOL. 4 1956

Diese Funktion gehört für $\varepsilon = \lambda = 1$ zu dem am tiefsten gelegenen schmalen Energieband, dem entspricht, dass die beiden sich am stärksten überlappenden Funktionen ϕ_5 und ϕ_7 ihren Hauptbestandteil bilden. Analoges gilt für alle anderen Bänder.

4. DIE BÄNDER VON $MoSi_2$ UND WSi_2

Besteht ein Gitter aus 2 Atomarten, so müssen wir zunächst 2 Extremfälle unterscheiden. Einmal können die Aussenelektronenterme einer Atomart A viel höher liegen als die der zweiten B; dann kann ein Elektron von B wegen des Pauliverbots nicht ohne grössere Energiezufuhr in Zustände von A übergehen. Die Atome A wirken nur mit ihrem Potential auf Elektronen von B. Entsprechend gehören zur Atomart A eigene höher gelegene Bänder, auf deren Form die Atome B nur mit ihrem Potential Einfluss haben. Als Folge dieser Bandverteilung ergibt sich eine stark ausgeprägte heteropolare Komponente der Bindung. Die dabei auftretende Coulombenergie senkt das gesamte Bandsystem.*

Im zweiten Fall haben die Aussenelektronen von A und B etwa gleiche Energie, so daß auf sie unser übliches Verfahren angewendet werden kann. Im $MoSi_2$ haben wir im wesentlichen den zweiten Fall verwirklicht. Sein $\mathscr{H}$-Operator ist also wie folgt anzusetzen:

$$\mathscr{H} = \begin{pmatrix} H^g W \\ W^\dagger H^M \end{pmatrix} \tag{15}$$

Darin bedeutet H^g den schon angegebenen H-Operator des idealisierten Galliumgitters. H^M ist der H-Operator des Molybdänteilgitters, in ihn gehen die Si-Atome nur mit ihrem Potential ein. Die Matrix W berücksichtigt die Möglichkeit, dass ein Elektron von Si zu Mo übergehen kann, also die Wechselwirkung der Bänder von H^g und H^M. Hier soll nur H^M angegebenen werden, während der Einfluss von W nur grob abgeschätzt werden soll. Die Matrixelemente von H^M lauten:

$$\begin{aligned} H_{11}{}^M = \mathscr{H}_{99} = \mathscr{H}_{10,10} &= (\phi_9{}^M \mid H_0 \mid \phi_9{}^M) \\ &\quad + 4(\phi_9{}^M \mid H_0 \mid \phi_9{}^N)\gamma_1 + \cdots \\ \mathscr{H}_{\mu\mu} &= (\phi_\mu{}^M \mid H_0 \mid \phi_\mu{}^M) + 4(\phi_\mu{}^M \mid H_0 \mid \phi_\mu{}^N)\gamma_1 \\ &\quad + \cdots \mu = 11, 12, 13, 14. \\ \mathscr{H}_{9,10} &= 4i(-i\phi_9{}^M \mid H_0 \mid \phi_{10}{}^N)\gamma_2 + \cdots \\ \mathscr{H}_{13,\mu} &= 4(\phi_{13}{}^M \mid H_0 \mid \phi_\mu{}^N)\gamma_2 \\ &\quad + \cdots \mu = 11, 12. \\ \mathscr{H}_{12,11} &= (\phi_{12}{}^M \mid H_0 \mid \phi_{11}{}^M) \\ &\quad + 4(\phi_{12}{}^M \mid H_0 \mid \phi_{11}{}^N)\gamma_1 + \cdots \end{aligned} \tag{16}$$

Alle weiteren Elemente von H^M enthalten nur Überlappungsintegrale mit übernächsten und noch weiter entfernten Mo-Atomen, sie sollen hier vernachlässigt werden. Die Eigenwerte von H^M lassen sich mit diesen Vereinfachungen leicht angeben. Es ist:

$$\begin{aligned} E_{9,10}{}^M &= \mathscr{H}_{99} \pm i\mathscr{H}_{9,10} \\ E_{14}{}^M &= H_{14,14} \end{aligned} \tag{17a}$$

Für die anderen 3 Eigenwerte gilt die Gleichung 3ten Grades:

$$\begin{aligned} &(\mathscr{H}_{11,11} - E^M)(\mathscr{H}_{12,12} - E^M)(\mathscr{H}_{13,13} - E^M) \\ &- (\mathscr{H}_{11,11} - E^M) \cdot \mathscr{H}^2_{12,13} + (\mathscr{H}_{12,12} - E^M)\mathscr{H}^2_{11,13} \\ &+ (\mathscr{H}_{13,13} - E^M)\,\mathscr{H}^2_{11,12} \\ &+ 2\mathscr{H}_{11,12} \cdot \mathscr{H}_{11,13} \cdot \mathscr{H}_{12,13} = 0 \end{aligned} \tag{17b}$$

Daraus folgen 3 Energiebänder, von denen $E_{13}{}^M$ der grössten Wechselwirkung mit den 4 nächsten Mo-Nachbarn entspricht und daher am tiefsten liegt. Nur wenig nach höheren Energien hin verschoben schliesst sich $E_{12}{}^M$ an. $E_{11}{}^M$ und $E_{14}{}^M$ sind hier die Bänder höchster Energie (Fig. 3).

Die Wechselwirkung der Si- und Mo-Atome, die in der Matrix W ihren Ausdruck findet, bewirkt nun eine starke von $\boldsymbol{k}$ abhängige Vermischung der dem Si- und Mo-Teilgitter zugeordneten Bandeigenfunktionen, was natürlich auch die Energieflächen im E-$\boldsymbol{k}$-Raum verändert. In Fig. 3 sind alle Bänder der Aussenelektronen für $MoSi_2$ angeführt, und zwar im Teil a die

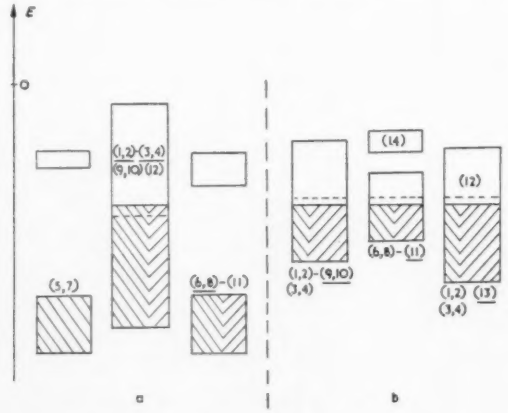

FIG. 3. Bänderschema für $MoSi_2$ und WSi_2.

* Vergl. die Zintl'sche Gruppe der Legierungen mit stark unedlen Metallen.

vom Si_2- im Teil b die vom Mo-Teilgitter. Die Mo-Si-Wechselwirkung ist in der weitgehenden Annäherung der Schwerpunkte beider Bandtypen und in der Verbreiterung der an sich schmalen d-Bänder des Mo-Teilgitters berücksichtigt. Jedes Band ist in Fig. 3 durch die Indizes der jeweils gleichwertigen Atomfunktionen gekennzeichnet, aus denen es entspringt. In Bändern, in denen eine starke Mischung der zu Si und Mo gehörigen Funktionen eintritt, ist dies durch entsprechende Schraffierung angedeutet. Dies ist vor allem bei den Bändern (6, 8)–(11), die der Wechselwirkung eines Mo-Atoms mit den beiden Si-Nachbarn auf der z-Achse (Fig. 1) entsprechen, und zwischen den Bändern (1, 2)–(9, 10)–(12), die die Wechselwirkung aller übrigen Si-Nachbarn mit dem Mo-Atom enthalten der Fall. Gegenüber Gallium ist hier das Band (6, 8)—(11) stark verbreitert und energetisch tiefer gelegen, so daß es sich mit dem Band (5, 7) überdeckt.

5. DISKUSSION DER ERGEBNISSE

Im Galliumgitter stehen 6 Elektronen je kleinster Zelle zur Besetzung der Bänder zur Verfügung, die an sich für 16 Elektronen pro Zelle Platz bieten. Die Bänder sind daher in der in Fig. 2 angegebenen Weise besetzt. Vier der sechs Elektronen besetzen die beiden schmalen Bänder (5, 7) und (6, 8) und nur zwei Elektronen die breiten die Gitterbindung bewirkenden Bänder. Für die Bindung an sechs der nächsten Nachbarn steht also pro Atom fast nur ein Elektron zur Verfügung. Die Bindung zwischen den Atomen des "Moleküls" A_1–A_2 kann näherungsweise durch ein Elekronenpaar mit abgesättigten Spins dargestellt werden. Ein drittes Elektron je Atom besetzt das Band (6, 8), dessen Atomfunktion nahezu ins Leere sticht; infolgedessen ist die Bindungsfestigkeit des Ga gering, was seinen Ausdruck im anomal niederen Schmelzpunkt findet. Damit sind die Bindungsverhältnisse des Ga erklärt.

Weiter erklärt sich aus den fast leeren breiten Bändern die elektrische Leitfähigkeit des Ga. Nach Messungen von Powell [6,7] ist diese stark anisotrop. In x-Richtung ist der Widerstand am größten ($54{,}3 \cdot 10^{-6}$ Ω cm), in y- und z-Richtung beträgt er dagegen nur 17,4 und $8{,}1 \cdot 10^{-6}$ Ω cm. Über diese Anisotropie kann bei Zugrundelegung des idealisierten Gitters keine Aussage gemacht werden, da dabei x- und y-Richtung gleichwertig behandelt werden. Erst beim Übergang zum richtigen Gitter ist dies nicht mehr der Fall. Die Gleichungen (12) stellen die Energieflächen $E(\boldsymbol{k})$ dar und ermöglichen damit die Angabe des Tensors der effektiven Masse m^*. Wie an anderer Stelle gezeigt werden soll, ist dieser stark anisotrop.[9] Der numerische Wert der elektrischen Leitfähigkeit ist jedoch wesentlich durch die Gitterschwingungen bedingt. Wenn durch die beim Übergang zum richtigen Galliumgitter erfolgende Drehung der Molekülachsen in x-Richtung das Potential in y-Richtung erhöht wird, haben die Gitterschwingungen in x-Richtung ihre grösste Amplitude, was dem hohen Widerstand entspricht. In z-Richtung dagegen ist ihre Amplitude am kleinsten wegen der starken Bindung der Atome A_1–A_2. Der starke Einfluss eines Magnetfeldes auf den elektrischen Widerstand ist eine Folge der stark anisotropen Masse m^*.[8] Gallium ist diamagnetisch, wie überhaupt die dritte Reihe des periodischen Systems ausser Aluminium. Dies erklärt sich durch die voll besetzten Bänder (5, 7) und (6, 8), die einen Beitrag zum Diamagnetismus geben, während der Paramagnetismus der Elektronen an der Besetzungsgrenze wegen des breiten Bandes (1, 2) klein ist. Aus der Lage der Besetzungsgrenze folgt für Gallium ein normaler Halleffekt.

Bei $MoSi_2$ sind die in Fig. 3 angegebenen Bänder mit 14 Elektronen je kleinste Elementarzelle zu besetzen. Acht stammen von den beiden Si-Atomen, sie füllen gerade die Bänder (5, 7) und (6, 8) ganz, (1, 2) dagegen gerade halb. Die Mo zuzuordnenden Bänder würden mit den 6 Aussenelektronen des Molybdäns bis zu der in Fig. 3b gestrichelten Linie zu füllen sein, die, wie wir sehen, über der Mitte des (1, 2) Bandes liegt. Es werden also Elektronen von den Mo-Bändern in die Si-Bänder überfliessen und es wird sich die stark gezeichnete Besetzungsgrenze einstellen. Dies hat das Auftreten einer heteropolaren Komponente bei der Bindung zur Folge. Sie ist hier nicht allzu stark, doch sehen wir, dass bei einer genaueren Rechnung Ionenzustände keineswegs zu vernachlässigen sind. Diese sind vom Einfluss auf die Fermienergie abgesehen, auch energetisch recht günstig. Unser Energieschema zeigt, dass Elektronen von den Mo-Bändern in Zustände der Bänder (1, 2) und (6, 8) überfliessen; die dazugehörigen Atomeigenfunktionen haben gerade ausgeprägte Maxima in Richtung eines Mo-Atoms. Die positive Ladung des Mo-Ions wird demnach durch die Elektronenzustände der Bänder (1, 2) und (6, 8) weitgehend in der nächsten Umgebung des Ions abgeschirmt. Die Polarisation der Atomrümpfe wird daher gering sein.

Nach dem Bandschema (Fig. 3) sind $MoSi_2$ und WSi_2 elektrische Leiter, was mit der Erfahrung übereinstimmt. Weiter sehen wir, dass alle besetzten Bänder einer gerichteten Bindung eines Atoms an seine nächsten Nachbarn entsprechen und dass diese entweder voll oder halb besetzt sind. Dies bedeutet

VOL. 4 1956

im Gegensatz zum Gallium einen stark homöopolaren Charakter der Bindung der Si- und Mo-Atome untereinander, sowie auch zwischen Si und Mo. So erklärt sich die grosse Härte dieser Stoffe. Es ist auch hier zu erwarten, dass $MoSi_2$ und WSi_2 diamagnetisch ist. Die Lage der Besetzungsgrenze in den oberen Bandhälften deutet auf einen anomalen Halleffekt hin.

LITERATUR

1. F. Bloch, *Z. Phys.*, **52,** 555 (1929).
2. P. O. Löwdin, *J. chem. Phys.*, **18,** 365 (1950).
3. H. Volz und H. Haken, *Z. phys. Chemie*, **198,** 61 (1951).
4. F. Bader, K. Ganzhorn, und U. Dehlinger, *Z. f. Phys.* **137,** 190 (1954).
5. C. Hermann, *Strukturbericht*, **2,** 2 (1928–1932).
6. R. W. Powell, *Nature*, **164,** 153 (1949).
7. W. Boas und J. K. Mackenzil, *Prog. in Metal Phys.*, **2,** 106, (1950).
8. A. Sommerfeld und H. Bethe, *Handb. d. Phys.*, **24/2,** 566 (1933).
9. H. Schenk, *Stüttgarter Dissertation*, 1955.

VOL
4
195

THERMODYNAMICS OF LIQUID Ag-Au AND Au-Cu ALLOYS AND THE QUESTION OF STRAIN ENERGY IN SOLID SOLUTIONS*

R. A. ORIANI †

The experimental details and the results of a galvanic cell investigation of the thermodynamics of liquid gold-copper and solid and liquid silver-gold solutions are described. The heats of solution are compared with the predictions of several theories. The concept of strain energy in a solid solution is discussed, and the suggestion of Lumsden and of Wagner that $\Delta(\Delta H)$ is a measure of misfit energy is supported by the present results and by arguments from the calculations of H. Jones. Elasticity-theory calculations are discussed, and misfit energy in a solid solution is defined as the energy change caused by the imposition of a lattice on a liquid solution; only the portion of the misfit energy arising beyond a certain radius about a solute atom is properly termed strain energy.

THERMODYNAMIQUE DES ALLIAGES LIQUIDES Ag-Au ET Au-Cu ET LA QUESTION D'ÉNERGIE DE DISTORSION DANS LES SOLUTIONS SOLIDES

Particularités expérimentales et résultats des mesures des caractéristiques thermodynamiques pour les solutions liquides or-cuivre et les solutions argent-or liquides et solides. Les chaleurs de dissolution sont comparées aux prévisions de diverses théories. La notion d'énergie de distorsion dans les solutions solides est discutée et l'idée de Lumsden et de Wagner que $\Delta(\Delta H)$ est une mesure de l'énergie de disconvenance est confirmée par ces résultats et par les calculs de H. Jones. Les résultats de la théorie de l'élasticité sont discutés et l'énergie de disconvenance dans une solution solide est définie comme le changement d'énergie provoqué par l'introduction d'un réseau dans une solution liquide; seulement la partie de l'énergie de disconvenance provenant du réseau hors d'un certain rayon autour d'une atome du soluté peut s'appeler proprement l'énergie de distorsion.

ÜBER DIE THERMODYNAMIK VON FLÜSSIGEN Ag-Au UND Au-Cu LEGIERUNGEN UND DIE FRAGE NACH DER SPANNUNGSENERGIE IN MISCHKRISTALLEN

Die experimentellen Einzelheiten und Ergebnisse einer Untersuchung zur Thermodynamik von flüssigen Gold-Kupfer- und flüssigen und festen Silber-Gold-Legierungen mit Hilfe einer galvanometrischen Methode werden mitgeteilt. Die Werte der Lösungswärmen werden mit den Voraussagen verschiedener Theorien verglichen. Der Begriff der Verzerrungsenergie in einem Mischkristall wird diskutiert. Die Vermutung von Lumsden und von Wagner, dass $\Delta(\Delta H)$ ein Mass für die Einpassungsenergie ist, wird sowohl durch die vorliegenden Ergebnisse als auch durch Argumente aus den Berechnungen von H. Jones unterstützt. Elastizitätstheoretische Berechnungen werden diskutiert. Die Einpassungsenergie in einem Mischkristall wird als die Energie definiert, die man aufbringen muss, um der flüssigen Lösung eine Gitterstruktur aufzuzwängen; als Verzerrungsenergie sollte man nur den Teil der Einpassungsenergie bezeichnen, der aus dem Gebiet ausserhalb einer bestimmten Entfernung von einem Fremdatom stammt.

VOL. 4 1956

1. INTRODUCTION

Recent papers[1–4] on the thermodynamics of solid metallic solutions have invoked the existence of a strain-energy contribution to the enthalpy of mixing in order to rationalize the large positive numbers obtained for the latter quantity. The concept of strain energy in solid solutions, though much used in many contexts, has remained rather vague; underlying most treatments of the subject, however, are the ideas that strain energy is to be associated with the disparity of size of the atomic constituents of the solid solution, and that strain energy is of mechanical origin and somehow to be dissociated from every other factor occurring in the formation of a solid solution.

Attempts at quantitative estimate of strain energy have always involved classical elasticity theory, but the methods of application have been varied. Lawson,[5] Heumann,[6] and Machlin[7] consider the elastic energy stored in the lattice surrounding a solute atom which occupies a "hole" too large or too small for it. Averbach, Flinn, and Cohen[2] consider the hydrostatic compression or expansion of a solute atom from its size in the pure (one-component) lattice to its size in the solid-solution lattice. Pines,[8] Jaswon, Henry and Raynor,[9] Friedel,[10] and Varley[11] apply elasticity theory both to the surrounding lattice and to the solute atom much in the manner of the Mott-Nabarro[12] treatment of precipitate particles within a solid matrix. Furthermore, some of these treatments consider that the elasticity-theory calculation furnishes a number that represents a contribution to the internal energy of the system, whereas others (Machlin, Friedel) consider that elasticity theory leads to a contribution to the free energy of the system, so that differentiation with respect to temperature of the applicable elasticity theory expression yields an entropy contribution.

Part of the reason for this diversity of approach is that there exists no experimental measurement of the strain energy of a solid solution against which to compare the calculations. Recently, Lumsden[13] and Wagner[14] have suggested that a comparison of the

* Received May 24, 1955

† General Electric Research Laboratory, Schenectady, New York, U.S.A.

relevant experimental thermodynamic quantities of the liquid and the solid solutions may yield satisfactory measures of the strain-energy contribution to the properties of the solid solutions. The present paper is an experimental exploration of that idea, as well as an attempt to clarify the concept of strain energy.

2. EXPERIMENTAL DETAILS

Because data of adequate accuracy exist for the solid alloys, and because both solid components have the same lattice structure (see below), the systems Au—Cu and Ag—Au were chosen for study in the liquid state. The thermodynamic properties were determined by the galvanic-cell technique. Cells of the type illustrated in Fig. 1 were constructed and charged with chips of copper, silver, or gold, each of at least 99.99 per cent purity. Connection was made to the liquid alloys by 0.010-in tungsten wires enclosed by thin-walled silica tubules. The electrochemical

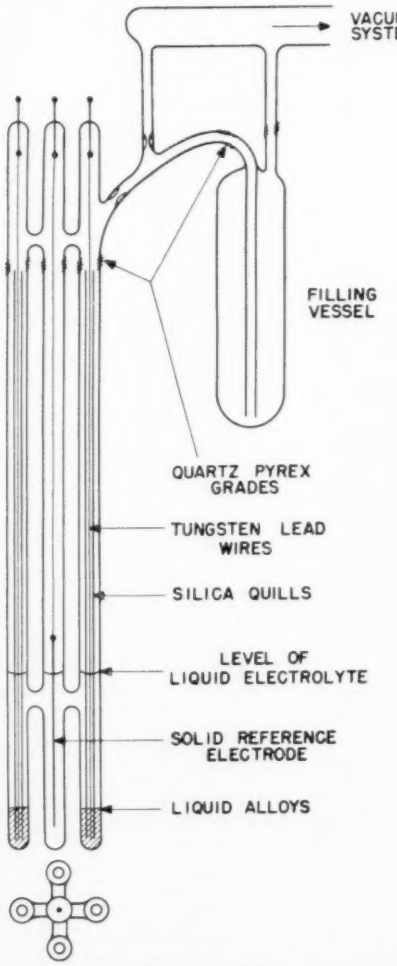

FIG. 1. Schematic diagram of the galvanic cell for liquid alloys and solid reference electrode.

cells established were $Cu_{(S)} \mid Cu^+, KCl, LiCl \mid Cu(Au)_{(L)}$, and $Ag_{(L)} \mid Ag^+, KCl, LiCl \mid Ag(Au)_{(L)}$; in the latter case the e.m.f. between solid pure Ag and solid alloys was also studied. The cell e.m.f. was measured by a Leeds-Northrup K-2 potentiometer; the thermal e.m.f. generated by the alloys and the lead wires was measured by separate experiments and found to be negligible. The temperature of the cell was measured by a calibrated Pt/Pt (10 per cent Rh) thermocouple maintained in contact with the outer surface of the cell.

The electrolyte, an equimolar mixture of KCl and LiCl plus a small amount of either AgCl or CuCl, was prepared in a separate container by holding at 500°C, in contact with pure silver or copper wire, for at least three days under a vacuum of about 1 μ Hg. Meanwhile, the cell itself was prepared by holding it under the same vacuum at a temperature above the melting temperatures of the alloys. After this treatment the seal-off in the vertical tube was sealed shut and the liquid electrolyte was forced into the cell by pressure of pure helium. The cell was subsequently sealed off from the vacuum system under about half an atmosphere of helium.

Once the cell was in readiness, the measurements over the accessible temperature range were carried out in only one day, since working in the liquid state makes it unnecessary to wait long periods for equilibrium. However, the measurements on the solid Ag-Au alloys were done at much longer waiting times. The alloys were chemically analyzed after the e.m.f. runs; the silver-gold alloys were analyzed for the gold content by a procedure developed and carried out by W. K. Murphy of this laboratory.

3. EXPERIMENTAL RESULTS

The e.m.f.-temperature curves obtained for solid copper against liquid gold-copper alloys are shown in Fig. 2. The deviations from linearity correspond to entrance into the two-phase region between the liquidus and the solidus lines. The departures from linearity occur in opposite directions for the two alloys because the compositions lie on opposite sides of the melting-point minimum. Fig. 3 presents similar information for liquid silver against liquid silver-gold alloys. The points of departure from linearity agree well with the temperature along the liquidus line. It is considered unnecessary to present the e.m.f.-temperature data for solid silver against solid silver-gold alloys, since the present results confirm literature values; only the derived values for the solid Ag-Au alloys will be presented.

The activity of copper in the liquid Au-Cu alloys was

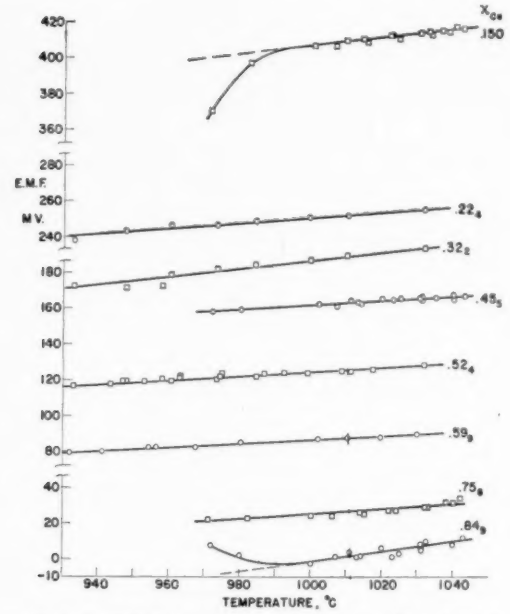

FIG. 2. E.M.F.-temperature relation for liquid Au-Cu alloys against pure solid copper.

calculated from the e.m.f. data at 985°C, and was reduced to refer to pure liquid copper as the reference state by the assumption that the entropy of melting of pure copper is independent of temperature. Fig. 4 shows the activities of copper and of gold, the latter calculated by a graphical integration of the Gibbs-Duhem equation, and both referred to the pure liquid alloys. This figure also shows the activity of copper in its liquid alloys calculated from extrapolation of the activity data for the solid state,[4] and from knowledge of the liquidus and solidus points of the phase diagram.

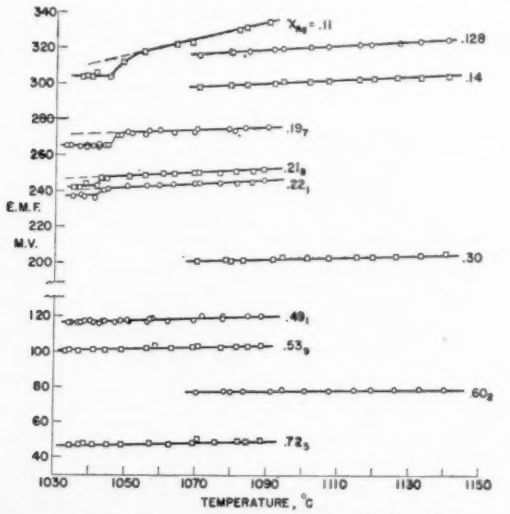

FIG. 3. E.M.F.-temperature relation for liquid Ag-Au against pure liquid silver.

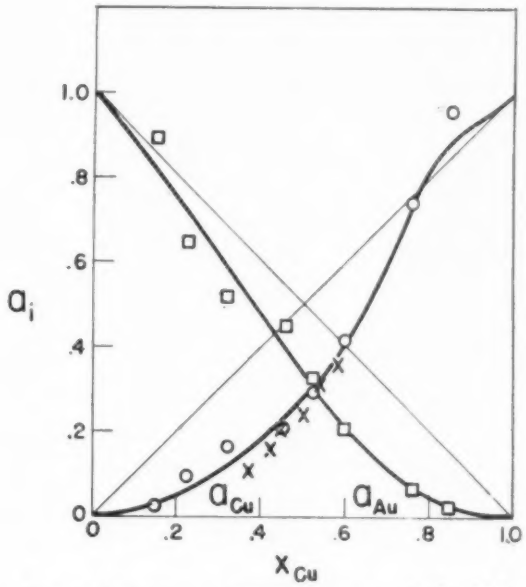

FIG. 4. Activities at 985°C of copper and of gold in their liquid alloys, relative to the pure liquids. The crosses are the values of a_{Cu} calculated from solid-state data and the phase diagram, $884° \leqslant T \leqslant 900°C$.

The agreement is gratifying in view of the large extrapolation involved.

The activity of silver, calculated from the e.m.f. data at 1071°C, and that of gold, calculated by a graphical integration of the Gibbs-Duhem equation, are given by Fig. 5. Each activity has as reference state the corresponding pure liquid component. The values obtained by Wagner and Engelhardt[15] at

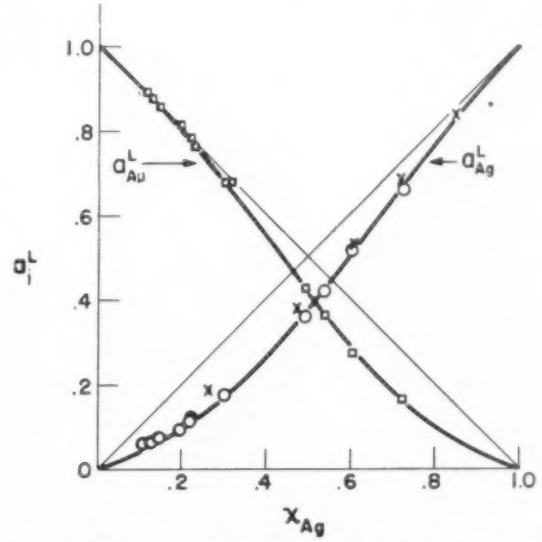

FIG. 5. Activities of silver and of gold in their liquid alloys, relative to the pure liquids.
○, □ Present data, 1071°C.
X 1085°C, ref. 15.

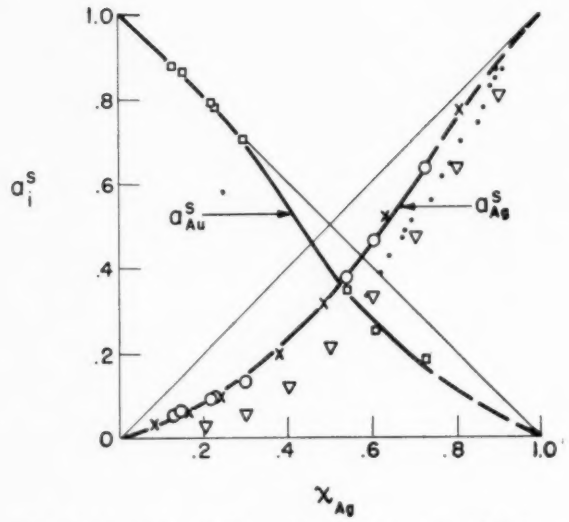

FIG. 6. Activities of silver and of gold in their solid alloys, relative to the pure solids.
○ □ Present data, 850°C.
X 745°C, ref. 15.
• 550°C, W. Bode, calculated by N. G. Schmahl, *Z. anorg. allg. Chem.*, **266,** 1 (1951).
▽ 200°C, A. Wachter, *J. Amer. Chem. Soc.*, **54,** 4609 (1932).

1085°C are also indicated. Fig. 6 presents similar data for the solid alloys of silver and gold, as well as various sets of values from the literature for the activity of silver.

The resulting integral Gibbs free energy and enthalpy of mixing are shown in Fig. 7 for liquid Au-Cu alloys, in Fig. 8 for liquid Ag-Au alloys, and in Fig. 9 for solid Ag-Au alloys. The enthalpy of mixing was calculated from the experimental e.m.f. values and their temperature derivatives, and then by graphical integration of the Gibbs-Duhem equation for the second component. Table 1 presents a résumé of the present

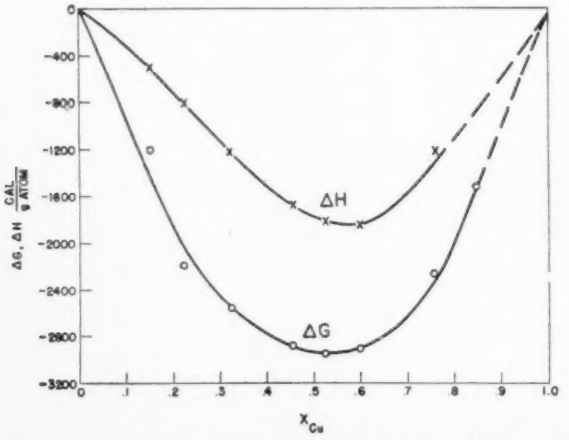

FIG. 7. The Gibbs free energy, ΔG, and the enthalpy, ΔH, of mixing of liquid Au-Cu alloys, 985°C.

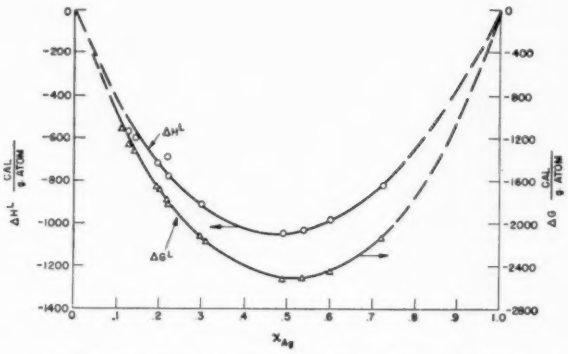

FIG. 8. The Gibbs free energy, ΔG, and the enthalpy, ΔH, of mixing of liquid Ag-Au alloys, 1071°C.

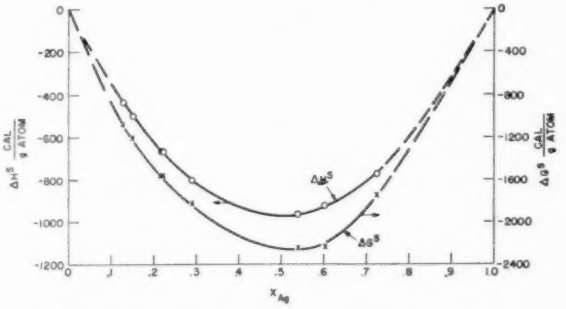

FIG. 9. The Gibbs free energy, ΔG, and the enthalpy, ΔH, of mixing of solid Ag-Au alloys, 850°C.

experimental results for a mole fraction of one-half together with quotations from all the relevant literature sources. The entropy of mixing, ΔS, was calculated from the relation $\Delta G = \Delta H - T\Delta S$. The four values tabulated for the ΔG at various temperatures for solid $Ag_{1/2}Au_{1/2}$ are plotted against temperature in Fig. 10; the slope of this line yields a value of 1.15 cal/deg g atom for the entropy of solution of solid $Ag_{1/2}Au_{1/2}$, in good agreement with the value obtained solely from present data.

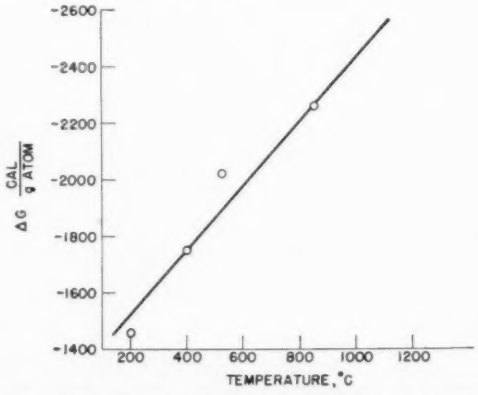

FIG. 10. The Gibbs free energy of mixing for solid $Ag_{1/2}Au_{1/2}$ at various temperatures; references in Table 1.

TABLE 1. Summary of experimental results.

	$Au_{1/2}Cu_{1/2}$	$Ag_{1/2}Au_{1/2}$
ΔG_{liq}	−2950† (985°C)	−2520† (1071°C)
ΔG_{sol}	−2200[a] (500°C); −2120[b] (427°C)	−2020[c] (527°C) −1750[d] (400°C) −1456[e] (200°C) −2260† (850°C)
ΔH_{liq}	0[f]; −1780†	0[f]; −430[g]; −1050†
ΔH_{sol}	−1230[a]; −1200[b]	−1010[h]; −947[e]; −950[d]; −1300[c]; −970†
ΔS_{liq}	0·93†	1·09†
ΔS_{sol}	1·26[a]; 1·31[b]	0·96[e]; 1·2[d]; 0·9[c]; 1·15†

† Present work.
[a] F. Weibke and U. van Quadt, *Z. Elektrochem.* **45,** 715 (1939).
[d] Ref. 4.
[c] A. Olander, *J. Amer. Chem. Soc.* **53,** 3577 (1931).
[d] O. Kubaschewski and O. Hichler, *Z. Elektrochem.* **52,** 170. (1948)
[e] A. Wachter, *J. Amer. Chem. Soc.* **54,** 4609 (1932).
[f] Ref. 16.
[g] Calculated in ref. 17 from C. Wagner and G. Engelhardt, ref. 15.
[h] Ref. 18; value for 0.42 mol fraction Ag, at 0°C.

4. DISCUSSION OF THE THERMODYNAMIC DATA

The strongest point of disagreement between the present data and those in the literature is with respect to Kawakami's[16] calorimetric results for the heats of formation of both liquid $Au_{1/2}Cu_{1/2}$ and liquid $Ag_{1/2}Au_{1/2}$ for the pure liquid components. However, Weibke and Kubaschewski[17] cast doubt on the accuracy of Kawakami's experimental technique, and the internal consistency of the present data leads us to give little weight to his values. With respect to the −430 cal/g atom for the ΔH of liquid $Ag_{1/2}Au_{1/2}$, it is not clear how Weibke and Kubaschewski[17] calculated this number from the e.m.f. data of Wagner and Engelhardt,[15] since these investigators present activity values at only one temperature. The present result for the heat of solution of solid $Ag_{1/2}Au_{1/2}$ agrees well with that obtained by the solution calorimeter of Ticknor and Bever.[18]

Both liquid alloys exhibit negative excess entropies of mixing, in contradistinction to the liquid alloys studied by Kleppa,[19] which have solution entropies larger than the entropy of random mixing. In the present case, the liquid alloys undoubtedly exhibit some short-range order, since the solid alloys do so,[20, 21, 22] but the degree of short-range order that probably exists is not sufficient to account for the observed negative excess entropies. For example, from the statistical equation of Takagi,[23] one may calculate that, for a co-ordination number of 12, if there are 5.05 A-nearest neighbors about any one A-atom, instead of the random distribution expectation of 6, the excess entropy of mixing would be −0.1 cal/deg g atom. Although the volume change upon mixing is not known for these liquid alloys, it is probable that it will have the same sign and roughly the same magnitude as that for the solid alloys. Solid Ag-Au solutions exhibit a very small negative deviation[24] from Vegard's law, so that one might expect that the entropy change due to the change of volume on formation of the liquid Ag-Au alloys is negligible. Solid Au-Cu alloys deviate positively[25] from Vegard's law, so that the volume change for the liquid solutions may contribute a small positive term to the ΔS of solution. Therefore, it would seem that these liquid alloys exhibit a negative vibrational contribution to the entropy of solution; that is, the stronger bonding between dissimilar atoms that is reflected in the negative heats of solution causes an increase in the vibration frequencies of the mass over what exists in the pure liquids.

Wagner[14] has developed a method of calculation of the quantity, $\Delta(\Delta G)$ at the melting-point minimum, of binary alloy systems which exhibit complete miscibility and have such a minimum. $\Delta(\Delta G)$ is defined as $\Delta G^S - \Delta G^L$ where ΔG^S is the Gibbs free energy of solution of the solid alloy referred to the pure solid constituents, and ΔG^L is the Gibbs free energy of solution of the liquid alloy referred to the pure liquid components. Assuming only that the entropies of fusion of the pure components are independent of temperature, and using the co-ordinates of the minimum, Wagner calculates for $Cu_{0.4}Au_{0.6}$ $\Delta(\Delta G) = 421$ cal/g atom. From the present data, correcting ΔG^S and ΔG^L to 884°C, $\Delta(\Delta G) = 160$ for the same composition. The discrepancy is probably due both to experimental error in our work and to the assumption that the ΔC_p upon melting of the pure components are zero and independent of temperature. The measured heat capacities of sodium[26] and of potassium[27] both above and below the melting points cast doubt on the validity of this assumption. The $\Delta(\Delta G)$ at 1000°C for $Ag_{1/2}Au_{1/2}$ is zero from our measurements; since there is no melting-point minimum in this system, Wagner's method cannot be applied.

We have pointed out that the thermodynamic properties of liquid metallic solutions reflect an appreciable contribution from the modification that the atomic vibrations undergo in the formation of the solution. It has been shown[1, 3] that the quasi-chemical theory of solutions does not describe the experimental results in the case of solid solutions which exhibit vibrational contributions, the reality of which has been demonstrated in a Au-Ni alloy.[28, 29] It is of interest therefore to try to apply to the present

VOL. 4 1956

liquid systems a statistical theory which explicitly considers the vibrational degrees of freedom. Prigogine and Bellemans[30] have extended the cell model for solutions of spherical molecules of different radii and having spherical fields of force. Although deviation from this last proviso would be serious for a calculation of the elastic constants, one may reasonably hope that the energetics would not be much affected. The other essential assumptions for this theory are (1) that the energy of the system can be expressed as a sum of pairwise interactions between nearest neighbors only, (2) that the potential energy between two molecules i and j is given by the Lennard-Jones expression $\epsilon_{ij}(r) = \epsilon_{ij}^*[(r_{ij}^*/r)^{12} - (r_{ij}^*/r)^6]$, (3) that $r_{ij}^* = \frac{1}{2}(r_{ii}^* + r_{jj}^*)$, (4) that the atomic distribution is random. In these expressions ϵ_{ij}^* and r_{ij}^* are respectively the energy and distance parameters of the minimum of the potential energy curve, and r is the actual distance apart of the neighboring atoms. The type of force law assumed is not important as Prigogine and Garikian[31] have shown, and the deviations of our liquid solutions from random distribution of species can lead only to very small error.

The important term in the relevant expression for the enthalpy of solution is

$$\frac{\Delta H}{NZ\,\epsilon_{AA}^*} = 1.435\,[-\theta + 4.50\rho^2]\,x_A x_B,$$

where N is the Avogadro number, Z the co-ordination number, x_i the mol fraction of component i, $\theta = [\epsilon_{AB}^* - \frac{1}{2}(\epsilon_{AA}^* + \epsilon_{BB}^*)]/\epsilon_{AA}^*$, and $\rho = (r_{BB}^* - r_{AA}^*)/r_{AA}^*$. The ρ-term can be evaluated from the lattice parameters of the pure components. The θ-term, analogous to the exchange energy term w in the regular solution theory,[32] can be evaluated from $(\epsilon_{BB}^* - \epsilon_{AA}^*)$ in the case where dispersion forces are operating. Since this is certainly not the case in metallic solutions, the θ-term may be approximated in the case of Au-Cu alloys from the theory of the critical temperature of ordering in the solid solution. By the quasi-chemical theory,[32] $w/(kT_\lambda) = Z \ln [Z/(Z-2)]$, from which $\theta = 0.016$ using $Z = 12$, $T_\lambda \approx 670°$K for the disordering temperature of the f.c. tetragonal $Au_{1/2}Cu_{1/2}$ superlattice. Employing the Kirkwood power series[32] up to and including the fifth term (the term $y = 20$ for a f.c.c. lattice) yields essentially the same value for θ. The Kikuchi[33] method for the f.c.c. lattice gives $\theta = 0.0176$, and is presumably the best approximation since it yields the highest[32] value of $w/(kT_\lambda)$. Using this value of θ, a value for ΔH of $+2720$ cal/g atom is calculated for liquid $Au_{1/2}Cu_{1/2}$, whereas the experimental number is -1780. This large disparity, extending even to the sign of the quantity, probably reflects the inadequacy of the third assumption, which is proper only for the case of operation of dispersion forces. Salsburg and Kirkwood[34] have shown that the calculated thermodynamic properties of mixtures are very sensitive to the values of the parameters of the Lennard-Jones potential, so that the arithmetic mean assumption for r_{AB}^* may cause serious error.

Varley[11] has considered the calculation of the heats of formation of metallic solutions from a less general point of view, but one specifically based on the electronic interactions in alloys. The calculation takes account of the decrease in energy of a system that occurs when charge is transferred, repulsive interactions, electron exchange interactions, the ground state of electronic energy, and the radii of the atomic polyhedra change. The contribution to the ΔH of solution from these effects must be negative, so that Varley depends on a strain-energy contribution to obtain a positive term in the calculation of a ΔH for solid solutions. Since, except for the strain-energy term, the method employed is equally valid for the liquid as for the solid state, a comparison of Varley's calculations with the present experimental results would be of interest, and is presented in Table 2. The degree of agreement is encouraging.

TABLE 2. Results of theoretical calculations of the heat of solution

Alloy	Expl. $\Delta H_{x=1/2}$	Cell Theory	Varley
$Cu_{1/2}Au_{1/2}$ liq.	-1780 cal/g atom	$+2720$ cal/g atom	-4030 cal/g atom
$Ag_{1/2}Au_{1/2}$ liq.	-1050	—	-1750

5. SOLUTION PROPERTIES OF SOLID PHASES vs. THOSE OF LIQUID PHASES

Conceptually, a comparison of the thermodynamic properties of solution for solid alloys (referred to the pure solid components) with those for liquid alloys (referred to the pure liquid components) is interesting for the evaluation of strain energy in the solid solution only if every other factor in the solution process remains the same. The latter becomes more probable, as the change in molar volume on melting is small and remains independent of alloy composition, as the packing in the two phases is nearly similar, and when the electron-to-atom ratio is independent of composition.[35] Empirically, such a comparison is satisfactorily in qualitative agreement with the original concept of strain energy when the $\Delta(\Delta G)$ and the $\Delta(\Delta H)$ are positive quantities the magnitudes of which vary roughly directly with the

disparity in atomic radii of the pure components.

The present writer criticized the proposal of Lumsden[13] as to the relevance of $\Delta(\Delta H)$ for the evaluation of strain energy in solid solutions on the strength of a tabulation[3] of experimental $\Delta(\Delta H)$ for many alloys of all types. However, Wagner[36] has pointed out that the comparison ought to be restricted to alloys having complete miscibility in the solid state. Nevertheless, even for Ag-Au, Au-Cu (see Table 1), and Cd-Mg,† the data then available were not conducive to the belief in the relevance of $\Delta(\Delta H)$. At present, however, the deductions of $\Delta(\Delta G)$ by Wagner[14] from phase-diagram data for binary systems having melting-point minima afford one some confidence that the numbers have something to do with strain energy, since they are positive quantities and depend roughly on $(r_A - r_B)$. Any deduction of $\Delta(\Delta H)$ from $\Delta(\Delta G)$, however, must depend upon some assumption concerning the entropies of solution of one or of both phases. The calculation of Brown[39] on the $\Delta(\overline{\Delta H})$ for dilute solutions of cadmium in zinc yields a positive number of reasonable magnitude. The present results on $\Delta(\Delta G)$ and $\Delta(\Delta H)$ for $Ag_{1/2}Au_{1/2}$ and $Au_{1/2}Cu_{1/2}$ also strengthen the idea that such a comparison is of help in evaluation of strain energy in a solid solution, since not only are all the quantities positive numbers, but also they vary in the right direction with $r_A - r_B$. It may be mentioned in passing that Lumsden's[13] proposed correlation between $\Delta(\overline{\Delta H}_2)/\Delta(\overline{\Delta S}_2)$, for vanishingly small concentrations of species 2, with $3R\beta_1/(4\alpha_1^2 V_1)$ of the pure solvent species (R = the gas constant, β = compressibility, α = thermal expansion coefficient, and V = molar volume) does not hold at all for Au-Cu and Ag-Au; however, our accuracy in the evaluation of $\Delta(\overline{\Delta H}_2)/\Delta(\overline{\Delta S}_2)$ from the present measurements is poor.

The work of H. Jones[35] lends added support to the correlation of $\Delta(\Delta H)$ with the strain energy in a solid solution. He has shown that, for solutions of randomly distributed species, and for which the heat capacities of the pure solvent in the solid phase, C_0^S, in the pure liquid phase, C_0^L, of the solid solution, C_x^S, and of the liquid solution, C_x^L, obey the relation

$$T\int_0^T \{(C_0^L - C_x^L) - (C_0^S - C_x^S)\} d \ln T - \int_0^T \{(C_0^L - C_x^L) - (C_0^S - C_x^S)\} dT = 0,$$

the change with mean solute concentration x of the difference in energy between the solid and the liquid phase is given by

$$\delta(\Delta U) \equiv (U^S - U^L)_{\bar{x}} - (U^S - U^L)_0 = \lambda_{1,0} - \frac{\lambda_{1,0} T}{T_{m,1}} - RT\left(\ln \frac{1 - x_S}{1 - x_L} + \bar{x} \ln \frac{x_S(1 - x_L)}{x_L(1 - x_S)}\right)$$

In this equation, U is the internal energy, which shall be taken as synonymous with the enthalpy H for condensed phases, $\lambda_{1,0}$ and $T_{m,1}$ are respectively the enthalpy of melting and the absolute melting point of pure solvent 1, and x_L and x_S are the solute mole fractions in the liquid and solid solutions respectively, which are in mutual equilibrium at the temperature T. It is easy to show that $\Delta(\Delta H) \equiv \Delta H^S - \Delta H^L$ is given by the same relation, except that $\lambda_{1,0}$ is replaced by the arithmetic mean of the enthalpies of melting of the two pure components. It is to be noted that the condition on the heat capacities is apt to be rather well obeyed, involving as it does a difference of differences, even for alloys which have appreciable deviations from the rule of additivity of the heat capacity and which therefore exhibit non-configurational contributions to the properties of solution.

Table 3 presents $\Delta(\Delta H)$, calculated as described above for three alloys, at a composition chosen to correspond to the melting-point minima for Au-Cu and Au-Ni, so that the logarithmic term is zero; the logarithmic term is essentially zero for the Ag-Au alloy also because of the very narrow two-phase region, as calculated by Wagner[14] for this system. The agreement for Au-Cu and Ag-Au alloys between the calculated and experimental $\Delta(\Delta H)$ is all that can be expected in view of the accuracy of the present data. The $\Delta(\Delta H)$ for $Ni_{0.4}Au_{0.6}$ leads to a ΔH^L for the corresponding liquid alloy of about 1650 cal/g atom, using the data of Seigle *et al.*[1] Since Wagner's[14] calculation leads to $\Delta(\Delta G) = 640$ for this alloy, one can obtain $\Delta G^L \approx -1450$ cal/g atom and $\Delta S^L \approx 2.5$ cal/deg g atom with the help of the experimental data[1] for the solid alloy. Thus, whereas these calculations agree with the conclusion of Seigle *et al.*[1]

TABLE 3. Property differences between solid and liquid solutions.

System		Temp. °C	$\Delta(\Delta H)$ calc'd.	$\Delta(\Delta H)$ expl.	$\delta\Delta U$	$900(v-1)\bar{x}$
2	1					
$Cu_{0.4}$	$Au_{0.6}$	884	440	535	410	0
$Ag_{0.4}$	$Au_{0.6}$	1025	−40	90	90	0
$Ni_{0.4}$	$Au_{0.6}$	850	950	—	480	360

† For $Cd_{1/2}Mg_{1/2}$ the available data were $\Delta H^L = -2000$ cal/g atom.[16] $\Delta H^S = -1940$ cal/g atom.[37] Discovery[38] of a mathematical error in the latter modifies the ΔH^S to -1302 so that the $\Delta(\Delta H)$ now acquires significance if one assumes the correctness of Kawakami's result.

that liquid Au-Ni alloys have activities that closely follow Raoult's law, it is seen that the liquid solutions are in reality very far from ideal, but that a large positive enthalpy of mixing is balanced by a large positive excess entropy of mixing. These large excess quantities have an important consequence that will be discussed in a later section.

Jones[35] showed that, for alloys of atoms of equal size, of simple structure in the solid state, and for which the volume-change upon melting is independent of composition, the variation of latent heat of melting with solute concentration will arise mainly from the variation of Fermi energy upon melting; and hence that the energy difference between solid and liquid alloys of the same composition will depend upon the number of extra electrons per atom introduced by the solute metal. Table 4 shows that, since the volume changes upon melting of the pure elements are so

TABLE 4. Change of molar volume on melting[40]

Pure metal	ΔV_f
Ag	0·42 cm³/g atom
Au	0·55 cm³/g atom
Cu	0·32 cm³/g atom
Ni	—

similar,[40] this quantity is likely to be essentially independent of composition for their alloys. The $\delta\Delta U$ calculated by the equation given above is tabulated in the fifth column of Table 3, and is to be compared with the quantity 900 $(v-1)\,\bar{x}$, the empirical expression deduced by Jones for $\delta\Delta U$ for various solutes of valence v in copper and silver as solvents. Since the e/a ratio remains constant for Au-Cu and Ag-Au, the valence effect leads to zero $\delta\Delta U$, so that the finite values of $\delta\Delta U$ in the fifth column of Table 3 may be ascribed to strain energy in the solid solution, and it is gratifying that they are about equal to the experimental values for $\Delta(\Delta H)$. Since $v=2$ for Ni, there is a finite contribution to the $\delta\Delta U$ from the Fermi energy effect, so that one can say that all of the calculated $\Delta(\Delta H)$ of 950 cal/g atom cannot be ascribed to strain energy in the solid solution.

6. RELEVANCE OF ELASTICITY-THEORY CALCULATIONS

When one solute atom is introduced into a solid solvent metal there occurs a change of volume and a change in lattice parameter of the system. If it is desired to apply classical elasticity theory to estimate the portion of the partial molar heat of solution that is due to "strain energy", it is necessary first of all to decide beyond what radial distance r_n away from the center of the solute particle shall the deformation of the lattice be deemed to be Hookean. Then from the observed change of volume of the assembly of an Avogadro number of atoms one may deduce the volume change suffered by the region of final radius r_n about the solute atom, whereupon, from the equations of elasticity theory and considering the image displacement,[41] one can calculate the Hookean elastic energy residing in the lattice beyond r_n. The choice of the cut-off radius r_n has been taken variously as the radius of the solute atom,[5] the radius of the cluster of twelve atoms about the solute atom,[9] and the radius of the third-nearest-neighbor shell[42] about an interstitial solute atom. Since the elastic energy varies inversely with the cube of r_n, the calculation is extremely sensitive to the choice made. As the concentration of solute particles increases, such a calculation can still be carried out in a meaningful fashion up to such a concentration of randomly distributed points of disturbance that the regions of non-Hookean deformation begin to impinge upon one another; beyond this point the elastic deformation will not sum up linearly.[41] It should be noted that it is not self-evident that a value of r_n (measured by the number of neighbor shells) adequate at infinite dilution is also adequate at appreciable concentration. In view of our ignorance of actual displacements of atoms about a solute atom, it seems wise to apply elasticity theory only to very dilute solutions, perhaps up to one atom per cent.

Before going further it should be pointed out that what the calculation that has been described yields is a contribution to the free energy, strictly the Helmholtz free energy, of the solid solution. This is because the isothermal bulk modulus, and the isothermal elastic constants in general, have to do with the work necessary to deform a body in a reversible, isothermal fashion. Therefore, in order to find the contribution to the energetics of solution one must add the entropy term, multiplied by the temperature, to the free-energy term. Since the entropy term is the negative of the derivative of the free-energy term with respect to temperature, and since bulk moduli generally decrease with temperature, the entropy contribution from the region in a solid solution beyond r_n will in general be positive.

Table 5 presents a comparison between the experimental $\Delta(\overline{\Delta H})$, the difference between the partial molar enthalpies of solution of solute in very dilute solid and liquid solutions, and the $\overline{\Delta G}_{el}$, the elastic contribution from $r > r_n$ to the partial molar free

TABLE 5. Elastic contribution calculated for region beyond r_n compared with experimental $\Delta(\Delta H)$ for very dilute solute

Solute	Solvent	Experimental cal/g atom			ΔV Å³/atom	$\overline{\Delta G}_{el.,\ calcd.}$ cal/g atom
		$\overline{\Delta H}^S$	$\overline{\Delta H}^L$	$\Delta(\overline{\Delta H})$		
Au	Ag	−3300	−3900	+ 500	$-0{\cdot}3_5$	~3
Ag	Au	−3600	−4250	+ 650	$-0{\cdot}0_5$	~0
Au	Cu	−3550	−5300	+ 750	$+6{\cdot}2_7$	910
Cu	Au	−1170	−2600	+1400	$-4{\cdot}2_8$	160
Au	Ni	11000	—	—	$+9{\cdot}8_0$	2960
Ni	Au	19400	—	—	$-3{\cdot}2_4$	87

energy of solution for the solute. The latter quantity was calculated by

$$\overline{\Delta G}_{el} = \frac{1 - 2\nu}{1 + \nu} Nk \frac{(\Delta V)^2}{V_n},$$

where ν and k are the Poisson ratio and the bulk modulus of the solvent, N is the Avogadro number, $V_n = (4\pi/3)r_n^3$, and ΔV is the change in volume, per atom, of the lattice. Following Moon,[42] $\Delta V = (a_1^3 - a_0^3)/m$, where a_0 is the lattice parameter of the pure solvent, a_1 is the value at which the tangent to the lattice parameter-composition curve cuts the axis for the pure solute (analogous to the apparent atomic diameter of Axon and Hume-Rothery),[43] and m is the number of atoms in a unit cell. The Poisson ratios were obtained from the Handbook of Metals, the bulk moduli from Waser and Pauling,[44] and the lattice parameter curves from refs. 24, 25, and 45. The r_n has been taken arbitrarily as the radius of the sphere just enveloping the shell of first neighbors in the pure solvent. The $\overline{\Delta G}_{el}$ was not corrected to the $\overline{\Delta H}_{el}$, for lack of data on the temperature variation of the bulk moduli. The table shows that there is no significant correlation between the observed $\Delta(\overline{\Delta H})$ and the calculated elastic-energy quantity.

It is seen, then, that application of elasticity theory and the continuum model to the Hookean region of a dilute solid solution leads to no conceptual difficulties only to serious ones of operational detail: how to choose an r_n, its variation with concentration (and temperature), and the limiting concentration. The problem with respect to the region containing the solute atom and bounded by a surface of radius r_n has conceptual difficulties as well. Qualitatively, in the region within r_n there will be a transfer of charge to or from the solute ion,[11] leading to a change in the "size" of the ion; there will be screening of the cation charge by the conduction electrons,[10] as well as a change in the closed ion-shell interactions; there will be a change in the radius of the first- and succeeding-neighbor shell, as well as a change in the atomic vibrations in that region. A popular approach, which incidentally conceals the difficulties associated with a specification of r_n, is to apply the Mott-Nabarro[12] treatment for the elastic strain produced by a solid precipitate within a solid matrix to the limiting case when the second phase is one solute atom, or the solute atom and its immediate neighbors.[8, 9, 10, 11] The calculation consists in computing the compressive free energy contributed by the cluster of atoms in going from a specific initial radius r_a to a final radius r', and in computing the elastic free energy stored in the lattice beyond r' by virtue of the change in radius of a spherical cavity in the material from an initial radius r_c to the final radius r'. The final radius r' is determined by a minimization of the sum of the two contributions with respect to final radius.

Thus, this method presumes that there is Hookean behavior beyond r', but what is much more important is, it presumes that the equilibrium radius of a cluster, or of a solute atom, is determined by the minimization of these two free-energy terms. This minimization has significance for the mechanical model contemplated, but has little relevance for the physical system. Actually, small changes in the electronic terms produce much larger changes in energy than are considered by these calculations. But of greater import is the realization that, since all of the effects discussed above that occur within a region r_n will occur in the liquid solution, the radius of, say, the second shell of neighbors will be determined in a liquid solution by the electronic interactions, and not by a non-existent elastic stress in the region beyond that shell. In the solid state, qualitatively the same interactions will determine the radius of the second shell of neighbors about a solute atom, but the existence of a lattice will lead to a second-order change in the radius of any one shell from what it would be in the corresponding glassy state, as well as to a non-zero stress field in the lattice beyond that shell. The first of these two effects of the imposition of a lattice consists of a slight redistribution of charge between the components, a small change in the co-ordination number and possibly in the ratio of species in the first-neighbor shell, and consequently a small change in the magnitude of the radius of any one shell of neighbors. Such changes cannot be calculated by elasticity theory, and properly should not be thought of as yielding a contribution to the strain energy. Therefore, it seems best to use the term misfit energy to cover the energetics of what happens both within and beyond r_n; both are associated with radius disparity between the

VOL. 4 1956

components, and their sum is what is measured by the $\Delta(\Delta G)$ and $\Delta(\Delta H)$ quantities discussed in a previous section. In short, the misfit-energy effect within r_n can be thought of as arising from the small change in the radius of the nth shell of neighbors, by the imposition of lattice periodicity; r_n, measured in angstroms, is primarily determined by the electronic interactions which are qualitatively the same in the solid as in the liquid state. The excellent numerical agreement obtained by Friedel[10] between elasticity-theory calculations and the experimental heats of solutions of solid Au-Ni alloys is itself an indication that what was calculated is not a strain energy, since incorporated in the ΔH^S, and a major part of it, is the sort of interaction that leads to a large positive number for the heat of solution in the liquid Au-Ni alloys.

Various authors have written of a strain (or misfit) energy in a liquid solution, without, however, further elucidation. The sense in which such a concept is meaningful is very restricted. It can be said that a liquid solution of species A and B will exhibit a more positive enthalpy of mixing than will a liquid solution of the same components if A were to have the same ionic size as B. This statement has no operational significance, but is simply an assertion concerning a physically unrealizable situation. The theory of Prigogine and Bellemans[30] is able to give an indication of such a hypothetical misfit energy. Nevertheless, in view of the lack of an operational definition of misfit energy in a liquid solution, it seems preferable to use the term with caution, and to measure the misfit energy in a solid solution with reference to the liquid solution as zero.

7. CONCLUSIONS

(i). The liquid binaries Ag—Au and Au—Cu exhibit negative deviations from Raoult's law, negative enthalpies of mixing, and negative excess entropies of mixing. The latter reflect a negative contribution from the changes in atomic vibrations caused by alloying.

(ii). The experimental heats of solution of the liquid alloys are not adequately calculable by the cell model or by a simple consideration of the electronic interactions between solute and solvent.

(iii). For binary alloy systems which exhibit complete miscibility in the solid state, which have composition-independent volume changes on melting, and in which the e/a ratio does not change with composition, a good measure of the misfit energy in the solid solution is given by the quantities $\Delta(\Delta G)$ and $\Delta(\Delta H)$.

(iv) The elasticity-theory calculation of the strain-energy contribution to the misfit energy in a very dilute solid solution from the region beyond the solute atom by a distance r_n is conceptually meaningful, and leads to a free energy quantity; however, because the numerical result is so sensitive to the value of r_n, it is necessary that the choice of r_n be justifiable by other considerations before the calculation can be fruitful. Such independent considerations are not apparent.

(v). The elasticity-theory calculation of the contribution to the misfit energy from the region within the distance r_n from the solute atom is conceptually meaningless.

(vi) Misfit energy in a solid solution is a term best used in connection with the energy and free-energy changes brought about by the imposition of lattice periodicity on a liquid solution of any concentration. There will then be contributions from both within and without the distance r_n, though the former cannot be computed from the theory of elasticity; the latter contribution may justifiably be called strain energy, since it is in principle calculable from elasticity theory.

(vii). The term strain energy or misfit energy in a liquid solution is operationally meaningless, and has conceptual significance only theoretically and with respect to an unattainable reference state.

(viii). The Au-Ni liquid solutions have large positive enthalpy and excess entropy of mixing. The misfit energy in solid $Au_{0.4}Ni_{0.6}$ is less than the calculated $\Delta(\Delta H)$ of 950 cal/g atom because of the change in e/a ratio with composition.

ACKNOWLEDGMENTS

It is a pleasure to acknowledge the benefit of discussions with Dr. E. W. Hart and with Professor I. Prigogine, and the help of Mr. W. K. Murphy with some of the experimental details. This work was supported by AEC contract No. W-31-109-Eng-52.

REFERENCES

1. L. L. Seigle, M. Cohen, and B. L. Averbach, *Trans. Amer. Inst. Min. Met. Eng., J. Metals*, **4**, 1320 (1952).
2. B. L. Averbach, P. A. Flinn, and M. Cohen, *Acta Met.*, **2**, 92 (1954).
3. R. A. Oriani, *Acta Met.*, **1**, 144 (1953).
4. R. A. Oriani, *Acta Met.*, **2**, 608 (1954).
5. A. W. Lawson, *J. Chem. Phys.*, **15**, 831 (1947).
6. T. Heumann, *Z. Metallkunde*, **42**, 182 (1951).
7. E. S. Machlin, *Trans. Amer. Inst. Min. Met. Eng., J. Metals*, **6**, 592 (1952).
8. B. J. Pines, *J. Phys. U.S.S.R.*, **3**, 309 (1940).
9. M. A. Jaswon, W. G. Henry, and G. V. Raynor, *Proc. Phys. Soc.*, **B64**, 177, 190, 195 (1951).
10. J. Friedel, *Adv. in Physics*, **3**, 446 (1954).
11. J. H. O. Varley, *Phil. Mag.*, **45**, 887 (1954).
12. N. F. Mott and F. R. N. Nabarro, *Proc. Phys. Soc.*, **52**, 86 (1940).

13. J. LUMSDEN, Thermodynamics of Alloys (London, Institute of Metals, 1952).
14. C. WAGNER, *Acta Met.*, **2,** 242 (1954).
15. C. WAGNER and G. ENGELHARDT, *Z. phys. Chem.*, **A159** 241 (1932).
16. M. KAWAKAMI, *Sci. Reports Tohoku Univ.*, **19,** 521 (1930).
17. F. WEIBKE and O. KUBASCHEWSKI, *Thermochemie der Legierungen* (Berlin), 1953.
18. L. B. TICKNOR and M. B. BEVER, *Trans. Amer. Inst. Min. Met. Eng.*, **194,** 941 (1952).
19. O. J. KLEPPA, *J. Amer. Chem. Soc.*, **73,** 385 (1951); **74,** 6052 (1952).
20. N. NORMAN and B. E. WARREN, *J. Appl. Phys.*, **22,** 483 (1951).
21. J. M. COWLEY, *J. Appl. Phys.*, **21,** 24 (1950).
22. B. W. ROBERTS, *Acta Met.*, **2,** 597 (1954).
23. Y. TAKAGI, *Proc. Phys. Math. Soc. (Japan)*, **23,** 44 (1941).
24. NYGAARD and OTTER, 1947, *in Vegard, Skrifter Norske Videnskaps. Okad., Oslo, Mat. Natur. Klasse*, No. 2, 37-40.
25. C. H. JOHANSSON and J. O. LINDE, *Ann. Phys.*, **25,** (ser. 5), 1 (1936).
26. D. C. GINNINGS, T. B. DOUGLAS, and A. F. BALL, *J. Res. Nat. Bur. Stand.*, **45,** 23 (1950).
27. T. B. DOUGLAS, A. F. BALL, D. C. GINNINGS, and W. D. DAVID, *J. Amer. Chem. Soc.*, **74,** 2472 (1952).
28. W. DESORBO, *Acta Met.*, **3,** 227 (1955).
29. R. A. ORIANI, *Acta Met.*, **3,** 232 (1955).
30. I. PRIGOGINE, and A. BELLEMANS, Faraday Soc. Discussions No. 15, 80 (1953).
31. I. PRIGOGINE and G. GARIKIAN, *J. Chem. Phys.*, **45,** 273 (1948).
32. E. A. GUGGENHEIM, *Mixtures* (Oxford) 1952.
33. R. KIKUCHI, *Phys. Rev.*, **81,** 988 (1951).
34. Z. W. SALSBURG and J. G. KIRKWOOD, *J. Chem. Phys.*, **21,** 2169 (1953).
35. H. JONES, *Proc. Phys. Soc.*, **49,** 243 (1937).
36. C. WAGNER, personal communication.
37. F. A. TRUMBORE, W. E. WALLACE, and R. S. CRAIG, *J. Amer. Chem. Soc.*, **74,** 132 (1952).
38. F. A. TRUMBORE, *J. Amer. Chem. Soc.*, **76,** 6417 (1954).
39. J. R. BROWN, *J. Inst. Metals*, **83,** 49 (1954-5).
40. R. A. ORIANI, *J. Chem. Phys.*, **19,** 93 (1951).
41. J. D. ESHELBY, *J. Appl. Phys.*, **25,** 255 (1954).
42. K. A. MOON, *J. Phys. Chem.*, **59,** 71 (1955).
43. H. J. AXON and W. HUME-ROTHERY, *Proc. Roy. Soc.*, **A193,** 1 (1948).
44. J. WASER and L. PAULING, *J. Chem. Phys.*, **18,** 747 (1950).
45. E. C. ELLWOOD and K. Q. BAGLEY, *J. Inst. Metals*, **80,** 617 (1951-2).

VOL.
4
1956

KINK-BANDS IN GERMANIUM*

FRED D. ROSI†

Coarse kink-bands were observed in single crystals of germanium extended above 700°C. The formation and appearance of these bands are discussed. Their crystallographic geometry was found by X-ray analysis to be similar to that reported for face-centered cubic metals. The occurrence of kink-bands appears orientation-dependent, and is associated with heterogeneities in the flow process. Kink-bands were not observed in crystals in which extensive slip occurred on several systems. Analysis of Laue spots revealed polygonization in crystals exhibiting extensive kinking at 850°C.

BANDES DE PLIAGE DANS LE GERMANIUM.

De larges bandes de pliage ont étéo bservées sur des monocristaux de germanium déformés au-dessus de 700°. La formation et l'aspect de ces bandes sont discutés; leurs propriétés cristallographiques, déterminées par rayons X, sont analogues à celles observées dans les métaux cubiques à faces centrées. Leur apparition dépend de l'orientation du cristal et est reliée aux hétérogénéités dans le mécanisme de la déformation. Les bandes de pliage n'ont pas été observées pour les cristaux présentant des glissements multiples. L'analyse des taches de von Laue indique une polygonisation pour les cristaux présentant un kin-king important à 850°C.

KNICKBÄNDER IN GERMANIUM

In Germanium Einkristallen, die oberhalb 700°C gedehnt worden waren, wurden grobe Knickbänder beobachtet. Die Entstehung und das Aussehen dieser Bänder werden diskutiert. Durch röntgenografische Untersuchungen wurde festgestellt, dass ihr kristallografischer Aufbau dem für kubischflächenzentrierte Metalle entspricht. Das Auftreten von Knickbändern scheint orientierungsabhängig zu sein. Es wird von Inhomogenitäten des Fliessvorganges begleitet. In Kristallen, bei denen ein ausgedehntes Gleiten auf mehreren Systemen auftrat, wurden Knickbänder nicht beobachtet. Eine Analyse der Lave Flecken zeigte, dass bei Kristallen, die bei 850°C eine ausgedehnte Knickbildung zeigen, Polygonisation auftritt.

1. INTRODUCTION

Recent studies[1–3] of the deformation mechanism in germanium crystals at elevated temperatures have shown that slip occurs on a {111} plane (see Fig. 1) and in a ⟨110⟩ direction, which are the planes and directions of closest packing in the diamond-type lattice. At present, however, there exists no evidence in the literature in connection with the occurrence of inhomogeneities of glide, such as kink-bands and bands of secondary slip. It is the purpose of this paper to describe observations of kink-band formation made in the course of investigation into the stress-strain characteristics of germanium single crystals extended above 700°C.

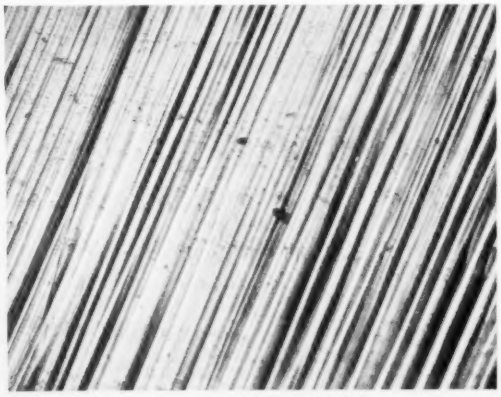

FIG. 1. Appearance of {111} slip in germanium at 750°C. ×150.

2. EXPERIMENTAL

The germanium used in these experiments was zone-refined to a resistivity of approximately 45 ohm-cm. Cylindrical single crystals were produced by withdrawl of a seed from the melt (Czochralski technique), which permitted the study of crystals of any desired orientation. The as-grown crystals were p-type, with resistivities ranging from 35 to 45 ohm-cm. Tensile specimens were cut from these cylindrical crystals in the form of sheets, 2 in. × 0.2 in. × 0.07 in. For purposes of gripping the specimen in tension, rods of similar-purity germanium were fused to the ends of the sheet. A typical example of a tensile specimen with fused grip-ends is shown in Fig. 2.

Tensile deformation was accomplished by the use of an Instron tester, which automatically recorded the load-extension curve at a constant crosshead speed of

* Received May 17, 1955

† RCA Laboratories, Radio Corporation of America, Princeton, New Jersey, U.S.A.

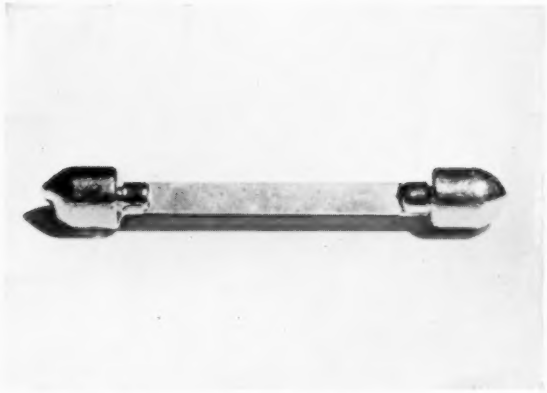

FIG. 2. Typical single-crystal specimen for tensile testing. ×1.

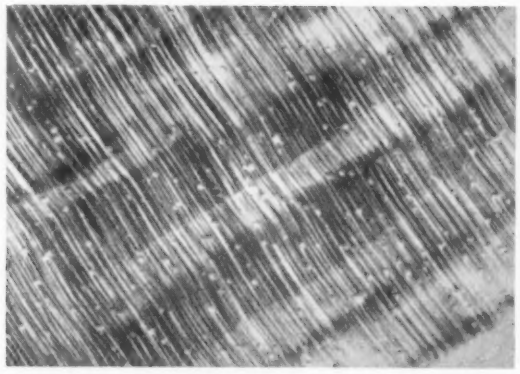

FIG. 3. Appearance of kink-bands in crystal extended approximately 25 per cent at 800°C. ×75.

0.02 in. min^{-1}. Heating of the specimens was done in a Hoskins furnace in an atmosphere of purified argon. Details of the tensile assembly will be given in a later work concerned with stress-strain characteristics.

Preparation of the surface of the crystals for optical microscopy consisted of surface grinding and then mechanically polishing with No. 305 American-Optical Compound. A final chemical polish in a dilute solution of hydrofluoric acid in nitric acid removed the cold-worked layer resulting from the mechanical treatment, and provided a surface satisfactory for examination of deformation markings.

The method of indentification of the slip-planes, as well as the bend-planes associated with kinking, was based on the use of a stereographic plot of a back-reflection Laue photograph describing the region where the slip and kinking were observed. Indentification resulted from the location in these plots of the poles of the planes responsible for the slip- and bend-planes.

3. RESULTS AND DISCUSSION

Frequent observations of coarse kink-bands were made in crystals in which extensive slip had occurred on a single, primary system. As shown in Fig. 3, these bands are very similar in appearance to those reported in a number of metals by various investigators,[4–8] in that they represent disoriented regions of the crystal which are bounded by parallel bend-planes making an angle of approximately 90° with the active {111} slip-planes. Moreover, from the relative angles which the {111} slip markings make with the tension axis, it is apparent that the lattice reorientation due to slip within the band lags behind that of the matrix material. This lag in lattice reorientation increases with deformation, and this is reflected in a higher density of slip markings in the crystal matrix as compared to the region within the band. It would appear from this that the bend-planes outlining the kink-band are effective in trapping dislocations moving along the active slip-planes, and that this effectiveness increases with deformation. In effect, this is to say that the kink-band is rotating toward the stress axis in an opposite sense to the primary slip-lines.

It may be noted that kink-bands were most frequently observed in regions of stress inhomogeneity, such as at the specimen edges and in the vicinity of the grips (see Fig. 4). This behavior would suggest that kinking can act as a stress-relief mechanism. In the disoriented region of the kink-band in Fig. 4, it may also be seen that slip has occurred on a different

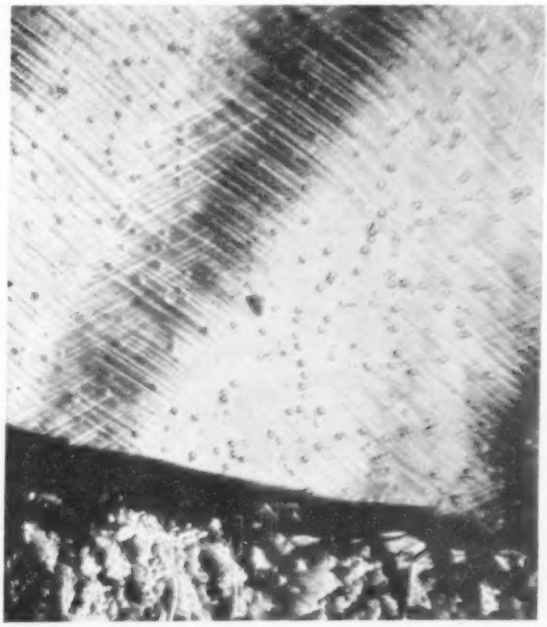

FIG. 4. Kink-band development in vicinity of grips. ×75.

VOL. 4 1956

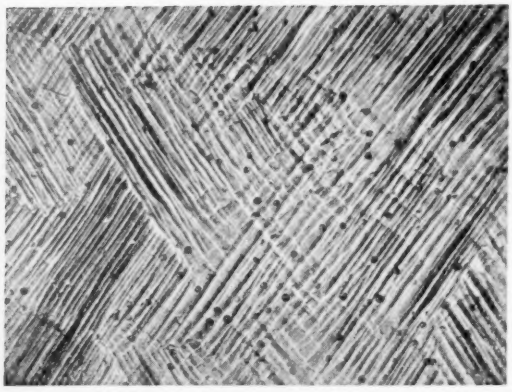

FIG. 5. Absence of coarse kink-bands in region of multiple glide on {111} planes. ×75.

set of planes. This observation was not uncommon at the higher deformations (>20 per cent elongation). It is apparent from the orientation of the secondary slip-planes with the stress axis, that their rotation, like that of the kink-bands, is in an opposite sense to the primary slip-planes. It is possible, therefore, that the occurrence of secondary slip within the lattice of the kink-band is to facilitate the rotation of the band toward the stress axis with increasing deformation.

Kink-bands were not optically detected in ⟨111⟩ and ⟨100⟩ crystals which had been extended as much as 80 per cent. It would appear from this that the occurrence of kink-bands in germanium is orientation-dependent in that, for critical orientations, where multiple slip can be expected at the onset of flow, kink-band formation is not necessary to the glide process. A similar behavior has been reported in aluminum[7, 10, 11] and titanium.[8] This orientation-dependence further supports the view that kinking is a stress-relief mechanism, since secondary slip systems could relieve those stresses which otherwise would necessitate kink-band formation. The absence of coarse kinking in a region of multiple slip on {111} planes is shown in Fig. 5.

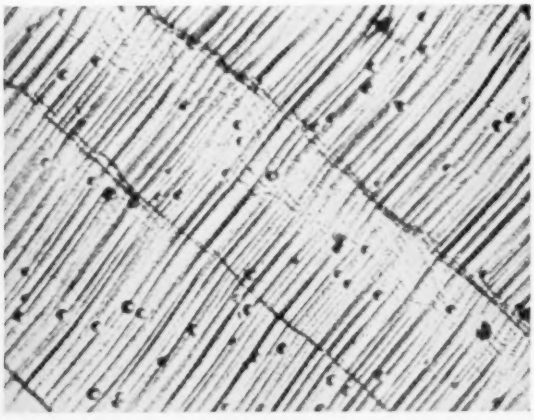

FIG. 6. Appearance of well-defined bend-planes outlining the kink-band in a crystal extended at 800°C. ×150.

Unlike kink-band development in metals, the bend-planes outlining the band in germanium often appear as well-defined lines, as shown in Fig. 6. These lines are probably a result of the banding of individual bend-planes, which can be expected to be very mobile at the high temperatures of deformation. Fig. 6 also reveals a tendency for the bend-lines to cluster, as well as an irregularity in their direction across the crystal. Optical examination of a number of these bend-lines indicated that this irregularity can be attributed to the formation of stepped secondary bend-planes, which make an angle of approximately 90° with the secondary slip-planes often appearing within the kink-band (see Fig. 4). The processes of banding of individual bend-planes have been described in detail in a recent study of kink-band development in titanium.[8]

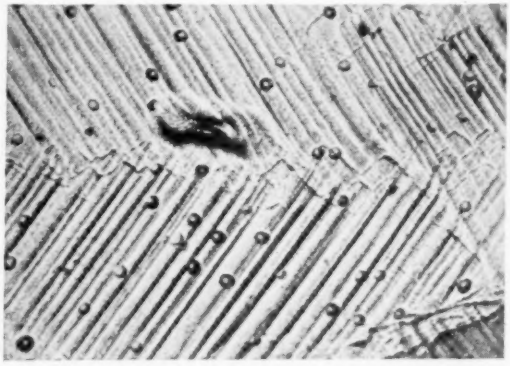

FIG. 7. Segmented bend-plane formation at boundary between slip on two sets of {111} planes. ×150.

Fig. 7 shows the unusual formation of segmented bend-lines in a region of the crystal representing the boundary between slip on two sets of {111} planes. Thus, the formation of bend-planes could be associated with an obstruction to the motion of edge dislocations on active slip-planes. In agreement with the topography of kinking, each segmented bend-plane in Fig. 7 is approximately normal to one of the two active {111} slip-planes.

The bend-planes of the kink-bands in moderately deformed crystals were found by X-ray analysis to coincide with {110} planes, the normal to which corresponded to the active slip direction. Moreover, from the appearance of the slip-line pattern in the as-deformed, unetched crystal the lattice rotation at the bend-plane is about an axis in the slip-plane, normal to the slip direction. This axis corresponds to a ⟨112⟩ direction, which represents the intersection of the

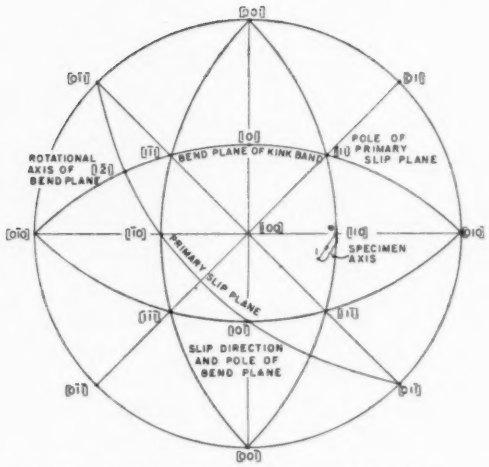
ROTATIONAL AXIS OF BEND PLANE
BEND PLANE OF KINK BAND
POLE OF PRIMARY SLIP PLANE
SPECIMEN AXIS
PRIMARY SLIP PLANE
SLIP DIRECTION AND POLE OF BEND PLANE

FIG. 8. Standard (100) projection indicating crystallography of bend-plane defining kink-band formation in crystal extended approximately 25 per cent.

{110} bend-plane with the active {111} slip-plane. These data are summarized in the standard projection of Fig. 8, which indicates, in addition to the rotation axis, the positions of the slip-plane, slip direction, and bend-plane in the crystal of Fig. 3. The movement of the specimen axis with deformation towards the [10$\bar{1}$] slip direction is also indicated. Thus, the crystallographic geometry of kinking in germanium is the same as that reported in the face-centered cubic metals, aluminum,[6,7] and copper.[12]

It has already been pointed out that in severely deformed crystals the operation of a second slip system was frequently observed in the lattice of the kink-band. From stereographic constructions of the lattice orientation inside the band, it was found in all cases that the secondary slip-plane corresponded to a {111} plane, which did not coincide with the conjugate plane of slip. For example, in the stereographic plot of Fig. 8, the secondary slip-plane corresponded to the (11$\bar{1}$) plane, which is the predicted plane of slip for crystal orientations in the triangle, [100] [110] [111].

One final observation of interest was the appearance of back-reflection Laue spots from crystals which had been extended above 25 per cent at 850°C, and in which extensive kinking or slip on several systems had occurred. As shown in Fig. 9, severe asterism was observed; but the streaks were broken up into a series of distinct segments, indicative of polygonization.[6] This would suggest that, at 850°C, recovery processes are occurring in germanium at a more rapid rate than work-hardening processes, which could account for the observed absence of any appreciable work-hardening in these crystals over a wide range of deformation. The present data also indicate that the break-up of the

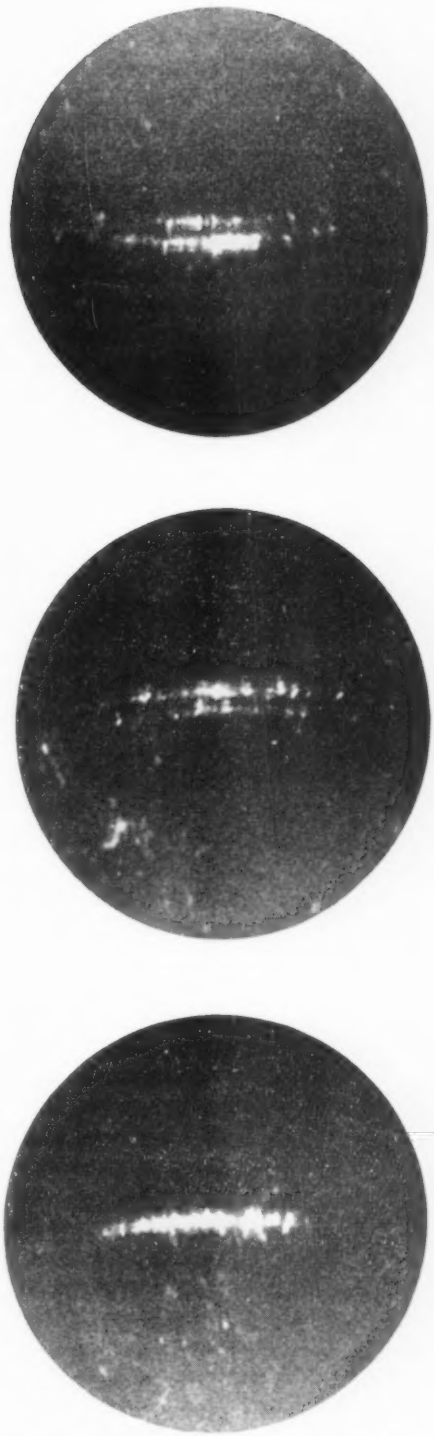

FIG. 9. Evidence of polygonization (break-up of asterism) in crystal extended approximately 80 per cent at 850°C.

VOL. 4 1956

asterism appears at earlier degrees of deformation, and is more complete in the crystals exhibiting slip on several systems.

4. SUMMARY

Tensile deformation of germanium single crystals above 700°C have led to the following observations in connection with kink-band formation:

1. The crystallographic and geometric features of kink-bands are very similar to those reported in a number of face-centered cubic metals.

2. The occurrence of kinking appears to be orientation-dependent, and is associated with stress inhomogeneities as a result of plastic flow. Kink-bands were never observed in crystals where extensive slip occurred on two or more slip systems.

3. The kink-band rotates in an opposite sense to the primary slip markings, and this rotation is accommodated by the appearance of secondary slip within the region of the kink-band.

4. Analysis of distorted Laue spots indicates that polygonization occurs simultaneously with deformation at 850°C.

ACKNOWLEDGMENTS

The author wishes to express his indebtedness to P. R. Celmer for his assistance in carrying out various aspects of the experimental program, and to J. J. Gannon for preparing the specimens for optical microscopy. He is also obliged to B. L. Rowe for the photomicrographs, and to G. W. Neighbor for X-ray orientation determinations.

REFERENCES

1. C. J. Gallagher, Plastic Deformation of Germanium and Silicon, *Phys. Rev.*, **88,** 721 (1952).
2. R. G. Treuting, *J. Metals*, **4,** p. 1044 (1952).
3. E. S. Greiner, Plastic deformation of germanium and silicon by torsion, *Trans. Amer. Inst. Min. Met. Eng.*, **203,** p. 203 (1955); *J. Metals* (January 1955).
4. J. B. Hess and C. S. Barrett, Structure and nature of kink bands in zinc, *Trans. Amer. Inst. Min. Met. Eng.*, **185,** p. 599 (1949); *J. Metals* (September 1949).
5. D. C. Jillson, An experimental survey of deformation and annealing processes in zinc, *Trans. Amer. Inst. Min. Met. Eng.*, **188,** p. 1009 (1940); *J. Metals* (August 1950).
6. R. W. Cahn, Slip and Polygonization in Aluminum, *J. Inst. Metals*, **19,** p. 129 (1951).
7. R. W. K. Honeycombe, Inhomogeneities on the Plastic Deformation of Metal Crystals, *J. Inst. Metals*, **80,** p. 45 (1951).
8. F. D. Rosi, Mechanism of plastic flow in titanium, manifestations and dynamics of glide, *Trans. Amer. Inst. Min. Met. Eng.*, **200,** p. 58, (1954), *J. Metals* (January 1954).
9. E. C. Burke, and W. R. Hibbard, Jr., Plastic deformation of magnesium single crystals, *Trans. Amer. Inst. Min. Met. Eng.*, **194,** p. 295 (1952), *J. Metals* (March 1952).
10. A. Lalouef and C. Crussard, Relation between the deformation and recrystallization of monocrystals of aluminum, *Rev. Metallurgie*, **48,** p. 462 (1951).
11. N. K. Chen and C. H. Mathewson, Structural studies of plastic deformation in aluminum single crystals, *Trans. Amer. Inst. Min. Met. Eng.*, **191,** p. 653 (1951), *J. Metals* (August 1951).
12. F. D. Rosi, Stress-strain characteristics and slip-band formation in metal crystals, effect of orientation, *Trans. Amer. Inst. Min. Met. Eng.*, **200,** p. 1009 (1954), *J. Metals* (September 1954).

THERMODYNAMIC PROPERTIES OF SOLID ALUMINUM-SILVER ALLOYS*

MATS HILLERT, B. L. AVERBACH, and MORRIS COHEN†

The relative thermodynamic properties of the Al-Ag system have been determined in the temperature range 642–820°K by means of emf measurements and compared with the local atomic arrangements determined from diffuse X-ray scattering. Qualitative agreement is obtained with both the quasi-chemical and Friedel's theory.

PROPRIÉTÉS THERMODYNAMIQUES DES ALLIAGES SOLIDES ALUMINIUM-ARGENT

Les propriétés thermodynamiques du système Al-Ag ont été mesurées dans l'intervalle de température 642–820°K par mesure des forces électromotrices et comparées aux arrangements atomiques locaux déterminés par la diffusion des rayons X. Un accord qualitatif est obtenu à la fois àvec la théorie quasi-chimique et celle de Friedel.

THERMODYNAMISCHE EIGENSCHAFTEN VON FESTEN ALUMINIUM-SILBER LEGIERUNGEN

Für den Temperaturbereich von 642–820°K wurden die relativen thermodynamischen Eigenschaften des Systems Al-Ag mit Hilfe von EMK-Messungen bestimmt. Sie wurden mit den örtlichen Atomanordnungen verglichen, die aus Aufnahmen der diffusen Röntgenstreuung bestimmt worden waren. Qualitative Übereinstimmung besteht sowohl mit der quasi-chemischen wie auch mit der Friedel'schen Theorie.

VOL. 4 1956

1. INTRODUCTION

Although the Al-Ag system, which is shown in Fig. 1,‡ has been investigated frequently in age hardening,[1] diffuse X-ray[2, 3] and equilibrium[4] studies, the thermodynamic properties of these alloys have not been measured. The thermodynamic quantities are of particular interest in connection with the various theories of solid solution formation which relate them to the local atomic arrangements in the solution. This system is especially significant in Friedel's theory,[5] which relies on the difference in valence between the components for the introduction of local electron energy levels. X-ray measurements which indicated a clustering of like atoms in the aluminum-rich solid solutions have been reported,[2, 3] and the present work provides the necessary thermodynamic data for a test of the solid solution theories.

From the result of this investigation it appears that Friedel's theory predicts the correct type of local order but unfortunately does not permit a quantitative correlation with the thermodynamic data. The quasi-chemical theory gives a qualitative correlation between the thermodynamic and the X-ray measurements, but does not allow a prediction of these properties from the form of the phase diagram.

The notation adopted by Wagner[6] is used here.

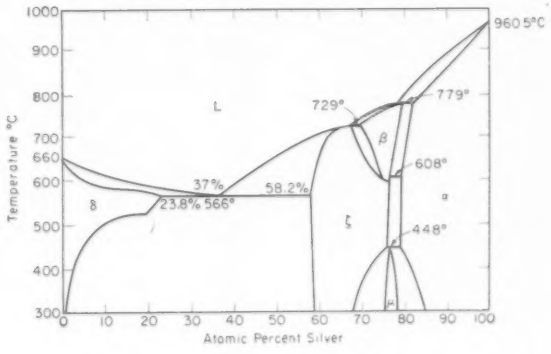

FIG. 1. Aluminum-silver equilibrium diagram.

2. EXPERIMENTAL PROCEDURE

A galvanic cell

Pure Al (anode)	Ionic conductor containing Al ions	Al-Ag alloy (cathode)

was used for measuring the activity of Al in a series of Al-Ag alloys. The electrolyte was an equimolar solution of $AlCl_3$ and NaCl, prepared as described elsewhere.[7] Fourteen alloys, covering the whole composition range, were made by melting 99.995 Al (supplied by the Aluminum Company of America) and high-purity electrolytic Ag under an atmosphere of argon. Rods of each alloy were sealed in separate Vycor tubes under vacuum and annealed at 540°C for 7 days. Electrodes 30 mm long and 2 mm diam. were obtained by filing the cast rods to shape. An Ag lead wire was welded to each electrode.

* Received May 24, 1955.

† Department of Metallurgy, Massachusetts Institute of Technology, Cambridge, Massachusetts.

‡ This diagram was drawn by J. E. Hilliard from selected experimental data.

The same electrolytic apparatus was used as in previous studies,[7, 9] but a new top was designed which permitted two electrodes to be put into the cell, and taken out without contaminating the purified argon atmosphere. The cell was brought to the desired temperature without the electrodes inside. A pure Al and an alloy electrode were then inserted into the cell and allowed to attain thermal equilibrium just above the surface of the electrolyte. They were then dipped into the electrolyte and the first potential reading was taken after about 15 seconds. The reason for this unusual procedure was as follows.

The Al-rich alloys gave rather stable emf values; alloys with a high Ag content were quite unstable, and there was a rapid change of potential with time. It was considered that at least two factors determined this rapid change, one increasing the potential and the other decreasing it. The first factor was probably the presence of moisture, which together with the electrolyte, dissolved Al from the electrodes and thus increased the Ag content at the surface of the alloy. The influence of this variable could be minimized by taking the potential readings as soon as possible after the electrodes were dipped into the electrolyte. Because of this chemical reaction, the surfaces of the electrodes were always cleaned by filing prior to each measurement.

The decrease of potential with time was very rapid and took place mainly during the first minute. If the electrodes were taken out from the cell, cleaned and inserted again, the potential started from a value lower than the original starting potential, and the decrease with time was less. After several repetitions, the starting value became constant and the effects of holding time became more difficult to detect. The rapid decrease in potential appeared again if the electrolyte was allowed to rest at temperature for some time. It was considered that the low, constant starting value was most representative of the activity of Al. After the bath had been conditioned to give constant emf values with one set of electrodes, measurements with the other alloys were made as quickly as possible. The heating period above the bath prior to the immersion of the electrodes was about 15 minutes, which was usually sufficient to achieve equilibrium in the alloy. Longer times were occasionally necessary for establishing equilibrium in the two-phase alloys.

It is obvious that the emf values obtained in this investigation and presented in Table 1 cannot be considered of high accuracy. The uncertainty increased with the Ag content, being about ± 0.1 mV in the Al-rich alloys, about ± 1 mV in the intermediate phase, and somewhat higher in the Ag-rich alloys.

TABLE 1. Experimental emf values for Al-Ag alloys

Alloy	x_{Ag}	mV		
		642°K	722°K	820°K
1	0.046			0.72
2	0.103			1.00
3	0.147			1.28
4	0.196			1.58
5	0.400	0.3	0.8	1.64
6	0.600	9	11	14
7	0.651	45	48	52
8	0.699	57	70	73
9	0.750	57	78	83
10	0.780	93	79	88
11	0.815	93	95	105
12	0.860	104	113	126
13	0.900	118	129	144
14	0.947	133	145	170

3. EXPERIMENTAL RESULTS

3.1. *Data and Method of Computation*

The activity of aluminum, a_{Al}, was obtained from the standard relationship

$$\ln a_{Al} = -\frac{3\mathcal{F}\varepsilon}{RT} \qquad (1)$$

Fig. 2 shows the values at 820°K. The activity of silver, a_{Ag}, was derived by evaluating the activity coefficient, f_{Ag}, using the Gibbs-Duhem equation in the form

$$\ln f_{Ag} = -\frac{1 - x_{Ag}}{x_{Ag}} \ln f_{Al} + \int_{x_{Ag}}^{1} \frac{\ln f_{Al}}{x_{Ag}^2}\, dx_{Ag} \qquad (2)$$

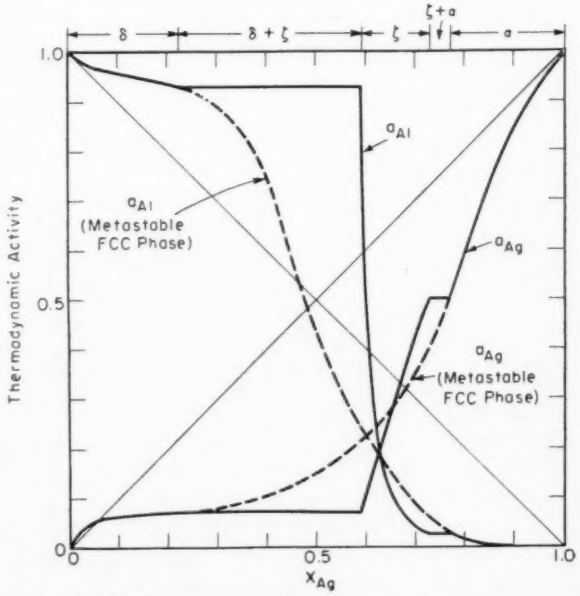

FIG. 2. Activities of components in Al-Ag alloys at 820°K.

The relative integral molar free energy, F^M, was computed from the excess integral molar free energy, F^E,

$$\frac{F^E}{RT} = x_{Ag}\int_{x_{Ag}}^{1} \frac{\ln f_{Al}}{x_{Ag}^2}\, dx_{Ag} \qquad (3)$$

It was thus necessary to know the quantity $\frac{\ln f_{Al}}{x^2_{Ag}}$ up to 100 per cent Ag. The extrapolation employed at 820°K is shown by the solid line in Fig. 3 at the high Ag contents. For the other two temperatures similar curves were drawn, but the experimental values for the alloy richest in Ag (0.947 Ag) had to be discarded because they were quite uncertain and did not fall in line with the other data.

Al and Ag both have face-centered cubic structure. Hence, the two terminal FCC regions can be joined by a metastable FCC region. Some interesting information concerning the metastable FCC alloys can be obtained from Fig. 3 by extending the curves for the stable Al-rich and Ag-rich FCC alloys into a smooth curve. This extension cannot be drawn arbitrarily because the excess free energy, according to equation (3), is obtained by integrating the area under the curve in Fig. 3 to $x_{Ag} = 1$. The result for Al-rich compositions must be the same whether the experimental stable curve or the metastable extension is used in the intermediate region. The two shaded areas must therefore be equal, and the course of the extension can be predicted fairly well. The thermodynamic quantities for metastable FCC alloys have been evaluated in this way.

The relative integral molar entropy, S^M, was computed from the change of F^M with temperature, assuming S^M to be independent of temperature. The S^M values in Fig. 4 were obtained from the two higher temperatures (820 and 722°K). Slightly different values were derived from the two lower temperatures (722 and 642°K). Because of the low solubility at the lower temperatures in the Al-rich FCC region, S^M could here be obtained only for the alloy richest in Al. Therefore, the S^M curve in Fig. 4 is to be regarded as tentative both for the other Al-rich alloys as well as for the metastable region. Fig. 4 also shows F^M at 820°K and the relative integral molar enthalpy, H^M, computed from F^M and S^M. The F^M values are considered fairly accurate, but the S^M and H^M values are more uncertain, mainly because of the experimental error in the emf data for the Ag-rich alloys.

However, the values for H^M and S^M obtained in this investigation are supported by the specific heat measurements of Hirano and Takagi[9] on Al-rich alloys. The specific heat determinations were corrected (by means of the present data for the ζ phase) for the entropy and enthalpy content of the ζ phase present in their starting specimens. The dotted curves in Fig. 4 show the corrected results; the agreement between the two sets of data is excellent up to $x_{Ag} = 0.2$. Beyond this composition, the H^M and S^M values based on the specific heat measurements undergo a sharp increase which has been interpreted in terms of Brillouin zone effects. If this increase is real (and it could have been missed in the present work because the alloys were not as closely spaced as those studied by Hirano and Takagi[9]) the smooth extrapolations used for the metastable FCC alloys are somewhat in error.

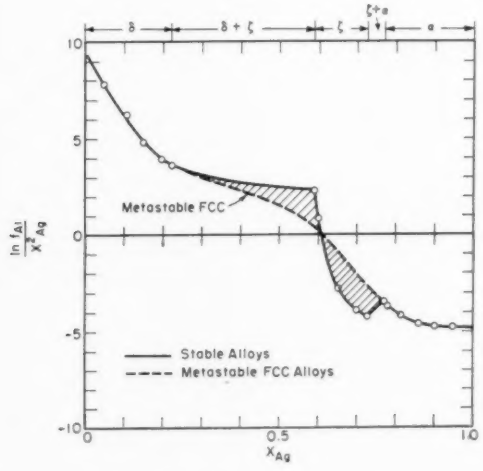

FIG. 3. $\frac{\ln F_{Al}}{X_{Ag^2}}$ *vs* X_{Ag} at 820°K for Al-Ag solid solutions.

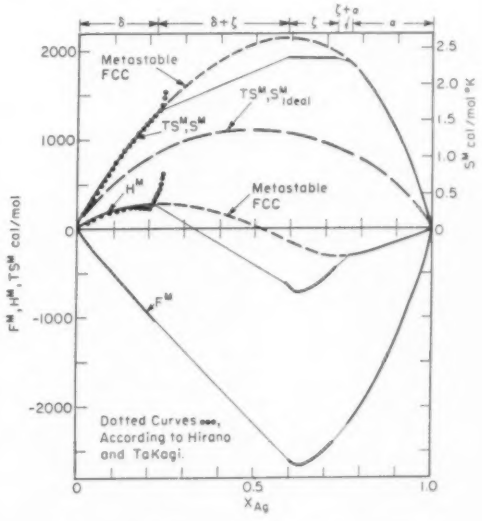

FIG. 4. Relative thermodynamic quantities in Al-Ag alloys at 820°K.

3.2. *Properties of Face-centered Cubic Phase*

Activity and enthalpy. The a_{Al} curve (Fig. 2) shows a positive deviation from Raoult's law on the Al-rich side and a negative deviation on the Ag-rich side. A similar kind of activity curve has been found for liquid Al-Ag alloys.[10]

The enthalpy curve (Fig. 4) also shows a positive deviation from ideality on the Al-rich side and a negative deviation on the Ag-rich side. Apparently, this has not been found experimentally for any other system, but it has been predicted by Meijering[11] for the Al-Ag, Al-Cu, and Ag-Pt systems.

Entropy. The relative integral entropy was found to be much higher than ideal. A high excess entropy has been usually associated with solutions in which the component atoms differ appreciably in size, as in the Au-Ni system.[12] However, the diffuse X-ray data indicate that there is no size difference between Al and Ag atoms in solution, and a similar situation prevails in the Al-Zn system.[2] New vibrational modes may be introduced as a consequence of the large difference in masses between the constituent atoms; however, this feature of solid solution formation is not well understood at present.

4. DISCUSSION

4.1. *Thermodynamic and X-ray Data*

Two approaches are usually taken in relating the thermodynamic properties to local atomic arrangements in solid solutions. The first is the quasi-chemical type which describes the internal energy of the solution entirely in terms of bond energies (E_{AA}, E_{BB}, E_{AB}) without considering the origin of these bond energies. The pertinent variable is the interaction energy, $\nu = E_{AB} - 1/2(E_{AA} + E_{BB})$, which is usually assumed to be independent of temperature and composition. Complications due to different atomic sizes are avoided in both the Al-Ag and Al-Zn solutions since the diffuse X-ray scattering shows that the atoms have the same size *in solution*.[2] The second approach, e.g., Friedel[5] and Varley,[13] attempts to predict the properties of the solution from data on the pure components.

Considering only nearest neighbors, the quasi-chemical theory expresses the number of unlike bonds, P_{AB}, in terms of the interaction energy:

$$\frac{(P_{AB})^2}{(x_A Z N_0 - P_{AB})(x_B Z N_0 - P_{AB})} = \exp(-2\nu/kT) \qquad (4)$$

and $$H^M = P_{AB}\nu \qquad (5)$$

where: x_A = mol fraction of component A
Z = number of nearest neighbors
T = temperature
N_0 = Avogadro's number
H^M = relative molar enthalpy

Equations (4) and (5) show that positive values of ν/kT indicate a positive relative enthalpy and clustering in the solid solution ($P_{AB}/x_A x_B Z N_0 < 1$), whereas negative values of ν/kT denote a negative relative enthalpy and short range order ($P_{AB}/x_A x_B Z N_0 < 1$).

X-ray results for the Al-rich FCC solutions in the Al-Ag system demonstrate that these solutions are clustered,[2, 3] and this correlates with the positive enthalpy values found in the present investigation. The quantitative agreement, however, is not impressive. The X-ray measurement for alloy $x_{Ag} = 0.10$ at 813°K[2] gives a value of $\nu/kT = 0.6$, using equation (4), whereas the enthalpy data determined here correspond to a value of $\nu/kT = 0.1$.

For Ag-rich FCC alloys, the thermodynamic data (Fig. 4) indicate negative values for H^M, implying short-range order. This was confirmed by diffuse X-ray scattering measurements on these alloys.[14] The quantitative agreement is only fair, however; for $x_{Ag} = 0.815$ at 733°K, the X-ray method gives $\nu/kT = -0.4$, whereas at 820°K the thermodynamic data yield $\nu/kT = -0.1$ for the same alloy. At any rate, both the X-ray and thermodynamic observations indicate a value of $\nu > 0$ in FCC Al-rich alloys and a value of $\nu < 0$ in FCC Ag-rich alloys.

It is not surprising that the values of ν/kT do not agree well when derived from X-ray vs. thermodynamic sources. It is assumed that either ν is independent of composition or E_{AB} alone varies with composition. Rudman[14] has pointed out, however, that equation (5) should be corrected to include the variation in E_{AA} and E_{BB} with composition in the form:

$$H^M = P_{AB}\nu + \tfrac{1}{2}ZN_0/2[x_A(E_{AA} - E_{AA}^\circ) + x_B(E_{BB} - E_{BB}^\circ)] \qquad (6)$$

where E_{AA}° refers to the bond energy in pure A. It is then possible to obtain good agreement between the thermodynamic and X-ray findings by assuming values of $(E_{AA} - E_{AA}^\circ)$ and $(E_{BB} - E_{BB}^\circ)$, but at the expense of introducing two new arbitrary variables.

Friedel's theory[5] predicts clustering and a negative second derivative of H^M with composition when the solvent has higher valence than the solute (e.g., at the Al-rich side of Al-Ag), but an ordering tendency and

a positive second derivative of H^M when the solvent has lower valency than the solute (e.g., at the Ag-rich side of Al-Ag). Thus, the thermodynamic and the X-ray measurements on the Al-Ag system lend support to this concept. However, the theory does not describe a solid solution in terms of nearest-neighbor bonds, and therefore it does not relate the thermodynamic and X-ray results by means of equations (4) and (5). Furthermore, it deals only with the sign of the second derivative of H^M, not with the sign of H^M itself. Accurate H^M data are needed for a critical test.

Friedel's theory is also consistent with the results on FCC Al-Zn alloys,[2] since a clustering tendency and a negative second derivative of H^M on the Al-rich side of the Al-Zn system have been found. The Zn-rich side of the system cannot be investigated in detail, due to the presence of the intermediate two-phase region, but the fact that the peak of the miscibility gap lies on the Al-rich side of the diagram indicates that the clustering tendency, if any, may be smaller on the Zn-rich side.

The thermodynamic properties of the hypothetical transformation Zn (HCP) → Zn (FCC) were estimated from the measured thermodynamic data of the Al-Zn alloys[7] and the phase diagram, giving $\Delta H = 500\ R$ and $\Delta S = 0.5\ R$. From these values, it is possible to approximate the relative thermodynamic properties of metastable FCC Al-Zn alloys in the Zn-rich region. These alloys show a positive second derivative of H^M vs. x_{Zn}, in agreement with Friedel's theory.

Varley's treatment[13] is not applicable to the Al-Zn and Al-Ag alloys. The only positive contribution to the enthalpy in this theory arises from the strain energy associated with the presence of atoms of different sizes. Hence, it does not account for the X-ray and thermodynamic data in these systems, since the solute and solvent atoms have the same sizes in solution.

4.2. *Early Stages of Age-hardening*

The variation of v with composition may provide an interesting picture of the early stages in age-hardening. Fig. 5 shows a free energy diagram for FCC Al-Ag alloys at 373°K. It has been constructed from the enthalpy and entropy data determined at 820°K, assuming these quantities to be independent of temperature. Consider an alloy of composition $x_{Ag} = 0.10$ quenched from a high temperature to 373°K. It is then within a miscibility gap and there is a tendency for the formation of Ag-rich clusters. If the strain and surface energy are assumed to be independent of composition, the most favorable composition for a cluster is found at the point which has a tangent with the same slope as the tangent through the point $x_{Ag} = 0.10$.[15] This represents the precipitate for which there is the largest decrease in volume free energy, and this composition is about $x_{Ag} = 0.65$, according to Fig. 5. It is thus to be expected that clusters of high Ag content are formed in the age-hardening alloy. These clusters might be identical with what Hardy calls GP zones [1].[1] Although v is positive for the matrix with low Ag content, it is negative at the composition of the clusters. Accordingly, there is a tendency for ordering within the clusters. Such ordered clusters may be identified with the next stage in the age-hardening of Al-Ag alloys, called GP zones [2] by Hardy.

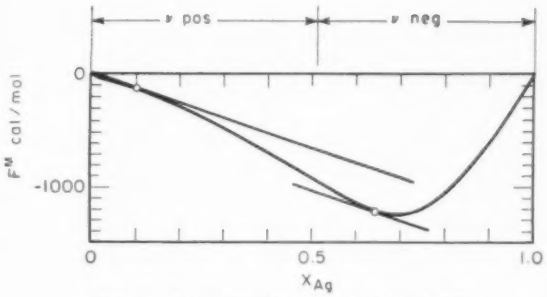

FIG. 5. F^M at 373°K in metastable FCC Al-Ag alloys.

5. SUMMARY

The thermodynamic data determined here indicate positive values of H^M in FCC Al-rich alloys and negative values in FCC Ag-rich alloys in the Al-Ag system. These results are consistent with the clustering and short-range order in the Al-rich and Ag-rich solutions respectively, as observed by X-ray methods. Both Friedel's theory and the quasi-chemical approach apply qualitatively, but neither theory is confirmed quantitatively.

The thermodynamic activities show positive deviations from Raoult's law in the Al-rich alloys, and negative deviations in the Ag-rich alloys. All of the solid phases examined in this system exhibit large excess entropies of mixing, despite the similarity in size of the component atoms. Possibly new vibrational modes are introduced because of the difference in atomic masses.

ACKNOWLEDGMENTS

This paper is based on a thesis submitted by Mats Hillert in partial fulfillment of the requirements for the S.M. degree at the Massachusetts Institute of

VOL. 4 1956

Technology in August 1954. The work was sponsored by the U.S. Atomic Energy Committee under Contract No. AT(30–1)–1002.

The authors are grateful to Dr. P. S. Rudman and Professor Carl Wagner for many helpful discussions, and to B. Howell and R. L. Goss for experimental assistance. The sponsorship of the U.S. Atomic Energy Commission is also gratefully acknowledged.

REFERENCES

1. H. K. Hardy and T. J. Heal, *Progress in Metal Physics*, **5**, 143 (1954).
2. P. S. Rudman and B. L. Averbach, *Acta Met.*, **2**, 576 (1954)
3. C. B. Walker, J. Blin, and A. Guinier, *Compt. rend.*, **235**, 254 (1952).
4. G. V. Raynor and D. W. Wakeman, *Phil. Mag.*, **40**, 404 (1949).
5. J. Friedel, *Adv. in Physics*, **3**, 446 (1954).
6. C. Wagner, *Thermodynamics of Alloys* (Cambridge, Mass., Addison-Wesley Press, 1952).
7. J. E. Hilliard, B. L. Averbach, and M. Cohen, *Acta Met.* **2**, 621 (1954).
8. L. L. Seigle, M. Cohen, and B. L. Averbach, *Trans. Amer. Inst. Min. Met. Eng.*, **192**, 1320 (1952).
9. K. Hirano and Y. Takagi, *J. Phys. Soc. Japan*, **9**, 730 (1954).
10. Y. H. Chou and J. F. Elliott, unpublished work, mentioned by J. Chipman, *Faraday Soc. Disc.*, **4**, 23 (1948).
11. J. L. Meijering, *Rev. de Metall.*, **49**, 906 (1952).
12. B. L. Averbach, P. A. Flinn, and M. Cohen, *Acta Met.*, **2**, 92 (1954).
13. J. H. O. Varley, *Phil. Mag.*, **45**, 887 (1954).
14. P. S. Rudman, Sc.D. Thesis, Dept of Metallurgy, M.I.T., Jan. 10, 1955.
15. M. Hillert, *Acta Met.*, **1**, 764 (1953).

VOL
4
195

CALORIMETRIC STUDY OF THE AUSTENITE : PEARLITE TRANSFORMATION*

W. C. HAGEL†, G. M. POUND‡, and R. F. MEHL†‡

A high temperature, continuously recording, constant heat-flow calorimeter was used to measure the specific heats of austenite and pearlite in eutectoid plain carbon and alloy steels and the enthalpy of the pearlite-austenite transformation as a function of alloy content. The precision of the present method is estimated to be ± 5 per cent.

The specific heats of austenite and pearlite of eutectoid composition are reported from 400 to 850°C. The addition of 0.80 per cent carbon causes an increase in specific heat relative to pure iron. Small additions of manganese, molybdenum, or cobalt, and variation of pearlite spacing, have no appreciable effect on specific heat.

The enthalpy of the austenite : pearlite transformation for a plain carbon eutectoid steel was found to be 19.6 cal gm^{-1} at the eutectoid temperature of 727°C. This is in good agreement with the value of 20.0 cal gm^{-1} calculated from the thermodynamic tables of Darken and co-workers. Additions of manganese (1.85 per cent) or molybdenum (0.51 per cent) lower the enthalpy of transformation to 18 cal gm^{-1}, and cobalt (1.91 per cent) increases it to 23 cal gm^{-1}.

The free energy of the transformation was calculated from the calorimetric data. The free-energy change is decreased by manganese and molybdenum and increased by cobalt. The effect of these alloying elements is in accord with Zener's prediction, and is of some consequence in the theory of pearlite growth.

ETUDE CALORIMÉTRIQUE DE LA TRANSFORMATION AUSTENITE-PERLITE

Un calorimètre pour hautes températures à enregistrement continu a été utilisé pour la mesure de la chaleur spécifique de l'austenite et de la perlite dans les aciers eutectoide et alliés et à la mesure de l'enthalpie de la transformation perlite-austenite en fonction de la composition. La précision de cette méthode est estimée à $\pm 5\%$. La chaleur spécifique de l'austenite et de la perlite à l'eutectoide est donnée entre 400 et 850°. L'addition de 0,8 de carbone accroît la chaleur spécifique du fer pur. De petites additions de manganèse, de molybdène, de cobalt ou des variations dans la périodicité de la perlite n'ont aucun effet appréciable sur la chaleur spécifique. L'enthalpie de la transformation austenite-perlite pour un acier eutectoide au carbone est de 19,6 cal g^{-1} à la température eutectoide de 727°. Ceci est en bon accord avec la valeur de 20,0 cal g^{-1} calculée à partir des tables de Darken et de ses callaborateurs. L'addition de manganèse (1,85%) ou de molybdène (0,51%) abaisse l'enthalpie de la transformation à 18 cal g^{-1}, celle de cobalt (1,91%) l'augmente à 23 cal g^{-1}.

L'énergie libre de la transformation a été calculée à partir des mesures calorimétriques. Le changement de l'énergie libre est diminué par le manganèse et le molybdène et accru par le cobalt. Cet effet des éléments d'addition est conforme aux prévisions de Zener et est important pour la théorie de la croissance de la perlite.

KALORIMETRISCHE UNTERSUCHUNGEN DER AUSTENIT-PERLIT UMWANDLUNG

Zur Messung der spezifischen Wärmen von Austenit und Perlit in eutektoiden Kohlenstoffstählen und in legierten Stählen, sowie zur Bestimmung der Enthalpie der Perlit-Austenit Umwandlung in Abhängigkeit vom Legierungsgehalt wurde ein Hochtemperaturkalorimeter mit kontinuierlicher Schreibvorrichtung und konstantem Wärmefluss herangezogen. Die Genauigkeit der Methode beträgt schätzungsweise $\pm 5\%$.

Die spezifischen Wärmen des Austenits und des Perlits bei der eutektoiden Zusammensetzung werden für einen Temperaturbereich von 400 bis 850°C angegeben. Bezogen auf reines Eisen verursacht die Zugabe von 0,8% Kohlenstoff eine Erhöhung der spezifischen Wärme. Geringe Zusätze von Mangan, Molybdän oder Kobalt und eine Veränderung des Lamellenabstandes des Perlits haben keinen wesentlichen Einfluss auf die spezifische Wärme.

Bei der Temperatur des Eutektoids von 727°C hat die Enthalpie der Perlit-Austenit Umwandlung eines reinen Kohlenstoffstahles einen Wert von 19,6 cal gm^{-1}. Der Wert zeigt gute Übereinstimmung mit dem aus den thermodynamischen Tabellen von Darken und Mitarbeitern berechneten Wert von 20,0 cal gm^{-1}. Zusatze von Mangan (1,85%) oder Moybdän (0,51%) erniedrigen die Enthalpie der Umwandlung auf 18 cal gm^{-1}, während Kobalt sie auf 23 cal gm^{-1} erhöht.

Aus den kalorimetrischen Werten wurde die freie Energie der Umwandlung berechnet. Die Änderung der freien Energie bei der Umwandlung wird durch Mangan und Molybdän erniedrigt, durch Kobalt erhöht. Der Einfluss dieser Legierungselemente ist in Übereinstimmung mit den Vorhersagen von Zener und hat gewisse Auswirkungen auf die Theorie des Perlitwachstums.

* Received 21 April, 1955. This paper is from part of a thesis presented by W. C. Hagel to The Committee on Graduate Studies of the Carnegie Institute of Technology, Pittsburgh, Penn., in partial fulfillment of the requirements for the degree of Doctor of Philosophy in Metallurgical Engineering, June 1954.

† Materials and Process Laboratory, General Electric Company, Schenectady, N.Y.; formerly with Department of Metallurgical Engineering, Carnegie Institute of Technology, Pittsburg, Penn.

‡ Department of Metallurgical Engineering, Carnegie Institute of Technology, Pittsburgh, Penn.

VOL. 4 1956

1. INTRODUCTION

Thermodynamic information on alloy systems is of obvious general importance. It is of especial importance to metal systems that exhibit transformation in the solid state, for, whatever the mechanisms of these transformations, thermodynamic data must be involved in theory. In the case of the austenite : pearlite transformation, for example, a transformation which, in either direction, proceeds by a nucleation and growth process, the free-energy change is currently an essential part of the theory of the rate of nucleation and of the rate of growth. These matters have recently been extensively reviewed for this particular transformation.[1]

The present paper reports an experimental attempt to measure the free-energy changes accompanying the austenite : pearlite transformation, for a simple-carbon eutectoid steel and for Mn-, Mo-, and Co-eutectoid steels.

2. EXPERIMENTAL METHOD

2.1. *Principle of Constant Heat-flow Calorimeter*

A constant heat-flow calorimeter similar to that described by C. S. Smith[2] was used to obtain the specific heats of austenite and pearlite and the latent heat of the transformation. The basic technique consists of surrounding the metal specimen with a refractory container of low thermal conductivity and placing the assembly in a furnace, the temperature of which is maintained at a constant level above the specimen temperature. The specimen temperature is measured by a thermocouple extending to the specimen's interior; for the determination of specific heat, a differential thermocouple with junctions inside and outside the container is used to control the furnace temperature. In this manner a constant temperature-difference is maintained across the container walls. Heat-flow through the refractory is then constant at a given temperature, since thermal conductivity of refractory remains constant; the heat gained by the specimen in a given time-interval is also constant. Therefore, the time taken to increase the specimen temperature a given interval is proportional to the heat absorbed. In practice, heat-flow varies slightly with temperature owing to changes in refractory thermal conductivity and e.m.f. difference of opposed thermocouples, but the variation can be determined by use of a specimen of known specific heat to give reproducible results.

The steady-state transmission of heat by conduction through the container walls can be expressed by the Fourier relationship

$$q = k S_F \Delta T \qquad (1)$$

where q = heat-flow,

k = thermal conductivity of container,

S_F = container-shape factor,

ΔT = temperature difference between inner and outer surfaces.

For a given calibrated container, K and S_F are constant, and ΔT is held constant experimentally. The resulting constant heat-flow serves to supply specimen specific heat, heat of transformation, and the specific heat of part of the container as follows

$$q\Delta t_1 = C_1 W_1 \Delta T_1 + W_1 \Delta H_1 + C_R W_R \Delta T_1 \qquad (2)$$

where ΔT_1 = temperature change in time Δt_1,

ΔH_1 = enthalpy of transformation occurring within ΔT_1,

C_1 and C_R = specific heats of specimen and container,

W_1 and W_R = masses of specimen and container.

When the container is empty, equation (2) reduces to

$$q\Delta t_R = C_R W_R \Delta T_R. \qquad (3)$$

If experiments are made with specimens of the same dimensions but of different weights and specific heats, omitting any heats of transformation, equations (2) and (3) can be combined as follows

$$q = \frac{C_2 W_2}{\left(\frac{\Delta t}{\Delta T}\right)_2 - \left(\frac{\Delta t}{\Delta T}\right)_R} = \frac{C_1 W_1}{\left(\frac{\Delta t}{\Delta T}\right)_1 - \left(\frac{\Delta t}{\Delta T}\right)_R}$$

$$C_1 = \frac{W_2}{W_1} \cdot C_2 \cdot \frac{\left(\frac{\Delta t}{\Delta T}\right)_1 - \left(\frac{\Delta t}{\Delta T}\right)_R}{\left(\frac{\Delta t}{\Delta T}\right)_2 - \left(\frac{\Delta t}{\Delta T}\right)_R} \qquad (4)$$

The quantities $\frac{\Delta t}{\Delta T}$ are the slopes of time-temperature heating curves for the empty container (subscript R), the calibration specimen (subscript 2), and the specimen under study (subscript 1). If the specific heat of the calibration specimen is known over a wide range, then the specific heat of the specimen under study can be determined at any temperature within that range.

When a heat of transformation is absorbed at a single temperature or within a very small temperature interval, it can be given by the equation

$$q\Delta t' = \Delta H_1 W_1 \qquad (5)$$

where $\Delta t'$ = arrest time when $\Delta T = 0$.

Combination with the expression for the calibration specimen gives

$$q = \frac{\Delta H_1 W_1}{\Delta t'} = \frac{C_2 W_2}{\left(\frac{\Delta t}{\Delta T}\right)_2 - \left(\frac{\Delta t}{\Delta T}\right)_R}$$

or

$$\Delta H_1 = \frac{W_2}{W_1} \cdot C_2 \cdot \frac{\Delta t'}{\left(\frac{\Delta t}{\Delta T}\right)_2 - \left(\frac{\Delta t}{\Delta T}\right)_R} \qquad (6)$$

Whenever a transformation occurs over a temperature range, its heat will appear as apparent specific heat, and a graphical integration is required for a complete solution.

2.2. *Furnace Assembly*

A diagram of the interior arrangement of specimen within the wire-wound furnace is presented as Fig. 1, and Fig. 2 shows the same parts photographed in a dismantled condition. The Nichrome-wire furnace is constructed by winding 20-gauge wire around a 1.5-foot collapsible mandrel. End losses are compensated by spacing turns more closely near the ends and using an excess of insulation. By taking temperature readings at 0.5-inch intervals within the furnace throughout the range of operation (400 to 850°C), it is eventually possible to arrive at a winding spacing which gives a 6-inch uniform heating zone completely surrounding the container. The life of a well-constructed furnace is about thirty heating and cooling cycles.

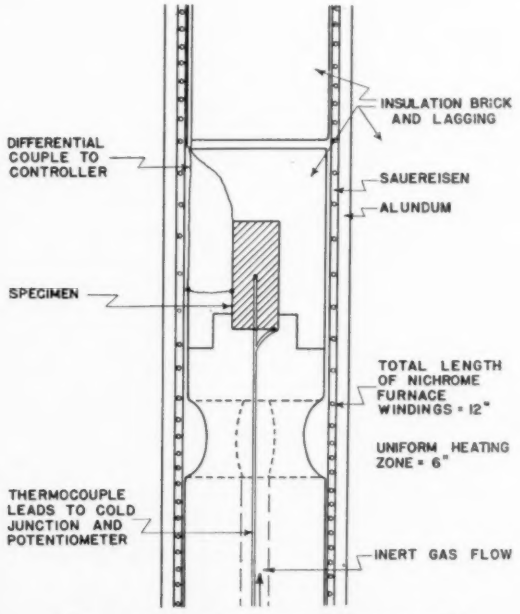

FIG. 1. Interior arrangement of apparatus for measuring specific and latent heats.

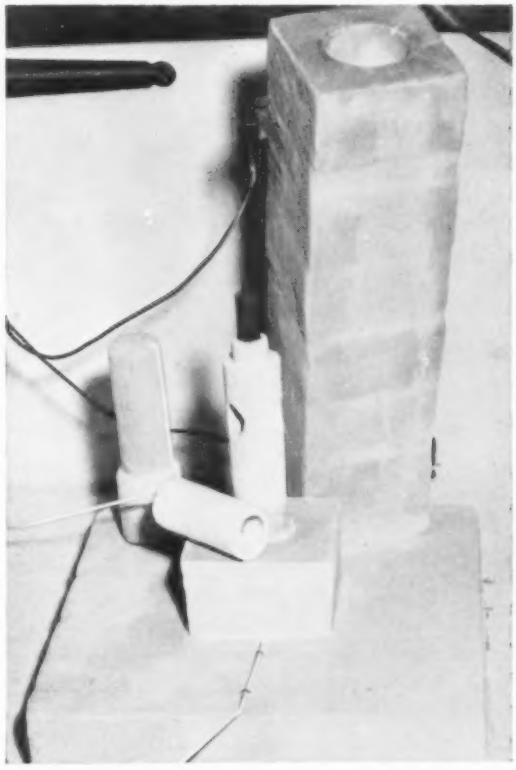

FIG. 2. Apparatus photographed in a dismantled condition.

The specimen has a diameter of 0.688 in., is 1.562 in. long, and weighs about 70 to 80 g, depending on material density. To give the same emissivity to the calibration specimens as the steel specimens, all specimen surfaces are rough-machined and evenly coated with colloidal graphite. The container, with wall 0.625 in. thick, is shaped by hand from a block of Armstrong LW-20 insulating brick. Careful shaping makes it possible to replace the specimen, container, and furnace in the same position over many heating cycles.

The specimen thermocouple, encased in thin ceramic tubing, is led up through the pedestal base to the center of the specimen. The differential thermocouple is positioned near the mid-portion of the container, and its leads are brought out the top of the furnace.

Prior to calorimeter operation, the specimen is placed on the pedestal, the container is positioned over the specimen, and the furnace is centered around the junction. An insulating cap is placed directly above the container, through which the differential thermocouple wires lead to the controller. The specimen

VOL. 4 1956

thermocouple remains intact until another container and pedestal must be used. Return of parts to their positions of original calibration is accomplished by means of fiducial markings, so that specimens can be inserted and removed with a minimum of disturbance to calibrated surroundings. Inert gas-flow is maintained under slight pressure from the center of the pedestal to the semi-sealed insulating cap. A large amount of lagging is placed around the furnace; though furnace interior approached 900°C, the exterior of the lagging is at room temperature.

The thermocouples used for temperature measurement and furnace control were made from 28-gauge chromel P-alumel wires, and calibrated by standard methods. It appeared that these thermocouples were accurate to ± 0.5°C.

2.3. *The Electrical System*

A Brown electronic two-second stripchart potentiometer is used to record time-temperature curves for slope determinations. For most experiments, a chart speed of 240 in. per hour, a span of 1.6 millivolts, and suppressions in steps of 1.60 millivolts are used. Since its 12-inch chart is evenly graduated from 0 to 100, a temperature calibration must be made against a potentiometer for millivoltage-temperature conversion of chart readings.

Satisfactory control of temperature difference is obtained by use of a Brown differential recording controller combined with an electronic position-proportioning relay with automatic reset. The circular chart is evenly graduated from 0 to 100°C in temperature difference, and makes one revolution every four hours, which is approximately the time required for recording one thermal curve. Differential temperature actuation is from chromel P-alumel thermocouple junctions positioned inside and outside the refractory container. Most experiments are conducted at temperature differences of 30 to 50°C, and maximum variation for short times from control temperature is of the order of ± 0.2°C.

2.4. *Gas Purification*

To prevent specimen oxidation and decarburization, a purified nitrogen gas atmosphere is maintained within the calorimeter at a pressure slightly greater than atmospheric. The gas is passed through a drying tower containing calcium chloride, and then over copper chips heated at 600°C, to the pedestal from which it rises out through the top of the furnace. Microscopic examination of specimen surface showed no evidence of decarburization or oxidation.

2.5. *Specimen Preparation*

Simple carbon and alloy eutectoid steels were received from Vanadium-Alloy Steel Company in the form of annealed 1-inch round bars. These materials were cast as 3-inch square ingots weighing about 30 lb. The ingots were annealed at 900°C, hammer-cogged to 1.75-inch square billets from 1120°C, rolled to 1-inch rounds from 1040°C, and annealed at 900°C for twenty hours to minimize banding. The chemical analyses of heats found suitable for use are as follows:

Composition—Weight per cent

C	Si	Mn	S	P	Mo	Co
0.80	0.22	0.27	0.016	0.011	—	—
0.79	0.22	1.85	0.011	0.020	—	—
0.79	0.19	0.12	0.005	0.005	0.51	—
0.79	0.22	0.12	0.014	0.005	—	1.91

Additional heat treatment, microscopic examination, and thermal analyses have shown these steels to be very close to eutectoid composition. The presence of ferrite or cementite is not observed outside the eutectoid structure, and temperature arrests take place over a narrow temperature range. The isothermal transformation techniques used to obtain suitable interlamellar spacings for these steels have long been standard procedure.

The oil-quenched 0.75-inch rounds were further machined to calorimeter specimen size, and a 0.25-inch endpiece was removed for metallographic examination and interlamellar spacing determination. Any traces of decarburization were removed by this machining operation. All the metallographic specimens were electropolished and given a light Nital etch. The procedure developed by Pellissier *et al.*[3] for determining interlamellar spacing was modified to avoid needless photography, and readings were made directly with a stage microscope at 850 diameters. Considering possible errors, these interlamellar spacing measurements are probably accurate from ± 5.0 to ± 10.0 per cent. The photomicrographs in Figs. 3 and 4 show the appearance of pearlites in the various eutectoid steels, and their spacing variation from coarse to fine structures.

2.6. *Operational Procedure*

The description which follows will outline the steps which must be taken to determine the specific and transformational heats of one steel specimen. A complete measurement cycle consists of first heating the furnace assembly to about 500°C to remove moisture held by the insulation brick. Time-temperature curves are then obtained (1) without a specimen in the apparatus, (2) with a copper calibration specimen, and (3) with the steel specimen under investigation.

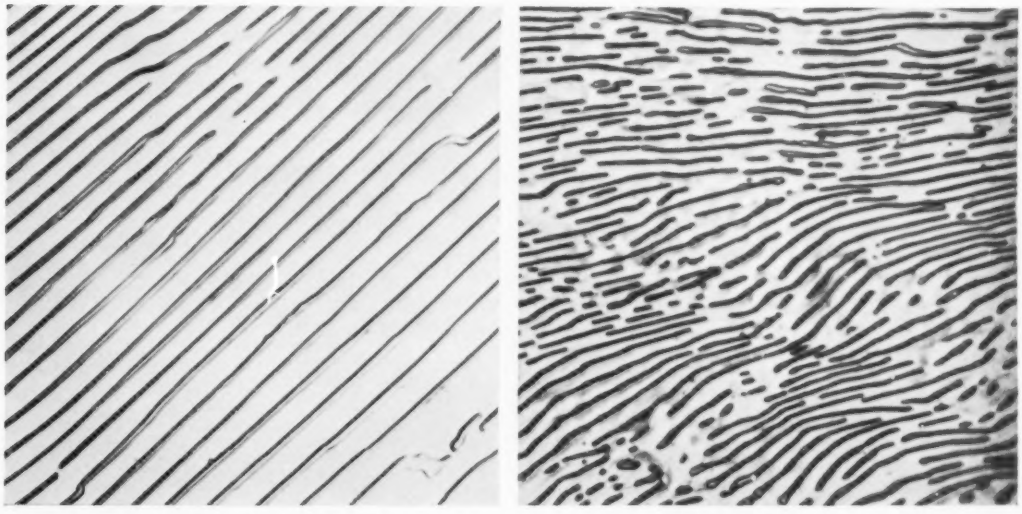

(i) Fe-C Spec. No. 79, 19,000 Å

(ii) Fe-C Spec. No. 22, 12,000 Å

(iii) Fe-C Spec. No. 6, 4440 Å

(iv) Fe-C Spec. No. 8, 2500 Å

FIG. 3. Photomicrographs of iron-carbon eutectoid steel electropolished ×1500 nital etch.

VOL. 4 1956

The rate of heating can be varied by changing container-wall thickness, container material, or temperature difference between the inside and outside of the container. Heating too rapidly is avoided in order to obtain a constant temperature of transformation, but too slow a rate causes spheroidization of the pearlite and decreases the sharpness of the transformation. In order to employ specimens of known interlamellar spacings, all reported measurements were made on a heating cycle.

2.7. *Determination of Thermal Values from Calorimetric Data*

Referring to equations (4) and (6), Kelley[4] reports that the specific heat of solid copper can be expressed as $C_2 = 8.52 \times 10^{-2} + 2.36 \times 10^{-5}\ T$ calories gram^{-1} °K^{-1}. The masses W_1 and W_2 of the steel and calibration specimens were weighed on an analytical balance. The ratios $\left(\frac{\Delta t}{\Delta T}\right)_1$, $\left(\frac{\Delta t}{\Delta T}\right)_2$, and $\left(\frac{\Delta t}{\Delta T}\right)_R$ are

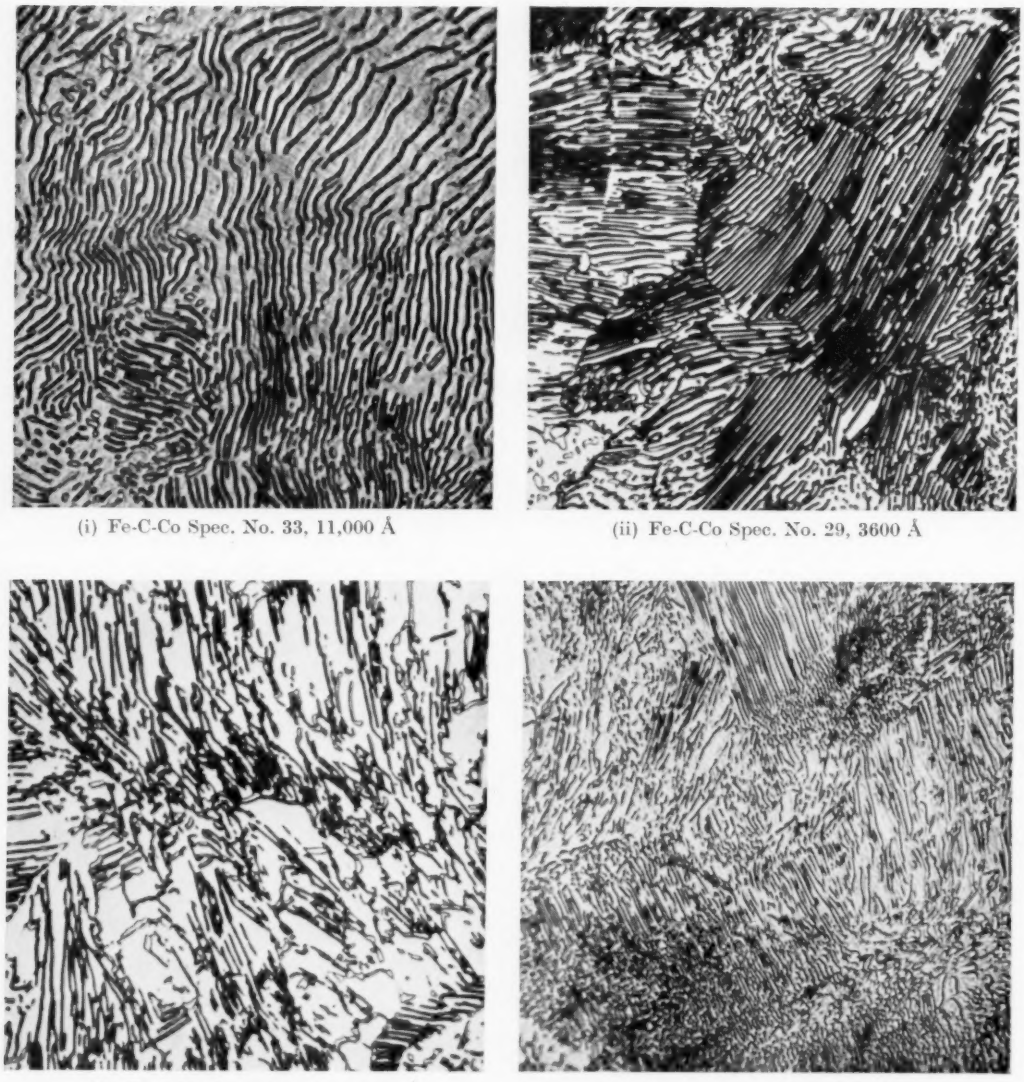

(i) Fe-C-Co Spec. No. 33, 11,000 Å

(ii) Fe-C-Co Spec. No. 29, 3600 Å

(iii) Fe-C-Mo Spec. No. 70, 10,000 Å

(iv) Fe-C-Mn Spec. No. 42, 3300 Å

FIG. 4. Photomicrographs of alloy eutectoid steels electro-polished ×1500 nital etch

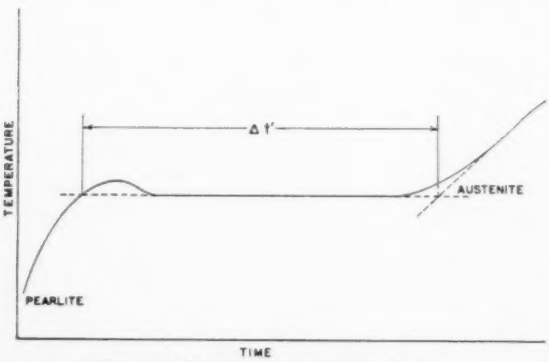

FIG. 5. Schematic representation of a temperature arrest.

the slopes at any given temperature of time-temperature curves obtained on heating the steel specimen, the calibration specimen, and the empty container. The arrest time $\Delta t'$ is measured as the time-interval intercepted by the minimum arrest temperature through the thermal curve of pearlite and the extended thermal curve of austenite. To illustrate this, a schematic representation of an arrest is given in Fig. 5. Fig. 6 is a photograph of the thermal curve for an empty container, and Fig. 7 shows the beginning of an arrest for pearlite-austenite transformation.

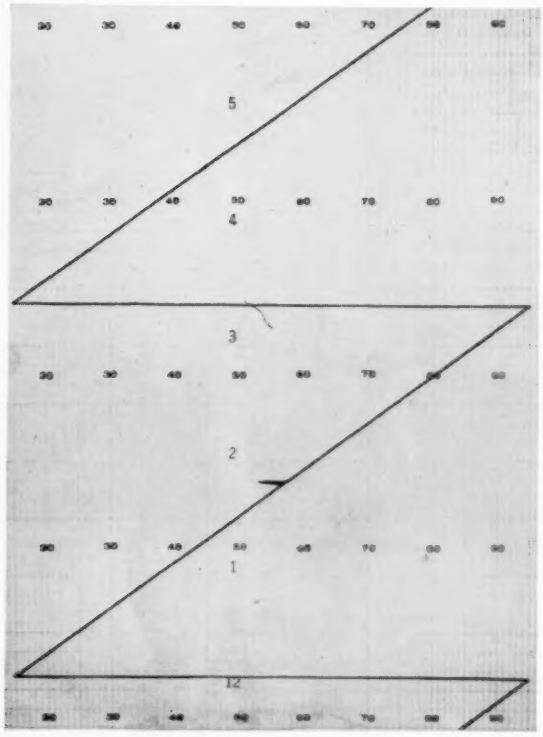

FIG. 6. Section of recorder time-temperature chart for a blank run.

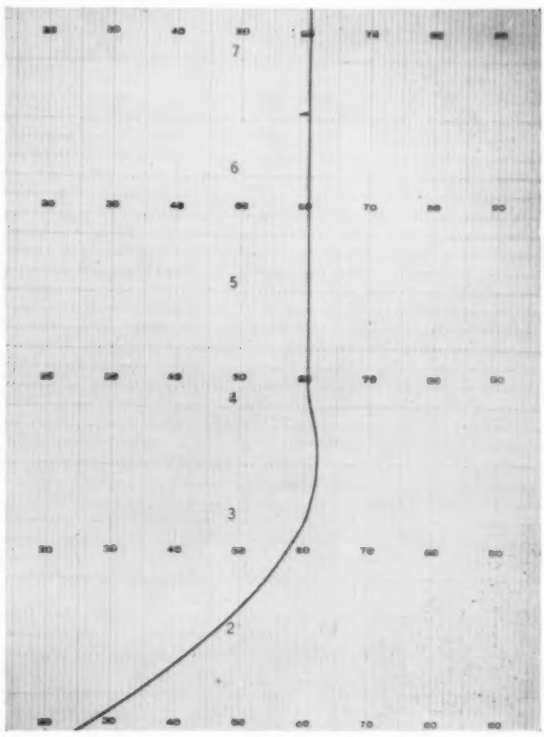

FIG. 7. Appearance of the beginning of a pearlite-austenite transformation.

VOL. 4 1956

3. EXPERIMENTAL RESULTS

3.1. *Specific Heats*

Fig. 8 is an example of an inverse heating curve for a steel specimen of mean interlamellar spacing equal to 4400 Å. One can see how the heating curve for pearlite increases prior to a transformation in accord with the increasing specific heat of the ferrite as it approaches its ferromagnetic transformation at 760°C. The arrest time for this steel is 1030 seconds at a temperature of 737°C. A heating rate of approximately 3°C minute^{-1} was obtained by a differential-controller temperature difference of 45°C. Based on equation (4), a sample specific heat calculation for a specimen (number 6) at 510°C is as follows:

$$C_S = \frac{83.7837}{72.4320} \times 0.1036 \times \frac{(83.5 - 28.0)}{(68.0 - 28.0)}$$

$$= 0.166 \text{ calories gram}^{-1}\ ^\circ\text{C}^{-1}$$

The calculation of about twenty specific heat curves for plain-carbon and low-alloy eutectoid steels was averaged to give the pearlite and austenite specific heats plotted in Fig. 9. Within the error of the calorimeter (± 5 per cent, as established by a specific heat

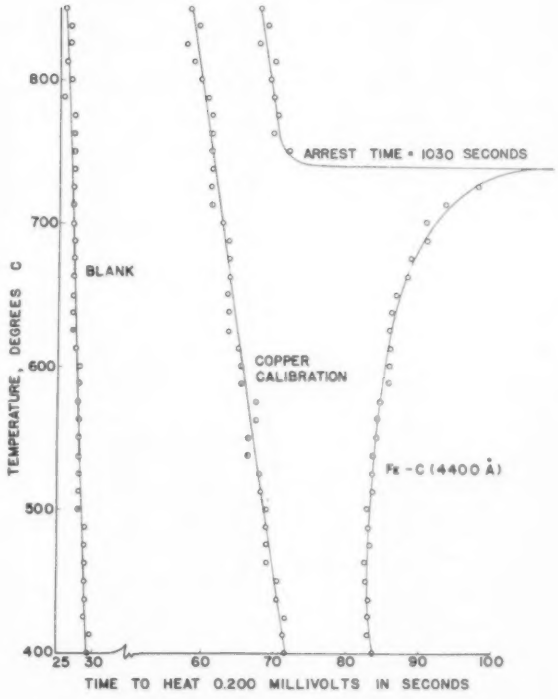

FIG. 8. Inverse heating curve for a carbon eutectoid steel.

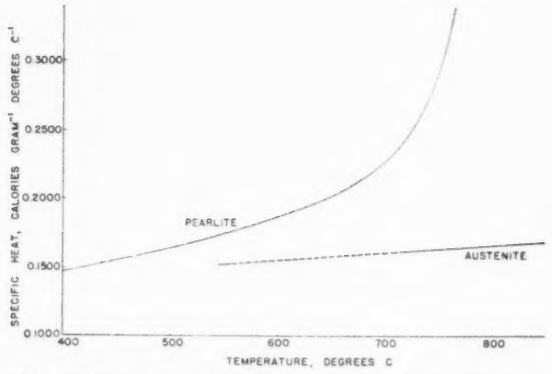

FIG. 9. Experimental specific heat of pearlite and austenite for plain-carbon and low-alloy eutectoid steels. (Best curves for all points of present work. Maximum deviation = ±5 per cent).

determination on pure nickel), variation in interlamellar spacing and low alloy content appears to cause no significant deviation from these average curves. The line connecting the pearlite specific heat curve to the austenite specific heat curve was not drawn for this average curve, since different transformation temperatures were observed for specimens of various spacings and alloy content. Comparison of the present data for steels with the specific heat of pure iron, as compiled by Darken and R. P. Smith,[5] shows that a carbon content of 0.80 per cent does slightly increase specific heat, as first observed by Esser and Baerlecken.[6] Little effect is caused by the presence of manganese, molybdenum, or cobalt on the specific heat. This might be expected, in view of the similarity in thermal properties of the latter elements to pure iron. Any heat effects caused by alloy partitioning were not observed. The present specific-heat data for plain-carbon eutectoid steel are in fair agreement with the results of Awbery and Snow[7] and Esser and Baerlecken,[6] except that the new pearlite specific-heat data are somewhat lower at temperatures (700–730°C) just preceding the transformation.

3.2. *Enthalpies of Transformation*

Table 1 gives the experimental results. All values refer to one gram of material. As an aid in explanation,

TABLE 1. Experimental results

	Specimen No.	s Å	α-Fe_3C A $\times 10^{-3}$cm²	T_T °C	ΔH_T cal g^{-1}	ΔH_{T_0} cal g^{-1}	$\Delta H_{T^0}{}^G$ cal g^{-1}
Fe—C	57	1,400	18.0	735.9	18.2	19.1	18.9
	8	2,500	10.1	735.8	18.1	19.0	19.2
	63	3,300	7.74	735.6	18.4	19.3	19.3
	12	3,400	7.4	737.0	18.1	19.1	19.3
	7	3,500	7.2	736.0	18.1	18.9	19.3
	13	3,800	6.8	737.5	17.9	19.0	19.3
	4	4,200	6.1	738.0	18.4	19.5	19.3
	6	4,400	5.8	737.2	18.3	19.3	19.3
	68	5,000	5.1	738.6	17.8	19.0	19.4
	9	5,900	4.3	737.7	18.2	19.3	19.4
	16	6,800	3.8	739.4	18.4	19.7	19.4
	19	8,100	3.2	738.6	18.5	19.7	19.4
	21	10,500	2.4	740.8	18.5	19.9	19.5
	22	12,400	2.1	740.7	18.4	19.8	19.5
	79	19,400	1.3	741.6	17.8	19.3	19.5
Fe—C—Mn	42	3,300	7.7	722.8	16.8	17.4	17.7
	38	3,600	7.2	720.8	17.1	17.6	17.8
	45	3,600	7.1	723.4	17.4	18.1	17.8
	44	4,000	6.3	723.8	17.0	17.7	17.8
	46	5,100	5.0	725.6	16.8	17.6	17.8
	74	5,700	4.5	725.5	17.2	18.0	17.9
Fe—C—Mo	71	54	4.8	734.4	16.8	17.2	17.5
	56	58	4.4	737.8	16.9	17.6	17.5
	73	6,500	3.9	738.2	16.9	17.6	17.5
	66	7,300	3.5	741.0	16.8	17.8	17.5
	67	9,300	2.7	742.7	16.6	17.8	17.6
	70	9,900	2.6	740.6	16.2	17.3	17.6
Fe—C—Co	29	3,600	7.1	745.4	21.4	22.6	22.6
	32	3,800	6.8	748.0	20.8	22.3	22.6
	35	3,900	6.5	747.4	21.5	22.9	22.7
	34	5,600	4.5	748.4	21.4	22.9	22.7
	27	7,000	3.6	748.7	21.2	22.8	22.8
	30	7,600	3.3	749.8	20.8	22.5	22.8
	33	11,200	2.3	748.8	20.9	22.5	22.8
	64	11,600	2.2	749.5	21.5	23.2	22.8

the formulae used will be described, and a sample calculation will be carried out for iron-carbon specimen number 6. Referring to Table 1, ferrite-cementite interfacial area

$$A = \frac{2V}{s} \tag{7}$$

where V = volume of 1 gram of steel $= 1/\rho$
ρ = density of eutectoid steel $= 7.83$ g cm^{-3}
s = mean interlamellar spacing

or

$$A_{\#6} = \frac{2 \times 1/7.83}{4.44 \times 10^{-8}} = 5.8 \times 10^{+3} \text{ cm}^2.$$

This expression assumes flat, regular surfaces similar to those seen in Fig. 3 for specimen number 79.

The transformation temperature T_T is reported as the average of several readings made during the minimum portion of an arrest. The enthalpy of pearlite-austenite transformation ΔH_T at the arrest temperature is calculated from equation (6):

$$\Delta H_T = \frac{W_C}{W_S} C_C \frac{\Delta t'}{\left(\frac{\Delta t}{\Delta T}\right)_C - \left(\frac{\Delta t}{\Delta T}\right)_R}$$

or

$$\Delta H_{T\#6} = \frac{83.783}{72.432} \times 0.1091 \times \frac{24.39 \times 1030}{(61.4 - 26.7)/0.200} = 18.3 \text{ cal gm}^{-1}$$

ΔH_{T_0} is the enthalpy change accompanying the transformation of austenite to pearlite at the eutectoid temperature $T_0 = 727$°C. This quantity is obtained from ΔH_T by graphical integration, according to the standard formula

$$\Delta H_{T_0} = \Delta H_T + \int_{T_0}^{T_T} [C_p(p) - Cp(\gamma)]\, dT. \tag{8}$$

The enthalpies of transformation, ΔH_{T_0}, at the bulk equilibrium temperature, T_0, for each steel* can then be plotted as a function of ferrite-cementite interfacial area A. The best straight lines through the data in Fig. 10 were determined by the method of least-squares, and the ordinate intercept at $A = 0$ is the enthalpy of transformation, ΔH_B, when no interfaces are present. Thus, the bulk enthalpy of the pearlite-austenite transformation for a plain-carbon eutectoid steel equals 19.6 cal gram^{-1} at T_0 (727°C). This is in good agreement with the value of 20.0 calculated from

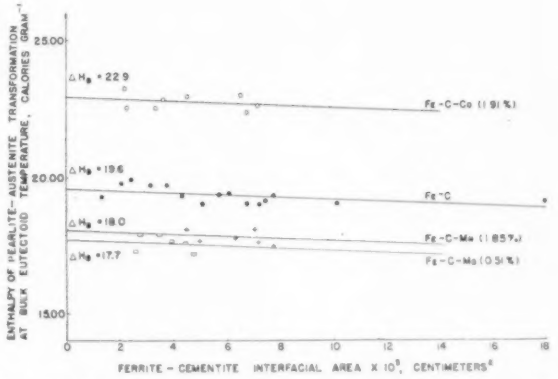

FIG. 10. Variation of enthalpy of transformation with pearlite spacing for plain-carbon and alloy eutectoid steels.

the data of Darken and co-workers, as noted previously.[1] Also, this result is in reasonable agreement with a value of 19.3 cal gram^{-1} obtained in a quenching experiment by Esser and Grass[8] for a 0.82 per cent carbon steel at 723°C. However, Awbery and Snow[7] heated 0.80 per cent carbon steel specimens at a rate of 3°C min^{-1} and obtained an enthalpy of transformation of 10.3 cal gram^{-1} at 730°C.

Additions of manganese or molybdenum lower ΔH_B to 18 cal gram^{-1}, and cobalt increases ΔH_B to 23 cal gram^{-1}. It is believed that the precision of the present method (± 5 per cent) is sufficient to preclude any doubt as to the order of these enthalpy values. Referring to Table 1, $\Delta H_{T_0}{}^G$ is the enthalpy change read from the curve of Fig. 10.

From Fig. 10 it is seen that there is a slight decrease of enthalpy of transformation ΔH_{T_0} with increase in ferrite-cementite interfacial area amounting to about 3 per cent in the present range of interlamellar spacing (1400-19,000 Å). This is about the decrease which would be expected if one assumed a ferrite-cementite interfacial energy of the order of 10^3 ergs/cm^2.[9, 10] However, the estimated precision (± 5 per cent) of the present work is believed not sufficient to demonstrate unequivocally any effect of capillarity. Recent refinements of the calorimetric technique should make possible certain detection of any appreciable capillary effect and estimation of the ferrite-cementite interfacial energy; a report on this work will shortly be forthcoming.

From the measured specific heats and enthalpy of the pearlite-austenite transformation and the equilibrium temperature T_0, the free-energy change can be calculated as a function of temperature by standard methods using the formula

$$\Delta F = T \int_{T_0}^{T} \Delta H\, d(1/T). \tag{9}$$

* The best values for bulk equilibrium temperature were taken from standard sources as 727°C for iron-carbon eutectoid, 715°C when 1.85 per cent Mn is present, 731°C when 0.51 per cent Mo is present, and 735°C when 1.91 per cent Co is present. Actually, this temperature for the alloy steels represents the mean of a small temperature-range of transformation.

VOL. 4 1956

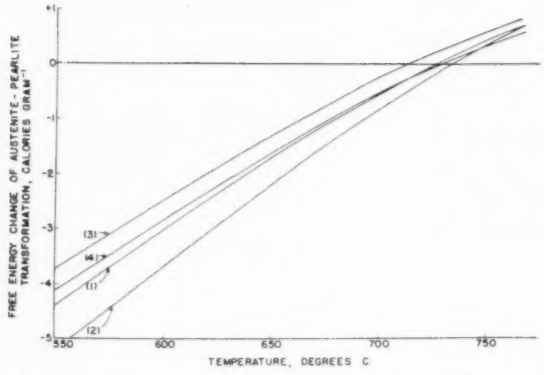

FIG. 11. Free-energy change of austenite-pearlite transformation versus temperature for plain-carbon and alloy eutectoid steels.

(1) Fe—C (bulk)
(2) Fe—C—Co (bulk, 1.91 per cent Co)
(3) Fe—C—Mn (bulk, 1.85 per cent Mn)
(4) Fe—C—Mo (bulk, 0.51 per cent Mo)

The results for representative specimens are plotted in Fig. 11. The values for the alloy steels represent the bulk free-energy changes for the formation of pearlite obtained by isothermal transformations under the conditions given in the section on Experimental Method. Thus, although the degree of alloy partitioning is unknown, the results are definite for these specific pearlites.

The free-energy change is increased by Co (1.91 per cent Co) and decreased by Mn (1.85 per cent Mn) and by Mo (0.51 per cent Mo). This is in accord with Zener's prediction.[10] Zener argued that one-half of the bulk free-energy change for the pearlite reaction must be expended in providing the energy for the ferrite-cementite interface, and the rest dissipated by the accompanying diffusional processes; on this basis it is the latter half that would be obtained from calorimetric measurements on fine pearlites. Assuming all this, then there is more free energy available for the ferrite : cementite interface in Co-steels than in the others, and accordingly the interlamellar spacing in Co-steels should be less and the rate of growth more than in the other steels, as is indeed the case. This relationship as derived should be one of simple proportionality, but there is no simple proportionality between the interlamellar spacing and the rate of growth,[11] and accordingly the principle proposed remains but a qualitative one.[1]

ACKNOWLEDGMENT

This work was supported by the U.S. Army Office of Ordnance Research under Contracts No. DA-36-061-ORD-205 and -350. Thanks are due Dr. G. A. Roberts of the Vanadium-Alloy Steel Co., who supplied the plain-carbon and alloy eutectoid steels.

The authors also wish to express their thanks to Mr. J. J. Kramer, who helped in making calorimeter measurements, and to Mr. Y. T. Chou, who assisted in specimen preparation.

REFERENCES

1. R. F. MEHL and W. C. HAGEL, *Progress in Metal Physics*, Vol. VI (1955).
2. C. S. SMITH, *Trans. Amer. Inst. Min. Met. Eng.*, **137,** 236 (1940).
3. G. E. PELLISIER, M. F. HAWKES, W. A. JOHNSON, and R. F. MEHL, *Trans Amer. Soc. Metals*, **30,** 1049 (1942).
4. K. K. KELLEY, Bureau of Mines Bulletin 476 (1946).
5. L. S. DARKEN and R. P. SMITH, *Industr. engng. Chem.*, **43,** 1815 (1951).
6. H. ESSER and H. BAERLECKEN, *Arch. Eisenhüttenwesen*, **14,** 617 (1941).
7. J. AWBERY and A. SNOW, Spec. Report No. 24-Second Report of the Alloy Steels Research Committee, p. 216 (1939).
8. H. ESSER and H. GRASS, *Stahl und Eisen* **53,** 92 (1933).
9. J. C. FISHER, Eutectoid decomposition in *Thermodynamics in Physical Metallurgy*, American Society for Metals, Cleveland (1949).
10. C. ZENER, *Trans. Amer. Inst. Min. Met. Eng.*, **167,** 550 (1946).
11. R. W. PARCEL and R. F. MEHL, *Trans. Amer. Inst. Min. Met. Eng.*, **194,** 771 (1952).

FRAGMENTATION IN TUNGSTEN CRYSTALS*

G. D. RIECK†

Micro-beam back-reflexion-Laue diagrams were made of W crystals.

The crystals showed often a special fragmentation with small angular differences. After cold bending this fragmentation was more pronounced. The fragmentation occurred mainly in the direction which is approximately perpendicular to the one which corresponds with the normal breaking up of the lattice in the direction of bending. The orientation differences between the particles were 1′–10′ and their dimensions about 10 μ.

As, during drawing, inclusions in the wire will have been stretched out in the wire direction, we may assume predisposition of the crystals to break along planes parallel to the axis.

FRAGMENTATION DANS LES CRISTAUX DE TUNGSTÈNE

Des cristaux de tungstène ont été étudiés avec un microfaisceau par la méthode des diagrammes de von Laue en retour. Les cristaux montrent souvent une fragmentation particulière avec de petites différences angulaires. Après flexion à froid, cette fragmentation est plus marquée et se produit principalement dans la direction perpendiculaire à celle correspondant à la rupture usuelle du réseau dans la direction de flexion. Les différences d'orientation entre les sous-grains sont de 1′ à 10′ et leur dimension de l'ordre de 10 μ. Lors du tréfilage, les inclusions sont allongées parallèle à l'axe du fil, aussi l'on doit admettre une tendance des cristaux à se rompre le long de plans parallèles à l'axe.

DAS AUFBRECHEN VON WOLFRAMKRISTALLEN

Von Wolframkristallen wurden Feinfokusaufnahmen nach dem Laue Rückstrahlverfahren angefertigt.

Die Kristalle zeigten häufig besondersartige Aufbrüche, die um kleine Winkel gegeneinander geneigt waren. Nach einer Kaltbiegung war das Aufbrechen besonders ausgeprägt. Die Bruchbildung trat hauptsächlich annähernd senkrecht zur Biegerichtung auf, in der normalerweise das Aufbrechen des Gitters vor sich geht. Die Orientierungsdifferenzen zwischen den Teilchen betrugen 1′–10′; ihre Grössenordnung betrug etwa 10 μ.

Weil während des Ziehens die Einschlüsse in Richtung der Drahtachse ausgestreckt werden, wird angenommen, dass die Kristalle besonders dazu neigen, parallel der Drahtachse aufzureissen.

VOL. 4 1956

1. INTRODUCTION

In making filaments for incandescent lamps, tungsten‡ is used to which a dope is added in order to obtain properties valuable to the life of the filament. Although this dope evaporates for the larger part from the metal during the preparation and accordingly the resulting tungsten can be considered as rather pure (e.g., 99.99 per cent W), it has still a large effect on the recrystallization. After recrystallization of doped polycrystalline tungsten wire rather large crystals of 1–10-mm length are found. These crystals in wires of 180 μ and 120 μ diameter were used for the experiments to be described in this paper. During the preliminary experiments it was often found that normal back reflexion Laue-diagrams of the crystals of this nature have spots originating from two adjacent crystals which differed only 1°–2° in their orientation. And zones of both crystals were frequently found to run parallel on the diagram. To get a better resolution the Laue-patterns were then made by means of a fine X-ray beam.

2. TECHNIQUE OF THE MICRO-LAUE METHOD

Use was made of a normal sealed-off X-ray tube with Mo-target. The distribution of the emitted radiation over the target surface is not homogeneous; a pinhole photograph reveals this fact (Fig. 1). With

FIG. 1. Pinhole photograph of a (rather bad) focal spot of a normal sealed-off tube (magnification 10 times). Strong vertical lines are seen and many horizontal ones originating from the windings of the coiled cathode.

* Received October 5, 1954; revised version February 17, 1955.

† Philips Research Laboratories, N. V. Philips' Gloeilampenfabrieken, Eindhoven-Netherlands.

‡ Although the International Union of Chemistry recommends the name of wolfram, we will use the name tungsten as is still common practise.

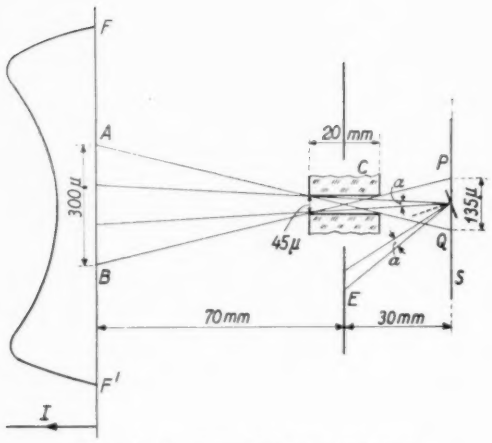

FIG. 2. Arrangement for microbeam back-reflexion diagrams.
C = lead glass capillary
FF' = plane of focal spot, its emitted intensity of radiation (I) at each place is plotted to the left.
PQS = specimen
E = film

normal collimators the effect of a splitting up in a crystal would get mixed up in the diffraction spot with the effect of the irregular focal spot. Therefore we used as collimator a leadglass capillary of about 45 μ internal diameter and of 20 mm length. Placed at about 70 mm distance from the anode of the tube, only part of the focal spot can be "seen" through it. A test film placed at some distance behind the collimator, as well as a back-reflexion Laue diagram of a good crystal, gives rather homogeneous spots. The small parallel lines originating from the coil windings of the cathode (Fig. 1) are normally not resolved. If however a deformation asterism should enlarge the reflexion spot very much and doubt might arise whether a spotty appearance of the streak is due to the focal spot or to irregularities in the crystal, turning the specimen over 90° around the X-ray beam and making another diagram provides a good and easy check.

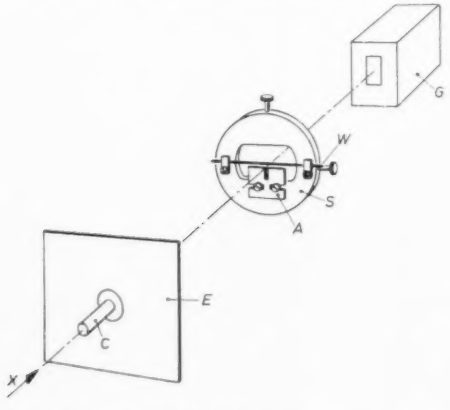

FIG. 3. Sketch of the arrangement.
Through the collimator (C), in the centre of the film (E) the X-ray beam (X) passes a slit in the brass shield (A) mounted below the wire (W) on the sample holder (S), which can be moved horizontally and vertically. The intensity of the beam is measured with a Geiger-counter (G).

Fig. 2 gives a sketch of the arrangement. The film was placed perpendicular to the leadglass capillary. The position of the collimator could be adjusted in a manner similar to that of Hirsch and Kellar.[1] Only one emulsion layer of the film was developed.

With this arrangement a resolution was possible of two reflexions of crystals with an orientation difference of 1′–2′. The irradiated spot of the specimen was about 120–150 μ in diameter.

The tungsten wire was fastened in a horizontal position. Half a mm under the wire a small brass shield in which a very narrow vertical slit was made, was screwed on the sample holder (Fig. 3). With a Geiger-counter the small X-ray beam can be traced and the sample-holder can easily be adjusted (by means of screws) in such a way that the beam passes the top of the slit. By moving the holder downwards the beam falls on the wire in a chosen spot, the Geiger-counter registering the absorption of the wire. With this method the same spot on the wire could always be found again as long as only one end of the wire remained fastened.

Exposure times of about 12–18 hours were necessary (at 45 kV and 20 mA; full wave rectified; Mo tube).

3. INVESTIGATION OF TUNGSTEN CRYSTALS

The tungsten wires, which after drawing have a fiber structure, were recrystallized by heating them by means of an electric current or by heating them in a tungsten tube furnace in which they were placed in a tungsten container. After recrystallizing they were slightly etched; they were handled carefully in order to avoid unintended deformations.

About fifty well developed crystals of at least 3 mm length were investigated with the above-described method. Sometimes the Laue spots occurred in pairs with orientation differences of 1°–2° as mentioned in the introduction.

In the separate spots sometimes no fine structure could be found, but often they were double, three-, or even five-fold (Fig. 4), with clear areas of up to 0.2 mm between the parts, corresponding to orientation differences of about 10′–30′. In some cases this split-up could only be seen under magnification, as darker lines in the spot (orientation differences 2′–10′). Generally the unblacked areas and the darker lines were approximately parallel to the wire direction in all parts of the diagram. About 60 per cent of the diagrams showed spots with this break up.

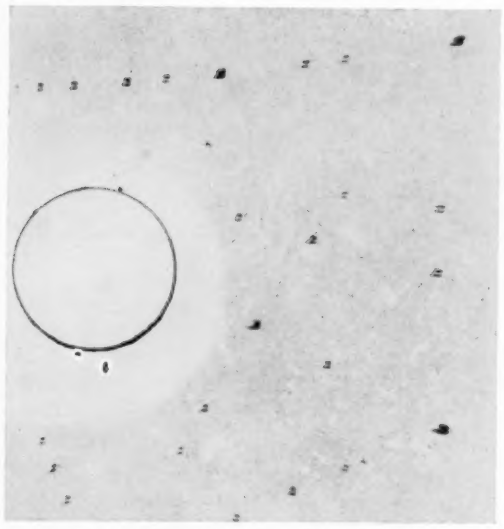

(a) double spots (enlargement 2.5×)

(c) fivefold spot (enlargement 5×)

(b) threefold spot (enlargement 2.5×)

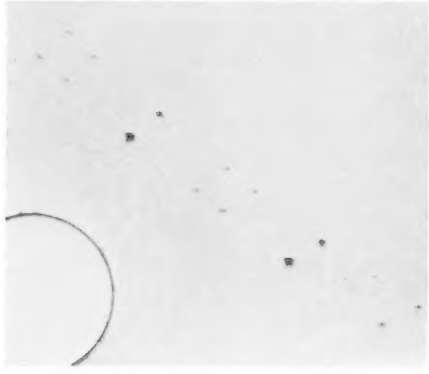

(d) split-up spots of two crystals with 2° orientation difference (enlargement 2.5×)

FIG. 4. Splitting of Laue spots in un-bent W crystals (the wire direction is horizontal).

In the investigated area of about 130 μ we counted from 2 to 7 fragments giving a diameter of 20–70 μ for each.

Of the fifty crystals investigated twenty were used for bending experiments. Before bending, about half of them showed single Laue spots, the other half diffraction spots that were split. The wires, of which the crystals were part, remained fastened on one end and were bent on the place of the chosen crystal with a radius of 1.5 or 2 mm over an angle of 20° or 90°. In some cases Laue diagrams were made in the bent state. Then the crystals were re-bent until they were as nearly as possible straight again. Some of them were bent in the plane through the X-ray beam and the wire, and some were bent in a direction perpendicular to that plane, which proved to give no appreciable differences.

In the bent condition the crystals gave of course Laue spots with large deformation asterism which were also very often broken up. This break-up happened sometimes in different directions; then the spots were more or less feather-shaped. The straightening of the bent crystal resulted in most casrs in a vanishing of the deformation asterism, but the re-bent crystals were much more broken up into fragments than before the bending. This break-up, which we consider as a form of "fragmentation", not only occurred in the direction of the bending of the lattice planes, but frequently in a direction perpendicular to the first. The second fragmentation not only happened

VOL. 4 1956

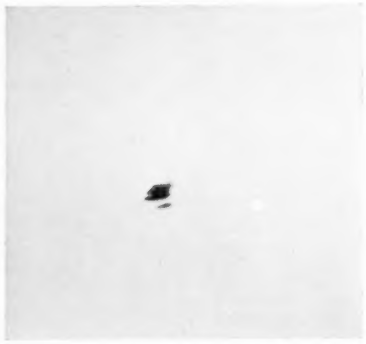

(a) split-up of a single spot perpendicular to the wire axis

(b) complicated split-up

(c and d) split-ups which suggest remaining deformations

FIG. 5. Splitting of Laue spots after bending and straightening of the W crystals (the wire direction is horizontal). Enlargement 5×.

in crystals in which before the bending a similar split-up was found to a lesser extent, but also in crystals in which with our set-up no splitting was detected. Of the twenty bent and re-bent crystals ten showed a split-up in a direction perpendicular to the wire axis (e.g. the fragments could be considered as being turned with respect to each other around the wire axis). Three had a split-up in the direction of this axis (as could be the result of bending the wire) and the remaining seven crystals showed a more complex break-up (perhaps sometimes as a result of a slight twisting). The various shapes of the spots are illustrated in Fig. 5.

The orientation differences between two adjacent spots amounted from 1′ to 10′. The number of separate spots was up to twenty. With an irradiated area of about 130 μ diameter, in the case of twenty spots, the average diameter of each fragment follows to be about 6–7 μ. (The penetration depth will be of the same magnitude, so we need not consider crystals lying under the surface layer.) The maximum orientation difference between extreme fragments in one irradiated spot is about 1.5°.

4. DISCUSSION OF THE RESULTS

Apart from the polygonization after annealing[2], in unannealed cold-worked metals a break-up of the crystals also occurs. This has been found in many lighter metals,[3, 4, 5] but also after bending molybdenum single crystals.[6]

In cases where the deformation asterism disappeared by rebending the crystals, we found the fragmentation to remain. Moreover, often a split-up was found to be present in carefully handled un-bent tungsten crystals, which corresponds to orientation differences which could be obtained by turning the fragments slightly around the wire axis. After bending and re-bending the wire, the same type of orientation defect dominates. The average dimensions of the crystals can diminish by bending from 70–20 μ to about 7 μ, which will be about the limit resolvable by our method (see also ref. 3). This leads up to the suggestion that crystal boundaries have a tendency to be parallel to the wire axis, and that in the crystals which have grown out of the fiber-structure of the wire the influence of this structure is still present. Although the so-called "dope" is still present in the recrystallized wire its amount is only of the order of, at the most, 0.01 per cent, a contamination which is to be considered as normal for a not extremely pure metal. This dope has however a very strong influence on the whole crystallization process, and we may assume a persisting influence on the behavior of the tungsten crystals which we normally consider as single crystals. As a result of the

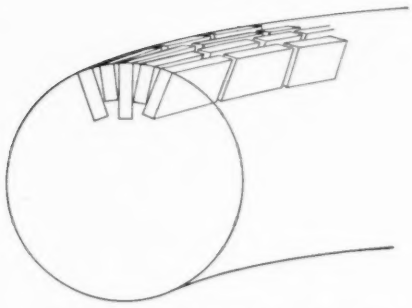

FIG. 6. Sketch of a bent wire with small crystals together normally considered as one single crystal but with orientation defects (fragmentation) in the direction of the wire and perpendicular to it.

drawing process of the wire the dope might, for instance, have been spread out in planes or threads parallel to the wire. If these planes functioned as boundaries of very small crystals with almost the same orientations, or as grooves in the single crystals, a similar split-up as found in our experiments could be expected before and after bending the wire. In bending there occur also forces perpendicular to the wire axis, and at the boundaries or grooves the crystal would yield to them, and show the increased split-up. Fig. 6 illustrates this fragmentation of a crystal.

The presence of these fragments with small disorientation in the un-bent wire and the further fragmentation in bending can also be explained as a result of the contaminations which are stretched like strings, instead of planes, through the wire. Probably these strings, or planes of strings, affect the recrystallization in the sense that they could act as capture-centres for the dislocations present in great number and probably in preferred orientation after drawing, and thus give rise to fragment boundaries as depicted in Fig. 7. In bending the recrystallized wire, new dislocations are formed which can interact in their turn with the contaminations. Although the majority of the dislocations formed in the bending experiment have their axes perpendicular to the wire axis, and should therefore be influenced but slightly by the strings parallel to the wire axis, the necessary change of shape of the cross-section of the wire must be caused by dislocations more or less parallel to that axis. It is these dislocations that could be responsible for the fragmentation of the second kind described above, as they

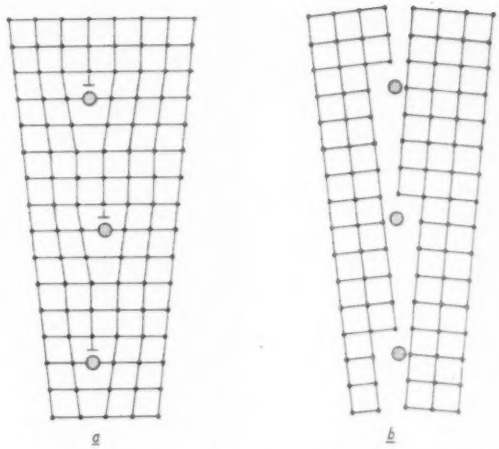

FIG. 7. Cross-section of a lattice in which strings of contaminations, perpendicular to the plane of drawing, combine with dislocations. One crystal with dislocations (left) and two fragments (right) both can give orientation defects.

will be captured by the strings and would not therefore be able to disappear in rebending the wire.

Similar experiments with tungsten of higher purity are started.

5. CONCLUSIONS

After re-bending cold-bent tungsten crystals in wires, the main part of the deformation disappears but fragmentation is found not only in the direction of the wire axis but very frequently perpendicular to that direction. The latter split-up is also present in un-bent crystals.

The distribution of the small amount of contaminations during the drawing process might be responsible for this fragmentation.

After bending, the average size of the individual crystals became smaller.

REFERENCES

1. P. B. HIRSCH and J. N. KELLAR, *Proc. Phys. Soc.*, **B64**, 369 (1951).
2. A. GUINIER and J. TENNEVIN, *Acta Cryst.*, **2**, 133 (1949).
3. P. B. HIRSCH and J. H. KELLAR, *Acta Cryst.*, **5**, 162 (1952).
4. P. GAY, P. B. HIRSCH, and A. KELLY, *Acta Cryst.*, **7**, 41 (1954).
5. C. A. JULIEN and B. D. CULLITY, *Acta Met.*, **1**, 588 (1953).
6. K. T. AUST, R. MADDIN, and N. K. CHEN, *J. Metals*, **5**, 1477 (1953).

VOL. 4 1956

VACANCIES AND INTERSTITIALS IN GERMANIUM AND SILICON*

SUMNER MAYBURG†

A search for the equilibrium solubility of vacancies or interstitials in silicon has led to the conclusion that such defects, if present at all, are at concentrations of less than 5×10^{12}/cc. However, there seems to be interstitial silicon frozen into most silicon crystals tested. The absence of frozen-in defects in germanium is explained by the effectiveness with which an equilibrium concentration of Frenkel defects aids the diffusion of extra defects out of the crystal. Interstitials may be frozen into silicon because there are essentially no Frenkel defects to aid the diffusion of the interstitials out of the silicon crystals during the growing process.

LACUNES ET ATOMES INTERSTITIELS DANS LE GERMANIUM ET LE SILICIUM

L'étude de la solubilitié d'équilibre des lacunes et atomes interstitiels montre que ces défauts, s'ils existent, sont à des concentrations inférieures à $5 . 10^{12}$/cc. Néanmoins, il semble y avoir des atomes interstitiels de silicium dans la plupart des cristaux de silicium étudiés. L'absence de tels défauts dans le germanium s'explique par l'action des défauts de Frenkel sur l'expulsion de ces défauts hors du cristal. Les atomes interstitiels peuvent être trempés dans le silicium, car l'absence de défauts de Frenkel ne permet pas leur expulsion du cristal pendant sa croissance.

LEERSTELLEN UND ZWISCHENGITTERPLÄTZE IN GERMANIUM UND SILIZIUM

Eine Untersuchung der Gleichgewichtslöslichkeit von Leerstellen der Zwischengitterplätze hat zu dem Schluss geführt, dass solche Fehler, wenn sie überhaupt vorhanden sind, bei Konzentrationen von weniger als $5 \times 10^{12}/cm^3$ auftreten. Es scheint jedoch, dass in den meisten untersuchten Siliziumkristallen Silizium auf Zwischengitterplätzen eingefroren war. Das Fehlen von eingefrorenen Defekten in Germanium wird der Wirksamkeit zugeschrieben, mit der eine Gleichgewichtskonzentration von Frenkel Defekten der Diffusion von Extradefkten aus dem Kristall hinaus verhilft. Da bei Silizium im wesentlichen keine Frenkel Defekte vorhanden sind, die das Hinausdiffundieren der Zwischengittereinlagerungen beim Wachstumsprozess unterstützen, werden hier die Zwischengittereinlagerungen eingefroren sein.

1. INTRODUCTION

The use of electrical measurements to study lattice defects in semi-conductors has allowed the study of lattice defect concentrations as low as one defect in 10^{10} atoms of the mother material. We have previously reported studies of the equilibrium concentration of Frenkel defects in germanium at temperatures near the melting point.[1] We wish to report here similar studies which were designed to detect the equilibrium solubility of vacancies and interstitials in silicon, but which resulted in the discovery of a considerable concentration of frozen-in interstitials.

2. EXPERIMENTAL OBSERVATIONS

The experimental apparatus is similar to the one used in the study of defects in germanium. The single-crystal silicon sample is a slab of about 1 mm thickness. It is heated by passing a current through it in a kinetic vacuum system at pressures less than 10^{-7} mm of Hg. The sample is quenched by turning off the current. It cools by radiation to room temperature with a typical initial cooling rate of 400°C/sec. The electrical resistivity is measured at room temperature after a given heat treatment, and any change in the resistivity can be ascribed to a change in the sample produced by the heat treatment. The heat-treatment temperature is determined by measuring the intrinsic resistivity of the specimen which is a sensitive function of the temperature.

There are two types of resistivity changes caused by heat treatment: irreversible and reversible changes. Irreversible changes can be related to the loss or gain of impurities, or to the loss of lattice defects which were introduced in the original growing of the crystal. Reversible changes in resistivity can be related to reversible changes in the equilibrium concentration of vacancies or interstitials or both when the heat treatment temperature is changed.[1] Reversible changes are only dependent on the heat-treatment temperatures, while irreversible changes depend on the total heat-treatment history as well.

From the work at Oak Ridge on the neutron bombardment of silicon, we know that the vacancy acts as an electron acceptor in n-type but not in p-type silicon, while the interstitial acts as a donor in

* Received February 17, 1955; revised version June 2, 1955.
† Sylvania Electric Products Inc., Bayside, Long Island, New York.

p-type but not in n-type silicon.[2] The room temperature resistivity, ρ, is given by the equation

$$1/\rho = |N_A - N_D| \, e\mu \qquad (1)$$

where N_A is the number of electron acceptors, N_D is the number of donors, μ is the mobility of holes in p-type material (500 cm²/volt sec)[3] or the mobility of electrons in n-type material (1200 cm²/volt sec).[3] We observed no reversible changes in the resistivity of silicon. Hence, we can deduce from equation (1) and the sensitivity of our resistivity measurement that the equilibrium concentration of defects near the melting point must be less than 5×10^{12} per cc. (In germanium we found 4×10^{14}/cc Frenkel defects near the melting point).[1] In the Appendix it is demonstrated that the heating times were long enough for equilibrium to be obtained, and that the quenching times were sufficiently short to capture the high-temperature equilibrium.

Another striking difference between the heat-treatment results on germanium and silicon was found in the nature of the irreversible changes we detected. In germanium, we found one simple irreversible process which could be ascribed to the evaporation of copper out of the specimen when it was first introduced into the vacuum system and heated.

In silicon the array of irreversible processes is more complex and implies the loss of various types of impurities from the sample. However, the largest irreversible change of resistivity is common to all p-type specimens so far tested, and takes place characteristically at 1100°C. Some of p-type samples were grown by pulling from a quartz boat in an argon atmosphere, and had a resistivity of 8 ohm-cm. Others were produced by the floating-zone technique in vacuum,[4] and had a resistivity of 20 ohm-cm p-type. By heat treatment at around 1100°C for several hours it was possible to reduce the gross resistivity of the 8 ohm-cm samples by a factor of 2, and the 20 ohm-cm material by a factor of 3. However, an n-type sample grown under the same conditions, except for the arsenic doping agent, as the 8 ohm-cm p-type material, exhibited no such irreversible change in resistivity. Thus the "impurity" involved is capable of influencing the resistivity of p-type but not of n-type silicon. Such an impurity might well be interstitial silicon which is introduced into the crystal during the growing process and is capable of diffusing out of the ingot when the temperature is raised to 1100°C.

We have etched several of the p-type samples in order to determine the region of the sample where the major resistivity change took place. Most of the change takes place within a few mils of the surface. We estimate from the magnitude of the resistivity changes observed and the depths to which such changes extended below the surface that these crystals contained at least 10^{16} interstitials/cc (see Fig. 1).* The diffusion observed corresponds to the decay of the "higher modes" in the solution of the diffusion equation.[5] The diffusion constant can only be estimated to an order of magnitude, and is found to be 10^{-9} cm²/sec.

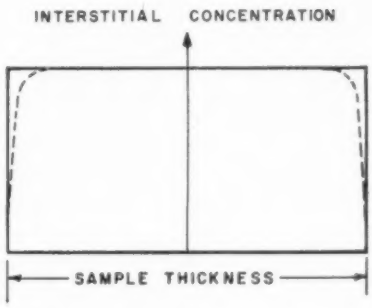

FIG. 1. The distribution of interstitial silicon through the sample. The heat treatment at 1100°C allows only the interstitials near the surface to leave the sample, indicating a very low diffusion constant for interstitial diffusion.
——— Initial concentration 10^{16}/cc
– – – – After several hours at 1100°C.

In Table 1, we summarize the available information on vacancies and interstitials in germanium and silicon as determined by resistivity measurements.

TABLE 1

	Ge	Si
Equilibrium solubility of vacancies or interstitials	$3 \times 10^{22} \, e^{-\frac{2 \text{ eV}}{kT}} \frac{\text{Frenkel defects}}{\text{cm}^3}$	Not detectable
Frozen-in vacancies or interstitials	Not detectable	$10^{16} \frac{\text{interstitials}}{\text{cm}^3}$

* The possibility of an impurity producing these effects seem very remote. Such an impurity would have to have the same electrical property as interstitial silicon. Furthermore, it must have a low diffusion constant but a high rate of evaporation from the solid surface in order for Fig. 1 to be explained. (The surface is an infinite sink for interstitials since they simply form a new layer of the crystal.) High evaporation from the solid implies high evaporation from the liquid. Since convection and diffusion are high in liquids, the impurity would have evaporated from the liquid during the crystal-growing process, and would not be found in the solid. A further argument favoring interstitials is that the p-type crystals grown with markedly different crucibles and atmospheres exhibited the same behavior. Under such different external conditions, it is hard to imagine that exactly the same impurity is introduced into the crystal during the growth process.

VOL. 4 1956

It is not unreasonable to expect that silicon would be grown with interstitial silicon present. Silicon liquid is denser than the solid, and some interstitials could well be dissolved during the growing process. As we shall see later, most crystals are grown at a rate which is too fast to allow the interstitials to diffuse out of the ingot during the growing process by a simple diffusion mechanism.

Liquid germanium is also denser than solid germanium. Why then did we not see interstitial germanium frozen into germanium single-crystals as grown from the melt? In germanium, it is proposed that the presence of an equilibrium concentration of Frenkel defects will greatly aid the diffusion of any added non-equilibrium number of interstitials. Therefore, for germanium the growing process is in effect slow enough to anneal out any extra interstitial germanium which may be introduced at the liquid crystal interface.

3. THE INFLUENCE OF FRENKEL DEFECTS ON DIFFUSION

In Fig. 2, we show schematically how an equilibrium concentration of Frenkel defects aids the diffusion of an extra interstitial out of the sample.

The solid enclosure represents a formed Frenkel defect; the cross on the left the added interstitial. There is no reason why the vacancies and interstitials could not, after allowing some time for diffusion, be reassociated as shown by the dashed enclosures. Now, the extra interstitial is found near the surface and can leave the sample. The important diffusion distance involved in this process is the average distance between vacancies and interstitials, but not the total distance from the extra interstitial to the surface. Thus the solid can lose an extra interstitial by this process much faster than if there were no Frenkel defects present, in which case the added interstitial would have to diffuse the whole distance to the surface.

The above picture is crude, but we can put it on a more exact basis in the following way. Into the equation describing the diffusion of interstitial germanium, we introduce terms relating to the generation of Frenkel defects and the recombination of vacancies and interstitials. In a germanium crystal where only Frenkel defects are present the approach to an equilibrium situation can be given by the equation[1]

$$\frac{dn_i}{dt} = -\frac{n_i \alpha n_v}{\tau N} + G,$$

where we assume for the sake of this argument that only the interstitials, n_i, are moving so that τ is the jump time for interstitials, N is the number of lattice positions per cm^3, n_v is the number density of vacancies, α is a geometrical factor which is 4 for the germanium structure,[6] and G represents the generation of Frenkel defects. At equilibrium

$$\frac{dn_i}{dt} = 0,\ n_i = n_v \equiv n_e, \text{ and hence } G = \frac{\alpha n_e^2}{\tau N}$$

where n_e is the number of Frenkel defects at equilibrium. The diffusion equation for the case when extra interstitials Δn_i are instantaneously added to the solid can be now written as

$$\frac{dn_i}{dt} = -\frac{\alpha}{\tau N}(n_i n_v - n_e^2) - D\nabla^2(\Delta n_i), \qquad (2)$$

where at $t = 0$,

$$n_i = \Delta n_i + n_e$$

$$n_v \approx n_e$$

Therefore,

$$\frac{d\Delta n_i}{dt} = -\frac{\Delta n_i \alpha n_e}{\tau N} - D\nabla^2(\Delta n_i). \qquad (3)$$

We assume that the extra interstitial concentration is sufficiently small so as not to appreciably alter the vacancy concentration. The term $\frac{\Delta n_i \alpha n_e}{\tau N}$ represents the contributions of the Frenkel defects to the diffusion process.

The diffusion equation has been solved previously for the case of vacancies or interstitials diffusing out of a slab of thickness $2L$.[5] The time dependence of the solution for the total concentration of defects after the higher modes of the solution have decayed is

$$e^{-\pi^2 \frac{Dt}{L^2}}.$$

The time dependence of the solution to equation (3) can readily be seen to be

$$e^{-\left(\frac{\pi^2 D}{L^2} + \frac{\alpha n_e}{\tau N}\right)t}.$$

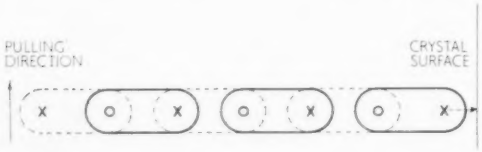

FIG. 2. The effect of Frenkel defects in aiding the removal of an extra interstitial from the crystal. The extra interstitial is originally on the left. The original Frenkel defects (solid enclosures) can reassociate (dashed enclosures) such that the extra-interstitial appears in the right and is lost to the surface.

Thus, the time to reach equilibrium t_e in a solid with no Frenkel defects is the well known

$$t_e = \frac{L^2}{\pi^2 D},$$

while in a solid with Frenkel defects is

$$t_{eF} = \left(\frac{\pi^2 D}{L^2} + \frac{\alpha n_e}{\tau N}\right)^{-1}.$$

The ratio of these two times is

$$t_e/t_{eF} = 1 + \frac{L^2 \alpha n_e}{\pi^2 D \tau N}.$$

The diffusion constant for interstitials can be related to their jump time, τ, by the usual "random walk" equation[7]

$$D = 4a^2/(6\tau) \tag{4}$$

where a is the jump distance between interstitial positions and is 2.4 Å in germanium. Also in germanium n_e/N near the melting point is of the order of 10^{-8}, so that for an ingot whose smallest dimension is 2 cm we have

$$\frac{t_e}{t_{eF}} \sim \frac{L^2(6\alpha)n_e}{\pi^2 4a^2 N} \sim 10^7.$$

Thus, the presence of Frenkel defects in germanium will speed up the diffusion of extra interstitials out of the sample by a factor of ten million over the time "normal" diffusion would require. The above or similar arguments would apply equally well for the diffusion of extra vacancies out of the crystal or for the case when the vacancies move instead of the interstitials.

VOL. 4 1956

4. DISCUSSION

Is the above mechanism essential to the removal of excess interstitials from germanium during the growth of a crystal, or is the normal diffusion process fast enough? The self-diffusion of germanium has been measured by Letaw, Slifkin and Portnoy,[8] to be

$$D_{\text{self Ge}} = 87e^{-\frac{73{,}500}{RT}} \text{ cm}^2/\text{sec}.$$

In our previous study of vacancies and interstitials in heat-treated germanium we found an equilibrium solubility of Frenkel defects of[1]

$$\frac{n_e}{N} = 6.7e^{-\frac{46{,}100}{RT}}$$

Furthermore, below 585°C we had experimental evidence to show that the interstitial is more mobile than the vacancy. Let us assume that self-diffusion proceeds interstitially in germanium at all temperatures.[9] Then, the interstitials have a diffusion constant

$$D_i = \frac{D_{\text{self}}}{n_e/N} = 13e^{-\frac{(27{,}400)}{RT}} \text{ cm}^2/\text{sec}$$

There is a sharp temperature drop along the length x of the crystal as it is pulled from the melt. The temperature gradient is determined by the radiation losses from the equation

$$K\frac{d^2T}{dx^2} = \frac{\sigma T^4(2\pi r)}{\pi r^2},$$

where we have written the radiation term as equivalent to a loss of heat per unit volume. For the sake of this argument we consider the bar as a circular rod of radius r, and we assume an emissivity of 1. The quantity σ is Stefan's radiation constant, and K is the thermal conductivity. If we multiply by dT/dx, integrate with respect to x and note that when T is small, $(dT/dx) = 0$, we have

$$\frac{K}{2}\left(\frac{dT}{dx}\right)^2 = \frac{2\sigma}{r}\frac{T^5}{5}$$

or

$$\left|\frac{dT}{dx}\right| = \sqrt{\frac{4\sigma}{5rK}}\,T^{5/2}$$

Whether our interstitials have time to diffuse out to the surface of the crystal depends on whether $\overline{Dt} > r^2$.

$$\overline{Dt} = \int D\,dt = \int D\frac{dt}{dx}\frac{dx}{dT}dT = \frac{D_0}{v}\int e^{-E/RT}\left(\frac{dx}{dT}\right)dT$$

where $v = \dfrac{dx}{dt}$ is the pulling rate.

If we substitute for $\dfrac{dx}{dT}$ and replace E/RT by y^2 we find

$$\overline{Dt} = \frac{D_0}{v}\sqrt{\frac{5rK}{4\sigma}\left(\frac{R}{E}\right)^3} \qquad 2\int_{y'}^{\infty} e^{-y^2}y^2\,dy$$

where y' is determined from the melting temperature of germanium.

$$y' = \sqrt{\frac{E}{R(1210°)}} = 3.3$$

One partial integration converts the integral into a gauss error function plus a calculable term. The integration results in

$$\overline{Dt} = \frac{D_0}{v}\sqrt{\frac{5rK}{4\sigma}\left(\frac{R}{E}\right)^3}\,e^{-y'^2}\left(y' + \frac{1}{2y'}\right)$$

The following values apply:

$$r = 1 \text{ cm}$$
$$K = 0.1 \text{ cal/cm sec } ^\circ\text{C}$$
$$\sigma = 5.7 \times 10^{-5} \text{ ergs/cm}^2 \text{ sec } (^\circ\text{C})^4$$
$$D_0 = 13 \text{ cm}^2\text{/sec}$$
$$R = 2 \text{ cal/mole}$$
$$E = 27{,}400 \text{ cal/mole}$$
$$v = 6 \text{ in./hour}$$

Hence $\overline{D}t = 0.03$ cm^2. Since $r = 1$ cm, $\overline{D}t \ll r^2$ and the interstitials would not diffuse out of the sample during the pulling process by a normal diffusion process. Evidently the accelerated diffusion produced by the Frenkel defects is essential to the removal of the extra interstitials.

5. CONCLUSIONS

Evidence has been presented for the presence of frozen-in interstitials in silicon crystals at a concentration of the order of 10^{16}/cc. A possible explanation is given which correlates the absence of an appreciable equilibrium concentration of Frenkel defects and the presence of the frozen-in interstitials.

Crystals studied had initial resistivities of 8 and 20 ohm-cm which corresponds to an uncompensated concentration of electron acceptors of the order of 10^{15}/cc. Since in p-type material the interstitial is a donor, the total acceptor concentration in these crystals must be of the order of 10^{16}/cc. The crystals were not intentionally doped with any acceptor impurity. One of the problems growing out of this work is to determine the impurity which is the source of this large number of acceptors.

ACKNOWLEDGMENTS

The writer would like to acknowledge the kindness of Dr. P. H. Keck for the gift of some of the crystals, the help of Mrs. Olga Kielbasa who prepared the samples from the crystals, and Dr. J. Birman's useful criticisms of this written presentation.

APPENDIX

In this section we propose to answer two questions which may be raised challenging the conclusion that no Frenkel defects are found in silicon:

(a) Was equilibrium for Frenkel defects achieved during the heat treatment?

(b) Were the quenching rates fast enough to trap the high-temperature equilibrium concentration of Frenkel defects at room temperature?

(a) The rate of approach to the equilibrium concentration of Frenkel defects is given by equation 2. If we set $n_i = n_e = n$, the number of Frenkel defects, and if we neglect the diffusion term which does not apply to this case where the concentration of defects is uniform throughout the crystal, we then have for the change in concentration of the Frenkel defects with time the equation

$$\frac{dn}{dt} = -\frac{\alpha}{\tau N}(n^2 - n_e^2) \qquad \text{(A1)}$$

where τ is the jump time for the fastest moving defect, most likely the interstitial. By use of equation (4), equation (A1) becomes

$$\frac{dn}{dt} = -\frac{\alpha 6D}{4a^2 N}(n^2 - n_e^2). \qquad \text{(A2)}$$

Equation (A2) may be integrated to give the time required for n to reach 90 per cent of its final value of n_e. We find

$$t_{(n=0.9n_e)} = \frac{(\ln 19)}{2\alpha}\frac{N}{n_e}\frac{4a^2}{6D}.$$

The following values apply

$$\alpha \sim 4$$
$$a = 2.3 \times 10^{-8} \text{ cm}$$
$$N \sim 5 \times 10^{22} \text{ cm}^{-3}$$

At 1100°C, $D \sim 10^{-9}$ and according to our measurements $n_e < 5 \times 10^{12}$ cm^{-3}. Under these conditions $t = 1200$ sec, which is a short time compared to most of our heat-treatment times.

If the Frenkel-defect concentration in Si were as high as in Ge (i.e., 4×10^{14} cm^{-3}), the diffusion constant for the faster moving defect would have to be at least as low as 10^{-14} cm^2/sec for equilibrium not to have been reached in our longest heat treatments, which lasted twenty-four hours. Such a low diffusion constant for vacancies or interstitials has never been reported. Our measurements at 1100°C, in fact, yield a value of 10^{-9} cm^2/sec for the diffusion constant for interstitials, and this is likely to be increased by an order of magnitude at the melting point of 1430°C. It, therefore, is certain that the equilibrium for Frenkel defects was established during our heat treatments, or else the equilibrium concentration was so low as to be immeasurable.

(b) Equation (A2) can also be used to show that the quenching rates were fast enough to capture whatever Frenkel defects were at the high-temperature equilibrium. The sample cools by radiation cooling; the change of temperature with time is given by

$$\frac{dT}{dt} = \left(\frac{dT}{dt}\right)_Q \frac{T^4}{T_Q{}^4}$$

where T_Q is the heat treatment temperature from which the sample is quenched and where $(dT/dt)_Q$ can be determined by measuring the power required to maintain the sample at the heat-treatment temperature. As was mentioned previously $(dT/dt)_Q$ is 400°C/sec near the melting point. As the sample cools, the term $n_e^2(T)$ in equation (A2) should rapidly become much less that n^2, because the production of Frenkel defects is an activated process and so the number of such defects at equilibrium should decrease sharply with temperature. Thus, we shall neglect the term n_e^2 in equation (A2). If anything, the neglect of this term should make the quench appear slower than it really is.

We can now integrate equation (A2) over time during the quenching process to see how many defects are lost.

$$N\int -\frac{dn}{n^2} = \frac{\alpha 6}{4a^2}\int_t D\,dt = \frac{\alpha 6}{4a^2}\int_{T_Q}^{300^\circ\mathrm{K}} D\left(\frac{dt}{dT}\right) dT$$

$$\frac{N}{n_r} - \frac{N}{n_Q} = \frac{6}{a^2}\int_{T_Q}^{300} T_Q{}^4\left(\frac{dt}{dT}\right)_Q D_0 e^{-E/RT}\frac{dT}{T^4}$$

where n_Q is the equilibrium concentration at the heat treatment temperature, n_r is the concentration measured at room temperature, and the usual temperature dependence of the diffusion constant has been substituted. The integration can be performed by substituting $x' = E/RT$, and yields

$$\frac{N}{n_r} - \frac{N}{n_Q} = \frac{6}{a^2} T_Q{}^4\left(\frac{dt}{dT}\right)_Q D_0\left(\frac{R}{E}\right)^3\int_{x_Q'}^{x'\sim\infty} e^{-x'}x'^2 dx'$$

$$= \frac{6}{a^2} T_Q{}^4\left(\frac{R}{E}\right)^3\left(\frac{dt}{dT}\right)_Q D_0\, e^{-x_Q'}\,(x_Q'^2 + 2x_Q' + 2)$$

where $x_Q' = E/RT_Q \gg 1$.
Hence

$$1 - \frac{n_r}{n_Q} = \frac{n_r}{N} T_Q\left(\frac{dt}{dT}\right)_Q \frac{D_Q}{x_Q'}. \qquad \text{(A3)}$$

The theory of Zener[10] on interstitial diffusion offers a method by which the activation energy for diffusion can be estimated from the diffusion constant at only one temperature. Following the calculations of Fuller, Struthers, Ditzenberger, and Wolfstirn[7] for copper in Ge, it is quite easy to get a rough estimate of the activation energy for the interstitial diffusion of Si in silicon from the measured value of D at 1100°C of 10^{-9} cm²/sec. We find $E \sim 40{,}000$ cal/mole. We can estimate the diffusion constant D_Q near the melting point of 1430°C from the value of D at 1100°C by the relation

$$\frac{D_Q}{D} = e\left(\frac{E\Delta T}{RT_1T_Q}\right)$$

where $D = 10^{-9}$ cm²/sec, $T_1 = 1370$°K, $T_Q = 1700$°K, and $\Delta T = T_Q - T_1 = 330$°C.

Hence,

$$D_Q \sim 2 \times 10^{-8}\ \mathrm{cm^2/sec}$$

and $$x_Q' \sim 12.$$

We now may estimate the fraction of defects lost in the quenching process as given by equation (A3) using the values given above, and the fact that $n_r \leq 5 \times 10^{12}$ cm^{-3}.

We find $$\frac{n_Q - n_r}{n_Q} \leq 4 \times 10^{-3}.$$

Thus a negligible fraction of defects fails to be quenched into the sample.

REFERENCES

1. S. Mayburg, *Phys. Rev.*, **95,** 38 (1954).
2. J. H. Crawford, Jr., *et al.*, personal communication (1954); H. M. James and K. Lark Horovitz, *Z. Phys. Chem.*, **198,** 107 (1951).
3. M. B. Prince, *Phys. Rev.*, **93,** 1204 (1954).
4. P. H. Keck and M. J. E. Golay, *Phys. Rev.*, **89,** 1297 (1953).
5. G. Esaki, *Phys. Rev.*, **89,** 1032 (1953).
6. The value of α is 4 if we assume that an interstitial combines instantaneously with a vacancy at any one of the four adjacent lattice points. If the interstitial can also recombine with vacancies on next-nearest neighbor lattice points, α is greater than 4.
7. Fuller, Struthers, Ditzenberger, and Wolfstirn, *Phys. Rev.*, **93,** 1182 (1954).
8. Letaw, Slifkin, and Portnoy, *Phys. Rev.*, **93,** 892 (1954).
9. By assuming that self-diffusion proceeds interstitially, we have maximized the chance that normal diffusion would be fast enough to remove the interstitials.
10. C. Zener, *J. Appl. Phys.*, **22,** 373 (1951).

VOL. 4 1956

THE MECHANISM OF DENSIFICATION DURING SINTERING OF METALLIC PARTICLES*

G. C. KUCZYNSKI†

The possible mechanisms which may bring about shrinkage of pores during sintering are discussed. In view of the Alexander-Baluffi experiment, only two such mechanisms are possible: (1) diffusion along grain boundaries, (2) volume diffusion with sinks at grain boundaries (Nabarro-Herring microcreep). The excess vacancies are transmitted to the grain boundaries and through their network out of the compact. The probability of occurrence of these mechanisms is discussed. It is concluded that the volume-diffusion mechanism is the more probable one.

MÉCANISME DE L'AUGMENTATION DE DENSITÉ LORS DU FRITTAGE DES PARTICULES MÉTALLIQUES

Les mécanismes possibles qui peuvent faire disparaître les pores pendant le frittage sont discutés. D'après les expériences d'Alexander et Baluffi, deux mécanismes seulement sont possibles: 1°—Diffusion le long des joints de grain. 2°—Diffusion en volume avec disparition des lacunes sur les joints de grain (mécanisme de Nabarro et Herring). Les lacunes en excès diffusent vers les joints de grain et, par leur réseau, hors du comprimé. La probabilité de ces divers mécanismes est discutée et il est conclu que la diffusion en volumes est le mécanisme le plus probable.

ÜBER DEN MECHANISMUS DER VERDICHTUNG BEIM SINTERN VON METALLISCHEN TEILCHEN

Die möglichen Mechanismen, die eine Schrumpfung von Poren während des Sinterns verursachen können, werden diskutiert. Nach dem Alexander-Baluffi Experiment sind nur zwei solche Mechanismen möglich; (1) die Diffusion entlang der Korngrenzen und (2) die Volumendiffusion mit Löchern an den Korngrenzen (Nabarro-Herring Mikrokriechen). Die überschüssigen Leerstellen werden zu den Korngrenzen und durch deren Netzwerk aus dem Sinterkörper hinaus befördert. Die Möglichkeit des Auftretens dieser Mechanismen wird diskutiert. Es wird der Schluss gezogen, dass die Volumendiffusion der wahrscheinlichere Vorgang ist.

INTRODUCTION

The process of sintering, the central process of powder metallurgy, long remained obscure despite imposing advances made in the last twenty years by that branch of technology. However, the results of investigations undertaken during recent years have gradually explained the mechanisms involved. Powder metallurgists usually divide the course of the process of sintering into two largely overlapping stages. The first, during which the mass of heated powder does not densify appreciably but gains in cohesion, is connected with the formation of metallic "necks" between adjacent particles. During the second stage the voids are gradually eliminated, resulting in an increase of density of powder compact. It has been well established that both stages are motivated by surface tension. C. Herring, in his excellent studies,[1, 2] discussed exhaustively the thermodynamics of this problem.

Two particles in mutal contact form a system which is not in thermodynamical equilibrium, because its total surface energy is not a minimum. If such a system is left for a sufficient period of time, bonding of the two particles will take place, resulting in a decrease of the total surface area. The mechanisms which would effect the bonding are those of surface and volume diffusion, evaporation from convex surfaces of the system and condensation on concave ones, and plastic or viscous flow. Studies of the initial growth of the "neck" joining an individual sphere of copper or silver and a flat plate of the same material on which it was loosely placed[3] and of wires wound around cylinders,[4] indicated that, for metals of not too high vapor pressure, volume diffusion seems to be the predominant mechanism during the early stages of sintering. Diffusion flow is caused by a gradient of vacancy concentration. In the area of a neck of radius of curvature r, the excess concentration of vacancies ΔC was shown to be roughly

$$\Delta C = \frac{\gamma \delta^3 C_0}{kTr}, \qquad (1)$$

where γ is the surface tension of the metal, δ the

* Received March 15, 1955; in revised form August 11, 1955.

† Department of Metallurgy, University of Notre Dame, Notre Dame, Indiana

interatomic distance, k Boltzmann's constant, T the temperature in degrees Kelvin, and C_0 the equilibrium concentration of vacancies underneath a flat surface. For glass spheres it has been demonstrated that sintering takes place by viscous flow.[5]

The second stage of sintering, which consists essentially of the elimination of the spheroidized voids, remained somewhat vague. Some years ago the author[6] suggested that the closing of the pores is brought about by a similar mechanism to that of the "neck" formation, and derived the following equation for the radius r of a pore after a sintering time t,

$$r^3 = r_0^3 - \alpha t, \tag{2}$$

where r_0 is the original radius of a pore and α a coefficient dependent on the diffusion constant. However, it has been pointed out by R. Shuttleworth[7] that in a single crystal such a mechanism would be too slow to account for observed rates of sintering. Whereupon J. K. Mackenzie and R. Shuttleworth concluded that plastic flow motivated by surface stress must be involved. However, all experiments they could refer to were not adaptable to a quantitative comparison of theoretical and observed sintering rates. Most sintering experiments are performed on powder compacts, and consist of measurements of density as a function of time and temperature. As Herring[2] states, "the details of geometry of the contacts between individual particles are so complex and so unknown that a quantitative prediction of result from theory would be hopeless, even if other disturbing influences were negligible." Experiments on systems of known geometry, similar to those mentioned above, were needed to furnish a sound basis for a theory of densification. Such an experiment has been supplied by Alexander and Baluffi.[8, 9, 10]

Following Geach and Jones'[11] method, they wound several layers of copper wire of 0.005-in. diameter on a copper cylinder. After sintering they obtained a parallel set of tubular voids, whose circular cross sections were easily measured under a microscope. They found that the diameter of a void decreased as long as the pores were interconnected by grain boundaries. By prolonged annealing they succeeded in the elimination of grain boundaries from large portions of their specimens, converting them into single crystals honeycombed by remnant tubular voids whose diameters ceased to decrease. Long before this experiment was performed, workers in the field of powder metallurgy noticed that it is impossible to obtain full densification of compacts by sintering alone without cold working and resintering, because as soon as the grain boundaries leave the voids, they cease to close. This behavior is obviously due to the effect found by Alexander and Baluffi. Their experiment seems to rule out the possibility of plastic flow as assumed by Mackenzie and Shuttleworth, or viscous flow, previously suggested by Shaler and Wulff,[12] as the chief mechanisms of densification of metallic powder compacts. If anything, plastic or viscous flow motivated by surface stress should be easier and faster in single crystals, than in systems containing grain boundaries. It remains therefore to discuss the mechanisms which, in view of the experimental evidence, are possible, and to evaluate their probability of occurrence.

POSSIBLE MECHANISMS OF DENSIFICATION

The fact that the elimination of the pores in a metallic system can be achieved only when the grain boundaries are present, suggests the following possible mechanisms: (1) grain-boundary diffusion, (2) volume diffusion with grain-boundary sinks (equivalent to so-called Nabarro-Herring microcreep). The latter mechanism has been previously suggested by the author.[6] These mechanisms will now be briefly discussed in connection with the cylindrical voids of the Alexander and Baluffi experiment.

1. *Grain Boundary Diffusion*

The closing of the pores by boundary diffusion can be visualized as follows. A pore may be considered as consisting of vacancies, which dissolve in the grain boundaries ending at the pore and are replaced by atoms from the boundaries. Dissolved vacancies are swiftly transmitted to the surface of the specimen by vacancy-grain-boundary diffusion, and in turn replaced by atoms from the surrounding crystals. At first glance this mechanism would appear to be a very slow process on account of the small breadth of the grain boundaries. If the excess vacancy concentration in a grain boundary near the surface of the pore is assumed to be roughly expressed by eq. (1), where r is the radius of the pore, the flux of vacancies through a unit length of the grain boundary, about one atomic distance thick, can be expressed by the following equation,

$$r^3 \frac{dr}{dt} = -D_b \frac{\gamma \delta^4}{2\pi k T},$$

where D_b is the grain-boundary diffusion coefficient.

VOL. 4 1956

After integration, the following relation is obtained.

$$r^4 = r_0^4 - \frac{2\gamma\delta^4}{\pi kT} D_b t. \tag{3}$$

If it is assumed that $D_b/D \sim 10^3$ near the melting-point of copper, as in the case of silver,[13] then the time necessary for complete closing of a pore of radius 10^{-3} cm should be at least 2.5×10^5 hours. It is therefore safe to rule out this mechanism as too slow.

2. *Volume Diffusion*

As in the case of "neck" formation discussed in the introduction, the crystal surrounding a tubular void of radius r will contain an excess concentration of vacancies expressed by eq. (1). There exists, therefore, a gradient of vacancy concentration of the order of magnitude of $\Delta C/r$. Under a steady-state condition, these vacancies migrate towards the nearest sinks provided by the grain boundaries, and are continuously replaced by vacancies from the pore. This is obviously another way of saying that atoms are flowing into the pore. As soon as the vacancies reach a grain boundary, they are swiftly removed by vacancy-grain-boundary diffusion to the surfaces of large radii of curvature, such as the surface of the specimen. It has been pointed out before that, near the melting-point, the grain-boundary diffusion of silver is about one thousand times faster than volume diffusion. Vacancy-grain-boundary diffusion is, of course, still faster. It is reasonable, therefore, to expect a very fast removal of excess vacancies through the network of grain boundaries. This model is equivalent to an assumption of a constant vacancy density in the grain boundary throughout the whole process. The rate of pore shrinkage will then be controlled by the slower process, namely, that of the diffusion of the vacancies through the crystal to the grain boundaries.

The flux of vacancies through a cylindrical surface of unit length is approximately

$$-2r\pi D' \frac{\Delta C}{r},$$

where D' is the coefficient of diffusion of vacancies in the crystal. Since $C_0 D' = D$, the coefficient of volume diffusion, and ΔC may be replaced by the expression in eq. (1), the flux will be $-2\pi r D \dfrac{\gamma\delta^3}{kTr^2}$. This must be equal to the rate of shrinkage of the pore, $\dfrac{d(r^2\pi)}{dt}$.

The resulting equation

$$r^2 \frac{dr}{dt} = -D \frac{\gamma\delta^3}{kT},$$

after integration, yields

$$r^3 = r_0^3 - \frac{3\gamma\delta^3 D}{kT} t, \tag{4}$$

which is identical with eq. (2).

This process as described here is essentially the same as the Nabarro-Herring micro-creep mechanism. According to Nabarro[14] and Herring,[15] it is possible for each grain of a polycrystalline solid to change its shape in response to an applied stress by the flow of self-diffusion currents away from the boundaries subject to compression towards those under tension. This flow is macroscopically describable by an effective viscosity proportional to the square of the linear dimensions of the grains. Therefore the flow equation can be written

$$\text{strain rate} = \frac{\sigma}{\eta'}$$

where σ is the acting stress and η' the effective viscosity. In our case the strain rate is the rate of shrinkage of the radius of the tubular void $dr/r\,dt$; stress $\sigma = -\gamma/r$ and $\eta' \sim r^2$. Therefore the flow equation is

$$\frac{dr}{dt} = -\frac{A\gamma}{r^2},$$

where A is a function of temperature only. It is obvious that after integration of this equation, an expression similar to eq. (4) will be obtained.

EXPERIMENTAL EVIDENCE

Equations (3) and (4) allow us to estimate the time t_c necessary for complete closure of a pore, provided the grain boundaries are present to the very end. These values calculated for $T = 1000°C$ are listed in Table 1. The calculations were based on measurements of r_0 and a, made on the photographs of sintered copper wires in Alexander and Baluffi's reports.[9, 10] They are listed in Table 1 together with the other constants used.

Table 1 indicates that the volume-diffusion

TABLE 1

Mechanism	t_c (hrs)
Grain-boundary diffusion	2.5×10^5
Volume diffusion	2.8×10^2

$r_0 = 1.1 \times 10^{-3}$ cm $a = 6.35 \times 10^{-3}$ cm (wire diam.)
$D = 2.5 \times 10^{-9}$ cm²/sec[16] $\gamma = 1.43 \times 10^3$ dyne/cm[17]

mechanism is definitely much faster than that of grain-boundary diffusion. Calculation of the self-diffusion coefficient of copper at 1000°C on the basis of eq. (4) also yields a very good result. For this purpose the average radius of pores was measured as a function of time, on the photographs mentioned before. The value for the coefficient thus obtained is 4.8×10^{-9} cm²/sec. This value compares very well with that obtained by Steigman, Shockley, and Nix,[16] namely, 2.5×10^{-9} cm²/sec. A plot of $(r_0^3 - r^3)/a^3$ against time for the temperatures of 1000° and 1050°C is given in Fig. 1. The points corresponding to short-time annealing (less than two hundred hours) fall fairly well on straight lines. The points corresponding to longer times deviate appreciably, due to the elimination of grain boundaries from the sintered compact, which was visible on the photographs. For this reason the results of sintering at 1075°C, though available, were not utilized, because the photographs indicated that the grain boundaries began to disappear even after annealing for a few hours at that temperature. It may therefore be concluded that the volume-diffusion mechanism as described above is the most probable mechanism of densification of sintered-powder compacts.

A powder metallurgical engineer may object to the value of time necessary for complete closing of a pore, given in Table 1, as unduly long. Indeed, from experience he knows that most powder compacts at elevated temperatures sinter within only a few hours to the vicinity of the theoretical density. Our estimates were closer to a few hundred hours, as the figure in Table 1 would indicate. The apparently faster rates observed during sintering of the commercial compacts are due chiefly to the much smaller original pore radius r_0. Indeed, if r_0 is approximately a few microns instead of 10, as in the experiment described above, a simple calculation would reveal that the time necessary to close such pores completely would be of the order of a few hours. The original pores are smaller because the particles of the powders used in powder metallurgical practice are never uniform in size. The fine particles tend to fill the large pores between the large particles. Pressing, which precedes practically every sintering operation, reduces the pore size still further. Slightly pressed coarse-powder compacts, such as those studied by Rhines *et al.*,[18] sinter much more slowly, with the development of large pores. The latter phenomenon is due to non-uniformity of pore diameter. Small pores, on shrinking, deposit—so to speak—their vacancies in the pores of large curvature; or, in other words, the atoms on the walls of large cavities dissolve in the grain boundaries and are deposited in smaller voids.

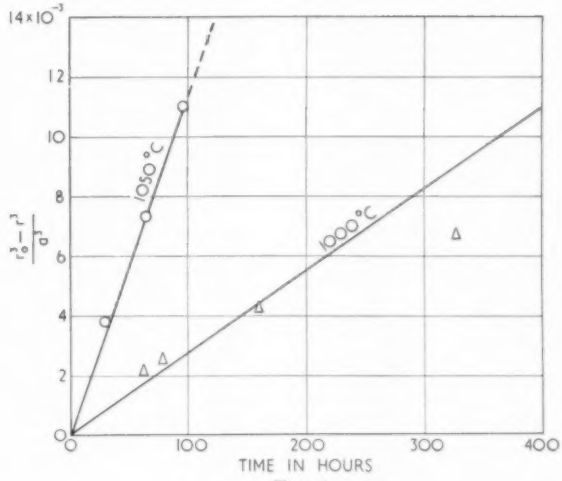

FIG. 1.

ACKNOWLEDGMENTS

The author is indebted to Dr. R. Landauer of I.B.M., Poughkepsie, New York, and Dr. P. Schwed of N.A.C.A., Cleveland, Ohio, for illuminating discussions, as well as to Mr. D. Lillie, formerly of the Atomic Energy Commission, Washington, for making pertinent unclassified reports available to the author. Thanks are also due Mr. I. Zaplatynskyj for his help in measuring the photographs and preparing the drawings.

REFERENCES

1. C. HERRING, *The Physics of Powder Metallurgy*, McGraw-Hill Book Company, p. 143 (1951).
2. C. HERRING, *Structure and Properties of Solid Surfaces*, University of Chicago Press, p. 5 (1953).
3. G. C. KUCZYNSKI, *Trans. Amer. Inst. Min. Met. Eng.*, **185,** 169 (1949).
4. G. C. KUCZYNSKI, *J. Appl. Phys.*, **21,** 632 (1950).
5. G. C. KUCZYNSKI, *J. Appl. Phys.*, **20,** 1160 (1949).
6. G. C. KUCZYNSKI, *Trans. Amer. Inst. Min. Met. Eng.* (discussion), **185,** 812 (1949).
7. J. K. MACKENZIE and R. SHUTTLEWORTH, *Proc. Phys. Soc.*, **62,** 833 (1949).
8. B. H. ALEXANDER and R. BALUFFI, *J. Metals*, **188,** 1219 (1950).
9. A.E.C. Report, AT-30-1, GEN 367, October 1, 1949–April 1, 1950.
10. A.E.C. Report, AT-30-1, GEN 367, April 1, 1950–October 1, 1950.
11. G. A. GEACH and F. O. JONES, *Research*, **2,** 493 (1949).
12. A. J. SHALER and J. WULFF, *Industr. Engng Chem.*, **40,** 838 (1948).
13. D. TURNBULL, *Atom Movement*, A.S.M., p. 129 (1950).
14. F. R. N. NABARRO, *Report of a Conference on the strength of solids*, (Physical Society, London, 1948).
15. C. HERRING, *J. Appl. Phys.* **21,** 437 (1950).
16. J. STEIGMAN, W. SHOCKLEY, and F. C. NIX, *Phys. Rev.*, **56,** 13 (1939).
17. J. C. FISHER and C. G. DUNN, *Imperfections in Nearly Perfect Crystals*, p. 317.
18. F. N. RHINES, C. E. BIRCHENALL, and L. A. HUGHES. *Trans. Amer. Inst. Min. Met. Eng.*, **188,** 378 (1950).

VOL. 4 1956

THE GROWTH OF WHISKERS BY THE REDUCTION OF METAL SALTS*

SIDNEY S. BRENNER†

The conditions for the growth of Fe, Cu, Ag, Ni, Co, Pt, and Au whiskers by the reduction of their halides are described. It is shown, at least in the case of copper, that the whiskers grow from the tip, and there seems little doubt that the growth occurs by the condensation of freshly-formed metal vapor. The supersaturation of the metal vapor appears to be extremely high during the whisker growth. Whiskers with a large variety of shapes and perfection grow under these conditions. Of greatest interest are the near-perfect whiskers which exhibit high strength and are bound by smooth planes. Whiskers larger than 8 μ are rarely near-perfect.

LA CROISSANCE DE BARBES PAR LA REDUCTION DE SELS METALLIQUES

Les conditions de croissance des barbes de Fe, Cu, Hg, Ni, Co, Pt, et Au pour la réduction de leurs halogénures sont décrites.

On montre que, dans le cas du Cu tout au moins, les barbes croissent à partir de l'extrêmité et il semble y avoir de doute que la croissance s'effectue par la condensation de vapeur métallique fraîchement formée.

La sursaturation de la vapeur métallique se révèle très élevée pendant la croissance de la barbe.

Des barbes de formes et de perfection très variables croissent dans ces conditions.

Les barbes presque parfaites sont du plus haut intérêt, car elles montrent une résistance élevée et sont limitées par des plans.

Des barbes d'une longueur supérieure à 8 μ ont rarement une perfection très élevée.

DAS WACHSEN VON "WHISKERS" DURCH REDUKTION VON METALLSALZEN

Es werden die Wachstumsbedingungen für "Whisker" aus Fe, Cu, Ag, Ni, Co, Pt, und Au beschrieben, die durch Reduktion der Halogenide erzeugt werden. Es hat sich gezeigt, dass mindestens im Fall des Kupfers die Whiskers von der Spitze her wachsen und es bestehen wenig Zweifel, dass das Wachstum durch die Kondensation von frisch gebildetem Metalldampf erfolgt. Die Übersättigung des Metalldampfes scheint während des Whiskerwachstums extrem gross zu sein. Unter diesen Bedingungen wachsen Whiskers in einer grossen Vielfalt bezüglich ihrer Form und Fehlerfreiheit. Von grösstem Interesse sind die "fast fehlerfreien" Whisker, die eine grosse Festigkeit aufweisen und die durch glatte Ebenen begrenzt werden. Whisker, die grösser als 8 μ sind, sind selten "fast fehlerfrei".

INTRODUCTION

Metals in the form of fine filaments or whiskers have been grown by the reduction of some of their salts as far back as 1877.[1] Of special interest was the growth of interwoven, cotton-like silver fibers (Haarsilber) by the reduction or oxidation of silver sulfide. This phenomenon was investigated by many authors. A growth mechanism was postulated by Kohlschütter[2] in 1932, and later supplemented by C. Wagner.[3] These authors proposed that the excess silver ions and electrons, formed on the sulfide surface by the reduction or oxidation, migrate in the sulfide until they can attach themselves to a metallic silver nucleus. If the nucleus lies at the surface and the silver ions are furnished at the base, the nucleus can be pushed out, forming a filament.

These filaments were found to be polycrystalline,[4] having a fiber structure with the axis parallel to the [112] direction. Upon heating to 900°C, the orientation became random.

Kohlschütter[2] briefly reported that silver and copper filaments can also be grown from AgCl and CuCl. He speculated that in this case the growth may be due to metal-vapor condensation.

More recent examples of whisker growth by the reduction of metallic salts were found by Gatti and Fullman[5] and Everett and Amick.[6] Gatti and Fullman grew iron whiskers by hydrogen reduction of ferric hydroxide precipitated from iron chloride solution. It was demonstrated by Doremus and Sears[19] that whiskers did not grow by reduction of a well-washed precipitate. It was therefore deduced that an iron chloride was the active ingredient.

Everett and Amick obtained silicon fibers by reducing diluted $SiCl_4$ with zinc. Both the iron and silicon fibers were shown to be single crystals. The iron whiskers, up to several cm in length, were reported to be bounded by four (100) planes. The silicon fibers up to 1 cm in length were parallel to the [111] direction.

Perhaps the most unusual property of the iron whiskers grown by Gatti and Fullman was their remarkable strength in bending. Elastic bending strains in excess of 1.4 per cent were reported.[7]

* Received July 21, 1955.

† General Electric Research Laboratory, Schenectady, New York.

The high bending strength of metal whiskers was first pointed out by Herring and Galt[8] for tin whiskers grown from tin plate.[9, 10] The high strength can be explained by assuming a low dislocation density (near-perfection) in the whisker. In the case of mercury whiskers grown by condensation from the pure vapor, Sears[11] proposed that in the ideal situation the whiskers contained one axial screw dislocation.

It is the purpose of this paper to report that many metals can be grown in the form of whiskers by the reduction of metal salts, particularly the halides. It is shown that, at least in the case of copper whiskers grown from CuI, the growth proceeds at the tip. The growth process and properties of some of the whiskers, especially copper, are discussed.

EXPERIMENTAL

Growth

The apparatus used for the growth of the whiskers is shown in Fig. 1. It consisted simply of a tube furnace containing either a quartz or mullite tube. A boat filled with the halide was pushed into the furnace by means of a tungsten rod. Hydrogen at a measured flow-rate was passed through the tube except in the case of gold and platinum, where reduction was carried out by thermal decomposition. The gaseous products were bubbled through water to separate the hydrogen halide.

When the reduction was stopped, the boat was pulled into the cooling chamber, the tube was flushed with helium, and the sample removed.

Vacuum pumps, manometers, and a palladium hydrogen bleeder were used to determine the effect of low pressure and small flow-rate.

For visual observation of the whisker growth the reduction was carried out in the more elaborate apparatus shown in Fig. 2. Its construction prevented fogging of the viewing window and allowed the access of sufficient light.

A Bausch and Lomb stereoscopic microscope with a magnification of up to 120× was used to examine the reduced halide. To measure the diameters of the fine whiskers and to examine their surface and geometry,

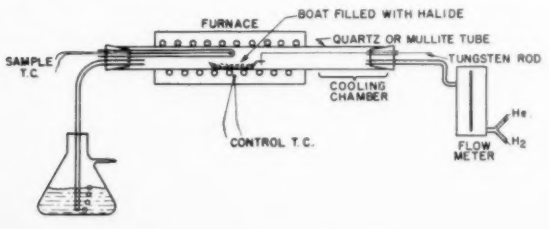

FIG. 1. Whisker growth apparatus.

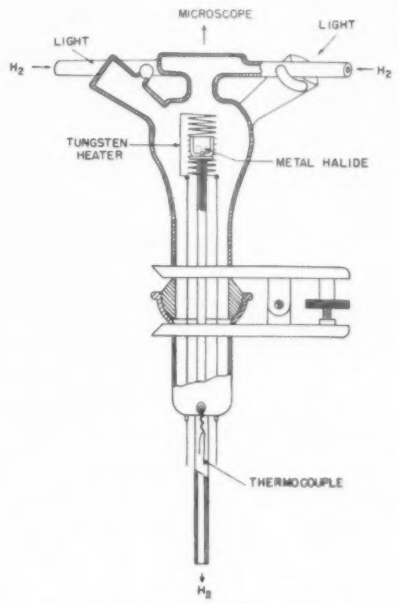

FIG. 2. Whisker growth apparatus for visual observation.

a high-powered microscope and an electron microscope were used.

X-Ray Diffraction

X-ray diffraction patterns were obtained from some of the whiskers for identification, crystallography, and crystal perfection. Both rotation and Laue cameras were used.

Strength Measurements

The elastic strength of the whiskers was determined by measuring the radius of curvature a whisker could sustain without deformation. The elastic bending strain is given by

$$e = \frac{r}{R}$$

where r = radius of whisker

R = radius of curvature

RESULTS

Growth

Whiskers of the following metals were grown from their halides:

Hydrogen reduction: Cu, Ag, Fe, Ni, Co

Thermal reduction: Au, Pt

Table 1 lists the halides from which these whiskers were grown, and the temperature range of reduction. The equilibrium vapor pressure of the halide and metal at the optimum temperature of reduction is

included. All of the halides were analytical reagent grade, and were not further purified.

Copper, silver, and iron whiskers were grown from several of their halides. However, best results were obtained with the one indicated in Table 1. In no case was it possible to grow whiskers from the more stable fluorides.

Only the chlorides were used in growing the gold and platinum whiskers. Examples of the copper, silver, platinum, and cobalt whiskers are shown in Figs. 3–6.

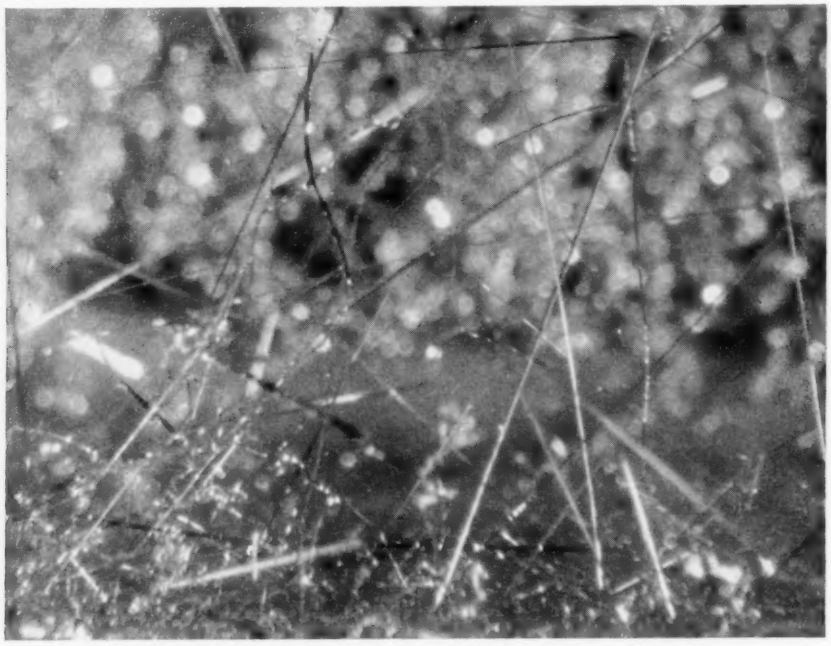

FIG. 3. Copper whiskers grown from CuI. Mag. 20×.

The shape of the whiskers varied greatly. In addition to straight and kinked whiskers, numerous odd shapes were observed. The regularity of the

TABLE 1

Metal	Halide	Temperature range (°C)	Optimum temperature	Maximum length (mm)	Po halide (mm Hg)	Po metal (13) (mm Hg)
Cu	CuCl, CuBr, CuI*	430–850	650	~50	10.4 (12)	2.23×10^{-10}
Ag	AgCl*, AgI	700–900	800	~10	0.14 (15)	3.71×10^{-5}
Fe	$FeCl_2$, $FeBr_2$	730, 760 (low H_2 flow)		~20	59 (17)	2.07×10^{-10}
Ni	$NiBr_2$	740		2	68 (15)†	8.18×10^{-15}
Co	$CoBr_2$	650		3	8 (15)†	
Pt	$PtCl_x$	800		3	Decomposes	7.23×10^{-16}
Au	$AuCl_x$	550		2	Decomposes	8.58×10^{-15}

* Best results.
† Vapor pressure only approximate because of insufficient data.

FIG. 4. Silver whiskers grown from AgCl. Mag. 20×.

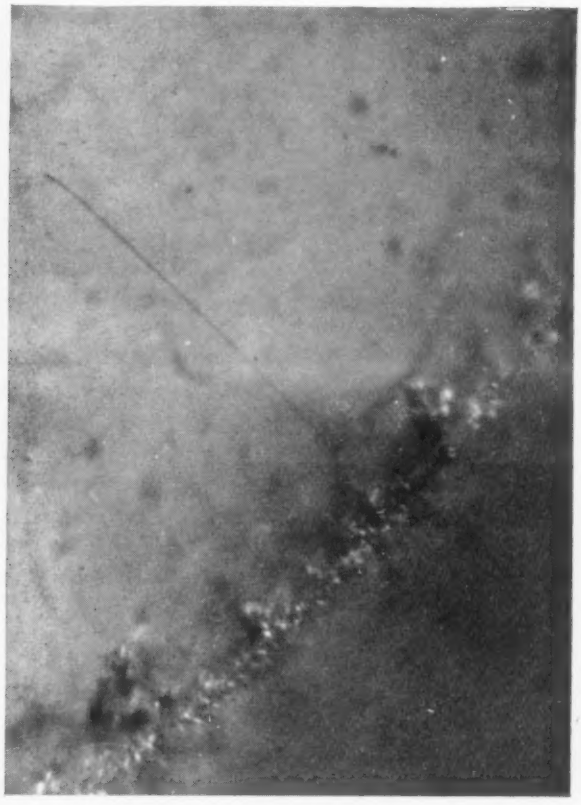

FIG. 6. Cobalt whisker grown from $CoBr_2$. Mag. 20×.

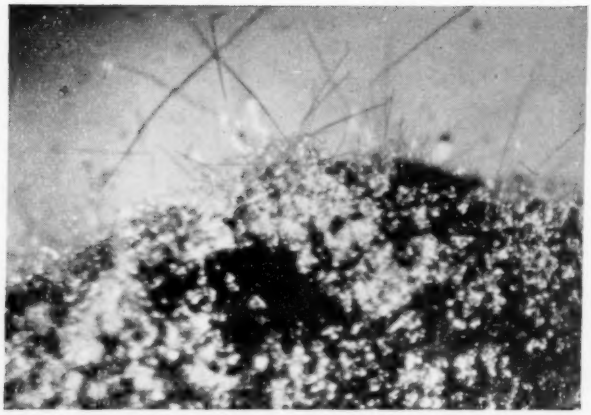

FIG. 5. Platinum whiskers grown from $PtCl_2$ at 720°C. Mag. 60×.

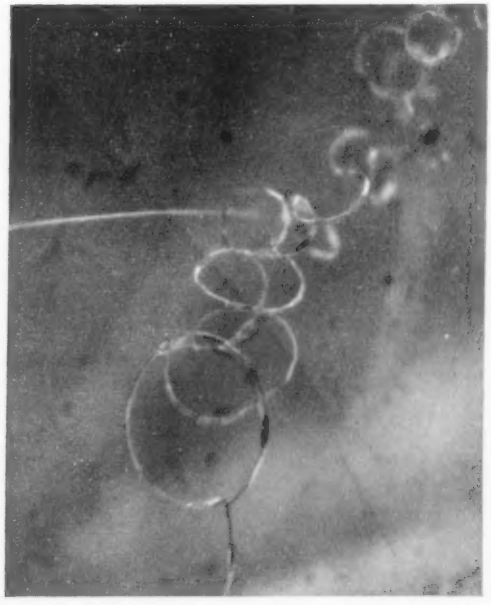

FIG. 7. Silver spiral. Mag. 60×.

VOL. 4 1956

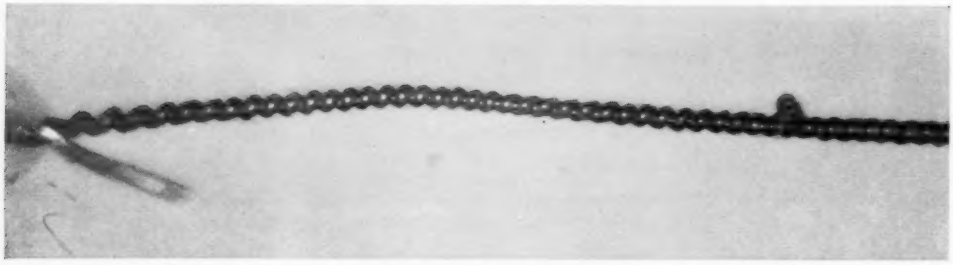

FIG. 8. Silver twist. Mag. 250×.

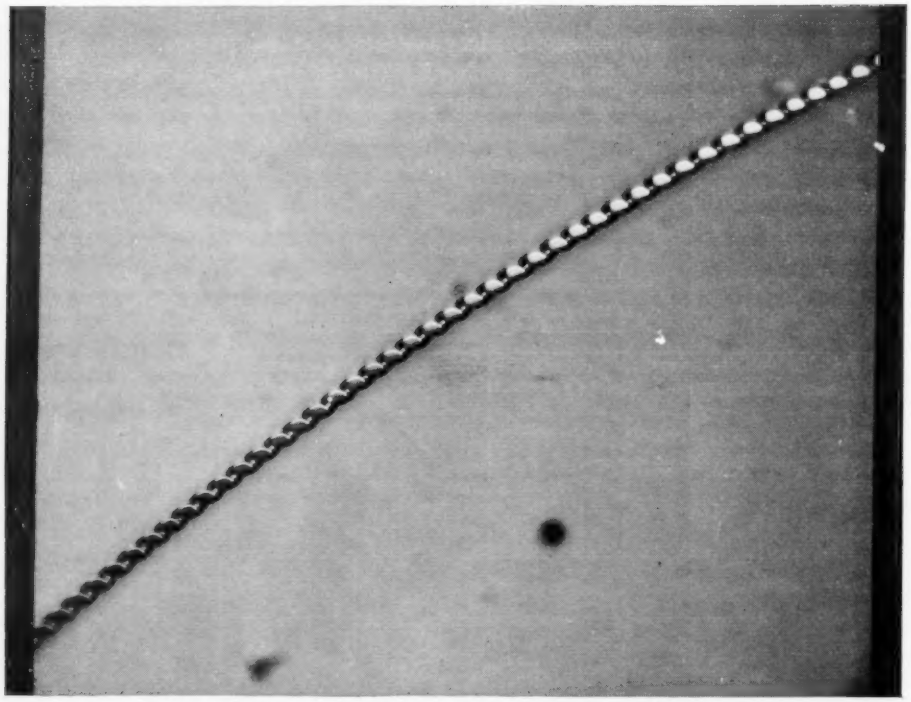

FIG. 9. Silver twist showing flat facets. Mag. 150×.

FIG. 10. Tip of silver whisker grown from AgCl + AgI at 660°C. Mag. 60×.

FIG. 12. Kinked and distorted copper whisker grown at 820°C. Mag. 13.3×.

growth pattern was often remarkable. Some of the growth shapes are shown in Figs. 7–13. No attempt was made to explain these shapes.

At this point, it may be appropriate to define the term "whisker" as used in this paper. It includes fibrous growth of all shapes, both single crystals and polycrystals, the only restriction being a high length-to-diameter ratio.

The maximum size and ease of growth of the whiskers varied greatly from one metal to another. While a great number of long copper, silver, and iron whiskers grew from each charge, only a few small whiskers of nickel, cobalt, and gold (up to 1 to 2 mm in length) could be grown during each reduction. Studies were, therefore, mainly restricted to the growth and properties of copper whiskers.

FIG. 11. Stack of silver plates grown from AgCl + AgI at 660°C. Mag. 60×.

FIG. 13. Platinum tube grown from $PtCl_2$ at mag. 60×.

VOL. 4 1956

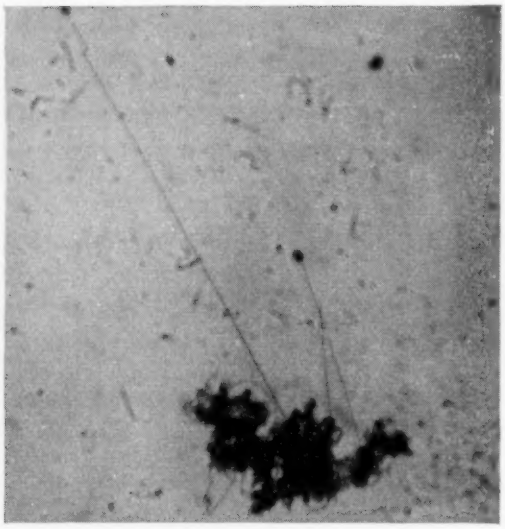

FIG. 14. Growth of copper whiskers from cotton-like copper deposit. 610°C. Mag. 60×.

COPPER WHISKERS

Growth

Copper whiskers were grown by hydrogen reduction of CuCl, CuBr, and CuI. Best results were obtained with CuI. This salt melts at 588°C and has a vapor pressure in excess of 1 mm above this temperature. The vapor pressure, as a function of temperature, is reported by Jellineck and Rudat[12] to be as follows:

	Equilibrium vapor pressure (mm)	
T (°K)	CuI	Cu
1373	316	4.4×10^{-4}
1273	182	4.3×10^{-6}
1173	100	2.8×10^{-6}
1038	32.4	3.1×10^{-8}
988	20.3	4.2×10^{-9}
948	13.4	7.2×10^{-10}
900 (extrap)	7.8	7.2×10^{-11}
800 (extrap)	2.1	2.4×10^{-13}

The equilibrium vapor pressure of Cu as taken from Smithells[13] is included for reference.

Jellineck and Rudat believe that cuprous-iodide vapor consists almost entirely of the monomer. Dissociation of the CuI to Cu and I_2 is negligible. At 675°C, the iodide dissociation pressure is only 5×10^{-3} mm.

Copper whiskers were grown in the temperature range of 430 to 850°C. The reduction of the CuI occurs very readily at the higher temperatures, and much less so at the lower temperatures. Whereas the reduction would take minutes at 850°C, the same charge required several days to be appreciably reduced at 430°C.

After reduction, the boat contained some massively reduced copper at the bottom, fine copper powder deposited along the walls, and whiskers growing from the sides. Visual observation of the whisker-growth

FIG. 15. Similar to Fig. 14. Mag. 3500×.

at 630°C indicated the sequence to be as follows. As soon as the boat containing the CuI heated sufficiently, small copper particles deposited along the walls of the boat. Shortly thereafter fine, vibrating copper whiskers were observed growing out from the sides of the boat. After some time the whiskers appeared to stop growing in length and began to broaden. At the same time other growth phenomena were observed. Balls of cotton-like copper resembling cactus-growth often formed, from which whiskers would grow out. This phenomenon is illustrated in Figs. 14 and 15. A peculiar growth pattern was

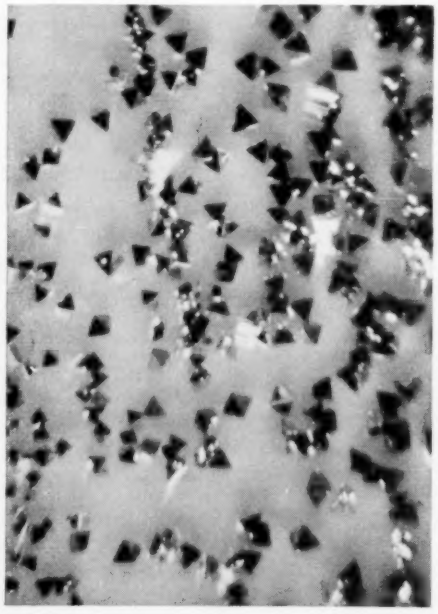

FIG. 16. Octahedral copper particles deposited along walls of boat at 850°C. Mag. 26×.

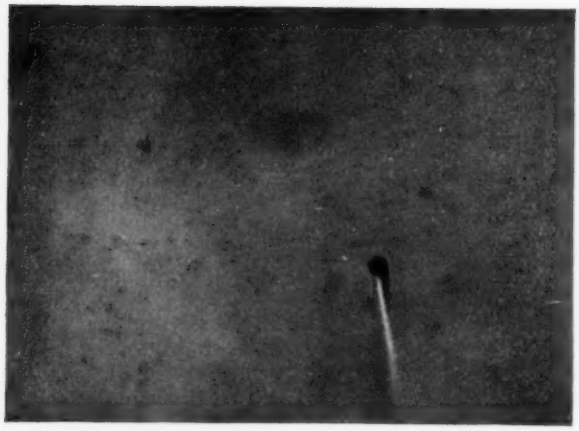

FIG. 17. Hexagonal cross-section of Cu whisker. Mag. 60×.

sometimes observed whereby a small rotating particle at the tip of a whisker appeared to weave out an irregular strand of copper. Welding of one whisker to another occurred when they came in contact.

Straight whiskers up to 5 cm in length and 1 to 200 microns in width were observed.

A number of the whiskers exhibited growth kinks. The distribution of the kink angles was not determined; however, 90° angles were frequently observed.

Temperature had a pronounced effect on the appearance and size of the whiskers. At lower temperatures (430 to 700°C) the majority of the whiskers were straight, narrow, and exhibited little overgrowth. From 700 to 850°C the whiskers were coarse and overgrown, and were frequently kinked and distorted. Above 850°C whiskers could only be observed occasionally. Instead, small, well-developed octahedral copper particles, as shown in Fig. 16, were observed along the walls of the boat.

The well-developed whiskers appeared to be predominantly hexagonal in cross-section (Fig. 17). When the iodide reduction was carried out for longer periods at temperatures below 600°C, the whiskers had a tendency to broaden into blades. The cross-section of a hexagonal whisker which began to broaden into a blade is shown in Fig. 18. Blades 5 cm long and 0.5 mm in width have been grown from CuI at 600°C. Some of these blades exhibited growth markings on their surfaces, as illustrated in Fig. 19.

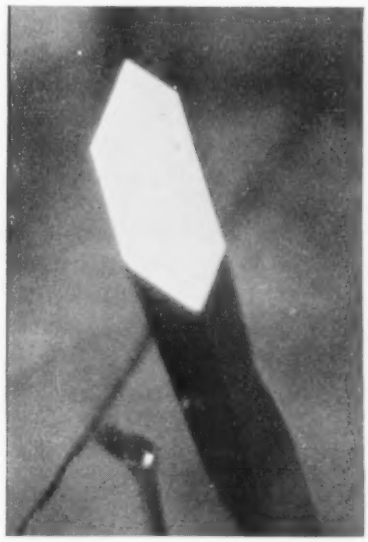

FIG. 18. Cross-section of hexagonal whisker broadening into a blade. Mag. 60×.

Hydrogen Flow-rate and Pressure

The flow-rate or partial pressure of the hydrogen had little effect on the whisker growth as long as they were above certain values. No whiskers could be grown from CuCl at 754°C when the hydrogen partial pressure was below 0.125 atm. Similarly, no whiskers could be grown from CuI at 620°C when the lineal velocity of the hydrogen was below 3 cm/sec. Above these values variations in hydrogen flow or pressure (up to 100 cm Hg) had little or no effect, except in the case of iron whiskers grown from $FeBr_2$, where a low hydrogen flow was favorable.

Crystallography

X-ray Laue and rotation patterns indicated that the straight, well-developed whiskers were single

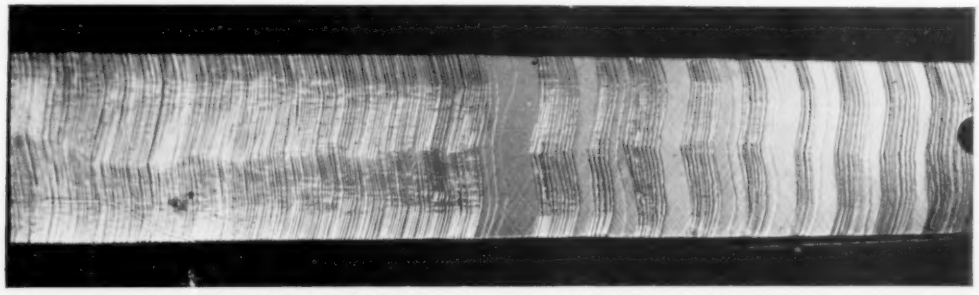

FIG. 19. Growth markings on copper blade. Mag. 100×.

VOL. 4 1956

crystals. Some distortion of the crystal lattice was evident at the larger sizes (>10 μ). The distortion was more prevalent with the silver whiskers.

The fiber axis of the copper whiskers was not constant. Of ten samples, the following distribution was found.

[111]	4
[110]	5
[100]	1

Four silver whiskers were examined, indicating three [100] fiber axis and one [110] axis. Two iron whiskers both showed a [100] fiber axis. The accuracy of the determinations was within two degrees.

An interesting feature of the whisker blades was the fact that the broad sides always corresponded to (110)

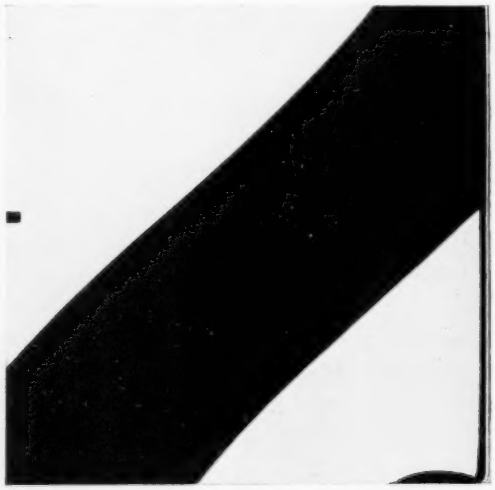

FIG. 20. Surface of copper whisker. Mag. 40,000×.

planes. Apparently the whiskers were predominantly bounded by these planes.

Growth Rate

An attempt was made to measure the growth-rate of the whiskers by means of motion pictures. This was difficult, due to the fact that the whiskers vibrated considerably at the start of the growth and infrequently grew in a horizontal plane. An approximate value of the growth-rate was obtained by reducing the CuI for a short period and measuring the length of the longest whisker. The minimum possible growth-rate thus determined varied irregularly from 4 to 23 microns per sec in the temperature range 550 to 670°C. One particular whisker, 5.5 microns in width, grew 14 mm in 10 minutes (23 μ/sec) at 670°C. The axis of this whisker was parallel to the [111] direction.

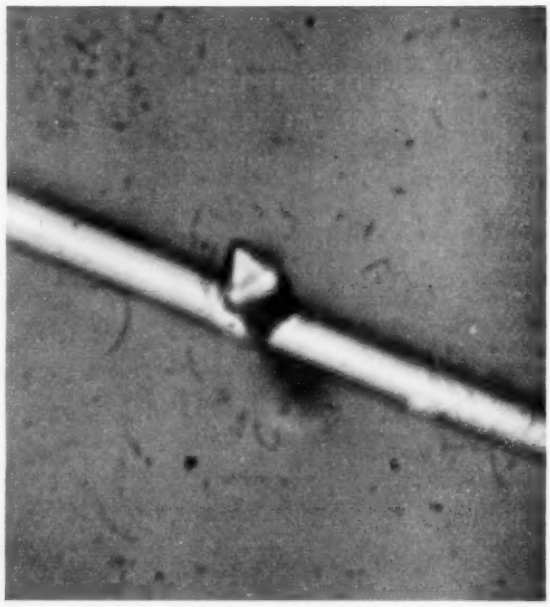

FIG. 21. Whisker nucleating on a whisker. Mag. 400×.

Surface and Ends of Whiskers

The surface of the whiskers varied from coarse and overgrown to extremely smooth. The surface of one whisker magnified 40,000× is shown in Fig. 20. An irregularity of 25 Å would be visible at this magnification. On other whiskers, nuclei of whisker branches such as shown in Fig. 21 could sometimes be observed.

FIG. 22. Tip of silver whisker. Mag. 400×.

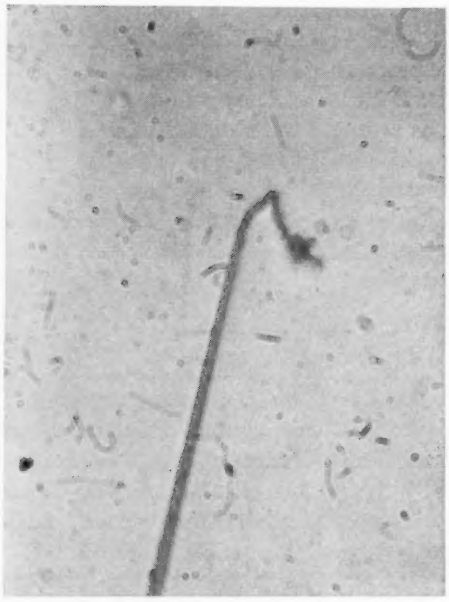

FIG. 23. Tip of copper whisker. Mag. 830×.

The appearance of the whisker tips was irregular. Examples are shown in Figs. 22, 23, and 24. Sometimes the tip came to a point as shown schematically in Fig. 25.

The surfaces of the whiskers after removal from the furnace were highly reflectant, but soon tarnished if left exposed to humid air.

Elastic Bending Strain

The elastic bending strains of a large number of the well-developed whiskers were determined. Strains of up to 2 per cent were measured. Fig. 26 shows a copper whisker of 2.3 μ-radius supporting a 1.5 per cent strain. When the radius of the whisker was 1 μ or less it became difficult to measure the maximum bending strain because of the small radius of curvature through which the whisker had to be bent.

When the whisker failed, it kinked at one or more points. The strength of the whisker including the region near the kink remained strong even after the failure.

FIG. 24. Tip of copper whisker. Mag. 10,000×.

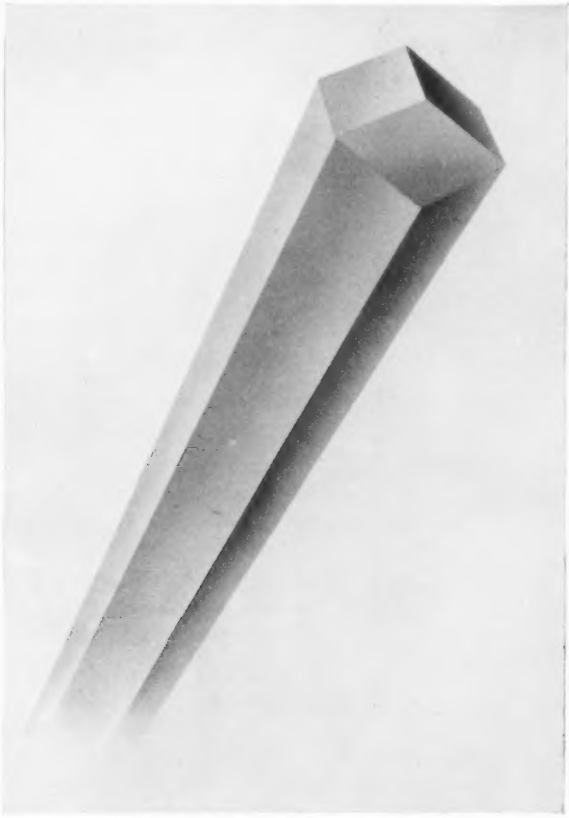

FIG. 25. Tip of whisker shown in Fig. 17 (schematic).

FIG. 26. Copper whisker strained 1.5 per cent.

VOL. 4 1956

There appeared to be a size-effect on the strength of the whisker; copper whiskers larger than 8 μ were usually not highly elastic. The strong whiskers have been defined as near perfect.

The overgrown and distorted whiskers exhibited little elastic strength, and are probably no stronger than bulk copper.

DISCUSSION

The growth mechanism of whiskers such as mercury grown from the pure vapor phase has been adequately described by Sears.[14] Sears postulated the following growth sequence. The supersaturated mercury vapor condenses around a screw dislocation emerging from a crystalline region of the container wall. Once started the whisker grows by means of metal atoms adsorbing on the whisker surface, which then migrate to the tip, where they are incorporated around the emerging screw dislocation. The primary requisite for the growth of whiskers is that the pressure is such that the two-dimensional nucleation frequency is negligible.

The supersaturation required for coherent two-dimensional nucleation can be shown to be

$$\ln \alpha = \frac{\pi a \sigma^2 M}{\rho k R T^2 \ln \frac{B}{\dot{N}}} \tag{1}$$

where α = supersaturation ratio $\frac{p}{po}$

a = interplanar distance

σ = surface energy

M = molecular weight

ρ = density

B = constant $\sim 10^{20}$ sec^{-1}

$\dot{N}$ = nucleation rate—nuclei/cm^2/sec

For non-coherent two-dimensional nucleation, a grain boundary has to be introduced. The supersaturation required to give the equivalent nucleation rate is only slightly higher than that required for coherent nucleation.[20]

Assuming that every striking atom becomes adsorbed, the axial growth-rate of the whiskers described by Sears was calculated to be

$$l = \frac{2\lambda p}{r\rho}\sqrt{\frac{M}{2\pi RT}} \tag{2}$$

where λ = mean free path of the adsorbed atoms

r = whisker radius

l = length of whisker

The growth of whiskers by the reduction of volatile metal salts is more difficult to interpret. For instance, in the case of CuI there are present $CuI_{(l)}$ or $CuI_{(s)}$, $CuI_{(v)}$, $Cu_{(v)}$, $Cu_{(s)}$, H_2, and HI. That the whisker growth proceeds at the tip is shown fairly conclusively in Fig. 27. Pictures of a growing kinked whisker were taken as a function of time. The distance from the kink to the base did not change perceptibly, indicating that material was *not* furnished at the base. There seems to be little doubt that the whisker grew by condensation of metal vapor. Although it is unlikely that the whisker in Fig. 27 was near-perfect, it is reasonable to assume that the axial growth process is the same for all whiskers.

The supersaturation ratio α of the freshly formed copper as a function of distance from the CuI-Cu surface probably varies as shown in Fig. 28. Very near the surface α is almost unity, because of the massively reduced copper which acts as a deposition sink. A small distance away α increases rapidly and finally decreases again beyond point a.

The shape of the curve and the maximum supersaturation is determined by the rates of evaporation and reduction of the CuI. Little is known concerning the kinetics of the CuI reduction. Above its melting-point the reduction is very rapid, and the Cu vapor pressure is probably determined mainly by the rate of evaporation of the CuI.

The supersaturation of the copper vapor during the whisker growth appears to be extremely high. An approximation of the supersaturation can be obtained by calculating the impingement rate that is required to give the observed growth-rate of 23 μ/sec at 943°K. Although the growth process is most likely more complicated than adsorption of atoms on the whisker surface, migration of these atoms to the tip, and finally incorporation at the tip, this model indicates the order of magnitude of the required supersaturation. Assuming then that the whisker radius initially was 10^{-6} cm and letting $\lambda = 1$ mm, from eq. (2), the supersaturation *near* the surface is $\sim 10^4$. The values of the radius r and mean free path λ were so chosen to minimize the supersaturation required for the given axial growth-rate. The supersaturation of the copper *on* the surface near the tip is undoubtedly less because of the tip which acts as a deposition sink; however, the supersaturation on the surface further away from the tip may well be the same as in the vapor phase $\sim 10^4$.

A supersaturation of 10^4 can be obtained without difficulty during the CuI reduction. The maximum obtainable supersaturation approaches

$$\frac{Po\ \text{CuI}}{Po\ \text{Cu}}$$

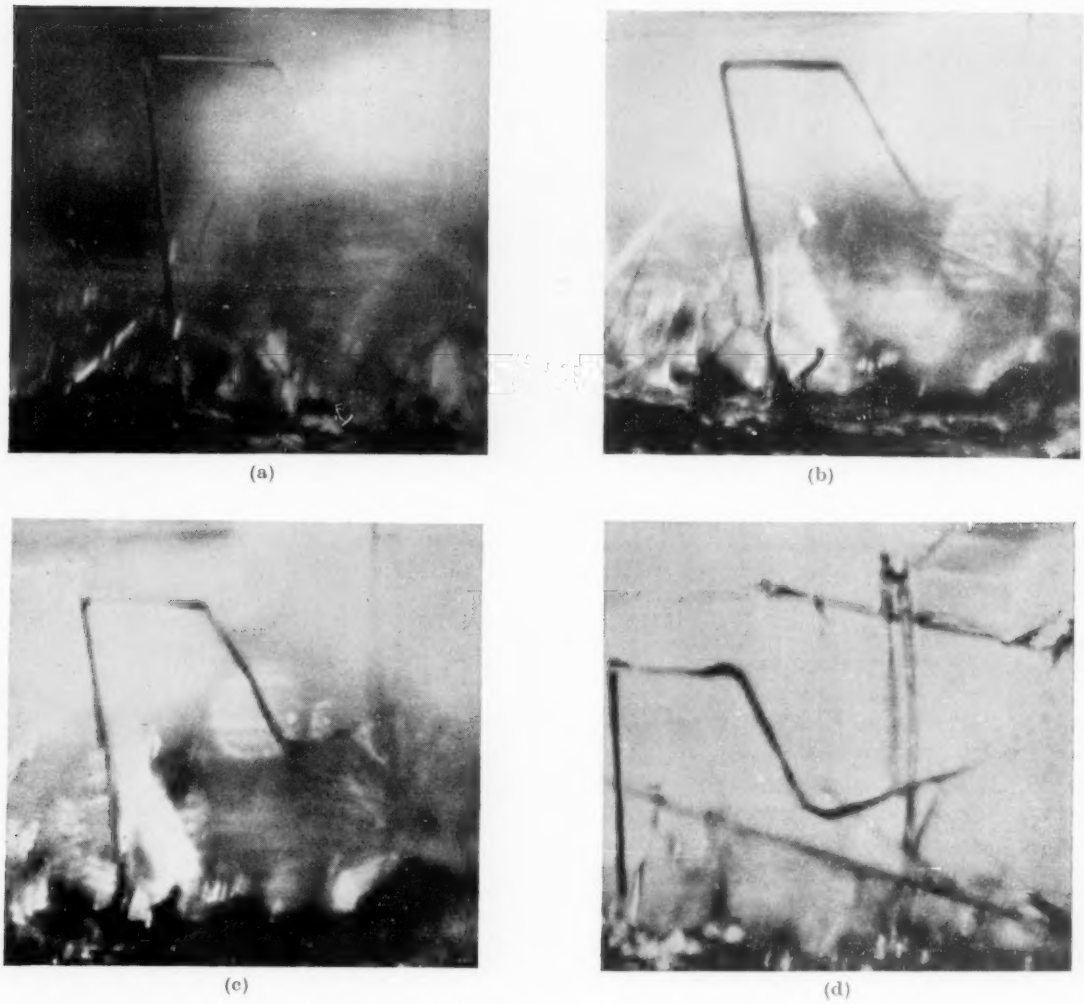

(a) (b) (c) (d)

FIG. 27. Growth sequence of a kinked copper whisker grown from CuI at 570°C.

where Po CuI and Po Cu are the equilibrium vapor pressure of CuI and Cu respectively. At 943°K this ratio is 2×10^{10}, a million times larger than that which is required.

The frequent appearance of overgrowth, especially at the higher temperatures, can now be understood. With a supersaturation of 10^4 the coherent nucleation rate at 943°K with $\sigma = 1900$ ergs/cm^2 (18) and $a = 2.56$ Å (d_{110}) equals from eq. (1) 2.2×10^{10} nuclei/cm^2/sec. The non-coherent nucleation rate is only a small amount less.

At the higher temperatures the supersaturation is most likely still greater than 10^4, and it is believed that the octahedral copper particles shown in Fig. 18 form by homogeneous three-dimensional nucleation At 1123°K the supersaturation required for homogeneous three-dimensional nucleation calculated from an equation similar to (2) is 3×10^3.

Since well-developed whiskers bound by smooth planes grew in the presence of high supersaturations, one is forced to conclude either that the growth mechanism of these whiskers is different from that

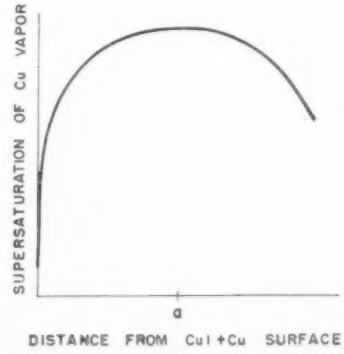

FIG. 28. Probable change of copper supersaturation as a function of distance from the Cu-CuI surface.

postulated by Sears, or that two-dimensional nucleation is more difficult than described by equation (1). One possibility is that the surface of the whisker is covered by an adsorbed layer of gas molecules such as HI, lowering the non-coherent two-dimensional nucleation frequency of the copper sufficiently to allow the growth of some whiskers, free of overgrowth.

Formation of the whiskers always occurred on deposited copper, and the initial substrate had no effect. In addition to porcelain, substrates of Pyrex, quartz, metal, and firebrick were used. One possible method of formation has been described by Brenner and Sears.[16] Briefly, it was proposed that, when the metal surface presents a low dislocation density, an isolated dislocation can form a growth hill. This hill then readily grows out from the surface into a fiber because of the change in the concentration configuration of the copper in the vapor surrounding the growth cone and fiber. Essentially it is dentritic growth in the vapor, the diffusion barrier being created by the foreign gases such as H_2 and HI.

It is more difficult to understand the cessation of the axial growth. As Figs. 22 and 23 show, disturbances at the tip of some of the whiskers can be observed. In the absence of these disturbances the axial growth may be limited by the decrease of the supersaturation at a distance (Fig. 28) from the Cu-CuI surface. It has been noticed that many of the longer whiskers grow at a small angle to the Cu-CuI surface.

The apparent decrease in the bending strength of Cu whiskers, when the diameter exceeds about 8 μ, requires further elucidation, and will be the subject of a future paper.

CONCLUSIONS

The growth of whiskers by the reduction of volatile metallic salts such as the halides seems to be a general phenomenon. It has been shown that the growth of the whiskers proceeds at the tip, and there seems little doubt that material is furnished by condensation of the freshly formed metal vapor.

The growth-rate of the whiskers requires a high supersaturation, far in excess of that required for two-dimensional nucleation from the pure vapor. Under these conditions many perplexing growth-forms occur, in addition to the straight and smoothly bound whiskers.

The thin, smoothly bound whiskers exhibit bending strains in excess of 1.5 per cent indicating near-perfection. There seems to be a size-dependence on the strength which will be investigated further.

REFERENCES

1. J. Margottet, Reproduction des sulfure, séléniure et tellurure d'argent cristallisés et de l'argent filiforme, *Compt. Rend.*, **85,** 1142 (1877).
2. H. W. Kohlschütter, Uber den Mechanismus der Haarsilberbildung auf Silbersulfid, *Z. Elektrochemie*, **38,** 345 (1932).
3. C. Wagner, Mechanism of the Reduction of oxides and sulphides to metals, *Trans. Amer. Inst. Min. Met. Eng.*, **194,** 214 (1952).
4. R. Schenck, R. Fricke, and G. Brinkman, Untersuchungen über metallische Fasern, *Z. Phys. Chem.*, **139** (1928).
5. A. Gatti and R. L. Fullman, to be published.
6. E. R. Everett and J. A. Amick, Formation of single-crystal silicon fibers, *J. Appl. Phys.*, **25,** 1204 (1954).
7. G. W. Sears, A. Gatti, and R. L. Fullman, Elastic properties of iron whiskers, *Acta Met.* **2,** 727 (1954).
8. C. Herring and J. K. Galt, Elastic and plastic properties of very small metal specimens, *Phys. Rev.*, **85** 1060 (1952).
9. K. G. Compton, A. Medizza, and S. M. Arnold, Filamentary growths on metal surfaces "whiskers," *Corrosion*, **7,** 327 (1951).
10. R. M. Fisher, L. S. Darken, and K. G. Carroll, Accelerated growth of tin whiskers, *Acta Met.*, **2,** 368 (1954).
11. G. W. Sears, Mercury whiskers, *Acta Met.*, **1,** 457 (1953).
12. K. Jellineck and A. Rudat, *Z. Phys. Chem.*, **143A,** 259 (1929).
13. C. J. Smithells, *Metals Reference Book*, Interscience Publishers Inc., New York (1949) 449.
14. G. W. Sears, Growth mechanism of mercury whiskers, *Acta Met.*, **3,** 361 (1955).
15. L. L. Quill, The chemistry and metallurgy of miscellaneous materials, McGraw-Hill, New York (1950).
16. S. S. Brenner and G. W. Sears, Mechanism of whisker growth III—Nature of growth sites, *Acta Met.*, to be published.
17. R. O. Macharen and N. W. Gregory, The vapor pressure of iron (II) bromide, *J. Phys. Chem.*, **59** 184 (1955).
18. H. Udin, Surface tension of Cu, *Trans. Amer. Inst. Min. Met. Eng.*, **191,** 63 (1951).
19. R. M. Doremus and G. W. Sears, Private communication.
20. R. L. Fullman and G. W. Sears, Private communication.

THE KINETICS OF RECOVERY AND RECRYSTALLIZATION OF COPPER FROM HARDNESS AND THERMOELECTRIC-POWER MEASUREMENTS*

T. LL. RICHARDS,† S. F. PUGH,‡ and H. J. STOKES†

Annealing of H.C. copper strip cold-rolled with reductions in thickness of 50 per cent and 96 per cent has been studied as a rate-process by parallel observations of changes in hardness and thermoelectric power. In accordance with earlier investigations, change in hardness is taken to be proportional to fraction of metal recrystallized, while thermoelectric power is assumed to be directly related to residual elastic lattice strain. While the hardness—isothermal annealing curve of strip rolled 50 per cent exhibits a definite discontinuity indicative of two processes, such as recovery (or polygonization) and recrystallization, the thermoelectric power curve is, in agreement with Brindley's earlier conclusion, pseudo first order. The rate of decrease of average lattice strain during both polygonization and recrystallization is apparently governed by similar processes of dislocation migration. The annealing of heavily rolled strip is more complex; hardness and thermoelectric power curves, however, are identical, and analysis of the curves, outlined in an appendix, indicates that the dominant process is one of second order in agreement with previous findings. The second-order character follows naturally from the concept that decrease in thermoelectric power and softening occurs by direct interaction and annihilation of stress fields associated with stable arrays of dislocations at grain interfaces. It is pointed out that this concept is also consistent with recrystallization as a process of nucleation and growth.

CINÉTIQUE DE LA RESTAURATION ET DE LA RECRISTALLISATION DU CUIVRE PAR MESURE DE DURETÉ ET DU POUVOIR THERMOÉLECTRIQUE

Le recuit de bandes laminées à froid en cuivre HC après réduction d'épaisseur de 50 et de 96% a été étudié par mesure des changements de dureté et du pouvoir thermoélectrique. Conformément à d'anciennes mesures, le changement de dureté est proportionnel au pourcentage du métal recristallisé, tandis que le pouvoir thermoélectrique est supposé dépendre directement des déformations réticulaires résiduelles. Tandis que les courbes de dureté après recuit de bandes laminées à 50% montrent une discontinuité bien définie caractéristique de deux processus tels que restauration (ou polygonisation) et recristallisation, la courbe du pouvoir thermoélectrique est, conformément aux anciennes conclusions de Brindley, du premier ordre. La vitesse de décroissance de la déformation réticulaire moyenne, pendant la polygonisation et la recristallisation, est apparemment régie par un mécanisme analogue à la migration des dislocations. Le recuit des bandes fortement laminées est plus complexe. Les courbes de dureté et du pouvoir thermoélectrique sont néanmoins identiques et leur analyse, faite dans un appendice, indique que le mécanisme prépondérant est du second ordre, en accord avec les mesures antérieures. Ce caractère est la conséquence naturelle de l'idée que la diminution du pouvoir thermoélectrique et celle de la dureté sont dues à l'interaction et à la destruction des champs de contraintes associées aux répartitions stables de dislocations dans les joints de grains. Il est remarqué que cette conception est en accord avec le mécanisme de germination et de croissance pour la recristallisation.

ÜBER DIE KINETIK DES ERHOLUNGS- UND REKRISTALLISATIONSVORGANGES BEI KUPFER HERGELEITET AUS HÄRTEMESSUNGEN UND BESTIMMUNGEN DER THERMOKRAFT

Durch gleichzeitige Beobachtung der Härteänderungen und der Änderungen der Thermokraft wurde die Zeitabhangigkeit des Anlassvorganges von Walzbändern aus Hochleitfähigkeitskupfer mit einem Verformungsgrad von 50 und 96% Dickenabnahme untersucht. In Übereinstimmung mit früheren Untersuchungen wird angenommen, dass die Härteänderung proportional dem rekristallisierten Anteil des Metalles ist, während die Thermokraft in direkter Beziehung zu den verbleibenden elastischen Gitterspannungen steht. Während die Härtekurve beim isothermen Anlassen des um 50% verformten Bandes eine definierte Unstetigkeit aufweist, die zwei Vorgänge anzeigt—die Erholung (oder Polygonisation) und die Rekristallisation—ist die Kurve der Thermokraft, in Übereinstimmung mit den früheren Folgerungen von Brindley, pseudo erster Ordnung. Die Geschwindigkeit des Abbaus der durchschnittlichen Gitterspannungen während der Polygonistion wie auch während der Rekristallisation wird offensichtlich durch ähnliche Vorgange der Versetzungswanderung beeinflusst. Die Vorgange beim Anlassen der stark verformten Bänder sind wesentlich verwickelter; die Kurven der Härte und der Thermokraft sind jedoch identisch. Eine Analyse dieser Kurven, die im Anhang umrissen wird, zeigt, dass der beherrschende Vorgang ein Prozess zweiter Ordnung ist, was mit früheren Beobachtungen übereinstimmt. Dass dieser Vorgang ein Prozess zweiter Ordnung ist, folgt naturgemäss aus der Annahme, dass der Abfall der Thermokraft und die Härteabnahme durch direkte Wechselwirkung und Vernichtung von Spannungsfeldern vorsichgehen unter gleichzeitigem Auftreten von stabilen Versetzungsgebieten an den Grenzflächen der Körner. Es wird gezeigt, dass diese Vorstellung mit der Rekristallisation als einem Keimbildungs- und Wachstumsvorgang im Übereinstimmung ist.

* Received October 27, 1954.

† Research Department, Imperial Chemical Industries Ltd., Metals Division, Birmingham, England.

‡ Formerly as above, now at Atomic Energy Research Establishment, Harwell, England.

VOL. 4 1956

1. INTRODUCTION

From analyses of observations of the rate of recrystallization, made directly or by following changes of various mechanical and physical properties, different investigators have concluded that recrystallization simulates a rate process of either the first,[1, 2] second,[3] or third[4] order. The divergent conclusions can be quite rationally explained on nucleation and growth theories,[5] but it is difficult to express such theories in terms of the more elemental and more widely applicable dislocation theory.

Changes in the observed values of different properties of the same cold-worked metal on annealing may occur at distinctly different rates, and, in attempting to analyse annealing curves, such differences must be taken into consideration. Some properties, for example, may be purely dependent on dislocation density, while others are affected by their distribution; or alternatively, as has been suggested,[6] while changes in one property may be associated with behavior of dislocations, those in other properties may be more directly related to lattice vacancies. Also the analysis of the form of annealing curves is highly dependent on the accuracy of the curves themselves, so that if such analysis is to have real significance it is desirable to select for observation a property which not only can be measured with sufficient accuracy, but which is quite representative of the average condition of the specimen examined. Furthermore, in the analysis, the possibility that more than one process is involved must be given consideration, and the problem treated accordingly.

The work described in the present paper was undertaken primarily with the object of studying recrystallization as a rate process, but a secondary objective was to explain the apparently conflicting observations of Brindley[2] and of Cook and Richards[3] on the recrystallization behavior of copper. The latter determined recrystallization rate in heavily cold-rolled copper strip by hardness measurements which they had first correlated with the proportion of each sample recrystallized, estimated by direct observation of changes in microstructure. From an analysis of their results they showed that the softening rate conformed to that of a second-order process, and therefore proposed a two-stage mechanism involving recovery and recrystallization. On the other hand, Brindley's[2] analysis of annealing curves determined by Brandsma[7] from thermoelectric-power measurements indicated a single first-order process. It was significant that, in their work on kinetics, Cook and Richards[3] dealt specifically with recrystallization of copper to cube-texture, while Brandsma's experiments[7] were, in all probability, concerned with recrystallization to random or to retained rolling texture.

For the present investigation, it was clearly desirable that thermoelectric-power and hardness measurements should be made on the same specimens and on material prepared so as to recrystallize in characteristically different manners. Accordingly, two batches of cold-rolled H.C. copper strip were produced in such a way that one recrystallized to cube-texture and the other to a random structure.

TABLE 1. Composition of the copper used

	per cent		per cent
Tin	0.0002	Arsenic	<0.0005
Lead	<0.0002	Bismuth	<0.0001
Iron	0.0010	Selenium	Nil
Nickel	0.0005	Tellurium	Nil
Manganese	<0.0005	Phosphorus	Nil
Silver	0.0022	Sulphur	0.0010
Antimony	<0.0001	Oxygen	0.032

2. PREPARATION OF MATERIAL

A cast slab of tough-pitch copper of H.C. quality and composition indicated in Table 1 was hot-rolled from an initial thickness of $3\frac{3}{4}$ in. to $1\frac{1}{2}$ in. The material was then annealed at 500°C for 3 hr and cold-rolled to 0.75 in., the direction of cold-rolling at this and all subsequent stages being transverse to that of the initial hot-rolling. Strip for the experimental work at a thickness of 0.030 in. was then prepared in the two following ways:—

(a) *Strip of Random Structure*

Strip, for the annealing experiments on material recrystallizing to random texture, was prepared from the 0.75 in. cold-rolled stock by annealing at 900°C, and then cold-rolling to the final gauge of 0.030 in. with intermediate anneals at 500°C at gauges of 0.150 in. and 0.060 in. The 0.030 in. strip was then sheared to $\frac{1}{2}$ in. widths. Some of the material was annealed at 350°C for use as reference leads, while the remainder was retained in the hard-rolled condition for the annealing experiments.

(b) *Hard-Rolled Strip for Recrystallization to Cube Texture*

Part of the 0.75 in. cold-rolled stock was annealed at 350°C to a grain size of 0.015 mm, and then rolled without further annealing to 0.030 in. Since this material recrystallizes slowly at room temperature,[8] the rolling was interrupted at a thickness of 0.15 in.,

rolling to final gauge being carried out immediately prior to the annealing experiments.

3. EXPERIMENTAL PROCEDURE

(a) *Thermoelectric-Power Measurement*

The thermoelectric power measurements were made with a Paschen astatic galvanometer, the control magnets being adjusted so as to provide a sensitivity of 3.4×10^{-9} volts/mm deflection. Since, with a temperature difference of 5°C between the junction of a cold-worked annealed copper thermocouple, an e.m.f. greater than 10^{-7} volts is developed, the error in its measurement is thus about 1 per cent. The galvanometer and leads were contained in a constant-temperature enclosure, on a heavy mounting to reduce vibration. The $\frac{1}{2}$ in. wide strip sample formed the detachable short element of a differential thermocouple, being bolted to annealed copper reference leads so that it could be removed for annealing treatment. A temperature difference was maintained between the junctions by immersing one of them in an oil-bath at room temperature, and the other in a bath about 5°C higher, the exact difference in temperature being measured by means of a chromel-alumel thermocouple calibrated against a Beckmann thermometer.

(b) *Determination of Isothermal Annealing Curves*

The progress of isothermal annealing of the strip reduced 50 per cent by cold-rolling, which recrystallized to a random crystal orientation, was followed by measuring thermoelectric power with respect to the fully annealed reference leads of random crystal orientation, and by D.P. hardness measurements after successive ten-minute annealing periods in an air circulation oven at 180°C.

In order to maintain a steady and uniform temperature and to hasten the attainment of thermal equilibrium, the specimen was inserted in a narrow space between two slabs of copper maintained continuously at a steady temperature in the oven. At the end of each annealing period the specimen was water-quenched. The cold-rolled strip, bent into a U-shape with arms 5 in. long, had holes drilled at the ends in order to bolt it to the reference leads, the thin oxide film formed during annealing being first removed at the contact points by rubbing lightly with metal polish. The sole purpose of the polishing was to ensure good electrical contact, any mechanical working of the surface having no effect, provided the whole junction was at uniform temperature. Hardness measurements were also made on the same sample after each annealing period.

TABLE 2. Diamond pyramid hardness and thermoelectric-power values on annealing at 180°C for H.C. copper strip cold-rolled 50 per cent reduction in thickness

Time of isothermal annealing at 180°C (min)	Diamond pyramid hardness		Thermoelectric power	
	Observed (D.P. No. 5 Kg load)	Per cent total change on annealing (123 − 50.4)	Observed (10^{-8} volts)	Per cent total change on annealing (5.38 − 0.925)
0	123	100	5.38	100
10	120	96.2	5.00	92.5
20	117	91.8	4.50	80.8
30	115	89.0	4.78	87.4
40	117	91.8	4.52	81.4
50	116	90.4	4.42	79.2
60	117	91.8	4.26	75.9
70	114	87.6	3.96	68.8
80	113	86.3	3.66	62.0
90	114	87.6	3.40	57.0
100	113	86.3	3.22	52.0
110	111	83.5	3.00	45.8
120	105	75.3	2.90	44.8
130	108	79.4	2.78	42.0
150	94.9	61.4	2.56	37.0
170	83.6	45.4	2.34	32.2
190	79.6	40.3	2.24	29.8
220	76.3	35.6	1.90	22.2
250	70.5	27.8	1.72	17.6
280	70.5	27.9	1.48	12.6
310	69.0	25.0	1.42	11.1
350	61.8	15.7	1.38	10.3
410	59.5	12.5	1.22	6.7
470	60.0	13.2	1.08	3.5
530	55.5	7.0	1.08	3.5
590	56.7	8.7	1.02	2.1(5)
680	52.1	2.3	0.96	0.8
800	50.8	0.6	0.96	0.8
980	50.4	0	0.88*	−1.0

* The asymptotic end value of thermoelectric power obtained from the smoothest curve through experimental points was estimated to be 0.925×10^{-8} volts.

Strip reduced 96 per cent by rolling, which recrystallized to cube-texture on annealing, was also made into a U-shaped specimen, and thermoelectric power again measured against random-orientation copper reference leads. Annealing of this strip was effected in boiling water, measurements being made after successive five-minute annealing periods until no further change in properties took place. Towards the end of annealing the periods were increased, since the rate of change was slower.

The observed values of hardness and thermoelectric power are recorded in Tables 2 and 3, from which it should be noted that the end value of the thermoelectric power in Table 3 is a small negative quantity. For the purpose of comparison of rates of change in hardness and thermoelectric power, the values of these quantities are also expressed in Tables 2 and 3 as the percentages of the total change on annealing from initial value to an asymptotic end

VOL. 4 1956

TABLE 3. Diamond pyramid hardness and thermoelectric-power values on annealing at 100°C for H.C. copper strip cold-rolled 96 per cent reduction in thickness

Time of isothermal annealing at 100°C (min)	Diamond pyramid hardness		Thermoelectric power	
	Observed (D.P. No. 5 Kg load)	Per cent total change on annealing per cent (126 − 44)	Observed (10^{-8} volts)	Per cent total change on annealing per cent (10.34 + 0.475)
0	126	100	10.34	100
5	125	98.8	9.40	91.26
10	123	96.3	9.30	90.35
15	125	98.8	9.50	92.19
20	123	96.3	9.16	89.04
25	123	96.3	9.06	88.12
30	124	97.6	8.78	85.57
35	121	93.8	8.46	82.58
40	118	90.2	8.58	83.68
45	121	93.8	8.18	80.00
50	106	75.6	7.76	76.12
60	110	80.5	6.72	66.39
70	92	58.5	5.64	56.52
80	82	46.3	4.30	44.14
90	87	52.4	3.30	34.93
100	72	34.2	2.50	27.50
110	59	18.3	1.78	20.84
120	60	19.5	1.36	16.96
130	58	17.1	0.98	13.45
140	54	12.2	0.68	10.68
155	48	4.9	0.40	8.09
175	49	6.0	0.14	5.72
200	48	4.9	−0.03	4.13
230	47	3.7	−0.17	2.84
275	46	2.4	−0.28	1.80
350	45	1.2	−0.36	0.95
420	44	0	−0.43	0.40
1140	44	0	−0.52*	−0.41

* The asymptotic end value of thermoelectric power was estimated to be −0.475 volts.

value derived from a smooth curve through experimental points. Isothermal annealing curves have been drawn in Fig. 1 from both the hardness and thermoelectric-power measurements on strip, rolled 50 per cent. Since, apart from a small initial lag in hardness values, the corresponding curves for strip, rolled 96 per cent, are exceedingly close to each other, in order to avoid confusion only the more accurate thermoelectric-power curve is plotted in Fig. 2.

4. ANALYSIS

Analysis of the recrystallization process by reference to changes in a secondary property depends on either the assumption of a linear relation between the measured value of the property and the corresponding fraction of metal recrystallized at any stage or on the experimental determination of the precise relationship. For a partly recrystallized metal, considered as a mixture of a residual cold-worked portion with that which has already transformed to the fully annealed

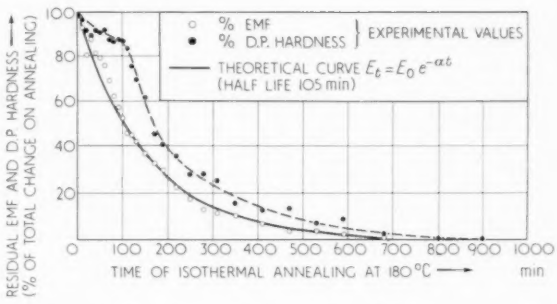
RESIDUAL EMF AND D.P. HARDNESS (% OF TOTAL CHANGE ON ANNEALING)
% EMF
% D.P. HARDNESS
EXPERIMENTAL VALUES
THEORETICAL CURVE $E_t = E_0 e^{-\alpha t}$
(HALF LIFE 105 min)
TIME OF ISOTHERMAL ANNEALING AT 180°C
min

FIG. 1. Isothermal annealing curves of H.C. copper strip cold-rolled 50 per cent reduction in thickness.

state, a linearly related property conforms to the simple rule of mixtures, so that an observed value is in simple proportion to the quantities of the two components present.

It has already been established[3] for the recrystallization of heavily cold-rolled H.C. copper strip, that apart from a small initial lag, during which no apparent change in average hardness of the strip occurs with the first microscopically observed signs of recrystallization, the relation between hardness and fraction recrystallized is, in fact, linear. No direct calibration of thermoelectric power was made for the purpose of the present investigation, although the close agreement between changes in this property and in hardness during isothermal annealing of heavily rolled copper indicates that, in this instance at least, it also is linearly related with the fraction recrystallized. This view is in direct opposition to one previously held,[9] namely that thermoelectric power might actually indicate the state of recovery of the continuous unrecrystallized matrix quite independently of the presence of discrete and therefore disconnected islands of recrystallized metal.

Crussard and Aubertin,[10] however, have shown that change in thermoelectric power of tensile specimens on unloading varies directly with applied stress and therefore with residual elastic strain. It thus appears that thermoelectric power provides a

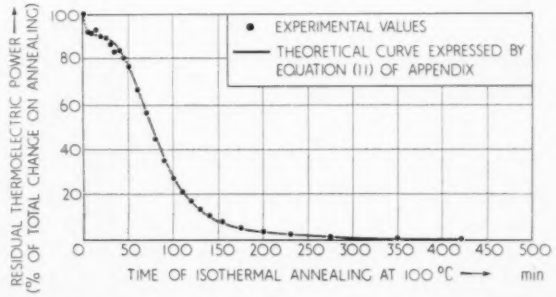
RESIDUAL THERMOELECTRIC POWER (% OF TOTAL CHANGE ON ANNEALING)
EXPERIMENTAL VALUES
THEORETICAL CURVE EXPRESSED BY EQUATION (11) OF APPENDIX
TIME OF ISOTHERMAL ANNEALING AT 100°C
min

FIG. 2. Isothermal annealing curve of H.C. copper strip cold-rolled 96 per cent reduction in thickness.

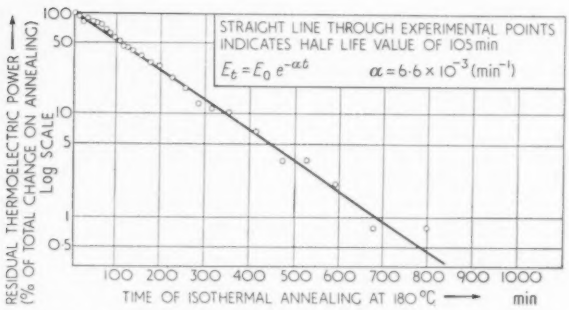
STRAIGHT LINE THROUGH EXPERIMENTAL POINTS
INDICATES HALF LIFE VALUE OF 105 min
$E_t = E_0 e^{-\alpha t}$
$\alpha = 6{\cdot}6 \times 10^{-3}$ (min^{-1})
RESIDUAL THERMOELECTRIC POWER (% OF TOTAL CHANGE ON ANNEALING) Log SCALE
100
50
10
5
1
0·5
100 200 300 400 500 600 700 800 900 1000
TIME OF ISOTHERMAL ANNEALING AT 180 °C
min

FIG. 3. Isothermal annealing curve of H.C. copper strip cold-rolled 50 per cent reduction in thickness.

means of following changes in lattice strains during isothermal annealing, and being truly representative of the average condition of the specimen, observation of thermoelectric power is ideally suited for rate-process analysis. The localized nature of the diamond-pyramid hardness test and the heterogeneous character of partly annealed metal are responsible, on the other hand, for a wide statistical fluctuation in results for a single specimen, which is reflected in the greater scatter of the observed hardness values about the estimated annealing curve in Fig. 1. Because of the relative inaccuracy of hardness determinations, full mathematical analysis of the kinetics of the isothermal annealing process is carried out only with the thermoelectric data.

(a) *Recrystallization of Strip Rolled* 50 *per cent*

The plot of residual thermoelectric power of strip rolled with reduction of 50 per cent against time of isothermal annealing at 180°C, Fig. 1, appears to follow a simple exponential curve, apart from a small, but significant, deviation in the initial stages. This deviation is probably connected with the more marked discontinuity in the hardness curve. To derive the exponential coefficient of decay of thermoelectric power with time, the experimental values are plotted in Fig. 3 on a semi-logarithmic scale. The points fall almost on a straight line, confirming the exponential nature of the relationship. From the slope of the line, the decay coefficient is 6.6×10^{-3} min^{-1}, corresponding to a half-value period of 105 minutes. The full curve in Fig. 1 is in fact the exponential curve of this half-life. Change in thermoelectric power is therefore either a simple first-order process or at least a pseudo first-order process. The significance of this finding, and the difference in character of the thermoelectric and hardness isothermal curves, will be discussed later.

(b) *Recrystallization of strip rolled* 96 *per cent*

The thermoelectric-power and hardness curves of strip rolled with reduction in thickness of 96 per cent and isothermally annealed at 100°C are, apart from an initial lag in hardness values, coincident. The curve, Fig. 2, is clearly more complex than the thermoelectric-power curve, Fig. 1, for strip rolled 50 per cent. As a first attempt at analysis, the experimental values of thermoelectric power were plotted on a semi-logarithmic scale, as in Fig. 4. The appearance of this curve is suggestive of three successive processes. The first is a rapid process accounting for an initial fall of about 10 per cent of the total change: the order of the second, accounting for the major proportion of the

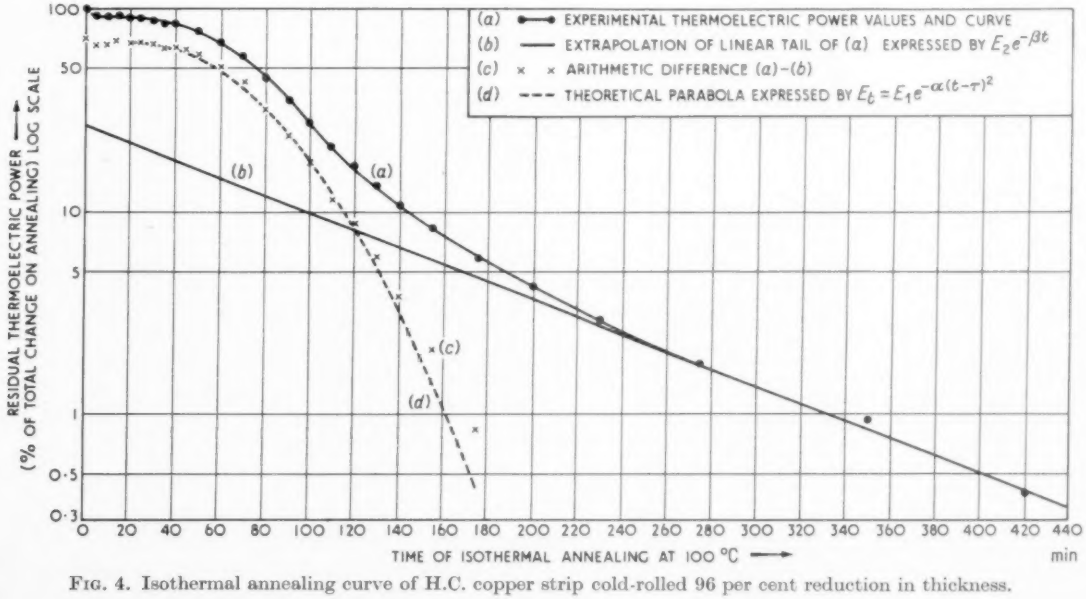
(a) EXPERIMENTAL THERMOELECTRIC POWER VALUES AND CURVE
(b) EXTRAPOLATION OF LINEAR TAIL OF (a) EXPRESSED BY $E_2 e^{-\beta t}$
(c) × × ARITHMETIC DIFFERENCE (a)−(b)
(d) THEORETICAL PARABOLA EXPRESSED BY $E_t = E_1 e^{-\alpha(t-\tau)^2}$
RESIDUAL THERMOELECTRIC POWER (% OF TOTAL CHANGE ON ANNEALING) LOG SCALE
100
50
10
5
1
0·5
0·3
(a)
(b)
(c)
(d)
0 20 40 60 80 100 120 140 160 180 200 220 240 260 280 300 320 340 360 380 400 420 440
TIME OF ISOTHERMAL ANNEALING AT 100 °C
min

FIG. 4. Isothermal annealing curve of H.C. copper strip cold-rolled 96 per cent reduction in thickness.

VOL. 4 1956

total change, is greater than unity, while the third and last is first order. The procedure for analysis of successive first-order reactions, which is not strictly applicable in the present instance, has been applied in order to obtain an approximate solution. The extrapolation (b) of the linear tail $E_2e^{-\beta t}$ of the full curve (a) in Fig. 4 is first subtracted arithmetically from the experimental curve yielding the thermoelectric-power values indicated by points marked $\times$. These points lie close to the theoretical parabola (c) expressed by $E_t = E_1e^{-\alpha(t-\tau)^2}$. The second process, accounting for the major proportion of change in thermoelectric power, thus simulates one of second order.

The above approach is only valid for successive first-order processes, but now that it is apparent that the second process is second order, a more rigorous mathematical treatment is possible. The first stage is so rapid that it is assumed to be a fast exponential decay process which is virtually complete in a few minutes, giving rise to an incubation period for the second stage. The complete mathematical treatment for a second-order process followed by one of first-order is set out in an appendix, the effect of the first process being represented by a zero shift or incubation period. Assuming values of the constants derived from analysis of Fig. 4, more exact values can be obtained by successive approximation. The equation derived for the complete annealing process is rather complex, but the constants can be determined fairly easily; and a comparison of experimental results with theoretical values, which are recorded in Table 4 and plotted in Fig. 2, shows agreement well within experimental error.

5. DISCUSSION

The possibility of interpretation of rate of change of a secondary property in terms of recovery and recrystallization naturally depends on there being a definite correlation between that property and fractions of metal in the recovered and recrystallized states. A simple and reasonable interpretation can be developed if it is assumed that, as Crussard and Aubertin[10] have shown, thermoelectric power varies directly with applied stress and therefore with residual elastic strain.

The first-order character of the thermoelectric curve of strip rolled 50 per cent is therefore equivalent to the simple exponential decay of internal stresses on isothermal annealing.[11]. These stresses would, in moderately deformed metal, be expected to vary more or less continuously throughout the processes of recovery (or polygonization) and subsequent recrystallization. The hardness curve of strip rolled 50 per cent, on the other hand, shows a definite discontinuity indicative of two such processes. These may well be the two processes which Stroh[12] envisages in explaining annealing behavior of cold-worked metal, namely a short-range rearrangement of dislocations in piled-up groups which is associated with appreciable change in stored energy and specific heat[13] but not in hardness, and with a long-range interaction of the stress fields of neighboring groups which is associated with a further liberation of stored energy and with appreciable softening. On this basis, it would seem that thermoelectric power is a measure not only of strain associated with dislocations, but also of stored energy which in moderately deformed metal varies continuously throughout the annealing process.

TABLE 4. Calculated values of the terms A and B together with their sum S* and the corresponding observed values

Time of isothermal annealing t (min)	A	B	S	Observed values (From Table 3)
0			100	100
5			91.7	91.26
10			90.3	90.35
15			90.04	92.19
20	90.0	0	90.0	89.04
25	89.5	0.08	89.58	88.12
30	87.9	0.14	88.04	85.57
35	85.0	0.50	85.5	82.58
40	82.7	1.0	83.7	83.68
45	78.6	1.6	80.2	80.00
50	74.0	2.0	76.0	76.12
60	62.5	3.0	65.5	66.39
70	52.5	4.8	57.3	56.52
80	40.6	5.3	45.9	44.14
90	30.8	6.0	36.8	34.93
100	22.6	6.6	29.2	27.50
110	15.0	6.9	21.9	20.84
120	9.8	6.9	16.7	16.96
130	6.2	6.7	12.9	13.45
140	4.0	6.4	10.4	10.68
155	2.7	5.8	8.5	8.09
175	0.4	4.8	5.2	5.72
200	0.07	3.9	3.97	4.13
230	0	2.9	2.9	2.84
275	0	1.8	1.8	1.80
350	0	0.9	0.9	0.95
420	0	0.4	0.4	0.40
1140	0	0	0	−0.41

* Values of S for t in the range 0–20 min are estimated on the assumption that initial fall from 100 to 90 per cent corresponds to a first-order process of 2 min half-life.

$$A = E_1e^{-\alpha(t-\tau)^2}$$

$$B = \frac{E_2}{K}e^{-\beta(t-\tau)}\left\{1 - e^{-\alpha(t-\tau)^2} - \frac{\beta}{\alpha}(t-\tau) + e^{\beta^2/4\alpha}\cdot\frac{\beta}{2}\sqrt{\frac{\pi}{\alpha}}\left[P\sqrt{\alpha}\left(t-\tau-\frac{\beta}{2\alpha}\right) + P\left(\frac{\beta}{2\alpha}\right)\right]\right\}$$

$S = A + B$, $\alpha = 2.2 \times 10^{-4}$ (min)$^{-2}$,
$\beta = 9.9 \times 10^{-3}$ (min)$^{-1}$, $\tau = 20$ min, $E_1 = 90$ per cent,
$E_2 = 23$ per cent, $K = 1.9$, $\frac{b}{2\alpha} = 22.5$ min.

In rolling, individual crystals are deformed in direct proportion to the strip itself, so that, with increasing reduction, initially equi-axed crystals are rolled progressively thinner, each crystal taking up the approximate orientation of one component or other of the standard rolling textures. The small initial fall in thermoelectric power on annealing of heavily rolled material is, on the present thesis, equivalent to a decrease in general lattice distortion with the establishment of dislocation arrays at the interfaces of adjacent crystals. Dislocations of opposite sign would be annihilated at the interfaces leading to an equilibrium density of dislocations of one sign corresponding to the definite orientation difference between the various components of texture, while the dislocations in neighboring interfaces would be of opposite sign. Further structural change can now only occur by direct interaction and cancellation of the dislocation stress fields across the thickness of individual crystals leading to an abrupt change in lattice orientation from rolling-texture to cube-texture. Such a mechanism would account both for the large change in thermoelectric power associated with the second process evident from the thermoelectric-power curve, and for its second-order character.

It has in fact been established[3] that, for heavily rolled copper, a linear relationship exists between hardness and fraction recrystallized to cube-texture. The similarity between the hardness and thermoelectric power curves of strip rolled 96 per cent indicates that, in this instance, the change in thermoelectric power is also proportional to fraction recrystallized. The change from rolling-texture to cube-texture must, of necessity, be one of localized atomic rearrangement such as nucleation and growth, otherwise large dimensional changes would be involved. The formation of cube-texture by annihilation of high-energy interfaces, however, is equivalent to two-dimensional growth from predetermined nuclei, which as Evans[14] has shown is a process of second order. The final first-order process is merely relief by grain growth of residual stresses at boundaries of cube-texture grains in slightly different orientations.

Analysis of changes in thermoelectric power and hardness purely as rate processes, making the basic assumptions that thermoelectric power is directly proportional to lattice strain and hardness to fraction recrystallized, has led to the following general picture of the annealing behavior of rolled copper strip. From the hardness curve, annealing of strip rolled with reduction of 50 per cent occurs by two distinct processes, polygonization and recrystallization. Thermoelectric power, and therefore lattice strain, however, varies more or less continuously in an exponential manner throughout, since both polygonization and recrystallization involve essentially similar processes of migration of dislocations. Annealing of heavily rolled strip may again be regarded as occurring by polygonization and recrystallization, although polygonization, being restricted within the boundaries of the now thin initial grains, is associated with only a small change in thermoelectric power and lattice strains, and none in hardness. Most of the change in hardness and thermoelectric power occurs by a second-order process which is interpreted as a process of annihilation of stable arrays of dislocations at the grain interfaces by direct interaction of their stress fields. The findings of the present investigation thus confirm the earlier observation of Cook and Richards[3] that recrystallization of heavily rolled copper is mainly a second-order process, and establish that the difference in order found by these authors and by Brindley[2] is due to the fact that the findings of the former refer to heavily rolled copper which recrystallizes to cube-texture, and of the latter to copper processed in such a way that it recrystallized in a different manner on annealing, probably to a retained rolling texture or perhaps a random texture. Furthermore, the picture of recrystallization derived by rate-process analysis is quite consistent with the structural observations and nucleation and growth concepts.

VOL. 4 1956

ACKNOWLEDGMENTS

The authors wish to thank several of their colleagues for much valuable discussion, and Dr. N. P. Inglis, Research Director, for his interest and encouragement.

REFERENCES

1. A. Krupkowski and M. Balicki, *Ann. Akad. Sci. Tech. Varsovie*, **4**, 270 (1937).
2. G. W. Brindley, Phys. Soc. Bristol Conference Report, 95 (1948).
3. M. Cook and T. Ll. Richards, *J. Inst. Metals*, **73**, 1 (1946).
4. B. F. Decker and D. Harker, *Trans. Amer. Inst. Min. Met. Engrs.*, **188**, 887 (1950).
5. J. E. Burke and D. Turnbull, *Progress in Metal Physics*, **3**, 220 (1952).
6. L. M. Clarebrough, M. E. Hargreaves, and G. W. West, *Phil. Mag.*, **44**, 913 (1953).
7. W. F. Brandsma, *Z. Phys.*, **48**, 703 (1928).
8. M. Cook and T. Ll. Richards, *J. Inst. Metals*, **70**, 159 (1944).
9. T. Ll. Richards, Phys. Soc. Bristol Conference Report, 105 (1948).
10. Ch. Crussard and F. Aubertin, *Rev. Met.*, **45**, 402 (1948).
11. W. G. Burgers, *Proc. K. Ned. Akad. Wetensch.*, **50**, 452 (1947).
12. A. N. Stroh, *Proc. Roy. Soc.*, **A218**, 391 (1953).
13. T. Suzuki, *Sci. Rel. Res. Inst. Tohoku University*, **1**, 193 (1949).
14. U. R. Evans, *Trans. Faraday Soc.*, **41**, 365 (1945).

Appendix

SUCCESSIVE RATE PROCESSES

The change in thermoelectric power of H.C. copper-strip cold rolled with a reduction in thickness of 50 per cent, on isothermal annealing, conforms to a first-order process, that is, the thermoelectric power E_t at time t can be expressed by the equation

$$E_t = E_0 e^{-\alpha t}$$

where E_0 is the initial thermoelectric power at time $t = 0$, and α a constant, the value of which is temperature-dependent.

Recrystallization of heavily rolled copper is complex, and an attempt was first made at analysis of the isothermal annealing curve, by following the standard procedure for successive first-order processes, such as a radioactive series for which a product A transforms to a product B, and B to C, and so on, the rate of decay of a product at any instant being proportional to the amount present at that instant. The analysis indicated that the recrystallization process of heavily rolled copper did not conform to successive first-order processes, but rather to a second-order process, followed by one of first order.

The mathematical analysis for successive first-order processes has long been established, but the authors are unaware of a similar treatment for a second-order process followed by one of first order, and they have accordingly developed their own treatment.

ANALYSIS OF SECOND-ORDER FOLLOWED BY FIRST-ORDER PROCESS

Let product A transform to B, and B to C, and let x, y, z be the amount of each present at time t, so that

$$x + y + z = 1$$

Let transformation $A \rightarrow B$ be a second-order process, so that

$$x = 1 \cdot e^{-\alpha t^2} \tag{1}$$

where α is a constant.

Let $B \rightarrow C$ be a first-order process such that, as a completely independent process, unit quantity of B decays according to the relation

$$y = 1 \cdot e^{-\beta t} \tag{2}$$

where β is a constant.

Consider now the successive transformations $A \rightarrow B \rightarrow C$. The rate of decay of A and therefore of formation of B at time t is obtained by differentiation of equation (1). The amount of B formed in time-interval dt_1 at t_1 is therefore

$$2\alpha t_1 \cdot e^{-\alpha t^2} \cdot dt_1. \tag{3}$$

The amount of B formed at t_1 which remains at subsequent time t is, by combination of (2) and (3),

$$= 2\alpha t_1 \cdot e^{-\alpha t_1^2} \cdot e^{-\beta(t-t_1)} \cdot dt_1,$$

and the total amount of y present at time t is therefore

$$= \int_0^t 2\alpha t_1 \cdot e^{-\alpha t_1^2} \cdot e^{-\beta(t-t_1)} \cdot dt_1,$$

where t_1 is the variable.

$$y = 2\alpha e^{-\beta t} \int_0^t t_1 e^{-(\alpha t_1^2 - \beta t_1)} \cdot dt_1 \tag{4}$$

Completing the square for the variable exponential coefficient,

$$y = 2\alpha \cdot e^{-\beta t} \cdot e^{\beta^2/4\alpha} \int_0^t t_1 \cdot e^{-\alpha(t_1 - \beta/2\alpha)^2} \cdot dt_1$$

and changing the variable from t_1 to $\sqrt{\alpha}\,(t_1 - \beta/2\alpha) = z$

$$y = 2\alpha \cdot e^{-\beta t} \cdot e^{\beta^2/4\alpha} \int_{-\beta/2\sqrt{\alpha}}^{(t-\beta/2\alpha)\sqrt{\alpha}} (z/\sqrt{\alpha} + \beta/2\alpha)\, e^{-z^2} \cdot dz/\sqrt{\alpha}$$

$$= e^{-\beta t} \cdot e^{\beta^2/4\alpha} \left\{ \int_{-\beta/2\sqrt{\alpha}}^{(t-\beta/2\alpha)\sqrt{\alpha}} 2z \cdot e^{-z^2} \cdot dz + \right.$$

$$\left. + \beta/\sqrt{\alpha} \int_{-\beta/2\sqrt{\alpha}}^{(t-\beta/2\alpha)\sqrt{\alpha}} e^{-z^2} \cdot dz \right\}$$

$$= e^{-\beta t} \cdot e^{\beta^2/4\alpha} \left\{ \left[-e^{-z^2} \right]_{-\beta/2\sqrt{\alpha}}^{(t-\beta/2\alpha)\sqrt{\alpha}} + \right.$$

$$\left. + \beta/\sqrt{\alpha} \int_{-\beta/2\sqrt{\alpha}}^{(t-\beta/2\alpha)\sqrt{\alpha}} e^{-z^2} \cdot dz \right\} \tag{5}$$

The last integral term in this expression corresponds to the error function, or integration of the Gaussian equation for normal distribution of errors, and can be written in a form, such that its value can be derived from standard tables. So that, on replacing $\sqrt{\alpha}\,(t - \beta/2\alpha)$ for z,

$$y = e^{\beta^2/4\alpha} \cdot e^{-\beta t} \left\{ \left[-e^{-\alpha(t - \beta/2\alpha)^2} \right]_0^t \right.$$

$$\left. + \frac{\beta}{2}\sqrt{\frac{\pi}{\alpha}} \left[P(t\sqrt{\alpha} - \beta/2\sqrt{\alpha}) + P(\beta/2\sqrt{\alpha}) \right] \right\} \tag{6}$$

where $P(\beta/2\sqrt{\alpha})$ and $P(t\sqrt{\alpha} - \beta/2\sqrt{\alpha})$ can be evaluated from tables. After simplification, equation (6) may be written in the form

$$y = e^{-\beta t} \left\{ 1 - e^{-\alpha(t^2 - \frac{\beta}{\alpha} t)} \right.$$

$$\left. + \frac{\beta}{2}\sqrt{\frac{\pi}{\alpha}} \cdot e^{\beta^2/4\alpha} \left[P(t\sqrt{\alpha} - \beta/2\sqrt{\alpha}) + P(\beta/2\sqrt{\alpha}) \right] \right\} \tag{7}$$

But since, as indicated in the text, it is reasonable to assume that thermoelectric power due to any product is linearly related with y, the quantity of that product present, equation (7) may be rewritten

$$E = E_2 e^{-\beta t}\left\{1 - e^{-\alpha\left(t^2 - \frac{\beta}{\alpha}t\right)}\right.$$

$$\left. + \frac{\beta}{2}\sqrt{\frac{\pi}{\alpha}} \cdot e^{\beta^2/4\alpha}\left[P(t\sqrt{\alpha} - \beta/2\sqrt{\alpha}) + P(\beta/2\sqrt{\alpha})\right]\right\}, \tag{8}$$

where E is the contribution to the observed thermoelectric power of the product B at any time T, and E_2 that of a thermocouple element composed wholly of product B with respect to the one composed wholly of the end product C.

It now remains only to demonstrate how the constants of the equation may be evaluated. By inspection, it is evident that the expression within brace brackets of equation (8) increases with time, and finally approaches a constant value K, when E subsequently decreases according to the relation

$$E = KE_2 e^{-\beta t}.$$

Identifying this relation with the linear tail of curve (a) in Fig. 4, the slope of line (b) corresponds to a β value of $9 \cdot 9 \times 10^{-3}$ min^{-1}. Some difficulty now arises in the evaluation of the remaining constants. Firstly, it is clear from Figs. 2 and 4 that a rapid decay process precedes the successive second-order and first-order processes to which the present analysis refers. For lack of sufficient data, this is presumed to be a simple first-order process of half-life of about two minutes. The complete decay of the initial product reduces the observed thermoelectric power from 100 per cent of the initial value to 90 per cent; that is, to a value E_1 corresponding to the thermoelectric power of the product A, which decays according to the relation

$$E = E_1 \cdot e^{-\alpha(t-\tau)^2},$$

an incubation period τ being introduced to represent the delay caused by the first process. The constants other than β of equation (8) are now evaluated by the method of successive approximation. First, the value of τ is assumed to be approximately 20 min, then a value for α is calculated for which the value of the expression reduces to a half in the appropriate time interval of $(t - \tau) = 80$ min. $K \cdot E_2$ is now the thermoelectric power corresponding to the time $\tau = 20$ min on line (b) of Fig. 4. The R.H.S. of equation (8) can now be evaluated for various times over the whole isothermal annealing range. K is the value of the expression in brace brackets of equation (8) corresponding to very long times. Bearing in mind that the annealing times are taken from $t = \tau$ (20 min) as zero, equation (8), thus evaluated, is plotted as curve (B) in Fig. 5, and then subtracted arithmetically from the experimental curve (S) to give curve (A). New values of α and τ are now found which satisfy curve (A), and the procedure repeated until a satisfactory agreement is obtained. The value of 20 min for τ was found to be sufficiently accurate, but the ultimate values of the other constants are, $\alpha = 2.2 \times 10^{-4}$ min^{-2}, $\beta = 9.9 \times 10^{-3}$ min^{-1}, $E_1 = 90$ per cent, $E_2 = 23$ per cent, $K = 1.9$, and $\beta/2\alpha = 22.5$ min. The terms,

$$A = E_1 e^{-\alpha(t-\tau)^2} \tag{9}$$

$$B = \frac{E_2}{K} \cdot e^{-\beta(t-\tau)}\left\{1 - e^{-\alpha\left((t-\tau)^2 - \frac{\beta}{\alpha}(t-\tau)\right)}\right.$$

$$+ \frac{\beta}{2} \cdot \sqrt{\frac{\pi}{\alpha}} \cdot e^{\beta^2/4\alpha}\left[P(t\sqrt{\alpha} - \tau\sqrt{\alpha} - \beta/2\sqrt{\alpha})\right.$$

$$\left. \left. + P(\beta/2\sqrt{\alpha})\right]\right\} \tag{10}$$

are evaluated in Table 4 for times corresponding to actual annealing periods after allowing for the incubation period $\tau = 20$ min, during which a simple first-order process of 2-min half-life is assumed to account for the initial 10 per cent change in thermoelectric power.

The sum of the terms

$$A + B = S \tag{11}$$

is plotted as the full curve in Fig. 2, the initial rapid decay being shown as a broken curve. Apart from some initial scatter, agreement with observed values is satisfactory.

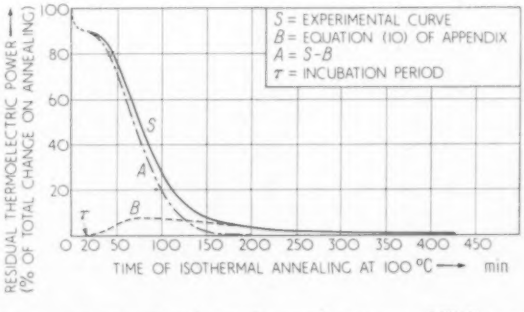

FIG. 5. Analysis of isothermal annealing curve of H.C. copper strip cold-rolled 96 per cent reduction in thickness.

VOL. 4 1956

THE INTERNAL FRICTION OF ALUMINUM SINGLE CRYSTALS AS A FUNCTION OF TEMPERATURE*

H. BIRNBAUM† and M. LEVY‡

The variation with temperature of the internal friction of aluminum single crystals was studied. In the temperature range, 77°K to 350°K, the decrement of undeformed crystals exhibited only a slight dependence on temperature. Some results were obtained which indicated that deformation and rapid cooling to 77°K resulted in a relaxation peak at about 100°K, as reported by Bordoni. In the temperature range, 350°K to 450°K, as-grown crystals exhibited what appeared to be discontinuous increases and decreases of decrement with temperature, and which appeared to be associated with the presence of an unstable disclocation configuration. An exponential dependence of decrement on temperature was observed in the temperature range 450°K to 650°K. An explanation of this behavior based on the formation of jogs at dislocation intersections is put forth. As predicted by the theory, variations of the activation energy for the exponential dependence with cold work and annealing are experimentally observed. The activation energy to form a jog at intersecting dislocations is calculated, and found to be about 17,000 cal/mole.

FROTTEMENT INTERNE DES MONOCRISTAUX D'ALUMINIUM EN FONCTION DE LA TEMPÉRATURE

En fonction de la température, le frottement interne a été étudié pour des monocristaux d'aluminium. Entre 77°K et 350°K, le décrément des cristaux non déformés ne dépend que peu de la température. Certains résultats indiquent que la déformation et le refroidissement rapide à 77°K provoquent un maximum vers 100°, comme l'a indiqué Bordoni. Dans l'intervalle 350–450°K, les cristaux "as grown" présentent une modification discontinue du décrément qui semble associée à des répartitions instables de dislocations. Entre 450 et 650°K, le décrément présente une variation exponentionnelle avec la température et il est proposé d'expliquer ce comportement par la formation de "jog," lors de l'intersection de dislocations. Des variations de l'énergie d'activation dans ce domaine ont été expérimentalement observées par écrouissage et recuit comme le prédit la théorie. L'énergie d'activation, pour former un "jog," serait de l'ordre de 17.000 cal/mol.

DIE INNERE REIBUNG VON ALUMINIUM EINKRISTALLEN IN ABHÄNGIGKEIT VON DER TEMPERATUR

Die innere Reibung von Aluminium Einkristallen wurde in Abhängigkeit von der Temperatur untersucht. Im Temperaturbereich von 77 bis 350°K zeigte die Reibungsabnahme unverformter Kristalle nur eine geringe Temperaturabhängigkeit. Einige Untersuchungsergebnisse zeigten, dass Verformung und rasche Abkühlung auf 77°K zu einem Relaxationsmaximum bei ungefähr 100°K führen, wie auch von Bordoni mitgeteilt wurde. Im Temperaturbereich von 350 bis 450°K traten bei unbehandelten ("as grown") Kristallen anscheinend Unstetigkeiten in den Kurven der Reibungsabnahme in Abhängigkeit von der Temperatur auf, die wahrscheinlich mit einer instabilen Versetzungskonfiguration im Zusammenhang stehen. Eine exponentielle Abhängigkeit der Reibungsabnahme von der Temperatur wurde im Temperaturbereich von 450 bis 650°K beobachtet. Eine Deutung dieses Verhaltens, die auf der Bildung von Sprüngen an Schnittpunkten von Versetzungen aufbaut, wird näher ausgeführt. Wie von der Theorie vorausgesagt, wurden experimentell Änderungen der Aktivierungsenergie für die exponentielle Abhängigkeit von der Kaltverformung und dem Anlassen festgestellt. Die Aktivierungsenergie, die zur Bildung eines Sprunges am Schnittpunkt von Versetzungen erforderlich ist, wurde berechnet. Sie liegt in der Grössenordnung von 17.000 cal/mol.

INTRODUCTION

The temperature dependence of the internal friction of metal single crystals measured at high frequencies, has been investigated by Pittenger,[1] Nowick,[2] and Bordoni.[3] Pittenger reported an activation energy of 14,000 cal/mole for the decrement of magnesium crystals measured at temperatures above 373°K. For aluminum crystals, he reported an increase in decrement with temperature above 300°K. Bordoni reported relaxation peaks in crystals of copper, silver, lead, and aluminum at 100°K, 65°K, 35°K, and 95°K respectively. These peaks were reported to be enhanced by cold work. The present work was attempted to establish the temperature dependence of the internal friction of aluminum single crystals, and to interpret the results on the basis of existing dislocation theory.

* Received June 16, 1955.

† Columbia University, Department of Metallurgy. Present address: University of Illinois, Department of Metallurgy.

‡ Columbia University, Department of Physics. Present address: The Haloid Corporation, Rochester, New York.

RESULTS AND DISCUSSION

The internal friction of high-purity aluminum single crystals was studied as a function of temperature, by the quartz composite oscillator method. The frequencies utilized were in the range of 30 to 80 kilocycles. The most interesting results were those obtained by studying the variation of the decrement, at a constant strain amplitude of the order of 10^{-6} in./in., with temperature in the range of 77°K to 650°K. All the aluminum crystals were grown from the melt. The bond used in the composite oscillator was Sauereisen, which was air dried.

It was established that the interface strains in the aluminum single crystals which accompanied changes in temperature and which were due to the different thermal coefficients of expansion of the quartz and the metal, had a negligible effect on the decrement of the crystals studied. In the temperature interval of 77°K to 300°K the change of decrement due to the interface strains was 1×10^{-4}. Since the decrements of the crystals studied were in the range of 10^{-4} to 10^{-3}, and the observed changes in decrement with temperature were of the order of 10^{-3} and 10^{-2}, the decrement changes due to interface strains may be neglected. Furthermore, the changes in decrement with temperature were reversible, indicating that interface straining and annealing does not appreciably affect the measured decrement.

A. *Decrement Discontinuities and Low-temperature Behavior*

Fig. 1 is typical of the results of the decrement measurements on an as-grown aluminum single crystal. The decrement exhibited only a slight increase with temperature in the range of 77°K to 350°K. In the temperature range of 350°K to 450°K, abrupt changes in the decrement took place as the temperature was increased. Within the limit of the experimental method, these changes were discontinuities in the decrement. A second series of measurements on the same crystal did not exhibit these discontinuities, indicating that the short anneal which occurred during the first series of measurements altered the structure of the crystal sufficiently to eliminate the discontinuities. If the crystals were deformed or annealed and slowly cooled prior to the initial measurement, these sharp changes in the decrement were not observed. This is shown in Fig. 2. The discontinuities appear to be the result of an "avalanche" process which may take place in an as-grown crystal acted on by an oscillating stress. Such a process could be of a type similar to the freeing of loosely pinned dislocations by the oscillating stress.

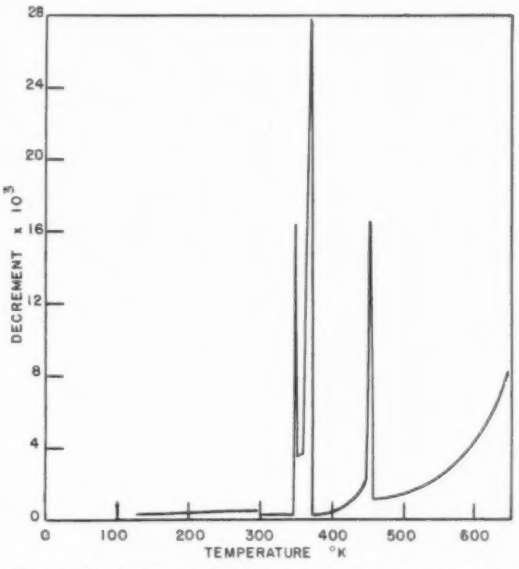

FIG. 1. Variation of the decrement of an as-grown crystal with temperature.

The low-temperature peaks in aluminum reported by Bordoni were not observed in as-grown or annealed crystals. It was observed, however, that relaxation peaks at a temperature of about 100°K could be produced if the crystals were plastically deformed by a strain of about 10^{-2} in./in. and rapidly cooled from room temperature to 77°K. The magnitude of these peaks decreased with time, indicating the annealing of the relaxation mechanism which caused the peaks.

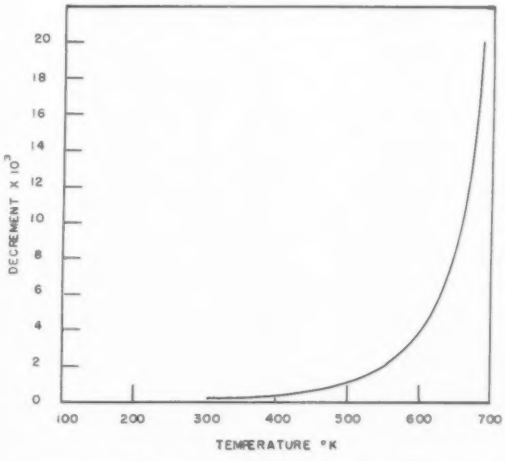

FIG. 2. Variation of the decrement of an annealed crystal with temperature.
Annealed for 1 hour at 400°C.
Cooled at 400°C per hour.

VOL. 4 1956

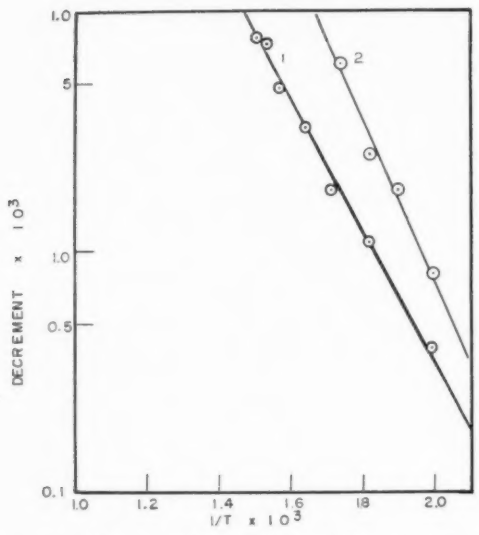

FIG. 3. High-temperature decrement.
Curve 1—Undeformed crystal. Annealed at 400°C and slow cooled.
Curve 2—After 0.5×10^{-2} in./in. torsional shear strain and 0.25×10^{-2} in./in. compressional shear strain.

B. *High-temperature Behavior*

As shown in Fig. 3, the decrement increases exponentially with temperature in the range 400°K to 650°K. This general behavior was observed in as-grown, in annealed, and in deformed crystals. The decrement in this temperature range may be expressed as

$$\log \Delta = -\frac{Q}{RT} + C. \tag{1}$$

The exact value of Q is sensitive to the previous treatment of the specimens.

It is of interest to consider the behavior under the oscillating stress of the internal friction measurement, of dislocation lines which are intersected by other dislocation lines. In the general case of such a grid of dislocations, the intersections act as effective pinning points. Except for certain specific configurations, movement of intersecting dislocations through each other requires the generation of vacancies or interstitial atoms. The temperature range in which the decrement increases exponentially with temperature is such that, for reasonable values of the binding energies of solute atoms to dislocation lines, the dislocations may be considered not being pinned by the solute atoms. Therefore, the dislocation lines will be considered as pinned only by intersections with other dislocation lines.

Seeger[4] has developed the following expression for the strain rate of dislocation lines which are pinned by dislocation intersections:

$$\dot{\epsilon} = K \exp\left\{-\frac{U_0 - \vartheta(\epsilon)[\tau - \tau_G]}{kT}\right\} \tag{2}$$

where U_0 is the activation energy to form a jog in the dislocation line at zero stress, τ is the applied shear stress, τ_G is the elastic stresses around the dislocation, $(\tau - \tau_G)$ is the total shear stress on the dislocation, and $\vartheta(\epsilon) = bdl_0$ where b = Burgers vector, d = the effective diameter of the dislocation, and l_0 is the distance between intersecting dislocations. The numerator of the exponential may be considered as the activation energy to form a jog in the dislocation line at the stress level of the measurement.

Koehler[5] has discussed the energy dissipation of a distribution of dislocation loops acted on by an oscillating stress. The movement of the oscillating dislocation line through an intersecting dislocation is equivalent to an added increment of displacement of the oscillating dislocation. On the basis of Koehler's calculation, the energy loss w', per cycle for a single loop, may be written as

$$w_1' = w_1 + \delta w_1 \tag{3}$$

where w_1 is the energy loss as calculated by Koehler and δw_1 is the energy loss due to the displacement of the dislocation intersections by the formation of jogs in the intersecting dislocations. The formation of jogs at dislocation intersections is essentially an irreversible process of energy dissipation, since interstitial atoms or vacancies must be created and destroyed. A simple calculation shows that the energy dissipated per jog by the oscillating stress is approximately

$$\delta w_1 = l_0 \sigma_0 \, (a^2/2) \tag{4}$$

where l_0 is the length of the dislocation line, $\sigma_0 a$ is the force per unit-length on the dislocation line, and $(a/2)$ is the average displacement of the dislocation line due to the formation of a jog consisting of one vacancy or interstitial. Following Koehler's analysis, the total energy loss per cycle is

$$\begin{aligned} w' &= w + \frac{\eta}{N_l} \int_0^\infty \frac{\sigma_0 a N c^2}{2} l_0 e^{-\frac{cl_0}{a}} \, dl_0 \\ &= w + \tfrac{1}{2}\sigma_0 a^3 N \left(\frac{\eta}{N_l}\right) \end{aligned} \tag{5}$$

where c is the concentration of pinning points, l_0 is the length of the dislocation segments, N is the atomic lengths of dislocation lines, w is the energy loss as calculated by Koehler, η is the number of jogs formed per cycle, and N_l is the number of dislocation loops acted on by the oscillating stress. It has been assumed that the length distribution

of loops at which jogs are formed is the same as the overall distribution of dislocation loop lengths.

$\dot{\epsilon}$, as given by eq. (2), is directly proportional to the rate of formation of vacancies or interstitials at the dislocation intersections. Since η is also directly proportional to the rate of formation of vacancies or interstitials, eq. (5) may be written;

$$w' = w + K\dot{\epsilon}.$$

Following Koehler's analysis, we arrive at

$$\Delta = \Delta_D + \Delta_J \tag{6}$$

where Δ is the total decrement, Δ_D is the decrement due to the oscillation of the dislocation loops, and Δ_J is the decrement due to the formation of jogs at dislocation intersections. Furthermore, Δ_J is proportional to $\dot{\epsilon}$, so eq. (6) may be written

$$\Delta = \Delta_D + K'\dot{\epsilon}. \tag{7}$$

If, as a first approximation, the energy dissipated by a moving dislocation is assumed to be independent of temperature, the temperature-dependence of the decrement is due to the $\dot{\epsilon}$ term. This assumption may be justified by the following argument. In the temperature range of 400°K to 650°K the dislocation lines may be considered as essentially not pinned by solute atoms, and the dislocation configuration as stable during the series of decrement measurements. This is indicated by the reproducibility of the data on subsequent series of measurements after the first series. Under these conditions, the temperature-dependence of the term Δ_D as derived by Koehler must arise from the dependence of the following terms on temperature: A, the effective mass per unit-length of the dislocation, given by Eshelby[6] as

$$A = \pi\rho a^2$$

where a is the lattice parameter and ρ is the density; C, the line tension of the dislocation, given by Mott and Nabarro[7] as

$$C = \frac{2Ga^2}{\pi(1-\vartheta)}$$

where G and ϑ are the appropriate elastic constants; and B, the damping force per unit-length acting on the dislocation. The variation of A and C with temperature is of the order of the variation of the elastic constants and density with temperature. These variations are too small to explain the observed temperature-dependence. The mechanisms proposed for the damping are thermoelastic damping,[8] radiation damping,[9] and scattering of sound-waves.[10] The temperature-dependence of these mechanisms is not determined, but is probably of the same order as the variation of the elastic constants. On this basis, the temperature-dependence of the term Δ_D may be neglected.

From eq. (7) we obtain

$$\log \Delta_J = \log (\Delta - \Delta_D) = A - \left\{\frac{U_0 - \vartheta(\epsilon)[\tau - \tau_G]}{kT}\right\} \tag{8}$$

The experimental data plotted in Fig. 3 shows that the variation of Δ is of this form, when

$$N_a\{U_0 - \vartheta(\epsilon)[\tau - \tau_G]\} \tag{9}$$

is taken equal to the measured activation energy Q. (N_a is Avogadro's number.) The dependence of the activation energy on the previous history of the specimen is also shown in Fig. 3. For an as-grown single crystal annealed at 400°C for one hour and slowly cooled, $Q = 13{,}000$ cal/mole (curve 1). After deformation of 0.5×10^{-2} in./in. in torsion and 0.25×10^{-2} in./in. in compression, the value of Q is 15,000 cal/mole (curve 2). Annealing after deformation was observed to cause a decrease in activation energy, as shown in Fig. 4.

The variation of Q with the state of the specimen may be accounted for by examining eq. (8). Plastic deformation causes an increase in the dislocation density and number of dislocation intersections, thereby decreasing l_0 and increasing τ_G. The increase in τ_G is due to the elastic interactions of the stress

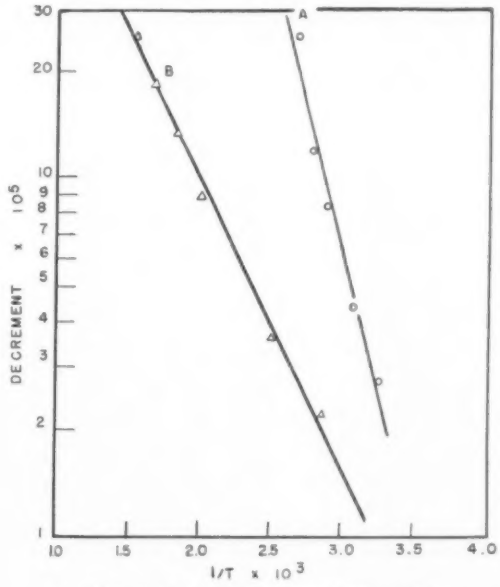

FIG. 4. High-temperature decrement.
Curve A—Crystal deformed 2.0×10^{-2} in./in. in compression.
Curve B—After a one-hour anneal at the temperatures of run A.

VOL. 4 1956

fields of nearby dislocations. This causes an effective increase in the value of Q. Annealing should decrease the dislocation density and number of intersections and therefore should result in a decrease in the value of Q. As outlined above, preliminary experiments have exhibited this behavior.

On the basis of the above discussion the measured activation energies are associated with the formation of vacancies or interstitials at dislocation intersections in the presence of an applied stress. The activation energy to form a vacancy or interstitial at a dislocation intersection may be obtained by extrapolating the values obtained at several stress levels to zero stress. An approximation to this value can be obtained by a simple calculation which also indicates the effect of plastic deformation.

Assume a dislocation density in an annealed crystal of 10^7 dislocation lines/cm^2. If a grid of dislocations is considered and the maximum number of intersections assumed, l_0 is 3.2×10^{-3} cm, b is of the order of 3×10^{-8} cm, as is d. The applied stress for the internal friction measurements is approximately 10^6 dynes/cm^2. Inserting these values in eq. (2), we obtain

$$\vartheta(\epsilon)[\tau - \tau_G] \simeq 0.18 \text{ eV}$$

where it is assumed that $[\tau - \tau_G] \approx \tau$. The measured activation energy for an annealed crystal is approximately 0.56 eV. The value of U_0 is calculated to be 0.74 eV, or 17,000 cal/mole. This is a reasonable activation energy for the formation of vacancies in aluminum. If the crystal is now deformed in torsion and compression and the dislocation density is assumed to be 10^8 dislocation lines/cm^2, a similar calculation gives

$$\vartheta(\epsilon)[\tau - \tau_G] \simeq 0.06 \text{ eV}$$

Assuming the value of U_0 previously calculated, Q is calculated to be 0.68 eV, or 15,600 cal/mole, again assuming $[\tau - \tau_G] \approx \tau$. This approximate calculation indicates that the observed changes in activation energy with deformation (Fig. 3) are of the proper order of magnitude.

The above calculations assume an isotropic distribution of dislocations. If, however, the deformation is such as to produce an increase in $(\tau - \tau_G)$, the measured activation energy may be decreased considerably below the value for an annealed crystal. Such an increase in $(\tau - \tau_G)$ may result from stress concentrations due to the dislocation configurations. An average stress concentration of 2 will result in a value for $\vartheta(\epsilon)[\tau - \tau_G]$ of 0.36 eV, and a value of the measured activation energy Q of 0.38 eV, or 8,700 cal/mole, for a dislocation density of 10^7 dislocation lines/cm^2. It is possible that the dislocation configuration produced by deformation in compression results in this stress concentration. The above calculations indicate the sensitivity of the value of the measured activation energy to the state of the crystal.

Recent results of Weertman and Salkovitz[11] on dilute alloys of lead have shown an exponential increase of decrement with temperature in the range of 400°K to 590°K. The activation energy for this increase is about 0.30 eV. It is suggested that the variation of decrement with temperature for these alloys may be treated in a manner similar to the previous analysis.

ACKNOWLEDGMENTS

The authors wish to thank Drs. T. A. Read and M. Metzger for many helpful discussions. The work was supported by Ordnance Contract DA–30–069–ORD–459.

REFERENCES

1. J. Pittenger, Navy Contract N6 ori 47 Technical Report, August 10, 1951.
2. A. S. Nowick, *Plastic Deformation of Crystalline Solids*, Mellon Institute (1950).
3. P. Bordoni, *La Ricerca Sci.*, **19,** 851 (1949).
4. A. Seeger, *Phil. Mag.*, **45,** 771 (1954).
5. J. Koehler, *Imperfections in Nearly Perfect Crystals*, J. Wiley (1950).
6. J. D. Eshelby, *Proc. Roy. Soc.*, **A197,** 396 (1949).
7. N. F. Mott and F. R. N. Nabarro, Report on a Conference on the Strength of Solids, Phys. Soc. (London) (1948).
8. J. D. Eshelby, *Proc. Roy. Soc.*, **A197,** 396 (1949).
9. E. Orowan, *Proc. Phys. Soc.*, **52,** 8 (1940).
10. G. Liebfried, *Z. Phys.*, **127,** 344 (1950).
11. J. Weertman and E. I. Salkovitz, *Acta Met.*, **3,** 1 (1955).

The High-Temperature Recovery of Deformed Copper Whiskers*

It has recently been observed by Z. Gyulai[1] that plastically kinked NaCl whiskers would recover and straighten out when the kinked region was heated.

Similar observations have been made on copper whiskers grown by Brenner.[2]

An elastically strong whisker about 2.5 microns in width was plastically deformed and then heated in hydrogen to 1015°C, where it was held for ten minutes. Upon removal, the whisker was again straight and possessed the initial high elastic strength at the point where it was deformed. The sequence of the experiment is shown in Fig. 1.

The recovery of kinked whiskers was subsequently visually observed several times. The time-sequence of the recovery of a kinked whisker, 8.5 microns in width, is shown in Fig. 2.

The recovery rate, $d\Delta\theta/dt$, where $\Delta\theta$ is the change in kink angle, appears to be constant except at the initial and final stages. This is shown for two whiskers in Fig. 3. The large initial recovery may be due to elastic strain.

* Received July 11, 1955.

VOL.
4
1956

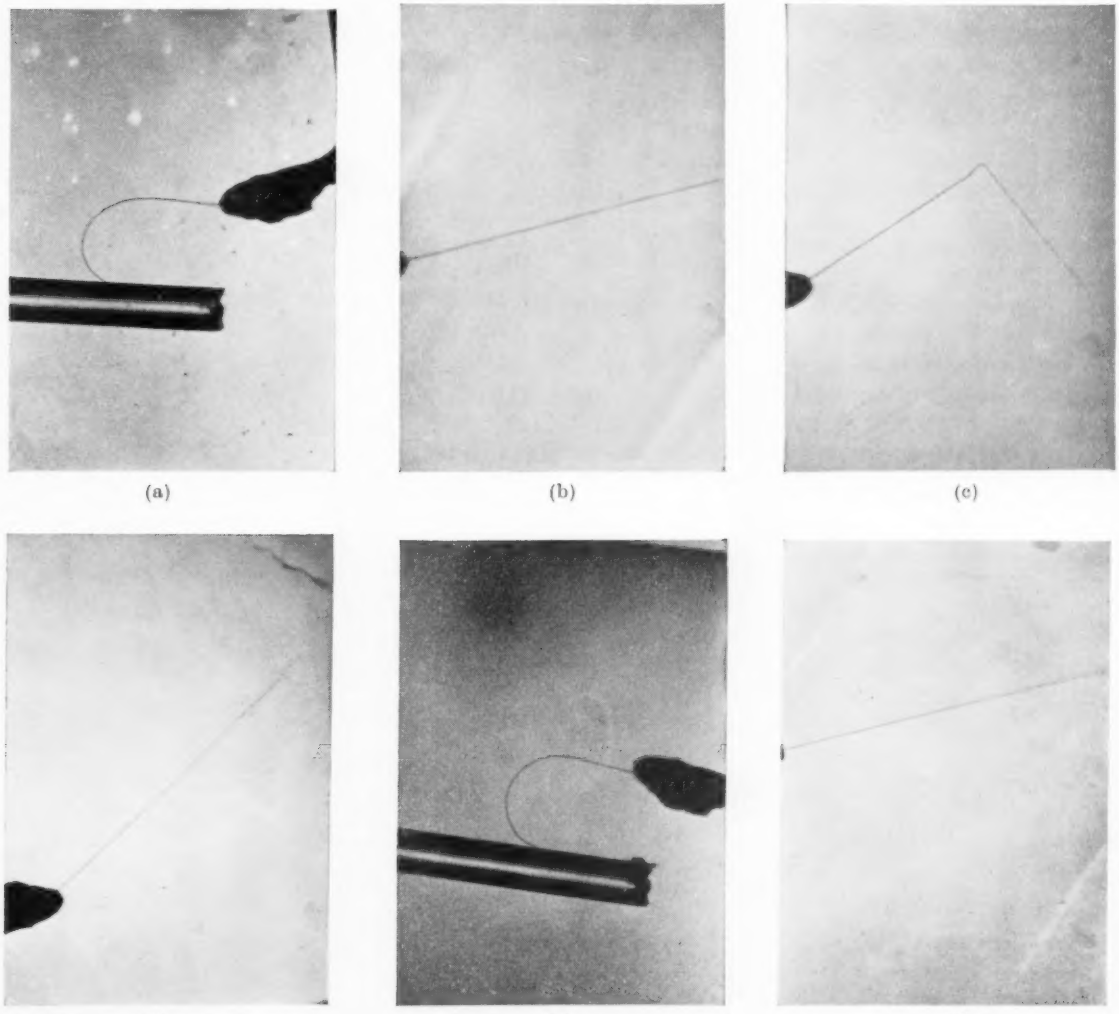

(a) (b) (c)

(d) (e) (f)

FIG. 1. Recovery of deformed copper whisker: (a) Strained ~0.3 per cent. (b) Unstrained. (c) Kinked. (d) After heating ten minutes at 1015°C. (e) Strained ~0.3 per cent. (f) Unstrained. Width of whisker 2.5 ± 0.5 microns. ×8.5.

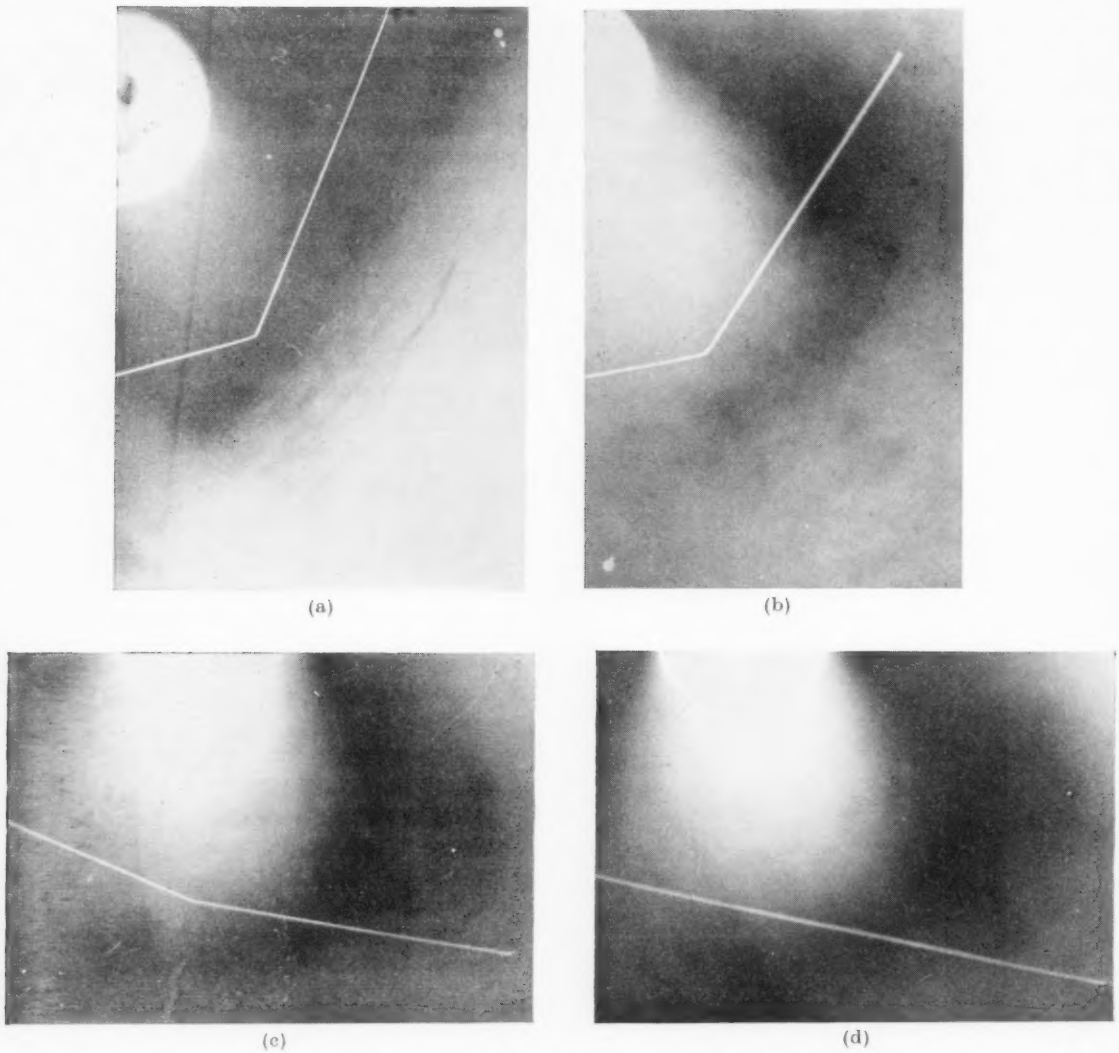

FIG. 2. Time sequence of recovery at 1015°C: (a) 0 sec. (b) 600 sec. (c) 1460 sec. (d) 2400 sec. Width of whisker 8.5 microns. ×6.5.

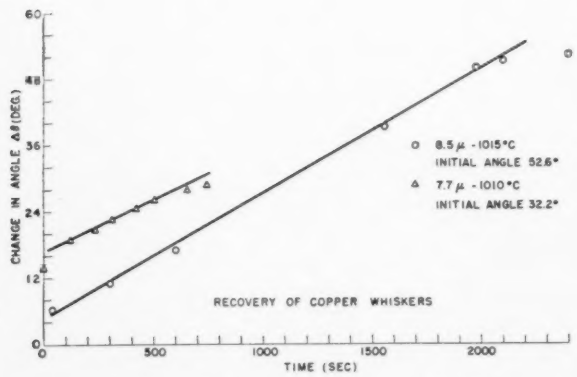

FIG. 3. Change of kink angle as a function of time. ○ 8.5 μ whisker—1015°C, initial angle 52.6°. △ 7.7 μ whisker—1010°C, initial angle 32.2°.

An oxide film formed at room temperature does not appear to retard the recovery. A deformed whisker maintained in air at room temperature for several hours recovered in helium at approximately the same rate as in hydrogen.

The effect of temperature, size of whisker, and angle of deformation will be studied further to clarify the mechanism of recovery.

S. S. BRENNER
C. R. MORELOCK

Metallurgical Ceramics Research Department, General Electric Company, Schenectady, New York

References

1. Z. GYULAI, Festigkeits und Plastizitätseigen-Schaften von NaCl-Nadelkristallen, *Z. Phys.*, **138,** 317 (1954).
2. S. BRENNER, Growth of whiskers by the reduction of metal salts. To be published.

Internal Friction Measurements on Tempered Martensite*

The diffusivity and solubility of carbon in alpha-iron can be determined from the internal friction peak that is associated with the stress-induced migration of interstitial atoms in a *bcc* lattice.[1] We have recently made such measurements on martensite in a high-purity iron—0.78 per cent carbon alloy, using a torsion pendulum at about one cycle per second. The internal friction peak due to carbon migration was observed as a function of the tempering temperature. The data may be summarized as follows:

(1) There is no carbon peak for the as-quenched martensite.

(2) The carbon peak is not detected until the martensite is tempered at about 900°F (485°C) for one hour. The peak then increases in magnitude as the tempering temperature is raised.

(3) The temperature and half-breadth of the internal friction peak are the same as that for carbon in alpha-iron, indicating that this is a true carbon peak and represents the same migration process.

(4) After the martensite has been tempered for twenty hours at 1200°F (650°C), the carbon peak is still not as pronounced as that exhibited by low-carbon alpha-iron quenched from the same temperature.

(5) A high-temperature internal friction peak is observed at 428°F (220°C), and the intensity of this peak decreases with increasing tempering temperature.

The absence of a carbon peak in as-quenched martensite is noteworthy. Evidently, the stress applied in the torsion pendulum is insufficient to produce migration of the carbon atoms from their preferred interstitial sites in the body-centered tetragonal lattice.

At the present time, we can only speculate concerning the delayed appearance and the relatively low intensity of the carbon peak when martensite is tempered. Probably the initial ferrite that appears on tempering (in the so-called third stage) is highly imperfect and contains many subgrain boundaries. Carbon atoms may be keyed at these low-angle boundaries as well as at random dislocations, and would thus be unavailable for stress-induced migration. It is also conceivable that the martensite may retain some degree of tetragonality on tempering up to 900°F (485°C), and this could also pin down carbon atoms. A third possibility is one suggested by Zener in private discussion. In the presence of numerous small carbides precipitated during the early stages of tempering, the precipitation of carbon from the ferrite may be so rapid as to essentially maintain the equilibrium concentration of carbon on quenching from 900°F (485°C). Since the equilibrium carbon concentration at room temperature is extremely low, a carbon peak would not be observed until the distance between the carbide particles became sufficiently large.

The high-temperature internal friction peak offers some support for the imperfection hypothesis, inasmuch as this peak may be associated with the presence of sub-boundaries. Such a peak should decrease as the tempering temperature is raised, and this is observed to be the case. However, more definitive experiments are necessary.

P. Stark
B. L. Averbach
M. Cohen

Department of Metallurgy,
Massachusetts Institute of Technology,
Cambridge, Mass.

References

1. C. Wert, *Modern Research Techniques in Physical Metallurgy*, ASM (1953), 225.

* Received July 1, 1955. This work was supported by the U.S. Air Force and the M.I.T. Instrumentation Laboratory.

VOL. 4 1956

Observations on the Deformation of Niobium*

There have been numerous references (unpublished) to the deformational behavior of niobium in that it does not strain-harden. The present results do, in fact, show that niobium single crystals experience no strain-hardening at room temperature.

In Fig. 1, the stress-strain curve for the as-received drawn wire is shown as D. After 13 per cent elongation the specimen failed, exhibiting a two-cup necking. Some strain-hardening was evident. The

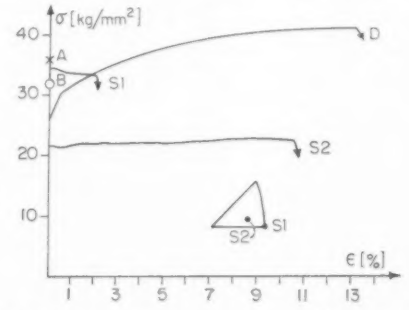

Fig. 1. Stress-strain curves for niobium specimens.
D: as-received, hard-drawn wire.
A: annealed.
B: bamboo-type structure.
S1, S2: single crystals.

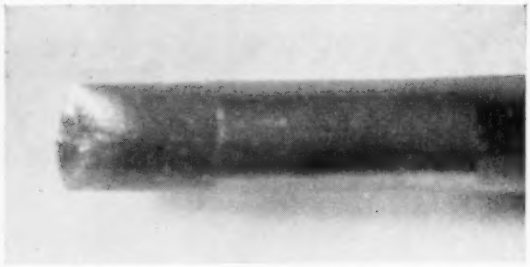

FIG. 2. Typical shear fracture in single crystal of niobium. ×20.

annealed wire, with a grain diameter of less than 0.1 mm, failed in a brittle manner at a stress indicated by A in Fig. 1. Two specimens with bamboo structure, consisting of 6 grains, each about 5 mm long, failed by cleavage on {100} planes the normal to which had, respectively, an angle of 40 and 25 degrees with the specimen axis. The cleavage occurred in the neighborhood of a grain boundary. The fracture stress is indicated by B in Fig. 1. Two single crystals (curves S1 and S2, orientation shown as an insert in Fig. 1) showed a small yield point and no work-hardening, in one case up to 10 per cent elongation. Both failed by a chisel-type necking (Fig. 2) in adjacent grains within the grips. The main crystals, however, were observed to deform to an extent comparable with the total elongation measured.

The niobium was obtained from the Fansteel Metallurgical Corporation, and contained solid impurities to the extent of 0.6 per cent. The major impurities were as follows:

Ta	0.16 per cent
C	0.2 per cent
Si, Ti, Fe	bring up the balance

The oxygen, nitrogen, and hydrogen contents, determined through the courtesy of Dr. O. Marske and Mr. D. I. Walter of the Metallurgy Division of the Naval Research Laboratories, were as follows:

	O_2 per cent	H_2 per cent	N_2 per cent
Sample A*	1.56	0.0390	0.047
B	0.058	0.0085	0.0047
D	0.058	0.0020	0.0026

* The extremely high gas content for sample "A" seems consistent with the extreme brittleness it exhibits.

The textures of the as-received and the recrystallized niobium were determined to be ⟨110⟩.

The samples were heated by means of their own resistance within five minutes up to a temperature of about 1300°C (sample A) and to just below the melting-point (samples B and S). They were maintained at these temperatures for times up to four hours in a dynamic vacuum of about 50 microns mercury. The deformation was performed in a Polanyi-type tensile apparatus at a strain-rate of 3×10^{-4}/sec. Strain was measured to ± 0.01 (strain differences to ± 0.0001), and the stress to an accuracy of ± 0.2 kg/mm^2. Specimens were 1 mm in diameter by 20 to 30 mm long.

A more thorough investigation of the effect of strain, strain-rate, temperature, grain size, and impurities on the absence of strain-hardening is now under way at the University of Pennsylvania. The work reported here was conducted at The Johns Hopkins University, Baltimore, Maryland, under the sponsorship of the Office of Naval Research.

Harvard University, U. F. KOCKS
Cambridge, Massachusetts
and R. MADDIN
School of Metallurgical Engineering,
University of Pennsylvania,
Philadelphia, Pennsylvania

* Received June 30, 1955.

Note on the Uniqueness of the Boltzmann-Matano Solution of the Diffusion Equation*

A special solution due to Boltzmann[1] of Fick's second law in one dimension

$$\frac{\partial C}{\partial t} = \frac{\partial}{\partial x}\left[D\frac{\partial C}{\partial x}\right], \qquad D = D(C), \tag{1}$$

with the initial conditions that

$$\left.\begin{aligned} C &= C_0 \quad \text{for } 0 < x < \infty \text{ and that} \\ C &= C_1 \quad \text{for } 0 > x > -\infty, \end{aligned}\right\} \tag{2}$$

has often been used in the experimental determination of the function $D(C)$.[2, 3] This solution is obtained by making the substitution $C = C(\lambda)$ with $\lambda = x/\sqrt{t}$, in which case equation (1) reduces to

$$-\frac{\lambda}{2}\frac{dC}{d\lambda} = \frac{d}{d\lambda}\left[D\frac{dC}{d\lambda}\right], \tag{3}$$

an ordinary differential equation. Thus corresponding boundary conditions are

$$\left.\begin{aligned} C &= C_0 \quad \text{for} \quad \lambda = +\infty \\ C &= C_1 \quad \text{for} \quad \lambda = -\infty. \end{aligned}\right\} \tag{4}$$

A first integration leads to

$$D(C) = -\frac{1}{2}\frac{dC}{d\lambda}\int_{C_0}^{C} \lambda \, dC. \tag{5}$$

Equation (5) is applied to experimental data, subject to the condition[2] that

$$\int_{C}^{C_1} \lambda \, dC = 0, \tag{6}$$

which allows for any volume changes or Kirkendall effects which may have occurred during diffusion. We will, for the present discussion, ignore such complications.

The question arises as to the uniqueness of solutions of the form $C = C(\lambda)$ as applied to the specified boundary conditions. Many writers, including Matano,[2] Rhines and Mehl,[3] Mehl,[4] Le Claire,[5] and Boas,[6] have erroneously taken the view that this relationship is an assumption which must be checked by experiment and at best can only be an approximation. Others, including Jost,[7, 8] Wagner,[9] and Barrer,[10] appear to be aware of the uniqueness of such solutions, although they have not stated this explicitly. Seitz[11] and Darken,[12] as far as the author knows are the only modern authors who have shown explicitly, though non-rigorously, that for the given boundary conditions, a unique solution $C = C(\lambda)$ can always be found.

It appears that we must appeal to Boltzmann for the first and last word.[1] He did not assume, as is often stated, that $C = C(\lambda)$ where $\lambda = x/\sqrt{t}$. Rather, he gave first the formal solution to equation (1) for the given boundary conditions; viz.,

$$C = C_0 + (C_1 - C_0)\frac{\displaystyle\int_{\lambda}^{\infty} \frac{d\lambda'}{D(\lambda')} e^{-\int_0^{\lambda'} \frac{\lambda'' d\lambda''}{2D(\lambda'')}}}{\displaystyle\int_{-\infty}^{\infty} \frac{d\lambda'}{D(\lambda')} e^{-\int_0^{\lambda'} \frac{\lambda'' d\lambda''}{2D(\lambda'')}}}, \quad \lambda = \frac{x}{\sqrt{t}}. \tag{7}$$

It is clear that this satisfies equations (1) and (3), that it meets all the boundary conditions, and that the integrals exist and are finite for any physically reasonable variation of D with $C(\lambda)$. The solution is therefore unique, and C is a function of λ.

It is, of course, unnecessary to know the above solution to prove the uniqueness of the statement, $C = C(\lambda)$. We note that this relation with $\lambda = x/\sqrt{t}$ provides for the possibility of a step-function as the initial condition, since $\sqrt{t}$ becomes the scale-factor for x and as such collapses any function of x into the origin as $t \to 0$. Any other ratio of positive powers of x to t would do this also, but this particular choice is the one which reduces equation (1) to (3). Now, considering equation (3) in the expanded form

$$\frac{-\lambda}{2}\frac{dC}{d\lambda} = \frac{dD}{dC}\left(\frac{dC}{d\lambda}\right)^2 + D\frac{d^2C}{d\lambda^2}, \tag{8}$$

we invoke the sufficient (and also physically reasonable) conditions that $D(C)$ and dD/dC are continuous and finite and that D is non-zero at all points of $C_0 \leq C \leq C_1$.

Then there must exist solutions of (8) such that as

$$\lambda \to +\infty \quad \text{and} \quad \frac{dC}{d\lambda} \to 0-, \ \frac{d^2C}{d\lambda^2} \to 0+$$

(concave upward)

and as

$$\lambda \to -\infty \quad \text{and} \quad \frac{dC}{d\lambda} \to 0-, \ \frac{d^2C}{d\lambda^2} \to 0-$$

(concave downward).

(The second term of (8) may be ignored, since in the limit it vanishes as $(dC/d\lambda)^2$.) These solutions are precisely those described by conditions (4). It follows therefore that since we can always find a solution to (3) (and therefore of (1)) that satisfies all the required boundary conditions, then that solution is unique.

It is concluded therefore that any significant observed deviation from the relationship $C = C(\lambda)$ is not to be attributed to any assumptions involved in the Boltzmann-Matano analysis, but rather to a failure of Fick's law or to an incorrect assessment of the boundary conditions.

J. S. KIRKALDY.

Aluminium Laboratories Limited,
Kingston, Ontario
(Now at the Department of Metallurgy,
McGill University, Montreal)

References

1. L. BOLTZMANN, *Ann. Phys* [*Leipzig*], **53,** 959 (1894).
2. C. MATANO, *Japan. J. Phys.*, **8,** 109 (1933).
3. F. N. RHINES and R. F. MEHL, *Trans. Amer. Inst. Mech. Engrs.*, **128,** 185 (1938).
4. R. F. MEHL. *Trans. Amer. Inst. Mech. Engrs.*, **122,** 11 (1936).
5. A. D. LE CLAIRE, Diffusion of metals in metals in Chalmers, B. *Progress in Metal Physics* **1.** Butterworth Scientific Publications, London (1949), p. 347.
6. W. BOAS, *Introduction to the Physics of Metals and Alloys.* John Wiley and Sons, Inc., New York (1947) p. 154.
7. W. JOST, *Z. Phys.*, **127,** 163 (1950).
8. W. JOST, W. *Diffusion in Solids, Liquids, Gases.* Academic Press Inc., New York (1952) p. 75.
9. C. WAGNER, *J. of Metals*, **4,** 91 (1952).
10. R. M. BARRER, *Diffusion in and through Solids.* Cambridge at the University Press (1951) p. 47.
11. F. SEITZ, Fundamental aspects of diffusion in solids in Smoluchowski, R. *Phase Transformations in Solids.* John Wiley and Sons, Inc., New York (1951) p. 120.
12. L. S. DARKEN and R. W. GURRY, *Physical Chemistry of Metals.* McGraw-Hill Book Company, Inc., New York p. 453.

* Received August 20, 1955.

VOL. 4 1956

Tin Whisker Studies. Observation of Some Hollow Whiskers and Some Sharply Irregular External Forms*

In a recent study of tin whiskers using high-resolution light microscopy two new features were revealed. The first was that some whiskers, for at least part of their length, were hollow in the sense that the tin phase did not extend completely across the section. The second was that many whiskers possessed heavily "fluted" surfaces with corresponding irregular cross-sections.

The whiskers were grown by S. M. Arnold[1,2] of these laboratories, from the tin constituent of a tin-aluminum alloy. For examination the whiskers were embedded together with the base in a commercial styrene polyester which was allowed to polymerize in situ. The sections were polished, metallographically, approximately transversely. Precautions, including the use of soft wax laps, were taken to prevent "burring-over" of whisker sections.

Figs. 1(a), (b), (c), and (d) show sections of a whisker after a first polishing and after three successive repolishings, each of several microns in depth. The magnification was 2000×, and the resolution, using an objective of numerical aperture 1.4 together with an interference filter with peak transmission at 5000 Å (0.5 micron), was of the order of 0.2 micron, about one-tenth the "diameter" of the whiskers under study. The microscopic appearance of the dark area, marked by the arrow, in the whisker at the left strongly suggested that it was a hole. This "hole" persisted through (b) and (c) and can still be seen near to the base of the whisker in (d). The whisker has changed in shape from (a) to (d), but the possibility of such change has been demonstrated.[3,4] The light-colored area in (d) near the whisker section is a high point of the somewhat irregular surface of the base material. The conclusion is that for at least part of its length this whisker was hollow.

(a) As originally seen.

(b) After first repolishing.

(c) After second repolishing.

(d) After third repolishing.

FIG. 1. Tin whisker sections.

While whisker sections containing holes were not in the majority, several other whiskers with holes were found. One of these was twice repolished and the hole found to persist. In this particular whisker the hole appeared to consist of a series of smaller intersecting holes grouped in a line near the center of the nearly-oval section.

The whisker sections generally did not correspond to any geometrically regular form of surface. The deep "fluting" mentioned, which corresponded to irregular and sharply outlined sections, was observed below the surface of the plastic mount.

Any mechanism proposed for the growth of tin whiskers should take the above findings into consideration.

E. E. THOMAS

Bell Telephone Laboratories,
Murray Hill, New Jersey

References

1. K. G. COMPTON, A. MENDIZZA, and S. M. ARNOLD, *Corrosion*, **7**, 327 (1951).
2. C. HERRING and J. K. GALT, *Phys. Rev.*, **85**, 1060 (1952).
3. S. E. KOONCE and S. M. ARNOLD, *J. Appl. Phys.*, **24**, 365 (1953).
4. S. E. KOONCE and S. M. ARNOLD, *J. Appl. Phys.*, **25**, 134 (1954).

* Received July 29, 1955.

Slip Patterns of Deformed Permalloy*

D. Kuhlmann-Wilsdorf and H. Wilsdorf have pointed out an essential difference between slip patterns of pure metals Al, Cu, Ag, and that of α-brass.[1] We have confirmed the same difference between pure nickel and permalloy by electron microscopic observation.

Specimens are prepared by melting commercially pure electrolytic nickel and iron in high vacuum. The polycrystalline plate specimens containing more

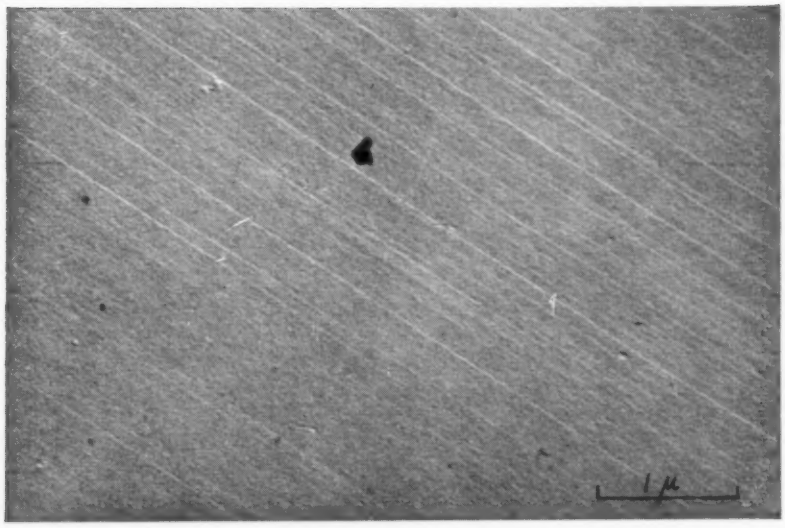

FIG. 1.
Typical elementary structure of pure nickel elongated 1 per cent.

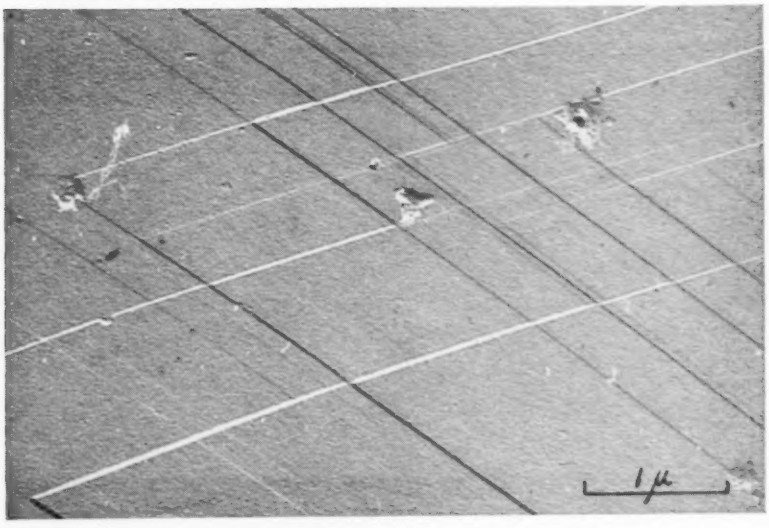

FIG. 2.
Typical cross slip in 80 per cent nickel permalloy elongated 3 per cent.

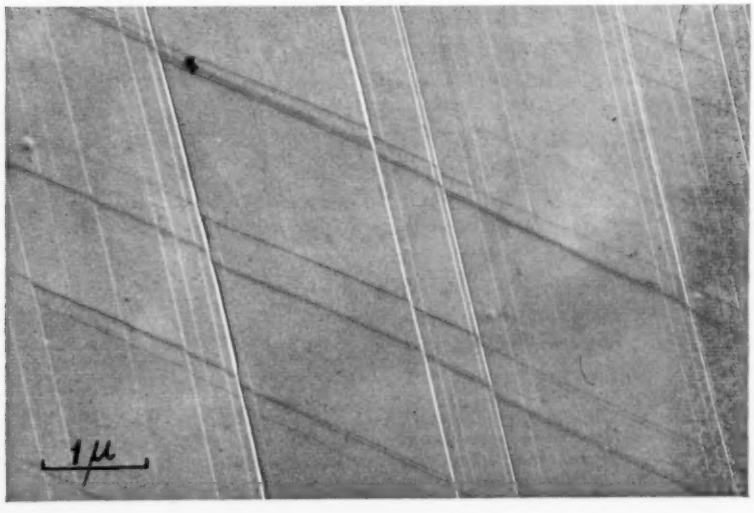

FIG. 3.
Double slip in 80 per cent nickel permalloy elongated 3.9 per cent.

VOL.
4
1956

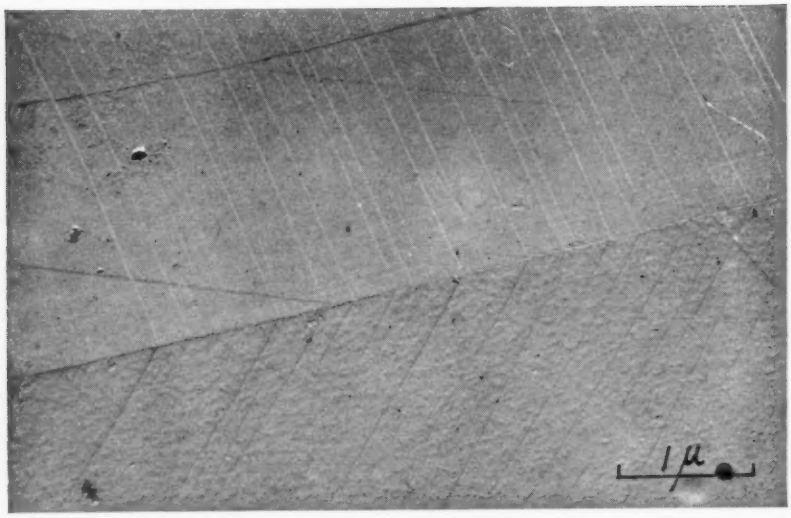

FIG. 4.
Slip lines crossing a twin boundary in 60 per cent nickel permalloy elongated 2.8 per cent.

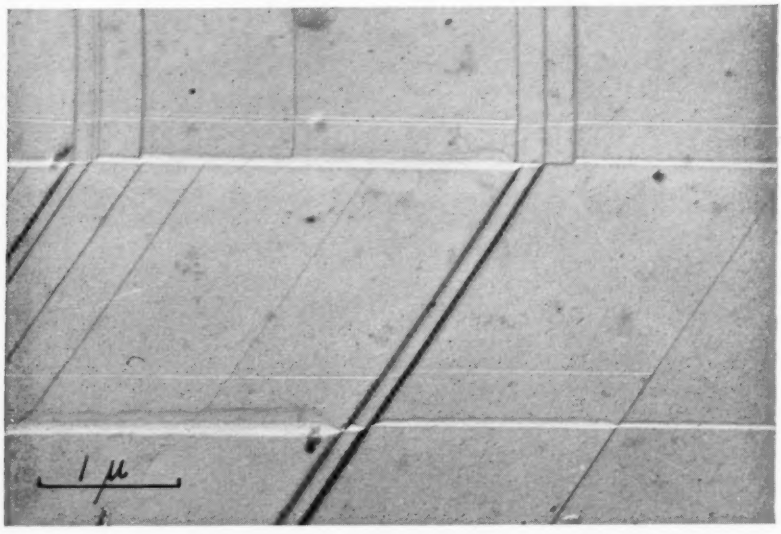

FIG. 5.
Slip lines crossing a twin boundary in 75 per cent nickel permalloy elongated 3.1 per cent.

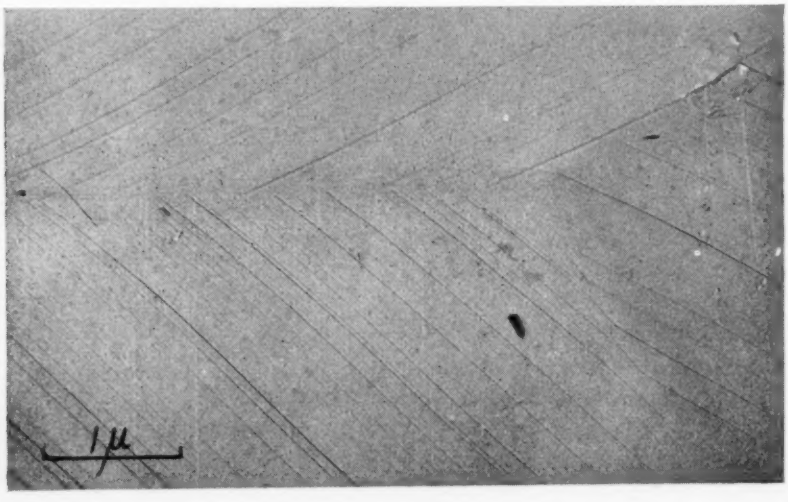

FIG. 6.
Slip pattern at the grain boundaries in 80 per cent nickel permalloy elongated 3.9 per cent.

than 50 per cent of nickel are, after careful polishing, annealed in pure hydrogen at 1300°C for a few hours. The average grain size is 0.1 to 0.3 mm in diameter. Then the specimens are electropolished, and elongated 1 to 5 per cent at room temperature. The microscopic replicas were prepared by Fukami's method, i.e., collodion one-step replica shadowed by palladium.

Fig. 1 shows that the typical elementary structure appeared on the surface of pure nickel, which can be observed in the range 100 to 95 per cent of nickel. In pure nickel, the average spacing between fine slip lines is about 350 Å, and the depth is roughly estimated at scores of Å. By adding iron, the spacing increases.

Further increase of iron content prevents slip lines from arranging themselves uniformly, and their spacing and depth become larger. On deformed permalloy with iron content of more than 20 per cent, often no slip line can be found within a randomly chosen space covering more than 1 μ, but in another place clustered slips with finer slip spacing of 500 to 1000 Å will be visible. Whereas the depth of slip is dependent on the grain size and straining condition, occasionally the deep slip line of 1000 Å or more in depth is observed. Fig. 2 shows the typical cross slip in 80 per cent nickel permalloy.

Cross and double slips are abundantly observed in permalloy, and in some cases the cross slip occurs prior to the formation of double slip as shown in Figs. 3 and 5. Annealing twins are visible quite often. At the twin boundary, change of slip direction, cross slip, and branching of slip lines occur as a common feature, as can be seen in Figs. 4 and 5. The disturbing influence of grain boundaries on slip lines is greater than that of twin boundaries, as shown in Fig. 6. Thus, the slip pattern of permalloy can be concluded to be similar to that of α-brass.[1, 2]

Further investigations on the dependence of spacing in the elementary structure on the magnitude of strain, the fine structure in a large slip, and the effect of superlattice formation on slip pattern are now under way.

The authors wish to thank Professor S. Kaya for his helpful suggestion and advice. Also a note of thanks goes to Dr. T. Taoka for his sincere guidance on electron microscopic techniques. There were many helpful discussions with Professor A. Ōkawa and Dr. F. E. Fujita.

Tomio Nagashima
Takaaki Yamamoto

Electrotechnical Laboratory,
2-Chome, Nagatacho,
Chiyoda-ku, Tokyo, Japan

7—(12 pp.)

VOL. 4 1956

References

1. D. Kuhlmann-Wilsdorf and H. Wilsdorf, *Acta Met.*, **1**, 394 (1953).
2. H. Czyzewski, *J. Appl. Phys.*, **22**, 846 (1951).

* Received October 5, 1955.

Anisotropy of Grain Boundary Self-Diffusion*

A recent publication[1] described the results of measurements of the rate of self-diffusion of silver along simple tilt boundaries in a direction parallel to the tilt axis (a common [100] direction of the two grains forming the boundary). The dependence of the rate of diffusion on crystal misorientation θ and on temperature was consistent with the dislocation model[2] of grain boundaries and with the concept that diffusion along edge dislocations is several orders of magnitude larger than lattice diffusion.

As pointed out in the discussion of reference [1], the dislocation model also leads to the prediction of anisotropic boundary diffusion rates. Specifically, for very low angle grain boundaries, we expect a very high anisotropy, since the dislocations are widely separated and diffusion through the boundaries in a direction normal to the dislocation pipes (i.e., normal to the tilt axis) should be only of the order of magnitude of lattice diffusion; for misorientations in the range 10–20°, the dislocation spacing becomes very small, and the anisotropy should decrease sharply; for very large-angle grain boundaries ($\theta \to 45°$) the dislocation model breaks down, and we expect a minimum, perhaps vanishing, anisotropy.

Quantitative measurements of the grain boundary diffusion anisotropy as a function of crystal misorientation should thus serve as a critical test of the dislocation model. The purpose of this note is to report the results of such measurements in tilt boundaries of silver. The experimental technique was the same as that used previously.[1] Measurements were made in directions parallel and perpendicular to the tilt axis over a range of misorientations, at a constant temperature of 450°C.

Unfortunately, quantitative results could not be obtained for $\theta < 16°$ because of the extremely slow diffusion normal to the tilt axis. However, this fact alone is a qualitative demonstration of the high anisotropy at low misorientations. For $16° \leqslant \theta \leqslant 45°$, the penetration curves for diffusion in both directions

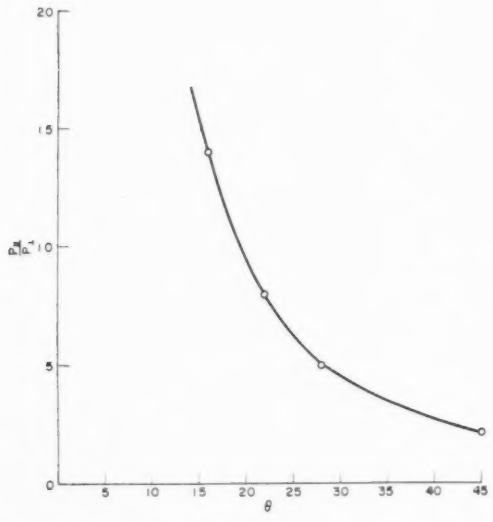

FIG. 1. The dependence of grain boundary diffusion anisotropy on crystal misorientation at $T = 450°C$.

were characterized by the usual exponential decrease of activity with the first power of the distance. The penetration curves were analyzed according to the method of Fisher[3] to give values of the parameter $P = D\delta$, where D is the boundary diffusion coefficient and δ is the effective width of the boundary. As a measure of the anisotropy, we use the ratio $P_{\|}/P_{\perp}$, the subscripts denoting the direction of diffusion relative to the common [100] direction of the two grains. The results are shown in Fig. 1, where $P_{\|}/P_{\perp}$ is plotted as a function of θ.

For as far as these measurements extend, the dependence of the anistropy on misorientation is entirely in accord with the dislocation model of grain boundaries, and constitutes further confirmation of the conclusions of the previous paper.[1]

It is also of interest to note that anisotropy persists in boundaries of maximum misorientation. Thus the concept of a large-angle grain boundary as a uniform slab of disordered material is not, in general, valid.

R. E. HOFFMAN

General Electric
Research Laboratory,
Schenectady, New York

References

1. D. TURNBULL and R. E. HOFFMAN, *Acta Met.*, **2**, 419 (1954).
2. J. M. BURGERS, *Proc. Phys. Soc.*, **52**, 23 (1940).
3. J. C. FISHER, *J. Applied Phys.*, **22**, 74 (1951).

* Received August 24, 1955. This work was supported by the United States Atomic Energy Commission under Contract No. W-31-109-Eng-52.

A Mechanism for the Formation of Intergranular Cracks when Boundary Sliding Occurs*

Greenwood, Miller, and Suiter[1] showed recently how some metals and alloys, particularly brass, when strained at elevated temperatures tend to break with intercrystalline fractures which develop from small cavities in the grain boundaries. They advanced a hypothesis to account for their observations, in which it was suggested that the cavities are formed by the agglomeration of vacancies. It was pointed out subsequently[2] that the kinetics of the agglomeration of vacancies at transverse boundaries are not easy to formulate, and there is also doubt whether vacancies will agglomerate at all, even under favorable conditions (see, e.g., Read[3] who quotes unpublished work of Brooks). The present note describes an alternative hypothesis which appears to fit the experimental observations remarkably well.

The main experimental observations of Greenwood *et al.*[1] were as follows:

1. Reduced ductility and grain-boundary cracking is associated with the prior formation of small cavities which are generally found only in the boundaries transverse to the applied stress.

2. Cavities only appear if the temperature of deformation is sufficiently high and the rate of deformation sufficiently low; their incidence is concurrent with the reduction in number and increased spacing of slip lines and with the onset of grain-boundary sliding.

3. Cavities are not found in twin boundaries; but where a twinned area terminates at a grain boundary, cavities are often associated with this part of the boundary and not the rest of it, or vice versa. That is, there appears to be a dependence on orientation difference across the boundary.

There is also evidence that the spacing of the cavities along the boundaries is about the same as that of optically visible or etched slip lines.

The model proposed now is similar to that suggested recently by Fisher[4] for the initiation of cracks within a crystal. Fig. 1(a) is a representation of a transverse boundary in which sliding is taking place between the grains A and B, with the applied stress as indicated. In Fig. 1(b) "dynamic" slip has occurred in grain B, as shown, and this may result in a "jog" in the boundary. The jog due to this slip will be much smaller than, for example, a slip step at a free surface. The size of the jog will depend on the number of dislocations which run through the boundary to initiate accommodating slip in grain A;

the remaining dislocations will remain piled-up, as indicated, and there will be a stress field[5] around them at the boundary. Slip across grain boundaries, similar to the postulated accommodating slip, has been observed and studied by Ogilvie.[6] However, since the boundary is sliding, the situation shown in Fig. 1(c) will tend to develop immediately before the jog can be straightened by boundary migration, provided that cohesion across the jogged portion of the boundary can be broken under this motion. The presence of Mott's "regions of bad fit"[7] in the boundary and the stress field of the remaining piled-up dislocations would appear to give the necessary conditions for this loss of cohesion to occur when the jog is small. The collapse of a void formed in this way in a transverse boundary is prevented by the applied stress, but would be assisted in a longitudinal boundary. A void once formed is then capable of enlargement by stress concentration as previously suggested[1] for the nuclei formed by agglomeration of vacancies.

It will be seen that this accounts for the experimental observations listed above; in particular, the fact that cavitation is only observed as a concomitant to boundary sliding is incorporated as an integral part of the hypothesis. The detailed application of the hypothesis to observation 3 above shows that there should be an orientation dependence for the formation of cavities. Consider two neighboring grains whose orientation difference is suitable for slip to run through their boundary; then, on the present hypothesis, this could lead to jogs and the formation of cavities. However, if part of this boundary pertains to a twin in one of the grains, the orientation difference is likely to be unsuitable for slip to cross the boundary, and the jogs necessary to initiate cavities will not be formed. The observed difference between the two parts of the boundary might also arise from the "herring-bone" pattern of slip in twinned grains, because this could imply jogs of opposing slopes, so that boundary sliding which opened one kind of jog would tend to make the others interlock. Such locking would not necessarily stop boundary sliding, since interlocking can be relieved by boundary migration.

Boundary sliding has been clearly demonstrated during creep of high-purity aluminum[8] and high-purity lead,[9] and it may be asked why these metals should not fail in a brittle manner by the cavitation mechanism. The metals used in the cavitation experiments were not high-purity to the same degree that the aluminum and lead were, and this could be important. Apart from this, boundary

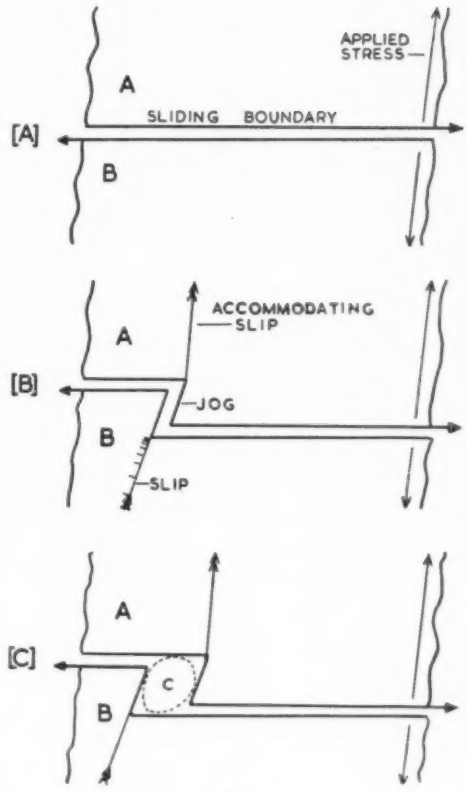

FIG. 1.

sliding in aluminum becomes prevalent only when optically visible slip has entirely disappeared. In both aluminum and lead, grain-boundary migration appears to occur more readily than in brass; thus the preservation of a jog for long enough to open up by boundary sliding appears less likely.

This work forms part of the programme of research of the Physical Metallurgy Section of Commonwealth Scientific and Industrial Research Organization, Australia.

R. D. GIFKINS

Commonwealth Scientific and Industrial Research Organization, Melbourne, Australia.

References

1. J. N. GREENWOOD, D. R. MILLER, and J. W. SUITER, *Acta Met.*, **2**, 250 (1954).
2. C. CRUSSARD and J. FRIEDEL, Paper 14 *Symposium on Creep and Fracture of Metals at High Temperatures*, N.P.L. Teddington (1954).
3. W. T. READ, Jr., *Dislocations in Crystals*, McGraw Hill, New York (1953), p. 105.
4. J. C. FISHER, *Acta Met.*, **3**, 109 (1955).
5. N. F. MOTT, *Phil. Mag.*, **43**, 1151 (1952).
6. G. J. OGILVIE, *J. Inst. Metals*, **81**, 491 (1952–53).
7. N. F. MOTT, *Proc. Phys. Soc.*, **60**, 391 (1948).
8. W. A. RACHINGER, *J. Inst. Metals*, **81**, 33 (1951–53).
9. R. C. GIFKINS, ibid., **82**, 39 (1953–54).

* Received August 26, 1955.

VOL. 4 1956

Au Sujet de la Mise en Evidence de la Polygonisation de l'Aluminium par la methode des Rayons X et par la Micrographie*

Un article récent de MM. Lambot, Vassamillet, et Dejace sur la polygonisation de l'aluminium[1] nous incite à rappeler quelques résultats obtenus au cours de nos recherches.

Ces auteurs montrent l'existence d'une striation très fine de toutes les taches de Laüe à grande distance obtenues par une méthode de focalisation en rayonnement monochromatique. Dans nos expériences, et en utilisant une méthode de focalisation à grande distance en rayonnement polychromatique (méthode de Guinier-Tennevin) nous avons constaté seulement une subdivision en une série de petites taches, à la suite de recuits à haute température; d'autre part, nous avons pu relier les aspects observés par micrographie et l'interprétation des taches de diffraction obtenues sur les mêmes cristaux.[2] Il semble donc que les striations fines et périodiques observées par M. Lambot dans toutes les taches obtenues et la subdivision en taches plus petites ne correspondent pas au même phénomène.

Nous avons aussi montré la nécessité de travailler avec un métal aussi bien défini que possible au point de vue de sa pureté et de son état de recristallisation. En effet, nous avons obtenu la subdivision des taches de rayons X après quelques heures à 630°C pour un aluminium, 99,999 pour cent, au lieu des quelques jours nécessaires avec un aluminium technique 99,5 pour cent.[3]

Nous avons souligné l'importance des tensions internes pour favoriser le réarrangement des dislocations en parois; la trempe, donnant une faible déformation plastique et créant des tensions internes élevées est une méthode de choix pour obtenir la polygonisation de grands cristaux. Des expériences récentes effectuées au laboratoire de Vitry soulignent encore ce point de vue.[4] On a montré que le simple fait de passer à faible vitesse un monocristal dans un four à 630°C provoque la polygonisation du cristal. L'influence, sur ce phénomène, de très faibles teneurs en certains métaux est actuellement à l'étude au laboratoire.

Nous avons aussi montré que la subdivision des taches de Laüe ne se produisait qu'à la suite d'un recuit à une température relativement élevée. Un monocristal d'aluminium 99,999 pour cent n'évolue pas après trempe pour des recuits prolongés à 400° au 500°. On observe les phénomènes de polygonisation uniquement vers 630°.

Tous nos résultats nous ont permis de considérer l'état polygonisé comme un état très stable, postérieur à la recristallisation. L'apport d'énergie produit par le chauffage à température élevée permet la diffusion des dislocations et leur réarrangement à l'intérieur d'un cristal encore imparfait.

CHRISTIAN DE BEAULIEU

Centre d'Etudes de Chemie Metallurgique (Laboratoire de Vitry du Centre National de la Recherche Scientifique), 15, rue Georges Urbain, Vitry, France

References

1. H. LAMBOT, L. VASSAMILLET, et J. DEJACE, *Acta Met.*, **3,** 157 (1955).
2. C. DE BEAULIEU, *Comptes Rendus*, **240,** 522 (1955).
3. C. DE BEAULIEU, J. TALBOT, et G. CHAUDRON, *Comptes Rendus*, **239,** 270 (1954).
4. J. MONTUELLE et G. CHAUDRON, *Comptes Rendus*, **240,** 1167 (1955).

* Received July 25, 1955.

Space Charge in Formation of Anodic Oxide Films*

Dewald in a recent letter[1] to this journal has advanced a theory (since published in more detail elsewhere[2]) to account for the apparently anomalous lack of temperature dependence reported by Vermilyea[3] for the range 0–80°C and confirmed over a smaller temperature range by the present author[4] of the Tafel slope $dE/d \ln i$ (where E = mean field strength in oxide, and i = ionic current density through oxide) in the formation by anodic polarization of oxide films on tantalum immersed in aqueous solutions of certain electrolytes. Dewald took into account the non-linearity of the potential in the oxide due to space charge by assuming that the latter is due solely to Ta^{5+} ions in transit; and, further instead of considering only, as do Mott and Cabrera,[5] the limiting cases of rate control by alternatively the barrier at the oxide/metal interface, or the succession of unit jumps in the diffusion of Ta^{5+} ions through the oxide, Dewald derived an expression involving dual control of the current by these two processes. Vermilyea,[6] also in a letter to this journal, has criticized Dewald's theory on the ground that the predicted variation of field with thickness has not been observed, and has concluded that the concentration of ions in transit is negligible. The purpose of the present letter is to report further observations which are consistent with Dewald's theory. Niobium was found to exhibit the same apparent anomaly, as does tantalum. A detailed examination (to be published later) of the results in

relation to Dewald's theory has shown that the latter accounts for the results giving reasonable values for all the parameters, except that, as with tantalum, the estimated jump distances are rather large. This, however, can be explained if the effective field-promoting ionic movement is greater than the Maxwell field because of polarization—as was suggested elsewhere might be so.[4] The predicted change of field with thickness is very small and could easily be masked if the current efficiency fell off at large thicknesses and high temperatures.

Impedance measurements gave what appears to be rather direct evidence that appreciable space charge is present during formation and decreases with increasing current density, as predicted by Dewald's theory for the case that $a/b > 1$, where b and a are approximately the half-jump-distances for diffusion into and through the oxide respectively. Fig. 1 shows $\log_{10}(C(t)/C(\infty) - 1)$ plotted against t, where $C(t)$ = equivalent series capacity at 1.0 kc/s and 30°C for a series of film thicknesses at time t after cessation of formation at constant current densities of about 1.0, 0.1, and 0.01 mA/cm^{-2}. The equivalent series resistance also falls with time. The capacity of a film of given thickness measured immediately after formation is larger, the smaller the current density. It falls with time by an amount of the order 1 per cent to a value independent of current density. It has been shown elsewhere[7] that the frequency dependence of the impedance of niobium oxide films can be accounted for on the assumption that the specific conductivity of the oxide (electronic conductivity at low fields) varies through at least part of the oxide in a manner which might be due to variation in non-stoichiometry. It is now suggested, following this theory, that the explanation of the results indicated above is that on ceasing formation the excess metal responsible for the space charge during formation is partly frozen or chilled in, and only slowly adjusts itself towards its equilibrium distribution. This adjustment happens to be such that the equivalent series capacity decreases—as it would if the specific conductivity of parts of the oxide decreased. (The equivalent circuit of the film may be taken as a series of capacities each with a parallel resistance, the time constants varying through the oxide due to the variation in the specific conductivity.) On this hypothesis the initial capacity is larger the smaller the current density, because of more space charge and hence more non-stoichiometry and greater conductivity.

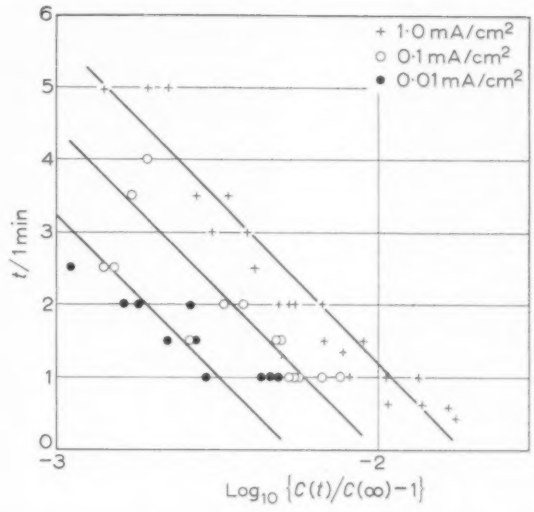

FIG. 1.

L. YOUNG.

Chemistry Department,
Imperial College of Science and Technology,
London, S.W.7.

References

1. J. F. DEWALD, *Acta Met.*, **2**, 340 (1954).
2. J. F. DEWALD, *J. Electrochem. Soc.*, **102**, 1 (1955).
3. D. A. VERMILYEA, *Acta Met.*, **1**, 282 (1953).
4. L. YOUNG, *Trans. Faraday Soc.*, **50**, 153 (1954).
5. N. CABRERA and N. F. MOTT, *Reports Prog. Physics*, **12**, 163 (1948-49).
6. D. A. VERMILYEA, *Acta Met.*, **3**, 106 (1955).
7. L. YOUNG, *Trans. Faraday Soc.*, 1955 (in press).

* Received July 22, 1955.

VOL. 4 1956

BOOK REVIEWS

X-Ray Diffraction Procedures for Polycrystalline and Amorphous Materials. By. H. P. KLUG and L. E. ALEXANDER. pp. xiii + 716 with 325 figs. New York, John Wiley and Sons, Inc.; London, Chapman and Hall. 1954. Price $15.00; £6.

X-Ray Diffraction by Polycrystalline Materials. Technical editors H. S. PEISER, H. P. ROOKSBY, and A. J. C. WILSON. (Physics in Industry Series.) pp. 725 with 263 figs. London, The Institute of Physics. 1955. Price 63s.; $9.00.

Much interest attends the arrival from opposite sides of the Atlantic of two weighty volumes both dealing with X-ray diffraction by polycrystalline materials. First to appear has been the book by H. P. Klug and L. E. Alexander, an ambitious project of private enterprise in which these two well-known American crystallographers build upon their considerable teaching and research experience in X-ray diffraction. The second book was sponsored by the Equipment Sub-Committee of the X-ray Analysis Group of the British Institute of Physics. The technical editors, H. S. Peiser, H. P. Rooksby, and A. J. C. Wilson, have through long effort succeeded in assembling a galaxy of British crystallographic talent to cover the diversity of topics now within the field of powder diffraction.

The aims of the two books differ considerably. Klug and Alexander have a double object in view. They wish to combine with a complete discussion of experimental techniques an introductory textbook of X-ray crystallography. Their book is intended to be a self-teacher; put in the hands of the worker who has no training in X-ray crystallography, and who lacks the self-reliance of an experienced researcher, it is intended to lead him by easy stages from basic concepts to the performance and understanding of advanced techniques. To further this end, the book is copiously illustrated, and the numerical analysis involved in many typical experiments is followed through in detail. The writers of the British book have been set a much easier task; they can assume prior knowledge of basic X-ray crystallography on the part of the reader, together with sufficient experience to proceed under his own steam through the analysis of experimental data when given only the basic formulae. Consequently, space has been available to them for the presentation of a greater number of facts on a wider range of topics. They have produced a handbook rather than a textbook, but it should be remembered that a good handbook, in the hands of a student able to do some thinking for himself, can also be a good textbook.

Bearing in mind the above-mentioned differences, the two books may now be examined more closely. The first three chapters of Klug and Alexander's volume follow fairly conventionally the lines of a general textbook on X-ray crystallography. Chapter 1 deals with the geometry and symmetry of crystals and space lattices. It is rather closely packed with material and will be found indigestible by the novice, though useful for reference purposes. Chapter 2, on the production and properties of X-rays, provides a simple but on the whole adequate introduction to a variety of topics in this field. To help the beginner, calculations of X-ray absorption, including those for β-filters, are given in detail. It is stated, however, that μ/p varies as Z^4, whereas this is the relationship between *atomic* absorption coefficients and Z (Bragg and Pierce's Law). Mass absorption coefficients are much more closely proportional to Z^3. Chapter 3 gives an elementary account of the basic geometry of X-ray diffraction, including a demonstration of the geometrical relationship between Bragg's equation and the Laue equations which is of interest to the student. The following section, on the intensity of diffracted beams, is unclear in many places. There is confusion between the number of atoms and number of unit cells in unit volume, and the statement that diffraction maxima become progressively more diffuse when the specimen is heated could be taken to imply a broadening of Bragg reflexions due to thermal motion. Following chapters are on the whole much stronger. A good survey of photographic powder techniques is offered in Chapter 4 and detailed instructions are given on specimen preparation and the adjustment of specimen and cameras, aided by many figures. Next comes the most interesting feature of the book, the first detailed account of the powder diffractometer technique. Chapter 5, of eighty-two pages, is devoted to this, and various applications of powder diffractometry are dealt with in subsequent chapters, adding roughly thirty-four more pages of material on this topic.

Diffractometer users will welcome the instructions on adjustment and calibration of the instrument and on the preparation of specimens. Valuable, too, is the discussion, summarized in three tables, of the best choice of instrumental variables such as apertures, scanning speed, and time constant. Certain criticisms of this chapter may be offered. Rather much attention is given to the X-ray optical characteristics of the first Norelco diffractometer, whereas the great majority of workers interested in high-quality records will now be using the much more refined later model. In contrast to the rather gentle pace of exposition in the rest of the book, the reader is led rather abruptly into the intricacies of convolution analysis. Here a little more explanation is required, and a figure should be included. In the expression for the displacement of center of gravity of a line as a result of vertical divergence, equation 5-17, the numerical factor should be 1/24, not 1/8. This chapter includes a rather detailed account of procedures for correcting for Geiger-Müller tube counting losses but no mention is made of the X-ray proportional counter. The value of this type of detector for obviating counting losses was demonstrated in 1951, and it is now commercially available in diffraction equipment. In the discussion of recording technique it is stated that a large time constant reduces both peak height and area of diffraction maxima, whereas the area is in fact unaffected.

VOL.
4
1956

The chief topic of Chapter 6 is the indexing of powder diffraction patterns of cubic and non-cubic crystals. The exposition, aided by several worked examples, is clear, but does not extend as far as discussion of the methods of Vand or Ito. Among various information contained in this chapter is a useful table of tungsten L spectrum lines likely to be found in contaminated X-ray sources. Chapter 7, on qualitative and quantitative analysis of powders, contains detailed instructions for using the A.S.T.M. index which will be helpful to the inexperienced worker, and describes some applications of the diffractometer in this field. A discussion of stability and reproducibility tests on the latter instrument will be found informative. The account of precision lattice parameter determination by the powder method, which follows in Chapter 8, is very well arranged. An elementary geometrical analysis of camera errors is given which is sufficient to familiarize the reader with the quantities involved. The results of more rigorous analyses are presented in graphical and tabular form. Extrapolation and analytical methods are explained through worked examples, and the discussion concludes with a tabular guide to the choice of the most appropriate method to apply in particular circumstances. Crystallite-size determination from line broadening is the subject of Chapter 9, including the extension to crystallite shape determination. The treatment of the corrections for instrumental broadening has particular relevance to the diffractometer technique and is well illustrated by a number of graphs. It is a little surprising, however, that no mention is made of graphical or numerical methods for obtaining line profiles from the pattern produced by overlapping $K\alpha$ doublet components. This is a frequently occurring problem, particularly to the diffractometer user. The discussion of stress measurement in metals and preferred-orientation determination which follows in Chapter 10 is along conventional lines. A strong feature of the book is Chapter 11, which deals with diffraction by materials lacking crystalline regularity. A very readable account is given of radial-distribution analysis by means of Fourier inversion of the scattered-intensity data. Illustrative examples are described and sources of error critically discussed. The final chapter, on small-angle X-ray scattering, offers a balanced if not exhaustive survey of this field. In Appendix I some suggestions are offered on planning the layout of a diffraction laboratory, and in Appendix II there are some sensible hints about film processing. X-ray data and trigonometrical functions contained in the remaining appendices are mainly reprinted from the Internationale Tabellen of 1935. Klug and Alexander write with a pleasing appreciation of the historical development of their subject and give a number of references to early and little known papers that will interest the connoisseur. For the benefit of the student they have put at the end of each chapter a short list of textbooks and special articles for further reading and reference.

The work edited by Peiser, Rooksby, and Wilson consists of three parts. The first deals with experimental techniques, the second with interpretive procedures, while the third contains a series of essays on the results obtained from X-ray diffraction by polycrystalline materials. The introductory chapter, by Peiser, Rooksby, and Wilson, presents a masterly summary of crystal geometry and the basic formulae of X-ray diffraction. The same authors then proceed to give a good general description of X-ray generators and film-measuring equipment. There follows a thorough account by J. B. Nelson of the design of Debye-Scherrer powder cameras and the preparation of specimens. G. W. Brindley contributes a chapter on monochromators and focusing cameras which is not as complete or up-to-date as could be desired, and another chapter on glancing-angle and flat-layer

techniques which serves a useful purpose in presenting a summary of his early analysis of the X-ray optics of flat specimens, which deserves to be better known, and of the more recent analysis by Wilson. A not very detailed description of the back-reflexion technique follows, by J. Adam. The chapter by U. W. Arndt on the diffractometer includes an account of Geiger, proportional, and scintillation counters, and of counting statistics, which many diffractometer users will find of interest. They will not, however, find in this article much practical guidance on diffractometer operation. In a brief discussion of the effects of mis-setting of the specimen away from the correct 2 : 1 ratio of counter angle to specimen angle a formula is given for the displacement of centre of gravity of diffraction lines due to this error combined with the 'flat-specimen' error which is quite wrong. A brief account of apparatus for small-angle scattering studies follows, contributed by D. P. Riley. In the next two chapters high-temperature and low-temperature methods are discussed, by H. J. Goldschmidt and E. G. Steward, respectively. Much information is given, with extensive literature references. P. B. Hirsch contributes a well-written article on X-ray microbeam techniques, and the last chapter of Part I is a fair account by A. Hargreaves of techniques for examining preferred-orientation textures. The authors of those articles in Part I describing apparatus and experimental techniques have had to try and steer a course between confining themselves to general descriptions on the one hand and offering a mere bibliography on the other, and they also have had to decide just how much geometrical analysis of experimental arrangements to give. On the whole, deviations from a satisfactory middle course are not great; perhaps Hirsch's article is the best-balanced.

Part II commences with a well-written chapter by A. Taylor on the identification of materials by powder diffraction patterns. The following chapter, by C. W. Bunn, on the determination of unit-cell dimensions, is excellent. The determination of accurate lattice parameters is discussed by I. G. Edmunds, H. Lipson, and H. Steeple. They give quite a good account of the principles of the extrapolation and least-squares methods; very little is said about the work of Straumanis. C. J. Brown enumerates the principal factors controlling the intensity of powder diffraction lines and quotes the formulae to apply in various experimental arrangements. In the next chapter, on line profiles, A. R. Stokes gives a brief but quite good summary of the theory of broadened reflections, and of the various methods for correcting for instrumental broadening. In a short chapter on background scattering in powder photographs D. P. Riley deals adequately with Compton scattering but gives scant attention to the diffuse scattering due to such effects as short-range order and clustering which are frequently encountered in alloy powder patterns. The following chapter, also by D. P. Riley, on scattering by non-crystalline media, indicates the intensity formulae to be applied to various physical systems and has an extensive bibliography. A variety of topics of interest is included in the short article by K. W. Andrews on the interpretation of non-continuous diffraction rings. T. Ll. Richards gives a good introduction to preferred orientation in metals in the next chapter. The last chapter of Part II, contributed by F. Happey, offers as its topic preferred orientation in organic polycrystalline materials, but it is in fact largely concerned with the geometrical interpretation of various types of preferred-orientation diffraction patterns. A number of interesting formulae are derived which are of quite general application in preferred-orientation studies.

The powder method in the industrial chemical laboratory forms the subject of the first essay in Part III. The author, E. Valerie Garner, writes chiefly about problems of identification, and thus overlaps somewhat the earlier contribution by A. Taylor. In this essay it is refreshing to see the opinion expressed that automation is no substitute for intelligent laboratory personnel. A stimulating contribution follows by V. Vand, on the powder method in organic chemical research. It includes a valuable discussion of resolution requirements in the recording of organic powder patterns, and of the intensity distribution of powder lines. A contribution by F. A. Bannister on the powder method in mineralogical research contains a good deal of information of general interest on matters of powder technique. Two rather specialized articles follow, one on powder and fibre methods in polymer and biological research, by F. Happey, and the other on the powder method in refractory and ceramic research, by H. J. Goldschmidt and H. M. Richardson. Happey summarizes structure investigations on a considerable number of natural and synthetic fibers. A historical approach is adopted but too much weight is attached to α-protein models of the pre-α-helix era. Goldschmidt and Richardson indicate briefly a variety of studies which are in fact fascinating experiments in synthetic mineralogy and petrology. The next three essays are concerned with metallurgical applications. E. A. Owen gives a general description of X-ray techniques for phase-boundary determinations, and stresses the advantages

VOL 4 195

of X-ray versus microscopic methods. An interesting account of the importance of experimental powder diffraction studies for the theoretical metallurgist is given by Mrs. A. M. B. Douglas. Order-disorder transformations, modulated and interstitial structures, and the role of Brillouin zones in determining alloy phase stabilities are among the topics considered in this review. Stress determinations from lattice-strain measurements form the topic of an article by G. B. Greenough. This considers the physical background of the X-ray measurements, and indicates both the scope and limitations of such experiments. Several different topics are touched upon in an article by J. Thewlis on the powder method in atomic-energy research. Of special interest are the notes on recent studies of the structures of uranium and graphite, and on the remarkable work done by Zachariasen on structures of compounds of the heavy elements. The final chapter, on photographic aspects of X-ray crystallography, really belongs to Part I. The author, R. H. Herz, gives some information on the physics of the photographic action of X-rays, discusses characteristic curves, and gives good advice for the correct use of X-ray film. A valuable feature of this work is the Appendix, compiled by A. J. C. Wilson, which contains a number of new tables. Specially to be noted are the following: interplanar angles in the cubic system, a considerable extension of Bozorth's table, of great value in single-crystal orientation determinations; a comparison of values of X-ray emission wavelengths, with a note on wavelength units by Mrs. Lonsdale; and a revised set of atomic scattering factors.

VOL. 4 1956

In view of the large number of independent contributions to this volume some degree of overlap and repetition is unavoidable. The operation of the tripartite division has also enforced a separation of some topics which are conventionally, and probably more satisfactorily, treated in a continuous development. An example of repetition may be cited: separation of the patterns due to various components in a mixture is often aided by noting differences in their degree of spottiness or sharpness. Statements to this effect appear four times, on pages 326, 461, 506, and 528. Certainly the reader will have no excuse for forgetting this advice.

Two criticisms of a specialized nature may be made; these apply both to Klug and Alexander and to Peiser, Rooksby, and Wilson. The discussion of monochromator crystals is inadequate and not up-to-date. In particular, old recipes are quoted for bending rock salt and lithium fluoride crystals while immersed in water under various conditions. In practice, the most satisfactory results are obtained by bending the crystals after thorough annealing; immersion is not necessary.

In the discussion of indexing of powder reflections of non-cubic crystals no mention is made of the technique proposed by Frevel (*J. App. Phys.*, **8** (1937) 553), and applied to soaps by Vand. This uses the relative shift of lines due to anisotropic thermal expansion to distinguish between reflections from different zones. With the high resolution nowadays available through use of the diffractometer and the relative ease of temperature variation of diffractometer specimens, this method deserves to be more widely employed.

Both books contain a valuable collection of references to original papers; an indication of the numbers involved is obtained by comparing the numbers of names in the author indices. These are roughly 540 for Klug and Alexander and 930 for Peiser, Rooksby, and Wilson. A fair impression of the relative number of topics considered is obtained by comparing numbers of entries in the subject indices, roughly 1450 and 2220, for Klug and Alexander, and for Peiser, Rooksby, and Wilson, respectively. A few trial searches suggest that the subject index in the British book is the better arranged.

Klug and Alexander's book is very well produced. The text is clear and there has been no stinting of the number and size of illustrations. The many large clear figures greatly aid the exposition in the text. There are remarkably few errors of a typographic nature; only the following were noticed. In equation 3–30 $\cos 2\theta$ should be $|\cos 2\theta|$, in the last line of Table 5–7, 1/8 should be 1/4; and V. W. Arndt should be U. W. Arndt.

The standard of printing in Peiser, Rooksby, and Wilson is also high, and the decimal numbering of paragraphs is a convenience when looking up particular topics. Unfortunately, the otherwise good impression made by the book is marred by the poor quality of the illustrations. Many of these are very badly designed and drawn. The text is creditably free from errors; among minor slips noted are the following. On page 108 "aromatic" should be "aliphatic." On page 222 it is stated that the probability of a count lying above or below the mean by three standard deviations is one in 300, whereas it is closer to one in 400. K. E. Ben should read K. E. Beu. The reviewer's name is misspelled on page 138: he thereby gains a double entry in the name index. Similarly honoured is A. Jevinš, who appears also as I. Jevinš. The page number in the latter reference should be 265; not 165. Reekie is misspelled Reeki on page 723,

and Andress is misspelled Andrass on pages 533 and 689.

To sum up, it is no exaggeration to say that the appearance of these two books is a landmark in the development of the art of X-ray diffraction. No laboratory in which powder diffraction work is done can afford to be without Peiser, Rooksby, and Wilson as a book of reference. The lesser-experienced worker will learn more rapidly from Klug and Alexander, and all classes of reader will benefit from reading some of their chapters, such as that on the precision determination of lattice constants. As a practical handbook on powder diffractometry, Klug and Alexander's work stands alone.

A. R. Lang.

Erratum

Acta Metallurgica, Vol. 3, No. 5
On page 513, line 15, column 1,
read "$(a/\sqrt{2})$ [110]"
instead of "$(a/2)$ 110"

SOME CURRENT PAPERS IN OTHER JOURNALS

Acta Crystallographica, Vol. 8

Part 10, October, 1955 (Partial Contents):

Messungen zur Röntgenstrahl-Optik des Idealkristalls. I. Bestätigung der Darwin-Ewald-Prins-Kohler-Kurve. M. RENNINGER.

Beitrag zur Kenntnis der röntgenographischen Unterschiede zwischen den beiden Diamant-Typen. M. RENNINGER.

Factors determining the choice of X-ray reflexions for the study of the elastic properties of certain non-cubic crystals. S. C. PRASAD and W. A. WOOSTER.

The crystal structure of trigonal U_3O_8. STANLEY SIEGEL.

A method for calculating thermal vibration amplitudes from spectroscopic data. P. W. HIGGS.

The calibration of microthermostats for X-ray measurements on crystals. J. C. McC. POLLOCK.

The refraction correction for lattice constants calculated from powder or rotation crystal patterns. M. E. STRAUMANIS.

Oblique projections. P. J. BLACK.

Part 11, November, 1955 (Partial Contents):

The use of shorter wavelengths in X-ray diffraction in relation to scintillation counting. J. C. M. BRENTANO.

The study of the elastic constants of white tin by diffuse X-ray reflexion. S. C. PRASAD and W. A. WOOSTER.

The determination of the signs of structure factors by optical methods. P. R. PINNOCK and C. A. TAYLOR.

The structure of $MoBe_{12}$. RICHARD F. RAEUCHLE and FRED W. VON BATCHELDER.

The crystal structure of $Na_{2-x}V_6O_{15}$. A. D. WADSLEY.

Polarization correction for crystal-monochromatized X-radiation. LEONID V. AZAROFF.

The crystal structures of KHg and KHg_2. E. J. DUWELL and N. C. BAENZIGER.

Symmetry of galvanomagnetic effects in antimony. HELLMUT J. JURETSCHKE.

The diffraction of X-rays by a cylindrical lattice. IV. E. J. W. WHITTAKER.

X-ray powder diffraction data for hexagonal zinc sulphide. M. A. SHORT and E. G. STEWARD.

A variation on the σ-phase structure: the crystal structure of the P phase, Mo–Ni–Cr. CLARA BRINK and DAVID P. SHOEMAKER.

A new type of X-ray diffraction picture (high-voltage Laue photographs). H. S. PEISER and J. R. RAIT.

Some lattice constants. J. W. MENARY.

Archiv für das Eisenhüttenwesen

Heft 9, September, 1955:

Die Grenzen der Entphosphorung des Eisens mit Kalk. GERHARD TRÖMEL und WILLI OELSEN.

Untersuchungen an einem Riemenfallhammer mit unterteiltem Hammerbär. PAUL GRÜNER und EDMUND KRAFT.

Zur thermodynamischen Analyse. III. Selbsttätige Aufzeichnung der Wärmeinhaltskurven von Metallen und Legierungen. WILLY OELSEN.

Spurenanalyse mit radioaktiven Isotopen Die Aktivierungsanalyse auf Phosphor im Eisen. WILFRID HERR.

Wirkung von Aktivierungszusätzen in festen Einsatzmitteln zur Aufkohlung von Stählen. HANS SCHRADER.

Abhängigkeit der Ummagnetisierungsverluste warm gewalzter Transformatorenbleche von den Glühbedingungen. FRANZ LIHL und PAUL ZEMSCH.

Die dehnungsfreien Richtungen des ebenen Spannungszustandes und ihre Bedeutung für röntgenographische Spannungsmessungen und Untersuchungen von Strukturen. FRITZ BINDER und ECKARD MACHERAUCH.

Das System Eisen-Phosphor-Vanadin. BERTHOLD STENGEL und RUDOLF VOGEL.

Das Dreistoffsystem Kobalt-Chrom-Kohlenstoff. WERNER KÖSTER und FRANZ SPERNER.

Ermittlung der Porengrößenverteilung in feuerfesten Baustoffen. LUDWIG ZAGAR.

Vielkristall-Makrohärte der Abschreckgefüge unlegierter Stähle und die Einkristall-Mikrohärte des Martensits. ROLAND MITSCHE und KARL L. MAURER.

Heft 10, Oktober, 1955:

Die Rektionen zwischen Eisen-Mangan-Schmelzen und den Schmelzen ihrer Aluminate. WILLY OELSEN und GERHARD HEYNERT.

Der Angriff eisengesättigter Zinkschmelzen auf schwefel- und phosphorhaltiges Eisen. DIETRICH HORSTMANN.

Beitrag zur Quarz-Cristobalit-Umwandlung. I. Einfluß der Oberflächengröße auf die Umwandlung von Findlingsquarziten. HANS-ERNST SCHWIETE und HANS STOLLENWERK.

Untersuchung über die Zwischenstufenumwandlung an Manganstählen. WINFRIED DAHL, WERNER JELLINGHAUS, und EDUARD HOUDREMONT.

Die Kaltwalzbarkeit von Transformatorenstählen mit mehr als 3,3% Si. FRANZ LIHL und PAUL ZEMSCH.

Versuche über die Leistung eines 15-MeV-Betatrons bei der Durchstrahlung von Stahl. HERMANN MÖLLER, WALTER GRIMM, und HELMUT WEEBER.

Kristallisation unterkühlter Metallegierungen. WERNER GELLER und HANS GARBECK.

Die Temperaturabhängigkeit der freien Energie von Mischkristallen. BERNHARD ILSCHNER.

Das Dreistoffsystem Nickel-Chrom-Kohlenstoff. WERNER KÖSTER und SIGRID KABERMANN.

Das Dreistoffsystem Eisen-Phosphor-Zinn. RUDOLF VOGEL und GERHARD ZWINGMANN.

Journal of the Institute of Metals, Vol. 84

September, Part 1, 1955–56:

A further study of the oxidation of titanium and its alloys at high temperatures. A. E. JENKINS.

Textures in face-centred cubic metals and alloys. R. E. SMALLMAN.

Intermediate precipitates in aged binary alloys of aluminium with cadmium, indium, or tin. (Miss) J. M. SILCOCK.

The structural ageing characteristics of ternary aluminium-copper alloys with cadmium, indium, or tin. (Miss) J. M. SILCOCK, T. J. HEAL, and H. K. HARDY.

October, Part 2, 1955–56:

Atmospheric corrosion of aluminium alloys in a large chemical factory and their protection by painting. W. D. CLARK.

Metallographic study of sodium, potassium, rubidium, and caesium after cooling to 1.2°K. CHARLES S. BARRETT.

The constitution of the titanium-oxygen alloys in the range 0–35 weight per cent oxygen. T. H. SCHOFIELD and A. E. BACON.

Relaxation of the precipitated copper atoms in the binary alloy AuCu. R. KAMEL.

November, Part 3, 1955–56:

The copper-rich alloys of the system copper-aluminium-indium. P. H. STIRLING and G. V. RAYNOR.

The constitution of the copper-rich copper-gallium-germanium alloys. G. V. RAYNOR and T. B. MASSALSKI.

Experiments on aluminium crystals subjected to slowly alternating stresses. N. THOMPSON, C. K. COOGAN, and J. G. RIDER.

December, Part 4, 1955–56:

Tensile properties of some titanium ternary solid solutions and duplex alloys up to 600°C. J. W. SUITER.

VOL. 4 1956

The relationship between the first development of slip lines and metallographic slip-line indications in 70 : 30 brass. L. E. SAMUELS and M. HATHERLY.
The effect of temperature on the lattice spacings of indium. J. GRAHAM, A. MOORE, and G. V. RAYNOR.
The mechanism of embrittlement by a liquid phase. R. EBORALL and P. GREGORY.
The crystal structures of some thorium compounds. (Miss) J. R. MURRAY.

Journal of Metals, Vol. 7

October, 1955, Section 1 (Partial Contents):
475°C embrittlement of chromized coatings on low carbon steel. W. L. CHU.
High nitrogen cast austenitic steels. J. F. CARLSON and V. F. ZACKAY.

November, 1955, Section 1 (Partial Contents):
Uniform density and structure possible with simultaneous high pressure and temperature. R. HUMPHREY, M. VILELLA, and L. W. TOMARKIN.
Iodide process produces ductile hafnium for fabrication. J. G. GOODWIN and W. J. HURFORD.
Residual lattice strains in sectioned bars of plastically deformed iron. C. J. NEWTON and H. C. VACHER.

November, 1955, Section 2 (Partial Contents):
Melting of high purity uranium. B. BLUMENTHAL.
Deformation mechanisms of alpha-uranium single crystals. L. T. LLOYD and H. H. CHISWIK.
Deformation and recrystallization textures of rolled uranium sheet. M. H. MUELLER, H. W. KNOTT, and P. A. BECK.
Uranium-chromium system. A. H. DAANE and A. S. WILSON.
Transformation kinetics in uranium-chromium alloys. D. W. WHITE, JR.
Compositional changes of the alpha phase in a eutectoid Cu-Al alloy during isothermal transformation. D. F. TONER, P. E. GAGE, and D. J. MACK.
Creep of polycrystalline tin. J. E. BREEN and J. WEERTMAN.
Aging effects in commercially pure beryllium. D. R. MASH.
Preliminary examination of the quenching of titanium alloys. L. D. JAFFE.
Hardenability of titanium alloys calculated from composition: a preliminary examination. L. D. JAFFE.
Recrystallization textures of a cold-rolled aluminum single crystal. Y. C. LIU and W. R. HIBBARD, JR.
Cleavage steps on zinc monocrystals: their origins and patterns. J. J. GILMAN.

VOL
4
195

SLIP IN CRYSTALS OF THE CAESIUM CHLORIDE TYPE*

W. A. RACHINGER† and A. H. COTTRELL‡

Crystals of ordered beta brass slip along ⟨111⟩; those of ammonium and thallium halides slip along ⟨100⟩. These observations can be interpreted in terms of partial dislocations in the simple cubic lattice of the caesium chloride structure. When the ordering forces are large, these partials are pulled together in pairs by the tension of the superlattice stacking faults between them, and the perfect dislocations thus created can produce slip along ⟨100⟩. When the ordering forces are small, the partials remain dissociated and can produce slip along ⟨111⟩. An estimate of the critical ordering energy leads to the view that some intermetallic compounds of this crystal type ought to slip along ⟨100⟩. Experiments were made to test this view on various single crystals, the conventional method of slip traces and the prismatic punching method of Smakula and Klein being used to determine the glide elements. The results show that CuZn and AgMg slip along ⟨111⟩, and that AuCd, AuZn, LiTl, MgTl, Tl(Br, I), and Tl(Cl, Br), slip along ⟨100⟩.

GLISSEMENTS DANS LES CRISTAUX DU TYPE CHLORURE DE CÉSIUM

Les cristaux de laiton β ordonné présentent un glissement le long de ⟨111⟩; ceux des halogénures d'ammonium et de thallium le long de ⟨100⟩. Ces observations sont expliquées par la présence de dislocations partielles dans le réseau cubique simple du type chlorure de césium. Quand les forces d'ordre sont grandes, ces dislocations partielles se rassemblent par paires sous l'action des "stacking faults" introduits entre elles dans la surstructure et les dislocations parfaites ainsi créées produisent un glissement le long de ⟨100⟩. Si les forces d'ordre sont faibles, les dislocations partielles restent dissociées et peuvent produire un glissement le long de ⟨111⟩. Une estimation de l'énergie d'ordre critique permet de conclure que certains composés intermétalliques de ce type doivent glisser le long de ⟨100⟩. Des expériences ont été entreprises pour vérifier ce point de vue sur différents monocristaux en utilisant, pour déterminer les les éléments du glissement, la méthode conventionnelle et la méthode de poinçonnage de Smakula et Klein. Les résultats montrent que CuZn et AgMg glissent le long de ⟨111⟩, tandis que AuCd, AuZn, LiTl, MgTl, Tl(Br, I), et Tl(Cl, Br) glissent le long de ⟨100⟩.

ÜBER DAS GLEITEN VON KRISTALLEN IN CÄSIUMCHLORID-STRUKTUR

Bei geordneten beta-Messing Kristallen findet die Gleitung in einer ⟨111⟩-Richtung statt; Ammonium- und Thalliumhalogenide gleiten nach ⟨100⟩. Diese Beobachtungen können aufgrund von Teilverstezungen im kubisch primitiven Gitter der Cäsiumchlorid-Struktur erklärt werden. Wenn die ordnenden Kräfte gross sind, so werden diese Teilversetzungen durch die Spannung der Überstrukturstapelfehler zu Paaren zusammengezogen. Die dadurch entstehenden vollständigen Versetzungen können dann das Gleiten nach ⟨100⟩ bewirken. Wenn die ordnenden Kräfte klein sind, bleiben die Teilversetzungen dissoziiert; sie können dann eine Gleitung in der ⟨111⟩-Richtung verursachen. Eine Abschätzung der kritischen Ordnungsenergie führt zu der Ansicht, dass die Gleitrichtung bei einigen intermetallischen Verbindungen dieses Kristalltypus die ⟨100⟩-Richtung sein müsste. Zur Prüfung dieser Ansicht wurden Versuche an verschiedenen Einkristallen ausgeführt. Zur Bestimmung der Gleitelemente wurden die übliche Methode mit Hilfe der Gleitlinienspuren und das Untersuchungsverfahren von Smakula und Klein herangezogen. Die Ergebnisse zeigen, dass CuZn und AgMg nach ⟨111⟩ und dass AuCd, AuZn, LiTl, Tl(Br, I), und Tl(Cl, Br) nach ⟨100⟩ gleiten.

VOL. 4 1956

INTRODUCTION

Crystals with structures of the caesium chloride type have the rare distinction of setting the theory of dislocations a problem involving a structure-insensitive property. For, whereas in a crystal of ordered beta brass (CuZn) the direction of slip is ⟨111⟩, in those of ammonium[1] and thallium halides[2] it is ⟨100⟩. An obvious interpretation is that ⟨111⟩ slip occurs when the bond is of metallic character, and the two kinds of ions that alternate along close-packed rows are practically indifferent to the species of their neighbors; and that ⟨100⟩ slip occurs when the bond is of ionic character, and electrostatic forces prevent like ions from becoming nearest neighbors. A similar view has been taken of differences in cleavage planes in crystals with structures of the zinc blende type.[3]

How large must the ordering energy be to change the slip direction from the "metallic" to the "ionic" type? This is a problem for the theory of dislocations.[4] Since the CsCl structure has a simple cubic lattice, the Burgers vectors available to unit-perfect dislocations in such crystals are $a[111]$, $a[110]$, and $a[100]$. These perfect dislocations do not disrupt the atomic order,

* Received July 15, 1955.

† Aeronautical Research Laboratories, Melbourne, Australia; formerly Department of Physical Metallurgy, University of Birmingham.

‡ Metallurgy Division, Atomic Energy Research Establishment, Harwell; formerly Department of Physical Metallurgy, University of Birmingham.

and so can exist in such crystals irrespective of the ionic character of the bonds. Suppose for the moment that they do not dissociate into *imperfect* dislocations. Then, as Nabarro[5] first pointed out, they can be expected to produce slip along ⟨100⟩; this is because the following dissociations into *perfect* dislocations,

$$\begin{aligned} a[111] &\rightarrow a[110] + a[001], \\ a[110] &\rightarrow a[100] + a[010], \end{aligned} \tag{1}$$

involve no change of elastic energy, so that a stress that acts more strongly on one component, e.g., $a[100]$, of an $a[111]$ or $a[110]$ dislocation can move this component independently of the others.

To produce slip along ⟨111⟩, the dislocations of $a[111]$ type must first dissociate into imperfect dislocations, thus

$$a[111] \rightarrow \tfrac{1}{2}a[111] + \tfrac{1}{2}a[111], \tag{2}$$

for this dissociation then renders them incapable of dissociating according to the first scheme. This second dissociation is encouraged by the reduction in elastic energy which accompanies it. In the limiting case where the atoms of the crystal are all identical the $\frac{1}{2}a[111]$ dislocations are simply unit-perfect dislocations in the body-centered cubic lattice.

In the CsCl structure, however, these two imperfect dislocations are partials, linked by a ribbon of stacking fault in the superlattice, and the surface tension of this fault prevents them from separating completely. A stable equilibrium is reached at which the surface tension is balanced by the elastic repulsion of the dislocations at a critical distance of separation r_0. When $r_0 \gg a$, the dissociated $a[111]$ dislocation can no longer undergo the reactions (1), and slip must then occur along [111]. But when $r_0 \simeq a$, the structure at the center of the $a[111]$ dislocation is not altered enough to prevent it from undergoing dissociations of the first type and so producing ⟨100⟩ slip.

For a rough quantitative criterion we shall assume that the critical surface energy γ_C of the stacking fault is that which exerts a force on the dislocation equal to the theoretical shear strength of the lattice. According as the fault energy is larger or smaller than this, so the direction of slip is ⟨100⟩ or ⟨111⟩. Thus

$$\gamma_C = \alpha\mu b, \tag{3}$$

where μ is the shear modulus, $\alpha\mu$ is the theoretical shear strength ($\alpha \simeq 1/30$), and b is the length of the Burgers vector. Taking the typical values $\mu = 3 \times 10^{11}$ dyne cm^{-2} and $b = 2.5 \times 10^{-8}$ cm, we obtain $\gamma_C \simeq 250$ erg cm^{-2}. The number of atoms per unit area in a (110) layer is $\sqrt{2}/a^2$, and each atom forms bonds with two nearest neighbors in the next layer. Hence, on the nearest-neighbor bond approximation,

$$V_{AB} - \tfrac{1}{2}(V_{AA} + V_{BB}) = -\gamma_C a^2/2\sqrt{2} \simeq -0.06 \text{ eV}. \tag{4}$$

This value, at which the ordering energy per atomic bond becomes critical, is not unduly large. Even in beta brass the observed ordering energy, although exceptionally small, nevertheless amounts to −0.015 eV per bond according to the formula $-kT_C/4$ (T_C is the Curie temperature) of the simple theory of long-range order.[6] Again, from the formula $-z^2e^2/r$ for the electrostatic energy of two ions with charges $+ze$ and $-ze$, respectively, and spacing r ($= 2.5 \times 10^{-8}$ cm), a charge of only ± 0.1 electron is required on each ion to give this pair a bond energy of −0.06 eV. An ionic character as small as this in the interatomic bond seems quite possible, even in highly "metallic" alloys, according to the calculations of Mott,[7] Friedel,[8] and Varley.[9]

We thus conclude that the occurrence of ⟨111⟩ slip is indicative of an exceptionally small electrochemical factor, and that ⟨100⟩ should be a common mode of slip in alloys with the CsCl structure. The experiments described below have been made to test this conclusion. The compounds studied were CuZn, AgMg, Tl(Br, I), Tl(Cl, Br), LiTl, MgTl, AuZn, and AuCd.

EXPERIMENTAL METHOD

With the exception of thallium chloro-bromide and thallium bromo-iodide, which were supplied in the form of large single crystals, the compounds were prepared by alloying spectroscopically pure metals, all melting or casting operations being carried out *in vacuo* or in purified argon. Single crystals were grown by cooling from the melt in a furnace with a gradient of 2°C per cm and a cooling rate of 0.5°C per minute. The crystals were checked for composition, homogeneity, and crystal structure by chemical analysis and by metallographic and X-ray diffraction methods. To obtain crystals free from gross misorientations, it was necessary to adjust the composition closely to that at which the liquidus and solidus of the compound reach a maximum. Otherwise coring occurred during the slow solidification, and the crystals contained a mosaic structure the elements of which were disoriented by several degrees. This is presumably due to the ease with which growth faults can form in the concentration gradients which accompany coring. All specimens were polished mechanically. Special precautions, described later, had to be taken with some of the reactive compounds to preserve the polished surface.

The slip plane and slip direction of the compounds

were determined by one or both of two methods: the examination of slip traces on a cylindrical crystal; and prismatic punching. To examine slip traces, polished cylindrical crystals were strained in tension or compression according as their ductility in tension was large enough or not to give well-defined slip traces before fracture. Each crystal was centered vertically in a Unicam X-ray goniometer fitted with a microscope having a magnification of 75×. A goniometer eyepiece in the microscope enabled the angle between the slip lines and the specimen axis to be measured for various rotations of the crystal about its axis. For each such reading the plane normal to the slip lines (i.e., the locus of all possible poles of the slip plane) was plotted on a stereographic projection, using the standard method described by Maddin and Chen.[10] The position of the pole of the slip plane was determined by the point of intersection of these traces.

The glide direction was found by the standard method of noting the position round the axis of the specimen at which the slip traces vanished. In this position the axis of the microscope was perpendicular to the glide direction. Thus, since the glide direction is contained within the slip plane, its pole could be plotted on the stereogram by making the appropriate intersection. The orientation of each such crystal was determined by taking back-reflection X-ray datterns in the same apparatus without disturbing the specimen. The need for reference marks on the crystal was thus eliminated and, by superposition of the stereograms for glide elements and crystallographic orientation, the indices of the slip plane and slip direction could be established. The method of prismatic punching was first used by Smakula and Klein[2] in their studies of the plastic properties of the thallium halides. They showed that, if a thin crystal plate is indented on one surface, a prism of material bounded by four sets of slip planes moves bodily through the crystal in the glide direction and produces a pyramidal bump on the reverse side. Fig. 1 shows a typical pyramidal bump produced by indentation on the opposite face. The figure also shows the "wings" which are developed in the neighborhood of the indentation.

Nabarro[11] has suggested that prismatic punching can occur only in cases in which deformation involves the movement of $a[100]$ dislocations. Thus it was expected that the method would be useful only for compounds which slip along ⟨100⟩. This proved to be the case, and in fact the appearance of well-defined wings at an indentation became a reliable first indication that the glide direction was ⟨100⟩. For these experiments, a thin single crystal plate (approx. 0.5-mm thickness) was prepared with both sides metallographically polished. The specimen, supported by a thin backing of soft rubber, was indented with a conical indenter under a load sufficient to produce an observable pyramidal bump on its reverse surface. Since the slip direction is the line joining the indentation and the bump, this direction could be found by measuring the thickness of the crystal and the relative positions of the indentation and the bump. In some cases the crystal plate had been cut so that its surface was a plane of low Miller indices, and in these the glide direction was obvious on inspection; thus a single square-based pyramid was produced on a (100) face, whilst two identical and symmetrically disposed bumps were produced on a (110) face. The slip planes were easily determined, since these contained both the measured slip direction and the observed slip traces on the crystal surface. The surface topology of typical pyramidal bumps was also studied by means of multiple beam interferometry; in general, however, the shape of the pyramid depended on the shape of the indenter, and the method was not suitable for the determination of glide elements.

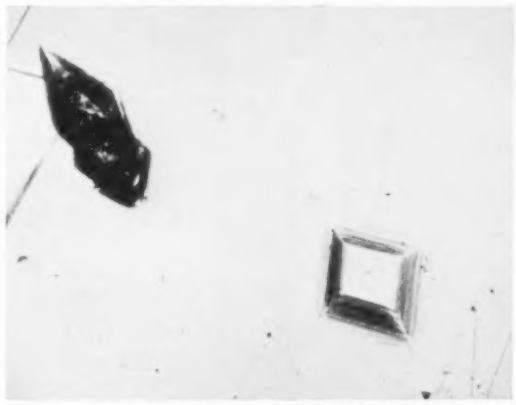

FIG. 1. Prismatic punching in thallium bromo-iodide (×55): (left) raised wings produced in the indented region; (right) pyramidal bump produced by indenting the reverse side of the slab.

EXPERIMENTS ON THE COMPOUNDS

(a) CuZn. The component metals were melted together by induction-heating in a small evacuated silica sheath. The alloy was remelted and cast under argon in a silica tube, 1-mm bore. Lengths of this wire were remelted and grown into single crystals in close-fitting silica tubes. These crystals were strained in tension and their glide elements determined by the slip-trace method. As was expected, the slip plane and direction were (110) and [111], respectively.

VOL. 4 1956

Prismatic punching did not occur, i.e., no well-defined pyramid was produced. Chemical analysis gave 48.4 per cent Zn, 51.5 per cent Cu, by weight.

(b) AgMg. The alloy and crystals were prepared by the same general method as for CuZn, although care had to be taken to adjust the composition to that of the maximum in the liquidus. Although the tensile elongation at fracture was only 4 per cent, it was sufficient to provide clear slip bands. The traces of these gave the slip plane and direction as (321) and [111], respectively. Prismatic punching did not occur. Chemical analysis gave 81.4 per cent Ag, 18.45 per cent Mg, by weight.

(c) Tl(Br, I) and Tl(Cl, Br). The thallium bromo-iodide (K.R.S. 5) and chloro-bromide (K.R.S. 6) crystals were obtained from the Engineer Research and Development Laboratory, Fort Belvoir, U.S.A. Thin slabs were cut from these and subjected to prismatic punching, which gave the slip plane and direction as (110) and [100], respectively. As a check, small cylinders were cut and deformed in compression; the same glide elements were obtained.

(d) LiTl. To minimize lithium losses by vaporization, a large quantity (60 gm) of the alloy was melted in a small sealed system, consisting of a steel crucible and mould contained in an argon-filled silica sheath. Cored structures in the crystals had to be eliminated by careful control of composition and by prolonged annealing, since cracking otherwise occurred at the dendrite boundaries. All metallographic preparations had to be made under liquids—paraffin for grinding, and a slurry of alumina, ether, and paraffin for polishing—to prevent rapid oxidation of the alloy. A polished surface could be preserved under liquid paraffin for about 30 min.

Single crystals were deformed both in tension and compression, but without producing visible slip lines. Thin crystal slabs were then prepared by cleaving in liquid nitrogen, the cleavage plane being identified as (110). Indentation of one face gave rise to two pyramidal bumps on the reverse face, in positions which established the slip direction as [100]. Although slip lines were not observed, the base lines of these pyramidal bumps, which are the traces of slip planes on the surface, established these planes as (110). No chemical analysis was made.

(e) MgTl. The experimental method was very similar to that for LiTl. Slip lines could not be observed on deformed specimens, and prismatic punching had to be used. Three crystal slabs were cut, two with random faces and one with faces parallel to (110). On indenting these crystals, pyramidal bumps formed in positions which established the slip plane and direction as (110) and [100], respectively. Chemical analysis gave 88.75 per cent Tl, 11.27 per cent Mg, by weight.

(f) AuZn. The alloy and crystals were made by the same methods as used for CuZn and AgMg. Cylindrical crystals were strained in tension and, from the slip lines thus developed, their slip plane and direction were identified as (110) and [100], respectively. As a check, thin crystal slabs were indented and the same glide elements were established by this method. Chemical analysis gave 75.36 per cent Au, 24.7 per cent Zn, by weight.

(g) AuCd. The general experimental method used was the same as that for AuZn, except that, after cooling to 350°C, the crystals were water-quenched to 20°C to suppress a low-temperature transformation.[12] X-ray and metallographic examinations showed no transformed phase in these quenched crystals. Single crystal wires were extended, and their slip plane and direction were established as (110) and [100], respectively, by the slip-trace method. Prismatic punching proved unsatisfactory for the determination of the glide elements, for the bumps produced on a (100) surface were too ill-defined to allow these elements to be established with certainty. It was observed generally that the punch marks produced in the ionic salts were better defined than those in the metallic compounds. Chemical analysis gave 62.2 per cent Au, 37.8 per cent Cd, by weight.

DISCUSSION

The results summarized in Table 1 show that slip is of "ionic" character in all the compounds studied except CuZn and AgMg. The view expressed in the introduction that ⟨100⟩ should be a common mode of slip in this class of compounds is thus confirmed. It is not surprising, of course, that CuZn slips along ⟨111⟩ since its ordering energy is well below the critical value given in equation (4); moreover, the alloy becomes disordered far below its melting-point. The alloy AgMg is probably a borderline case, since silver is more electronegative than copper,[13] and magnesium is more electropositive than zinc. It is ordered up to

TABLE 1. Planes and directions of slip in compounds of the CsCl type

Compound	Plane	Direction
CuZn	(110)	[111]
AgMg	(321)	[111]
Tl(Br, I), Tl(Cl, Br), LiTl MgTl, AuZn, AuCd	(110)	[100]

its melting-point (820°C), which implies, according to the formula $kT_C/4$, that the ordering energy per atomic bond is certainly greater than 0.023 eV. The alloys AuZn and AuCd are probably also borderline cases in which the ordering forces are just large enough to produce ⟨100⟩ slip. One indication of this is the fact that the prismatic markings were particularly ill-defined in the case of AuCd, which is the alloy nearest to AgMg in order of increasing electrochemical factor. Diffuseness of the punch markings implies a certain wandering of the slip direction out of the strict ⟨100⟩ axis, as would be expected if a minor component of the slip were transmitted along ⟨111⟩ directions. Presumably the decisive factor in these alloys is the much greater electronegativity of gold, relative to copper and silver, which ensures a correspondingly larger electrochemical factor when this metal is alloyed with zinc or cadmium.[13] It would be extremely interesting to have values for the ordering energies in AgMg, AuZn, and AuCd, so that a quantitative comparison with the theoretical predictions could be made, thus providing an unexpected link between the theory of alloys and the theory of dislocations which could be exploited to the benefit of both theories.

VOL.
4
1956

ACKNOWLEDGMENTS

This investigation was made in the Department of Physical Metallurgy, University of Birmingham, and the authors are grateful to several of their colleagues, especially Professor G. V. Raynor, for valuable discussions and advice during the course of the work.

REFERENCES

1. H. SEIFERT, LANDOLT-BORNSTEIN, *Phys.-Chem. Tab., Berlin, Suppl.*, **1,** 35 (1927).
2. A. SMAKULA and M. W. KLEIN, *Phys. Rev.*, **84,** 1013 (1951).
3. H. PFISTER, *Z. Naturforschg.*, **10a,** No. 1, 79 (1955).
4. A. H. COTTRELL, Interactions of dislocations and solute atoms, *Relation of Properties to Microstructure, Amer. Soc. Metals* (1954).
5. F. R. N. NABARRO, *Advances in Physics*, **1,** 269 (1952).
6. W. L. BRAGG and E. J. WILLIAMS, *Proc. Roy. Soc.*, **A151,** 540 (1935).
7. N. F. MOTT, *Proc. Camb. Phil. Soc.*, **32,** 281 (1936); *Proc. Phys. Soc.*, **49,** 258 (1937).
8. J. FRIEDEL, *Phil. Mag.*, **43,** 153 (1952); *Advances in Physics*, **3,** 446 (1954).
9. J. H. O. VARLEY, *Phil. Mag.*, **45,** 887 (1954).
10. R. MADDIN and N. K. CHEN, Progress in Metal Physics, **5,** 53 (1954).
11. F. R. N. NABARRO, *Phys. Rev.*, **79,** 894 (1950).
12. E. A. OWEN and W. H. REES, *J. Inst. Metals*, **67,** 141 (1941).
13. W. HUME-ROTHERY, P. W. REYNOLDS, and G. V. RAYNOR, *J. Inst. Metals*, **66,** 191 (1940).

THE INFLUENCE OF HYDROGEN ON THE YIELD POINT IN IRON*

H. C. ROGERS†

Armco iron normally exhibits a sharp yield point when tested in tension at room temperature and below. After electrolytically charging the iron with hydrogen, however, a yield point no longer is observed at room temperature. When the tensile test temperature is lowered, a yield point returns at about −12°C and increases in magnitude with decreasing test temperature. Two related mechanisms for the suppression of the yield point in iron by hydrogen are discussed.

L'INFLUENCE DE L'HYDROGÈNE SUR LA LIMITE ÉLASTIQUE DU FER

Le fer Armco présente normalement une limite élastique bien définie au cours de l'essai de traction à la température ambiante et à des températures inférieures.

Cependant, une telle limite n'est plus observée à la température ordinaire quand le fer a été chargé électrolytiquement d'hydrogène.

En abaissant la température d'essai, la limite élastique réapparaît vers −120°C et sa valeur augmente lorsque la température diminue.

Deux mécanismes relatifs à la suppression de la limite élastique du fer par l'hydrogène sont discutés.

DER EINFLUSS VON WASSERSTOFF AUF DIE STRECKGRENZE VON EISEN

Armco-Eisen weist im Zugversuch bei Raumtemperatur und darunter normalerweise eine scharfe (obere) Streckgrenze auf. Wurde das Eisen jedoch vorher elektrolytisch mit Wasserstoff beladen, so ist eine Streckgrenze bei Raumtemperatur nicht mehr zu beobachten. Bei Erniedrigung der Temperatur des Zugversuchs kehrt die Streckgrenze bei −120°C wieder; ihre Grösse nimmt mit abnehmender Versuchstemperatur zu. Zwei miteinander verwandte Mechanismen für die durch Wasserstoff in Eisen hervorgerufene Unterdrückung der Streckgrenze werden diskutiert.

Hydrogen has been found to affect strongly the tensile yield behavior in SAE-1020 steel, Armco iron, and rimmed steel. The yield point normally observed in a room-temperature tensile test can be eliminated from Armco iron and from rimmed steel, and can be substantially reduced in SAE-1020 steel merely by a short-time cathodic charge at room temperature.

Cracknell and Petch[1] have just reported the complete elimination of the yield point in fifteen annealed steels ranging in carbon content from relatively pure iron to a 0.62% carbon steel. Their successful elimination of the yield point in the higher carbon steels is undoubtedly due to the use of more severe charging conditions than were used in the present experiments.

The variation in yield behavior both with test temperature and with charging time was studied for cathodically charged Armco iron. In addition, the influence of charging time upon embrittlement was determined for fixed charging conditions.

Cylindrical specimens, 0.200-in. in diameter, were electrolytically charged in 4% sulfuric acid, using a platinum anode and a current density of 0.2 amperes per square inch. Fig. 1 shows that the room-temperature yield point in Armco iron is partially eliminated after 16 min charging, and completely eliminated after 30 min. Fig. 2 shows the reduction of area at fracture for these same tests as a function of the charging time. It is evident that the 30-min charge which eliminates the yield point causes only 60% of the maximum embrittlement obtained after a prolonged charge.

When similar Armco iron specimens were charged for four hours and tested at successively lower temperatures, a yield point began to appear at about −12°C. As in the uncharged iron, the yield point increased in magnitude with decreasing temperature (Fig. 3). However, other work with SAE-1020 steel[2], prestrained about 10% prior to charging, has shown that the hydrogen yield point does not begin to appear until about −100°C. In these earlier tests, prestraining was presumed to eliminate the possibility of a yield point due to carbon or nitrogen.

Preliminary aging experiments between room temperature and 200°C indicate that the yield point returns, at least in part, after its elimination by electrolytic charging.

Dislocation theory explains the yield point in steel as follows: Atoms of carbon and/or nitrogen diffuse to dislocations during annealing of the steel, and during cooling while the steel is still warm. At room

* Received September 2, 1955.

† General Electric Research Laboratory, Schenectady, N. Y.

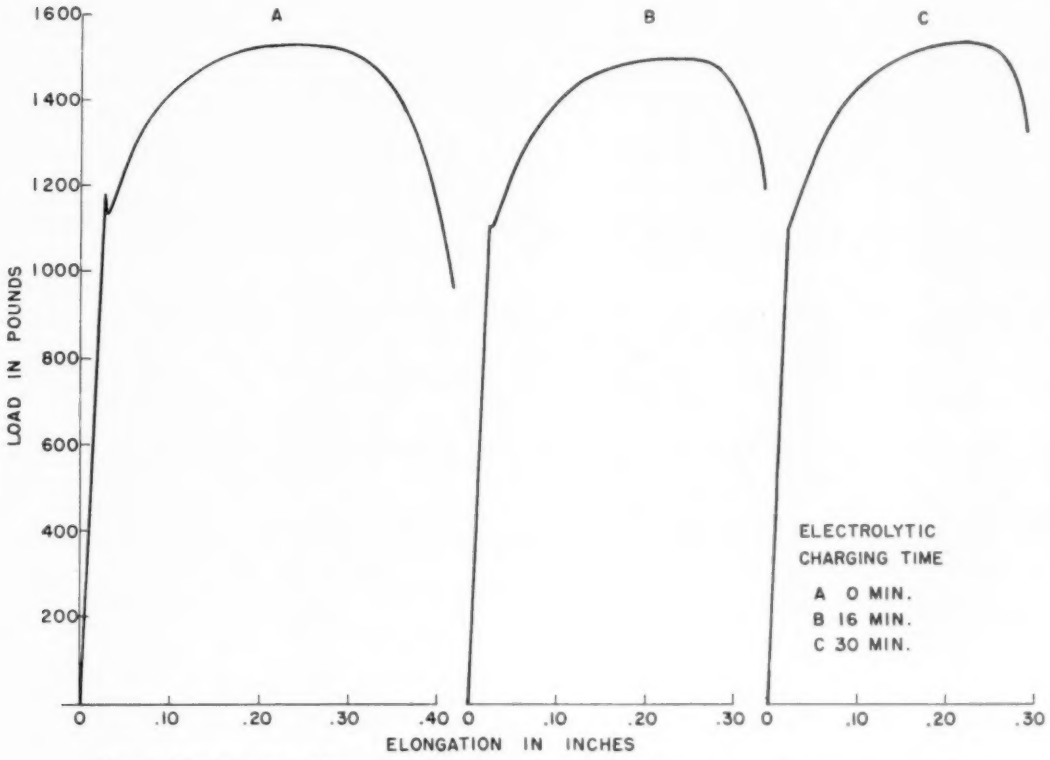

FIG. 1. The influence of increasing amounts of hydrogen on the yielding of Armco iron. Hydrogen introduced by electrolytic charging.

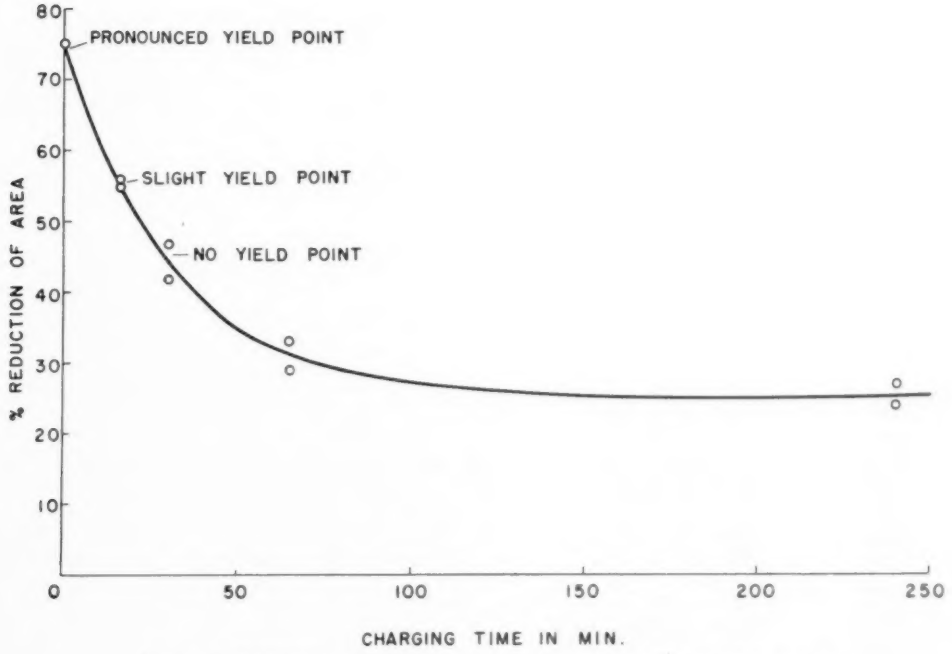

FIG. 2. The influence of electrolytic hydrogen on the ductility of Armco iron.

VOL.
4
1956

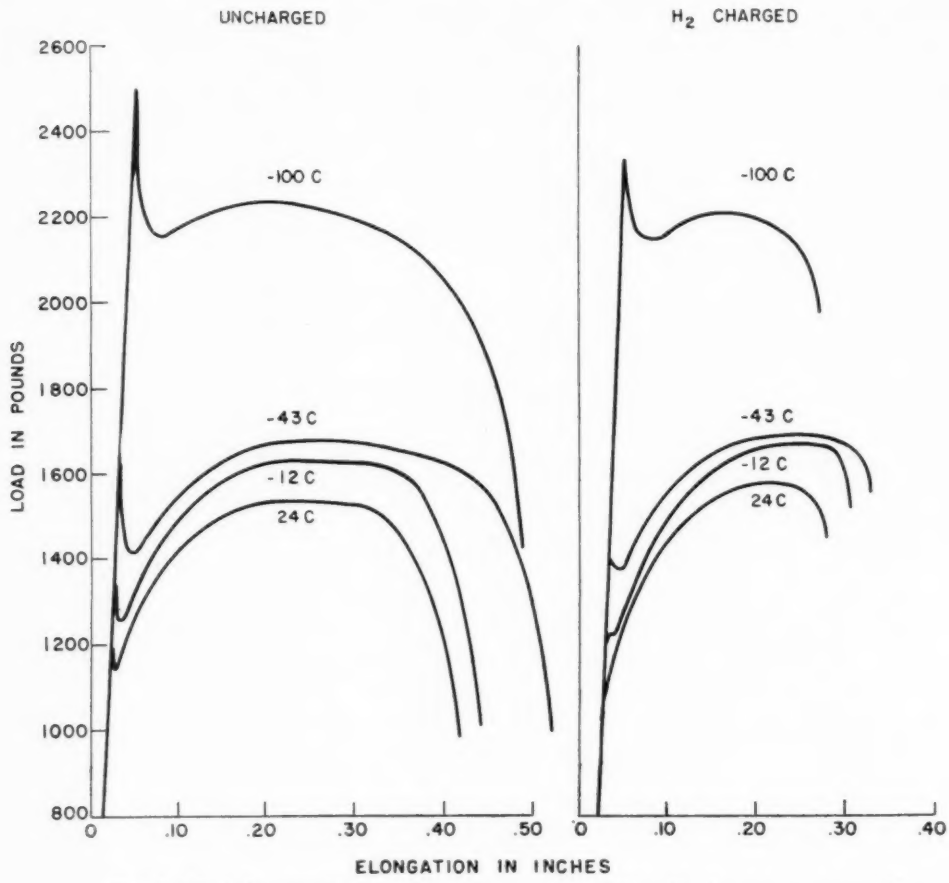

FIG. 3. The influence of testing temperature on the ability of hydrogen to suppress the yield point in Armco iron.

temperature they are firmly bound by an elastic interaction. When a stress is applied at room temperature or below, the dislocations are held up by the attached solute atoms which do not diffuse rapidly at low temperature. High stresses are required to cause the pinned dislocations to break away, and since they then can move more freely, the stress drops, giving rise to a yield point.

In terms of dislocation theory there appear to be at least two possible explanations for the fact that hydrogen eliminates the carbon or nitrogen yield point at room temperature. First, it may be that hydrogen is bound to dislocations more tightly than is carbon or nitrogen. After charging with hydrogen, each dislocation then would be surrounded by a cloud of tightly bound hydrogen atoms that would displace most of the previously bound carbon or nitrogen atoms. Assuming that hydrogen atoms can diffuse rapidly at room temperature, dislocations and their surrounding hydrogen clouds could move readily together under an applied stress, and there would be no yield point at this temperature. Only at much lower temperatures, when hydrogen itself becomes sufficiently immobile that it alone could pin the dislocations, would a yield point appear. According to this model, aging would allow the hydrogen to diffuse out of the specimen, where its free energy is still lower than on a dislocation. The carbon and nitrogen atoms then would diffuse to the dislocations and pin them, causing the yield point to return as in normal strain aging.

A second explanation could be that hydrogen is bound less tightly to dislocations than is carbon or nitrogen. Hydrogen would not now displace any significant number of carbon or nitrogen atoms, but would attach itself to loops of dislocations that are freed from carbon or nitrogen by thermal fluctuations, lowering the energy—and thereby the stress—necessary for formation of a critical-size loop. At room temperature, hydrogen could depress the yield stress sufficiently to reduce or eliminate a sharp yield point. Lowering the temperature then would raise the yield stress and cause the discontinuity in the flow-curve to increase or become apparent. The yield

stress would increase with decreasing temperature as in uncharged iron, always being smaller than that of the uncharged iron at any given temperature. As with the previous model, aging would occur with the diffusion of hydrogen out of the specimen where its free energy is lower than on the dislocation. However, since carbon and nitrogen are not displaced, the yield point would return merely upon the disappearance of the hydrogen.

Two observations suggest that the second of the proposed mechanisms—that in which hydrogen is less strongly bound to dislocations than is carbon or nitrogen—is the more likely. The first observation is that hydrogen-charged material develops a yield point near −12°C. If all carbon and nitrogen had been displaced by hydrogen, there should be no yield point until much lower temperatures, near −100°C, where the hydrogen yield point is known to appear.[2] The fact that a yield point is present near −12°C demonstrates that dislocations are more strongly held than can be accomplished by hydrogen. The second observation is that unbound nitrogen, as revealed by internal friction measurements, does not increase in concentration when hydrogen is added to strained and aged steel. If hydrogen displaced nitrogen from dislocations and returned it to free solution, the concentration of unbound nitrogen and the associated internal friction should rise.

The internal friction experiments were performed with a wire specimen and a torsional pendulum. Electrolytic iron, heat-treated in wet hydrogen to remove carbon and nitrogen, was nitrided for half an hour at 500°C in hydrogen saturated at −78°C with ammonia, then water-quenched to retain maximum nitrogen in solution. A damping peak was observed. The wire then was strained to provide a large number of dislocations, and aged to allow the nitrogen to move to the dislocations. This treatment almost completely eliminated the damping peak. After electrolytic charging with hydrogen until the yield point was almost completely eliminated, there was no increase in the damping peak. As a final check to demonstrate that an observable amount of nitrogen remained bound to dislocations, a tensile test was performed and the strained wire immediately tested in the torsional pendulum. A smaller damping peak had reappeared, showing that dislocation motion returned nitrogen to free solution, as expected. It is to be noted that the damping measurements detected no damping peak over a temperature range of 25°C to 100°C, so that it is unlikely that hydrogen interacts with carbon or nitrogen to shift the temperature of the internal friction-peak.

Tests with carbon as the interstitial atom also were negative, but less conclusively so, because no damping peak appeared upon straining after hydrogen charging. The reason for dislocation motion not returning an observable amount of carbon to free solution may be that too little strain could be introduced before the wire fractured. Another problem encountered with both carbon and nitrogen was the amplitude dependence of the damping, particularly when the specimen was not in the strain-aged condition.

VOL. 4 1956

ACKNOWLEDGMENTS

I am indebted to G. Ardley, J. C. Fisher, J. H. Hollomon, and J. R. Low, jun., for their stimulating and helpful discussions, and to R. W. Powers for providing equipment and advice for the internal friction measurements.

REFERENCES

1. A. Cracknell and N. J. Petch, *Acta. Met.*, **3**, 200 (1955).
2. H. C. Rogers, *Acta. Met.*, **2**, 167 (1954).

AN ISOTHERMAL ANNEAL STUDY OF QUENCHED AND COLD-WORKED COPPER-PALLADIUM ALLOYS*

F. E. JAUMOT, Jr., and A. SAWATZKY†

The annealing behavior of quenched and cold-worked copper-palladium alloys in the composition range from 6 to 30 atomic per cent palladium has been studied at temperatures from room temperature to 450°C. It is concluded that ordering probably takes place by a nucleation and growth process. The growth of ordered domains is a singly activated process with activation energies in the range from 34 to 46 kcal/mol, depending on the composition and the condition of the sample. Nucleation is probably not a singly activated process, but the "average" activation energy in the temperature range considered is of the order of 20 kcal/mol.

A survey of the order-disorder phenomena in light of the present data suggests that the phase diagram is in need of serious revision. The probable form of the revised diagram is discussed.

ETUDE DES TRAITEMENTS THERMIQUES ISOTHERMES DES ALLIAGES DE CUIVRE-PALLADIUM TREMPÉS ET ÉCROUIS

Le comportement d'alliages de Cuivre-Palladium trempés et écrouis de compositions atomiques variant entre 6 et 30% de palladium, a été étudié entre température ambiante et 450°C.

On conclut qu'un phénomène d'ordre se développe par un mécanisme de nucléation et croissance. La croissance des domaines ordonnés est un processus mono-activé avec une énargie d'activation variant de 34 à 46 kcal/mol, suivant la composition et l'état de l'échantillon. La nucléation n'est probablement pas mono-activée, mais l'énergie d'activation moyenne dans le domaine de température considéré est de l'ordre de 20 kcal/mol.

L'examen des phénomènes d'ordre—désordre à la luminière des résultats présents suggère la nécessité d'une révision sérieuse pour le diagramme d'état. La forme probable de ce diagramme est discutée.

EINE UNTERSUCHUNG DES ISOTHERMEN ANLASSVERHALTENS VON ABGESCHRECKTEN UND KALTBEARBEITETEN KUPFER-PALLADIUM—LEGIERUNGEN

An abgeschreckten und kaltbearbeiteten Kupfer-Palladium-Legierungen wurde im Konzentrationsbereich von 6 bis 30 Atom-Prozent Palladium das Anlassverhalten bei Temperaturen zwischen Raumtemperatur und 450°C studiert. Es wird der Schluss gezogen, dass die Ordnungseinstellung wahrscheinlich durch eine Keimbildung und einen Wachstumsprozess erfolgt. Das Wachstum von geordneten Bereichen ist ein einfach aktivierter Prozess mit einer Aktivierungsenergie zwischen 34 und 46 kcal/Mol, je nach der Zusammensetzung und dem Zustand der Probe. Die Keimbildung stellt wahrscheinlich keinen einfach aktivierten Prozess dar, ihre "mittlere" Aktivierungsenergie in dem betrachteten Temperaturbereich ist jedoch von der Grössenordnung 20 kcal/Mol.

Ein Überblick über die Ordnungs-Unordnungs-Erscheinungen an Hand der vorliegenden Ergebnisse weist auf die Notwendigkeit einer gründlichen Revision des Zustandsdiagramms hin. Die wahrscheinliche Gestalt des revidierten Diagramms wird diskutiert.

1. INTRODUCTION

A recent study[1] of order-disorder and cold-work phenomena in copper-palladium alloys in the composition range from 0 to 30 atom per cent palladium indicated that the isothermal anneal behavior of these alloys would be of some interest. Specifically, three features of the behavior of these alloys indicated that the change in resistivity with time at constant temperature could yield interesting information: (a) the disorder-order transition is sluggish, (b) cold-work produces a marked decrease in the electrical resistivity of these alloys; (c) alloys containing less than about 19%‡ palladium appear to order as face-centered cubic, while alloys containing from 19 to 26% palladium order in a tetragonal structure.

2. EXPERIMENTAL TECHNIQUES

All resistivity measurements were made at 0°C by standard potentiometric techniques which employed a Rubicon Type-B potentiometer and a Type-T-3210 Rubicon galvanometer. The potential leads were provided by alloy wires of the same composition as the sample, spot-welded to the sample about 10 cm apart and 2 cm from the ends of the sample. The current leads were simply clipped to the ends of the sample.

The pulse-annealing was accomplished by placing the sample in one end of a long Vycor tube which

* Received April 18, 1955; in revised form September 16, 1955.

† Franklin Institute Laboratories for Research and Development, Philadelphia.

‡ All percentages refer to atomic per cent.

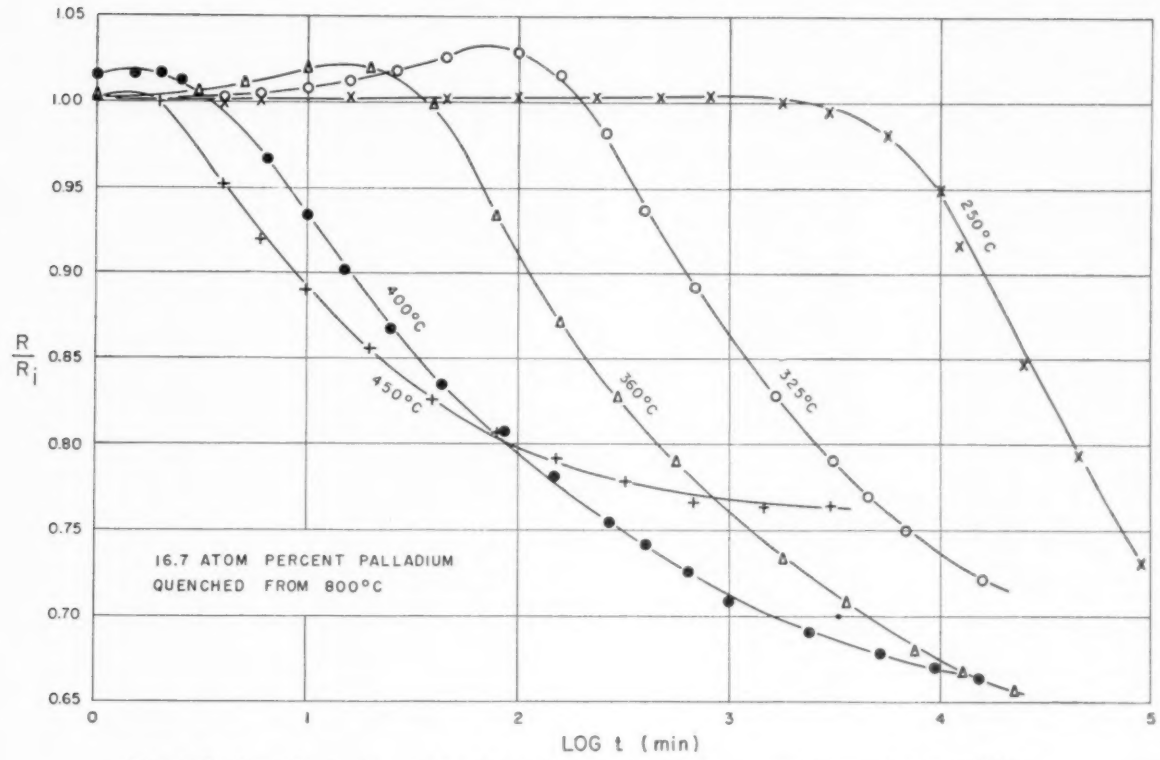

FIG. 1. Isothermal anneal curves for 16.7 atom per cent palladium samples quenched from 800°C.

contained an over-pressure of helium. The other end of the tube was placed in the furnace and allowed to come to the desired equilibrium temperature. The sample was then projected into the furnace so that it was brought into contact with a helium bath at temperature, at time $t = 0$. After the desired time had elapsed, the tube was unplugged and the sample quenched directly into non-conducting oil at 0°C. The resistivity was measured with the sample in the bath. Tests using chromel-alumel thermocouple wires indicated that the error in the time of anneal, when this method is used, is only a few seconds. This error is significant only for the one-minute anneal and then was probably no more than 5%.

3. RESULTS AND DISCUSSION OF RESULTS

The behavior of these alloys in the course of isothermal anneals was studied for 6.4, 16.7, 20.9, and 29% palladium alloys. Both cold-worked and quenched alloys were studied at temperatures from 250°C to 450°C. Runs were also made at room temperature and 100°C, with negative results. That is, after four months at 100°C, quenched and cold-worked alloys showed only a very small change in resistivity, about 0.1% increase; after one year at room temperature none of the samples exhibited any change in resistance. Typical results at the higher temperatures are shown in Figs. 1, 2, and 3, where R/R_i is plotted as a function of the logarithm of the time of anneal; here, R_i is the initial resistance of the sample, so that R_i is smaller for cold-worked samples than for quenched samples. Complete sample descriptions are given in Table 1.

Figs. 1 and 2 give the results for quenched and cold-worked 16.7% alloys; the 20.9% results are entirely similar in general behavior. The first striking thing one notices on annealing is that the resistance first increases before decreasing, for the quenched as well as for the cold-worked samples. This is in marked contrast to the behavior of other order-disorder alloys which have been studied in these laboratories (Fe-Pd near Fe-Pd_3, Cu-Au near Cu_3Au, Fe-Pt near Fe_3Pt), none of which exhibited a marked incubation period before the decrease in resistance associated with ordering began.

Two possibilities occur for the explanation of the initial rise in resistivity of quenched samples of these alloys. If one assumes that quenching produces similar results to cold work (e.g., introduction of imperfections), one might expect to find, since cold work reduces the resistivity, that the samples would

VOL. 4 1956

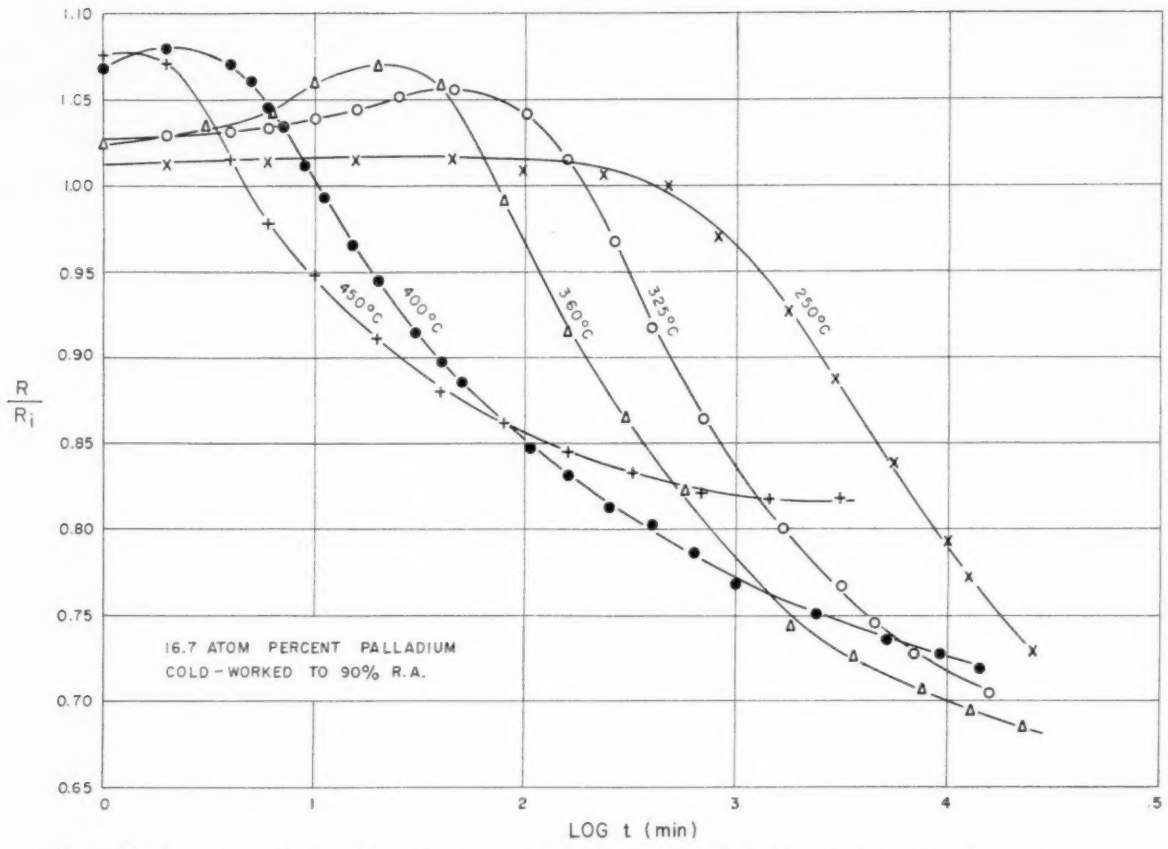

FIG. 2. Isothermal anneal curves for 16.7 atom per cent palladium samples cold worked to 90% reduction in area.

have a lower resistance the higher the temperature of quench. Then, it would be possible to attribute the initial increase in resistivity to an attempt on the part of the sample to reach equilibrium for a disordered state at the annealing temperature involved. However, the available experimental evidence does not support this view, since samples quenched from 600°C and 500°C have slightly lower resistivities than samples quenched from 800°C. The second, and most reasonable, explanation of this initial rise is a nucleation of the ordered phase. Although one cannot obtain direct micrographic or X-ray diffraction evidence in the case of these rather special alloys (this is discussed in Section 4), there are plausible arguments based on general theoretical expectations and the experimental evidence which support the latter explanation. In any nucleation process, the nuclei are initially smaller in linear dimensions than the mean free path of the conduction electrons. Thus, one would expect the nuclei to behave as additional scattering centers in the lattice and increase the resistivity. As the number of nuclei increase, the resistivity will increase until the nuclei have grown to a size such that the mean linear

TABLE 1. Description of samples used for isothermal anneals.

Composition (atom % Pd)	Electrical resistivity (micro-ohm cm)		Ordered material	Temp. (°C)	References
	Quenched from 800°C	Cold-worked to 90% *RA*			
6.4	7.35	7.15	Does not order	—	1, 8
16.7	15.60	14.0	Face-centered cubic	$450 < T_c < 475$	1
20.9	18.53	17.0	Complex tetragonal	~475	2, 1
29	23.16	20.9	Mixture of tetragonal and body-centered cubic ordered phases	$360 < T_c < 400$	1

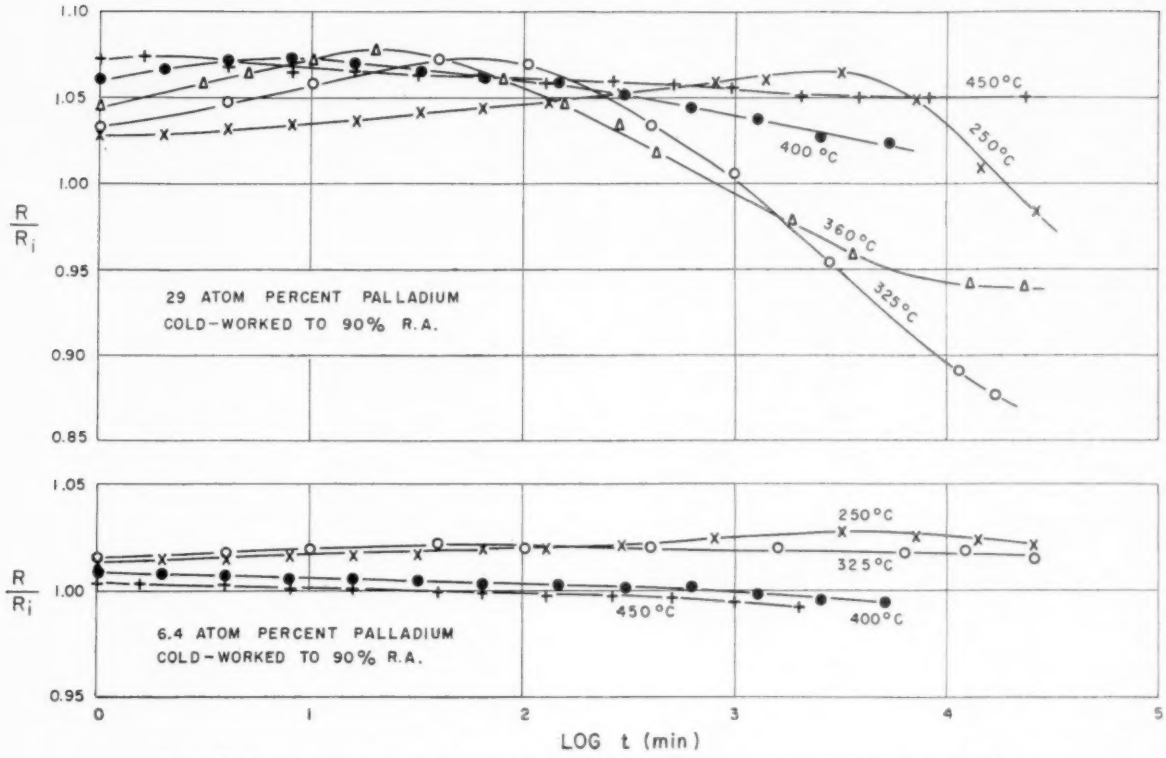

FIG. 3. Isothermal anneal curves for cold-worked 29 and 6.4 atom per cent palladium samples.

VOL. 4 1956

dimensions are greater than the appropriate mean free path. Then, since the resistivity of the ordered material is lower than that of the disordered material, further growth of the domains will cause the resistivity to decrease.

The experimental evidence (which is described in detail below) which supports the contention that the initial rise in resistivity is due to a nucleation of ordered domains, is threefold. First, the values of R/R_i at the maxima in the annealing curves for quenched alloys are larger for lower temperatures. Second, the curves are very similar to those obtained from alloys which exhibit nucleation and growth of a second phase. Third, maxima do not appear in the annealing curves of quenched samples which do not exhibit ordering; for example, the 6.4% Pd samples or the 29% quenched samples annealed at 400°C and 450°C. It may be possible to argue, in view of the fact that superstructure lines were not observed in this region, that the above reasoning would also apply if the rise in resistivity were due to an increase in short-range order. However, the authors feel that this becomes a matter of definition.

For annealing of the quenched samples at temperatures between 450°C and 325°C, the maxima in the R/R_i versus log t curves (Fig. 1) are progressively higher for lower temperatures. This is attributed to nucleation being faster and growth being slower at the lower temperatures. On the other hand, the cold-worked samples show more or less the opposite behavior. This is due, we believe, to the fact that recovery, which causes the resistance to increase more than does nucleation, is the most rapid of all the processes occurring. Then, recovery to a nearly equilibrium, disordered (and single-phase) condition occurs for the high temperatures before growth of ordered domains begins competing. The speed of recovery is well illustrated by the values of R/R_i after one minute of annealing (log $t = 0$) for the cold-worked alloys. For temperatures below about 360°C, the recovery apparently aids the combined process of nucleation and growth in such a way that appreciable growth occurs at lower values of t in the cold-worked alloys.

The 20.9% samples behaved in an entirely similar fashion, except for the 250°C anneal. At the latter temperature, neither quenched nor cold-worked samples exhibited an appreciable decrease in resistance until times exceeding 20,000 minutes. Thus it would seem that for the 20.9% sample, which is near the composition of maximum ordering temperature[1, 2] 250°C is bordering on the lower limit of temperature

at which ordering proceeds at a significant rate. For this reason, the 250°C anneal results were not used in any additional calculations.

The cold-worked curves for 29% palladium samples are included (Fig. 3), since they not only show ordering at temperatures below 360°C but also a difference in the general behavior of the peaks. The increase in resistivity due to recovery and nucleation (which probably cannot be separated) proceeds to nearly the same value at all temperatures before growth of ordered domains occurs to any appreciable extent. For the 400°C and 450°C anneals, this may be due to the fact that we do not have the competing process of growth of ordered domains. (The change in resistance of the quenched samples, for which the data are not shown, at these temperatures is less than a 1% decrease in 10,000 minutes.) At the lower temperatures, the explanation may be in the sluggish character of the ordering.

In Fig. 3 we have also included the results for the 6.4% palladium cold-worked sample. Although the scale is double that of the other samples, very little change in the resistivity beyond the recovery is some starting-point for the decrease in resistance. The only convenient starting-point was at the maxima in the R/R_i versus log t curves. Since the equilibrium resistance R_∞ (R at $t = \infty$) is a function observed on prolonged annealing. There does seem to be an increase in resistivity at 250°C which is slightly more than would be expected on the basis of pure recovery. It is possible, but by no means definite, that this could be a reflection of a tendency to form ordered nuclei, even for this low palladium content.

The principal quantity one hopes to derive from isothermal anneal curves is, of course, an activation energy. In the present case, it is fairly obvious that the entire process is not a singly activated one. We investigated the possibility that the annealing curves represent two competing processes, each singly activated. We found that they could be treated approximately in this manner, although the data indicate that only the growth of domains is definitely a singly activated process.

To obtain an activation energy for the growth portion of the curve, it was necessary to assume of the temperature of anneal, it was necessary to normalize to R_∞ in order to obtain cuts at equivalent points in the process for different temperatures. Thus the function

$$R' = \frac{R - R_\infty}{R_0 - R_\infty}$$

was plotted as a function of log $(t - t_{max})$. Here R is the value of the resistance at time $(t - t_{max})$; R_0 is the value of the resistance at time $t = t_{max}$; and t_{max} is the time for which the peak in the R/R_i curves was reached. Typical curves of this function are shown in Fig. 4. From these curves, values of log $(t - t_{max})$ obtained for various values of R' were plotted against the reciprocal of the absolute temperatures. The activation energy is then obtained from the slopes of these curves. Typical curves are shown in Fig. 5; they illustrate why we have some confidence in the observation that the growth process is singly activated. The points from the 450°C anneals were not considered reliable until after large times had elapsed; small errors in the time of anneal greatly affect the results at this temperature. Also, the maxima in the R/R_i curves are not determined by the data at 450°C.

Activation energies obtained by this method are given in Table 2 for quenched and cold-worked samples. Values of Q for growth of ordered domains are given only for the 16.7 and 20.9% samples, although the 29% samples show ordering at low temperatures (Fig. 3). The activation energies for the latter samples are not included, since ordering occurs in two different lattice structures which, among other things, causes greater scatter than is found in the other cases. It would appear from Fig. 3, however, that any activation energy for ordering based on the 360°C and 325°C curves would be lower for the 29% samples.

Included in Table 2 are the maximum scatter observed (for the range $R' = 0.9$ to 0.3) in the

TABLE. 2. Activation energies obtained from isothermal anneal data.

A. *For growth of ordered domains.*

Composition (atom % Pd)	Q (kcal/mol)	
	Quenched samples	90% RA
16.7	42.1 ± 1.1	34.0 ± 1.7
20.9	45.2 ± 4	37.0 ± 1.3

B. *For nucleation and/or recovery.*

Composition (atom % Pd)	Q (kcal/mol)	
	Quenched samples	90% RA
16.7	21.5 ± 4	21.1 ± 5
20.9	21.0 ± 6	20.6 ± 7
29.0	—	21.4 ± 6

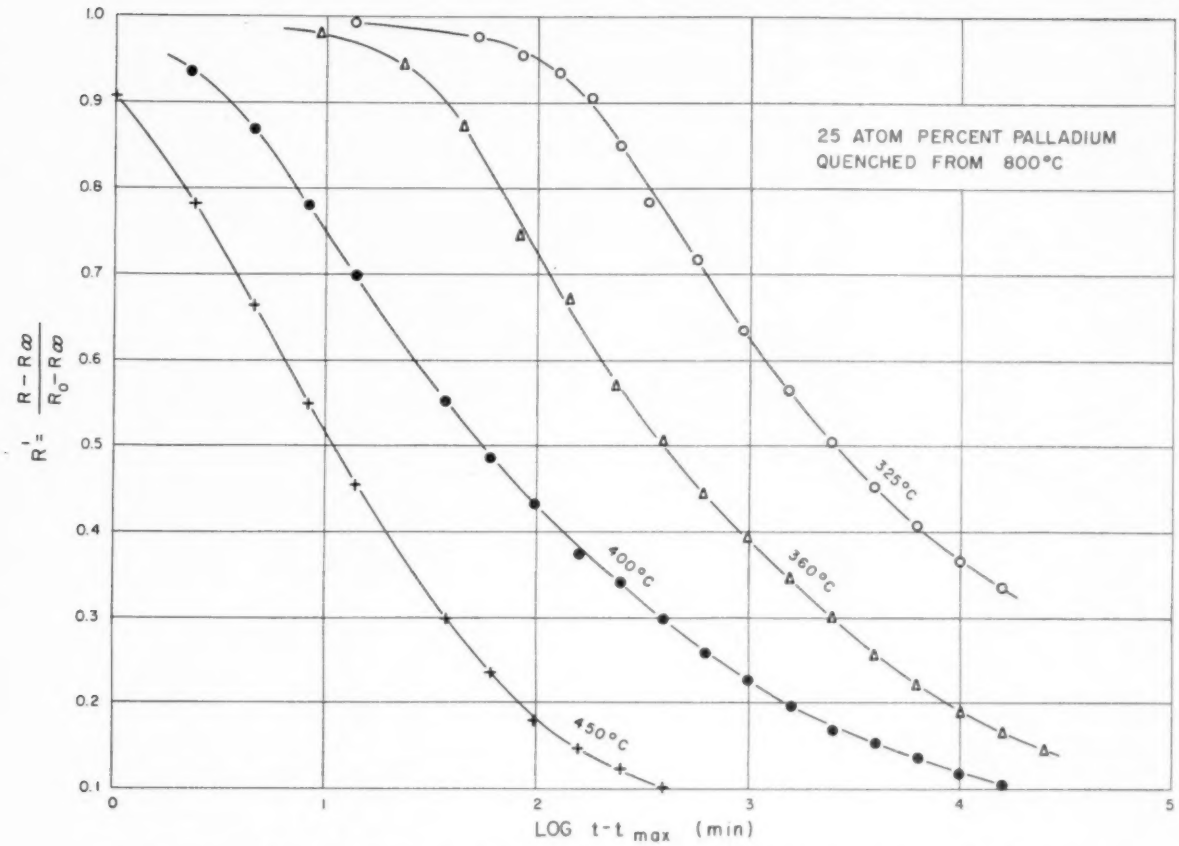

FIG. 4. Rationalized curves representing the effect of the growth of ordered domains on the fractional resistance.

activation energies. We do not believe that the absolute accuracy is as good as the scatter would indicate. There are too many factors involved to determine the probable accuracy, although an estimate leads us to believe that these values should be correct to within 10–15%.

Although the spread between the values for 16.7 and 20.9% palladium samples is not great enough to be outside of experimental error, the indications are that the higher palladium samples require slightly higher activation energies. This would be reasonable on the assumption that diffusion is the governing mechanism, and the values found for the activation energies seem to indicate that this is the case. The best value for the self-diffusion of copper is 47.1 kcal/mol.[3] The diffusion of palladium in copper should require lower activation energies depending on the composition. Thomas and Birchenall[4] found values of the activation energy for this system between 31 and 40 kcal/mol, with increasing energies for increasing palladium content, but they pointed out that their values are probably low. The activation energies found in the present work are definitely in the correct range, and this, coupled with the evidence for a singly activated process, provides strong evidence for a diffusion-controlled mechanism.

Assuming that the growth of the ordered domains is controlled by diffusion, it remains to consider why the cold-worked samples exhibit lower activation energies than the quenched samples, even though, in general, appreciable growth does not occur until after comparatively long times. This probably results from the formation of more nuclei during the nucleation process as a consequence of the release of stored energy during recovery. This is then presumed to increase the probability that an atom desiring to diffuse to an existing nucleus will find itself near an imperfection which can help provide a short circuit path for the diffusion.

The activation energies for the nucleation and/or recovery processes (Table 2) are not nearly so uniquely determined. The scatter is much greater even though the range of values of R/R_i was much smaller. Undoubtedly, the energies given represent averages of more than one temperature-dependent process. These "average" activation energies were obtained

simply by taking "cuts" at fixed values of R/R_i, plotting the values of log t obtained against $1/T$, and computing Q from the slopes. This method involves the implicit assumption that if no growth of domains occurred, all values of R/R_i would be the same at $t = \infty$. This assumption is open to argument and this would be a relatively easy value to explain; that is, it could be considered the energy for motion of imperfections. However, it seems reasonable that nucleation, at least initially, occurs by a very similar mechanism; that is, the ordered domains are nucleated at those positions in the solid at which

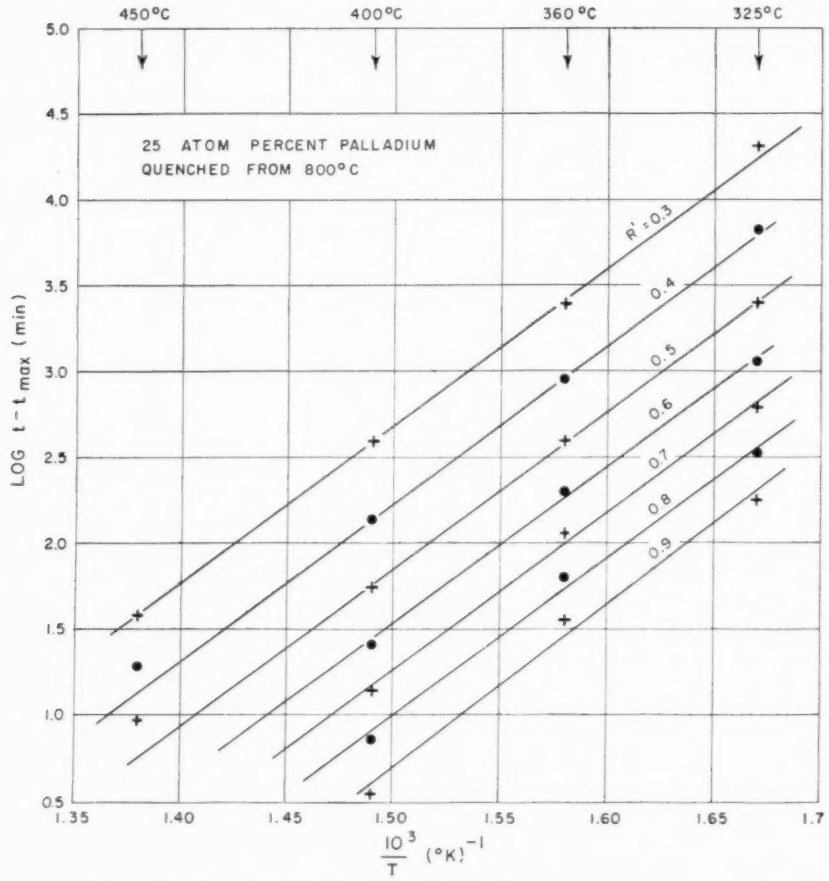

FIG. 5. Curves of the values of log $(t - t_{max})$ as a function of the reciprocal of the absolute temperature for various values of R'.

could be partly responsible for the large scatter in the values of the activation energies.

There is no activation energy listed for the 29% quenched sample, since only two temperatures of anneal, 360°C and 325°C, produced any increase in resistance. Based on only two temperatures, the activation energy was 23 ± 10 kcal (with no definite trend to the scatter), which we consider meaningless. Except for this value, however, and in spite of the large scatter, the activation energies all seem to be approximately 21 kcal/mol. This is only about one-half of the values found for growth, and is probably too low to be diffusion. If only recovery were involved, the atoms find motion easiest. Since quenched samples also contain a small excess of imperfections, it is not unreasonable to conclude that nucleation occurs principally by movement of the atoms over small distances in regions where the lattice imperfections can aid such movement.

In summary, we believe that the evidence, although certainly not absolutely conclusive, strongly supports a nucleation and growth process. The growth of ordered domains is a singly activated process. Nucleation is almost certainly not a singly activated process, so that the values given represent average values, at best.

4. THE ORDER-DISORDER TRANSITION AND THE EQUILIBRIUM DIAGRAM

The order-disorder phenomena in these alloys were discussed in connection with the previous work.[1] There is, however, an interesting point raised by the isothermal anneal data concerning the nature of the ordering process. The data indicate that ordering takes place by a nucleation and growth process (as has been suggested previously for other alloys reference 5), in which the nucleation is not particularly rapid. This, in turn, raises the question as to what the situation is in the region where Jones and Sykes[6] draw a fixed boundary between the face-centered cubic and tetragonal ordered phases, and, in particular, as to what the situation is where this boundary (or boundaries) joins the disordered phase. The region of interest of the phase diagram, as given by Jones and Sykes, is reproduced in Fig. 6(a).

Although no work has been done which specifically aimed at determining the phase diagram, a considerable number of X-ray diffraction patterns were made of samples quenched from a number of different temperatures.[1] The results are summarized in Fig. 6(b). These X-ray data combined with the indication (from the isothermal anneal data) that ordering occurs by a nucleation and growth process, lead us to believe that the phase diagram needs serious revision and is probably of the form given by Fig. 6(b).

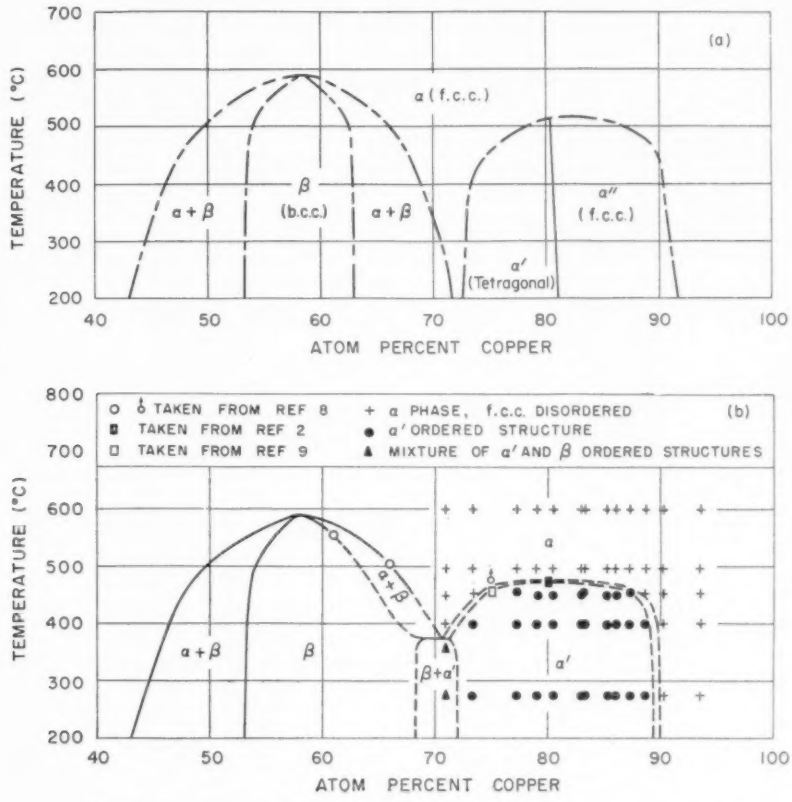

FIG. 6. The copper-palladium phase diagram in the region of ordering.
(a) After Sykes and Jones[6]
(b) Proposed form based on present work

The solid lines in Fig. 6(b) are taken from Jones and Sykes,[6] and the dotted lines represent the form of the revision necessary, in the authors' opinion. The two open circles represent the two highest-copper-content samples used by Jones and Sykes to study the region near 50% copper, and the open circle with an arrow, the lowest-copper-content sample used for the Cu_4Pd region. The filled square at Cu_4Pd is taken from the work of Geisler and Newkirk,[2] who found no two-phase region (within 1°C) at this composition. Tentatively then, Cu_4Pd can be considered as being very nearly the stoichiometrically correct composition for the ordered structure.

VOL. 4 1956

It is the authors' opinion that no boundary exists between the face-centered cubic and tetragonal region, but rather that the entire ordered region tends to be tetragonal with a c/a ratio too close to unity for tetragonality to be observed until the palladium content is about 19%. This view is upheld by the data of the present and the previous work,[1] which indicate that nearly all properties measured are relatively smooth functions of the composition. Also, since the presence of a nucleation and growth process indicates a classical phase transformation, this boundary is unlikely, simply because there is no way thermodynamically to draw a reasonable phase diagram which includes it.

The details of the diagram given in Fig. 6(b) are purely speculative, based on the evidence mentioned, and no accuracy is claimed for the details of the temperatures or the widths of the two-phase regions. It probably can be assumed that the widths of the two-phase regions in the composition range around 20% palladium are quite small, since two phases were not detected by previous workers.[2, 7] However, since there is no change in atomic volume (or for all practical purposes, in lattice parameters) for compositions below 20% Pd, it would be virtually impossible to pick up a two-phase region by X-ray techniques. This is also true to some extent for compositions above 20% Pd, particularly since the defining lines in the diffraction pattern for the tetragonal ordered structure proposed by Geisler and Newkirk[2] are weak under the most ideal conditions. Resistivity measurements of the type described by Rhines and Newkirk[5] would probably decide the issue.

ACKNOWLEDGMENTS

The authors gratefully acknowledge the support of the Office of Ordnance Research, U.S. Army. They would also like to thank E. Klockholm and A. D. Franklin for many helpful discussions.

REFERENCES

1. F. E. Jaumot, jr., and A. Sawatzky—to be published.
2. A. H. Geisler and J. B. Newkirk, Report No. RL-1001, G.E. Res. Lab., Dec. 1953.
3. A. Kuper, H. Letaw, jr., L. Slifkin, E. Sonder, and C. T. Tomizuka, *Phys. Rev.*, **96,** 1224 (1954).
4. D. E. Thomas and C. E. Birchenall, *J. Metals*, **4,** 867 (1952).
5. F. N. Rhines and J. B. Newkirk, *Trans. Amer. Soc. Metals*, **194,** 1029 (1952).
6. F. W. Jones and C. Sykes, *J. Inst. Metals*, **65,** 419 (1939).
7. D. Madoc Jones and E. A. Owen, *Proc. Phys. Soc.*, **67B,** 297 (1954).

ORDER-DISORDER AND COLD-WORK PHENOMENA IN Cu-Pd ALLOYS*

F. E. JAUMOT, Jr., and A. SAWATZKY†

The copper-palladium system, in the composition range from 6 to 30 at. per cent palladium, has been studied. The order-disorder phenomena have been investigated and some disagreement with the work of Jones and Sykes observed. The effects of cold-work distortion on disordered and partially ordered samples were determined. When disordered Cu-Pd alloys are cold-worked at room temperature, the electrical resistivity decreases, the magnetic susceptibility increases, the temperature coefficient of resistivity decreases, and the thermoelectric power becomes increasingly negative. Similar effects are observed for partially ordered samples only after initial effects which are attributed to the destruction of order are completed. This produces an unusual marked maximum in the resistivity as a function of the degree of cold-work. It is suggested that the primary effects of cold-work are consistent with an electronic-structure change due to a shift in the relative centers of gravity of the s-p and d bands.

PHÉNOMÈNES D'ORDRE-DÉSORDRE ET D'ÉCROUISSAGE SUR DES ALLIAGES Cu-Pd

Le système cuivre-palladium a été étudié par des compositions atomiques variant entre 6 et 30% en palladium.

Les phénomènes d'ordre-désordre ont été examinés et un certain désaccord avec le travail de Jones et Sykes a été observé. Let effets de distorsion par écrouissage sur des échantillons désordonnés et partiellement ordonnés ont été déterminés.

Quand des alliages désordonnés de Cu-Pd sont écrouis à température ambiante, la résistivité électrique diminue, la susceptibilité magnétique augmente, le coefficient de température de résistivité diminue et la force thermoélectrique devient de plus en plus négative.

Ce n'est que lorsque certains effets initiaux attribués à la destruction de l'ordre ont pu se dérouler que des phénomènes similaires sont observés sur des échantillons partiellement ordonnés.

Ceci donne lieu à un maximum inhabituel dans la valeur de résistivité en fonction du degré d'écrouissage.

Il est suggéré que les effets primaires d'écrouissage sont en relation avec un changement de la structure électronique, due à un déplacement des centres de gravité relatifs des couches s, p, et d.

ORDNUNGS-UNORDNUNGS- UND KALTBEARBEITUNGSPHÄNOMENE IN Cu-Pd-LEGIERUNGEN

Das System Kupfer-Palladium wurde im Konzentrationsbereich von 6–30 At.-Prozent Palladium studiert. Es wurden die Ordnungs-Unordnungserscheinungen untersucht und dabei eine gewisse Abweichung von der Arbeit von Jones und Sykes beobachtet. Die Auswirkungen einer Kaltverformung auf ungeordnete und teilweise geordnete Proben wurden bestimmt. Wenn ungeordnete Cu-Pd-Legierungen bei Raumtemperatur kaltverformt werden, nimmt der elektrische Widerstand ab, die magnetische Suszeptibilität zu, der Temperaturkoeffizient des Widerstands ab und die Thermokraft wird stärker negativ. Ähnliche Erscheinungen werden an teilweise geordneten Proben nur beobachtet, nachdem anfängliche Effekte, die der Zerstörung der Ordnung zugeschrieben werden, abgeschlossen sind. Dadurch kommt ein ungewöhnlich ausgeprägtes Maximum im Widerstand als Funktion des Kaltverformungsgrads zustande. Es ist anzunehmen, dass die primären Folgen der Kaltverformung konsistent sind mit einer Änderung der Elektronenstruktur, die von einer Verschiebung der relativen Schwerpunktslagen des s-p und d-Bandes herrührt.

VOL. 4 1956

1. INTRODUCTION

To study the effects on various properties of the distribution of the atoms in solid solution, one naturally chooses an alloy system which exhibits order-disorder phenomena; at present, this is the only way in which the distribution of the atoms can be known or controlled. The copper-palladium system was chosen for the present work partly because of its unusual ordering properties. Instead of being isomorphous with Cu-Au alloys, which exhibit an ordered face-centered cubic structure in the composition range from 17 to 34 at. per cent gold, the Cu-Pd alloys order when less than 10%‡ palladium is present. Jones and Sykes[1] report that, in the range from 9 to 27% palladium, these alloys exhibit two types of ordered structure. Jones and Sykes found that there is little or no change in atomic volume on ordering in Cu-Pd alloys, while Cu-Au alloys decrease considerably in volume on ordering. Finally, in view of the recent evidence[2, 3, 4] supporting the view that the ordering transition in Cu-Au alloys is a classical phase-change, interest was attached to the nature of the order transition.

The rather different nature of the ordering in these alloys indicated that the interatomic forces might be of a special kind; and, particularly, the apparent change of the structure of the ordered material with composition indicated that the interatomic distances might be quite critical. Thus, there was interest in the effects of cold-work distortion, and this work was included as a routine part of the

* Received April 18, 1955; in revised form, September 16, 1955.

† The Franklin Institute Laboratories for Research and Development.

‡ All percentages refer to *atomic* per cent.

program. However, very early in the course of the measurements on the effects of cold-work, it became evident that distortion produced some very unusual effects in the electronic properties of these alloys, and the major emphasis of the program was shifted to the study of the cold-work phenomena.

2. EXPERIMENTAL TECHNIQUES

The following parameters were measured, as a function of the degree of order and the degree of cold-work in the alloys: The electrical resistivity, the thermoelectric power, the temperature coefficient of resistivity, the magnetic susceptibility, the mechanical hardness, and the X-ray lattice parameters. Inasmuch as these measurements involved several different techniques, most of which were standard, the techniques will be described briefly, and only the departures from the standard techniques will be discussed in any detail.

Preparation of the Alloys

Originally, commercial alloys were purchased, but these contained too much oxygen and were soon discarded in favor of alloys prepared in these laboratories. High-purity metals (Cuprovac R, 99.99+% Cu, from Vacuum Metals Co; and 99.99+% Pd from J. Bishop Co.) were melted in vacuum. The melts were fabricated into wires by forging and swaging, and all compositions were given an initial anneal in vacuum at 800°C for two hours.

Cold-work

The cold-work was accomplished by drawing the initial wires through steel or carbide dies. The amount of cold-work is measured by the per cent reduction in area, per cent R.A. $= 100\dfrac{A_0 - A}{A_0}$, where A_0 is the initial area and A the final area.

Heat Treatments

Whenever the term "quenched" is used alone to describe the sample condition (or "quenched from 800°C"), we mean that the sample was annealed for two hours at 800°C, in a vacuum of 10^{-5} mm of Hg, and quenched into water or oil at ice- or room-temperature. The actual quenching was accomplished in two ways, and no noticeable differences in the properties of samples were observed. In the first method, the sample was sealed in an evacuated Vycor tube, annealed, and the tube broken in a quenching bath. In the second method, the sample was placed directly into an evacuated furnace tube, onto one end of which a large glass bulb was attached. The other end of the furnace tube was connected to the vacuum system and to a reservoir of water at the desired quench temperature. At the desired time, the valve connecting the vacuum system to the furnace tube was closed, and the valve to the reservoir opened. The vacuum in the tube drew the water into the furnace tube, sweeping the sample and a large volume of water into the glass bulb. This latter method provided a very rapid quench, and was used whenever the temperatures involved were near the critical temperatures.

Various degrees of lattice order were obtained by several different heat treatments. It was found that a reasonable degree of order could be obtained by furnace cooling (about six hours to 150°C) from 800°C, or by holding the samples at 400°C for twenty-four hours, followed by either rapid or slow cooling. When a high degree of order was desired, the samples were cooled at the rate of 2°C per day from 600°C to the desired temperatures, and then quenched.

X-ray Analyses

All X-ray work was done at room temperature, using CuKα radiation (35 kV, 16 mA) and the GE-XRD powder camera of 14.23-cm effective diameter. The beam was collimated with either a slit (0.01 in. × 0.080 in.) or a pinhole (0.030-in. diameter). Exposure times were as long as twelve hours, when it was desirable to detect faint superstructure lines. The parameters listed below are estimated to be accurate to about one part in 10,000.

Magnetic Susceptibility Measurements

The magnetic susceptibility measurements were made using the Gouy method[6] with maximum field strengths of 5,426; 10,467; 14,052; and 17,563 oersteds. The field at the upper end of the specimens never exceeded 100 oersteds. Values of apparent susceptibility were plotted as a function of the reciprocal field strength, and extrapolated to infinite field strength to eliminate the effects of ferromagnetic impurities.[6]

Magnetic susceptibilities were determined for samples of all compositions in the quenched condition (disordered), partially ordered, and for various degrees of cold-work. Measurements were made at room temperature and at liquid-nitrogen temperature.

Thermoelectric Power Measurements

All thermopower measurements were made using a very simple and standard technique. Small wires of copper and constantan were soldered to the tips of both ends of the sample wires, making as small a

joint as possible. The thermocouples thus formed were used to measure the temperatures of the ends of the samples, and the two copper leads were used to measure the difference in e.m.f. across the wires. One end of the sample was placed in an ice-bath and the other end was imbedded in a large aluminum block which was fitted into a dewar-flask assembly. Liquid nitrogen was then added to the dewar flask in controlled amounts, and the aluminum block allowed to come to thermal equilibrium. Using this technique, measurements could be made at temperatures from room temperature to the temperature of liquid nitrogen, in any size increments desired. In practice, the temperature increments used were 10°C.

The thermopower relative to copper was computed from the slope of the curve of ΔE vs. ΔT, where ΔE is the difference in e.m.f. of the two ends of the wire (measured with a Rubicon Type-B potentiometer), and ΔT is the temperature-difference between the ends of the wire. The relative thermopower was then converted to absolute thermopower by correcting for the absolute thermopower of copper.

Hardness Measurements

The Knoop hardness numbers were obtained for the various compositions as a function of the degree of order and the amount of cold-work. The technique used was the standard one (Wilson "Tukon" tester; diamond indentor; 1-kg load). Wherever a hardness number is given, it represents the mean value of at least twenty-five determinations.

Electrical Resistivity Measurements

The values of the electrical resistivities were required as a function of several different parameters; consequently the techniques involved in sample treatment and measurement varied. However, in all cases, the actual values of the resistivity were obtained by standard potentiometric techniques which employed a Rubicon type-B potentiometer and a Type T-3210 Rubicon galvanometer. The current through the sample was determined by measuring the potential drop across a Rubicon 0.1-ohm standard resistor. The cross-sectional areas of the wires were determined either volumetrically or with a micrometer; no appreciable differences were noted for the two methods. Errors in the cross-sectional areas increase with decreasing diameters, so that for a given specimen the error in the initial resistivity probably does not exceed 0.1%. However, the error for all specimens reduced in area by 90% could be as large as 1.5 or 2%. Other details are given below, in conjunction with the technique of sample treatment.

When a sample was to be cold-worked after the resistivity measurement, it was inconvenient to have permanent potential leads affixed to the sample. Because of this, a specially designed measuring board was constructed which employed knife-edge potential contacts whose separation was known accurately. The error in the length of the sample was then ± 0.02 cm. This board was used for the measurement of the resistivity as a function of the degree of order and for the measurements as a function of cold-work. Both sets of measurements were made at 27°C. This was the temperature of interest for the cold-worked samples, but it was used as the measuring temperature for ordered samples, because the difference in the resistivities of quenched and partially ordered samples is much greater at room temperature than at the equilibrium temperature of the degree of order in question.

In order to determine the *temperature coefficient of resistance* of these alloys, wires of the same composition as the samples were spot-welded to the sample (about 10 cm apart and 2 cm from the ends of the sample wire). The resistivity was measured as a function of temperature from liquid-nitrogen temperature to 100°C. The measurements could not be made to higher temperatures because of the danger of annealing the quenched and cold-worked samples. For these measurements, a nonconducting oil bath was used from 100°C to 0°C; an acetone bath was used from 27°C to dry-ice temperatures; and the samples were placed directly into liquid nitrogen. The spot-welded wires were used as potential leads, and the current leads were clamped to the ends of the samples with modified alligator clips.

3. RESULTS AND DISCUSSION OF RESULTS

3.1. *Order-disorder in the Alloys*

Thirteen alloys in the composition range from 6 to 29 at. per cent palladium were prepared (the actual compositions were: 6.4, 9.7, 11.3, 12.6, 13.9, 14.7, 16.7, 17.0, 19.5, 20.9, 22.7, 26.6, and 29.0 at. per cent palladium) and the lattice parameters and electrical resistivity of these alloys were determined for a variety of heat treatments. Fig. 1 gives the lattice parameters as a function of per cent palladium for three heat treatments. The lattice parameters of the quenched (disordered) samples appear to be accurately linear with composition, but to have two different slopes in this composition region. That is,

VOL. 4 1956

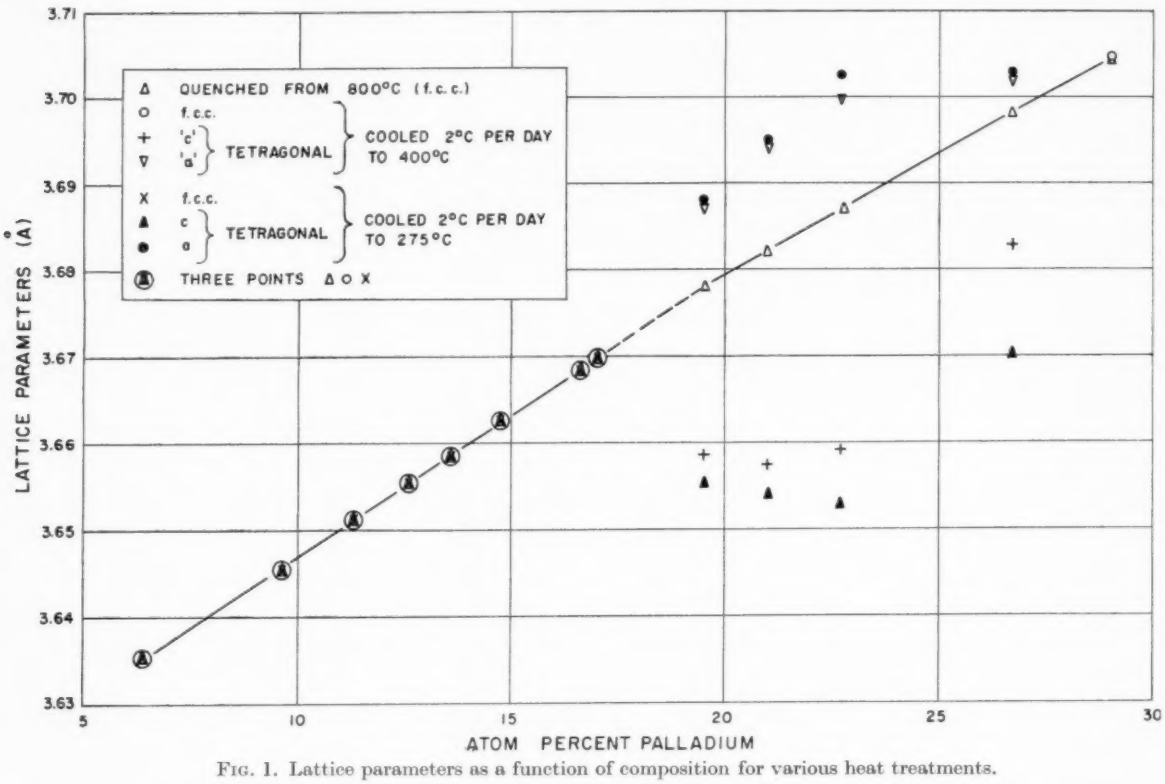

FIG. 1. Lattice parameters as a function of composition for various heat treatments.

lattice parameter vs. composition is a straight line of one slope up to the composition at which tetragonality becomes evident, and a straight line of a different slope thereafter.

The lattice parameters of the alloys which were slowly (2°C per day) cooled exhibit several interesting features. First, in the cubic region there is no change in atomic volume on ordering. Although the intensity and sharpness of the superstructure lines in this region increase considerably with increasing order, the lattice parameters remain rigorously constant. Second, it is obvious from Fig. 1 that the c/a ratio of those alloys in the tetragonal region provides a measure of the degree of order. This has been discussed by Madoc-Jones and Owen[5] for 25% palladium, and they derived an empirical relation between the c/a ratio and the order parameter S. The validity of relationships of this type is always questionable over a range of compositions, and particularly so in this case, since Madoc-Jones and Owen worked on the basis of a unit cell, which according to Geisler and Newkirk[7] is not the true unit cell. The present authors are inclined to agree with Geisler and Newkirk both on the unit cell and on the fact that the Cu_4Pd composition is the most favorable composition for ordering, in spite of the smaller c/a ratio at Cu_3Pd. Fig. 2(a) gives curves of c/a for 20.9 and 25% palladium and Fig. 2(b) gives the c/a values for quench temperatures of 400°C and 275°C as a function of composition. The latter curves in the region of 23 to 25% palladium represent extrapolated values obtained from our data and that of Jones and Sykes.[1]

Notice that in Fig. 1 there are no points for the 29 at. per cent sample at 275°C. This is because the 29% sample overlaps the region in the neighborhood of the 50-50 composition which orders with a body-centered cubic structure. This alloy will be discussed in more detail later. Finally, if one considers the ordered tetragonal lattice to be a simple face-centered tetragonal cell, there is a slight volume change on ordering. The maximum volume change is about 0.06%, which is extremely small, but the lattice parameters were accurate to about 0.01%, so that from this standpoint the volume change is real. However, it is entirely possible that the change observed is actually a reflection of the assumption of the wrong unit cell. The X-ray diffraction results obtained agree with those of Geisler and Newkirk, and support the suggestion that the tetragonal unit cell is a "2-*hi* inverted Ni_4Mo-type" structure.[7]

The second parameter used to determine the

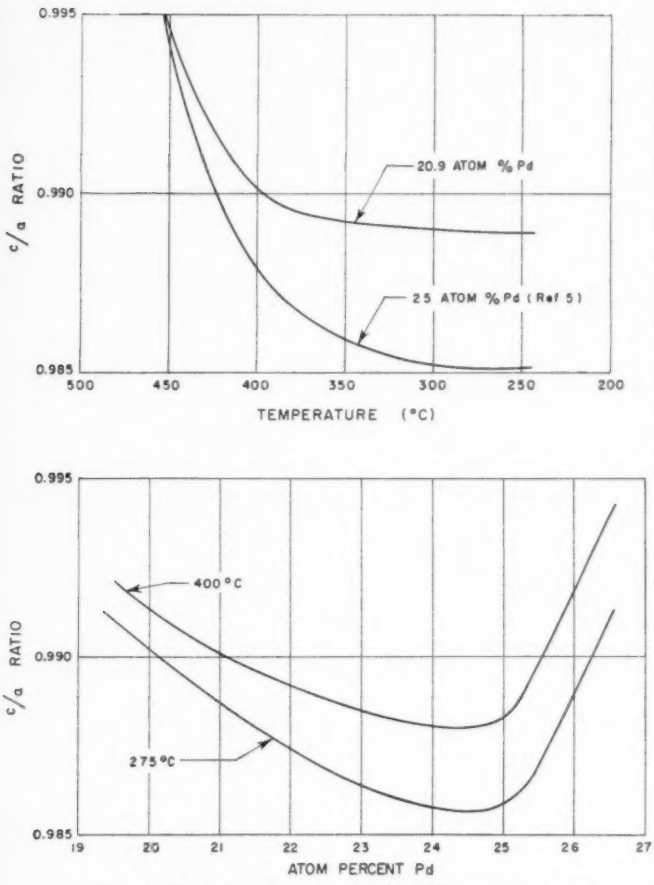

FIG. 2. Variation of the ratio c/a with temperature of quench and composition for the ordered tetragonal lattice.

presence of order was the electrical resistivity. Fig. 3 gives the values of the electrical resistivity as a function of composition for five of the heat treatments investigated. The values of resistivity for samples quenched from 600°C and 500°C are not included, since they are nearly the same as the values for the samples quenched from 800°C. The dotted lines in Fig. 3, indicating the boundaries for the various regions, are taken from reference (1). When examining the curve, it is well to remember that the composition may be in error by 0.2%.

The behavior of the resistivity of quenched (disordered) samples is very similar to the behavior of the lattice parameter. That is, the curve can be represented by two straight lines of different slopes with the break occurring in the neighborhood of the composition at which tetragonality is first observed. The remaining values, in the range from 10 to 25% palladium, illustrate the effects of various amounts of order, or alternately, indicate the degree of order obtained from a particular heat treatment. The points outside this range have some interesting individual features. Contrary to the work of Jones and Sykes, we found no evidence of ordering in a 9.7% sample, even at 275°C. Therefore, an equilibrium diagram based on the present work would have to have the order-disorder boundary above 10% palladium. Similarly, the high palladium boundary would have to be moved to a slightly higher palladium content, since the 26.6% sample was definitely ordered at 400°C, whereas Jones and Sykes indicate the limit of composition at this temperature to be 26.2%. The 29% sample presents a very interesting special case. This sample showed no tendency to order for any heat treatment except the very slow cooling to 275°C. In the latter case, two phases are observed. The main "constituent" is a tetragonal lattice with a c/a ratio slightly less than unity. There is also a body-centered cubic phase present (lattice parameter $a = 2.969$ Å) which is highly ordered, as evidenced by the fact that the superstructure lines are comparatively intense. Thus it appears that at 275°C there is an overlapping of the two ordered regions, which is in disagreement with Jones and Sykes's work (see reference 18 for a discussion of this point).

There is some disagreement between the present data and those of Jones and Sykes as to the maximum temperature of ordering. They show the ordering temperatures to be higher than 500°C over a considerable range of composition. The present work indicates that the maximum temperature of ordering is in the neighborhood of 475°C, and this is in substantial agreement with other recent work.[5, 7]

A considerable amount of effort was expended in attempting to detect effects of short-range order on the X-ray diffraction patterns or resistivities. However, in no case was there observed any appreciable effect of short-range order.

The effects of order on the thermoelectric power, the magnetic susceptibility, and the thermal coefficient of resistivity are discussed in those sections which deal with the cold-work phenomena.

3.2. *The Cold-work Phenomena*

The alloys of copper-palladium in the composition range studied, exhibit very unusual behavior when deformed, quite unlike either a "normal" alloy or an ordered alloy such as copper-gold. To have a comparison with what is often thought to be a "standard" order-disorder alloy, similar measurements were made on Cu_3Au and Cu-5% Au alloys which received treatments equivalent to those given the Cu-Pd alloys. Since most of the data obtained on Cu_3Au

VOL. 4 1956

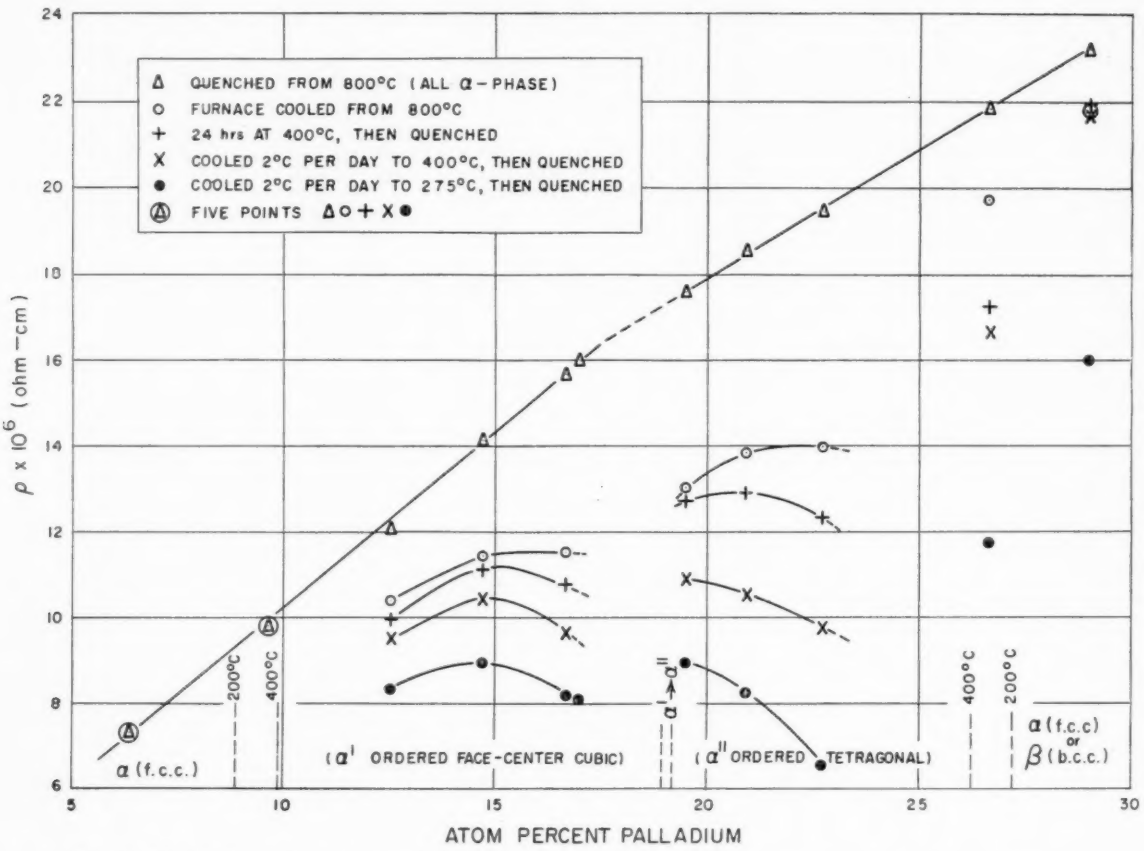

FIG. 3. Electrical resistivity at room temperature as a function of composition for various heat treatments.

alloys already appear in the literature, only those comparison curves that are not available and those which are useful for emphasizing the point in question will be shown.

The Electrical Resistivity as a Function of Cold-work and Temperature

The electrical resistivity as a function of per cent reduction-in-area was measured on quenched (disordered) samples, and on samples which had received a variety of heat treatments designed to introduce (partial) order. Since the degree of order did not affect the results beyond the first few points, which is in itself a remarkable fact, we will discuss, as our partially ordered samples, those samples which were slowly cooled (2°C per day) to 400°C. These samples contained considerable order (Figs. 1 and 3) except for the 29% Pd sample, and the behavior of that sample is rather unusual for all anneals.

Fig. 4 shows the behavior of the electrical resistivity as a function of cold-work for the 6.4 and 16.7 at. per cent palladium samples. Fig. 5 gives similar curves for the 19.5 and 29% samples. For comparison, Fig. 6 gives curves for copper-gold alloys. The general features of the curves given in Fig. 6 are in good agreement with the data of Dahl.[8]

Figs. 4 and 5 are typical curves for each of the four "regions" studied in this work; other compositions in corresponding regions behaved qualitatively the same. Specifically, the 6.4% samples are typical of the low palladium region which does not show order; the 16.7% samples are typical of the composition region which tends to order as face-centered cubic; the 19.5% samples are typical of the region which orders as tetragonal; and the 29% sample is again outside these regions, but, as previously mentioned, if slowly cooled to 275°C it tends to be a mixture of ordered phases.

Notice that in all cases the quenched samples (and the slowly cooled 6.4% sample) *decrease* in resistivity with increasing cold-work. On the other hand, the partially ordered samples show first an increase and then a decrease in resistivity. To the best of our knowledge this is the only homogeneous alloy which shows a marked maximum in the resistivity with cold-work, independent of order.

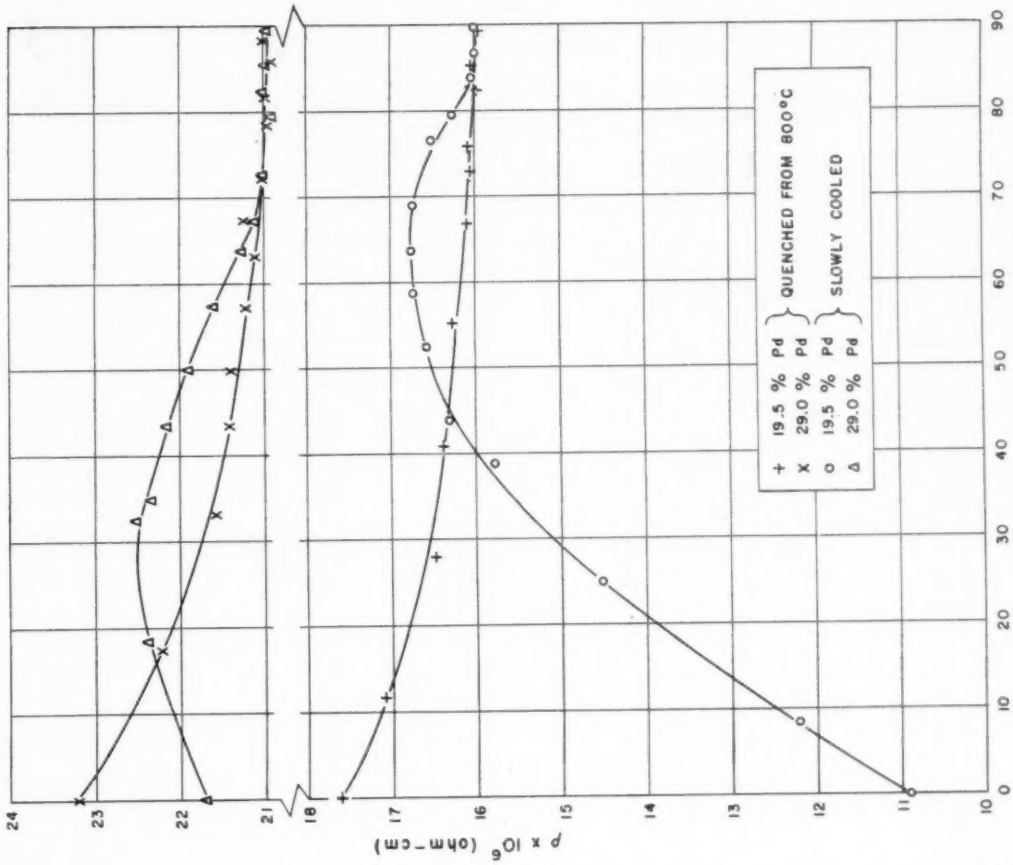

FIG. 5. Resistivity as a function of cold-work for the 19.5 and 29 at. per cent palladium samples.

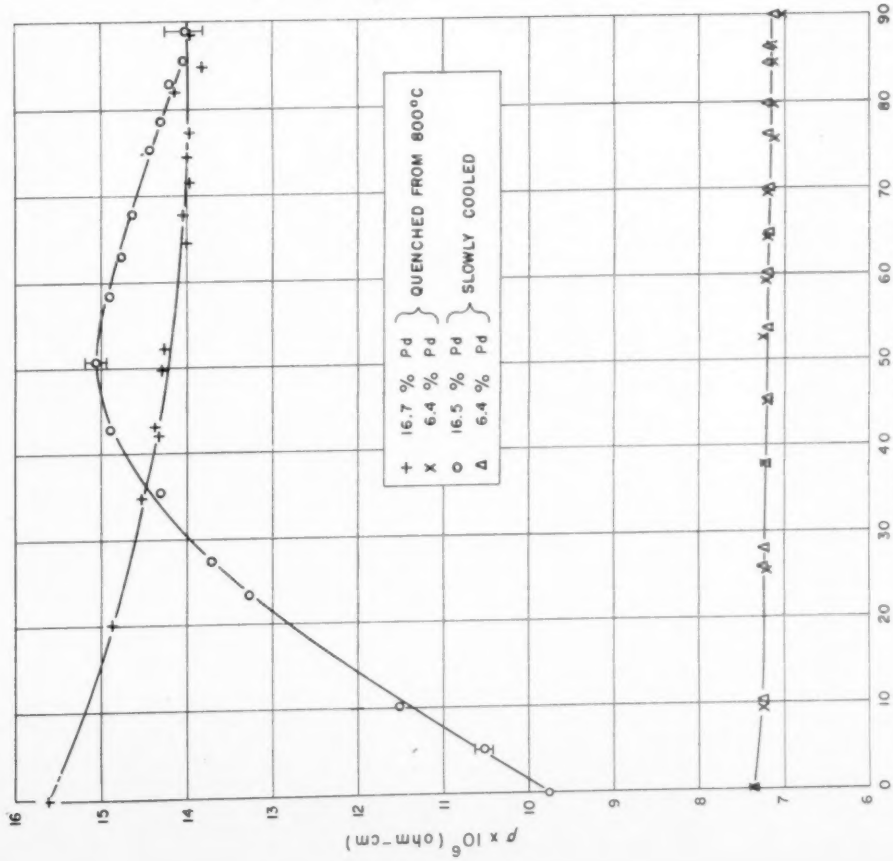

FIG. 4. The electrical resistivity as a function of cold-work (by cold-drawing) for the 6.4 and 16.7 at. per cent palladium samples.

VOL. 4 1956

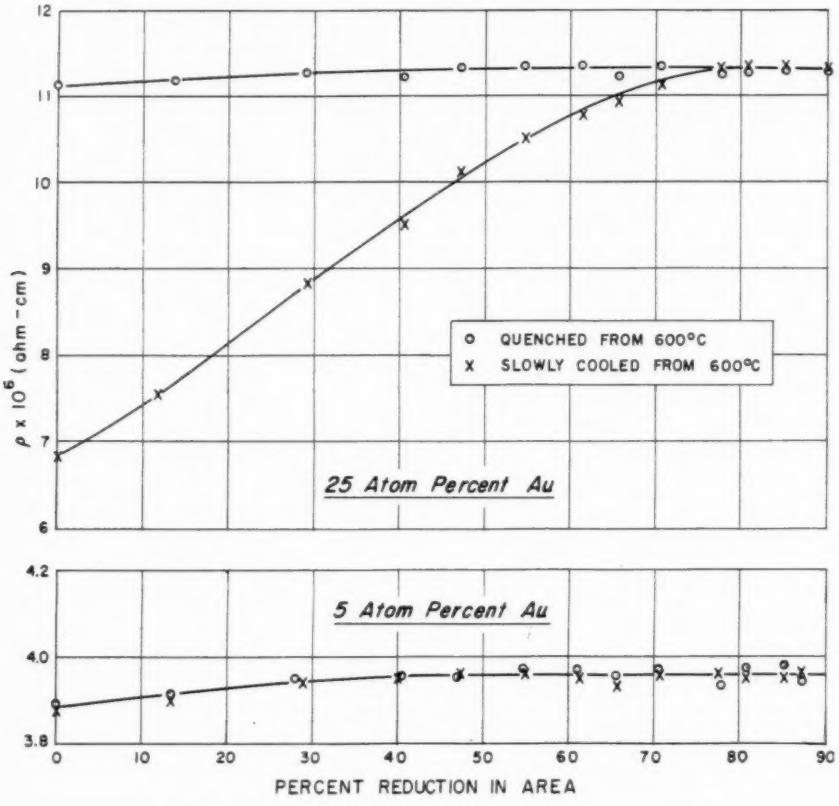

FIG. 6. Resistivity as a function of cold-work for copper-gold alloys.

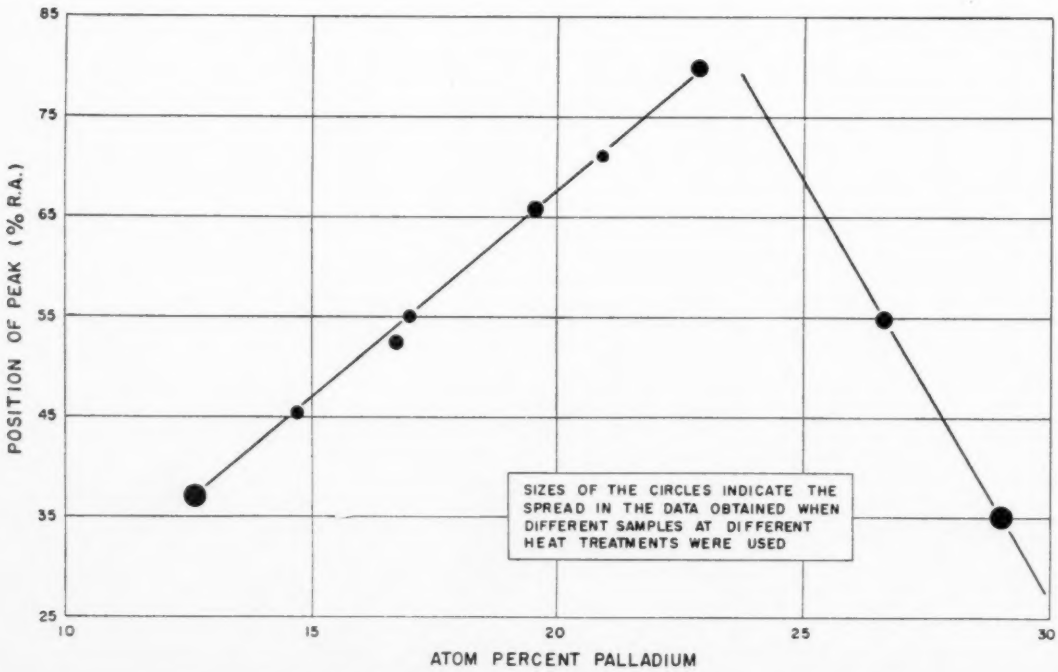
POSITION OF PEAK (% R.A.)
SIZES OF THE CIRCLES INDICATE THE SPREAD IN THE DATA OBTAINED WHEN DIFFERENT SAMPLES AT DIFFERENT HEAT TREATMENTS WERE USED
ATOM PERCENT PALLADIUM

FIG. 7. The position of the peak in the resistivity vs. per cent reduction in area curves as a function of composition.

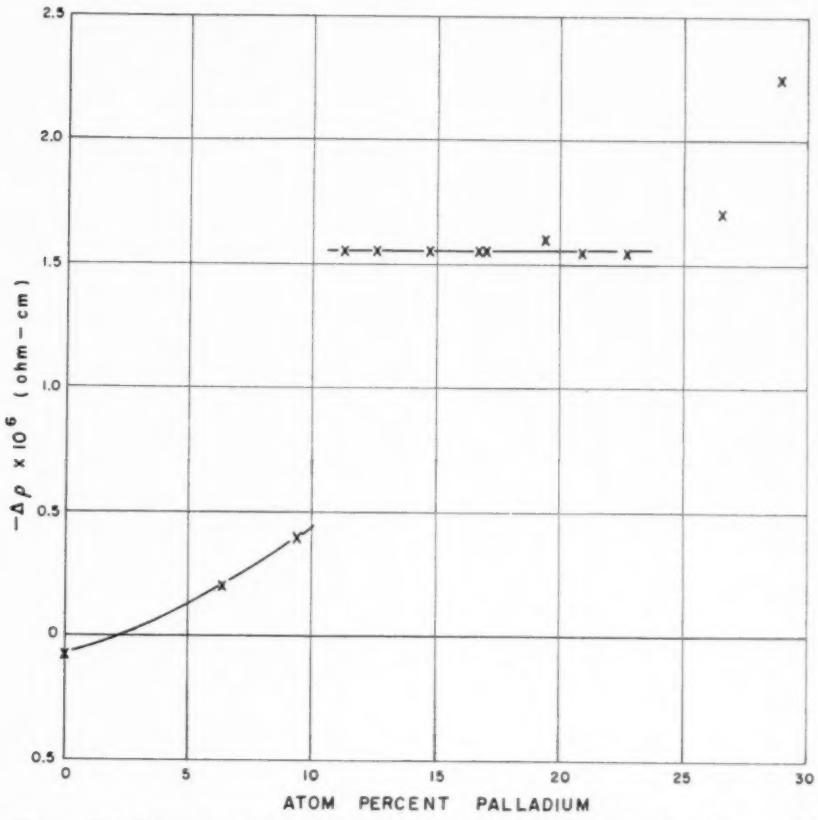

FIG. 8. The change in resistivity for 90% reduction in area, as a function of composition.

It is not clear why one should observe this maximum; it is not improbable that it is simply a case of the primary effect, order, having to be removed before the (secondary) effects of cold-work can be observed.

Since the absolute values of the initial resistivities of the ordered samples depend to a considerable degree on the heat treatment, it is difficult to discuss the data quantitatively. The height of the peak (maximum) depends to some extent on the order present; apparently the higher the degree of order the higher the maximum value of the resistivity, so that in some cases this peak actually exceeds the quenched (initial) resistivity. There are, however, two unvarying quantities exhibited by the partially ordered samples. The resistivity of any sample which has been reduced 90% in area is the same as any other sample of the same composition, independent of any heat treatment that was originally applied. Also, the position of the maxima on the curves of resistivity versus the per cent-reduction-in-area seems to be only a function of composition. Any dependence on the amount of order initially present, if present, is so slight as to be within the error of locating the maximum (less than 5%). We have plotted, on Fig. 7, the average position of the maximum in terms of per cent R.A. as a function of composition for all determinations. It is to be emphasized that the different values involved in each of these average points were taken from data obtained from samples which had been heat-treated in as many as four different ways (see Fig. 3 for the different treatments involved). The linear relationship is as yet unexplained.

The 29% sample used in Fig 5. exhibited no ordering (either body-centered cubic or tetragonal), but the behavior of the resistivity with cold-work indicates that severe annealing produces a "knowledge" on the part of the sample that it is capable of being ordered. Additional ordering simply bends the initial portion of the curve down.

The data obtained from the quenched samples can be treated in a more quantitative fashion, since the initial resistivity varied less than 0.3% when the samples were quenched at temperatures from 800°C to 500°C. The decrease in resistivity with cold-work is unusual, but it is even more unusual that the decrease is so marked. Further, the quantitative features of decrease are very unusual as shown in

VOL. 4 1956

Fig. 8, where the change in resistivity with cold-work is given as a function of composition. The pure-copper data was obtained in this laboratory, but agrees well with previous data.[9] We see from the figure that the absolute value of the decrease in resistivity, in the composition region which tends to show ordering, is rigorously constant. The actual data are tabulated in Table 1, where the maximum deviations from the average values for different determinations are also given. The usual quantities, $\Delta\rho/\rho$, are also given in Table 1.

TABLE 1. Reduction in resistivity of Cu-Pd alloys with cold-work
(*All alloys initially quenched from* 800°C)

Ordered structure	Composition	$-\Delta\rho$ (micro-ohm cm) for 90% R.A.	% change in resistivity	
			$\frac{-\Delta\rho}{\rho_0} \times 100$	$\frac{-\Delta\rho}{\rho_t} \times 100$
do not order	6.4	0.2	2.7	2.8
	9.7	0.4	4.2	4.3
	11.3	1.55 ± 0.05	13.7	15.9
	12.6	1.55 ± 0.05	12.5	14.3
f.c.c.	14.7	1.55 ± 0.05	10.9	12.3
	16.7	1.55 ± 0.05	9.9	11.0
	17.0	1.55 ± 0.05	9.6	10.6
	19.5	1.60 ± 0.05	9.1	10.0
tetragonal	20.9	1.55 ± 0.05	8.4	9.1
	22.7	1.55 ± 0.05	7.9	8.6
tetragonal	26.6	1.7 ± 0.10	7.9	8.6
mixed phases	29.0	2.25 ± 0.10	9.7	10.7

Note: ρ_0 = resistivity of alloy after quenching;
ρ_t = resistivity of alloy after 90% reduction in area, by drawing.

There appear to be plausible reasons for the qualitative aspects of the general behavior of the resistivity (see Section 4), but the explanation of the result that $\Delta\rho$ is a constant for the composition range in which ordering occurs, is pure speculation. It is possible that this comes from a "saturation" of the effects discussed, or from a competition of the mechanisms. However, it should be pointed out here that the decrease in resistivity with cold-work is not due to lattice-ordering. First of all, there is no evidence of order in the X-ray patterns, and it has been determined (Section 3.1) that short-range order does not appreciably affect the resistivity. However, more important in this respect, cold-work produces the opposite effect from order in the case of the magnetic and thermoelectric properties.

The temperature coefficient of resistivity is a useful parameter for obtaining insight into the relative roles played by the composition (impurities) and the lattice vibrations in the electrical properties of the material. It was found that all samples in the composition range from 10 to 25% palladium exhibited resistivities which were perfect linear functions of the temperature in the temperature-range considered. The 6.4, 26.6, and 29 per cent palladium samples indicated a very slight increase (0.5%) in $d\rho/dT$ at temperatures near that of liquid nitrogen. Thus, over a considerable temperature-range these alloys obey the usual relation

$$\rho = \rho_0(1 + \alpha T).$$

Fig. 9(a) gives α as a function of composition, and Fig. 9(b) gives the more informative quantity $d\rho/dT$ as a function of composition. In Fig. 9(b), the width of the lines indicate the spread in the data (maximum deviation less than 0.5%) for the quenched and cold-worked samples. The actual points were plotted for the slowly-cooled samples which show a somewhat greater spread (about 2.4% maximum deviation), presumably due to the sensitivity of the samples to slight changes in the heat treatment.

The first important fact that we obtain from Fig. 9 is that Matthiessen's rule, which states that $d\rho/dT$ is independent of composition (for small changes in composition), is obeyed over a very wide range of composition; much wider, in fact, than one expects. Further, Matthiessen's rule is obeyed with respect to composition independently of the heat treatment or cold-work. On the other hand, Matthiessen's rule is not obeyed with respect to cold-work. This is at variance with the usual belief that the rule should hold for cold-worked materials since the scattering from the imperfections is not considered to be dependent upon temperature. Concerning this last point, α decreases with cold-work, as expected. However, in the present case ρ also decreases, so that the product, $\alpha\rho$, is not constant as in the usual case, but is definitely different for quenched and cold-worked samples. The results given in Fig. 9 for the ordered samples also illustrate why the temperature coefficient α frequently does not provide a meaningful quantity. In the present case, α simply reflects the initial resistivity, as is obvious when Fig. 9(a) is compared with Fig. 3, with due respect for the differences in scale.

The Thermoelectric Power as a Function of Cold-work and Lattice Order

The electrical resistivity can be thought of as a measure of the electronic scattering due to the lattice vibrations, the impurities, and other imperfections

of all types. The thermoelectric power can be thought of, in a crude way, as the way this scattering changes with the energy of the electrons. For conceptual purposes we can think of the thermopower as the slope of the curve of scattering cross-section versus the energy of the electrons, the slope to be evaluated at the Fermi energy. From this naïve point of view, one can see that the thermopower is potentially a useful source of information when a change in the electronic structure is suspected.

The thermoelectric power was measured, as previously described, for representative compositions and for partially ordered samples, disordered samples, and samples which had received various degrees of cold-work. Typical results are shown in Fig. 10. Fig. 10(a) gives the results for the low palladium alloy; Fig 10(b) gives the results for an alloy which orders in a face-centered cubic lattice; Fig. 10(c) gives the results for an alloy which orders in a tetragonal structure; and Fig. 10(d) gives the results for a 29% sample, the slowly-cooled sample showing no order. In all of the figures, the absolute thermopower is plotted against the centigrade temperature.

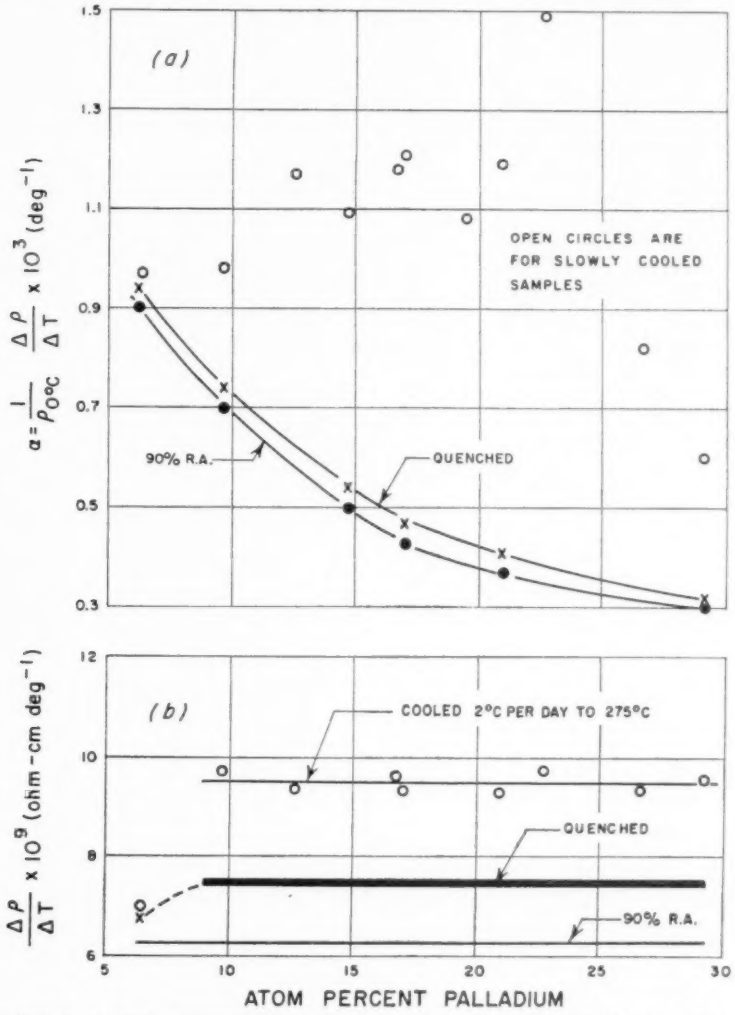

FIG. 9. (a) The temperature coefficient of resistivity. (b) $d\rho/dT$ as a function of composition for quenched, partially ordered, and cold-work samples.

The data indicate that there is no appreciable difference in the thermopower of the low-palladium-content alloys when the samples are quenched, slowly cooled, or severely cold-worked. Actually, the scatter is large enough that a small difference might exist as in copper-gold alloys containing small amounts of gold. We have plotted the copper-gold case in Fig. 11.

The samples which fall in the composition region of ordering, exhibit marked changes in the thermopower with heat treatment and cold-work. We

VOL. 4 1956

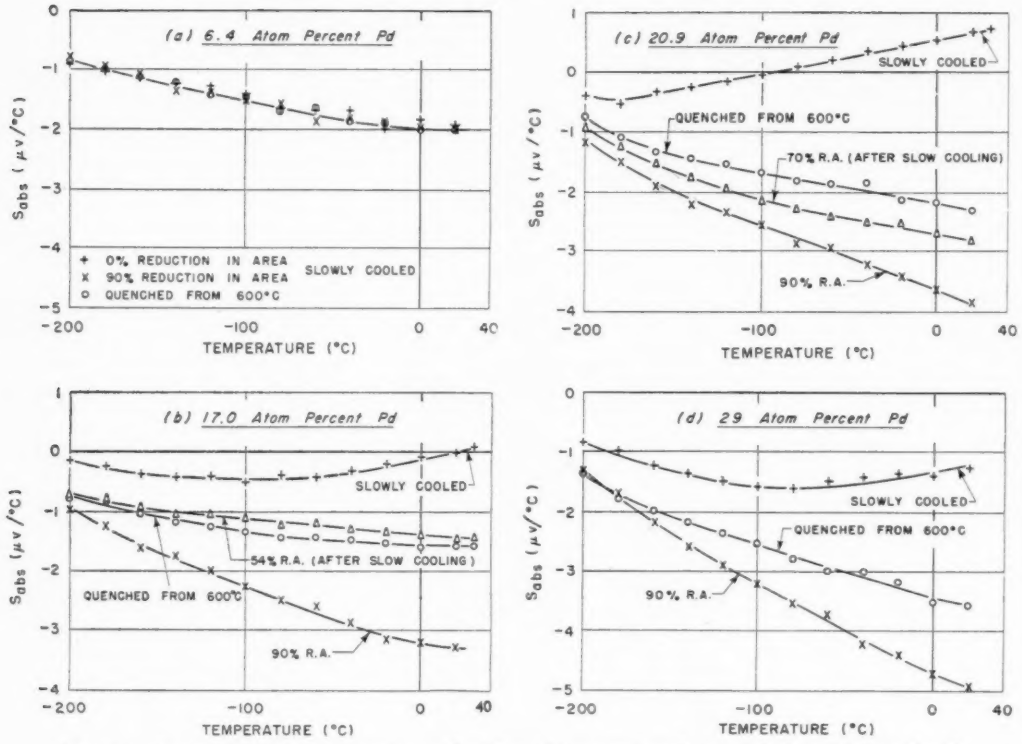

FIG. 10. The absolute thermopower as a function of temperature for quenched, partially ordered, and cold-worked samples of various compositions.
(a) 6.4% Pd. (b) 17.0% Pd. (c) 20.9% Pd. (d) 29% Pd.

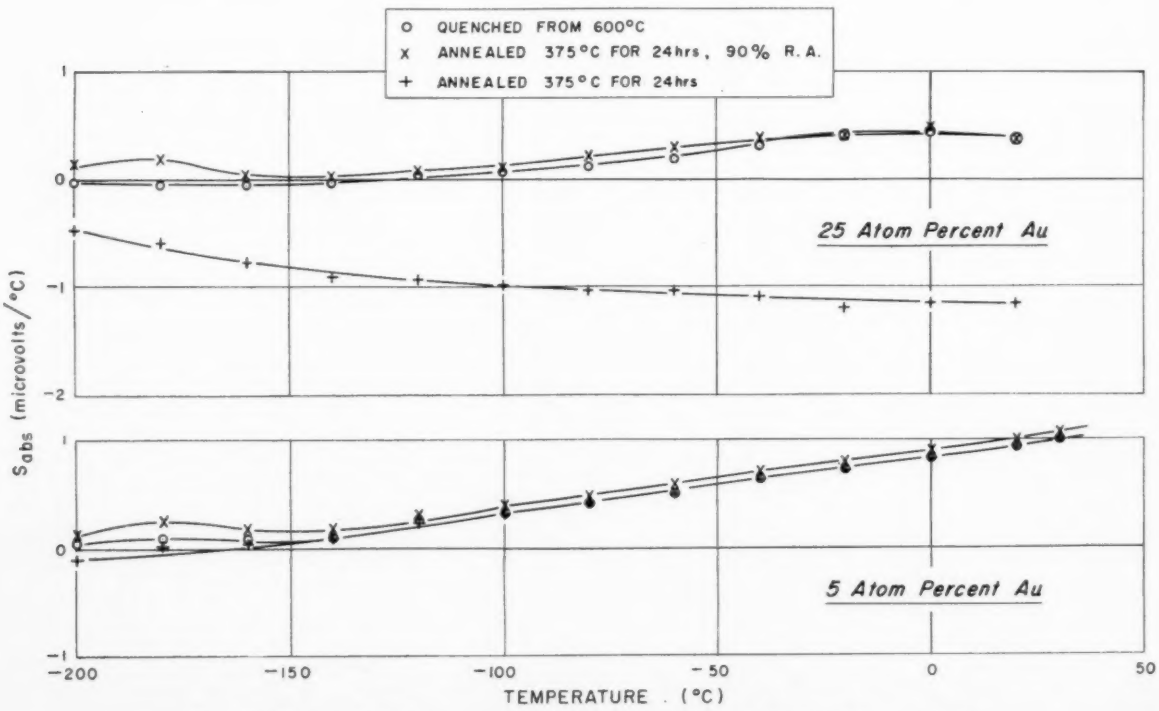
○ QUENCHED FROM 600°C
x ANNEALED 375°C FOR 24hrs, 90% R.A.
+ ANNEALED 375°C FOR 24hrs
25 Atom Percent Au
5 Atom Percent Au
Sabs (microvolts/°C)
TEMPERATURE (°C)

FIG. 11. The absolute thermopower of Cu-Au alloys as a function of temperature for various samples treated similarly to the Cu-Pd alloys.

have included in Figs. 10(b) and 10(c) the results for ordered samples cold-worked to the amount necessary to bring them near the region of the resistivity maximum in the curves of Figs. 4 and 5; the general trends of the S vs. T curves for these samples are not substantially different from initially quenched samples which have been cold-worked. On the other hand, when S is plotted as a function of cold-work, as in Fig. 12, there are considerable differences between quenched and slowly-cooled samples, and between slowly-cooled samples of different compositions. Very little reliance can be placed on the

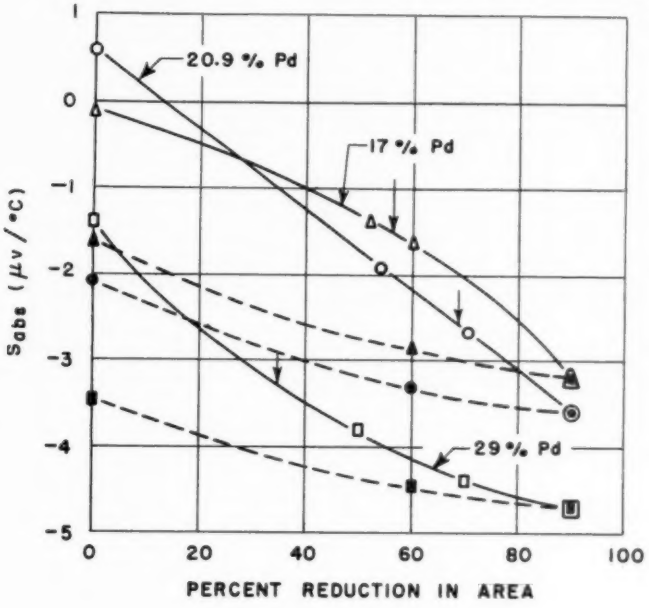

FIG. 12. The thermopower as a function of cold-work.
The solid lines are for samples which were initially slowly cooled.
The dotted curves with similar symbols are for quenched samples of corresponding composition.
The arrows give the positions of the peaks in the ρ vs. % R.A. curves for partially ordered samples.

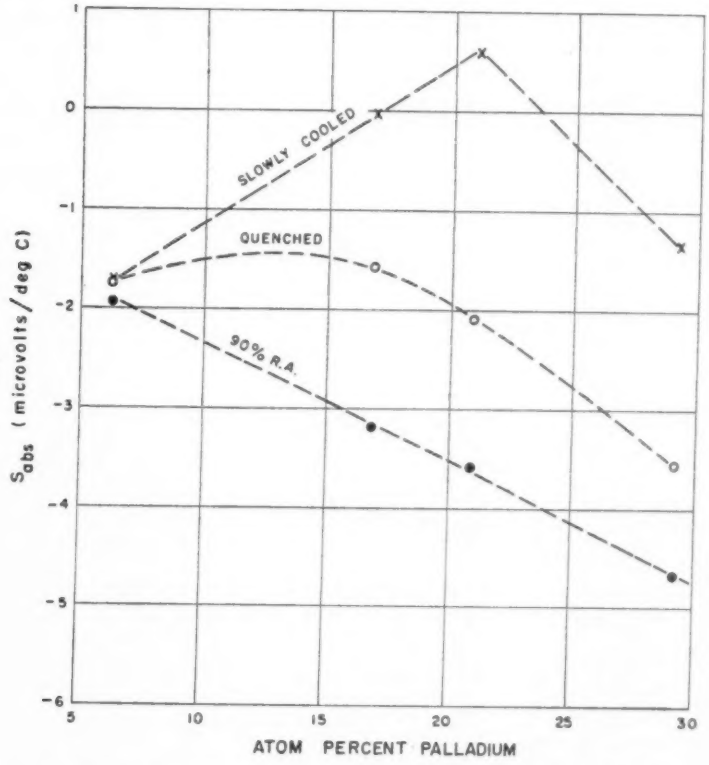

FIG. 13. Absolute thermopower at 0°C of quenched, partially ordered, and cold-worked Cu-Pd alloys.

VOL. 4 1956

actual forms of the curves in Fig. 12, but they do indicate that the behavior of quenched samples of different compositions is very similar. Also, they point out the most interesting fact that the thermopower of a slowly-cooled sample which has been cold-worked to the region of maximum resistivity is very nearly equal to the thermopower of a quenched sample of the same composition, which has not been cold-worked.

In general, the thermopower of partially ordered samples is very slightly negative at low temperatures and becomes increasingly positive with increasing temperature. On the other hand, the thermopowers of quenched and cold-worked samples are considerably more negative at low temperatures and become increasingly negative with cold-work. Thus, the thermopower data are consistent with the general tendency for these copper-palladium alloys to behave oppositely from the usual or more "normal" case. This is illustrated by a comparison with the copper-gold results (Fig. 11). All other ordered alloys with which the authors are familiar behave in a similar fashion to the copper-gold alloys. That is, the ordered alloys show a tendency to have a more negative thermopower than the quenched alloys, and cold-work usually causes the thermopower of pure metals and ordered and disordered alloys to become slightly more positive.

One final point of interest is illustrated in Fig. 13, where the absolute thermopower at 0°C is plotted as a function of composition for partially ordered, quenched, and cold-worked alloys. Of particular interest here is the considerable difference between disordered (quenched) and partially ordered samples. Using a sufficiently elaborate set-up, the thermopower can be detected to an accuracy represented by better than 0.001 of the spread between these two curves. Therefore, it is proposed that the thermoelectric power could be used as a sensitive means of detecting order. In connection with this, an attempt was made to detect the presence of short-range order by means of thermopower measurements. The best curve through the points obtained for a quench from 480°C did show a slight increase compared to the results for a quench from 800°C, but unfortunately the accuracy of our method is such that we cannot claim that short-range order effects were observed.

The Magnetic Susceptibility

As the work progressed, the idea that cold-work deformation causes a fundamental change in the electronic structure became increasingly attractive (and plausible). Thus, it was natural to suspect that this change involved changes in the "*d*" shell of the atoms. The pure-metal palladium exhibits a "*d*" shell defect, as evidenced by its paramagnetism; and copper, although considered a "well-behaved" metal, occurs in forms (the cupric ion) which have "*d*"-shell defects. To check this possibility, the magnetic susceptibility of the various samples was measured. The results are given in Fig. 14. These results agree almost perfectly with the work of Svensson.[11] This agreement is not obvious until the individual points are examined, since Svensson had only four points over the entire range and drew his curve differently.

The susceptibility of quenched samples show nearly the identical behavior, except for absolute values, of the classical case of silver-palladium alloys. Ordering causes the alloy to become increasingly diamagnetic as it does for Cu_3Au. However, if quenched Cu_3Au alloys are cold-worked, very little change in the susceptibility is observed; it is roughly of the same order as pure copper (Fig. 14). If ordered Cu_3Au is cold-worked, the susceptibility approaches that of the quenched and cold-worked sample. In the present case, cold-work causes the diamagnetic susceptibility to decrease as a function of cold-work independently of the initial heat treatment. Further, the sample which was most diamagnetic in the quenched state becomes least diamagnetic when cold-worked to 90% R.A. This latter phenomenon is probably related to the fact that the alloy in question is very close to the composition Cu_4Pd.

It should be pointed out here that the actual curve drawn through the points representing partially ordered samples is virtually meaningless. That is, these samples were all treated in the same way, which means roughly that the fractional degree of order (S/S_{max}) is greatest for the low palladium samples and least for the samples which tend to show the maximum c/a ratio in the tetragonal range. (Experimentally, it was found that the most severe ordering treatments were required for samples in the composition range which orders in a tetragonal structure.) Thus, the curve for very well-ordered samples could even be a straight line or the reverse of the present curve; in any event, it would certainly be at more negative values of the susceptibility.

Before the decrease in diamagnetism with cold-work could be attributed to any fundamental change in the electronic structure of the alloys, it was necessary to satisfy the possibilities that it could be due to ferromagnetic impurities introduced during cold-work or due simply to imperfections. The

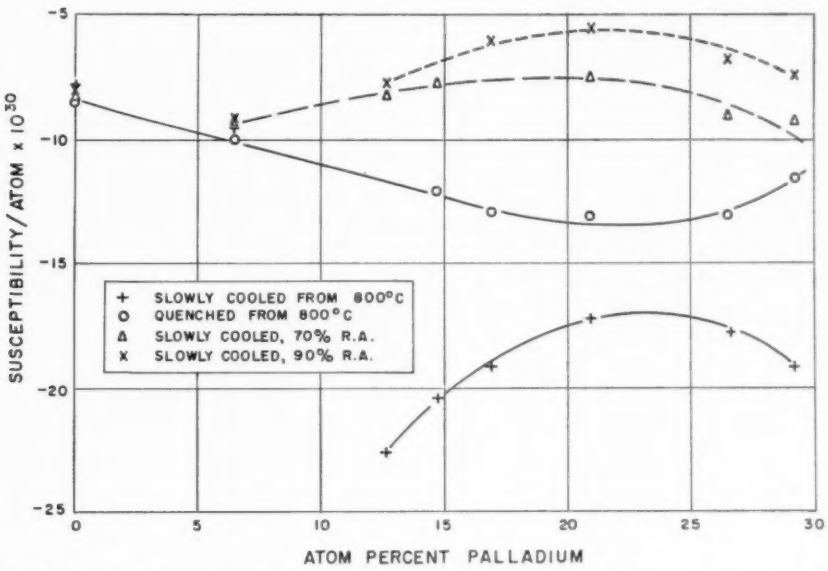

FIG. 14. The magnetic susceptibility, at room temperature, as a function of composition of quenched, partially ordered, and cold-worked Cu-Pd alloys.

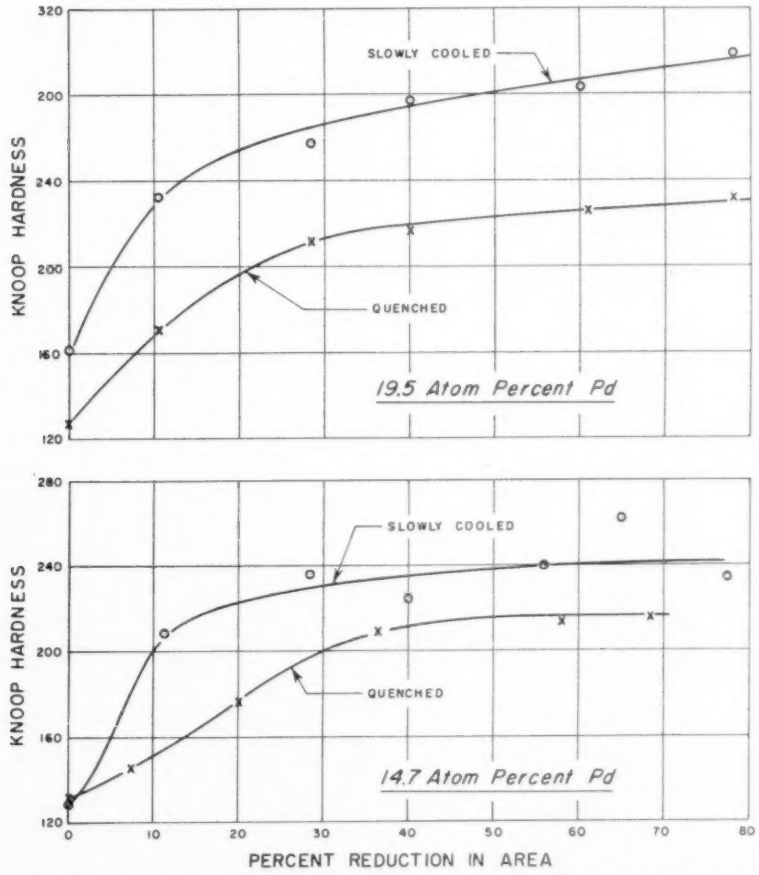

FIG. 15. The microhardness of quenched and partially ordered Cu-Pd alloys as a function of cold-work.

VOL. 4 1956

experimental technique used (Section 2 or reference 13) permitted effects of ferromagnetic impurities to be extrapolated out.

The possibility that the decrease in diamagnetism could be due to lattice imperfections had to be considered, since it had been reported in the literature[12] that the cold-work increased the susceptibility. Later work,[13] however, indicated that cold-work does not affect the susceptibility of pure metals, and this is in agreement with our data on pure copper (Fig. 14). We also found that cold-work did not appreciably affect the susceptibility of the 6.4% palladium sample.

Therefore, the problem became one of whether or not a paramagnetic component was introduced (or one present, increased) or whether diamagnetism was simply decreased. In order to check whether a simple paramagnetic component of the type found, for example, in pure palladium was present, the susceptibility was measured at liquid-nitrogen temperatures. In all cases, the susceptibility was, within experimental error, identical to that measured at room temperature. To be sure, the temperature range is not large enough to say conclusively that there is no temperature dependence, but it is large enough to say that any paramagnetism present is not of the type found in pure palladium.

Peierls[14] has shown that the Landau diamagnetism is inversely proportional to the effective mass, and we know that the Pauli spin-susceptibility[15] (also temperature-independent) varies directly as the effective mass. On this basis, we could account for the entire effect in terms of the conduction electrons, or, more precisely, in terms of electrons taking part in the conduction, if we can make plausible an increase in the density of states at the top of the Fermi distribution (by definition of the effective mass). We shall discuss this further in Section 4.

Mechanical Hardness

Koster,[16] in a review of the mechanical properties of alloys, found that the hardness of order-disorder alloys changes appreciably only when the structure of the alloy changes, and in that case the hardness increases on ordering. Presumably a dislocation can move through an ordered cubic alloy more easily than through a disordered one, if the disordered phase is also cubic, and so the hardness should decrease slightly if it changes at all. If, on the other hand, there is a difference between the ordered and disordered structures, the existence of out-of-phase domains of different structure supposedly represents an obstacle to the motion of a dislocation, and in this case the ordered alloy is harder.

The results obtained for the copper-palladium alloys support this view, as the results given in Fig. 15 indicate. Considering the points at zero-reduction-in-area, we see that the 14.7% alloy, which orders in a face-centered cubic structure, exhibits very little change in microhardness on ordering. An average of twenty-five determinations on each indicates that the ordered material may be slightly softer, but for any single determination the difference is well within experimental error. On the other hand, the 19.5% alloy, which orders in a well-defined tetragonal structure, is appreciably harder than the disordered structure.

The increase of the microhardness as a function of the cold-work is very similar to that observed for many alloys. The fact that the hardness apparently behaves "normally" supports the conclusion that the unusual results occur mainly for those properties which are relatively structure-insensitive, and are primarily the result of electronic rather than structural changes.

4. GENERAL DISCUSSION OF THE COLD-WORK PHENOMENA

The principal experimental facts are:

(a) The resistivity decreases markedly with cold-work for quenched samples (Figs. 4 and 5).

(b) The value of $d\rho/dT$ is lower for cold-worked samples than for quenched samples (Fig. 9).

(c) The thermoelectric power becomes increasingly negative with cold-work (Fig. 13).

(d) The magnetic susceptibility becomes less negative with cold-work, but the alloys remain diamagnetic (Fig. 14).

(e) The susceptibility is temperature-independent (over the range from room temperature to liquid-nitrogen temperature) for both quenched and cold-worked material.

(f) The change in resistivity with 90% reduction-in-area is constant over the composition range of 10 to 25 at. per cent palladium (Fig. 8).

(g) The microhardness appears to behave normally with cold-work (Fig. 15).

(h) The resistivity-decrease with cold-work is completely recoverable on annealing at temperatures above the ordering temperatures (reference 18).

(i) The curve of resistivity vs. cold-work for partially ordered samples passes through a maximum before decreasing to follow the behavior of quenched samples (Figs. 4 and 5).

(j) The value of $d\rho/dT$ is independent of composition for both quenched and cold-worked samples (Fig. 9).

We should perhaps first clear up the possibility of preferred orientation or segregation producing the observed results. Orientation was looked for in detail (by means of X-ray techniques), and only very small effects were observed, and these not in all samples. Segregation could have occurred, but it does not seem likely, for two reasons. First, an attempt was made to observe it directly through lattice parameter measurements, but none was observed. Second, the cold-work effects are completely recoverable at low temperatures, and at high temperatures the recovery is much too rapid for appreciable diffusion (homogenization) to occur (see reference 18).

We are left with three obvious possibilities for the behavior of these alloys with cold-work:

(a) Cold-work introduces order.

(b) The unusual behavior is simply a reflection of imperfections introduced by cold-work.

(c) The cold-work produces a fundamental change in electronic structure.

VOL. 4 1956

The first possibility, order, has been discussed at length in previous sections, and has been discarded principally on the grounds that, for every quantity except the resistivity, cold-work produces the opposite effect of order.

The second possibility is not so easily discarded and, in fact, in a broad interpretation the imperfections introduced must cause the observed effects. However, we mean by (b) the effects produced by imperfections in so far as dislocations, stacking faults, vacancies, and interstitials are produced which provide additional scattering centers, or otherwise behave as quantities added to the lattice without affecting the basic electron structure of the atoms or of the alloy as a whole. This, of course, is the general explanation for the increase in resistivity observed on cold-working most alloys. Probably this effect is also present in the alloys considered in this work, but since this effect is usually quite small, it is masked by the large effects tending to decrease resistivity. Also, the argument against this type of imperfection-effect is strengthened by the results of the thermopower, temperature dependence of the resistivity, and the magnetic susceptibility. That is, it is generally believed that imperfections should make the thermopower become more positive.[10, 17] The resistivity due to imperfections as scattering centers should be temperature-independent so that $d\rho/dT$ should remain constant; and recent work[13] as well as the present results (Fig. 16) indicate that for otherwise "well-behaved" metals the magnetic susceptibility does not change with cold-work. Thus, the observed effects are probably not due to added imperfections.

We are left with the conclusion that cold-work produces a fundamental change in the electronic configuration. The actual physical process which brings about this change is not determined by the present work. However, the present work does shed light on the electronic configuration changes produced.

Several more or less specific possibilities are suggested by individual results, which turn out not to be upheld when all the data are considered. For example, a decrease in ρ combined with a decrease in $d\rho/dT$ would most easily be explained on the basis of a decrease in the scattering of electrons from s-p to d bands as the material is cold-worked. However, the magnetic measurements and, in fact, the values of $d\rho/dT$ itself strongly indicate that the d band is filled in both cases (quenched and cold-worked samples).

We are thus led to consider the usual simplified picture of the density of states, $N(E)$, as a function of energy E in the conduction band. From the well-known dependencies of the major quantities investigated in this work on the densities of states, we see that all the points (a) to (j) above are satisfied (or not violated) if we can assume that the density of states near the top of the Fermi distribution is increased by cold-work. There are actually two ways in which an increase in the density of states could be brought about; either a narrowing of the d band, or a shift in the relative positions of the centers of gravity of the s-p and d bands. An appreciable narrowing of the d band seems hard to achieve, but a shift in the relative positions of the centers of gravity of the s and d bands would not be as difficult. One way, in fact, of achieving such a shift is simply to move the atoms farther apart.

Although these alloys exhibit order, this fact has not been used explicitly in arriving at the above conclusions, since, generally, ordered alloys are essentially different alloys than disordered ones of the same composition. The suggestions were, however, influenced by the fact that AB pairs of atoms are strongly favored over AA or BB. Also, the tendency of the alloy to assume different structures on ordering is an indication that interatomic distances are critical in this substance.

The authors do not claim that the above suggestions are more than qualitative possibilities. There are

a number of experiments which are needed to decide the causes of the observed phenomena. Certainly, a detailed structure determination is needed. The amount of stored energy should be very large. Low-temperature measurements, particularly of the Hall coefficient and of the specific heat, would provide most valuable information concerning the number of carriers and the variation in the density of states. By and large, the study reported was in the nature of a survey, but it indicates that these alloys could provide an interesting experimental exercise in the band theory of metals.

ACKNOWLEDGMENTS

The authors would like to express their gratitude for the financial support of the Office of Ordnance Research, U.S. Army.

We should like to acknowledge the aid of P. J. Flanders, who made the magnetic measurements; J. L. Rutherford and R. L. Smith, who prepared the alloys; and Miss P. A. Parkin, who performed the chemical analyses. We are also indebted to C. A. Domenicali, F. J. Donahoe, A. D. Franklin, and E. Klockholm for many interesting discussions.

REFERENCES

1. F. W. Jones and C. Sykes, *J. Inst. Metals*, **65,** 419 (1939).
2. F. N. Rhines and J. B. Newkirk, *Trans. Amer. Soc. Met.*, **194,** 1029 (1952).
3. F. E. Jaumot, jr., and C. H. Sutcliffe, *Acta Met.*, **2,** 63 (1954).
4. R. A. Oriani, *Report No. RL*-1061, *G.E. Res. Lab.*, March 1954.
5. D. Madoc Jones and E. A. Owen, *Proc. Phys. Soc.*, **67B,** 297 (1954).
6. L. F. Bates, *Modern Magnetism* (Cambridge, 1951).
7. A. H. Geisler and J. B. Newkirk, *Report No. RL*-1001, *G.E. Res. Lab.*, December 1953.
8. O. Dahl, *Z. Metallkunde*, **28,** 133 (1936).
9. See for example, T. Broom, *Phil. Mag.*, **42,** 56 (1951).
10. W. B. Pearson, *Phys. Rev.*, **97,** 666 (1955).
11. B. Svensson, *Ann. Phys.* (*Leipzig*), **14,** 699 (1932).
12. F. Bitter, *Phys. Rev.*, **36,** 978 (1930).
13. J. D. McClelland, *Acta Met.*, **2,** 406 (1954).
14. R. Peierls, *Z. Phys.*, **80,** 763 (1933).
15. W. Pauli, jr., *Z. Phys.*, **41,** 81 (1927).
16. W. Koster, *Z. Metallkunde*, **32,** 277 (1940).
17. A. W. Saenz, *Phys. Rev.*, **91,** 1142 (1953).
18. A. Sawatzky and F. E. Jaumot, jr. (to be published).

VOL
4
195

THE RATES OF OXIDATION OF SEVERAL FACES OF A SINGLE CRYSTAL OF COPPER AS DETERMINED WITH ELLIPTICALLY POLARIZED LIGHT*

FRED W. YOUNG, Jr.,† JOHN V. CATHCART,‡ and ALLAN T. GWATHMEY†

The rates of oxidation of the (100), (111), (110), and (311) faces of a copper single crystal were determined at the temperatures 70°, 106°, 130°, 159°, and 178°C by measuring the increase in thickness of the oxide film as a function of time. A polarizing spectrometer was used to measure film-thickness. Particular emphasis was placed on preparing a smooth, clean, strain-free surface of known orientation. The relative order of the rates of oxidation of these faces was found to be (100), (111), (110), (311) in decreasing order. The results showed the great difference in the rate of oxidation with crystal face at these temperatures, the ratio of the thickness of the oxide on the (100) face to that on the (311) face being 12.5 for oxidation at 178°C. An analysis of the results, according to the present theories of the oxidation of metals, was presented.

DÉTERMINATION DES VITESSES D'OXYDATION DE DIVERSES FACES D'UN MONOCRISTAL DE CUIVRE, DÉTERMINÉES AU MOYEN DE LUMIÈRE POLARISÉE ELLIPTIQUEMENT

Les vitesses d'oxydation des faces (100), (111), (110), et (311) d'un monocristal de cuivre ont été déterminées à des températures de 70°, 106°, 130°, 159°, et 178°C par la mesure de l'augmentation d'épaisseur du film d'oxyde en fonction du temps. Cette épaisseur a été déterminée à l'aide d'un spectomètre polarisant. Un soin tout particulier a été apporté à la préparation de surfaces d'orientation connue, bien planes, propres et exemptes de toute déformation. La vitesse d'oxydation de ces faces va décroissant dans l'ordre (100), (111), (110), (311). Les résultats obtenus montrent la grande différence de vitesse d'oxydation suivant ces plans: ainsi pour une oxydation à 178°C, le rapport des épaisseurs d'oxyde pour (100) et (311) est 12.5. Une analyse des résultats est présentée, à la lumière des théories actuelles de l'oxydation des métaux.

DIE MIT ELLIPTISCH POLARISIERTEM LICHT BESTIMMTEN OXYDATIONS—GESCHWINDIGKEITEN AUF VERSCHIEDENEN FLÄCHEN EINES KUPFER-EINKRISTALLES

Die Oxydationsgeschwindigkeiten auf den (100), (111), (110), und (311)-Ebenen eines Kupfereinkristalls wurden bestimmt bei den Temperaturen 70°C, 106°, 159°, und 178°C durch Messen der Dickenzunahme des Oxydfilms in Abhängigkeit von der Zeit. Zur Messung der Filmdicke wurde ein Polarisations-Spektrometer verwendet. Besondere Bedeutung wurde der Herstellung einer glatten, sauberen und spannungsfreien Oberfläche mit bekannter Orientierung zugemessen. Es wurde gefunden, dass die Oxydationsgeschwindigkeit auf diesen Flächen in der Reihenfolge (100), (111), (110), (311) abnimmt. Die Ergebnisse zeigten bei den genannten Temperaturen grosse Unterschiede zwischen den Oxydationsgeschwindigkeiten auf verschiedenen Kristallflächen. Das Verhältnis der Oxyddicke auf der (100)- Ebene zu derjenigen auf der (311)-Ebene ist für eine Oxydation bei 178°C 12,5. Auf Grund der derzeitigen Theorien für die Oxydation von Metallen wurde eine Diskussion der Ergebnisse durchgeführt.

INTRODUCTION

The first evidence of the anisotropic oxidation of copper crystals was obtained by Tammann,[1] who noted that the different grains of a piece of polycrystalline copper showed different interference colors after oxidation. The oxidation of large single crystals of copper was first studied by Gwathmey and associates,[2] who used interference colors as the means of determining the thickness of the oxide. They concluded that the rate of oxidation varied greatly with crystal face, and determined the relative order of the rates of oxidation of the various faces. Lustmann and Mehl[3] measured the rate of oxidation of a number of orientations of copper single crystals, using a polarizing spectrometer as a means of measuring film-thickness. They obtained a very complicated variation of the rate of oxidation with crystallographic orientation, with temperature, and with pressure of oxygen. More recently Rhodin[4] made careful measurements of the rate of oxidation of the (100), (111), and (110) faces of copper in the temperature range —195° to 50°C, using a microbalance to determine the film-thickness. A preliminary report on the use of the polarizing spectrometer in measuring the rate of oxidation of several faces of copper was published by two of the authors.[5] Studies of the structure of oxide films on a copper crystal have been made by Lawless and Gwathmey.[6]

* Received March 30, 1955; in revised form July 15, 1955.
† Cobb Chemical Laboratory, University of Virginia.
‡ Present address: Oak Ridge National Laboratory.

VOL. 4 1956

EXPERIMENTAL METHOD

Although there have been many studies made of the oxidation of metals, there has been a tendency to overlook the importance of the preparation of the surface. In the present studies, emphasis has been placed on the preparation of a clean, strain-free copper surface of known orientation.

A $\frac{3}{4}$-in. sphere, with a cylindrical shaft $\frac{1}{4}$ in. in diameter by $\frac{1}{2}$ in. in length on one side, was cut from a copper single crystal rod of 99.99% purity in such a manner as to have a [110] direction along this shaft. Four flat surfaces $\frac{3}{8}$ in. in diameter, corresponding to the $(00\bar{1})$, $(\bar{1}11)$, $(1\bar{1}0)$, and $(1\bar{1}3)$ faces, were cut on this sphere. (Obviously the chemical properties of the (100), (010), $(\bar{1}00)$, etc., surfaces are equivalent.) Thus, by turning the sphere on its axis through the shaft, the four faces could be rotated consecutively to the same given position. The crystal was etched to remove the strained layer, which resulted from the cutting, and polished mechanically with metallographic polishing papers through No. 0000. The flat faces were then polished on a metallographic lapping wheel with a 20-min suspension of levigated alumina and finally polished electrolytically in a phosphoric acid-water solution.[7] With great care in polishing, optically flat surfaces were obtained which were of such smoothness that it was not possible to focus on the surface with a metallographic microscope at 1000×. The smoothness of electropolished copper surfaces has been previously discussed.[8] The orientations of these faces were checked periodically with X-ray diffraction.

After completion of the electrolytic polishing, it was necessary to wash the crystal very carefully to remove traces of phosphate ion. Many methods of washing were tried, and the following procedure was adopted. The crystal was immediately rinsed with water, immersed in a 10% solution of phosphoric acid in water for one minute, washed in a stream of water for one minute and again immersed in the phosphoric acid solution for one minute. Finally, the crystal was washed in a stream of water for four minutes, dried with a jet of pure oxygen, and then fixed in place in the oxidation apparatus. The wash water was prepared by distilling demineralized water, and approximately eight gallons were used in washing each crystal. A short piece of No. 24 copper wire 99.999% pure, which had been carefully polished, washed, and dried, was used to tie the crystal in place in the oxidation chamber.

The crystal was annealed in purified dry hydrogen for one hour at 500°C. It was then cooled in hydrogen to the temperature of oxidation, the hydrogen was evacuated to $\sim 10^{-2}$ mm of Hg, and an atmosphere of purified dry oxygen was admitted.

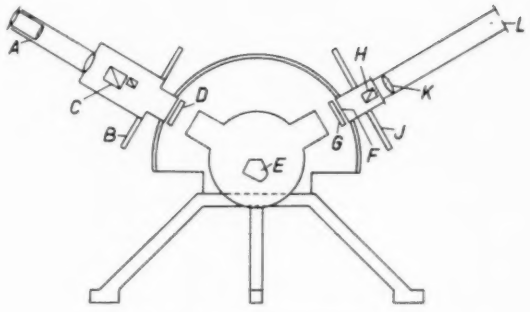

FIG. 1. Polarizing spectrometer.

A—Telescope
B—Analyser scale
C—Analyser nicol with lippich assembly
D—Ellipticity half-shade
E—Crystal
F—Iris diaphram
G—Quarter-wave plate
H—Polarizer nicol
J—Polarizer scale
K—Collimating lens
L—Adjustable slit

The rate of oxidation was determined by measuring the increase in thickness of the oxide film as a function of time, using a polarizing spectrometer to measure film-thickness. The polarizing spectrometer has been described by various authors.[9] The one used in these experiments was designed and built at the University of Virginia, following somewhat the one described by Winterbottom.[10] A diagram of this instrument is shown in Fig. 1. The optics of the instrument were set so that it was necessary to read only the polarizer angle J and the analyser angle B in order to determine the change in the ellipticity on reflection. The refractive index of the Cu_2O film on copper was determined by one of the authors of this paper by a graphical method.[11] As previously reported, the film-thickness measurements obtained by this method compared very favorably with those obtained by other methods.[5]

The crystal was fixed in place in the glass oxidation chamber so that the four flat faces could be successively brought exactly into the plane of incidence of the light by turning the ground joint, as shown in Fig. 2. Great care was necessary in this optical alignment. Thus it was possible to measure the thickness of the oxide on the four faces consecutively. One reading per minute could be made, so that the film-thickness on each face could be determined as often as once per four minutes.

The temperature was controlled to ± 0.1°C by thermocouples which were placed on the outside wall of the oxidation chamber. These thermocouples were calibrated against a thermocouple placed inside the chamber in the position which the crystal normally occupied.

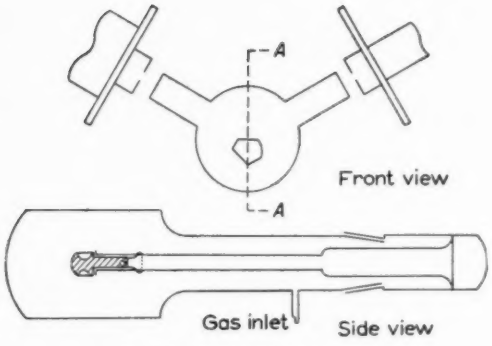

FIG. 2. Oxidation chamber.

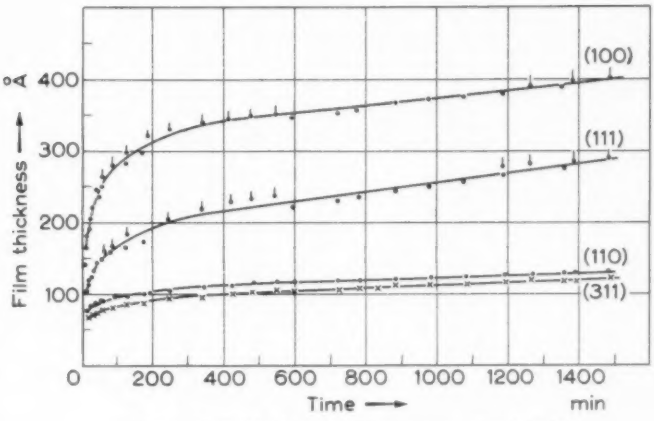

FIG. 5. Oxidation of copper monocrystal 130°C.

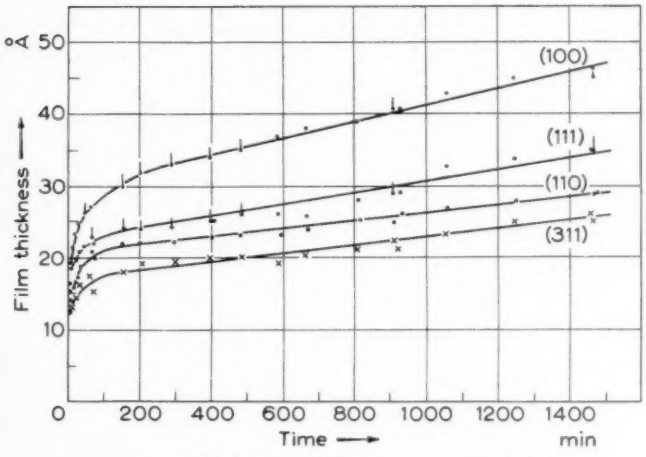

FIG. 3. Oxidation of copper monocrystal 70°C.

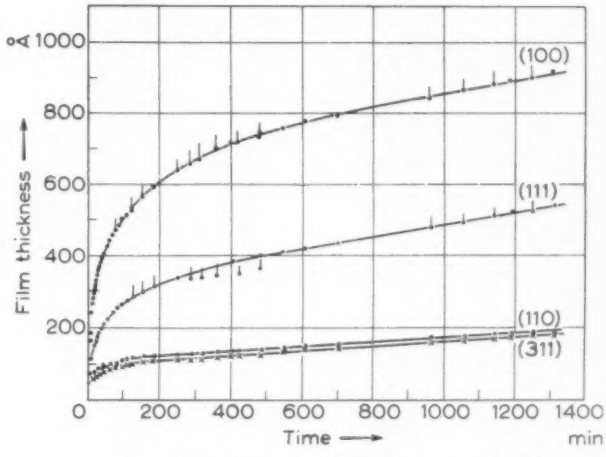

FIG. 6. Oxidation of copper monocrystal 159°C.

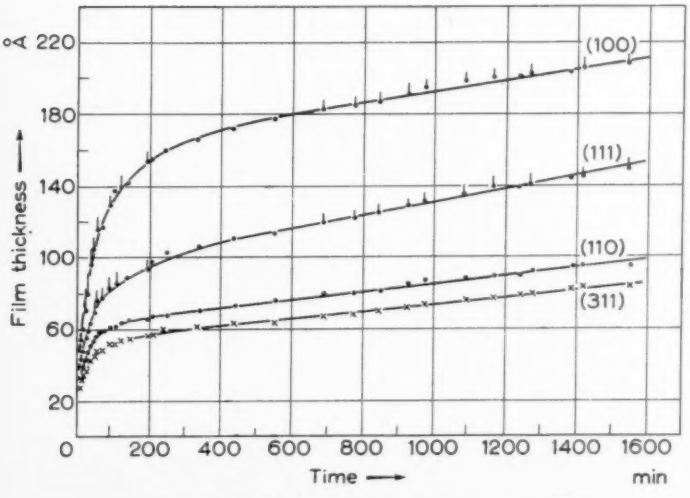

FIG. 4. Oxidation of copper monocrystal 106°C.

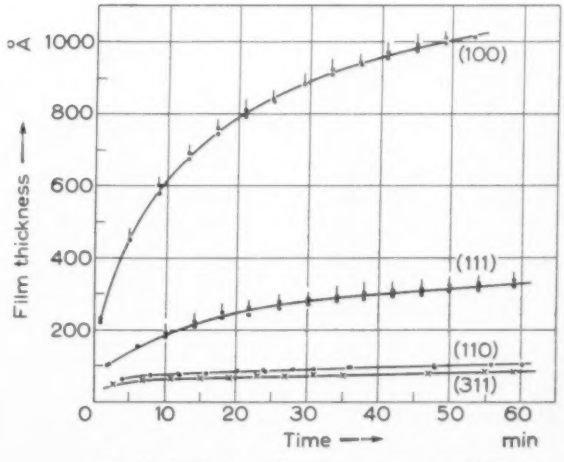

FIG. 7. Oxidation of copper monocrystal 178°C.

VOL.
4
1956

RESULTS

As reported earlier by Gwathmey and associates,[2] the relative order of the rates of oxidation of the principal faces was found to be (100), (210), (111), (110), (311), in decreasing order. Rectilinear plots of oxide thickness versus time for the (100), (111), (110), and (311) faces at the temperatures 70°, 106°, 130°, 159°, and 178°C, are shown in Figs. 3 to 7. The results of two experiments carried out under the same conditions were plotted on each curve, the points with tails indicating one experiment and the untailed points the other one. The tails were omitted from all points for the (311) and (110) faces because of the closeness of the curves. Since the crystals were gradually reduced in size and regularity of shape by the polishing processes, it was necessary to use two crystals cut from the same crystal rod in making these measurements. The first crystal was used for the measurements at 178° and 159°C and the second for those at 70°C, while measurements at 106° and 130°C were carried out with both crystals in order to serve as a check on the two specimens. The same results within the limits of the method were obtained with the two crystals. In addition, many measurements were made with a number of crystals under slightly different conditions, and results within at least 10% of those given were obtained.

EVALUATION OF RESULTS

The polarizing spectrometer is especially suited to determining rates of oxidation on the different faces of a single crystal. It is one of the most accurate and sensitive methods for measuring film-thickness, and it has the unique advantage that continuous, non-destructive measurements can be made of film-thickness in one desired area exclusive of that in other areas.

The thickness of a film of Cu_2O on copper can be determined to ± 1 Å over the range 0–1000 Å with this polarizing spectrometer if the film is not changing in thickness. However, this accuracy cannot be maintained for rapid measurements on films which are changing in thickness. Thus, the measurements at 70°C are believed to be accurate to ± 1 Å, while the accuracy for the measurements at 178°C is believed to be at least ± 5 Å. These are average thicknesses.

A spherical crystal with flat faces cut on it has special advantages in studying the rates of surface reactions. Since all faces are on the same small piece of metal, they must be at the same temperature, and since they have been prepared in exactly the same manner prior to oxidation, the relative rates should be especially significant under the conditions of the experiment.

The presence of impurities adsorbed on the surface either prior to or during oxidation, henceforth called contamination, can greatly affect the rate of oxidation. It appears that this fact has often not been appreciated. A number of studies have been made of the effect of impurities within the metal on the rate of oxidation,[12] but this effect is generally much smaller than that of surface contamination.

The problem of the removal of contaminating atoms on the surface is a most important one. However, there is no completely satisfactory method of detecting or analysing for very small traces of impurities on a surface. The single crystal in the form of a sphere has special advantages in detecting surface contamination. It has been previously described that when a copper single crystal sphere is oxidized, a color-pattern results. This is due to the fact that the various crystal faces oxidize at different rates, thereby building up oxide films of different thickness on the various faces, and these oxide films show interference colors. This color-pattern is extremely sensitive to traces of contamination. It was determined that less than a monolayer of contaminant on the surface can visibly alter the oxidation color-pattern.

After experimenting with many methods of preparing the surface, the procedure described was thought to give the most satisfactory surface in terms of ease of reproducibility and of freedom from contamination, facet formation, and strain. The oxidation pattern obtained with this procedure was therefore referred to as the characteristic or "standard" pattern (see Fig. 8), but there is admittedly no method at the present time of making absolutely sure that even these measurements were not made under a constant state of contamination. In the procedure used, every effort was made to remove all contaminants without, at the same time, giving the surface such drastic treatment that its structure would be unknown. If the oxide pattern on the spherical part of the crystal did not show the standard pattern, inconsistent results on the flat faces with the spectrometer were always obtained. The effects of traces of such contaminants as stopcock grease, impurities in the wash water, phosphate ions from the polishing-bath, and sulfide fumes in the air, were studied qualitatively by noting their influence on the pattern. Thus the oxidation pattern was used as a criterion for detecting the presence of contaminants.

It is to be emphasized, therefore, that the results which are reported herein apply only for the described experimental conditions. However, a number of experiments were carried out to show that the choice of experimental conditions was a good one. Some preliminary experiments were made using a polishing-bath of HNO_3—CH_3OH in which there was no possibility of phosphate ion being present as a contaminant. Essentially the same results were obtained with both polishing solutions. Also, several experiments have subsequently been carried out which indicated that when the crystal was cleaned with hydrogen bombardment after electropolishing and washing prior to annealing in hydrogen, the same oxidation results were obtained.

For the quantitative measurements reported in this paper the hydrogen was evacuated from the system prior to oxidation at a pressure of approximately 10^{-2} mm of Hg. However, a series of experiments was conducted in another all-glass apparatus containing no stopcocks to determine the effect of outgassing of the crystal and apparatus. The experimental procedure was the same as that described above, except that the system was evacuated to $\sim 1 \times 10^{-7}$ mm of Hg. The temperature of outgassing was that at which the oxidation was to take place. Using the interference colors of the oxide films to determine the film-thickness, the same order of activity of the crystal faces as reported above was obtained. Also the rates of oxidation were the same as those reported above, within the limit of error of the interference color method of measuring film-thickness.

There are several factors which may be important in studying the oxidation of copper crystals, and which were not thoroughly investigated. First, there is no satisfactory method of outgassing a copper crystal preparatory to measuring rates of surface reactions. If the crystal is not heated in a vacuum at a temperature near its melting-point, it is doubtful whether contaminating gases are completely removed. On the other hand, recent results in this laboratory show that such treatment will cause facet formation, and thus the surface is no longer smooth and of one orientation. Second, it is known that there are always various types of imperfections present in a single crystal which cannot be removed by annealing. These imperfections may play an important role in surface reactions. For example, the activity of regions where dislocations end in the surface may be different from that of the remaining surface. At present, the effects of these imperfections are not known.

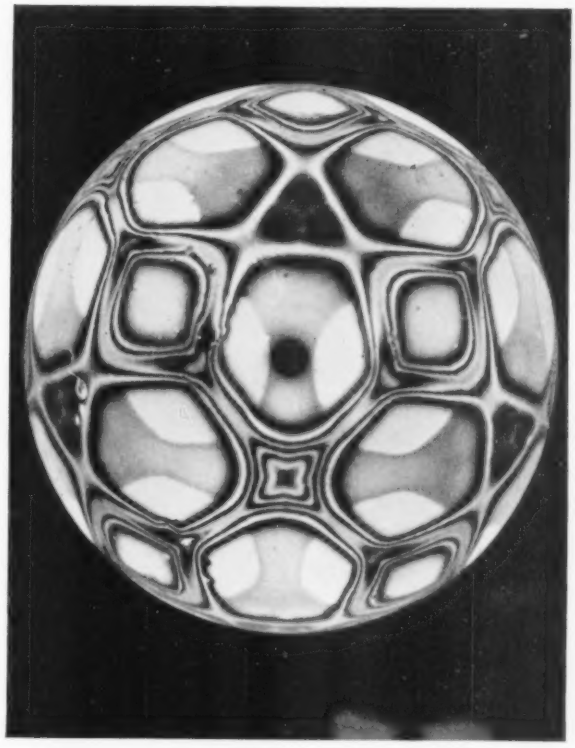

FIG. 8. Pattern resulting from oxidation of a single crystal copper sphere at 250°C in oxygen.

DISCUSSION

The relative order of the rates of oxidation of the different faces in this study was, in decreasing order, the (100), (111), (110), and (311) faces, while in the studies of Rhodin,[4] the relative order was the (100), (110), and (111) faces. Thus in the first case the rate of the (111) was found to be faster than the (110), while in the studies of Rhodin, the reverse was found. Very small amounts of impurities on the surface will reverse the relative rates of these two faces, the (110) having been found to be especially susceptible to surface contamination. With the present lack of analytical methods for detecting traces of impurities on metal surfaces, it is impossible to resolve this difference. The (100) face was reported to have the greatest rate in both studies. Also when the thicknesses for (100) face reported in these studies over the temperature range of 70° to 178°C are extrapolated to 50°C, the value agrees reasonably well with that reported by Rhodin for the (100) face at this temperature. At the present time this agreement has a limited significance. The rate of the (311) face was determined only in this study.

The results shown in Figs. 3 to 7 emphasize the large difference in the rate of oxidation with crystal

VOL. 4 1956

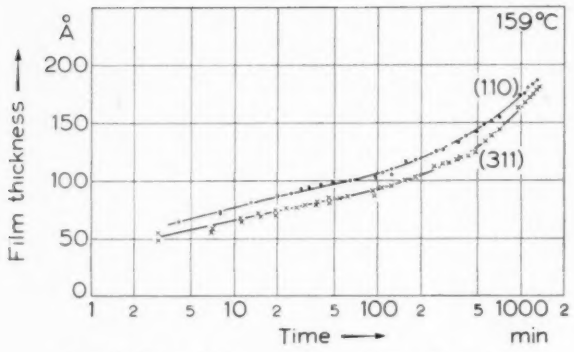

FIG. 9. Film thickness vs. logarithm of time for (110) and (311) faces at 159°C.

face. It can be seen that this difference is increasing with temperature. The ratio of the thickness of the oxide on the (100) face to that on the (311) face is 1.8 at 70°C, while at 178°C this value has increased to 12.5. As determined from interference colors, this value increases still further to >20 at 250°C.

It is desirable to examine the results shown in Figs. 3 to 7 with the aid of existing theories of oxidation of metals, particularly that of Mott and Cabrera.[13] The following analyses will show, however, that these results cannot be satisfactorily interpreted by the present theories.

1. In no case is a logarithmic relationship of the form $X = A \ln t + B$ obeyed (X = film thickness, t = time). Logarithmic plots of the data for 159°C are given in Figs. 9 and 10,* and it can be seen that the plots definitely curve upward. This is true for the data at all temperatures, even 70°C. This is in agreement with Mott and Cabrera.

2. At 70°C the results for all faces can be expressed as $1/X = A - B \ln t$. This relation can be used to express the results for the two low-rate faces, the

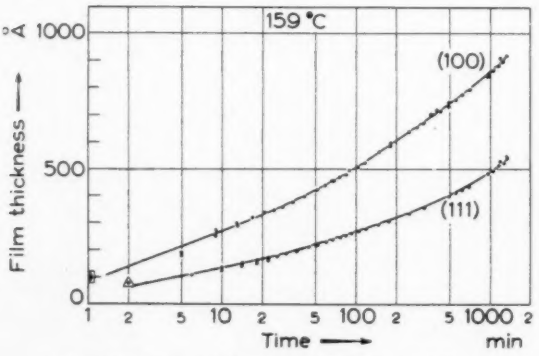

FIG. 10. Film thickness vs. logarithm of time for (111) and (100) faces at 159°C.

* Figs. 9 to 14, and that part of the discussion indicating that activation energies cannot be calculated from these data, using present theories, were added at the request of the referees.

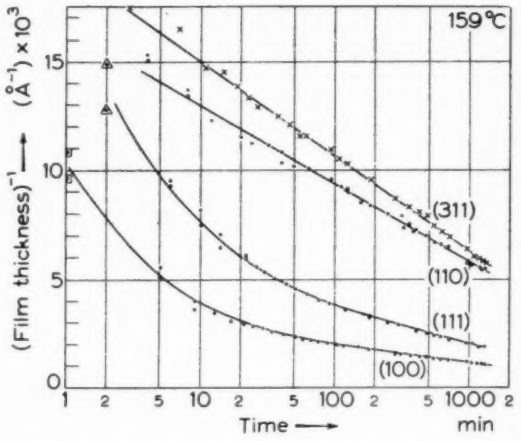

FIG. 11. Reciprocal of film thickness vs. logarithm of time for all faces at 159°C.

(311) and (110), at all temperatures. Fig. 11 shows a reciprocal logarithmic plot of the data for 159°C. It is clear that the (311) and (110) data are best represented by straight lines, while the (100) and (111) are definitely represented by curves.

3. At the temperatures above 70°C the results for the (100) and (111) faces can be expressed by a relation of the form $X^n = Ct$, with n decreasing with increasing temperature, the value of n being 4.4 at 106°C, 4.8 at 130°C, 4 at 159°C, and 3 at 178°C. Fig. 12 shows a log-log plot of the data for 159°C. It is clear that the (100) and (111) data are best represented by straight lines, while it is not possible to draw either straight lines or continuous curves through the (110) and (311) data. However, it can be seen that the (110) and (311) data seem to be slightly concave upward.

4. As suggested by the theory of Mott and Cabrera, the results for all temperatures can be expressed by a relation of the form $dX/dt = 2A \sinh X_1/X$ ($X_1 = qaV/2kT$; $A = ave^{-W/kT}$; V = difference in

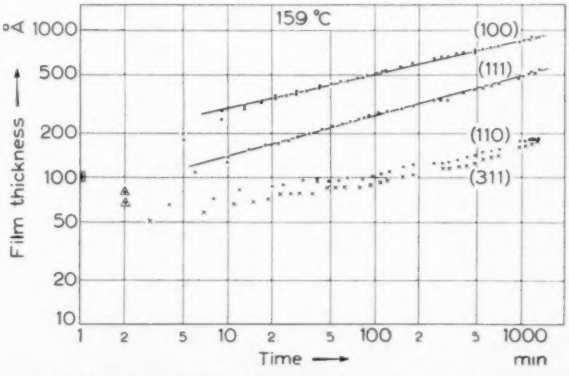

FIG. 12. Logarithm of film thickness vs. logarithm of time for all faces at 159°C.

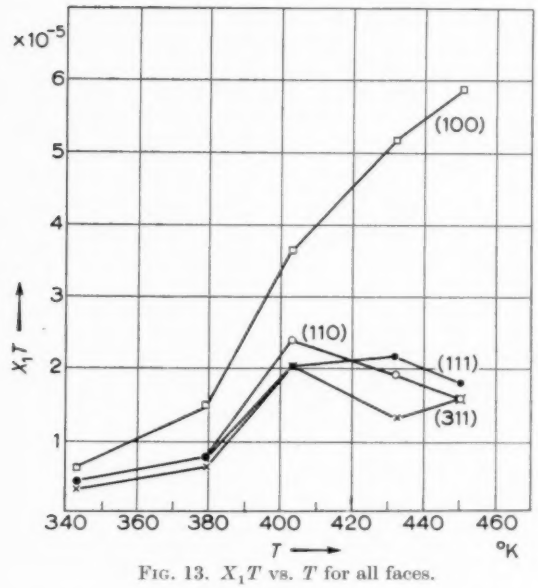

FIG. 13. X_1T vs. T for all faces.

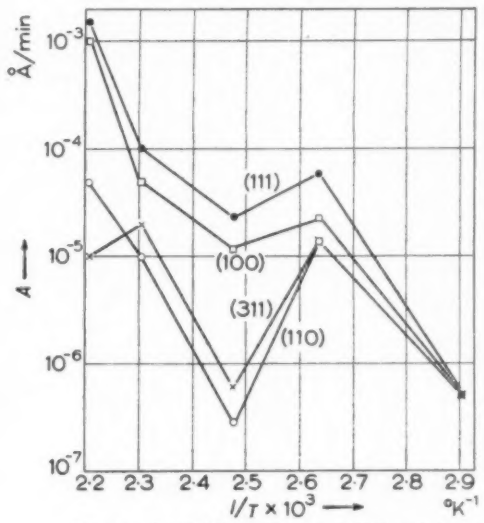

FIG. 14. Logarithm of A vs. $1/T$ for all faces.

potential between metal-oxide interface and oxide-oxygen interface; q = charge on the diffusing ion; a = interatomic distance in the oxide; ν = atomic frequency of vibration; W = heat of solution for a vacancy plus the activation energy for diffusion). A plot of this equation after numerical integration as $\ln X/X_1$ vs. $\ln At$ is a curve with gradually increasing slope, the maximum value being 0.5. Thus the equation predicts that the oxidation curves can be described as a series of curves of the form $X^n = Ct$ with n decreasing with temperature, since the range of thicknesses measured increases with temperature. Therefore, the results reported in this paper agree qualitatively with this prediction, since the relation $1/X = A - B \ln t$ can also be described as $X^n = Ct$, where n is a fairly large number. In this connection it may be noted that the log-log plots of the (311) and (110) data shown in Fig. 12 are slightly concave upward, and this fact conforms with this generalization.

It is possible to evaluate the constants A and X_1 by superimposing $\ln X$ vs. $\ln t$ plots of the experimental data on the $\ln X/X_1$ vs. $\ln At$ plot of the numerically integrated curve. The values of A and X_1 obtained in this way are shown in Table 1.

Although the numerical values of these constants seem to be of the right order of magnitude, a more careful consideration of these constants shows that they are not consistent with the theory. It can be seen from the expression for X_1 that it is proportional to $1/T$, and therefore a plot of X_1T vs. T should be a straight line of zero slope. Fig. 13 shows that this does not hold for any of the faces. Also, since $A = A_0e^{-W/kT}$, a plot of $\ln A$ vs. $1/T$ should be a straight line, the slope of which should be $-W/k$. Fig. 14 shows such a plot for the experimental data. Obviously activation energies cannot be calculated from this data using the theory of Mott and Cabrera.

A numerical integration of the relation $dX/dt = A'/X \sinh X_1/X$ which was suggested by Mott and

TABLE 1

Temp.	(100)		(111)		(110)		(311)	
	A (Å/min)	X_1 (Å)	A (Å/min)	X_1 (Å)	A (Å/min)	X_1 (Å)	A (Å/min)	X_1 (Å)
178°C	1×10^{-3}	1300	1.5×10^{-3}	400	5×10^{-5}	345	1×10^{-5}	355
159°C	5×10^{-5}	1200	1×10^{-4}	500	1×10^{-5}	450	2×10^{-5}	300
130°C	1.3×10^{-5}	900	2.3×10^{-5}	500	2.8×10^{-7}	600	6×10^{-7}	500
106°C	2.7×10^{-5}	390	6×10^{-5}	200	1.4×10^{-5}	200	1.4×10^{-5}	170
70°C	5×10^{-7}	178	6×10^{-7}	130	5×10^{-7}	125	5×10^{-7}	105

VOL. 4 1956

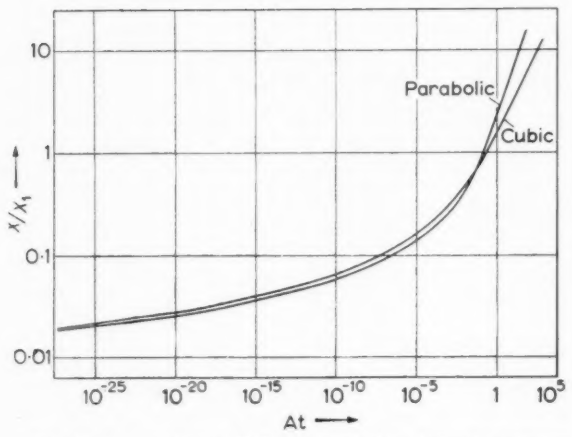

FIG. 15. Logarithm of X/X_1 vs. logarithm At for the relation $dX/dt = 2A \sinh X_1/X$ (parabolic) and $dX/dt = A'/X \sinh X_1/X$ (cubic).

Cabrera to be more applicable to the oxidation of copper, showed that this relation and the above relation $dX/dt = 2A \sinh X_1/X$ were nearly numerically identical over the thickness range covered in this paper. Fig. 15 shows $\ln X/X_1$ vs. $\ln At$ plots for these two relations. Since A' should obey a similar relation with temperature to A, it is clear that quantitative agreement with this equation is also not satisfactory.

Although qualitative agreement with the theory of Mott and Cabrera is surprisingly good, the fact that quantitative agreement is poor is not unexpected, for the following fundamental reasons. First, all existing theories assume a uniform oxide film on a single crystal face of a metal. The work which has recently been done by Harris,[14] Gulbransen,[15] and Benard[16] indicates that this assumption must be modified. These investigators have shown that there are nuclei of oxide in the film which differ in thickness from the remainder of the film. Also, the work of Harris shows a difference in the nature of the film and in the number of nuclei with crystal face for copper. Second, the theory of Mott and Cabrera cannot explain the large difference in rate of oxidation with crystal face; indeed, it cannot predict the correct relative order of the rates of oxidation of the different crystal faces. The large difference in the rate of oxidation with crystal face is probably the most significant fact in these studies.

It is likely that the roles of imperfections and grain boundaries in promoting diffusion through the oxide may be more important than has been realized. From this point of view, studies of the orientation relationships of Cu_2O on Cu may help in explaining in part why the different crystal faces of copper oxidize as they do. For example, it is found by Lawless and Gwathmey[6] that the (111) Cu_2O is parallel to (100) Cu, and (111) Cu_2O is parallel to (111) Cu. However, there are four energetically equal ways by which the (111) planes of the Cu_2O may form parallel to the (100) planes of the Cu, while there are only two ways for the (111) planes of Cu_2O to form parallel to the (111) planes of copper. Thus the former system has more grain boundaries than the latter, and the rate of diffusion through the oxide may be enhanced.

These considerations point out the necessity for modification of the present theory of the oxidation of metals to account for the large differences in rate with crystal face and the smaller differences in rate within any one face.

ACKNOWLEDGMENT

The authors wish to thank Professor N. Cabrera of this laboratory for valuable aid in the preparation of this paper, especially the theoretical interpretation of results. This work was supported in part by the Office of Naval Research.

REFERENCES

1. G. TAMMANN, *J. Inst. Metals*, **44,** 29 (1930).
2. A. T. GWATHMEY and A. F. BENTON, *J. Chem. Phys.*, **8,** 431 (1940). *J. Phys. Chem.*, **46,** 969 (1942); A. T. GWATHMEY, H. LEIDHEISER, and G. P. SMITH, Technical Note No. 1460, National Advisory Committee for Aeronautics, Washington, 1948.
3. B. LUSTMAN and R. F. MEHL, *Trans. Amer. Inst. Mining Met. Engrs.*, **145,** 246 (1941).
4. T. N. RHODIN, *J. Amer. Chem. Soc.*, **72,** 5102 (1950).
5. A. T. GWATHMEY and F. W. YOUNG, *Rev. Metallurgie*, **48,** 434 (1951).
6. A. T. GWATHMEY and K. R. LAWLESS, see following article.
7. P. JACQUET, *Trans. Electrochem. Soc.*, **69,** 629 (1936).
8. T. N. RHODIN, *J. Appl. Phys.*, **21,** 791 (1950).
9. A. B. WINTERBOTTOM, *Trans. Faraday Soc.*, **42,** 203 (1946).
10. A. B. WINTERBOTTOM, *J. Sci. Instrum.*, **14,** 203 (1937).
11. F. W. YOUNG, Dissertation, University of Virginia, 1950.
12. O. KUBASCHEWSKI and B. E. HOPKINS, *Oxidation of Metals and Alloys*, New York Academic Press Inc., 1953, page 68.
13. N. CABRERA and N. F. MOTT, *Rep. Progr. Phys.*, **12,** 163 (1948–49).
14. W. W. HARRIS and FRANCES L. BALL, *J. Appl. Phys.*, **24,** 1416(A) (1953); **25,** 1459 (1954).
15. E. A. GULBRANSEN, W. R. MCMILLAN, and K. F. ANDREW, *J. Metals*, **6,** *Amer. Inst. Metall. Engrs. Trans.*, **200,** 1027 (1954).
16. J. BARDOLLE and J. BENARD, *Rev. Metall.*, **49,** 613 (1952).

THE STRUCTURE OF OXIDE FILMS ON DIFFERENT FACES OF A SINGLE CRYSTAL OF COPPER*

KENNETH R. LAWLESS and ALLAN T. GWATHMEY†

The composition and structure of oxide films formed on electropolished single crystals of copper were studied for eight different crystal faces, using X-ray diffraction techniques. Particular care was taken to assure the best possible surfaces as concerns smoothness and freedom from contaminants. The effects of crystal face, temperature, pressure, oxide thickness, and contaminants were studied.

Cu_2O was found to be the major oxide formed between 170° and 450°C and at pressures from 0.8 mm of Hg to atmospheric. CuO formed above certain minimum thicknesses, the values of which depended on crystal face and temperature.

The degree of orientation varied with all the above variables, being, in general, greater for higher temperatures and for lower pressures. The type of orientation (epitaxy) varied with crystal face, but did not vary with the other variables studied. Four different classes of orientations were found for Cu_2O on Cu, and in all cases a [110] direction of Cu_2O was parallel to a [110] direction of Cu. CuO when formed was not oriented.

LA STRUCTURE DES FILMS D'OXYDE SUR LES DIFFÉRENTES FACES D'UN MONOCRYSTAL DE CUIVRE

La composition et la structures des films d'oxydes formés sur des monocristaux de cuivre polis électrolytiquement ont été étudiées pour huit faces cristallines différentes à l'aide des rayons X. Un soin particulier a été pris pour assurer les meilleures surfaces possible en ce qui concerne le poli et l'absence d'agents de contamination. Les effets de face cristalline, température, pression, d'épaisseur d'oxyde et d'agents contaminants ont été étudiés.

On a trouvé que Cu_2O est le principal oxyde formé entre 170°C et 450°C et entre 0,8 mm de mercure et à la pression atmosphérqiue. CuO se forme au-dessus de certaines épaisseurs minima dont les valeurs dépendent de la face cristalline et de la température.

Le degré d'orientation varie avec tous les paramètres cités ci-dessus. Il est en général plus grand pour des températures élevées et de basses pressions. Le type d'orientation (épitaxie) varie avec la face cristalline mais est indépendant des autres variables étudiées. Quatre classes d'orientations différentes ont été trouvées pour Cu_2O sur Cu et dans tous les cas, une direction (110) de Cu_2O est parallèle à une direction (110) du cuivre. CuO, lorsqu'il se forme, n'est pas orienté.

DIE STRUKTUR VON OXYDSCHICHTEN AUFVERSCHIEDENEN FLÄCHEN EINES KUPFER-EINKRISTALLS

Mit Hilfe von Röntgen-Beugungsverfahren wurden Zusammensetzung und Struktur von auf elektrolytisch polierten Kupfereinkristallen gebildeten Oxydschichten für acht verschiedene Kristallflächen untersucht. Besondere Sorgfalt wurde angewandt, um möglichst glatte und verunreinigungsfreie Oberflächen zu erhalten. Der Einfluss der Kristallfläche, der Temperatur, des Drucks, der Oxyddicke und der Verunreinigungen wurde untersucht.

Es wurde gefunden, dass zwischen 170° und 450°C bei Drucken von 0,8 mm Hg aufwärts bis zu Atmosphärendruck Cu_2O das hauptsächlich gebildete Oxyd ist. CuO bildete sich erst oberhalb einer bestimmten Minimaldicke, deren Grösse von der Kristallfläche und der Temperatur abhängt.

Der Grad der Ausrichtung (Verwachsung) variiert mit allen obengenannten Veränderlichen. Er ist im allgemeinen grösser bei höheren Temperaturen und bei niedrigeren Drucken. Der Typ der Verwachsung (Epitaxie) variert mit der Kristallfläche, aber nicht mit den anderen untersuchten Variablen. Vier verschiedene Arten von Verwachsungen wurden für Cu_2O auf Cu gefunden. Bei allen war eine (110)-Richtung des Cu_2O parallel zu einer (110)-Richtung im Cu. CuO, sofern es auftrat, zeigte kein orientiertes Aufwachsen.

VOL. 4 1956

INTRODUCTION

The purpose of this study is to determine the nature of the oxide film formed on different faces of a single crystal of copper under various conditions of experiment. A thorough knowledge of the composition and structure (including texture and epitaxy) of the oxide film is required in order generally to understand the mechanism of oxidation and especially to explain the large differences in rate with face.

Although considerable work has been done on the composition of the oxide formed on polycrystalline copper,[1, 2, 3, 4, 5] only a few studies have been made of the composition of the oxide formed on single crystals of copper.[6, 7] The structural relationships of the oxides on single crystals of copper have been studied by a number of workers,[8, 9, 10, 11] the most complete study being that of Menzel,[12] which was

* Received March 30, 1955; in revised form July 15, 1955.
† Cobb Chemical Laboratory, University of Virginia.

made primarily on etched spherical surfaces. In general, most studies have been made on etched surfaces or surfaces of an unknown character.

The present studies were made of thin oxide films in the range from 250 Å to 5000 Å, using an X-ray technique. The oxidations were carried out on carefully electropolished single-crystal surfaces. The effects of temperature, pressure, thickness of oxide, and contaminants on the nature of the oxide were studied for several faces, and epitaxial relationships were determined for eight different faces.

EXPERIMENTAL METHOD

Since both the rate of oxidation and the structure of the oxide film depend on the preparation of the surface of the metal, great emphasis in these studies was placed on obtaining surfaces which were as clean, flat, and as strain-free as possible. There is no completely satisfactory method of preparing a metal surface for rate or structure studies. Dissolved and adsorbed foreign gases may best be removed by heating in a vacuum at an elevated temperature, but on the other hand the structure of a copper surface so treated is not known at the present time. The exact preparation of the surface for these studies and the advantages of using the crystal in the form of a sphere with flat faces cut on it have been discussed by Young and Gwathmey and others.[13]

It should be emphasized that the use of crystals in this form made it possible to utilize the oxidation patterns on the spherical surface as a reference standard for the conditions used for surface preparation and carrying out the reaction. Addition of trace amounts of impurities, whether as adsorbed gases, or as foreign compounds such as grease, caused marked changes from the standard. Etching or development of facets destroyed the homogeneity of the surface, and this also showed up as a change in the oxidation pattern.

The crystals were oxidized at temperatures from 170° to 450°C and at pressures from 0.8 mm of Hg to atmospheric. The oxidation reactions were stopped at a given thickness by evacuating the system with a high-capacity pump and then cooling to room temperature. The rate of cooling was varied for different experiments. A fast rate of cooling was used to minimize solid-phase reactions[5] for studies in which the determination of the composition of the oxide was the primary purpose. Experiments indicated that the rate of cooling did not affect the oxide structure appreciably, and in general a moderate to slow rate of cooling was used for the structure studies.

Oxide-film thicknesses were determined by means of interference colors, using values for the first-order colors as determined by a polarized light technique.[14, 15] In some cases, thicknesses were checked directly with the polarizing spectrometer, and agreement with thicknesses estimated from interference colors was always very good. For thicknesses above the first order, the increment between successive orders as determined from the optical formulae[14] was used. This amounted to 1050 Å between successive orders of reds. Thicknesses determined in this way were sufficiently accurate for these studies, since in general, sharp changes of composition and structure did not occur over narrow thickness ranges.

The oxide structure and composition were determined by glancing-angle X-ray diffraction methods, using Cu radiation. Both oscillating-crystal and stationary-crystal techniques were used, the radiation being filtered through Ni foil in the former case. The face of the specimen being studied was adjusted normal to the X-ray beam in such a way that the axis of oscillation was in the plane of that face and normal to the X-ray beam. The crystal was then rotated about the oscillation axis until the face being studied made a definite angle of inclination with the X-ray beam, this angle being determined by consideration of the Bragg angles for the metal and oxide faces concerned.

The diffraction patterns were recorded on a cylindrical film concentric about the axis of oscillation. If the oxide was highly oriented, the resulting films showed layer-line patterns with X-ray reflections from both the flat face of the substrate and from the oxide plane parallel to the substrate falling on the zero layer-line, provided the Bragg conditions were satisfied. As an additional check in determining the oxide orientation, the specimen was rotated through an angle of about 45° to 90° about an axis perpendicular to the flat face, and a second layer-line pattern obtained. This gave at once, in many cases, the plane of the oxide which was parallel to the given substrate plane. In some cases where a sufficient number of X-ray reflections was recorded, the complete orientation of the oxide could be determined simply by inspection of one or two oscillation X-ray patterns. In other cases, it was necessary to take a number of diffraction patterns, using both oscillating-crystal and stationary glancing-angle techniques, before the complete orientation could be fixed with certainty. The use of reciprocal lattice relationships simplified the determination of the orientation relationships in cases in which they were not obvious from inspection.

The degree of orientation was estimated by comparing a particular diffraction pattern with each

of a series of X-ray diffraction patterns of cuprous oxide classified as to the amount of orientation, ranging from essentially random (0–10%) to nearly perfect (95–100%). The orientations of the classified series were determined on the basis of the length of the arc of the diffraction maxima, weighted according to the distribution of intensity in the arc. As the orientation deviates from perfect alignment, the diffraction maxima are no longer sharp spots, but become arcs which vary in length depending on the degree of disorientation. This method can give a reasonable estimate of the degree of orientation.

Studies were made of the oxide on eight different crystal faces, the (001), (111), (011), (113), (112), (012), (122), and (133), the studies being more complete on the first six faces listed. All faces studied were prepared as flat surfaces cut on a spherical crystal. It should be noted that results were the same on the (100), (010), (0$\bar{1}$0), etc., planes as for the (001). Thus it is necessary to indicate results for the faces of only one unit stereographic triangle.

VOL. 4 1956

RESULTS

The results of this study are divided into two sections, the first concerning the complex interrelated effects of temperature, pressure, oxide thickness, and contamination on the composition and texture (or degree of orientation), and the second concerning epitaxy. Epitaxy may be generally defined as the mutual orientation relationships between two different crystal substances.

COMPOSITION AND TEXTURE

Composition of the Oxide Film

The major oxide formed under the conditions of these experiments was Cu_2O, the X-ray diffraction patterns giving d_{hkl} values which agreed very closely with those given for Cu_2O by Swanson and Fuyat,[16] including the very weak 211 reflection. If the crystal was allowed to remain in an oxidizing atmosphere after the rate of oxidation had become very slow, monoclinic CuO was formed also. No CuO was detected below certain oxide thicknesses, which depended on the particular crystal face and the temperature of oxidation. Table 1 shows the least thicknesses for which CuO was found under the specified conditions.

Since the X-ray techniques used were not capable of detecting trace amounts of CuO, it was not possible to say that no CuO was present for smaller film thicknesses, but only that the amount must have been very small. Thermodynamic calculations[5] reveal that both Cu_2O and CuO are stable throughout the entire ranges of pressure and temperature covered in these experiments, and the Cu_2O is the more probable oxide. The formation of CuO is explained as follows. When the rate of formation of Cu_2O has become very slow, the number of copper ions available for reaction at the oxide-oxygen interface is very small. Since CuO is stable under these conditions and a ready supply of copper ions is not available, the reaction $Cu_2O + \frac{1}{2}O_2 \rightarrow 2\ CuO$ is more likely to take place. Since the rates become very slow at different thicknesses on different crystal faces, the formation of large amounts of CuO will begin at different thicknesses on different faces. CuO would not be expected at smaller thicknesses where a greater supply of copper ions is more readily available.

TABLE 1

Crystal face	Temperature	Pressure	Least thickness for which CuO was found
(001)	250°C	atm	3000 Å
(011)	250°C	atm	1100 Å
(113)	250°C	atm	800 Å
(001)	350°C	20 mm of Hg	5000 Å
(011)	350°C	20 mm of Hg	2000 Å
(113)	350°C	20 mm of Hg	1200 Å
(111)	350°C	20 mm of Hg	2500 Å

These results are in general agreement with experiments by both electron diffraction,[4, 5, 6] and electrolytic reduction[4] methods. No indication of the oxide CuO′ was found.[1] In general, the methods used by most previous workers for preparing the surface and forming the oxide on the metal were different from those used in these experiments and were not comparable.

The CuO, whenever present, was completely polycrystalline, with no evidence of preferred orientation. The Cu_2O was in general oriented, the degree of orientation depending on the crystal face of copper, oxide thickness, oxygen pressure, temperature, and the presence of impurities. The remainder of this paper is devoted to the effect which these different variables have on the texture and epitaxy of the Cu_2O.

Influence of Oxygen Pressure on Orientation

The effect of oxygen pressure on the degree of orientation of oxide on the (001) and (111) faces is shown in Fig. 1 for oxidation at 200°C. The curves show markedly that for pressures below about 200 mm the degree of orientation increases with decreasing

pressure. For pressures greater than 200 mm, there seems to be no change in the amount of orientation with pressure. In general, for all faces studied, the degree of orientation was greater the lower the pressure. This held true over the whole temperature range studied and for all oxide thicknesses over about 500 Å. With decreasing pressure, the increase in the degree of orientation was greater for the lower temperatures (<250°C). The increase was also greater for larger film thicknesses (>500 Å). For oxide thicknesses less than 500 Å, the oxide was in general highly oriented and showed either a very slight increase in the amount of orientation or no appreciable increase. In no case was the amount of orientation found to decrease with decreasing pressure.

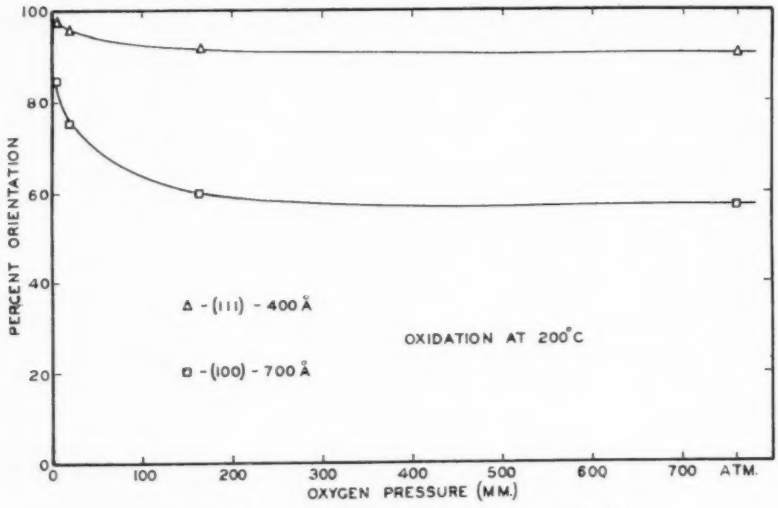

FIG. 1. Effect of pressure on the degree of orientation of the oxide on the (100) and (111) faces of Cu.

Since the oxide film formed at atmospheric pressure is highly oriented for low thicknesses due to the strong orienting effect of the substrate, the degree of orientation can increase only slightly with decreasing pressure. This increase is probably due to the fact that, at the lower pressures, few oxide nuclei are formed with unfavorable orientations. The number of possible adsorption sites occupied by oxygen ions will in general be greater at atmospheric pressure than at low pressure. Since more adsorption sites are always available than are needed for oxide of the observed orientations, the higher pressure will lead to the formation of additional nuclei of different and less stable orientations. The state of knowledge concerning the influence of pressure on the rate of oxidation of single crystals of copper is very limited at the present time, and this makes a more complete interpretation of the effect of pressure on the orientation difficult. Preliminary experiments in this laboratory indicate that a slower rate of oxidation at pressures under 9 mm of Hg may account partially for the improvement in orientation observed for thicker films formed at low pressures.

It was found that the type of orientation (epitaxy) did not vary with pressure; i.e., when a particular crystal plane of the oxide was found parallel to a given substrate face for oxidation at atmospheric pressure, the same relationship was present at lower pressures.

Influence of Temperature and Film Thickness on Orientation

There was a general increase in the degree of orientation of the oxide with increasing temperature for all faces studied, the amount of the increase depending on oxide thickness, oxygen pressure, and crystal face. In no case did an increase in temperature produce a decrease in the degree of orientation. The complex relationships between the degree of orientation, temperature, and oxide thickness may best be described by a type of existence diagram in which points are designated by the amount of orientation for a given temperature and oxide thickness. This is done in Fig. 2 for the (111) face and in Fig. 3 for the (001) face oxidized at atmospheric pressure.

For oxidation at atmospheric pressure, the oxide films formed were generally highly oriented for low thicknesses and could be considered as pseudomonocrystalline, i.e., consisting of small crystallites aligned in a small angular region about a given orientation. With increasing thickness above 600 Å,

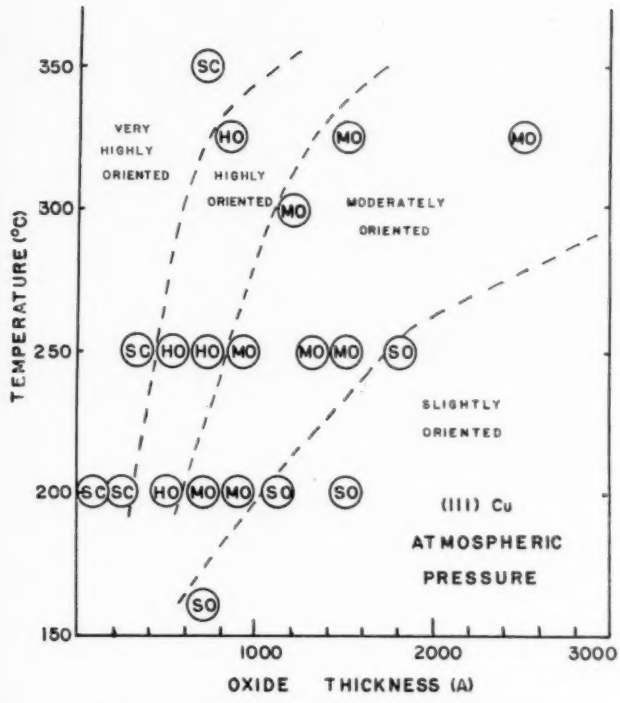

FIG. 2. Orientation variation with temperature and oxide thickness for Cu_2O on (111)Cu.

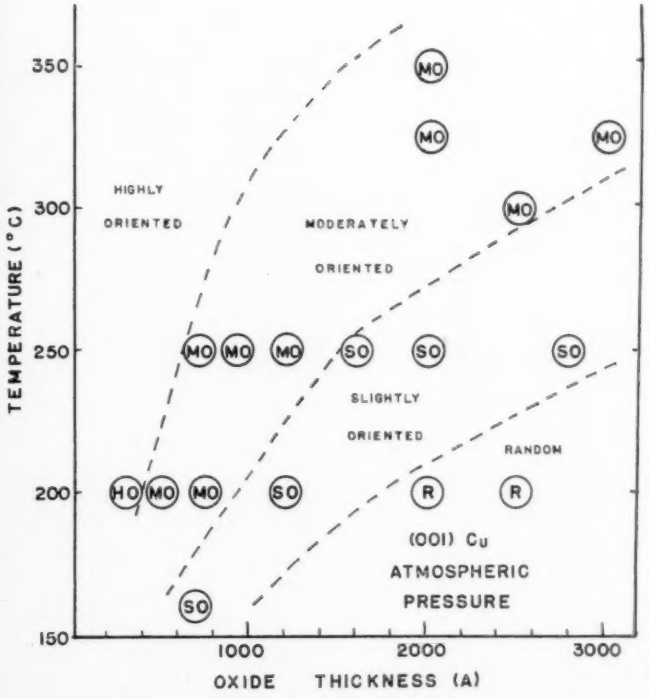

FIG. 3. Orientation variation with temperature and oxide thickness for Cu_2O on (001)Cu.

the amount of orientation decreased, the decrease being rapid at the lower temperatures but gradual at the higher temperatures. This can be seen in Fig. 4 for the (111) face. Oxide on the (012) and (001) faces showed this same general behavior, i.e., a high initial orientation for low film thicknesses followed by a fairly rapid decrease in the amount of orientation with increasing thickness over a certain minimum. It was not possible to compare all the faces studied over a large range of thicknesses because of the large differences in rates of reaction on different faces.

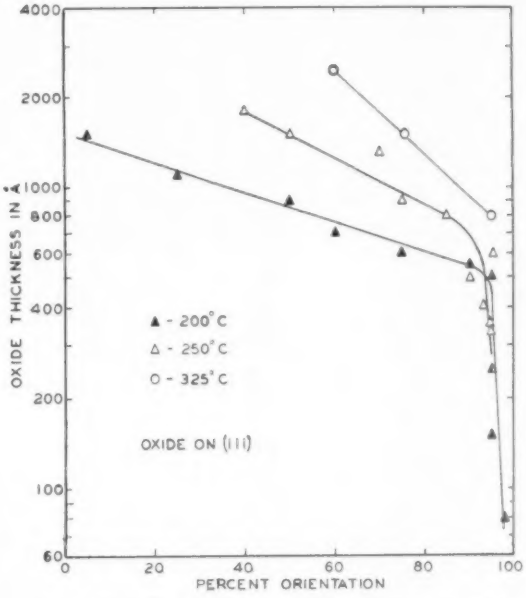

FIG. 4. Variation of the degree of orientation with thickness for Cu_2O on (111) face of Cu.

Oxide films formed at pressures of 0.8 mm to 25 mm of Hg were highly oriented for all thicknesses from 200 Å up to 3000–5000 Å on all faces studied. The amount of orientation either increased slightly [oxide on (001), (111), (012), and (011) planes] or remained about the same [oxide on (112) and (113) planes] with increasing temperature. The disorientation amounted to less than 10° of arc on the X-ray diffraction film in all cases, with the oxide on the (001) showing the greatest amount of disorientation.

It should be pointed out that it is difficult to separate the effects of temperature from those due to initial low-pressure oxidation, when oxidizing at atmospheric pressure. In general, 0.7 to 0.8 sec was required for the pressure in the reacting system to reach 200 mm of Hg; and at temperatures of 300°C and over, an oxide film greater than 500 Å formed in this short time. The evidence indicates that a

large part of the increase in degree of orientation observed with increasing temperature over 300°C for oxidation at so-called atmospheric pressure is due to the initial low-pressure oxidation.

Two factors in general could lead to disorientation of the oxide film with increasing thickness. The first of these is the rapid falling off of the substrate influence with increasing oxide thickness. The second factor is the rearrangement of the oxide due to slip or rotation in such a way as to relieve compressive stresses in the oxide film. The first of these would be the same whether the oxidation was carried out at low or atmospheric pressure. The second, however, could depend on pressure, since oxide films formed at atmospheric pressure contain more imperfections than those formed at low pressures. This would enable slip or rotation of the oxide to take place at lower compressive forces than would be the case for oxide films formed at low pressures. This means that the high initial orientation can extend to greater thicknesses for oxidation at low pressures, as is observed.

The greater amount of energy available to the crystal at higher temperatures gives greater mobility to the oxide. Since the less favorably oriented units of oxide are more weakly bound, it is more likely that these will move about under the influence of temperature than the stronger bound, favored orientations. This then leads to an overall increase in the degree of orientation with increasing temperature.

Influence of Contamination

Trace amounts of such contaminants as SO_2, H_2S, silicone grease, phosphate from polishing solution, residual gases from gas used in glass blowing, silicates or chloride from wash-water, and many others, caused marked changes in the oxidation patterns on the crystal sphere. Crystals showing an oxidation pattern differing from a "normal" or "standard" pattern could then be considered as contaminated, and in many cases the contaminant could be identified from the oxide pattern.

In all cases, at temperatures of 200° to 250°C, it was found that the oxide, when formed in the presence of impurities, showed a marked decrease in the amount of preferred orientation for all thicknesses. In general, the amount of disorientation was almost complete, i.e., the oxide was polycrystalline, with random orientation. For oxidation at 300°C to 400°C, the oxide showed a marked decrease in the amount of orientation, but not the randomness shown for the lower temperatures.

In general, it would be expected that a contaminant which is adsorbed on the surface of the metal would reduce the orientation of the oxide by a simple blocking and reduction of the substrate influence. In general, less than a monolayer of contaminant could cause effective disorientation by blocking the adsorption sites on the metal surface. Gaseous contaminants could also produce disorientation by creating imperfections in the oxide as it is formed.

EPITAXY

The epitaxial relationships reported in this section are those of Cu_2O formed on electropolished flat faces of a single crystal. The type of orientation observed on a particular face did not change with temperature, pressure, or oxide thickness within the ranges covered in these experiments [170°C–450°C; 0.8 mm of Hg to atmospheric pressure; 200 Å to 5000 Å]. The degree of orientation did change with these variables, as described previously.

The epitaxial relationships observed are summarized in Table 2, the second column showing the plane of the oxide which is parallel to the Cu plane listed in column 1, and the third column giving the directional relationships necessary to define the complete orientation, i.e., the alignment of given rows of atoms of the oxide with rows of atoms of the substrate.

All the orientations observed can be placed in one of four different classes. These are designated as I (*A*, *B*, *C*, and *C′*), II (*D*), III (*E*, *E′*, and *E″*), and IV (*F*). These orientations are shown in Figs. 5 (a, b, c, and d). The diagrams represent a section through the oxide and the copper normal to the particular face of copper indicated. The $[1\bar{1}0]$ direction is normal to the page in each case. The rectangular figures in each drawing serve as an aid to visualizing the relative orientations of corresponding units of the metal and oxide. Fig. 6 is a schematic representation of these orientations for six different faces of copper. The large areas of Fig. 6 represent the plane faces of copper, and the small figures represent the oxide with all faces shown being cube faces.

Orientations *A*, *B*, *C*, and *C′* occurred only on the (001) face of copper. The (001) plane of the oxide is parallel to the $(\bar{1}\bar{1}1)$ plane of Cu in *A* and to the (111) plane of copper in *B*. In *C* the (010) plane of Cu_2O is parallel to the $(\bar{1}11)$ plane of Cu.

Orientation *D*, in which the oxide has the same orientation as the Cu substrate, occurred in only minor amounts in a few cases on the (001) plane of Cu, but was a major orientation of the oxide on the

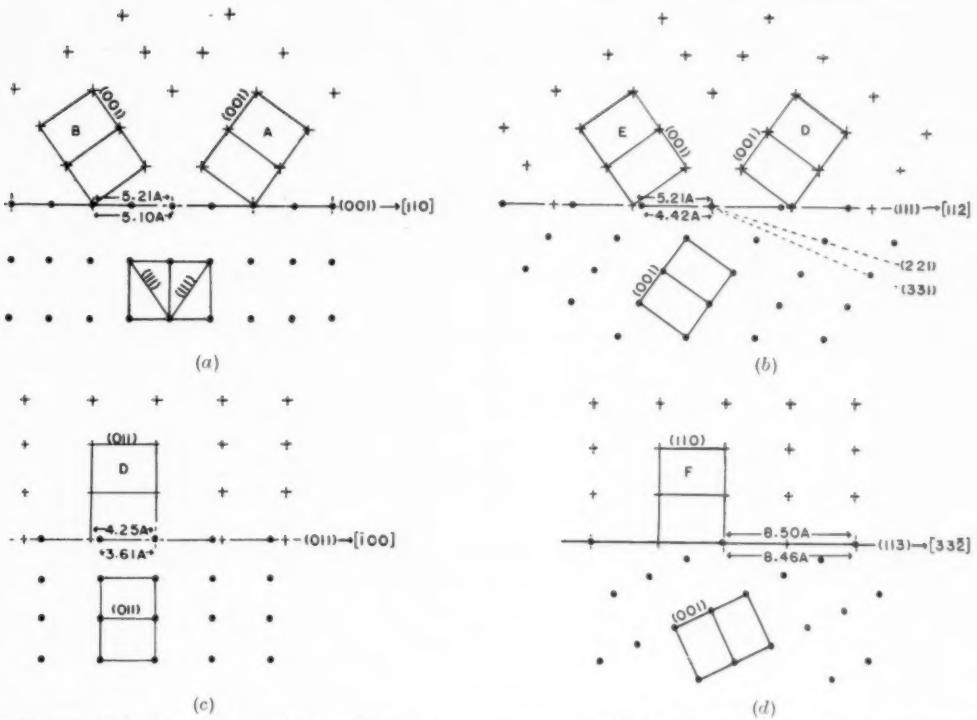

FIG. 5. Positions of Cu ions (+) of Cu_2O with respect to Cu atoms (●) of single-crystal substrate viewed parallel to the faces indicated and with the [1$\bar{1}$0] direction normal to the page. (a) orientations *A* and *B* on (001)Cu; (b) orientations *D* and *E* on (111)Cu; (c) orientation *D* on (011)Cu; (d) orientation *F* on (113)Cu.

VOL. 4 1956

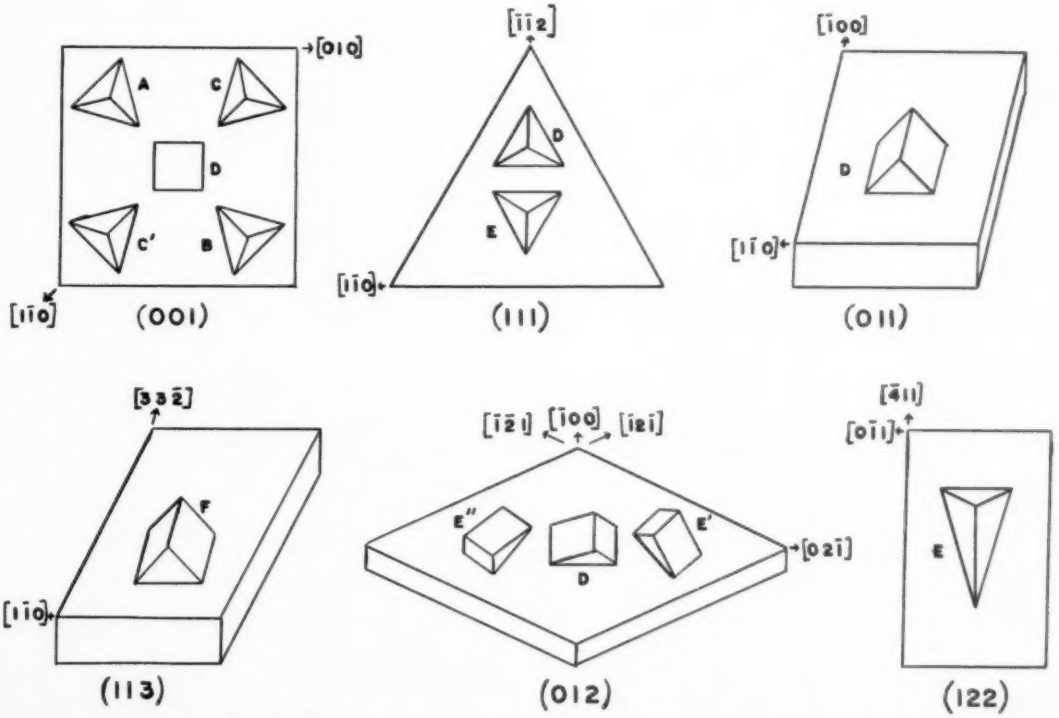

FIG. 6. Schematic representation of oxide orientations on Cu.

TABLE 2.

Crystal face Cu substrate	Parallel face Cu_2O	Major directional relationships	Class	Remarks
(001)	(111)	*A* $[1\bar{1}0]Cu_2O//[1\bar{1}0]Cu$	I	*A*, *B*, *C*, and *C′* are exactly equivalent orientations.
		B $[0\bar{1}1]Cu_2O//[1\bar{1}0]Cu$		
		C $[10\bar{1}]Cu_2O//[110]Cu$		
		C′ $[01\bar{1}]Cu_2O//[110]Cu$		
	(001)	*D* $[1\bar{1}0]Cu_2O//[1\bar{1}0]Cu$	II	Found only in a few cases
(111)	(111)	*D* $[1\bar{1}0]Cu_2O//[1\bar{1}0]Cu$	II	Orientation *E* may also be expressed as: $(11\bar{1})Cu_2O//(111)Cu$ $[1\bar{1}0]Cu_2O//[1\bar{1}0]Cu$
		E $[\bar{1}10]Cu_2O//[1\bar{1}0]Cu$	III	
(011)	(011)	*D* $[1\bar{1}0]Cu_2O//[1\bar{1}0]Cu$	II	
(012)	(012)	*D* $[1\bar{1}0]Cu_2O//[1\bar{1}0]Cu$	II	*E′* and *E″* are equivalent orientations, but are not equivalent to *D*.
		E′ $[\bar{1}10]Cu_2O//[0\bar{1}1]Cu$	III	*E′* may also be expressed as: $(120)Cu_2O//(012)Cu$ $[1\bar{1}0]Cu_2O//[1\bar{1}0]Cu$
		E″ $[110]Cu_2O//[011]Cu$		
(113)	(110)	*F* $[1\bar{1}0]Cu_2O//[1\bar{1}0]Cu$	IV	
(112)	$(44\bar{1})$	*F* $[1\bar{1}0]Cu_2O//[1\bar{1}0]Cu$	IV	
(122)	$(47\bar{4})$	*E* $[1\bar{1}0]Cu_2O//[1\bar{1}0]Cu$	III	
(133)	High index face near (112)	*E* $[1\bar{1}0]Cu_2O//[1\bar{1}0]Cu$	III	

(111) and (012) faces in all cases, and was the only orientation found on the (011) face of Cu. It is probable that the occurrence of *D* on the (001) face was due to sub-microscopic etching with the development of (110) or (111) facets prior to oxidation.

Orientations *E*, *E′*, and *E″* were found in addition to *D* on both the (111) and (012) planes of Cu. It was also the only orientation found on the (122) and (133) faces of Cu. The orientations *D* and *E* on the (111) face are exactly equivalent as far as the surface layer of atoms is concerned. *E* may be derived from *D* on the (111) face by a 180° rotation of the oxide about the [111] axis. On the (012) face of Cu, *E* is not equivalent to *D*, and may be thought of as being derived from *D* by a rotation of the oxide of 131° 49′ about the normal to the (012) face (counter-clockwise rotation giving *E′* and clockwise giving *E″*). The counter-clockwise rotation brings the densely-packed row $[1\bar{2}1]$ of Cu_2O into coincidence with the $[12\bar{1}]$ row of Cu, the (111) plane of Cu_2O with the $(\bar{1}11)$ plane of Cu, and makes three pair of [110] directions parallel.

On the (113) and (112) faces of Cu, the orientation *F* was found. For both of these faces, the (110) plane of the oxide is accurately parallel to the (113) face of the copper, and the $[1\bar{1}0]$ directions of oxide and metal are parallel. No other densely-packed rows of atoms or planes of atoms coincided.

It should be emphasized that the results reported in this paper were obtained on flat electropolished and annealed surfaces, and both the conditions of oxidation and the nature of the metal surface were different from those used by previous workers.[8, 9, 10, 11, 12] The results are thus not strictly comparable.

Neither the preparation of the surface nor the conditions of the oxidation are reported by Mehl, McCandless, and Rhines.[8] Their observation, that the Cu_2O grows with its cube axes parallel to the cube axes of the substrate, was borne out for the parallel orientations on the (011), (012), and (111) faces, but not for any other faces studied.

Thiessen and Schütza used surfaces which had been etched in HNO_3 and then annealed at 1000°C before oxidation was carried out at 325°C and 150-mm pressure. Their results on the (001), (011), and (111) faces are in agreement with those reported here.

Yamaguti[10] etched his specimens in HNO_3 and HCl, and then oxidized them in air at 1000°C. The orientations observed cannot be compared directly, since the faces used were not specified except for one specimen. On a (001) face the orientation observed did not agree with that found here.

Elam[11] used surfaces which were characterized

as "polished," but no other specifications were given. In some cases specimens were used from which the oxide had been removed by heating in a high vacuum. The orientations seem to be in good agreement with those found here.

Menzel[12] carried out oxidations at 450°C and 50-mm pressure, followed by a high-vacuum heat treatment, for surfaces which had received a variety of preparations, including application of various etchants, electropolishing, and high-temperature–high-vacuum treatment. The results obtained are in general agreement with those of this paper if consideration is made of the various facets developed by the different methods of surface preparation.

Consideration of the data of Table 2 reveals that the only relationship present in all cases is that of at least one pair of [110] directions being parallel in metal and oxide. The [110] directions are the ones of greatest density in both the metal and oxide. Since this one condition does not completely define the oxide orientation with respect to a given substrate face, one or more other conditions must be important for determining the complete oxide orientation.

It is necessary to consider the fitting of the oxide lattice on the metal substrate, and to determine whether small misfit for a given direction or for two directions is controlling the orientation. There are two ways of considering this. The first considers the misfit between oxygen positions in the oxide and the most probable adsorption sites on the copper surface, and the second considers the matching of copper positions in the oxide with those in the substrate. Consideration of the first of these indicates that a good match or fit for oxygen ions on the adsorption sites on the metal surface is not necessary for oriented growth of the oxide film.

If the copper-ion positions of the oxide planes are superimposed on the copper positions of the substrate faces, as in Fig. 7, according to the orientations of Table 2, it is seen that a misfit of 18% is present in at least one [110] direction in each case. The misfit here is defined as $b/a - 1$, where b and a are the distances between lattice points for the oxide and metal respectively in a given direction for which the misfit is being determined. From Fig. 7 it is seen that the matching of the two lattices is good for oxide on the (111) and (011) planes of copper (the misfit is 18% in any direction on the surface). For oxide on the (001) and (113) planes of copper, the matching of lattices is not so good, but there is present a striking near-coincidence of the rows of closest-packed Cu ions of the oxide with the closest-packed

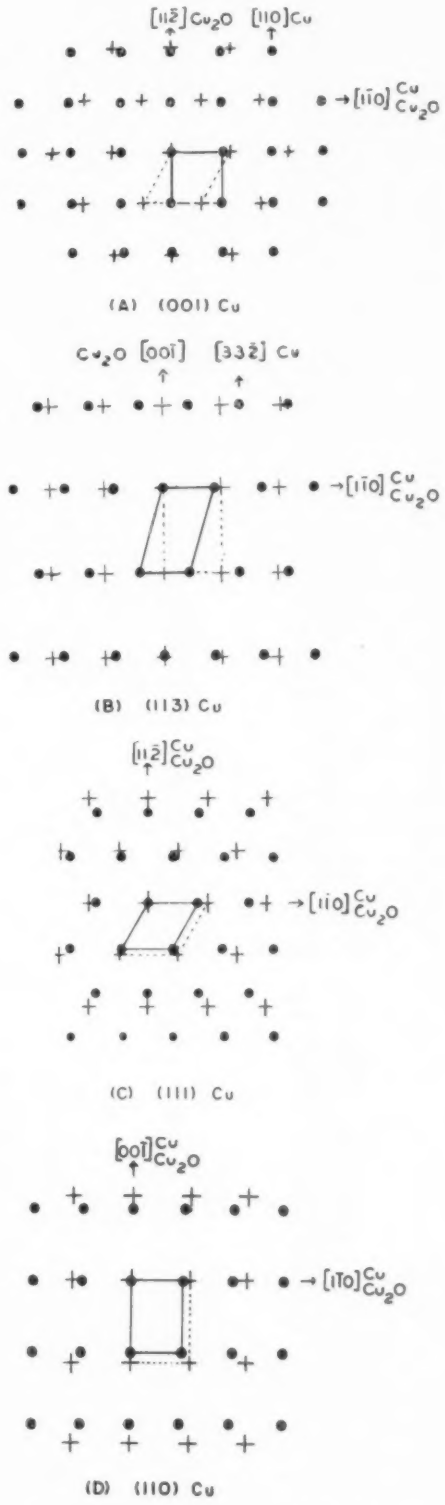

FIG. 7. Positions of Cu ions (+) of Cu_2O superimposed on Cu atoms (●) of the substrate viewed normal to faces indicated.

rows of the metal face. Table 3 lists the misfits between the closest-packed rows of atoms and ions in the interface plane for seven substrate faces. The misfit here is defined as above, except that B and A are the perpendicular distances between closest-packed rows in the oxide-metal interface.

From Table 3 it is seen that this misfit between closest-packed rows for oxide on the (001) is only 2%, and for oxide on the (113) it has the exceptionally small value of 0.5%. These small misfits are apparently the determining factor in fixing the oxide orientation on these two planes.

It is also apparent from Table 3 that a small misfit between rows in the interface plane cannot be the deciding factor for oxide on the (112) and (122) planes. The (112) face can be considered as composed of steps of (111) and (113) faces, the (122) and (133) of (111) and (011) faces. The orientation of the oxide on these faces seems to be controlled by these steps, specifically the (113) for the (112) face and the (111) for the (122) and (133) faces.

SUMMARY

The composition and structure of oxide films on single crystals of copper were studied for eight different crystal faces, using X-ray diffraction techniques. The effects of crystal face, temperature, pressure, oxide thickness, and contaminants were studied, using carefully prepared electropolished specimens.

Studies between 170° and 450°C showed that Cu_2O was the major oxide which was formed on all faces initially. CuO formed above a certain minimum oxide thickness, the value of which depended on crystal face and temperature.

The type of orientation (i.e., the major face of the oxide tending to be parallel to a particular substrate face) did not vary with temperature, pressure, or oxide thickness, but did vary with crystal face.

The degree of orientation varied with all the above variables. It was essentially constant (for a given face and given oxide thickness) with change in pressure above 200 mm of Hg; but below this, the degree of orientation increased markedly with decreasing pressure for all faces and at all temperatures studied. The degree of orientation of the oxide increased with increasing temperature in all cases, the amount of the increase being greater for oxidation at atmospheric pressure and large oxide thicknesses.

Oxide films formed at atmospheric pressure were highly oriented for the first 500 to 600 Å, but became disoriented with increasing thickness above this. Oxide films formed at pressures from 0.8 to 25 mm of Hg were highly oriented for all thicknesses up to 3000 to 5000 Å.

Contaminants in general caused a marked decrease in the amount of orientation of the oxide.

Four different classes of epitaxial relationships were found for Cu_2O on the eight crystal faces studied. The controlling factors in determining these orientations can be summarized as follows:

1. At least one pair of [110] directions (the closest-packed directions for both Cu and Cu_2O) must be parallel. This gives 18% misfit in one direction.

2. For low-index planes, a good fit (small misfit) between closely-packed rows of atoms is more

TABLE 3.

Crystal plane Cu	Parallel plane Cu_2O	Orientation class	Distance between closest-packed parallel rows of Cu atoms in boundary plane (in Å)		Misfit $\frac{B-A}{A}$ (%)
			Cu (A)	Cu_2O (B)	
(001)	(111)	I (A, B, C, C')	2.55	2.61	2
(111)	(111)	II (D), III (E)	2.21	2.61	18
(011)	(011)	II (D)	3.61	4.25	18
(012)	(012)	II (D)	4.03	4.75	18
(012)	(012)	III (E', E'')	3.29	3.88	18
(113)	(110)	IV (F)	4.23	4.25	0.5
(112)	(44$\bar{1}$)	IV (F)	6.25 12.50 ($2A$) 18.75 ($3A$)	17.27	— 38 −8
(122)	(47$\bar{4}$)	III (E)	7.65 15.31 ($2A$)	18.78	— 23

important than the requirement of parallelism of densely-packed planes. This is illustrated by the (110)Cu_2O//(113)Cu.

3. For high-index planes such as the (122) and (133), the amount of misfit in the interface plane is not important. The orientation is determined by the steps of which the face is composed, i.e., by the major faces near the high-index face. If there is a choice between (110) and (111) planes as the determining plane, the (111) seems most likely; and of the two orientations directed by the (111) plane, the non-parallel orientation seems to be the preferred one.

In general, CuO, when present, was polycrystalline and completely disoriented.

Consideration of these results in terms of the rates of oxidation on different crystal faces reveals one interesting correlation. Although the rates of oxidation of the (001) and (111) faces are considerably different, both faces have (111) planes of the oxide parallel to them. There are, however, four energetically equivalent orientations on the (001), whereas there are only two on the (111). Oxide on the (001) therefore shows more grain boundaries and the possibility of enhanced diffusion through the oxide. The slow-oxidizing (011) and (113) faces show only one orientation of the oxide. This may partially account for the large rate differences between different crystal faces.

ACKNOWLEDGMENT

This work was supported in part by the Office of Naval Research.

REFERENCES

1. C. A. MURISON, *Phil. Mag.*, **17**, 96 (1934).
2. G. D. PRESTON and L. L. BIRCUMSHAW, *Phil. Mag.*, **20**, 706 (1935).
3. H. DUNHOLTER and H. KERSTEN, *J. Applied Phys.*, **10**, 523 (1939).
4. C. G. CRUZAN and H. A. MILEY, *J. Applied Phys.*, **11**, 631 (1940).
5. E. A. GULBRANSEN and W. R. MCMILLAN, *J. Electrochm. Soc.*, **10**, 393 (1952).
6. H. FRISBY, *Compt. rend.*, **228**, 1291 (1949).
7. G. P. THOMSON, *Proc. Roy. Soc.* (London), **A133**, 1 (1931).
8. R. F. MEHL, E. L. MCCANDLESS, and F. N. RHINES, *Nature*, **134**, 1009 (1934).
9. P. A. THIESSEN and H. SCHÜTZA, *Z. anorg. u. allgem. Chem.*, **233**, 35 (1937).
10. T. YAMAGUTI, *Proc. Phys. Math. Soc. Japan*, **20**, 230 (1938).
11. C. F. ELAM, *Trans. Faraday Soc.*, **32**, 1604 (1936).
12. E. MENZEL, *Ann. Phys.* [Leipzig] **5**, 163 (1949).
13. F. W. YOUNG, Jr., J. V. CATHCART, and A. T. GWATHMEY; Submitted for publication this journal.
14. A. B. WINTERBOTTOM, *Trans. Faraday Soc.*, **42**, 487 (1946).
15. A. T. GWATHMEY and F. W. YOUNG, Jr., *Rev. Métallurgie*, **48**, 434 (1951).
16. H. E. SWANSON and R. K. FUYAT, National Bureau of Standards Circular 539, Vol. II, 23 (1953).

VOL.
4
1956

THE TEMPERATURE DEPENDENCE OF THE ELASTIC CONSTANTS OF GOLD-CADMIUM ALLOYS*

STANLEY ZIRINSKY†

The temperature dependence of the dynamic elastic constants (Moduli of Compliance, S_{11}, S_{12}, and S_{44}) of body-centered cubic Au-Cd alloys that undergo diffusionless phase change, has been determined as a function of composition variation within the beta phase, and heat treatment prior to measurement. The results are consistent by comparison with compressibility calculations and data available for an isomorphous material, beta brass. Derived quantities are similarly comparable. The abnormally high elastic shear anisotropy, $2(S_{11} - S_{12})/S_{44}$, increasing with decreasing temperature, leads to the consideration of an elastic shear anisotropy criterion for diffusionless transformation of body-centered cubic beta-phase alloys. 47.5 at. per cent Cd alloys water-quenched from 500°C and 550°C yield elastic constant data and a diffusionless transformation temperature consistent with that for a 50 at. per cent Cd alloy. An interpretation of the latter phenomena is offered, based upon the elastic interaction of quenched-in vacancies with neighboring metal ions.

L'INFLUENCE DE LA TEMPÉRATURE SUR LES CONSTANTES ÉLASTIQUES D'ALLIAGES OR-CADMIUM

La dépendance thermique des constantes d'élasticité dynamique ("moduli of compliance" S_{11}, S_{12}, S_{44}) des alliages or-cadmium (cubiques centrés) au cours d'une modification de phase s'effectuant sans diffusion, a été déterminée en fonction de la variation de composition en phase β et du traitement thermique antérieur à la mesure.

Les résultats sont en accord avec les calculs de compressibilité et les données connues pour un matériau isomorphe, le laiton β.

Une comparaison similaire peut être effectuée pour des grandeurs dérivées.

L'anisotropie de cisaillement $2(S_{11} - S_{12})/S_{44}$ anormalement élevée et augmentant lorsque la température décroit, conduit à considérer un critère d'anisotropie de cisaillement pour la transformation sans diffusion des alliages cubiques centrés à phase β.

Les alliages à pourcentage atomique de 47,5 de cadmium, trempés à l'eau à partir de 500–550°C présentent des constantes élastiques et une température de transformation (sans diffusion) en accord avec celles d'un même alliage à 50% de cadmium.

Une interprétation de ces derniers phénomènes est proposée sur la base de l'interaction élastique des lacunes conservées par trempe et des ions métalliques voisins.

DIE TEMPERATURABHÄNGIGKEIT DER ELASTISCHEN KONSTANTEN VON GOLD-CADMIUM-LEGIERUNGEN

An kubisch-raumzentrierten Au-Cd-Legierungen, die einer diffusionslosen Phasenumwandlung unterliegen, wurde die Temperaturabhängigkeit der dynamischen elastischen Konstanten (Elastizitätskoeffizienten S_{11}, S_{12}, S_{44}) als Funktion der Zusammensetzung im Bereich der Betaphase und in Abhängigkeit der vor der Messung vorgenommenen Wärmebehandlung bestimmt. Die Ergebnisse sind konsistent im Vergleich mit Berechnungen der Kompressibilität und vorhandenen Daten für ein isomorphes Material (Beta-Messing). Abgeleitete Grössen sind in ähnlicher Weise vergleichbar. Die abnormal grosse elastische Schub-Anisotropie, $2(S_{11} - S_{12})/S_{44}$, die mit abnehmender Temperatur zunimmt, führt zu Betrachtungen über ein auf der elastischen Schub-Anisotropie beruhendes Kriterium für die diffusionslose Umwandlung von Legierungen mit kubisch-raumzentrierter Beta-Phase. Von 500°C und 550°C in Wasser abgeschreckte Legierungen mit 47,5 Atom-Prozent Cd weisen Werte der elastischen Konstanten und eine Temperatur der diffusionslosen Umwandlung auf, die mit denjenigen für eine Legierung mit 50 Atom-Prozent Cd übereinstimmen. Diese zuletzt genannten Erscheinungen werden auf Grund der elastischen Wechselwirkung eingefrorener Leerstellen mit benachbarten Metallionen interpretiert.

INTRODUCTION

Interest in the elastic properties of body-centered cubic alloys has arisen from the results obtained for beta brass, which were obtained for the purpose of studying the influence of order-disorder changes upon the elastic properties. In the temperature range below that for completion of ordering, the positive temperature dependence of Young's modulus for most orientations was inverse to that considered normal for other cubic materials not undergoing any transitions.[1] The shear anisotropy, $2(S_{11} - S_{12})/S_{44}$, at room temperature[1, 2] was shown to be higher than that determined for any other cubic material.

The unusually high value for the body-centered cubic (110) [$\bar{1}$10] shear compliance modulus $2(S_{11} - S_{12})$,

* Received April 15, 1955; in revised form, July 18, 1955.

† Special Defense Projects Dept., General Electric Company, Schenectady, N.Y.

for beta brass and its positive temperature coefficient,[3] was interpreted in terms of the combination of the body-centered cubic structure and closed shell ions. An analogous physical model would be the zero resistance to a face diagonal shear of hard balls packed in a body-centered cubic structure.

The positive temperature coefficient[3] of E_{100} and E_{110} was shown to result from the contribution of the face diagonal shear compliance modulus, $2(S_{11} - S_{12})$. E_{111} has a negative temperature coefficient as a result of similar temperature coefficients for S_{44} and the compressibility, $3(S_{11} + 2S_{12})$.

These results were embodied by Zener[4] in a proposed mechanism for diffusionless transformation in materials body-centered cubic in their high-temperature phase. The phase change occurred upon cooling as a result of change in relative phase stability, which can be derived as a result of the lowering of the (110)[$\bar{1}$10] shear compliance modulus with decrease in temperature. These considerations led to the discovery of a low-temperature diffusionless transformation in lithium and Li-Mg alloys.[5]

Though beta brass (around 50-50 at. per cent) is highly anisotropic, the body-centered cubic phase is retained at all temperatures.[6] Beta-phase Au-Cd alloys are isomorphous to beta brass and do undergo diffusionless transformation. These alloys are convenient for study, because they transform close to room temperature, are reversible with little hysteresis, and no decomposition products are formed.[7]

VOL. 4 1956

EXPERIMENTAL PROCEDURE

A. *Crystal Preparation*

Ingots of 47.5 at. per cent Cd-Au and 50.0 at. per cent Cd-Au were prepared by melting accurately weighed quantities of 99.99 per cent Au (supplied by Baker and Co.) and 99.99 per cent Cd (supplied by N. J. Zinc Co.) in evacuated, sealed-off, uncoated clear fused quartz tubes. The high vapor pressure of the Cd necessitated the use of sealed-off tubes. Composition control was insured by observing weight losses after each melting operation. Single crystals of arbitrary and controlled orientation were grown from ingot sections, also in quartz, using a modified Bridgman technique.[8] The combination of a sharp temperature gradient and narrow liquidus region for the beta alloys favored crystals with little segregation and good structures. The orientations of the cube axis with reference to the crystal cylindrical axis were determined by obtaining back-reflection Laue patterns and mapping stereographically with the aid of a Greninger chart and Wulff net.[9]

Seeded crystals were grown with their cylindrical axis paralleled to the following three principal cube directions; [100], [110], [111]. The angle between the desired zone axis in the seed (which the crystal to be grown will follow), and the seed cylindrical axis, positioned the seed with regard to the ingot above it. A single bend in the container quartz tube plus proper rotational positioning of the seed fulfilled the above requirement. The tubing was placed in the furnace so that the ingot and only part of the seed melted, and then lowering yielded the desired results. Crystals obtained were within $\frac{1}{2}$ to 2° of the orientations desired. A drawback to this procedure is the possibility of obtaining pronounced lineage structures due to the wide solid-liquid interface at the melting zone. (Ordinarily, crystals are grown from a sharp tip to suppress multiple nucleation.) This can be avoided by placing a narrow restriction in the containing vessel just above the interface. The as-grown crystals were then annealed for 100 hours at 590°C, 20° below the melting-point, and then furnace-cooled.

B. *Method of Measurement*

The composite oscillator as originated by Quimby[10] and modified by Zacharias[11] was used to obtain the dynamic elastic constants. Determinations of Young's modulus for right-circular cylindrical single-crystal specimens were obtained in longitudinal oscillation, using Straubel cut-quartz drivers. Rigidity moduli of the same crystals were obtained, using torsional oscillation with "Y" cut-quartz circular cylinders. The quartz electrodes' arrangement, as devised by Giebe and Schiebe,[12] was modified to allow the use of the same dual electrode mount as that for the Straubel drivers.

The circuits used were adapted from those recommended by previous investigators.[22] A transitron-type oscillator[23] provided a stable variable-frequency oscillator for driving the composite oscillator. Auxiliary circuits allowed for resonance measurements by means of impedance variation and accurate frequency determination, using an audio beat-note technique. Fig. 1 indicates the circuits used in the investigation.

A six-position vertical mount was used for the composite oscillators, this being surrounded by a $\frac{1}{16}$-in.-wall copper tube, and above it an independently controlled-resistance wound heater. Temperatures were measured by a Cromel-Alumel thermocouple adjacent to the mount, this being previously

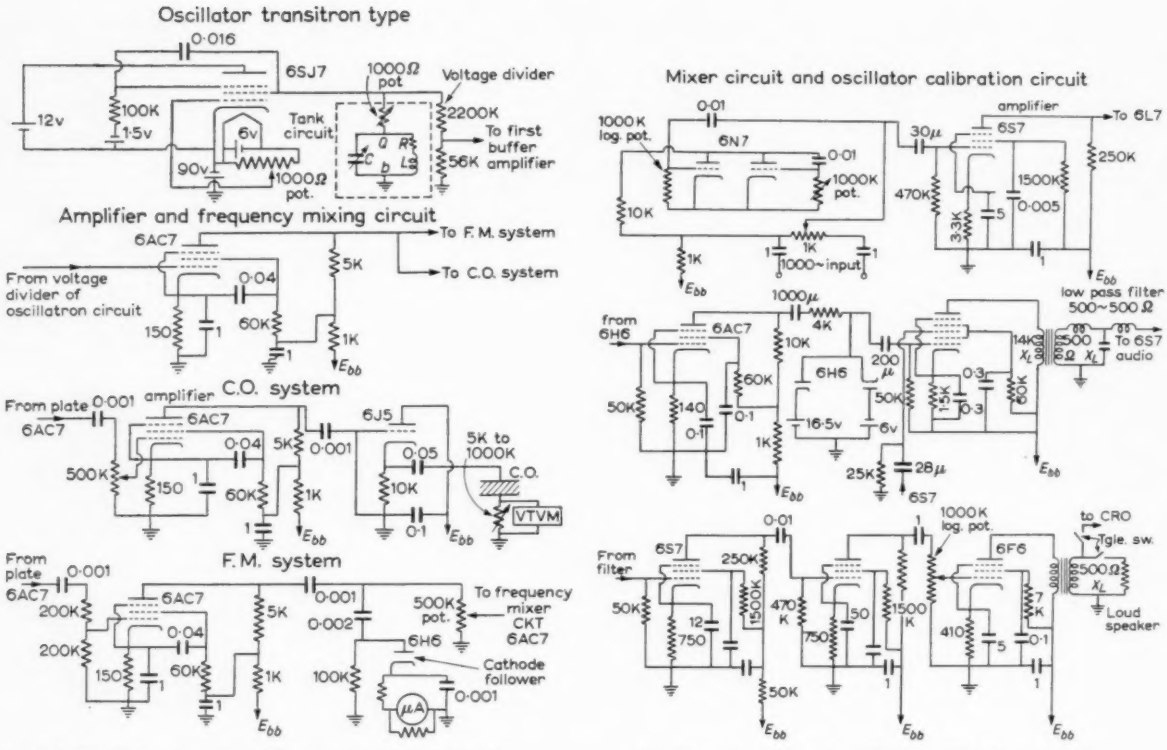

(a) Oscillator circuit and frequency mixing circuit
legend: F.M.—frequency measurement circuit,
C.O.—quartz-specimen composite oscillator,
VTVM—vacuum-tube voltmeter,
CRO—cathode-ray oscilloscope.

(b) Mixer circuit and oscillator calibration circuit.

FIG. 1. Electronic circuit for composite oscillator system.

calibrated by dummy specimens having thermocouples welded on, placed in the positions of the composite oscillators. Surrounding this assembly was an enclosed 4-in. diameter Pyrex tube providing both evacuation and argon-atmosphere control within, the entire assembly suspended vertically in a resistance wound-tube furnace.

Thermal expansion data were obtained experimentally both by X-ray technique and fused-quartz dilatometer. The former involved the determination of isotherms of lattice parameter as a function of composition. These data were obtained using a modified back-reflection Laue technique, whereby a particular plane reflection yielding a very large Bragg angle was selected and the interplanar distance measured. Excellent agreement between the two methods was obtained. The lattice parameters were also used for non-destructive composition analysis of the specimens.

Suitable bonding of the quartz and specimen was obtained with the use of mixtures of silicone resins, properly cured and baked prior to measurement.

RESULTS

A. *X-ray and Thermal Expansion Measurements*

Within the composition range studied (47.00 to 50.25 at. per cent Cd), the dilatometric studies indicated a linear thermal expansion. The dilatometer was checked by calibration, using pure copper, the data obtained agreeing very well with values in the literature. The linearity and values for thermal expansion also agreed fairly well with data obtained using the X-ray lattice parameter determination:

TABLE 1. Coefficient of thermal expansion as a function of composition for Au-Cd

Specimen composition	(units of) (10^{-6}/°C) Dilatometer	(units of) (10^{-6}/°C) X-ray	% difference
47.00 at. per cent Cd	20.7 ± 0.3	20.3 ± 0.8	2
48.75 at. per cent Cd	21.4 ± 0.2	21.7 ± 0.8	1.4
50.25 at. per cent Cd	21.8 ± 0.3	21.2 ± 0.8	2.8

The difference between these independent determinations lies within the individual errors. Fig. 2

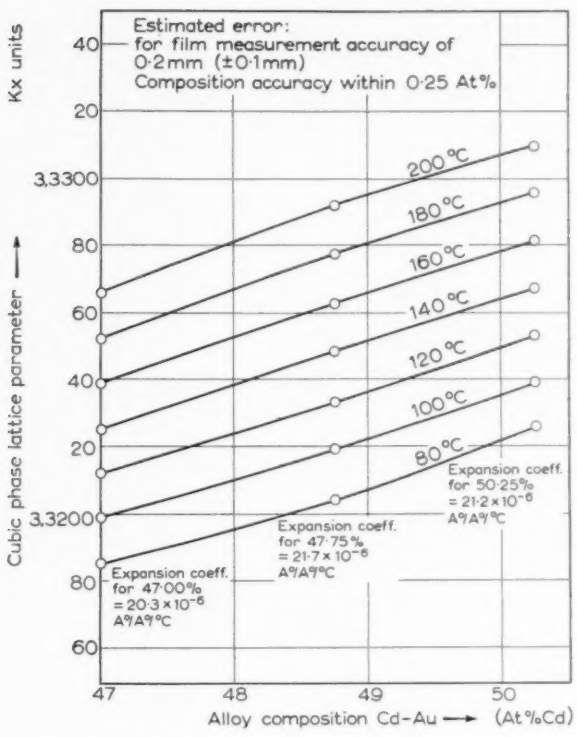

FIG. 2. Variation of lattice parameter of cubic phase Cd-Au alloys for various temperatures (tungsten $L\alpha_2$ radiation reflected from (420) plane).

shows the isothermal variation of lattice parameter with composition.

B. *Elastic Constants*:

The standard wave-velocity equation is used to determine the Young's and free rigidity moduli respectively,

$$E = (2/n)^2 \rho_a L_a^2 (L_a/L_T) f_L^2 \left(1 + \frac{n^2\pi^2\bar{\sigma}^2 r^2}{2L_a^2}\right) \quad (1)$$

$$G_F = (2/n)^2 \rho a L_a^2 (L_a/L_T) f_T^2 \quad (2)$$

Where ρ_a and L_a are the density and length at the temperatures of diffusionless transformation, L_T the length at the temperature of measurement, n the number of half-waves in the specimen, $\bar{\sigma}$ the average Poisson's ratio, r the cross-sectional radius, $f_{L,T}$ the measured resonant frequency for longitudinal and torsional oscillations, respectively.

It may be pointed out that only crystals with symmetrical orientations were used for torsional measurements to avoid erroneous determinations due to the bending-torsion interaction.[13]

TABLE 2. Temperature dependence of elastic constants and derived parameters (all moduli in units of 10^{-12} cm²/dyne).

T°C	$S_{11} = 1/E_{100}$	$1/E_{111}$	$S_{44} = 1/G_{100}$	$-S_{12}$	k
47.5 at. per cent Cd					
50	11.24	0.9024	2.363	5.446	1.032
52.5	11.15	0.9031	2.363	5.404	1.038
55	11.07	0.9021	2.387	5.364	1.029
57.5	10.99	0.9021	2.364	5.323	1.028
60	10.91	0.9021	2.364	5.284	1.026
65	10.76	0.9022	2.365	5.210	1.024
70	10.61	0.9027	2.366	5.136	1.026
75	10.47	0.9033	2.368	5.065	1.026
80	10.35	0.9038	2.370	5.003	1.023
90	10.12	0.9058	2.376	4.889	1.024
100	9.892	0.9076	2.383	4.776	1.021
110	9.681	0.9097	2.391	4.672	1.014
120	9.481	0.9125	2.401	4.572	1.011
130	9.292	0.9155	2.410	4.478	1.011
140	9.122	0.9189	2.420	4.393	1.012
160	8.809	0.9260	2.440	4.236	1.013
180	8.536	0.9333	2.462	4.099	1.014
200	8.310	0.9411	2.485	3.986	1.016
220	8.106	0.9503	2.510	3.883	1.024
240	7.942	0.9595	2.537	3.800	1.026
260	7.785	0.9685	2.564	3.722	1.024
280	7.626	0.9781	2.592	3.642	1.027
300	7.484	0.9881	2.621	3.570	1.031
320	7.365	0.9990	2.650	3.509	1.041
340	7.280	1.011	2.680	3.464	1.056
360	7.234	1.023	2.709	3.438	1.076
370	7.229	1.029	2.723	3.433	1.089
50 at. per cent Cd					
30	8.919	0.8817	2.275	4.275	1.110
32.5	8.863	0.8820	2.276	4.247	1.110
35	8.803	0.8824	2.277	4.217	1.110
37.5	8.747	0.8828	2.279	4.189	1.109
40	8.692	0.8832	2.280	4.161	1.109
45	8.589	0.8842	2.283	4.110	1.109
50	8.491	0.8851	2.288	4.060	1.111
60	8.311	0.8871	2.297	3.973	1.094
70	8.148	0.8897	2.304	3.892	1.091
80	7.999	0.8923	2.316	3.818	1.088
90	7.864	0.8954	2.325	3.751	1.085
100	7.744	0.8984	2.334	3.691	1.084
120	7.536	0.9044	2.353	3.588	1.080
140	7.353	0.9120	2.375	3.496	1.084
160	7.185	0.9198	2.397	3.412	1.087
180	7.039	0.9287	2.420	3.337	1.098
200	6.908	0.9382	2.444	3.269	1.111
220	6.787	0.9488	2.468	3.205	1.134
240	6.676	0.9593	2.493	3.146	1.154
260	6.574	0.9698	2.520	3.094	1.167
280	6.482	0.9817	2.547	3.042	1.195
300	6.397	0.9937	2.574	2.995	1.221
320	6.318	1.006	2.601	2.951	1.247
340	6.249	1.018	2.630	2.913	1.270
360	6.196	1.030	2.658	2.882	1.295
370	6.183	1.036	2.672	2.873	1.310

The elastic constants, S_{11}, S_{12}, and S_{44}, are related to Young's and the rigidity modulus by

$$1/E = S_{11} - 2\,.\,SF(\gamma) \quad (3)$$

$$1/G_F = S_{44} + 4S\,.\,F(\gamma) \quad (4)$$

where $S = S_{11} - S_{12} - \frac{1}{2}S_{44}$

and $F(\gamma) = \gamma_1^2\gamma_2^2 + \gamma_2^2\gamma_3^2 + \gamma_1^2\gamma_3^2$

VOL. 4 1956

where the γ's are the direction cosines of the specimen cylinder axis with respect to the crystallographic axes. The elastic moduli, C_{11}, C_{12}, C_{44}, are related to the principal moduli of compliance by

$$C_{11} = (S_{11} + S_{12})/(S_{11} - S_{12})(S_{11} + 2S_{12}) \quad (5)$$

$$C_{12} = -S_{12}/(S_{11} - S_{12})(S_{11} + 2S_{12}) \quad (6)$$

$$C_{44} = 1/S_{44} \quad (7)$$

Simplicity of interpretation of relations (5) and (6) in terms of experimentally derived elastic-modulus data is not easily apparent, but suitable combinations of the principal elastic moduli are more useful as follows,

$$(C_{11} - C_{12}) = 1/(S_{11} - S_{12}) \quad (5a)$$

$$(C_{11} + 2C_{12}) = 1/(S_{11} + 2S_{12}) \quad (6a)$$

As previously indicated, equations (5a) and (7) are related to elastic shear moduli in the (110)[$\bar{1}$10] and (100)[0$\bar{1}$0] plane and direction respectively, while equation (6a) is related to the compressibility.

The elastic-constant data, as calculated by a least-squares method for each temperature of measurement, from the individual specimens', Young's, and rigidity-modulus determinations, are presented along with derived elastic parameters in Table 2 and plotted in Figs. 3 to 5. The percentage error for the elastic constants is estimated to be under 0.8%.

C. *Additional Modulus Measurements*

The data presented above are for annealed and slow-cooled material. The same 47.5 at. per cent Cd specimens were reannealed for five minutes in a salt-pot at 500°C, 550°C, and rapidly water-quenched. Subsequent elastic-modulus measurements were obtained from 30°C to 100°C, using Duco cement bonds between the quartz drivers and specimens. Some of the elastic-modulus data subsequently obtained are presented in Table 4. The specimens reverted to their normal behavior by annealing between 125°C to 150°C for a half-hour. The quenching

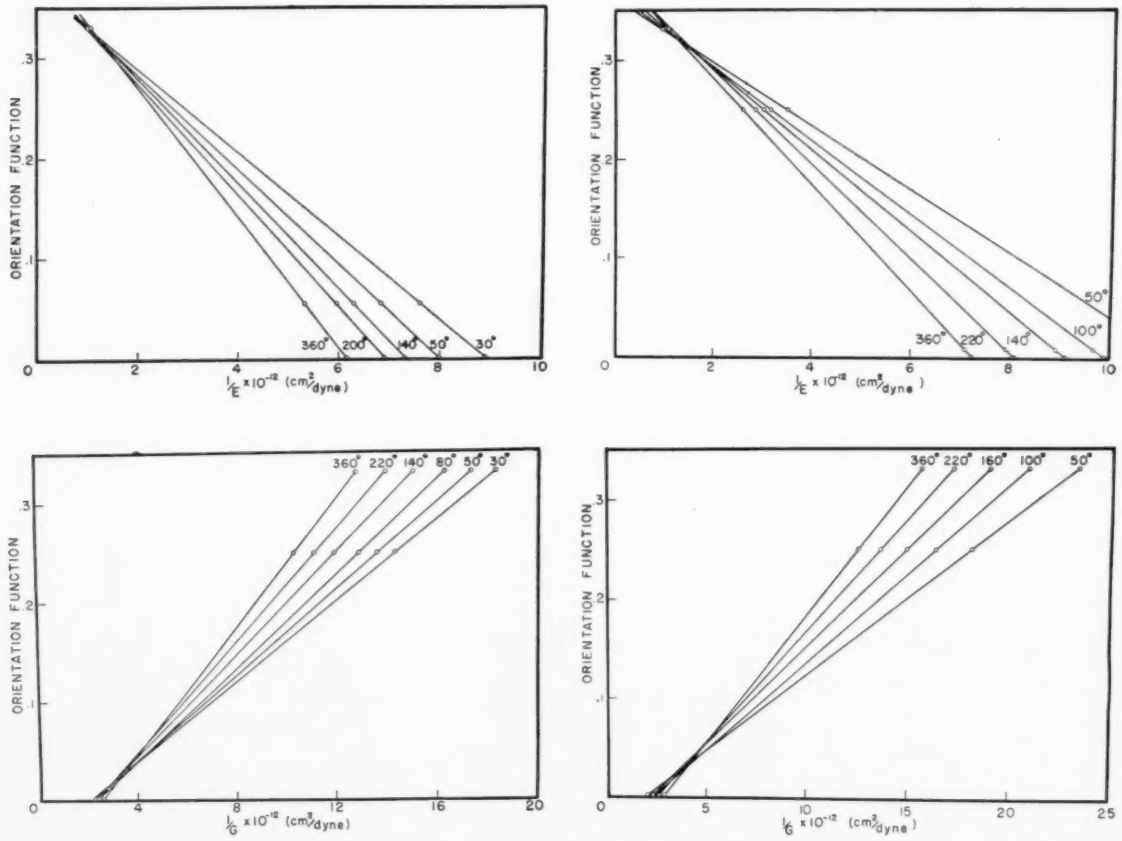

FIG. 3. Reciprocal Young's and rigidity moduli versus the cubic orientation function of beta Au-Cd alloys:
(a) Upper left and upper right—50 at. per cent Cd-Au alloys.
(b) Lower left and lower right—47.5 at per cent Cd-Au alloys.
These are the reciprocal moduli calculated from equations (3) and (4) where E, G_γ are obtained from the experimental frequency data using equations (1) and (2), and orientation function as determined experimentally from the crystal orientation determination.

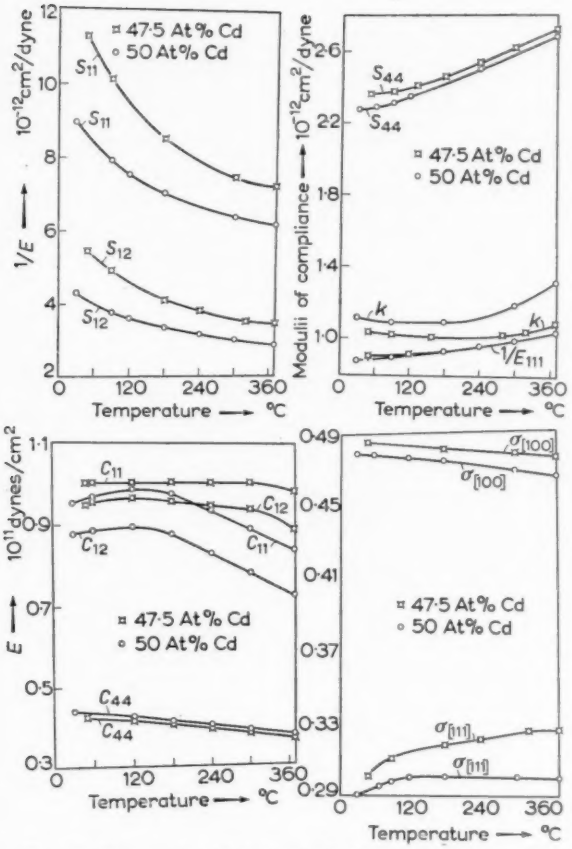

FIG. 4. Measured and derived elastic parameters of beta Au-Cd alloys. $\Delta_{(100)}$ and $\Delta_{(111)}$ represent the Poisson's ratio for the indicated single crystal axial orientations.

effect was found to be reproducible with subsequent similar heat treatments.

DISCUSSION

The temperature variation of some of the elastic parameters parallel that for beta brass.[2] Zener[3] has shown that for this type of alloy, a linear increase with temperature is to be expected for S_{44} and k. No immediate explanation is available for the slight deviations present at temperatures in the proximity of the transformation. Lattice parameter measurements indicated no anomalous change in this region.

The reliability of the compressibility data is estimated by comparison: (1) with beta-brass data, determined as in this investigation, (2) a calculation based upon data determined directly (no direct determination upon Au-Cd has been made). Bridgman has attempted the prediction of compressibilities based upon the following relationship.[19]

$$k_{A_mB_n} = \frac{m \cdot \text{at. vol. } A \cdot k_A + n \cdot \text{at. vol. } B \cdot k_B}{m \cdot \text{at. vol. } A + n \cdot \text{at. vol. } B} \quad (8)$$

k_A, k_B, = compressibility of indicated component, at. vol. A, B = atomic volume of the indicated component

Bridgman used the above values as obtained experimentally for the free state in using equation (8). Very poor correlation was obtained for the calculated compressibilities as compared to the experimentally determined compressibilities. Weibke[14] used Bridgman's relation, but made certain assumptions concerning changes in the compressibilities and atomic volumes of the components in the combined state. Excellent correlation between compressibilities calculated by Weibke and those determined experimentally was then obtained. Similar calculations for Au-Cd alloys were then obtained, using values published by Weibke. The results in Table 3 indicate the data to be reliable within the order of magnitude of error of the experimental data. This is also an indication of the absolute reliability of the elastic modulus determination.

Comparison of the elastic properties between different systems is simplified by the use of dimensionless ratios such as E_{111}/E_{100} and $A = 2(S_{11} - S_{12})/S_{44}$. These are indicative of the elastic anisotropy of the

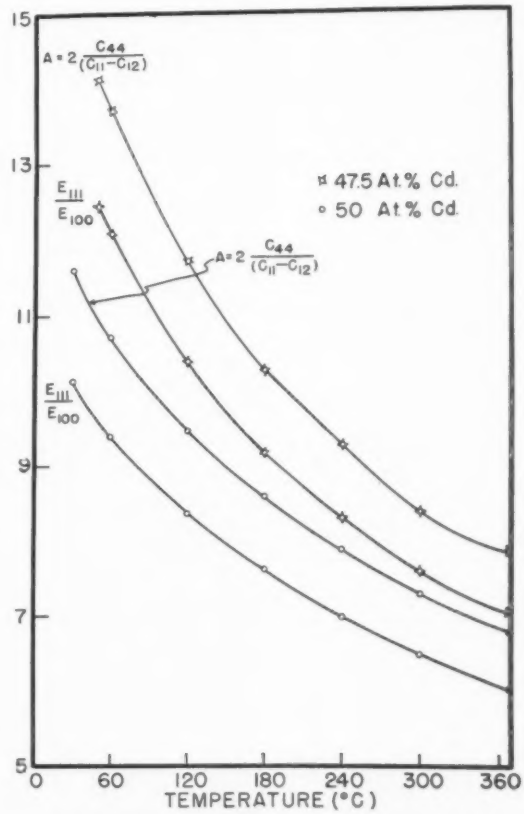

FIG. 5. Dimensionless ratios of elastic parameters of Au-Cd alloys.

TABLE 3. Calculated and experimentally determined compressibilities (units of 10^{-12} cm²/dyne)

Alloy	$3(S_{11} + 2S_{12})$	Equation (8)	Experimental	Per cent difference
CuZn[14]		0.938	0.948	1.0
CuZn[14]		0.942	0.913	2.0
55 at. per cent CuZn[1]	0.927	0.924		0.3
52 at. per cent CuZn[2]	0.861	0.808		6.3
47.5 at. per cent CdAu	1.03	0.998		5.0
50 at. per cent CdAu	1.11	1.02		8.5

material. Examination of Table 4 shows that for the lowest temperature of measurement of elastic properties of beta brass, which does not go through a diffusionless transformation, the degree of elastic anisotropy does not reach that obtained for Au-Cd alloys at their intervals of transformation. This gives rise to the possibility of pronounced elastic anisotropy as a principal criterion for structural instability resulting in diffusionless transformation for body-centered cubic materials. This argument does not necessarily imply a particular mechanism for transformation.

As discussed previously, Zener[3] has explained the low value for the (110)[$\bar{1}$10] shear modulus. Fuchs[16] considered interatomic electrostatic and exchange forces, and calculated their effect on the cubic elastic constants. The closed ion shells will result in a negative contribution to the shear constant, compensating somewhat for the positive electrostatic contribution, with a result that all beta-type alloys with closed inner shells should have unusually low body-centered cubic-face diagonal-shear moduli.

Jones[17] has quantitatively shown, for the case of beta brass, that its (110)[$\bar{1}$10] shear modulus is positive as a result of the stabilizing influence of a positive-energy contribution due to the interaction between the Fermi energy of the valence electrons and the first (110) Brillouin zone. His stabilization criterion can be applied for a comparison of the transformation characteristics of the Cu-Zn and Au-Cd alloys as a function of composition within the beta-phase region. Similar data for other isomorphous alloys in the periodic subgroups Ib and IIb are not available.

Comparison of (1) with (2) and (3) with (4) shows that a lower electron/atom ratio yields a greater tendency toward transformation. With a lower valence electron density, the Fermi energy is lowered,[18] thereby lessening the positive-energy contribution to the (110)[$\bar{1}$10] shear modulus, causing its value to be lowered. Arguments based upon differences in behavior due to changes in lattice parameter are not easily interpretable, because both the Fermi energy and Brillouin-zone energy vary as the reciprocal of the lattice parameter squared.

The data for quenched 47.5 at. per cent Cd show that, with lowering of the temperature of transformation, elastic moduli are obtained similar to that for the 50 at. per cent Cd alloy. No direct explanation for the cause of this behavior is as yet available. Arguments based upon a possible suppression of ordering by the quench are untenable, because these would require the reverse of the modulus changes observed.[15] Metallographic and X-ray investigations covering the range from 47 to

TABLE 4. Comparison of elastic properties of beta brass and gold-cadmium alloys

	Beta brass			47.5 at. per cent Cd-Au‡			50 at. per cent Cd-Au‡ annealed
	Lazarus[2]	Rhinehart[1]	Artman[1]	Annealed	Quenched from 500°C	Quenched from 550°C	
T°C	R.T.	R.T.	R.T.	50	30	28	30
E_{111}*	20.0	21.1	18.2	11.1	11.1	11.1	11.3
E_{100}*	2.84	2.58	2.44	0.890	1.06	1.10	1.12
E_{111}/E_{100}	7.04	8.17	7.45	12.5	10.5	10.1	10.1
$\frac{2(S_{11} - S_{12})}{S_{44}}$	8.47	—	8.93	14.1	12.0	11.6	11.6
T°C	−200	−200	−200				
E_{111}*	22.0	23.3	23.2				
E_{100}*	2.70	2.45	2.32				
E_{111}/E_{100}	8.15	9.50	8.55				
$\frac{2(S_{11} - S_{12})}{S_{44}}$	10.0	—	10.4				

* Units of $E \times 10^{11}$ dynes/cm².

† Rhinehart's E_{111}/E_{100} does not compare favorably with those of Lazarus and Artman. His temperature dependence checks favorably, so his low-temperature data can be used for low-temperature extrapolation of the other data.

‡ Temperatures for Au-Cd are those prior to transformation.

TABLE 5. Comparison of the transformation characteristics of the Cu-Zn and Au-Cd systems

System	Atomic comp.	Transformation temperature °C	Transformation product
(1) Cu-Zn	50% Cu	None	None
(2) Cu-Zn*	62.5% Cu	−14	Face-centered tetragonal (revers.)
(3) Au-Cd	50% Cd	30	Face-centered tetragonal (revers.)
(4) Au-Cd	47.5% Cd	50	Orthorhombic (reversible)

* Homogeneous beta is retained at low temperatures only by rapid quenching from 900°C.

50 at. per cent Cd have not revealed the presence of an additional phase.

A possible alternative explanation for the anomalous data for quenched 47.5 at. per cent Cd alloys in Table 4 would be to consider the influence of the presence of a non-equilibrium vacancy concentration obtained during the quenching operation. Indirect physical evidence for the presence of vacancies is indicated by a very rapid relaxation of the abnormal behavior to normal behavior at around 100°C. X-ray measurements upon similar alloys undergoing similar quenching treatments, by J. Intrater of Rutgers University (results to be published), have also been interpreted in terms of the quenching in of a non-equilibrium vacancy concentration.

An accurate estimate of the high-temperature equilibrium concentration of vacancies for Au-Cd is not available, but estimates for other materials have been given, ranging from $10^{-4}\%$[19] to as high as 0.4%[20]. An interpretation of the elastic interactions can be made whereby the vacancies take on the properties of cadmium ions, because it would be expected that the mutual repulsion due to ion overlap, from the ions neighboring the vacancy, would compress the vacancies to a smaller volume than that available for either of the metal ions. Since it is well established that doubly-charged ions are smaller than singly-charged ions,[21] then the cadmium-ions properties are assumed. This will yield elastic property changes in the direction indicated experimentally.

This admittedly very rough picture has its obvious faults, such as the wide discrepancy in estimated vacancy concentration versus the actual apparent composition shift indicated experimentally, and that the excessive distortion of the ion shells around a vacancy could conceivably either increase the ion-exchange repulsion or yield a positive effect due to positive quadrupole interactions.

ACKNOWLEDGMENTS

This paper constitutes part of a thesis submitted in partial fulfillment of requirements for the degree of Doctor of Philosophy to the Graduate Faculty of Columbia University, N.Y.C.

This work was supported jointly by the United States Atomic Energy Commission (Contract No. At(30-1)-904), and the office of Ordnance Research, U.S. Army (Contract DA-30-069-ORD-59), under the guidance of Dr. T. A. Read, whose maintained interest and encouragement is appreciated.

REFERENCES

1. R. A. ARTMAN, *J. Appl. Phys.*, **23,** No. 4, 470 (1952); J. S. RHINEHART, *Phys. Rev.*, **58,** p. 365 (1940); **59,** p. 308 (1941).
2. D. LAZARUS, *Phys. Rev.*, **74,** 1726 (1948); **76,** 547 (1949).
3. C. ZENER, *Phys. Rev.*, **71,** 846 (1947).
4. C. ZENER, *Elasticity and Anelasticity of Metals*, U. of Chi. Press, 1948, Chap. 4.
5. C. S. BARRETT, *Phys. Rev.*, **72,** 245 (1947).
6. Cu-Zn in the beta range (about 47 to 50 at. per cent Zn) will not transform regardless of the temperature cooled to, but an alloy with 62.5 at. per cent Cu when quenched to retain all beta, will show diffusionless transformation at −14°C. See: A. B. GRENINGER and V. G. MOORADIAN, *Trans. Amer. Inst. Metall. Engrs.*, **128,** 337 (1938).
7. L. C. CHANG and T. A. READ, *Trans. Amer. Inst. Metall. Engrs.*, **191,** 47 (1951).
8. M. BURKHART, Ph.D. thesis, Columbia U., 1953.
9. C. S. BARRETT, *The Structure of Metals*, McGraw-Hill, N.Y.
10. S. L. QUIMBY, *Phys. Rev.*, **25,** 558 (1925).
11. J. ZACHARIAS, *Phys. Rev.*, **44,** 116 (1933).
12. GIEBE and SCHIEBE, *Z. Phys.*, **33,** 760 (1925).
13. W. F. BROWN, JR., *Phys. Rev.*, **58,** 998 (1940).
14. F. WEIBKE, *Z. Metall.*, **30,** 322 (1938).
15. Y. SHIBYYA, Report No. 527, Japanese Research Inst. for Metals (1949).
16. K. FUCHS, *Proc. Roy. Soc.*, **A151,** 585 (1935); **153,** 622 (1936).
17. H. JONES, *Phil. Mag.*, **43,** 105 (1952).
18. Using the Sommerfeld relation:
$$\varepsilon_{\text{Fermi}} = \frac{h^2}{2m^*}\left(\frac{3n_0}{8\pi}\right)^{2/3}$$
where n_0 is the electron/atom ratio
it should be noted that "m^*" is an "effective" electron mass and is constant only in the case of a free electron.
19. N. M. NACHTRIEB and G. S. HANDLER, *Acta Met.*, **2,** 800 (1954).
20. C. J. MEECHAN and R. R. EGGLESTON, *Acta Met.*, **2,** 683 (1954).
21. J. R. NEIGHBORS and C. S. SMITH, *Acta Met.*, **2,** 595 (1954).
22. T. A. READ, *Phys. Rev.*, **48,** 371 (1940).
23. C. BRUNETTI, *Proc. Inst. Radio Engrs.*, **27,** 88 (1939).

VOL. 4 1956

STRUCTURAL RELATIONSHIPS BETWEEN INTERMETALLIC COMPOUNDS*

P. J. BLACK†

Structural features of aluminum-rich transition metal compounds are correlated and classified. They all possess, in common with structures involving other elements of groups IIIB and IVB, a polyhedral grouping of electronegative atoms around transition metal atoms, but they have a distinctive place in a broader scheme of compounds, because the polyhedra are 9- or 10-fold instead of 8-fold. The linking of such polyhedra gives a three-dimensional pattern which can be built up from characteristic plane patterns, so that structures can be simply described in terms of sequences of these patterns. The co-ordination of transition metal atoms is not controlled by size factors alone, and in the aluminum-rich structures it shows a trend from ten neighbors for manganese to eight for nickel and copper.

RELATIONS STRUCTURALES ENTRE COMPOSÉS INTERMÉTALLIQUES

Les caractères structuraux des composés de métaux de transition riches en aluminium sont comparés et classés. Ils présentent tous, à côté de structures comprenant d'autres éléments des groupes IIIB et IVB, un groupement polyédrique d'atomes électronégatifs autour des atomes du métal de transition, mais ils occupent une place différente dans une classification plus large des composés, car ces polyèdres sont d'ordre 9 ou 10 au lieu d'ordre 8.

L'assemblage de tels polyèdres conduit à un réseau tridimensionnel qui peut être construit à partir de réseaux plans caractéristiques, si bien que ces structures peuvent être simplement décrites comme une séquence de tels réseaux plans.

La coordination des atomes de transition n'est pas uniquement contrôlée par le facteur de taille seulement et pour les structures riches en aluminium et elle montre une évolution de 10 voisins pour le manganèse vers 8 pour le nickel et le cuivre.

STRUKTURELLE BEZIEHUNGEN ZWISCHEN INTERMETALLISCHEN VERBINDUNGEN

Strukturelle Erscheinungen an aluminiumreichen Verbindungen von Übergangsmetallen werden miteinander in Beziehung gebracht und klassifiziert. Alle diese Verbindungen zeigen ebenso wie Strukturen, bei denen andere Elemente der Gruppen IIIB und IVB beteiligt sind, eine durch Polyeder zu beschreibende Gruppierung der elektronegativen Atome um die Übergangsmetallatome herum. Sie nehmen jedoch eine ganz bestimmte Stellung innerhalb einer umfassenderen Ordnung der Verbindung insofern ein, als ihnen neun- oder zehnflächige Polyeder entsprechen statt achtflächiger. Durch Aneinanderfügen derartiger Polyeder ergibt sich eine dreidimensionale Anordnung, die aus charakteristischen ebenen Mustern aufgebaut werden kann. Die Strukturen können somit einfach durch die Aufeinanderfolge solcher Muster beschrieben werden. Die Koordination der Übergangsmetallatome wird nicht allein durch die Grössenverhältnisse bestimmt; sie zeigt bei den aluminiumreichen Strukturen einen Gang von zehn Nachbarn bei Magnesium, zu acht Nachbarn bei Nickel und Kupfer.

1. INTRODUCTION

For many classes of compounds, the geometrical features of different structures can be correlated and explained by means of rules which have an established theoretical basis. Amongst intermetallic compounds, however, there is little clarity or simplicity. For between two main groups of electron compounds and normal valency compounds, each of which groups is characterized by a few relatively simple structures adopted by many different compounds, is found a large number of compounds with many different and often complicated structures for which there is little or no theoretical explanation. It is generally supposed that such compounds represent a type of binding intermediate between the metallic and the homopolar or ionic, and that this fact, together with the varying size factors involved, accounts for their diversity and complexity (see, e.g., Hume-Rothery and Raynor[1]).

The primary aim of this paper is to consider the structures of Al-rich compounds of the transition metals from Mn to Ni. As a preliminary to any comprehensive theory of their formation it is necessary to compare and correlate the known features of their structures and to attempt to build an empirical scheme to relate or classify them. As soon as some progress has been made in this direction, it is of interest to examine other types of compound with respect to this scheme. For this reason, compounds of transition metals with other electronegative elements‡ and of the noble metals with electronegative elements, will also be considered.

The second section of this paper will consist of a

* Received August 11, 1955.

† Crystallographic Laboratory, Cavendish Laboratory, Cambridge, England. Royal Society Mr. and Mrs. John Jaffe Donation Student.

‡ This term is used in this paper to denote Al and elements of groups IIIB and IVB.

VOL 4 195

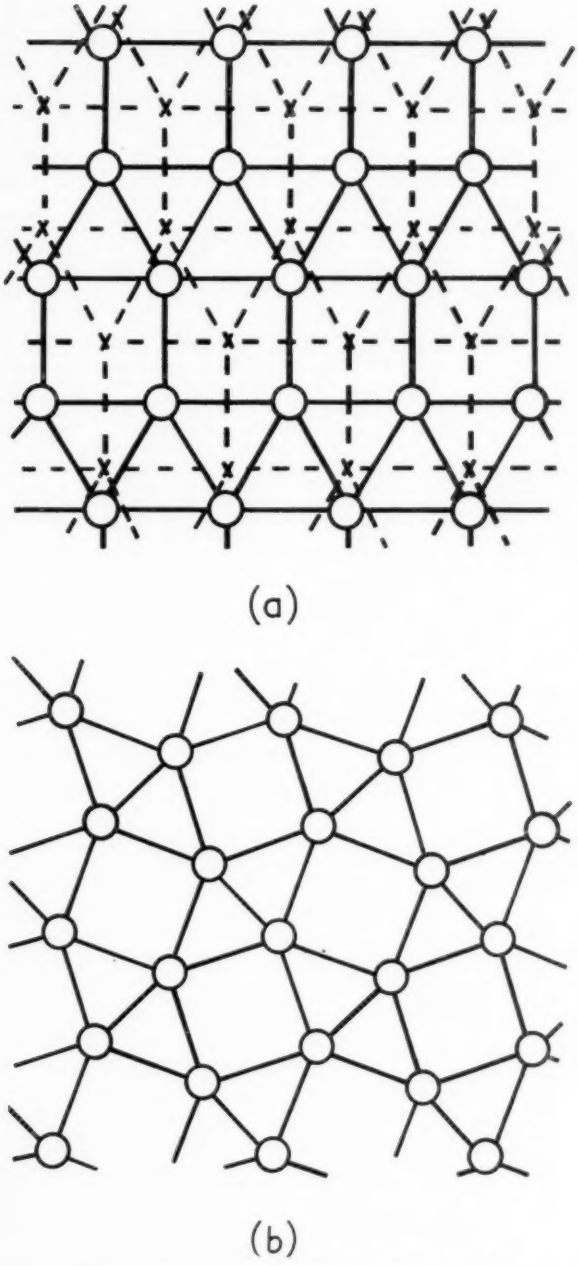

FIG. 1. Five-connected square-triangle arrays:

(a) Successive (full lines and broken lines) layers of the (10$\bar{1}$1) type of a close-packed hexagonal structure. They are not quite flat in the structure.

(b) Al atoms at $z = 0$ in $CuAl_2(\theta)$. This is an A-type layer.

systematic description of structures which hitherto have not been considered (*qua* structures) in relationship to one another. This section will be concerned with the overall pattern of the structures, whilst the third and fourth sections will deal with the most prominent aspect of their first-order co-ordinations, the polyhedral co-ordination of the transition-metal atoms.

Previous discussions of the Al-rich compounds have been concerned with their Brillouin-zone properties, the electron absorption behavior of transition metals, and the peculiarities in interatomic distances.[2, 3, 4, 5] It cannot be said that these features have indicated any satisfactory general theory, so that, with the accumulation of structural data, it has become both possible and necessary to collect and correlate some of the structural effects that such a theory must explain.

2. THE STRUCTURAL PATTERNS

It is observed that in all of these compounds the T.M.* atoms are surrounded by polyhedra of 8, 9, or 10 electronegative atoms. Two modes of geometrical description will be considered here. The first is constructed with respect to the different modes of linking of such polyhedra, the second in terms of the patterns of planes of electronegative atoms.

One might expect *a priori* that the Al-rich structures would contain layers of Al atoms corresponding to some form of close packing of the Al atoms. If a condition is imposed that a sequence of these layers must build up suitable sites for the T.M.'s, then close-packed ((111) of f.c.c.) layers might be expected to give high–co-ordination sites, whilst, for the 8– or 9–co-ordinations, layers which are square arrays ((100) of f.c.c. and b.c.c.) or a linking of squares and triangles (Fig. 1a) might be more suitable. This can be illustrated by the example of $CuAl_2$ (θ-phase[6]), for which the plan of one cell in projection is shown in Fig. 2. The plan of Al atoms in one plane, which is

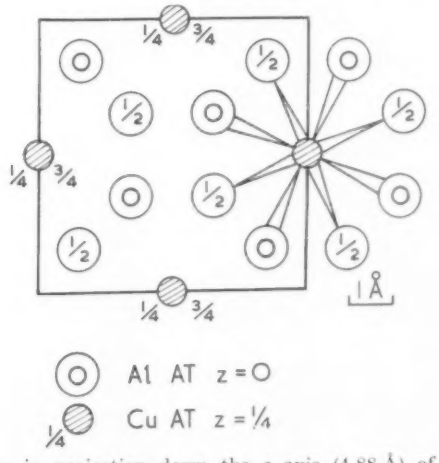

FIG. 2. Plan in projection down the c axis (4.88 Å) of the $CuAl_2$-θ structure [6]. The Al-neighbors of one Cu atom are shown.

* The abbreviation T.M. will be used for transition metal.

shown in Fig. 1(b), may be described as a collapsed-square array.[7] Cu atoms are placed over the square gaps and the next Al layer is the same pattern translated by one-half of the face diagonal. A layer having the pattern of Fig. 1(b) may be called an A layer, and in $CuAl_2$ the A–$A_{\frac{1}{2}\frac{1}{2}}$–$A$ sequence forms 8-fold polyhedra for the (smaller) Cu atoms placed between the squares of successive layers. Table 1 is a list of structures which may be described by such sequences. In this table, a simple square array is called a B-type layer. Corresponding relationships between the unit cells of such structures can easily be explained and may be useful in considering unknown structures.

The data of Table 1 will be discussed in the following paragraphs, in order to relate them to the polyhedral type of description.

(i) In $CuAl_2$, 8-fold polyhedra share faces, with their central Cu atoms in contact, to form continuous chains along the c direction. In the a-b plane, each pair in contact has one edge in common (see Fig. 3a).

(ii) $PtPb_4$ is the same as $CuAl_2$ with every other polyhedron centre along the c direction vacant, so that Pt atoms are not in contact.

(iii) δ(AlFeSi) is a succession of (a) $CuAl_2$-type sections followed by (b) directly superposed A layers. The latter give cubic 8-fold gaps in which the Si atom is fitted, so that each Fe in the 8-fold gap of (a) also has two silicon neighbors.*

(iv) $PtSn_4$ contains $CuAl_2$-type layers of polyhedra, but these are separated in the c direction and each layer shifted by $a/2$ with respect to its neighbors, so that there is no contact of Pt atoms.

(v) $CoGe_2$ builds 8-fold polyhedra between the squares of A and (expanded) B layers and is a succession of $CuAl_2$ and CaF_2 type stacking.

(vi) Both CaF_2 and Ni_2Al_3 can be regarded as CsCl-type arrangements with ordered vacancies.

(vii) In Co_2Al_9, the sequence B–A–$B_{\frac{1}{2}}{}^{45}$ builds a 9-fold polyhedron by the sequence of a square in B, a larger square in A (cf. $CoGe_2$) and a single point of $B_{\frac{1}{2}}{}^{45}$. The unit cell can be divided into two identical layers perpendicular to the c axis, each of which is a layer of polyhedra linked to share corners only in the layer (Fig. 3b), with a shift between successive layers so that polyhedra share edges between layers.

(viii) In $FeCu_2Al_7$, the B–A–$B_{\frac{1}{2}\frac{1}{2}}{}^{45}$ sequence forms a layer of 9-fold polyhedra for Fe atoms in the same manner as in Co_2Al_9, but interleaved between such layers is a body-centred-cubic sequence of Al around Cu, with ordered vacancies on the Cu sites.

(ix) The relationship for $NiAl_3$ is more tenuous. In Fig. 4(a), Ni atoms are placed in regular alternation in half of the triangular gaps between two A layers, and Al atoms in the square gaps. (If all the triangle gaps are filled, then Fig. 4(a) represents the Al_2Th_3 structure in which Al is the small atom.[10]) This gives Ni nine neighbors, but then the distances of Al(X) from its four neighbors are too short if the superposed

* Some of the A-layer members may also be Si's.[15]

TABLE 1. Description of intermetallic compound structures in terms of stacking of plane nets

A—Five-connected array of squares and triangles (Fig. 1b)
B—Four-connected square array
$\frac{1}{2}$—Translation by half a unit cell side. $\frac{1}{2}\frac{1}{2}$—by half a face diagonal
45—Rotation of a net by 45° about origin, which precedes any translation if one is also indicated

Sequence[a]	Compounds
A—A—A	$NiAl_3$,[8] $PdAl_3$,[9] (Th_3Al_2)[10]
A—$A_{\frac{1}{2}\frac{1}{2}}$—$A$	$CuAl_2$-θ,[6] $FeSn_2$, $CoSn_2$, $MnSn_2$, $RhSn_2$,[11] $AgIn_2$,[12] $PtPb_4$,[13] $FeGe_2$, $RhPb_2$, $PdPb_2$, $AuPb_2$[14]
A—$A_{\frac{1}{2}\frac{1}{2}}$—$A_{\frac{1}{2}\frac{1}{2}}$—$A$—$A$	δ-(AlFeSi)[15]
A—$A_{\frac{1}{2}\frac{1}{2}}$—$A_{\frac{1}{2}}$—$A_{\frac{1}{2}\frac{1}{2}}$— A	$PtSn_4$, $PdSn_4$, $AuSn_4$[16]
B—($B_{\frac{1}{2}\frac{1}{2}}$)[b]—$B$ All sites occupied with ordered vacant (T.M.) sites with ordered vacant (T.M.) sites (CaF_2 type)	FeAl[17], CoAl,[18] NiAl[19] Ni_2Al_3,[8] Pd_2Al_3,[9] Ni_2Ga_3, Ni_2In_3, Pt_2Ga_3, Pt_2In_3, Pd_2In_3,[12] $PtGa_2$, $AuGa_2$, $PtIn_2$, $AuIn_2$, $PtAl_2$,[12] $AuAl_2$,[20] $PtSn_2$, $IrSn_2$,[11] $CuAl_2$-θ'[21]
B—A—B—$A_{\frac{1}{2}\frac{1}{2}}$—$B$	$CoGe_2$, $PdSn_2$, $RhSn_2$,[22] $AuSn_2$[23]
B—A—$B_{\frac{1}{2}}{}^{45}$[c]—$A_{\frac{1}{2}\frac{1}{2}}$—$B$	Co_2Al_9[24]
B—A—$B_{\frac{1}{2}\frac{1}{2}}{}^{45}$[c]—($B^{45}$)—$B_{\frac{1}{2}\frac{1}{2}}{}^{45}$—$A$—$B$—($B_{\frac{1}{2}\frac{1}{2}}$)—$B$	$FeCu_2Al_7$,[25] $CoCu_2Al_7$[26]

[a] The last member of each sequence is identical with the first.
[b] A bracket shows that this is a layer of T.M. or Cu atoms. Otherwise, the position of such atoms is not included.
[c] These appear to be different, because the unit cell origins are not equivalent, so that the effect of a rotation is changed.

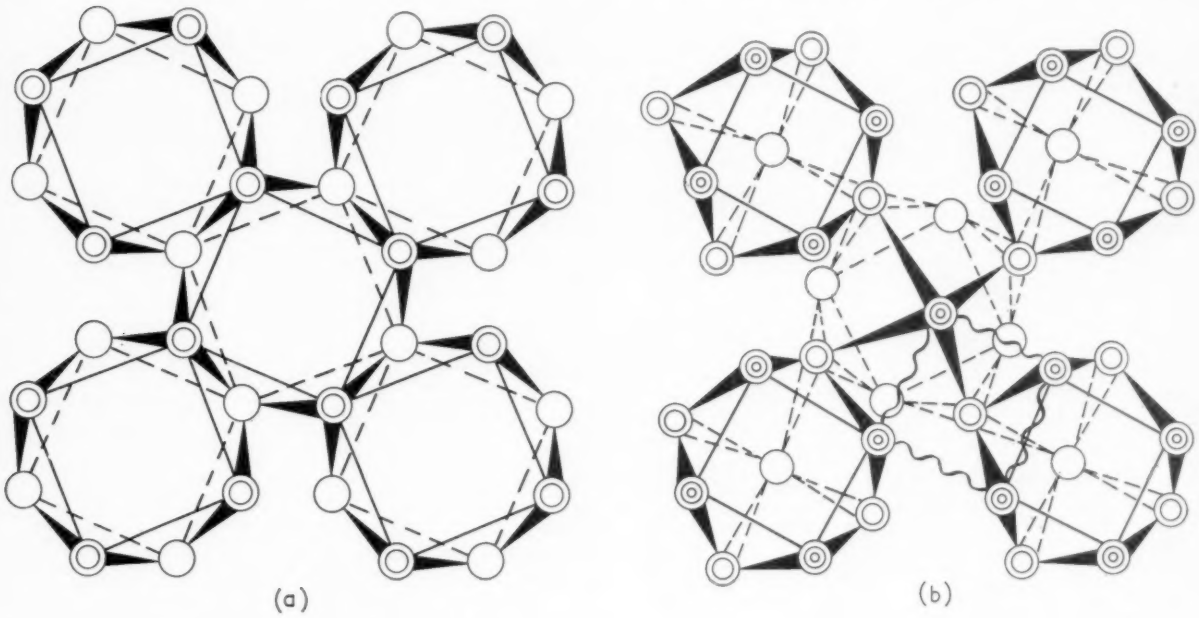

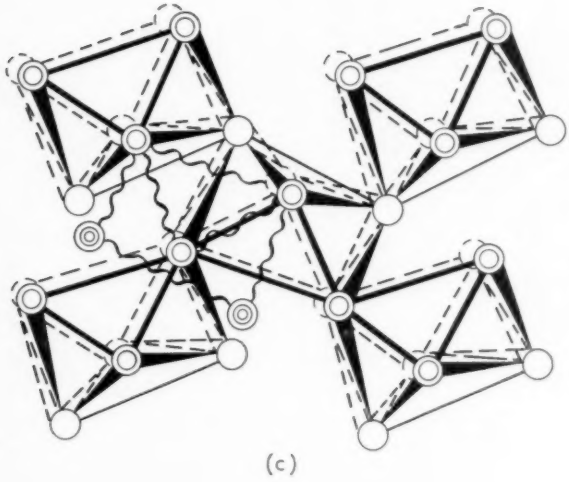

FIG. 3. Illustrating the mode of linking polyhedra in three different structures and its relationship to A-type layers:

(a) 8-fold polyhedra of Al in $CuAl_2$. One-cell thickness viewed along the c axis.

(b) 9-fold polyhedra of Al in Co_2Al_9. Half-a-cell-thickness viewed along the c axis. The same pattern is found in $FeCu_2Al_7$. Wavy lines indicate the square base for polyhedra in the next layer in Co_2Al_9.

(c) 8-fold polyhedra of Al in $NiAl_3$. Half-a-cell-thickness viewed along the b axis. Wavy lines show how the layer in the next half-cell is linked.

Centres of polyhedra are not marked. Connecting lines are all polyhedron edges.

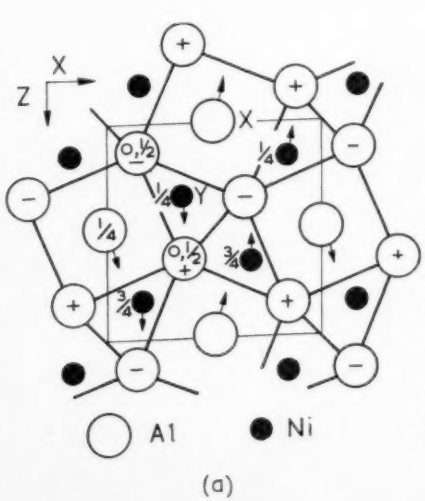

FIG. 4.
The $NiAl_3$ structure.

(a) Ideal plan of A–A layers. Ideal y parameters are marked and changes in these indicated by (+) and (−). Movements in the x-z plane are shown by arrows. Expansion along x then gives:

(b) Plan in projection down b axis (7.35 Å) of $NiAl_3$, with y parameters marked. Al neighbors of one Ni atom are indicated.

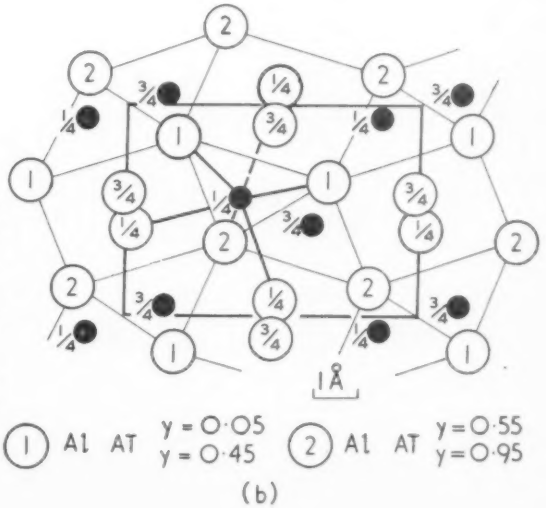

A layers are in contact, and if Ni(Y) is to be much closer to the A layer than Al(X). The adjustments, of puckering the A layers and expanding in the a direction, are indicated in Fig. 4(a), and give the observed structure of 4(b). The Ni co-ordination is then effectively 8, as one neighbor is at 2.72 A compared with 2.42–2.52 A for the other eight. The polyhedra share faces (if the ninth neighbor is included), but Ni atoms are not in contact across these faces; their arrangement is illustrated in Fig. 3(c).

All of the above structures have 8- or 9-fold polyhedra for T.M. atoms. The diagrams of Fig. 3 indicate that the linking of such polyhedra is based on the linking of A layer squares; this can be compared with the linking of chains in the fibrous zeolites.[27] For 10-fold polyhedra, the system of Table 1 does not apply, but a description in terms of close-packed layers may be useful. Two examples will be considered.

The first is $FeAl_3$, for which the features of interest here have been discussed elsewhere.[4] The structure consists of misoriented close-packed regions with regions of misfit between them which allow the iron atoms as members of the close-packed layers to have only ten instead of twelve neighbors, whilst iron atoms placed between these regions have nine neighbors.

For Co_2Al_5,[28] Fig. 5(a) shows the pattern in projection down the c axis, of atoms with z parameters between (but not equal to) 0 and $\frac{1}{2}$. This is repeated with an inversion about the center of the cell to give the atoms in the other half of the cell. It can be seen that the layer is a close-packed one, split at Y to fit in cobalt atoms; the effect is shown in a schematic view of one cell along a [11.0] direction in Fig. 5(b). The displaced parts of adjacent close-packed layers form a layer about $z = 0$ or $z = \frac{1}{2}$, as shown in Fig. 5(c), which resembles the A layer discussed above. Cobalt atoms at X and Y between layers have nine neighbors, whilst those of type P within layers have ten (cf. 9- and 10-fold Fe atoms in $FeAl_3$).

Further discussion of structures with 10-fold co-ordination (e.g., $MnAl_6$,[29] Fe_2Al_5[23]) and of other structures which may be described in terms of close-packed layers (e.g., $CuMg_2$, $NiMg_2$[30]) will not be developed here. It seems that the determination of some new structures of this type by J. A. Bland[31] in this laboratory will provide a valuable link between such structures and will suggest a new scheme of relationships for them.

This section can be summarized by saying that

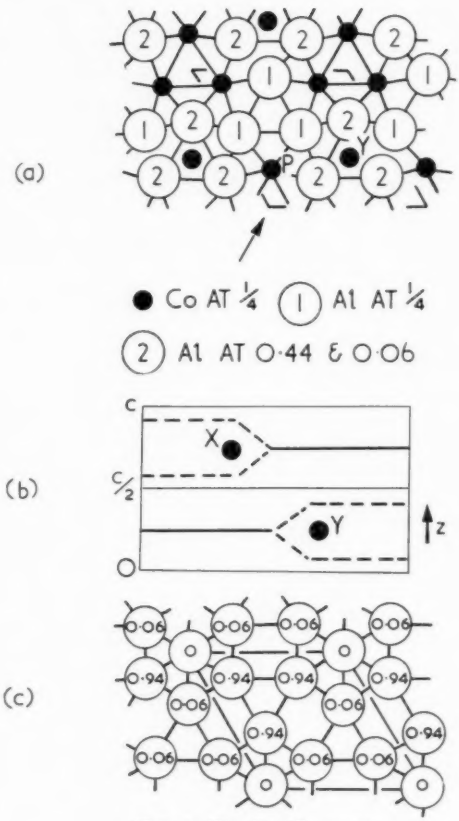

FIG. 5. The Co_2Al_5 structure.

(a) Plan in projection down c axis (7.6 Å) of atoms about height $\frac{1}{4}$.

(b) Schematic view of one cell along direction shown in (a). Full and broken lines indicate close-packed planes of (a). X and Y are Co atoms which split such planes into two mirrored halves.

(c) Projection as in (a) showing atoms about height zero.

certain characteristic plane patterns of atoms are often found in structures which build up 8, 9, or 10-fold polyhedra, and that these structures can be simply described in terms of sequences of such patterns. The patterns may also be significant in the growth mechanism of the crystals, e.g., the $CuAl_2\theta'$-phase grows with the B layers coherent with identical (100) layers of the Al-matrix.[32] The planes of Al atoms are members of the families of planes which build up characteristic strong (Brillouin-zone) reflexions for these structures (see discussion by Black).[5]

3. POLYHEDRA

(i) In the Al-rich T.M. compounds it is natural to focus attention on the T.M. atoms and to discuss structures in terms of their co-ordination polyhedra. For the purposes of this paper, it should be emphasized that the polyhedral description is not suggested for or supported by any specific theory of the structures,

TABLE 2. Transition metal co-ordinations in aluminum-rich structures

Mn		Fe		Co		Ni		Cu	
(29) $MnAl_6$	10†	(4) $FeAl_3$	$9(\frac{1}{3})$‡ $10(\frac{2}{3})$	(24) Co_2Al_9	9	(8) $NiAl_3$	8 or 9	(6) $CuAl_2(\theta)$	8
(34) Mn_3SiAl_9	10	(23) Fe_2Al_5	10	(28) Co_2Al_5	$9(\frac{1}{4})$ $10(\frac{3}{4})$	(8) Ni_2Al_3	8	(21) $CuAl_2(\theta')$	8
		(25) $FeCu_2Al_7$	9	(26) $CoCu_2Al_7$	9	(26) NiCuAl	8	(26) NiCuAl	8

† This is the number of Al neighbors of the T.M. atom.
‡ Where the structure contains T.M. atoms with different environments, the proportion of T.M. atoms concerned is given after each co-ordination number.

but arises from observation of their peculiarities and the most general inferences that can be drawn from these. Thus it is observed that T.M. atoms are usually distributed so as to avoid contact with one another, whilst from the contraction of T.M.-Al distances and the occurrence of holes on T.M. sites it is inferred that T.M.-Al interactions play a decisive role in stabilizing the structures.[33, 4] At the same time, there are no obvious regularities in the Al-Al co-ordinations, except perhaps for a tendency to contract the mean T.M.-Al distance as the number of T.M. neighbors of an Al atom is decreased.[4] Each Al atom has about ten neighbors, of which between two and four are T.M. atoms.

In Table 2 are reviewed the T.M. co-ordinations in the Al-rich structures; the first compound in each section is the binary that is most rich in Al. There is a trend of preference from ten neighbors for Mn to eight for Cu.

(ii) If these preferred numbers are significant, they should influence, for example, the formation of isomorphic compounds and the solid solubilities of one T.M. in compounds of another. Some evidence for such effects can be suggested:—

(a) Mn_3SiAl_9 is an isomorph of Co_2Al_5 such that one-quarter of the T.M. sites of the latter are vacant in the former. This has been explained in terms of electron concentration,[34] but this explanation cannot account for the ordering of the vacant sites. The 10-fold sites (P of Fig. 5) are all occupied by Mn, whilst the 9-fold sites (X, Y of Fig. 5) are vacant.

(b) Iron and nickel replace cobalt to form an isomorph of Co_2Al_5 whose composition is approximately Fe_3NiAl_{10}.[35] The 3 : 1 ratio of Fe : Ni is the ratio of 10-fold to 9-fold sites in the structure; there is as yet no experimental proof that the atoms are ordered in this way.

(c) In $FeAl_3$, iron shows a preference for 10-fold co-ordination; it would seem that a compound $FeAl_6$ isomorphic with $MnAl_6$ is almost stable, for a ternary (FeCu) $(CuAl)_6$ is found which contains only 4 at. per cent Cu.[25, 36] Iron replaces up to half the Mn in $MnAl_6$,[37] and 38% of the Co in the 9-fold sites of Co_2Al_9.

(d) Cobalt replaces one-third of the iron in $FeAl_3$[38] which is sufficient to fill the 9-fold sites of that structure. It does not go into the 8-fold sites of $NiAl_3$ to any great extent, whilst Ni replaces two-thirds of the cobalt in 9-fold sites of Co_2Al_9.[39]

The above section is a speculative interpretation and as such is a digression from the main descriptive theme of the paper. It has been included because it illustrates how a generalization arising from structural data may provide an (otherwise unsuspected) clue to the formation and stability range of compounds.

(iii) For the other compounds of Table 1, it can be said that they show many of the characteristics of the Al-rich compounds, viz., contraction of the distance between unlike atoms, holes on T.M. sites ($PtPb_4$ and the CaF_2 types), a large range in interatomic distances (including short distances between electronegative atoms), and, for some of them, avoidance of contact between T.M. atoms ($CoGe_2$, $PdSn_2$, and the $CuAl_2$ types contradict this latter rule). They are all 8-neighbor systems, but most of them are compounds of end members of the transition series or of noble metals, which might be expected to resemble Ni and Cu. The Pd-Al equilibrium diagram, for example, is similar to the Ni-Al diagram, and structures occurring in the two systems are isomorphous.[9] Some bismuth-rich compounds of T.M.'s have been systematically described in terms of 7- and 8-fold polyhedra by Zdanov.[40]

4. SIZE FACTORS

It is important to establish whether the trend of eight-nine-ten neighbors is governed by size factors.

TABLE 3. Mean interatomic distances in Al-rich T.M. structures

Compound		Number of Al neighbors	Mean Al-Al distance (Å)	% variation of Al-Al distance	Mean T.M.-Al distance (Å)	Radius ratio
$MnAl_6$		10	2.82[1] 2.75[2]	10	2.56	(1.225) 1.16
Mn_3SiAl_9		10	2.80[1]	11	2.59	1.18
$FeAl_3$[5]	1	10 or 11	2.71[1] 2.68[1]	19	2.60 2.62	1.09 1.05
	2	10	2.74[1]	17	2.53	1.18
	3	10	2.82[1] 2.78[4]	14	2.54	(1.245) 1.21
	4	10	2.83[1] 2.78[4]	22	2.56	(1.235) 1.19
	5	9	2.85[3] 2.76	30	2.53	(1.28) 1.20
Co_2Al_9		9	2.83[1] 2.78[4]	9	2.47	(1.34) 1.285
Co_2Al_5		9 10	2.88[1] 2.78[1]	14 16	2.43 2.57	1.455 1.18
$NiAl_3$		8 (or 9)	2.85[1] 2.78[4]	11	2.46 (for 8)	(1.375) 1.30

[1] This is the mean of contact distances on the polyhedron surface.
[2] This is the mean of contact distances between polyhedra.
[3] This is reckoned by including five distances >3.0 Å as contacts: these are neglected in the next row.
[4] This is the mean Al-Al distance in the structure.
[5] The numbering of Fe atoms corresponds to reference (4).

In Table 3 is given a survey of the numbers and distances for Al neighbours of T.M. atoms. The radius ratios quoted correspond to the sizes of atoms in the structure. The mean Al-Al distances are in the first instance average values of the distance between atoms on the surface of one polyhedron, but in some cases other mean distances are also quoted, for these sometimes show that the Al atoms can be more closely packed between polyhedra than on their surface, and in such cases the second radius ratio may provide a better estimate of possible atomic sizes.

An attempt has been made to determine whether these numbers of neighbors correspond to the maximum numbers of larger atoms that can be packed around a smaller atom for the radius ratios observed. Twelve neighbours are most efficiently packed on a regular icosahedron for which the radius ratio is 1.12 (see discussion of β-Mn by Pauling).[41] For ten or eleven neighbors it is not easy to make an explicit calculation, especially if a range of variation in contact distances is allowed. The results of Table 4 have been derived by using a stereogram to adjust a polyhedron empirically, radius ratios being calculated from the angles between points on the stereogram. Each result is the maximum radius ratio found for the quoted conditions of number of neighbors and variation of distance from the mean. Since the process is empirical, it cannot be asserted that these are the maximum possible ratios. Comparison of Tables 3 and 4 shows that in most cases it would be possible to fit one or two more neighbors around a T.M. atom without changing the mean interatomic distances or their range of variation from those found in the structures. There is a trend in the mean T.M.-Al distance in the Al-rich binary compounds from 2.56 Å in $MnAl_6$ to 2.46 Å in $NiAl_3$, which might be correlated with the preferred coordination trend of 3(ii), although the size factors would indicate a change from eleven neighbours for Mn to nine for Ni instead of the observed range of ten to eight.

It is therefore probable that the number of Al-atoms in contact with a T.M. is reduced either by some specific factor characteristic of the T.M.-Al interaction, or by long-range ordering and packing conditions of the structure. To investigate the second

TABLE 4. Ideal radius ratios calculated empirically

Number of neighbors	Radius ratio	Variation of distance
12	1.11	0 (regular)
11	1.15	10%
11	1.185	22%
10	1.25	8%
10	1.28	25%
9	1.42	5%
9	1.51	15%
8	1.55	0

possibility, one would have to compare alternative hypothetical structures to prove, for example, that a structure can be built by linking 11-fold polyhedra. It would seem *a priori* that this should be possible, since these structures can tolerate holes (Ni_2Al_3, β(AlMnSi)), misfit regions between polyhedra ($FeAl_3$), and a large range of interatomic distances.

Similar conclusions can be drawn for the other compounds of Table 1. In the CaF_2 types, the radius ratios obtained by assuming normal sizes for the electronegative atoms (which in some of the structures are not in contact) and a contracted radius for each T.M. (as derived from the structure concerned) are in the range 1.05–1.25, so that there is room for more than eight neighbors. For the $PtSn_4$ types, the ratio is 1.33–1.37, sufficient for nine neighbors instead of eight, but in $PtPb_4$ the ratio (1.51) would only allow eight. Consideration of other members of the list is complicated by the contact between T.M. atoms. It is not, of course, suggested that previous analyses which correlate the $CuAl_2$- and CaF_2-type phases in terms of size factors are mistaken, but rather that such factors alone cannot dictate the choice of eight-co-ordination for T.M.'s in these structures.[42, 14, 11]

5. CONCLUSION

It may be suggested that the aim of a theory which would account for these intermetallic-compound structures should be a set of rules analogous to (say) Pauling's rules for complex ionic compounds. If such an attitude is accepted, then it is not surprising that attempts to account for a set of compounds like the Al-T.M. compounds and to construct rules governing their formation without an intimate knowledge of their structures has produced "no real understanding" (Hume-Rothery and Coles).[43] The work described above should be regarded as a necessary and preliminary descriptive analysis. It cannot yet be in any way complete: for example, comparisons among existing data show distinctive features for the Al-rich compounds, but this cannot be generalized in the absence of extensive data for gallium- and indium-rich compounds. Nevertheless, attempts to align existing details and to interpret the data for discussion of theories about these compounds are suggested by this work. Apart from section 3(ii), such attempts have been avoided here and will be discussed elsewhere.

VOL. 4 1956

ACKNOWLEDGMENTS

I wish to thank Professor N. F. Mott and Dr. W. H. Taylor for provision of facilities, and for their interest in the progress of this work, and the Council of the Royal Society for financial support. I am indebted to several colleagues, particularly Dr. P. Vousden and Mr. J. A. Bland, for many valuable discussions. I am grateful to Dr. P. Spiegelberg for permission to quote unpublished results.

REFERENCES

1. W. Hume-Rothery and G. V. Raynor, *The Structure of Metals and Alloys*, Institute of Metals, London (1954).
2. W. H. Taylor, *Acta Met.*, **2,** 684 (1954).
3. P. J. Black, *Phil. Mag.*, **46,** 155 (1955).
4. P. J. Black, *Acta Cryst.*, **8,** 175 (1955).
5. P. J. Black, *Phil. Mag.*, **46,** 401 (1955).
6. A. J. Bradley and P. Jones, *J. Inst. Met.*, **51,** 131 (1933).
7. M. J. Buerger, *Phase Transformations in Solids* (New York, Wiley, 1951), Chapter 6.
8. A. J. Bradley and A. Taylor, *Phil. Mag.*, **23,** 1049 (1937).
9. Y. P. Simanov, *Zh. fiz. Khim.*, **27,** 1503 (1953).
10. P. B. Braun and J. H. N. van Vucht, *Acta Cryst.*, **8,** 117 (1955).
11. O. Nial, *Svensk. Kemisk Tidskrift*, **59,** 165, 172, 177 (1948).
12. E. Hellner and F. Laves, *Z. Naturforsch.*, **2a,** 177 (1947).
13. U. Rösler and K. Schubert, *Z. Metallkunde*, **42,** 395 (1951).
14. H. J. Wallbaum, *Z. Metallkunde*, **35,** 218 (1943).
15. P. Spiegelberg, Private Communication (1955).
16. K. Schubert and U. Rösler, *Z. Metallkunde*, **41,** 298 (1950).
17. A. J. Bradley and A. H. Jay, *J. Iron Steel Inst.*, **125,** 339 (1932).
18. A. J. Bradley and G. C. Seager, *J. Inst. Met.*, **64,** 81 (1939).
19. A. J. Bradley and A. Taylor, *Proc. Roy. Soc.*, **A159,** 56 (1937).
20. C. D. West and A. W. Peterson, *Z. Krist.* **A88,** 93 (1934).
21. G. D. Preston, *Proc. Phys. Soc.* [London], **52,** 77 (1940).
22. K. Schubert and H. Pfisterer, *Z. Metallkunde*, **41,** 433 (1950).
23. K. Schubert, U. Rösler, M. Kluge, K. Anderko, and L. Härle, *Naturwissenschaften*, **40,** 437 (1953).
24. A. M. B. Douglas, *Acta Cryst.*, **3,** 19 (1950).
25. G. Phragmen, *J. Inst. Met.*, **77,** 489 (1950).
26. M. G. Bown, Thesis for Doctor of Philosophy (Cambridge, 1955).
27. L. Pauling, *Proc. Nat. Acad. Sci.*, **16,** 453 (1930).
28. A. J. Bradley and C. S. Cheng, *Z. Krist.*, **99,** 480 (1938).
29. A. D. I. Nicol, *Acta Cryst.*, **6,** 285 (1953).
30. K. Schubert and K. Anderko, *Z. Metallkunde*, **42,** 321 (1951).
31. J. A. Bland, Private Communication (1955).
32. W. L. Fink and D. W. Smith, *Trans. Amer. Inst. Min. Met. Engrs.*, **137,** 107 (1940).
33. P. Vousden, Private Communication (1955)—to be published.
34. K. Robinson, *Acta Cryst.*, **5,** 397 (1952).
35. A. J. Bradley and A. Taylor, *J. Inst. Met.*, **66,** 53 (1940).
36. H. W. L. Phillips, *J. Inst. Met.*, **82,** 197 (1954).
37. G. V. Raynor, *J. Inst. Met.*, **70,** 531 (1944).
38. G. V. Raynor and M. B. Waldron, *Proc. Roy. Soc.*, **A194,** 362 (1948).
39. G. V. Raynor and P. C. L. Pfeil, *J. Inst. Met.*, **73,** 609 (1946/7).
40. G. S. Zdanov, *Proc. Inst. Cryst., U.S.S.R. Acad. Sci.*, **10,** 249 (1954).
41. L. Pauling, *J. Amer. Chem. Soc.*, **69,** 542 (1947).
42. E. Zintl, A. Harder, and W. Haucke, *Z. phys. Chem.*, **35** (B) 354 (1947).
43. W. Hume-Rothery and B. R. Coles, *Advances in Physics*, **3,** 149 (1954).

PROPAGATION OF LÜDER'S BANDS IN STEEL WIRES*

J. C. FISHER and H. C. ROGERS†

Annealed SAE-1010 steel wires were deformed in tension at three temperatures. The tests were performed at constant load by hanging weights on the wires. Propagation was observed visually through the cracking of a brittle lacquer coating.

Lüder's band-fronts propagate with a velocity V that depends upon stress σ and temperature T through a relationship of the form

$$\log V = C - \frac{D}{\sigma T}$$

where C and D are constants.

PROPAGATION DES BANDES DE LÜDER DANS DES FILS D'ACIER

Les fils d'acier SAE 1010 préalablement recuits ont été déformés par traction à trois températures. Les essais ont été effectués à charge constante en suspendant des poids aux fils. La propagation a été observée visuellement grâce aux fissures apparaissant dans une couche de vernis fragile recouvrant les fils.

Les fronts des bandes de Lüder se déplacent avec une vitesse V qui dépend de la tension σ et de la température T suivant une relation de la forme:

$$\log V = C - \frac{D}{\sigma T}$$

où C et D sont des constantes.

AUSBREITUNG VON LÜDERS-BÄNDERN IN STAHLDRÄHTEN

Geglühte Drähte aus SAE-1010-Stahl wurden bei drei Temperaturen gedehnt. Die Versuche wurden unter konstanter Last durch Anhängen von Gewichten an die Drähte durchgeführt. Die Ausbreitung der Lüders-Bänder wurde durch das Aufreissen eines spröden Lacküberzuges visuell beobachtet.

Die Fronten der Lüders-Bänder breiten sich mit einer Geschwindigkeit V aus, die von der Spannung σ und der Temperatur T entsprechend einer Beziehung von der Form

$$\log V = C - \frac{D}{\sigma T}$$

abhängt, wobei C und D Konstante sind.

When an annealed low-carbon steel wire is stressed in tension, the nature of the associated extension depends upon the magnitude of the stress. At low stresses the extension is elastic. At somewhat higher stresses the elastic extension is followed by a small amount of homogeneous plastic strain that rapidly approaches a limiting value, which increases with stress.[1] At still higher stresses, when the limiting amount of homogeneous plastic strain is as great as 10^{-5} or 10^{-4}, one or more local constrictions appear in the wire and grow along it, as sketched in Fig. 1. The strain in these constrictions is relatively large, and is nearly independent of time. In the unconstricted portion of the wire the homogeneous plastic strain runs its course and ceases. Later, the boundary of a constricted region reaches this portion of the wire and passes by it. As the boundary passes a given point on the wire, the plastic strain very rapidly increases and approaches a new limiting value as great as 10^{-2} or 10^{-1}. Boundaries traverse the wire until the entire gage length has been consumed by constricted regions.[2]

The constricted region of a wire in which a relatively great amount of plastic deformation has occurred is called a Lüder's band, and the moving boundary of the band behind which the plastic strain occurs is called the band front. This investigation was undertaken to measure the influence of applied stress and of temperature upon the velocity of band-fronts. For a given stress and temperature they usually were found to move at a uniform velocity, and they moved more rapidly as the temperature or stress was increased.

EXPERIMENTAL PROCEDURE

Dead-weight tensile tests were conducted on wire specimens that were mounted inside a double-walled tube 30 in. long with a 1-in. inside diameter. Specimens were gripped by squeezing a $\frac{3}{4}$-in. length at each end between grooved blocks, and by flattening down with a setscrew a small length of wire that extended

* Received May 11, 1955.

† General Electric Research Laboratory, Schenectady, N.Y.

beyond these blocks. The top grip was hung by $\frac{1}{8}$-in. rod from a plastic block at the top of the tube, and the load was applied by means of a weight-pan hung on the bottom cross-arm of a rectangular frame, which in turn was fastened to a T bar attached to the bottom grip. A dial gage was mounted inside the rectangular frame so that it measured the motion of the lower grip relative to the frame of the tensile machine.

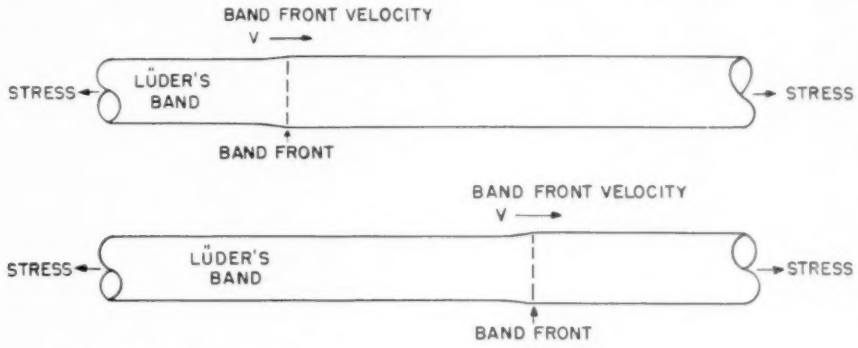

FIG. 1. Propagation of a constricted region (Lüder's band) along a wire, schematic. The band-front moves with velocity V, and plastic strain occurs in its wake. The lower sketch refers to a later time.

The specimens were 0.030-in.-diameter wires with 9-in.-gage lengths. Long wires were used primarily to reduce the influence of end constraints upon the band-front velocity. The wire was drawn from $\frac{3}{4}$-in.-diameter SAE-1010 steel rod, cut into 11-in. lengths, and hand-straightened. The specimens then were packed in alundum in an SAE-1010 steel tube, and were heated for ten minutes at 1000°C in dry hydrogen. The tube and contents then were cooled in a water-jacketed chamber with a hydrogen atmosphere, producing ASTM No. 8 grain size. An X-ray check indicated practically no fiber texture in the cold-drawn wire.

The test temperature was obtained by means of a constant-temperature bath between the two walls of the tube. The bath was insulated by an unsilvered, evacuated, double-walled glass cylinder surrounding the tube.

Preliminary experiments showed considerable variability in extension rate for a given stress and temperature, because of changing numbers of band-fronts. In order to make the fronts visible and countable, the specimens were dipped in Stresscoat and allowed to dry before testing. The Stresscoat, which is a brittle lacquer, then flaked when subjected to the plastic strain of a Lüder's band, rendering the band easily visible under the oblique illumination of a small microscope light. The effect of the radiation from this light-source on the specimen temperature was checked and found to be negligible.

A test consisted first of placing grips on the coated wire, hanging it in the tube, and waiting for the specimen and grips to reach the temperature of the bath surrounding the inner tube. Next, the rectangular frame was attached to the bottom grip and the weight-pan hung on its lower cross-arm. A 0.001-in. dial gage was placed against the lower flat side of its upper cross-arm, to measure the extension of the specimen. Such weights as preliminary tests had shown would only elastically deform the specimen were then added, taking up all slack in the specimen train, and the initial dial-gage reading was taken. Finally, the last weight was added to give the desired stress, and measurement of time, elongation, and the number of band-fronts was continued until the entire wire was consumed by Lüder's bands. Measurements were continued for a short additional period after the Stresscoat had completely cracked, to see if further deformation would occur.

Usually band-fronts moved into the wire from each grip, and often other Lüder's bands were nucleated at imperfections along the wire, producing two band-fronts that moved apart along the wire. Occasionally, a Lüder's band would appear long after the final stress was reached, but usually they appeared as soon as the final stress was applied.

RESULTS

The following symbols are defined:

t = time.

T = temperature in °C.

t_s = time from initiation of plastic flow to the complete cracking of the Stresscoat along the entire specimen gage length.

VOL. 4 1956

σ = stress.
V = velocity of propagation of band-front.
ε_b = strain associated with the band.
Δl = extension of wire.
n = number of moving band-fronts.

Figs. 2 through 4 show typical curves of extension as a function of time for tests at 0°C, 24°C, and −78°C. At 0°C, extension is linear with time for any fixed number of band-fronts, as shown in Fig. 2. When two fronts meet, there is a sharp decrease in the extension

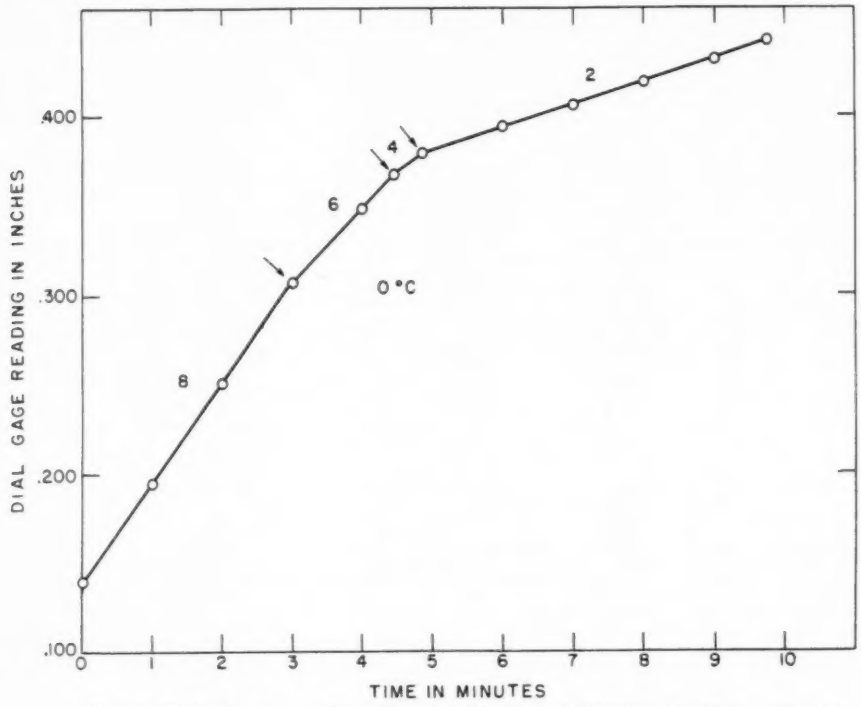

FIG. 2. Extension versus time for a test at 0°C and 37,300 p.s.i. The number of moving band-fronts is indicated, and decreases at the positions marked by arrows.

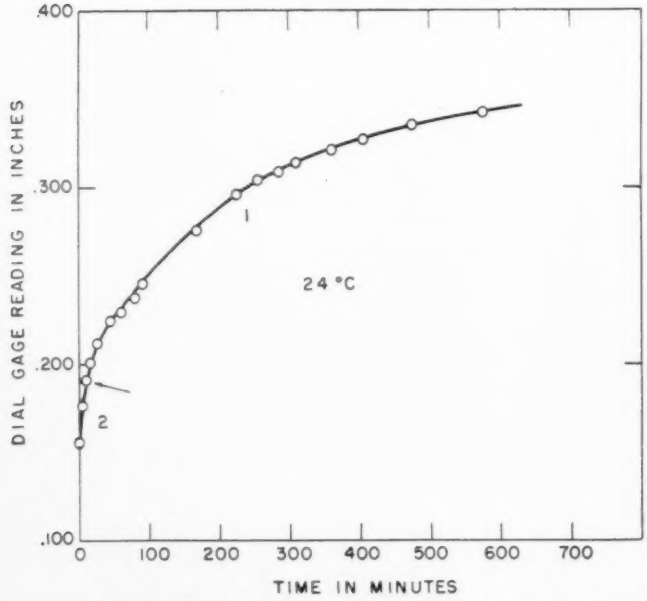

FIG. 3. Extension versus time for a test at 24°C and 33,000 p.s.i. The number of moving band-fronts is indicated, and decreases at the position marked by the arrow. (One of the band-fronts ceased moving after ten minutes.)

rate. No further deformation is observed after time t_s. This behavior corresponds to the motion of band-fronts at constant velocity, and to a rapid cessation of plastic flow in the Lüder's band shortly after the front passes by.

The behavior at 24°C is somewhat different, in that the extension rate for any fixed number of band-fronts decreases as a function of time, as shown in Fig. 3. Still, the extension ceases after t_s. This behavior could result from a reduction in the velocity of band-front motion, or from a reduction in the strain in a Lüders' band. Measurement of Lüder's band-strain shows it to be constant, so that the reduction in extension rate must be interpreted as a reduction in band-front velocity as the band moves along the specimen.

Testing at −78°C is again somewhat different, as may be seen in Fig. 4. At this temperature, the extension rate is approximately constant for a fixed number of band-fronts, but the specimen continues to elongate after time t_s. Moreover, the extension rate changes more gradually to its new value after two

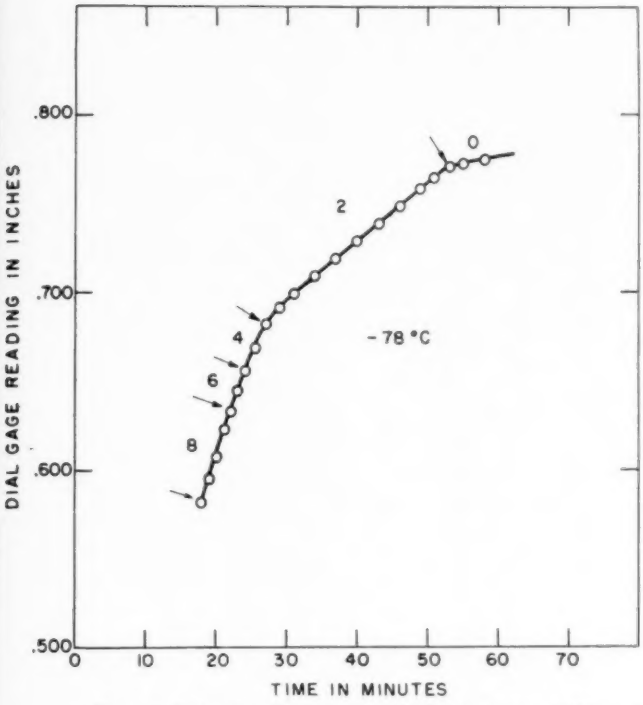

FIG. 4. Extension versus time for a test at −78°C and 47,100 p.s.i. The number of moving band-fronts is indicated, and decreases at the positions marked by arrows. The initial portion of the curve is not shown.

band-fronts meet. This behavior results because the plastic deformation in the wake of each front continues for a long time. It continues after the specimen is completely traversed, accounting for extension after time t_s, and slows down only gradually after two fronts meet, accounting for the gradual change in extension rate following their junction.

Several approximations had to be made in order to calculate the velocity of propagation of the band-fronts from the measured extension rates, the number of fronts, and the strain in the Lüder's bands. These approximations would not have been necessary had the band-front velocity been measured directly.

Assuming the strain associated with a Lüder's band to be constant during any one test, an assumption that was found experimentally to be satisfactory, the extension rate can be approximated by the equation

$$d(\Delta l)/dt = nV\varepsilon_b \qquad (1)$$

where the band-strain is calculated from the elongation at time t_s by the relationship $\varepsilon_b = \ln(l/l_0)$. This equation can be solved for the band-front velocity V when the extension rate, the strain ε_b, and the number of band-fronts n are known; a procedure that can be followed straightforwardly for tests at 0°C.

In the tests at room temperature, the decrease of the extension rate with time results primarily from a decreasing band-front velocity rather than a decreasing strain associated with the band. Hence, the band-front velocity can be determined in the same manner as at 0°C, except that the velocity is variable with time, rather than being a constant of the test.

The band-front velocities deduced for tests at −78°C are more ambiguous, because the Lüder's band-strain ε_b is not strictly constant with time at −78°C. Velocity calculations for tests at −78°C were made by assuming that, just before the last pair of band-fronts met, the wire was extending in the Lüder's bands at the rate measured after time t_s. This homogeneous extension rate then was subtracted from the measured total extension rate just before t_s, and the band-front velocity was obtained from this corrected value of the extension rate.

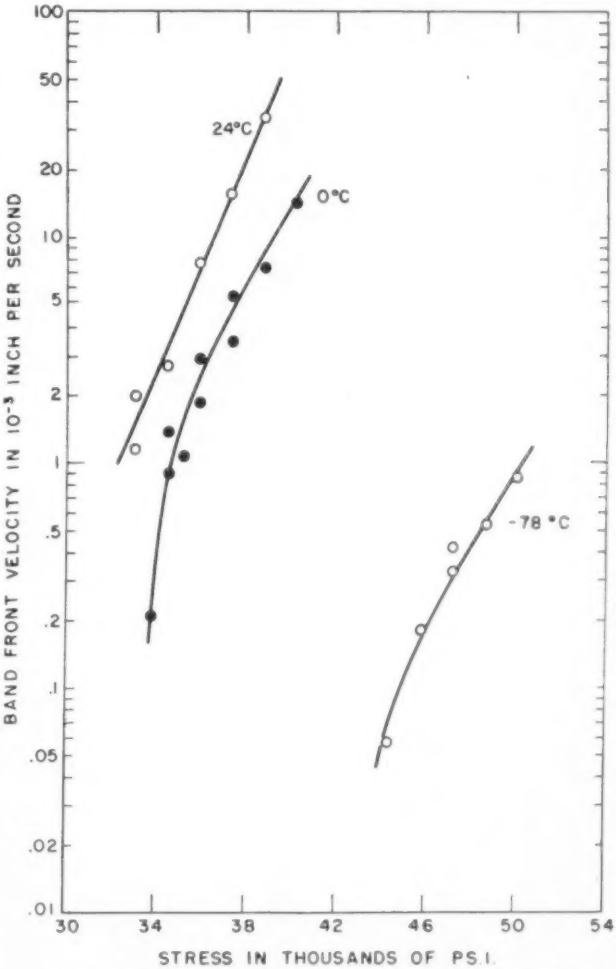

FIG. 5. Band-front velocity versus stress for tests at 24°C, 0°C, −78°C. Because the velocity is variable at 24°C (see Fig. 3), only the initial velocity is plotted for this temperature.

VOL. 4 1956

The band-front velocities for tests at all three temperatures are plotted as a function of the applied stress in Fig. 5. Only the initial velocity is plotted for tests at 24°C.

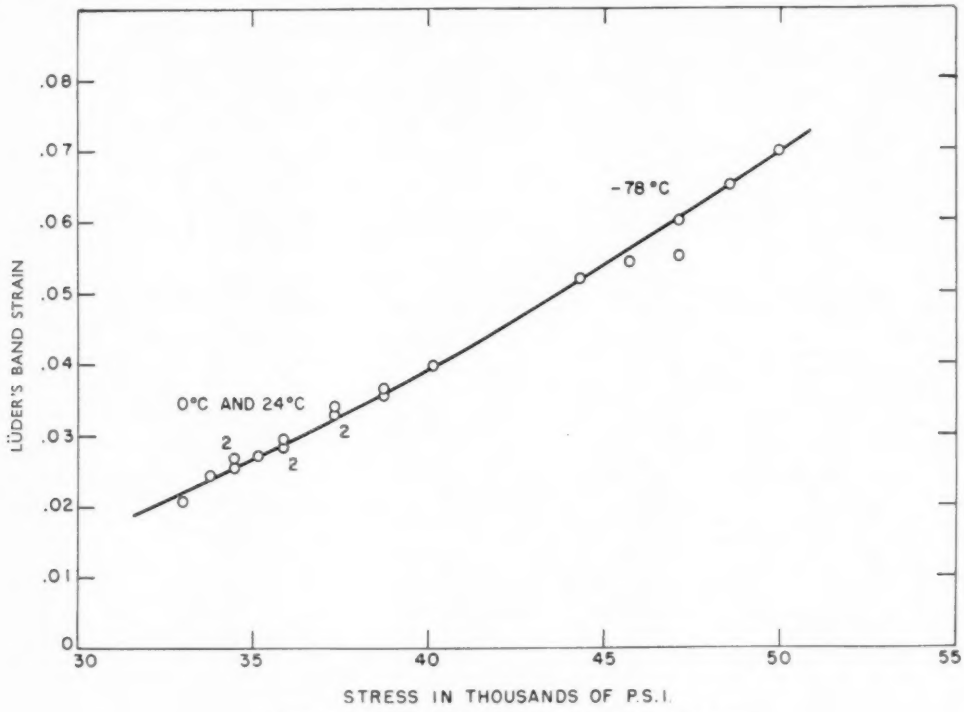

FIG. 6. Lüder's band-strain as a function of stress.

Fig. 6 shows that the Lüder's strain ε_b depends primarily upon stress, and increases rapidly with stress.

DISCUSSION OF RESULTS

The dependence of the Lüder's band-front velocity upon stress and temperature may be related to the delay time for yielding as observed by Clark and Wood,[3, 4, 5] which is based upon the pinning of dislocations by solute atoms in the manner described by Cottrell.[6] One might look upon the motion of a band-front as the yielding of many successive small increments of length along the wire. These regions could be individual grains or subgrains in the wire. As each region yields, it increases the stress on the region ahead of it, which region in turn yields after an appropriate delay time. The succession of delay times, for the yielding of successive increments of length of the wire, leads to a definite band-front velocity. This velocity should then depend upon stress depends upon stress and temperature through a relationship of the form

$$\log (\text{delay time}) = A + BG^2/\tau T$$

where A and B are constants, G is the shear modulus, and temperature just as does the reciprocal of the delay time.

An analysis of the delay time for yielding, based upon dislocation theory, shows that the delay time and τ is the resolved shear stress on the slip plane.[7]

The band-front velocity, then, should be of the form

$$\log V = C - D/\sigma T.$$

The experimental data are so plotted in Fig. 7, and do give a linear relationship for the velocities at −78°C, at 0°C, and for the initial velocity at 24°C. Final velocities for the room-temperature tests fall well below the curve, however.

The decrease in propagation velocity at 24°C with time probably is due to aging of the material following the homogeneous plastic strain that precedes Lüder's band formation. According to this view, the properties of the stressed and aging material should change with time at room temperature, in the absence of Lüder's bands. Aging of this type has been observed by Holden and Kunz, who studied it with reference to the upper yield-point.[8] They stress-aged steel specimens at stresses below the yield-stress, and found that the yield-stress thereby was raised above its value for specimens aged without stressing.

Similarly, the absence of creep at 0°C and 24°C probably results from aging of the material in the Lüder's band at these temperatures.

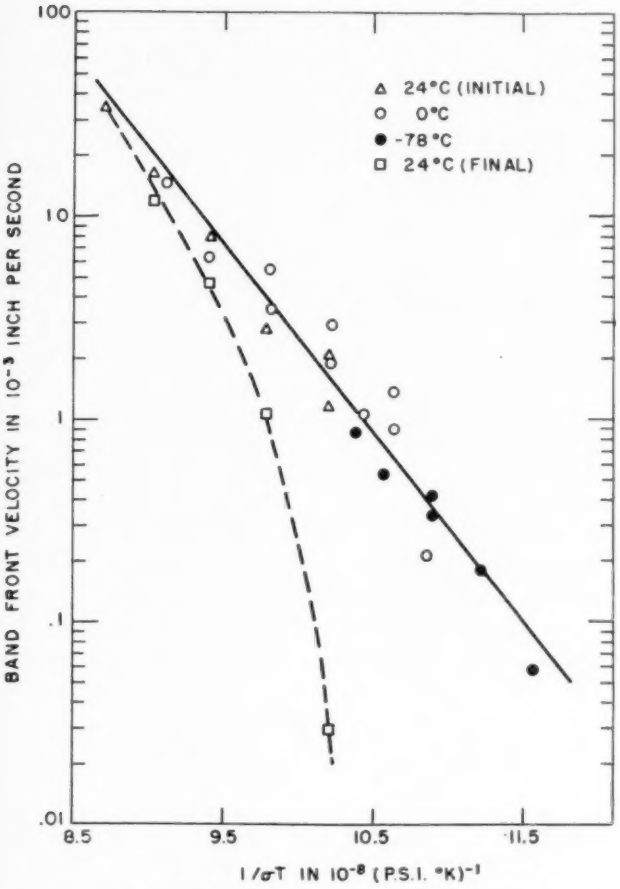

FIG. 7. Band-front velocity as a function of the reciprocal of stress × absolute temperature. Because of aging at 24°C, only the initial 24°C velocities fall on the curve, and the final 24°C velocities fall below it.

CONCLUSION

For a given material, Lüder's band-fronts propagate with a velocity that depends upon stress and temperature through a relationship of the form

$$\log V = C - D/\sigma T,$$

where σ is the applied stress, and T is the absolute temperature. This relationship suggests that the front propagates as the result of a series of "delay times" in the propagation of yielding from grain to grain similar to that observed for the initiation of a Lüder's band itself.

The Lüder's strain increases with stress in the same way that strain increases with stress for a polycrystalline material that has no Lüder's bands.

Strain-aging of the Lüder's band prevents creep in the band at 0°C and 24°C, but not at −78°C. At 24°C, aging of the material ahead of the band causes the band velocity to decrease with time.

REFERENCES

1. T. VREELAND, JR., D. S. WOOD, and D. S. CLARK, *Acta Met.*, **1,** 414 (1953).
2. W. SYLWESTROWICZ and E. O. HALL, *Proc. Phys. Soc.*, **B64,** 495 (1951).
3. D. S. CLARK and D. S. WOOD, *Proc. Amer. Soc. Test. Mtrls.*, **49,** 717 (1949).
4. D. S. WOOD and D. S. CLARK, *Trans. Amer. Soc. Metals.*, **43,** 571 (1951).
5. D. S. WOOD and D. S. CLARK, *Trans. Amer. Soc. Metals.*, **44,** 726 (1952).
6. A. H. COTTRELL, *Dislocations and Plastic Flow in Crystals*, The Clarendon Press, Oxford, 1953.
7. J. C. FISHER, *Trans. Amer. Soc. Metals.*, **47,** 451 (1955).
8. A. N. HOLDEN and F. W. KUNZ, *J. App. Phys.*, **23,** 799 (1952).

VOL. 4 1956

PHYSICAL EVIDENCE OF DISLOCATIONS IN CHROMIUM*

M. J. FRASER, D. CAPLAN, and A. A. BURR†

Chromium sheet, thermally etched at 1300°C and 1500°C in purified hydrogen, was found to exhibit a number of surface structures which are conceived as resulting from the presence of dislocations.

PREUVE PHYSIQUE DE LA PRÉSENCE DE DISLOCATIONS DANS LE CHROME

Des plaquettes de chrome attaquées thermiquement à 1300 et 1500°C dans l'hydrogène pur montrent en surface un ensemble de structures que l'on peut concevoir comme résultant de la présence de dislocations.

PHYSIKALISCHER NACHWEIS VON VERSETZUNGEN IN CHROM

Es wurde gefunden, dass bei 1300°C und 1500°C in reinem Wasserstoff thermisch geätztes Chrom-Blech eine Anzahl von Oberflächenstrukturen zeigt, von denen anzunehmen ist, dass sie von der Anwesenheit von Versetzungen herrühren.

Although the importance of the dislocation concept in deformation, solidification, diffusion, and in crystal structure is well known, until recently direct experimental observation of dislocations has been lacking. Examples of the various types of observations have been reviewed by Forty.[1] Most of these have been made in non-metals, with relatively few examples of dislocation configurations in metals.

On the basis of the dislocation model of a small-angle boundary, simple calculations indicate that the spacing of individual dislocations along a sufficiently low-angle boundary is well within the resolving power of the optical microscope.[2–6] Since a dislocation is a structural discontinuity involving an energy-differential in the lattice, it is possible, with sufficiently sensitive techniques, to reveal dislocation sites in low-angle boundaries as well as the position of randomly-spaced dislocations and other related phenomena.[7–21]

In general, two methods may be employed to do this. The first, applicable only to multiphase systems, is local precipitation.[9, 13] The second, which is most generally used, involves sensitive etching.[7, 8, 10–12, 14–21]

The metallurgist employs various etching techniques to reveal structural discontinuities. The basis for such delineation of structure is the differential rate of removal of atoms from the surface near discontinuities relative to the average rate of removal from the surrounding matrix. This may be accomplished by chemical or electrochemical solution, by ionic bombardment,[22] or by thermal-etching.[23] Thermal-etching is a method of delineating structure by heating the surface in a vacuum or in an atmosphere with which it does not react to form a stable compound. The increased mobility at high temperature allows the surface atoms to produce a configuration of lowest free-energy, consistent with the temperature, pressure, and atmosphere conditions imposed.[24] Migration is away from high-energy sites, revealing these as depressions in the surface. This method has recently been used to show dislocation sites in silver.[12]

The purpose of this paper is to describe some of the structural discontinuities revealed by the thermal-etching of chromium. Only those effects which are conceived as resulting from the presence of dislocations will be illustrated. A more general treatment of the thermal-etching of chromium will be presented in another publication.

Assuming the possibility of revealing individual dislocation sites by a sufficiently sensitive etching treatment, the following details might be observed in the general case:

1. General dislocation density and distribution.
2. Small-angle boundaries developed as rows of pits.
3. Dislocation distribution along slip traces and other deformation discontinuities.
4. Interaction of dislocations with inclusions.
5. Interaction of dislocation loops produced during plastic deformation.

Generally, the high-temperature treatment required for thermal-etching precludes the observation of possibilities 3 and 5 unless the dislocation lines are anchored by some means.

* Received May 27, 1955.
† Department of Metallurgical Engineering, Rensselaer Polytechnic Institute, Troy, New York.

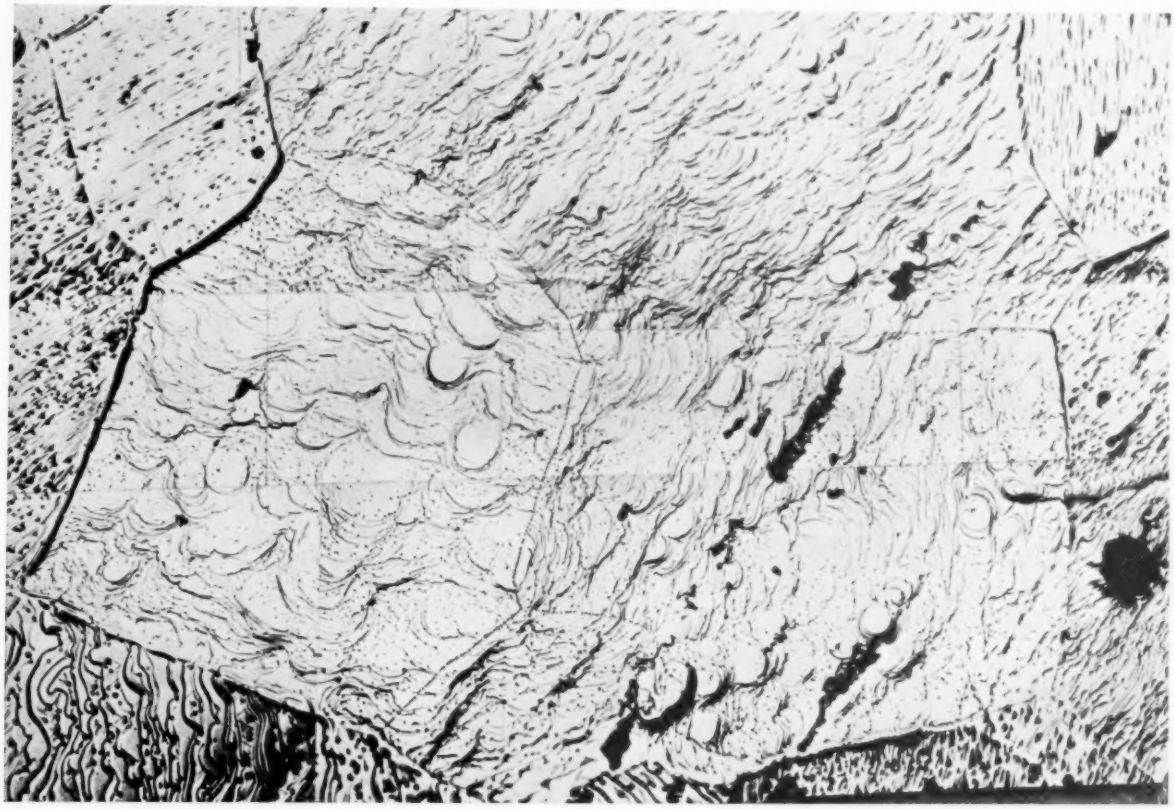

FIG. 1. Composite photomicrograph showing a portion of a large grain divided into subgrains—×500.

EXPERIMENTAL

Relatively pure chromium sheet, rolled to approximately 0.020 in., was pickled in 1:1 HCl at room temperature to remove the rolling scale. The sheet was then thermally etched under controlled conditions without further surface treatment.

For the work described below, two etching temperatures were employed: 1300°C and 1500°C. At 1300°C, the sample was etched in an iron muffle and at 1500°C in a molybdenum muffle. In both cases, the atmosphere was purified hydrogen flowing at 1-atm pressure through the muffle. The times employed were sixty-six hours for the 1300°C etch and twenty hours for the 1500°C etch.

The thermally-etched surfaces were examined by optical microscopy. Where the orientation of specific grains (0.2- to 0.4-mm diameter) was studied, a simple micro-X-ray technique was employed.[25]

RESULTS AND DISCUSSIONS

The structures which are illustrated are reproducible under the conditions outlined above.

Fig. 1 shows a composite photomicrograph of a portion of a single grain. This structure is typical of the 1300°C thermal-etch where the {100} plane of the grain is slightly inclined to the surface (approximately 5°). The following features are apparent:

1. The existence of sub-boundaries developed as rows of pits.
2. The occurrence of generally spaced pits within the subgrains.
3. The dihedral angles between sub-boundaries themselves and between the sub-boundaries and the grain boundaries.

Fig. 2 shows a section of one of the boundaries of Fig. 1. The mismatch across the boundary is qualitatively illustrated by the change in reflected light intensity from one side of the boundary to the other. Fig. 3 shows another section of this boundary. The fact that the discontinuities which cause the pits extend into the metal is evident from the path of the boundary up and down the ridge in the center of the field. On thin-sheet specimens, boundaries were noted to be continuous through the sheet.

The degree of mismatch across the boundary of Fig. 2 has been estimated at about ten minutes from X-ray analysis. Unfortunately, there is no

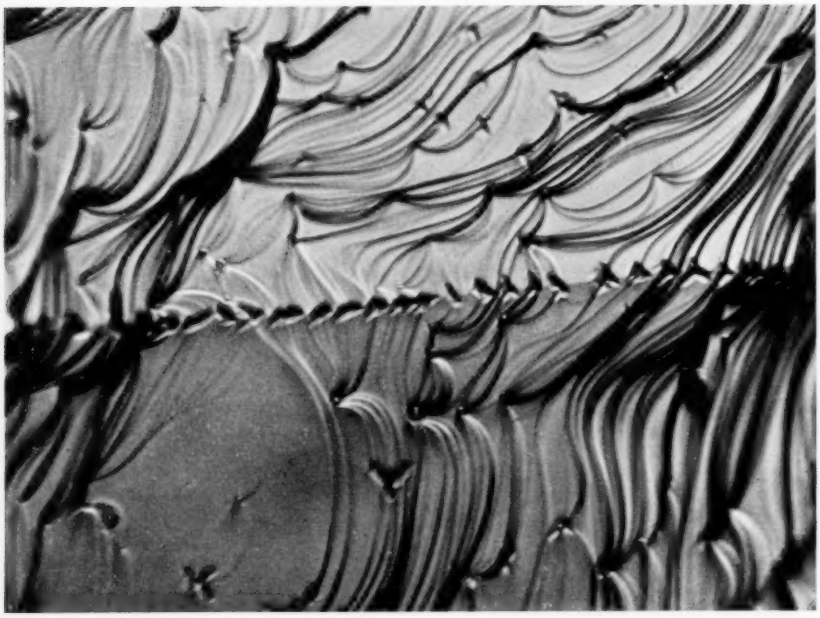

FIG. 2. Section of a subgrain boundary shown in Fig. 1—×2000.

FIG. 3. Section of a subgrain boundary shown in Fig. 1—×2000.

control over the angle of intersection of the dislocation lines with the surface, and therefore no precise correlation between pit-spacing and the angle of mismatch can be made at this time. The reported mismatch would seem to require a closer spacing of pits on the basis of a simple boundary model.[5, 11] A valid analysis would require, however, a section normal to the dislocation lines, since any section other than the normal one constitutes a taper section. Therefore, the observed pit-spacing is probably greater than the actual spacing of dislocations along the boundary by some taper factor. The interpretation of the exact geometry of the dislocation array along the boundary is further complicated by the fact that the boundaries are not crystallographically dependent (Fig. 4). The model for these boundaries does not appear to be a simple one, and further experiments to determine their geometry are anticipated.

The scarcity of the subgrains may be due to coarsening during the long thermal treatment.[7] However, there is an alternate explanation for such boundaries which has recently been proposed by Nielsen,[26] called "geometrical coalescence." This mechanism could produce the observed boundaries, and is indicated in many boundary configurations which have been noted during this investigation.

VOL. 4 1956

Grain-boundary migration was easily observed because of the difference in striae configuration between neighboring grains. It is interesting to note that when a grain boundary migrated, the sub-boundaries, when observable, extended or contracted with the movement of the grain boundary. This behavior was also noted by Dunn and Daniels in silicon iron.[27]

The observed dihedral angles at the intersection of the sub-boundaries with the grain boundaries are not to be expected, due to the relatively low energy associated with the sub-boundaries. However, the grain boundaries themselves are not very high-energy boundaries, relative to the sub-boundaries, because of a rather strong texture developed during thermal etching. Experiments are in progress to measure the dihedral angles accurately and estimate the interfacial energy of a sub-boundary. This should allow an independent determination of the density of dislocations along the sub-boundary.[4, 5]

The density of the randomly-spaced pits intersecting the surface is of the order of 10^5–10^7 per square centimeter. This is consistent with the range generally quoted for the density of dislocations in a well-annealed metal (approximately 10^6–10^8 per square centimeter)[28] and agrees well with a similar determination in thermally-etched silver.[12] One is therefore tempted to attribute their occurrence to dislocations. Fig. 5 shows the configuration of the generally-spaced pits at higher magnification. This field was not taken in the grain shown in Fig. 1 and illustrates a configuration where the {100} plane intersects the surface at a slightly greater angle. However, this does not affect the conclusions drawn.

Pits lying along crystallographic directions within a single grain are shown in Fig. 6. The spacing in this type of array is quite uneven. However, this is to be expected, considering these pits to be indications of dislocations lying in slip planes.

It should be noted that these pit phenomena are crystallographically dependent to the extent that they are observed only in grains oriented so that a {100} plane is within about 10° of the surface. A certain degree of crystallographic dependence of the observation of the intersections of dislocations with the free surface is expected, but it seems questionable that the limits would be so narrow. One factor influencing the observability of the dislocation pits is the degree of interference caused by thermal-etch striae. Fig. 7 illustrates small-angle boundaries in a grain where the angle of intersection of the {100} plane with the surface is somewhat greater than 10°. The resolution of individual pits in the boundaries is poor with this orientation.

Fig. 8 shows a boundary of greater mismatch than those illustrated previously. A grain boundary is present on the left-hand edge of Fig. 8. The pit-spacing is obviously greater as the sub-boundary approaches the grain boundary. This is probably a result of climb of the dislocations from the sub-boundary into the grain boundary at the high etching temperature.

Fig. 9 illustrates a type of configuration observed in chromium thermally etched at 1500°C, where a {100} plane of the grain is in the surface. Two interesting features are noted in this structure:

1. The nature of the intersections of the lamellae with the grain boundaries.
2. The configuration around an inclusion.

It is suggested that the configuration near the grain boundaries represents, on a gross scale, the movement of dislocation loops from the boundaries across the grain. Fig. 10 is a higher magnification of the area around point *A* in Fig. 9.

Recent moving pictures of thermal-etching of mercuric iodide taken by J. B. Newkirk allow a reasonable interpretation of this pattern.[29] The mercuric iodide striae configuration was in many cases very similar to that observed in chromium,

FIG. 4. Section of a subgrain boundary shown in Fig. 1—×2000.

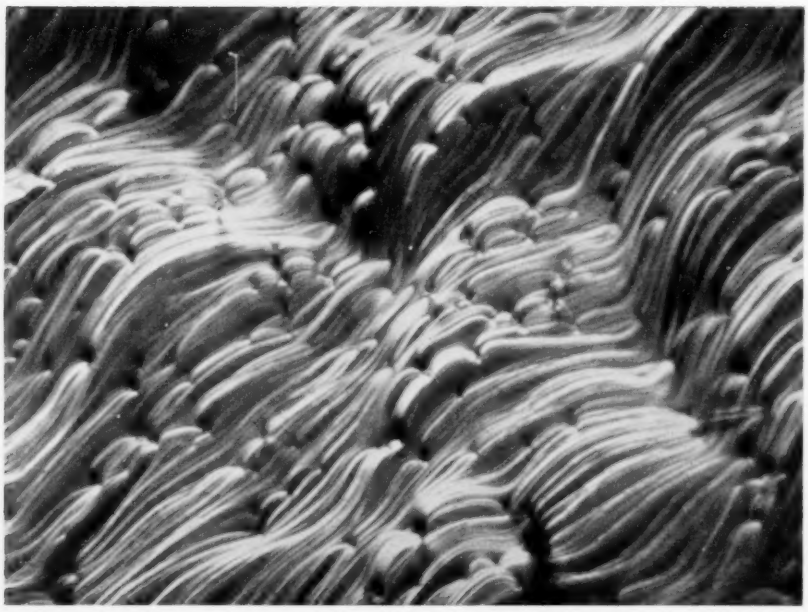

FIG. 5. Generally spaced pits within a grain—×1500.

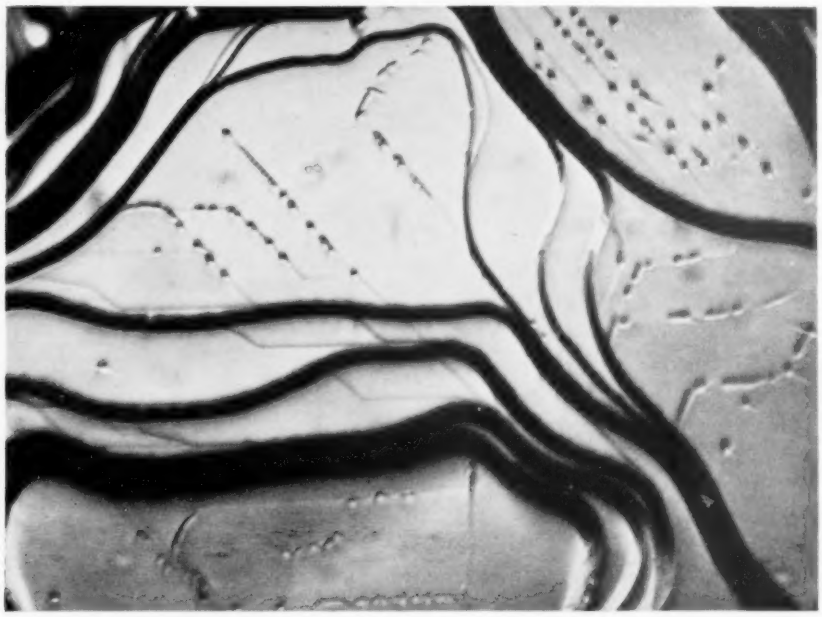

FIG. 6. Interior of grain showing pits positioned along crystallographic directions—×2000.

VOL.
4
1956

FIG. 7. Subgrain triple point within a large grain—×2000.

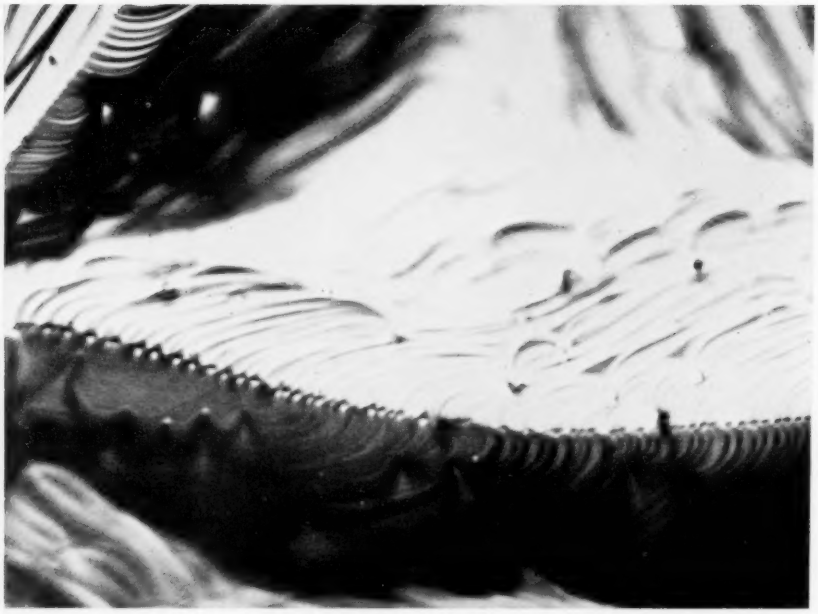

FIG. 8. Subgrain boundary showing variation of pit-spacing along the boundary—×2500.

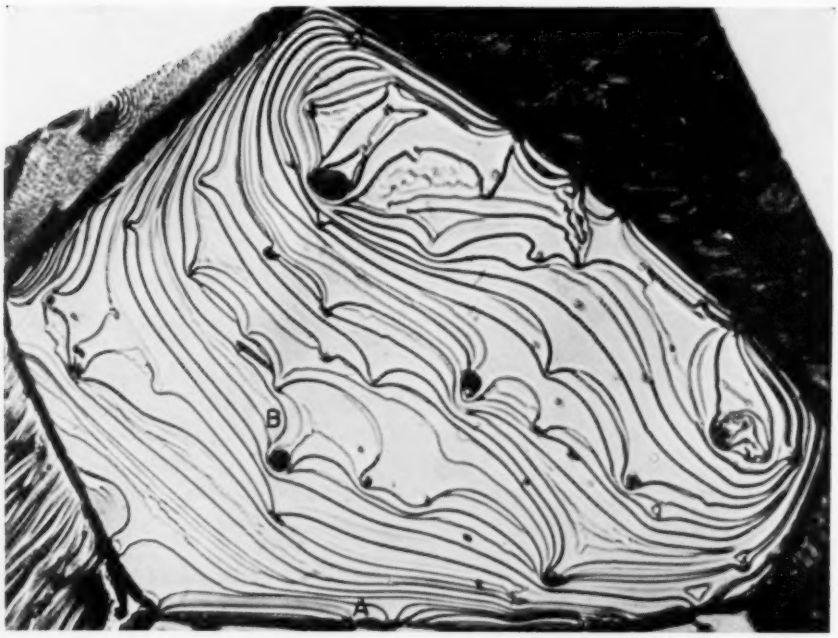

FIG. 9. Thermal-etching configuration showing interaction between striae and inclusions—×500.

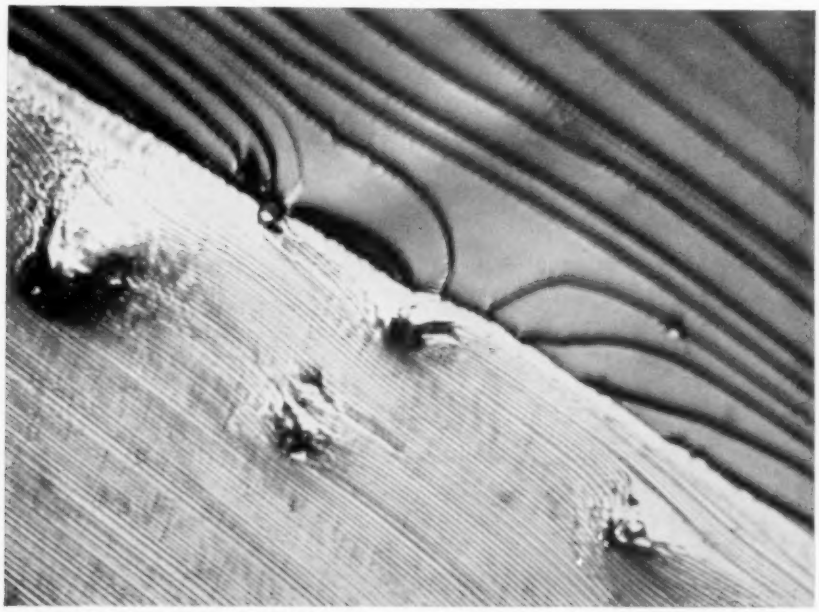

FIG. 10. Detail of area around point A in Fig. 9—$\times 2000$.

VOL.
4
1956

FIG. 11. Detail of area around point B in Fig. 9—$\times 2000$.

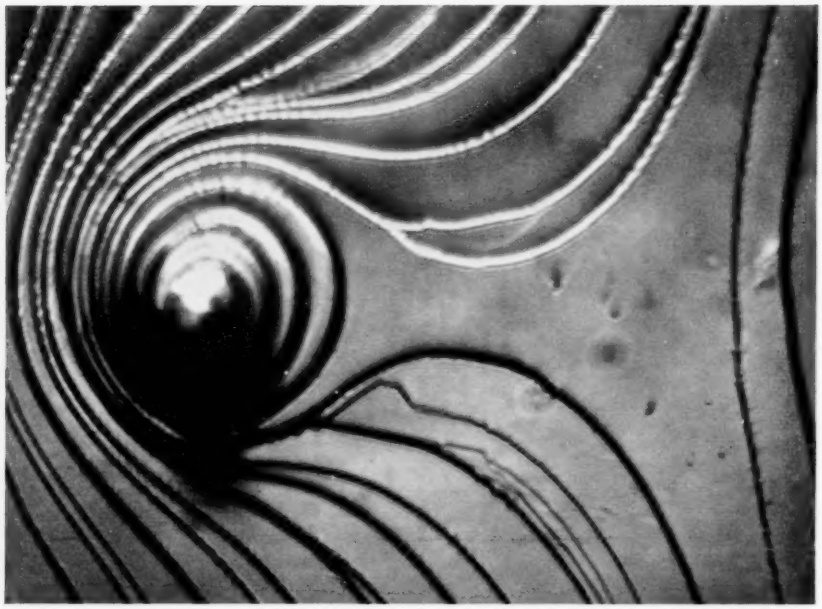

FIG. 12. Interaction of striae with an inclusion showing closed loops around the inclusion—×2000.

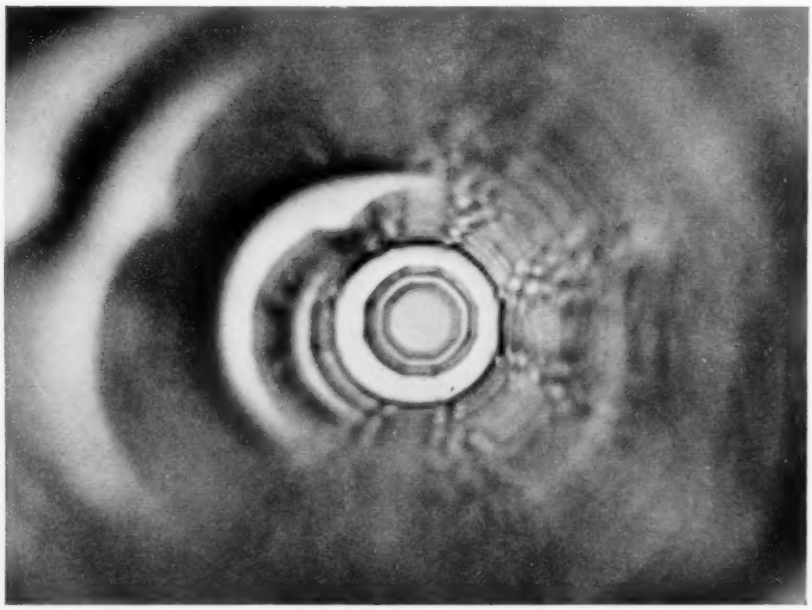

FIG. 13. Deep pit with octagonal symmetry—×2800.

with the lamellae originating at grain boundaries and moving across the grain. It is believed that the surface pattern in chromium illustrated in Fig. 9 was also produced by this mechanism. The lamellae do not necessarily leave the boundary with their final thickness. Layers of one atomic height probably move individually from the boundary and collect at some point close to it. The stable height reached before the lamellae move as a unit is a function of the orientation of the grain with the specimen surface. As soon as the collective lamella moves away from the boundary as a unit, a new one begins to form. This series of events could be realized by the degeneration of favorably oriented screw dislocations in the boundary.

The intersection of the loops with inclusions (area around point *B*, Fig. 9) is shown in Fig. 11. Fig. 12 illustrates another interaction where pinched-off loops are seen around the inclusions. It is evident that these interactions are analogous in configuration to those proposed by Orowan,[30] and Fisher, Hart, and Pry,[31] for dispersion hardening.

It should be noted that no pit-boundaries or generally-spaced pits, as illustrated in chromium etched at 1300°C, were observed in that etched at 1500°C. Low-angle boundaries are present in the latter, but these are not delineated by pits. Also, the striae configuration, except for grains of the orientation very close to that shown in Fig. 9, is generally straight and crystallographically dependent. These two observations indicate the decreased sensitivity at the higher etching temperature.

Fig. 13 shows a configuration which was noted only in the chromium etched at 1500°C. This is a relatively deep pit which, at its base, exhibits octagonal symmetry. There is an obvious tendency in the second and third levels from the base toward dodecahedral symmetry, and further up on the wall of the pit the section appears to be a regular polygon of many sides approaching a circle. Pits of this type are observed in grains which have a {100} plane nearly in the plane of the surface. It is proposed that this represents the reverse process of spiral growth as proposed by Frank[32] and directly observed in cadmium iodide crystals by Newkirk.[33] The polygonal symmetry of the pit is due to anisotropy of atom removal.

Fig. 14 illustrates a growth-mound which exhibits the same symmetry characteristics as the pit mentioned above; the opposite nature of these two structures was verified by the light profile method.[34] This structure is probably the result of spiral growth. The apparent anomaly of growth occurring under

FIG. 14. Growth-mound with octagonal symmetry—×1500.

so-called etching conditions may be resolved by considering the observations of Johnson,[35] who noted growth-mounds on thermally-etched tungsten. It is probable that a relatively stationary gas-jacket exists around the whole specimen while it is being thermally etched. Metal atoms, diffusing in this jacket, have a high probability of return to the solid surface.[22, 36] It is not unlikely that local fluctuations of metal-vapor content of the gas, temperature of gas or metal surface, or energy of the surface, could lead to local growth. The probability of such occurrences is small, and indeed growth-mounds were rarely observed in this study.

Continuously connecting spirals were not resolved either in the pits or in the mounds. However, this is to be expected, since the strength of growth- or etch-spirals in metals under the imposed conditions is one atomic diameter, and special techniques on relatively open structures are required to resolve the spiral.[1]

CONCLUSIONS

It may be concluded from the illustrations of thermally-etched chromium presented above that in this metal, at least, thermal-etching reveals structures related to the presence of dislocations.

ACKNOWLEDGMENTS

The authors are indebted to Mr. Edward Bahm of the General Electric Research Laboratory, Niskayuna, New York, for carrying out the thermal-etching treatments. Many thanks are also due Dr. J. B. Newkirk of the General Electric Research Laboratory for helpful discussions.

The authors are also grateful for the continued interest of Dr. P. R. Kosting of the Watertown Arsenal Laboratory. This research was conducted as part of a contract sponsored by the Ordnance Corps.

VOL. 4 1956

REFERENCES

1. A. J. Forty, *Adv. in Phys.*, **3, No. 9,** 1 (1954).
2. J. M. Burgers, *Proc. Kon. Ned. Akad. Wet.*, **42,** 293 (1939).
3. W. L. Bragg, *Proc. Phys. Soc.*, **52,** 54 (1940).
4. W. Shockley and W. T. Read, *Phys. Rev.*, **75,** 692 (1949).
5. W. Shockley and W. T. Read, *Phys. Rev.*, **78,** 275 (1950).
6. J. H. van der Merwe, *Proc. Phys. Soc.*, **A63,** 616 (1950).
7. A. Guinier, *Imperfections in Nearly Perfect Crystals*, p. 402 (1950), Symposium, John Wiley and Sons, New York.
8. F. H. Horn, *Phil. Mag.*, **43,** 1210 (1952).
9. R. Castaing, *Compt. Rend.*, **228,** 1341 (1949).
10. F. L. Vogel, *Acta Met.*, **3,** 95 (1955).
11. F. L. Vogel, W. G. Pfann, H. E. Corey, and E. E. Thomas, *Phys. Rev.*, **90,** 489 (1953).
12. A. A. Hendrickson and E. S. Machlin, *Acta Met.*, **3,** 64 (1955).
13. H. Wilsdorf and D. K. Wilsdorf, *Phil. Mag.*, **45,** 1096 (1954).
14. R. P. Steijn, *Trans. Amer. Inst. Met. Eng.*, **203,** 406 (1955).
15. P. Lacombe and L. Beaujard, *J. Inst. Met.*, **74,** 1 (1948).
16. J. J. Oberly, *Trans. Amer. Inst. Met. Eng.*, **200,** 1025 (1954).
17. E. S. Greiner, *Trans. Amer. Inst. Met. Eng.*, **203,** 203 (1955).
18. P. A. Jacquet, *Acta Met.*, **2,** 752 and 770 (1954).
19. S. Amelinckx, *ibid*, 848.
20. A. H. Abdou, *Phil. Mag.*, **45,** 105 (1954).
21. S. Amelinckx, *Phil. Mag.*, **44,** 1048 (1953).
22. T. R. Padden and F. M. Cain, *Jr., Met. Prog.*, **66, No. 1,** 108 (1954).
23. R. Shuttleworth, *Metallurgia*, **Vol. 38,** No. 225 (1948).
24. B. Chalmers, R. King, and R. Shuttleworth, *Proc. Roy. Soc.*, **A193,** 465 (1948).
25. M. J. Fraser and A. A. Burr (in press).
26. J. P. Nielsen, *Trans. Amer. Inst. Met. Eng.*, **200,** 1084 (1954).
27. C. G. Dunn and F. W. Daniels, *Trans. Amer. Inst. Met. Eng.*, **191,** 147 (1951).
28. P. Gay, P. B. Hirsch, and J. W. Kelley, *Acta Met.*, **1,** 315 (1953).
29. J. B. Newkirk, private communication.
30. E. Orowan, *Symposium on Internal Stresses in Metals and Alloys*, The Institute of Metals, London (1948).
31. J. C. Fisher, E. W. Hart, and R. H. Pry, *Acta Met.*, **1,** 336 (1953).
32. F. C. Frank, *Disc. Faraday Soc.*, **5,** 48 (1949).
33. J. B. Newkirk, private communication.
34. S. Tolansky, *Nature*, **169,** 445 (1952).
35. R. P. Johnson, *Phys. Rev.*, **54,** 459 (1938).
36. I. Langmuir, *A.I.E.E.*, **32,** 1913 (1913).

VOL
4
195

THE CRITICAL SHEAR STRESS IN α-BRASS AS A FUNCTION OF ZINC CONCENTRATION AND TEMPERATURE*

R. E. JAMISON and F. A. SHERRILL†

Single-crystal tensile specimens of α-brass of various compositions up to 30 at. per cent Zn were pulled at four temperatures (4.2, 78, 195, and 297°K) to measure the critical shear stress. The ratios of the critical shear stress at each of the lower temperatures to that at 297°K show a sharp increase from unity for 0% zinc (measured by previous workers) to a plateau at about 7% and then another rise starting at about 20% zinc. A significant result is that for small percentages of zinc (up to about 4%) the critical shear stress at 4.2°K is actually lower than that at 78°K. An explanation of this anomaly is offered in terms of jog formation in the dislocations during their movement prior to yielding of the specimen.

DE LA TENSION CRITIQUE DE CISAILLEMENT DANS LE LAITON α AU POINT DE VUE DE LA CONCENTRATION EN Zn ET DE LA TEMPÉRATURE

Des échantillons de mono-cristaux de laiton α tenant plus de 30 pour cent de Zn ont été soumis à une traction sous 4 températures (4,2, 78, 195, 297°K) pour mesurer la tension critique de cisaillement.

Les rapports de la tension critique de cisaillement à la température la plus haute (297°K) à celle obtenue pour les autres températures indiquent un accroissement rapide lorsque la teneur en Zn croit de 0 à 7%.

Pour cette valeur, on obtient un palier puis une nouvelle augmentation pour des teneurs de 20% Zn environ.

Un résultat significatif obtenu ainsi est que pour les faibles teneurs en Zn (4% et plus), la tension critique de cisaillement à 4,2°K est actuellement plus faible que celle à 76°K. On propose un explication de cette anomalie en relation avec la formation de Jog dans les dislocations au cours de leur mouvement avant que l'échantillon n'ait atteint sa limite élastique.

DIE KRITISCHE SCHUBSPANNUNG VON α-MESSING ALS FUNKTION DER ZINK-KONZENTRATION UND DER TEMPERATUR

Einkristalline Zugstäbe aus α-Messing verschiedener Zusammensetzung bis zu 30 At.-Prozent Zn wurden bei vier Temperaturen (4,2, 78, 195, und 297°K) gedehnt, um die kritische Schubspannung zu messen. Die Verhältniswerte der kritischen Schubspannung bei jeder der tieferen Temperaturen zu derjenigen bei 297°K zeigen einen scharfen Anstieg von eins für 0% Zink (von früheren Bearbeitern gemessen) zu einem Plateau bei ungefähr 7% und daraufhin einen weiteren Anstieg der etwa bei 20% Zink beginnt. Ein bemerkenswertes Ergebnis ist, dass für kleine Zinkgehalte (bis zu etwa 4%) die kritische Schubspannung bei 4,2°K tatsächlich kleiner ist als diejenige bei 78°K. Es wird eine Erklärung dieser Anomalie durch Sprung(jog)-Bildung in den Versetzungen während ihrer Bewegung vor Beginn des plastischen Fliessens der Proben vorgeschlagen.

VOL.
4
1956

INTRODUCTION

The data presented here are the result of preliminary work in a study of neutron-irradiation effects on the mechanical and electrical properties of α-brass single crystals. The results supplement early room-temperature data by Göler and Sachs[1] and Masima and Sachs[2] on α-brass, and more recent data by Ardley and Cottrell[3] on β-brass in the range 78°K to 673°K.

PROCEDURE

High-purity copper (99.999%) and zinc (99.99%) in the approximate proportion desired were inserted into a closed graphite mold which was then sealed into a fused-quartz tube at 400°C under a vacuum of approximately 2×10^{-5} mm of Hg. The metals were melted and mechanically agitated to obtain homogenization, then crystals were grown from the melt by the Bridgman technique.

Because of the differences in coefficients of thermal expansion between the crystals and the graphite mold, some deformation ($< 0.8\%$ elongation) occurred during cooling. After the crystals were removed from the mold, they were etched, sealed again in an evacuated quartz tube, and annealed for seventeen hours at 550°C.

The single crystals, which were grown in the shape of tensile specimens with the gage section $1\frac{1}{2}$ inches long by $\frac{7}{32}$ inch in diameter, were then strained in an Instron Tensile Testing Machine, at a constant rate of extension (0.02 in./min). The crystals were pulled at various temperatures in the following

* Received August 6, 1955.

† Oak Ridge National Laboratory, Oak Ridge, Tennessee.

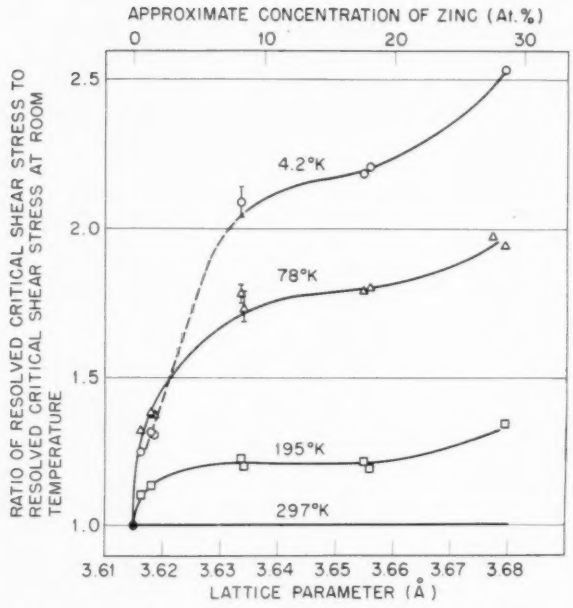

FIG. 1. The ratios of the resolved critical shear stress at each of three lower temperatures to that at room temperature are plotted as a function of lattice parameter (or approximate zinc concentration). The absolute values of the critical shear stress may be obtained by use of Table 1.

order: 297 (twice), 78, 4.2, 297, and 195°K. During each test the samples were extended to just exceed the elastic limit. After these six tests, the samples were again annealed (72 hours at 550°C) and were pulled again at the various temperatures, but not in the same order, to check the first measurements. Except for samples 5A and 5B, the reproducibility

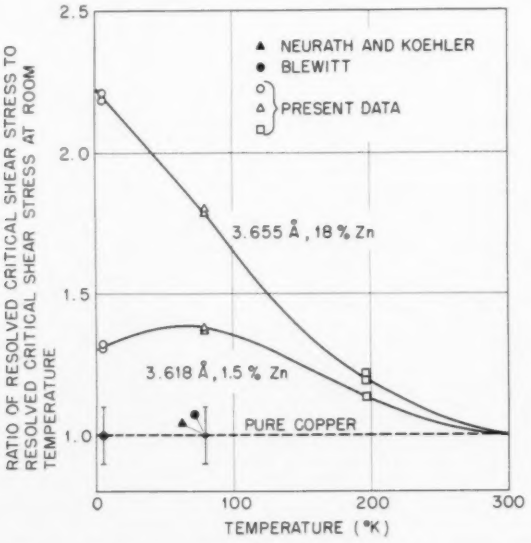

FIG. 2. The ratios of the resolved critical shear stress which were plotted in Fig. 1 are plotted here as a function of temperature for two concentrations of zinc. The results by previous workers on pure copper are also shown.

was within 2%. Total extension during the first set of tests was never more than 1%, and was generally less than 0.5%.

Upon completion of the critical shear-stress measurements, sections from the ends of the samples were removed for single-crystal lattice parameter measurements. These measurements, taken at 22°C, were accurate within 0.001 Å.[4]

Although we are perhaps primarily interested in the zinc concentration, we will refer to it and the lattice parameter interchangeably (as one of the experimental variables): we have used the linear relation between the two to determine its value indirectly. This linear relation is commonly accepted and is expressed as follows: atomic per cent zinc $= 444$ (lattice parameter in angstroms $- 3.615$). The proportionality constant used here is accurate within two per cent. We have designated the values of the zinc concentration as approximate even though they are more accurate than could easily be obtained by chemical analysis, particularly on small samples.

Some samples varied slightly in zinc concentration from end to end; so in these cases the measurements were interpolated to the region where slip lines were seen in the gage length.

OBSERVATIONS

Since the concentration dependence of the critical shear stress at room temperature is well known, and since a relative value is much more accurately determined, the ratio of the critical shear stress at each of the lower temperatures to that at room temperature is plotted in both figures.

Fig. 1 shows the complete data with the critical shear stress (henceforth referred to as the CSS) ratio as a function of zinc concentration at 4.2, 78, 195°K. Fig. 2 shows the most accurate of this data for two concentrations of zinc, along with the data from previous experiments on pure copper, as a function of temperature.

Except where indicated, the values of the ratio plotted in Fig. 1 are accurate to within 2%. The values of the ratio (except those for pure copper) plotted in Fig. 2 are accurate to within 1.5%. The inaccuracy of the measurements on pure copper[5, 6] results from a yield point being undefined in this material.

The values of the critical shear stress measured at room temperature for all samples are listed in Table 1 along with values corresponding to the same concentrations which are taken from a smooth curve drawn as an average through all data available.[1, 2, 3]

TABLE I. Critical resolved shear stress at room temperature, orientation lattice parameter, and approximate composition

Sample[a]	Orientation[b] (deg)	Lattice parameter (Å)	Approximate composition (at. per cent Zn)	Critical resolved shear stress at room temp. (Kg/mm²)	
				Measured	Corrected[c]
CuZn 1	30, 63, 78	3.6792 ± 0.0010	28.5	1.52 ± 0.15	1.43
CuZn 2	46, 56½, 63	3.6770 ± 0.0010	27.5	1.56 ± 0.15	1.425
CuZn 3	43, 53, 73 43½, 51½, 72½	3.6548 ± 0.0005	17.5	1.49 ± 0.13	1.33
CuZn 5A	41, 56½, 70	3.6335 ± 0.0005	8.2	1.08 ± 0.12	1.07
CuZn 5B	41, 56½, 70 Assumed	3.6340 ± 0.0005	8.5	1.03 ± 0.12	1.08
CuZn 6	4½, 86½, 87	3.6162 ± 0.0005	0.5	0.51 ± 0.08	0.50
CuZn 7A	43½, 48½, 79½	3.6179 ± 0.0005	1.4	0.76 ± 0.10	0.64
CuZn 7B	44, 48, 82	3.6185 ± 0.0005	1.6	0.72 ± 0.10	0.67
CuZn 8	17½, 73, 84	3.6558 ± 0.0010	18.0	1.31 ± 0.13	1.34

Notes:
[a] Samples 5A and 5B were grown together as were samples 7A and 7B.
[b] The angles between the specimen axis and the three [100]-type poles.
[c] These values are from a smooth curve, drawn through the plot of data from ref. (1), (2), and (3), and the authors' own values. These would be very reasonable values to use in determining the absolute resolved shear stress from the ratio plotted in Figs. 1 and 2.

Sharp upper yield points were found at room temperature (for the first test after annealing) in those samples where the zinc concentration was more than about 1 atomic per cent. This is in agreement with the findings of Ardley and Cottrell.[3] However, all our data correspond to lower yield-point values, since only the first test in each set of tests showed an upper yield point.

The curve through the values of the ratio taken at 4.2°K in Fig. 1 is shown to be indefinite for zinc concentrations less than 10%, and the other curves (for 78°K and 195°K) might not actually run through a common point. However, it should be emphasized that, as shown in both Figs. 1 and 2, for zinc concentrations less than about 4%, the critical shear stress at 4.2°K is definitely lower than that at 78°K. This result is not affected by the order of testing or the temperature history between tests.

DISCUSSION

The large difference in mobility between zinc and copper in α-brass[7] causes formation of vacancies and voids by dezincification at elevated temperatures. In our growing of crystals by the Bridgman technique, the vacancy formation is enhanced by the crystals remaining for two or three hours in the dezincification temperature range and by the vaporized zinc having a sink at the cold end of the crucible.

In discussing our results, we plan to place major emphasis on the role of these vacancies rather than on the role of zinc as an alloying element. We are then afforded the most simple explanation of our results.

The knee (not typical of substitutional alloys) in the plot of CSS vs. zinc concentration at room temperature[1, 2] might, for example, be explained by saying there is an optimum concentration of zinc (around 10%) for the creation of vacancy effects on the critical shear stress. This statement would be supported by our data, which shows poorer reproducibility in this region and by the even more pronounced knee at the lower temperatures (Fig. 1). There is a complication in the fact that, even though the number of vacancies created may increase consistently with the zinc concentration, they might group in such a way as to have a maximum effect on the CSS at a certain concentration.

The most important and interesting result described here (Fig. 2) is the maximum in the critical shear stress at about 80°K for low zinc concentrations. This indicates the existence (in α-brass at least) of two distinct, and perhaps independent, effects of temperature on the critical shear stress. They are:

(i) The usual decrease in the CSS with increasing temperature. This has been discussed in other papers at length[8, 9] but a general argument can be stated here. That is, that the thermal energy of a dislocation can aid it in overcoming barriers, such as the necessary generation of vacancies or interstitials by a jog.[10] The higher the temperature, then the higher the mean thermal energy of the dislocation, and the lower the critical shear stress or the external force required to cause displacement of the dislocation.

(ii) An increase in the CSS with increasing temperature for low concentrations of solute only. To

the authors' knowledge this effect has not been observed before and requires at least a possible explanation.

The existence of the Bauschinger effect[11] and the elastic after effect[12] in α-brass single crystals would indicate that this increase in the CSS with increasing temperature might be caused during the so-called elastic extension. These two effects indicate that, prior to the yielding of α-brass under stress, there is displacement and locking of dislocations away from their potential minima.

If we say that the locking is by vacancies or groups of vacancies, we can assume that the extent of the locking (or the jog configuration) is temperature dependent, since, in general, the vacancies picked up by the moving dislocation (or moving extended dislocation) would not lie directly in the path of the dislocation and would be required to diffuse to it (perhaps by moving only one lattice spacing) from planes adjacent to the plane in which the dislocation is moving. The lower the temperature, the lower would be the rate at which such diffusion could take place; and the lower the concentration, the lower the diffusion rate as well as the number of vacancies available to the dislocation at any particular temperature.

If the concentration of vacancies is high enough, then even at the lowest temperatures the moving dislocation could pick up enough vacancies directly in its path to have an optimum or perhaps saturating effect on the CSS without any maximum in the CSS vs. temperature curve. We see this in the curve (Fig. 2) corresponding to 18% zinc. Although there might still be an inflection at about 100°K which would indicate a slight diffusion effect, if it exists at all it is not pronounced and there is no actual maximum in the CSS as there is for concentrations below about 4% zinc.

FURTHER OBSERVATIONS

The standard annealing temperature was 550°C, but in two instances (CuZn-3 and CuZn-5A) the second anneal was made at 850°C, and this caused a 5% rise in the ratio at 78°K while the actual yield strength was lowered slightly at room temperature. Also there were visible voids formed in the sample during the anneal at 850°C. When the sample was annealed again at 550°C for 72 hours, the ratio nearly returned to its original value. The increase in the ratio could be caused by additional dezincification and vacancy formation at the higher temperature, while the void formation with consequent reduction in cross-section area would account for the slightly reduced yield strength at room temperature. Annealing afterwards at 550°C conceivably alters the jog configuration in such a way as to lower the temperature effect on the CSS.

The curve plotted in Fig. 2 corresponding to approximately 18% zinc is very similar to the same curve plotted for pure copper with approximately 3×10^{18} fast neutrons/cm^2 irradiation.[13] Among other defects the irradiated copper would contain a large number of vacancies and interstitials.

When CuZn-1 (approximately 28.5% zinc) was pulled at 4.2°K, it yielded discontinuously and with audible clicks. This was definitely a real effect and is thought to be like the phenomenon reported for irradiated copper at 78°K[14] and deformed copper at 4.2°K.[15]

ACKNOWLEDGMENTS

The authors are indebted to D. S. Billington, Director of the Solid State Division at this laboratory, for his encouragement and valuable criticism, and to T. H. Blewitt, R. H. Kernohan, M. S. Wechsler, R. R. Coltman, J. T. Gray, and G. E. Klein for helpful suggestions, criticism, and aid. We are also indebted to J. S. Koehler of the University of Illinois, whose interest resulted in our refinement and publication of the data.

REFERENCES

1. V. Göler and G. Sachs, *Z. Phys.*, **55,** 581 (1939).
2. M. Masima and G. Sachs, *Z. Phys.*, **50,** 161 (1928).
3. G. W. Ardley and A. H. Cottrell, *Proc. Roy. Soc.*, **A219,** 328 (1953).
4. R. J. Fox, F. A. Sherrill, M. C. Wittels, A single-crystal adapter for the Norelco wide-range diffractometer, *ORNL*-1807 (Jan. 6, 1955).
5. P. W. Neurath and J. S. Koehler, *J. Appl. Phys.*, **22** 621 (1951).
6. T. H. Blewitt, *Phys. Rev.*, **91,** 1115 (1953).
7. D. D. VanHorn and W. J. Cooley, *Phys. Rev.*, **98,** 245 (1955).
8. A. F. Mott, *Phil. Mag.*, **43,** 1152 (1952).
9. A. H. Cottrell and B. A. Bilby, *Proc. Phys. Soc. (London)*, **49,** A62, (1949).
10. W. T. Read, *Dislocations in Crystals*, McGraw Hill, p. 85 (1953).
11. G. Sachs and H. Shoji, *Z. Phys.*, **45,** 776 (1927).
12. R. E. Jamison, to be published.
13. T. H. Blewitt, R. R. Coltman, R. E. Jamison, unpublished.
14. R. E. Jamison and T. H. Blewitt, *Phys. Rev.*, **91,** 237 (1953).
15. T. H. Blewitt, J. K. Redman, F. A. Sherrill, and R. R. Coltman, APS Bulletin, **30,** No. 2, 32 (1955).

FORMATION DE MONOCRISTAUX DE Cu_2O ET ZnO PAR OXYDATION SELECTIVE D'UN FILM DE LAITON α PREPARE PAR EVAPORATION SOUS VIDE*

N. TAKAHASHI† et J. J. TRILLAT‡

De minces films de laiton α ont été préparés par évaporation successive sous vide de Cuivre et de Zinc, puis oxydés par chauffage dans le vide du diffractographe électronique (~10^{-3} m/m Hg). On a réussi à obtenir ainsi des monocristaux des oxydes Cu_2O et ZnO dont l'orientation relative avec le support a été déterminée. On a étudié également les phénomènes d'oxydation sélective.

Cu_2O AND ZnO SINGLE CRYSTAL FORMATION BY SELECTIVE OXIDATION OF AN α-BRASS FILM, PREPARED BY VACUUM EVAPORATION

α-Brass thin films were prepared under vacuum by successive deposition of copper and zinc. The films were then oxidized by heating in the specimen chamber of the electron diffraction unit (10^{-3} mm/Hg). In this way, it was possible to obtain Cu_2O and ZnO single crystals whose relative orientations with respect to their base were determined. Processes of selective oxidation were then studied.

DIE HERSTELLUNG VON Cu_2O- UND ZnO-EINKRISTALLEN DURCH SELEKTIVE OXYDATION EINER IM VAKUUM AUFGEDAMPFTEN DÜNNEN SCHICHT AUS α-MESSING

Durch stufenweise Verdampfung von Kupfer und Zink im Vakuum wurden dünne Schichten aus α-Messing hergestellt, die anschliessend im Vakuumraum des Elektronenbeugungsgerätes durch Erhitzen oxydiert wurden (~10^{-3} mm/Hg). Auf diese Weise erhalt man Einkristalle der Oxyde Cu_2O und ZnO, deren relative Orientierung zu ihrer Unterlage bestimmt wurde. Gleichzeitig wurden die Vorgänge bei der selektiven Oxydation untersucht.

VOL. 4 1956

1. INTRODUCTION

On sait que lorsqu'on chauffe dans l'air certains alliages, l'un des composants s'oxyde sélectivement;[1] les conditions de cette oxydation varient selon la température et la pression.[2] En ce qui concerne le laiton, c'est l'oxyde de cuivre Cu_2O qui apparaît à basse température et l'oxyde de zinc ZnO qui se forme à haute température.[1] Toutes les recherches sur l'oxydation sélective effectuées jusqu'à présent par diffraction électronique ont été effectuées par la méthode de réflexion; nos expériences ont pour but de les compléter en utilisant la méthode plus précise de transmission.

Nous avons préparé dans ce but un monocristal de laiton α à l'état de film mince par évaporation dans le vide et effectué des expériences d'oxydation de cet échantillon en le chauffant dans le vide contrôlé du diffractographe électronique.[3]

2. EXPERIENCES

Un monocristal de laiton α est préparé par évaporation *successive* dans le vide de cuivre et de zinc sur une surface fraîchement clivée de sel gemme portée à 420°C. L'appareil d'évaporation est semblable à celui que Göttsche a utilisé pour préparer des monocristaux des alliages Al-Ag.[4] La température doit être supérieure à 400°C afin d'obtenir de bonnes plages unicristallines; des essais nous ont montré que la température de 420°C était particulièrement convenable.

L'évaporation *simultanée* de Zn et de Cu à partir d'un même four est au contraire très difficile, car le cuivre s'évapore après qu'il est fondu et forme une sphère liquide, tandis que le zinc s'évapore directement sans passer par cet état.

Dans ce travail, nous avons évaporé le cuivre et le zinc successivement en utilisant deux fours placés tout près l'un de l'autre, les deux opérations se faisant sans rompre le vide entre chacune d'elles. Il est important d'évaporer d'abord le cuivre et ensuite le zinc, car sinon l'on ne peut obtenir de monocristal.

Après refroidissement lent du support, celui-ci est dissout dans l'eau distillée et le film composite recueilli sur une grille de nickel. Le film est ensuite étudié par diffraction électronique en transmission, sous incidence normale; il est chauffé dans le diffractographe lui-même,[5] sous un vide de $2 \cdot 10^{-3}$ m/m Hg, ce qui permet de suivre sur l'écran fluorescent le phénomène d'oxydation progressive dû à la présence de l'oxygène résiduel.

* Received May 7, 1955.
† Université de Yamanashi, Kofu, Japon.
‡ Laboratoire de Rayons X du C.N.R.S.-Bellevue (S. and O.) France.

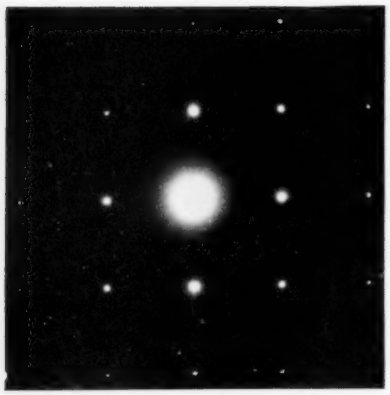

FIG. 1. Laiton α.

3. RESULTATS

1. *Monocristal de laiton α*

D'après le diagramme d'équilibre, le laiton α existe entre 0 et 40% en poids de zinc; on sait qu'il consiste en une solution solide de substitution. Par substitution d'atomes de Zn aux atomes de Cu dans la maille cristalline de Cu, celle-ci passe de 3,608 Å (Cu) à 3,68 Å (laiton α) pour 30% en poids de Zn, mais le réseau cristallographique reste toujours cubique à faces centrées.

La Fig. 1 montre le diagramme de diffraction correspondant à un monocristal de laiton α ainsi préparé; son plan (100) est toujours parallèle à la surface clivée (100) du support de sel gemme.

Quand la préparation est inclinée d'environ 30° par rapport au faisceau électronique, l'intensité de quelques-unes des taches principales s'affaiblit et de nombreuses taches supplémentaires apparaissent, dont certaines sont disposées en croix (Fig. 2).

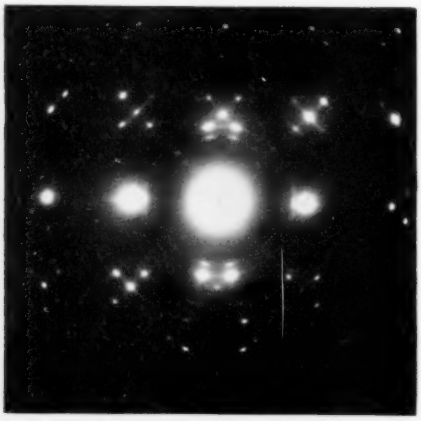

FIG. 2. Laiton α. Film incliné de 30° par rapport au faisceau d'électrons. Quelques taches dues à l'oxyde de cuivre Cu_2O apparaissent aussi, mais les taches correspondant au laiton α sont aisément identifiables par comparaison avec la Fig. 1.

Un tel phénomène a déjà été observé par Brück[6] dans le cas de monocristaux métalliques et discuté en détail par Menzer,[7] v. Laue,[8] Göttsche.[4] En particulier, Göttsche explique l'apparition de toutes les taches supplémentaires par formation de mâcles submicroscopiques et de défauts de réseau; nous en publierons ultérieurement les détails.

2. *Monocristal de Cu_2O*

Le monocristal de Cu_2O se forme souvent très facilement après une simple action de l'eau sur le film composite de Cu et de Zn; il se forme aussi quand on chauffe l'échantillon dans le vide du diffractographe (2×10^{-3} m/m Hg) à une température *inférieure à* 300°C; il se dissocie ensuite aux températures supérieures. En général, cependant, la structure n'est pas parfaite et le diagramme de diffraction montre une organisation plus ou moins fibreuse (Fig. 3). Trois orientations relatives entre Cu_2O et le support sont observées, dont la principale est:

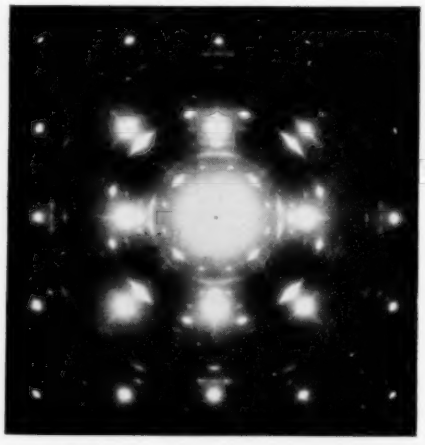

FIG. 3. Oxyde de cuivre Cu_2O formé sur le film monocristallin de laiton α. Trois orientations sont observables.

$$(001)\ Cu_2O \parallel (001)\alpha \quad \text{et} \quad [010]\ Cu_2O \parallel [010]\alpha \quad (1)$$

(plan et arête du cube des deux cristaux respectivement parallèles). Les deux autres orientations sont:

$$(111)\ Cu_2O \parallel (001)\alpha \quad \text{et} \quad [1\bar{1}0]\ Cu_2O \parallel [1\bar{1}0]\alpha \quad (2)$$

$$\text{et} \quad (111)\ Cu_2O \parallel (001)\alpha \quad \text{et} \quad [1\bar{1}0]\ Cu_2O \parallel [110]\alpha \quad (3)$$

Ces trois orientations sont schématisées sur la

Fig. 4; les arcs provenant de l'orientation (1) présentent la plus forte intensité.

L'effet de diffusion secondaire est observable et conduit à l'apparition de nombreuses taches irrationnelles. Leurs positions théoriques sont indiquées sur la Fig. 5 en même temps que les taches principales de l'oxyde Cu_2O. Cet effet se manifeste encore plus nettement dans le cas de ZnO que nous étudierons plus loin.

L'un de nous a déjà constaté que l'oxyde de cuivre Cu_2O se forme toujours pour le laiton α comme pour le laiton β, à partir des directions correspondant aux groupements atomiques les plus denses, soit [110] pour le laiton α et [111] pour le laiton β. Ceci est confirmé pour d'autres processus d'oxydation; ainsi, dans le cas de l'oxydation anodique du laiton α, on observe des orientations relatives entre l'oxyde et l'alliage identiques à celles indiquées plus haut pour l'oxydation par chauffage.

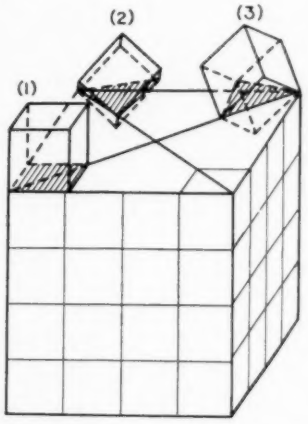

FIG. 4. Schéma montrant les trois orientations relatives entre l'oxyde de cuivre Cu_2O et le support de laiton α. Les petits cubes indiquent les mailles élémentaires de Cu_2O et le grand cube 64 mailles élémentaires du laiton α. Les plans hachurés sont parallèles aux faces du cube du laiton α. Les chiffres correspondent aux orientations (1), (2), (3) mentionnées dans le texte.

L'apparition de l'orientation (1) se comprend facilement par le fait que les atomes d'oxygène entrent dans la maille du laiton α pour former l'oxyde de cuivre; le réseau se dilate de 3,68 Å (laiton α) à 4,25 Å (Cu_2O).

Les orientations (2) et (3) semblent apparaître après que l'orientation (1) se soit développée; les atomes de Cu traversent la couche d'oxyde Cu_2O déjà produite et, du côté extérieur à cette couche, se combinent avec les atomes d'oxygène.

La direction $\langle 110 \rangle$ suivant laquelle les atomes de Cu ont la disposition la plus dense, jouerait le rôle principal dans la formation de l'oxyde et il en résulterait le développement privilégié des plans octaédriques (111) définis par ces directions.

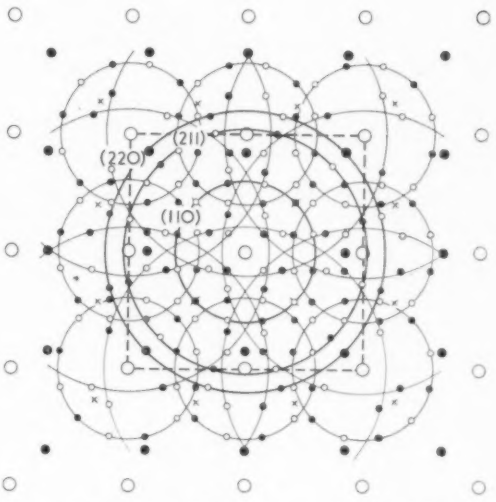

FIG. 5. Diagramme théorique relatif à la Fig. 3. Les grands cercles blancs sont relatifs aux taches du laiton α; les moyens, noirs, correspondent à l'orientation (1) et les petits cercles blancs et noirs respectivement aux deux orientations (2) et (3). Celles-ci se répètent autour de chaque tache du laiton α par effet de diffusion secondaire; les details sont representés dans le carré délimité par des tirets.

Les orientations (2) et (3) sont équivalentes; elles peuvent se développer en même temps. On peut les expliquer par l'hypothèse du glissement de rotation ("rotational slip") proposée par Wilman,[10] qui, dans ce cas, aurait lieu suivant le plan octaédrique.

3. *Formation de l'oxyde de zinc*

L'oxyde de zinc apparaît à l'état de plages monocristallines quand on chauffe des plages monocristallines de laiton α au-dessus de 450°C dans le vide partiel du diffractographe électronique. La structure

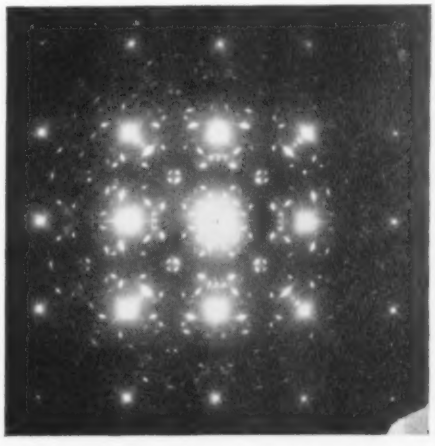

FIG. 6. Oxyde de zinc formé sur un film de laiton α.

VOL. 4 1956

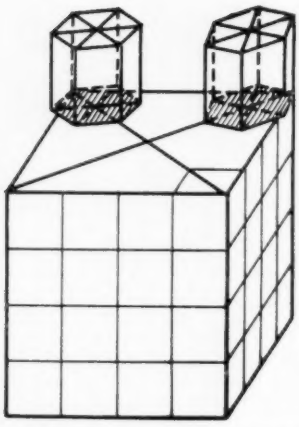

FIG. 7. Schema montrant les deux orientations relatives entre l'oxyde de zinc et le support de laiton α.

monocristalline est d'autant plus parfaite que la température est plus élevée et que la durée de chauffage est plus longue. La Fig. 6 montre le diagramme de ZnO obtenu à partir de l'échantillon ainsi chauffé à 450°C pendant trente minutes. Les grosses taches correspondent au réseau cubique à faces centrées du laiton α. Les petites taches sont dues à l'oxyde de zinc; elles peuvent être facilement indicées et leur disposition indique que le cristal hexagonal ZnO se développe de façon à ce que le prisme hexagonal soit perpendiculaire à la face du cube et que les diagonales du plan de base (0001) soient parallèles à celle de la diagonale [110] du laiton α. En considérant les deux directions équivalentes de cette dernière diagonale,

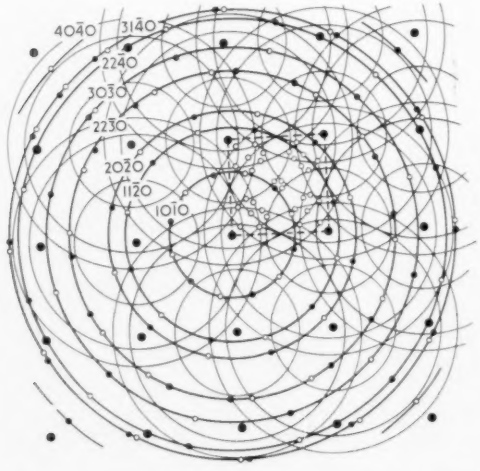

FIG. 8. Diagramme théorique qui explique le cliché 6. Les gros cercles noirs montrent les taches dues au laiton α. Les petits cercles noirs et blancs correspondent aux orientations de ZnO (4) et (5) respectivement. Les taches dues à la diffusion secondaire sont montrées, de la même manière que sur la Fig. 5, dans le premier quadrant des taches de laiton α, en tenant compte des reflexions à partir de (10$\bar{1}$0) jusqu'à (20$\bar{2}$0).

il apparaît deux orientations de ZnO schématisées sur la Fig. 7, à savoir:

$$(0001\ \mathrm{ZnO}) \parallel (001)\alpha \quad \text{et} \quad [11\bar{2}0]\ \mathrm{ZnO} \parallel [1\bar{1}0]\alpha \qquad (4)$$

et

$$(0001)\ \mathrm{ZnO} \parallel (001)\alpha \quad \text{et} \quad [11\bar{2}0]\ \mathrm{ZnO} \parallel [110]\alpha \qquad (5)$$

Autour de la trace du faisceau direct, les taches correspondant à ces deux orientations de ZnO apparaissent en même temps que de très faibles anneaux de Debye-Sherrer, qui indiquent la formation de microcristaux orientés au hasard. Elles sont représentées sur la Fig. 8 par des petits cercles noirs et blancs disposés sur des anneaux de Debye-Scherrer de grand diamètre. Dans le cas présent, l'effet dynamique est si intense que de nombreuses taches dues à la diffusion secondaire apparaissent aussi très nettement. Nous avons représenté ces taches, pour le premier quadrant des taches du laiton α, en tenant compte des réflexions à partir de (10$\bar{1}$0) jusqu'à (20$\bar{2}$0). Il existe encore d'autres taches correspondant à des réflexions multiples d'ordre plus élevé que nous avons supprimées pour plus de clarté.

En ce qui concerne l'orientation relative entre ZnO et le support de laiton, on trouve, comme pour Cu_2O, que c'est encore la direction de densité atomique maxima ⟨110⟩ du laiton α qui est parallèle à la direction ⟨11$\bar{2}$0⟩ de ZnO. Par remplacement des atomes de Cu par ceux de Zn dans la couche superficielle, cette direction ⟨11$\bar{2}$0⟩ de ZnO se développe parallèlement à la direction ⟨110⟩ du laiton α et le plan (0001) de ZnO apparaît pour la même raison que les plans (111) dans le cas de Cu_2O. On peut expliquer de la même façon l'apparition des orientations (4) et (5).

4. *Discussion sur l'oxydation sélective*

Pour de faibles pressions d'oxygène et à des températures nettement inférieures au point de fusion du zinc, on peut admettre que la pression de vapeur du zinc étant beaucoup plus grand que celle du cuivre, et la mobilité des atomes de cuivre plus grande que celle des atomes de zinc, la surface du laiton α s'enrichit en atomes de cuivre, ce qui favorise la formation de l'oxyde Cu_2O.

A haute température au contraire (supérieures au point de fusion du Zn, 419°C), les atomes de Zn se déplacent facilement vers la couche superficielle où la pression de vapeur de Zn est très grande et où sa combinaison avec les atomes d'oxygène a lieu facilement. L'oxyde de cuivre Cu_2O a tendance à être réduit, soit sous l'action réductrice du zinc, soit par dissociation de l'oxyde lui-même dans le vide. (Nous avons en effet observé que l'oxyde de cuivre

a tendance à se dissocier dans le vide à une température de l'ordre de 450°C), ce qui explique sur les clichés la disparition des taches dues à Cu_2O. En outre, la position des taches principales du laiton α montre que la maille de celui-ci varie par suite de la formation de ZnO, qui, en provoquant un départ d'atomes de Zn, amène la contraction du réseau de ce dernier.

BIBLIOGRAPHIE

1. S. MIYAKE, *Sci. Pap. Inst. Phys. Chem. Res.*, **29,** 167 (1936).
2. G. HONJO, *Proc. Phys. Soc. Jap.*, **8,** 113 (1953).
3. N. TAKAHASHI, *Compt. Rend.*, **238,** 462 (1954).
4. H. GÖTTSCHE, *Z. Phys.*, **134,** 517 (1953).
5. J. J. TRILLAT et N. TAKAHASHI, *Compt. Rend.*, **236,** 790 (1953).
   J. J. TRILLAT, *Colloque de Microscopie électronique*, Toulouse, Avril 1955 (sous presse, éditions C.N.R.S.).
6. L. BRÜCK, *Ann. Phys.*, **26,** 233 (1936).
7. G. MENZER, *Z. Kristall.*, **A99,** 410 (1938).
8. M. VON LAUE, *Ann. Phys.*, **26,** 55 (1936).
9. N. TAKAHASHI, *Rikagakukenkyujo-iho* (en japonais), **27,** 536 (1939).
10. H. WILMAN, *Proc. Phys. Soc.*, **A64,** 329 (1951); D. M. EVANS, D. M. LAYTON, and H. WILMAN, *Proc. Roy. Soc.*, **A205,** 17 (1951).

VOL.
4
1956

CEMENTITE MORPHOLOGY IN PEARLITE*

F. C. FRANK and K. E. PUTTICK†

Some characteristic growth patterns of cementite in pearlite, revealed by electron microscopy, are discussed in terms of the geometry of growth and of diffusion and surface energy factors. These include (a) linear discontinuities in the lamellar structure, which are shown to be one possible origin of branching, (b) curved and striated lamellae, (c) acicular growth of cementite. It is concluded that lamellar precipitation of cementite has its origin in anisotropy of ferrite-cementite interfacial energy.

LA MORPHOLOGIE DE LA CÉMENTITE DANS LA PERLITE

Quelques modes caractéristiques de croissance de la cémentite dans la perlite, observés au microscope électronique, sont discutés au point de vue de la géométrie de la croissance et des facteurs de diffusion et d'énergie de surface.

Ceux-ci comportent:

(a) des discontinuités linéaires, origine possible des embranchements.

(b) des lamelles courbes et striées.

(c) une croissance aciculaire de la cémentite.

On peut conclure que la précipitation de la cémentite en lamelles a son origine dans l'anisotropie de l'énergie interfaciale ferrite-cémentite.

MORPHOLOGIE DES ZEMENTITS IM PERLIT

Einige charakteristische Wachstumsfiguren von Zementit in Perlit, die elektronenmikroskopisch gefunden wurden, werden anhand der Geometrie des Wachstums und von Diffusions- und Oberflächenenergie-Betrachtungen diskutiert. Diese umfassen (a) lineare Diskontinuitäten in der Lamellenstruktur, von denen gezeigt wird, dass sie eine mögliche Ursache der Verzweigung sind, (b) gekrümmte und gestreifte Lamellen, (c) nadeliges Wachstum von Zementit. Es wird der Schluss gezogen, dass die lamellare Ausscheidung von Zementit ihren Ursprung in der Anisotropie der Grenzflächenenergie zwischen Ferrit und Zementit hat.

The object of this note is to interpret certain features in the structure of pearlite colonies in steel. One such feature is a line of discontinuity in the pearlite pattern, as shown in Figs. 1 and 2. Such lines of discontinuity are found to be fairly common when pearlite is examined electron-microscopically.‡ A possible explanation is simply that two pearlite colonies growing with the same orientation in the same austenite grain have met along this line: we shall, however, indicate a way in which the same feature could be produced in a single colony.

If a convex body grows with a uniform rate of advance of every surface element normal to itself, it remains a convex body. An orthogonal trajectory to all the instantaneous growth surfaces (a growth trajectory) can be constructed through every point of any one of them. The growth trajectories through neighboring points on any one of the growth surfaces, except the first, pass through neighboring points on any other. The first surface, but no other, may have edges or corners; if it does, growth trajectories through non-neighboring points on the later surfaces meet at these edges or corners. The requirement that the rate of normal advance be uniform over the surface is not critically essential. If the growth-rate is a function of the orientation of the surface element, these statements remain true if the function is a sufficiently smooth one; namely, if a three-dimensional polar diagram of the reciprocal of the growth-rate as a function of the orientation of the normal is itself a convex body. A proof may be given on the lines of Herring's discussion of Wulff's theorem,[1] bearing in mind that the inverse of a sphere through the origin is a plane.

We apply these considerations to the growth of a pearlite colony. If at any stage considered as initial the boundary of the colony is convex, and growth is sufficiently uniform for it to remain so, the pattern of edges of cementite sheets in any portion of its surface area can be continuously propagated into the later boundaries. The spacing between sheets will increase, unless branching or folding of the sheets occurs, or new sheets are nucleated. It is indeed possible, and probable, that some of these events do happen, but inexplicable that, with a convex growth boundary,

* Received August 3, 1955.

† H. H. Wills Physical Laboratory, University of Bristol, Bristol, England.

‡ The experimental techniques used in this work have been described in another publication by one of us (K. E. P.), to appear shortly.

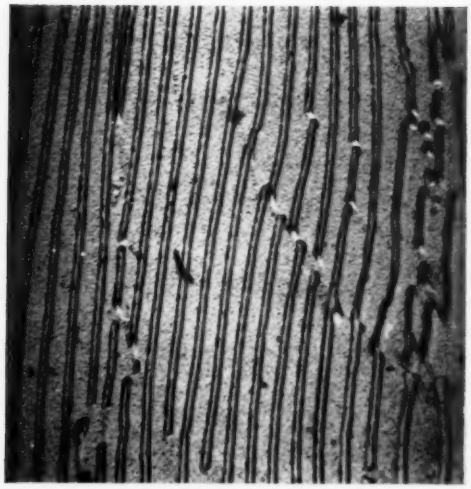

FIG. 1. Linear discontinuity in lamellar pearlite—×7500.

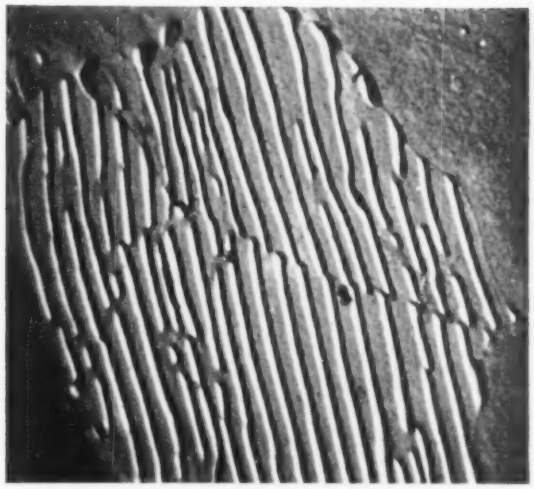

FIG. 2. Linear discontinuity in lamellar pearlite—×7500.

branching should occur in various sheets at points along a line to produce Fig. 1.

The situation is altered if there is a concavity in the growth front: for then, unless the concavity gives rise to accelerated growth, growth trajectories from the concave region meet either in a point or a line focus. The latter, i.e., an astigmatic focus in the optical analogue, will be the more general case. Beyond the focus there will be a groove in the growth surface, and neighboring points either side of the groove derive from non-neighboring points in earlier growth surfaces. The locus of this groove in three dimensions will be a surface at which, in pearlite, there is a discontinuity in the three-dimensional pattern of cementite sheets. This will be seen as a line of discontinuity in the pattern in any arbitrary cross-section.

It is not essential for this conclusion that the pattern in the growth surfaces should be propagated along the growth trajectories defined, as above, as normal to the growth surfaces. The cementite pattern probably extends in directions intermediate between the trajectories so defined and crystallographically determined preferred directions: but in any case, as the pattern is inherited through successive positions of the growth front, if some part of the growth front has finally no inheritance along the normal trajectories, then some part, in general a different part, has finally no inheritance. A definite area of the continuous pattern is eliminated, shrinking to a singular point or (more usually) line at which a discontinuity of pattern will be visible.

At least two ways can be suggested by which a concavity in the growth surface of the colony can be produced. One is pre-existing inhomogeneity in the austenite (Fig. 3). Since the radii of curvature of the boundary continually increase during growth, the severity of such a perturbation necessary to produce concavity diminishes. Even in perfectly homogeneous austenite, we can anticipate irregularity in the growth-rate of pearlite from the dependence of growth-rate on spacing. In an analysis which should be at least qualitatively correct, Zener[2] indicates that the opposing influences of diffusion (favoring fine spacing) and interfacial energy (favoring coarse spacing) determine an optimum spacing at which the pearlite grows fastest. In an expanding colony the actual spacing will no doubt be greater than the optimum. This will make for uniformity of spacing, for any group of cementite sheets closer together than the average will grow ahead, spread apart a little, and make the spacing more uniform. If the spacing were optimum or closer, a group closer than average would be retarded and left behind. Any branching processes must give rise to temporary crowding and will be ineffective in increasing the number of growing sheets if this increased crowding retards the growth. Hence, as the colony grows, the spacing between sheets should increase until it is such that branching will accelerate the growth. Any such event produces an irregularity in the growth front. From these considerations we may see, however, that concavity in the cross-sections transverse and parallel to the cementite sheets can have different consequences. In the case of the former, growth into the concavity will close up the spacing, and this may cause sufficient acceleration to remove the concavity without the production of a focal groove. No such effect operates in the other

VOL. 4 1956

FIG. 3.

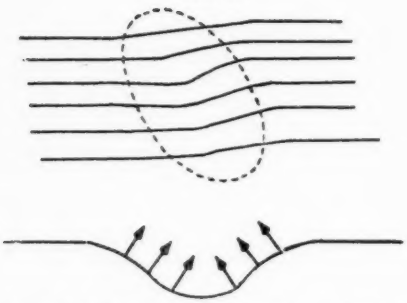

(a) A trough is formed in the growing colony surface by inhomogeneity in the austenite, or anomalous interlamellar spacing. Arrows indicate growth trajectories.

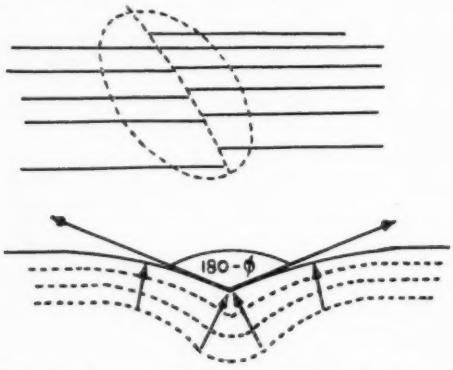

(b) Growth of cementite sheets normal to their boundaries at such a point results in a focal groove, with discontinuity in the lamellar pattern.

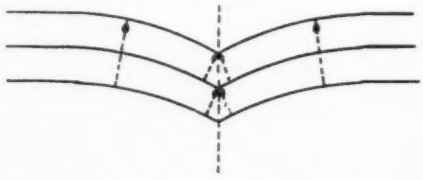

(c) If growth-rate is not sufficiently increased by interleaving, the groove and accompanying discontinuity will continue during further growth.

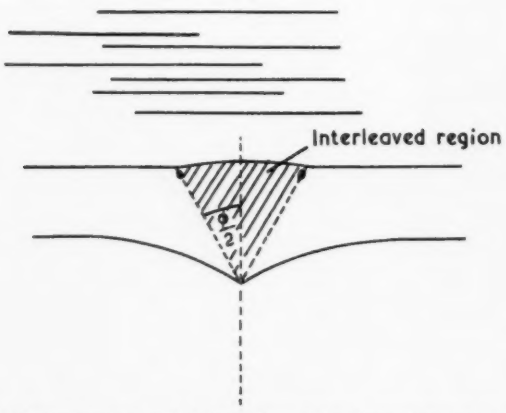

(d) Interleaving will follow from this discontinuity if the consequent decrease in spacing gives a growth-rate greater than the existing velocity by a factor $>\sec \frac{1}{2}\phi$.

direction, so that focal grooves should be more easily produced transverse to the cementite: they will, of course, also be more easily recognized in this position.

The process described may itself be one of the chief branching mechanisms: for the discontinuity in the pattern gives an opportunity for the sheets of cementite to interleave and give a closer spacing. This will only occur if the resulting acceleration in growth-rate is by a factor exceeding $\sec(\frac{1}{2}\phi)$ where $180^\circ - \phi$ is the groove angle. The groove angle ultimately diminishes with continuing growth, so that the simple discontinuity in the pattern may continue for a while and then be followed by interleaving.

Fig. 4 shows another feature of pearlite structure revealed by electron microscopy and requiring interpretation. The cementite sheets have striations all running in one direction. This direction may reasonably be (a) the growth direction, (b) a crystallographic direction of low index in the cementite, (c) a crystallographic direction of low index in the ferrite: these are not necessarily exclusive. It is further noted that certain regions on the cementite sheets are free from striation, and that all these regions have parallel orientation. The same plane of orientation occurs frequently in the steps of the striated portions. This suggests very strongly that the plane in question is one of relatively low interfacial free energy, γ, for the contact between cementite and ferrite. If this orientation gave a sufficiently deep minimum of γ (the precise meaning of "sufficiently deep" being given by Herring's discussion already cited), the consequence would be that where possible the cementite would grow as a plane sheet in this orientation, but that when constrained to grow out of this plane (e.g., by

FIG. 4. Curved and striated cementite lamellae (specimen tilted 30° from normal), ×10,000.

neighboring cementite-growth depriving it of a supply of carbon from one side), it would still utilize this plane over part of its area, alternating with strips of other orientations of higher free energy sufficient to produce the required mean orientation at the lowest cost in interfacial free energy. The preferred plane will almost certainly be one of low crystallographic indices in either the ferrite or the cementite, or both. The striation direction lies in the preferred plane, but we have no evidence on which to choose between the two possibilities that it is the component of the growth direction in that plane or that it is a crystallographic zone axis.

Dependence of the interfacial free energy γ on crystallographic orientation has a direct bearing on the fundamental sheet-like rather than rod-like habit of cementite growth in pearlite. Consider the alternative patterns of parallel sheets, with spacing period p, and parallel rods in a hexagonal array with lattice parameter a (Fig. 5). Then the thickness of a cementite sheet must be αp and the radius of a cementite rod must be

$$r = (\sqrt{3}/2\pi)^{\frac{1}{2}}\,\alpha^{\frac{1}{2}}a$$

where α is the volume ratio of cementite. The interfacial free energy per unit total volume is for sheets

$$s = 2\gamma/p$$

and for rods

$$s' = 2\pi r\gamma'/(\sqrt{3}/2)a^2 = (8\pi\alpha/\sqrt{3})^{\frac{1}{2}}\,\gamma'/a$$

where we have distinguished γ', a mean value over the surface of a rod, from the single value γ appropriate to a sheet.

The greatest transverse distance of diffusion required for carbon to reach the cementite is, in the case of sheets

$$d = \tfrac{1}{2}p(1-\alpha)$$

and in the case of rods

$$d' = a/\sqrt{3} - r$$
$$= a[1/\sqrt{3} - (\alpha\sqrt{3}/2\pi)^{\frac{1}{2}}].$$

If we set $s' = s$, we have

$$a/p = (2\pi\alpha/\sqrt{3})^{\frac{1}{2}}\,(\gamma'/\gamma)$$

And thus

$$d'/d = 2\,[1/\sqrt{3} - (\alpha\sqrt{3}/2\pi)^{\frac{1}{2}}\,(2\pi\alpha/\sqrt{3})^{\frac{1}{2}}\,\gamma'/(1-\alpha)\gamma$$
$$= 2\,[(2\pi\alpha/3\sqrt{3})^{\frac{1}{2}} - \alpha]\,\gamma'/(1-\alpha)\gamma$$
$$= 2\,(1.105\alpha^{\frac{1}{2}} - \alpha)\gamma'/(1-\alpha)\gamma.$$

If $\gamma' = \gamma$, this ratio is less than unity for any value of $\alpha < 0.78$: in normal pearlitic steels $\alpha \sim 1/7$, making the ratio 0.64. Thus, if $\gamma' = \gamma$, rods have the advantage over sheets. Our treatment is an inexact one, and probably unduly favorable to the sheet pattern, since this gives a large fraction of the cross-sectional area at nearly the maximum distance from cementite. The inference is that the sheet-like habit is not to be expected if the interfacial free energy is independent of orientation, but can be readily understood if the interfacial free energy in preferred planes is two or three times smaller than in other orientations of the interface.

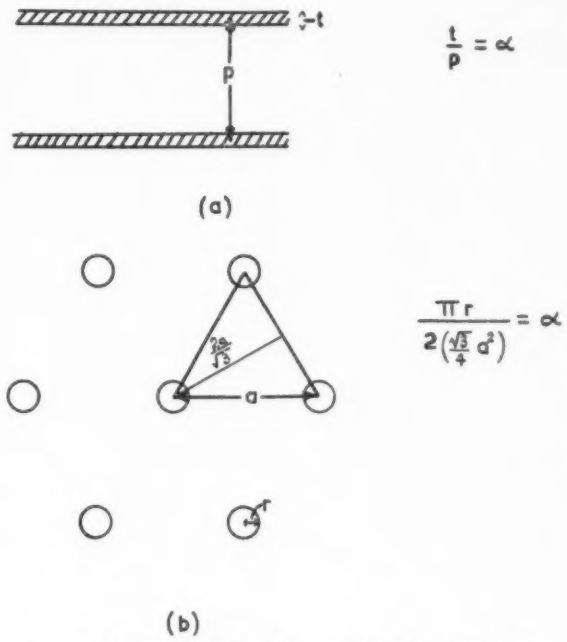

FIG. 5. Comparison of lamellar and acicular growth of pearlite (growth direction normal to paper).

FIG. 6. Laths and rods of cementite, ×11,250.

VOL. 4 1956

A corollary to this is that when the cementite growth is forced out of the preferred planes and the interface becomes a composite one, partly in preferred planes and partly in others of higher free energy, the growth may be expected to break up into rods if the departure from the preferred plane exceeds a limiting magnitude. Examples of this type of growth are not uncommon (Fig. 6).

Once the rods grow away from the disturbing environment which forced the growth into an unpreferred direction, they have the opportunity to spread out again as sheets in the preferred plane: this gives us another mechanism for multiplying the number of sheets in a pearlite colony.

ACKNOWLEDGMENT

One of us (K. E. P.) wishes to express his gratitude to the Royal Society and the Armourers' and Brasiers' Company for the award of their Research Fellowship in Metallurgy.

REFERENCES

1. C. Herring, *Phys. Rev.* **82,** 87 (1951).
2. C. Zener, *Trans. Amer. Inst. Mech. Met. Eng.* **167,** 405 (1946).

Crystal Boundary Hardening in Deformed Metals revealed by Scratch Tests*

Tuchschmid[1] has pointed out that only by statistical analysis of a great many microhardness measurements on strained crystalline aggregates may one obtain definite information regarding any concentration of strain-hardening at the crystal boundaries. He reviews the work of Boas and Hargreaves[2] in this connection, but I should like to mention some earlier work[3] using scratch tests. The data then

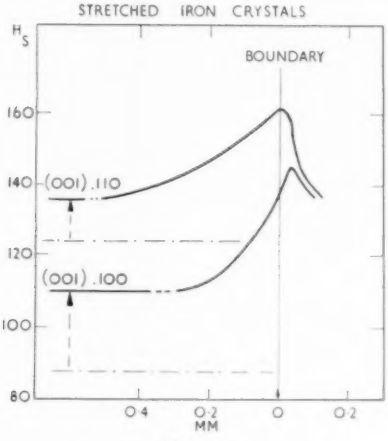

FIG. 1.

obtained on stretched coarse-grained iron have been plotted in Fig. 1, and are independent evidence suggesting that strain-hardening increases as boundaries are approached.

HUGH O'NEILL.

University College,
Singleton Park,
Swansea, Wales.

References

1. TUCHSCHMID, *Acta Met.*, **3**, No. 2, 215 (1955).
2. W. BOAS and M. E. HARGREAVES, *Proc. Roy. Soc.*, **A193**, 89 (1948).
3. H. O'NEILL, Carnegie Schol. Mems. Iron and Steel Inst., **17**, 109 (1928).

*Received July 29, 1955.

The Relation between the Electrical Resistivity and the Yield Strength of Deformed Copper*

During the past five years the influence of cold-working on the resistivity of metals has been the subject of a number of publications.[1] The main reason for this interest is the possibility of describing this increase of the resistivity as the sum of at least four different effects. One separates these effects by annealing at different temperatures. We made experiments on commercial copper with a residual resistivity of $6 \times 10^{-11}\ \Omega$m in the annealed state.

Fig. 1(a) gives the resistivity at -195°C after stretching 20% and annealing for 30 min at different temperatures. The dotted curve was obtained from the results of Manintveld,[2] and the drawn curve was composed after our own measurements. Also the yield value (the stress at a plastic strain of 0.15%) is given (b).

The resistivity and the yield stress are measured on the same wire in liquid nitrogen. For every annealing pulse of 30 minutes a new wire was used.

From Fig. 1 it appears that in this case at 280°C the dislocations disappear.

More information is obtained when we plot the yield stress as a function of the resistivity for constant strain and variable annealing temperature. Fig. 2 shows the results for copper wires strained 5, 10, 15, 20, and 25%. About this figure we can make the following remarks:

1. The horizontal part of the curves of Fig. 2 represents the three restoration steps (I, II, and III) of Fig. 1. The resistivity varies only with the yield stress in step IV when the dislocations disappear.

2. We assume that step III does not influence the yield stress and that in the first stage of mechanical recovery the decrease of the yield stress is proportional to the decrease of step IV. The crossing point E represents then the resistivity of the dislocations and the yield stress after 20% deformation. In this way five crossing points B, C, D, E, F are obtained.

Fig. 3 shows these points. In this figure A–B–C–D–E–F represents the yield stress at -195°C as a function of the resistivity of the dislocations during stretching. The curves like F–S–A give the same relation during annealing.

3. As in the recrystallization region the yield stress and the resistivity vary much with the heating temperature, inhomogeneous annealing of the wire might cause a larger decrease of the yield stress than of the resistivity. Experiments arranged in this direction showed that the influence of the inhomogeneity of the temperature was negligible.

VOL. 4 1956

4. Pry and Hennig[3] have shown that there exists a single-valued relation between the extra resistivity due to dislocations and the yield stress. The same result was obtained by Korevaar.[4] This dependence

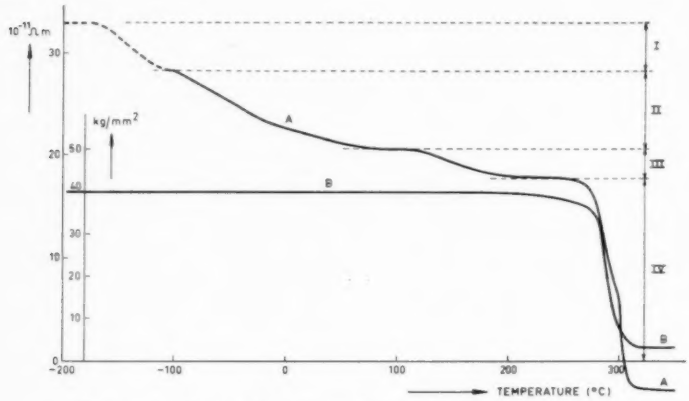

FIG. 1(a). Remaining part of the extra-resistivity, after annealing 30 min, as a function of the annealing temperature. (b). Yield strength at −195°C after the same heat-treatment.

clearly does not exist in the general case. One can obtain, e.g., at a dislocation resistivity of $10 \cdot 10^{-11}\,\Omega$m any yield stress between 8 and 30 kg/mm^2.

For the sake of completeness we note that we define the resistivity of the dislocations in a way different from that of Pry and Hennig. This difference does not influence the conclusions.

5. This result shows that, when the resistivity is proportional to the concentration of dislocations,

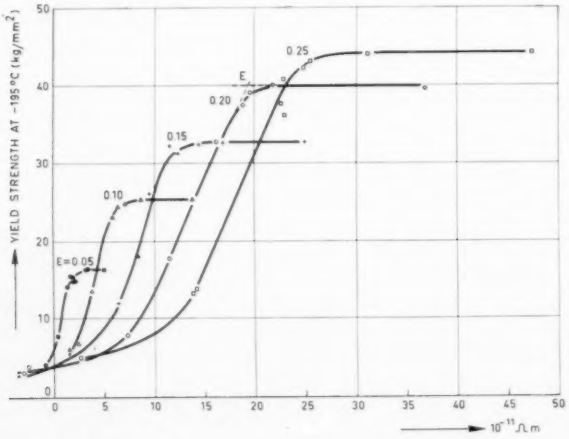

FIG. 2. Yield strength at −195°C as a function of the extra resistivity during annealing.

the yield strength depends markedly on the position of the dislocations. It is a good example of the difficulties of the theory of work-hardening.

6. The curves of Fig. 3 (e.g., F–S–A) can be divided in a part where the yield strength varies strongly (F–S) and a part where the yield stress is almost constant (S–A). The part F–S might be attributed to polygonization. The recrystallization then takes place between S and A.

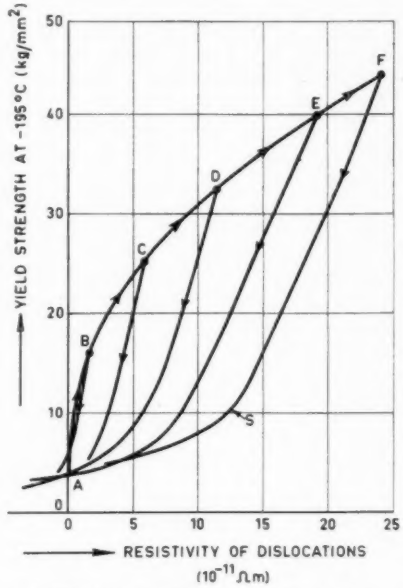

FIG. 3. Yield strength at −195°C as a function of the resistivity of the dislocations (this figure is obtained from Fig. 2).

This view was supported by X-ray diffraction. It appeared that the texture, which remains unchanged during deformation and the first stage of mechanical recovery (F–S), changes markedly between S and A.

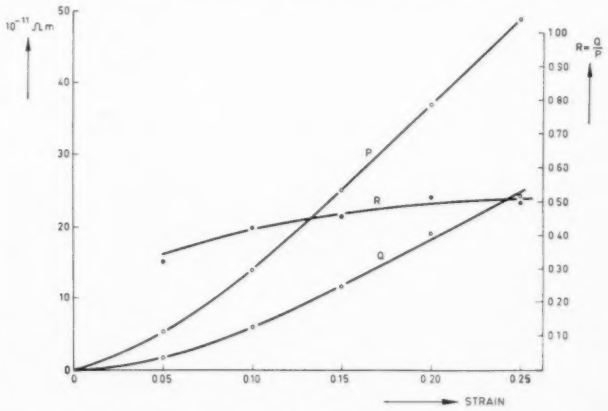

FIG. 4. The total increase of the resistivity (P), the resistivity of the dislocations (Q), and their ratio (R) as a function of the strain.

7. Fig. 4 (obtained from Fig. 3) gives the total increase of the resistivity P and the resistivity due to dislocations Q as a function of the strain. Curve R gives the ratio of the effects. This ratio is almost constant (between 0.4 and 0.5).

8. The resistivity of the dislocations is not in accord with the calculations of Hunter and Nabarro.[5] To illustrate this, we take for example the dislocation resistivity at a strain of 25%. According to Hunter and Nabarro,[5] this resistivity must be caused by 1.2×10^{12} dislocations cm^{-2}. When the low value of 2 eV per atomic plane is the energy of a dislocation, we find a stored energy of 2.3 cal/cm^3. This is about 20% of the work done in stretching. It is about ten times larger than the measured values.[6]

This work is part of the research programme of the research group "Metals F.O.M.–T.N.O." of the "Stichting voor Fundamenteel Onderzoek der Materie" (F.O.M.), and was also made possible by financial support from the "Nederlandse Organisatie voor zuiver wetenschappelijk Onderzoek" (Z.W.O.).

C. W. Berghout.

Laboratorium voor Technische Physica,
Delft, Holland.

References

1. T. Broom, *Adv. Phys.*, **9,** 26 (1954).
2. J. A. Manintveld, Thesis, Delft, 1954.
3. R. H. Pry and R. W. Hennig, *Acta Met.*, **2,** 318 (1954).
4. B. M. Korevaar, private communication.
5. S. C. Hunter and F. R. N. Nabarro, *Proc. Roy. Soc.*, **A220,** 542 (1953).
6. L. M. Clarebrough *et al.*, *Proc. Roy. Soc.*, **A215,** 507 (1952).

*Received September 20, 1955.

VOL. 4 1956

Internal Friction in α-Iron due to Interstitial Solutes*

Recently Lagerberg & Joseffson[1] obtained expressions for the anelasticity of an aggregate of randomly oriented crystals and of a wire with a ⟨110⟩ texture. Being unable to integrate their expressions, they obtained approximate solutions only. Methods for obtaining exact solutions are given below. Where possible, the notation of Lagerberg and Joseffson is used.

(a) *Wire with a random orientation*—A similar expression was used by Rawlings and Tambini,[2] and is solved by changing to polar co-ordinates, viz., $x^2 + y^2 = \theta$, $z^2 = 1 - \theta = \cos^2\psi$, and $y/x = \tan\varphi$.

$$Q\max_{\text{mean}}^{-1} = \frac{A}{\pi}\int_0^{\pi/2}\int_0^1 \left\{\frac{3}{b} + \frac{\frac{3a}{b} - 1}{bf(\theta,\varphi) - a}\right\}\frac{d\varphi d\theta}{\sqrt{1-\theta}}$$

where $f(\theta,\varphi) = \theta\{1 - \theta(1 - \cos^2\varphi\sin^2\varphi)\}$

$$a = S_{11}$$

$$b = 2\{(S_{11} - S_{12}) - \tfrac{1}{2}S_{44}\}$$

This reduces to

$$Q\max_{\text{mean}}^{-1} = \frac{A}{\pi}\left(\frac{3}{b} + \frac{b - 3a}{b}\cdot\bar{E}\right)$$

where $\bar{E}$ = Young's modulus for an aggregate of randomly oriented crystals. Using the same constants as Lagerberg and Joseffson, we calculate

$$a = 0.757 \times 10^{-12}\ \text{cm}^2/\text{dyne}$$

$$b = 1.216 \times 10^{-12}\ \text{cm}^2/\text{dyne}$$

Taking $\bar{E} = 2.06 \times 10^{12}$ dyne/cm^2, we obtain

$$Q\max_{\text{mean}}^{-1} = A \times 0.647 \times 10^{12} \qquad (1)$$

(b) *Wire with a ⟨110⟩ texture*—Starting from equation (18) of Lagerberg and Joseffson, we have

$$\langle 110\rangle\, Q\max_{\text{mean}}^{-1} = \frac{2C}{\pi}\int_0^{\pi/2}\left\{1.866 + \frac{0.866}{1.608F(w) - 1}\right\}dw$$

The second part of the integral is

$$0.866\int_0^{\pi/2}\frac{dw}{1.608F(w) - 1}$$

$$= -0.866\int_0^{\pi/2}\frac{dw}{0.4975 + 0.201\cos^2 w + 0.3015\cos^4 w}$$

$$= I_2$$

Substitute, $\tan w = x \qquad dw = \dfrac{dx}{1 + x^2}$

Then, $$I_2 = -1.74\int_0^{\infty}\frac{(1 + x^2)\,dx}{x^4 + 2.405x^2 + 2.01}$$

$$= -1.74\int_0^{\infty}\left\{\frac{Ax + B}{x^2 + Sx + t} + \frac{Cx + D}{x^2 - Sx + t}\right\}dx$$

where $$A = -C = 1/2S(1/t - 1)$$

$$B = D = 1/2t.$$

and $$s = 0.655, \quad t = 1.417$$

$$I_2 = -1.74\int_0^{\infty}\left\{\frac{\frac{A}{2}(2x + s) + B - \frac{sA}{2}}{x^2 + sx + t} + \frac{-\frac{A}{2}(2x - s) + B - \frac{sA}{2}}{x^2 - sx + t}\right\}dx$$

$$= -1.74\,\frac{A}{2}\left[\ln\frac{x^2 + sx + t}{x^2 - sx + t}\right]_0^{\infty} - 1.74$$

$$\int_0^{\infty}\left\{\frac{Y}{\left(x + \frac{s}{2}\right)^2 + Z^2} + \frac{Y}{\left(x - \frac{s}{2}\right)^2 + Z^2}\right\}dx$$

where $Y = B - \frac{sA}{2}$ $\quad Z^2 = t - \frac{s^2}{4}$

$$I_2 = -1.74\,\frac{Y}{Z}\left[\tan^{-1}\frac{x+s/2}{Z} + \tan^{-1}\frac{x-s/2}{Z}\right]_0^{\infty}$$

$$= -1.74\,\frac{Y}{Z} = -1.74 \cdot \frac{1}{4} \cdot \left(\frac{1}{t}+1\right) \cdot \frac{\pi}{\sqrt{t - s^2/4}}$$

$$= 1.295\,\frac{\pi}{2}$$

Inserting this value in the original equation, we obtain

$$\langle 110\rangle\, Q\max^{-1}_{\text{mean}} = \frac{2C}{\pi}\,(1.866\pi/2 - 1.295\pi/2)$$

$$= 0.571C$$

$$= A \cdot 0.754 \cdot 10^{12} \qquad (2)$$

That is, the anelasticity of a wire with a ⟨110⟩ texture is greater than one without, agreeing qualitatively with the approximately calculated solution of Lagerberg and Joseffson, but disagreeing with the experimental observation of Fast and Verrijp.[3] The latter found that the internal friction of a wire with a ⟨110⟩ texture is *less* than that of a randomly oriented wire. Both wires had a fine-grained structure.

This suggests that the method of calculation is wrong. It has been shown[2] that the value given by equation (1) is in good agreement with the observed values of Fast and Verrijp[4] and of Rawlings and Tambini.[5] A different mode of calculation by Smit and Bueren[6] gives even better agreement (see 2). Smit and Bueren treat the problem of the damping of wire as a problem in shear and not as one of tension at 45° to the axis (as is implied in the present analysis). It is difficult to see how a shear strain can result in this type of anelasticity (Smit and Bueren do not suggest a mechanism). It seems possible, however, that, if their method of analysis were used, the low value obtained by Fast and Verrijp for a wire with a ⟨110⟩ texture may be explained.

R. Rawlings

Department of Metallurgy,
University College,
Cardiff

References

1. G. Lagerberg and Åke Joseffson, *Acta Met.*, **3**, 236 (1955).
2. R. Rawlings and D. Tambini, *J. Iron Steel Inst.* (to be published).
3. J. D. Fast and M. B. Verrijp, *J. Iron Steel Inst.*, **180**, 337 (1954).
4. J. D. Fast and M. B. Verrijp, *Acta Met.*, **3**, 203 (1955).
5. R. Rawlings and D. Tambini, *Acta Met.*, **3**, 212 (1955).
6. J. Smit and H. G. van Bueren, *Philips Res. Reports*, **9**, 460 (1954).

*Received September 13, 1955.

Elasticity of Zinc Whiskers*

A large variety of crystalline solids have been grown as whiskers by controlled vapor deposition.[1, 2, 3, 4, 5, 6] The mechanism of whisker growth has been inferred from studies of the growth kinetics of mercury whiskers.[1, 7] It has been deduced that a nucleus bearing a single screw dislocation will grow as a whisker of constant cross-section at supersaturations in the vapor phase insufficient to cause a sensible rate of two-dimensional nucleation.[2]

Consistent with the proposed near-perfection of the whiskers grown by vapor deposition are the observations on a variety of whiskers[3, 8, 9, 10] that their elastic properties approximate the theoretical properties of perfect crystals.[11] With the exception of zinc sulfide whiskers,[3] all of the whiskers tested mechanically have been produced by the vapor-phase reduction of volatile metal salts. The growth mechanism has been established for the vapor deposition of a pure phase. While it has been presumed that the whisker-growth mechanism operates independently of the manner in which the vapor phase is supersaturated, a mechanical test of a metal whisker grown from its pure vapor has been lacking.

The authors[12] have grown zinc whiskers up to 2 cm in length by vapor deposition of pure zinc in a temperature gradient. It is the purpose of this note to report that zinc whiskers, so grown, have elastic properties in bending, approximately the expected properties for perfect crystals.

It was observed that a few whiskers were bent elastically in the growth process when neighboring crystals sterically interfered with their growth. Since zinc whiskers oxidize rapidly when exposed to air, the oxidation problem was avoided by microphotographing whiskers in situ.

The most severe elastic bend of this kind had a radius of curvature of 150 μ as measured at 100×. The whisker thickness was 2 μ. The maximum elastic strain was 0.7 per cent. To demonstrate that the bending was elastic, the whisker-growth vessel was opened and the whisker was observed to straighten out when the bending constraints were removed.

The maximum strain above is not the upper limit of elastic strain for a zinc whisker. The reported strain is sufficient to demonstrate that zinc whiskers approximate the theoretical value for perfect crystals. The results support the premise that the whisker-growth mechanism is independent of the method of attaining supersaturation.

R. V. Coleman.
G. W. Sears.

General Electric Research Laboratory,
Schenectady, New York.

References

1. G. W. Sears, *Acta Met.*, **1,** 453 (1953).
2. G. W. Sears, *Acta Met.*, **3,** 367 (1955).
3. W. W. Piper and W. L. Roth, *Phys. Rev.*, **92,** 503 (1953).
4. S. S. Brenner, *Acta Met.* (to be published).
5. E. R. Everett and J. A. Amick, *J. Appl. Phys.*, **25,** 1204 (1954).
6. A. W. Cochardt and H. Wiedersich, *Naturwissenschaften*, **42,** 342 (1955).
7. G. W. Sears, *Acta Met.*, **3,** 361 (1955).
8. G. W. Sears, A. Gatti, and R. L. Fullman, *Acta Met.*, **2,** 727 (1954).
9. S. S. Brenner (to be published).
10. R. L. Eisner, *Acta Met.*, **3,** 414 (1955).
11. L. Bragg and W. M. Lomer, *Proc. Roy. Soc.*, **A196,** 71 (1949).
12. R. V. Coleman and G. W. Sears, *Growth of Zinc Whiskers* (to be published).

*Received October 5, 1955.

The Two-step Anneal of Cold-worked α-Brass and Silver-zinc*

It is well known that when cold-worked α-brass is heated to about 200°C, the hardness, elastic limit, and other properties related to the motion of dislocations increase slightly. This increase is followed, upon further heating, by the normal decrease caused by the removal of dislocations by recrystallization. The increase of the elastic limit upon heating is accompanied by an upper yield-point. If the application of stress is continued, a lower yield-point occurs which corresponds to the elastic limit obtainable prior to heating. If the brass is then reheated, the upper yield-point returns. It is also known that if cold-worked α-brass is annealed isochronally, the decay of resistance occurs in two steps. The high-temperature step arises from the removal of dislocations and, as expected, occurs in the same temperature range as the loss of hardness. The low-temperature step occurs in the same temperature range as the small increase of hardness. This low-temperature step of resistance-decay has been studied by the writer and shown to arise from short-range order. This experiment will be discussed below. It will be shown that the kinetics of the hardness-increase in brass, as measured by Averbach,[1] compares with the resistance change of the first step. Hence Fisher's[2] proposal, that short-range order can impede the motion of dislocations, is the probable mechanism for the hardness-increase.

Tammann[3] has shown that many alloys exhibit the two-step decay of cold-work resistance. The resistance kinetics of one of these, silver-zinc, was studied, and will be compared to the behavior exhibited by α-brass. Although it cannot be concluded that any alloy which exhibits the two-step decay of cold-work resistance possesses short-range order, the results indicate that the converse may be true, and that, in the examination for order in an alloy, the cold-work resistance-decay characteristics should be included.

Evidence has been shown by Rosenblatt, Smoluchowski, and Dienes,[4] and by the writer[5] for resistivity effects of short-range order in α-brass. The following is a brief review of the writer's findings which will hereafter be referred to as I. Annealed brass wires (30% Zn) were quenched from 320°C and then annealed isothermally at a temperature in the range 200–220°C. During the anneal the resistivity measured at liquid-nitrogen temperature was found to decrease in nearly an exponential fashion. Relaxation times were evaluated at the inflection point of a log-time vs. resistance plot. The relaxation times obtained in this manner were found to agree identically with relaxation times obtained by anelastic methods. Pile-neutron irradiation at 50°C decreased the resistance of α-brass, and subsequent anneals in the 200–220°C range returned the resistance to an equilibrium value at the temperature of anneal. The relaxation times for the return of resistance again agreed with those obtained by anelastic methods. Measurements of resistance as a function of temperature of brass quenched from 320°C and then annealed at 210°C and remeasured showed that the anneal decreased ρ_0, the residual resistance, and increased ρ_T, the thermal part of resistance. An anneal causes larger resistance changes at low temperatures due to this behavior of ρ_0 and ρ_T. Therefore, all measurements were made at liquid-nitrogen temperature. According to current theories, anelastic effects in substitutional solid solutions arise from stress-induced changes in local order.[6] The agreement of the relaxation times of the resistance changes with those of anelastic measurements leads to the explanation that the resistance changes are caused by changes in short-range order. The examination of the annealing kinetics of the first step of cold-work resistance in α-brass will be discussed in the next section, in conjunction with the new data on silver zinc.

Brass (30% Zn) and Ag-Zn (33% Zn) wires were annealed at 350°C, and then drawn at room temperature to 60% R.A. (reduction in area). They were first given isochronal anneals to obtain the annealing spectra. The resistance measurements were made in a liquid-nitrogen bath by comparing the potential drop across the cold-worked wire with the drop across a dummy wire of the same alloy. The anneals were performed in a wax-bath with the temperature

VOL. 4 1956

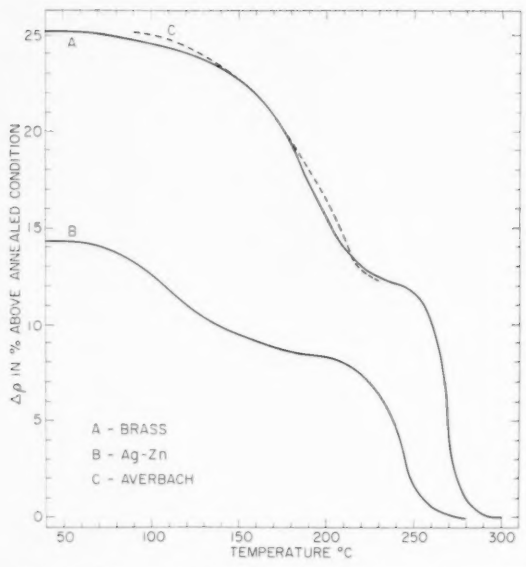

FIG. 1. Curves *A* and *B*—15-min isochronal anneals of cold-work resistance in α-brass and Ag-Zn respectively. Resistance measurements made at liquid-nitrogen temperature. Curve *C* (dashed)—Averbach's measurements of the hardness increase caused by anneal of cold-worked α-brass. The curve is inverted and normalized to the magnitude of the first step of the resistance charge.

controlled to ± 0.2°C. The time of anneal was 15 min, after which the wire was quenched in a room-temperature air-stream. A more detailed report in 1 discusses the adequacy of this technique. Curve *A* (Fig. 1) shows the 15-min isochrone measured at liquid nitrogen for cold-worked brass. Curve *B* (Fig. 1) shows the isochrone for silver-zinc subjected to the same treatment. The two-step decay is evident for both alloys. The low-temperature annealing step was studied isothermally for both alloys. The results for brass are shown in curve *B* (Fig. 2) and for silver-zinc in curve *D* (Fig. 2). Curves *A* and *C* (Fig. 2) are the relaxation time vs. reciprocal temperature curves for brass (30% Zn) and silver-zinc (33% Zn) respectively, as determined by anelastic methods. Curve *A* is a portion of the curve obtained from the combined data of Childs and LeClaire[7] and reference 1. Curve *C* is a portion of the curve obtained by Roswell and Nowick.[8] Overhauser[9] has shown that a spread in activation energies about a mean will result in a lowered relaxation time for a rate-controlled process. It is reasonable to suppose that the dislocation damage of the high-temperature step which remains during the anneal of the low-temperature step will cause such a spread of activation energies for atomic migration and cause the observed lowered relaxation times. This, however, does not alter the mechanism, and the close comparison to stress-induced changes in local order indicates that changes in local order give rise to the low-temperature step of cold-work resistance in both alloys.

It was concluded in 1 from the resistivity behavior and related data that short-range order occurs in α-brass and that small changes in the degree of order cause the resistivity to change. Cold-work can be expected to destroy short-range order, and the time and temperature required to restore it to the equilibrium value at the temperature of anneal can be determined from curve *B* (Fig. 2). The similar behavior of cold-worked silver-zinc permits the conclusion that short-range order also occurs in that alloy, is destroyed by cold-work, and can be restored by an anneal at a temperature lower than that required for recrystallization.

Fisher[2] has shown that, in an alloy in which short-range order exists, the energy of ordering will increase the stress required to move a dislocation. This mechanism will explain the small increase in hardness which occurs when cold-worked brass is heated. Cold-work destroys the short-range order, and a subsequent heating can restore it to equilibrium before removal of dislocations by recrystallization. Examination of Curve *A* (Fig. 2) shows that about one hour at 200°C will essentially restore short-range

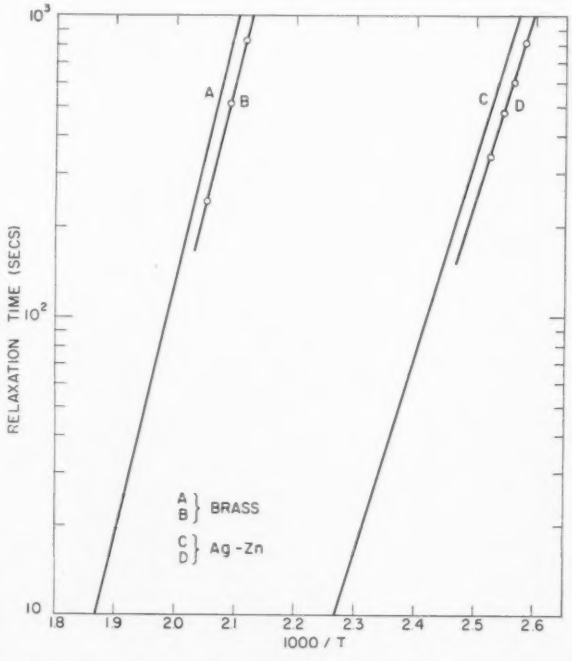

FIG. 2. Relaxation times vs. T^{-1} obtained as follows. Curves *A* and *C*—anelastic measurements of α-brass and Ag-Zn respectively. Curve *B* and *D*—isothermal anneals of the low-temperature resistance step of cold-worked α-brass and Ag-Zn respectively.

order to equilibrium at that temperature. This is the time-temperature value reported by investigators to be required for maximum hardness. The rate process for hardening is shown in a curve by Averbach,[1] who, with Rudman, has suggested that the hardness-increase may be due to order.[10] Averbach's curve for the increase in hardness was inverted and normalized in magnitude to the first step of curve *A* (Fig. 1). Curve *C* (dashed) (Fig. 1) is his hardness curve plotted in this manner. Admittedly, the precision for small hardness changes is low and his time and temperature spacings differ from those of the resistivity measurements, but quite a latitude of error can be allowed before the fit to the resistance-decay curve is impaired. The conclusion is evident. The restoration of short-range order destroyed by cold-work not only causes the first step of resistance-decay, but by increasing the stress required to move a dislocation causes an increase in the gross properties related to dislocation motion.

A numerical estimate of the quantities involved may be made from existing data. Because of the many factors affecting hardness in brass, it will be more reasonable to compare Fisher's estimate of the short-range-order effect on dislocation motion to the yield-point measurements of Ardley and Cottrell.[11] They have shown that the upper yield-point on single crystals of 30% Zn α-brass which have been cold-worked and annealed for half an hour at 200°C lies about 0.13 kg/mm^2 above the lower yield-point. The upper yield-point decays upon further stress to the preheated value, and Cottrell[12] has suggested that Fisher's mechanism, among others, can explain this behavior. On the basis of lattice parameter changes which accompany the changes in short-range order in 70–30 α-brass, Feder and Nowick[13] have made an estimate that the short-range order coefficient for this alloy lies in the range 0.01–0.05. When these order coefficients are included in a calculation of the increase in stress required to move a dislocation, the resulting range contains the experimental value. Thus it is seen that Fisher's mechanism agrees within a factor of 5 with experimental behavior. The magnitude of the difference between the upper and lower yield-points measured by Ardley and Cottrell for the 10% Zn brass is about one-quarter of that of 30% Zn. Examination of Tammann's annealing kinetics for ρ show that the magnitude of the first step of the resistivity anneal for 10% Zn brass is about one-quarter of that for 30% Zn brass. Agreement again is obtained in favor of Fisher's mechanism.

Appreciation is expressed to Drs. G. J. Dienes and A. S. Nowick for helpful discussions.

This work was performed at Brookhaven National Laboratory, Upton, New York, where the writer is a guest scientist, and supported in part by the United States Atomic Energy Commission.

A. C. Damask.

Pitman-Dunn Laboratories,
Frankfort Arsenal,
Philadelphia, Pennsylvania.

References

1. B. L. Averbach, *J. Met.*, **185,** 491 (1949).
2. J. C. Fisher, *Acta Met.*, **2,** 9 (1954).
3. G. Tammann, *Z. Metall.*, **28,** 6 (1936).
4. D. B. Rosenblatt, R. Smoluchowski, and G. J. Dienes, *J. Appl. Phys.*, **26,** 1044 (1955).
5. A. C. Damask, to be published (*J. Appl. Phys.*).
6. A. D. LeClaire and W. M. Lomer, *Acta Met.*, **2,** 731 (1954).
7. B. G. Childs and A. D. LeClaire, *Acta Met.*, **2,** 718 (1954).
8. A. E. Roswell and A. S. Nowick, *J. Met.*, **189,** 1259 (1953).
9. A. W. Overhauser, *Phys. Rev.*, **90,** 393 (1953).
10. B. L. Averbach and P. S. Rudman, *Phys. Rev.*, **98,** 1554(A) (1955).
11. G. W. Ardley and A. H. Cottrell, *Proc. Roy. Soc.*, **219A,** 328 (1953).
12. A. H. Cottrell, *Relation of Properties to Microstructure*, Amer. Soc. Metals, 1954.
13. R. Feder and A. S. Nowick, private communication.

*Received December 1, 1955.

The Dependence of Grain-boundary Precipitation Rates on the Orientation of Adjoining Grains*

Recently Gruehl and Ammann[1] published some results of experiments on precipitation in specimens of Cu-Ni-Mn and Cu-Be which had a 100-fiber axis. They found that the thickness of the cellular or discontinuous grain-boundary precipitate perpendicular to the common 100-axis depended on the relative orientation of the adjoining grains. They attributed this effect to differences in nucleation rates on the boundaries. Since they believe that differences in growth rates arise only from strains, they discarded the notion that their results might be due to differences in growth rates.

It is unlikely that the data of Gruehl and Ammann can be explained by nucleation rate alone. Nucleation on grain boundaries in these systems proceeds until the boundary has been covered by precipitate nodules. Thereafter, nucleation ceases, and further growth results in a slab of precipitate which thickens. The thickest portions of the slab are due to precipitate nodules which nucleated earliest, and if one assumed no effect of boundary orientation on growth rate, these would be equally thick for all slabs. The only

effect that nucleation rate would have is in determining the thinnest portion of the slab, since these are due to the last nuclei to form. The micrographs of Gruehl and Ammann show (1) that the precipitate slabs are quite uniform in thickness for a given boundary and (2) that there are wide differences in maximum thickness. The first indicates that nucleation ceased quite early, the second indicates that it is growth and not nucleation which determines the thickness. Smith[2] has suggested that such precipitates are related in orientation to one of the grains adjoining the boundary, and that they grow into the other grain. Turnbull[3] explained that the mechanism by which the precipitate advances into the grain is by grain-boundary diffusion of the segregating material along the boundary, which sweeps through the unprecipitated material ahead of the grain. The growth rate would then be proportional to the diffusion coefficient in this boundary. Turnbull and Hoffman[4] have measured self-diffusion of bicrystals of silver tilted about a 100-axis and have found that, parallel to the common axis, the diffusion constant D times the effective boundary thickness δ can be expressed up to a tilt of 28° by the theoretical expression

$$D\delta = A \sin \theta/2.$$

Figs. 1 and 2 are plots of the data of Gruehl and Ammann compared with a sin $\theta/2$ plot. Although the data scatter considerably, the fit is quite good, and one is led to the conclusion that this is grain-boundary diffusion-controlled precipitation and not nucleation which determines the thickness. Much of the scatter in the data may be due to tilts about the 100-fiber axis, which was obtained by directional cooling.

Hoffman has measured the anisotropy of grain-boundary self-diffusion in silver and has found that

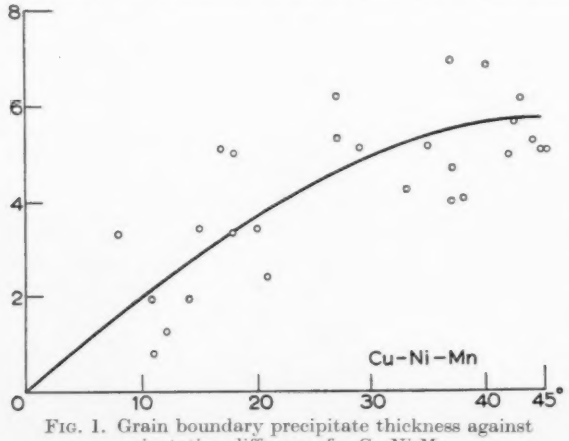

FIG. 1. Grain boundary precipitate thickness against orientation difference for Cu-Ni-Mn.

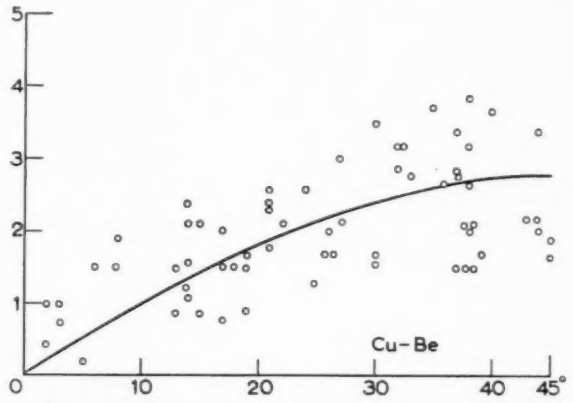

FIG. 2. Grain boundary precipitate thickness against orientation difference for Cu-Be.

the diffusion perpendicular to the common 100-axis is slower and is much more strongly dependent on relative orientation. It appears, therefore, that diffusion in the boundary occurs along the easy direction and that the platelets which act as sinks for the diffusing material are probably oriented perpendicular to the common axis; that is, perpendicular to this easy direction. One can also conclude that the spacing of the platelets is apparently unaltered by the orientation differences across the boundary.

JOHN W. CAHN.

General Electric Research Laboratory,
Schenectady, New York.

References

1. W. GRUEHL and D. AMMANN, *Acta Met.*, **3**, 347 (1955).
2. C. S. SMITH, *Trans. Amer. Soc. Metals*, **45**, 533 (1953).
3. D. TURNBULL, *Acta Met.*, **3**, 1 (1955).
4. D. TURNBULL and R. HOFFMAN, *Acta Met.*, **2**, 419 (1954).

*Received December 13, 1955.

Geiger-counter Determinations of X-ray Lattice Strains in Plastically Deformed Aluminum Alloy*†

It has been reported previously that past the yield-stress the X-ray lattice strain-stress diagrams of polycrystalline metals in tension depart markedly from proportionality. The observed deviations are in many instances of an order of magnitude larger than the deviations predicted on the basis of Taylor's *homogeneous* five-slip mechanism.[1] In more recent tests[2, 3] performed on various materials at subzero- as well as room-temperature, it was found that for

* Work supported by the United States Air Force, through the Office of Scientific Research of the Air Research and Development Command.

the so-called soft orientations the trends in the plastic stage were in reality of a twofold nature. There was first a departure from proportionality at the start of the plastic flow, following which the lattice strain-stress diagram showed an opposite trend, toward the recovery of the initial slope. In an endeavor to secure additional evidence of this tendency, a new series of tests was performed in compression instead of tension, and the Geiger-counter technique of recording the X-ray intensity was substituted for the previously used photographic procedure.

A special compression loading device was built to mount on the goniometer table. The loading shaft passed through the center of hollow specimens, and load was applied by tightening nuts at the end of the shaft. Load was measured by a calibrated hollow load-cell adjacent to the specimen. The whole assembly was rotated in order to average out stress variations due to possible eccentric loading, to insure a more representative sampling of grains, and to attenuate spurious effects of grain size on the profile of the diffracted X-ray intensity chart. The specimens were 6061 annealed aluminum alloy.

Lattice strains were determined from the diffraction records of the (420)-planes which were tangent to the specimen surface. The reproducibility in terms of lattice strains was $\pm 15 \times 10^{-6}$, which is at least twice as good as for the photographic procedure.

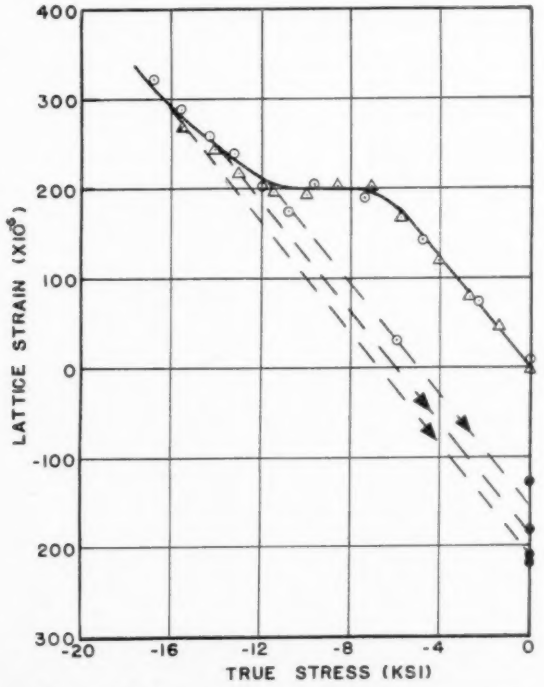

FIG. 1. Lattice strain-stress diagram in compression, 6061 aluminum alloy. Dashed lines indicate unloading.

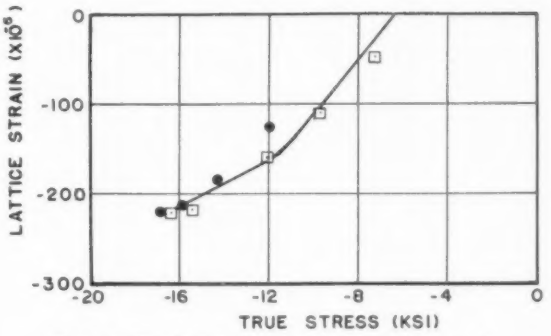

FIG. 2. Residual lattice strain-stress diagram in compression, 6061 aluminum alloy.

The applied stress was measured to within ± 250 p.s.i.*

Several preliminary tests were made to ascertain the existence of the jog shown in Fig. 1. They have been omitted from the final results because they contained also other variables, such as different waiting periods, which shifted slightly the position of the jog without affecting its shape. The two symbols shown in Fig. 1 refer to two specimens tested under identical conditions. The slope in the elastic range corresponds to a modulus of elasticity of 9.5×10^6 p.s.i., which is in excellent agreement with the previously determined tensile data.[2, 3] At about the external yield (6000 p.s.i.) the initial departure from proportionality begins. The reverse trend starts at about 11,000 p.s.i., which corresponds to 0.8% plastic strain.

The above two trends are also reflected in the diagram of the residual lattice strains Fig. 2. The data marked by full circles are those shown in Fig. 1, but the squares represent an independent set of data from a third specimen investigated only for the residual strains. The full line has been derived from the diagram (Fig. 1) by assuming elastic unloading. The reasonable agreement between experiment and computation provides additional proof of the twofold trend observed in the plastic range under load.

The observed lattice-strain results suggest that in the early stages of plastic deformation the bulk of the grains contributing to the (420) orientation might deform by a mechanism which is much simpler than the five-slip mechanism. Recent work on single crystals, bicrystals, and polycrystalline materials seems to support this point of view.[5–9] Whatever the nature of the new mechanism, it is clear that the

* The angular position of the peak intensity was obtained by following two procedures suggested previously:[4]
(a) extension of the linear portions of the record until intersection, and
(b) parabolic interpolation.
The strains computed by these two procedures differed by no more than $\pm 30 \times 10^{-6}$.

VOL. 4 1956

trend revealed at the start of the plastic flow constitutes the major reason for the failure of Taylor's homogeneous five-slip mechanism to account quantitatively for the observed deviations in the lattice strain-stress diagrams.

D. HASANOVITSH.
M. KAUFMAN.
D. ROSENTHAL.

Department of Engineering,
University of California,
Los Angeles, California.

References

1. G. B. GREENOUGH, *Progress in Metal Physics*, Interscience, **3,** 176 (1952).
2. M. KAUFMAN, X-ray lattice strains in plastically deformed metals. Ph.D. Thesis, University of California, Los Angeles, 1953.
3. R. M. ASIMOW, Influence of grain size on X-ray lattice strain in an aluminum alloy, M.S. Thesis, University of California, Los Angeles, 1955.
4. A. L. CHRISTENSEN and E. S. ROWLAND, *Amer. Soc. Metals*, **45,** 638, and written discussions by S. R. MALOOF and H. R. ERARD, and J. T. NORTON and R. E. OGILVIE, pp. 669 and 674.
5. CH. CRUSSARD and B. JAOUL, *Revue Metall.*, **47,** 590 (1950).
6. C. R. CUPP and B. CHALMERS, *Acta Met.*, **2,** 803 (1954).
7. K. T. AUST, *Acta Met.*, **2,** 632 (1954).
8. A. E. JOHNSON and S. B. BATDORF, A study of slip formation in polycrystalline aluminum, *NACA*, T.N. 2567, 1951.
9. P. A. JACQUET, *Acta Met.*, **2,** 752 (1954).

† Received December 8, 1955.

Birefringence and Twinning in Silicon *

Polished silicon specimens exhibit complex birefringence patterns[1] when observed between crossed nicols with an infra-red image tube ("snooperscope"). In the present study, parallel, sharply-defined birefringence bands, oriented with respect to the silicon structure (Fig. 1), have been observed and are discussed.

When the samples were etched, fine parallel traces extending over a width of approximately 10^{-1} mm could be observed coincident with each birefringence band. These structural features permitted accurate positioning of an X-ray beam for orientation studies. Laue back-reflection patterns disclosed the presence of first-degree twinning. Furthermore, the segmentary character of each reflection corresponding to the twinned orientation evidenced the multiple nature of the twinning. The twinning planes are octahedral and parallel to the surface tracings, i.e., parallel to the direction of the birefringence bands (Fig. 1).

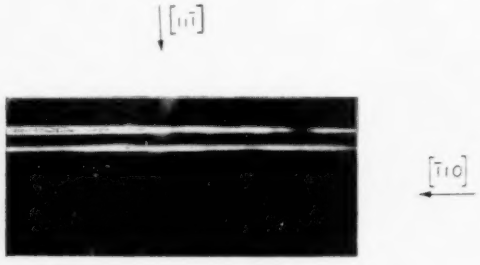

FIG. 1. Birefringence bands in silicon observed along the pulling direction [112]. (Sample thickness 1 mm; magnification 10×.)

Examination of the silicon specimens between crossed nicols with parallel, essentially monochromatic light (Si absorption edge $\approx 1.1\,\mu$; "snooperscope" limit $\approx 1.2\,\mu$), led to the following observations:

(a) Direction of observation along the twinning planes (i.e., perpendicular to the plane of Fig. 1): The birefringence bands were extinguished at 90° intervals (direction of polarization parallel and perpendicular to the band direction) upon rotation of the specimen about the line of sight.

(b) Direction of observation perpendicular to the twinning planes: Essentially no birefringence was observed.

(c) Direction of observation as in (a): Each birefringence band was compensated in turn over its full length with a quartz wedge inserted perpendicular to the band direction. When the quartz wedge was inserted parallel to the band direction, a compensated region covering separated birefringence bands moved in the direction of wedge insertion; band sections corresponding to the same quartz-wedge thickness were compensated simultaneously. These latter experimental findings indicate that the optical difference is identical not only over the full length of a given band but from one band to another. Since the specimen thickness was constant for these observations, the birefringence (Δn) must be the same for the observed bands. Δn was measured with the quartz wedge as approximately 8×10^{-3}; the optical character is positive. Upon compensation of the birefringence bands with the quartz wedge, no residual birefringence was observed along the band edges. From this it can be implied that in the specimens studied, the contribution of strain (due to twinning) is relatively minor. In this connection it should also be mentioned that the Laue pattern discussed earlier gave no indication of a directional stress along the twinning axis.

The behavior of the birefringence bands as noted above is analogous to that of optically uniaxial crystalline layers. In this respect, the optic axis of the uniaxial layers is perpendicular to the bands, i.e., parallel to [111]. A possible explanation for the uniaxial layers is as follows:

Twinning introduces into the cubic silicon structure

a layer having a hexagonal configuration and extending a few atomic planes on either side of the twin boundary.[2] The c axis of the anisotropic layer is perpendicular to the twin plane. The layer acts as a uniaxial crystalline lamella and gives rise to birefringence.

Etched specimens were studied microscopically to determine the degree of multiplicity of the twin traces. At 1300×, using an oil immersion objective, the upper (brighter) band of Fig. 1 was resolved into approximately twenty twin boundaries. The lower (weaker) band showed approximately ten boundaries. Specimens with somewhat weaker bands showed fewer boundaries. It is to be expected, of course, that higher magnification would reveal a larger number of boundaries in each case.

It is suggested, then, that the birefringence bands observed in silicon are due to anisotropic zones introduced by multiple, parallel twinning. In this respect, fine traces which "resembled twins in silicon" have been noted[3] in electron micrographs as little as 100 Å apart. It has also been suggested[4] that the anomalous double refraction commonly observed in cubic tetrahedral structures and attributed to strain is actually due to repeated parallel twinning.

An alternative explanation for the observed optical behavior lies in the presence of discrete layers of hexagonal silicon structure. The latter would bear the same relationship to the normal, cubic form of silicon as wurtzite bears to sphalerite. Conceivably, the postulated layers of hexagonal structure could be interleaved with the multiple twinning and account for the observed birefringence. Evidence for such an allotropic modification of silicon[5] and germanium[6] has been offered by König, who indicated the presence of the hexagonal form in the formation of the cubic structure from an initial amorphous film. By comparison, however, his annealing temperature for silicon (900°C) was significantly lower than that used (1450°C) in pulling the present specimens from a melt. Nevertheless, attempts were made to identify such a structure by X-ray and electron-diffraction techniques. Long-exposure X-ray rotation patterns taken about the twinning axis (potential c axis of the hexagonal) did not disclose the expected c_0 spacing of the suggested modification. A similarly negative result was obtained using the electron reflection-diffraction technique.[7] In this respect, surface-energy calculations have shown[8] that a hexagonal modification of a diamond-type substance is unlikely beyond the stage of nuclei.

W. Kaiser.
Signal Corps Engineering Laboratories, J. A. Kohn.
Fort Monmouth, N.J.

References

1. W. C. Dash, *Bull. Amer. Phys. Soc.*, **30,** 13 (1955).
2. C. B. Slawson, *Amer. Mineral.*, **35,** 193 (1950).
3. J. Franks, G. A. Geach, and A. T. Churchman, *Proc. Phys. Soc.*, **B68,** 111 (1955).
4. C. B. Slawson and J. A. Kohn, Polymorphic twinning in tetrahedral structures, Amer. Crystallog. Assoc. Meeting, Penn. State Univ., April 1950.
5. H. König, *Optik*, **3,** 419 (1948).
6. H. König, *Reichsber. Phys.*, **1,** 4 (1944).
7. The authors are grateful to R. Lefker for the electron reflection-diffraction studies.
8. G. A. Wolff, personal communication.

*Received November 14, 1955.

Internal Stresses during Ordering*†

During the disorder-to-order transformation in CuAu, the crystalline structure changes from cubic to orthorhombic or tetragonal.[1] This transformation is accompanied by an internal stress field.[2] It has been observed that polycrystalline wires, when ordered for a short time, were bent or even curled. Single crystal rods, as large as $\frac{1}{8}$ in. in diameter, underwent considerable bending during ordering annealing.

* Supported by ONR.

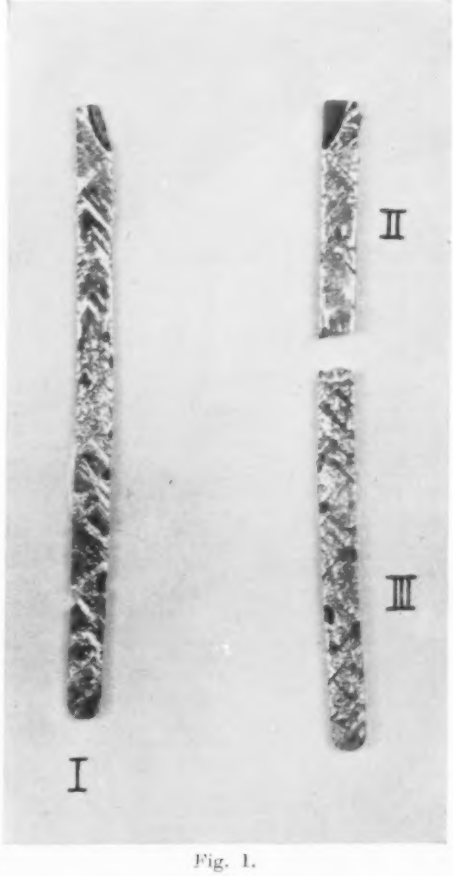

Fig. 1.

VOL. 4 1956

A very dramatic manifestation of the internal stresses accompanying the ordering transformation was observed in a three-crystal rod $\frac{1}{8}$ in. in diameter. In that specimen one grain boundary, almost planar, was parallel to the specimen axis, and the other was almost perpendicular to it. The rod was heated for 3 h at 800°C, followed by 24-h disordering at 425°C. After this heat treatment, the specimen was transferred to the ordering bath at 350°C. At this temperature the equilibrium structure is tetragonal. After about 45 sec of ordering, the specimen split three ways, exactly along the grain boundaries. A view of the three single crystals resulting from splitting is given in Fig. 1. The visible surfaces are unetched grain boundaries, covered with markings caused by twins[2] in crystal I (the markings on the interfaces of crystals II and III are impressions of twin plates grown from the interior of crystal I). The crystal orientation of all three grains was determined. It was found that the angle between boundary normal and the [100] direction in crystal I was only 9°, the angle between $[100]_I$ in the first crystal and $[100]_{II}$ in crystal II was 42°, between $[100]_I$ and $[100]_{III}$ 31°, and between $[100]_{II}$ and $[100]_{III}$ 60°. From these it follows that the twinning plane is of the (110)-type.

From the electrical-resistance measurements and Muto's relation,[3] it has been established that the disintegration of the three-crystal specimen took place when the long-range-order parameter S reached the value of about 0.5.

S. Kohara.
G. C. Kuczynski.

Metallurgy Department,
University of Notre Dame,
Notre Dame, Indiana.

References

1. C. H. Johansson and J. O. Linde, *Ann. Phys.*, **25,** 1 (1936).
2. G. C. Kuczynski, R. F. Hochman, and M. Doyama, *J. Appl. Phys.*, **26,** 871 (1955).
3. R. Muto, *Inst. Phys. Chem. Res. Sci. Papers (Tokyo)*, **30,** 99 (1936).

†Received November 14, 1955.

Variation of Anodic Film Growth with Grain Orientation in Zirconium*

Previously, a black low-resistance anodic oxide was reported for zirconium in nitric acid.[1] The existence of an orientation dependence was also noted. Further study of this effect is reported here. A large-grained zirconium specimen was produced from rolled iodide crystal bar by a strain-anneal treatment. Spectrographic analysis showed less than 0.1% As, Ba, Ca, Mo, P, V, Zn, Hf, with all other elements less than 0.01% except for 0.04% Fe. Several sections of this specimen were mounted, metallographically polished, and etched.* The sections were then anodized in

Fig. 1. Appearance of large-grained zirconium after anodizing in 70% nitric acid. The lightest grains have no anodic film. 17,390 100×.

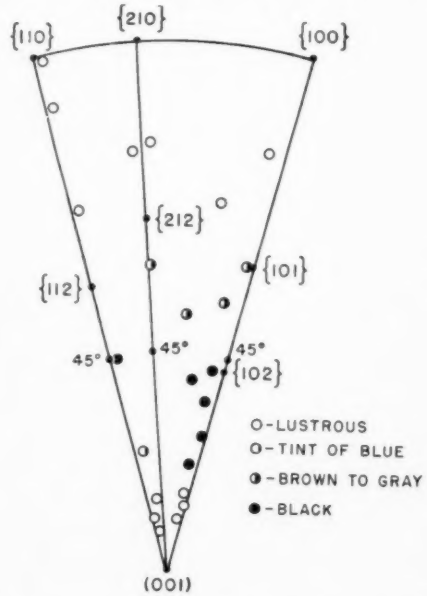

Fig. 2. Locations of normals to grain faces on a basal-plane standard projection.

* 8 ml concd. hydrofluoric acid (48%), 50 ml concd. nitric acid (70%), 50 ml hot tap water. One minute with agitation and hot water rinse.

70% nitric acid at 5°C for 3½ h at a current density of 0.025 mA/cm². These conditions were not critical. The anodizing was stopped initially when the appearance of individual grains was noted to vary from the original metallic luster to a dull black.

A portion of the anodized surface is shown in Fig. 1 at 100× (bright field). The orientations with respect to the anodized surface of twenty-four of the largest grains were determined by the back-reflection Laue method. The grains were selected to represent all shades of darkening. The composite results are presented in Fig. 2 in the form of an inverse pole figure based on the standard projection for zirconium on the (001)-plane. One-twelfth of the projection is given, since this covers all possible orientations. The circles are projections of normals to the anodized surfaces, and are designated according to the degree of anodization. It is evident that the rate of film-growth is low when the plane of anodizing is close to the basal plane. The rate is high at approximately 40° from the basal plane, and appears to decrease on planes at larger angles.

R. D. Misch.
E. S. Fisher.
Argonne National Laboratory,
Lemont, Illinois

VOL. 4 1956

References

1. R. D. Misch and W. E. Ruther, *J. Electrochem. Soc.*, **100,** 531–537 (1953).

*Received July 29, 1955; revised version, October 24, 1955.

Hysteresis of the Cobalt Transformation in Thin Films*

This letter describes quantitatively the influence of the surface upon the hysteresis of the cobalt transformation. Dehlinger *et al.*[1] established that the transition from the face-centered cubic to the close-packed hexagonal modification in single crystals of cobalt first occurs in those cubic (111) planes which are parallel to the largest external surface of the crystal. From this observation, Dehlinger concluded that the hysteresis could be attributed to the increase in surface energy incurred in the glide process of transformation (thus, the larger the surface perpendicular to the glide planes, the greater the hysteresis). In a more recent publication, which describes a possible dislocation mechanism for the cobalt transformation, this phenomenon is only casually mentioned as being compatible with a glide mechanism.[2] We have studied the transformation from the c.p.h. to the f.c.c. modification in thin films, because they allow quantitative control of the surface/volume ratio. The films were obtained by evaporation of Baker 98–99% pure cobalt upon a substrate of microscope cover glass in a vacuum of $2 \cdot 10^{-4}$ mm Hg. The temperature of the substrate was kept at 380°C during evaporation, so that the film was obtained in the hexagonal modification (heating was necessary to ensure continuity of the film and to obtain sharp diffractions). Grain orientation was random, with a superposed [0001] fiber texture, where the fiber axis is normal to the surface. The film thickness was measured by weighing, after optical determinations of thickness in transparent samples showed that the variation in thickness between the center and the extreme edges of the substrate never exceeded 10%. The films remained in the vacuum during the transformation, to minimize gas absorption. The (upper) hysteresis temperature lies between the last temperature at which there was no evidence of the cubic phase and the first temperature at which the cubic (200) diffraction appeared. Both temperatures are indicated in the diagram, and the solid curve is the assumed hysteresis temperature. (Evidence of transformation to the cubic modification, once obtained, was not removed by subsequent cooling to room temperature.) The samples were analysed in a Norelco wide-angle diffractometer with the substrate surface in the reflecting position, so that those (200) planes were "seen" whose corresponding glide planes were 55° away from the surface. For this arrangement, in which the glide planes terminate in a large surface, a large hysteresis was to be expected. A hyperbolic relation was found between hysteresis temperature and film thickness, wherefore the hysteresis temperature was plotted versus the reciprocal of the thickness (or half of surface/volume when the grain diameter is much greater than the film thickness). The resulting straight line can be extrapolated to the equilibrium temperature for a surface/volume ratio of unity, for which hysteresis from this cause must be negligible.

From the experimental information of Fig. 1, an estimate can be made of the energy of hysteresis. This is based upon the simple thermodynamic analysis of the cobalt transformation due to Dehlinger.[3] Therein the equilibrium temperature of the two modifications is given as $T_e = \Delta U_0/\Delta S_0$, where the energy and entropy differences are those of zero degrees Kelvin. Contrary to the third law, ΔS_0 is nonzero. If the temperature-dependence of the cause of hysteresis can be neglected, the hysteresis temperature is simply

$$T_h = \frac{\Delta U_0 \pm U_h}{\Delta S_0} = T_e \pm \frac{A}{V}\frac{U'_h}{\Delta S_0/V}$$

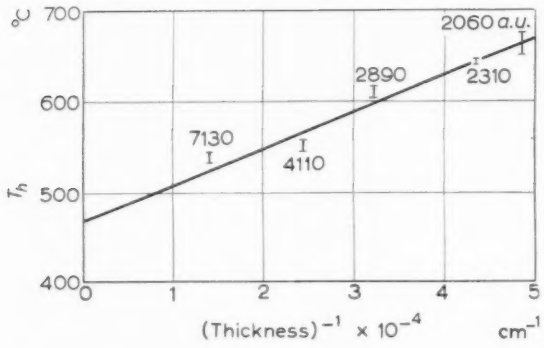

FIG. 1. Hysteresis temperature versus reciprocal of thickness. Listed with each point is the film thickness in Ångstrom units.

where U_h is the energy of hysteresis. A is the surface area and V the volume, so that U'_h has the dimension of a surface energy. The positive sign is for the transition from the low-temperature phase to the high-temperature phase, and the negative sign for the reverse transition (U_h does not necessarily have the same magnitude in both directions). From the slope of the straight line in Fig. 1, the magnitude of U'_h is obtained if Dehlinger's value (per gram atom) of R ln 1.04 is used for ΔS_0. This leads to a value U'_h of about 1000 erg/cm², which lies between that of the energy of the free surface (1400 for copper)[4] and the estimated energy of the glass/metal interface (order of grain-boundary energy). While the results of this experiment cannot furnish any direct clues to the mechanism of hysteresis in the cobalt transformation, they show that the transition from the c.p.h. to the f.c.c. modification cannot commence until an energy barrier of the magnitude of the surface (or interfacial) energy is overcome.

H. H. STADELMAIER.
R. C. HOCK.
North Carolina State College, Raleigh, N.C.

References

1. U. DEHLINGER, *Chemische Physik der Metalle und Legierungen*, p. 130 (Akademische Verlagsgesellschaft, Leipzig, 1939); further references listed there.
2. A. SEEGER, *Z. Metallkunde*, **44**, 247 (1953).
3. U. DEHLINGER, *Handbuch der Metallphysik*, Vol. I, 1—Der metallische Zustand der Materie, p. 133 (Akademische Verlagsgesellschaft, Leipzig, 1935).
4. H. UDIN, A. J. SHALER, and J. WULFF, *Trans. Amer. Inst. Min. Met. Eng.*, **185**, 186 (1949).

*Received November 21, 1955.

The Influence of Hydrogen on the Yield-point of Mild Steel*

In a recent letter to this journal, Cracknell and Petch[1] indicated that hydrogen, when introduced cathodically into a mild steel, eliminated the yield-point. They ascribed the disappearance of the yield-point to the inhomogeneous stresses set up at internal cavities containing hydrogen under pressure. Similar work by the writers, but at lower current densities and for shorter charging times, has indicated the same effect, but because of the absence of internal cavities after this treatment, a somewhat different explanation seems possible.

Using this less severe rate of charging, i.e., 2 amp/sq. in. for 1 h, elimination of the lower yield-point from the mild-steel specimens was observed. Moreover, as previously shown by Seabrook *et al.*,[2] a change of slope of the work-hardening part of the stress-strain curve occurred just below the old level of the upper yield-point, as shown in Fig. 1, curve (b). On allowing diffusion of the hydrogen from a tensile specimen (de-gassing) before straining, it was noted that the yield-point phenomenon (i.e., a definite upper and lower yield-point) began to reappear within four hours. The normal behaviour of the steel was completely regained after aging for three days at room temperature. During this period, as confirmed from other tests, substantially all diffusable hydrogen would have diffused from the specimen, the resulting tensile test indicating no embrittlement. The removal of the lower yield-point, and a lowering of the value of the flow-stress, indicate the influence of diffusible hydrogen on dislocation movement.

Because of the effect of hydrogen on the yield-point, strain-aging effects were also studied. Three

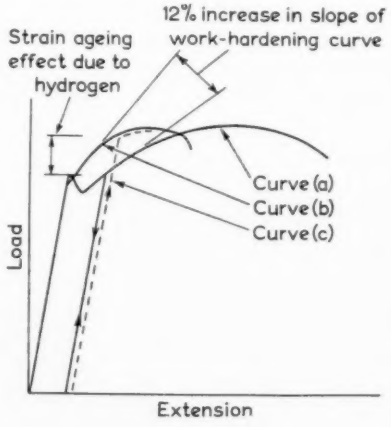

FIG. 1.

Curve (a) Normal stress-strain curve for non-treated material.

Curve (b) Stress-strain curve for hydrogen-charged material.

Curve (c) Stress-strain curve after loading to 2% strain. Unloading, charging with hydrogen, and re-testing.

stress-strain curves are shown in Fig. 1, and designated as follows:

(a) normal curve of nontreated material.

(b) curve of hydrogen-charged material.

(c) curve after loading to 2% strain, unloading, charging with hydrogen, and re-testing.

It will be noted that in the case of curve (c) the effect of introducing hydrogen, after an initial loading, is to increase the stress from the normal flow-stress to the flow-stress of the original hydrogen-charged specimen, i.e., the strain-aging effect is equal to the increase in flow-stress between the normal specimen and the hydrogen-charged specimen. The time taken for an equivalent strain-aging effect to occur at room temperature, due presumably to nitrogen, is of the order of several days.

The strain-aging effect was also studied in a virtually nonstrain-aging steel (Al and Ti killed), and here a definite strain-aging effect, due to hydrogen, was observed. These tests showed that, after 2% strain, unloading and aging for 70 h at room temperature, the additional load necessary to reinitiate yielding (stated as a percentage of the first applied load) was 1.9%. If, however, the specimen was charged with hydrogen after the 2% strain and tested within 30 min, an effective increase of the new flow-stress of 4.9% was observed. If diffusion of hydrogen from the specimens was allowed and the specimen tested 70 h after straining 2% and charging with hydrogen, the former value of 1.9% was again found. It would appear that diffusible hydrogen can collect at the dislocation sites—denuded of their former atmospheres by straining—and so cause an increase of the stress required to reinitiate yielding. This phenomenon is diffusion-dependent, since if the test is conducted after the diffusible hydrogen has degassed, the steel behaves normally.

The facts appear to be consistent with experimental evidence of Rogers[3], who, by reducing the diffusion rate of nitrogen by testing at a low temperature, showed an effect of hydrogen consistent with interference of dislocation movement and the production of an upper and lower yield-point. This also agrees with the suggestion of Bastien and Azou[4] that, because of the higher mobility, hydrogen might diffuse along with moving dislocations at room temperature, thus eliminating the lower yield-point.

H. G. Vaughan.
M. E. de Morton.

British Welding Research Association, 29 Park Crescent, London, W.1.

References

1. A. Cracknell and N. W. Petch, *Acta Met.*, **3**, 200 (1955).
2. J. B. Seabrook, N. J. Grant, and D. Carey, *Trans. Amer. Inst. Min. Met. Eng.*, **188**, 1317 (1950).
3. H. C. Rogers, *Acta Met.*, **2**, 167 (1954).
4. P. Bastien and P. Azou, *Rev. Met.*, **49**, 837 (1952).

*Received October 13, 1955.

Antiferromagnetism in the System Ti-H*

Investigations on the phase diagram of the system Ti—H, reviewed in reference,[1] have recently been supplemented by magnetic investigations[2] covering the composition range H/Ti = 0–1.98 and the temperature range 80°–470°K. The observed susceptibility-temperature curves present a number of interesting features, and their tentative qualitative interpretation, as outlined in the present note, may help to supplement other investigations in clarifying the structure of this system.

On adding hydrogen to hexagonal α-Ti at temperatures below about 590°K, a phase boundary is reached at low values of the hydrogen concentration, separating the α phase from a two-phase region $\alpha + \gamma$, the γ phase having face-centered cubic structure. In the neighborhood of 50% H and at room temperature the α phase has disappeared and the system is again single phase γ. At somewhat higher hydrogen concentrations the lattice-constant, so far practically constant at about 4.40 A.U., begins to increase, tending to about 4.45 A.U. when $H/Ti \to 2$. There is evidence by Gibb *et al.*[3, 4] and by Chrétien *et al.*[5] that at H/Ti values considerably less than 2, a new phase appears, and both these authors give strong reasons for identifying this new phase with the compound TiH_2, although its range of stability is uncertain. To summarize, the system appears to be two-phase, $\alpha + \gamma$, up to near H/Ti = 1, and again $\gamma + TiH_2$ between H/Ti equal to about 1.3–1.5 and 2; and, as far as can be judged, the lattice-constant increase coincides with the appearance of the TiH_2 phase.

The paramagnetic susceptibility isotherms[2] parallel this picture of the phases in the Ti-H system. At room temperature the mass susceptibility χ increases from 3.17×10^{-6} for pure α-Ti to 3.61×10^{-6} at H/Ti = 1. Between this composition and $H/Ti \simeq 1.3$, χ remains almost constant at about 3.60×10^{-6}, but then increases again, attaining the value 4.24×10^{-6} at H/Ti = 1.8. Between this composition and H/Ti = 2 the room-temperature isotherm passes through a slight minimum at H/Ti = 1.9 ($\chi = 4.11 \times 10^{-6}$) and finally tends to high values as $H/Ti \to 2$ ($\chi = 4.58 \times 10^{-6}$ at H/Ti = 1.98).

The susceptibility-temperature curves for H/Ti less than about 1.3 show an increasing susceptibility with increasing temperature. At the same time the slope $d\chi/dT$ decreases as the hydrogen concentration increases. For H/Ti values above about 1.7 the $\chi - T$ curves exhibit sharp maxima at about 300°K, the maxima becoming more pronounced the higher H/Ti is. There is evidence that a maximum already appears at lower concentrations, but unfortunately the measurements in this range do not in general extend to 300°K; for H/Ti = 1.55 they do, however, and the existence of a slight maximum at this temperature is already evident.

The results of the magnetic investigations may be tentatively interpreted as follows: The temperature increase of the susceptibility of pure α-Ti may be ascribed to the detailed structure of the density-of-states curve of the metal.[6] In the two-phase $\alpha + \gamma$ region the susceptibility is the sum of that of the two phases, and the results show that the γ-phase is more strongly paramagnetic than pure α-Ti, but that its temperature coefficient $d\chi/dT$ is much smaller if not zero, as appropriate to a metallic phase. The appearance of the susceptibility maxima seems to coincide with the appearance of TiH_2 as a separate phase at H/Ti $\simeq$ 1.3–1.5 and also with the first signs of an increase of the lattice-constant. Since the maxima all occur at one temperature and become more pronounced the higher H/Ti is, they must necessarily be a property of this phase, occurring in stronger concentrations as H/Ti $\to 2$. The measurements thus suggest that the compound TiH_2 is antiferromagnetic (for a review, see reference 7), with a transition temperature $T_c = 300$°K. The ratio χ_0/χ_{T_c} is about 0.82, and thus lies in the range $\frac{2}{3} - 1$ common to previously-known antiferromagnetic substances. It is here tentatively suggested that the antiferromagnetism of this compound is caused by superexchange[7] between Ti atoms through the intermediary of hydrogen in *molecular* form, the H-H axis being collinear with two neighbouring Ti atoms.

The situation is then in many respects analogous to that occurring in the more familiar antiferromagnetic compound MnO. Here an oxygen ion acts as the intermediary between two manganese ions, the superexchange mechanism being a transfer of one of the oxygen p electrons to one of the neighboring Mn ions, and the subsequent interaction of the other p electron, with opposite spin, with the Mn ion diametrically opposed to the first. In the present case the transfer is envisaged to be of one of the s electrons of the H_2 molecule to one of the neighbouring Ti atoms, i.e., the formation of the molecular ion H_2^+, followed by the interaction of the other s electron, with opposite spin, with the oppositely placed Ti atom. In both cases the electronic charge of the intermediary is a maximum along the line joining the transition atoms. Although the H-H separation is likely to be different in this compound from its value for the normal H_2 molecule, the tolerance is large enough for molecular hydrogen to fit easily into the interstices even between nearest neighbouring Ti atoms. The increase of the lattice-constant at H/Ti values close to those at which TiH_2 is first formed would also be explicable by the presence of interstitial molecular rather than atomic hydrogen, the latter having a much smaller "size."

For the above mechanism it is obviously essential for the hydrogen to be in molecular form. It is, therefore, significant that, in the two-phase region $\alpha + \gamma$, antiferromagnetism does not occur. Here the lower hydrogen concentration in the γ phase makes it more likely for it to be in atomic form, so that the above mechanism is ruled out.

In discussing superexchange, Anderson[8] and van Vleck[9] suggested that it would lead to antiferromagnetism only if the transition atoms had d shells which are more than half-full, ferromagnetism being predicted if they are less than half-full. This rule was found to apply in many, but not all cases. Among the exceptions to it[7] are the antiferromagnetic substances V_2O_3 and $CrCl_2$ and the recently investigated[10] titanium compound Ti_2O_3, which has a transition temperature 248°K. The measurements under discussion show TiH_2 to be another exception to Anderson's rule.

Two other mechanisms of antiferromagnetism in the Ti-H system may be suggested. First, the properties described may be due to the direct interaction of Ti atoms. The onset of antiferromagnetism, absent in the γ phase, is then closely linked to the onset of lattice expansion at H/Ti $\simeq$ 1.3–1.5. This would imply a very strong sensitivity of the interaction and hence of the transition temperature on the lattice-constant, and hence on the hydrogen concentration beyond the above values. Since the transition temperature is constant, however, this mechanism is apparently inappropriate. Secondly, the interaction between the d shells of the Ti atoms may be via an atmosphere of conduction electrons produced by the ionization of the hydrogen atoms. Here again the interaction is implied to be very sensitive to the hydrogen concentration since, if it is too low, as in the γ phase, it does not produce antiferromagnetic coupling. Constancy of the transition temperature in the range of H/Ti values where antiferromagnetism

occurs again seems to rule out this mechanism. The model suggested above appears to be the only one capable of accounting for the experimental findings.

It is obviously desirable to obtain independent evidence for or against the suggested explanation. The most direct evidence would be obtainable from neutron diffraction measurements. Other measurements which are likely to be of value in supplementing the magnetic work described include those of specific heat, both at low temperatures and near the transition point, and of electrical resistance.

ACKNOWLEDGMENTS

I wish to acknowledge the help obtained from discussions with Dr. A. D. and Mrs. M. K. McQuillan about the constitution of the Ti-H system.

Department of Mathematics, E. P. WOHLFARTH.
Imperial College,
London, England

References

1. M. HANSEN, D. J. MCPHERSON, and W. ROSTOCKER, *Constitution of Titanium Alloy Systems*, WADC Technical Report 53-41, p. 60 (1953).
2. W. TRZEBIATOWSKI and B. STALIŃSKI, *Bull. Acad. Polon. Sci.*, (Cl III), **1,** 131 (1953).
3. T. R. P. GIBB and H. W. KRUSCHWITZ, *J. Amer. Chem. Soc.*, **72,** 5364 (1950).
4. T. R. P. GIBB, J. J. MCSHARRY, and R. W. BRAGDON, *J. Amer. Chem. Soc.*, **73,** 1751 (1951).
5. A. CHRÉTIEN, W. FREUNDLICH, and M. BICHARA, *Compt. Rend.*, **238,** 1423 (1954).
6. C. J. KRIESSMAN and H. B. CALLEN, *Phys. Rev.*, **94,** 837 (1954).
7. A. B. LIDIARD, *Phys. Soc. Rep. Progr. Phys.*, **17,** 201 (1954).
8. P. W. ANDERSON, *Phys. Rev.*, **79,** 350 (1950).
9. J. H. VAN VLECK, *J. Phys. Radium*, **12,** 262 (1951).
10. S. ADLER and P. W. SELWOOD, *J. Amer. Chem. Soc.*, **76,** 346 (1954).

*Received November 10, 1955.

VOL. 4 1956

Sur l'Oxydation du fer dans l'Air dans l'Intervalle 400°–700°C*

Nous nous proposons dans cette lettre d'énumérer quelques particularités que présente l'oxydation du fer dans l'air dans l'intervalle 400°–700°C.

Nous avons opéré sur des plaquettes de 0,5 mm d'épaisseur et de quelques cm² de surface, de fer Armco ou de fer dénommé Puron par la Westinghouse. Ces échantillons polycristallins à grains équiaxes furent préalablement soumis à une préparation soignée de surface[1] comportant un polissage au papier émeri (000) suivi éventuellement d'un polissage électrolytique dans le bain de Jacquet.[2]

Dans une premiére série d'expériences les échantillons polis étaient réduits dans une atmosphère d'hydrogène pur et sec à 700°C, refroidis dans cette

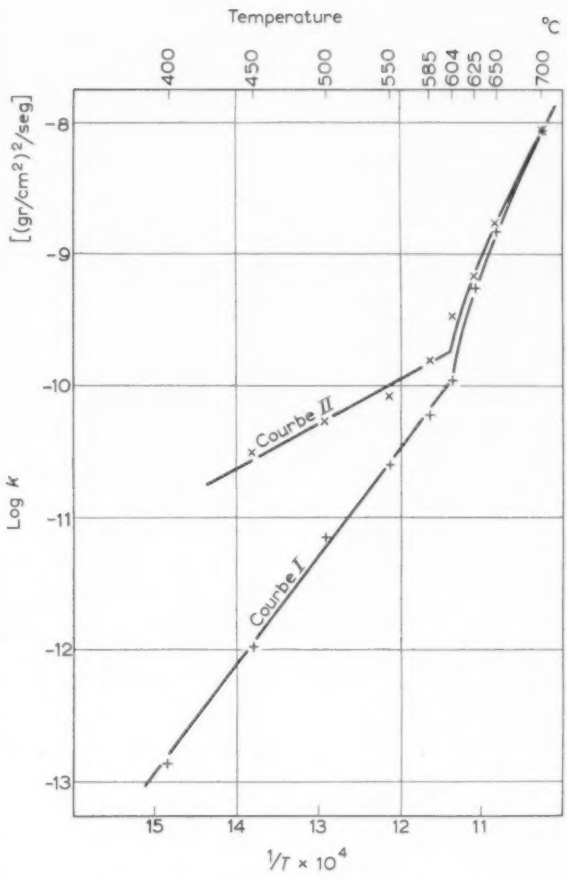

FIG. 1. Variation des constantes d'oxydation k_1 et k_2 en fonction de l'inverse de la température absolue.

atmosphère jusqu'à la température d'oxydation après quoi l'hydrogène était rapidement évacué et remplacé par de l'air purifié (1ère technique opératoire).

Dans une autre série d'expériences les échantillons étaient directement introduits dans la zone à température constante d'un four où l'air était constamment renouvelé et l'oxydation s'y effectuait par conséquent sans aucun préchauffage. (2ème technique opératoire).

Dans les deux séries d'expériences à une température T quelconque de l'intervalle étudié, l'augmentation de poids par cm² de surface d'échantillon obéit à la loi parabolique: $\Delta m = k\sqrt{t}$ où t est la durée d'oxydation et k une constante.

Il est à noter que la valeur de k_1 est en général beaucoup plus faible que celle de k_2, en appelant k_1 et k_2 les constantes d'oxydation correspondant respectivement aux techniques 1 et 2. L'expérience montre d'ailleurs que c'est l'inobservance dans la technique 2 de la condition de préchauffage des

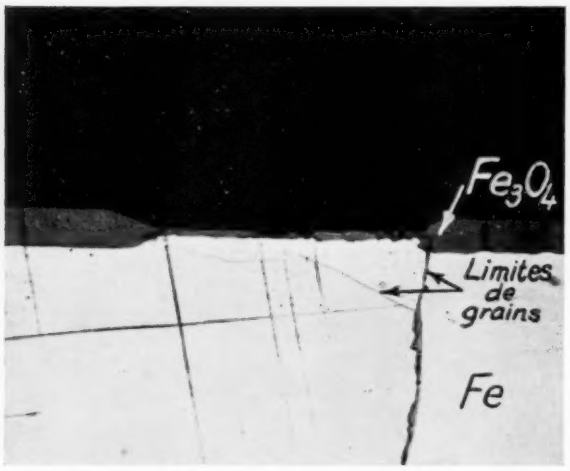

FIG. 2. Pellicule formée par oxydation du fer suivant la technique 2, à 500°C durant 3 heures (×750).

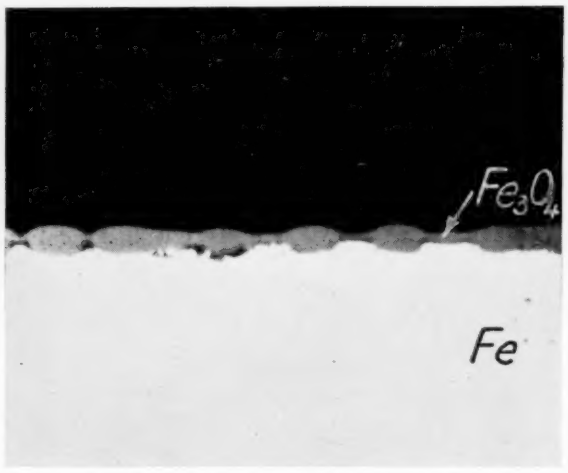

FIG. 4. Coupes des irrégularités d'épaisseur de la pellicule: 500°C—22 min 30 sec (×1250).

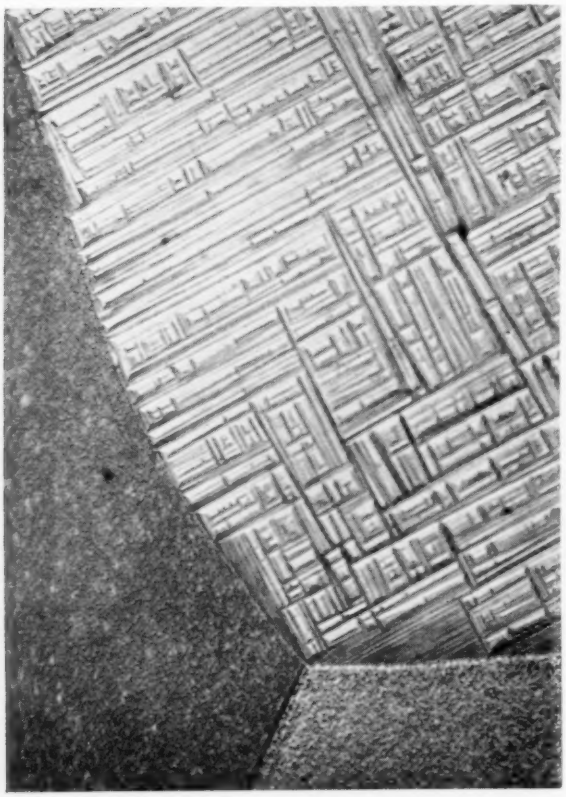

FIG. 3. Aspect de la surface extérieure d'une pellicule sur support de fer, formée par oxydation suivant la technique 1, à 400°C pendant 22 min 30 sec (×300).

FIG. 5. Aspect de la surface extérieure de la pellicule: 604°C—22 min 30 sec (×800).

échantillons jusqu'à la température de l'essai d'oxydation qui conduit à des augmentations de poids anormalement élevées.

Dans la fig. 1 nous avons représenté la variation de k_1 (courbe I) et de k_2 (courbe II) en fonction de l'inverse de la température absolue. (Ces courbes sont très sensiblement indépendantes de la pureté des échantillons et de leur préparation de surface dans les limites où nous avons étudié l'influence de ces facteurs.)

On constate que tant que la température ne dépasse pas 600°C, c'est-à-dire tant que n'apparaît pas la phase FeO dans les pellicules[1] le processus d'oxydation est régi, pour chacun des deux groupes d'expériences par une chaleur d'activation trouvée égale respectivement à $Q_1 = 36.300$ cal/mol et $Q_2 = 15.100$ cal/mol. On voit de plus que l'influence du préchauffage, très importante à 450°C, diminue constamment quand augmente la température, pour devenir négligeable à 600°C.

Nous pensons que la cause de la croissance plus rapide de la pellicule sur un échantillon non préchauffé doit être recherchée dans les tensions développées dans la pellicule par la dilatation du support au cours de sa mise à la température de l'expérience.

Si on procède maintenant à l'examen micrographique des échantillons oxydés, on constate que tant que la température d'oxydation reste inférieure à 550°C, la vitesse de croissance de la pellicule varie avec l'orientation du cristal de fer, comme on peut le constater sur la coupe de la fig. 2.

Cette croissance épitaxique de la pellicule peut d'ailleurs prendre un autre aspect. Nous avons observé effectivement sur des échantillons oxydés dans des conditions rigoureuses dans l'intervalle 400°–550°C, que pour certains grains, la pellicule, au lieu de présenter une surface lisse, porte des striations parallèles (fig. 3). Ces striations peuvent prendre, dans l'intervalle 550°–625°C un relief assez accentué pour qu'il soit possible d'en étudier le faciès sur des coupes polies (figs. 4 et 5). Cet aspect épitaxique de l'oxydation du fer dans l'air à la pression atmosphérique est à rapprocher du phénomène mis en évidence par Bénard et Bardolle au cours de leur étude sur l'oxydation du fer aux faibles pressions d'oxygène.[2]

Ces quelques observations montrent la complexité du phénomène d'oxydation du fer polycristallin dans l'intervalle 400°–600°C, même si pour l'étudier on prend la précaution d'adopter un mode opératoire qui élimine dans la mesure du possible les facteurs perturbateurs. Il en résulte que les courbes isothermes d'augmentation de poids ou celles donnant la variation de la constante d'oxydation k en fonction de la température absolue, ne traduisent, même dans le cas d'un mode opératoire rigoureux, qu'un état moyen de la cinétique de l'oxydation.

Les résultats complets de cette recherche, realisée en liaison avec le Professeur J. Bernard, et qui a fait l'objet du contrat No. 43 entre l'auteur et le "Consejo de Investigación Cientifica" de l'Université de Concepción (Chili), seront publiés prochainement.

J. Païdassi.

Département de Métallurgie,
Escuela de Ingenieria Quimica,
Université de Concepción (Chili).

Bibliographie

1. J. Païdassi, *Boletin Soc. Chilena de Química*, **5**, 46 (1953).
2. J. Benard et W. Bardolle, *Compt. Rend.*, **232**, 2317 (1951).

*Received October 6, 1955.

VOL. 4 1956

BOOK REVIEW

Metals Reference Book. Edited by C. J. SMITHELLS. Second Edition, 1955. Butterworths Scientific Publications, London; Interscience Publishers Inc., New York. 2 volumes; Price: £8 8s; $25

The appearance of a second, expanded, edition of *Smithells* will be welcomed by all whose interests include the properties and behavior of metals and alloys. This edition, in two volumes, has been considerably revised, and contains several new sections, dealing with friction, physical properties of molten salts, and elastic properties and damping capacity.

The sections that appeared in the first edition are all retained, but have all been revised, and some drastically enlarged; for example the number of equilibrium diagrams has been substantially increased; they now occupy almost a quarter of the total space. Another welcome change is the inclusion of much more extensive bibliographies, which will further increase the usefulness of this essential reference book.

BRUCE CHALMERS.

VOL
4
195

SOME CURRENT PAPERS IN OTHER JOURNALS

Acta Crystallographica, Vol. 8

Part 12, December, 1955 (Partial Contents):
A single-crystal automatic diffractometer. I. W. L. Bond.
A single-crystal automatic diffractometer. II. T. S. Benedict.
A new method for calculating the effect of the collimating system on the small-angle X-ray scattering pattern. Paul W. Schmidt.
The geometry of lattice planes. II. Crystallography of edge dislocations. M. A. Jaswon and D. B. Dove.
Fonctions de Répartition: Application à l'Approche directe des structures. E. F. Bertaut.
Some lattice constants. J. W. Menary.
A table of dispersion corrections for X-ray scattering of atoms. Carol H. Dauben and David H. Templeton.
X-ray dispersion effects in crystal-structure determinations. David H. Templeton.
Temperature-diffuse scattering for powder patterns from cubic crystals. F. H. Herbstein and B. L. Averbach.
Precision measurement of dimensional changes in beryllia on neutron irradiation. G. E. Bacon and S. A. Wilson.
Twinning in barium titanate crystals. E. A. D. White.
The crystal structure of indium (I) iodide. Robert E. Jones and David H. Templeton.
Solid-solution effects, structural transitions and ferroelectricity in sodium–cadmium niobates. B. Lewis and E. A. D. White.
The δ phase found in the U–Zr alloys. Melvin H. Mueller.

Vol. 9, Part 1, January, 1956 (Partial Contents):
A new aid to the determination of the point-group symmetry of transparent crystals. J. W. Davisson.
Growth features on crystals of long-chain compounds. II. S. Amelinckx.
The anomalous X-ray background scattering from β-tin. S. C. Prasad and W. A. Wooster.
The elasticity of single crystals of lead. S. C. Prasad and W. A. Wooster.
An apparent anisotropic Debye-Waller Factor in cubic crystals. R. J. Weiss, J. J. DeMarco and G. Weremchuk.
Notation for felspar structures. Helen D. Megaw.
Anomalous absorption of slow neutrons and X-rays in nearly perfect single crystals. J. W. Knowles.
Kristallgittermodelle infolge von elektrischer Aufladung bei Kristallisation. Brigitte Krause und M. Renninger.
Double reflexion in aluminium—copper alloys. J. M. Silcock.
On the ordered structure proposed for Li_3Mg_5. F. H. Herbstein and B. L. Averbach.
Structures of the compounds Th_2Cu, $ThCu_2$, Th_2Zn and $ThHg_2$. N. C. Baenziger, R. E. Rundle and A. I. Snow.

Vol. 9, Part 2, February, 1956 (Partial Contents):
Progrès Réalisés dans la construction des tubes à rayons X pour cristallographie. Stanislas Goldsztaub.
Détermination de la Structure de Ti_2CaO_4 par le méthode self-consistante d'approche directe. E. F. Bertaut et P. Blum.
On the valence and atomic size of silicon, germanium, arsenic, antimony, and bismuth in alloys. Linus Pauling and Peter Pauling.
X-ray and neutron diffraction study of ferroelectric $PbTiO_3$. Gen Shirane, Ray Pepinsky and B. C. Frazer.
An explanation of the structures of hexagonal barium titanate and titanium dioxide. P. Vousden.
The probability distribution of X-ray intensities. VII. Some sesquisymmetric distributions. A. J. C. Wilson.
A new rationale of structure-factor measurement in neutron-diffraction analysis. R. D. Lowde.
Calculation of the electron distribution in the hydrogen atom for different values of the temperature factor. T. R. R. McDonald.
The elasticity of iron pyrites, FeS_2. S. C. Prasad and W. A. Wooster.
Fehlordnungserscheinungen in Elektronenbeugungsdiagrammen. (Zur Deutung der kontinuierlichen Streifen und der Zwillingsreflexe.) Hans Göttsche.
The probability distribution of X-ray intensities: atoms in special positions. A. Hargreaves.
Compounds with the α-U_3O_8-type structure. William T. Holser.
The lattice energies of the alkali halides. D. F. C. Morris.
The unit cell and space group of barium tetratitanate, $BaO.4TiO_2$. F. W. Harrison.
Systematic absences corresponding to false symmetry. David H. Templeton.
Sur quelques composes du type M_2O_3–Cu_2O. Claude Delorme.
The accuracy of atomic co-ordinates derived from Fourier syntheses. G. J. Dickins.

Archiv für das Eisenhüttenwesen

Heft 11, November, 1955:
Beeinflussung des Kohlenstoffes des Gießereiroheisens beim direkten Guß vom Hochofen. Willy Oelsen, Karl Roesch und Kurt Orths.
Formänderungsfestigkeit von unlegierten und niedrig legierten Stählen beim Warmstauchen unter einem Fallhammer. Kurt Fink, Werner Lueg und Günter Bürger.
Anlage zur Spannungserzeugung für die Spektralanalyse mit Schalteinrichtung. Kurt Möhl, Ernst Schael und Joachim Bruch.
Die potentiometrische Bestimmung des Vanadins in chromreichen Stählen. Johannes Bünger.
Umwandlungskinetik der Sigmaphase in einer Eisen-Chrom-Legierung mit 48% Cr. Ewald Baerlecken und Heinz Fabritius.
Untersuchungen im System Eisen-Eisenoxyd-Kalk. Gerhard Trömel, Willi Jäger und Eberhard Schürmann.
Die Eisenecke des Dreistoffsystems Eisen–Beryllium–Phosphor. Rudolf Vogel und Gerhard Zwingmann.
Prämienlohnabkommen auf technisch-statistischer Grundlage. Wilhelm Bauer.
Heft 12, Dezember, 1955:
Phosphorschnellbestimmung im Thomaswerk mit radioaktiven Isotopen. Friedrich Eberhard, Helmut Knüppel und Hermann-Josef Kopineck.
Die Röntgen-Fluoreszenz-Spektralanalyse und ihre Bedeutung für die Metallkunde. Otto Werner.
Metallographische Untersuchungen über Verformungserscheinungen an der Oberfläche biegewechselbeanspruchter Proben aus St 37. Franz Wever, Max Hempel und Angelica Schrader.
Untersuchung von Phasenumwandlungen in austenitischem Manganstahl, besonders mit Magnetitsuspension. Kurt Hans v. Klitzing und Elfriede Wesselhöft.
Die Verfestigung bei der Tiefziehprüfung. Alfred Krisch.
Passivierung von Chromstählen in 6,5 prozentiger Salpetersäure, schwefelsaurer Kupfersulfatlösung und Leitungswasser. Carl Carius.
Die Grundlagen zur Ermittlung der Gasdurchlässigkeit von feuerfesten Baustoffen. Ludwig Žagar.
Berechnung der wirtschaftlichsten Sicherheitsabschnitte bei Massekopfblöcken für Radreifen. Ludwig von Bogdandy.
Heft 1, Januar, 1956:
Untersuchungen über Reaktionsgleichgewichte zwischen flüssigen Eisen und kieselsäuregesättigten Schlacken. Hermann Schenk und Günther Wiesner.
Mikroanalytische Untersuchungen in der Eisenforschung. I. Die Technik der Mikroanalyse. Walter Koch und Hans Malissa.
Streuung und Trennschärfe verschiedener Verfahren zur Prüfung der Sprödbruchempfindlichkeit von Stahl. Helmut Knüppel und Karl Ernst Mayer.

VOL. 4 1956

Die Eigenschaften handelsüblicher warm gewalzter Dynamobleche. ERNST CZERLINSKY.
Diffusion von Kohlenstoff in Eisen durch elektrolytisch erzeugte Wanderung bei Anwesenheit von Phosphor. FRIEDRICH ERDMANN-JESNITZER und WOLFGANG GUNKEL.
Zur Ausscheidung von Kohlenstoff aus übersättigter Lösung in α-Eisen während der Auslagerung. WOLFGANG PITSCH und KURT LÜCKE.
Ermittlung kleiner Kohlenstoffgehalte im α-Eisen durch Dämpfungsmessung. WOLFGANG WEPNER.
Die Löslichkeit des Vanadinkarbids im Austenit. KARL BUNGARDT, KARL KIND und WILLY OELSEN.
Verkürzung der Belichtungszeit bei Röntgeninterferenzaufnahmen durch geeignete Anordnung und Formgebung der Blenden. FRITZ BINDER und ECKARD MACHERAUCH.
Ein Beitrag zum Dreistoffsystem Eisen–Phosphor–Kalzium. RUDOLF VOGEL und HELMUT KLOSE.

Journal of the Institute of Metals, Vol. 84

January, Part 5, 1955–56:
On the recrystallization of cold-rolled commercially pure titanium. ICHIJI OBINATA and KEIZO NISHIMURA.
The intergranular brittleness of single-phase copper-antimony alloys. L. M. T. HOPKIN.
Rotational slip in zinc single crystals. A. D. WHAPHAM.
Plastic laps for the preparation of specimens for metallographic examination. V. J. HADDRELL, E. C. SYKES and B. W. MOTT.
Observations on the mechanical properties of two age-hardenable copper–aluminium alloys. J. P. DENNISON.
A miscibility gap in the face-centred cubic phase of the copper–nickel–chromium system. J. L. MEIJERING, G. W. RATHENAU, M. G. VAN DER STEEG, and P. B. BRAUN.

February, Part 6, 1955–56:
Symposium on the final forming and shaping of wrought non-ferrous metals.
The machining properties of non-ferrous metals. D. F. GALLOWAY.
The deep drawing and spinning of sheet metal, with particular reference to non-ferrous materials. JOHN A. GRAINGER.
Rubber pressing. J. FIELDING.
(Symposium to be completed next month).
The manufacture and properties of high-strength nickel–tungsten alloys. M. DAVIS, C. E. DENSEM, and J. H. RENDALL.

Journal of Metals, Vol. 7

January, 1956, Section 1 (Partial Contents):
The present status of titanium development. D. J. MCPHERSON.
Status of titanium fabrication and use. J. H. GARRETT.
Background for practical heat treatment of various titanium alloy types. P. D. FROST.
The future use pattern for titanium. B. S. MESICK.
Interaction between metals and atmospheres during sintering. J. T. NORTON.
Surface tensions of silicates. R. E. BONI and G. DERGE.
Surface structure of nonoxidizing slags containing sulphur. R. E. BONI and G. DERGE.

La Metallurgia Italiana, Vol. XLVII

November, 1955:
Influence of small work-hardenings on mechanical and technological properties of steel strip. L. DAINELLI and L. COCCIOLO.
Interpreting inhibitors operation in steam phase by observing their behaviour at various temperatures. C. BIGHI and E. MANTOVANI.
Considerations on the behaviour of refractory materials against thermal stresses. L. MASSIMILLA and S. BRACALE.
December, 1955:
Operating experiences with basic furnace roofs. C. KREUTZER.
Researches on salty fog corrosion tests—Note III. About the effect of sample shape. G. BIANCHI and U. GANDOLFI.
Etch figures of pure copper examined at electronic microscope. G. BONFIGLIOLI and A. FERRO.
Extending the Lingane-Karplus method of potentiometric determination of Mn to high-silicon ores and steel products. L. BRAICOVICH and M. F. LANDI.

VOL 4 195

INTERNAL FRICTION IN SOLID SOLUTIONS OF TANTALUM*

R. W. POWERS and MARGARET V. DOYLE†

The internal friction in tantalum arising from the diffusion of interstitial oxygen can be described as the sum of two peaks. The peak at 137°C (applied frequency ~ 0.6 c.p.s.), whose height is directly proportional to the oxygen concentration, is interpreted as arising from the diffusion of free, non-interacting interstitial oxygen. On the other hand, that at 162°C, whose height is a quadratic function of the oxygen concentration, is believed to arise from the diffusion of oxygen atoms, each of which is interacting with another oxygen atom in its neighborhood.

In a very similar manner, the internal friction arising from the diffusion of nitrogen can also be described as the sum of two peaks, one at 334°C and the other at 362°C ($\nu \sim 0.6$ c.p.s.). The peak at 362°C is shown to be a quadratic function of the nitrogen concentration.

With both oxygen and nitrogen present in tantalum, a peak appears at 175°C, whose height is proportional to the product of the oxygen and nitrogen concentrations. This peak is described as arising from the diffusion of oxygen atoms, each of which is interacting with a nitrogen atom in its neighborhood.

The activation energy associated with the diffusion of free oxygen atoms was found to be less than those measured for the diffusion of oxygen interacting either with other oxygen atoms or with nitrogen. These interactions between interstitial solute atoms in tantalum are believed to take place over short atomic distances.

FROTTEMENT INTERNE DANS LES SOLUTIONS SOLIDES DE TANTALE

Le frottement interne du tantale dû à la diffusion de l'oxygène interstitiel est décrit comme la somme de deux pics. Celui à 137° (fréquence de 0,6 c.p.s.), dont la hauteur est proportionnelle à la concentration en oxygène, est expliqué par la diffusion des atomes interstitiels libres. Par contre, celui à 162°, dont la hauteur est une fonction quadratique de la concentration en oxygène, est attribué à la diffusion d'atomes d'oxygène en interaction avec un autre atome d'oxygène situé dans le voisinage.

De la même manière, le frottement interne dû à la diffusion de l'azote peut être expliqué comme la somme de deux pics, l'un à 334°, l'autre à 362° (ν de l'ordre de 0,6). Le pic à 362° est une fonction quadratique de la concentration en azote. Quand l'oxygène et l'azote sont présents simultanément dans le tantale, un pic apparaît à 175°, dont la hauteur est proportionnelle au produit des concentrations en oxygène et en azote; il est expliqué comme dû à la diffusion des atomes d'oxygène en interaction avec un atome d'azote situé dans son voisinage.

L'énergie d'activation associée à la diffusion des atomes libres d'oxygène est plus petite que celle mesurée pour la diffusion de l'oxygène en interaction, tant avec l'oxygène qu'avec l'azote. Ces interactions entre atomes interstitiels dans le tantale seraient à courte distance.

ÜBER DIE INNERE REIBUNG BEI TANTAL MISCHKRISTALLEN

Die innere Reibung von Tantal, die durch die Diffusion von eingelagertem Sauerstoff hervorgerufen wird, kann als die Summe zweier Maxima beschrieben werden. Das Maximum bei 137°C (angewandte Frequenz ~0.6 cm/s), dessen Höhe direkt proportional der Sauerstoffkonzentration ist, wird der Diffusion von freiem, eingelagerten Sauerstoff zugeschrieben, der keinerlei Wechselwirkungen unterliegt. Auf der anderen Seite scheint das Maximum bei 162°C, dessen Höhe eine quadratische Funktion der Sauerstoffkonzentration ist, von der Diffusion von solchen Sauerstoffatomen herzurühren, von denen ein jedes mit einem anderen aus seiner Nachbarschaft in Wechselbeziehung steht.

In ähnlicher Weise kann die innere Reibung, die durch die Diffusion des Stickstoffs hervorgerufen wird, ebenfalls als die Summe zweier Maxima beschrieben werden, von denen das eine bei 334°C und das andere bei 362°C liegt ($\nu \sim 0.6$ cm/s). Es wird gezeigt, dass das Maximum bei 362°C eine quadratische Funktion der Stickstoffkonzentration ist.

Bei Anwesenheit von Sauerstoff und Stickstoff in Tantal entsteht bei 175°C ein Maximum, dessen Höhe proportional dem Produkt aus der Sauerstoff- und der Stickstoffkonzentration ist. Dieses Maximum wird der Diffusion von Sauerstoffatomen zugeschrieben, von denen ein jedes mit einem Stickstoffatom aus seiner Nachbarschaft in Wechselwirkung steht.

Die Aktivierungsenergie des Diffusionsvorganges von freien Sauerstoffatomen hat einen niedrigeren Wert als die des Diffusionsvorganges von Sauerstoff, der entweder mit Sauerstoffoder mit Stickstoffatomen in Wechselwirkung steht. Die gegenseitige Beeinflussung der eingelagerten, gelösten Atome in Tantal reicht anscheinend nur über kurze Atomabstände.

* Received July 20, 1955.

† General Electric Research Laboratory, Schenectady, New York.

VOL. 4 1956

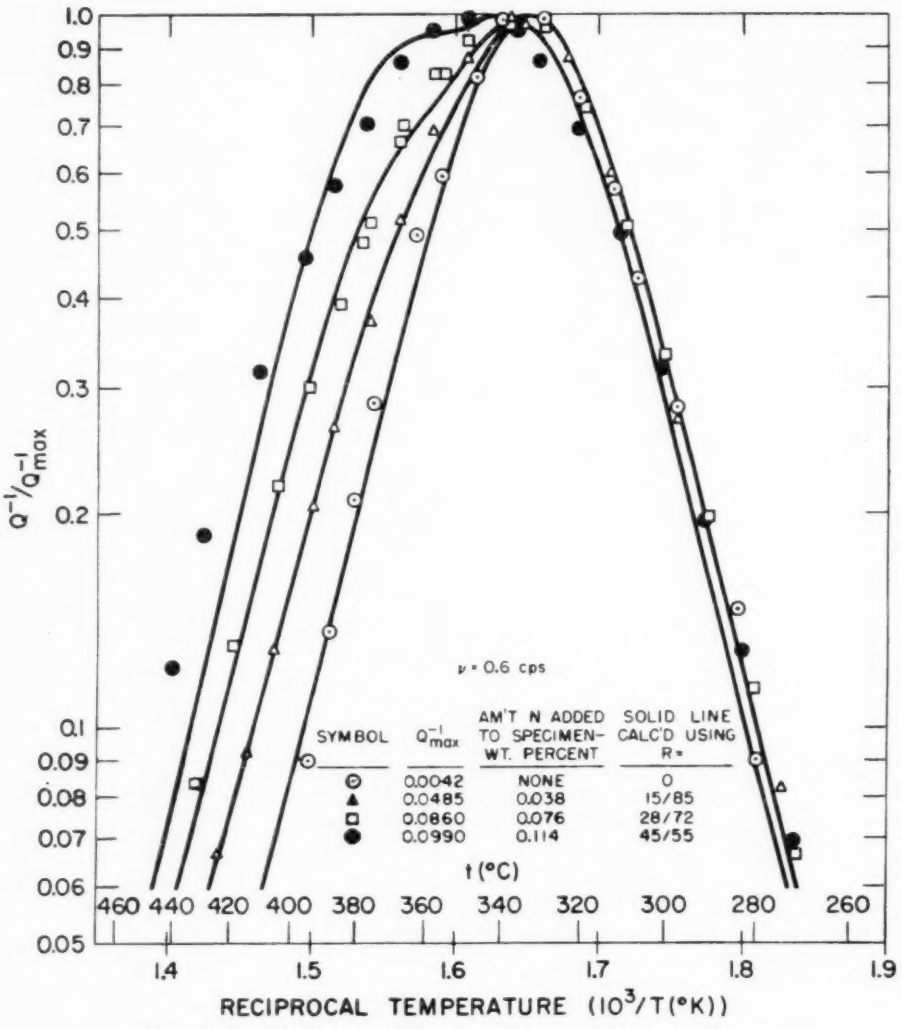

FIG. 1. Normalized internal friction peaks of nitrogen in tantalum.

INTRODUCTION

The internal friction in tantalum arising from the diffusion of interstitially dissolved oxygen at low concentrations can be described with a single relaxation time.[1] However, at higher oxygen concentrations, the experimentally determined internal friction curve (Q^{-1} vs. $1/T$) becomes broadened and skewed, with the internal friction considerably higher on the high-temperature side of the peak than that computed for a single relaxation time. At least one additional, longer relaxation time is needed to represent the data at these higher concentrations.

In this report we present additional experimental evidence that concentration broadening in oxygen-tantalum solutions is brought about by an interaction between interstitial oxygen atoms. Moreover, there are indications that concentration broadening of this kind is not confined to solid solutions of oxygen in tantalum, but is found in all oxygen and nitrogen solid solutions of the five-B elements. Part of the evidence for this general behavior is illustrated by the influence of nitrogen concentration on the shape of the internal friction peak associated with the diffusion of nitrogen in tantalum.

THE TANTALUM-NITROGEN INTERNAL FRICTION PEAK

In order to reveal the influence of nitrogen concentration upon the shape of the internal friction peak, we measured the damping in four specimens, containing different quantities of nitrogen, as a function of temperature in a low-frequency torsional pendulum. The internal friction in these specimens, as well as that in all others discussed in this report, was strictly

independent of the strain-amplitude up to strains of at least $2 \cdot 10^{-4}$. The samples were prepared in a manner analogous to that already described in detail for oxygen-tantalum solutions.[1] We estimate that the concentration of nitrogen in the specimens prior to loading was about 0.005 weight per cent. The normalized damping curves are presented in Fig. 1. They are similar to those previously reported for oxygen solutions. Thus, as can be seen in Fig. 2, the width of the nitrogen peak, in terms of $\Delta(1/T)$ measured at half the peak height, increases with the nitrogen concentration or nitrogen peak height. At 0.6 c.p.s., the internal friction for small amounts of nitrogen can be described with a single relaxation time corresponding to a peak at 334°C. At higher concentrations a second relaxation time corresponding to a second peak at 362°C is needed to fit the experimental data. The solid lines in Fig. 1 have been computed for various combinations of the 334° and 362° peaks. The ratio of the height of the 362° peak to that of the 334° peak is indicated on the graph. Up to roughly 0.1 weight per cent nitrogen, it is possible to fit the experimental data using combinations of only two peaks. However, for a specimen containing about 0.12 weight per cent nitrogen, the fit is imperfect, indicating the presence of additional relaxation times at very high nitrogen concentrations. For purposes of curve fitting, an activation energy of 37.5 kcal was used for the 334° peak and 40.0 kcal for the 362° peak.

The nitrogen internal friction peak is not as stable as that for oxygen. If a specimen is aged above 450°C, the internal friction arising from the diffusion of nitrogen declines noticeably. Similar observations have been made by Ke.[2] Because of this instability, which it seems reasonable to associate with the precipitation

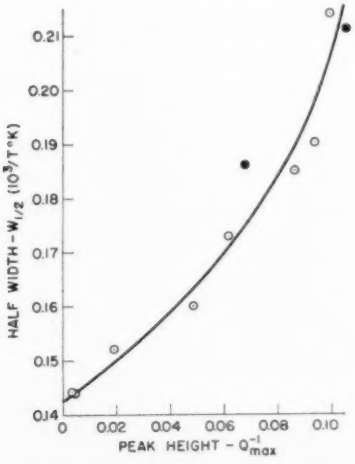

FIG. 2. Half-width of tantalum-nitrogen damping peak as a function of peak height.

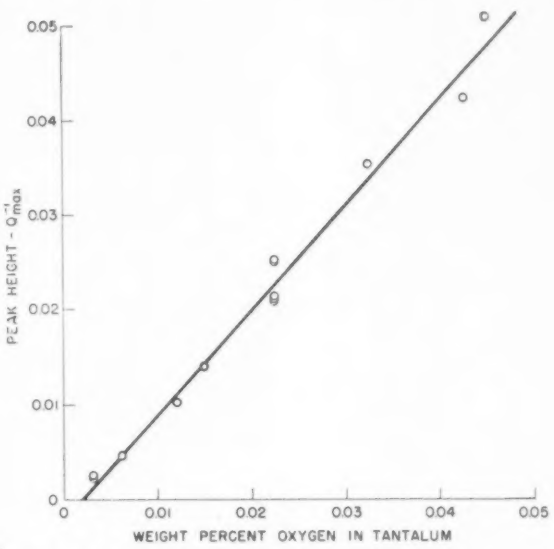

FIG. 3. The height of the normal tantalum-oxygen damping peak as a function of oxygen concentration.

of tantalum nitride, our study of the nitrogen peak has not been as comprehensive as that of the oxygen peak.

THE EFFECT OF CONCENTRATION ON THE HEIGHT OF THE NORMAL (137°C) TANTALUM-OXYGEN PEAK

By Snoek's theory,[3] the height of an internal friction peak should be proportional to the interstitial solute atom concentration, if no interaction occurs between the solute atoms. Consequently, we thought it would be of value to check this aspect of Snoek's theory for solutions of tantalum containing oxygen at low concentrations. A large number of tantalum-wire specimens were prepared with the oxygen content varying over a fifteen-fold range from 0.003 to 0.045 weight per cent. The preparation of tantalum-oxygen alloys of known interstitial atom content has been described previously.[1] The results of measurements of the peak heights at 0.6 c.p.s. in a torsional pendulum are shown in Fig. 3. The equation of the least-square line that best represents these data is

$$Q^{-1} = 1.10 \text{ (concentr. in weight per cent)} - 0.0020.$$

With the exception of the lowest points, all points fall within ten per cent of this line. Some of this scatter may be associated with variations in grain-size and orientation from specimen to specimen. Usually most of the cross-section of a wire specimen is occupied by one grain with, however, a number of smaller grains lying along the periphery.

VOL. 4 1956

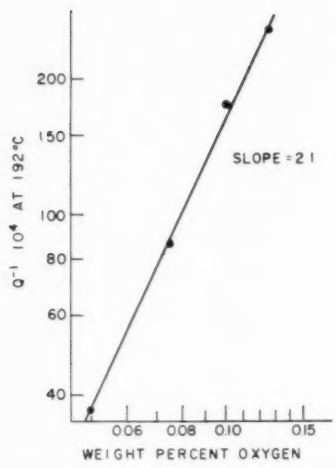

FIG. 4a. Plot showing quadratic dependence of the height of the oxygen interaction peak on the oxygen concentration.

THE EFFECT OF CONCENTRATION ON THE EXTRAORDINARY OXYGEN AND NITROGEN (162° AND 362°) PEAKS

As reported previously, the internal friction data for somewhat higher concentrations of oxygen in tantalum can be represented empirically as the sum of two peaks, one of which occurs at 137° and the other at 162°C ($\nu = 0.6$ c.p.s.). We have just shown that the height of the normal peak at 137°C varies linearly with concentration. In Fig. 4a, the logarithm of the internal friction found at 192°C in a number of specimens is plotted against the logarithm of the oxygen concentration. The oxygen concentration was varied from 0.05 to 0.125 weight per cent. At 192°C, the internal friction is due principally to the 162° peak, that from the tail of the 137° peak being relatively small. The measured data have been adjusted for this contribution from the 137° peak, as indicated in Table 1. The slope of 2.1 indicates that the height of the extraordinary peak at 162°C is a quadratic function of the oxygen concentration. These facts suggest that the 162° peak may arise from diffusion of oxygen atoms, each of which has another oxygen atom in its neighborhood with which it is interacting.

TABLE 1. Internal friction data on tantalum-containing oxygen at relatively high concentrations. All internal friction data observed at 0.6 c.p.s.

Weight per cent oxygen	Height of oxygen peak $\sim Q_{max}^{-1} \cdot 10^4$	Measured internal friction at 192°C $\cdot 10^4$	Calculated contribution from 137° Peak $\cdot 10^4$	Internal friction from 162° Peak $\cdot 10^4$
0.050	410	77	40	37
0.075	599	145	59	86
0.100	833	258	82	176
0.125	913	347	90	257

In a completely analogous manner, we interpret the 362° peak as arising from the diffusion of nitrogen atoms, each of which is interacting with another nitrogen atom. This assumption is justified in Fig. 4b, where data for nitrogen in tantalum (taken from Fig. 1) are presented similar to those for oxygen in Fig. 4a. The internal friction was measured at 417°C, where the contribution from the tail of the normal (334°) peak is relatively small. These data have been corrected for the contribution from the tail of the 334° peak, however. The slope of 1.9 indicates that the 362° peak is a quadratic function of the nitrogen concentration.

We interpret the peaks at 137° and 334°C in the conventional manner. They arise from diffusion of free oxygen or nitrogen atoms that are not interacting with neighboring solute atoms.

THE INFLUENCE OF NITROGEN ON THE OXYGEN PEAK

Not only does increasing nitrogen concentration broaden the nitrogen peak, but nitrogen also broadens the oxygen peak, concomitantly with reducing its height, as shown in a previous report.[1] The damping data can be fitted fairly well as the sum of the normal peak at 137°C and a second peak at 175°C ($\nu = 0.6$ c.p.s.). An interpretation of this latter peak, consistent with that given the 162°C, is that it arises from the diffusion of oxygen atoms, each of which is interacting with a nitrogen-atom neighbor. Should this interpretation be correct, we would expect the height of the 175° peak to be proportional to the product of the oxygen and nitrogen concentrations. An experiment to check this point was conducted on specimens all loaded with the same amount of oxygen (0.0225 weight per cent), but with varying quantities of nitrogen. The oxygen concentration was kept low in order that the interaction between oxygen atoms might be neglected. The internal friction data obtained from measurements

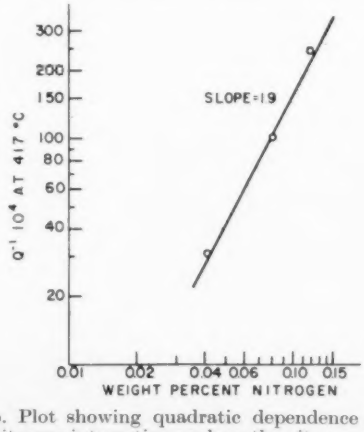

FIG. 4b. Plot showing quadratic dependence of the height of the nitrogen interaction peak on the nitrogen concentration.

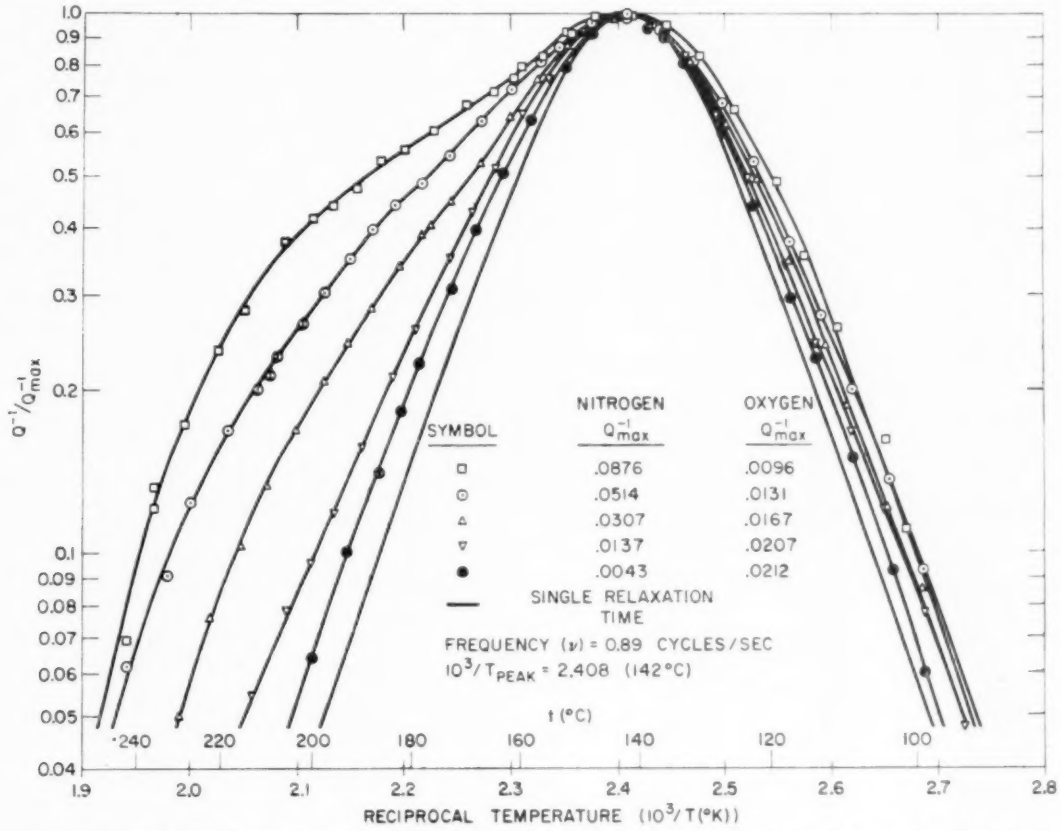

FIG. 5a. Normalized internal friction peaks of oxygen in tantalum broadened by varying amounts of nitrogen.

made on these specimens are shown in Fig. 5a. The data in Fig. 5a have been normalized to unity at the normal oxygen peak (142°C at 0.9 c.p.s.).

The oxygen dissolved in these specimens can be considered distributed between two classes of atoms, those interacting with nitrogen and those that are free. From mass-action considerations we would expect

$$C_{O_N} = C_{O_f} \cdot C_{N_f}$$

where C_{O_N} is the concentration of oxygen atoms interacting with nitrogen,

C_{O_f} is the concentration of free oxygen, and

C_{N_f} is the concentration of free nitrogen.

The nitrogen content of the specimens in the as-received condition varies considerably, as indicated by variations in the nitrogen peak height from 0.002 to 0.014. Since this nitrogen is difficult to remove, requiring temperatures above 2500°C and pressure of about 10^{-6} mm, the amount of nitrogen subsequently loaded into the specimens cannot be used as a very good measure of the total nitrogen content. It is perhaps better to use the height of the nitrogen peak itself as a measure of the nitrogen concentration. The magnitude of the damping at 142°C can be used as a measure of the free oxygen concentration, since at this temperature the contribution from the 175°C peak is relatively small.

In Fig. 5b there is presented a plot of the damping measured at 215°C, where the contribution from the tail of the normal oxygen peak is negligible, against the product of the heights of the normal oxygen peak

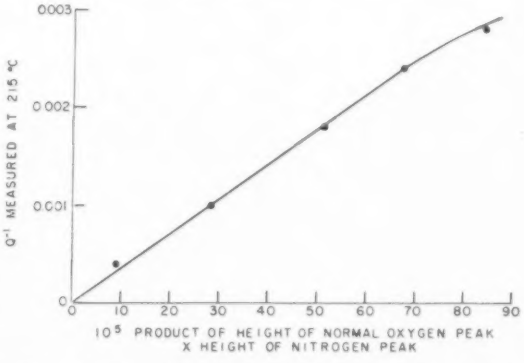
Q⁻¹ MEASURED AT 215 °C
0.003
0.002
0.001
0
0 10 20 30 40 50 60 70 80 90
10⁵ PRODUCT OF HEIGHT OF NORMAL OXYGEN PEAK X HEIGHT OF NITROGEN PEAK

FIG. 5b. Plot illustrating linear dependence of the height of the 175°C peak on the product of oxygen and nitrogen concentrations.

VOL. 4 1956

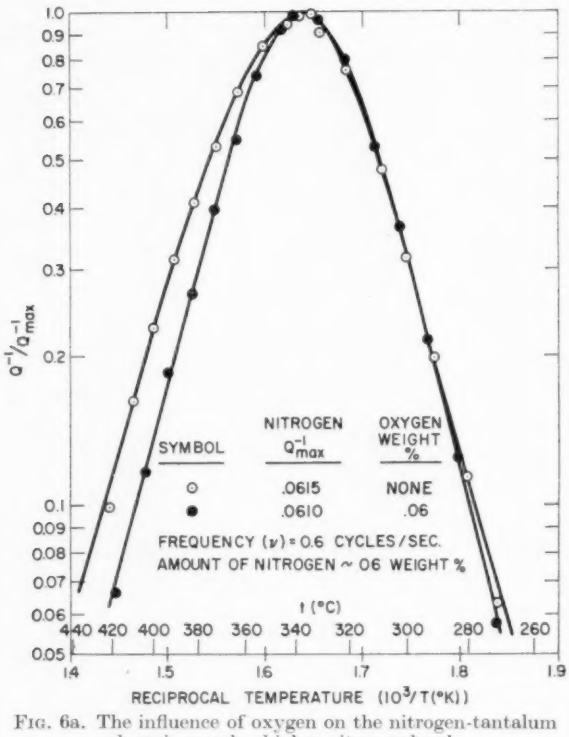

FIG. 6a. The influence of oxygen on the nitrogen-tantalum damping peak—higher nitrogen level.

and of the nitrogen peak. A linear relationship is observed between damping and this product up to those concentrations at which deviations occur in the proportionality between nitrogen peak height and nitrogen concentration.

THE INFLUENCE OF OXYGEN ON THE NITROGEN PEAK

Since nitrogen was found capable of affecting both the height and breadth of the oxygen peak, it was of some interest to study the complementary case, to investigate the influence of oxygen on the nitrogen peak. Four samples were prepared, with high and low oxygen concentrations in samples containing two different amounts of nitrogen.

The results of damping measurements on the four test specimens are to be found in Fig. 6a and 6b. At neither nitrogen level, 0.06 nor 0.04 weight per cent nitrogen, was oxygen found to broaden the nitrogen damping peak. On the contrary, the influence of oxygen was to decrease slightly the breadth of the nitrogen peak. The fact that oxygen does not broaden the nitrogen peak is perhaps not too surprising if it is borne in mind that oxygen diffuses about 25,000 times faster than nitrogen at 350°C. In the time-interval required for a nitrogen atom to diffuse from one site to an adjacent one, any interaction influence of oxygen might be smeared out.

THE UNIQUE POSITION OF THE INTERACTION PEAKS AND THEIR RESOLVABILITY

We shall now refer to the 162, 175, and 362°C peaks as interaction peaks. To reduce the apparent arbitrariness of this description, perhaps at least two questions need be considered further. The first concerns the uniqueness of the position of an interaction peak at a fixed frequency of vibration. If the position of an interaction peak were to vary continuously with changes in interstitial solute concentration, the term "peak" would be a description of little value. In Figs. 7a, 7b, and 7c there are shown plots of the interaction peaks at various concentrations. It can be seen that, through a range of concentration, the interaction-peak temperatures do not vary with concentration. The positions of the oxygen and nitrogen interaction peaks at 162°C and 362°C respectively appear constant within about a degree. On the other hand, that for the oxygen-nitrogen peak (175°C) changes by 4 degrees. A large part of this apparent variation arises from the contribution from the 162°C peak. At low nitrogen concentrations, where the relative magnitude of the oxygen-nitrogen and oxygen interaction peaks are more nearly of the same magnitude, this contribution is relatively greatest.

The interaction peaks in Figs. 7a, 7b, and 7c were obtained by subtracting a damping curve of unit

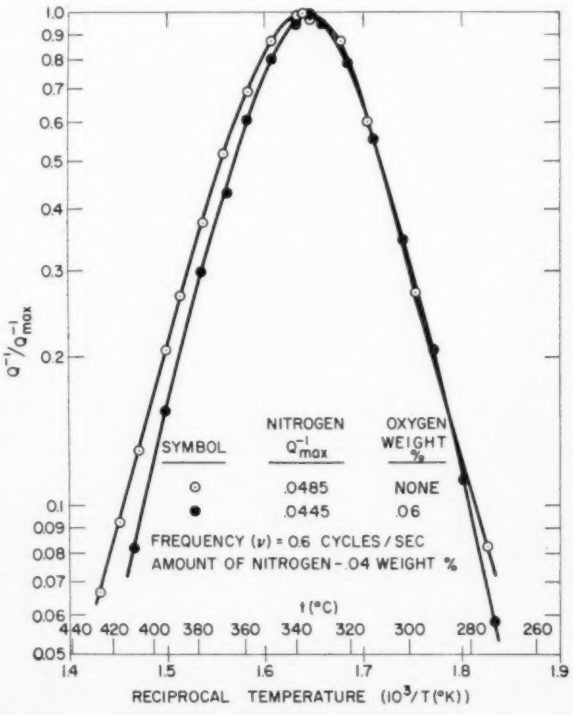

FIG. 6b. The influence of oxygen on the nitrogen-tantalum damping peak—lower nitrogen level.

height, corresponding to the "normal" peak, from the experimental damping curve normalized to unity at its maximum. There can be objection to this procedure on the grounds that the height of the normal peak to be subtracted should be somewhat less than unity. However, the precise height of the normal peak that should be subtracted is unknown. Moreover, knowledge of its precise height is not required, as can be shown by the following argument:

If a hypothetical damping curve is synthesized from two peaks of equal height, is normalized to unity at its maximum, and if one of the peaks of unit height is subtracted from the synthesized curve, the position of the second peak can be determined within 1.5 degrees.

Although the positions of the interaction peaks in Figs. 7a, 7b, and 7c are well established, little can be said about their shapes from this procedure. Consequently, the fact that the curves shown in Figs. 7a, 7b, and 7c are skewed reveals nothing about the shape of the interaction peaks.

It is true that, at extremely high concentrations, the position of the interaction peak appears to move in the direction of higher temperatures. This we interpret as an indication of the presence of more than one neighboring solute atom in the vicinity of a jumping atom.

The second question with respect to the interaction peaks concerns the possibility of resolving an experimental internal friction curve into separate and distinct normal and interaction peaks. Since an internal-friction peak near 150°C, with an activation energy of about 25 kcal, has a half-width of about 35 degrees, no distinct separation of the 162° interaction peak and the 137° peak is possible. On the other hand, a partial separation of the 137° oxygen peak and the nitrogen-oxygen interaction peak at 175°C is possible. Inspection of Fig. 5a discloses a readily discernable inflection point, which is the best that can be done with respect to the resolution of distinct peaks.

ACTIVATION ENERGY MEASUREMENTS

Relaxation times for diffusional processes can usually be described in the exponential form, $\tau = \tau_0 \exp(E/RT)$. It is of interest to find out whether the relaxation times corresponding to the interaction peaks are longer than those for the normal peaks because of differences in the pre-exponential constant τ_0, or in the activation energy E, or perhaps in both. Therefore, activation energies for diffusion in various specimens have been determined by noting the change in peak temperature that results from varying the

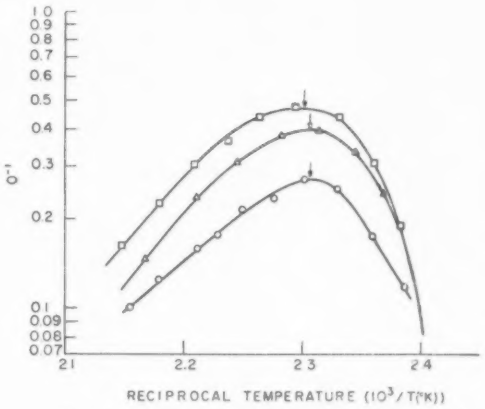

FIG. 7a. Determination of the position of the oxygen interaction peak.

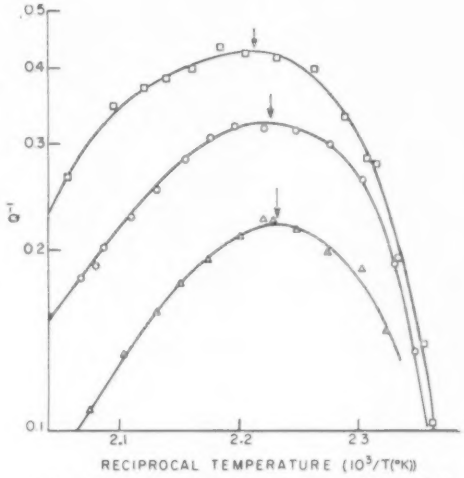

FIG. 7b. Determination of the position of the oxygen-nitrogen interaction peak.

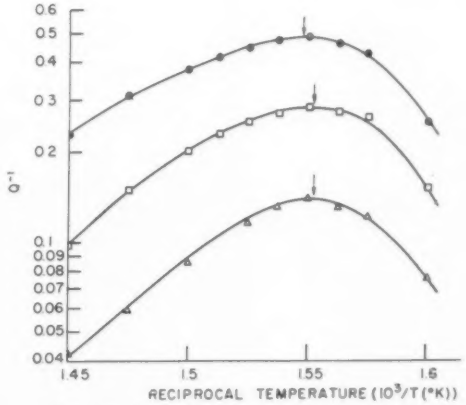

FIG. 7c. Determination of the position of the nitrogen interaction peak.

VOL. 4 1956

TABLE 2. Fundamental data used in computing activation energies

System	Freq. of applied stress c.p.s.	Reciprocal peak temp. $1/T \cdot 10^3$	Activation energy kcal/mole	τ_0 10^{14} sec	Comment
O in Ta (low conc. 0.015 weight per cent)	0.285 0.612 1.673	2.494 2.438 2.358	25.8	0.5	$E = 25.9$ kcal from peak-breadth meas.
O in Ta (high conc. 0.12 weight per cent)	0.266 0.559 1.541	2.431 2.381 2.305	27.8	0.1	Value $E = 27.8$ is some average of that for normal and interaction peaks
Low O conc. High N conc. (0.0225 weight per cent O 0.08 weight per cent N)	0.293 0.891 1.722	2.492 2.408 2.357	26.1	0.3	Normal oxygen peak
	0.293 0.891 1.722	2.275 2.191 2.147	27.3	1.0	Oxygen-nitrogen interaction peak
N in Ta (low conc. *ca.* 0.02 weight per cent)	0.285 0.570 0.927 1.662	1.689 1.652 1.625 1.596	37.5	0.8	$E = 37.0$ kcal from peak-breadth measurement

frequency of the torsional vibration of the tantalum wire. Results of these measurements are summarized in Table 2, and are depicted graphically in Figs. 8a, 8b, and 8c. In all cases, the temperature at which the internal friction is a maximum was determined from plots of the midpoint of the low- and high-temperature sides of the damping peak versus the normalized damping. Such a procedure, which enhances greatly the precision of the measurements, has been described in detail in a previous report.[4]

Data taken on specimens containing only oxygen are shown in Fig. 8a. The significant result is that the measured activation energy (27.8 kcal) for the specimen containing a high concentration of oxygen

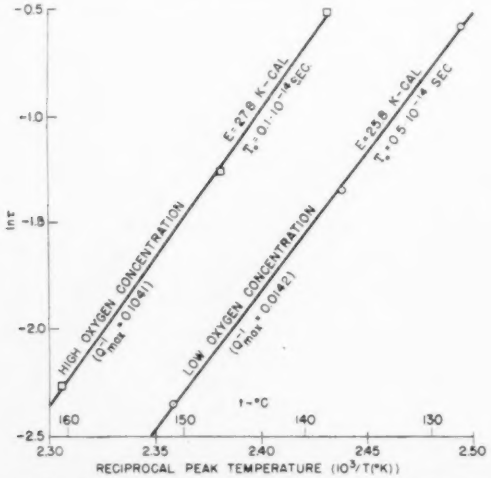

FIG. 8a. Activation energy determination for the diffusion of oxygen in tantalum.

is greater than that (25.8 kcal) for the specimen containing only a little oxygen. Since the normal and interaction peaks are too close to resolve well enough for our purpose here, the value 27.8 kcal must represent some average activation energy of that for the normal and that for the interaction peak. Moreover, since the experimental high-oxygen peak is broadened, its activation energy cannot be measured as precisely as that for the low-oxygen peak. There can be no doubt, however, that the activation energy is greater for the interaction peak than that for the normal peak. It is doubtful that the values obtained for τ_0 in the two cases, $0.5 \cdot 10^{-14}$ sec and $0.1 \cdot 10^{-14}$ sec, are significantly different.

Data on a specimen containing a small amount of oxygen and a large amount of nitrogen are shown in Fig. 8b. This sample is the same as the one corresponding to the largest amount of nitrogen in Fig. 5a. For this sample, the interaction peak at 175°C is separated by 38° from the normal peak. It is possible to measure separately, reasonably well, the shifts in the normal and the interaction peak temperatures with changes in the frequency of vibration. The position of the interaction peak was located by subtracting from the experimental curve, a calculated damping peak corresponding to normal peak. The data obtained for the normal peak are in good agreement with those found with the specimen containing oxygen alone in small amounts (26.1 vs 25.8 kcal in the activation energy and 0.5 vs $0.3 \cdot 10^{-14}$ sec in τ_0). The activation energy for the oxygen-nitrogen interaction peak was found to be greater than that for the

normal oxygen peak, 27.3 against 26.1 kcal. The values obtained for τ_0, 0.3 vs. $1.0 \cdot 10^{-14}$ sec, are not significantly different within our experimental error.

The activation energy for the diffusion of nitrogen in tantalum at low concentration has also been measured. The results are shown in Fig. 8c. We obtained a value of 37.5 kcal for the activation energy and 0.8×10^{-14} sec for τ_0 with a specimen in which the nitrogen peak height was about 0.019.

The activation energies measured for the normal peaks, 25.8 and 26.1 kcal for oxygen, and 37.5 kcal for nitrogen, should be compared with some values obtained by an entirely different method. It has been shown that the half-breadth, $W_{1/2}$, of a damping peak corresponding to a single relaxation process, bears the following relationship to the activation energy.[1]

$$E \text{ (kcal)} = 5.28/W_{1/2}.$$

If a plot of the half-breadth of a damping curve for various interstitial concentrations is extrapolated to zero concentration, where interactions do not occur, the value of the half-breadth so obtained should correspond to that for only one relaxation process. Previously, we reported a value of 25.0 kcal for oxygen in tantalum by this method.[1] This number was obtained by an extrapolation of a half-breadth plot to zero oxygen concentration. More properly the extrapolation should have been made to zero total interstitial concentration. With the data available in Fig. 5a, we can now correct for the broadening arising from the small amount of residual nitrogen left in the "oxygen" specimens. A half-breadth of $0.204 \cdot 10^{-3}$ is thus obtained corresponding to an activation energy of 25.9 kcal. This is in good agreement with the values 25.8 and 26.1 kcal obtained in the more conventional manner.

An extrapolated half-breadth of $0.143 \cdot 10^{-3}$ is obtained from Fig. 2 for nitrogen in tantalum. This corresponds to an activation energy of 37.0 kcal. This number should be compared with the value 37.5 kcal obtained from the measurement of the shift in the peak temperature with changes in the frequency of vibration.

The compilation made by Marx, Baker, and Sivertsen[5] shows a wide variation in the activation energies for the diffusion of oxygen and nitrogen in niobium and tantalum, as measured by various workers. Undoubtedly a factor contributing to this variation is that due to concentration which has not always been controlled very well. The extra relaxation times found as a result of interactions at the higher concentrations have higher activation energies, and thereby increase the average activation energy as

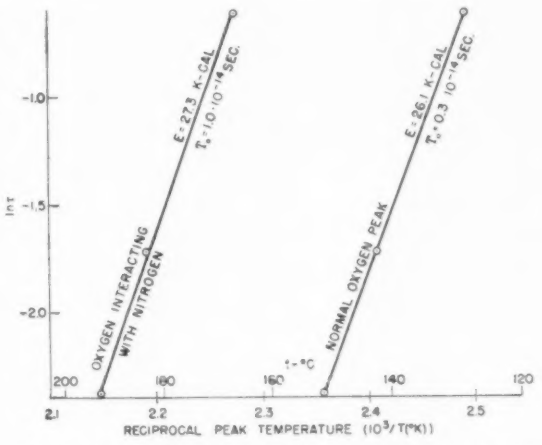

FIG. 8b. Activation energy determination for the diffusion of oxygen in tantalum as affected by nitrogen.

measured in a damping experiment. Therefore, to obtain unambiguous results, activation-energy measurements should be carried out on specimens containing interstitial solute atoms at low concentrations.

SOME COMMENTS ON THE NATURE OF THE INTERACTION BETWEEN INTERSTITIAL SOLUTE ATOMS

It has been shown that, over a range of concentration, the internal friction associated with the diffusion of a single solute element can be described rather well by only two relaxation times. Moreover, the positions of the two peaks appear to be constant as a function of composition. These facts suggest perhaps that interactions between solute atoms can take place from a rather limited number of relative configurations, and

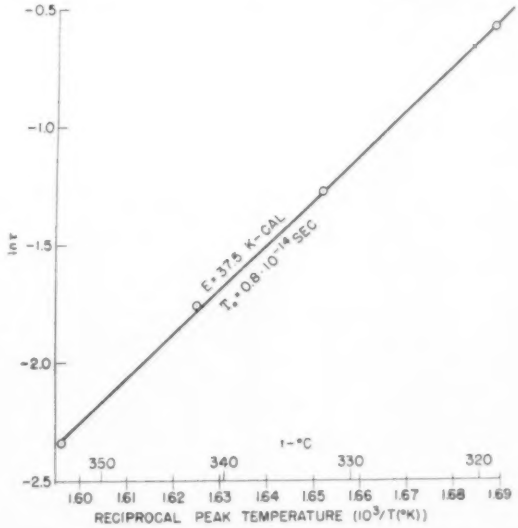

FIG. 8c. Activation energy determination for the diffusion of nitrogen in tantalum.

VOL. 4 1956

that the interaction forces extend over only short atomic distances.

Other experimental observations lend some support to this viewpoint. Should a strain interaction occur over relatively large distances, it might be expected that plastic deformation or the presence of a large number of precipitate particles would alter the breadth of an experimental internal friction peak. Neither do, however.

A tantalum wire was loaded with 0.20 weight per cent nitrogen and aged at 600°C for one day. The maximum damping was 0.105 and the half-width $0.211 \cdot 10^{-3}$. This specimen was aged further for a week in a furnace whose temperature was lowered gradually from 600° to 400°C. The peak height declined to 0.0676 and the half-width to $0.186 \cdot 10^{-3}$. Metallographic examination disclosed the presence of a large amount of precipitate compared with that in a specimen loaded with 0.12 weight per cent nitrogen for which the maximum damping was 0.10. The values of the half-width subsequent to the two aging treatments have been plotted on Fig. 2. These data correspond to the shaded circles. It is seen that the breadth for this specimen with a large amount of precipitate is no greater than those containing no such quantity of precipitate.

The cold-work experiments have been described briefly in a previous report.[1]

CONCLUSIONS

The internal friction arising from the diffusion of oxygen in tantalum can be represented as the sum of two peaks, one occurring at 137°C and the other at 162°C (applied frequency ~ 0.6 c.p.s.). The peak at 137°C, whose height is directly proportional to the oxygen concentration, is interpreted as arising from the diffusion of free, non-interacting oxygen atoms. The second peak, whose height is proportional to the square of the oxygen concentration, is interpreted as arising from the diffusion of oxygen atoms, each of which is interacting with a neighboring oxygen atom.

Similarly, the damping arising from the diffusion of nitrogen in tantalum can also be represented as the sum of two peaks, one at 334°C and the other at 362°C ($\nu \sim 0.6$ c.p.s.). The second peak, whose height varies as the square of the nitrogen concentration, is interpreted as arising from the diffusion of nitrogen atoms, each of which is interacting with another nitrogen atom in its neighborhood.

When both oxygen and nitrogen are present in tantalum, a peak is found at 175°C, whose height varies as the product of the oxygen and nitrogen concentrations. This peak is interpreted as arising from the diffusion of oxygen atoms, each of which has a nitrogen atom with which it is interacting in its neighborhood.

The activation energies found for the diffusion of oxygen interacting with other oxygen atoms or with nitrogen atoms are higher than that measured for the diffusion of free, non-interacting oxygen.

The interactions between interstitial solute atoms appear to occur over short atomic distances from a limited number of relative configurations.

ACKNOWLEDGMENT

The authors are indebted to J. C. Fisher for many stimulating conversations and for reviewing the manuscript.

REFERENCES

1. R. W. Powers, *Acta Met.*, **3**, 135 (1955).
2. T. S. Ke, *Phys. Rev.*, **74**, 914 (1948).
3. J. L. Snoek, *Physica*, **8**, 711 (1941).
4. R. W. Powers, *Acta Met.*, **2**, 604 (1954).
5. Marx, Baker, and Sivertsen, *Acta Met.*, **1**, 193 (1953).

THE GROWTH OF DISPERSED PRECIPITATES IN SOLUTIONS*

G. W. GREENWOOD†

When dispersed particles of a second phase exist in a saturated solution, there is a tendency for smaller particles to dissolve and larger ones to grow, by the transfer of solute through the solvent from particle to particle. The driving force is derived from the consequent reduction in total interfacial energy. This process is analysed theoretically in terms of a resultant diffusion flow from the smaller to the larger particles, and formulae are derived for the rate of change of particle size. The theory is applied to the particular case of the growth of solid particles dispersed in a liquid solution and shown to agree in order of magnitude with observed rates of growth in uranium-lead and uranium-sodium slurries.

LA CROISSANCE DE PRÉCIPITÉS DISPERSÉS DANS LES SOLUTIONS

Quand des particules dispersées d'une seconde phase existent dans une solution saturée, il y a une tendance à la dissolution des petites particules et à la croissance des plus grosses, ce processus s'effectuant par le transfert de particules en particules des atomes en solution.

Celui-ci résulte de la réduction de l'énergie interfaciale totale.

Ce procédé est analysé théoriquement aux termes d'un "courant" de diffusion résultant, allant des plus petites particules aux plus grosses et des formules sont déduites pour la vitesse du changement de taille des particules.

La théorie est appliquée au cas particulier de la croissance des particules solides dispersés dans une solution liquide et montre un accord sur l'ordre de grandeur des vitesses de croissances observées dans des suspensions uranium-plomb et uranium-sodium.

DAS WACHSTUM DISPERSER AUSSCHEIDUNGEN IN LÖSUNGEN

Sind in einer gesättigten Lösung feinverteilte Teilchen einer zweiten Phase vorhanden, so besteht die Tendenz, dass infolge eines Übergangs des gelösten Stoffes von Teilchen zu Teilchen durch das Lösungsmittel die kleineren Teilchen sich auflösen und die grösseren wachsen. Die treibende Kraft rührt dabei von der sich insgesamt ergebenden Verringerung der Grenzflächenenergie her. Der Prozess wird theoretisch behandelt als resultierender Diffusionsstrom von den kleineren zu den grösseren Teilchen. Dabei werden Formeln für die Änderungsgeschwindigkeit der Teilchengrösse abgeleitet. Die Theorie wird auf den speziellen Fall des Wachsens feinverteilter fester Teilchen in einer flüssigen Lösung angewendet und es wird gezeigt, dass sie grössenordnungsmässig mit beobachteten Wachstumsgeschwindigkeiten in Uran-Blei- und Uran-Natrium-Schlamm übereinstimmt.

VOL. 4 1956

INTRODUCTION

It is inherent in all systems where there are dispersed particles of varying size having some solubility in the surrounding medium, that the smaller particles tend to dissolve and precipitate onto larger particles; in the final state the system tends to form a single particle. The driving force is derived from the consequent reduction in interfacial energy. This process underlies many practical phenomena, and the rate at which it takes place is therefore of some importance. A rigorous analysis is likely to be immensely difficult, and the purpose of the present work is to analyse the process in just sufficient detail to deduce approximate formulae, on the basis of a diffusion flow, from which the rate may be reasonably estimated. Particular attention will be given to the case of solid particles dispersed in a liquid solution.

A number of observations of the growth of solid particles in a liquid medium at the expense of smaller particles have previously been reported.[1] The process is analogous to the greater evaporation rate of small droplets because of their higher vapor pressures with subsequent condensation of vapor on the larger drops under saturation conditions. To analyse it quantitatively, use is made of the well-known Thomson-Freundlich equation[2] relating solubility to particle size.

$$\ln \frac{S_a}{S} = \frac{2M\sigma}{RT\rho a} \tag{1}$$

where S is the true solubility, S_a the solubility in contact with a particle of radius a, ρ the density of the solid of molecular weight M, σ the interfacial tension between solid and liquid, and RT has the usual meaning.

Equation (1) determines the increase in solubility with decrease in particle size. Ostwald[3] observed that very finely divided mercuric oxide was more soluble in normal solutions of potassium bromide and sodium thiosulfate than when it was in coarser

* Received September 15, 1955.

† Atomic Energy Research Establishment, Harwell, Didcot, Berks, England.

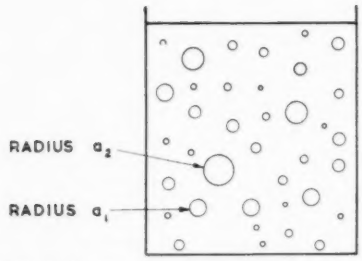

FIG. 1. Dispersed precipitates in a saturated solution.

form. He obtained similar results for various salts in water. Hulett[4] found increasing solubility of gypsum and barium sulfate in water with decreasing particle size, but the effect was only measurable for particle radii less than about 2 μ. It was noted that larger particles tended to grow at the expense of the smaller particles. The absence of very small particles in the neighborhood of a large particle has been cited as an example of the same effect.[5]

It has been argued that the Thomson-Freundlich equation has limited application,[1] since it is based on the assumptions that the solution is ideal and that the interfacial tension and density are independent of particle size. There have been some demonstrations of the variation of interfacial tension with radius of curvature,[6, 7] but the effect is insignificant for particles greater than 1-μ radius. For particles above this size and with a low solubility in the liquid, the equation should apply with a fair degree of accuracy.

A GENERAL ANALYSIS OF PARTICLE GROWTH

Consider two particles of radii a_1 and a_2 in a system as shown in Fig. 1; these are surrounded by solute concentrations in the liquid S_{a_1} and S_{a_2} respectively. If $\frac{2M\sigma}{RT\rho a_1}$ and $\frac{2M\sigma}{RT\rho a_2}$ are both small compared with unity, then from equation (1) the concentration difference is

$$S_{a_1} - S_{a_2} = \frac{2M\sigma S}{RT\rho}\left(\frac{1}{a_1} - \frac{1}{a_2}\right)$$

If the diffusion coefficient of the solute in the liquid is D and the effective area-to-length ratio of the diffusion path between two particles (A/x), then from Fick's law the mass of solute transferred per unit time dQ/dt is given by

$$\frac{dQ}{dt} = D\left(\frac{A}{x}\right)\left(S_{a_1} - S_{a_2}\right)$$

or

$$\frac{dQ}{dt} = D\left(\frac{A}{x}\right)\frac{2M\sigma S}{RT\rho}\left(\frac{1}{a_1} - \frac{1}{a_2}\right)$$

Now, dQ/dt is the rate of gain of mass of a_2, and this is equal to the rate of mass loss of a_1.

$$\frac{dQ}{dt} = \rho 4\pi {a_2}^2 \frac{da_2}{dt} = -\rho 4\pi {a_1}^2 \frac{da_1}{dt}$$

The growth equation for a_2 is

$$\rho 4\pi {a_2}^2 \frac{da_2}{dt} = D\left(\frac{A}{x}\right)\frac{2M\sigma S}{RT\rho}\left(\frac{1}{a_1} - \frac{1}{a_2}\right)$$

Extending these considerations to an entire system of n particles of radii $a_1, a_2, a_3, \ldots, a_i, \ldots, a_n$, the growth of a particle of radius a is given by the equation

$$\rho 4\pi a^2 \frac{da}{dt} = DS\,\frac{2M\sigma}{RT\rho}\sum_{i=1}^{n}\left(\frac{A}{x}\right)_i\left(\frac{1}{a_i} - \frac{1}{a}\right) \qquad (2)$$

where $(A/x)_i$ refers to the area-to-length ratio of the effective diffusion path between the particles a and a_i.

Equation (2) implies that the larger particles of the system are growing at the expense of the smaller ones, which are dissolving. When very small particles are present on the verge of dissolving completely, for which $\frac{2M\sigma}{RT\rho a_i}$ is not small compared with unity, $S_{a_i} - S$ cannot be replaced by $\frac{2M\sigma}{RT\rho a_i}S$. In most cases, however, this modification is unlikely to be of significance, since particles of this size are dissolving rapidly and their number at any instant must be small. Let a_u be the radius of the particle which is instantaneously neither growing nor dissolving, then $\frac{da_u}{dt} = 0$. The radius a_u is thus determined from

$$\sum_{i=1}^{n}\left(\frac{A}{xa}\right)_i = \frac{1}{a_u}\sum_{i=1}^{n}\left(\frac{A}{x}\right)_i$$

Using this relation, equation (2) can be written

$$\rho 4\pi a^2 \frac{da}{dt} = DS\,\frac{2M\sigma}{RT\rho}\left(\frac{1}{a_u} - \frac{1}{a}\right)\sum_{i=1}^{n}\left(\frac{A}{x}\right)_i \qquad (3)$$

Equations (2) or (3) can be used in principle to determine exact rates of growth. However, in general cases the evaluation of the expressions for a_u and $\sum_{i=1}^{n}\left(\frac{A}{x}\right)_i$ presents great difficulties. The rate of growth or solution of a particle is chiefly influenced by its nearest neighbors, and the overall growth-rate of the system is consequently dependent on the distribution of particle sizes throughout the volume.

THE CALCULATION OF GROWTH RATE FOR HIGHLY DISPERSED PARTICLES

The problem of evaluation of the effective diffusion paths is much simplified in the case of particles

which are highly dispersed and have a uniform size distribution throughout the volume. Under these conditions the solute concentration around each particle is assumed to be spherically symmetrical, and an average value is found for the solute concentration at an infinite distance from the particles. The case of a single particle dissolving into an infinite liquid is first considered, and the growth-rate of a system of particles is developed from this.

The diffusion equation for a dissolving particle can be written

$$\rho 4\pi a^2 \frac{da}{dt} = D4\pi r^2 \frac{ds}{dr} \tag{4}$$

when ds/dr is the concentration gradient of solute at a distance r from the centre of the particle. If the solute concentration at a distance r is S_r and S_∞ at a great distance from the particle,

$$\int_r^\infty \frac{\rho a^2}{D}\left(\frac{da}{dt}\right)\frac{dr}{r^2} = \int_{S_r}^{S_\infty} ds\,.$$

On integration

$$\frac{\rho a^2}{D}\left(\frac{da}{dt}\right)\frac{1}{r} = S_\infty - S_r \tag{5}$$

The variation of $S_\infty - S_r$ with r plotted from equation (5) is shown in Fig. 2. If S_a is the solute concentration at the particle surface when $r = a$, then equation (5) becomes

$$\frac{\rho a}{D}\left(\frac{da}{dt}\right) = S_\infty - S_a \tag{6}$$

In a whole system of n highly dispersed particles, their total mass is constant, providing their solubility is small. Hence

$$\sum_{i=1}^{n} \rho 4\pi {a_i}^2 \frac{da_i}{dt} = 0.$$

Substituting for $\dfrac{da_i}{dt}$ from equation (6),

$$\sum_{i=1}^{n} 4\pi a_i D(S_\infty - S_{a_i}) = 0,$$

and substituting for S_{a_i} from equation (1),

$$\sum_{i=1}^{n} 4\pi a_i D\left(S_\infty - S - \frac{2M\sigma S}{RT\rho a_i}\right) = 0.$$

Therefore $(S_\infty - S)\sum_{i=1}^{n} a_i = \sum_{i=1}^{n} \dfrac{2M\sigma S}{RT\rho} = \dfrac{2M\sigma S}{RT\rho}\, n$

and since $\dfrac{\sum_{i=1}^{n} a_i}{n}$ is the arithmetic mean radius of the system a_m.

$$S_\infty - S = \frac{2M\sigma S}{RT\rho a_m}\,.$$

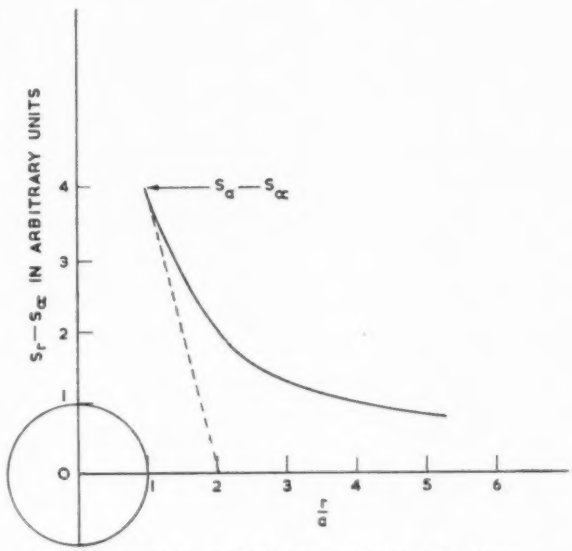

FIG. 2. Variation of solute concentration with distance from a sphere dissolving into an infinite medium.

Substituting for S from equation (1),

$$S_\infty - S_a = \frac{2M\sigma S}{RT\rho}\left(\frac{1}{a_m} - \frac{1}{a}\right)$$

and from equation (6), the particle-growth equation

$$\frac{da}{dt} = DS\,\frac{2M\sigma}{RT\rho^2 a}\left(\frac{1}{a_m} - \frac{1}{a}\right) \tag{7}$$

is obtained. Equation (7) is a special case of the more general formulae (2) and (3), where $\sum_{i=1}^{n}\left(\dfrac{A}{x}\right)_i = 4\pi a$ and $a_u = a_m$. The graph of da/dt against a in Fig. 3 plotted from equation (7) shows some interesting features. Particles of radius less than a_m are dissolving at increasing rates with decreasing values of a. Particles of radius greater than a_m are growing, but the graph shows a maximum value for the growth rate $(da/dt)_{\max}$ for $a = 2a_m$. Thus at any instant, particles of radius twice the arithmetic mean radius of the distribution are growing at the fastest rate.

Over a period of time the value of n decreases discontinuously when particles dissolve completely and thus disappear. It is a consequence of this that the system ultimately tends to form one large particle. The mean particle radius a_m increases as n decreases, and thus the growth-rate slows down.

APPLICATION OF THE FORMULAE

The difficulties of exact evaluation of equations (2) and (3) were mentioned for the case where the particles are close together; this is often the case

of most practical importance, as for example where the particles have settled out under gravity. These difficulties arise from the complex diffusion processes which are occurring, and the growth-rate depends upon the precise mode of particle packing. However, it is of interest to determine how equation (7) is affected as a system of highly dispersed particles is brought close together. The rate of growth or solution depends on the value of ds/dr at the particle surface from equation (4). Its value for a sphere in a highly dispersed distribution from equations (4) and (6) is $\frac{S_a - S_\infty}{a}$, and it corresponds to the gradient of the dotted line in Fig. 2. As particles are brought closer together, the value of $|ds/dr|$ increases. At adjacent points on neighboring particles $|ds/dr|$ becomes very large, and as a result these points rapidly assume the same curvature. However, approximate geometrical considerations indicate that the overall value of ds/dr is unlikely to be greater than a factor of about five times $\frac{S_a - S_\infty}{a}$. Moreover, if the range of particle sizes is not uniformly distributed throughout the volume, then ds/dr is decreased; for particles of similar sizes clustered together, the value of ds/dr can be very small. Thus the two factors, increasing closeness of particles and lack of uniformity of particle-size distribution throughout the volume, have opposite effects on ds/dr. It appears that equation (7), derived for a system of highly dispersed particles, can therefore provide a fair estimation of particle growth-rate for particles close together and with a reasonably uniform distribution of particle sizes throughout the volume.

The solid particles have been assumed to be spherical, though in many cases particles in liquids are bounded by crystallographic faces. The formulae can still be expected to apply if the particles are considered to have effective radii equal to those of spheres having the same surface area. For markedly anisotropic crystals the theory requires further development, to take into account the dissolution and reprecipitation processes which can take place on different crystallographic faces of the same particle.

The formulae (2), (3), and (7) have been derived on the assumption that the growth process is dependent on a diffusion mechanism. Where there is any relative motion of parts of the system, the formulae are invalid. Dispersions of particles of colloid size will have growth-rates affected by Brownian motion. The formulae will be inaccurate when temperature fluctuations occur and the steady-state diffusion is destroyed. The theory has assumed that particle aggregation and sintering do not occur, though in some cases these phenomena contribute to particle growth. Finally, it has been assumed that the particle solution rates are sufficient to maintain the diffusion currents. This can be expected to apply because of the large interfacial areas involved.

COMPARISON WITH EXPERIMENTAL RESULTS

Some measurements have been made of growth-rates of settled slurries of particles of UPb_3 phase in liquid lead, and of uranium particles in sodium. For UPb_3 in lead the specimens were sectioned before and after heating at certain temperatures, and the maximum dimensions of the particles in a given direction in the section were measured. The measured-size distribution was related to the true-size distribution as described by Herdan,[8] but the true-size distribution was not calculated, since the correction was within the range of error for approximations in the theory and in some metallurgical data used. Table 1 shows some results for UPb_3 in lead.

TABLE 1

Measured increase in mean radius	Conditions
from 2 to 6 μ	after 5 days at 500°C
from 5 to 10 μ	after 5 days at 600°C
from 3 to 9 μ	after 5 days at 600°C
from 6 to 10 μ	after 30 hours at 750°C
from 4 to 12 μ	after 30 hours at 750°C
from 3 to 16 μ	after 5 days at 750°C
from 3 to 27 μ	after 20 days at 750°C
from 3 to 29 μ	after 50 days at 750°C

For comparison with Table 1, graphs are plotted of da/dt against a calculated from equation (7). Fig. 3 shows growth rates for distributions of mean radii 2 μ, 4 μ, and 8 μ at 500°C; Fig. 4 for mean radii of 5 μ, 10 μ, and 20 μ at 600°C; and Fig. 5 for mean radii of 5 μ, 10 μ, and 20 μ at 750°C.

In the calculations, the Stokes-Einstein equation[9] has been assumed valid, the diffusion coefficient D being given by the expression

$$D = \frac{RT}{N}\frac{1}{3\pi\eta d}$$

where η is the viscosity of the liquid, d the diameter of the diffusing atom, and N Avogadro's number. Substituting for D in equation (7),

$$\frac{da}{dt} = \frac{S}{N}\frac{2M\sigma}{3\pi\eta d\rho^2}\frac{1}{a}\left(\frac{1}{a_m} - \frac{1}{a}\right) \qquad (8)$$

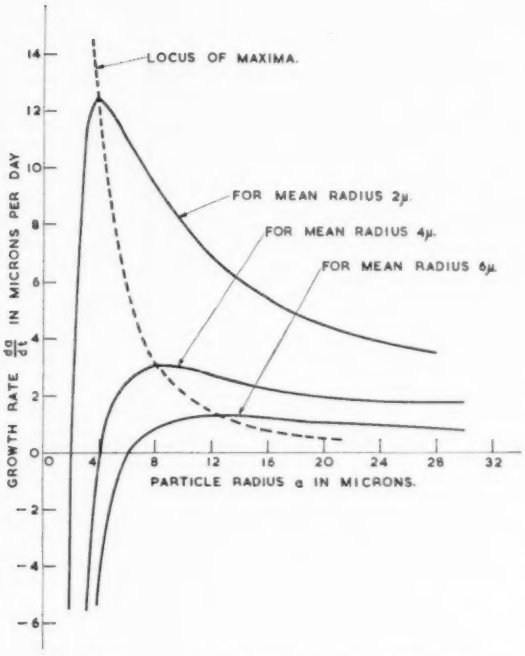
LOCUS OF MAXIMA.
FOR MEAN RADIUS 2μ.
FOR MEAN RADIUS 4μ.
FOR MEAN RADIUS 6μ.
GROWTH RATE $\frac{da}{dt}$ IN MICRONS PER DAY
PARTICLE RADIUS a IN MICRONS.

FIG. 3. Curves of da/dt against a for UPb_3 in lead at 500°C.

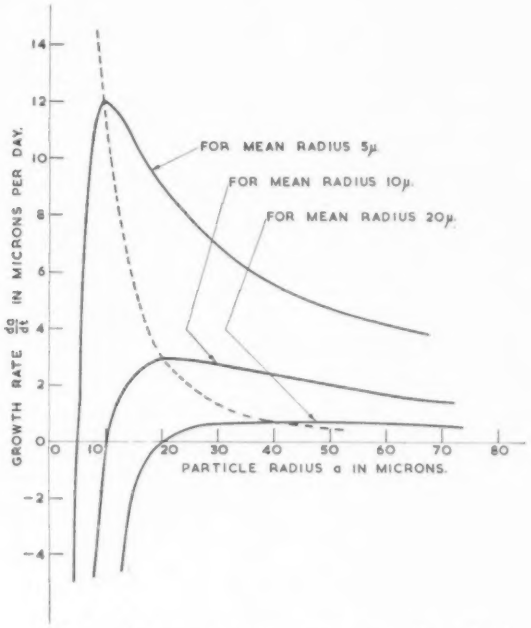
FOR MEAN RADIUS 5μ.
FOR MEAN RADIUS 10μ.
FOR MEAN RADIUS 20μ.
GROWTH RATE $\frac{da}{dt}$ IN MICRONS PER DAY.
PARTICLE RADIUS a IN MICRONS.

FIG. 4. Curves of da/dt against a for UPb_3 in lead at 600°C.

The data used in plotting Figs. 3, 4, and 5 from equation (8) are:

S = solubility of uranium in lead,[10]
$= 10^{-3}$ g/cm^3 at 500°C,
$= 10^{-2}$ g/cm^3 at 600°C,
$= 3 \times 10^{-2}$ g/cm^3 at 750°C,

N = Avogadro's number $= 6 \times 10^{23}$,

σ = interfacial tension between UPb_3 and lead,[11]
$\sim$100 ergs/cm^2,

M = gram molecular weight of uranium = 238 g,

ρ = density of uranium in UPb_3 = 3.75 g/cm^3,[10]

η = viscosity of lead,[12]
$= 2 \times 10^{-2}$ poise at 500°C
$= 1.6 \times 10^{-2}$ poise at 600°C
$= 1.3 \times 10^{-2}$ poise at 750°C

d = atomic diameter of uranium[10]
$= 3 \times 10^{-8}$ cm.

An alternative approximate method of calculating particle growth can be obtained by considering the growth of the particles which are always twice the mean radius and are thus growing at the fastest rate. The maximum growth-rate $\left(\frac{da}{dt}\right)_{\max}$, from equation (7), is given by

$$\left(\frac{da}{dt}\right)_{\max} = DS \frac{2M\sigma}{RT\rho^2} \frac{1}{4a_m^2} \qquad (9)$$

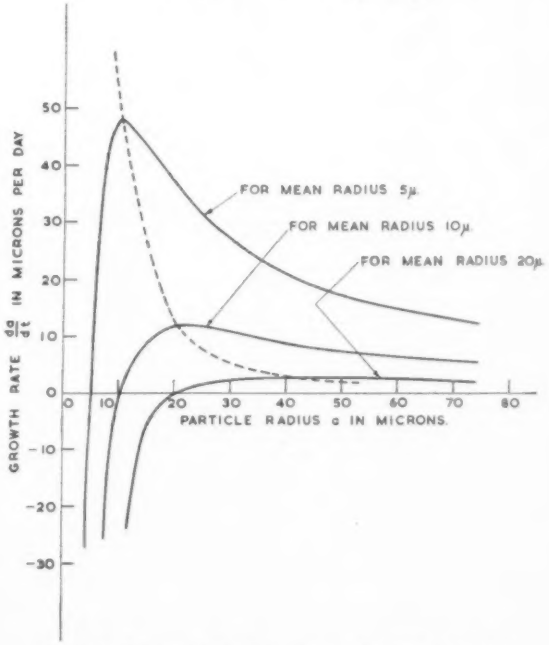
FOR MEAN RADIUS 5μ.
FOR MEAN RADIUS 10μ.
FOR MEAN RADIUS 20μ.
GROWTH RATE $\frac{da}{dt}$ IN MICRONS PER DAY
PARTICLE RADIUS a IN MICRONS.

FIG. 5. Curves of da/dt against a for UPb_3 in lead at 750°C.

VOL. 4 1956

and thus the growth equation for a particle of radius of equal to $2a_m$ is:

$$\frac{da}{dt} = DS\frac{2M\sigma}{RT\rho^2}\frac{1}{a^2}$$

On integration

$$a_F^3 - a_I^3 = 3DS\frac{2M\sigma}{RT\rho^2}t \qquad (10)$$

where a_I and a_F are the initial and final radii of the particles growing at the fastest rate throughout. This assumes that initially the particle-size distribution is of a sufficient range to include particles of radius $2a_m$, and that such particles are present throughout the growth of the system. The distribution as a whole will grow at a rate slower than this, but since the cube of a occurs in equation (10), the equation should yield the correct orders of magnitude. For given values of a_I the values of a_F have been calculated and are shown in Table 2. This affords comparison with the experimental results in Table 1, which are somewhat smaller than the calculated values, as expected.

In the measurement of particle sizes of uranium powder before and after heating in sodium for a week at 500°C, no change was found in distributions of mean radius about 1 μ. Data for calculating the maximum growth-rate in a distribution of this size at 500°C from equation (9) are:

S = solubility of uranium in sodium $\sim 10^{-7}$ g/cm^3,[13]

σ = interfacial tension between sodium and uranium[11] $\sim$500 ergs/cm^2,

ρ = density of uranium, 19 g/cm^3,

η = viscosity of sodium = 2.5×10^{-3} poise.[12]

Other values are as used for UPb_3 in lead. The calculated maximum growth-rate is 4×10^{-3} μ per day. Thus the growth-rate was too small to be detected under the experimental conditions, and a stable slurry can be formed of uranium particles of mean radius less than 1 μ contained in sodium.

TABLE 2

a in microns	a_F in microns	Time	Temperature (°C)
3	13	5 days	500
5	27	5 days	600
5	27	30 hours	750
3	42	5 days	750
3	66	20 days	750
3	87	50 days	750

CONCLUSIONS

The growth of dispersed particles in a saturated solution by a diffusion mechanism depends on the many variables discussed. The chief factors promoting stability (slow growth-rate) are particles of large mean radius, high density, and low molecular weight, with low values of the solute diffusion coefficient, the solubility, and the interfacial tension. All these variables may change considerably from system to system. A strictly rigorous approach to the problem would be immensely difficult and has not been attempted, but the approximate formulae derived are capable of predicting growth-rates of the correct order of magnitude.

ACKNOWLEDGMENTS

The author is grateful to Dr. W. M. Lomer for valuable discussion and to Mr. B. Sharpe for experimental measurements.

REFERENCES

1. S. L. Bigelow and H. M. Trimble, *J. Phys. Chem.*, **31,** 1798 (1927).
2. H. Freundlich, *Kapillarchemie*, Leipzig, 1922.
3. W. Ostwald, *Z. Phys. Chem.*, **34,** 495 (1900).
4. G. A. Hulett, *Z. Phys. Chem.*, **37,** 385 (1901), and **47,** 357 (1904).
5. F. B. Kenrick, *J. Phys. Chem.*, **16,** 516 (1912).
6. W. Thomson, *Proc. Roy. Soc., Edinburgh*, **7,** 63 (1870).
7. W. A. Patrick and N. F. Eberman, *J. Phys. Chem.*, **29,** 227 (1925).
8. G. Herdan, *Small Particle Statistics*, Elsevier Publishing Corp., p. 237 (1953).
9. A. M. Samarin and L. A. Shavartsman, *Izv. Akad. Nauk. U.S.S.R.* (Tekhn), **12,** 1649 (1947).
10. B. R. T. Frost and J. T. Maskrey, *J. Inst. Metals*, **8,** 171 (1953).
11. J. W. Taylor, private communication.
12. R. N. Lyon, *Liquid Metals Handbook*, U.S. Gov. Printing Office, 2nd ed. (1952).
13. G. W. Horsley, private communication.

CLOSED MISCIBILITY GAPS IN TERNARY AND QUATERNARY REGULAR ALLOY SOLUTIONS*

J. L. MEIJERING† and H. K. HARDY‡

Although the regular-solution model is only an approximation, it may yield useful semi-quantitative results in predicting the form of ternary miscibility gaps from binary data. The spinodal equation of quaternary regular solutions has been derived and the co-ordinates of second-order critical points are given as a function of the six binary interaction parameters. Quaternary critical points are of special interest, as they are connected with closed miscibility gaps. The conditions which cause a ternary critical temperature to be raised by the addition of a fourth component are given. The results are applied to miscibility gaps in liquid and f.c.c. alloys.

LACUNES DE MISCIBILITÉ FERMÉES DANS LES SOLUTIONS IDÉALES D'ALLIAGES TERNAIRES ET QUATERNAIRES

Bien que le modèle de solution idéale soit seulement une approximation, il peut conduire à des résultats semi-quantitatifs utiles, en prévoyant la forme des lacunes de miscibilité ternaires à partir des données obtenues sur des alliages binaires.

L'équation spinodale des solutions idéales quaternaires est déduite et les coordonnées des points critiques du second ordre sont données, comme fonction des six paramètres binaires d'interaction.

Les points critiques quaternaires sont d'un intérêt spécial car ils sont en relation avec des lacunes de miscibilité fermées.

Les conditions qui provoquent une élévation de la température critique ternaire, par addition d'un quatrième composé, sont données.

Les résultats sont appliqués à des lacunes de miscibilité de liquides et d'alliages cubiques à face centrée.

GESCHLOSSENE MISCHUNGSLÜCKEN IN TERNÄREN UND QUATERNÄREN REGULÄREN LÖSUNGEN VON LEGIERUNGEN

Obwohl das Modell der regulären Lösung nur näherungsweise gilt, kann man mit ihm aus den Daten binärer Systeme brauchbare halbquantitative Voraussagen über die Form ternärer Mischungslücken gewinnen. Die Spinodalgleichung quaternärer regulärer Lösungen wurde abgeleitet; die Koordinaten der kritischen Punkte zweiter Ordnung sind als Funktion der sechs binären Wechselwirkungsparameter angegeben. Quaternäre kritische Punkte sind von besonderem Interesse, da sie mit dem Auftreten geschlossener Mischungslücken zusammenhängen. Es werden die Bedingungen angegeben, unter denen eine ternäre kritische Temperatur durch Zufügen einer vierten Komponente erhöht wird. Die Ergebnisse werden auf Mischungslücken in flüssigen und kubisch-flächenzentrierten Legierungen angewendet.

VOL. 4 1956

1. INTRODUCTION

Some years ago one of the authors made an analysis of phase separation in ternary regular solutions.[1] These are characterized by the free energy

$$F = axy + bxz + cyz + RT(x \ln x + y \ln y + z \ln z) \tag{1}$$

where x, y, and z are the mole fractions of the three components X, Y, and Z, and a, b, and c are three interaction-energy parameters, each being connected with one of the binary boundary systems (see Fig. 1). Of course, (1) is only a rough approximation. Firstly, all short-range effects (and superstructures) are disregarded. Secondly, each binary system is taken

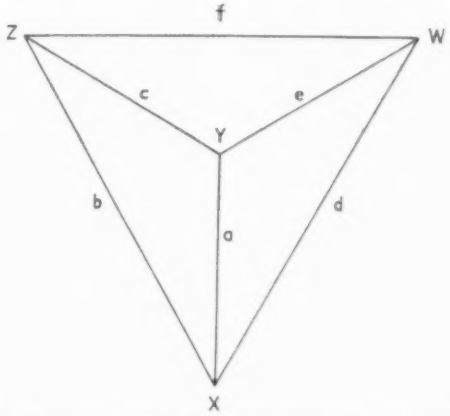

FIG. 1. The interrelation of the binary interaction-energy parameters and the compositional tetrahedron.

* Received September 26, 1955.

† Philips Research Laboratories, Eindhoven, Netherlands.

‡ Previously Fulmer Research Institute, Stoke Poges (Bucks), England, now U.K. Atomic Energy Authority, Industrial Group, Springfields Laboratory.

to be thermodynamically symmetrical. To take care of these shortcomings would lead to serious complications, at least when an overall picture of the effect of different combinations of the parameters is desired.* This applies particularly in the case of regular quaternary solutions, examined by the authors.[3] In the present paper we wish to apply the results to a discussion of closed miscibility gaps in alloys.

2. SECOND-ORDER CRITICAL POINTS AND PSEUDOBINARY SECTIONS IN TERNARY SOLUTIONS

In spite of the simplicity of the regular approximation, it yields results that are not trivial. For instance, in many cases a miscibility gap in a ternary system contracts by a growing tendency towards phase separation in one of the binary systems. There is a well-known qualitative rule due to Timmermans and Bancroft, which says that miscibility in a binary phase X–Y is diminished by adding a third component Z, when the affinity between Z and X is widely different from that between Z and Y. In the regular approximation one obtains[1] the inequality

$$|b - c| \gtrless a \tag{2}$$

which is a quantitative form of the above-mentioned rule. When the absolute value of the difference between the parameters describing the interactions of Z with X and with Y is greater than the interaction parameter between X and Y—which is positive when there is a miscibility gap in the X–Y system—this gap is widened by a small addition of Z; it becomes narrower when $|b - c| < a$. Inequality (2) is valid for all temperatures up to the binary critical point at $x = y = \frac{1}{2}$, $RT = \frac{1}{2}a$. It was derived earlier implicitly for the critical point by Prigogine.[4]

When $0 < a > b > c < 0$, so that the binary critical point at $x = y = \frac{1}{2}$ is the highest or only one, $(b - c) > a$ causes a *ternary critical point* at[1]

$$x_c = \tfrac{1}{2}, \qquad y_c = \tfrac{1}{4} + \frac{a-b}{-4c}, \qquad z_c = \tfrac{1}{4} - \frac{a-b}{-4c},$$

$$T_c = \frac{L}{-8cR} \tag{3}$$

where L is short for

$$L = a^2 + b^2 + c^2 - 2ab - 2ac - 2bc. \tag{4}$$

A ternary critical point can also appear when all three parameters are negative, namely when L is positive, that is to say: $\sqrt{-c} > \sqrt{-a} + \sqrt{-b}$. The closed miscibility gap growing in the concentration triangle from the ternary critical point on decreasing T then does not attain any of the binary sides in a binary critical point; at $T = 0$ it covers the whole triangle, however.

A ternary critical point is one sort of *second-order critical point*, the other being a *saddle point*. In both, two first-order critical points merge together: in the former at increasing T, the miscibility gap vanishing; but in the latter at decreasing T, two miscibility gaps flowing together. One, two, or three saddle points may appear in a system, but only when a, b, and c, are positive and L negative.

A second-order critical point in a regular system always forms the culminating point of a symmetrical (regular) miscibility gap in a pseudobinary section through one of the triangle corners and a point on the opposite side. In the case of a ternary critical point, this side has the strongest negative interaction of the three; the pseudobinary section corresponding with equations (3) goes through the X corner and a point with

$$y = \tfrac{1}{2} + \frac{a-b}{-2c}, \qquad z = \tfrac{1}{2} - \frac{a-b}{-2c}.$$

The pseudobinary section through a saddle point is metastable at low temperatures, owing to three-phase equilibria. Even the saddle point itself may be metastable.

3. CLOSED MISCIBILITY GAPS IN TERNARY ALLOYS

The shift towards higher temperatures of the binary critical point in the liquid phase of Pb–Zn by addition of Ag—and the existence of a ternary critical point in Pb–Zn–Ag—as found by Seith and collaborators,[5] would be expected. Although the Pb–Zn gap is rather asymmetrical, the Zn–Ag affinity is strong enough to leave a safe margin. Ternary critical points can be predicted also in the systems Bi–Zn–Ag and Bi–Zn–Cu. After this prediction was made by us, we found that Henglein and Köster[6] had examined both systems, and also Pb–Zn–Ag. The investigation was more concerned with the three- and four-phase equilibria (with solid phases participating) than with the miscibility gap in the liquid phase itself. The fact that they did not discover closed miscibility gaps in the two systems with silver is therefore not in conflict with the result of Seith *et al.* or with our prediction concerning Bi–Zn–Ag.

In all three systems Henglein and Köster determined the critical end-point, where a first-order critical liquid is in equilibrium with a solid phase. In such

* So long as each binary interaction can be described by one parameter ("affinity"), the regular-solution approximation appears to be satisfactory. When a *specific* case is to be considered, and the binary data are sufficiently accurate (or asymmetrical) to warrant the introduction of additional parameters, the "subregular" approximation[2] will not present unsurmountable difficulties in the ternary case.

a tie-line a series of three-phase triangles (liquid$_1$ + liquid$_2$ + solid) ends with increasing T when the two liquids become identical. In the Bi–Zn–Cu system this critical point was found at about 15 at. per cent Bi, 20 at. per cent Zn, and 65 per cent Cu (coexisting with a practically bismuth-free α-brass) and 930°C. Now, this is at least 100° higher than the binary critical point of Bi–Zn. Therefore, we must conclude that there is indeed a closed miscibility gap in the Bi–Zn–Cu liquid phase; at still higher T it will disappear in a ternary critical point.*

Closed miscibility gaps have also been found in the liquid phase of Al–Mg–Sb and of Bi–Cu–Sb.[7]† In the former, all three binary interactions will probably be negative, but in the latter Bi and Sb, and certainly Bi and Cu, mix endothermically; the corresponding binary sides are only prevented from being attained by the miscibility gap by the appearance of solid phases.

We now look at two binary critical points in *face-centered cubic* phases, namely in Au-Pt and Au–Ni. As their critical temperatures do not differ very much, a not-too-weak Ni–Pt affinity would mean that both are raised in the ternary Au–Pt–Ni system. The stability of the Ni_3Pt superstructure (greater than that of Cu_3Au) is in favour of a strong Ni–Pt affinity. This in itself is an uncertain argument when magnetic phenomena may be involved, but the Fe–Pt affinity resulting from activity measured in f.c.c. Fe–Pt alloys by Larson and Chipman[8] is so strong that it seems justifiable to predict that the Au–Pt critical point is raised by Ni additions, and the Au–Ni critical point by Pt additions. This would lead to a ternary critical point in Au–Ni–Pt, but this is probably not stable with respect to the liquid phase.

The Au–Ni binary critical point can be expected to be raised also by Ag, or Co. This is rather trivial, because Ni–Ag and Au–Co have very limited miscibility and would have high critical temperatures if the liquid phase did not interfere. Si should behave similarly. As the solubility of Si in solid gold (practically pure silicon being the coexisting phase) is quite small, the differential solution energy of Si in Au will be positive. That of Si in Ni is strongly negative. It is true that we need the quantities with reference to *f.c.c.* silicon, but the unknown energy-difference between this hypothetical modification and Si with diamond structure vanishes when the Si–Au and Si–Ni affinities are subtracted (cf. inequality 2).

The ternary critical point in Ni–Au–Cu, found by Raub and Engel,[9] is the only one discovered in solid solutions so far. Its theoretical "explanation" is made rather uncertain by the asymmetry of the Ni–Au miscibility gap, and the lack of quantitative thermodynamical data on Ni–Cu. However, the heats of mixing in the liquid and solid Ni–Cu phases cannot be very different, as can be concluded from calorimetric measurements[10] and by a consideration of the liquidus and solidus curves. Therefore, it looks probable that the Ni–Cu solid solutions will be roughly ideal, in agreement with the absence of distinct tendencies towards ordering or segregation. If the Ni–Cu interaction parameter is taken to be zero, inequality (2), in order to have a closed miscibility gap, becomes

$$-c > a = 2RT_c. \qquad (5)$$

Here T_c is the absolute critical temperature of Ni-Au, and c the Au–Cu interaction parameter. The latter is about −5.0 kcal according to e.m.f. measurements, by Oriani and by earlier authors.[11] Recent activity measurements by Balesdent[12] by means of the equilibria $2\,Cu + H_2S \rightleftarrows Cu_2S + H_2$ yield about −6.2 kcal. As $2RT_c$ is 4.5 kcal, inequality (5) is satisfied, but the margin is small. A thermodynamical evaluation of the Cu–Ni–Cr system indicates that the Cu–Ni interaction is weakly positive rather than weakly negative.[13] This strengthens the contention that Cu should raise the Ni–Au critical temperature (cf. inequality 2).

Inequality (5) is also satisfied when we use as the right-hand side the Ni–Au interaction parameter a as deduced from the measurements by Seigle *et al.*[14] But we must take axy $(= ax(1-x)$ in the binary system) to be the nonideal part of the free energy of mixing. This is equal to the energy minus T times the non-Gibbsian entropy of mixing. This extra entropy by definition is zero for regular solutions, but in Au–Ni it is strongly positive. When the extra entropy—like the energy—can be approximated by a parabolic function, the system behaves as though regular, but with its interaction parameter a linear function of temperature.

When a/T, b/T, and c/T are plotted as Cartesian co-ordinates (a, b, and c being permitted to be linear functions of T), each point stands for a ternary isothermal section identical with an isothermal section

* *Note added in proof*—
Quite recently Seith, Johnen, and Wagner have indeed found that Bi–Zn–Ag and Bi–Zn–Cu show closed miscibility gaps. The same holds for Pb–Zn–Cu, Tl–Zn–Ag and probably also Tl–Zn–Cu. With their binary data on Tl–Zn and Pb–Cu one can predict closed gaps in Pb–Zn–Cu and Tl–Zn–Cu. Lack of thermodynamic data on Tl–Ag prevents doing the same for Tl–Zn–Ag. (W. Seith, H. Johnen, and J. Wagner, *Z. Metallkde*, **46**, 773, 1955).

† In this section (and also in the last one) we write the three components in such a way that the second and third have the strongest mutual affinity (negative interaction parameter).

VOL. 4 1956

through some regular system. The points depicting the sections through such a system lie on a straight line. If the system is really regular, this line goes through the origin; which is approached asymptotically for infinite T.

Naturally, the parameter describing the extra entropy can be negative. If the entropy of mixing S in a binary system is given by

$$-R\{x \ln x + (1-x) \ln (1-x)\} - fRx(1-x),$$

d^2S/dx^2 is positive around $x = \frac{1}{2}$ if $f > 2$. Therefore *lower* critical points—such as in the liquid phase of H_2O-triethylamine, and probably also Cu–Fe and Cu–Co—can be treated in this scheme. Indeed, such a critical point is characterized (besides by d^2F/dx^2 and d^3F/dx^3 being zero) by $d^2S/dx^2 > 0$.[15, 16, 17]

4. THE SPINODAL EQUATION OF REGULAR SOLUTIONS

When, at a given temperature, the free-energy surface of a regular ternary solution is everywhere convex from below, no phase separation occurs at this temperature. When the free-energy surface is both concave and convex, double (or triple) tangent planes are possible. Each double-tangent plane is associated with a tie-line in a two-phase domain. The calculation of such a tie-line necessitates numerical computation of three (in the case of quaternary regular solutions four) equations,[1, 3] except in pseudobinary sections.

The end-points of the tie-lines lie on the solubility ("binodal") surface* (for a ternary isothermal section it is a curve). It separates the domain where the homogeneous solution is absolutely stable from that where it is only metastable. For an overall survey of phase separation it is much more practical to use the equation of the *spinodal* surface.* This forms the boundary between metastable and unstable domains. Its relative importance lies in the fact that a nonconvex part of the free-energy surface is necessary and sufficient for phase separation.† Its simplicity lies in the fact that it is defined by one single equation only, being governed by the F-curvature at one point and not by the geometry over a finite concentration area.

For *binary* regular solutions $d^2F/dx^2 = 0$ leads to the spinodal equation

$$2axy - RT = 0 \qquad (6)$$

For *ternary* regular solutions d^2F/ds^2 must be zero in one direction s and positive in all other directions in the x, y plane. Thus

$$(\partial^2F/\partial x^2)(\partial^2F/\partial y^2) = (\partial^2F/\partial x\,\partial y)^2,$$

leading to the spinodal equation

$$Lxyz + 2RT(axy + bxz + cyz) - (RT)^2 = 0 \qquad (7)$$

where L is defined by (4).

For *quaternary* regular solutions we use the free energy of mixing

$$F = axy + bxz + cyz + dxw + eyw + fzw + RT(x \ln x + y \ln y + z \ln z + w \ln w) \qquad (8)$$

Fig. 1 shows the inter-relation of the six binary interaction parameters and the compositional tetrahedron. Naturally, the sum of the mole fractions $x + y + z + w$ equals 1.

The determinant[3]

$$\begin{vmatrix} \partial^2F/\partial x^2 & \partial^2F/\partial x\,\partial y & \partial^2F/\partial x\,\partial z \\ \partial^2F/\partial x\,\partial y & \partial^2F/\partial y^2 & \partial^2F/\partial y\,\partial z \\ \partial^2F/\partial x\,\partial z & \partial^2F/\partial y\,\partial z & \partial^2F/\partial z^2 \end{vmatrix} = 0$$

leads to the spinodal equation

$$2Kxyzw + RT(xyzL_{abc} + xywL_{ade} + xzwL_{bdf} + yzw\,L_{cef}) + 2(RT)^2(axy + bxz + cyz + dxw + eyw + fzw) - (RT)^3 = 0 \qquad (9)$$

where L_{ade}, etc., are defined like $L = L_{abc}$ in (4) and

$$K = af(-a + b + c + d + e - f) + be(a - b + c + d - e + f) + cd(a + b - c - d + e + f) - abc - ade - bdf - cef. \qquad (10)$$

For a fixed concentration, (7) is a quadratic in T and (9) a cubic in T. When there is no positive T root, the homogeneous solution remains stable down to $T = 0$.‡ There may be more than one positive T root, which is discussed most easily for the ternary case: At sufficiently high temperatures the F surface is fully convex. When, on decreasing T, the higher T root is crossed, it becomes concave-convex. When the lower T root (if any) is crossed, the F surface becomes fully concave from below. In the quaternary case, where we are concerned with F, x, y, z four-dimensional space, this is more complicated.[3]

The question whether a solution is unstable with regard to concentration fluctuations in all directions or in one or a few only may have a bearing on kinetic

* The surface *may* consist of two or more separate parts.

† This is due, of course, to the fact that we have to consider only one continuous F surface. If there are two phases with different structure (say f.c.c. + b.c.c., or f.c.c. + liquid), and their F surfaces intersect each other, double-tangent planes appear even when both F surfaces are convex everywhere. In general, therefore, a two-phase region does not necessarily comprise an unstable region.

‡ Ordering effects are not taken care of by the regular approximations.

precipitation problems in some instances, but is of no consequence for phase diagrams. However, it is not feasible to split off the physically relevant spinodal equation from the total mathematical one. This is demonstrated by Fig. 2, where it is seen that internal sectioning may happen. The (physically important) upper spinodal surface shows two discontinuities here.

5. SECOND-ORDER CRITICAL POINTS AND PSEUDOBINARY SECTIONS IN QUATERNARY SOLUTIONS

A two-phase domain in an isothermal section of a quaternary system is filled by an infinite number of tie-lines. Each tie-line joins two points at the solubility (binodal) surface and cuts the spinodal surface at two* points in between. Binodal and spinodal surfaces may touch each other along a curve. At this (first-order) critical curve the tie-lines are degenerated into critical points. In sections at definite temperatures a critical curve may show a double point or an isolated point. These special points are second-order critical points. There are *three* kinds, against two in the ternary case (see first section).

(i) Firstly, we have *quaternary critical points*. In such a point a closed—more or less ellipsoidal—two-phase domain shrinks to a point with increasing temperature. It is comparable to a ternary critical point in a ternary solution.

In a ternary saddle point contact is established—at rising T—between two homogeneous regions, and this automatically means that contact between two heterogeneous regions is severed. In the quaternary case, where an isothermal section is three-dimensional, this is not so. We have two sorts of "confluence points":

(ii) Two two-phase domains coalesce at decreasing T. Slightly below the second-order critical temperature we have a heterogeneous tunnel through a homogeneous block.

(iii) Two homogeneous domains coalesce at increasing T. Slightly above the second-order critical temperature we have a homogeneous tunnel through a heterogeneous block.

Sketches of tie-lines and the transformations of first-order critical curves around these three kinds of second-order critical points are given in Fig. 4 of reference 3.

So far, the discussion in this section is qualitative and valid for quaternary solutions in general, apart from the direction of temperature influence, which in abnormal cases may not be throughout towards

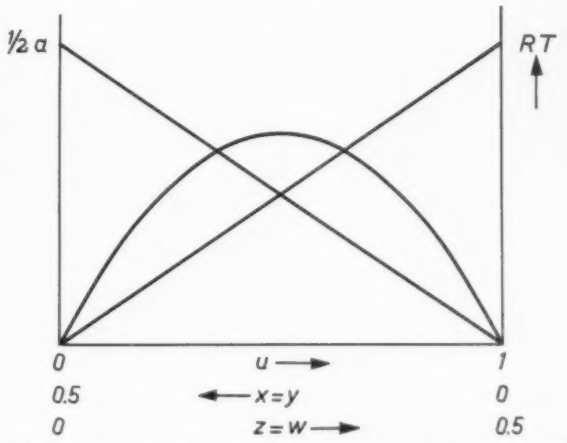

FIG. 2. Section, along the line $x = y$, $z = w$, of the spinodal surface of a system with parameters $f = a > 0$, $e = d = c = b = 1.2a$. The parabola has the equation $RT = 1.4au(1 - u)$.

increasing miscibility with increasing T over the whole compositional range. In our regular approximation (8) the co-ordinates of the second-order critical points can be calculated.[3]

One finds two types: "apex" type and "edge-edge" type. This division is independent of the three kinds mentioned above (i to iii).†

Either one of the concentrations is $\frac{1}{2}$, ($x = \frac{1}{2}$ in Table 1) or the sum of two concentrations is $\frac{1}{2}$, ($x + y = z + w = \frac{1}{2}$ in Table 1). For example, when $z = \frac{1}{2}$ or $x + z = y + w = \frac{1}{2}$, the parameters in the table must be interchanged according to Fig. 1. The derived parameters K and L_{cef} have been defined earlier (cf. equations 10 and 4), while

$$J_{af} = (c - e + d - b)^2 - 4af. \qquad (11)$$

Fig. 3 shows the seven planes in the concentration tetrahedron to which second-order critical points are limited. For each system (combination of energy-interaction parameters a, b, c, d, e, and f) one obtains seven mathematical solutions for a second-order critical point. In most cases, several or all of these solutions have no physical meaning, as T, x, y, z, and w have to be positive. Even then, such a point may be practically meaningless, namely when it lies on a lower spinodal level; this can be checked by examining whether, for the critical concentration, equation (9) has a T root higher than the critical T.

The remaining relevant second-order critical points can be distinguished[3] as follows: When K is negative, it is a point of confluence between two miscibility gaps. When K and all six binary parameters are positive, we have a confluence point

* In nonregular cases the number of intersections may be 4, 6, etc.

† Numerical examples of five out of the six possible combinations can be found in reference (3).

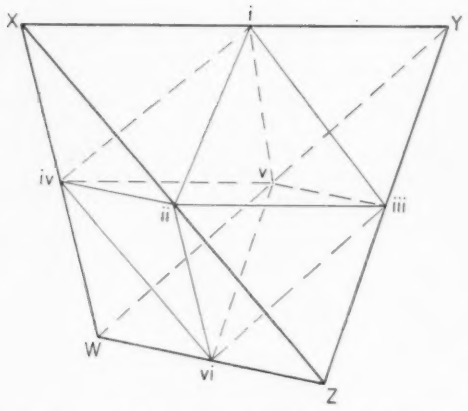

FIG. 3. Planes in the compositional tetrahedron to which second-order critical points are restricted.

$x = y + z + w = \frac{1}{2}$,	i	ii	iv	
$y = x + z + w = \frac{1}{2}$,	i	iii	v	
$z = x + y + w = \frac{1}{2}$,	ii	iii	vi	
$w = x + y + z = \frac{1}{2}$,	iv	v	vi	
$x + y = z + w = \frac{1}{2}$,	ii	iii	v	iv
$x + z = y + w = \frac{1}{2}$,	i	iii	vi	iv
$x + w = y + z = \frac{1}{2}$,	ii	i	v	vi

between two homogeneous domains. In other cases the point in question is a quaternary critical point.

Second-order critical points of one kind only (i, ii, or iii) can appear together in a regular system, and no more than one quaternary critical point at a time. Just as in ternary regular solutions (cf. first section), a quaternary second-order critical point is the T maximum of miscibility gap in a *pseudobinary section*. For the "apex" type, say with $x = y + z + w = \frac{1}{2}$, this joins the X apex with a point on the opposite face of the tetrahedron. For the "edge-edge" type, say with $x + y = z + w = \frac{1}{2}$, this joins a point on the X–Y edge with a point on the opposite Z–W edge.*

Such a pseudobinary section has the same properties as a regular normal binary system, That is to say, the binodal curve obeys the equation

$$T = 2T_c(1 - 2u)/\ln\{(1 - u)/u\}, \qquad (12)$$

where T_c is the critical temperature and u is the co-ordinate (from 0 to 1) along the pseudobinary axis; in the "apex" case u can be identified by x, for example. The spinodal section is $T = 4T_c u(1 - u)$; this parabola (cf. that in Fig. 2) touches the binodal curve[12] in its summit at $u = \frac{1}{2}$.

In the case of a ternary or quaternary critical point, T_c is a T maximum on the binodal and spinodal surfaces in *all* directions through the second-order critical concentration. In the case of a ternary saddle point, T_c is a T minimum along the line $u = \frac{1}{2}$. When T is viewed as a function of concentration in the plane $u = \frac{1}{2}$ through a second-order critical point in a quaternary solution, it is a maximum, or a minimum, or on a saddle in that point: cases i, iii, and ii respectively.

The tie-lines in pseudobinary sections through confluence points (ii and iii) are not absolutely stable at low temperatures, owing to the appearance of three-phase triangles. Even the confluence points themselves may be metastable.[3]

Quaternary (like ternary) critical points of regular solutions, however, are always† absolutely stable, and probably no three-phase equilibria appear when the system shows such a point. In this connection it is worth mentioning that each pseudo-component of the pseudobinary section through a quaternary critical point is not subject to phase separation at any temperature. In the "edge-edge" case the binary systems in question both have a negative interaction

* Two other sorts of pseudobinary sections, not associated with second-order critical points, are described in reference (3).

† This, of course, does not apply when two or more regular solutions are considered together, e.g., liquid + f.c.c.

TABLE 1. Co-ordinates of second-order critical points in regular quaternary systems

Co-ordinate	"Apex" type	"Edge-edge" type
T	$-\frac{K}{2RL_{cef}}$	$-\frac{K}{2RJ_{af}}$
x	$\frac{1}{2}$	$\frac{(c-e)(c-e+d-b) - f(2a+c+e-d-b)}{2J_{af}}$
y	$\frac{f(f+2a-c-e) - d(c-e+f) - b(e+f-c)}{2L_{cef}}$	$\frac{(d-b)(c-e+d-b) - f(2a-c-e+d+b)}{2J_{af}}$
z	$\frac{e(e+2b-c-f) - d(c+e-f) - a(e+f-c)}{2L_{cef}}$	$\frac{(d-e)(c-e+d-b) - a(2f-c+e+d-b)}{2J_{af}}$
w	$\frac{c(c+2d-e-f) - b(c+e-f) - a(c-e+f)}{2L_{cef}}$	$\frac{(c-b)(c-e+d-b) - a(2f+c-e-d+b)}{2J_{af}}$

parameter. In the "apex" case the ternary system opposite to the pure component in question shows complete miscibility at all T.

At temperatures below a second-order critical temperature of "apex" type—say, with $x = \frac{1}{2}$—the spinodal and binodal surfaces have tangent planes parallel to the Y–Z–W plane at the intersections with the pseudobinary axis. When, for example, the second-order critical point is a quaternary critical point, the tie-line along this axis joins two solutions whose concentrations x are (at constant T) a maximum and a minimum respectively. One also finds that the chemical potential μ_X in solutions of constant x is a maximum at the pseudobinary axis. This means that, e.g., a minimum in the solubility of pure solid X in ternary liquid mixtures Y–Z–W is correlated with the existence of a quaternary critical point in the liquid phase. For the ternary case these things are treated more fully in the last section of reference 1.

6. INFLUENCE OF A FOURTH COMPONENT ON A TERNARY CRITICAL POINT

We now look at a quaternary regular isothermal section at the temperature of a ternary critical point in one of the boundary systems, say X–Y–Z, with co-ordinates given by equations (3). Apart from some degenerate symmetrical cases there are two possibilities:

(I) The ternary critical temperature is raised by adding a small amount of W. Then there is a miscibility gap in the tetrahedron with its (first-order) critical curve tangent to the ternary face in its ternary critical point.

(II) The critical temperature is lowered by adding W. Now there is no miscibility gap in the tetrahedron, at least not in the vicinity of the ternary critical point. Analysis shows[3] that the inequality

$$\left| ey_c + fz_c - 2cy_cz_c - \tfrac{1}{2}d \right| \gtrless RT_c \qquad (13)$$

decides which of the two possibilities applies. When the absolute value of the left-hand side is greater, we have I, in the opposite case II.

Inequality (13) can be expressed in a more comprehensible way when the pseudobinary section in the ternary X–Y–Z system through the X corner and the ternary critical point is treated as a binary system.

The terminal solution (with $y \equiv y_0 = 2y_c$ and $z \equiv z_0 = 1 - y_0 = 2z_c$) will be called U, the U–X interaction parameter η and the U–W interaction parameter ζ.* Naturally $\eta = 2RT_c > 0$, while $\zeta = y_0e + z_0f - y_0z_0c$. Thus (13) becomes simply

$$\left| \zeta - d \right| \gtrless \eta \qquad (14)$$

in complete analogy with inequality (2) for the influence of an addition on a normal regular binary critical point.

If the ternary critical point in question has the highest of the critical temperatures (ternary or binary) in the boundary systems of X–Y–Z–W, then $\left| \zeta - d \right| > \eta$, raising it, necessarily leads to a quaternary critical point. When, moreover, $\zeta - d$ is negative, W mixes more readily with the Y–Z mixture (called U) than with X. The quaternary critical point will then be of the "apex" type, lying in a pseudobinary section with X and a Y–Z–W mixture as pseudocomponents. When, however, $\zeta - d$ is positive, W prefers X over the Y–Z mixture, and we get a quaternary critical point of "edge-edge" type.

It should be mentioned that a quaternary critical point can also appear when none of the ternary boundary systems shows phase separation. The closed miscibility gap then attains the tetrahedron faces at $T = 0$ only.

7. CLOSED MISCIBILITY GAPS IN QUATERNARY ALLOYS

The physical clarity of (14) allows its semi-quantitative extension to systems which show more or less considerable deviations from regularity. For ternary critical points in general the following rule analogous to that of Timmermans-Bancroft may be expected to hold: A ternary critical point in X–Y–Z is the culminating point of a two-phase domain whose central tie-lines can be idealized as directed from one or the components (say X) to a binary solution (y_0, z_0). Addition of a fourth component W will raise† the critical temperature when W has strongly different affinities for that solution and for X.

As (2) governs also the widening or narrowing of of a binary miscibility gap at temperatures below T_c, the rule above may be extended to the widening‡ of a ternary gap, at constant T below T_c, by addition of W. Miscibility is increased when the affinities are not very different.

It is felt that (13) can be used with some confidence for predicting the influence of various additions on the miscibility in ternary solutions, provided the inequalities show a sufficient margin. As in the second section, approximate values for binary interaction parameters were deduced with the aid of thermodynamic data (most of which were taken from the

* Along the section U–W both energy and entropy of mixing are regular. In general, however, it will not be pseudobinary (in contrast with the section along U–X), tie-lines crossing the line U–W at an angle.

† Provided miscibility is increased by heating. In the abnormal case of a lower critical point, T_c is lowered.

‡ In the tie-line direction.

VOL. 4 1956

compilation by Weibke and Kubaschewski[10] and the phase diagrams).

The ternary critical point of the f.c.c. phase in Ni–Au–Cu would, e.g., be raised by Co and by Ag. The idealized pseudobinary section joins Ni with an Au–Cu solution. Co prefers nickel, and Ag the other side. In general, a ternary critical point will be raised more easily by an addition preferring the single component than by an addition preferring the exothermic binary solution, because of the energy of dilution (viz., the term $-2cy_cz_c$ in (13)), which must be added to the appropriately averaged affinities of Y and Z for W.

The ternary critical point of the liquid phase in Pb–Zn–Ag would be raised by Bi (which prefers Pb) and perhaps also by Al (preferring the Zn–Ag side). The ternary critical point in Bi–Zn–Ag, predicted in the second section, may possibly be raised by Pb. This would lead to a quaternary critical point in the liquid phase of Pb–Bi–Zn–Ag. Qualitatively speaking, it would be of "edge-edge" type; that is to say: coexisting liquids in the closed miscibility gap would be relatively rich in (Pb + Bi) and (Zn + Ag) respectively.

The miscibility gap in liquid Al–Mg–Sb can be predicted to widen (in the tie-line direction) by addition of Fe, which prefers the Al side. That in Bi–Cu–Sb would be widened by Al and perhaps also by Zn; both prefer the Cu_3Sb side.

REFERENCES;

1. J. L. Meijering, *Philips Res. Rep.*, **5,** 333 (1950); **6,** 183 (1951).
2. H. K. Hardy, *Acta Met.*, **1,** 202 (1953); **2,** 348 (1954).
3. H. K. Hardy and J. L. Meijering, *Philips Res. Rep.*, **10,** 358 (1955).
4. I. Prigogine, *Bull. Soc. Chim. Belg.*, **52,** 115 (1943).
5. W. Seith and G. Helmold, *Z. Metallkde.*, **42,** 137 (1951); W. Seith and H. Johnen, *Z. Elektrochem.*, **56,** 140 (1952).
6. E. Henglein and W. Köster, *Z. Metallkde.*, **39,** 391 (1948).
7. E. Jänecke, *Handbuch aller Legierungen*, 2nd ed., Winter, Heidelberg, 1949.
8. H. R. Larson and J. Chipman, *Acta Met.*, **2,** 1 (1954).
9. E. Raub and A. Engel, *Z. Metallkde*, **38,** 11 (1947).
10. F. Weibke and O. Kubaschewski, *Thermochemie der Legierungen*, Springer, Berlin, 1943.
11. R. A. Oriani, *Acta Met.*, **2,** 608 (1954).
12. D. Balesdent, *Compt. Rend.*, **240,** 760 (1955).
13. To be published.
14. L. L. Seigle, Morris Cohen, and B. L. Averbach, *Trans. Amer. Inst. Min. Met. Eng.*, **194,** 1320 (1952).
15. J. L. Meijering, *Philips Res. Rep.*, **3,** 281 (1948), last section.
16. O. K. Rice, *Chem. Rev.*, **44,** 69 (1949).
17. I. Prigogine and R. Defay, *Thermodynamique Chimique*, Desoer, Liège, 1950.

DISLOCATION ARRAYS AND ROWS OF ETCH-PITS*

B. A. BILBY and A. R. ENTWISLE†

Measurements have been made of some arrays of etch-pits in α-brass observed by Jacquet. The positions of these pits have been compared with those predicted by Eshelby, Frank, and Nabarro for a linear array of dislocations of like sign piled up under a shear stress against a barrier. The arrangement of pits was found to be consistent with the assumption that each corresponds to an individual dislocation in such an array. The etch-pit spacings are, however, too irregular for a critical examination of their exact distribution. A slight systematic deviation of the etch-pit positions from those calculated could not be accounted for by considering other simple distributions of dislocations. Approximations to the roots of the first derivatives of the Laguerre and Legendre polynomials, which are required for the analysis, are discussed.

ACCUMULATIONS DE DISLOCATIONS ET ALIGNEMENTS DE PIQÛRES DE CORROSION

Des mesures ont été faites sur quelques accumulations de piqûres de corrosion dans le laiton α, observées par Jacquet.

Les positions de ces piqûres ont été comparées avec celle prédites par Eshelby, Frank, et Nabarro pour un arrangement linéaire de dislocations de même signe, empilées par une tension de cisaillement contre une barrière. L'arrangement des piqûres a été trouvé en accord avec l'hypothèse que chacune d'elles correspond à une dislocation individuelle dans une telle accumulation. Les distances entre les piqûres sont toutefois trop irrégulières pour permettre un examen critique de leur distribution exacte. Une légère déviation systématique des positions de piqûres, par rapport à celles calculées ne peut être attribuée, dans ce cas, à d'autres distributions simples des dislocations.

Des approximations sur les racines des dérivées premières des polynomes de Laguerre et Legendre, requises par l'analyse, sont discutées.

VERSETZUNGSANORDNUNGEN UND REIHEN VON ÄTZGRÜBCHEN

An einigen von Jacquet beobachteten reihenförmigen Anordnungen von Ätzgrübchen auf α-Messing wurden Messungen angestellt. Die Lage dieser Grübchen wurde verglichen mit den Voraussagen von Eshelby, Frank, und Nabarro für eine lineare Anordnung von Versetzungen gleichen Vorzeichens, die unter einer Schubspannung gegen ein Hindernis aufgestaut sind. Es wurde gefunden, dass die Anordnung der Grübchen in Übereinstimmung ist mit der Annahme, dass jedes Grübchen einer einzelnen Versetzung innerhalb einer solchen Aufreihung entspricht. Die Abstände der Ätzgrübchen sind jedoch zu unregelmässig, um ihre genaue Verteilung kritisch zu prüfen. Eine schwache systematische Abweichung der Lagen der Ätzgrübchen von den berechneten konnte auch durch In-Betracht-ziehen anderer einfacher Versetzungsverteilungen nicht erklärt werden. Näherungslösungen für die Wurzeln der ersten Ableitungen der Laguerreschen und Legendreschen Polynome, die für die Auswertung benötigt werden, werden diskutiert.

VOL. 4 1956

1. INTRODUCTION

Jacquet[1, 2] has recently reported experiments on the etching behavior of polycrystalline α-brass (64.5% Cu), deformed by tension under very low stresses (1–4.5 kg/mm²). The material, originally electropolished, was etched with $Na_2S_2O_4$ solution, using a special technique, and lines of etch-pits appeared along the traces of the slip planes. Through the kindness of Madame Weill and Dr. Jacquet, a number of unpublished photographs of these arrangements of etch-pits were made available to the authors. In most groups, the etch-pits were distributed along the slip planes in an approximately uniform way, but in some, the spacing between etch-pits decreased systematically as an obvious obstacle to the slip was approached. In the present note it is tentatively assumed that in such groups each etch-pit corresponds to an individual dislocation, and the arrangement of etch-pits is then correlated with that predicted for linear groups of dislocations piled up under shear stress (Eshelby, Frank, and Nabarro).‡[3]

2. MEASUREMENT OF THE PHOTOGRAPHS

Measurements were made with a travelling microscope of the etch-pit positions in four linear groups selected as indicated above. In three of these (arrays 1–3) the obstacle to slip was apparently a grain boundary, and in one (array 4), another line of etch-pits indicating slip on a different plane intersecting the first. (Several examples of two piled-up groups on different slip planes meeting each other at a point were noticed, suggesting the locking process proposed by Cottrell[4] and Lomer[5]). Photographs of arrays 4 and 2 have been published (Jacquet);[1, 2] arrays 1

* Received September 13, 1955.

† Department of Metallurgy, The University, Sheffield, England.

‡ Referred to as EFN in the sequel.

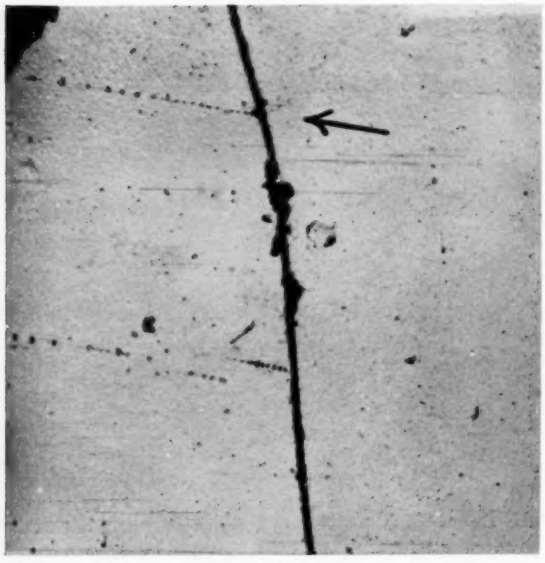

(a)

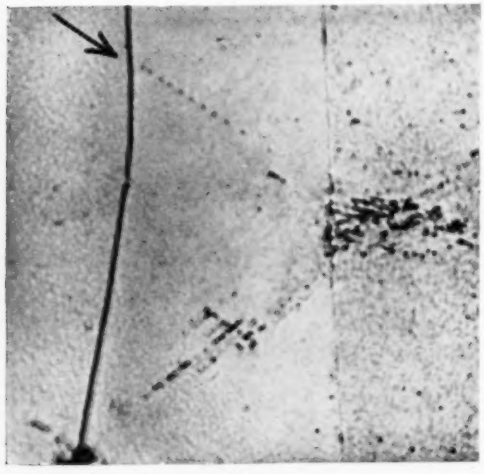

(b)

FIG. 1. Arrays of etch-pits in α-brass (after unpublished photographs of Dr. Jacquet).
(a) Array 1: electron micrograph, ×3500.
(b) Array 3: optical micrograph, ×2000.

and 3 are shown in Figures 1(a) and 1(b) respectively, which are unpublished photographs by Dr. Jacquet. In most groups the etch-pits merged into a continuous line near the barrier, and it was not possible to assign to any etch-pit its correct ordinal number in the group. (Occasionally, also, there was a small region free from etch-pits, immediately adjacent to the barrier.) Accordingly, only the positions y_{k+m}, $k = 0, 1, 2, 3, 4, \ldots, (N-1)$, of N discrete etch-pits, and the position y_0 of the barrier could be measured. Thus, taking the latter as origin, $x_{k+m} = y_{k+m} - y_0$ give the positions of the mth to the $(m+N)$th etch-pits in the group, where m is unknown. However, it was usually possible, from the absence of further etch-pits at the "free" end of the group, to infer that the Nth dislocation was the last. The following analysis is based on this assumption.

3. ANALYSIS OF THE MEASUREMENTS

When $n-1$ similar straight dislocations are piled under a stress $-\tau_0$, against one locked dislocation at the origin, their positions x are given by the roots of the first derivative of the nth LaGuerre polynomial of argument z, where $z = 2\tau_0 x/A$ (EFN). The constant A depends on the angle between the Burgers vector and the dislocation line. For screw and edge dislocations in an isotropic medium, A has the values $\mu b/2\pi$ and $\mu b/2\pi(1-\nu)$ respectively, where μ is the shear modulus and b the strength of the dislocations. $-\tau_0$ is the component in the direction of the Burgers vector of the traction in the plane $y = 0$ due to the applied stress.

When
$$z/4n \ll 1 \tag{1}$$
it is shown by these authors that the positions of the free dislocations are given approximately by $z_i = j_i^2/4n$; $i = 1, 2, \ldots, (n-1)$, where j_i is the ith zero of the Bessel function $J_1(z)$. When $i \gg 1$, $j_i \simeq \pi i$, so that then, in the notation of Section 2 above,
$$k + m = C\sqrt{x_{m+k}} \tag{2}$$
where $C = (2/\pi)/\sqrt{(2n\tau_0/A)}$. The graph of k against $\sqrt{x_{m+k}}$ should be a straight line whose intercept on the k axis is $-m$. If the $(m+N-1)$th dislocation is the last in the group, $m+N = n$, and so n and τ_0 can be determined. Values of n and τ_0 obtained in this way by fitting regression lines of $\sqrt{x_{m+k}}$ on k for the four sets of measurements are shown in columns (2) and (3) of Table 1. Columns (7) and (8) show N and the experimental τ_0 where this is known. τ_0 was assumed to be one-half the nominal applied tensile stress, although, of course, in the polycrystalline specimens used, the local stresses may have differed considerably from this. The value of A was taken to be 2.86×10^3 dyne cm^{-2}. Although the results fit the relation (2) quite well, the Bessel-function approximation is best for the smallest zeros, while the data refer to the largest, and the further approximation (2) is valid only for an intermediate region where $1 \ll i \ll n$. An approximation which is best for the largest roots is obtained in the Appendix. It is shown there that if
$$2\sqrt{nz} \gg 1 \tag{3}$$

the zeros of $L'_n(z)$ are given by

$$z_r = 4n \cos^2 \theta_r \qquad r = 1, 2, \ldots, (n-1) \quad (4)$$

where

$$2\theta_r - \sin 2\theta_r = (r - \tfrac{1}{4})(\pi/n). \quad (5)$$

In the previous notation, $r = n - m - k$, and $r = 1$ corresponds to the largest zero. Thus we have

$$\log_{10}(x_r) = \log_{10}(1 + \cos 2\theta_r) - \log_{10}(n\tau_0/A) \quad (6)$$

$$\log_{10}(r - \tfrac{1}{4}) = \log_{10}(2\theta_r - \sin 2\theta_r) - \log_{10}(\pi/n). \quad (7)$$

For any array these ratios should all equal $2\tau_0/A$. For each set of ratios $R_r(n)$, the mean $\bar{R}(n)$ and standard deviation $\sigma(n)$ were computed and that value of n selected for which $\sigma(n)/\bar{R}(n)$ was less than both $\sigma(n+1)/\bar{R}(n+1)$ and $\sigma(n-1)/\bar{R}(n-1)$. The final τ_0 value was then calculated from the $\bar{R}(n)$. The roots z_r were obtained by iteration from (5) for array 3, and by the aid of a large graph of v against u for arrays 1, 2, and 4. The final values of n, τ_0, and $\sigma(n)$ are shown in columns (4), (5), and (6) respectively of Table 1, and Fig. 2 shows the quantities $R_r(n)/\bar{R}(n)$ plotted against r for each array.

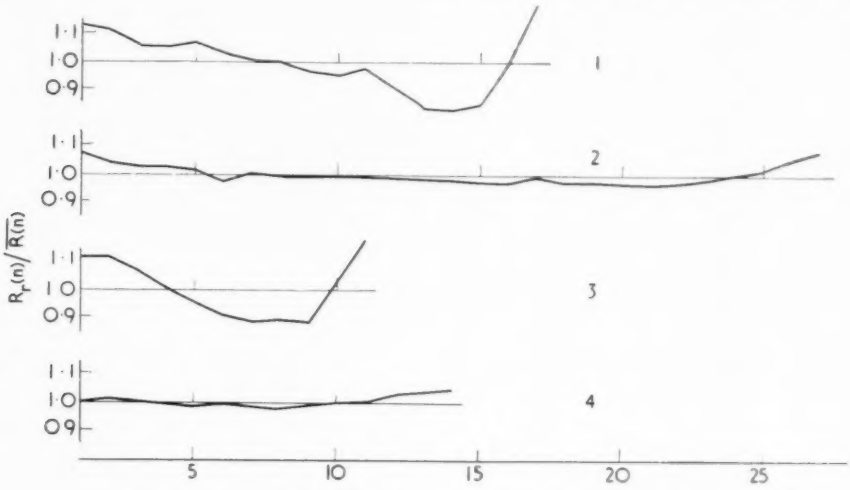

FIG. 2. Graphs of $R_r(n)/\bar{R}(n)$ against r for the four arrays. $R_r(n)/\bar{R}(n)$ is a measure of the deviation of the position of a pit from that predicted by the theory, and would be unity for all pits if the fit were exact.

From a master graph of $v = \log_{10}(1 + \cos 2\theta)$ against $u = \log_{10}(2\theta - \sin 2\theta)$, the zeros $z_r = (2\tau_0 x_r/A)$ can therefore be obtained for any value of n, provided (3) is satisfied. Preliminary estimates of n and τ_0 were obtained by plotting graphs of $\log_{10}(x_r)$ against $\log_{10}(r - \frac{1}{4})$ for each experiment and determining the translations $u_0 = \log_{10}(n/\pi)$ and $v_0 = \log_{10}(n\tau_0/A)$ required to superpose them on the graph of v against u. Final estimates of n were then obtained by varying n by a few units, and calculating z_r, $r = 1, 2, \ldots, N$ and the ratios $R_r(n) = z_r/x_r$.

TABLE 1

(1) Array	(2) n from eq. (2)	(3) τ_0 from eq. (2)	(4) n from eq. (5)	(5) τ_0 from eq. (5)	(6) $\sigma(n)/\bar{R}(n)$	(7) N visible	(8) Experimental τ_0
1	24	0.58	25	0.70	0.104	18	?
2	57	0.54	69	1.3	0.032	27	0.5
3	15	0.76	16	0.45	0.108	11	1.8
4	42	0.36	58	1.0	0.021	14	1.5

The units of τ_0 are kg mm^{-2}.

4. DISCUSSION

It is clear from the above analysis that the arrangement of these etch-pits is quite consistent with the assumption that each corresponds to an individual dislocation in a group piled against a barrier by a shear stress. From this assumption the correlation of the observed and calculated positions leads to reasonable values of τ_0* and for the $n - N$ dislocations lying between the N visible dislocations and the barrier. Fig. 2 shows, however, that the etch-pit spacings are too irregular for a critical examination of their exact distribution. Nevertheless, there appears to be a slight systematic deviation from the positions given by the roots of $L'_n(z) = 0$, for the values of z_r/x_r are higher at each end of the group than in the middle. This means for example that, if the outer etch-pit

* If the dislocations are not normal to the trace of the slip plane in the surface of observation, the values of τ_0 given in the table should be increased by a trigonometrical factor of order unity.

VOL. 4 1956

positions are weighted more heavily so that the deviation appears at the inner end, the dislocations near the barrier are closer to it than the theory predicts. This deviation cannot be removed by any reasonable adjustment of the barrier position, but it can be reduced by abandoning the assumption that the outermost visible etch-pit corresponds to $r = 1$. The estimates of n and τ_0 are not, however, radically altered thereby. For example, if array 2 is fitted graphically with r running from 21 to 47, we obtain $n = 82$ and $\tau_0 = 0.714\,\text{kg mm}^2$. $R_r(n)$ still oscillates about $\bar{R}(n)$, but more rapidly and with $\sigma(n)/\bar{R}(n) = 0.0172$. There is no evidence on the photograph, however, for the presence of the twenty additional dislocations external to the visible group which this assumption implies.

It is, of course, not certain that the arrays were formed under a constant shear stress τ_0 alone, and two other possibilities have been examined for the array 2. Firstly, the influence of a similar array of opposite sign at the other end of the slipped region might be important. The discrete solution for this case is not known, but an approximate treatment using a continuous distribution of dislocations has been given (Leibfried).[6]

If the origin is taken at the centre of the slipped region and the barriers at $w = \pm a$, and if the dislocations extend from $-a < w < -b$ and $b < w < a$, the number $r(w)$ of dislocations between b and w is:

$$r(w) = n - \frac{\tau_0 a}{\pi A}[E(\lambda, k) - k'^2 K(\lambda, k)] \qquad (8)$$

where $\lambda = [1 - (w/a)^2]^{\frac{1}{2}}/k$, $k' = b/a$ and $k^2 + k'^2 = 1$. $K(\lambda, k)$ and $E(\lambda, k)$ are the incomplete elliptic integrals of modulus k of the first and second kinds respectively. Clearly $r(a) = n = (\tau_0 a/\pi A)[E(1,k) - k'^2 K(1,k]$ where $E(1, k)$ and $K(1, k)$ are the complete elliptic integrals. Assuming again that the outermost etch-pit corresponds to b, $a - b$ is known, $a = (a - b)/(1 - k')$, and $w_r = a - x_r$. The right-hand side of (8) was evaluated for $k' = 0.766$ and 0, and varied approximately linearly with r. Linear relations fitted by the method of least-squares gave values for n and τ_0 as follows: $k' = 0.766$, $n = 75$, $\tau_0 = 1.7\,\text{kg mm}^{-2}$; $k' = 0$, $n = 89$, $\tau_0 = 0.5\,\text{kg mm}^{-2}$. Both showed a systematic deviation for large r in the same sense as that in the previous analysis. This was much more pronounced, however, for $k' = 0$. The deviation could no doubt have been reduced by assuming again that the etch-pits began at some $b' > b$.

Secondly, the etch-pit positions have been compared with these predicted for part of a group of M like dislocations under no shear stress, the outer two being locked at $w = \pm L$. Their positions are given by the roots of $P'_{M-1}(z) = 0$, P'_M being the first derivative of the Mth Legendre polynomial (EFN), where $z = w/L$. An approximate formula for these roots is given in the Appendix, where it is shown that $\sin^{-1}[1 - x_r/L]$ should vary linearly with r. This was found to be true approximately, but again the deviation was systematic, both for $L = d$ and $L = 10d$. d is the distance of the furthest visible dislocation from the barrier; that is, in the previous notation $d = x_1$. These two choices of L gave widely differing values, 106 and 394, for M, and this, coupled with the lack of visual evidence for the additional dislocations, suggests that this analysis has little significance.

Thus, these two further possibilities do not account for the systematic deviation, and the latter is probably due to some kind of perturbation of the stress field under which the arrays were formed. The photographs indeed usually suggest the presence of other dislocations near the groups measured. In array 4, for example, the influence of the smaller piled-up group lying on the intersecting slip plane must be important. Also, when the barrier is at a grain boundary, the discontinuity in the elastic constants there may introduce forces not discussed in the simple theory (EFN).

It does not seem worth while to attempt to analyse further these detailed perturbations until more regular data obtained in single crystals under controlled stresses are available.

5. ACKNOWLEDGMENTS

We wish to express our thanks to Madame Weill and Dr. Jacquet for making available to us the unpublished data on which the analysis is based. We are also indebted to Mr. A. R. Curtis for the analysis in part (a) of the Appendix, and for suggesting the graphical method of comparison.

The work was carried out during the tenure of the United Steel Companies Research Fellowship (A. R. E.) and the Royal Society Sorby Research Fellowship (B. A. B.).

6. REFERENCES

1. P. A. Jacquet, *Compt. Rend.*, **237,** 1248 (1953).
2. P. A. Jacquet, *Acta Met.*, **2,** 752, 770 (1954).
3. J. D. Eshelby, F. C. Frank, and F. R. N. Nabarro, *Phil. Mag.*, **42,** 351 (1951).
4. A. H. Cottrell, *Phil. Mag.*, **43,** 645 (1952).
5. W. M. Lomer, *Phil. Mag.*, **42,** 1327 (1951).
6. G. Leibfried, *Z. Phys.*, **130,** 214 (1951).
7. H. Jeffreys and B. S. Jeffreys, *Methods of Mathematical Physics*, Cambridge University Press (1946).

Appendix

(a) The differential equation satisfied by $u_n(z) \equiv L'_n(z)$ is

$$zu''_n(z) + (2 - z)\,u'_n(z) + (n - 1)\,u_n(z) = 0 \quad \text{(A1)}.$$

Put $z = 4nt$, $v_n(t) = ze^{-\frac{1}{2}z}u_n(z)$,

then
$$\frac{d^2v_n}{dt^2} = 4n^2\left(1 - \frac{1}{t}\right)v_n(t)\,. \qquad \text{(A2)}$$

The asymptotic solutions for large n of Green's type are (Jeffreys and Jeffreys) (7):

$$v_n \sim k_n\left(\frac{t}{t-1}\right)^{\frac{1}{4}}\exp\left[\pm 2n\int_1^t\left(1 - \frac{1}{w}\right)^{\frac{1}{2}}dw\right]. \qquad \text{(A3)}$$

Since, for large z, $L'_n(z) \sim z^{n-1}$ and so $v_n(t) \sim t^n e^{-2nt}$, the negative sign in the exponential must be taken. The continuation for $t < 1$ is then

$$v_n \sim 2k_n\left(\frac{t}{1-t}\right)^{+\frac{1}{4}}\sin\left[\frac{\pi}{4} + 2n\int_t^1\left(\frac{1}{w} - 1\right)^{\frac{1}{2}}dw\right]. \qquad \text{(A4)}$$

There are thus zeros for $t = t_r$ where

$$I_r = \int_{t_r}^1\left(\frac{1}{w} - 1\right)^{\frac{1}{2}}dw = \left(r - \frac{1}{4}\right)\left(\frac{\pi}{2n}\right) \qquad \text{(A5)}$$

or, putting $t_r = \cos^2\theta_r$, the zeros are

$$z = z_r = 4n\cos^2\theta_r \qquad \text{(A6)}$$

where

$$2\theta_r - \sin 2\theta_r = \left(r - \frac{1}{4}\right)\left(\frac{\pi}{n}\right). \qquad \text{(A7)}$$

The $(n - 1)$ zeros of u_n are given by $r = 1, 2, \ldots, (n - 1)$ and $r = n$ gives an approximation to the root $z = 0$ of v_n. The error, which arises because $(1 - 1/t) \to \infty$ as $t \to 0$, may be estimated by setting $\theta_n = \pi/2\varepsilon$. Then $\varepsilon \simeq \pi/16n$ and $z_n \simeq \pi^2/64n$ instead of zero.

If t is small,

$$v_n \sim 2k_n\left(\frac{t}{1-t}\right)^{\frac{1}{4}}\sin\left[\frac{\pi}{4} + n\pi - 2n\int_0^t\left(\frac{1-w}{w}\right)^{\frac{1}{2}}dw\right]$$
$$\simeq 2k_n(-)^{n-1}t^{\frac{1}{4}}\sin\left[4nt^{\frac{1}{2}} - \pi/4\right]. \qquad \text{(A8)}$$

Since, if $4nt^{\frac{1}{2}}$ is large,

$$J_1(4nt^{\frac{1}{2}}) \sim \frac{1}{\sqrt{2n\pi}}\,t^{-\frac{1}{4}}\sin\left(4nt^{\frac{1}{2}} - \frac{\pi}{4}\right) \qquad \text{(A9)}$$

(A8) agrees with the solution

$$v_n = 2(nt)^{\frac{1}{2}}J_1(4nt^{\frac{1}{2}}) \qquad \text{(A10)}$$

given by EFN, if $k_n = (-)^{n-1}/\sqrt{2\pi}$.

(b) $p_n(z) \equiv P'_n(z)$ satisfies the differential equation:

$$(1 - z^2)p''_n(z) - 2zp'_n(z) + n(n+1)p_n(z) = 0. \qquad \text{(A11)}$$

If
$$q_n(z) = (1 - z^2)p_n(z),$$

then
$$q''_n(z) = \frac{n(n+1)}{z^2 - 1}\,q_n(z) \qquad \text{(A12)}$$

Since $q_n \sim z^2p_n \sim z^{n+1}$ for large z, the asymptotic solution of Green's type for $z > 1$ is:

$$q_n \sim (z^2 - 1)^{\frac{1}{4}}\exp\left[+\left(n + \frac{1}{2}\right)\int_1^z(w^2 - 1)^{-\frac{1}{2}}\,dw\right]$$

with the continuation (Jeffreys and Jeffreys) for $z < 1$,

$$q_n \sim (1 - z^2)^{\frac{1}{4}}\cos\left[\left(n + \frac{1}{2}\right)\int_z^1(1 - w^2)^{-\frac{1}{2}}dw + \pi/4\right]. \qquad \text{(A13)}$$

This has roots when $z = z_k$, where

$$\left(n + \frac{1}{2}\right)\int_{z_k}^1(1 - w^2)^{-\frac{1}{2}}\,dw + \frac{\pi}{4} = (2k + 1)\pi/2$$

or,

$$z_k = \cos\left\{\frac{\pi(4k+1)}{2(2n+1)}\right\} \qquad \text{(A14)}$$

$k = 0$, $z_0 \simeq 1 - \pi^2/8(2n + 1)^2$, is an approximation to the root $z = 1$ of q_n. The positive roots of p_n are given by $k = 1, 2, 3 \ldots, s$, where $s \leq n/2$ according as n is odd or even. (The negative roots are minus these values, since $P'_n(z)$ is either an odd or even function of z.) From (A14) the linear relation stated in the text follows at once.

VOL. 4 1956

LOW-FREQUENCY STUDIES OF DISLOCATION INTERACTIONS WITH SOLUTE ATOMS*

S. WEINIG† and E. S. MACHLIN‡

An investigation of the internal friction of 99.999% Cu and copper binary alloys was performed at 40°C in a high-vacuum torsion pendulum at a one c.p.s. frequency of vibration. The effect of solute additions of 0.01 to 1 at. per cent of Al, Ni, and Si was studied. It was observed that the Ni was almost ineffective in diminishing the logarithmic decrement, whereas the Si and Al lowered the decrement. The rate of decrease with concentration was most rapid for the Cu-Al alloys.

Calculation of the elastic interaction energy between a solute atom and an edge type of dislocation reveals that there should be negligible binding energies for Ni and Si solutes in copper due to their very small atomic size difference. However, computation of the electrical interaction between a solute atom and a dislocation results in an appreciable binding energy for a Cu-Si alloy. The summation of the various interaction energies for the binary consistuents indicates that the order of effectiveness in pinning dislocation singular lines in copper should be Al, Si, and Ni in the ratio of 4.9 : 2.8 : 1. This analysis is in agreement with the experimental results and gives additional support for an electrical interaction between solute atoms and dislocations.

ETUDES PAR FRICTION INTERNE EN BASSE FRÉQUENCE DES INTERACTIONS DE DISLOCATION AVEC LES ATOMES EN SOLUTION

La friction interne de Cu très pur (99,999%) et d'alliages de cuivre a été étudiée à 40°C sous vide poussé à l'aide d'un pendule de torsion, avec une fréquence de vibration d'un cycle par seconde.

On a étudié l'influence d'additions solubles de Al, Ni et Si en pourcentage atomique variant de 0,01 à 1%.

Il a été observé que Ni est presque sans effet sur le décrément logarithmique, tandis que Si et Al l'abaissent.

Le degré de diminution avec la concentration est plus rapide pour des alliages de cuivre-aluminium.

Un calcul de l'énergie élastique d'interaction entre un atome soluble et une dislocation du type coin, indique qu'il existerait des énergies de liaison négligeables pour les atomes Ni et Si en solution dans le cuivre, ceci étant dû à leur très petite différence de rayon atomique.

Cependant, un calcul de l'interaction électrique entre un atome en solution et une dislocation révèle une énergie de liaison appréciable pour un alliage Cu-Si. L'addition des différentes énergies d'interaction pour les constituants binaires montre que l'ordre de blocage des lignes de dislocation dans le cuivre devrait être Al-Si-Ni dans la proportion de 4,9 : 2,8 : 1.

Cette analyse est en accord avec les résultats expérimentaux et renforce l'idée d'une interaction électrique entre atomes en solution et dislocations.

UNTERSUCHUNGEN BEI NIEDERFREQUENZ ÜBER DIE WECHSELWIRKUNG VON VERSETZUNGEN MIT GELÖSTEN ATOMEN

Mit einem Hochvakuum-Torsionspendel wurde eine Untersuchung über die innere Reibung von 99,999 prozentigem Kupfer und binären Kupferlegierungen bei 40°C und einer Schwingungsfrequenz von 1 Hz durchgeführt. Die Wirkung von Lösungszusätzen von 0,01 bis 1 Atom-Prozent Al, Ni, und Si wurde studiert. Dabei wurde beobachtet, dass Ni fast unwirksam ist hinsichtlich einer Verringerung des logarithmischen Dekrements, während Al und Si das Dekrement erniedrigen. Die Abnahme des Dekrements mit wachsender Konzentration ist am steilsten für die Cu-Al-Legierungen.

Eine Berechnung der elastischen Wechselwirkungsenergie zwischen einem gelösten Atom und einer Stufenversetzung lässt erkennen, dass die Bindungsenergien von gelöstem Ni und Si in Kupfer wegen der geringen Atomradiendifferenzen vernachlässigbar klein sein sollten. Jedoch ergibt sich bei einer Berechnung der elektrischen Wechselwirkung zwischen einem gelösten Atom und einer Versetzung eine beträchtliche Bindungsenergie für Cu-Si-Legierungen. Summiert man die verschiedenen Wechselwirkungsenergien für die einzelnen Zulegierungen, so zeigt sich, dass deren Wirksamkeit hinsichtlich des Verankerns von einzelnen Versetzungslinien in Kupfer in der Reihenfolge Al, Si, Ni sich wie 4,9 : 2,8 : 1 verhalten sollte. Diese Analyse ist in Übereinstimmung mit den experimentellen Ergebnissen und stellt eine zusätzliche Stütze für das Vorhandensein einer elektrischen Wechselwirkung zwischen gelösten Atomen und Versetzungen dar.

---

* Received June 5, 1955. This paper represents part of a thesis by S. Weinig submitted in partial fulfillment of the requirements for the degree of Doctor of Engineering Science in the School of Engineering of Columbia University.

† Now at Department of Metallurgy, New York University, New York 3, N.Y.

‡ School of Mines, Columbia University, New York 27, N.Y.

It has been previously demonstrated that the room-temperature energy dissipation observed with a single crystal specimen oscillating at a high frequency manifests the characteristics of a static hysteresis process, i.e., the logarithmic decrement and the dynamic modulus* are strain-amplitude dependent.[1] Although the static hysteresis or nonlinear effect should be independent of the frequency, it has been suggested by Nowick[2] that the mechanical behavior which is describable in terms of static hysteresis at high frequencies may completely change its character to a visco-elastic type of mechanism at low frequencies (~1 c.p.s.). If this is so, then the low-frequency logarithmic decrement may exhibit considerably less, if any, strain-amplitude dependence as compared to the high-frequency damping.

This investigation concerned itself with the determination of whether or not an amplitude-dependent logarithmic decrement could be obtained at a low frequency of vibration, with the study of the effect of small solute additions on the room-temperature internal friction at a constant amplitude of vibration, and with the high-temperature-background internal friction-rise above the grain-boundary stress-relaxation peaks.

MATERIALS AND EXPERIMENTAL PROCEDURE

The solvent metal used in this investigation was high-purity copper which was obtained from the American Smelting and Refining Company. The nominal spectrographic analysis reported by A. S. and R. is given in Table 1.

The material will be henceforth designated as 99.999%. The alloy series were prepared in a high-vacuum melting apparatus and the specimens were cold-swaged and wire-drawn to 0.030 in. without any intermediate annealing. The detailed procedure used in the specimen preparation has been reported by the authors in a previous paper.[3]

The specimens were tested in a high-vacuum torsion pendulum which permits a complete test to be performed on a single wire without manual manipulation of the sample or exposure to atmosphere from a time prior to annealing until completion of the measurements.[4] The logarithmic decrement and vibrational frequency were measured at approximately 1 c.p.s. at 40°C with the vacuum maintained at 10^{-5} mm of Hg. The frequencies were determined with an electrical timer which reads to 0.01 sec.

The logarithmic decrement values could be reproduced on any single wire specimen to within a few per cent. For different specimens of the same composition the variation was as great as 10–15%. The values given in the tables represent an average value for all specimens of the particular concentrations that were tested.

TABLE 1. Spectrographic analysis of American Smelting and Refining Company high-purity copper

Element	Detectable percentage	Element	Detectable percentage
Fe	0.00007	As	0.0002
Sb	0.0001	Cr	0.00005
Pb	0.0001	Si	0.00001
Sn	0.0001	Te	0.0002
Ni	0.0001	Se	0.0001
Bi	0.00001	S	0.0001
Ag	0.00003		

Note: The above are the minimum percentages detectable by spectrographic analysis. None of the elements were observed.

* Young's modulus is obtained for longitudinal or flexural vibration, whereas the rigidity modulus or dynamic shear modulus is obtained for torsional vibrations.

EXPERIMENTAL RESULTS AND DISCUSSION

A. *Pure Copper*

Tests were performed on a 99.999% copper wire subsequent to a two-hour anneal in situ at 600°C. The strain-amplitude of the vibrational frequency was varied between 10^{-6} and 10^{-5} in order to ascertain whether the aforementioned characteristics of a static-hysteresis process could be observed. Actually the magnitude of the amplitude of strain is continually decreasing during the free decay of a torsion pendulum, hence the values reported are the mean between the maximum and minimum amplitude over which the decay was measured. The results of these tests at 40°C are given in Table 2.

TABLE 2. The strain-amplitude dependence of the internal friction and dynamic modulus of 99.999% Cu (Measurement at 40°C).

Strain amplitude	Logarithmic decrement ±0.00003	(Frequency)^2 ±0.001
3.2×10^{-6}	2.38×10^{-3}	1.308
4.8×10^{-6}	2.58×10^{-3}	1.305
9.2×10^{-6}	2.73×10^{-3}	1.304

It is noted that the ambient level of the internal friction is somewhat higher for these polycrystalline specimens than for the single-crystal specimen tested by Read,[1] although the strain-amplitude dependence of both the logarithmic decrement and

VOL. 4 1956

the dynamic modulus* is as large as observed in the single crystals at high frequencies. Consequently, it appears that the static hysteresis which is observed at high frequencies can likewise be observed at low frequencies, as expected from the frequency-independent character of the static-hysteresis phenomenon. Nowick[5] and Read[1] have suggested that the static-hysteresis effect is due to the stress-induced migration of dislocations. Actually, the area swept out by the moving dislocations cannot be independent of stress for a static-hysteresis effect. This area must change with stress. One mechanism suggested for this change[5] requires that increasing stress should free increasing lengths of dislocation lines from the solute atoms pinning them. Let us assume this interpretation of the source of room-temperature decrement. It is then possible to discuss the effect of alloying elements upon the internal friction of high-purity copper in terms of solute atom interaction with dislocations.

From the studies on grain-boundary stress-relaxation of high-purity copper performed both by Ke[6] and the authors,[3] it was found that upon successive annealing the magnitude of the relaxation peak as well as the background component of internal friction decreased in a monotonic fashion.

Although the specimen-annealing was performed in an evacuated chamber of 10^{-5} mm of Hg, this does not preclude the possibility that oxygen may have diffused into the wire specimen during the heat treatment, as the partial pressure of the oxides of copper have considerably lesser values at the annealing temperature.

If the oxygen atoms do diffuse into the high-purity Cu wire specimen, they should interact with the edge type of dislocations within the matrix, and it would be possible to observe this effect by measuring the internal friction at room temperature after successive annealing treatments. The interaction between a solute atom and a Taylor dislocation will hinder the motion of the dislocation and hence lower the observed logarithmic decrement. Measurements were made at 40°C of the logarithmic decrement after a series of anneals at 600°C, and it was found that the internal friction decreased after each heat treatment. A similar series of tests were performed on a specimen of 1 at. per cent Cu-Si, and it was observed that within the experimental accuracy no change in the decrement at 40°C resulted. The values obtained for this series of measurements as well as the former are given in Table 3.

* The modulus in torsion, i.e., rigidity modulus, is proportional to the square of the vibrational frequency.

TABLE 3. The effect of successive annealing on the logarithmic decrement for 99.999% copper and a 1.0 at. per cent Cu-Si alloy (Measurements at 40°C).

99.999% Cu		1.0 at. per cent Cu-Si	
Annealing time at 600°C	Logarithmic decrement	Annealing time at 600°C	Logarithmic decrement
2 h	0.00252 ± 0.00001*	1 h	0.00011 ± 0.000005*
+1 h	0.00249 ± 0.00001		
+1 h	0.00244 ± 0.00001	+2 h	0.00011 ± 0.000005
+3 h	0.00189 ± 0.00001		

* The precision of the readings is a function of the absolute value of the decrement, as it depends upon the rate of decay of the free oscillation relative to the rapidity of the operator in making a reading.

These results indicate that during the annealing period the oxygen atoms diffuse into the matrix probably along dislocation pipes, and pin the dislocations by interacting with the strained regions around the dislocation singular lines. The constancy of the logarithmic decrement of the Cu-Si alloy will be shown later in this paper to be due to a saturation of the existing dislocation sites for solute atoms at a concentration of 1 at. per cent Cu-Si.

B. *Effect of Solute Additions on the Room-temperature Decrement*

It was previously shown in this paper that the observed internal friction at low temperatures (40°C) is the manifestation of a static-hysteresis phenomenon, and therefore may possibly be ascribed to the motion of dislocations. The effect of various solutes should be qualitatively the same as that of oxygen, i.e., they should act to restrain the motion of dislocations and hence decrease the energy dissipated. The relative ability of the various binary constituents in diminishing the decrement will depend upon the magnitude of the interaction between the solute atom and the edge type of dislocation. If the total interaction is divided into the component parts of elastic and electrical interactions, then the magnitude of the binding energies may be calculated from Cottrell's analysis.[7]

The elastic interaction may be obtained from the assumption of linear elasticity theory in that a solute atom is considered to distort the lattice equally in all directions and therefore only interacts with the hydrostatic component of the dislocation stress field. If the hydrostatic component is p, and Δv is the change in volume caused by the solute atoms,

then the elastic interaction energy may be expressed as

$$V = p\Delta v. \tag{1}$$

Substituting numerical values in equation (1) for Cu as the solvent metal, the approximate binding energy in electron volts is -2ε, where ε is the degree of misfit of the solute atom, and is defined as

$$\varepsilon = (1/a)(da/dc). \tag{2}$$

The lattice parameter is a, and c is the concentration.

The electrical interaction is believed to be caused by the redistribution of the free electrons in order to equalize the Fermi energy level about the edge type of dislocation. This transfer of electrons causes an effective dipole to be formed about the dislocation which acts to attract solute atoms. The magnitude of the interaction between the dipole and a solute atom is a function of the excess charge on the atom as calculated from conductivity measurements. Cottrell estimates the binding energy due to the electrical interaction between a solute atom and a dislocation in copper to be approximately

$$V_e = -0.0175(z - 1), \tag{3}$$

where z is the valence of the binary constituent.

Table 4 gives the interactions between an edge dislocation and the various solutes used in this investigation. The lattice parameters which were used in the calculation of the elastic binding energy are the apparent atomic diameters based upon the extrapolation of the terminal solid solution.[8]

TABLE 4. The elastic and electrical interactions between a solute atom and an edge dislocation in copper

Solute	Apparent atomic diameter	Elastic interaction	Electrical interaction	Total (eV)
Al	2.71 Å	0.125	0.035	0.160
Ag	2.95 Å	0.180		0.180
Ni	2.51 Å	0.033		0.033
Si	2.59 Å	0.036	0.051	0.087
Cu	2.55 Å			

The ratios of the calculated total binding energies for the solutes Ag, Al, Si, and Ni are as follows:

$$5.4 : 4.8 : 2.6 : 1 = \text{Ag} : \text{Al} : \text{Si} : \text{Ni}. \tag{4}$$

The values of the logarithmic decrement at 40°C for the various solutes obtained at a strain amplitude of 5×10^{-6} are given in Table 5, and these decrements are plotted against concentration in Fig. 1. It is seen that the experimental trends corroborate the theoretical predictions in regard to the effectiveness of the various solutes in pinning the edge type

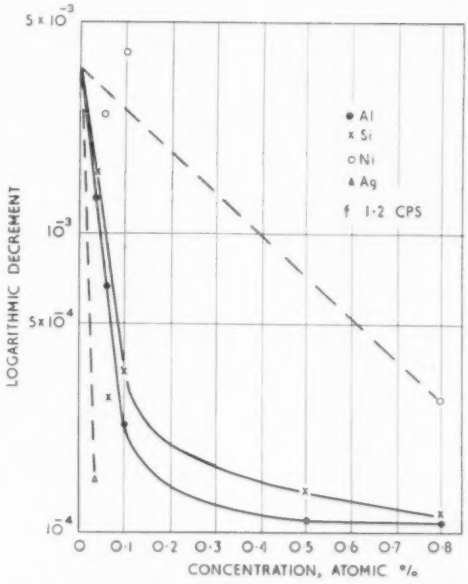

FIG. 1. Variation of logarithmic decrement with solute concentration at 40°C.

of dislocations. If the initial slope of the decrement against concentration curve for each solute is calculated, the ratios are as follows:

$$4.6 : 3.4 : 1 = \text{Al} : \text{Si} : \text{Ni}. \tag{5}$$

Comparison of these values with the ratios computed from Cottrell's analysis of the interaction between solute atoms and edge dislocations gives good agreement. A significant point is that the electrical interaction has generally been considered to be a second-order reaction, but these results indicate that it may be appreciable in the case of a four-valent atom interacting with a dislocation in a

TABLE 5. Logarithmic decrements measured at 40°C at 1 c.p.s.

Specimen (at. per cent)	Logarithmic decrement
0.03 Al	1.3×10^{-3}
0.06 Al	6.7×10^{-4}
0.10 Al	2.3×10^{-4}
0.50 Al	1.1×10^{-4}
0.80 Al	1.1×10^{-4}
0.03 Si	1.6×10^{-3}
0.06 Si	2.8×10^{-4}
0.10 Si	3.4×10^{-4}
0.50 Si	1.4×10^{-4}
0.80 Si	1.1×10^{-4}
1.00 Si	8.0×10^{-5}
0.05 Ni	2.5×10^{-3}
0.10 Ni	4.0×10^{-3}
0.50 Ni	2.8×10^{-4}
0.03 Ag	1.5×10^{-4}

Note: These readings are accurate to ± 0.00003.

VOL. 4 1956

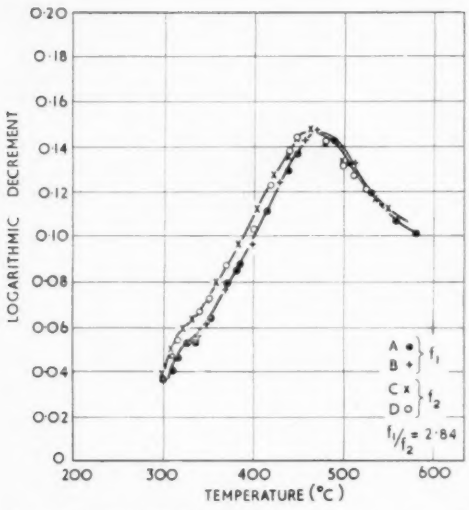

FIG. 2. Variation of internal friction with temperature for a 0.10 at. per cent Cu-Si alloy.

univalent metal. Although only one point has been obtained from a Cu-Ag alloy, it qualitatively confirms the theoretical expectations in that it is more effective than either the Al, Si, or Ni in depressing the logarithmic decrement.

If the Goldschmidt relation is considered, i.e., for a given metallic element the interatomic distance is about 12% less when the co-ordination number is 4 than when it is 12, then it is found that Si is about 2–3% larger than Cu. This difference cannot explain the magnitude of the Si-atom interaction with the dislocations, and hence gives further support to the possibility of an electrical interaction.

It is interesting to note that a saturation value is

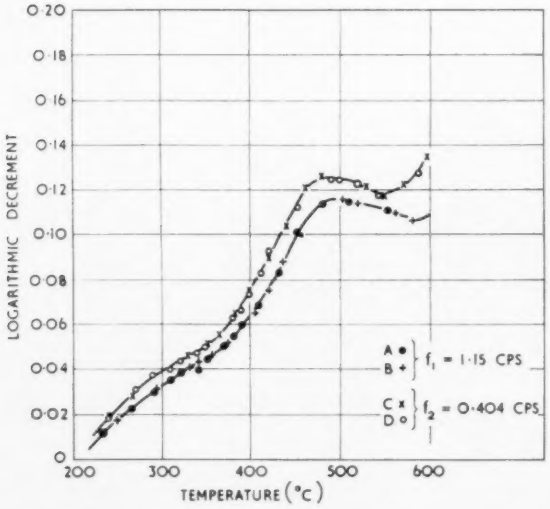

FIG. 3. Variation of internal friction with temperature for a 0.10 at. per cent Cu-Al alloy.

reached for the logarithmic decrement at approximately 0.1–0.2 at. per cent Al. This decrement of 10^{-4} could not be the lower limiting value obtainable with the high-vacuum torsion pendulum as values of the logarithmic decrement of 3×10^{-5} have been obtained. If the same criterion is used for the pinning as for the yield point, i.e., the concentration should approach unity at the sites in the center of the dislocation, then the overall concentration in the specimen required for appreciable lowering of the decrement may be calculated from the following formula:

$$c = c_0 \exp(+V/kT.) \qquad (6)$$

where c_0 is the bulk concentration and c is the excess concentration at the dislocation. Utilizing the interaction energy V for Al given in Table 4, and a

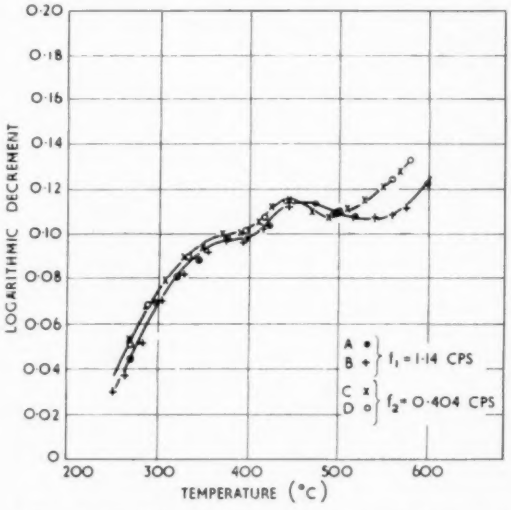

FIG. 4. Variation of internal friction with temperature for a 0.06 at. per cent Cu-Si alloy.

temperature of 300°K, a concentration of approximately 0.21% results which is in good agreement with the empirical value obtained from the curve of the decrement against concentration.

Note added in proof.

Further experiments and theoretical considerations indicate that the concentration should not be unity at the sites in the center of the dislocation. However, the magnitude of the result is not appreciably changed by the modification. The authors discuss this point more fully in a forthcoming paper.

HIGH-TEMPERATURE EFFECTS

If the background internal friction which is manifested at higher temperatures than the grain-boundary stress relaxation peak is examined for equal atomic

per cents of Si and Al in Cu (Figs. 2 and 3), it is noted that the Si appears to be the more effective in diminishing the decrement. A reversal in the order of effectiveness between the Al and Si in lowering the logarithmic decrement of the Cu seems to have occurred.

An activation energy was obtained for the background internal friction observed above the grain-boundary peak in an 0.06 at. per cent Cu-Si alloy (Fig. 4). The energy of activation was calculated from the relaxation spectrum for horizontal displacement of two different frequencies of measurement, and the resulting value was $25{,}000 \pm 3000$ cal/mole. This value of the activation energy is in good agreement with the average value of 26,500 cal/mole which Pearson obtained for various binary copper alloys over a range of solute composition.[9]

The subject of high-temperature pinning and the source of the background contribution to the relaxation spectrum will be the subjects of further investigation.

SUMMARY AND CONCLUSIONS

1. The logarithmic decrement measured at 1 c.p.s. and 40°C is strain-amplitude dependent, and hence may be associated with the static-hysteresis phenomenon of dislocation motion.

2. The effect of successive annealing is to diminish the room-temperature logarithmic decrement, presumably due to oxygen atoms diffusing through the dislocation pipes and pinning the edge type of dislocations.

3. The magnitude of the internal friction observed at low temperatures, e.g., 40°C, is a function of the solute concentration and the total interaction energy between the solute atoms and the edge type of dislocations.

4. Electrical interactions between solute atoms and Taylor dislocations are shown to be significant in their effect upon dislocation pinning. The experimentally obtained values are somewhat greater than the approximate theoretical values of Cottrell, Hunter, and Nabarro.

5. An activation energy of 25 kcal/mole was obtained for the high-temperature background contribution to the relaxation spectrum.

ACKNOWLEDGMENTS

The authors wish to acknowledge the valuable assistance of Gerald Pincus in the experimental phase of the research.

This research was supported by the United States Air Force, through the Office of Scientific Research of the Air Research and Development Command.

REFERENCES

1. T. A. READ, *Trans. Amer. Inst. Met. Engrs.*, **143,** 30 (1941).
2. A. S. NOWICK, *Progress in Metal Physics*, **IV,** 1.
3. S. WEINIG and E. S. MACHLIN, *J. Metals*, to be published.
4. S. WEINIG, *Rev. Sci. Instrum.*, **26,** 91.
5. A. S. NOWICK, *J. App. Phys.*, **25,** 1129.
6. T. S. KE, *J. App. Phys.*, **20,** 274 (1949).
7. A. COTTRELL, *Relations of Properties to Microstructure*, A.S.M. publication 131 (1953).
8. H. J. AXON and W. HUME-ROTHERY, *Proc. Roy. Soc.*, **A193,** 1.
9. S. PEARSON, Royal Aircraft Establishment, Farnborough, Hants. Report No. Met. 67.

VOL. 4 1956

MECHANISM OF WHISKER GROWTH—III
NATURE OF GROWTH SITES*

S. S. BRENNER and G. W. SEARS†

A mechanism is described for the formation of whiskers on a crystal which is growing by vapor deposition. A necessary condition is the existence of diffusion-limited transfer of material or heat. The mechanism is supported by Brenner's observations that metal whiskers formed by vapor-phase reduction invariably grow from previously deposited material.

MÉCANISME DE CROISSANCE DES BARBES—III
NATURE DES SITES DE CROISSANCE

Un mécanisme est décrit pour la formation des barbes sur un cristal qui grossit par dépôt de vapeur. Une condition nécessaire est l'existence d'un transport limité par diffusion de matière ou de chaleur. Le mécanisme est appuyé par les observations de Brenner, d'après lesquelles des barbes de métaux formés par réduction de la phase vapeur, grossissent indépendamment de la matière préalablement déposée.

MECHANISMUS DES WHISKER-WACHSTUMS—III
NATUR DER WACHSTUMSSTELLEN

Es wird ein Mechanismus für die Bildung von "Whisker" auf einem aus der Dampfphase wachsenden Kristall beschrieben. Eine notwendige Bedingung ist dabei das Vorhandensein eines durch Diffusion begrenzten Material- oder Wärmeübergangs. Der Mechanismus wird durch die Beobachtungen von Brenner gestützt, nach denen durch Reduktion aus der Dampfphase gebildete Metall-Whisker ohne Ausnahme aus dem vorher abgeschiedenen Material heraus wachsen.

The growth of crystalline whiskers from the vapor phase was first observed with mercury.[1] Since the whisker-growth occurred at supersaturations insufficient for two-dimensional nucleation, it was postulated[2] that the whiskers were perfect except for a single axial-screw dislocation. Thus, the whisker grew axially by the Frank mechanism[3] at constant diameter. A number of other crystalline substances in the form of whiskers have since been grown by deposition[4, 5] from the pure vapor phase. A large variety of crystalline whiskers also have been grown by vapor-phase reduction of metallic salts.[6]

Although the growth-behavior of a crystal bearing a single screw dislocation has been satisfactorily rationalized, the nature of the growth site and the mechanism of formation of the whisker have not been fully described. It has been postulated in the growth of mercury whiskers[2] that the whisker inherited its screw dislocation from a tiny devitrification crystallite in the pyrex condensing surface.

A second mechanism of whisker formation has been used to explain the growth of potassium-halide rods[7] from aqueous solution. The potassium halides are known to nucleate heterogeneously on nucleation catalysts. When the halide nucleus grows around its impurity particle, occasionally a single screw dislocation is generated. The resulting halide crystallite bearing a single screw dislocation grows at constant radius to form a rod. The generation of screw dislocation by growth around foreign particles has been previously described.[8]

It is the purpose of the present paper to postulate a third mechanism of whisker formation for systems in which diffusion of either material or heat is the limiting factor for crystal growth.

It is recognized that any real surface presents screw dislocations and therefore acts as a deposition-sink at low supersaturations. When such an imperfect crystal face is immersed in its own sufficiently supersaturated vapor in the presence of a foreign gas, deposition will occur at screw-dislocation steps. The vapor concentration in the neighborhood of the advancing face will decrease. The concentration gradient normal to the growing face will become less steep.

If the actual vapor pressure at the surface is p and the equilibrium vapor pressure is p_0, the supersaturation ratio α is defined as p/p_0, and the supersaturation σ is defined by

$$\sigma = \alpha - 1. \tag{1}$$

The supersaturation at the growing face is very small, $\sigma \sim 0.01$, only sufficient to cause growth by

* Received September 26, 1955.
† General Electric Research Laboratory, Schenectady, New York.

the Frank mechanism. Screw dislocations, which are closely spaced, will yield a smoothly advancing surface. The occasional screw, which is somewhat separated from its nearest neighbor, will form a growth cone as shown in Fig. 1. The gradient in vapor concentration is schematically shown with three densities of dots.

As the summit of the cone rises, it no longer depends on unidimensional diffusion to grow. It begins to rob the growth steps at its base of their share of diffusing molecules. Slowly it approaches a spherical diffusion configuration. The more it deviates from linear diffusion, the faster it grows. The more it outgrows its base, the more nearly it

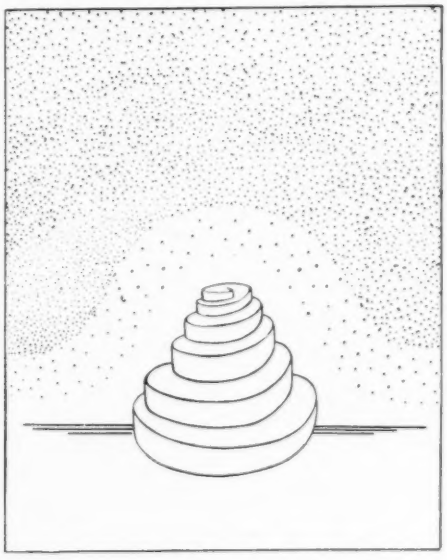

FIG. 1.

grows by spherical diffusion. The process is self-propagating. In Fig. 2 the growth cone is shown in an intermediate stage of growth. Since the diffusion rate is faster to the summit of the cone, the distance between steps is less and a tapered hill is produced.

In Fig. 3 the growth cone has reached the stage of having a columnar summit. The growth steps are widely spaced at the base and closely spaced on the tapered section. The top tapers to a uniformly cross-sectioned whisker.

When the summit has moved well out from the original surface and has attained a uniform cross-section it will grow in length at a constant rate. The whisker should thicken simultaneously as layers grow upwards from the shank. The base crystal will slowly advance and overgrow the original tapered base.

The ultimate cross-section of a whisker will be a

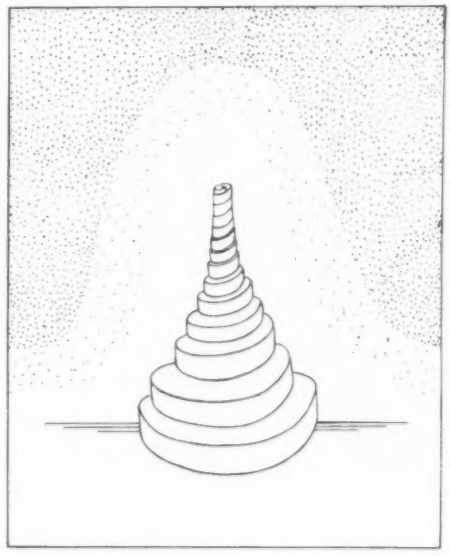

FIG. 2.

function of supersaturation and rates of gaseous and surface diffusion. There will be an initial critical supersaturation, σ_c, necessary to grow a whisker from a screw dislocation characterized by its least separation distance R from neighbors. As R decreases, the necessary critical supersaturation to grow a whisker at this site increases. In practice, higher initial supersaturations will yield more closely spaced whiskers. There will be, however, an upper limit of supersaturation at which whiskers will form at all. The individual screw dislocations spaced too closely or exposed to an excessive supersaturation

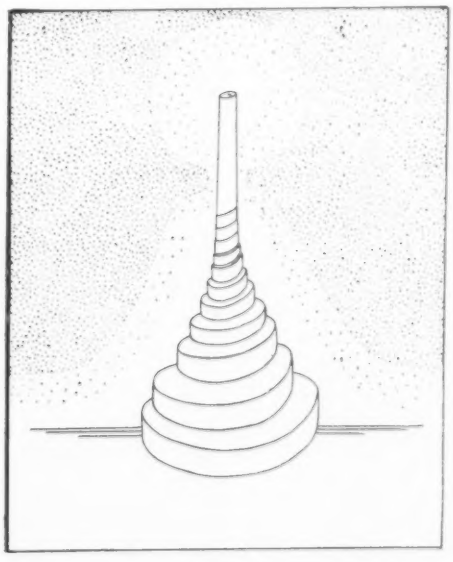

FIG. 3.

VOL. 4 1956

will not form growth cones, but will cause the surface to advance continuously.

The proposed mechanism of whisker formation is supported by the observation of Brenner[4] that metal whiskers formed by vapor-phase reduction invariably grow from previously deposited metal. The behavior has been observed for copper, iron, nickel, cobalt, gold, and platinum. In these experiments the freshly formed metal vapor diffused through hydrogen to reach the deposition surface. Material transport was therefore limited by gaseous diffusion.

Brenner also observed that whiskers would only grow at calculated supersaturations far in excess of the critical value for two-dimensional nucleation. The proposed mechanism would only yield a prolific growth of whiskers at very high initial supersaturations. The supersaturation at the growth steps is very low, and the high supersaturation implies there only a steep concentration gradient. Further evidence for the high supersaturations in the vapor-reduction experiments is furnished by frequent evidences of overgrowth on whiskers.

It should be noted in conclusion that the proposed mechanism of whisker growth is merely a description of dendritic growth from the vapor phase.

REFERENCES

1. G. W. Sears, *Acta Met.*, **1,** 457 (1953).
2. G. W. Sears, *Acta Met.*, **3,** 361 (1955).
3. F. C. Frank, *Disc. Faraday Soc.*, **5,** 48 (1949).
4. G. W. Sears, *Acta Met.*, **3,** 367 (1955).
5. W. Piper and W. Roth, *Phys. Rev.*, **92,** 503 (1953).
6. S. S. Brenner, *Acta Met.*, **4,** 62 (1956).
7. J. B. Newkirk and G. W. Sears, *Acta Met.*, **3,** 110 (1955).
8. J. C. Fisher, R. L. Fullman, and G. W. Sears, *Acta Met.*, **2,** 344 (1954).

VOL
4
195

AN EXPERIMENTAL INVESTIGATION ON THE MODE OF SLIP IN α-BRASS*

H. WILSDORF and J. T. FOURIE†

Replicas showing slip lines on α-brass are examined with the electron microscope in order to decide whether slip in this metal is "homogeneous" or "inhomogeneous," i.e., whether it takes place in atomistic steps on many successive atomic planes or in big steps on single atomic planes. The replicas used are subjected to a critical examination, to assess the reliability of measurements obtained from them.

Five different methods are used. In four of these, slip lines selected at random are investigated, while in the fifth the average shear of all slip lines present on the portion of the specimen is deduced from that fraction of the surface which appears to be covered with slip lines when viewed perpendicularly. All five methods lead to the result that slip in α-brass is inhomogeneous.

RECHERCHES EXPERIMENTALES SUR LE PROCESSUS DE GLISSEMENT DANS LE LAITON α

Des répliques montrant des lignes de glissement sur du laiton α ont été examinées au microscope électronique en vue de déterminer si le glissement est homogène ou hétérogène, c'est-à-dire s'il procède par bonds unitaires sur de nombreux plans atomiques successifs, ou par glissements importants sur quelques plans atomiques bien déterminés.

Les répliques utilisées sont soumises à un examen critique pour s'assurer de la valeur des mesures obtenues.

Cinq méthodes différentes ont été employées. Pour quatre d'entre elles, des lignes de glissement arbitrairement choisies sone examinées. Dans la cinquième, on a examiné la face perpendiculaire à celle contenant les lignes de glissement. La valeur moyenne du cisaillement de toutes les lignes de glissement est déduite de la fraction de surface où apparaissent les traces de ces lignes de glissement.

EINE EXPERIMENTELLE UNTERSUCHUNG ÜBER DIE ART DER GLEITUNG IN α-MESSING

Mit dem Elektronenmikroskop wurden Abdrücke von Gleitlinien auf α-Messing untersucht, um zu entscheiden ob die Gleitung in diesem Metall "homogen" oder "inhomogen" ist, d.h. ob sie in atomistischen Stufen auf vielen aufeinanderfolgenden Atomebenen oder in grossen Stufen auf einzelnen Atomebenen erfolgt. Die verwendeten Abdrücke wurden einer kritischen Prüfung unterzogen, um die Zuverlässigkeit der von ihnen erhaltenen Messungen abzuschätzen.

Fünf verschiedene Verfahren wurden angewendet. In vier von ihnen wurden Gleitlinien untersucht, die wahllos herausgegriffen waren, während in dem fünften die durchschnittliche Scherung aller auf einem gewissen Probenabschnitt vorhandenen Gleitlinien erhalten wurde, wobei der Bruchteil der Oberfläche, der senkrecht von oben betrachtet mit Gleitlinien bedeckt erscheint, in die Betrachtung eingeht. Die fünf Verfahren führen übereinstimmend zu dem Ergebnis, dass die Art der Gleitung in α-Messing inhomogen ist.

VOL. 4 1956

1. INTRODUCTION

In previous investigations concerning the process of translation and of slip-band formation it has usually been presupposed that slip takes place on single atomic planes, separated by layers of undeformed material. More recently it was shown by electron microscopy that the slip bands on aluminum,[1] seen as single lines in the light microscope, are in reality series of lamellae, and later the same phenomenon was also observed on silver, copper, and lead.[2, 3] Nevertheless, the idea of slip on single atomic planes was not radically altered, but it was generally assumed that the slip between the lamellae took place on single planes, with no slip within the lamellae. Yakutovitch, Yakovleva, Lerinman, and Buinov,[4] however, who repeated the work of Heidenreich and Shockley on aluminum, came to the conclusion that the slip between the lamellae in a band was composed of one-unit slip-step each, in a series of adjacent atomic planes. Suzuki and Fujita[5, 6] were led to the same view by theoretical as well as experimental investigations, and claimed that in face-centered cubic metals generally—including α-brass—homogeneous slip, i.e., slip in the form of one atomic glide step in each of a number of successive planes, takes place almost exclusively. Bilby,[7] in a theoretical examination of possible dislocation sources, found sources which would lead to homogeneous slip, as well as sources which would lead to slip on single atomic planes, and showed that the number of sources of the two types should be roughly equal. Thus it appears desirable that conclusive experimental evidence should be obtained for the type of slip which actually occurs, whether it be homogeneous, or slip on single atomic planes. In the following, the terms "homogeneous" and "inhomogeneous" slip will be used respectively for slip

* Received August 26, 1955.

† National Physical Laboratory, South African Council for Scientific and Industrial Research, Pretoria.

on successive atomic planes, in the sense of the above authors, and for slip on a single atomic plane.

In transmission electron microscopy, which appeared to be the best available method for this investigation, surface phenomena are examined by means of replicas. The resolution of electron microscopes, and, even more important, of the replicas, is, however, not sufficient to resolve the slip steps of a few angstroms height and width which are to be expected for homogeneous slip. Fortunately, other methods exist by means of which it is possible to distinguish between the two types of slip. These are all ultimately based on an investigation of whether or not an angular difference exists between the slip plane and the surface exposed within the slip zones.

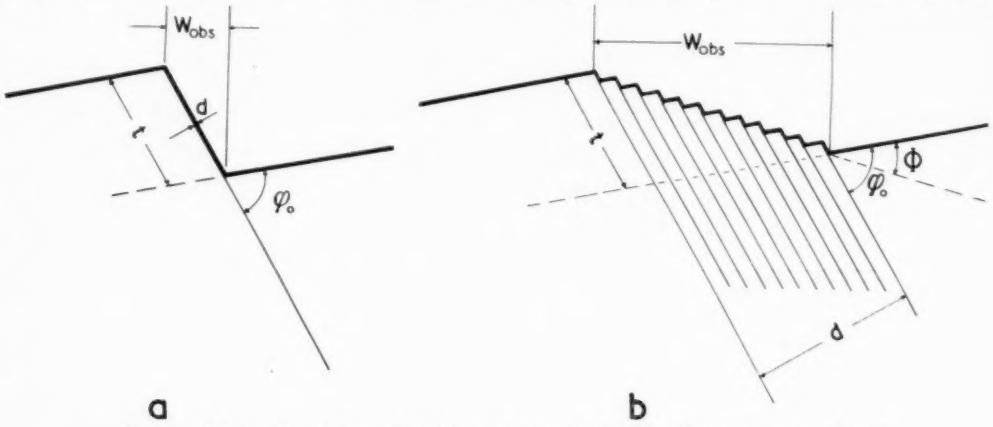

FIG. 1. Two modes of slip: (a) "Inhomogeneous" slip of a distance t on *one* plane; (b) "Homogeneous" slip on a *number* of neighboring (111) planes, with a total slip distance of t.

The problem is demonstrated in Fig. 1. Slip on an individual atomic plane is schematically represented in Fig. 1(a), homogeneous slip in Fig. 1(b). It is immediately evident that the angle between the newly-formed surface and the crystal surface is different in the two cases. In Fig. 1(a) this angle is equal to that between the slip plane and surface as determined by X-rays, while in Fig. 1(b) the angle is smaller. As the slip steps on the pure metals so far investigated rarely exceed 1000 Å, these metals are unsuitable for the present experimental investigation, and instead, α-brass was chosen, which exhibits steps with slip of up to and even exceeding 10,000 Å.

Since the micrographs are obtained from replicas, and not directly from the surfaces, it proved necessary to examine the extent to which peculiar properties of the replicas have to be taken into account in order to avoid possible misinterpretation of the photographs.

2. EXPERIMENTAL PROCEDURES

(i) *Preparations of Samples*

Single crystals of α-brass were prepared by the Bridgman method of gradual solidification from the molten state[8] in an inert atmosphere of argon or nitrogen. Cartridge brass, containing 71% copper and traces of Fe (<0.01%), Pb (<0.01%), and Ni (<0.03%), was melted in a pointed graphite crucible 120 mm long and of a uniform rectangular cross-section of $1.3 \times 3\ \text{mm}^2$. The crucible was cooled from the point upwards, so that the crystal grew at a rate of about 5 cm per hour. Analysis of the composition of single crystals, carried out on sections taken from both the lower and upper portions, showed the final composition to be 79% copper, with a variation of approximately 1% over the length of the sample. The orientations of the crystals, before and after extension, were determined by means of Laue back-reflection photographs. Without any preliminary treatment, the crystal surfaces were polished electrolytically in a bath of 35% H_3PO_4.[3] A small tensile machine was used for extending the crystals, and the rate of deformation was approximately 1% per second.

(ii) *The Production and Critical Examination of Replicas.*

One-step silicon monoxide replicas were used as described by Wilsdorf.[3] They were produced by the evaporation of SiO in a high vacuum on to the specimen. After removal of the SiO films from the crystal surface with a solution of 30% HNO_3 and 10% HCl in distilled water, they were washed, placed on specimen carriers, and shadow-cast with tungsten oxide at an angle of approximately 45°.

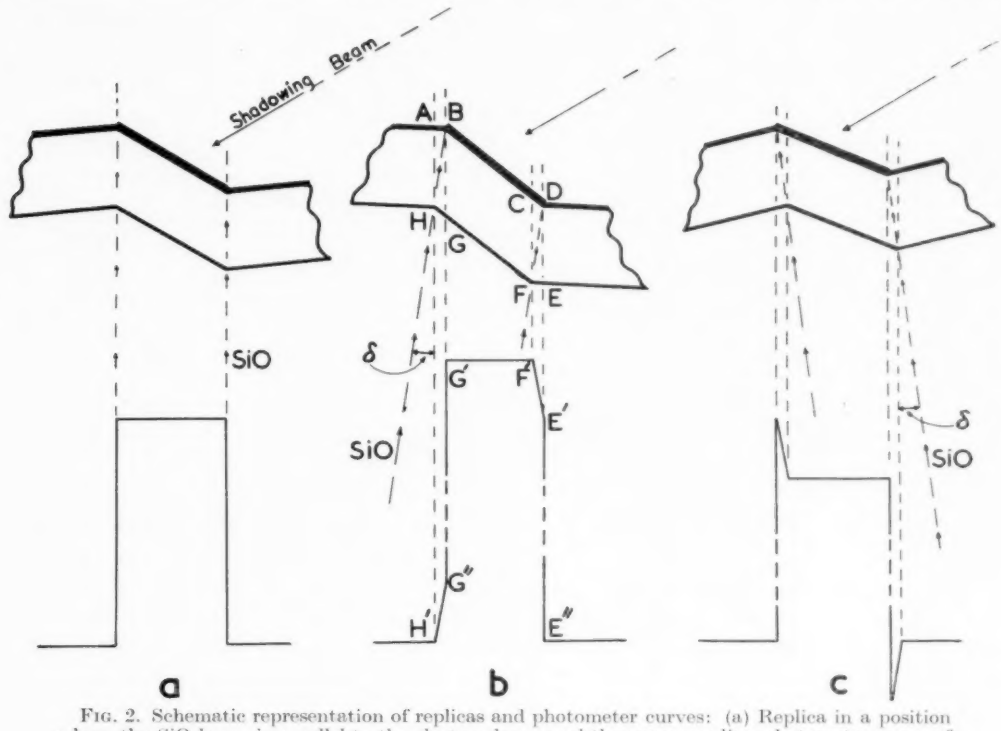

FIG. 2. Schematic representation of replicas and photometer curves: (a) Replica in a position where the SiO beam is parallel to the electron beam and the corresponding photometer curve of the final image. (b) and (c) As in (a), but replica rotated with respect to the electron beam.

VOL. 4 1956

The application of this replica method was preferred to others, as it yields a high resolution, and many replicas from any sample could be obtained with ease and certainty. The replicas, however, showed a slight irregular waviness when placed over a slit of area 1.0×0.1 mm^2 on the specimen carrier. Since it is the aim of the present investigation to obtain quantitatively reliable measurements, it was therefore necessary first to investigate whether artefacts are introduced by the replicas, and, in particular, what influence the waviness may have on the measurements.

The replicas were obtained by evaporating SiO under high vacuum *perpendicularly* onto the samples, which were placed at a distance of about 13 cm from the source. The length of the samples was usually approximately 5 cm, and consequently the angle of incidence at the extreme ends was no longer 90°, but about 80°. This deviation from normal incidence has to be considered as soon as the thickness of the replica exceeds 200 Å. Because of the very deep slip steps on deformed α-brass, together with the fact that these steps make angles of up to 80° or even more with the specimen surface, it was necessary to make the replicas much thicker than usual. If the thickness on a plane parallel to the surface is d, the replica thickness on a plane making an angle φ_0 with the surface is $d' = d \cos \varphi_0$. For $d = 700$ Å and $\varphi_0 = 70°$, then $d' = 240$ Å.

The artefacts which may be caused by these thick replicas after shadow-casting are discussed with the aid of Fig. 2. It is obvious that, in a direction parallel to the SiO beam, the thickness of the replica traversed by an electron beam is constant, and that there is no contrast due to the unshadowed replica. If, however, the electron beam deviates from this direction by an angle δ, which can happen either because of the finite dimensions of the sample, as mentioned above, or because of a bending in the replica after removal from the specimen surface, which thus induces the virtual SiO beam to deviate from the direction normal to the projection plane, the finite thickness of the replica begins to have an effect. The drawing represents the ideal case, where the SiO molecules do not undergo surface diffusion while subliming on the sample, thus forming sharp contours on both sides of the replica. From experiments carried out in a previous investigation,[3] this assumption seems to be justified. By means of the photometer curve in Fig. 2(a), the contrast in the final image of the shadowed replica in the case of $\delta = 0$ is shown, and in Fig. 2(b) and 2(c) the two types of $\delta \lesssim 0$ are demonstrated.

The density curve in Fig. 2(b) is easily understood.

For electron illumination to the right of ED, scattering which causes the normal background takes place. At ED, the variation in the tungsten oxide layer causes a sudden increase in scattering, and the density on the negative decreases sharply, causing the photometer curve to rise accordingly to the point E'. From points E to F there is a further increase in scattering, resulting from the change in thickness of the SiO layer in the direction of the electron beam, while from F to G it remains constant. Immediately to the left of G there is a sharp decrease in scattering, caused by the discontinuity in the thickness of the tungsten oxide film, while from G to H the scattering gradually diminishes to that of the background. It is obvious, from the description, that the right-hand side of the line will be clearly defined with respect to the background, while on the left the line will gradually fade into the background.*

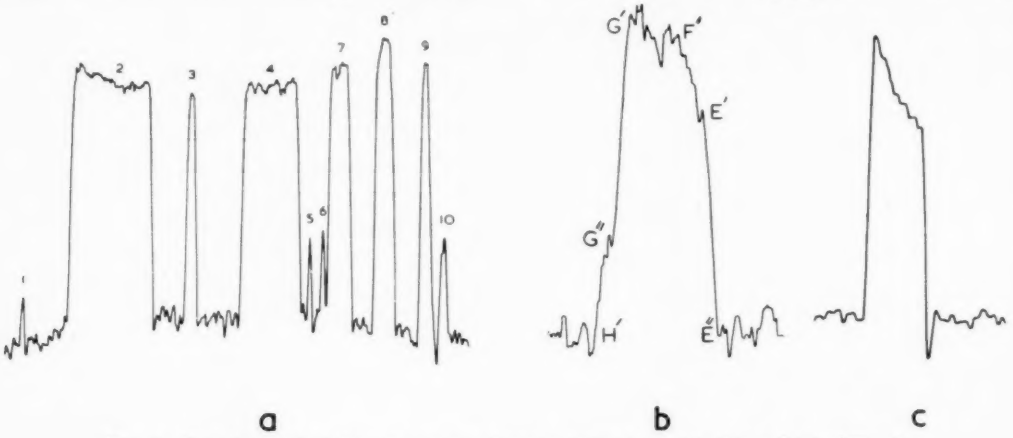

FIG. 3. Experimental photometer curves demonstrating cases (a), (b), and (c) of Fig. 2

The case where $\delta > 0$ can be explained in a similar manner. Here both sides of the line are sharply defined, one side being bordered by a white line, while the other edge shows greater scattering than the rest of the line.

From the curve of Fig. 2(b) it is immediately evident that any slip line which is smaller than CD will give a contrast which is lower than the maximum contrast of a wider line. The lower limit to the observed width of a line which will still give the maximum contrast can be expressed by

$$D_{\min} = Md_0 \sin \delta ,$$

where M is the magnification on the micrograph, d_0 the thickness of the replica, measured parallel to the SiO beam, and δ the angle between electron and SiO beam. For $d_0 = 700$ Å, $M = 20{,}000$, and $\delta = 10°$, $D_{\min} = 0.25$ mm. The formula neglects the resolution of the microscope, which will also have an effect on the minimum width of lines. Similar considerations apply to the curve in Fig. 2(c).

In order to test the validity of these arguments, replicas of a single crystal, showing large and small steps, were placed on specimen carriers in such a manner that the slip lines were parallel to the length of the slit. As it was possible to rotate the specimen holder about an axis parallel to this direction during operation of the microscope, photographs were obtained of the same spot but with the replica oriented in such a manner as to illustrate the different cases. Micrographs were taken with an attachment plate camera at a magnification of 20,000. Photometer traces obtained from the plates show approximately the curves predicted (Fig. 3). In Fig. 4 a micrograph is shown where the electron beam is nearly parallel to the molecular beam, i.e., for $\delta = 0$, while its photometer trace is reproduced in Fig. 3(a). The very fine lines show intensities which are lower than the maximum because of resolution effects of the electron microscope, the replica, and the photometer. Electron micrographs and their corresponding photometer traces demonstrating the effects of $\delta \lesssim 0$ are shown in Figs. 5 and 6, 3(b) and 3(c) respectively.

The above investigation is of great importance when considering the waviness of the replica. The waviness is actually caused by the superposition of two effects. The first is due to a slight ripple on the crystal surface produced during electrolytic polishing, while the second and more serious one is due to the replica film itself. The latter effect seems to come into existence when the replica is removed from the

* From a comparison of the thickness of the SiO layer (say 700 Å) and that of the tungsten oxide film (approximately 30 Å), it is clear that the geometrical effect caused by the latter is negligible in this discussion.

metal surface or while it is drying on the specimen carrier. Fig. 7 was obtained with an interference microscope, and gives an impression of the waviness which is present on the electrolytically polished surface of a deformed α-brass single crystal. The "wavelength" of the ripple is normally of the order of 1 mm. The waviness of the replica itself is demonstrated in Fig. 8 by an interferometer micrograph of a replica obtained from the cleavage plane of a rocksalt crystal. Here it can be seen that many crinkles are present over distances smaller than 0.1 mm, parts of the replica often making an angle of 10° or more with the plane of the specimen carrier. Replicas with line structures on them are, however, somewhat planer than the one shown in Fig. 8.

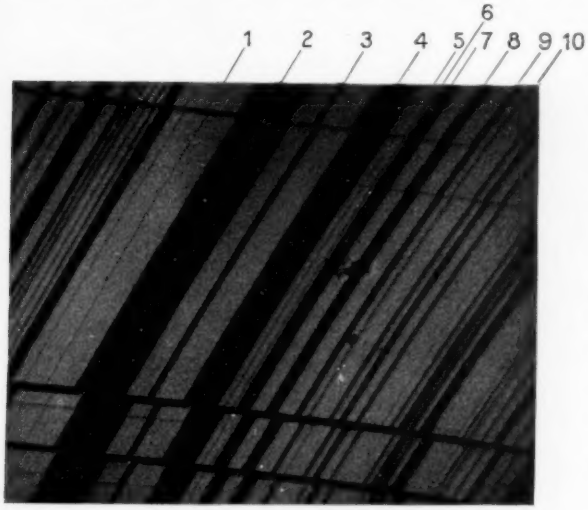

FIG. 4. Electron micrograph corresponding to 3(a); ×20,000. Elongation 51%.

From the above considerations it follows that conclusions which are based on the contrast of different slip lines in electron micrographs are not reliable and, further, that data which are concerned with geometrical measurements can be expected to scatter widely around the actual value.

3. OBSERVATIONS

(i) *A Method to Determine the Angle between the "Surface" of a Slip Line and the Crystal Surface, using Shadows cast by Spherical Particles*

A number of uniform spherical particles, brought on to the replica before shadow-casting, throw shadows which can be used to determine the angle between the surface exposed in the slip lines and the crystal surface, as has already been mentioned in a paper by Wilsdorf and Kuhlmann-Wilsdorf.[9] Here

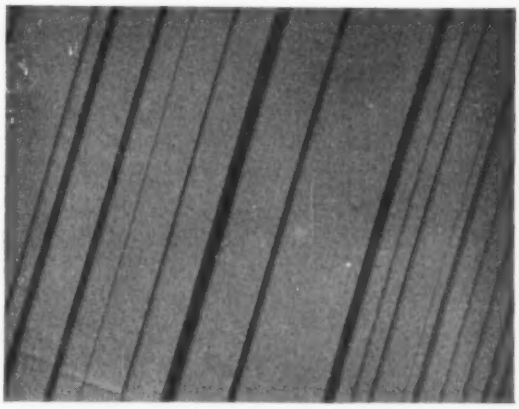

FIG. 5. Electron micrograph corresponding to 3(b); ×20,000. Elongation 15%.

use is made of the relative difference in length of shadows from two particles, situated near each other, and arranged so that the shadow of one falls on the undisturbed surface between the slip lines, while the shadow of the other crosses a slip line. Two particles are necessary because the angle of shadowing, with respect to the wavy replica, varies slightly from place to place and must be determined locally for each set of measurements. The first particle serves to determine the angle of shadowing, while the second determines the angle between the undisturbed crystal surface and the "surface" of a slip line.

In the following, the undisturbed sections of crystal surface between the slip lines after straining will be referred to as the "old surface," and the plane of the specimen surface after straining, i.e., the plane of the replica, which is at right angles to the electron beam in the microscope, as the "new surface." The term "surface of a slip line" will indicate the newly exposed surface within the slip

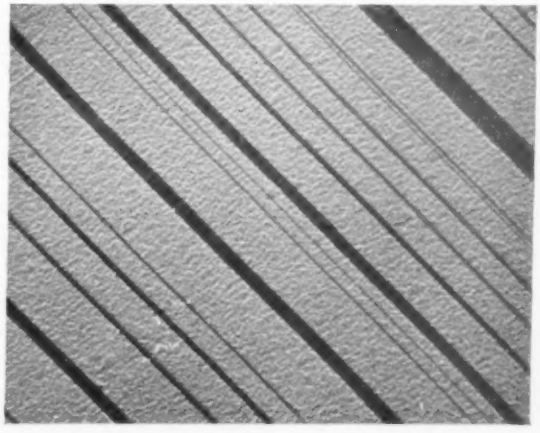

FIG. 6. Electron micrograph corresponding to 3(c); ×20,000. Elongation 15%.

VOL. 4 1956

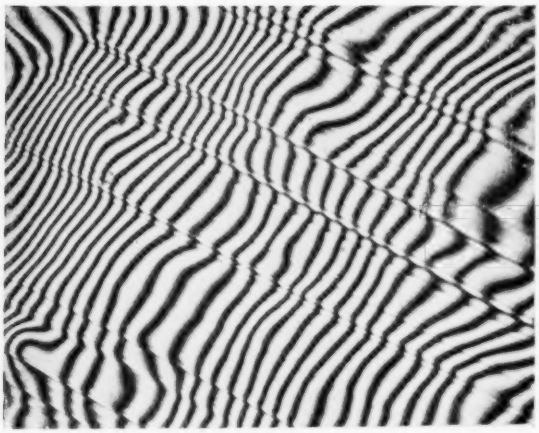

FIG. 7. Interference micrograph of an electrolytically polished α-brass single crystal surface after deformation. Tl light. ×530.

line. Obviously if slip should take place on one atomic plane only, the surface of the slip lines would be the slip plane, and the angle between the surface of the slip plane and the old surface would be found to be equal to φ_0, the stereographically determined angle between the slip plane and the surface. If, on the other hand, slip should take place in the form of "homogeneous" slip, the slip-line surface would make an angle with the crystal surface which would be considerably smaller than φ_0.

Figs. 9 and 10 give typical examples of photographs which are suitable for these measurements, while Fig. 11(a) and (b) illustrate the geometry of the method. The symbols used should be clear to the reader. The angle α, in particular, is the angle between the "new" and the "old surface" taken perpendicularly to the direction of the slip lines. It can be determined from Laue photographs taken

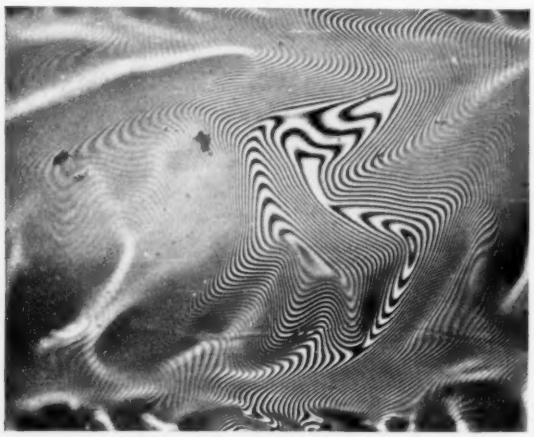

FIG. 8. Interference micrograph of a SiO replica, taken from a rock-salt cleavage plane. Tl light. ×530.

FIG. 9. An electron micrograph demonstrating the latex-particle shadow method for obtaining Φ, the angle between band "surface" and crystal surface. ×18,100.

before and after deformation. Except for the angle Φ to be determined, all other quantities such as shadow-lengths l'_1, l'_2, and l_3, the angle ξ, and the particle diameters d_1 and d_2, can be measured on the photograph.

A formula for the calculation of Φ from the measureable quantities follows from a fairly involved geometrical consideration of the problem which is given in Appendix I. Because of the rather complicated form of the final equation, this calculation is somewhat tedious. On the other hand, it is possible to find the angle Φ by a simple geometrical construction, illustrated in Fig. 11(b), which represents a section parallel to the shadowing beam and the shadow itself. Here AC is the old surface and $A'B'$ the new surface. These include the angle α', which, as can be seen from Fig. 11(a), can be expressed as $\tan \alpha' = \tan \alpha \cos \xi$, where ξ is the angle between the direction of the shadow and the normal to the slip lines in the plane of the new surface. The circle represents the particle which throws the shadow, and the direction of the shadowing beam is found as the tangent to

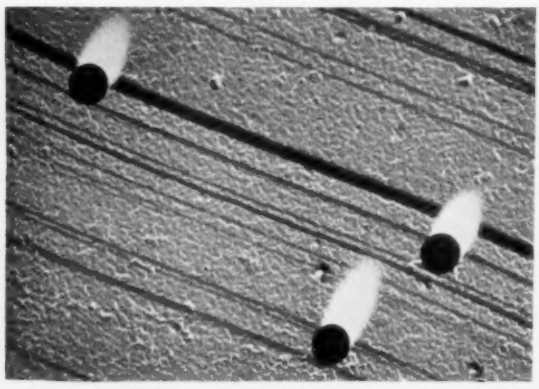

FIG. 10. As in Fig. 9. ×21,600.

the circle which cuts the direction of the old surface at a horizontal distance of l_1 from the center of the circle. The surface of the slip line in the direction of the shadow can then be represented by the line

number of measurements obtained from different replicas and different positions on them is taken. The effect of the waviness should be eliminated by taking the mean, while that of α' will remain. The

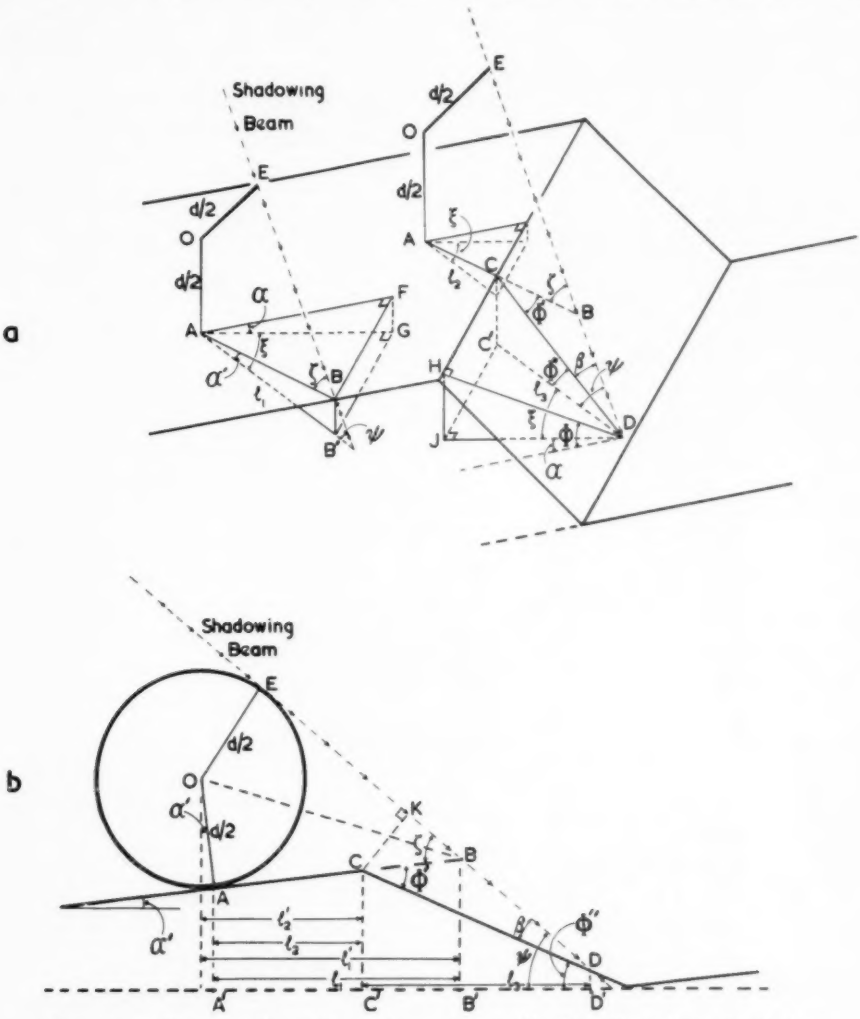

FIG. 11. (a) The geometry of the "latex-particle method" in three-dimensional view. For particles, only centers O and radii are drawn. (b) A section of the above, taken along the direction of the shadow, and containing the shadowing beam.

connecting C, the point on the old surface at a horizontal distance of l_2 from the center of the particle, with D, the point on the line representing the shadowing beam which has a horizontal distance of $l_2 + l_3$ from the center of the circle. To be quite exact, the point of contact of the circle and the line representing the old surface has to be substituted for the center of the circle in the above geometrical construction. Although the angular "waviness" of the replica is of the same order as α', the correction for the position of the point of contact of the particle and the surface is necessary when the mean of a

angle Φ'' thus found is connected with the actual angle between new surface and surface of the slip line by the equation $\tan(\Phi - \alpha) = \tan \Phi''/\cos \xi$.

In practice, the shadow of the particle used to determine the direction of shadowing often crosses one or two very narrow slip lines. In such cases a small correction has to be applied. Altogether twenty-eight slip lines of three different crystals were investigated by these methods.* The results are given in Table 1.

* The values obtained by the two methods agree to within 1°.

TABLE I

1	2	3	4	5
Crystal No.	Number of measurements	Extreme values of Φ	Average value of Φ	Angle determined by X-rays φ_0
25(1)	13	29°, 51°	39° ± 1.3°	39° ± 1°
11(2)	9	29°, 52°	42° ± 1.4°	40° ± 1°
4(6)	6	23°, 43°	35° ± 2.2°	34° ± 1°

In addition to the average values of Φ, the extreme values measured are also given in the table, since the scattering of the measurements is considerable.

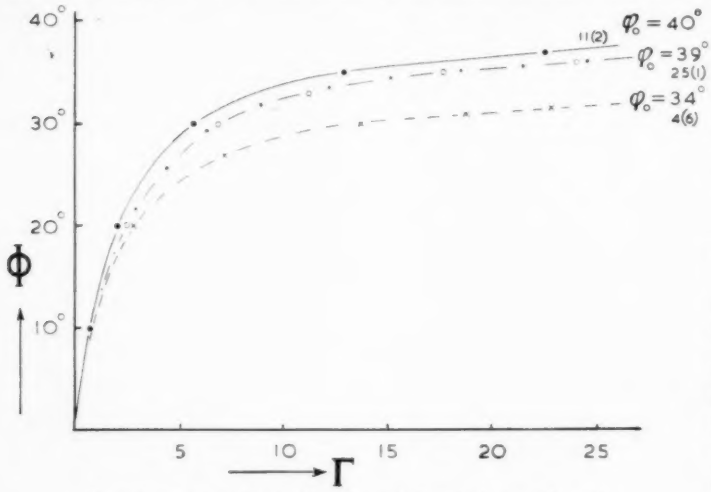

FIG. 12. Curves illustrating the relation between the net shear in bands Γ and Φ.

The error given in column 4 of the table is the probable error calculated from the measurements in the usual way. The chief source of error lies in the measurement of the respective lengths of shadows which are used in the calculations. Further errors are introduced by electrolytic polishing, which causes a rippled surface with angular variations from the mean surface, and by the wavy form the replica tends to take on after being removed from the sample surface. Consequently it seemed desirable, when measuring a single slip step, to find within what limits of experimental error it would be possible to make a distinction between homogeneous and inhomogeneous slip.

A sensitive criterion would be the determination of the shear Γ in a slip band from the above measurements, as Γ ought to be infinite in the case of glide on one plane only while it is close to 1 for homogeneous slip (Fig. 1). The relationship between Γ and Φ is given by

$$\Gamma = \frac{\cot(\varphi_0 - \Phi) - \cot\varphi_0}{\sin\Theta}$$

where φ_0 and Φ are used as defined above and Θ is the angle between slip line and slip direction. A graphical representation for the three crystals examined is given in Fig. 12. The curves show that Γ for the lowest measured values of Φ (column 3) is always higher than 4, while the lower limits of the mean values of Φ (column 4) correspond to a shear Γ of 50 or more.

In conclusion, it may be stated that, despite the wide scattering of the measurements, the average values of Φ and the angle φ_0, as determined by X-rays, coincide within the limits of the probable error, thus indicating inhomogeneous slip.

(ii) *A Method to Determine the Orientation of the Surface Exposed in Deep Slip Lines by Examining Slip Traces within Them*

Occasionally very deep slip lines are found, within which two sets of fine slip lines of other slip systems are visible, as shown in Fig. 13. Such cases afford a further method of distinguishing between homogeneous and inhomogeneous slip, for, if the slip in the deep band was of the inhomogeneous type, the surface exposed in it would be a (111) plane, on which the other sets of slip traces would include angles of 60°. If, on the other hand, the slip was of the homogeneous type, then the angle included by any two sets of slip traces would not be 60°.

Although this idea is very simple in principle, it is not altogether easy to use it quantitatively, because the angle in question is not directly measurable, but only its projection in the plane of observation. Furthermore, the angle between the crystal surface and the surface in the deep slip line is unknown. However, knowing the orientation of the crystal, and with the help of its stereographic projection, it is possible to calculate what the observed angle ρ' included by the slip traces, should be for any given angle between the slip-line surface and the projection plane. The calculated curve $\rho'(\Phi)$ is then plotted (see Fig. 14), and with measured values for ρ' the angle Φ is directly obtained from the graph. The method of calculating the curve is explained in Appendix II.

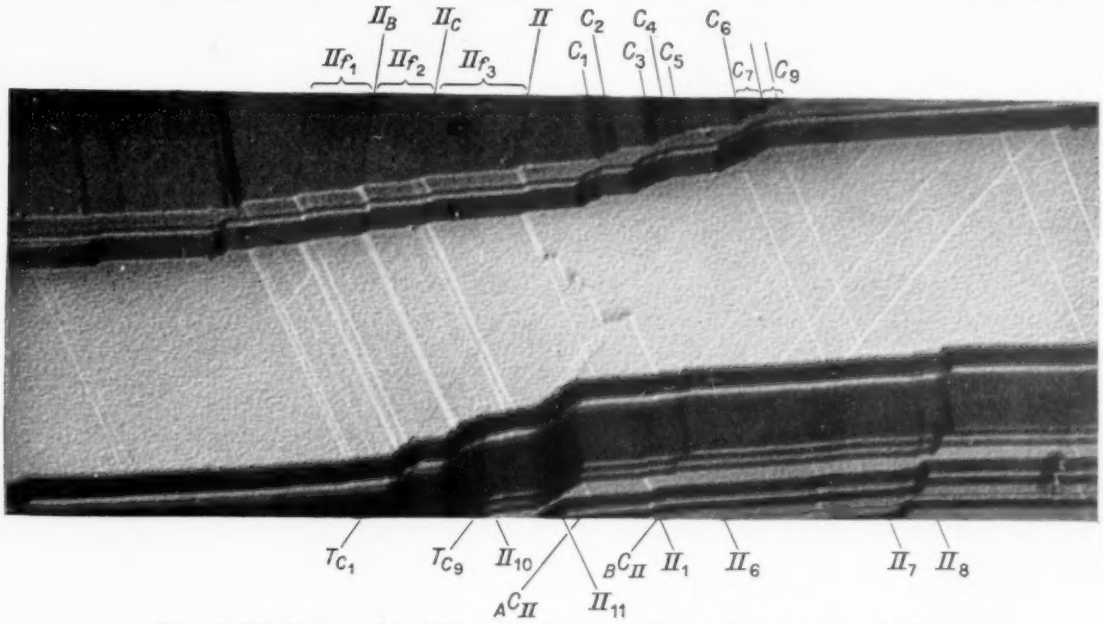

FIG. 13. Slip line caused by glide over a distance of about 2 microns, crossed by lines of the second and cross-slip systems; ×30,000. Elongation 38%.

The actual measurements were all obtained from crystal No. 24(1), which showed the desired deep slip steps. It was deformed up to $\epsilon = 38\%$, practically all in single slip, giving an angle φ equal to $45° \pm 1°$ with the angle Θ equal to 43°. All results are given in Table 2. It can be seen that the values for Φ are mostly somewhat smaller than $\varphi = 45°$, the angle which corresponds to ideally inhomogeneous slip. The authors believe that this is due to the random waviness of the SiO replicas discussed above, rather than to homogeneous slip. As the average value for Φ obtained by the measurements is 42°, this value deviates only 3° from the expected value for pure inhomogeneous shear. This deviation is only slightly bigger than the average error. Finally, the value which would be obtained in the case of homogeneous slip can be read from the curve $\Gamma(\Phi)$ in Fig. 14, namely $\Phi \simeq 15°$, which is well beyond the most extreme experimental value of Φ.

(iii) *Measurement of the Thickness of Slip Lines using Slip-line Intersections*

Wilsdorf and Kuhlmann-Wilsdorf[9] have described two methods by which the thickness of a slip band, i.e., the thickness D of the material perpendicular to the slip plane which takes part in the deformation, can be determined from measurements made at slip-band intersections. The formulae which are applicable and which have been derived in the paper mentioned, are

$$D_{II} = (W_{II} - T \cdot \tan \Theta_{II} \cos \varphi_{II}) \sin \varphi_{II} \qquad (1)$$

and

$$D_I = (W_I - X \tan \varphi_{II} \cot \varphi_I) \sin \varphi_I \qquad (2)$$

Here the symbols have the following meaning: Index I indicates the slip line which has been crossed; index II the slip line which arose later and crossed the first; φ is the angle between slip plane and

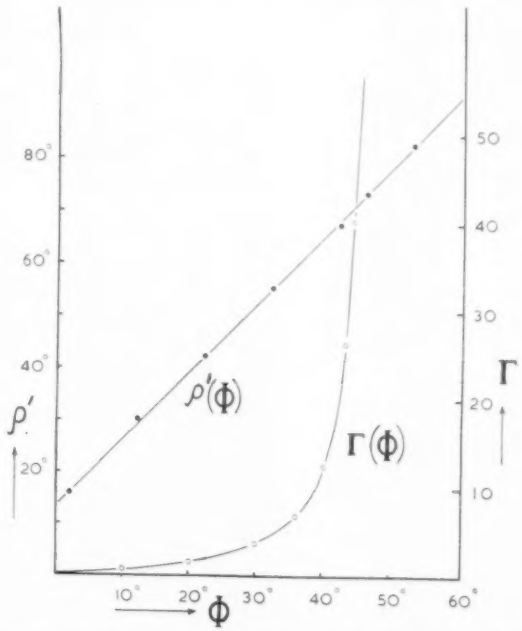

FIG. 14. The relation between ρ' (the observed angle between different sets of slip traces crossing a deep slip line) and Φ, and also between Γ and Φ, for crystal 24(1).

VOL. 4 1956

TABLE 2

1	2	3	4	1	2	3	4
No.	ρ' Observed angle between slip traces in slip band	Φ Angle between "new surface" and slip-band "surface"	$(\varphi - \Phi)$ Angle between slip-plane and slip-band "surface"	No.	ρ' Observed angle between slip traces in slip band	Φ Angle between "new surface" and slip-band "surface"	$(\varphi - \Phi)$ Angle between slip-plane and slip-band "surface"
1	67	42	+3	14	69	43	+2
2	66	41	+4	15	66	41	+4
3	60	36	+9	16	70	44	0
4	62	38	+7	17	77	48	−3
5	62	38	+7	18	66	41	+4
6	78	50	−5	19	61	37	+8
7	64	39	+6	20	62	38	+7
8	67	42	+3	21	73	46	−2
9	69	43	+2	22	62	38	+7
10	71	45	0	23	84	57	−12
11	71	45	0	24	73	46	−1
12	55	32	+13	25	67	42	+3
13	54	31	+14	26	74	47	−2

Probable error calculated from scatter of results: $\pm 1°$. Mean value of $\varphi - \Phi = 3° \pm 1°$; it should be noted that φ has been determined with an accuracy of $\pm 1°$.

surface; Θ is the angle between the slip direction and the direction of the line on the surface; W is the width of the slip line as observed; T is the lateral shift of the intersected slip line; and X is the apparent displacement of the cutting slip line at the intersection (Fig. 15).

A great number of photographs were studied in order to find suitable slip-line intersections. It soon became evident that the intersections between slip lines of the first and second systems were generally unsuitable. This is peculiar to brass, because in this case, unlike that of the pure metals previously studied, double slip is impeded and is in a large measure replaced by cross slip.[2] Thus the lines of the second system were too weak to allow even moderately accurate measurements of T and X. On the other hand, intersections between lines of the first system and lines of its own cross-slip system are rather frequent, and many were found to be suitable for the determination of slip-line thicknesses (see, for instance, Fig. 16). Altogether twelve intersections, all on the same crystal, were chosen, and for each of these the thicknesses of lines I and II were determined. The crossings were chosen only with a view of obtaining accurate measurements. Table 3 gives the result of these measurements. The scatter in the value of $1/\Gamma$ suggests a probable error of 0.004. Undoubtedly the scatter is due to errors in the measurements and to the waviness of the replica,

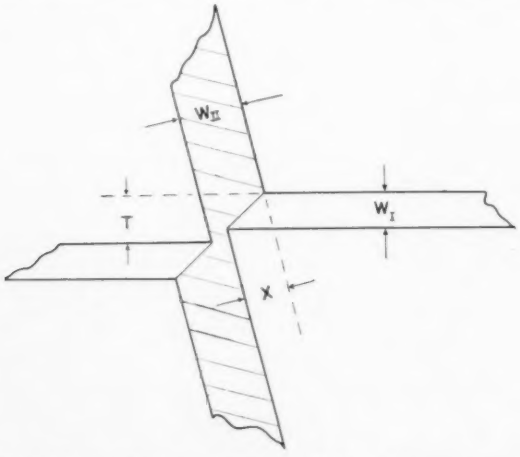

FIG. 15. Evaluation of Γ from slip-line intersections. T is the lateral shift of the intersected slip line (I), while X is the apparent displacement of the intersecting slip line (II).

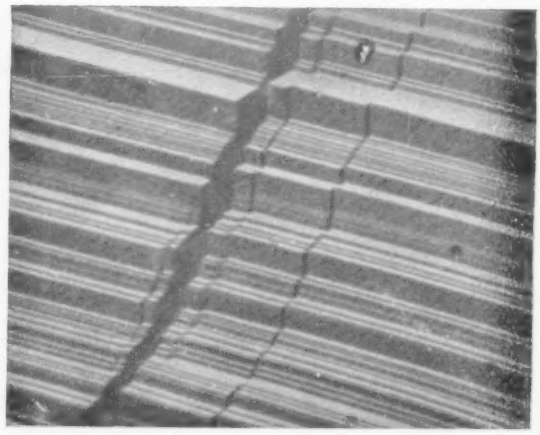

FIG. 16. Electron micrograph, suitable for determining Γ from the line intersection; ×20,000.

TABLE 3

Method 1						Method 2					
1	2	3	4	5	6	7	8	9	10	11	12
T Lateral shift of intersected slip line (mm)	W_{II} Observed width of slip line II (mm)	D_{II} Thickness of material perpendicular to slip plane which has taken part in the deformation (mm)	D_{II} (Å)	Γ Shear in slip band	$1/\Gamma$	X Apparent displacement of intersecting slip line (mm)	W_I Observed width of slip line I (mm)	D_I Thickness of material perpendicular to slip plane which has taken part in the deformation (mm)	D_I (Å)	Γ Shear in slip band	$1/\Gamma$
1.3	1.7	+0.07	+35	37	0.027	2.7	2.6	−0.07	−35	−80	−0.013
1.2	1.4	−0.05	−25	−48	−0.021	2.4	2.5	+0.07	+35	81	0.014
2.3	2.8	−0.014	−7	−330	−0.003	2.8	2.6	−0.14	−70	−41	−0.024
2.2	3.0	+0.212	+107	21	0.048	2.2	2.1	−0.07	−35	−66	−0.015
2.6	3.3	+0.085	+43	61	0.016	2.7	2.8	+0.07	+35	80	0.013
2.7	3.5	+0.13	+65	42	0.024	2.8	2.6	−0.14	−70	−41	−0.024
2.8	3.2	−0.16	−80	−35	−0.029	2.0	2.1	+0.07	+35	60	0.017
2.5	2.9	−0.11	−55	−45	−0.022	0.9	1.0	+0.07	+35	27	0.037
2.5	3.0	−0.04	−20	−125	−0.008	0.9	1.0	+0.07	+35	27	0.037
3.2	3.6	−0.23	−115	−28	−0.036	2.2	1.9	−0.21	−105	−22	−0.045
3.4	4.0	−0.113	−57	−60	−0.017	2.8	2.8	0	0	∞	0
2.0	2.8	+0.25	+125	16	0.062	2.5	2.2	−0.21	−105	−25	−0.040

All measurements were made on micrographs having a magnification of ×20,000.

VOL. 4 1956

as negative values for D could not be explained otherwise. The mean value of $1/\Gamma$ for all twenty-four measurements is -0.0002. For D it is -9 Å with a probable error of ± 10 Å for slip steps of approximately 1000-Å depth. Consequently it may be said that, in the group of twenty-four slip lines measured, the average shear corresponds to slip on one atomic plane only.*

(iv) *A Criterion for Homogeneous or Inhomogeneous Slip in connection with Slip-line Crossings*

The single quantitative measurements described in the preceding sections are subject to considerable error, due to the inaccuracy of the measurement itself, the waviness of the replica, and the ripples on the surface of the sample. It is, however, possible, by a simple argument, not involving measurements, to come to a conclusion as to whether a slip line has been caused by glide on a single atomic plane, or whether many atomic planes have acted in that region.

It is known from the geometry of slip in face-centered cubic crystals that the same slip direction belongs to both a slip system and its cross-slip system, and that this slip direction lies along the intercept of the two corresponding (111)-planes. Consequently, if either system crosses the other, no visible trace should be found along the junction of the relatively displaced sections of the initial slip line, since there is no component of slip perpendicular to the intersected slip plane which can be made visible by shadow-casting. Examples of this phenomenon are shown in Figs. 17, 18, 19, and 20, which are micrographs taken from different crystals. All the micrographs show areas where the first system was initially active, to be cut later by the cross slip lines, which in their turn leave no visible traces in the original lines. Naturally, the question as to which system was initially active does not affect the argument in this specific case, as any deviation of the initial slip-line surface from the position of the

* The term "one single atomic plane" is used throughout this paper for the sake of simplicity; it is realized that, say, three atomic planes may be involved in the slip process over these long distances, due to lattice irregularities.

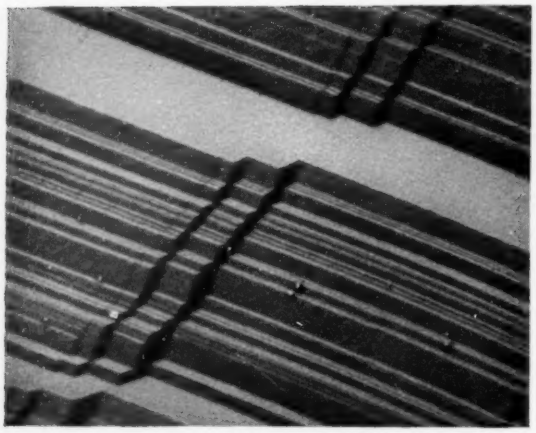

FIG. 17

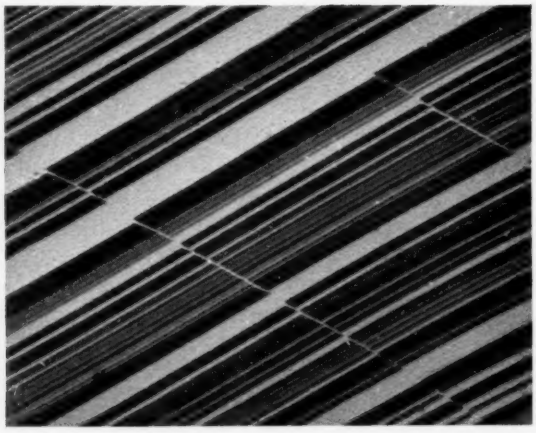

FIG. 18

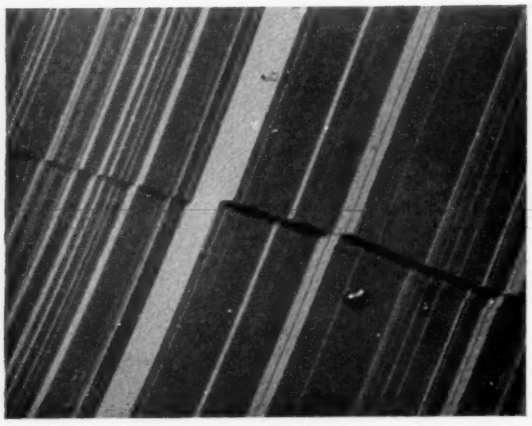

FIG. 19

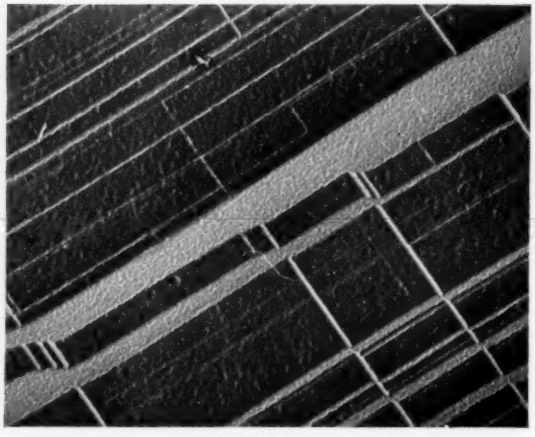

FIG. 20

FIGS. 17–20. Cross-slip lines intersecting deep slip lines of the first system, without leaving traces; all ×20,000.

(111)-plane would result in the formation of a visible trace by the crossing system.

Fig. 13 shows a micrograph of a slip line representing slip to the extent of about 2 μ (about 7000 atomic distances). It was felt that this micrograph merited a separate discussion, and it is explained with the aid of the descriptive Table 4. All the markings on the edges of the micrograph in Fig. 13 are continuations of lines, referring either to slip lines on the crystal surface (symbols on the top of the figure), or to lines on the newly exposed surface (symbols on bottom of the figure). In the descriptive table, the lines are listed in the order in which they took part in the slipping process.

The most remarkable feature of this photograph, from the standpoint of this paper, is the displacement of line II by the cross-slip lines C_2, C_3, C_4, C_6, C_7, and C_8, as drawn in detail in Fig. 21. This affords evidence that the cross-slip lines mentioned definitely acted *after* the formation of the big step. Although the direction of the shadowing beam was such that any steps on the slip plane should have been observed, these lines leave no visible traces on its undisturbed surface.* The only explanation for this phenomenon is that slip takes place on one plane only, over the entire slip distance of 2 μ which can be seen in the micrograph. However, a slip line which had been caused by the deepest cross-slip line in Fig. 13, on a plane deviating less than 5° from the (111)-plane, would not have been visible, due to limited resolution.†

* For the trace T_c see Table 4.

† The smallest deviation observable depends mainly on the depth of the cross-slip line, and in more favorable cases (e.g., Fig. 17) can be as small as 1°.

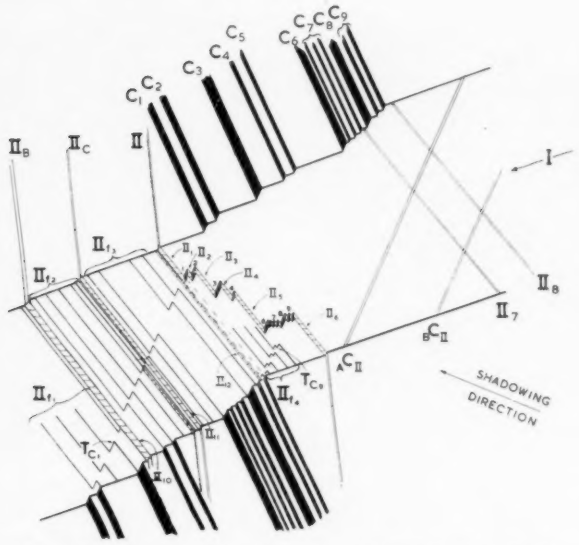

FIG. 21. Diagrammatical representation of the slipping processes in Fig. 13. The *very* fine lines in II_{f_1}, II_{f_2}, II_{f_3}, and II_{f_4} have been greatly enlarged for the sake of clarity, being hardly visible in Fig. 13.

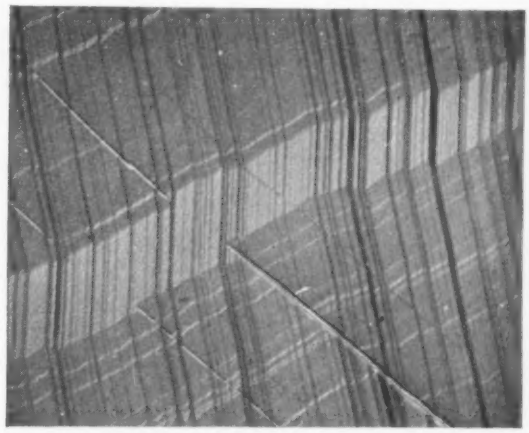

FIG. 22. A slip line formed by slip on the slip plane of the cross-slip system, but in a different direction, causes a visible trace when crossing a slip line of the first system. ×20,000.

In several micrographs of different crystals, examples were found where a system, which was active on the normal cross-slip plane, caused a clear and definite trace on the slip lines of the first system (Fig. 22); but in these cases the cross-slip lines were due to slip in a different direction. This is evident from the appearance of the two types of lines causing the phenomena, which always show a different measure of blackening.

(v) *Statistical Method*

In the previous paragraphs of this paper it has been shown that the examination by different methods of groups of individual slip steps consistently

TABLE 4

Line No.	Description (see micrograph Fig. 13 and Fig. 21)
I	Large white slip line, caused by first system ($\varphi_0 = 55°$, $\Theta = 43°$)
II	Faint black line, being in the direction of second-system lines on crystal surface, and hardly visible because $\Theta = 0$, $\varphi_0 = 68°$, and cuts across I (where $\Theta = 61°$, $\varphi_0 = 70°$), to form a trace II_1
II_1	Original position of the trace of II, caused by its crossing slip plane I
C_2, C_3, C_4, C_6, C_7, C_8, and junctions 2, 3, 4, 6, 7, 8	Cross-slip lines on crystal surface which cut across large slip plane I, displacing sections of II, alternatively, for distances equivalent to the black junctions 2, 3, 4, 6, 7, and 8 between the corresponding sections of II.
II_3, II_4, II_5	Sections of II_1, displaced by C_2, C_3, C_4, C_6
II_{f_1}, II_{f_2}, II_{f_3}, and II_{f_4}	"Bands" of second-system lines on I, which are all less than 100 Å in width, and closely spaced, forming in regions where black traces of C_1 and C_9 are observable
C_1 and C_9 and junctions 1 and 9. T_{c_1} and T_{c_9}	Cross-slip lines cutting I to form black junctions 1 and 9 between corresponding sections of II_1, and also black junctions between relatively displaced sections of fine lines in II_{f_1}, II_{f_2}, II_{f_3} and II_{f_4}, which then give the impression of black traces T_{C_1} and T_{C_9} on the slip plane
II_{10}, II_{11}, and others	White second system traces formed by lines such as II_A, II_B, and II_C
${}_AC_{II}$, ${}_BC_{II}$	Lines such as these belong to a system acting on the cross-slip plane and in the slip direction of the second system.
$*C_5$	Evidently this line crossed the slip plane I before II, as it did not displace II_1

* Order of activity is not in accordance with position in table. The fine white line II_{12} which crosses the large slip plane and almost coincides with the original position of II_1 before its displacement by the cross-slip lines, can only have been caused by slip after the latter event, as it has in no way been displaced.

VOL. 4 1956

led to a result which indicated that slip in α-brass is inhomogeneous, i.e., probably takes place on one atomic plane only. The result would, however, be even more conclusive if, instead of examining individual slip steps selected at random, one examined all the slip lines, irrespective of their depth, that appear on a certain area of the specimen. To attempt this by the methods described so far would involve an enormous amount of work, as it would be necessary to investigate hundreds of slip lines lying side by side. Fortunately, a statistical method is available in which the average shear in the slip bands on a specimen is calculated from the proportion of the surface of the specimen, which appears to be covered with slip lines when viewed from above. This method was developed for an earlier investigation of slip bands on aluminum,[9] and was adapted to the present study by the elimination of an approximation used in the earlier paper. The final formula used has the form

$$\frac{1}{\Gamma} = B \frac{(1+\epsilon)\sin\beta \cdot \sin\varphi_0}{(\sqrt{(1+\epsilon)^2 \cdot \sin^2\lambda_0} - \cos\lambda_0)\cos(\varphi_0 - \varphi) - \sin\Theta\{\sin\varphi_0 \cdot \cos\varphi_0 + \sin^2\varphi_0 \tan(\varphi_0 - \varphi)\}},$$

where B is the fraction of the surface which appears to be covered with slip lines when viewed from above, ϵ is the tensile strain, λ_0 is the angle between slip direction and axis before deformation, β is the angle between the direction of the slip lines on the surface and the axis after deformation, and φ_0, φ, and Θ have the same meanings as before. The derivation of the formula is given in Appendix III.

For the successful application of the statistical method, a number of precautions have to be taken: the specimen should be moderately strained, so that the value of B is not too small, and it should have slipped on one system only; also (this is most important) many photographs must be taken. The distribution of the slip lines is by no means uniform, but varies greatly over distances which are large compared with the field of view in a photograph taken at a magnification of say 20,000. In an investigation of slip lines, not made with the specific aim of finding a reliable value for B, photographs would be taken to show particular surface features such as cross slip, exceptionally deep slip steps, areas with unusually fine slip lines, etc., and not to show the average distribution of slip lines. Therefore, it would be useless to attempt the application of the statistical method to an arbitrary set of photographs, as for instance may be found in publications, but it is imperative that series of photographs be taken, showing adjoining surface areas, and covering as large a distance perpendicular to the slip lines as possible.

For these reasons the statistical method was used on a considerable number of photographs taken of a crystal with an angle φ_0 between the slip plane and the surface equal to 52°, and strained to $\epsilon = 15\%$. The total length of the areas investigated, measured perpendicularly to the slip lines, was more than 0.5 mm. The photographs with a magnification of 20,000 were obtained from fourteen replicas, taken from different parts of the specimen. In order to ensure further that a specimen with random slip-line distribution was obtained, each of the two authors took a number of photographs. The value of B was obtained by measuring every slip line appearing on the photographs, using a glass rule with 0.5-mm divisions. Again both authors took measurements and occasional checks showed good agreement. The width of the slip lines on the photographs varied between 0.1 and 2.6 mm, corresponding to an observed width on the replica of 50 to 1300 Å.

An independent check was made on the measurements by using photometer traces of the densities of slip lines, photographed on plates at a magnification of 20,000. The total area under all peaks was measured with a planimeter and, with the aid of a calibration curve obtained from measurements of wide and clearly defined lines, the equivalent slip-line width of this area was derived. The results obtained in this way were compared with the direct measurements taken from the photographic prints. Rather surprisingly, the values of B obtained from the photometer recordings deviated from the direct measurements, giving values which were from 1% to 15% lower than the direct measurements, with an average error of −6%. The reasons for this discrepancy are not entirely clear. As discussed in Section 2(ii), the contrast between the smallest slip lines and the undisturbed surface is less than for wider slip lines, resulting in lower peaks on the recordings. Since, with the planimeter, the area under the peaks is measured and not the half-peak breadth, this may be one reason for this phenomenon. Another possible reason is that an observer tends to make a small positive error in all measurements of line widths, when viewing lines on a darker or lighter background. Furthermore, there may be a slight error introduced when obtaining a print from a photographic plate, depending on the grade of paper taken. All in all, the average error of −6% seems entirely satisfactory, particularly when taking into account the narrowness of the average line.

TABLE 5

1	2	3	4	5
No. of replica	Length of area (μ)	B Fraction of surface covered with slip steps	Γ Average shear in slip steps	$\frac{1}{\Gamma}$
1	26	0.175	+4	+0.23
1	21	0.0164	−3	−0.37
2	6	0.106	−33	−0.03
2	28	0.202	+3	+0.33
3	56	0.150	+8	+0.13
4	60	0.106	−33	−0.03
5	28	0.119	+67	+0.02
5	20	0.154	+7	+0.15
6	23	0.105	−25	−0.04
7	24	0.137	+12	+0.08
8	21	0.157	+6	+0.16
9	27	0.0827	−8	−0.12
10	29	0.100	−17	−0.06
10	36	0.149	+8	+0.13
11	24	0.144	+9	+0.11
11	13	0.097	−14	−0.07
12	24	0.064	−5	−0.19
12	19	0.160	+6	+0.17
12	17	0.119	+67	+0.02
13	7	0.032	−3	−0.31
13	27	0.0567	−5	−0.22
14	7	0.0868	−9	−0.11
14	46	0.0868	−9	−0.11
$\epsilon = 15\%$		$\Theta = 38°$	$\lambda_0 = 38°$	
$\varphi_0 = 52°$		$\varphi = 44°$	$\beta = 47°$	

Table 5 gives the result of the direct measurements. The first column indicates the replica from which the photographs were obtained. Each line in the table refers to one series of consecutive photographs covering an area, with a length perpendicular to the slip lines, which is given in the second column. The fourth column indicates the average shear in the slip lines, as found from that particular series of photographs, by making use of the formula given above. Negative values indicate that, *if* the strain in the observed section of the specimen were exactly equal to the average strain of the specimen, which is obviously not true, the thickness of the slip lines, perpendicular to the slip plane, would be negative. In other words, less new surface is exposed than would have been the case if the strain had been caused by slip on one atomic plane only. This, of course, is physically impossible. Conversely, a positive value indicates shear which spreads over a certain thickness of material, as would have been the case in homogeneous slip proposed by Suzuki. However, it would appear that the real reason for the scatter in the values is a statistical variation of the strain, varying from place to place. To form an accurate idea of the average shear in the slip lines, it is necessary first to calculate the average value of B from all the photographs and then to insert it into the formula. When this is done, we find $B = 0.118$, with a probable error of about 6%, giving $\Gamma = 91$, while $B = 0.115$ is the theoretical value for slip on one atomic plane. The relationship between Γ and B can be seen from the curve in Fig. 23. Furthermore, by introducing the correction of −6% found from the photometer recordings, we obtain $B = 0.110 \pm 0.007$, in excellent agreement with the concept of inhomogeneous slip.

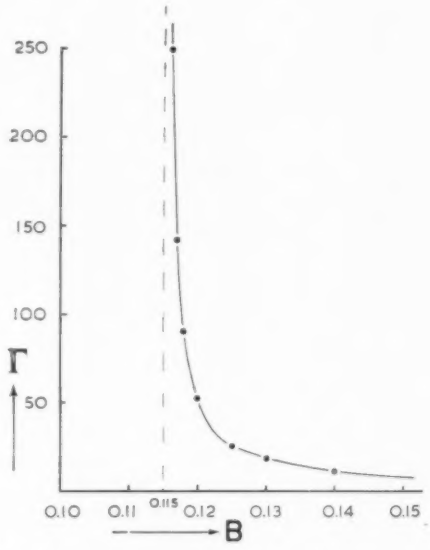

FIG. 23. The dependence of the shear Γ on the fraction B of a surface covered with bands, for a given ϵ.

4. CONCLUSIONS

An investigation on the mode of slip in α-brass was made in order to find whether, for a single slip line, glide takes place on successive atomic planes ("homogeneous" slip) or on one atomic plane only ("inhomogeneous" slip). Five methods of examination were used, and the results obtained are as follows:

(i) The measurements of the angle Φ between the "surface" of a slip line and the crystal surface, using shadows cast by spherical particles, agreed within the limits of the probable error with the angle φ_0 between slip plane and crystal surface, as determined by X-rays.

(ii) From two sets of different slip lines in deep slip lines, it was possible to determine the angle Φ. Its mean value was found to deviate only three degrees from the value which is to be expected for inhomogeneous shear, which is slightly more than the probable error.

VOL. 4 1956

(iii) By means of slip-line intersections, the thickness D of a line perpendicular to the active slip plane was measured, and found to be practically zero.

(iv) The close observation of crossings between deep slip lines and their own cross-slip lines showed that slip in those lines was inhomogeneous.

(v) A statistical method was applied, in which the average shear Γ in the slip lines is calculated from the proportion of the specimen's surface which appears to be covered with slip lines. The measurements give a value for $1/\Gamma$ which is very close to zero, indicating inhomogeneous slip.

The authors regard these results as conclusive evidence that homogeneous slip does not occur in α-brass to any marked extent. While four methods show that individual slip lines, selected at random, are not due to homogeneous slip, a statistical method shows that in addition even the small slip lines are almost certainly single steps. It is therefore concluded that homogeneous slip, if present at all, must be a rare occurrence on the surface of deformed α-brass.

ACKNOWLEDGMENTS

The authors wish to thank Dr. Doris Wilsdorf, Department of Physics, University of the Witwatersrand, Johannesburg, for valuable suggestions and for reviewing the manuscript.

The paper is published with permission of the South African Council for Scientific and Industrial Research.

Appendix 1

A FORMULA FOR CALCULATING THE ANGLE BETWEEN A "BAND SURFACE" AND THE CRYSTAL SURFACE, FROM THE SHADOWS OF PARTICLES

For the derivation of the formula, use is made of Figs. 11(a) and (b), from which it can be seen that the measurable quantities are l'_1, l'_2, l_3, d, and ξ, while α is known.

In Fig. 11(a), it follows from the relation between triangles ABB', $AB'G$, and AFG, that

$$\tan \alpha' = \tan \alpha \cdot \cos \xi, \tag{1}$$

but

$$\alpha' = \zeta - \psi, \tag{2}$$

thus,

$$\tan (\zeta - \psi) = \tan \alpha \cdot \cos \xi. \tag{3}$$

The *actual* projected length l_1 of the shadow (see Fig. 11*b*), is given by

$$l_1 = l'_1 \pm \frac{d_1}{2} \cdot \sin \alpha', \tag{4}$$

where the + and − signs apply respectively to slip lines which appear darker and lighter than the background.

The angle of incidence of the shadowing beam, on the crystal surface, is given by

$$\tan \zeta/2 = \frac{d_1/2}{l_1 \cdot \sec \alpha'} . \tag{5}$$

Thus ζ is known, and ψ can be obtained from (2), (3), and (5).

For the particle casting a shadow on the slip plane,

$$l_2 = l'_2 \pm d_2/2 \sin \alpha'. \tag{6}$$

Usually, $d_1 = d_2$ in the case of latex particles, but for generality this is not assumed in the formulae, although they are shown to be equal in the figure. For $d_1 \neq d_2$ an obvious alteration in Fig. 11(b) will follow.

Now, in Fig. 11(b),

let

$$CB = q \text{ (say)}, \tag{7}$$

then

$$q = d_2/2 \cdot \cot \zeta/2 - l_2 \sec \alpha'. \tag{8}$$

From triangles CKD and CKB, it follows that

$$\sin \beta = (q \cdot \sin \zeta)/p , \tag{9}$$

where

$$p = CD ,$$

and also

$$p = l_3 \sec (\psi - \beta) , \tag{10}$$

where

$$\psi - \beta = \Phi'' . \tag{11}$$

By combining (9) and (10) and solving for β, it follows that

$$\sin \beta = \pm \sqrt{\frac{1}{v+1}} , \tag{12}$$

where

$$v = \left\{ \frac{l_3/q \sin \zeta - \sin \psi}{\cos \psi} \right\}^2 . \tag{13}$$

As in the case of α', the relation between triangles DCC', $DC'J$, and DJH leads to

$$\tan (\Phi - \alpha) = \frac{\tan \Phi''}{\cos \xi} . \tag{14}$$

Appendix II

A METHOD OF OBTAINING THE CURVE OF ρ' VERSUS Φ

After the crystal has been deformed, a Laue back-reflection photograph is made, with the crystal parallel to the film. This plane also is the plane of projection of all micrographs.

In order to obtain the angle of inclination Φ of the surface of a slip line to the projection plane, use

is made of the angle ρ', which is the observed angle between the two sets of slip traces within the deep slip line (Fig. 24). To do this, it is necessary to draw the poles and great circles representing the "new surface" (S), and the first, second, and cross slip systems (I, II, and C) on the stereographic projection of the crystal. This is illustrated in Fig. 25, where the poles of the planes and their respective great circles are given similar notations. Thus, in Fig. 25, L_1 gives the direction of the slip lines of the first system, while T_1 and T_2 represent the two sets of traces of II and C on I. The angles between L_1 and T_1 (σ_1), and L_1 and T_2 (σ_2) can be measured from the stereographic projection.

As shown in Fig. 1, the angle Φ is dependent on the shear Γ, being equal to φ_0 for $\Gamma = \infty$ and decreasing with diminishing values of Γ. The pole of the "band surface" must always lie on the great circle passing through poles I and S. Now poles such as 1, 2, 3, and 4 and their great circles representing various possible slip-band surfaces with values of Φ corresponding to the angular separation between the poles 1, 2, 3, 4, and S are marked, and on each great circle the angles σ_1 and σ_2 are measured.

The values of σ'_1 and σ'_2, as observed in the plane of projection, are then calculated by the formula

$$\tan \sigma' = \cos \Phi \tan \sigma ,$$

and ρ', the angle between the two sets of observed traces, is given by

$$\rho' = 180^\circ - (\sigma'_1 + \sigma'_2).$$

Thus a curve $\rho'(\Phi)$ is obtained (see Fig. 14), and observed values of ρ' can directly be expressed in terms of Φ.

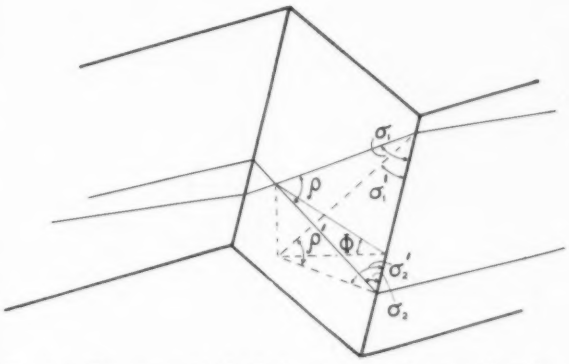

FIG. 24. The geometrical relation between the actual angle ρ included by the traces, and ρ', the observed angle.

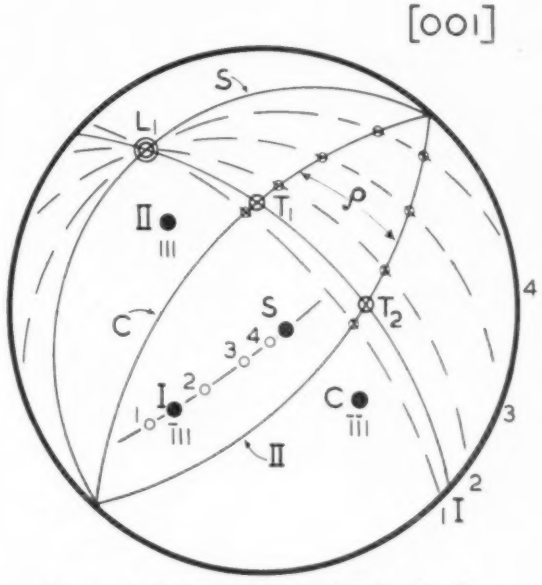

FIG. 25. The stereographic method for obtaining the curve $\rho'(\Phi)$.

Appendix III

DERIVATION OF A FORMULA FOR THE AVERAGE SHEAR IN SLIP BANDS

If a single crystal is elongated and shows slip bands due to fine slip, the fraction B of a surface covered with bands is given by

$$B = \frac{W_{\text{obs}}}{L_0(1 + \epsilon) \sin \beta}, \qquad (1)$$

where W_{obs} is the observed width of all bands on the crystal section, measured perpendicular to the bands, β the angle between the slip bands and the crystal axis, and $L(1 + \epsilon)$ the length of the crystal after an elongation strain of $\epsilon\%$. From Fig. 26 follows that

$$W_{\text{obs}} = \cos (\varphi_0 - \varphi) \frac{d}{\sin \varphi_0} + s \cdot \cos \varphi_0 + s \sin \varphi_0 \cdot \sin (\varphi_0 - \varphi). \qquad (2)$$

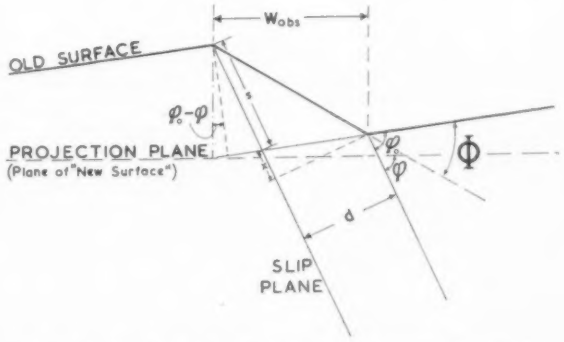

FIG. 26. Drawing for the derivation of a formula for Γ as a function of B.

The total slip in the band is

$$S = \frac{s}{\sin \Theta}, \tag{3}$$

Θ being the angle between the slip direction in the slip plane, and the direction of the slip line.

Since we wish to obtain a formula connecting B with the net average shear Γ, this quantity has to be expressed in terms used before. Thus

$$\Gamma = \frac{S}{d}, \tag{4}$$

and it follows that

$$B = \frac{S/\Gamma \cdot \cos(\varphi_0 - \varphi) + S \cdot \sin\Theta \cdot \cos\varphi_0 \cdot \sin\varphi_0 \cdot \cos(\varphi_0 - \varphi) + S \cdot \sin\Theta \sin^2\varphi_0 \sin(\varphi_0 - \varphi)}{L(1+\epsilon)\sin\beta \cdot \sin\varphi_0}. \tag{5}$$

S can be expressed in terms of the average shear γ, of the crystal, and hence in terms of the strain ϵ; thus

$$\gamma = \frac{S}{L_0 \sin\chi},$$

i.e., $$\gamma = \frac{1}{\sin\chi}(\sqrt{(1+\epsilon)^2 - \sin^2\lambda_0} - \cos\lambda_0),$$

where λ_0 and χ are the angles between the axis and slip direction, and the axis and slip plane, respectively. Hence

$$S = L_0(\sqrt{(1+\epsilon)^2 - \sin^2\lambda_0} - \cos\lambda_0) \tag{6}$$

By inserting (6) in (5), the final formula is obtained.

REFERENCES

1. R. D. Heidenreich and W. Shockley, *J. Appl. Phys.*, **18,** 1029 (1947).
2. D. Kuhlmann-Wilsdorf and H. Wilsdorf, *Acta Met.*, **1,** 394 (1953).
3. H. Wilsdorf, *Z. Metallk.*, **45,** 14 (1954).
4. M. V. Yakutovitch, E. S. Yakovleva, R. M. Lerinman, and N. N. Buinov, *Izv. Akad. Nauk. S.S.S.R.* (Physical Series), **15**, 383 (1951), quoted by A. F. Brown, *Adv. in Physics*, **1,** 455 (1952).
5. H. Suzuki and F. E. Fujita, *J. Phys. Soc., Japan*, **9,** 428 (1954).
6. H. Suzuki, *J. Phys. Soc., Japan*, **9,** 531 (1954).
7. B. A. Bilby, Report of the Conf. on Defects in Cryst. Solids, Bristol 1954. Phys. Soc., 1955, p. 124.
8. H. L. Burghoff, Thesis, Yale University, 1930.
9. H. Wilsdorf and D. Kuhlmann-Wilsdorf, *Z. angew. Phys.*, **4**, 418 (1952).

MECHANIK UND KINETIK DER DIFFUSIONSLOSEN MARTENSITBILDUNG*

H. KNAPP und U. DEHLINGER†

Die empirischen Befunde beim Martensit schliessen eine Keimbildung durch Schwankungen aus, obwohl die Kurve der Verzerrungsenergie je Mol einschliesslich der Grenzflächenenergie mit abnehmender Keimgrösse gegen Unendlich geht. Dieses thermodynamische Dilemma löst sich nur, wenn wie bei der Co-Umwandlung ein präformierter Keim vorhanden ist, der aus zwei überlagerten Versetzungen der Grundstruktur bei Annäherung an die Umwandlungstemperatur sich ohne jede Diffusion ausbildet. Aus den empirischen Orientierungsbeziehungen wird die Verzerrungsenergie als Funktion der Keimgrösse berechnet. Wegen der Kohärenz der beiden Gitter treten dabei an der Grenze auch Schubspannungen auf. Nach Einsetzen der Grösse des präformierten Keims erhält man so eine Verzerrungsenergie von 300 cal je Mol Martensit, was die beobachtete Martensittemperatur befriedigend erklärt. Beim Wachstum der Nadel müssen die Schraubenversetzungen der Grenzfläche in das Austenitgitter hineinwandern Da man die Abhängigkeit der Geschwindigkeit wandernder Versetzungen von der treibenden Schubspannung, die von der akustischen Dämpfung herrührt, theoretisch kennt, kann man aus der zur Verfügung stehenden freien Energie die Geschwindigkeit der Nadelbildung zahlenmässig berechnen. Sie steigt von Null sehr schnell an, für die zur Bildung einer Nadel benötigte Zeit erhält man $5 \cdot 10^{-8}$ sec. Wenn das Längenwachstum beendet ist, kann die Nadeldicke weiterwachsen, bis die freie Energie erschöpft ist.

MECHANICS AND KINETICS OF MARTENSITE FORMATION WITHOUT DIFFUSION

The empirical results with martensite exclude nucleation owing to fluctuations, though the curve of distortion energy per mol, including the interfacial energy, tends to infinity with decreasing nuclear size. This thermodynamic dilemma is only to be solved if, as with the transformation of Co, a preformed nucleus is present, which is formed without any diffusion out of two superposed dislocations of the "Grundstruktur" (dislocation network) when the transformation temperature is approached. The distortion energy is computed from the empirical orientation relations as a function of the nuclear size. Owing to the coherence of the two lattices, there are shear stresses at the interface. After having put in the size of the preformed nucleus, there results a distortional energy of 300 cal per mol martensite, which satisfactorily explains the observed martensite temperature. With increasing size of the needle, the screw dislocations of the interfaces have to move into the austenite lattice. As the dependence of the speed of moving dislocations on the driving shear stress resulting from acoustic attenuation is known theoretically, the rate of the needle formation can be computed quantitatively from the free energy available. This rate increases rapidly from zero; for the time required for the formation of a needle we obtain $5 \cdot 10^{-8}$ sec. When the length-growth is finished, the thickness of the needle may increase up to exhaustion of the free energy.

DYNAMIQUE ET CINETIQUE DE LA TRANSFORMATION MARTENSITIQUE SANS DIFFUSION

Les résultats empiriques relatifs à la martensite excluent la nucléation due aux fluctuations, bien que la courbe de l'énergie de distorsion par môle, y compris l'énergie interfaciale, tende vers l'infini avec la décroissance de la dimension du germe. Ce dilemme thermodynamique peut seulement se résoudre si, comme pour la transformation du cobalt, un germe pré existe. Celui-ci serait formé sans aucune diffusion à partir de 2 dislocations superposées de la "Grund-Struktur" (réseau de dislocation) lorsque la température approche celle de la transformation.

L'énergie de distorsion est calculée à partir de relations empiriques d'orientation en fonction de la dimension du germe.

A cause de la cohérence des deux réseaux, il y a des tensions de cisaillement à l'interface. Après avoir introduit la dimension du germe préexistant, il en résulte une énergie de distorsion de 300 calories par môle de martensite, ce qui explique d'une façon satisfaisante la température mart ensitique observée. Avec l'augmentation de la dimension de l'aiguille, les dislocations vis des interfaces doivent se diriger dans le réseau austénitique. Comme la dépendance de la vitesse des dislocations en mouvement avec la tension de cisaillement qui résulte de l'amortissement acoustique est connue théoriquement, la vitesse de la formation de l'aiguille peut être calculée quantitativement à partir de l'energie libre disponible.

VOL. 4 1956

* Received October 7, 1955.

† Aus dem Institut für theoretische und angewandte Physik der Technischen Hochschule und dem Max-Planck-Institut für Metallforschung, Stuttgart.

1. THERMODYNAMIK DER KEIMBILDUNG

Unter Keimbildung soll jeder Vorgang verstanden werden, bei dem sich an einzelnen Stellen eines Systems in atomistischen Dimensionne eine neue Atomkonfiguration bildet. Nur in einem speziellen Fall, der Keimbildung durch Schwankungen, muss methodisch streng zwischen Keimbildung und darauffolgendem Keimwachstum unterschieden werden, in anderen Fällen ist dies nicht möglich. Die durch den Keim hervorgerufene Änderung ΔF der freien Energie (bezw. der freien Enthalpie) des Systems zerlegen wir in den von der Keimgrösse unabhängigen, aus thermischen Messungen an den homogenen Phasen zu gewinnenden "chemischen Anteil" ΔF_C und die "Verzerrungsenergie" ΔE_v, die sich im allgemeinen wieder aus der Oberflächenenergie ΔE_o und der Spannungsenergie ΔE_{el} zusammensetzt. Wenn wir diese Grössen auf ein Mol oder ein Atom des Keims beziehen, schreiben wir

$$f = f_c + e_v = f_c + e_o + e_{el}$$

Zunächst sind inkohärente und kohärente Keime zu unterscheiden. Inkohärente Keimbildung ist selbstverständlich in Flüssigkeiten und Dämpfen, im kristallinen Zustand ist ein Keim inkohärent, wenn er durch eine flüssigkeitsähnliche Grosswinkelkorngrenze von der Matrix getrennt ist. Kohärente Keime können entweder eine definierte Grenzfläche besitzen, die nach Art einer Kleinwinkelkorngrenze von nahezu parallelen Versetzungslinien gebildet wird, oder sie können stetig in das Matrixgitter übergehen. Eine besondere Oberflächenenergie ist dann in der Verzerrungsenergie nicht zu unterscheiden.

Wird die Geometrie des Keims in seinen verschiedenen Stadien als bekannt angenommen, so kann die Verzerrungsenergie. e_v je Atom oder Mol als Funktion der Zahl der Atome im Keim i theoretisch berechnet werden. Diese Kurve ist die wichtigste Grundlage der Kinetik des Vorgangs. Da die Grenzflächenenergie e_o, wenn sie auftritt, in allen Fällen mit abnehmendem i gegen Unendlich geht, hat die Kurve für alle Keime mit definierten Grenzflächen die Form der Fig. 8, wie sie auch der bekannten Theorie der Keimbildung durch Schwankungen von Volmer u.a. zugrundeliegt. Für Keime ohne definierte Grenzflächen, z.B. die Komplexe der Kaltaushärtung in übersättigten Mischkristallen dagegen ist e_v bei kleinen Werten von i unabhängig von i, nimmt bei grösseren Werten vielfach etwas ab, geht aber nicht gegen Null.

Die chemische freie Energie f_c ist wesentlich temperaturabhängig und zwar näherungsweise proportional dem Abstand ΔT der Arbeitstemperatur von der wahren Gleichgewichtstemperatur. Dagegen sind e_v, e_o, und e_{el} nahezu unabhängig von T. Daher gibt es bei fehlender Grenzflächenenergie stets eine bestimmte Temperatur, von der ab für $i = 0$ die freie Energie f negativ wird und weiterhin negativ bleibt. Von da ab kann also dem zweiten Hauptsatz entsprechend durch diffusionsartige Anlagerung eines Atoms nach dem anderen (negative Diffusion) der Keim gebildet werden und wieterwachsen.

Im erstgenannten Fall dagegen, wenn die Verzerrungsenergiekurve für kleine i gegen Unendlich geht, ist eine Keimbildung, die dem zweiten Hauptsatz gehorcht, bei der also die freie Energie des Systems ständig abnimmt, offensichtlich zunächst bei keiner Temperatur möglich. Statt dessen kann der von Volmer u.a. betrachtete, dem zweiten Hauptsatz widersprechende Vorgang eintreten, bei dem die notwendig vorhandene Schwelle der freien Energie des Systems durch eine statistische Schwankung überwunden wird. Durch Turnbull[24] ist experimentell nachgewiesen, dass ein Vorgang dieser Art die Erstarrung besonders gereinigter Metallschmelzen beherrscht, dagegen ist im kristallinen Zustand noch nie eine Keimbildung durch Schwankungsvorgänge mit einiger Sicherheit nachgewiesen worden. Insbesondere beim Martensit kann ein Schwankungsvorgang, der zweifellos stark von der Temperatur abhängen müsste, als experimentell direkt widerlegt betrachtet werden, da die Bildungsgeschwindigkeit einer Martensit-Nadel aus dem Austenit unterhalb der Martensittemperatur von der Temperatur nicht merklich abhängt und noch bei 4°K gross ist.

Offensichtlich löst sich diese Schwierigkeit durch die naheliegende Annahme, dass die mit Oberflächenenergie verbundenen Keime im kristallinen Zustand an bestimmten Gitterfehlstellen entstehen, also aus den von Cohen[1] erstmals eingeführten "präformierten Keimen" herauswachsen. Es sind dies Fehlstellen im Gitter, vor allem Bereiche des Versetzungsnetzes der Grundstruktur, in deren Nähe die Lagen der Atome schon denjenigen im neuen Gitter ähnlich sind. Diese Ähnlichkeit braucht zunächst nur gering zu sein; sie wird bei Annäherung an die Gleichgewichtstemperatur aus thermodynamischen Gründen stets grösser. Bezeichnen wir nämlich mit γ_k die geometrischen Parameter (meistens Winkelgrössen), welche die Atomverschiebungen vom alten zum neuen Gitter kennzeichnen, dann können wir als verallgemeinerte Schubmoduln in Bezug auf diese Verschiebungen die Grössen

$$G_k = \frac{\partial^2 f_c}{\partial \gamma_k^2} = \frac{\partial \sigma_k}{\partial \gamma_k} \approx \frac{\sigma_k}{\gamma_k}$$

definieren. Da weiterhin gilt

$$f_c = \sum_k \frac{\partial f_c}{\partial \gamma_k} \gamma_k = \sum_k \sigma_k \gamma_k$$

werden die G_k gleichzeitig mit f_c am Gleichgewichtspunkt zu Null und nehmen bei Annäherung an diesen entsprechend ab. Das bedeutet aber, dass bei Annäherung an die Gleichgewichtstemperatur die von den inneren Spannungen der Grundstruktur erzeugten Verschiebungen in Richtung auf das neue Gitter zu immer grösser werden; begrenzt werden sie durch die aus f_o und f_{el} entspringenden Spannungen. Die so entstandenen Fehlordnungsstellen nennen wir präformierte Keime.

Anstatt die freie Energie der Zustände mit den thermodynamischen G_k und für eine bestimmte Grundstrukturstelle einzeln zu berechnen, können wir schematisch in der ohne Berücksichtigung von Gitterfehlern berechneten Verzerrungsenergiekurve die Grösse i_p des präformierten Keims einsetzen, der in der Nähe der Umwandlungstemperatur zu erwarten ist. Wir erhalten damit die Verzerrungsenergie je Atom, die beim Wachstumsbeginn des präformierten Keims anzusetzen ist. Die Temperatur, bei der entsprechend dem zweiten Hauptsatz dieser Vorgang beginnen kann, der die äusserlich beobachtbare Umwandlung darstellt, erhält man durch Gleichsetzen dieser Verzerrungsenergie mit der negativen chemischen freien Energie, also für $f = 0$.

Ebenso wie die Entstehung des präformierten Keims aus der Fehlordnungsstelle geht auch sein Wachstum so vor sich, dass dabei die freie Energie des Systems ständig abnimmt. Für die Geschwindigkeit solcher in der Nähe ihrer Gleichgewichtstemperatur verlaufender irreversibler Vorgänge gilt:[25]

$$\frac{\partial i}{\partial t} = -C \frac{\partial F}{\partial i} = -Cf = -C(f_c + e_v)$$

Bei Vorgängen, die mit diffusionsartigen Bewegungen einzelner Atome gekoppelt sind, das sind Ausscheidungsvorgänge in Legierungen sowie Wachstum inkohärenter Keime auch in Elementen, ist zu setzen

$$C = Ae^{-\frac{B}{KT}}$$

Dagegen ist bei den diffusionslosen Umwandlungen, bei denen die Atome ähnlich wie beim Wandern einer Versetzung nur kleine Verschiebungen auszuführen haben, die aus mechanischen Gründen weitgehend miteinander in Phase sind, der Faktor C nahezu unabhängig von der Temperatur.

Nun ist f_c bei kleinen Werten von i, also bei Beginn des Vorganges, stets von i unabhängig. Somit hat die Kurve, welche die Umwandlungsgeschwindigkeit bei konstantgehaltener Temperatur als Funktion der Zeit (und näherungsweise auch der umgewandelten Menge i) angibt, die Form der umgekehrten Verzerrungsenergiekurve. Insbesondere hat sie bei Keimbildung mit Oberflächenenergie die Form der Fig. 9. Die integrierte Kurve, die man meist als kinetische Kurve bezeichnet, beginnt also mit einem flachen Anstieg, der sich erst später vergrössert, dann aber wieder gegen Null geht. Bekanntlich werden solche S-förmigen kinetischen Kurven, oder bei weniger genauer Beobachtung statt dessen die sogen. Latenzzeiten, bei allen wirklichen Ausscheidungen (Warmaushärtungen) beobachtet.

2. DIE KOBALTUMWANDLUNG

Das einfachste Beispiel eines präformierten Keims bietet die Umwandlung kubisch-hexagonal des Kobalts nach A. Seeger.[2] Geometrisch besteht sie darin, dass in jeder zweiten Ebene (111) des kubisch flächenzentrierten Gitters sich ein Stapelfehler (staking fault) ausbildet. Nun besitzt aber jeder flächenzentrierte Kristall von vornherein kleine Netzebenenbereiche mit solchen Stapelfehlern, die durch Aufspaltung der in der Grundstruktur häufig vorkommenden Versetzungen mit dem Burgersvektor $a/2$ [110] in zwei Halbversetzungen entstehen. Die Energie eines solchen Bereichs setzt sich zusammen aus der der beiden Halbversetzungslinien und einem Anteil, der als Grenzflächenenergie bezeichnet werden kann und proportional ist der von dem Stapelfehler eingenommenen Fläche sowie dem Schubmodul für die den Stapelfehler kennzeichnende Verschiebung. Dazu kommen meist noch positive oder negative Beiträge, die von den Wechselwirkungen mit anderen solchen Bereichen sowie mit der Oberfläche des Kristalls herrühren. Wenn nun nach 1. der genannte Schubmodul bei Annäherung an die Gleichgewichtstemperatur der hexagonalen Modifikation gegen Null geht, wird die Fläche des Stapelfehlers der durch die Wechselwirkung begünstigten Bereiche immer grösser. Ein flächenhafter präformierter Keim hat sich ausgebildet, der etwa den Bereich einer Masche des Grundstrukturnetzwerks umfassen wird.

Unterhalb der Gleichgewichtstemperatur wird der erwähnte Schubmodul negativ; mit anderen Worten, es besteht jetzt eine positive chemische Kraft (Schubspannung), die die Halbversetzungslinien auseinander zu treiben und den Stapelfehlerbezirk zu vergrössern sucht. Seeger[2] hat einen Versetzungsknoten mit einer Schraubenkomponente gleich

VOL. 4 1956

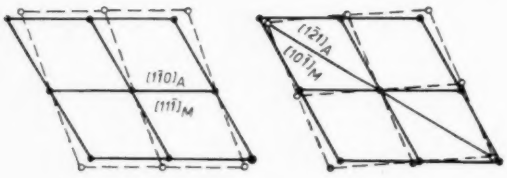

FIG. 1.

dem Doppelten des Netzebenenabstandes (111) angegeben, der es den Halbversetzungslinien geometrisch ermöglicht, unter dieser Schubspannung spiralartig einen räumlichen Bezirk zu durchlaufen. So kann der präformierte Keim weiterwachsen.

Da sich das spezifische Volumen bei der Umwandlung nicht merkbar ändert, ist die Verzerrungsenergie (nach Ausbildung des präformierten Keims) wesentlich durch die genannten Wechselwirkungen bestimmt. In einem unversehrten Einkristall wird den grössten Betrag ein Glied geben, das von der Wechselwirkung der beiden Halbversetzungslinien herrührt, wenn sie beim Durchlaufen der Spiralfläche gerade untereinander zu liegen kommen. Im Mittel ist in diesem Fall die Verzerrungsenergie weitgehend unabhängig von i. Daher kann, wie es auch der Beobachtung entspricht, von einer wenig unter der Gleichgewichtstemperatur liegenden Hysteresetemperatur ab die Umwandlung bei konstanter Temperatur fast vollständig vor sich gehen. Die verbleibenden Reste flächenzentrierter Anordnung sind ebenso zu erklären wie die Stapelfehler im kubischen Gitter oberhalb der Umwandlungstemperatur. Im vielkristallinen Material, wo die bei der Umwandlung notwendigen Scherungen an den Korngrenzen mehr oder weniger behindert sind, ist die Verzerrungsenergie stark von i abhängig, weshalb bei bestimmter Temperatur nur ein bestimmter Bruchteil des Volumens umgewandelt werden kann.

3. DIE ATOMVERSCHIEBUNGEN BEIM MARTENSIT

Beim Übergang vom Austenit zum Martensit vergrössert sich das spezifische Volumen um etwa 5%; daher kann die Umwandlung nicht wie die des Kobalts durch eine einfache Scherung beschrieben werden. In Fig. 1 sind die geometrischen Beziehungen

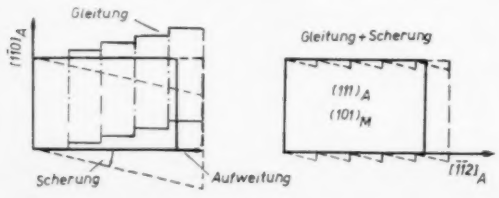

FIG. 2.

zwischen den Orientierungen der beiden Gitter nach Kurdjumow und Sachs[3] sowie nach Nishiyama[4] gekennzeichnet. Es handelt sich dabei um Grenzfälle, die nur bei bestimmten Verhältnissen der beiderseitigen Gitterkonstanten eintreten. Im folgenden soll die etwas einfachere Kurdjumow-Sachs-Beziehung zugrundegelegt werden.[6–10,15]

Wie aus Fig. 1 zu schen ist, bleiben die Abstände innerhalb der dichtbesetzten Atomreihen $[1\bar{1}0]_A = [11\bar{1}]_M$ praktisch erhalten. Die Umwandlung lässt sich also darstellen als eine Verschiebung dieser Reihen und zwar: (1) Eine Vergrösserung der Abstände zwischen diesen Reihen um 6% in der $[11\bar{2}]_A$ Richtung; (2) Eine Scherung in Richtung der Reihen um einen Winkel γ, für den gilt : $tg\gamma = 1/3$.

Die erstgenannte Verschiebungskomponente ergibt unvermeidlich eine makroskopisch merkbare Deformation (vgl. Fig. 2). Die Scherung dagegen wird nach der Untersuchung an Schliffen[5] durch plastische Deformationen, also aus einer gewöhnlichen Gleitung hervorgehende parallele Scherung so kompensiert,

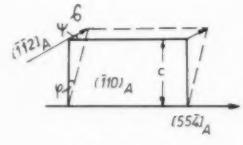

FIG. 3.

dass keine makroskopische Deformation zu sehen ist. Die Bedingungen für eine solche Ableitung erscheinen günstig, da im Martensit die entsprechende Ebene $(112)_M$ und die Richtung [111] Elemente der Zwillingsbildung, also bevorzugte Bewegungselemente sind.

Makroskopisch ändert die Ebene $(225)_A$ bei der Umwandlung ihre Richtung nicht und bleibt unverzerrt; sie ist die Invariable Ebene der Umwandlung und die Mittelebene der Martensitnadeln, also auch Habitusebene. Diese Netzebenen werden also bei der erwähnten Abstandsvergrösserung nur parallel verschoben. Eine von ihnen, die Mittelebene, ist dadurch gekennzeichnet, dass der Verschiebungsvektor $[11\bar{2}]_A$ der makroskopisch sichtbaren zweiten Deformation, der die Abstandsvergrösserung ergibt, dem Betrag nach proportional dem Abstand von ihr ist[11] (vgl. Fig. 3).

Da nur eine der beiden überlagerten Verschiebungen makroskopisch sichtbar wird, bleibt nicht nur die invariable Ebene, sondern die ganze Zone senkrecht zu dem genannten Verschiebungsvektor bei der Umwandlung parallel. Daher kann man die kristallographische Orientierungsbeziehung nach Kurdjumow-Sachs in der üblichen Weise formulieren:

$(111)_A$ $(110)_M$ und $[1\bar{1}0]_A$ $[1\bar{1}1]_M$. Berechnet man sich danach die der Ebene (225) des Austenits entsprechende Ebene des Martensits, so findet man (734). Jedoch ist die Atombelegung in diesen beiden Ebenen nicht dieselbe. Nach Fig. 4 bedarf es einer inhomogenen, makroskopisch nicht sichtbaren Verzerrung, um die beiden ineinander überzuführen. Wie Frank[11] bemerkt hat, müssen dazu in die Grenzfläche zwischen Martensit und Austenit (die sogen. Wachstumsfläche), die man näherungsweise der Ebene $(225)_A$ parallel setzen kann, die in Fig. 5 angedeuteten parallelen Schraubenversetzungen eingefügt werden, die durch Stufenversetzungen an den Seiten der platten-förmigen Nadel zu "Versetzungsrahmen" zu ergänzen sind. Wenn diese Versetzungen in jeder sechsten Atomreihe angebracht werden, wird die durch das oben erwähnte Gleiten hervorgerufene Inhomogenität gerade kompensiert. Fügt man die so vorbereitete $(225)_A$ Oberfläche an eine spannungsfreie $(734)_M$-Oberfläche, dann passen

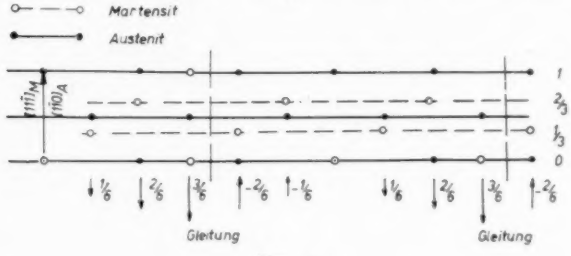

FIG. 4.

sie genau aufeinander. Denkt man sich nun die beiden Flächen miteinander verlötet, dann wird sich auch im Martensit eine Verzerrung einstellen. Da die elastischen Konstanten in beiden Gittern nahezu gleich sind, wird im mechanischen Gleichgewicht nahezu die Hälfte des ursprünglichen Verzerrungen, damit auch die Hälfte des ursprünglichen Burgersvektors im Austenit, und der gleiche Betrag mit umgekehrten Vorzeichen im Martensit zu finden sein. Dieser Zustand wird der Berechnung der Grenzflächenenergie zugrunde gelegt.

Beim Wachstum einer Nadel müssen also die Versetzungen in das Austenitgitter hineinwandern, die Versetzungsrahmen sich vergrössern und an den Enden der Nadel neue Rahmen gebildet werden. Im Anschluss daran müssen die oben gekennzeichneten Atomverschiebungen geschehen. Es ist zu betonen, dass die Atome bei diesen keine Potentialschwellen zu überschreiten haben. In dieser Beziehung liegen die gleichen Verhältnisse vor wie bei der von Chang und Read[22] geometrisch untersuchten, anscheinend ebenfalls diffusionslosen Umwandlung von Au-Cd.

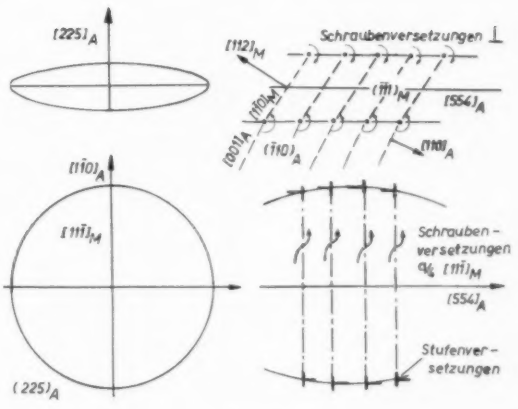

FIG. 5.

In Fig. 6 sind zwei Schnitte durch die Gitter in der Nähe der Grenzfläche gezeichnet. Die Reihen 9–7 sind noch in der stabilen Lage des Austenitgitters, die Reihe 6 ist ein wenig daraus verschoben, sie wird durch die elastische Kraft K_A in die alte Lage zurückgetrieben. Die Reihe 5 ist in einer strukturell labilen Zwischenlage, die Reihen 1–3 sind in der neuen Gleichgewichtslage des Martensitgitters, die Reihe 4 ist schon in deren Nähe und wird durch die elastische Kraft K_M in das Martensitgitter eingereiht. Ist der Martensit thermodynamisch stabiler, dann wird K_M grösser als K_A, somit resultiert eine Kraft, die die Grenzfläche zugunsten des Martensits verschiebt. Potentialschwellen werden dabei von den Atomen nicht überschritten, dagegen müssen sich die angegebenen Versetzungslinien senkrecht zu K_M bewegen. Sie stehen dabei ebenfalls unter dem Einfluss einer Schubspannung der Gröse $K_M - K_A$. Nach (1) ist nun zu untersuchen, ob sich im Austenit ein Gitterbaufehler, im vorliegenden Falle eine Kombination von Versetzungen als präformierter Keim finden lässt, in dessen Nähe die vom Austenit zum Martensit führenden Verschiebungen vorhanden sind. In der Tat zeigt sich nach Fig. 7, dass die dort eingezeichnet

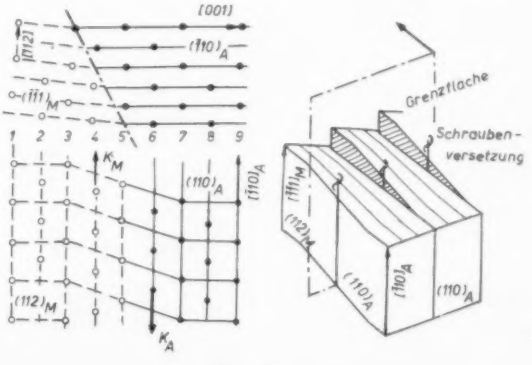

FIG. 6.

Versetzung mit dem Burgersvektor a $[\bar{1}\bar{1}2]$ gerade die erste dieser Verschiebungen innerhalb des umrahmten Gebietes ausmacht. Dieser Burgersvektor ist $2\sqrt{3}$ mal länger als derjenige der kleinsten normalen Versetzung im flächenzentriert kubischen Gitter und und wird daher zunächst in mehrere kleinere aufspalten. Jedoch wird nach dem in (1) gesagten bei Annäherung an den Umwandlungspunkt die thermodynamische Stabilität der grösseren, martensitähnlichen Versetzung zunehmen. Die zweite Verschiebung, die eine Scherung um 1/3 ergibt, kann durch eine überlagerte Stufenversetzung mit dem Burgersvektor a $[\bar{1}10]$ zustandekommen.[19]

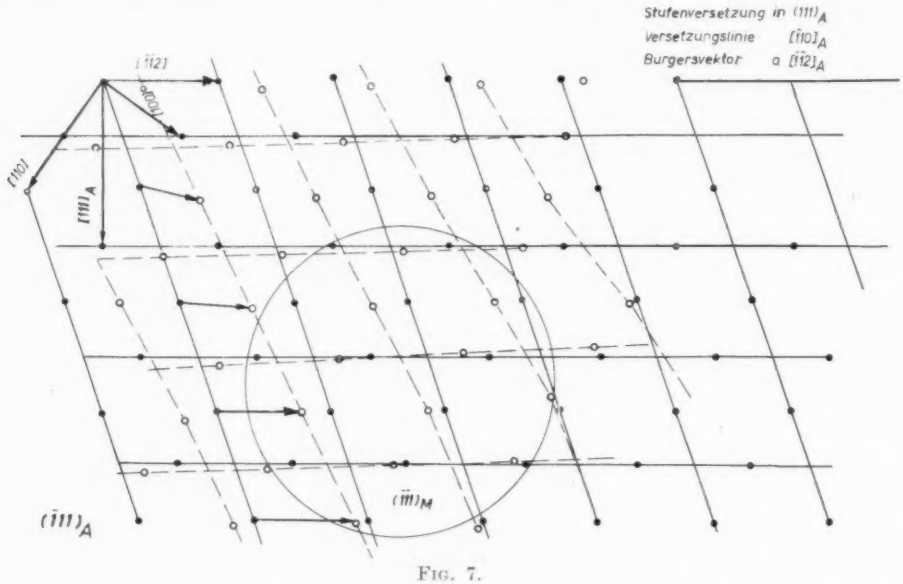

FIG. 7.

4. DIE VERZERRUNGSENERGIE DES MARTENSITS

Die freie Energie der Eisenmodifikationen wurde von Johansson[12] aus calorischen Daten berechnet, die des C-haltigen Austenit und Ferrits (Martensits) von Cohen[1] aus Aktivitätsmessungen von R. P. Smith abgeleitet.[14,15] Wird die Differenz $f_A - f_M = f_c$ gleich Null gesetzt, so erhält man die wahre Gleichgewichtstemperatur (ohne Entmischung) zwischen den beiden Phasen. Sie liegt nahezu unabhängig vom C-Gehalt 220° über der gemessenen Martensittemperatur M_s, bei der die Nadelbildung gerade beginnt. Damit findet man, dass bei dieser eine chemische freie Energie von 290 cal je Mol zur Verfügung steht. Nach (1) muss ebenso gross die Verzerrungsenergie $e_v = e_{el} + c_o$ sein. Da die bisherigen Berechnungen dieser Grösse nur 60–80 cal ergaben, wurden neue, genauere Formeln hierfür aufgestellt.

In e_{el} wurde bisher meist nur der von der Volumvergrösserung herrührende Anteil beachtet, der übrigens nach Nabarro[17] und Kröner[18] von der Gestalt des Keims abhängt, und zwar so, dass er für sehr dünne Scheiben am kleinsten, aber auch für Nadeln noch kleiner als für Kugeln ist. Da aber beim Wachstum die Kohärenz sicher gewahrt bleibt (weil sonst keine diffusionslose Umwandlung möglich wäre), führt auch die Verschiebungskomponente parallel zur Grenzfläche zu einer elastischen Verzerrung in der Matrix und im Keim, deren Energie nicht vernachlässigt werden kann. Wenn die elastischen Konstanten nicht stark verschieden sind, ist der im Keim steckende Anteil der elastischen Energie e_{el} klein gegenüber dem in der Matrix. Daher wurde der erstere vernachlässigt.

Somit sind die elastischen Spannungen zu berechnen, die dadurch entstehen, dass die Matrix an der Grenzfläche diejenige Verschiebung erfährt, durch welche die Atome des Austenits in die Lagen des Martensits gerückt werden. Es handelt sich also um die Lösung der ersten Randwertaufgabe der Elastizitätstheorie, bei der die Verschiebungen $s(r)$ an der Oberfläche eines Bereichs gegeben, die in seinem Innern gesucht sind. Wenn die s gefunden sind, lässt sich die elastische Energie entweder als Oberflächenintegral

$$\tfrac{1}{2}\int s(r)\, A\, df \qquad (1)$$

(wo A die Kraftdichte der äusseren Kräfte an der Oberfläche ist) oder als Volumintegral über die elastische Energiedichte W

$$\int W(r)\, d\tau \qquad (2)$$

berechnen. Das hier einzusetzende s ist nach (3) in Fig. 3 dargestellt. Die Martensitplatten werden näherungsweise als Rotationsellipsoide mit dem Achsenverhältnis c/a betrachtet, so dass das Problem in elliptischen Koordinaten zu behandeln ist.

Bekanntlich lässt sich jedes reguläre Verschiebungsfeld durch Entwicklung nach einem abgeschlossenen Funktionensystem annähern. Sie konvergiert gut, wenn man dazu Lamé'sche Produkte s_ν verwendet, die Lösungen der Potentialgleichung in elliptischen Koordinaten sind. Die Koeffizienten der Reihenentwicklung $s = \Sigma a_\nu s_\nu$ werden aus dem Minimalprinzip bestimmt, nach dem die richtigen s den obenerwähnten Randbedingungen genügen und ausserdem das elastische Potential

$$P = \int W\, d\tau - \int sM\, d\tau - \int sA\, df$$

zu einem Minimum machen müssen (dabei ist M die Dichte der Volumkräfte). Hier wurden nur die ersten Glieder der Reihenentwicklung benützt, mit denen sich die Randbedingungen genau erfüllen liessen. Mit dieser Näherung[16] erhielt man dann für das Integral (1), bezogen auf die Volumeinheit Martensit, den numerischen Wert:

$$E_{el}/V = 6{,}04\,\frac{c}{a}\,10^2 \text{ cal/cm}^3$$

Andererseits ergab das Volumintegral (2) den Wert:

$$E_{el}/V = 5{,}06\,\frac{c}{a}\cdot 10^2 \text{ cal/cm}^3$$

Wenn die elastizitätstheoretische Rechnung genau durchgeführt würde, müssten die beiden Integrale den gleichen Zahlenwert haben. In Anbetracht der guten Übereinstimmung wurden höhere Näherungen nicht gerechnet. Da bei diesen die Energie stets kleiner wird, wurde der kleinere der beiden Energiewerte für das weitere benützt.

Die Grenzflächenenergie wurde in bekannter Weise als die Energie einer Reihe von Versetzungen berechnet. In der Formel

$$E/F = E_0\,\theta[0{,}5 + \ln\theta]$$

wurde die Konstante E_0 aus den Messungen der Grenzenergie zwischen α- und γ-Fe von Van Vlach[26] entnommen und $tg\theta = 1/12$ gesetzt. Dann erhält man für E/F einen Wert von $100\,\text{erg/cm}^2 = 1{,}4\cdot 10^{-6}$ cal/cm². Dagegen würde eine absolute Berechnung von E_o nach Read und Shockley einen wesentlich grösseren Wert ergeben.

Insgesamt erhält man also für die Verzerrungsenergie je Mol Martensit

$$e_v = \left(5\cdot 10^2\,\frac{a}{c} + \frac{3}{2}\cdot 1{,}4\cdot 10^{-6}\,\frac{1}{c}\right)\frac{\mu}{\rho}\text{ cal}$$

wo μ das Molgewicht und ρ die Dichte ist.

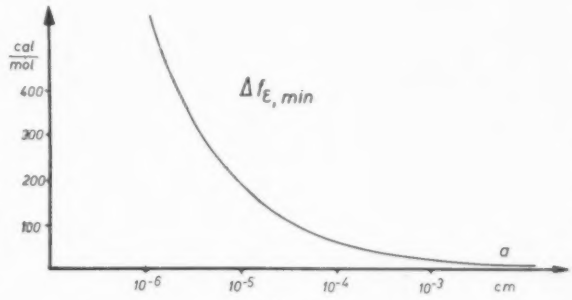

FIG. 8.

Wie man sieht, ist e_v wesentlich von dem Verhältnis c/a der Plattendicke und Plattenlänge abhängig. Da nach (1) die Umwandlungsgeschwindigkeit mit abnehmender Verzerrungsenergie wächst, wird sich bei der Entstehung des präformierten Keims und beim Wachstum jeweils die Plattenform einstellen, die einem Minimum von e_v entspricht. Für diese günstigste Plattenform gilt:

$$\frac{c}{a} = \sqrt{\frac{3}{2}\cdot\frac{1{,}4\cdot 10^{-6}}{5\cdot 10^2}}\cdot\frac{1}{\sqrt{a}}$$

Die danach berechnete minimale Verzerrungsenergie, die noch wesentlich von der Plattengrösse a abhängt, ist in Fig. 8 aufgetragen.

Die Dicke c des in (3) beschriebenen präformierten Keims in der Richtung $[\bar{1}10]$ ist etwa $20\cdot 10^{-8}$ cm. Ihr entspricht ein günstigstes a von etwa $5\cdot 10^{-6}$ cm. Setzt man diesen Wert in e_v nach Fig. 8 ein, so erhält man eine bei Beginn des Keimwachstums aufzubringende Verzerrungsenergie von 300 cal je Mol, also einen Wert, der dem experimentell geforderten sehr nahe kommt.

5. DIE GESCHWINDIGKEIT DES NADELWACHSTUMS

Der wesentliche Teil der Gitteränderung bei der Umwandlung wird bewirkt durch die in Fig. 3 dargestellte Verschiebung in der $(\bar{1}10)_A$-Ebene, die man näherungsweise als Scherung mit dem Scherungswinkel $\gamma = 1/3$ auffassen kann. Dann ist die partielle freie Energie $\partial F/\partial i$, die nach (1) proportional der Umwandlungsgeschwindigkeit ist, proportional mit $\partial f_c/\partial\gamma$, einer Grösse, die die Dimension einer Schubspannung hat. Dabei gilt

$$\tau = \frac{\partial f_c}{\partial\gamma} \approx \frac{f_c}{\gamma}$$

wo f_c die bei der Umwandlung bei einer bestimmten Temperatur zur Verfügung stehende freie Energie ist.

VOL. 4 1956

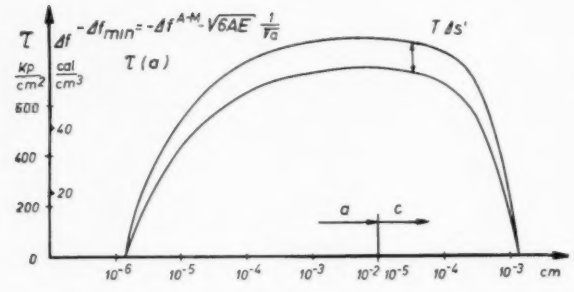

FIG. 9.

Zahlenmässig erhält man für $f_c = 1$ cal/Mol = 5,9 cmKg/cm³ einen Wert $\tau = 18$ Kg/cm².

Diese Schubspannung ist nach 3 dieselbe, die die Schraubenversetzungen bei der Wanderung in das Austenitgitter hinein antreibt. Nun hat Burkhard[19] zahlenmässig die Dämpfung einer wandernden Versetzung durch die von ihr ausgestrahlten Schallwellen und damit auch die Wanderungsgeschwindigkeit als Funktion der Schubspannung ausgerechnet. In Fig. 9 ist die aus Fig. 8 berechnete freie Energieänderung und Schubspannung als Funktion der Plattengrösse aufgetragen, in Fig. 10 die damit berechnete Zunahme der Plattengrösse a in der Zeiteinheit.

Nach den mikroskopischen Beobachtungen wächst die Platte so lange, bis ihre Enden an andere Platten, oder an Korngrenzen anstossen (bezw. in den Bereich von deren Spannungsfelder kommen). In Fig 9 und 10 ist hierfür ein Wert $a = 10^{-2}$ cm angenommen. Weil aber bis dahin die Verzerrungsenergie minimal war, steht auch für die Vergrösserung der Plattendicke c allein noch freie Energie zur Verfügung. Während dieses zweiten Vorgangs wird aber die Verzerrungsenergie je Mol nicht mehr, wie beim ersten, abnehmen, sondern stets zunehmen, so dass sie schliesslich die chemische Energie kompensiert und das Wachstum aufhört. Die danach für das Wachstum von c berechnete Geschwindigkeit ist in Fig. 10 eingetragen. Die bei dem oben angenommenen Endwert von a zu berechnende Enddicke ergibt sich ohne weitere

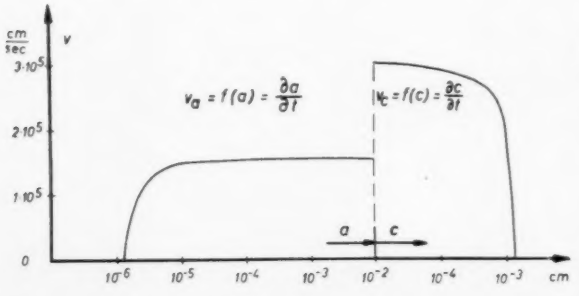

FIG. 10.

Annahmen zu etwa 10^{-3} cm, ein Wert, der den mikroskopischen Befunden gut entspricht. Durch Integration über die Geschwindigkeitskurve Fig. 10 erhält man die Zeitdauer für die Bildung einer Nadel zu $5 \cdot 10^{-8}$ sec, während nach Förster und Scheil[21] sowie Bunshaw und Mehl[22] Zeiten von $5 \cdot 10^{-8}$ bis $5 \cdot 10^{-7}$ sec experimentell beobachtet wurden.

Die während des Plattenwachstums freiwerdende Umwandlungswärme $u - f$ wird innerhall dieser kleinen Zeiten nur zum geringste Teil abgeführt, verursacht also eine Temperaturerhöhung ΔT des Martensits. Die zur Verfügung stehende freie Energie wird dadurch um den Betrag $T\Delta s'$ verringert, wo $\Delta s'$ die mittlere, infolge der Temperaturerhöhung eintretende Zunahme der Entropie ist. Man berechnet für ΔT einen Wert von etwa 100°, damit wird

$$\Delta s' = \frac{u - f}{T} - c_M \ln \frac{T + \Delta T}{T}$$

(c_M spezifische Wärme)

und die Grösse $T\Delta s' \approx 70$ cal/Mol. Dieser Betrag wurde von der treibenden Kraft in Fig. 9 abgezogen.

Jedoch ist zu betonen, dass diese Wärmeentwicklung und ihre Folgen erst im Verlauf des Nadelwachstums eintreten, also auf die Martensittemperatur, d.h. auf den Beginn des Wachstums mit sehr kleiner Geschwindigkeit keinen Einfluss haben. Wegen der ausserordentlich starken Abnahme der Verzerrungsenergie je Mol beim Nadelwachstum nach Fig. 8 steht ja auch bei konstanter Temperatur sehr bald nach Beginn des Vorgangs eine grosse freie Energie zur Verfügung, die die beobachtete grosse Geschwindigkeit zur Folge hat, während die kleine Geschwindigkeit am Anfang des Nadelwachstums, die für die Berechnung der Martensittemperatur entscheidend ist, nicht beobachtbar ist.

Mit erhöhter Abkühlungsgeschwindigkeit des Präparats muss grundsätzlich, wie stets in solchen Fällen, zwar nicht die Lage, aber die Schärfe des bei der Martensittemperatur zu beobachtenden Knicks in den Kurven der Magnetisierung usw. abnehmen, so dass er schliesslich nicht mehr erfassbar ist und statt dessen das Geschwindigkeitsmaximum allein aufgenommen wird, dessen Lage sich selbstverständlich mit der Abkühlungsgeschwindigkeit verschiebt.

Beim Abkühlen unter die Martensittemperatur vergrössert sich die chemische freie Energie, daher können nunmehr weitere Nadeln gebildet werden, deren Verzerrungsenergie infolge ungünstiger Lage ihrer Keime grösser ist. Ausserdem können die schon vorhandenen Nadeln in der Dicke wachsen, wie es von Kurdjumow und Khandros[27] beobachtet wurde.

REFERENCES

1. M. COHEN, *Phase Transformations in Solids*, Cornell Report, New York und London 1951.
2. A. SEEGER, *Z. Metallkunde*, **44,** 247 (1953).
3. G. KURDJUMOW und G. SACHS, *Z. Phys.*, **64,** 325 (1930).
4. Z. NISHIYAMA, *Sci. Rep. Res. Inst. Tohoku Univ.*, **23,** 637 (1933/34).
5. A. B. GRENINGER und A. R. TROIANO, *Trans. Amer. Inst. Min. Met. Eng.*, **145,** 289 (1945); **185,** 590 (1949).
6. M. A. JASWON und J. A. WHEELER, *Acta Cryst.*, **1,** 216 (1948).
7. J. S. BOWLES, *Acta Cryst.*, **4,** 162 (1951).
8. J. S. BOWLES und J. K. MACKENZIE, *Acta Met.*, **2,** 129 und 224 (1954).
9. E. S. MACHLIN und M. COHEN, *Trans. Amer. Inst. Min. Met. Eng.*, **191,** 10, 19 (1951).
10. M. S. WECHSLER, D. S. LIEBERMANN und T. A. READ, *Trans. Amer. Inst. Min. Met. Eng.*, **197,** 1503 (1953).
11. F. C. FRANK, *Acta. Met.*, **1,** 15 (1953).
12. C. H. JOHANSSON, *Arch. Eisenhüttenw.*, **11,** 241 (1937/38).
13. C. ZENER, *Trans. Amer. Inst. Min. Met. Eng.*, **167,** 513 (1946).
14. J. C. FISHER, *Trans. Amer. Inst. Min. Met. Eng.*, **170,** 691 (1949).
15. H. KNAPP, *Arch. Eisenhüttenw.*, **24,** 497 (1953).
16. H. KNAPP, *Stuttgarter Diss.*, 1954.
17. F. R. N. NABARRO, *Proc. Roy. Soc. A.*, **175,** 519 (1940).
18. E. KRÖNER, *Acta Met.*, **2,** 30, 2 (1954).
19. W. BURKHARDT, Diplomarbeit Stuttgart 1954, Vgl. U. Dehlinger, *Theoretische Metallkunde*, Berlin 1955.
20. O. KRISEMENT, *Arch. Eisenhüttenw.*, **24,** 191 (1953).
21. F. FORSTER und E. SCHEIL, *Z. Metallkunde*, **28,** 245 (1936); **32,** 165 (1940).
22. R. F. BUNSHAH und R. F. MEHL, *Trans. Amer. Inst. Min. Met. Eng.*, **187,** 1251 (1953).
23. L. C. CHANG und T. A. READ, *Trans. Amer. Inst. Min. Met. Eng.*, **189,** 47 (1951).
24. D. TURNBULL und J. H. HOLLOMON, *Progr. Met. Phys.*, **4,** 333 (1953).
25. U. DEHLINGER, *Theoretische Metallkunde*, Berlin 1955.
26. A. VAN VLACH, *J. Metals*, 251 (1951).
27. G. V. KURDJUMOW und L. G. KHANDROS, *Ber. Akad. UDSSR*, **66,** 211 (1949).

VOL.
4
1956

BEITRÄGE ZU EINER THEORIE DER PLASTISCHEN DRAHTDEHNUNG*

HORST LIPPMANN†

Setzt man die plastische Dehnung eines Drahtes proportional der Zahl neugebildeter Versetzungen im Kristallgitter, so muß man Versetzungsneubildungen untersuchen. Seit Becker hat sich eine statistische Betrachtungsweise eingebürgert. Es sind verschiedene Funktionen bekannt, welche die Wahrscheinlichkeit eines Gleitsprunges in Abhängigkeit von der angelegten Spannung darstellen sollen. Diese Wahrscheinlichkeit ist aber an verschiedenen Stellen des Gitters verschieden. Hierauf wird eine konsequente Theorie aufgebaut, die es gestattet, experimentelle Befunde quantitativ und qualitativ richtig zu beschreiben. Wesentliche Ergebnisse sind Formel (2) für die spontane Dehnung und Formel (11) für das Kriechen. Als neue Form der genannten Wahrscheinlichkeit wird (25) vorgeschlagen. Ferner wurde zum Vergleich Abschnitt 4 über die Taylor'sche Verfestigungstheorie aufgenommen.

CONTRIBUTIONS TO A THEORY OF PLASTIC STRAIN OF WIRES

If we assume the plastic deformation of a wire to be proportional to the number of newly-formed dislocations in the crystal lattice, then the generation of dislocations must be studied. Since Becker, a statistic view has been in use. Different functions are known, which represent the probability of a glide-step dependent on the applied stress. This probability is, however, different in different regions of the lattice. Thereupon a consequent theory is established, which permits us to describe experimental observations quantitatively and qualitatively. Essential results are equation (2) for the spontaneous elongation, and equation (11) for the creep behavior. As a new form of the above probability, equation (25) is proposed. In addition, paragraph 4 on Taylor's theory of work-hardening is presented for comparison.

CONTRIBUTION A UNE THÉORIE DE L'ELONGATION PLASTIQUE DES FILS

Dès que l'on suppose que la déformation plastique d'un fil est proportionnelle au nombre de dislocations nouvellement formées dans le réseau cristallin, il est nécessaire d'étudier la formation des dislocations.

Depuis les travaux de Becker, une méthode statistique est utilisée. Différentes fonctions sont connues, qui représentent la probabilité d'un pas de glissement dépendant de la tension appliquée. Cette probabilité est cependant variable pour différentes régions du réseau.

Partant de là, on a établi une théorie qui nous permet d'interpréter les observations experimentales qualitativement et quantitativement.

Les résultats essentiels sont donnés par l'équation (2) pour les élongations instantanées, et l'équation (11) pour le comportement au fluage.

L'équation (25) est proposée comme une forme nouvelle de la probabilité déjà mentionnée.

En plus, le paragraphe IV relatif à la théorie de Taylor sur l'écrouissage permet d'établir une comparaison.

EINLEITUNG

Die Engelhardt'sche Theorie der Drahtdehnung unterscheidet sich von der bisher üblichen statistischen Auffassung dadurch, daß der von Orowan[10] in die Becker'sche Gleichung (Becker[1]) eingeführte Kerbwirkungsfaktor q als veränderlich über den sogenannten Bauanomalien betrachtet wird, was u. a. bereits Kochendörfer[6] (S. 64/65) vorschlug. Bauanomalie heißt jede Stelle im Gitter, von welcher eine Versetzung ausgehen kann (Quelle). Wanderungen, gegenseitige Beeinflussungen etc. von solchen werden mit Ausnahme von Abschnitt 4 nicht betrachtet. Man kann sie beim weiteren Ausbau in die Theorie einbeziehen. Vielmehr soll eine erste mathematische Behandlung der schon mehrfach niedergelegten Thesen (Engelhardt[4]) unter Berücksichtigung experimenteller Ergebnisse folgen.

Wir formulieren explizite unsere Voraussetzungen.

1. Die Dehnung des Metalldrahtes ist proportional der Anzahl der neugebildeten Versetzungen.
2. Wirkt an einer Anomalie die effektive Kraft $\sigma \leqq a$, so wird die Wahrscheinlichkeit eines Gleitsprunges in der Zeiteinheit gegeben durch eine bei gewissem endlichen a für $0 \leqq \sigma \leqq a$ stetige Funktion $w(\sigma)$ mit $w(0) = 0$ und $w(a) = 1$. $w(\sigma)$ wächst eigentlich monoton.

Wir sehen also von irgendeiner der speziellen Formen der Becker'schen Gleichung ab, die ohnehin nicht zwingend hergeleitet sind, und versuchen am Ende dieser Abhandlung, $w(\sigma)$ aus den Experimenten zu bestimmen. $w(0) = 0$ rührt daher, daß nur im Sinne der Spannung gerichtete Sprünge als wesentlich angesehen werden. Die Monotonie von w ist plausibel.

* Received October 7, 1955.

† Forschungsinstitut für bildsame Formung der Metalle, Zwickau, Germany.

Ein endliches a mit $w(a) = 1$ (übrigens auch in der Becker'schen und Vitovec'schen (Vitovec[12]) Form) erklärt zwanglos die bislang umstrittene spontane Dehnung (vgl. etwa Kochendörfer,[5] S. 36; Andrade,[0] Kuhlmann,[6] Müller[8, 9]) mittels der zusätzlichen Annahme:

3. Für $\sigma > a$ findet ein sofortiger Gleitsprung unabhängig von Wärmeschwingungen statt.

Wir beachten, daß $w(\sigma)$ in 2 proportional der Größe der Zeiteinheit ist, a nach 3 davon jedoch nicht abhängt. Durch die Forderung, a von 2 soll gleich dem von 3 sein, wird daher der Zeitmaßstab festgelegt. a bedeutet eine "kritische Spannung."

Den Zusammenhang mit der von außen wirkenden Spannung τ gibt der jetzt als variabel angesehene Orowan'sche Faktor q:

4. Zieht am Draht die Spannung τ, so errechnet sich die effektiv an der Anomalie angreifende Kraft σ zu

$$\sigma = q \cdot \tau \tag{1}$$

mit von Anomalie zu Anomalie veränderlichem q.

Wir werden aus den Experimenten die Engelhardt'sche Annahme rechtfertigen, q sei gaußverteilt. — Schließlich sehen wir von der Bildung neuer oder der Regenerierung alter Anomalien während des Versuches ab:

5. An jeder Anomalie findet höchstens ein Gleitsprung statt. Es bilden sich während des Versuches keine neuen Anomalien.

Charakteristisch für die betrachtete Theorie sind eigentlich allein Voraussetzung 2, 3, 4, während 1 und 5 vorläufig der mathematischen Vereinfachung dienen. Nur zum Zwecke eines Vergleiches schränken wir 5 in Abschnitt 4 ein.

VOL. 4 1956

1. DIE SPONTANE DEHNUNG $\gamma(\tau)$

Zieht am Draht die Spannung τ, so findet nach den Voraussetzungen 3 und 4 sofortiger Gleitsprung für alle Anomalien mit $\sigma = q\tau > a$ statt. Die Größenverteilung von q über die Werte von 0 bis ∞ sei durch die Dichtefunktion $f(x)$ gegeben, also die Zahl der Anomalien mit $q > a/\tau$ im wesentlichen durch $\int_{a/\tau}^{\infty} f(x)\,dx$. Nach Voraussetzung 1 ist diesem die sich ergebende "spontane Dehnung" $\gamma(\tau)$ proportional:

$$\gamma(\tau) = A \cdot \int_{a/\tau}^{\infty} f(x)\,dx. \tag{2}$$

Umgekehrt folgt

$$f(x) = -\frac{1}{A}\frac{d}{dx}\gamma\left(\frac{a}{x}\right). \tag{3}$$

Ist also $\gamma(\tau)$ bekannt, so kann daraus $f(x)$ berechnet werden. A bestimmt sich aus der Normierungsforderung $\int_0^{\infty} f(x)\,dx = 1$. Es gleicht der möglichen Gesamtdehnung, die nach Vor. 5 dann eintritt, wenn an allen Anomalien Versetzungen entstanden sind:

$$A = c \cdot N, \tag{4}$$

wo c etwa als mittlere Weite einer Versetzung, N größenordnungsmäßig als Zahl der Anomalien deutbar ist. c liegt folglich in der Größenordnung eines Atomabstandes im Metallgitter.

Bestimmt man experimentell die Dehnung eines Drahtes $D(\tau, t)$ in Abhängigkeit von Spannung τ und Zeit t, so genügt diese näherungsmäßig im Zeitintervall zwischen 5 und 900 sec der Gleichung

$$D(\tau, t) = C(\tau) \cdot t^{\alpha} + \gamma(\tau) = d(\tau, t) + \gamma(\tau) \tag{5}$$

mit $\alpha \approx 0{,}3$ und einer nur von τ abhängigen wachsenden Funktion $C(\tau)$ (Kuhlmann,[6] Müller[8]). $\gamma(\tau)$ errechnet sich demnach durch Rückwärtsverlängern der experimentellen Dehnungskurve gemäß (5) bis $t = 0$, ist somit vom empirischen $C \cdot t^{\alpha}$-Gesetz abhängig. $\gamma(\tau)$ besitzt dann nach Müller[9] bei Kupfer den in Bild 1 dargestellten gestrichelten Verlauf, dessen relativ starker Streubereich für $\tau \geq 6$ kg/mm² schraffiert ist. Andere Versuchsmetalle bedingen lediglich eine Maßstabsänderung der Ordinatenachse.

Die ausgezogene Kurve paßt sich diesem Verlauf gut an. Wesentliche Abweichungen treten wohl nur für sehr hohe Spannungen auf und können theoretisch durch Verletzung der Voraussetzungen 1 und 5 verursacht werden. Jene Kurve entspricht der Gleichung (2) mit

$$f(x) = \frac{2h}{\sqrt{\pi}} e^{-h^2 x^2}; \tag{6}$$

dabei wird ungefähr $a \cdot h = 4{,}8$ kg/mm²; $A = 0{,}7$ mm bei einer Drahtlänge von 1260 mm.

a ist zahlenmäßig frei wählbar. Dies kommt nach Vor. 2 einer Maßstabsfestlegung für σ gleich. Derselbe ist ja durch Maßstabswahl für τ (hier kg/mm²) keineswegs fixiert, da (1) gleichzeitig neben der eigentlichen Bedeutung Maßstabstransformation auszudrücken vermag. Nach Vorgabe von a ist freilich h und damit die Verteilung der q eindeutig bestimmt. Etwa für $a = 1$ erscheint $h = 4{,}8$ als Konstante der kubisch flächenzentrierten Metalle, weil sich deren Kurven $\gamma(\tau)$ wesentlich nur im Ordinatenmaßstab unterscheiden.

(6) bedeutet Gaußverteilung. Eine solche wurde von Engelhardt[4] wegen ihres in der Natur bevorzugten Auftretens a priori vorausgesetzt. Sie erweist sich hier im Einklang mit den Experimenten.

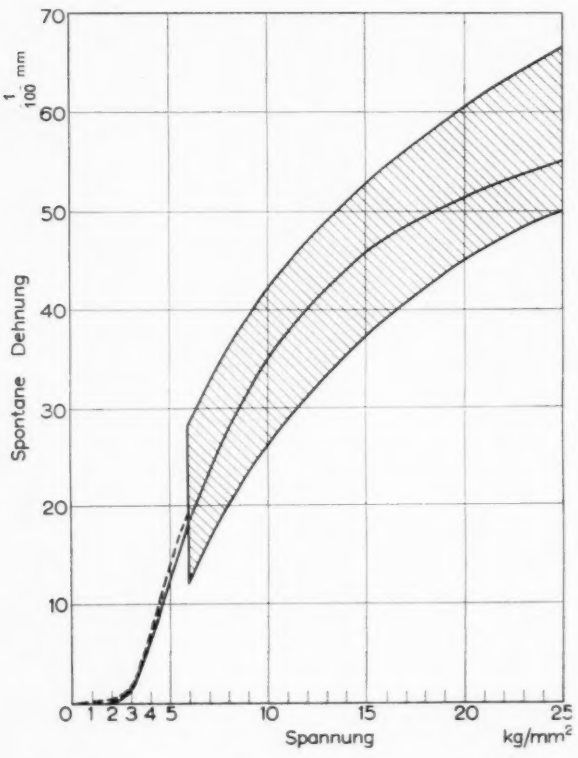

ABB. 1. Spannungsabhängigkeit der spontanen Dehnung.
– – – – – – Experimentell für kleine Spannungen.
\\\\\\\\\\\\ Streubereich für große Spannungen.
———— Theoretisch.

2. DIE KRIECHDEHNUNG $d(\tau, t)$

Durch spontane Dehnung baut sich unsere Anfangsverteilung (6) so ab, daß alle Anomalien mit $q > a/\tau$ ausscheiden. Sie gewinnt die Form

$$f(0,x) = \begin{cases} \dfrac{e^{-h^2x^2}}{\int_0^{a/\tau} e^{-h^2x^2}\,dx} & \text{für } 0 \le x \le a/\tau \\ 0 & \text{für } x > a/\tau \end{cases} \tag{7}$$

Integrale von 0 bis ∞, deren Integrand $f(0,x)$ als Faktor enthält, können dann als Integrale von 0 bis a/τ, also über ein endliches Intervall, geschrieben werden. Unter der letzten Voraussetzung sind die folgenden Entwicklungen des Abschnittes 2 für beliebige stetige Funktionen $f(0,x)$ gültig.

Stellt $N(0)$ die Zahl der Anomalien zu Beginn des Kriechens dar; d.h. in unserem Falle

$$N(0) = N \cdot \int_0^{a/\tau} f(x)\,dx; \tag{8}$$

so betrachten wir neben $f(0,x)$ die Funktion $g(0,x) = N(0) \cdot f(0,x)$. Sie bedeutet anschaulich den "Berg" der Anomalien über den Werten von q, wo jede Anomalie durch die Flächeneinheit repräsentiert wird. Der Berg verringert sich und besitzt zur Zeit t die Gestalt $g(t,x)$; $N(t) = \int_0^{a/\tau} g(t,x)\,dx$ ist die Anomalienzahl zur Zeit t. $g(t,x)$ wird für jedes feste x als stetig differenzierbar nach t vorausgesetzt.

Die relative Abnahme der Anomalien mit $x \le q \le y$ ist wegen des Wachstums von w nicht kleiner als $w(\tau x)$, nicht größer als $w(\tau y)$:

$$w(\tau x) \le \left| \frac{\dfrac{\partial}{\partial t}\int_x^y g(t,\ x)\ dx}{\int_x^y g(t,x)\,dx} \right| \le w(\tau y);$$

und da wegen Voraussetzung 5 $\dfrac{\partial}{\partial t} g \le 0$, folgt für $y \to x$

$$\frac{\partial}{\partial t}\, g(t,x) = -g(t,x) \cdot w(\tau x),$$

oder
$$g(t,x) = g(0,x) \cdot e^{-t \cdot w(\tau x)}, \tag{9}$$

was für das einfachste Beispiel $w(\sigma) = \sigma$; $N(0) = \dfrac{\sqrt{\pi}}{2}$; $a = \tau = h = 1$ (ohne Rücksicht auf Dimensionen) in Bild 2 dargestellt ist.

Die Kriechdehnung $d(\tau, t)$ ist bei konstantem τ nach Vorausdetzung 1 mit der Konstanten A von Abschnitt 1 gleich

$$d(\tau,t) = \frac{A}{N}\int_0^{a/\tau} (g(0,x) - g(t,x))\,dx, \tag{10}$$

folglich unter Benutzung der in Abschnitt 1 gebrauchten Anfangsverteilung $f(x)$

$$d(\tau,t) = A\left\{ \int_0^{a/\tau} f(x)\,dx - \int_0^{a/\tau} f(x)\, e^{-t\cdot w(\tau x)}\,dx \right\}. \tag{11}$$

Dies stellt einen wohlbestimmten funktionalen Ablauf dar, falls $w(\sigma)$ bekannt ist und $f(x)$ etwa nach (6) eingesetzt wird. Lucas und Lücke[7] gaben in etwas anderem Zusammenhange und unter spezielleren Voraussetzungen einen sehr ähnlichen an, leiteten ihn jedoch nicht überzeugend her. Ein zu (9) ähnlicher und entsprechend errechneter Ausdruck findet sich bei Cottrell[3] (vgl. auch die dortigen Literaturhinweise).

3. DISKUSSION DER DEHNUNGSKURVEN

Es kann bereits die allgemeine Form (11) diskutiert werden. Für feste äußere Spannung τ entsteht eine

monoton wachsende Kurve ohne Wendepunkt, deren Tangente sich jedoch immer mehr der Waagerechten nähert. Das folgt wegen

$$\frac{\partial}{\partial t} d = A \int_0^{a/\tau} wf \cdot e^{-tw}\, dx > 0;$$

$$\frac{\partial^2}{\partial t^2} d = -A \int_0^{a/\tau} w^2 f\, e^{-tw}\, dx < 0$$

und erklärt die sogenannte "Verfestigung." Schließlich strebt sie asymptotisch dem Werte $A \int_0^{a/\tau} f\, dx\, zu$, wie es schematisch Abbildung 3 darstellt.

Für wachsendes τ wird der Endwert kleiner. Dies ist nach Vor. 5 klar: Für größeres τ vollzieht sich ein größerer Teil der möglichen Gesamtdehnung A spontan; für das Kriechen bleibt nur noch der dann kleinere Rest.

Die Aenderung der Anfangstangente

$$h(\tau) = \frac{\partial^2}{\partial t\, \partial \tau} d(\tau, t)\Big|_{t=0}$$

errechnet sich nach (11) zu

$$h(\tau) = A\left\{\int_0^{a/\tau} \frac{\partial}{\partial \tau} w(\tau x) f(x)\, dx - \frac{a}{\tau^2} f\left(\frac{a}{\tau}\right)\right\}$$

$$= \frac{A}{\tau} \int_0^{a/\tau} w(\tau x)(2h^2x^2 - 1) f(x)\, dx, \quad (12)$$

wenn man $\frac{\partial}{\partial \tau} w = \frac{x}{\tau} \frac{\partial}{\partial x} w$ beachtet, partiell integriert und dann gemäß (6) $f'(x) = -2h^2 x f(x)$ einsetzt. w wird dabei als stetig differenzierbar angenommen. Wir behaupten:

Für kleine τ und beliebige für $\sigma > 0$ wendepunktfreie Funktionen $w(\sigma)$ wächst die Anfangstangente des Kriechens mit der Spannung.

Das gilt somit für alle "vernünftigen" w (z.B. $w(\sigma) = \sigma, \sigma^2, \ldots, \sigma^n$; aber auch für die von Becker, Vitovec, etc. angegebenen Formen) und ist in Bild 3 schematisch dargestellt. Beide dortigen Kurven schneiden sich notwendig an genau einer Stelle, weil sie verschiedenen Grenzwerten zustreben und keine Wendepunkte besitzen. Zum Beweis unterscheiden wir zwei Fälle:

1. $\int_0^{a/\tau} \frac{\partial}{\partial \tau} w(\tau x) f(x)\, dx = \int_0^{a/\tau} w'(\sigma)\Big|_{\sigma=\tau x} \cdot x f(x)\, dx \to$

$$w'(0) \int_0^{\infty} x f(x)\, dx > 0$$

für $\tau \to 0$ I: $w'(0) > 0$.

2. $w'(0) = 0$. Dann muß $w'(\sigma) > 0$ für das ganze Intervall $0 < \sigma < a$ gelten, weil wegen des Wachstums alle Stellen σ mit $w'(\sigma) = 0$ Wendepunkte sind. w ist daher bei 0 nach unten konvex; es gilt $\left(\frac{w(\sigma)}{\sigma}\right)' \leq 0$ für $0 < \sigma < a$; daher $w'(\sigma) \leq \frac{w(\sigma)}{\sigma}$, und für kleine τ

$$h(\tau) = A\left\{ - \int_0^{1/(h\sqrt{2})} \frac{w(\tau x)}{\tau x} \cdot x(1 - 2h^2x^2) f(x)\, dx \right.$$

$$\left. + \int_{1/(h\sqrt{2})}^{a/\tau} \frac{w(\tau x)}{\tau x} x(2h^2x^2 - 1) f(x)\, dx \right\}$$

$$\geqq A \frac{w(\sigma)}{\sigma}\Big|_{\sigma=\tau/(h\sqrt{2})} \left\{ - \int_0^{1/(h\sqrt{2})} x(1 - 2h^2x^2) f(x)\, dx \right.$$

$$\left. + \int_{1/(h\sqrt{2})}^{a/\tau} x(2h^2x^2 - 1) f(x)\, dx \right\}$$

$$= A \frac{w(\sigma)}{\sigma}\Big|_{\sigma=\tau/(h\sqrt{2})} \int_0^{a/\tau} x(2h^2x^2 - 1) f(x)\, dx > 0,$$

weil $\int_0^{a/\tau} x(2h^2x^2 - 1) f(x)\, dx = -(a/\tau)^2 f(a/\tau)$

$$+ \int_0^{a/\tau} x f(x)\, dx \text{ mit } \tau \to 0 \text{ gegen}$$

$$\int_0^{\infty} x f(x)\, dx > 0 \text{ strebt.}$$

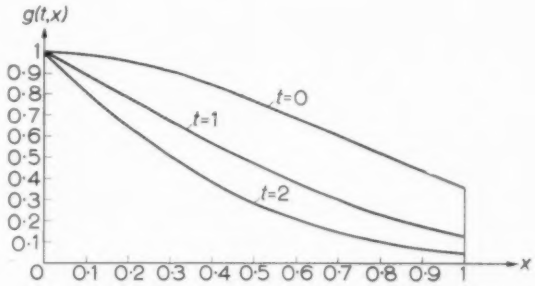

Abb. 2. Beispiel für den Abbau des Anomalienberges gemäß Formel (9).

$d(\tau, t)$ ist für jedes τ eindeutig für komplexe t erklärt

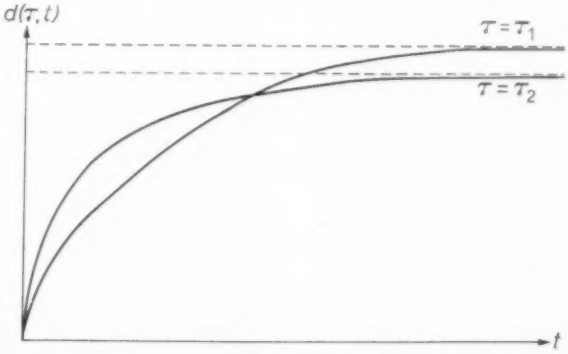

Abb. 3. Schematische Darstellung der fließenden Dehnung für zwei Spannungen $\tau_1 < \tau_2$ nach Formel (11).

VOL. 4 1956

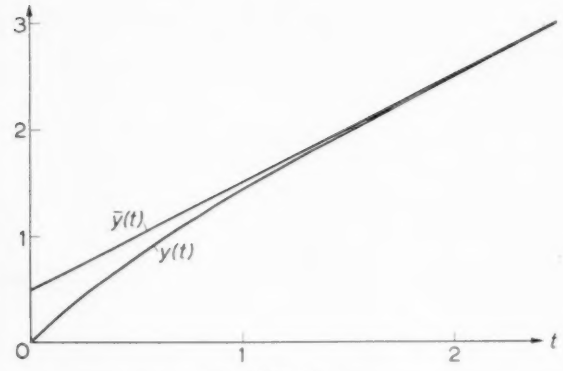

ABB. 4.
$y(t) = t + \frac{1}{2}(1 - e^{-2t})$
als Beispiel einer Kriechkurve nach der Taylor'schen Hypothese mit ihrer Asymptote $\bar{y}(t) = t + \frac{1}{2}$.

und in eine beständig konvergente Potenzreihe nach t entwickelbar. Denn es gilt

$$\frac{\partial^n}{\partial t^n} d(\tau, t) = (-1)^{n+1} \int_0^{a/\tau} (w(\tau x))^n f(x)\, e^{-tw(\tau x)}\, dx;$$

also konvergiert das $(n-1)$-te Restglied der Taylorentwicklung

$$\left| R_{n-1}(\tau, t) \right| \leq \left| \frac{t^n}{n!} \right| \int_0^{a/\tau} f(x) \left| e^{-\vartheta t w(\tau x)} \right| dx \quad (0 < \vartheta < 1)$$

für jedes feste t gegen 0.

Wir vergleichen diese Ergebnisse mit der experimentellen Formel (5): $d(\tau, t) = C(\tau) \cdot t^{\chi}$; und finden, daß sie im Rahmen der hier dargelegten Theorie nur näherungsweise gültig sein kann. Denn sie ist erstens nicht analytisch um $t = 0$, zweitens unbeschränkt für große t. Immerhin können wir aus dem theoretischen Wachstum der Anfangstangente auf das Wachstum von $C(\tau)$ mit τ für kleine Kräfte schließen. Das dann nach Bild 3 nötige Schneiden zweier zu verschiedenen τ gehörigen Kurven ist noch nicht beobachtet worden. Abgesehen davon, daß bei langen Zeiten Anomalien regenerieren und folglich unsere auf den Voraussetzungen 1–5 aufgebaute Theorie nur für beschränkte t anwendbar ist, kann dies dadurch bedingt sein, daß für kleine τ der Schnittpunkt der Kurven weit nach rechts wandert und außerhalb der bisherigen Meßbereiche liegt.

4. DIE TAYLOR'SCHE HYPOTHESE

Wir verlassen vorübergehend unsere bisherigen Gedankengänge und wenden uns den Taylor'schen zu, um Vergleichsmöglichkeiten zu gewinnen.

Wir setzen wie bisher die Dehnung proportional der Zahl der neugebildeten Versetzungen, räumen jedoch allen Quellen die gleiche Bildungschance ein (was konstantes q bedeutet) und erklären die Verfestigung wie folgt: Jede Versetzung verspannt das umliegende Atomgitter, solange sie noch nicht aufgelöst ist; behindert daher eine Bildung weiterer Versetzungen in ihrer Nähe. Dieses Bild geht auf Taylor[11] (vgl. Kochendörfer[5]) zurück.

Wir stellen uns ein einfaches Modell vor: N sei die Zahl sämtlicher etwa gleichmäßig im Gitter verteilter Quellen; v_1 die (überall konstante) Bildungswahrscheinlichkeit einer Versetzung; v_2 die für alle Versetzungen konstante Auflösungswahrscheinlichkeit. Wir nehmen ferner an, jede gebildete Versetzung behindere ihre eigene Quelle sowie $g - 1$ umliegende an der Versetzungsneubildung. Schließlich seien alle unbehinderten Quellen zur Versetzungsbildung und alle bestehenden Versetzungen zur Auflösung gleichberechtigt—das letzte, weil die Fortpflanzungszeit der Versetzungslinie vernachlässigbar ist (Kochendörfer[5] S. 91ff). $\rho(t, dt)$ Versetzungen mögen sich im Zeitintervall zwischen t und $t + dt$ neubilden. Dann ist

$$\rho(t) = \lim_{dt \to 0} \frac{\rho(t, dt)}{dt} \tag{13}$$

deren Bildungsgeschwindigkeit. $W(t)$ bezeichne die Zahl der Versetzungen zur Zeit t; $W \ll N$. Dann sind $gW(t)$ Quellen behindert*; $N - gW(t)$ frei und damit mit $v_1(N - gW(t))\, dt$ zur Bildung prädestiniert:

$$\rho(t) = v_1(N - gW(t)). \tag{14}$$

Da sich das $v_2 dt$-fache aller zur Zeit t bestehenden Versetzungen zur Zeit $t + dt$ aufgelöst hat:

$$W(t + dt) = (1 - v_2\, dt)\,(W(t) + \rho(t)\, dt);$$

$$W'(t) + v_2 W(t) = \rho(t); \text{ oder wegen (14)}$$

$$W'(t) + (gv_1 + v_2) W(t) - v_1 N = 0.$$

Mit der Normierung $W(0) = 0$ gibt dies integriert

$$W(t) = \frac{Nv_1}{gv_1 + v_2} (1 - e^{-t(gv_1 + v_2)}) \tag{15}$$

und strebt dem Grenzwert $\dfrac{Nv_1}{gv_1 + v_2}$ zu. Die Drahtdehnungsgeschwindigkeit ist proportional (14): $\dot{y}(t) = c\rho(t)$;

$$y(t) = c \cdot \frac{Nv_1}{gv_1 + v_2} \left\{ v_2 t + \frac{gv_1}{gv_1 + v_2} (1 - e^{-t(gv_1 + v_2)}) \right\}, \tag{16}$$

welcher Verlauf für $\frac{1}{2} cNv_1 = gv_1 = v_2 = 1$ in Bild 4 gezeichnet ist. Das anfängliche parabelförmige

* Wegen $W \ll N$ kann nämlich von einer überschneidung der behinderten zonen abgesehen werden.

Steigen entspricht wegen seiner Flachheit keineswegs dem $C \cdot t^{\varkappa}$-Gesetz; doch ist der (durch das erste Glied in (16) bedingte) Uebergang in eine Gerade (parallel zu $c \cdot \dfrac{N v_1 v_2}{g v_1 + v_2} \cdot t$) experimentell geläufig.*

Es wird möglich sein (und im nächsten Abschnitt versucht werden), durch passende Wahl der Wahrscheinlichkeit $w(\sigma)$ in der Engelhardt'schen Theorie den Anfangsverlauf des Kriechens richtig zu gewinnen. Für den weiteren Verlauf sind nach obigem Taylor'sche Auffassungen geeignet, so daß eine Koppelung beider Ideenkreise gerechtfertigt scheint. Das bedeutet Modifikation von Voraussetzung 5. Man muß darüber hinaus eine Neubildung von Quellen (Anomalien) in Betracht ziehen, wie sie auf Grund der Frank-Read'schen Theorie beispielsweise von van Bueren[2] errechnet wurde.

Uebrigens liefern bereits schwächere Voraussetzungen, als sie zu Anfang dieses Abschnittes gemacht wurden, gleiche Resultate. Dies danke ich Herrn cand. phys. K. Müller. — Spannungsabhängigkeit der Vorgänge wurde hier außer acht gelassen. v_1, v_2, die Formeln (14), (15), (16), etc. sind also mit konstanter Spannung zu verstehen.

Wir kehren zu unseren Voraussetzungen 1–5 zurück.

VOL. 4 1956

5. DIE WAHRSCHEINLICHKEIT $w(\sigma)$

Obgleich die Becker'sche und Vitovec'sche Form von $w(\sigma)$ nach Abschnitt 3 qualitativ richtige Kurven liefert, zeigt ein quantitativer Vergleich mit dem Experiment schlechte Uebereinstimmung. In beiden Fällen nähern sich die zugehörigen Dehnungskurven zu rasch ihrem Grenzwert, wenn sie durch passende. Wahl der freien Konstanten wenigstens richtige Anfangsverläufe aufweisen. Daher wählen wir den umgekehrten Weg, nehmen die experimentellen Kurven als gegeben an und versuchen, daraus $w(\sigma)$ zu bestimmen. Leider sind jene nur auf begrenztem Zeitintervall gemessen worden, und die Formel

$$d(\tau, t) = C(\tau) \cdot t^{\varkappa} \tag{17}$$

kann nach Abschnitt 3 über dasselbe hinaus nicht gültig sein. Darin liegt die Hauptfehlerquelle der folgenden Ueberlegungen, welche dennoch Bedeutung haben, als sie eine Methode demonstrieren. Außerdem gewinnen wir ein von vornherein nicht unmögliches *Er*gebnis.

Ist $w(\sigma)$ stetig differenzierbar und $u(\rho)$ die zugehörige Umkehrfunktion, so folgt für festes τ nach (11) mit

$$y(z) = f\left(\frac{u(z)}{\tau}\right)\frac{u'(z)}{\tau}, \qquad g(t) = \int_0^{a/\tau} f(x)\,dx - \frac{d(\tau, t)}{A} \tag{18}$$

die Beziehung

$$g(t) = \int_0^1 y(z)\, e^{-tz}\, dz \tag{19}$$

als lineare Integralgleichung 1. Art für $y(z)$. Nach (18) gewinnt man hieraus wegen $u(0) = 0$ ($w(0) = 0$ nach Voraussetzung 2)

$$\int_0^{\rho} y(z)\,dz = \int_0^{\rho} f\left(\frac{u(z)}{\tau}\right)\frac{u'(z)}{\tau}\,dz = \int_0^{u(\rho)/\tau} f(v)\,dv;$$

$$\int_0^{w(\sigma)} y(z)\,dz = \int_0^{\sigma/\tau} f(v)\,dv; \tag{20}$$

wo sich τ beiderseitig herausheben muß. (20) ist nach $w(\sigma)$ auflösbar.

Die Hauptaufgabe liegt in der Behandlung von (19). Wir suchen—wie bei Integralgleichungen üblich—nur Funktionen y mit $\int_0^1 |y(z)|^2\,dz < \infty$. Dann ist y sofort als komplexe Fourierreihe angebbar:

$$y(z) = \sum_{n=-\infty}^{\sigma} g(2\pi i n)\, e^{2\pi i n z} \;\dagger. \tag{21}$$

Leider existiert durchaus nicht für jedes g eine Lösung. z.B. muß g beschränkt und analytisch um $t = 0$ sein (Abschnitt 3 zusammen mit (18)), weshalb Dehnungsformel (17) unbrauchbar ist. Wir begnügen uns mit einer Näherungsrechnung. Die Formel

$$C \cdot r^{\varkappa} \cdot \frac{t^{\varkappa}}{(t + r)^{\varkappa}}$$

kann für hinreichend großes r experimentell nicht von (17) unterschieden werden; sie ist darüber hinaus beschränkt. Wir benutzen sie künftig statt (17). Sie muß nach (11) für $t \to \infty$ gegen $A \int_0^{\varkappa/\tau} f(x)\,dx$ streben, woraus

$$C = \frac{A}{r^{\varkappa}} \int_0^{a/\tau} f(x)\,dx$$

und zusammen mit (18)

$$g(t) = \int_0^{a/\tau} f(x)\,dx \left[1 - \frac{t^{\varkappa}}{(t + r)^{\varkappa}}\right] \tag{22}$$

* Vgl. Cottrell[3]; insbes. entspricht dessen Formel (6) unserer Formel (16), wenn deren zweiter Term durch $\beta \cdot t^{1/2}$ ersetet wird.

† Die Funktionen $e^{2\pi i n z}$ bilden nämlich für unseren Fall ein sog. "vollständiges Orthonormalsystem."

folgt, welche Funktion ebenfalls beschränkt ist. Dennoch kann sie keiner Gleichung (19) genügen*; wohl aber können das gewisse Funktionen $g_1(t)$, die sich von $g(t)$ für reelle t praktisch nicht unterscheiden. Leider sind uns die $g_1(t)$ nicht bekannt. Vereinbaren wir jedoch, in (21) näherungsweise nur die Glieder $n = 0, \pm 1$ zu berücksichtigen, für die $2\pi i n$ in der Gaußischen Zahlenebene nahe der reellen Achse liegt, so werden sich auch $g(2\pi i n)$ und $g_1(2\pi i n)$ wenig unterscheiden, weshalb wir die Rechnung mit g selbst durchführen.

Zunächst muß (22) für komplexe t eindeutig erklärt werden; wir benötigen bloß $Re\, t \geq 0$. Mit $s > 0$ sei $t + s = |t + s| \cdot \exp(i\lambda + 2k\pi i)$; $k = 0, \pm 1, \pm 2, \ldots$. $(t+s)^\alpha = |t+s|^\alpha \exp(i\alpha\lambda + 2k\alpha\pi i)$. Für t reell, $\lambda = 0$, soll $(t+s)^\alpha$ reell werden. Daraus folgt $k\alpha = m$ ganzzahlig. Als Grenzwert ergibt sich für imaginäre t:

$$t^\alpha = |t|^\alpha \exp\left(\pm i\alpha\frac{\pi}{2}\right), \text{ wenn } t = \pm|t|i. \text{ Also}$$

$$g(\pm 2\pi i n) = 1 - K_n \exp\left(\pm i\alpha\left[\frac{\pi}{2} - \lambda_n\right]\right). \quad (23)$$

Hier bedeutet $\cos\lambda_n = \dfrac{2\pi n}{\sqrt{r^2 + (2\pi n)^2}}$

$$K_n = \left(\frac{2\pi n}{\sqrt{r^2 + (2\pi n)^2}}\right)^\alpha.$$

(21) mittels $\exp 2\pi i n z = \cos 2\pi n z + i \cdot \sin 2\pi n z$ umgeformt, ergibt

$$y(z) = g(0) + \sum_{n=1}^{\infty}\{[g(2\pi i n) + g(-2\pi i n)]\cos 2\pi n z + i\,[g(2\pi i n) - g(-2\pi i n)]\sin 2\pi n z\}.$$

Aus (23) folgt

$$\left(\int_0^{a/\tau} f(x)\,dx\right)^{-1}[g(2\pi i n) + g(-2\pi i n)] = 2\left(1 - K_n\cos\left[\left(\frac{\pi}{2} - \lambda_n\right)\alpha\right]\right);$$

$$\left(\int_0^{a/\tau} f(x)\,dx\right)^{-1} \cdot i \cdot [g(2\pi i n) - g(-2\pi i n)] = 2K_n \sin\left[\left(\frac{\pi}{2} - \lambda_n\right)\alpha\right].$$

Daher $y(z) = \displaystyle\int_0^{a/\tau} f(x)\,dx\left[1 + 2\sum_{n=1}^{\infty}\left\{\cos 2\pi n z - K_n\cos\left(2\pi n z + \alpha\left[\frac{\pi}{2} - \lambda_n\right]\right)\right\}\right]$,

was, von 0 bis x integriert, nach (18)

$$\int_0^{u(x)/\tau} f(x)\,dx = \int_0^{a/\tau} f(x)\,dx\left[x + 2\sum_{n=1}^{\infty}\left\{\frac{\sin 2\pi n x}{2\pi n} - K_n\frac{\sin\pi n x}{\pi n}\cos\left(2\pi n x + \alpha\left[\frac{\pi}{2} - \lambda_n\right]\right)\right\}\right]$$

liefert. Wir beschränken uns nunmehr auf das Glied mit $n = 1$. Hier wird $\alpha\left[\dfrac{\pi}{2} - \lambda_1\right]$ sehr klein. Nehmen wir ferner noch kleine x, so kann $\cos\left(\pi x - \alpha\left[\dfrac{\pi}{2} - \lambda_1\right]\right)$ $= 1$ gesetzt werden, weil der cos bei 0 in erster Näherung konstant ist. Für kleine x setzen wir ferner den sin gleich dem Argument und haben, wenn wir $x = w(\sigma)$ substituieren:

$$w(\sigma) = \frac{\displaystyle\int_0^{\sigma/\tau} e^{-h^2x^2}\,dx}{[1 + 2(1 - K_1)]\displaystyle\int_0^{a/\tau} e^{-h^2x^2}\,dx}; \quad (24)$$

also

$$w(\sigma) \sim \int_0^{B\sigma} e^{-x^2}\,dx \qquad (B = \text{const.}) \quad (25)$$

proportional dem Gaußschen Fehlerintegral für kleine σ. In (24) ist $w(\sigma)$ noch von τ abhängig. Dies können wir den Vernachlässigungen zuschreiben.

Offenbar genügt (25) den in Abschnitt 3 gestellten Forderungen, so daß Dehnungsverläufe gemäß Bild 3 sicher sind. Genauer erhielten wir, wenn wir $\dfrac{a}{\tau} f\left(\dfrac{a}{\tau}\right)$ für kleine τ vernachlässigen,

$$h(\tau) \sim \frac{1 - \exp\left[-a^2\left(\left(\dfrac{a}{\tau}\right)^2 + 1\right)\right]}{h^2 + \tau^2} \approx 1/h^2,$$

weil die Exponentialfunktion im Zähler $\ll 1$ und $\tau \ll h$. Mit $C'(\tau) \sim h(\tau)$ gibt dies näherungsweise für kleine τ:

$$C(\tau) \sim \tau. \quad (26)$$

Doch entnehmen wir diesem nur noch einmal das monotone Wachsen von C. Den im einzelnen richtigen Verlauf können wir auf Grund der Vernachlässigungen nicht erwarten.

Der Verfasser dankt dem Forschungsinstitut für bildsame Formung der Metalle in Zwickau für die Gelegenheit zur Durchführung vorliegender Untersuchungen sowie die Genehmigung zur Veröffentlichung derselben; ferner dessen Direktor, Herrn

* Die mathematische Durchführung dieser und folgender *allgemeiner* Betrachtungen wird unterdrückt.

Dipl-Ing. W. Engelhardt, für seine Anregungen. Fördernde Diskussionen mit ihm, Herrn G. Müller und Herrn K. Müller trugen viel zur endgültigen Form dieser Arbeit bei.

LITERATUR

0. E. N. da C. Andrade, *Proc. Roy. Soc.* **A84,** 1 (1910); **90,** 329 (1914).
1. R. Becker, *Phys. Z.*, **26,** 919 (1925); *Z. techn. Phys.*, **7,** 547 (1926).
2. H. G. van Bueren, *Z. Metallkde.*, **46,** 222 (1955).
3. A. H. Cottrell, *J. Mech. Phys. Sol.*, **1,** 53 (1952).
4. W. Engelhardt, *Z. Metallkde.*, **43,** 128 (1952); *Freiberger Forschungshefte*, **1,** 134 (1951); *Die Technik*, **7,** 515 und 659 (1952); *Metall*, **6,** 762 (1952); *Freiberger Forschungshefte*, **B5,** 7 (1954).
5. A. Kochendörfer, *Plastische Eigenschaften von Kristallen und metallischen Werkstoffen*, Berlin, 1941.
6. D. Kuhlmann und G. Masing, *Z. Metallkde.*, **39,** 361 (1948).
7. G. Lucas und K. Lücke, *Z. angew. Phys.*, **6,** 64 (1954).
8. G. Müller und W. Engelhardt, *Ann. Phys.*, VI, **9,** 357 (1951); G. Müller, *Metallurgie und Gießereitechnik*, **3,** 67 (1953).
9. G. Müller, demnächst in *Ann. Phys., Leipzig*, und *Technik*.
10. E. Orowan, *Z. Phys.*, **89,** 605 (1934); **97,** 573 (1935); **98,** 382 (1935).
11. G. I. Taylor, *Z. Kristallographie*, **89,** 375 (1934); *Proc. Roy. Soc.*, **A14,** 362 (1934).
12. F. Vitovec, *Z. Metallkde.*, **43,** 128 (1952).

VOL. 4 1956

A STUDY OF ⟨112⟩ EDGE DISLOCATIONS IN BENT SILICON-IRON SINGLE CRYSTALS*

W. R. HIBBARD Jr. and C. G. DUNN†

Good agreement between calculated and measured dislocation densities for ⟨112⟩ edge dislocations was obtained in bent single crystals of silicon iron. A density of about 2×10^6 cm^{-2} was found for original unbent crystals. Cancellation of unlike dislocations was observed in detail during removal of a polygonization structure and also during removal of a cold-worked structure. The change in distribution of edge dislocations after bending and annealing was investigated. Observations included thermally activated slip, first rearrangements of dislocations into short-range polygon walls, and later rearrangements and combinations leading to polygon growth. Some semi-quantitative data on polygon growth were obtained.

UNE ÉTUDE DES DISLOCATIONS COINS ⟨112⟩ SUR DES MONOCRISTAUX COURBES DE FER-SILICIUM

Une bonne concordance a été obtenue pour les densités de dislocations coin ⟨112⟩ calculées et mesurées sur des monocristaux courbés de fer-silicium.

Une densité d'environ 2×10^6 cm^{-2} a été trouvée pour des cristaux non courbés.

L'annulation des dislocations de signes contraires a été observée en détail pendant l'évolution d'une structure polygonisée et d'une structure d'écrouissage.

Le changement de distribution des dislocations coins après courbure et revenu a été examiné.

Les observations comprennent le glissement thermiquement activé, les premiers réarangements des dislocations en parois polygonales (short range) et subséquemment les réarangements et combinaisons conduisant á la croissance des polygones. Quelques données semi-quantitatives sont obtenues sur la croissance des polygones.

EINE UNTERSUCHUNG ÜBER ⟨112⟩-STUFENVERSETZUNGEN IN GEBOGENEN SILIZIUM-EISEN-EINKRISTALLEN

Bei gebogenen Einkristallen aus Silizium-Eisen wurde eine gute Übereinstimmung zwischen berechneten und gemessenen Versetzungsdichten für ⟨112⟩-Stufenversetzungen erhalten.

Für ungebogene Kristalle im Ausgangszustand wurde eine Dichte von ungefähr 2×10^6 cm^{-2} gefunden. Die Auflösung von Versetzungen entgegengesetzten Vorzeichens wurde während des Abbaus einer Poligonisierungsstruktur und ausserdem bei der Beseitigung einer durch Kaltbearbeitung entstandenen Struktur im Einzelnen verfolgt. Die Änderung in der Verteilung der Stufenversetzungen nach Biegen und Tempern wurde untersucht. Die Beobachtungen schlossen ein: thermisch aktiviertes Gleiten, die erste Umordnung der Versetzungen in kurze Polygonwandstücke sowie spätere Umordnungen und Zusammenlagerungen, die zum Wachstum der polygonisierten Bereiche führen. Über das Wachstum der Polygonbereiche wurden einige halbquantitative Daten gewonnen.

A number of investigators have developed etch pits which appear to correspond satisfactorily to the sites of individual edge dislocations, and a few investigators have studied the density of edge dislocations in plastically bent single crystals. The present paper gives some quantitative data on the density of dislocations as a function of radius of curvature of the slip lamellae obtained by plastically bending $3\frac{1}{4}\%$ silicon-iron crystals and studying the density of etch pits; it describes the course of slip and of polygonization and it presents some semi-quantitative data on the kinetics of increase in wall spacing following the first stage of polygonization. The work reported in the literature on dislocation sites will not be summarized, but work on dislocation densities produced by plastic bending and the work on kinetics is reviewed below.

Hendrickson and Machlin[1] used a thermal etch technique and studied the densities of dislocations in crystals of silver bent to various radii of curvature. The densities obtained were found to be in good agreement with predicted values based on the formula of Cahn[2]. This agreement must be weighed against an error in their calculations, because the radius of curvature of the slip lamellae (r') should have been used instead of the radius of curvature of the neutral axis (r).‡ Another important result obtained by

* Received October 6, 1955.

† General Electric Research Laboratory, Schenectady, New York, U.S.A.

‡ According to the geometry of the bent slip planes (see, for example, Nye[3] and Gilman[4]) the following relation holds, at least approximately:

$$r' = r \cos \chi_0,$$

where χ_0 is the angle between the slip plane and the neutral axis.

Hendrickson and Machlin is a dislocation density of about 2×10^6 cm^{-2} in original unbent crystals.

Dunn and Hibbard[5] used an electrolytic etch-pit technique on a bent and polygonized single crystal of silicon iron, and measured the spacing between etch pits (dislocations) along polygon walls and the spacing between walls. From these data, the Burgers vector, and the orientation of the polygon walls, they calculated a radius of bend for the crystal and obtained good agreement with the actual radius (mathematically this is equivalent to a check of the Cahn formula). They also found that the spacing of dislocations along polygon walls was variable, becoming widely spaced as the walls in certain instances ended within a crystal. It was suggested that the removal of boundaries with open ends might occur by migrations of individual dislocations, leading to an increase in wall spacing.

Vogel[6] has studied the distribution of dislocations and dislocation densities before and after polygonization in bent single crystals of germanium. Dislocation densities checked the Cahn formula after polygonization, but were too high before polygonization. Annealing was shown to reduce the total average density (the reduction was explained in terms of cancellation of unlike dislocations), to produce a more uniform distribution of dislocations, and finally to align the dislocations into polygon walls.

Aust and Maddin[7] have obtained data on dislocation densities in bent and annealed single crystals of molybdenum.

Jacquet[8] has followed the course of substructure changes from the slightly deformed condition to the fully polygonized state in polycrystalline brass. He interprets his results in terms of two kinds of subgrains and subgrain boundaries designated as primary and secondary. The primary boundaries are more stable and of higher angle than the secondary boundaries. Instead of boundary movement, he considers the migration of individual dislocations. Thus, on annealing, the secondary boundaries tend to disappear, while the primary boundaries remain more of less unchanged in position.

Amelinckx[9] has obtained excellent resolution of dislocations along both slip planes and polygon walls in crystals of rock-salt. He also noted differences in etch-pit geometry.

Forty[10] has summarized information on the identification of dislocations, particularly those of the screw type. His review of the data on observed dislocation densities points to lower densities than have been usually predicted; for example, about 10^6 cm^{-2} for aluminum grown from the melt and

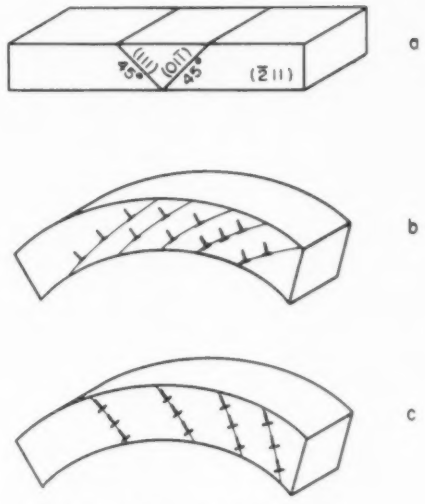

FIG. 1. Orientation relationships.
(a) showing position of (111), (01$\bar{1}$), and ($\bar{2}$11) planes.
(b) showing dislocations on the slip plane.
(c) showing dislocations along polygon walls.

10^4 to 10^6 cm^{-2} for a number of various crystals grown from their vapour. The predicted values—for example, those of Cottrell[11]—are 10^7 to 10^9 cm^{-2}.

Gilman[4] has obtained quantitative data on the kinetics of polygon growth in bent zinc monocrystals, and also has found that annealing is required to initiate polygonization, i.e. polygonization does not occur spontaneously at room temperature in bent single crystals of zinc.

Dunn and Hibbard[12] also found that annealing is required to initiate polygonization in bent silicon-iron single crystals. The present paper reports this work in detail.

EXPERIMENTAL PROCEDURE

Single crystal specimens in sheet form, 1.25 mm thick, were prepared with one predetermined orientation[13] as shown in Fig. 1(a). Fig. 1(b) depicts the position of positive edge dislocations expected if the crystal is bent about a [$\bar{2}$11] axis producing bend gliding and slip on the (01$\bar{1}$) plane. Fig. 1(c) depicts the new arrangement of edge dislocations expected if the bent crystal is annealed and polygonization occurs.

All unbent crystals were annealed eight hours at 1175°C in pure dry hydrogen, and given a slow cool. The chemical analysis at this point was: $3\frac{1}{4}$% silicon, 0.001 carbon, 0.008 phosphorus, 0.005 sulfur, 0.038 manganese, 0.078 nickel, 0.098 copper, 0.008 tin, and traces of chromium and aluminum.

Bending of crystals to different radii of curvature was done at room temperature. In this operation

VOL. 4 1956

FIG. 2. (211) surface of crystal bent around [$\bar{2}11$] axis to a 2.55-cm radius of curvature. Chrome-acetic acid electroetch. 750×.

the specimens were greased and pressed between a round steel cylinder and a matching block. The matching block was a cylindrical concave block for specimens bent to 25-mm radius of curvature and a thick sheet of solder which deformed with the specimens for specimens bent to larger radii of curvature.

Samples for annealing and subsequent examination were cut from the bent crystals. Annealing was accomplished in an atmosphere of dry hydrogen, using a nichrome form which retained the curvature of the specimen. After the samples were mounted in bakelite, metallographic preparation consisted of mechanical polishing followed by electrolytic polishing and etching in a chrome-acetic acid bath, as described by Morris.[14]

RESULTS AND DISCUSSION

Proof of (01$\bar{1}$) *Slip*

Lines of etch pits in a bent single crystal observed on a ($\bar{2}$11) plane (Fig. 2) and on a plane tilted about the 49$\bar{1}$ direction 30° to the ($\bar{2}$11) plane showed that slip had occurred on the (01$\bar{1}$) plane. For example, the angle made by each line of etch pits and the [49$\bar{1}$] direction normal to the top surface of the specimen was 45° in the first section (i.e., the line coincided with the [111] slip direction) and 48° in the second section. Angles expected on the second section for (01$\bar{1}$), ($\bar{1}$3$\bar{2}$) and ($\bar{1}$2$\bar{1}$) planes having [111] as a common slip direction are 49°+, 59°−, and 65°, respectively; so the agreement is with the (01$\bar{1}$) plane within experimental error.

The average distance between dislocations and the average distance between slip lines as revealed in Fig. 2 are 1.1 μ and 2.3 μ respectively. The latter figure is of the correct order of magnitude for the spacing of slip bands, which would appear on other surfaces of the specimen during deformation.

A Statistical Proof That Etch Pits Locate Individual Edge Dislocations

Quantitative Relations in Bent Crystals

Although Vogel, Pfann, Corey, and Thomas,[15] and Vogel[16] obtained agreement between angles measured from X-ray data and those calculated from etch-pit spacings along low-angle boundaries, which established a one-to-one correspondence between dislocation sites and etch pits, there is need for further proof, particularly for the edge dislocations developed by bend gliding. Dunn and Hibbard[5] confirmed the one-to-one relationship for the polygonized structure of a bent and annealed single crystal of silicon iron, but it could be argued that this result may have been fortuitous. On the other hand, the method used by Hendrickson and Machlin,[1] which attempts to correlate dislocation density and radius of curvature, should provide data for a statistical proof.

Cahn[2] has derived a formula that predicts the number of excess dislocations required to satisfy a given geometry of a bent specimen; namely,

$$\rho = 1/br',$$

where ρ is the number of excess dislocations of one kind per unit area normal to the slip plane, b is Burgers vector, and r' is the radius of curvature of the slip lamellae. In terms of the radius of curvature r of the specimen, ρ is given by $(br \cos \chi_0{}^5)^{-1}$.

In the present work, a range of specimen curvatures was investigated, but the angle between slip plane and the neutral axis χ_0 was held constant at 45°. The number of etch pits observed in one or more areas of 48-cm^2 size on photomicrographs taken at a magnification of 750 were counted and used to obtain a measured dislocation density, assuming each pit to be the site of one dislocation. Cahn's formula, with Burgers vector taken as 2.47×10^{-8} cm for the unit of slip along a ⟨111⟩ direction, gave the calculated densities. Results appear in Table 1 and Fig. 3.

Complete agreement between calculated and measured densities would appear as a 45° line in the plot. Above a density of about 10^6 cm^{-2} the densities

observed in annealed specimens actually do fall close to this line; so the conclusion is reached that the etch pits correspond to sites of individual dislocations.

In unbent crystals a density of dislocations of about 2×10^6 cm^{-2} was counted by the same technique; this agrees quite well with results of other workers, particularly those of Hendrickson and Machlin[1] and of Noggle and Koehler.[17]

The higher densities obtained in as-bent specimens can be explained in terms of departure from lamellar slip, i.e. by the generation of both positive and negative dislocations during bend gliding.[6] During annealing, these dislocations come together and cancel in pairs, leaving the excess dislocations that satisfy Cahn's formula. The following section will consider the cancellation process in greater detail.

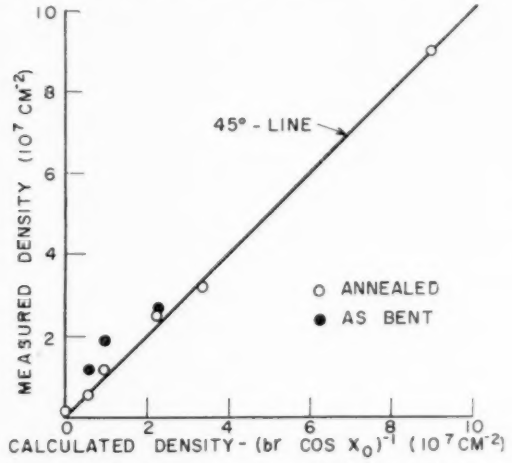

FIG. 3. Plot showing variation of dislocation density with amount of bending.

The Cancellation of Edge Dislocations of Opposite Sign

(a) *Removal of a polygonization structure*

A specimen with identifiable positive and negative dislocations was obtained in the following manner. First, a single crystal was bent to a radius of curvature of 2.55 cm and annealed for one hour at 1100°C to produce a set of dislocations arranged in polygon walls. Secondly, the polygonized crystal was flattened, giving the conditions shown in Fig. 4. The widely-spaced dark boundaries are the polygon walls that have been retained during the flattening operation. The other lines 90° to the polygon walls are arrays of dislocation with opposite sign lying on slip planes that become active during flattening.

Measurements for dislocations lying on slip planes gave a density of 3.3×10^7 cm^{-2}. A density of 2.5×10^7 cm^{-2} was taken for the dislocations of

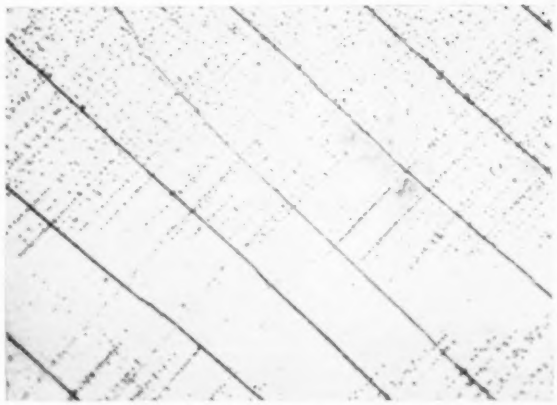

FIG. 4. (211) surface of crystal bent around [$\bar{2}$11] axis to a 2.55-cm radius of curvature, annealed one hour at 1100°C, flattened, and electro-etched. 750×.

opposite sign lying on the polygonized boundaries (see Table 1). The sum of these two densities is 5.8×10^7 cm^{-2}. The theoretical number is twice 2.25×10^7 cm^{-2}, or 4.5×10^7 cm^{-2}.

Fig. 5 shows the microstructure after a one-hour anneal at 1000°C. Both the polygon wall and the slip-line arrangements of dislocations have disappeared. The measured density is 0.73×10^7 cm^{-2}. This is considerably less than either 2.5×10^7 cm^{-2} or 3.3×10^7 cm^{-2}, and can be explained only by the cancellation process. If the theoretical total number 4.5×10^7 cm^{-2} is used, the reduction in density is 84%; if the higher or measured density 5.8×10^7 cm^{-2} is used, the reduction in density is 87%. Apparently with dislocations of opposite sign on a single set of slip planes, cancellation is favored over rearrangement into a network of subgrains with a dislocation density near the total density introduced by the deformations.

The drop in density observed here demonstrates the reliability of the detection method for edge dislocations as well as proof of the cancellation process for unlike

FIG. 5. Same as Fig. 4 after one hour at 1000°C.

VOL. 4 1956

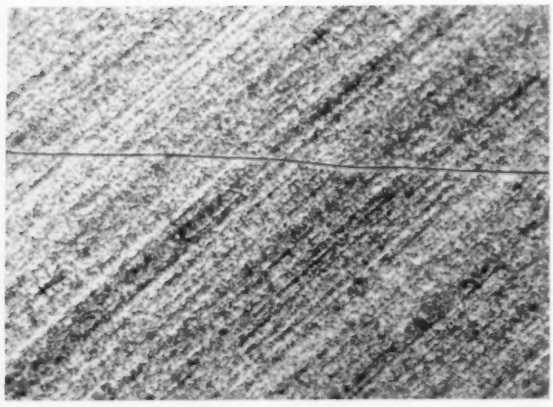

FIG. 6. Worked structure obtained after nine bends, the first bend producing a radius of curvature of 8.5 cm, the second bend flattening the sample, etc. 750×.

dislocations. This means that the density 2×10^6 cm^{-2} found in original unbent crystals is probably not in error on the low side because of the detection method —higher values could easily have been detected.

(b) *Removal of a worked structure*

If bending is followed immediately by flattening and the process is repeated a number of times, the dislocation density is found to rise. Apparently extensive cancellation of unlike dislocations does not occur at low temperatures. Fig. 6 shows the worked structure after bending to an 8.5-cm radius, flattening, bending, etc., for a total of nine operations. As in Fig. 2, slip is confined to (01$\bar{1}$) slip planes, but the repeated bends have extended slip to the neutral axis (there is a 4° boundary near the neutral axis due to growth imperfections in the preparation of this crystal). Annealing one hour at 750°C removed the slip-line arrangement of dislocations and produced the configuration shown in Fig. 7. Fig. 8 shows the configuration after one hour at 950°C, and Fig. 9

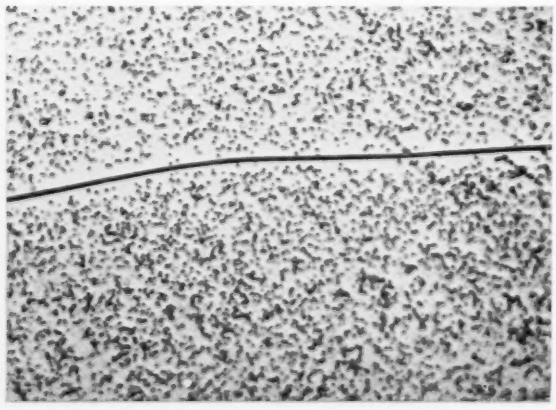

FIG. 7. Same as Fig. 6 after one hour at 750°C. 750×.

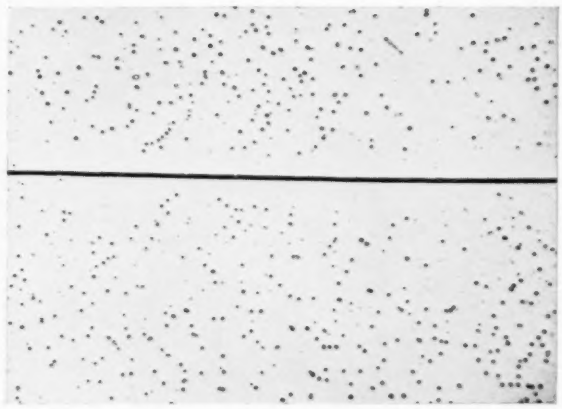

FIG. 8. Same as Fig. 6 after one hour at 950°C. 750×.

after one hour at 1020°C. It appears that cancellation of unlike dislocations occurs before polygonization, which is just beginning at the 1020° point.

Poor resolution of pits prevented a measurement of dislocation density for Fig. 6, but those for Figs. 7, 8, and 9 are 3.9×10^7, 0.58×10^7, and 0.70×10^7 cm^{-2} respectively. The latter figure is in good agreement with Cahn's formula or the value 0.67×10^7 cm^{-2} required for a radius of curvature of 8.5 cm. The intermediate density of 0.58×10^7 cm^{-2} is too low, due to either an error in measurement or a deficiency of excess dislocation near the neutral axis. The change in density from 3.9×10^7 cm^{-2} to 0.70×10^7 cm^{-2} is a reduction of 80%, and indicates a near-100% cancellation of unlike dislocations.

Course of Annealing Changes in Bent Crystals

The results shown in Figs. 2 and 10 to 19 were obtained on a crystal bent to a 2.55-cm radius of curvature and annealed for one hour in a temperature gradient giving annealing temperatures from about room temperature to 1100°C. They are selected points

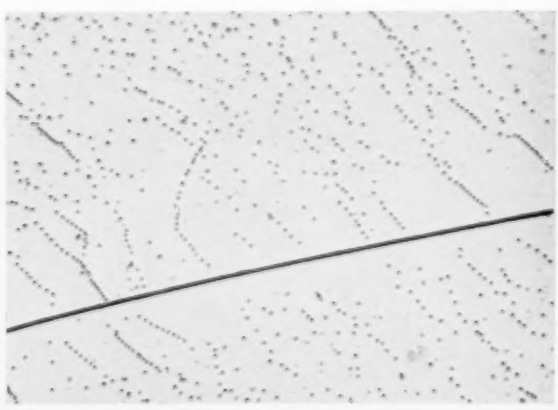

FIG. 9. Same as Fig. 6 after one hour at 1020°C. 750×.

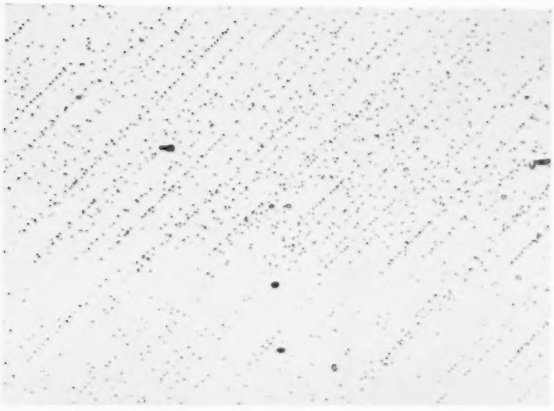

FIG. 10. (2̄11) surface of crystal bent around [2̄11] axis to a 2.55-cm radius of curvature. After one hour at 650°C. 750×.

FIG. 11. Same as Fig. 10, but after one hour at 700°C. 750×.

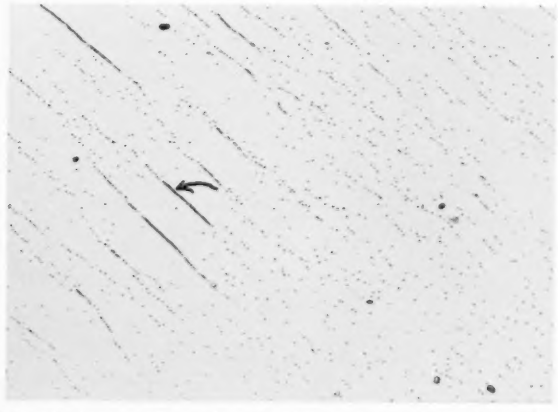

FIG. 12. Same as Fig. 10, but after one hour at 750°C. 750×.

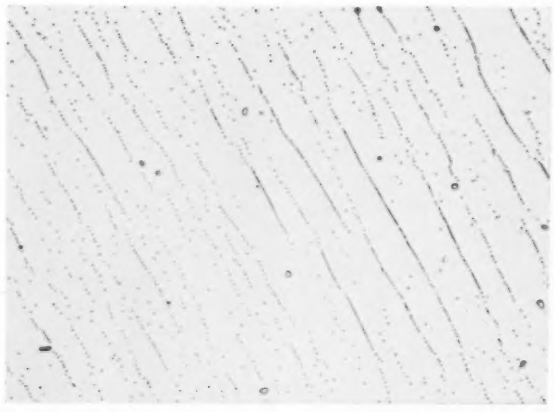

FIG. 13. Same as Fig. 10, but after one hour at 850°C. 750×.

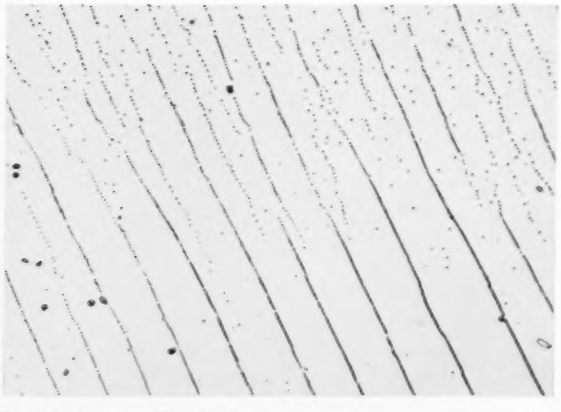

FIG. 14. Same as Fig. 10, but after one hour at 875°C. 750×.

FIG. 15. Same as Fig. 14. 1500×.

VOL. 4 1956

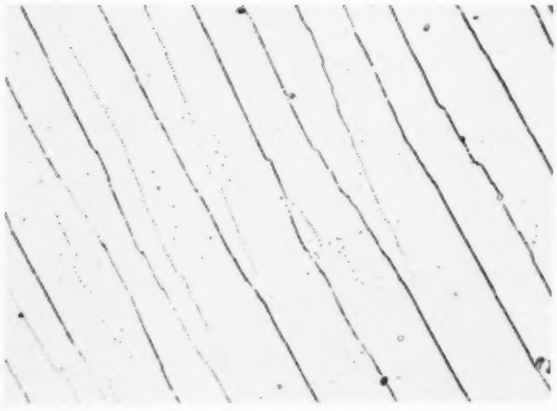

FIG. 16. Same as Fig. 10, but after one hour at 925°C. 750×.

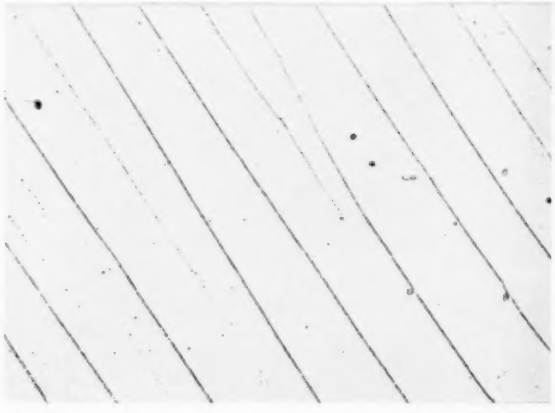

FIG. 17. Same as Fig. 10, but after one hour at 975°C. 750×.

FIG. 18. Same as Fig. 10, but after one hour at 1025°C. 750×.

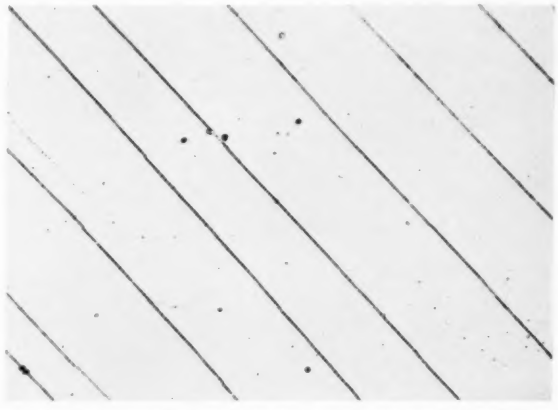

FIG. 19. Same as Fig. 10, but after one hour at 1060°C. 750×.

along the central portion or neutral axis of the crystal.

Fig. 2, corresponding to room temperature, shows arrays of resolved etch pits that form lines parallel to the [111] slip direction; these are due to [$\bar{2}$11] edge dislocations that have been generated by bend gliding.* It is clear that the central region is entirely elastically bent.†

Observations along the bent crystal for regions annealed at high temperatures disclosed a narrowing of the width of the unslipped zone. This narrowing was continuous, beginning at 300°C and ending near 600°C. It indicates a relief of elastic stress through glide which is activated by the lowering of the yield point with a rise in temperature.

Fig. 10 shows the configuration after complete bend gliding, slip occurring through the neutral axis at a temperature near 650°C. The lines of etch pits still define the active slip planes. The dislocations clearly lie on slip planes, and present little evidence for

TABLE 1. Calculated and measured dislocation densities for crystals bent to various radii of curvature

Radius (cm)	Sample condition	Density (10^7) cm^{-2}	
		Calculated	Measured
0.635	Annealed 24 h 950°C	9.02	9.0
1.70	Annealed 4 h 1300°C	3.37	3.2
2.55	Annealed 1 h 750°C	2.25	2.5
	As bent	2.25	2.7
5.92	Annealed 1 h 750°C	0.97	1.2
	As bent	0.97	1.9
10.25	Annealed 1 h 720°C	0.56	0.57
	Annealed 1 h 960°C	0.56	0.57
	As bent	0.56	1.2

* Note that slip lines should not occur on this surface, since it is parallel to the slip direction.

† The maximum elastic strain in the center region is calculated as 0.002. This strain corresponds to a yield strength of about 50,000 p.s.i., a value in agreement with the results of Benford.[19]

incipient arrangements that could be described as subgrain boundaries. Compared with the as-bent crystal, the density of dislocations after complete bend gliding was found to be much more uniform across the thickness of the crystal.

Figs. 11 and 12, for temperatures of about 700° and 750°C respectively, show beginning stages of climb leading to polygonization. That is to say, there are arrays of dislocations in lines or walls, 90° to the slip direction, while there are arrays of dislocations still in lines on the slip planes. The latter are particularly prominent in Fig. 11, and they are parallel to the slip lines shown in Figs. 2 and 10.

The arrays of dislocations in polygon walls such as appear in Fig. 12 certainly can be treated as unique groups, even though there are still no obvious subgrain boundary arrangements. A polygon wall may be described in terms of the spacing between dislocations, which determines a linear dislocation density. It can also be described in terms of the disorientation across the wall. For instance, the maximum disorientation angle noted in Fig. 12 for the marked boundary is 5.4×10^4 radians, or about 1.6 min, which was calculated from a measured spacing of 4.4×10^{-5} cm and a Burgers vector of 2.47×10^{-8} cm. The linear density for this boundary (2.2×10^4) is fairly uniform for a distance of 13 μ; it then changes quite rapidly on both ends, as may be inferred from the micrograph. Directly adjacent to the 1.6-min wall and extending over to the neighboring wall, the density of dislocations can be seen to be relatively low.

Fig. 13 shows a region that reached 850°C. Most of the dislocations are in walls approximately 90° to the slip direction; so polygonization has occurred to the extent of attaining this new alignment. Polygonization is not complete, however, in the sense of producing uniform boundaries of constant dislocation density that would be required for dividing the crystal into well-defined subgrains. The spacing of dislocations in the walls is far from uniform. Interestingly, a check on maximum linear density disclosed none above the 2.2×10^4 value noted in Fig. 12. Also, very few of these boundary segments include more than about thirty etch pits. Clearly, the new array of dislocations represents a large but incomplete step toward developing a system of relatively stress-free subgrains.

The series of micrographs given in Figs. 14 to 19 show what may be described as polygon growth, i.e. the spacing between walls increases as the annealing temperature increases. Dunn and Daniels[18] obtained such coarsening for similar anneals, and also for isothermal anneals, upon lengthening the time at temperature. Therefore, the picture obtained going from low to high temperatures represents stages in the same overall process of movement of dislocations into new configurations. The mechanism can be viewed in terms of glide and climb of dislocations that bring about a lowering of the elastic strain energy.

Although isolated dislocations between walls or at the end of an incomplete wall may move individually to neighboring walls during polygon growth, groups of dislocations such as those discussed in Fig. 12 have enough stability to tend to hang together. Therefore, displacements of groups of dislocations or even walls probably occur. Whether dislocations move singly or in groups to lower the stress fields, they have to move by glide and climb processes.

Kinetics of Polygon Coarsening

Fig. 20 gives the course of polygon coarsening or the increase in wall spacing with time for several annealing temperatures. The wall spacing increases rather rapidly at first and then suddenly levels off, the leveling-off spacing depending markedly on temperature. Such a behavior cannot be accounted for on the basis of one simple mechanism, thus precluding a detailed analysis for activation energies of the process.

The increase in wall spacing can be accounted for only by the movement of dislocations. These movements involve glide and climb processes,[11] and they occur whenever a reduction in energy is possible. It has been shown[18] that coalescence of low-angle boundaries into higher-angle boundaries effects a reduction in energy.

On the other hand, the leveling off of the growth curves, particularly at the lower temperatures, can only be explained by something stopping the movement of the dislocations. Impurities in some form are probably responsible for the observed effect. According to this point of view, the dislocations become anchored, particularly at low temperatures, and this occurs only when the active driving force on the dislocations becomes sufficiently low.

The wall spacing for the initial stages of growth taken at the point of disappearance of slip configurations was difficult to measure. The average spacing of dislocations measured along lines parallel to the slip direction was used. Above a value of about 4×10^{-4} cm, however, the measurements should correspond quite well to true wall spacings. If the five curves in Fig. 16 were drawn to converge on a spacing of 4×10^{-4} cm, the general form would be retained.

VOL. 4 1956

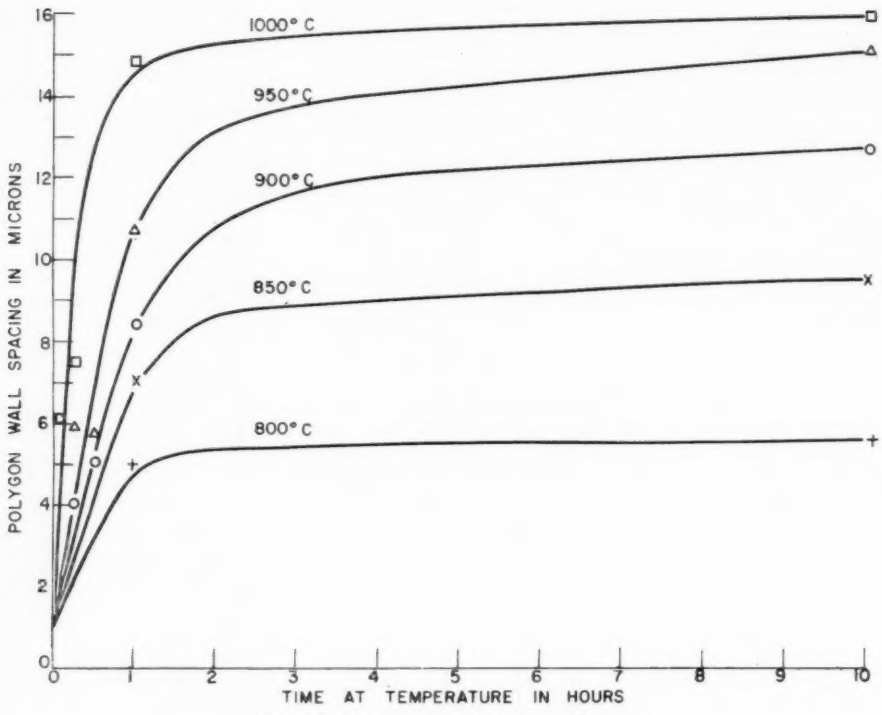

FIG. 20. Isothermal polygon growth curves.

SUMMARY

The chrome-acetic acid electropolish and etch procedure used to develop etch pits in silicon-iron crystals was found to be a reliable method for locating the sites of individual dislocations.

Good agreement was obtained between dislocation densities measured in bent and annealed specimens and densities calculated by Cahn's formula. A density of about 2×10^6 cm^{-2} was found for the original unbent crystals.

Cancellation of unlike dislocations was observed and the drop in dislocation density was measured upon annealing a polygonized crystal which had been subjected to a reversed bend (i.e. flattening, which introduced dislocations of opposite sign).

Cancellation of unlike dislocations in the removal of a cold-worked structure (obtained by several cycles of bending and flattening treatments) occurred upon annealing a specimen left in the bent condition. At relatively high densities the dislocations left the single slip-line arrangement and produced a more or less random pattern. This pattern persisted while the density decreased to approximately the final value, which agreed well with the density of excess dislocations required for the residual curvature. Further annealing resulted in the formation of polygonization structures in accordance with bending geometry.

The course of annealing changes in a single bent crystal with slip extending part-way to the neutral axis were the following. Up to about 600°C further slip occurred until no unslipped region remained. Near 700°C the first stages of polygonization occurred; this consisted of the formation of short-range polygon walls. Additional annealing completed the formation of these incomplete wall arrangements. Above about 850°C further rearrangements and combinations of dislocations produced polygon structures of increased wall spacing (polygon growth).

In a semiquantitative investigation of isothermal polygon growth it was found that growth occurred rather rapidly for a short time, after which growth was extremely slow.

ACKNOWLEDGMENT

The authors wish to thank H. T. Sagendorph for preparing the single crystals used in the present work, E. F. Koch for much of the metallographic work, and H. Brandhorst for determining dislocation densities.

REFERENCES

1. A. A. HENDRICKSON and E. S. MACHLIN, *Acta Met.*, **3,** 64 (1955).
2. R. W. CAHN, *J. Inst. Metals*, **76,** 121 (1949).
3. J. F. NYE, *Acta Met.*, **1,** 153 (1953).
4. J. J. GILMAN, *Acta Met.*, **3,** 277 (1955).
5. C. G. DUNN and W. R. HIBBARD, JR., *Acta Met.*, **3,** 409 (1955).

6. F. L. VOGEL, JR., "Dislocations in Plastic Bending of Germanium Single Crystals," Research in Progress. Amer. Inst. Min. Met. Eng. Chicago Meeting (1955).
7. K. T. AUST and R. MADDIN, "Subgrain and Electrical Resistivity Studies of Molybdenum Single Crystals." Research in Progress, Amer. Inst. Min. Met. Eng. Chicago Meeting (1955).
8. P. A. JACQUET, *Acta Met.*, **2,** 752, 770 (1954).
9. S. AMELINCKX, *Acta Met.*, **2,** 848 (1954).
10. A. J. FORTY, *Advances in Phys.*, **3,** No. 9, 1 (1954).
11. A. H. COTTRELL, "Dislocations and Plastic Flow in Crystals" (Oxford, 1953), p. 102.
12. C. G. DUNN and W. R. HIBBARD, JR., "Polygonization in a Bent Single Crystal of Silicon Iron." Research in Progress, Amer. Inst. Min. Met. Eng. Chicago Meeting (1955).
13. C. G. DUNN and G. C. NONKEN, *Metal Progress*, **64,** No. 6,71 (1953).
14. C. E. MORRIS, *Metal Progress*, **56,** No. 5,696 (1949).
15. F. L. VOGEL, W. G. PFANN, H. E. COREY, and E. E. THOMAS, *Phys. Rev.*, **90,** 489 (1953).
16. F. L. VOGEL, JR., *Acta Met.*, **3,** 245 (1955).
17. T. S. NOGGLE and J. S. KOEHLER, *Acta Met.*, **3,** 260 (1955).
18. C. G. DUNN and F. W. DANIELS, *Trans. Amer. Inst. Min. Met. Eng.*, **191,** 147 (1951).
19. F. G. BENFORD, *Metal Progress*, **46,** 94 (1946).

VOL.
4
1956

A CRYSTALLOGRAPHIC STUDY OF MERCURIC IODIDE*

J. B. NEWKIRK†

Mercuric iodide crystals grow from the liquid or vapor state by the spread of successive parallel layers over the crystal surface. The crystals also sublime and melt by the recession of layers. Transformation from the yellow to the red form occurs by two distinctly different mechanisms. The red transformation product has a definite and known orientation with respect to the parent lattice. The nucleation kinetics of the yellow $\rightleftarrows$ red transformation indicate that the interfacial energies between red-yellow, yellow-vapor, and red-vapor phases increase in that order. Approximate values for these interfacial energies are given.

ÉTUDE CRISTALLOGRAPHIQUE DE L'IODURE MERCURIQUE

Les cristaux d'iodure mercurique croissent à partir du liquide ou de la vapeur par le développement de couches parallèles successives sur la surface du solide. Inversément les cristaux se subliment ou fondent par la récession de ces couches.

La transformation de la variété jaune en variété rouge s'effectue par deux mécanismes bien distincts.

Le produit de la transformation rouge a une orientation connue et bien définie sur le réseau de base.

La cinétique de nucléation de la transformation jaune $\rightleftarrows$ rouge montre que les énergies interfaciales entre phase rouge–phase jaune, phase jaune–phase vapeur et phase rouge–phase vapeur vont en croissant dans le même ordre.

Des valeurs approchées sont données pour ces énergies interfaciales.

KRISTALLOGRAPHISCHE UNTERSUCHUNG VON QUECKSILBERJODID

Das Wachstum von Quecksilberjodid-Kristallen aus der flüssigen oder der Dampf-Phase erfolgt durch Ausbreiten aufeinanderfolgender, paralleler Schichten über die Kristalloberfläche hinweg. Ausserdem sublimieren und schmelzen die Kristalle durch schichtweisen Abbau. Die Umwandlung von der gelben in die rote Modifikation geht durch zwei deutlich verschiedene Mechanismen vor sich. Das rote Umwandlungsprodukt hat eine definierte und bekannte Orientierung bezüglich des Mutterkristalls. Die Keimbildungskinetik der gelb $\rightleftarrows$ rot- Umwandlung zeigt, dass die Grenzflächenenergien zwischen den Phasen rot-gelb, gelb-Dampf und rot-Dampf in der genannten Reihenfolge zunehmen. Näherungswerte für diese Grenzflächenenergien werden angegeben.

1. INTRODUCTION

Mercuric iodide, first chosen for study because of its interesting polymorphic transformation at 127°C, has proven to be an appropriate subject for the study of several other fundamental phenomena. Among these are the mechanisms of nucleation and growth of crystals from the vapor, and the melting and freezing characteristics of a crystalline substance. It is the purpose of this report to describe experimental observations regarding these phenomena in mercuric iodide and to discuss their interpretation in terms of fundamental processes which may operate in metallic and other nonmetallic systems. Although they are closely related, the different types of phenomena are discussed individually, in so far as possible, in separate sections of this report.

2. EXPERIMENTAL OBSERVATIONS

When mercuric iodide powder is heated above 127°C, it turns from it characteristic red color to a bright yellow as the tetragonal crystal structure transforms to the orthorhombic structure. As the temperature is raised, the yellow crystals sublime, producing a vapor of molecular mercuric iodide. A cool glass slide held in the vapor becomes covered with many crystals of the red or yellow phase. These crystals take the shape of red rectangular parallelepipeds, yellow parallelogram platelets, or yellow needles, depending upon the temperature and the degree of supersaturation of the vapor (see Fig. 1). The long sides of a yellow parallelepiped are parallel with [110] and [$\bar{1}$10] respectively; the thin plane is parallel with (001). (See Appendix for experimental verification.) If the glass slide is warm, the yellow crystals sometimes grow as large as several millimeters across.

* Received August 6, 1955.

† General Electric Research Laboratory, Schenectady, New York.

(a)

600× 60°C

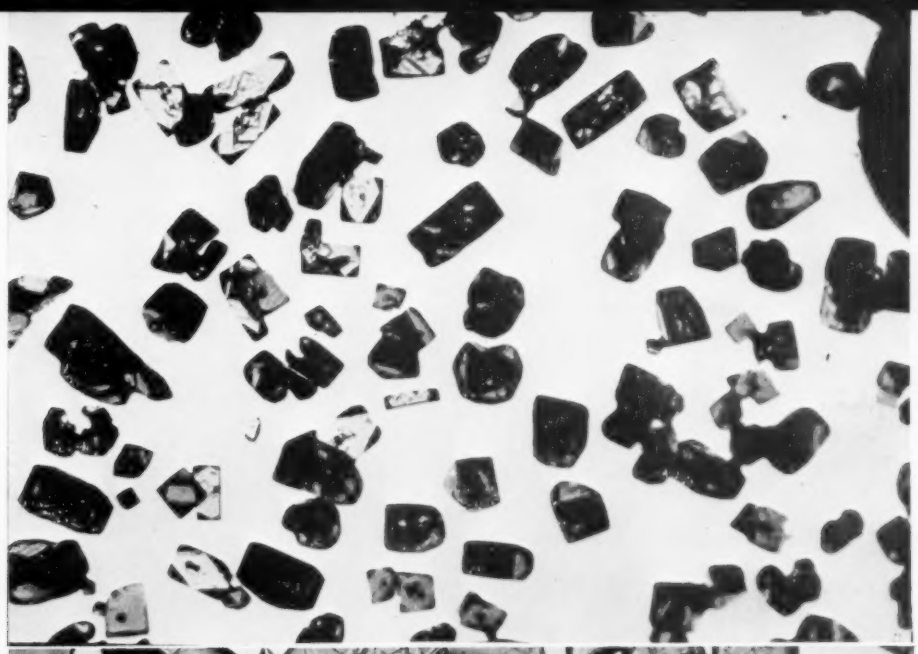

(b)

600× 200°C

(c)

600× 150°C

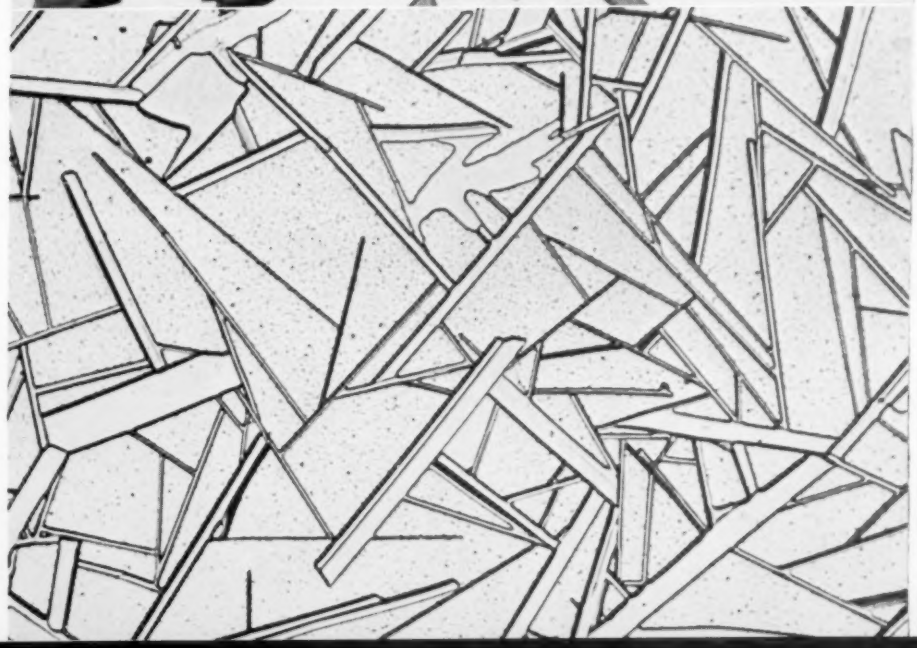

FIG. 1. Depending upon temperature and vapor super-saturation, HgI_2 crystals form as (a) red rectangular parallelepipeds, (b) yellow non-rectangular parallelepipeds or platelets, or (c) yellow needles. Approximate temperatures are indicated.

VOL.
4
1956

Crystals on a glass slide can be conveniently watched, at magnifications up to 750×, by means of the apparatus sketched in Fig. 2. The crystals resting on the heated lower glass slide provide HgI_2

Growth of HgI_2 Crystals from the Vapor Phase

At a magnification of about 100×, some of the crystals appear to have on them curved lines resembling terrace edges or contours as in Fig. 3. The lines move

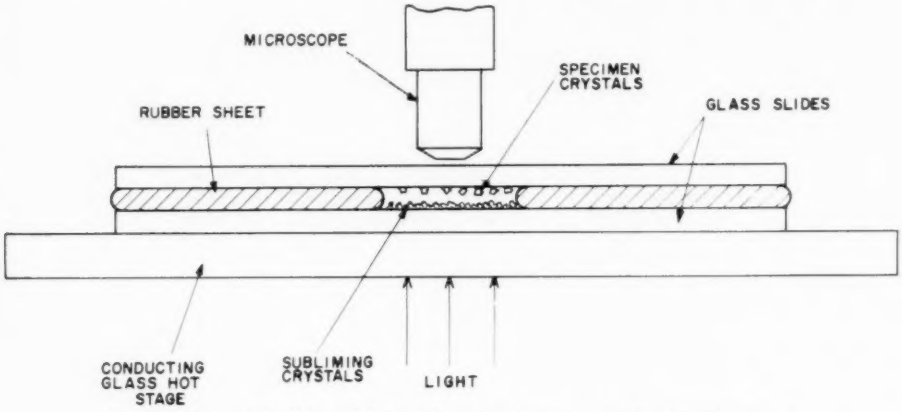

FIG. 2. Mercuric iodide, subliming from the hot lower slide, deposit on the under side of the cooler top slide.

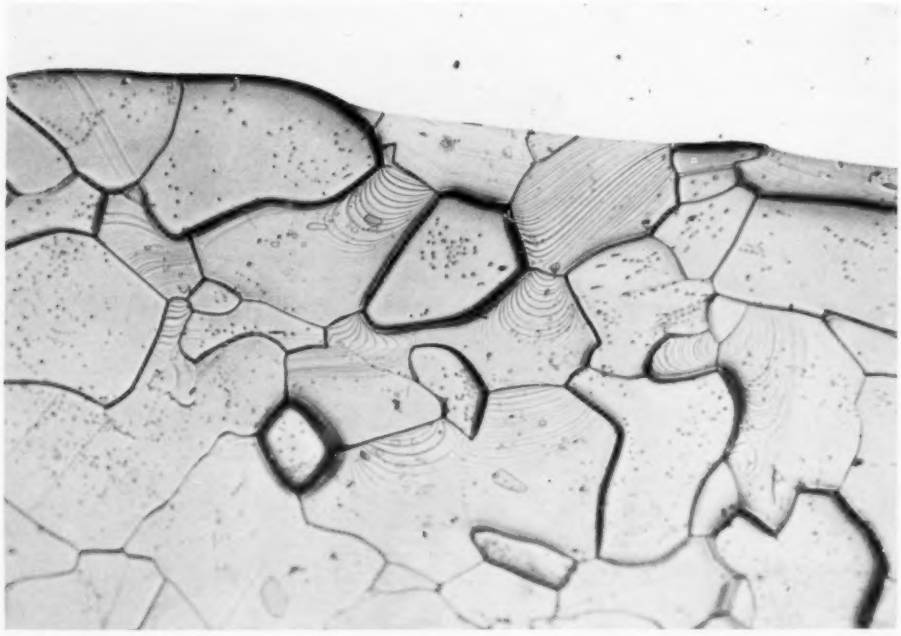

600× ~225°C

FIG. 3. Lines resembling contours move continuously across the surface of some crystals as they grow or sublime.

vapor, which condenses on the under side of the top slide. Since the forming crystals are transparent, a clear image of their underneath surface can be seen through them, and the underneath surface appears as it would if it were viewed from below the crystal instead of through it.

steadily across the surface of the crystals. The lines are first seen as small loops and spread successively across the (C01) surface, moving in the direction of their convex side. When this occurs on crystal platelets, which are so thin that they exhibit interference colors, the spreading lines mark the boundary

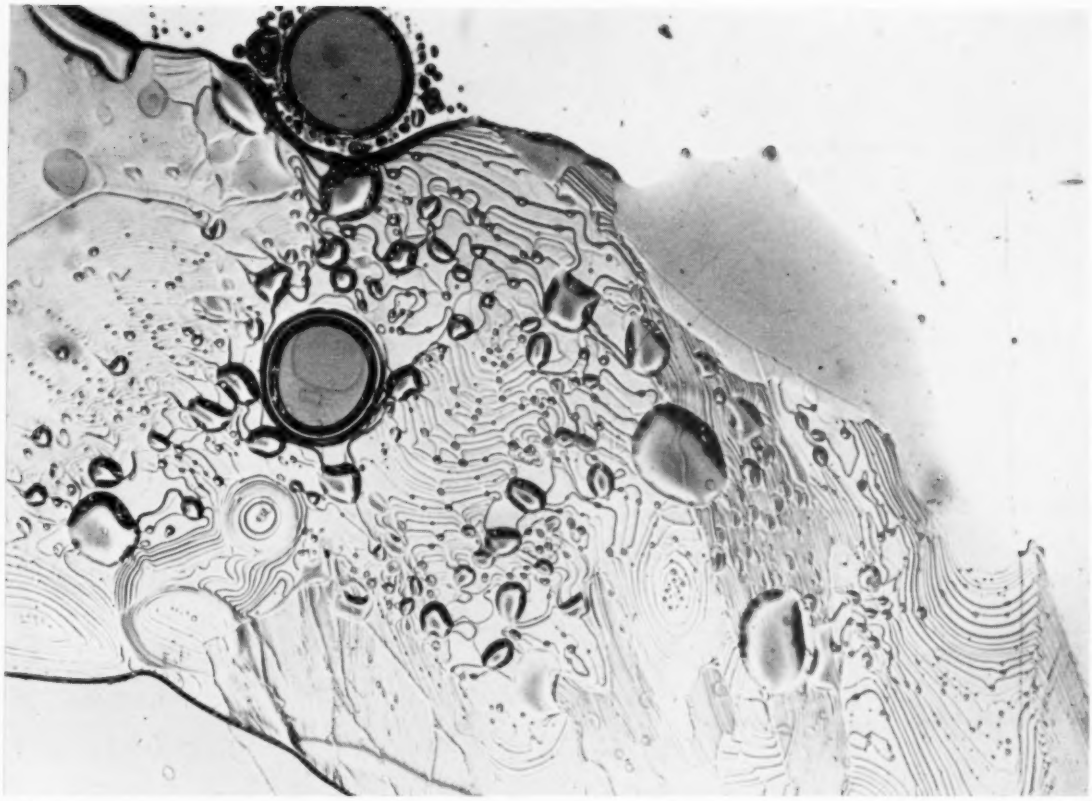

600 × ~250°C

FIG. 4. Melting seems to occur by the recession of crystalline layers, not by the random sloughing-off of material. Droplets, forming on the receding layers, grow and coalesce until large liquid areas are formed.

VOL. 4 1956

between an area of one uniform color and an area of another.

Among the hundreds of mercuric iodide crystals examined, not one definite spiral has been seen. When they occur on isolated crystals, the loops sometimes seen to come from a point well within the bounding edges of the crystal. When several crystals are in intimate contact, having grown until they impinge, the loops appear to come from a section of the grain boundary or, infrequently, from a point away from the grain boundaries. Occasionally, crystals are seen on which the loops apparently spring into existence with a relatively large radius of curvature.

Sublimation

If conditions are adjusted so that the space over a hot mercuric iodide crystal is unsaturated with respect to mercuric iodide vapor, the crystal will sublime. As in the case of growth, sublimation of these crystals is sometimes accompanied by the movement of lines across the crystal surface. The lines start as a boundary around the periphery of a crystal and move toward the interior. The motion of the lines appears to be much the same as during crystal growth, except that the lines move in the direction of their concave side. This process of line movement continues until all visible trace of the crystal has vanished.

Melting

As a vapor-deposited crystal is heated to the melting-point, the lines on the surface stand out in greater contrast. The first evidence of melting is the formation of minute drops at random locations on the lines as the lines move back, as in sublimation (Fig. 4). The droplets are in rapid motion, but seem to stay on one line. The liquid does not appear to wet the surface of its own crystal between lines. Occasionally, a droplet hesitates a moment at one place. The line then recedes more rapidly at the point of hesitation than it does where no drop is present, though the temperature must be very nearly the same. Continued melting appears to occur by the recession of terrace

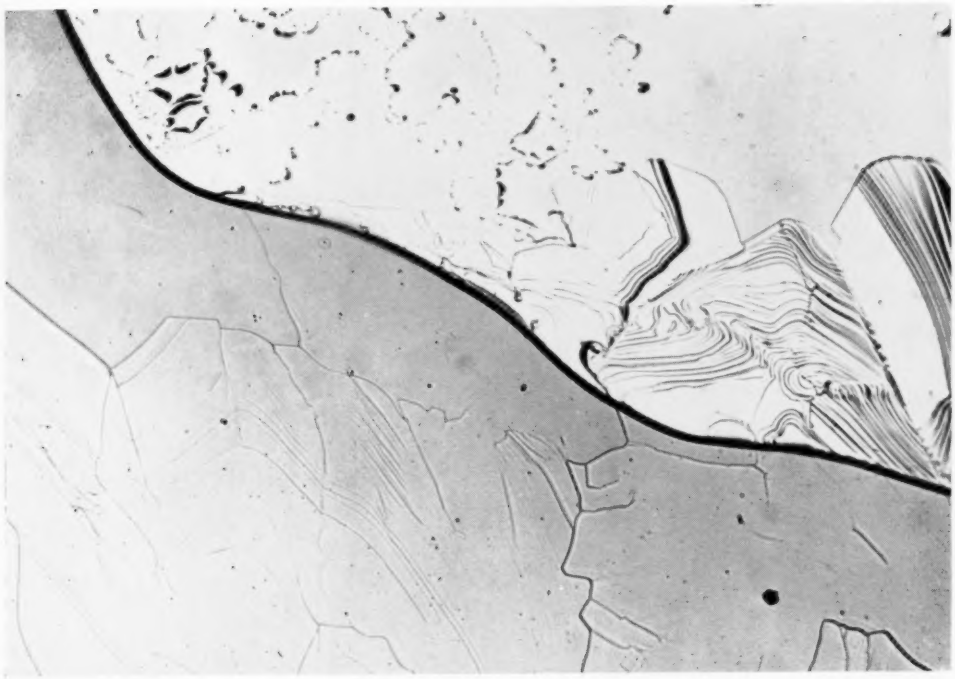

600× ~256°C

FIG. 5. Surface striations on crystals grown in the liquid are easily seen where the liquid has drawn back from a newly frozen crystal. They are barely visible on other parts of the crystal which are covered with the melt.

edges, accompanied by the formation and coalescence of droplets as described above. The layers do not appear to become thinner. Only where there is some sort of a visible crystalline singularity does the surface become pitted. At such a place a hole develops, which becomes lined within as though it were contoured. The contours then recede and droplets form as melting proceeds.

Freezing

Molten mercuric iodide is a reddish-brown liquid somewhat darker than bromine. When the bulk liquid is cooled below the melting point, dendrites quickly grow into the body of the liquid. If the liquid is only slightly undercooled so that the dendrites grow slowly, one can see very faint lines, resembling terrace edges, spreading over the faces of the crystals. The lines are much less distinct than they are on crystals growing from the vapor phase, probably because the refraction between liquid and solid is less than between vapor and solid. If the liquid is quickly drawn back from a newly frozen crystal, the surface striations can be clearly seen (Fig. 5). Spirals have not been observed on crystals grown from the liquid.

Solid-Phase Transformation

Mechanism. When the yellow-red transformation in a loose polycrystalline aggregate is viewed through a microscope, the advancing red front can be seen to move through individual crystals, and from one crystal to another wherever they are in physical contact. Sometimes the advancing front proceeds through a crystal in an apparently random manner with various areas billowing ahead of others (Fig. 6 top). Frequently one or more parallel red bends resembling twins suddenly shoot out into the yellow matrix (Fig. 6 bottom). These bands then widen more or less uniformly until the entire crystal is transformed. Sometimes two nonparallel sets of red bands form, making a lattice-work of red against yellow. The exact conditions favoring one mode of growth over the other are not well understood, but it is suspected that crystal stresses and mechanical restraints are involved in promoting the formation of red bands.

Occasionally a large isolated yellow crystal, say $3 \times 1 \times 0.5$ mm, which has been grown from the vapor can be cooled to room temperature without transforming if it is handled with great care. The yellow-red transformation seems to be suppressed if

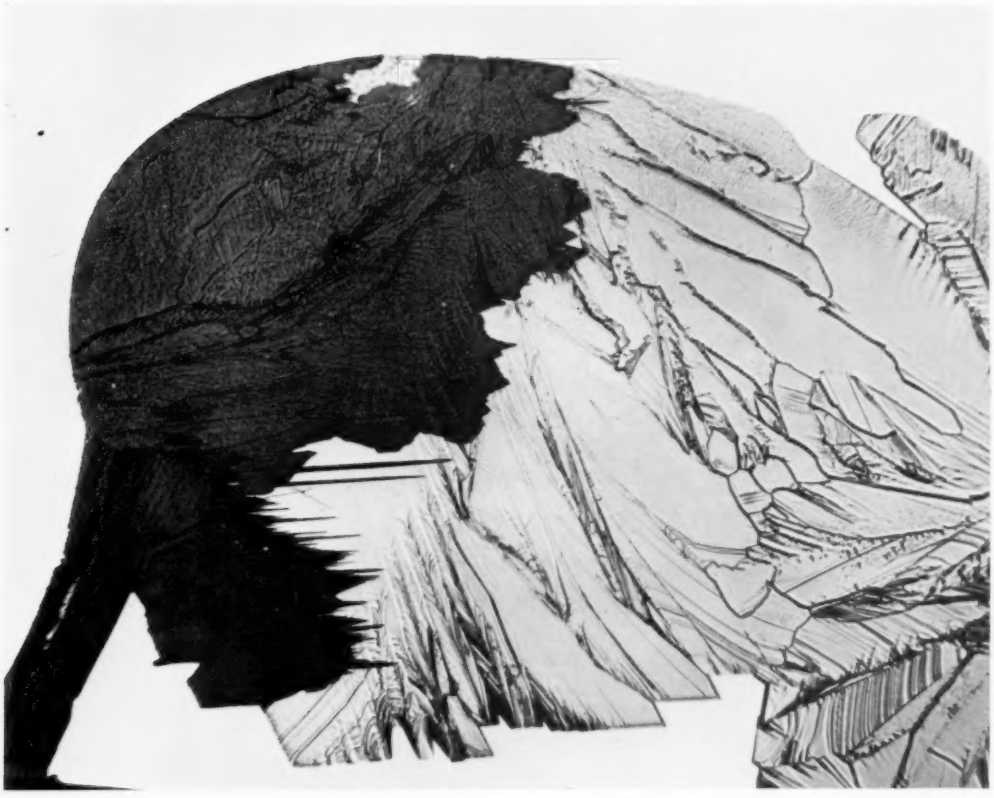

600× ~70°C

FIG. 6. Two modes of transformation from yellow HgI_2 to red.
Top: Random advance of incoherent interface. Bottom: Formation of red bands.

the crystal is coated with a liquid such as acetone which wets the surface. If a yellow crystal is mechanically distorted while at temperatures between 0° and 127°C, the transformation will begin at the point of distortion and spread throughout the entire crystal. When the transformation occurs by the formation of red bands, the bands are invariably parallel with an edge of the crystal and are therefore parallel with a [1$\bar{1}$0] or [110] direction. When a red crystal is heated above 127°C it invariably transforms by the random advance of the red-yellow interface.

By the method described in the Appendix, it was determined that the tetragonal lattice of a red crystal bears the following orientation relationship to the orthorhombic lattice of its parent yellow crystal:

$$(100)_{\text{tetragonal}}//(110)_{\text{orthorhombic}}$$

$$[001]_{\text{tetragonal}}//[001]_{\text{orthorhombic}}$$

Kinetics. In the present investigation the nucleation behavior was of greater interest than the growth rate. Therefore, no attempt was made to measure growth rate of the new phase. It was necessary, however, to determine the temperature limits beyond which growth of the red phase from the yellow is so slow that observations of nucleation behavior would be masked. To test this, several small samples of red mercuric iodide powder were placed in the bottom of each of several small test tubes which were then held in an oil bath at 150°C. Within one minute, all the powder had turned yellow. After fifteen minutes the tubes were removed individually, quickly shaken to provide nuclei for the yellow-red transformation and plunged into one of five constant-temperature oil baths which were held at 100°, 50°, 0°, —78° and —218°C, respectively. The test tubes were observed continuously while in the oil baths, and the times required for the powder to complete one-third, one-half, etc., of the transformation (estimated visually by color change) were recorded for each reaction temperature. The results are shown graphically in Fig. 7.

Effect of Mechanical Distortion. It was mentioned above that the slightest plastic distortion of a yellow crystal held at room temperature will induce its complete transformation to the red phase. Although

VOL. 4 1956

large yellow crystals (average diameter >1 mm) would usually transform spontaneously in a matter of minutes, even if left undisturbed at room temperature, crystals smaller than 0.1 mm could be cooled to room temperature and held there for days (presumably indefinitely) without transforming. However, small crystals which had been rapidly cooled by plunging them directly into liquid nitrogen would turn red within a few minutes after reheating above 0°C. Very slow cooling to liquid nitrogen temperature, over a period of several hours, did not cause the small crystals to transform on returning to room temperature.

Nucleation of Yellow in Red HgI_2. The characteristics of the nucleation of yellow in red mercuric iodide were studied by observing small, isolated, red crystals while they were being heated. These crystals were originally red, having been slowly grown from the vapor on a glass slide at a relatively low temperature. During the test the temperature was observed by means of a very small chromel-alumel thermocouple, the junction of which was placed near the crystals being observed. Photomicrographs were made (35 mm color film) every 2° as the crystals were heated (above 127°C). Pictures were taken until all the crystals were yellow. Then, on each developed photograph, the number of crystals which had turned yellow since the preceding picture was counted. The results of this experiment for crystals of two different sizes are plotted in Fig. 8.

Nucleation of Yellow HgI_2 from the Vapor. If mercuric iodide is heated to a known temperature in a continuous cloud chamber[1] (Fig. 9) so that the vapor is cooled under controlled conditions, a distinct line will be seen below which "snowflakes" of solid yellow mercuric iodide form directly from the vapor. Since the dependence of vapor pressure upon temperature is known for yellow mercuric iodide,[2] by comparing the temperature of the vapor source (e.g. 260°C) with the highest temperature at which snowfall occurred (e.g. 160°C), the vapor supersaturation at the snowline could be calculated. Due to the high molecular weight of HgI_2 there was inevitable turbulence within the chamber, which limited the accuracy to which the vapor supersaturation at the snowline was known.

A 10-minute 16 mm color film has been made which shows many of the effects described above. The film is entitled "Growth, Evaporation and Phase Transformation of Mercuric Iodide Crystals" and is available for loan on request.

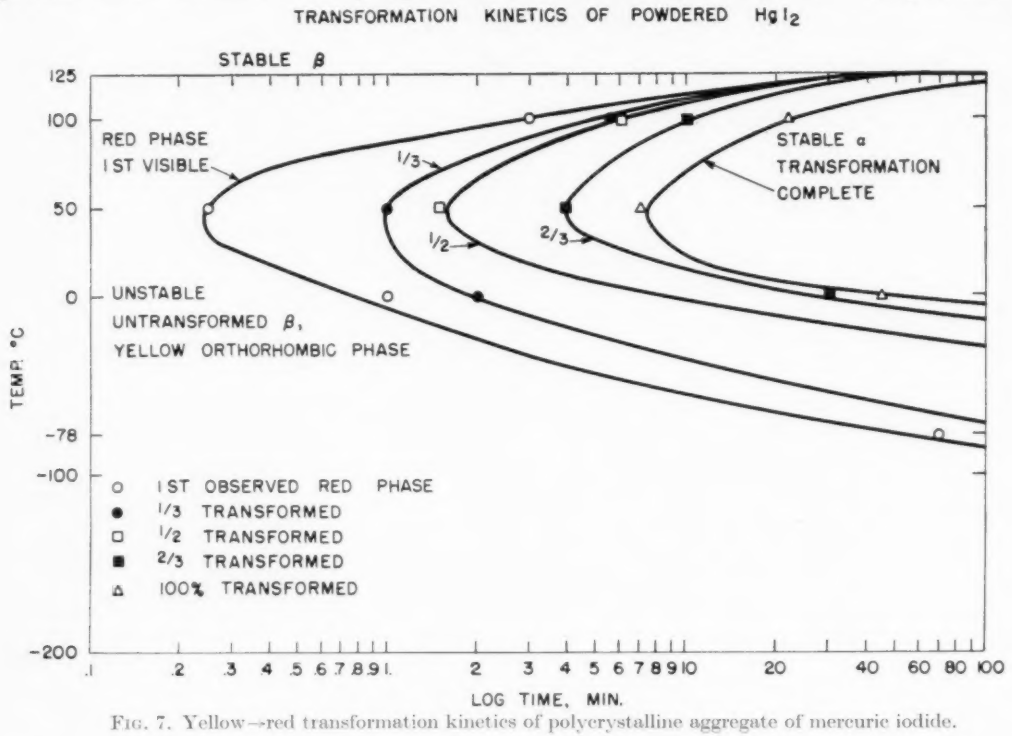

FIG. 7. Yellow→red transformation kinetics of polycrystalline aggregate of mercuric iodide.

3. DISCUSSION

Crystal Growth, Sublimation, and Melting

It was evident that the curved contour-like lines moving across the surface of a crystal marked the edges of layers by which the crystal was growing or

evaporating. When the lines moved toward their convex side the crystal grew. Therefore, layers were being deposited. Conversely, lines moving toward their concave side occurred only on shrinking crystals.

to which it is hanging, the terrace would break away and proceed across the crystal surface. Thus a visible terrace having a relatively large radius of curvature and step height could appear to spring into

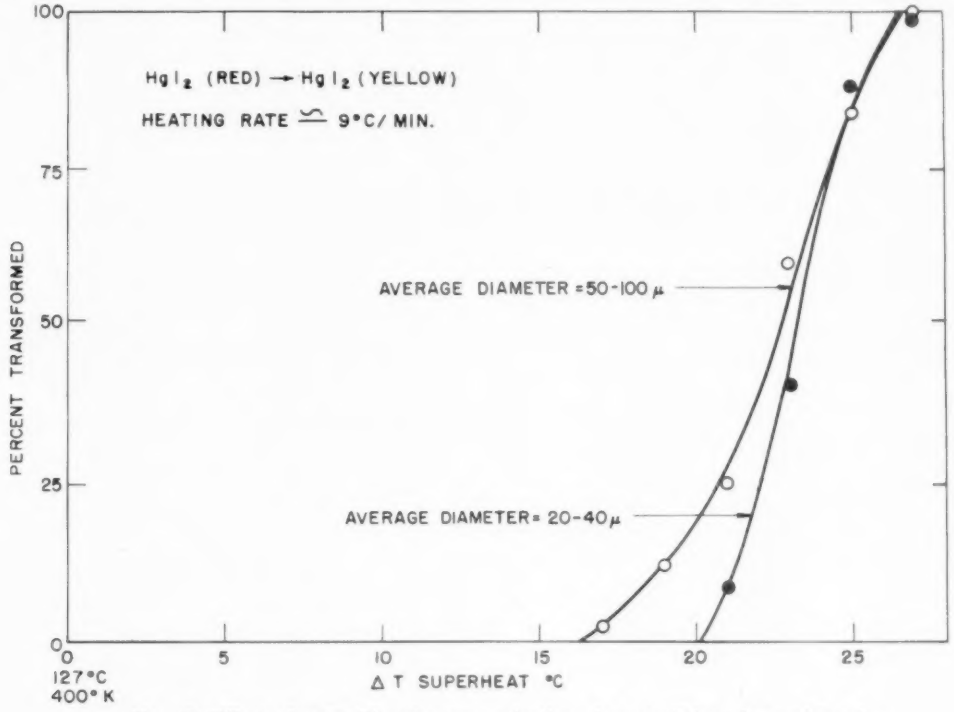

FIG. 8. Effect of crystallite size on nucleation characteristics of superheated red crystals of mercuric iodide.

The mechanism of growth by layers has been observed in many metallic and non-metallic systems.[3,4] However, it is unusual that definite spiral growth sources are not seen on HgI_2 crystals.

The mechanism by which the visible growth steps suddenly appear is not understood. It is possible that many sub-microscopic spiral growth sources of the usual type are present at a grain boundary or in a particular area of a crystal, each source generating a growth step too small to be seen by itself. Many steps of this sort may then catch up with a slower-moving step ahead and thus accumulate into one single large step. This large step could then proceed coherently across the face of the crystal while another large step gathered behind it. Accumulation of small steps could be brought about by the presence of a crystal singularity, such as an included foreign particle or a crystal lineage formation, at a distance from the individual sources. The singularity would retard an invisible advancing step until other smaller (therefore, faster moving) steps could catch up to it. When the step acquires sufficient energy through a concentration fluctuation or other means to overcome the singularity

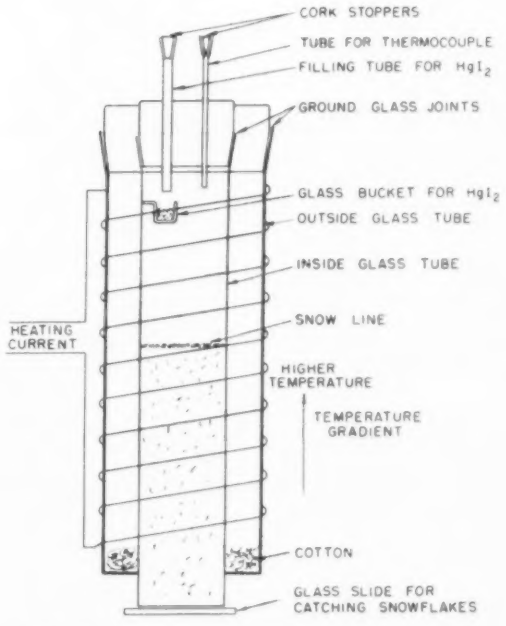

FIG. 9. Diagram of continuous cloud chamber used to form HgI_2 "snow" directly from the HgI_2 vapor.

VOL. 4 1956

existence. It would not be necessary for the visible step to spread from a point of origin as is commonly observed in the growth of cadmium iodide crystals in water solution.[5,6]

The process of sublimation also appears to occur by the removal of successive layers. However, it is not clear how the layer thickness is established during sublimation. When a crystal grows by layering, one may reasonably assume that a crystalline imperfection is present in the surface, which defines the height of the layers at their point of origin. On sublimation, however, some other mechanism must act to define the thickness of the layers since the bounding edge first appears at the periphery of the grain and contracts until the layer disappears at a point. Possibly each layer becomes coated, as it first forms, with an adsorbed film of oxygen or nitrogen, which separates it from the layer immediately below. Thus, the crystal would be built up of a sandwich of layers separated from each other by these thin films. Such a structure might be expected to sublime by the successive removal of the layers in the reverse of the order in which they formed. By an evaporation etching technique, Frasier, at Rensselaer Polytechnic Institute,[7] has found surface figures on chromium metal which are remarkably similar to those observed on mercuric iodide. Also electron micrographs of "natural-fired" barium titanate shows similar steps on the surface.[8]

The fact that a melting terrace edge recedes more rapidly in the vicinity of a droplet, suggests that the solid is at a temperature slightly above its own melting-point. On the other hand the effect of the droplet may alternatively be explained by assuming that impurities present in the droplet lower the melting point of the solid salt with which the droplet is in contact. The latter explanation seems less likely, because the salt was purified by subliming several times before being used for these observations. Furthermore, as a droplet grows, any impurity originally present must become greatly diluted: yet the droplet remains potent in causing the terrace to recede.

Solid-Phase Transformation

Mechanism and Kinetics. The orientation relationship found to exist between a red HgI_2 crystal and its parent yellow crystal, offers no pair of conjugate planes having similar symmetry by which a coherent interface might be formed. Therefore, the yellow-red interface must advance into the yellow phase by the passage of HgI_2 molecules across an incoherent interface. The activation energy required for this process in a strain-free orthorhombic crystal may be represented by Fig. 10(a). No coherency stresses would be generated by this transformation. However, there is generally a volume change accompanying the yellow-red transformation which could provide a source of stress leading to the generation and growth of twins in the yellow phase.

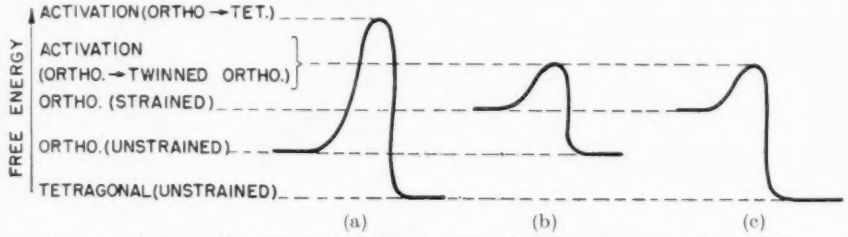

FIG. 10. Schematic representation of free energy changes accompanying twinning and transformation in orthorhombic HgI_2 crystals.

It is probable, though unverified, that orthorhombic mercuric iodide twins on $(1\bar{1}0)$ and (110) planes. A twin forms by the rapid advance of an incoherent twin interface through a yellow crystal in a direction which is parallel with the twin plane. The activation energy required for the movement of this twin interface is represented by Fig. 10(b). If the orthorhombic phase were stable, the molecules passing the incoherent twin interface would be expected to recombine in the orthorhombic arrangement. However, since the twin is made to form at a temperature where the stable crystal structure is tetragonal, the system can enjoy a lowering of free energy if the molecules crossing the interface reorganize as the more stable tetragonal red phase. The free energy change accompanying this mode of transformation is represented by Fig. 10(c). In this case the final state is the stable tetragonal structure, but it was only necessary to reach the twinning activation energy to achieve it. In this case mechanical strains could provide the bulk of the driving force. The effects of mechanical distortion by a probe in initiating and accelerating the yellow-red transformation may come about through a similar mechanism.

This process of phase transformation across an incoherent twin interface provides a mechanism by which a transformation can proceed at a much more

rapid rate than it could if twinning were not involved. It is, of course, limited to systems which will form twins. Furthermore, it would be expected to operate only for allotropic transformations, not for those where composition changes require long range diffusion, since the relatively rapid advance of the twin interface would not allow time for diffusion to occur. This mechanism is similar to the well-known tendency of mechanical distortion in an unstable precipitation alloy to initiate precipitation on active slip planes where lattice disturbance has occurred.

Other investigators[9,10] have made semi-quantitative tests of the rate of (yellow→red) transformation in loose polycrystalline aggregates over limited temperature ranges. Data from these tests are limited by the fact that the transformation occurs mostly by growth rather than extensive nucleation. In a mass of crystals the spread of the red phase is strongly affected by the amount and geometry of the contact area between the adjoining grains. Therefore, a measure of the linear velocity of the average macroscopic interface between the red and yellow areas in a polycrystalline mass is not a quantity having fundamental significance. Furthermore, since two modes of growth of the red phase occur, viz., random interface advance and twin formation, the overall rate represents at best only a combination of these two growth mechanisms.

From the isothermal transformation experiments with monocrystalline samples it was established that nuclei of the red phase will not form spontaneously in yellow crystals at temperatures as low as 0°C. At lower temperatures slow growth rate makes it uncertain as to whether nuclei form or not. Therefore, 127°C was taken as a minimum amount of undercooling to which yellow HgI_2 can be subjected without inducing spontaneous nucleation. If a crystal is distorted at a low temperature where atomic mobility is small, the lattice apparently becomes activated by the disturbance so that, on reheating, nucleation and growth can occur.

According to nucleation theory[11] the change in free energy ΔG^* accompanying the formation of a spherical isotropic nucleus of critical size is:

$$\Delta G^* = \frac{16}{3}\frac{\pi\sigma^3_{ry}}{(\Delta G_V{}^T)^2} \qquad (1)$$

where σ = interfacial energy between nucleus and matrix

$\Delta G_V{}^T$ = change in free energy per unit volume at the temperature T

I = nucleation frequency per unit volume

k = Boltzmann's constant

T = temperature.

At constant pressure $\frac{dG_V{}^T}{dT} = -\Delta S_V$, the entropy change accompanying the transformation from yellow to red. It follows from this that

$$\Delta S_V = -(C_p{}^R - C_p{}^Y)\left(\ln\frac{T}{T_0}\right) + \Delta S_0\, dT, \qquad (2)$$

where ΔS_0 is the entropy change at T_0, the equilibrium transformation temperature and C_p is the specific heat of the red or yellow phase. This provides the following expression, by means of which $\Delta G_V{}^T$ can be evaluated in terms of known thermodynamic constants[12]:

$$\Delta G_V{}^T = -\Delta S_0(T - T_0) - \Delta C_p\left[T\ln\frac{T}{T_0} - (T - T_0)\right]. \qquad (3)$$

A reasonable value for ΔG^* can be approximated by assuming that nuclei of the yellow phase form at the rate of one per second per cc. Following the theory and notation of Turnbull and Fisher,[13]

$$I \simeq 1 = 10^{30}\exp\frac{-\Delta G^*}{kT}, \qquad (4)$$

where k = Boltzmann's constant. The pre-exponential factor is discussed in reference 13. Using equations (1–4), a minimum value of 14 ergs/cm² for σ_{ry} is found corresponding to minimum undercooling of 127°C.

Red → Yellow Nucleation

In contrast with the stable behavior of yellow crystals on cooling, crystals which are originally red invariably turn yellow before they are superheated more than 27°C above the equilibrium transformation temperature. As is shown in Fig. 8, crystals of smaller size are more resistant to transformation, an expected effect of isolation if nucleation is normally catalyzed by foreign particles. Since the highest temperature at which the most resistant crystal would remain red was 154°C, this is assumed to be the temperature at which surface nucleation occurs spontaneously. Crystals which turned red at temperatures below 154°C were presumably nucleated by an impurity particle or some other crystalline inhomogeneity.

One can rationalize this difference in transformation behavior of red and yellow crystals by assuming that the first bit of yellow phase, which forms from an originally red crystal, occurs at the surface of the crystal. For purposes of calculation it may be further assumed that the nucleus takes the form of an

VOL. 4 1956

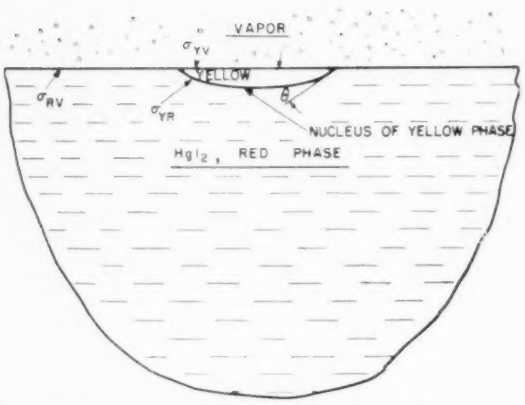

FIG. 11. In an unstable red crystal the yellow phase may nucleate as a spherical segment on the surface.

isotropic spherical segment, as in Fig. 11. The relative values, σ_{vr} and σ_{vy}, of the energies of the red and yellow phases against mercuric iodide vapor are given by the angle θ and to assume θ is less than 90° is equivalent to assuming $\sigma_{vy} < \sigma_{vr}$. This is consistent with the concept that the low temperature phase, having stronger interatomic binding than the high, has a larger surface energy. It is also consistent with the observation by the author and the statement by Mellor that yellow crystals can form from the vapor on a glass slide at temperatures as low as 25°C. In forming the vapor-yellow (VY) interface an equal amount of vapor-red (VR) interface is lost, resulting in a net lowering of surface energy.

The activation energy required to form a critical size nucleus of the type sketched in Fig. 11 is[14]

$$\Delta G^* = \frac{16\,\pi\,\sigma^3_{ry}}{3\,(\Delta G_V{}^T)^2}\,\frac{(2\,+\,\cos\theta)(1\,-\cos\theta)^2}{4}, \quad (5)$$

where $\Delta G_V{}^T$ is the change in free energy per unit volume of transformed material at temperature T. Using the value for σ_{RY} (min) found in the preceding section, one finds a maximum value of 24° for θ.

Assuming that the surface nucleus is isotropic,

$$\sigma_{RV} = \sigma_{YV} + \sigma_{RY}\,(\text{min})\cos\theta\,(\text{max}). \quad (6)$$

Since $\sigma_{RV} > \sigma_{YV}$, a red-vapor surface could be replaced by a yellow-vapor surface with a decrease in surface energy, and nucleation of the yellow phase upon the surface of a red crystal is favorable. Similar reasoning leads to the conclusion that transformation from yellow to red by surface nucleation is unfavorable. This would account in part for the large amount of undercooling which yellow crystals will suffer without transforming spontaneously.

Thus far only relative values for σ_{RV}, σ_{YV}, and σ_{RY} have been found. Their values can be approximated on an absolute energy scale by using the data from the cloud chamber experiment.

The maximum supersaturation ratio, S, which was required to form mercuric iodide snow crystals by homogeneous nucleation from the vapor at 160°C was found to be approximately 90. This figure is a maximum value because the turbulence caused by the high molecular weight of the HgI_2 inevitably resulted in some dilution of the vapor with air before it reached the snow level. From this value, $\Delta G_V{}^T$ can be calculated since

$$\Delta G_V{}^T = -\frac{kT}{v}\ln S, \quad (7)$$

where v = molecular volume and

$$S = \frac{\text{vapor pressure } HgI_2}{\text{saturation vapor pressure } HgI_2}.$$

Combining equations (1) and (7), and using the approximation $I \simeq 1 = 10^{25}\,\exp\dfrac{-\Delta G^*}{kT}$, one finds that $\sigma_{VY} \simeq 102$ ergs/cm².

This, with equation (6), predicts a maximum value of 115 ergs/cm² for σ_{RV}.

4. SUMMARY AND CONCLUSIONS

(1) Crystals of the yellow orthorhombic phase of mercuric iodide normally form from the vapor in the shape of flat parallelograms with edges parallel to [110] and [1$\bar{1}$0]. The thin plane of a crystal is normal to [001]. The crystals are sometimes twinned on a (110) or (1$\bar{1}$0) plane. When supersaturation is low the growing crystals take the shape of needles.

(2) The yellow crystals grow from the melt or from the vapor by the formation of successive layers thousands of Å thick. These layers are parallel with $(001)_{\text{orthorhombic}}$. The thickness of a given layer appears to be constant as it advances, although the thicknesses of successive layers are nonuniform. The visible layers probably form by the occasional accumulation of many invisible layers of much smaller step height. No growth spirals have been observed and the origin of the small layers is not definitely known.

(3) Yellow mercuric iodide crystals sublime and melt by the recession of layers over their surface. It is not clear how the step height of a receding layer is originally fixed. A melting crystal first develops droplets at terrace edges. The droplets appear to wet the edge but not the flat surface of a layer. Wherever a droplet occurs, the layer recedes more rapidly, indicating that the solid may be superheated. Melting proceeds by the coalescence of droplets accompanied by layer recession, not by the thinning of layers or the random sloughing-off of material.

(4) Orthorhombic mercuric iodide transforms to the tetragonal structure by two different mechanisms, viz.,

(a) The random advance of the red-yellow interface through the crystal.

(b) The rapid darting through the crystal of red bands parallel with [110] and [1$\bar{1}$0]. It is proposed that these are regions where transformation is accelerated by the passage of an incoherent twin boundary through the unstable crystal lattice. The twinning may arise from strains resulting from the volume change accompanying previous transformation.

The orientation relationship between the tetragonal lattice of a red crystal and the orthorhombic lattice of its parent yellow crystal is as follows:

$$(100)_{\text{tetragonal}}//(110)_{\text{orthorhombic}}$$
$$[001]_{\text{tetragonal}}//[001]_{\text{orthorhombic}}.$$

Since this relationship does not offer the possibility of conjugate planes having close atomic matching, the interface is probably not a coherent one.

(5) Crystals which were originally of the low-temperature red tetragonal phase could be heated as much as 27°C above the equilibrium transformation temperature without spontaneously turning yellow; crystals which were originally of the high-temperature yellow orthorhombic phase could be undercooled at least 129° without turning red. This asymmetrical nucleation behavior is explained on the hypothesis that the yellow phase nucleates on the surface of a red crystal and the red phase nucleates in the interior of the yellow. On the basis of this hypothesis, reasonable values of interfacial energies between the two phases, and between each phase and mercuric iodide vapor, are estimated from superheating and undercooling data.

ACKNOWLEDGMENTS

Throughout this study the author has had the benefit of stimulating discussions with D. Turnbull and G. W. Sears, both of this laboratory.

REFERENCES

1. A. Langsdorf, jr., *Ind. and Eng. Chem.*, **44,** 1298–1300 (1952).
2. J. W. Mellor, *A Comprehensive Treatise on Inorganic and Theoretical Chemistry*, Vol. IV, 901–921, Longmans, Green and Co., London (1923).
3. H. E. Buckley, *Structures and Properties of Solid Surfaces*, Chap. VIII, Univ. of Chicago Press (1953).
4. *Crystal Growth, Disc. Farad. Soc.*, No. 5, Gurney & Jackson, London (1949).
5. A. J. Forty, *Phil. Mag.*, **43,** 377–92 (1952).
6. J. B. Newkirk, *Acta Met.*, **3,** 121–5 (1955).
7. Malcolm Frasier (To be published), Rennselaer Polytechnic Institute, Troy, N.Y. (1954).
8. C. R. Mingins, Dept. of Physics, Tufts College, Medford, Mass. Private Communication (1954).
9. J. B. M. Coppock, *Nature*, **133,** 570 (1934).
10. D. G. Eade and N. H. Hartshorne, *J. Chem. Soc.*, (*Trans.*), 1636–46 (1938).
11. R. Becker and W. Doring, *Ann. d. Physik* (5), **24,** 719 (1935).
12. K. K. Kelley, *U.S. Bureau Mines Bull.*, No. 476 (1949).
13. D. Turnbull and J. C Fisher, *J. Chem. Phys.*, **17,** 71 (1949).
14. M. Volmer, *Z. Elektrochem.*, **35,** 555 (1929).

Appendix

By **W. G. MARTIN**

Determination of the Orientation Relation Between the Orthorhombic and the Tetragonal Phases

Yellow crystals grown slowly from the vapor upon a glass fiber often have the shape sketched in Fig. 12. If all but one of these crystals is removed from the

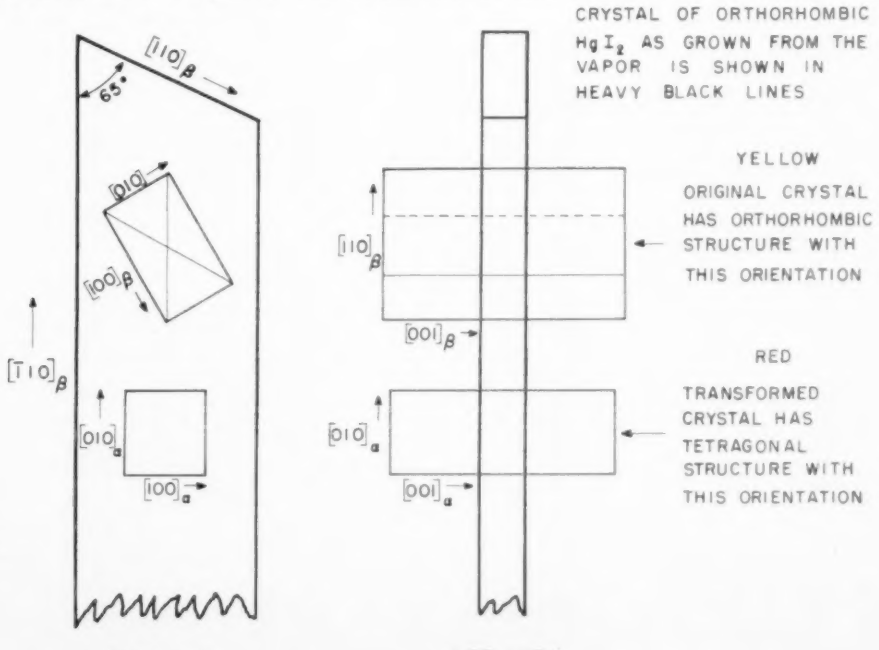

Fig. 12. Yellow crystals grown from the vapor upon a glass rod usually take the form of long flat rods of the shape sketched here.

VOL. 4 1956

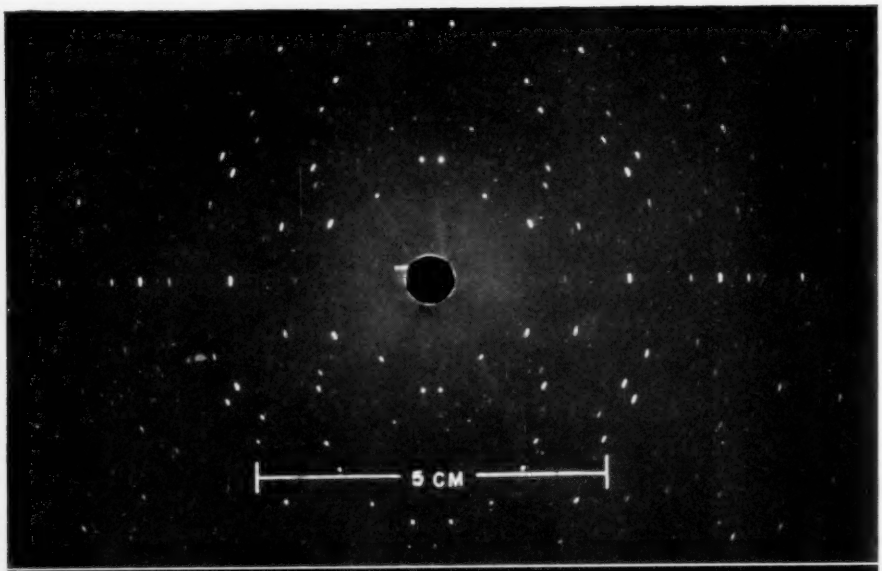

(a) Transmission Laue. [110] vertical, [001]//beam.

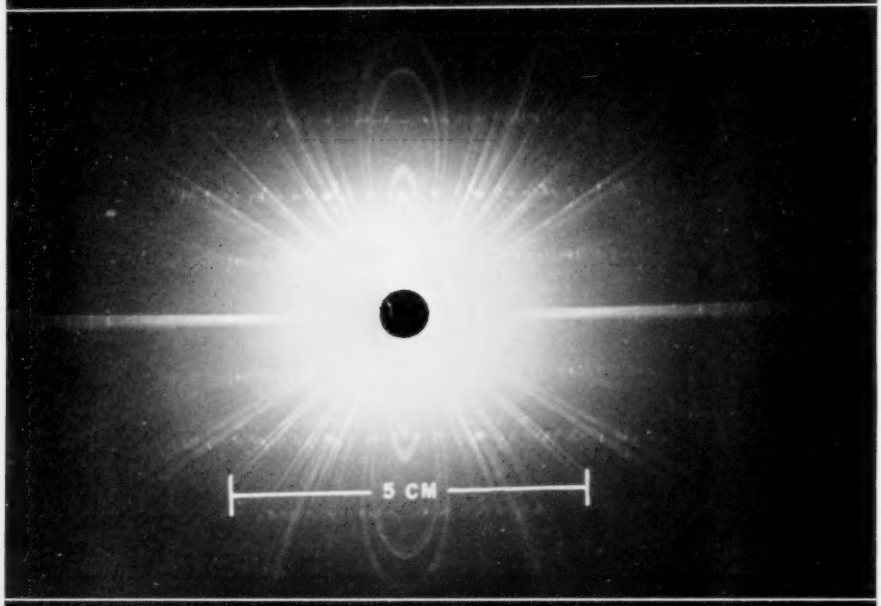

(b) Rotation. [110] vertical and rotation axis.

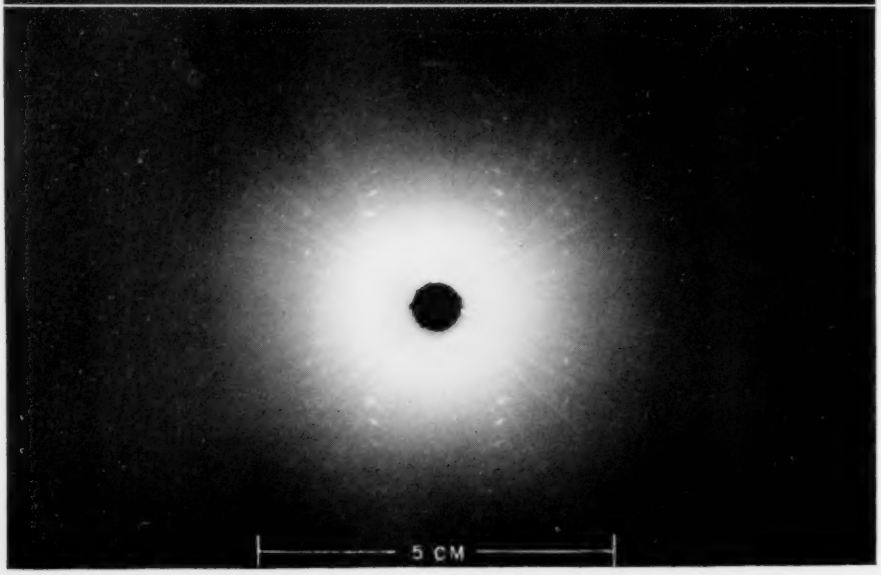

(c) Rotation. [001] vertical and rotation axis.

FIG. 13. X-ray diffraction photographs of the unstable yellow phase. (Room temperature, Mo radiation, Rad. = 5 cm)

VOL
4
195

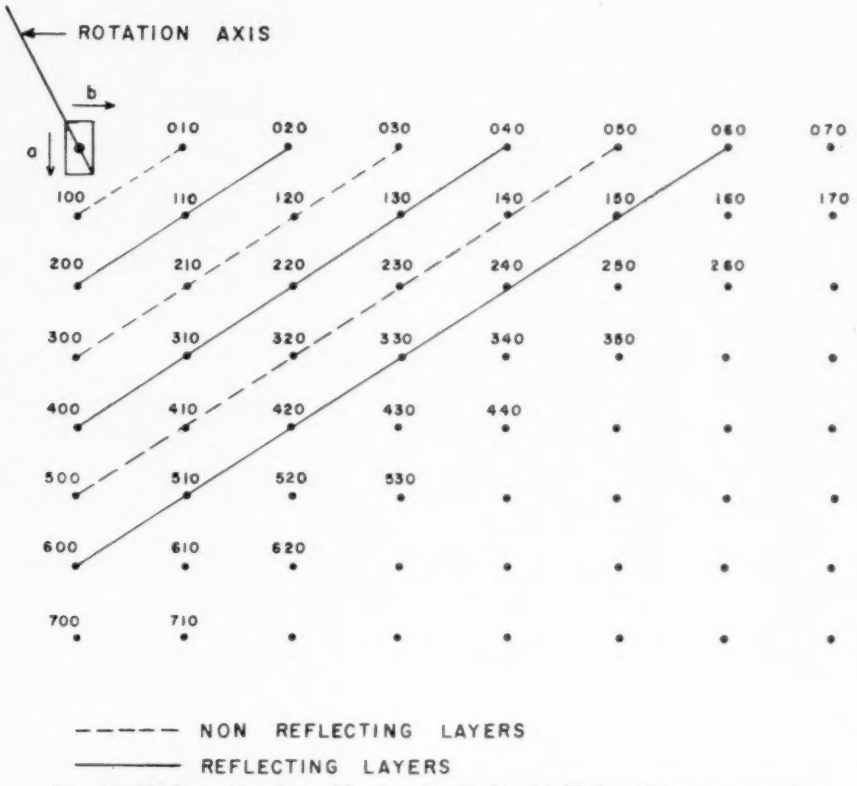

FIG. 14. $hk0$ layer of reciprocal lattice of orthorhombic HgI_2. (Space group C_{2v}^{12}.) Reflection occurs from points with indices $h + k = 2n$. These and corresponding points where $l \neq 0$ give layer lines seen on Fig. 13(b).

VOL. 4 1956

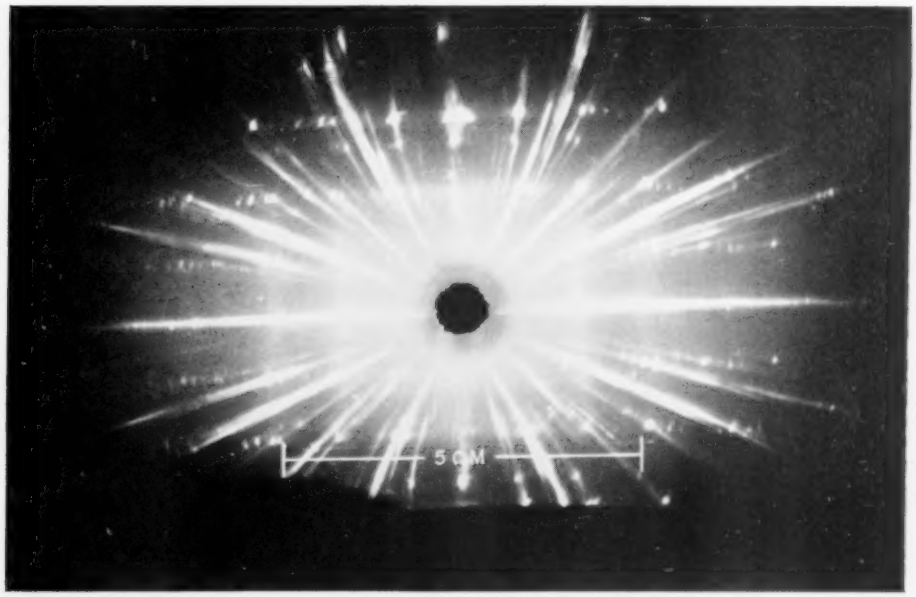

FIG. 15. Transmission Laue photograph of red crystal which was originally yellow. Layer lines correspond to a dimension of unit tetragonal cell.

fiber, the remaining crystal can be conveniently studied by conventional x-ray diffraction methods. Fig. 13(a) shows a transmission Laue photograph of a single crystal of the orthorhombic phase with [001] parallel with the beam and [110] vertical. Unfiltered molybdenum radiation and a cylindrical camera of radius 5 cm were used throughout this study. For Fig. 13(a) the long axis of the macroscopic crystal was vertical.

During the exposure for Fig. 13(b), the crystal, mounted as for Fig. 13(a), was rotated about the vertical axis. The layer lines correspond to the indicated (110) planes of the reciprocal lattice in Fig. 14 and have a ζ-value corresponding to even layers of the orthorhombic HgI_2 reciprocal lattice. Reflection from points on odd layers of the reciprocal lattice is forbidden for this space group (C_{2v}^{12}). For Fig. 13(c), the crystal was turned so that its flat side was horizontal and then was rotated about a vertical axis during the exposure. The layer lines in Fig. 13(c) correspond to the c-dimension of the mercuric iodide$_{\text{(orthorhombic)}}$ unit cell.

To establish the orientation relationship between a yellow crystal and a red one descended from it, the orientation of a yellow single crystal was determined as described in the preceding paragraph and then the crystal was lightly touched, thereby causing it to transform to the red phase. A Laue photograph was then made with the now red crystal still in place in the camera. From this photograph the orientation of the red crystal was directly determined and could be related to that of its parent yellow crystal. Fig. 15 shows a transmission Laue photograph of a red crystal descended from a yellow crystal which had been oriented with $[001]_{\text{ortho.}}$ parallel with the beam and $[110]_{\text{ortho.}}$ vertical. For Fig. 15 $[001]_{\text{tet.}}$ is parallel with the x-ray beam and $[100]_{\text{tet.}}$ is vertical. Severe distortion indicated by the heavy streaks is probably a result of mechanical warping which is characteristic of single crystals of mercuric iodide after they have transformed from yellow to red. According to Fig. 15, the warping amounts to a 20° twist of the crystal about the vertical [100] axis. Layer lines made visible by this distortion correspond to the a dimension of tetragonal mercuric iodide.

The orientation relationship given by this method is:

$$(100)_{\text{tetragonal}}//(110)_{\text{orthorhombic}}$$

$$[001]_{\text{tetragonal}}//[001]_{\text{orthorhombic}}$$

and is shown in Fig. 12.

On the Role of Grain Boundaries in Creep*

There are numerous examples of the influence of crystallographic orientation of grain boundaries on their properties and behavior.[1] One of the first to show this effect was Chalmers,[2] who measured creep strengths of tin bicrystals grown in such a manner that both crystals were similarly oriented with respect to the specimen axis, which was also the tensile axis. The [001] axes of the tetragonal lattice were perpendicular to the tensile axis, while the [101] directions were at 45 deg to it. The angle A between the [001] axes of the two crystals was varied so as to cover the whole range, and the results are reproduced in Fig. 1. The deviations of experimental points from the straight-line average seem to indicate a certain systematic trend, and thus a closer analysis of the observed facts was made.

It is natural to expect that the variation of such a quantity as creep strength as a function of the angle A will be irregular whenever the grain boundary is in proximity of a prominent crystallographic plane. A typical example of this behavior is, for instance, the rate of diffusion along grain boundaries.[1] The rate of creep will be influenced by the availability of dislocations and the ease with which they can move across the grain boundary. A grain boundary parallel to a plane of high density would provide a better fit between the lattices of the two grains than a low-density plane, and would facilitate creep, A calculation was made to show what angles A correspond to high-density, low-index planes in Chalmers' experiments. Referring to Fig. 2, it can be seen that the last index of the tensile axis must be zero, since the axis is perpendicular to the [001] direction.

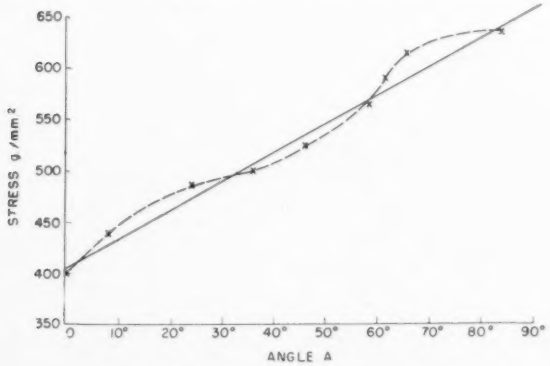

FIG. 1. Chalmers' data on creep strength vs. angle between grains.

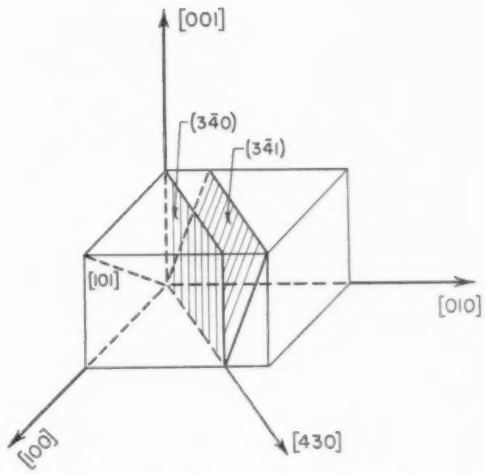

FIG. 2. Orientation of grain boundaries with respect to crystal axes.

The condition that the axis is 45 deg from the [101] direction gives the ratio of the two other indices of the axis, and so one obtains [1 0.735 0], or approximately [430]. Thus the grain boundaries in these experiments belong to the [430] zone and must be of the (3$\bar{4}l$) type, where l varies from 0 (at $A = 0°$) to 2·37 (at $A = 90°$). Apart from the limiting case $l = 0$, the lowest index is (3$\bar{4}$1), which corresponds to $A = 40°$, in good agreement with a broad minimum in the array of experimental points as shown in Fig. 1. This plane is outstanding among all the possible (3$\bar{4}l$) planes ($l \neq 0$) because it has the highest density of atoms and also because it contains [111], the most densely packed direction of all directions contained in these planes. The density of atoms in the (3$\bar{4}$1) plane is only a few per cent lower than in the (3$\bar{4}$0) plane, which is the most densely packed of all planes in the [430] zone. The next plane, the (342), does not seem to show up as a dip in the experimental curve, presumably because its density is already 15% lower than in (3$\bar{4}$1). The low creep strength for A near 0° and 90° may be related to the (3$\bar{4}$0) and (3$\bar{4}\bar{3}$) planes respectively, but there are not enough experimental points available to justify that conclusion.

It would be of considerable interest to conduct similar measurements for a variety of bicrystals and

VOL. 4 1956

obtain a more complete picture of the "permeability" of grain boundaries to dislocations.

This work was supported by an AEC contract; the first author had an AEC Fellowship.

M. R. Achter†
R. Smoluchowski

Carnegie Institute of Technology.

References

1. M. R. Achter and R. Smoluchowski; Carnegie Institute of Technology Thesis, 1950; *J. App. Phys.* **22**, 1260 (1951).
2. B. Chalmers, *Proc. Roy. Soc.* **162**, 120 (1937).

* Received August 24, 1955; in revised form January 3, 1956.

† M. R. Achter, now at the Naval Research Laboratory, Washington, D.C.

Dislocations at Compositional Fluctuations in Germanium-Silicon Alloys*

Unusual arrays of dislocations have been found in germanium-alloy single crystals grown from the melt. The arrays are presumably layers of edge dislocations which lie parallel to successive positions taken by the liquid-solid interface during freezing. They arise from fluctuations in solute concentration, and hence of lattice constant, at the interface. The dislocations form presumably because they reduce the energy of elastic strain between adjacent crystal layers which differ in lattice constant.

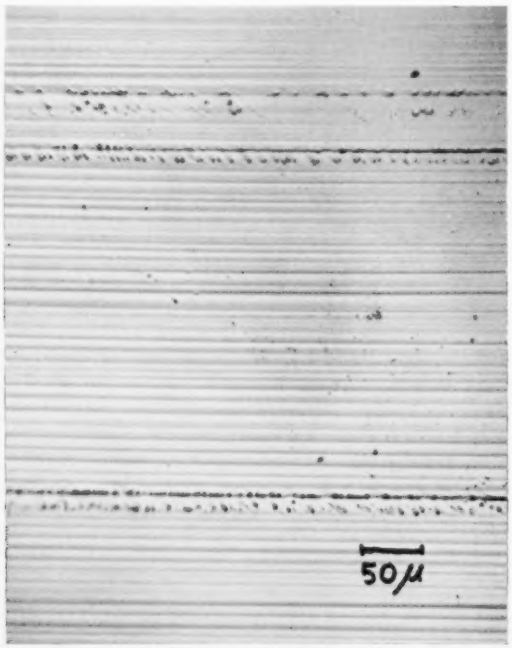

Fig. 1. Dislocation etch-pits lying along growth striae in germanium–6 at. per cent silicon single crystal.

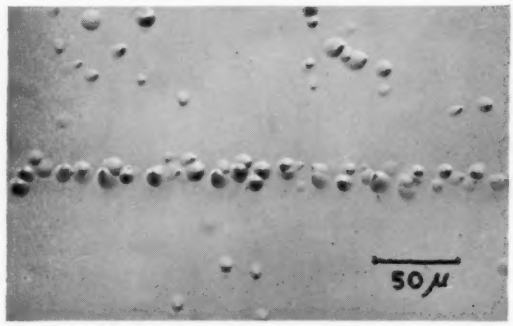

Fig. 2. A section similar to that of Fig. 1, at higher magnification.

Such dislocations have been observed in single crystals of germanium–6 at. per cent silicon, germanium–0.2 at. per cent tin, and germanium–0.2 at. per cent boron, but *not* in germanium or silicon single crystals containing $< \sim 10^{-4}$ at. per cent of solute. A section of a germanium–6 at. per cent silicon crystal, in a (111) plane nearly parallel to the growth direction, is shown in Fig. 1. The surface has been ground and etched in CP-4, a mixture which reveals edge dislocations in germanium alloys as etch-pits,[1] and which, because etch-rate varies with composition, reveals fluctuations in silicon concentration as striae lying parallel to interface-positions. Note that: (a) the pits are distinctly lined up parallel to the striae, which is in accord with the reason advanced for their origin; (b) the rows tend to appear in pairs, which can be attributed to a rise, followed shortly by a fall in silicon concentration; and (c) the pits appear only at certain striae, which is presumably because dislocations are formed only if the concentration gradient exceeds a critical value related to the elastic strain required to form dislocations. As shown in Fig. 2, for another specimen at higher magnification the spacing and alignment of the etch-pits is less regular than in typical lineage boundaries in germanium.[1]

A maximum value for the linear density, ρ, of edge dislocations arising from an abrupt change, ΔC, in solute concentration at the interface can be estimated by assuming that all of the macroscopic elastic strain is relieved by dislocations. Each edge dislocation relieves an elastic strain equal to the Burgers vector b, which is $(a/\sqrt{2})$ [110] for germanium. It is readily shown that if a change ΔC causes a change Δa_0 in lattice constant, ρ will be given by:

$$\rho = (\Delta C)\,(da_0/dc)\,(\sqrt{2}/a_0^2) \qquad (1)$$

where (da_0/dc) is the change in lattice constant per unit change in solute concentration. For germanium-silicon alloys of low silicon content, da_0/dc is about

-2.8×10^{-11} cm per atomic per cent of silicon;[2] and a_0 for germanium is 5.6×10^{-8} cm. Hence, a ΔC of 0.1 at. per cent silicon (which appears reasonable for these crystals) will produce according to equation (1), about 1200 dislocations per cm. Fig. 2 shows a dislocation density of about 1400, and Fig. 1 perhaps twice that. From evidence of this kind it appears that, at a discontinuity in solute concentration of perhaps 0.1 at. per cent or more, an array of edge dislocations may be expected in germanium.

Since edge dislocations materially lower carrier lifetime in germanium,[3] arrays such as those described here may be the cause of the relatively low lifetimes observed in germanium-silicon alloys. We, and also S. G. Ellis,[4] have observed them at p-n junctions such as are produced by the alloy process. They should increase the saturation current and to some extent decrease storage of injected carriers at a p-n junction.

In general, microscale fluctuations of solute concentration such as described here provide an effective mechanism for the formation of dislocations in crystals grown from the melt, even in the absence of macroscale segregation, which has previously been proposed as a source of dislocations.[5]

The writers wish to thank W. C. Ellis, D. F. Gibbons, J. N. Hobstetter, W. T. Read, and F. L. Vogel for helpful discussions.

A. J. Goss†
K. E. Benson‡
W. G. Pfann‡

VOL. 4 1956

References

1. F. L. Vogel, W. G. Pfann, H. E. Corey, and E. E. Thomas, *Phys. Rev.* **90,** 489 (1953).
2. E. R. Johnson and S. M. Christian, *Phys. Rev.* **95,** 560 (1954).
3. F. L. Vogel, W. T. Read, and L. C. Lovell, *Phys. Rev.* **94,** 1791 (1954).
4. S. G. Ellis, *J. App. Phys.* **26,** 1140 (1955).
5. B. Chalmers, *Trans. Amer. Soc. Metals* **47A,** 84–106 (1955).

* Received December 30, 1955.
† Now with Marconi Research Establishment, Great Baddow, Essex, England.
‡ Bell Telephone Laboratories, Murray Hill, New Jersey.

On Thermodynamical Analysis by Calorimetry Alone*

Recently Oelsen, Schürmann, and Heynert[1] have made a circumstantial and well-founded plea for "thermodynamical analysis" by a purely calorimetric method. It is based essentially on two simple facts:

(i) The increase in entropy of a substance when heated (at constant pressure) from T_1 to T_2 is given by $\int_{T_1}^{T_2} \frac{dH}{T}$, where H is the enthalpy (heat content) and T absolute temperature. This classical definition of entropy is valid irrespective of whether the substance is heterogeneous at T_1 and/or T_2, or somewhere in between, provided equilibrium is established everywhere.

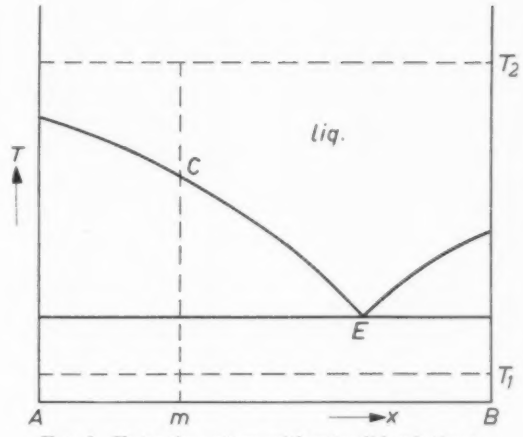

FIG. 1. Eutectic system without solid solutions.

(ii) In a binary two-phase (or ternary three-phase, etc.) region, all thermodynamic quantities are linear functions of concentration.

For example (cf. Fig. 1), when H as a function of T is measured between T_1 and T_2 for the mixture m and for both components A and B, not only ΔH, but also ΔS and ΔG, are known for the liquid mixture, with reference to liquid A and B at the same temperature. This method yields primarily the free enthalpy G. The chemical potentials μ_A and μ_B can only be obtained—by differentiation of the G, x curve—when several mixtures have been measured. The authors point out that two G values in a two-phase region (e.g. two liquids, as in Fig. 2) are sufficient for deter-

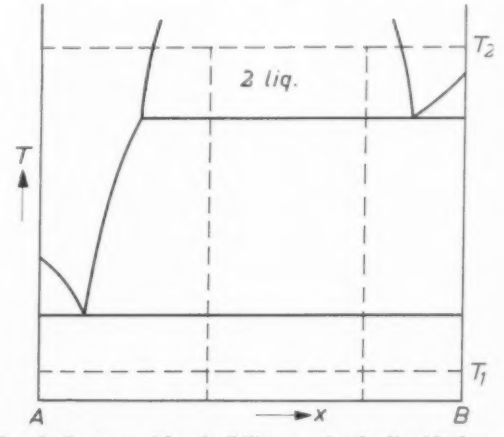

FIG. 2. System with miscibility gap in the liquid phase.

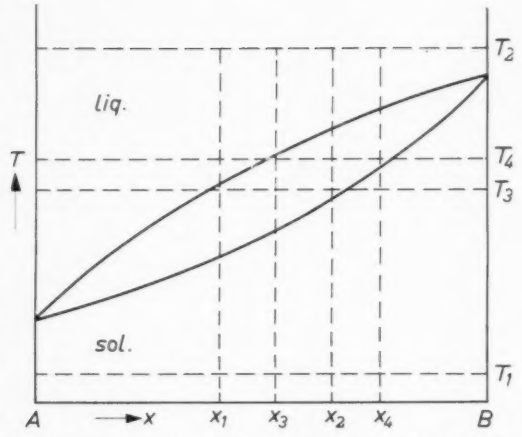

FIG. 3. System with complete solid and liquid miscibility.

mining the activities of saturated solutions, without precise knowledge of their concentrations. In the case of Fig. 1, even one measured concentration† (m for example) is sufficient for the chemical potentials in the two-phase region between T_E and T_C. It may be remarked that the values of H and S of the saturated liquids E to C can also be calculated, provided this liquidus curve itself is known. Suppose that the specific heat c_p of the liquid may be assumed to be linear with concentration (Kopp). Then H, S, and G are known at T_2 for all concentrations between x_C and x_E.

On the other hand, if an appreciable number of mixtures is measured, the detailed course of their H, T curves is not necessary, provided Kopp's rule may be applied and the liquidus curves‡ in the phase diagram are known. Then the mixing enthalpy curve of the liquid phase is independent of T, and its knowledge combined with the phase diagram yields the entropy and free-enthalpy data. The counterpart of this, calculating the mixing enthalpy from the phase diagram and mixing entropy—assumed to be Gibbsian—is often carried out.

However, complete "thermodynamical analysis" with several mixtures makes Kopp's approximation unnecessary, and constitutes an elegant and self-contained method. The authors[1] express well-founded astonishment that it is not mentioned in textbooks on thermodynamics. The writer is only aware of a paper in Japanese[2] which—judging from the abstract—might perhaps treat the same method. Oelsen *et al.* also stress the advantage for instructive purposes of mixing A and B reversibly through the solid + liquid region instead of using hypothetical semipermeable membranes, as in the van't Hoff method. Their method can also be applied[1] in systems with intermediate phases (but no solid solutions).

Systems with solid solutions are especially important for alloys. But here difficulties arise, at least when solid solutions are still present after cooling, so that no two-phase equilibria of, e.g., solid A + solid B are obtained. Oelsen *et al.* propose to have recourse to low-temperature calorimetry, using a tentatively extended version of Nernst's theorem. The supposition that an undercooled solid solution would have zero entropy at $T = 0$ cannot be correct, however. Alternatively, the authors propose supplementing their method by vapour-pressure or e.m.f. measurements. But it is just in cases where these measurements are not feasible that the "thermodynamical analysis" is most attractive.

It seems to the writer that Oelsen's method can be independently applied even in systems with solid solutions. This may be shown in Fig. 3, an example with complete solid miscibility (type Cu—Ni). Suppose the heat content of a number of mixtures ranging from x_1 to x_2 is measured between T_1 and T_2. At T_3 both H and S are linear functions of x; these may be chosen arbitrarily, as a reference basis. We then have H, S, and G in this concentration range at all temperatures between T_1 and T_2.

It may be, for instance, that this piece of G, x curve becomes concave at temperatures so low that diffusion is extremely slow. Then we know that there is a (hidden) miscibility gap in the equilibrium diagram. In such a way, useful information could be obtained, with pure A and B not coming into the picture. To stress the completely nonstatistical nature of these calorimetric methods, it may be remarked that it is not necessary to know the atomic (or molecular) weights of A and B or even their identities, provided A-B is really a binary system. Working with weights percentages and H, S, and G per kilogram is just as good for arriving at conclusions on miscibility.

The thermodynamically explored concentration range x_1–x_2 in Fig. 3 may be widened as follows. At T_4 both H and S are known between x_3 and x_2. Linear extrapolation further yields these quantities between x_2 and x_4, and so furnishes the reference basis for H, S, and G between T_1 and T_2 in this concentration region. This procedure might be repeated at both sides towards A and B. It goes without saying that experimental inaccuracies will grow rather rapidly with each linear extrapolation, but in principle this method is quite sound.

† Besides both pure components of course.
‡ For their construction, the kinks in the H, T curves may be used.

The most obvious difficulties arise from segregation during solidification. Each alloy cooled from above the solidus curve will have a range of concentrations. It is necessary to determine the difference in heat content between such a cored ingot and a homogeneous one obtained by annealing. In principle, this could be done directly in a calorimeter, but presumably an indirect method will be generally more feasible. Körber and Oelsen's method[3] could be used: liquid A (or a third substance) is poured into the calorimeter on the ingot, so that temporarily the whole content liquifies. By doing this, both with a cored and a homogenized ingot, in such a way that the compositions are equal also after adding A, the necessary correction is obtained. The segregation in the two ingots solidified in the calorimeter will be practically equal and thus without influence.

It thus appears that purely calorimetric thermodynamical analysis has an even wider field of applicability than was described by Oelsen *et al.* themselves.

Finally, the writer wishes to point out that an analogous method is possible, using pressure p and volume v as variables. Fig. 4 shows a p, x diagram of a simple binary system at constant temperature above the melting-points of both A and B at normal pressure. These two components are assumed to contract on solidification; to be completely miscible in the liquid state and nonmiscible in the solid state (above the eutectic pressure p_e). It is easily seen that the free enthalpy of mixing of a liquid mixture (say m) is obtained simply by graphical integration of the v, p curves of m, A, and B, measured from normal pressure up to a pressure above p_e, provided

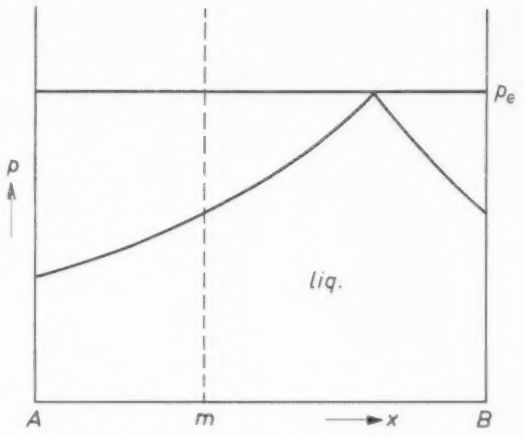

FIG. 4. Pressure-concentration diagram, at constant temperature, of a system without solid solutions.

equilibrium is preserved during compression. This method will have less practical value than the calorimetric one. But the underlying principles they have in common are shown somewhat more simply, owing to the fact that volumes are more directly measurable than entropies.

J. L. MEIJERING

Philips Research Laboratories
N.V. Philips' Gloeilampenfabrieken,
Eindhoven, Netherlands.

VOL. 4 1956

References

1. W. OELSEN, E. SCHÜRMANN, and G. HEYNERT, *Archiv. Eisenhüttenwesen* **26,** 19 (1955).
2. S. NAGASAKI and E. FUJITA, *Nippson Kinzoku Gakkai-Si* **16,** 313 (1952), cf. *Metallurg. Abstr.* (*Inst. Metals*) **20,** 466 (1952/53).
3. F. KÖRBER and W. OELSEN, *Mitt. Kais. Wilh. Inst. f. Eisenforschung* **18,** 109 (1936).

* Received December 23, 1955.

SOME CURRENT PAPERS IN OTHER JOURNALS

Acta Crystallographica, Vol. 9

Part 3, March 1956 (partial contents):

The crystal structure of the intermetallic compound $Mg_6Si_7Cu_{16}$. GUNNAR BERGMAN and JOHN L. T. WAUGH.

Growth features on crystals of long-chain compounds. III. S. AMELINCKX.

Three examples of accurate crystal-structure analysis by low-temperature X-ray photography. F. L. HIRSHFELD and G. M. J. SCHMIDT.

Die Kristallstruktur des Lithiummetasilikates, $(Li_2SiO_3)_x$. H. SEEMANN.

High-temperature structure transitions in sodium niobate. M. H. FRANCOMBE.

Scattering of X-rays by defect structures. W. COCHRAN.

The structure of mercuric oxide. W. L. ROTH.

Ordering of Atoms in the σ phase. J. S. KASPER and R. M. WATERSTRAT.

A crystallographic study of the tellurium-iodine system. W. R. BLACKMORE, S. C. ABRAHAMS and J. KALNAJS.

The crystal structure of the Co–Cr σ phase. G. J. DICKINS, AUDREY M. B. DOUGLAS and W. H. TAYLOR.

K-Surfaces and diffuse X-ray reflexions. S. C. PRASAD and W. A. WOOSTER.

The crystallography of two compounds containing the oxides of copper and molybdenum. IVOR D. THOMAS, ARNO HERZOG, and DAN MCLACHLAN, JR.

The Laue goniometer and its use as a proportional diffractometer. A. R. B. SKERTCHLY.

Part 4, April 1956 (partial contents):

The crystal structures of $SrZn_5$ and $BaZn_5$. N. C. BAENZIGER and J. W. CONANT.

Compounds of thorium with transition metals. II. Systems with iron, cobalt and nickel. JOHN V. FLORIO, N. C. BAENZIGER, and R. E. RUNDLE.

Lattice parameter and coefficient of thermal expansion of thorium. W. J. JAMES and M. E. STRAUMANIS.

A modified Patterson function. J. M. COWLEY.

"Stereoscopic" three-dimensional structure analysis. J. M. COWLEY.

Archiv für das Eisenhüttenwesen

Heft 2, Februar 1956:

Entwicklung und Blaseigenschaften eines basischen Kleinstkonverters. WILHELM ANTON FISCHER und MANFRED WAHLSTER.

Der Angriff eisengesättigter Zinkschmelzen auf kohlenstoffhaltiges Eisen. DIETRICH HORSTMANN.

Der Wachstumsdruck des Kohlenstoffs. ROLF BAUKLOH, OTTMAR KNACKE, und WERNER LÖSCHER.

Doppelätzung zum Nachweis sulfidischer Einschlüsse in technischen Eisenlegierungen. JOSEFINE WALLNER.

Bestimmung der Seltenen Erden in Stahl. HEINZ KRAPP.

Weitere ausländische Versuche und Überlegungen über die Sprödbruchempfindlichkeit von Stahl. KARL RÜHL.

Untersuchung des isothermischen Austenit- und Martensitzerfalls bei unlegierten Stählen im Temperaturbereich von 100 bis 400° durch Anwendung des Lösungsätzverfahrens. HANS-KURT GÖRLICH und HANS GOOSSENS.

Ausscheidungsvorgänge in einem mit Titan stabilisierten austenitischen Chrom-Nickel-Stahl und ihre Beziehung zur interkristallinen Korrosion. KARL BUNGARDT und GUSTAV LENNARTZ.

Das Überschall-Sichtgerät und seine Anwendung bei der zerstörungsfreien Werkstoffprüfung. HERBERT TROMMLER.

Das System Silber-Eisen-Silizium. RUDOLF VOGEL und WALTER VON MÄSSENHAUSEN.

Anwendung der Zephirolätzung bei Untersuchungen über Anlaßversprödung, Alterungsversprödung und Spannungskorrosion von Stählen. RICHARD WERNER.

Heft 3, März 1956:

Der Einfluß des Sauerstoffzusatzes zum Gebläsewind auf die Kornzusammensetzung der Thomaskonverter- und Ofenabgase beim Lichtbogenofen. ROBERT MELDAU und DIETHELM LAUFHÜTTE.

Untersuchungen der Walz- und Rekristallisationstexturen von Karbonyleisen. FRANK HAEßNER und HELMUT WEIK.

Der Angriff eisengesättigter Zinkschmelzen auf aluminiumhaltiges Eisen. DIETRICH HORSTMANN.

Mikroanalytische Untersuchungen in der Eisenforschung. II. Die spektrochemische Untersuchung isolierter Gefügebestandteile in Stählen. WALTER KOCH und SIEGFRIED ECKHARD.

Die Kennzeichnung von Farben bei der Tüpfelanalyse. HANNS MALISSA.

Der Hall-Effekt an reinem Eisen und an Stahl mit 1,2% C. WERNER JELLINGHAUS und MIGUEL PEDRO DE ANDRÉS.

Einfluß der Walz- oder Glühhaut auf die Korrosion von Stahl und die Haltbarkeit von Schutzüberzügen. FRANZ EISENHECKEN.

Leitpaket-Streifenjoch und Ganztafel-Meßjoch zur Ermittlung der magnetischen Kenngrößen von Elektroblechen. WILLI KRUG.

Anwendung statischer Verfahren auf einige Fragen der Zeitstandfestigkeit. HANS BÜHLER und WALTER SCHREIBER.

Aufbau und Aushärtung von Eisen-Kobalt-Zink-Legierungen. WERNER KÖSTER und HEINZ SCHMID.

La Metallurgia Italiana, Vol. XLVIII

January 1956:

The problem of natural gas pipelines protection from the point of view of electrolytic corrosion. G. BOMBARA.

To-day's tendencies in the evaluation of mechanical strength of refractory products at high temperatures. J. BARON.

Studying the deformation of zinc polycrystals. P. GONDI.

February 1956:

The pre-refining of pig iron in the ladle by means of pure oxygen. P. LEROY and L. SEPTIER.

Testing refractoriness. R. ZOJA.

On hot corrosion in common hypochlorite of 18–8 Ti, 18–8 and 8–T welded stainless steels. C. BIGHI and G. PANCALDI.

SINGLE CRYSTAL ELASTIC CONSTANTS OF SILVER AND SILVER ALLOYS*

R. BACON† and CHARLES S. SMITH‡

The elastic constants of single crystals of silver and of dilute alloys of Mg, Zn, Pd, Cd, In, and Sn in silver have been measured by the ultrasonic pulse-echo method. For all solutes except Pd, there is a large fractional decrease, upon alloying, in the shear constant $(C_{11} - C_{12})/2$, and a relatively small decrease in C_{44}. This result has been interpreted as indicating a decrease in the short-range crystal forces, because of a local weakening of nearest-neighbor repulsive bonds, and an increase in the long-range electrostatic forces, because of the increase in the average ion-core charge. The two shear constants increase upon alloying with Pd, and a similar interpretation is not inconsistent with this result.

LES CONSTANTES ÉLASTIQUES DE MONOCRISTAUX D'ARGENT ET D'ALLIAGES D'ARGENT

Les constantes élastiques de monocristaux d'argent et d'alliages d'argent à faibles teneurs en Mg, Zn, Pd, Cd, In et Sn ont été mesurées par la méthode d'écho d'impulsions ultrasoniques. Pour tous les éléments étudiés sauf Pd, on constate une diminution importante de la constante de cisaillement $(C_{11}–C_{12})/2$ et une diminution relativement petite de C_{44} à la suite de la formation de ces alliages. Ce résultat est interprété comme indiquant une diminution de faces cristallines d'action à courte distance, à cause d'un affaiblissement des liaisons répulsives entre proches voisins, et une augmentation des forces électrostatiques d'action à longue distance, due à une augmentation de la charge moyenne des couches autour des ions. Les deux constantes de cisaillement augmentent lors de l'addition de Pd et une interprétation similaire n'est pas incompatible avec les résultats.

DIE ELASTISCHEN KONSTANTEN VON EINKRISTALLEN AUS SILBER UND SILBERLEGIERUNGEN

Mit der Ultraschall-Puls-Echo-Methode wurden die elastischen Konstanten von Einkristallen aus Silber und verdünnten Legierungen von Mg, Zn, Pd, Cd, In und Sn in Silber gemessen. Abgesehen von Pd tritt beim Zulegieren eine starke relative Abnahme des Schubmoduls $(C_{11}–C_{12})/2$ und eine verhältnismässig schwache Abnahme von C_{44} auf. Dieses Ergebnis wurde interpretiert als Anzeichen für eine Abnahme der kurzreichenden Gitterkräfte aufgrund einer lokalen Verminderung der Abstossungskräfte zwischen nächsten Nachbarn und ein Anwachsen der weitreichenden elektrostatischen Kräfte infolge der Zunahme der mittleren Ladung der Ionenrümpfe. Beim Zulegieren von Pd nehmen die beiden Schubmoduln zu; eine ähnliche Interpretation ist mit diesem Ergebnis nicht im Widerspruch.

VOL. 4 1956

INTRODUCTION

The elastic constants of single crystals of silver and several dilute alloys of silver have been measured as a part of a program aimed toward investigating the nature of crystal-binding forces. This paper is concerned primarily with the effect of alloying on the two shear constants of silver. An interpretation of the experimental results is made in a manner similar to that of previous investigations of one of the authors.[1, 2]

EXPERIMENTAL PROCEDURE

Single crystals of silver alloys were prepared, and their elastic constants measured, in the manner which has been described for copper alloys.[2]

Crystals of $\frac{5}{8}$-in. diameter were grown from the melt in a hydrogen-atmosphere furnace by cooling through the solidus point of the alloy. The sample was positioned in the furnace in a region of high temperature gradient, and in addition a water-cooled copper rod was screwed into the lower end of the graphite crucible in order to increase the gradient.

The sample was examined for any possible grain boundaries by etching the surface. Then an approximate orientation of the cylinder axis was obtained optically, by reflecting a focused beam of light from the sides of the crystal and observing the specular reflection from the {111} etch planes. A section of the crystal approximately $\frac{1}{2}$–$\frac{3}{4}$ in. long was cut out on an abrasive wheel with the faces nearly perpendicular to the [110] direction. After waxing the specimen in a steel lapping block, the faces were polished on metallographic paper until flat and parallel.

The longitudinal and the two transverse acoustic-wave velocities were then measured by the pulsed ultrasonic method.[3] A back-reflection Laue photograph was made after etching in order to obtain an

* Received October 27, 1955; revised version, December 5, 1955.

† Formerly at Case Institute of Technology, Cleveland, Ohio. Now at the National Carbon Company, Research Laboratories, Cleveland, Ohio.

‡ Case Institute of Technology, Cleveland, Ohio.

exact orientation of the specimen faces,[4] and the elastic constants were calculated, using the approximation method.[5] The density of each alloy was obtained from X-ray lattice parameter data[6] along with the known chemical composition. The latter was obtained from chemical analyses, by the James H. Herron Company, of two slices of the crystal taken from each end of the specimen. The starting material was Handy and Harman "fine silver."

RESULTS

The values of the three elastic constants for pure silver and the different alloys are shown in Table 1, where Zener's notation for the two shear constants, $C = C_{44}$ and $C' = (C_{11} - C_{12})/2$, has been used. The absolute accuracy for most of the numbers is felt to be within one-half of one per cent, whereas the relative accuracy should be better than this. The adiabatic bulk modulus for pure silver in Table 1 is about two-tenths per cent lower than that calculated from Bridgman's value[7] of the isothermal bulk modulus ($B_T = 1.017 \times 10^6$ kg cm^{-2}) by means of the equation

$$B_S \cong B_T (1 + TV\beta^2 B_T/C_P)$$

where the cubical coefficient of thermal expansion is $\beta = 5.76 \times 10^{-5}$ (C°)$^{-1}$, and the specific heat is $C_P = 6.00$ cal (mole-C°)$^{-1}$.[8] V is the molar volume, and T is room temperature taken as 300°K. The value of B_S obtained in this way is 1.038×10^{12} dyne cm^{-2}.

It will be seen from Table 1 that there is a decrease in all three constants upon alloying in every case except that of Ag-Pd, where the solute is to the left of silver in the periodic table. A striking fact is that the fractional change in C' is greater than that of C in every case. This qualitative result was previously observed also in the case of the alloys of copper, and the interpretation which was presented at that time[2] is now felt to be further justified.

TABLE 1. Elastic constants of silver alloys in units of 10^{12} dyne cm^{-2}

Alloy	Atom composition* (per cent)	$C = C_{44}$	$C' = (C_{11} - C_{12})/2$	$B_S = (C_{11} + 2C_{12})/3$
Ag	0	0.4613	0.1528	1.036
AgMg	3.07 ± 0.04	0.4600	0.1498	0.998
	7.33 ± 0.38	0.4524	0.1462	0.964
AgZn	2.40 ± 0.18	0.4612	0.1484	1.032
	3.53 ± 0.03	0.4577	0.1462	1.014
AgCd	1.34 ± 0.08	0.4611	0.1516	1.026
	1.92 ± 0.14	0.4593	0.1505	1.014
AgIn	8.36 ± 0.24	0.4505	0.1379	0.982
AgSn	3.17 ± 0.14	0.4581	0.1437	1.018
AgPd	6.22 ± 0.56	0.4809	0.1596	1.064

* The average composition of each alloy is given along with the deviations from this average obtained from chemical analyses of material taken from each end of the specimen. The composition gradient was in the same direction as expected from conditions of crystal growth, with the exceptions of 1.34 Cd and 2.50 Zn.

INTERPRETATION

In the interpretation of the above results, it is assumed that there are only two important contributions to the shear constants C and C', one arising from long-range electrostatic forces, the other from short-range repulsive forces between closed-shell ion cores. The elastic constants are obtained from the crystal-binding energy by taking the second derivative with respect to the appropriate strain. Any contributions to this energy other than the two mentioned above are assumed to depend only on the volume, and hence do not contribute to the shear constants.

The long-range electrostatic contribution for both shear constants of FCC metals has been calculated by Fuchs,[9] using as a model a lattice of positive point charges imbedded in a uniform electron sea. His results, which may be termed the electrostatic stiffnesses C_E and C_E', are

$$C_E = 0.9479(2e^2/a^4) \qquad C_E' = 0.1058(2e^2/a^4)$$

where a is the lattice parameter.

In this work with silver the ion-core stiffnesses C_I and C_I' are then obtained by taking the difference between the measured stiffnesses and Fuchs's electrostatic stiffnesses. The resulting values for pure silver, in units of 10^{12} dyne cm^{-2}, are:

$$C_E = 0.1569, \quad C_E' = 0.0175, \quad C_I = 0.3044, \quad C_I' = 0.1353$$

The change in shear constant upon alloying is presumed to be the result of changes in both the long-range and the short-range stiffnesses.[2] The former depends on the square of the net ion charge, and it is hence assumed that the electrostatic stiffness for the alloy is equal to that for pure silver multiplied by an empirical parameter Z^2, which is expected to be close to unity. The ion-core stiffness is proportional to the average short-range bond energy between pairs of ion cores, and the change in this stiffness is hence expected to be proportional to the concentration of solute x, so long as we are in the dilute range. The constant of proportionality has been designated by α, which should be a constant characteristic of a particular solute element.

The shear constants for the alloy will thus be given by

$$C = C_E Z^2 + C_I(1 + \alpha x)$$
$$C' = C_E' Z^2 + C_I'(1 + \alpha x) \quad (1)$$

where the coefficients of Z^2 and $(1 + \alpha x)$ are the values for pure silver quoted above. If we subtract from C and C' the constants for pure silver, and then divide by the latter, we obtain the fractional change in C and in C':

$$\Delta C/C = 0.34\,(Z^2 - 1) + 0.66\alpha x$$
$$\Delta C'/C' = 0.11\,(Z^2 - 1) + 0.89\alpha x$$

In the case of all the alloys for which C and C' decrease, $Z^2 - 1$ is a small positive number, while αx is a negative number of the same order of magnitude as $Z^2 - 1$. The relative sizes of the coefficients of these terms show clearly that the equations (1) formally account for the large fractional decrease in C' relative to that in C.

It must be cautioned that there is a lattice parameter change upon alloying, and that the values for pure silver must be corrected for this change, so that the net change in shear stiffness is the result of alloying alone. The change in the electrostatic stiffness due to lattice parameter change only may be shown to be

$$\delta C_E/C_E = \delta C_E'/C_E' = -4\delta a/a$$

and the change in ion-core stiffness is approximately given by

$$\delta C_I/C_I \approx \delta C_I'/C_I' \approx -16\delta a/a$$

The value 16 is an estimated value for r_0/ρ in the Born-Mayer repulsive potential:

$$W = Ae^{-(r-r_0)/\rho}$$

The estimate has been made from Bridgman's value of dB/dP for silver.[7] In the case of copper, r_0/ρ has been estimated by Huntington[10] to be about 14. Since any sort of calculation of this number yields a somewhat higher value for silver than for copper, it was decided to use 16 in the case of silver. Strictly speaking, the fractional changes in C_I and C_I' are only approximately given by r_0/ρ times the fractional change in lattice parameter, but the differences are negligible in their effects on the parameters Z and α.

Thus the values for C_E, C_E', C_I, C_I', after being corrected for change in lattice parameter, are introduced into equations (1) along with the two measured shear constants for the alloy, and these equations are then solved for Z and α, resulting in the following working equations:

$$Z^2 - 1 = \left[\frac{\Delta C - \Delta C' A_I}{C_E(1 - A_I A_E^{-1})} + 4\frac{\delta a}{a}\right]\frac{1}{1 - 4\dfrac{\delta a}{a}}$$
$$\alpha x = \left[\frac{\Delta C' - \Delta C A_E^{-1}}{C_I'(1 - A_I A_E^{-1})} + 16\frac{\delta a}{a}\right]\frac{1}{1 - 16\dfrac{\delta a}{a}}, \quad (2)$$

where $A_E = C_E/C_E'$, $A_I = C_I/C_I'$ and $\delta a/a$ is the fractional change in lattice parameter. The results for Z and α are listed in Table 2.

The accuracies claimed for the listed values of Z and α can best be indicated simply by saying that there is always some question about the last figure quoted, and that $Z^2 - 1$ and α are relatively better known when their magnitudes are large. As a rule, it is true that any conceivable errors, aside from gross errors (such as in chemical analysis) would cause less than 10 per cent error in $Z^2 - 1$ and α.

Two possible sources of error which deserve particular attention are the effect of long-range composition gradients, and the effect of short-range segregation. The former has been discussed by Neighbours and Smith[2] in connection with alloys of copper. Briefly, since the acoustic velocity, as measured, is a bulk property, any variations in velocity owing to composition variations along the direction of wave propagation will average out, to a very close approximation, to the true value for the average composition. This average composition is felt to be well known, in spite of the difference in composition found at each end of the crystal. In Table 1 the atom composition is given along with the actual deviations from the mean obtained from the two chemical analyses. These deviations are not to be interpreted as limits of error, for they are not random variations. The direction of the composition gradient was what one would expect to result in the growing process, with two exceptions. The exceptions are the 1.34 per cent Cd alloy and the 2.40 per cent Zn alloy. Both could well be accounted for by the fact that there was considerable boiling-out of the solute, especially in the case of Cd, which would cause a gradient of increasing solute toward the lower end. In any case the deviation of each reported composition never differs by as much as 10 % from the mean value, and even if these deviations were to be considered as uncertainties in the average composition, the corresponding uncertainties in the computed values of $Z^2 - 1$ and α would also be under 10 per cent.

VOL. 4 1956

The presence of short-range segregation was inferred from observations of a wood-grain appearance on the sides of the crystal, and a series of ridges spaced about one-half millimeter apart on the polished face which appeared after etching (and in one case was just visible before etching). These ridges were quite obviously due to effects which extended through the entire crystal, and could be seen to correspond to the wood-grain ridges on the sides. They were in fact the cross-section of a series of strata parallel to (001) planes containing the [110] direction nearest the direction of crystal growth. They are quite possibly the "prismatic substructure" observed by Rutter and Chalmers.[11]

The section of crystal which was used for velocity measurements was always cut from a point near the lower end of the crystal where the wood-grain appearance had not yet developed, and hence where impurity segregation was presumably not so severe (probably because the lower end of the crystal was grown under a higher-temperature gradient than the upper end). The ridges usually, though not always, appeared upon etching, but in no case was the segregation severe enough to interfere with measurement of sound velocities. As has been pointed out,[2] the acoustic attenuation is very sensitive to such structure.

DISCUSSION

The remarks which follow first will be limited to solutes to the right of silver in the periodic table, that is, all except the Pd alloy, which will be discussed separately.

An inspection of Table 2 shows that the parameter Z is nearly the same as the electron-atom ratio, q. An extension of Fuchs's idealized model for the pure metal of positive point charges imbedded in a *uniform* sea of electrons would lead one to look for a mean-square ion-core charge for the alloy crystal. By assuming that each ion core has a charge (in units of e) equal to its valence, it can be shown[2] that the proper mean-square charge is q^2. Hence, as a first guess, we expect Z to be equal to q. On second guess it is known that the more highly charged solute ion cores will be partially screened by the valence electrons, so that Z will be somewhat less than q. This is indeed the case for all but the Zn alloys. This fact is also in qualitative agreement with the previous results for copper alloys,[2] which have been recalculated on the basis of the present empirical treatment of C_I and C_I' and using more recent values[12] of the shear constants of pure copper. The copper results now show that Z is in every case equal to or less than q.*

TABLE 2. The empirical parameters Z and α for silver alloys computed from equations (2)

Alloy	Composition (atomic (per cent)	Change in lattice parameter (per cent)	α	Z	q electron-atom ratio
AgMg	3.07	0.06	−0.6	1.024	1.031
	7.33	0.15	−0.4	1.028	1.078
AgZn	2.40	−0.11	−2.5	1.039	1.024
	3.53	−0.16	−2.4	1.044	1.035
AgCd	1.34	0.07	−0.1	1.012	1.013
	1.92	0.10	−0.3	1.015	1.019
AgIn	8.36	0.67	−0.4	1.105	1.167
AgSn	3.17	0.33	−1.1	1.078	1.095
AgPd	6.22	−0.34	−0.1	1.011	0.938

The values of α which appear in the table are all negative. This result implies a decrease in the ion-core contribution to the two shear constants, and implies a weakening of the repulsive ion-core forces. This is to be expected, since in every case the solute ions are smaller than the silver ions. It may be seen that in the alloy sequence Cd, In, Sn, in which the solute ion-core electron configuration is the same as for Ag, but the net charge is increasing, the values of α increase in magnitude in a reasonable manner. We might offhand expect a similar variation in α for the alloy sequence Cd, Zn, Mg. While it is true that the magnitude of α for both Zn and Mg is larger than that for Cd, it is also true that the relative magnitudes for Zn and Mg are opposite to what one would expect on the basis of relative ion-core sizes. However, it is in agreement with the results for copper alloys, in which there was a decrease in the magnitude of α in going from Ga to Al and from Ge to Si. With these three pieces of evidence, we are led to the conclusion that the net charge and the number of electrons in the ion core are not the only important factors determining the magnitude of α. We may speculate that the apparent anomaly in the relative effects of the solute element pairs Zn-Mg, Ga-Al, Ge-Si, on the shear constants of silver or copper, is due to the difference in the types of outer shell configuration. That is, in the case of Ag-Zn, the solvent-solute interaction is between two d-shells, while for Ag-Mg it is between d and p shells, and similarly for the other two pairs in the case of copper.

In the case of Ag-Pd, the solute element (which has atomic number one less than silver) is expected to have its $5d$ shell at least partly filled when it is

* This treatment of the copper-alloy data will be submitted for publication to *Acta Metallurgica*, together with recent data for Cu-Ni alloys for comparison with our Ag-Pd results.

introduced into a silver crystal. In so doing, it would reduce the electron-atom ratio below 1.00, and we hence expect Z to be less than 1.00. Similarly, we expect the Pd ion core to be somewhat larger than that of silver, yielding a positive value for α. These predictions are not strictly met, for α and $Z^2 - 1$ both turn out to be essentially zero. However, both values are in the right direction relative to the values for the alloying elements to the right of silver, and in this sense they fall into line with the present interpretation. There is considerable experimental uncertainty in the results for Pd, since the magnitudes of the increases in C and in C' are such as to nearly cancel each other in their effects on the parameters Z and α. It seems pointless therefore to speculate on possible explanations for their values, especially in view of the fact that Pd, being a transition element, does not lend itself to easy interpretation.

If the shear constants for each of the three sets of alloys in which crystals of two different composition were used are plotted as a function of composition, it is found that the C' constant extrapolates to zero composition reasonably well to the value for pure silver, whereas C seems to extrapolate to a higher value. This discrepancy is about 1%, and an experimental error of that magnitude for pure silver seems unlikely. Furthermore, even if such an error were assumed to exist and were corrected for, there would be an accompanying decrease in the adiabatic bulk modulus of pure silver by at least the same absolute magnitude as the increase in C, bringing B_s at least four-tenths per cent lower than the value listed in Table 1. In view of the agreement of B_s as reported with Bridgman's measurement, and the fact that such an error seems unlikely in any case, it is believed that the value of C as reported is correct.

It is interesting, however, to speculate on the possibility that a low value of C is caused by dislocations, which for some reason affect C more than C'. (The value of B_s as measured by the present technique will not be affected by the presence of dislocations.) Dislocations have been suggested to account for results such as reported by Bradfield and Pursey,[13] showing the initial rise and then fall in the elastic moduli of polycrystalline copper alloys as the solute concentration is increased from zero. If such an effect is occurring in this investigation, a correction for it would cause a lowering of the values of Z, while causing very little change in α, thus not changing the interpretation advanced here in a qualitative way. It is felt, however, that an attempt to assess a possible dislocation effect quantitatively is not justified with the present data, which were not planned for this purpose. A quantitative extrapolation would require data at high compositions, which were avoided deliberately in this work.

ACKNOWLEDGMENTS

This research was supported by the office of Naval Research. One of the authors, Roger Bacon, is indebted to the Standard Oil Company, and to the National Carbon Company, for their assistance provided through fellowships. The authors wish to thank Mr. A. Hruschka and Mr. T. R. Long for their valuable help.

REFERENCES

1. CHARLES S. SMITH and J. W. BURNS, *J. Appl. Phys.*, **24**, 15 (1953).
2. J. R. NEIGHBOURS and CHARLES S. SMITH, *Acta Met.*, **2**, 591 (1954).
3. H. B. HUNTINGTON, *Phys. Rev.*, **72**, 321 (1947).
4. J. R. NEIGHBOURS, F. W. BRATTEN, and CHARLES S. SMITH, *J. Appl. Phys.*, **23**, 389 (1952).
5. J. R. NEIGHBOURS and CHARLES S. SMITH, *J. Appl. Phys.*, **21**, 1338 (1950).
6. Abstracted in K. POLMANTEER's Master's Thesis, TM 65 (1950), Case Institute of Technology.
7. J. C. SLATER, *Phys. Rev.*, **57**, 744 (1940).
8. LANDOLT-BORNSTEIN, *Physikalish-Chemische Tabellen, Supp.* 2 (Julius Springer, 1931), 1152, 1240.
9. K. FUCHS, *Proc. Roy. Soc.*, **A153**, 622 (1936).
10. H. B. HUNTINGTON, *Phys. Rev.*, **91**, 1092 (1953).
11. J. W. RUTTER and B. CHALMERS, *Canad. J. Phys.*, **31**, 15 (1953).
12. W. C. OVERTON, JR., and JOHN GAFFNEY, *Phys. Rev.* **98**, 969 (1955).
13. G. BRADFIELD and H. PURSEY, *Phil. Mag.*, **44**, 437 (1953).

VOL. 4 1956

STRUCTURE-DEPENDENT CHEMICAL REACTION AND NUCLEATION OF FRACTURE IN Cu_3Au SINGLE CRYSTALS*

R. BAKISH† and W. D. ROBERTSON‡

The associated phenomena of structure-dependent chemical removal of copper from Cu_3Au and the nucleation and growth of fracture have been investigated in single crystals. Copper is selectively removed from Cu_3Au by ferric chloride from imperfections originating during crystal growth. Selective removal of copper also occurs from local areas in slip clusters, apparently unrelated to growth imperfections. Under applied stress, both sites of reaction become nuclei of fracture cracks. Fracture propagates only in the presence of stress and the chemical reagent. The fracture path is normal to the stress axis and independent of crystallography, after initial nucleation occurring in areas of clustered slip bands. The fact that the fracture path is not a rational crystallographic plane indicates that deformation at the leading edge of the crack is highly complex. In accordance with the observed chemical activity localized in slip clusters, possibly at sites of cross slip, it is proposed that fracture occurs as a result of the selective removal of copper from the zone of complex deformation at the leading edge of the crack.

RÉACTION CHIMIQUE DÉPENDANT DE LA STRUCTURE ET NUCLEATION DE FRACTURE DANS LES MONOCRISTAUX DE Cu_3Au

Les phénomènes associés de l'élimination chimique (dépendant de la structure) du cuivre hors de Cu_3Au d'une part et la nucléation et croissance de fracture, d'autre part, ont été étudiés sur des monocristaux. Par l'action du chlorure ferrique, le cuivre contenu dans Cu_3Au est sélectivement éliminé des défaut sui se sont formés au cours de la croissance des cristaux. Le même phénomène se déroule également dans des régions localisées de concentrations de glissements, qui apparemment ne sont nullement relevées aux défauts de croissance. Sous l'action d'une tension appliquée, les deux types de régions deviennent des amorces de fracture. Celle-ci se propage seulement sous tension et en présence du réactif chimique. Après une amorce initiale dans certaines régions des bandes de glissement, le parcours de la fracture est normal à l'axe de tension et n'est pas de nature cristallographique. Le fait que la fracture ne se développe pas suivant un plan cristallographique indique que la déformation au front de fracture est très complexe. En accord avec l'acitivité chimique observée dans les bandes de glissement, et peut-être "cross-slips," il est suggéré que la fissure résulte de l'élimination sélective du cuivre hors de la zone de déformation complexe se trouvant au front de fracture.

STRUKTUREMPFINDLICHE CHEMISCHE REAKTION UND KEIMBILDUNG DES BRUCHS IN Cu_3Au-EINKRISTALLEN

Die miteinander zusammenhängenden Erscheinungen der strukturempfindlichen chemischen Entfernung von Kupfer aus Cu_3Au sowie der Keimbildung und des Wachstums des Bruchs wurden an Einkristallen untersucht. Aus Cu_3Au wird—ausgehend von Fehlstellen, die während des Kristallwachstums entstehen—Kupfer durch Eisenchlorid selektiv gelöst. Ein solches selektives Herauslösen des Kupfers erfolgt, offenbar ohne Zusammenhang mit den Wachstumsfehlern, auch von lokalen Bereichen in Gleitbandbündeln aus. Unter einer angelegten Spannung werden beide Arten von Reaktionsstellen zu Keimen von Bruch-Anrissen. Der Bruch breitet sich nur bei Vorhandensein der Spannung und des chemischen Agens aus. Nach der anfänglichen, in Bereichen von gebündelten Gleitbändern erfolgenden Keimbildung ist die Ausbreitungsrichtung senkrecht zur Spannungsrichtung und unabhängig von den kristallographischen Verhältnissen. Die Tatsache, dass die Bruchausbreitung nicht in einer rationalen kristallographischen Ebene erfolgt, zeigt, dass die Verformung an der Rissfront ausserordentlich komplex ist. In Übereinstimmung mit der beobachteten, in Gleitbandbündeln—möglicherweise an Stellen mit Quergleitung—lokalisierten chemischen Aktivität wird vorgeschlagen, dass der Bruch als eine Folge der selektiven Entfernung von Kupfer aus der Zone komplexer Verformung an der Rissausbreitungsfront entsteht.

INTRODUCTION

An investigation of polycrystalline Cu_3Au[1] has shown that copper is preferentially removed from structural sites by ferric chloride. Active sites are located at grain boundaries, incoherent twin boundaries, and subgrain boundaries in annealed structures; in plastically deformed Cu_3Au, active sites are located in slip clusters, and the concentration of active sites is greatest near grain boundaries and twin boundaries. Qualitatively, the intensity of reaction depends on the magnitude of imperfections; for example, the relative orientation of adjacent grains. The activity of specific sites appears to be an intrinsic chemical and structural property of the homogeneous solid solution, and it is not associated with precipitation.

Because of the relatively high activity of grain

* Received July 30, 1955.

† Sprague Electric Company, North Adams, Massachusetts.
‡ Hammond Metallurgical Laboratory, Yale University, New Haven, Connecticut.

boundaries and associated fracture under stress, it is difficult to study the nucleation and growth of active sites as they relate to crystallography and imperfections, other than grain boundaries. Accordingly, a study has been made of the relative chemical activity of various structural sites in single crystals, together with the associated nucleation and growth of fracture.

Previous work in this field is limited to a few experiments on stress corrosion cracking of brass; most of it precedes the development of a detailed understanding of crystal imperfections.

Wasserman[2] studied the fracture of alpha-brass single crystals in ammonia, and he found that fracture did not follow any identifiable crystallographic plane; fracture did, however, appear to start at surface traces of slip planes. Edmunds[3] also did not find any simple relation between crystallography and fracture; from the micrograph of this crystal it is evident that it was extermely inhomogeneous with respect to composition, and it had also been previously deformed by bending.

Tragert,[5] using well-homogenized crystals of dilute copper-phosphorus alloys, which are susceptible to failure in ammonia, found no crystallographic dependence of fracture path except that surface traces of slip planes were preferentially attacked in accordance with previous observations of Wasserman; after duplex slip, the distribution of active sites was apparently quite uniform.

Skorcheletti and Titova[4] show that the time to failure of alpha-brass single crystals at constant stress is dependent on relative orientation of the slip plane to the axis of the specimen. However, no details of orientation are given and the reported stress dependence may be that of plastic deformation for differently oriented crystals.

Priest, Beck, and Fontana,[6] working with a magnesium alloy containing 6% Al, 1% Zn, and 0.2% Mn in an environment of 3% NaCl-3% K_2CrO_4, found that both transgranular and intergranular cracking occurred, depending on heat treatment. Transgranular fracture was associated with a grain-size larger than ASTM No. 7 and water-quenching from 345°C; the fracture path appeared to follow the basal plane. Metzger,[7] in an independent investigation, also observed transgranular cracking in the same magnesium alloy. However, in the latter investigation, planes other than the basal plane were found to contribute to the propagation of fracture.

The two preceding investigations are the only cases in which the fracture path is reported to be related to crystallography, and it should be noted that both are in an age-hardenable, hexagonal close-packed alloy. While there are suggestions of fracture nucleated at surface traces of slip bands in alpha-brass, no detailed structural observations appear to have been made, particularly in the initial stages of deformation where nucleation of fracture may be associated with the structure, and distinguished from the growth, of a macroscopic fracture.

To provide information regarding structure-dependent chemical reactions and fracture, it is desirable to employ an alloy in which only one component reacts with the environment and a system that does not produce opaque films; the later condition makes it possible to study the reaction under the microscope without subsequent polishing and possible loss of evidence. Copper-gold alloys and ferric chloride meet both these requirements and, accordingly, the following aspects of the problem were investigated with a homogeneous solid solution of composition corresponding to Cu_3Au.

1. The effect of order and disorder on stress-cracking susceptibility of Cu_3Au single crystals.
2. The preferential removal of copper by ferric chloride from structural imperfections and associated composition gradients resulting from crystal growth.
3. The removal of copper from structural imperfections produced by plastic deformation, slip bands, and clusters of slip bands.
4. The relative activity of specific crystallographic planes.
5. Nucleation and growth of fracture under applied and residual stress, with particular reference to crystallography and nucleation at the preceding structural sites.

EXPERIMENTAL PROCEDURE

Single crystals were produced from polycrystalline Cu_3Au, analysing 48.92 per cent copper and a total impurity content of 0.04 per cent (the latter indicated by spectrographic analysis). The alloy was cast under vacuum in quartz tubes of 3.5- and 2.0-mm diameter. Crystals were grown by the Bridgman technique of lowering through a temperature gradient; it was found by trial that in the particular furnace used a maximum temperature of 1150°C and lowering rate of 7 in. per hour produced crystals with small dendrite spacing and a minimum lineage structure.

All crystals were subsequently homogenized for 150 h at 850°C, to eliminate concentration gradients. Single crystals were obtained in the disordered state by an ice-water quench from 850°C. To produce long-range

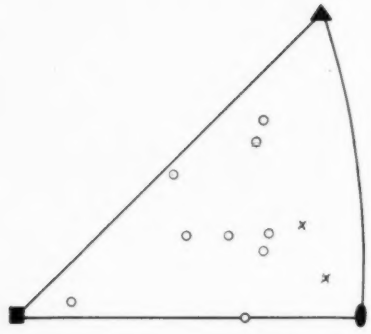

FIG. 1. Orientation of crystal axes; (○) disordered, (×) ordered.

order, single crystals were quenched from 850°C in ice-water, after which they were held for 100 h at 350°C, and cooled over a 100-h period to 250°C followed by quenching in ice-water.

The back-reflection Laue technique developed by Greninger[8] was used for the determination of orientation. White radiation from a copper target at 20 kV and 12 milliamperes gave satisfactory patterns after 2 h exposure.

For the purpose of studying the relation of fracture to crystallography, two planes, with a known angular relation, were ground by hand on cylindrical crystals. Because of the importance of surface conditions, special care was taken in the grinding operation to avoid distortion, and all surfaces were subsequently electropolished to remove strained material. The orientations of the axes of the different crystals used in this work are indicated in Fig. 1.

The study of nucleation and growth of cracks in single crystals was conducted with a specially constructed machine (Fig. 2) having the following features: axial strain was applied through a lead screw device and gear-reduction train in which one revolution of the driving shaft corresponds to a movement of 5×10^6 in. The crystal was mounted in series with a compression spring, so that strain was controlled at all times by the lead screw, and the growth of fracture cracks could be stopped at any point within the limits of elastic strain of the machine bed, which was very small, or the stress-measuring dynamometer in series with the specimen, in which case the elastic strain was defined by the sensitivity of a resistance strain gage. Specimens were mounted horizontally and could be observed and photographed with a microscope through a drop of ferric chloride while the stress was applied. It may be appropriate to emphasize here that a machine of this type is essential to the study of fracture. With strain under the control of the observer, it is possible to study the nucleation and growth of fracture at any instant without fracture becoming catastrophic as the section diminishes at constant load and increasing unit stress.

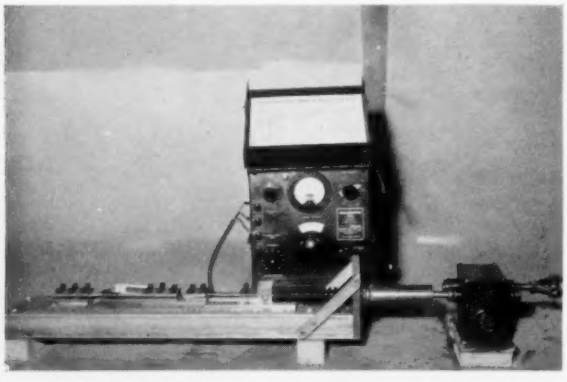

FIG. 2. Tensile machine for microscopic study of fracture at constant strain.

EXPERIMENTAL RESULTS

Plastic Deformation

The elements of plastic deformation of ordered and disordered Cu_3Au single crystals were redetermined, prior to fracture studies, as a means of evaluating crystal preparation and behavior under stress. Movement of the pole of the (111) plane over the stereographic projection, followed in one crystal and checked by observations on slip traces in four other crystals, demonstrated the expected slip system of (111) [110]. The critical resolved shear stress of ordered and disordered crystals averaged 2.3 and 4.5 kg/mm^2, respectively, in agreement with Sachs and Weerts[9] and Ardley.[10]

A typical set of stress-strain diagrams is shown in Fig. 2. The intermittent type of plastic flow observed in ordered polycrystalline specimens,[1] and in single crystals,[10] was detected in the ordered single crystals, as is indicated in Fig. 3. A noise, similar to that accompanying twinning in tin, and previously observed in ordered polycrystals when passing through the yield-point, was heard when the single crystals were in the "intermittent" flow range of strain.

Effect of Order and Disorder on Stress-Cracking Susceptibility of Cu_3Au Single Crystals

Experiments with polycrystalline specimens[1] demonstrated that intergranular fracture was not affected by long-range order. Before investigating nucleation and growth of fracture of single crystals, it was necessary to determine the significance of the state of order. For this purpose, ordered and disordered crystals were loaded in a tensile test machine

TABLE 1. Time for fracture of ordered and disordered single crystals of Cu_3Au in ferric chloride

Condition	Applied load (pounds)	Per cent of critical resolved shear stress	Time for drop in load (min)	Time for fracture (min)
Ordered	160	120	—	28
Ordered	160	120	5	12
Ordered	105	90	53	57
Disordered	195	90	—	No failure in 240
Disordered	201	90	51	59
Disordered	195	90	33	35
Disordered	195	90	—	120
Disordered	225	120	32	38
Disordered	225	120	1	4
Disordered	225	120	1	4

to 90 and 120 per cent of their respective critical resolved shear stresses, surrounded by ferric chloride, and the time for the first drop in load and for failure was observed. The data are given in Table 1. It appears quite certain that no significant difference exists between the fracture behavior of ordered and disordered states. Examination of the fracture also showed no evidence of a difference between the two states. It is clear, however, that fracture time is related to the magnitude of stress relative to the critical resolved shear stress and to the corresponding strain. It appears that plastic strain is a prerequisite for rapid fracture, a conclusion substantiated by subsequent work. The fact that failure occurred at 90 per cent of the critical resolved shear stress is probably due to the difficulty of mounting and conducting the test in the total absence of local strain and imperfections arising from specimen preparation. As a result of these experiments it was decided to conduct all subsequent investigations with crystals in the disordered state, as quenched from 850°C.

Composition Gradients and Imperfections Associated with Crystal Growth

Laue patterns of single crystals indicated a structure of subgrain boundaries with a maximum of about 2 deg relative rotation. Concentration gradients, associated with subgrain boundaries in crystals that were insufficiently homogenized, were revealed by etching polished sections.

Immersion of an incompletely homogenized, disordered crystal in ferric chloride for three months resulted in the pattern of attack shown in Fig. 4, which is an etched cross-section of a single crystal. It is evident that copper has been preferentially removed from the subgrain boundaries and that the rate of

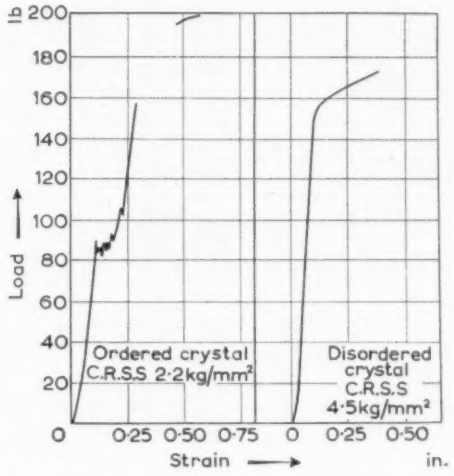

FIG. 3. Typical stress-strain diagram for ordered and disordered single crystals of Cu_3Au.

penetration in the boundaries is high, relative to the average rate through the crystal normal to its surface. When a crystal containing these boundaries is strained, subsequent to immersion, failure is initiated at the subgrain boundaries. It appears very probable that the previous investigations with alpha-brass were influenced by this factor. Obviously, crystals of greater perfection are required, and metallographic evidence indicates that 150 hours at 850°C is sufficient to produce homogeneous crystals, though the crystallographic subboundaries are, of course, still present and microscopically visible under oblique illumination.

It should be emphasized at this point that the subboundary penetration seems to be related to the concentration gradient that is evident in Fig. 4. Prolonged immersion of homogenized crystals in which concentration gradients were absent did not

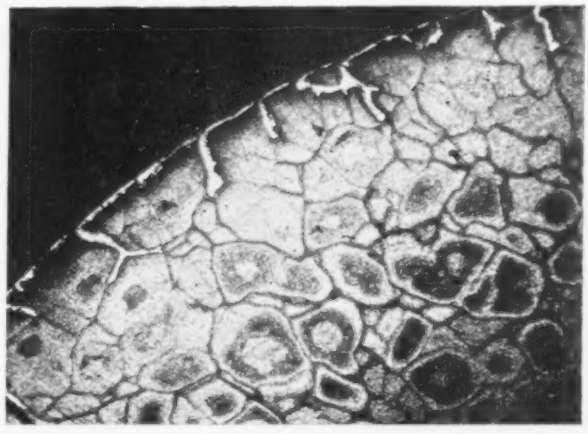

FIG. 4. Preferential solution of copper from substructure boundaries in an inhomogeneous single crystal of Cu_3Au. 150×.

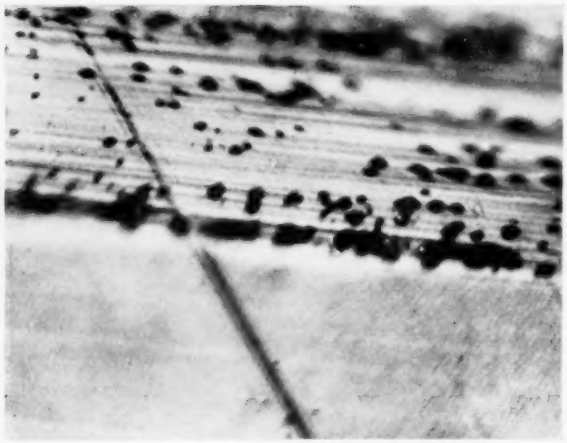

FIG. 5. Sites of chemical reaction in a slip cluster. 2000×.

result in subgrain boundary penetration, which was in accordance with the previously indicated conclusion that penetration is orientation-dependent and correspondingly small at low-angle boundaries.

Application of ferric chloride to polished surfaces of unstrained Cu_3Au single crystals resulted in reaction at randomly distributed small areas of circular form, very similar in appearance to those shown in Fig. 5, but in the absence of strain. The number of these sites varied from one crystal to another, and they did not all appear simultaneously with the application of the reagent; in one crystal, for example, a few sites were detected in several minutes, and the number grew to forty-five in twenty minutes. Significantly, these point sites become crack nuclei after straining a few per cent (Fig. 6). Detailed analysis of the structure of these "point sites" was not made, but it seems very probable that they originate in the growth history of the crystals, particularly as the number and distribution varied widely from one crystal to another.

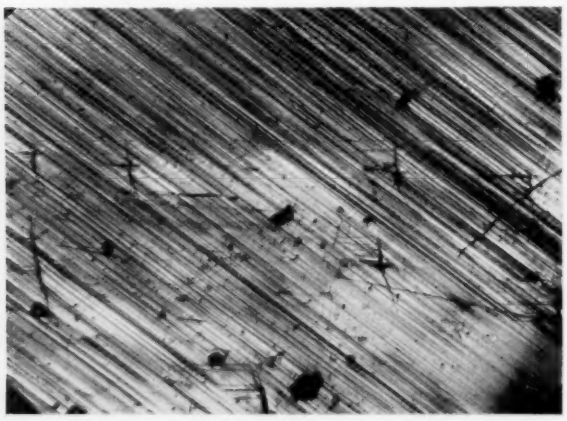

FIG. 6. "Point sites" of reaction after plastic strain. 300×.

It was considered possible that point sites are associated with the cell structure, particularly with points of intersection of boundaries, but no direct evidence in support of this hypothesis was observed.

Reaction Sites Associated with Strain

In order to distinguish growth imperfections from those produced by plastic deformation, microscopic areas of crystals that were free of the preceding "point sites" were chosen for the study of the interaction of strain and chemical reaction. Crystals with flat, polished surfaces were strained under the microscope and the reagent was applied.

Sites of reaction appeared on the surface almost immediately after application of the ferric chloride. These sites were invariably associated with the deformation structure and usually with slip clusters (Fig. 5). While occasional reaction sites appeared at single slip bands, a definite preference for slip clusters was observed, and the reaction was invariably localized at microscopic sites within the surface area of the slip cluster.

No quantitative correlation was observed between the degree of strain and the magnitude of attack. In fact, one crystal was deformed 60% without activating a significant number of sites. It is, of course, difficult to evaluate the strain associated with the microscopic processes observed; obviously, average strain is not very significant. A measure of microscopic strain, combined with observations of the present type, is required, but was not available; even more significant would be a measure of the degree of homogeneous strain characteristic of the range of "easy glide."

Relative Activity of Crystallographic Planes

Further investigation demonstrated that the degree of attack was dependent on the specific crystallographic plane of the reacting surface. A crystal was prepared with one surface 3 deg from the (111) plane and the other 4 deg from the (110) plane. It was observed that the surface parallel with the octahedral plane was essentially unreactive even after 4.5 per cent average strain, while the other was relatively active. To verify this observation, the entire crystal was immersed in ferric chloride for twenty-four hours, with the result shown in Fig. 7, which is a picture of the surfaces as they appeared without further polishing. To preclude possible galvanic protection of the relatively noble face by the active face, all surfaces except the (111) surface were masked with wax and the crystal was completely immersed in ferric chloride for eight days. After this additional period, the (111) surface was not significantly changed.

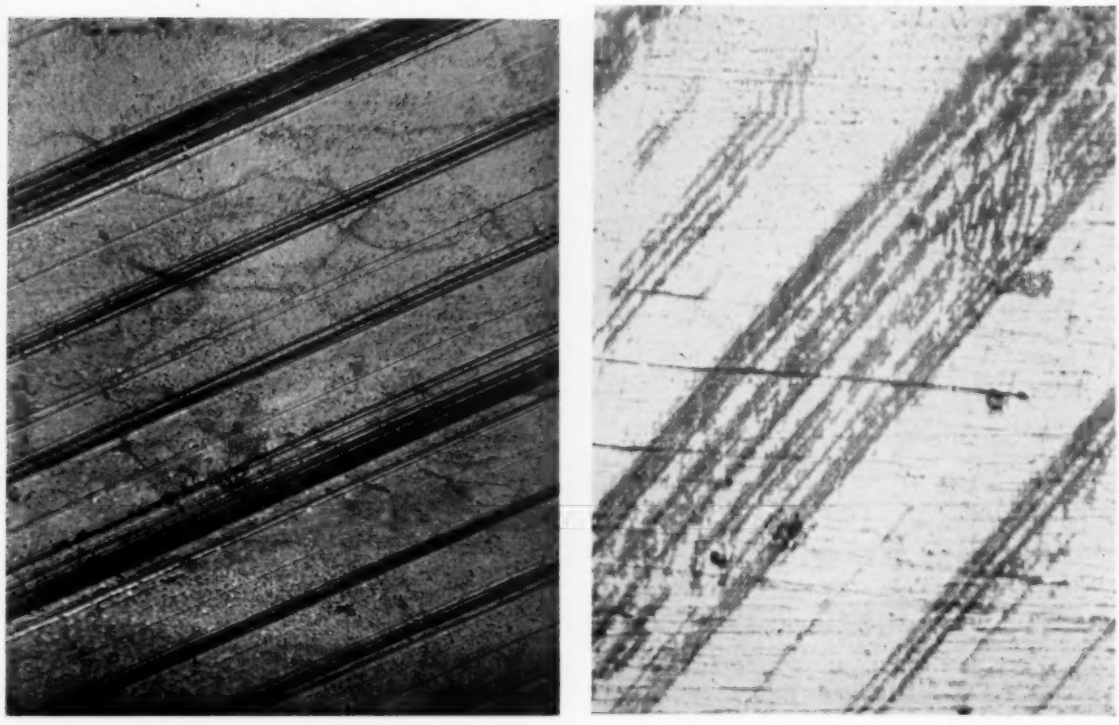

FIG. 7. Two faces of the same crystal after straining and immersion in ferric chloride for twenty-four hours. Left, (111) plane; right, (110) plane. 300×.

VOL. 4 1956

This result is in complete accord with the work of Tragert and Robertson,[11] which demonstrated that the (111) plane of copper is the only thermodynamically stable plane, and all others revert to this configuration in time by an etch-faceting process. It is interesting that the relative stability of the octahedral plane is preserved even after being crossed by slip traces, with the slip vector parallel to the plane of the surface. There is evidence, however, that more sensitive and greatly prolonged etching would show discrete sites of attack, apparently distributed at random along slip traces.[12]

Sites of Reaction and Fracture

Each of the preceding sites of chemical activity becomes the nucleus of a crack when stress is applied. An early stage of the process of crack formation is shown in Fig. 8, where it is evident that cracks have originated in a slip cluster at discrete sites distributed along the traces of the cluster. As indicated in Fig. 8, the general plane of the crack is normal to the principal axis of tension.

Investigation of cracks produced on two polished surfaces at a known angle to each other, in six different disordered crystals of random orientation, conclusively demonstrated that the plane of initial crack growth is normal to the axis of tension and unrelated to any particular crystallographic plane. The only observed exception occurred with a crystal having a (111) plane normal to the tensile axis in which fracture was initiated at a trace of the (111) plane. Fig. 9 shows this particular configuration and the associated strain required to accommodate the extension of the crystal.

It may be conclusively stated that in the absence of growth imperfections, fracture is nucleated preferentially within the volume of deformed material in a

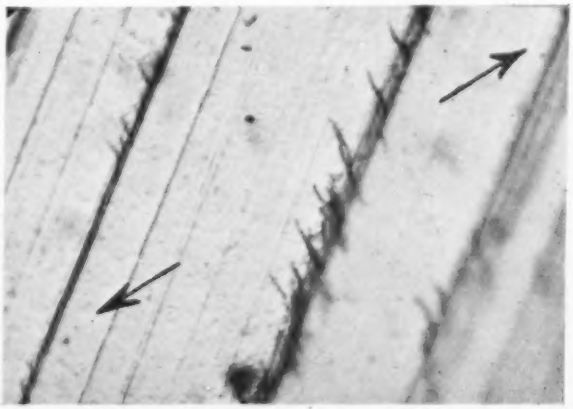

FIG. 8. Cracks nucleated in slip clusters and growing normal to the axis of tensile stress. 2000×.

FIG. 9. Crack, perpendicular to the axis of tensile stress and coincident with a trace of a (111) plane; point sites of attack above and below crack and accommodation strain at both ends of crack. 100×.

slip cluster, and that the growth of a fracture surface is defined by the axis of tensile stress. Macroscopic fracture proceeds by growth of fracture cracks accompanied by local plastic deformation, which becomes complex as the stress pattern is changed by the presence of cracks; finally, isolated cracks join together and complete separation occurs.

The process requires the simultaneous presence of stress and a chemical reaction removing at least one component of the alloy. In the absence of ferric chloride, the crystals are normally ductile and they deform in accordance with the (111) [110] slip mechanism at the previously observed critical resolved shear stress. In the presence of ferric chloride, active areas, associated either with "point sites" or with slip clusters, become crack nuclei that grow into macroscopic cracks. If the stress is maintained, brittle fracture occurs; the extent to which a normally ductile crystal cracks and fails in minutes is clearly shown in Fig. 10. If the ferric chloride is removed after initiation of a crack, the crystal deforms plastically, and typical ductile failure occurs after extensive deformation and duplex slip. Brittle failure can also be prevented by galvanic protection with copper, as already shown for polycrystalline Cu_3Au[1]. It seems clear that this effect results from the suppression of the solution of copper from the advancing crack by the imposed galvanic current derived from a copper anode, which is about 0.5 V more active than Cu_3Au in ferric chloride. In the absence of point sites, plastic deformation is necessary to nucleate fracture, which then propagates at stresses small compared to the yield stress.

FIG. 10. Macroscopic fracture cracks and accommodation strain. 100×.

Maintenance of applied stress is necessary for the propagation of cracks in single crystals. Residual stress associated with slip clusters in single crystals does not produce microscopically detectable cracks after prolonged immersion of strained crystals; in this respect, single crystals differ from polycrystalline aggregates, which fail under conditions of constrained plastic bending in the absence of additional stress. These contrasting results are almost certainly associated with the low level of residual stress in single crystals and, possibly, with the presence of the relatively more susceptible grain-boundary paths in the polycrystal.

The relative reactivity of the (111) and (110) faces is also evident in the relative cracking susceptibility of these two surfaces (Fig. 11). A considerable number of large cracks are present on the (110) plane, while the cracking of the (111) plane is limited to the slip clusters.

DISCUSSION

Copper is preferentially removed from sites produced in a relatively perfect crystal by plastic deformation, particularly in the volume of a slip cluster. Significantly, the whole volume of the cluster is not involved, but only regions of small cross-section (Fig. 5), leading from the external surface into the interior of the crystal along crystallographically defined directions.[12] It has also been shown that if a structural path exists for the exit of copper from the interior, reaction slowly spreads into the matrix, normal to the reaction path, at a rate similar to that characteristic of the surface of a crystal; thus, the observed "pipe" is resolvable as a region of some width even though the dimensions of the initial structural path may be very small. The distribution of sites along surface traces of slip bands and slip clusters, and the observed segments of curved reaction paths parallel to the octahedral plane inside the crystal,[12] all indicate that copper is

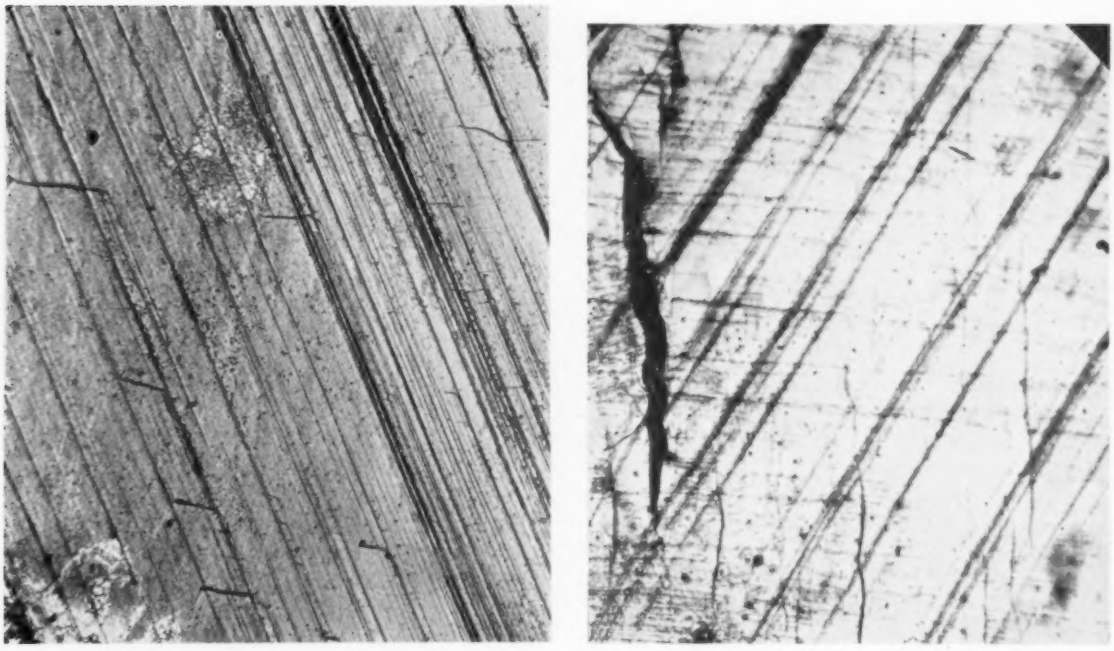

FIG. 11. Cracks on two faces of the same single crystal; left, (111) face; right, (110) face. 100×.

VOL. 4 1956

being removed from strained regions that correspond to various arrays of dislocations. Similar phenomena have been observed previously as a result of plastic strain of different materials.[13, 14, 15]

The simplest case is that in which the surface is parallel to a (111) plane and the slip vector lies in this plane. Movement of dislocations across the slip plane in homogeneous shear will leave a relatively undisturbed crystal behind. The evidence (Fig. 7) seems to be in agreement with this. A (111) surface plane is not appreciably disturbed by slip traces, as indicated by the complete absence of reaction with ferric chloride; also, the absence of cracks after prolonged immersion indicates that residual stresses must be of a very low magnitude. A more detailed investigation should be undertaken to verify that the crystal is indeed in the range of "easy glide"; however, it may be pointed out that Cu_3Au in the disordered state is very similar to alpha-brass, in everything except price, and that homogeneous slip is relatively easily obtained in the latter case.[16]

On the other hand, the corresponding (110) surface containing the slip step exhibits immediate and extensive reaction, not confined to individually resolvable sites, but distributed more or less continuously along the length of slip clusters. Several reasons for the activity of slip traces on the (110) plane may be proposed, though none has been experimentally proved. It seems most probable that the high activity is caused by complex strain associated with the emergence of a slip step at the surface; alternative explanations may be found in the activity of the exposed slip plane or the corner of the slip step. Again, resolvable cracks were not observed on this surface after the removal of the stress which produced the plastic strain. However, extensive cracking occurs if the stress is maintained.

A more complex problem is that of the discrete sites in a slip cluster (Fig. 5). In view of the evidence with respect to homogeneous shear, it is understandable that single slip bands are not particularly active. But, in a cluster of closely spaced slip bands (planes), dislocation interaction on parallel planes and possible cross slip[16] are involved; both may contribute to a state of high internal stress. Indeed, there is evidence for a high level of chemical activity parallel with the intersection of two planes operating in cross slip,[12] in conformity with the high stress and complex faulting that results from intersecting dislocation lines.[17] The fact that sites of high activity remain after removal of external stress demonstrates that dislocation arrays are locked in positions originally defined by the operating shear stress. In a polycrystalline aggregate, grain boundaries act as barriers to the passage of dislocations; and the evidence derived from a study of the annealing temperature necessary to reconstitute regions containing piled-up dislocations, and thereby lower the chemical activity,

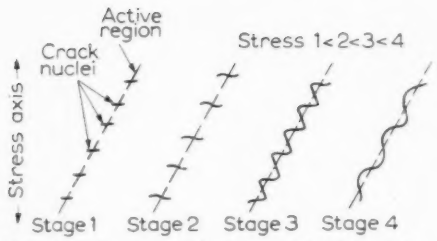

FIG. 12. Characteristic shape of initial cracks nucleated in a slip cluster.

shows that a temperature and time in the range of recrystallization is necessary (300°C and 100 h); in other words, a range where diffusion is significant is required. Thus, while there is undoubtedly some relaxation, it seems probable that the major part of the disorganization produced by complex slip is permanent at a temperature below that where diffusion is important in the alloy in question.

The preceding discussion concerns the location and relative activity of various reaction sites in the absence of a continuously applied stress. If, and when, an axial tensile stress is applied, the identical sites become centers from which cracks develop. Cracks appear almost immediately after applying ferric chloride and, on the other hand, do not appear in the absence of ferric chloride. It seems, therefore, that two stages of the process may be clearly differentiated: nucleation of a crack and growth of a fracture path.

The preferential nucleation of cracks in slip clusters, in the absence of "point sites," is indicative of fracture initiated at a site of stress concentration. However, in the present case, the stress concentration, shown by its high level of chemical activity, is not sufficient to produce a stable crack in the absence of chemical reaction. It is probable that a sufficient number of dislocations cannot be concentrated in a face-centered cubic single crystal to initiate spontaneous fracture, a number estimated by Stroh[18] to be 1000.

On the other hand, given a reaction site to start the process and a medium preferentially removing one component of an alloy, it is almost certain that reaction proceeds rapidly at the leading edge of a growing crack, at which point the stress is a maximum and inversely proportional to the square root of the radius of curvature at the crack tip.[19, 20] Extensive experiments with numerous crystals of varying orientation demonstrated that initial crack growth is invariably normal to the axis of tensile stress and, accordingly, independent of crystallography; this feature of crack growth is in conformity with a principal stress-reaction site mechanism rather than a path of growth defined by a crystallographic array of dislocations or a cleavage plane. After a crack has grown some distance, defined by strain imposed by the machine used in the present experiments, the general line of the crack deviates from a transverse path at both ends; the shape of such cracks is shown in Fig. 12. This typical crack-shape may be reproduced by a combination of axial tensile stress and shear stress; in fact, a simple demonstration, attributed to Mott, may be made by cutting through the center of a sheet of paper and applying both a tensile stress normal to the cut and a shear stress which will produce essentially the form of crack growth observed.

That chemical reaction is a necessary part of the mechanism in the present case is shown by the fact that, when ferric chloride is removed from the cracked crystal and stress reapplied, the crystal deforms in a ductile manner, modified by the presence of pre-existing cracks. Furthermore, when a strip of copper is attached to the crystal and ferric chloride introduced between the two, copper is removed from the pure copper strip instead of Cu_3Au, and no fracture is nucleated; immediately after removal of the copper, the crystal fails.

Summarizing the preceding results with respect to the mechanism of stress corrosion cracking, it appears that brittle fracture in ductile crystals is nucleated at sites produced by plastic deformation, sites apparently associated with blocked arrays of dislocations arising from complex deformation. However, cracks do not grow under stress in the absence of a reacting medium. Orowan has suggested two possibilities for the growth of a crack under these conditions: (1) the crack-tip has a high free energy with respect to the environment as a result of inherent structural or compositional conditions, such as a precipitated phase and/or a structural boundary; (2) in advance of the moving crack there is a volume of plastically deformed crystal that is chemically active as a result of deformation. Priest, Beck, and Fontana[6] have in fact shown, by a moving picture of the process, that a plastic wave precedes a growing fracture crack in a magnesium alloy.

In so far as this work is concerned with single crystals, only the latter hypothesis is involved. The function of plastic deformation in producing active sites of reaction has been demonstrated; it has also been shown that cracks grow normal to the principal tensile stress. It seems apparent, therefore, that plastic deformation in advance of a crack, propagating under a localized stress concentration of the order of three times the average stress[21] in a nonrational crystallographic direction, must proceed in a highly complex manner; and accordingly an extremely

disorganized volume of material of high chemical activity is produced.

The function of chemical reaction is, then, to dissolve the plastically deformed and disorganized material at the leading edge of a crack. The rate of advance of a crack is defined by the rate of solution of the particular alloy in a given environment; depending on the alloy and the environment, one or both components may be dissolved by the corrosive reagent. Stress and plastic deformation are not, however, sufficient to cause corrosion-cracking in a ductile crystal, since a pure metal crystal does not fracture in this manner. Given the necessary structural characteristics of a crack nucleus, it appears that an additional driving force is required in the form of a chemical potential difference between two components of an alloy with respect to a specific environment.*

CONCLUSIONS

1. A redetermination of the critical resolved shear stress of ordered and disordered Cu_3Au has shown that the values are 2.2 and 4.5 kg mm^{-2} respectively, are in accordance with previous determinations.

2. Copper is selectively removed by ferric chloride from Cu_3Au single crystals at imperfections originating during crystal growth and from imperfection centers located in slip clusters produced by plastic strain; the latter are apparently associated with blocked arrays of dislocations.

3. In the absence of growth imperfections, the imperfection centers located in slip clusters become nuclei of fracture cracks.

4. Under applied stress, cracks nucleated at reaction sites grow normal to the axis of the principal tensile stress during the initial stages of crack growth.

5. Residual stresses, present in a plastically deformed single crystal, do not produce a microscopically observable crack.

6. A chemical reaction is necessary for the growth of a fracture crack in the present ductile crystals; it appears that sufficient stress cannot be concentrated in a face-centered cubic crystal to produce a stable crack in the absence of chemical removal of at least one component of the alloy.

7. Under applied stress, crack growth is apparently determined by chemical activity of a highly disorganized volume of plastically deformed crystal in advance of the leading edge of a crack. Observed minimum stresses for fracture in transgranular corrosion-rupture tests probably are related to the minimum stress necessary for local plastic deformation.

* *Note added in proof*—Subsequent to this work, direct electrochemical potential measurements have been made [R. Bakish and W. D. Robertson, *Trans. Electrochem. Soc.*, **103,** (1956)] between grains and grain boundaries in copper, Cu_3Au, and alpha brass which have demonstrated the structure and composition dependence of galvanic potential differences in homogeneous alloys.

ACKNOWLEDGMENTS

The authors are indebted to Handy and Harman (particularly to Mr. John L. Christie and Mr. Ernest Chamer) for assistance rendered in preparation of the alloys. We are also indebted to The Office of Naval Research for financial support of this work, and, accordingly, reproduction in whole or in part is permitted for any purpose of the United States Government.

REFERENCES

1. Robert Bakish and W. D. Robertson, *Trans. Amer. Inst. Min. Met. Eng.*, in press. W. D. Robertson *Impurities and Imperfections*, Amer. Soc. Met., Cleveland, 1955, p. 170.
2. G. Wasserman, *Z. Metallkunde*, **34,** 297 (1942).
3. G. Edmunds, *A.S.T.M.-A.I.M.E. Symposium on Stress Corrosion Cracking, Philadelphia*, 67 (1944).
4. Skorcheletti and Titova, *J. App. Chem., U.S.S.R.*, **26,** 37 (1953).
5. W. E. Tragert, Master's Thesis, Yale University (1951).
6. D. K. Priest, F. H. Beck, and M. G. Fontana, *Trans. Amer. Soc. Met.*, **47,** 473 (1955).
7. M. Metzger, private communication.
8. A. B. Greninger, *Trans. Amer. Inst. Min. Met. Eng.*, **117,** 61 (1935).
9. G. Sachs and J. Weerts, *Z. Phys.*, **67,** 507 (1931).
10. G. W. Ardley, *Acta Met.*, **3,** 525 (1955).
11. W. E. Tragert and W. D. Robertson, *Trans. Electrochem. Soc.*, **102,** 86 (1955).
12. Robert Bakish and W. D. Robertson, *Acta Met.*, **3,** 513 (1955).
13. P. A. Jaquet, *Comptes Rendus*, **237,** 1248 (1953); *Rev Metallurgie*, **52,** 307 (1955).
14. A. H. Abdou, *Phil. Mag.*, **45,** 105 (1954).
15. S. Amelinckx, *Acta Met.*, **2,** 848 (1954).
16. R. Maddin, C. H. Mathewson, and W. R. Hibbard, *Trans. Amer. Inst. Min. Met. Eng.*, **175,** 85 (1948); **185,** 527 (1950).
17. A. H. Cottrell, *Dislocations and Plastic Flow in Crystals*, Oxford, 1953, p. 171.
18. A. N. Stroh, *Proc. Roy. Soc.*, **223,** 404 (1954).
19. A. A. Griffith, *Phil. Trans.*, **A221,** 163 (1920).
20. E. Orowan, *Z. Krist.*, **A89,** 327 (1934).
21. E. Orowan, *Repts. on Prog. in Phys.*, **12,** 185 (1949).

VOL. 4 1956

THE BAUSCHINGER EFFECT IN SUPER-PURE ALUMINUM SINGLE CRYSTALS AND POLYCRYSTALS*

S. N. BUCKLEY† and K. M. ENTWISTLE†

The Bauschinger effect has been investigated in both polycrystalline and single-crystal specimens of 99.996% aluminum stressed uniaxially in tension and compression. The magnitude of the effect, defined as the difference between the plastic strains in the forward and reverse directions at a constant fractional stress level, has been found to be uniquely related to the degree of strain hardening induced during prestrain, both in single crystals and polycrystals. In the former case the results become independent of the orientation of the crystal if they are expressed in terms of resolved shear stress and glide strain along the line of prestrain slip. The rate of increase of Bauschinger effect with prestress is high in the easy glide range in single crystals, and falls sharply at the easy glide limit to a much lower value which is about one-fifteenth of this and about half of the corresponding rate of increase in polycrystals. The easy-glide behavior gives rise to a larger Bauschinger effect in single crystals than in polycrystals for low prestresses, but at higher stresses than those used in this work the polycrystalline effect is likely to be greater.

Two dislocation redistribution processes which can give rise to a Bauschinger effect are outlined.

L'EFFET BAUSCHINGER DANS LES MONO- ET POLYCRISTAUX D'ALUMINIUM DE HAUTE PURETE

L'effet Bauschinger a été étudié sur des échantillons poly- et monocristallins d'aluminium très pur (99,996%) déformés unixiallement en traction et compression. Dans les deux cas, on a trouvé que la grandeur de cet effet définie comme la différence des déformations plastiques respectivement dans les directions avant et arrière pour un niveau constant de tension est uniquement relié au degré de consolidation créé au cours de la déformation préalable.

Dans le cas des monocristaux, les résultats sont indépendants de l'orientation du cristal, si on les exprime en fonction de la tension critique de cisaillement et de la déformation le long du glissement dû à la déformation préalalbe. La vitesse d'accroissement de l'effet Bauschinger avec la tension préalable est grande dans le domaine du glissement facile pour les monocristaux et elle diminue brusquement à la limite de ce domaine. Cette vitesse tombe ainsi à 1/15 de sa valeur et vaut à peu près la moitié de la vitesse d'accroissement correspondante dans les polycristaux. Pour de faibles tensions préalables, le glissement facile donne lieu à un effet Bauschinger plus grand dans les monocristaux que dans les polycristaux. Mais à des tensions plus élevées que celles insérées dans ce travail, les polycristaux présentent un effet plus grand.

Deux processus de redistribution de dislocations qui peuvent donner lieu à l'effet Bauschinger sont décrits.

DER BAUSCHINGEREFFEKT IN EIN- UND VIELKRISTALLEN AUS REINSTALUMINIUM

Der Bauschingereffekt wurde sowohl in vielkristallinen als auch in einkristallinen Proben aus Aluminium 99,996% unter einachsiger Zug- und Druckbeanspruchung untersucht. Es wurde gefunden, dass in Vielkristallen die Grösse des Effekts, definiert als die Differenz zwischen den plastischen Verformungen in Vorwärts- und Rückwärtsrichtung bei konstantem Spannungsverhältnis, eindeutig mit der Grösse der durch Vorverformung hervorgerufenen Verfestigung zusammenhängt. In Einkristallen wird das Ergebnis von der Kristallorientierung unabhängig, wenn man es in Schubspannung und Abgleitung, bezogen auf das bei der Vorverformung betätigte Gleitsystem, ausdrückt. Der Anstieg des Bauschingereffekts mit der Vorspannung ist in Einkristallen im easy-glide-Bereich gross und nimmt am Ende des easy-glide-Bereichs rasch auf einen wesentlich niedrigeren Wert ab, der etwa ein Fünfzehntel des vorhergehenden beträgt und etwa halb so gross ist wie der entsprechende Anstieg bei Vielkristallen. Für kleine Vorspannungen verursacht das easy glide-Verhalten in Einkristallen einen grösseren Bauschingereffekt als in Vielkristallen. Bei höheren Spannungen, als den in dieser Arbeit verwendeten, ist jedoch wahrscheinlich bei Vielkristallen der Effekt grösser.

Zwei Prozesse für eine Umordnung der Versetzungen, die Anlass zu einem Bauschingereffekt geben können, werden diskutiert.

INTRODUCTION

Bauschinger[1] observed that the strain hardening of plastically deformed steel was directional, and that, for example, an annealed rod which had been overstrained in tension exhibited increased resistance to a tensile stress but reduced resistance to compression. Later work by Masing[2, 3] and others[4, 5, 6, 7, 8, 9] has established that this phenomenon, the Bauschinger effect, is evident in a wide range of polycrystalline metals, and indeed is now regarded as an intrinsic feature of the strain-hardening process.

Masing[10] has suggested that the effect could be explained by the development of a residual intergranular stress system, assisting a reverse

* Received August 2, 1955.

† Department of Metallurgy, University of Manchester, England.

stress, and arising from the heterogeneous deformation pattern of an aggregate of anisotropic grains. This view was until fairly recently widely accepted, even in the face of conflicting evidence by Sachs and Shoji[4] of a large Bauschinger effect in single crystals of alpha-brass—which was ascribed to the high elastic anisotropy of this material. However, an estimate by Woolley[9] predicts that Heyn stresses can account for at most one-tenth of the observed effect in polycrystals. No precise measurements appear to be available to check this prediction. The results of Sachs and Shoji, for example, are not free from objection on account of possible composition gradients in their crystals, and although appreciable effects in single crystals of iron,[12] cadmium, and zinc[13, 14] have been reported, no parallel measurements on polycrystals were made by their investigators.

The present work had as its first objective a comparison between the Bauschinger effect in single-crystal and polycrystalline specimens of 99.996% pure aluminum, stressed in uniaxial tension and compression. The early results indicated that, although precise comparison is difficult, under certain circumstances the single-crystal effect could be predominant, and most of the work to be described was devoted to it, in particular the variation of Bauschinger strain with crystal orientation and prior deformation.

QUANTITATIVE DESCRIPTION OF THE BAUSCHINGER EFFECT

The Bauschinger effect describes the existence in overstrained metal of different stress-strain curves obtained on the one hand by loading in the direction of overstrain and on the other hand with loads in the reverse direction. The parameter used in the present work to express the magnitude of this difference is defined in Fig. 1, which shows a typical stress-strain history for the tests to be described.

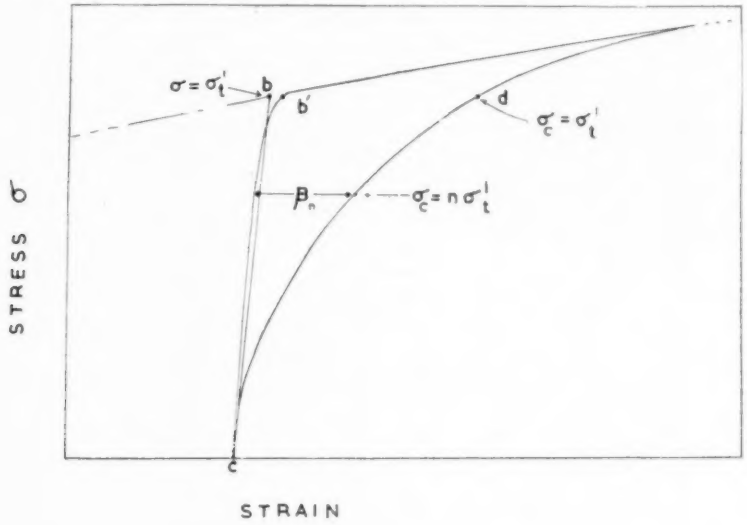

FIG. 1. Typical axial stress-strain history for a Bauschinger test.

An annealed specimen is stressed in tension along ob. At b, the prestress value, it is unloaded to c, and the tensile stress is reapplied to the same value b, giving the curve cb'. After unloading, the specimen is now stressed in compression along cd, the reverse strain curve, which is plotted in the same direction as cb' for compactness. The Bauschinger effect is measured by the Bauschinger strain, β_n, defined as the strain difference between cd and cb' at an arbitrarily chosen stress of n times the prestress value. n here is either 3/4 or unity. The consistent use of cb' eliminates ambiguity arising from hysteresis, which was always detected along cb but which never exceeded 4% of the maximum elastic strain. Thus for $n > \frac{1}{2}$ the difference between cb and cb' is not important.

The definition of β_n is based on that of Woolley,[9] but differs slightly from his in that it describes the anisotropy of the *unloaded* specimen. Woolley's β_n values will be a little greater, since they include the small but measurable inelastic strain associated with removal of the prestress.

It is important to note that because the shape of cd varies in a complex manner, the apparent Bauschinger behavior depends on the value of n selected. However, β_n is found to be an acceptable measure of the Bauschinger effect, since the general conclusions

VOL. 4 1956

do not depend on the value of n selected, at least in the range $\frac{1}{2} < n < 1$. No single parameter has been found *completely* to describe the Bauschinger effect.

Creep was evident only near the prestress level, where creep strains of about 10% of the total plastic strain could arise at normal testing rates. Consequent errors in the value of β_n are claimed to be small, since β_n is the difference between cd and cb', both of which suffer creep modification. The compensation is not complete, however, since the reverse creep rate was observed to be higher than the forward rate for $\frac{3}{4} < n < 1$. No creep was detected and no error in β_n exists for $n \leq \frac{3}{4}$.

EXPERIMENTAL METHOD

Application and Measurement of Strain

In the present work the spurious Bauschinger effect associated with macroscopically inhomogeneous strain was in principle avoided by stressing cylinders in uniaxial tension and compression. The torsion of thin-walled tubes, used with success by Woolley for polycrystals, is basically unsuited to single-crystal tests, and the ability of the Kochendörfer type of straining to produce homogeneous shear is put in some doubt by the work of Read[15] and Sawkill and Honeycombe.[16]

Complex stresses almost invariably arise in the end-regions of uniaxially strained specimens from either frictional constraint to radial expansion in compression or the support from the understressed undeformed metal in headed specimens. Influence from such effects was reduced to negligible proportions by using specimens with a uniform cylindrical section of length at least three times its diameter and by measuring the strain over a gage-length of not more than one-third of the length of the cylinder.

The specimens were strained in a tensile testing machine fitted with axial loading shackles, which were designed to allow free rotation of the specimen during test and so to prevent the generation of torsional stresses. The load was measured from the deflection which it produced at the mid-point of a simply supported elastic beam. Headed tensile specimens were gripped in split collets, and compression specimens were strained between accurately faced and aligned plungers. All strain measurements were made over a gage-length of about $\frac{3}{4}$ in. with two light-weight mirror extensometers of the Martens type fixed to the specimen at diametrically opposite points, and the associated optical system was arranged to indicate the mean strain which is equal to that on the specimen axis. A mean-strain difference of 2×10^{-7} could be detected.

The calibration of the extensometers and the degree of nonaxiality of the applied load were investigated simultaneously with an interferometric device which separates the axial and bending strains. The degree of bending measured at 1% elongation was never greater than 1/100 deg/in., which corresponds to a maximum bending strain of less than 1% of the strain on the axis. No correction has therefore been made for it.

Specimen Preparation and Material

S.P. aluminum of purity 99.996%† was chosen for the experiments on account of its high purity, absence of strain aging, low elastic anisotropy, and reasonably low rate of recovery at room temperature.

Cylindrical polycrystalline specimens were vacuum-cast into chilled graphite molds. Single crystals of either 0.5-in. or 0.65-in. diameter and up to 12-in. long were grown by controlled solidification from the melt, again *in vacuo*, and could be used to give three specimens of identical orientation.

Initial tests were made with headed specimens prepared from the 0.65-in. diameter rods by reducing the center section down to 0.4-in. electrolytically. An alternative method was later devised to reduce the time taken for specimen preparation. Duralumin end-pieces were bonded with shellac to the ends of the 12-in. crystals (Fig. 2), and after tensile prestrain, compression cylinders were parted off either electrolytically or with a jeweller's saw. The ends of the specimen were lapped parallel to each other and normal to the axis to within 20 sec of arc, to preserve axial loading.

All specimens were annealed *in vacuo* for 24 hours at 620°C and then electropolished in a 10% perchloric acid-acetic acid electrolyte immediately before prestraining.

Occasional crystals, which were presumed to have been strained in the mold, showed a compression curve consistently above the tensile curve in the nominally undeformed condition even after annealing at 620°C and electropolishing. Fig. 3 is typical, and implies a residual Bauschinger effect from a compressive prestrain, which is unexpected; but so far as the present work is concerned, all the results quoted are for crystals which showed no such anisotropy and were presumably not strained in growth.

† Principal impurities: Si 0.0020%, Fe 0.0015%, Cu 0.0005%.

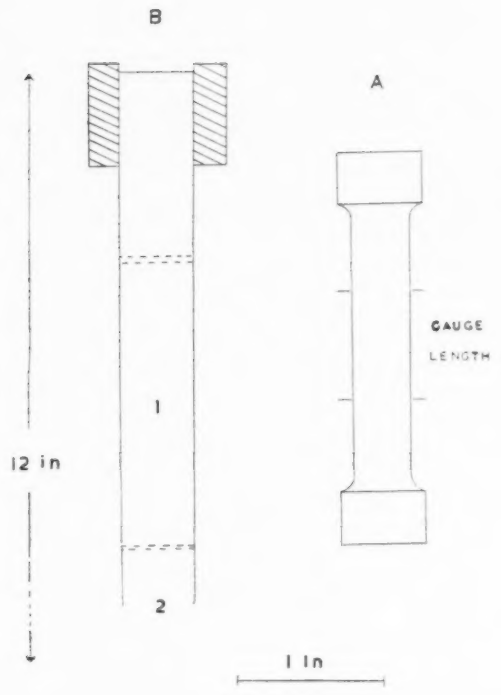

FIG. 2.
(a) Form and dimensions of headed specimens.
(b) Long crystal with duralumin end-piece, showing disposition of compression specimens 1 and 2.

Clearly the direct and reverse stress-strain curves give a sensitive indication of freedom from internal strains.

RESULTS

All the measurements of Bauschinger strain quoted in this section were obtained in compression following tensile prestrain. Other measurements on headed specimens have confirmed that similar conclusions are reached with compressive prestrains.

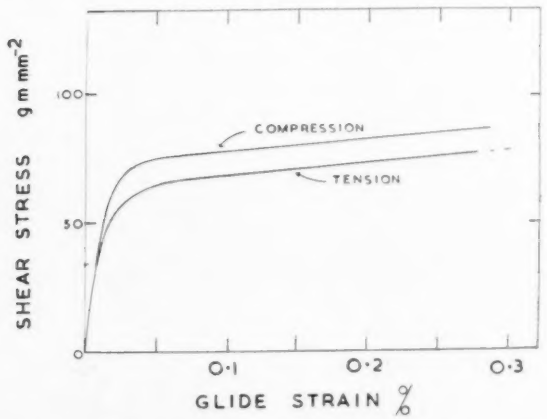

FIG. 3. Stress-strain curves in tension and compression for two identical specimens sectioned from the same single crystal in the as-grown and annealed condition.

Polycrystalline Aluminum

Results are collected in Fig. 4 of a series of tests, each on a different specimen, undertaken to establish the relation between the Bauschinger strain and the extent of prestrain. It is apparent that a linear relation between prestress σ' and β_n exists above about 0.1% prestrain for n equal to 3/4 and unity. This has previously been reported by Woolley[9] for $n = \frac{3}{4}$, but to be valid only for prestrain above about 1% shear, corresponding to an equivalent tensile strain of about 0.5%.

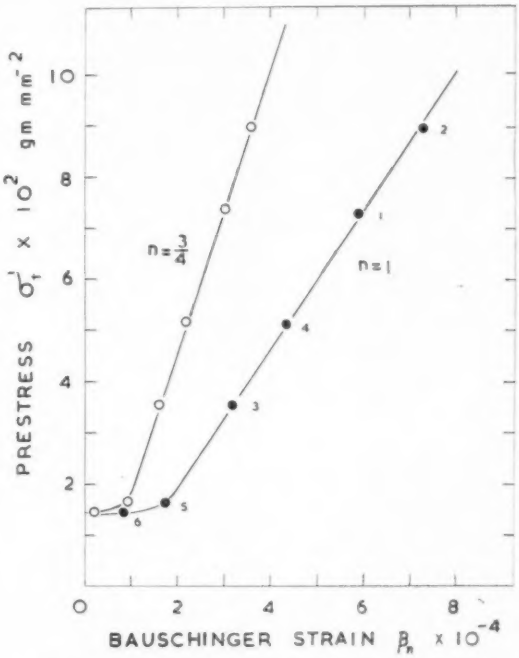

FIG. 4. Relation between Bauschinger strain and prestress for polycrystalline specimens.

A plot of the form of the reverse strain-curve, in terms of log β against log n (Fig. 5), shows that no simple equation can be fitted to it, although its shape was observed to vary little with prestress—a fact consistent with the form of the curves in Fig. 4.

Single Crystals

The values of λ_0 and χ_0, the initial angles between the specimen axis and the primary slip direction and primary slip plane respectively, were measured by the Laue back-reflection X-ray method, and were used to compute the resolved shear stress τ in the operative [110] direction, using the usual relation[17]

$$\tau = \sigma \sin \chi \cos \lambda$$

where σ is the nominal stress.

Instantaneous values of χ were deduced from χ_0, using

$$\frac{l_1}{l_0} = \frac{\sin \chi_0}{\sin \chi},$$

where l_1/l_0 is the ratio of current to initial length.

The glide prestrains were calculated from

$$a = \frac{1}{\sin \chi_0}\left(\sqrt{\left(\frac{l_1}{l_0}\right)^2 - \sin^2 \lambda_0} - \cos \lambda_0\right)$$

The Bauschinger glide strains a_n were calculated on the assumption, in part justified later, that they operated in the reverse direction to the prestrain (i.e. $[\bar{1}\bar{1}0]$) and therefore, because of the small strains involved, could be derived from $a = \dfrac{\varepsilon}{\sin \chi \cos \lambda}$,

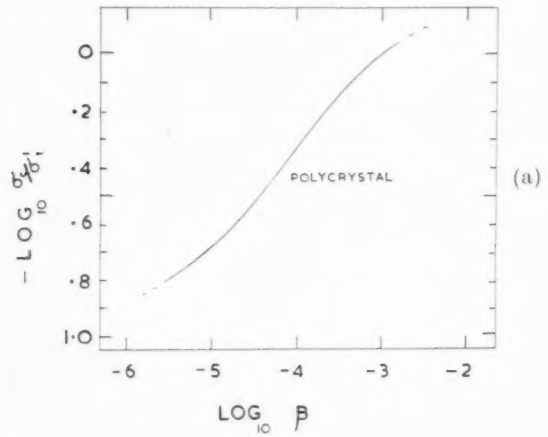

FIG. 5.
(a) Relation between stress and the difference between the forward and reverse strains for polycrystalline aluminum.
(b) Relation between resolved shear stress and the difference (a_β) between the forward and reverse glide strains for an aluminum single crystal prestressed above the easy-glide limit.

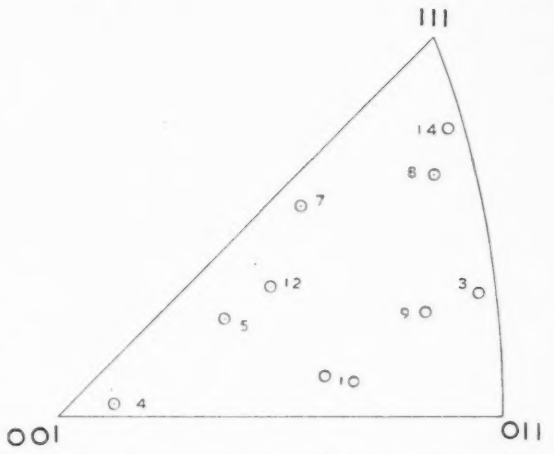

FIG. 6. Stereogram showing the orientation of the crystals for which results are given in Figs. 7 and 8.

where χ and λ are assumed constant and equal to the values obtaining at the end of the prestrain, and ε is the axial plastic strain.

The range of orientation of the crystals tested is given in the stereogram of Fig. 6. In contrast to the behavior of aluminum of commercial purity, the relation between resolved shear stress and glide strain for super-pure aluminum is not unique, and depends an crystal orientation. Thus for crystals such as 9 and 10, with axes near the [110] pole, the initial part of the curve shows a low and constant rate of hardening, which is the region of "easy glide" and persists up to a critical stress τ^*, beyond which the rate of hardening increases sharply. Less favourably oriented crystals, for example 4, show higher hardening rates in the easy-glide range, so that τ^* is attained at very small strains, and the range of easy glide is often in consequence imperceptible.

Fig. 7 shows the magnitude of the Bauschinger strain as a function of prestrain in five specimens of identical orientation, corresponding to point 5 in the stereogram, and each given different prestrains some within and others beyond the limit of easy glide. The specimens were cut from two long crystals, the second seeded with a part of the first. The rate of increase of a_1 is high in the easy-glide range and drops to about one-fifteenth beyond it.

Information from a number of similar tests on crystals of orientations shown in Fig. 6 is given in Fig. 8. All the Bauschinger glide strains a_1, irrespective of orientation and prestrain, fall on a single curve when plotted against $\Delta\tau$, the increase of yield-point above that of the unstrained crystal. The curve gives some support to the suggestion that the reverse strain operates on the same crystallographic plane but in the opposite direction to the prestrain,

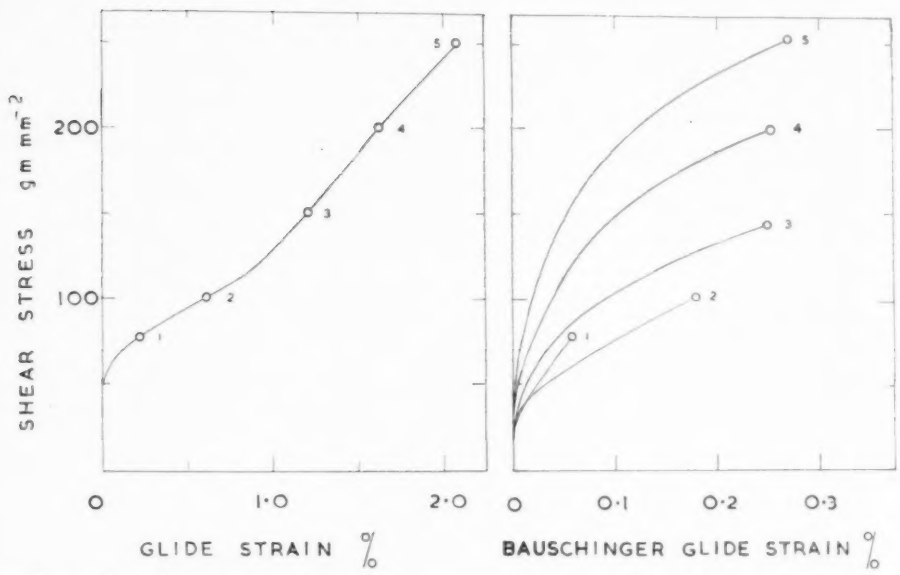

FIG. 7.
(a) Relation between shear stress and glide-strain for crystal No. 5 measured during tensile prestrain. The numbered points on the curve correspond to the prestress values at which a compression curve was measured.
(b) Relation between reverse shear stress and the difference (a_β) between the forward and reverse glide strains for five identical specimens of orientation of crystal No. 5 and each prestressed to a different value, shown in (a). Closed circles show the points corresponding to a Bauschinger glide strain a_β, and crosses $a_{\beta_{3/4}}$

and, further, shows a rapid rate of increase of a_1 in the easy-glide range, and a sharp transition to a reduced rate at a point which closely corresponds to the stress at the easy-glide limit. The form of the curve depends on the value of n, but the high rate of increase in the easy-glide range is still evident for $n = \frac{3}{4}$. The important conclusion is reached, therefore, that the Bauschinger glide strain measured at a constant fractional resolved shear-stress level is uniquely related to the degree of strain-hardening generated during prestraining.

The shape of the plastic component of the reverse strain curve for prestresses above τ^* conforms to a close approximation to $a = kn^3\Delta\tau$ (see Fig. 5).

For prestress within the easy-glide range the shape is markedly different from this. The curve is almost linear above a fairly well defined stress and up to the prestress value.

The difference of shape in the two regions explains the difference between the curves for $n = 1$ and $n = \frac{3}{4}$ in Fig. 8.

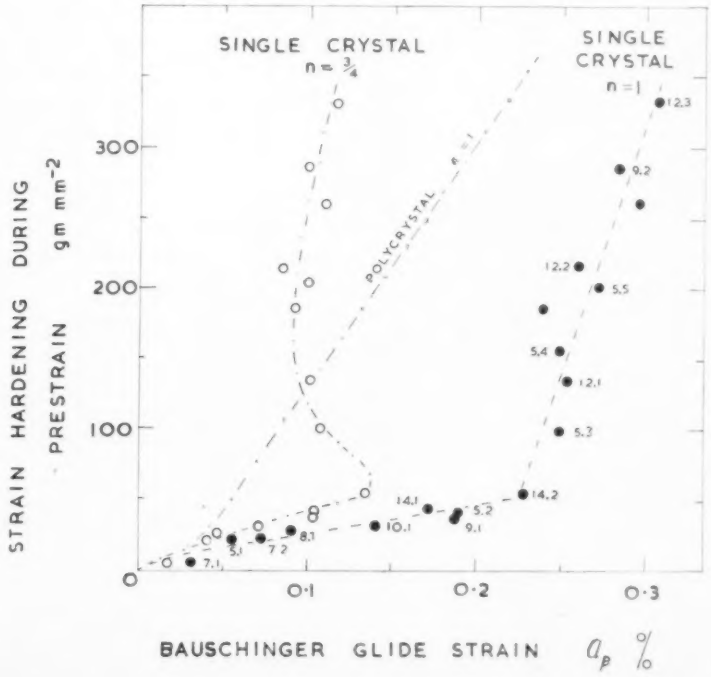

FIG. 8.
Relation between degree of shear strain-hardening developed during prestrain and the Bauschinger glide strain for crystals of orientation shown in Fig. 6. Closed circles are a_{β_1} and open circles $a_{\beta_{3/4}}$.
The polycrystalline curve, shown for comparison, is a replot of Fig. 5(a) after the axial stresses and strains have been resolved in the direction $\sin\chi\cos\lambda = 1/3.1$.

VOL. 4 1956

Surface Observations

Observations with an optical microscope of the surface of prestrained specimens during reverse straining failed to reveal any changes which might indicate the location of the Bauschinger strain.

The surface slip which developed in individual grains of a polycrystal during prestraining was always operative on at least two sets of planes, and for small prestrains was visible in only a few crystals. Specimens from which the slip lines generated during prestrain had been removed by electropolishing showed no evidence of slip during compressive straining until the stress was very near the prestress value τ'. No slip bands were detected until the later stages of prestrain of electropolished single crystals, when both coarse-slip bands ($\sim$2000 Å) and fine-slip were evident. Crystals from which the prestrain markings had been electropolished (proved to be without detectable influence on the Bauschinger strain) developed no indication of slip during reverse stress below τ'. Further tests using the multiple-beam interferometric technique showed that the slip bands which developed above τ' were located between the prestress bands, and possibly correspond to the increase of slip-band density induced by continued tensile prestress above τ'. As such they are not necessarily part of the Bauschinger effect.

It is of interest to note that the maximum Bauschinger glide strain observed in this work (about 0.0025, or one-tenth of the prestrain) could easily be accommodated by a reasonable density of slip bands each with steps below resolvable height.

DISCUSSION

It is possible to make only an indirect comparison between the polycrystalline results and the most closely equivalent published figures of Woolley, because of the different kinds of straining. If the axial stresses and strains in the present work are translated into maximum shear stresses and strains, and these figures are used to derive ρ, the ratio used by Woolley to specify his results, a figure of 3.8 is obtained, which is in good agreement with the range of 3.7 to 4.3 quoted by him.[9]

A similar kind of difficulty is presented in any comparison between single-crystal and polycrystalline measurements; however, for this purpose, the axial stresses and strains of the polycrystal measurements have been resolved into equivalent shear stresses and glide strains along the direction considered by Taylor[18] to represent an average slip direction for the crystals of the aggregate, namely $\sin\chi\cos\hat{\lambda} = \frac{1}{3.1}$. The $\Delta\tau - a_1$ curve derived on this basis is shown with the single-crystal curve in Fig. 8, and it is apparent that within the stress range investigated the single-crystal effect exceeds that in polycrystals. However, the order appears likely to be reversed at Bauschinger glide strains above about 4×10^{-3}, because of the steeper polycrystal curve compared to the single-crystal curve above the limit of easy glide. The relatively large effect in single crystals at small strains is thus a consequence of the easy-glide behavior, and it may well be that in crystals which show no easy glide when stressed in a favorable direction, the polycrystalline effect may be consistently greater. If the trends evident in the present results extend to higher stresses, it is not unreasonable to expect a Bauschinger effect in polycrystals at least double that in single crystals. This indicates that, under certain circumstances, either the contribution from textural stresses in polycrystals is greater than that predicted by Woolley, or that additional factors, such as the resistance to slip propagation across crystal boundaries, are operative.

The high order of the single-crystal Bauschinger strain in the range in which no appreciable disorientation in substructures would be expected suggests that an important source of anisotropic strain-hardening arises on the scale of the individual dislocations. Woolley[9] considers that the measured ratio of the Bauschinger strain to the elastic strain at the yield-point is consistent with all the dislocations in the crystal moving during reverse straining a distance equal to their mean separation. He reached this conclusion after analyzing both a symmetrical Taylor dislocation lattice and the large piled-up groups proposed by Mott. However, before this redistribution process can be accepted as an explanation of the Bauschinger effect, it is essential to show that the dislocations move between potential troughs which are consistently higher on the side to which they are forced by the prestress. The symmetry of the Taylor lattice must mean that the forward and reverse stress-strain curves are identical and no Bauschinger effect is possible.

Consider now the case of dislocations piled up by the prestress against an internal sessile barrier. In order to get a Bauschinger effect from redistribution of the group, it is first necessary to prevent extensive movement on unloading. Mott suggests[19] that this stabilization is effected by cross-slip occurring at frequent intervals along the pile-up and in the wake of the advancing dislocations. Cross-slip thus forms

secondary barriers of the same order of magnitude as the obstacle at the head of the pile-up.

On unloading, the dislocations will rearrange themselves in a reversible manner within the secondary barriers—a process which can affect only the elastic modulus if interactions from neighboring pile-ups are negligible. Under the conditions assumed here, a Bauschinger effect would result only if the dislocations passed over the secondary obstacles, and did so more easily in the reverse than in the forward direction. The essential force asymmetry exists if the dislocation density between any two barriers increases regularly towards the head of the pile-up—a very likely situation—and, further, the asymmetry is automatically reduced and ultimately reversed by dislocation transfer. It is difficult, however, to accept the ability of the dislocations to surmount the cross-slip barriers, since they are obstacles of a primary magnitude. In short, the redistribution of dislocations over barriers confining a regularly increasing dislocation density is a feasible explanation of the Bauschinger effect, but the barriers are unlikely to be of the cross-slip type.

If surmountable barriers exist, then the single-crystal results of Fig. 8 can be interpreted by considering that the Bauschinger strain is produced by the redistribution of a number of dislocations N through a mean distance L. If during easy glide, L is constant and N is proportional to the amount of strain-hardening, then the observed linear increase of a_n with $\Delta\tau$ results. The alternative explanation, that L increases with prestress, does not appear feasible. Beyond the easy-glide limit, the product NL appears to be constant to a first order, that is the reduction of L with increased hardening just balances the increase in number of operative dislocations.

It is possible that another contribution to the Bauschinger strain will be made by dislocations moving between potential wells formed by the interaction between dislocations in closely neighboring slip planes. This idea is attractive in view of Mott's recent theory[20] of strain-hardening based on the force between individual dislocations in planes about 200 Å apart. The present work gives experimental support to the view that strain-hardening and Bauschinger behavior are intimately related.

If the dislocation density at low prestrains is assumed to be not more than $10^{10}/\text{cm}^2$, and is distributed on planes 200 Å apart, then the mean separation in the plane (s) is about $25d$ (where $d = 200$ Å). Referring to Fig. 9, the force F_x on a negative-edge dislocation exerted in its slip direction by an infinitely long uniformly-spaced row of positive-edge dislocations is

$$\frac{\pi D \sin 2\pi x/s}{S(\cosh 2\pi d/s - \cos 2\pi x/s)} \times \left[1 - \left(\frac{2\pi d/s \sinh 2\pi d/s}{\cosh 2\pi d/s - \cos 2\pi x/s}\right)\right],$$

where D is a constant and x is defined in Fig. 9. The variation of F_x with x is shown in Fig. 10 for $s/d = 6$, 10, and 20. Two stable sites (a and d in Fig. 9) exist between any dislocation pair if $S > 4.1d$. Thus stress-induced migration of the negative dislocation between a and d will contribute hysteresis corresponding to the loop *abcef*, but no Bauschinger effect arises because $|F_3| = |F_4|$. An alternative irreversible forward translation from h to d requires a higher stress than the reverse translation from d to a, and thus gives a Bauschinger effect if $F_5 > F_1$, so that the dislocation can be arrested at j. Thus in both cases a Bauschinger effect would arise if some asymmetry of the force distribution existed so that the peaks became higher towards the right of the diagram. An asymmetrical distribution of dislocations could give rise to this situation in the following way: consider a group of negative dislocations confined between cross-slip barriers and lying below a positive group similarly confined in a parallel slip plane. (This would arise if a barrier is formed in each of two neighboring pile-ups by a single cross-slip process.) During forward straining the negative group is piled towards the end opposite to the positive group. The forces of interaction oppose redistribution of dislocations on unloading, but the external force required for reversed movement will be less than the force required to pile the dislocations up, since the reverse stress is assisted by both back-stress within a group and unbalanced interaction between the groups caused by the displacement of the centers of gravity of the two dislocation distributions. This is just the force asymmetry required. Reverse redistribution of dislocations causes a reduction of asymmetry and ultimately a reversal of sign, which is consistent with observed behavior. It is seen, then, that a Bauschinger effect can arise by rearrangement of dislocations in asymmetrical potential wells within sessile cross-slip barriers.

If the Bauschinger strain is assumed to arise from dislocation jumps of the type similar to d to a in Fig. 9, then if $s/d = 20$, the elastic strain associated with the reversible recovery fa is less than 1/40 of the plastic strain, and the ratio falls as s/d increases.

VOL. 4 1956

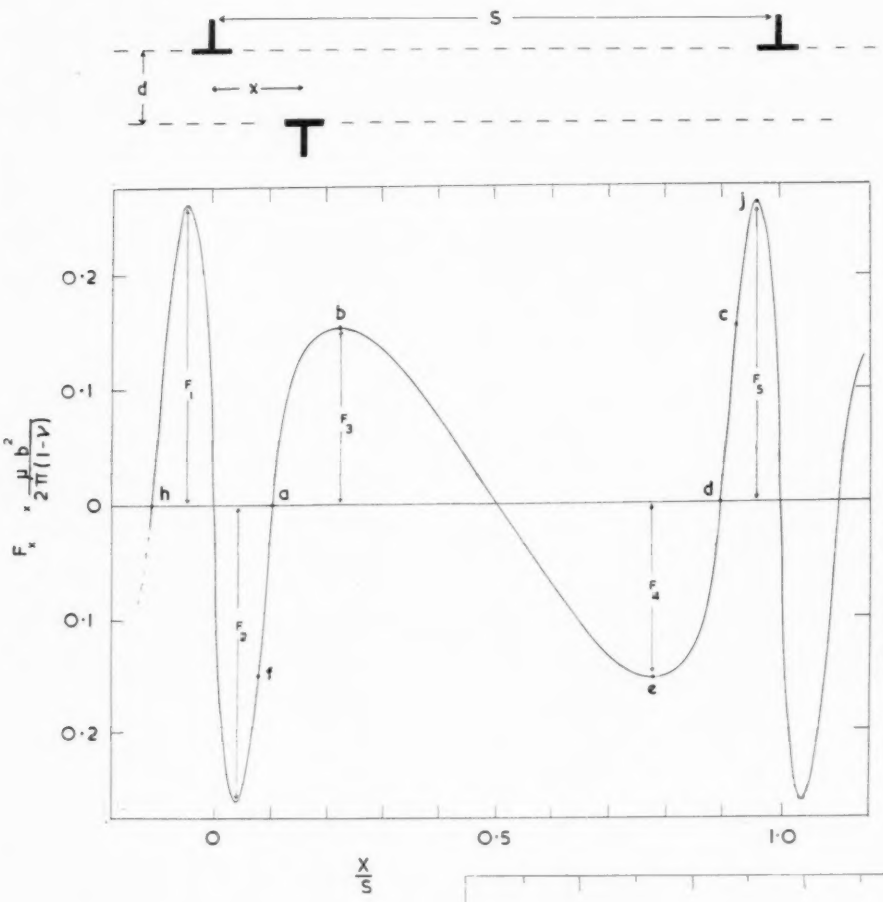

FIG. 9.
Schematic diagram showing variation with distance x of the force on a negative dislocation T moving parallel to and distance d away from an infinite plane containing uniformly distributed positive dislocations ⊥ separated by a distance S. The force on T is shown as positive if it operates to the left.

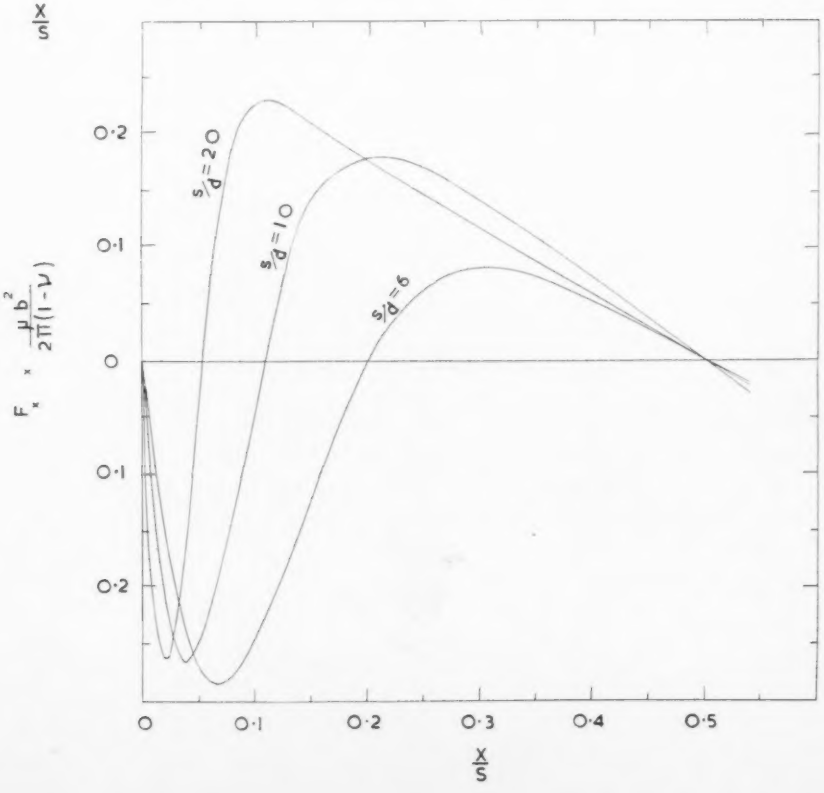

FIG. 10.
Computed variation of F_x with x/s for $s/d = 6$, 10, and 20.

This is of the right order. For *polycrystalline* cubic metals a reduction of elastic modulus of about 10% results from cold working,[21] and since the Bauschinger strain β_1 is five or more times the associated elastic strain, it would be expected that the above ratio would be at least 1/50.

As s approaches d, the elastic redistribution strains become impossibly large; Andrade and Henderson,[22] for example, have shown that for a uniform dislocation lattice with $S = d$, the shear modulus is reduced by dislocation movement to a value of about half of that for a perfect crystal.

There are features of close similarity between the deformation of aluminum during easy glide and the behavior of hexagonal metal crystals; in particular, both show low and linear hardening rates. It is of interest to enquire therefore if the conclusion of a high rate of increase of Bauschinger strain in easy glide is of more general validity by seeking similar effects in hexagonal metals. The measurements of Edwards, Washburn, and Parker on Cd and Zn crystals, although not primarily concerned with the Bauschinger effect, do indicate that the expected steep increase of Bauschinger strain is observed. It is further germane to note that alpha-brass crystals show large Bauschinger strains and are known to deform extensively by easy glide. Unfortunately, the results of Sachs and Shoji do not lend themselves to analysis in terms of the rate of increase of Bauschinger strain.

An extension of the present measurements is in hand to investigate the effect on the Bauschinger strain of elements in solid solution in aluminum, which are known to influence the rate of hardening in the easy-glide range. Preliminary results indicate that for aluminum —0.4% silver single crystals, the rate of increase of a_1 with strain-hardening, $\Delta\tau$, is about double that for pure aluminum. It is hoped to report these experiments fully in the near future.

VOL. 4 1956

ACKNOWLEDGMENTS

The authors wish to thank Professor F. C. Thompson for his continued interest in this work and Dr. H. E. Buckley for the loan of crystallographic equipment. They are grateful to Mr. C. R. Illingworth for mathematical assistance, and one of them (S. N. B.) is indebted to the Department of Scientific and Industrial Research for a maintenance grant.

REFERENCES

1. J. Bauschinger, *Mitt. Mech.-Tech. Lab. München*, **Heft 13,** 1 (1886).
2. G. Masing and W. Maukch, *Wissen Ver. Siemens-Konzern*, **4,** 244 (1925).
3. G. Masing, *ibid.*, **5,** 135 (1926).
4. G. Sachs and H. Shoji, *Z. Phys.*, **45,** 776 (1927).
5. N. Kunze and G. Sachs, *Metallwirtschaft*, **9,** 85 (1930).
6. H. Schwartzbart, M. H. Jones, and W. F. Brown, *Nat. Advis. Cttee. Aeronautics Research Memorandum*, No. RME51013.
7. P. Rahlfs and G. Masing, *Zeit. Metallk.*, **41,** 454 (1950).
8. N. H. Polakowski, *J. Iron Steel Inst.*, **169,** 337 (1951).
9. R. W. Woolley, *Phil. Mag.*, **353,** 597 (1953).
10. G. Masing, *Z. Tech. Phys.*, **3,** 167 (1922).
11. M. J. Druyvesteyn and C. F. Etienne, *Appl. Sci. Res.*, **A4,** 100 (1953).
12. N. H. Polakowski, *Research*, **5,** 143 (1952).
13. E. H. Edwards, J. Washburn, and E. R. Parker, *Trans. Amer. Inst. Min. Met. Eng.*, **197,** 1525 (1953).
14. E. H. Edwards and J. Washburn, *ibid.*, **200,** 1239 (1954).
15. W. T. Read, *Symposium on the Plastic Deformation of Crystalline Solids, Pittsburg*, 1950, p. 111.
16. J. Sawkill and R. W. K. Honeycombe, *Acta Met.*, **2,** 854 (1954).
17. E. Schmid and W. Boas, *Plasticity of Crystals* (F. A. Hughes, London), 1950.
18. A. H. Cottrell, *Dislocations and Plastic Flow in Crystals* (Clarendon Press, Oxford), 1953, p. 117.
19. N. F. Mott, *Phil. Mag.*, **43,** 1151 (1952).
20. N. F. Mott, *Nature*, **175,** 365 (1955).
21. M. Cook, T. Ll. Richards, and G. F. Bidmead, *J. Inst. Metals*, **83,** 41 (1954–55).
22. E. N. Da C. Andrade and C. Henderson, *Phil. Trans.*, **244,** 198 (1951–52).

ON THE ENERGETICS OF TlCl-TlBr SOLID SOLUTIONS*

VÄINÖ HOVI†

Heats of formation corresponding to the equilibrium at 25°C are calculated on the basis of Wasastjerna's statistical theory for some TlCl-TlBr solid solutions of different crystal composition. The theoretical heats of formation are in good agreement with the experimental data.[1] Thus, it is possible to apply the above-mentioned theory also to ionic solid solutions having caesium chloride structure.

SUR L'ÉNERGÉTIQUE DES SOLUTIONS SOLIDES TlCl-TlBr

Des chaleurs de formation correspondant à l'équilibre à 25°C sont calculées, en se basant sur la théorie statistique de Wasastjerna, pour quelques solutions solides de TlCl-TlBr à différentes compositions cristallines. Les chaleurs de formation théoriques sont en bon accord avec les données expérimentales. Il est ainsi possible d'appliquer le théorie susmentionnée également à des solutions solides ioniques ayant la structure du chlorure de caesium.

ÜBER DIE ENERGETIK VON TlCl-TlBr-MISCHKRISTALLEN

Auf der Grundlage der Wasastjernaschen statistischen Theorie wurden für einige TlCl-TlBr-Mischkristalle verschiedener Kristall-Zusammensetzung die dem Gleichgewicht bei 25°C entsprechenden Bildungsenergien berechnet. Die theoretischen Bildungsenergien sind in guter Übereinstimmung mit den experimentellen Daten. Daher ist es möglich, die erwähnte Theorie auch auf Jonenkristalle mit Cäsium-Chlorid-Struktur anzuwenden.

1. INTRODUCTION

Nurmia[1] measured recently heats of formation for some TlCl-TlBr solid solutions of different crystal composition by using high-temperature differential calorimetric method. These solid solutions were prepared from purified component salts by fusion in closed Pyrex glass tubes and then annealed either 140 hours at 150°C or 400 hours at 175°C. Because of the poor solubility of TlCl and TlBr in water, the solid solutions and the corresponding mechanical mixtures of the components were dissolved simultaneously at 175°C in nearly eutectic molten salt mixtures of CuCl, CuBr, TlCl, and TlBr.

The object of the investigation now reported was to obtain *theoretical* data for the heat of formation of some TlCl-TlBr solid solutions and, in this way, to verify the suitability of Wasastjerna's statistical theory[2, 3] for a new case, an ionic mixed lattice having caesium chloride structure.

2. HEATS OF FORMATION

For the calculations of the heats of formation, the ion displacement phenomenon and the ordering state of the mixed lattice in the case of TlCl-TlBr were assumed to be similar to those of KCl-KBr solid solutions. Thus, the heats of formation were calculated from the formula[3]

$$Q_{IV} = Q_I \left[\frac{\vartheta_1}{8} \left(1 + \sigma (1 - 4q) \right) + \frac{\vartheta_2}{8} \left(1 + \sigma(1 - 4p) \right) + \frac{1 + \sigma}{2} \right]. \qquad (1)$$

The meaning of the symbols of this formula is explained in the papers (3) and (4). The characteristic constants of the components, ϑ_1 and ϑ_2, were determined for the caesium chloride structure from Wasastjerna's equation[5]

$$\vartheta = \frac{3 + 4T\gamma}{\kappa_T \frac{\sqrt{3}}{8} \frac{Ce^2}{R^4} - T\gamma}. \qquad (2)$$

Here κ_T is the coefficient of compressibility of a cubic-body-centered lattice, γ stands for the cubic expansion coefficient at constant pressure, C for $c\alpha^2$, where c is Madelung's constant (= 1.7627), and α the ionic charge expressed in elementary units (= 1), e for the charge of an electron, and R for the shortest interionic equilibrium distance in the lattice.

In the numerical calculations the values of the atomic constants N, e, and k, and of the energy equivalent, were the same as in paper[4]. The shortest interionic equilibrium distances in the lattice of TlCl and TlBr, $R_1 = 3.32088 \cdot 10^{-8}$ cm and $R_2 = 3.44489 \cdot 10^{-8}$ cm, respectively, were calculated from the X-ray data measured at room temperature by Straumanis, Ievins, and Karlsons.[6] The interionic distances of the solid solutions were obtained from the corresponding values of the components according to Vegard's rule.

For the compressibilities of TlCl and TlBr, the values $4.86 \cdot 10^{-12}$ bar^{-1} and $5.26 \cdot 10^{-12}$ bar^{-1} by Saerens[7] were accepted. The cubic expansion coefficients of the components, $15.80 \cdot 10^{-5}$ and $15.22 \cdot 10^{-5}$ for TlCl and TlBr at 25°C, respectively, were obtained graphically from the experimental data by Jones and Jelen.[8]

* Received November 30, 1955.

† Institute of Physics, University of Turku, Finland.

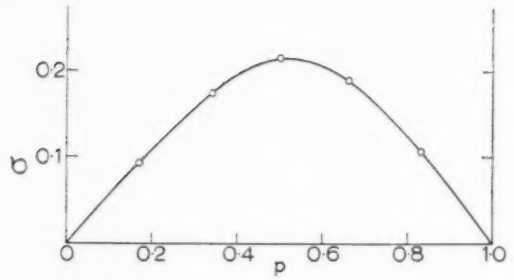

FIG. 1. The degree of local order, σ, corresponding to 25°C, as a function of crystal composition.

Fig. 1 shows the degree of local order σ of the TlCl-TlBr mixed lattice as a function of crystal composition. This curve corresponds to the equilibrium at 25°C. Table 1 contains the values of p, σ, Q_{I}, Q_{IV}, and Q_{exp}. The theoretical and experimental heat of formation values, corresponding to the equilibrium at 25°C and 150–170°C, respectively, are plotted against the TlCl mole fraction in Fig. 2. As seen from Table 1 and Fig. 2, the theoretical results of the present paper are in good agreement with the experimental data by Nurmia. Furthermore, the theoretical values corresponding to the equilibrium at a lower temperature are at every composition smaller than the experimental data, which were obtained for solid solutions annealed at considerably higher temperatures. This is in agreement with the earlier observations made for the difference $Q_{\mathrm{exp}} - Q_{\mathrm{IV}}$ in the cases of KCl-KBr and KCl-RbCl.[3, 9, 10, 11, 12] With the exception of the experimental data by Nurmia, the writer has found neither experimental nor theoretical investigations dealing with the energetics of TlCl-TlBr solid solutions. The results represented in Table 1 may so give first information about the magnitude of the heat of formation of this particular case and also the applicability of Wasastjerna's statistical theory to the ionic solid solutions having caesium chloride structure.*

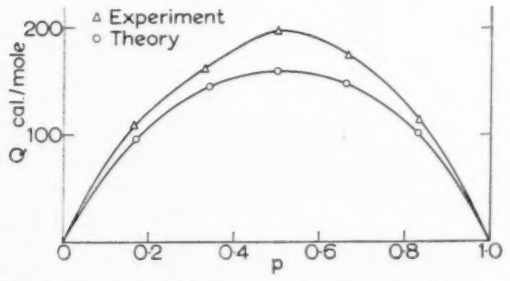

FIG. 2. The heat of formation of TlCl-TlBr solid solutions as a function of crystal composition according to experiment and Wasastjerna's theory.

TABLE 1

Solid solution	Mole fraction of the lighter component p	Degree of local order σ	Electrostatic part Q_{I} (cal/mole)	Heat of formation (cal/mole)	
				Q_{IV}	Q_{exp}
TlCl-TlBr	0.1666				109*
	0.1700	0.092	31.6	96	
	0.3333				162
	0.3400	0.174	51.3	145	
	0.5000	0.214	58.1	159	
	0.5007				198
	0.6600	0.189	53.1	148	
	0.6666				175
	0.8300	0.106	34.0	101	
	0.8332				114
	0.5000				195†

* Experimental data by Nurmia[1] for solid solutions annealed 140 h at 150°C.

† Experimental data by Nurmia[1] for a solid solution annealed 400 h at 175°C.

ACKNOWLEDGMENTS

The writer wishes to record his indebtedness to the Chancellor of the University of Turku for a research scholarship from the Finnish Academy.

The writer is obliged to Miss Anna-Liisa Aalto, University of Turku, for her assistance in the performance of the numerical calculations.

REFERENCES

1. M. J. NURMIA, Dissertation at the University of Helsinki (1956).
2. J. A. WASASTJERNA, *Soc. Sci. Fenn., Comment. Phys.-Math.* XV No. 3 (1949).
3. V. HOVI, *Soc. Sci. Fenn., Comment. Phys.-Math.* XV No. 12 (1950).
4. V. HOVI, *Acta Met.*, **2**, 334 (1954).
5. J. A. WASASTJERNA, *Phil. Trans. Roy. Soc.*, **237**, 105 (1938).
6. M. STRAUMANIS, A. IEVINS, and K. KARLSONS, *Z. phys. Chem.*, **B42**, 149 (1939).
7. E. SAERENS, *Bull. Soc. chim. Belg.* **33**, 53 (1924).
8. G. JONES and F. C. JELEN, *J. Amer. Chem. Soc.*, **57**, 2536 (1935).
9. N. FONTELL, *Soc. Sci. Fenn., Comment. Phys.-Math.* X No. 6 (1939).
10. V. HOVI, *Ann. Acad. Sci. Fennicae*, AI, No. 55 (1948).
11. N. FONTELL, V. HOVI, and A. MIKKOLA, *Ann. Acad. Sci. Fennicae*, AI, No. 54 (1948).
12. N. FONTELL, V. HOVI, and L. HYVÖNEN, *Ann. Acad. Sci. Fennicae*, AI, No. 65 (1949).

* Theoretical and experimental studies on heats of formation of CsCl-CsBr solid solutions are in progress.

VOL. 4 1956

THE DELAY-TIME PHENOMENON IN METAL SINGLE CRYSTALS*

TIEN-SHIH LIU,† I. R. KRAMER,‡ and M. A. STEINBERG§

The effects of strain duration on the critical resolved shear stress of copper, zinc, and beta-brass single crystals were studied by impact tests which produce short-duration compressions. These tests were carried out at 25°C, −50°C, and −190°C. It was found that CPH zinc and BCC beta-brass crystals exhibit a definite increase of critical resolved shear stress at temperatures below room temperature, when the stress duration is decreased to below 10^{-3} sec. This phenomenon was not observed on FCC-copper single crystals. It was shown that the delay-time for the initiation of slip was not affected by the orientation of the stress axis with respect to the slip plane. Activation energies for slip of zinc and beta-brass single crystals were derived from the data obtained.

LE PHENOMENE DU TEMPS D'INCUBATION DANS LES MONOCRISTAUX METALLIQUES

L'influence de la durée de déformation sur la tension critique de cisaillement de monocristaux de cuivre, de zinc et de laiton bêta a été étudiée par des essais de choc produisant des compressions de courte durée. Ces essais furent effectués aux températures de 25°C, −50°C et −190°C. On a constaté qu'aux températures inférieures à l'ambiante, les cristaux de zinc (h.c.) et de laiton bêta (c.c.) présentent un accroissement déterminé de la tension critique de cisaillement lorsque la durée d'application de la charge est inférieure à 10^{-3} sec. Ce phénomène ne s'observe pas pour des monocristaux de cuivre (c.f.c.). On a pu montrer que le temps d'incubation du glissement initial était indépendant de l'orientation relative de l'axe des tensions vis-à-vis du plan de glissement. Les énergies d'activation du glissement pour les monocristaux de zinc et de laiton bêta ont été calculées à partir des résultats obtenus.

VERWEILZEIT (DELAY-TIME)-PHÄNOMEN IN METALLEINKRISTALLEN

Mit Schlagversuchen, die kurzzeitige Stauchungen hervorrufen, wurde der Einfluss der Belastungsdauer auf die kritische Schubspannung von Einkristallen aus Kupfer, Zink und Beta-Messing untersucht. Diese Versuche wurden bei 25°C, −50°C und −190°C durchgeführt. Es wurde gefunden, dass hexagonal dichtest gepackte Zinkkristalle und kubisch-raumzentrierte β-Messingkristalle bei Temperaturen unterhalb Raumtemperatur einen deutlichen Anstieg der kritischen Schubspannung zeigen, wenn die Beanspruchungsdauer kleiner als 10^{-3} sec wird. Diese Erscheinung wurde bei kubisch-flächenzentrierten Kupfereinkristallen nicht beobachtet. Es hat sich gezeigt, dass die Verweilzeit für die Einleitung des Gleitvorgangs von der Orientierung der Spannungsrichtung bezüglich der Gleitebene nicht beeinflusst wird. Aus den gewonnenen Daten wurden Aktivierungsenergien für das Gleiten von Zink- und β-Messingkristallen abgeleitet.

INTRODUCTION

In the study of plastic flow of metals, it is generally known that the yield-point increases with increase of strain rate for polycrystalline metals. This rise of yield-point indicates that a larger force is necessary to start plastic flow when the stress duration is short, or that an incubation period or delay-time exists. The delayed yielding phenomenon of steel was extensively studied by Clark and his associates.[1,2,3,4,5] They concluded that a delay-time for the yield-point existed in low-carbon steels and fine grained molybdenum. They found that as the temperature was lowered, the delay-time for the initiation of the yield-point was increased. The effect of interstitial elements in steel and molybdenum, such as carbon and nitrogen, was found to increase the stress level of the delay-time versus stress relationship.

Kramer and Maddin[6] studied the initial appearance of slip in metal single crystals. They concluded that a delay-time for initial slip occurred in body-centered cubic metals, but was either nonexistent or was very small in face-centered cubic metals. The delay-time increased rather rapidly with decreasing temperature. They also proposed a theory for the brittle-fracture transition which occurs in BCC and CPH metals.

In the present investigation, delay-time measurements were made on copper, beta-brass, and zinc single crystals. These metals were chosen because of their different crystal structures and the fact that, in the case of beta-brass, a sharp rise of critical resolved shear stress with decreasing stress duration was obtained.

EXPERIMENTAL PROCEDURE

Loading Method

To obtain short strain durations under simple compression, a horizontal pendulum similar to the

* Received May 2, 1955; in revised form, July 24, 1955. This paper is based in part on work carried out by Horizons Incorporated for the Watertown Arsenal, Watertown, Massachusetts, under Contract DA-36-034-ORD-871-RD.

† Metallurgy Department, Horizons Incorporated, Cleveland, Ohio.

‡ Mercast Corporation, New York, New York.

§ Metallurgy Department, Horizons Incorporated, Cleveland, Ohio.

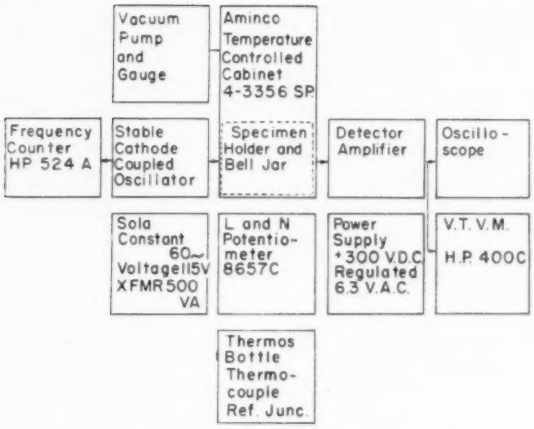
Vacuum Pump and Gauge
Aminco Temperature Controlled Cabinet 4-3356 SP
Frequency Counter HP 524 A
Stable Cathode Coupled Oscillator
Specimen Holder and Bell Jar
Detector Amplifier
Oscillo-scope
Sola Constant 60~ Voltagell5V XFMR500 VA
L and N Potentio-meter 8657C
Power Supply +300 V.D.C. Regulated 6.3 V.A.C.
V.T.V.M. H.P. 400C
Thermos Bottle Thermo-couple Ref. Junc.

FIG. 1. Block diagram of resonance-frequency measuring equipment.

one described by Kramer and Maddin,[5] was used with some modifications. Since the longest strain duration employed in this investigation is of the order of 1.5×10^{-3} sec, a 6-ft pendulum (total length of two sides is 12 ft) was used. To avoid undesirable reflected waves from the specimen-pendulum interface, the pendulum materials used were such that their Young's moduli and densities corresponded closely to that of the specimens being tested; e.g., for copper specimens, copper bars were used.

The pendulum bars rest on knife-edged supports; these bar supports are in turn hung on a top support with *B* and *S* gage-30 nichrome wire. The knife edges are used to decrease the transmission of impact energy to the supports, thus minimizing the consequent complications of undesirable wave patterns.

For the low-temperature experiments, a cryostat was constructed on a steel sleeve, allowing the coolant to come in direct contact with the specimen.

Measurement of Strain

The method used for indicating the strain experienced by the specimens is similar to that of Kramer and Maddin.[6]

The initiation of plastic flow was judged by observing the residual strain in the specimen after each impact. It is characterized by a sudden increase of the residual strain readings obtained. Since the tests were conducted within the elastic range, stresses in the specimens could be computed from the strains and suitable Young's moduli.

Determination of Young's Modulus

The Young's moduli of the crystals used were determined by a dynamic method, using the resonance frequency of the specimens put into longitudinal vibrations by electrostatic means.

The rod-type specimen, whose Young's modulus was to be measured, was clamped at its first node of vibration between two knife edges. It was then driven electrostatically at its mechanical resonance by a polarized plane electrode at one end, and detected electrostatically at the other end with a similar electrode. This signal was amplified and fed into a cathode-ray oscilloscope or detected by a vacuum-tube voltmeter. This is shown in the block diagram in Fig. 1.

The frequency was measured by a Hewlett-Packard Model 524A frequency counter, which read to an accuracy of ± 1 count. With accurate measurement of specimen dimension, the value of E can be obtained within $\pm 0.5\%$. The specimen-holder assembly was enclosed in an Aminco temperature chamber so that the Young's moduli of the specimens at various temperatures could be obtained directly.

Preparation of Single Crystals for Test

Single crystals of copper, beta-brass, and zinc were grown, using the Bridgman technique. OFHC copper was used for growing copper single crystals. Spectrographic analysis of a typical copper single crystal produced showed 99.98 wt. per cent purity. The beta-brass single crystals used in this investigation have a copper content between 50.8 and 53.7 wt. per cent. After crystal growth, they were analyzed chemically at several spots to determine the zinc content along the length of the crystal. In each case the composition variation was less than 0.20 wt. per cent. Zinc crystals were grown from 99.99% pure electrolytic zinc. To eliminate the oxidation of the molten metal and gas entrapment when the molten melt was poured into the mold, the technique described by Miller[7] was followed wherein a vacuum was used to pull the molten zinc into a glass mold. Copper crystals were grown under a nitrogen atmosphere; beta-brass and zinc crystals were grown *in vacuo*.

Copper and beta-brass specimens were then machined to 5/16-in. lengths with parallel ends perpendicular to the specimen axis. After annealing (four hours at 200°C), the specimens were electropolished to a highly reflective surface. The specimens, in this condition, were essentially strain-free, as evidenced by examination of X-ray diffraction spots produced from these crystals. For zinc crystals, machining caused considerable strain in the resulting specimen. For this reason, zinc test specimens were obtained by hand-grinding on a sanding belt and then chemically polished.

VOL. 4 1956

EXPERIMENTAL RESULTS

To observe the strain-time relationship in the elastic range up to the onset of slip, the single crystal specimens were placed in the pendulum and subjected to increasing amounts of impact loads. This was accomplished by drawing the pendulum back from its equilibrium position in $\frac{1}{4}$-in. increments. At the instant the pendulum made contact, a signal was flashed across the screen of the oscilloscope. Any residual strain after the impact was detected by means of a Baldwin Type-L strain indicator. As reported by Kramer and Maddin,[6] within the limits of visual observation the appearance of slip lines occurred at the same time that a plastic strain was indicated. This plastic strain was, therefore, used to indicate the end of the elastic region.

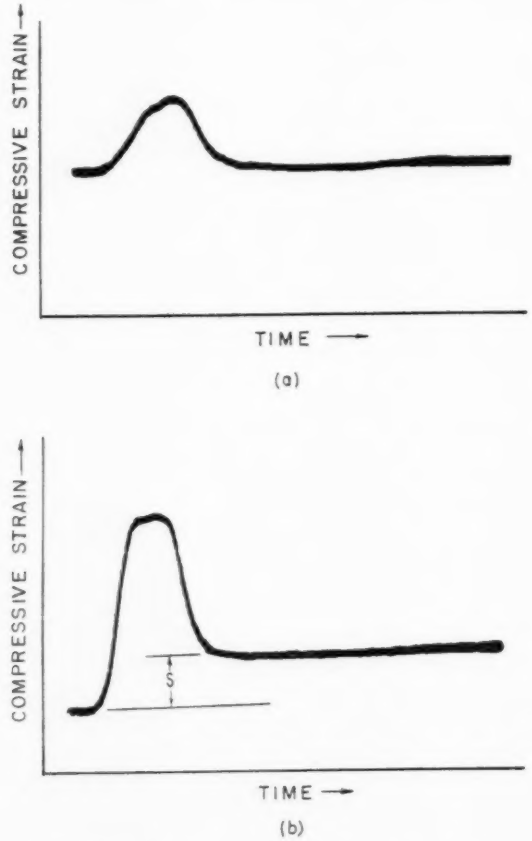

FIG. 2. (a), (b) Strain-time oscillographic signals.

The residual strain was also evidenced in the strain-time signals on the oscilloscope screen. This is indicated in Fig. 2, where two signals are shown. In these signals, the vertical direction represents strain, with increasing negative strain (compression) in the upward direction. Signal (a) was obtained when the crystal was still in its elastic range, the trace returning to its original horizontal level. Signal (b) was obtained when the strain indicator showed residual strain; this was evidenced in the signal by the fact that the trace did not return to its original horizontal level, but to a higher level, indicating permanent strain. The vertical distance s represents the residual strain, which offers an excellent check of the strain-indicator readings obtained.

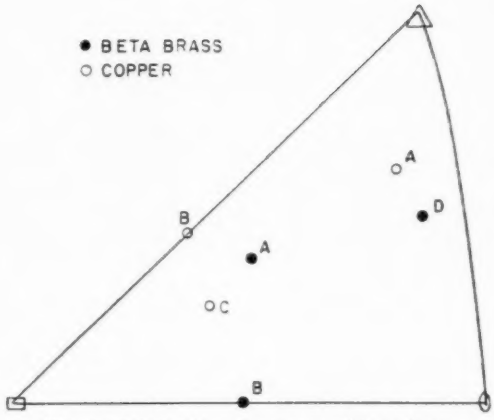

FIG. 3. Orientation of copper and beta-brass single crystals used.

Orientations of all the single crystals used were determined by the back-reflection Laue method. These are shown in Figs. 3 and 4.

To obtain suitable values of Young's moduli for use in the calculations, the resonance-frequency method described above was employed to make actual measurements on the single crystals used. This was carried out at temperatures ranging from room temperature down to —50°C. To obtain values for

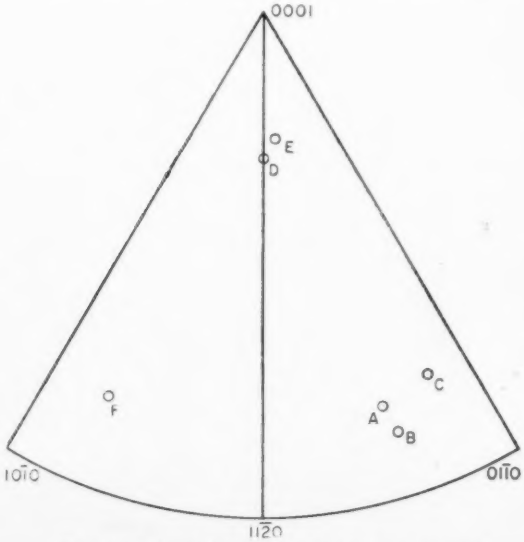

FIG. 4. Orientation of zinc single crystals used.

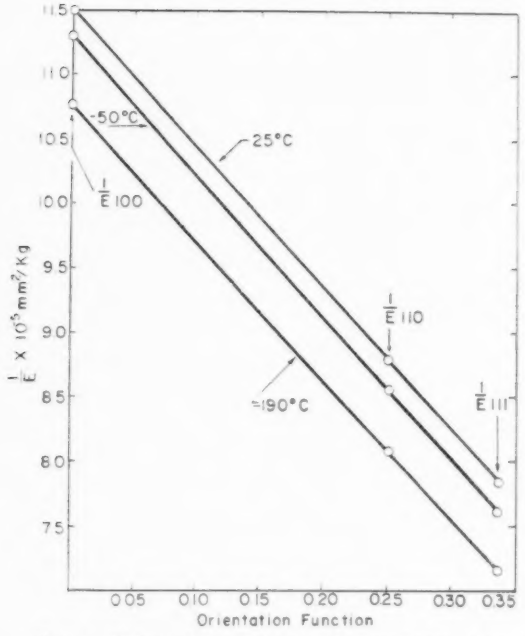

FIG. 5. Effect of orientation on the reciprocal elastic moduli of copper single crystals.

use in connection with —190°C experiments, extrapolation is resorted to where E varied linearly with temperature. In the case of beta-brass, the change of elastic modulus with respect to temperature is not linear; therefore, the measured values of Reinhart[8] were adopted.

Values of the Young's moduli for the single crystals measured in this laboratory are summarized in Figs. 5 and 6, for copper and zinc, respectively. In Fig. 6, the data of Reinacher and Scheil[9] is also included for comparison. For beta-brass, the variation of Young's moduli with temperature is irregular, depending on the orientation; therefore, the values are only presented in table form (Table 1).

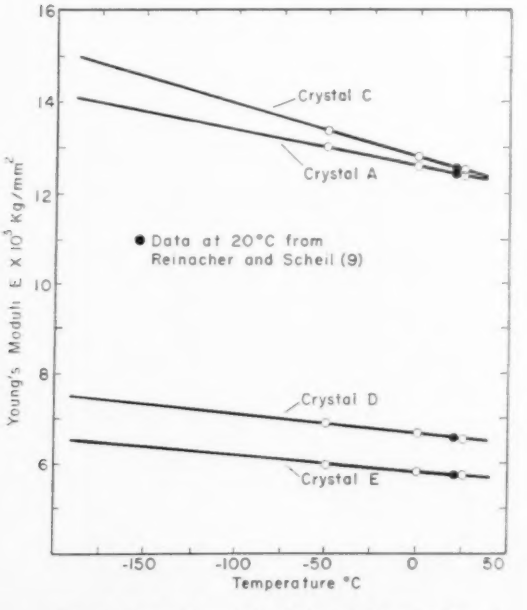

FIG. 6. Young's moduli of zinc single crystals vs. temperature.

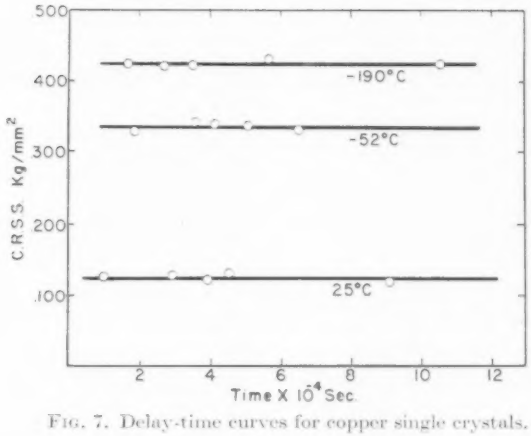

FIG. 7. Delay-time curves for copper single crystals.

The strain duration versus critical resolved shear-stress relations observed at room temperature and at the low temperatures investigated are plotted in Figs. 7, 8, and 9. For beta-brass single crystals at —190°C, it was found that, using the present pendulum arrangement, no plastic deformation could be obtained even under the most favorable strain-duration and

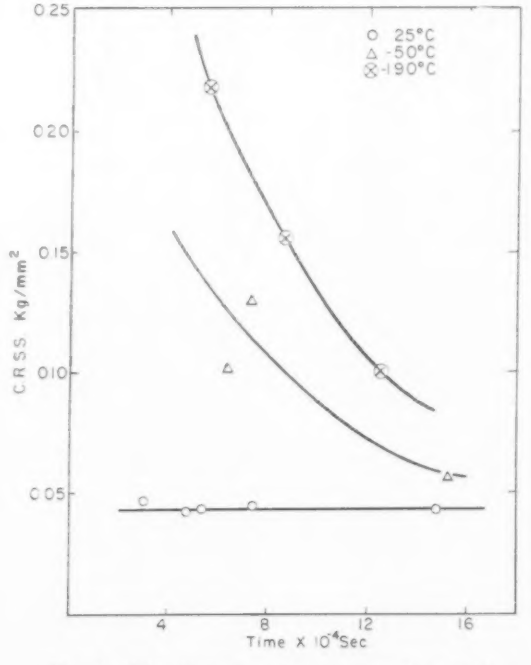

FIG. 8. Delay-time curves for zinc single crystals.

impact condition. The values of critical resolved shear stress listed in these tables were obtained by applying the proper elastic moduli at the temperatures of the tests; thus they were temperature corrected.

TABLE 1. Young's moduli of beta-brass single crystals

Temperature	Crystal A $\times 10^3$ kg/mm^2	Crystal B $\times 10^3$ kg/mm^2	Crystal D $\times 10^3$ kg/mm^2
25°C	5.242	—	12.46
−48°C	5.401	—	10.23
−183°C	5.062*	3.829*	10.12*

* Based on J. S. Rhinehart's data.[8]

DISCUSSION OF RESULTS

From the results obtained, it can be observed that for CPH zinc and BCC beta-brass there is a definite increase of critical resolved shear stress at temperatures below room temperature when the strain duration is decreased to about 10^{-3} sec. This is, however, not evident in FCC copper crystals.

At room temperature, the value of critical resolved shear stress for copper obtained in the present investigation, 0.122 kg/mm^2, is lower than the value of 0.156 kg/mm^2 reported by Hibbard[10]. This may be due to the difference in the nitrogen content of the resulting single crystals used. The values of critical resolved shear stress for copper single crystals grown *in vacuo* are much lower, being 0.10 kg/mm^2, as reported by Sachs and Wurtz,[11] and 0.094, as reported recently by Rosi.[12] From the strain-duration–critical resolved shear-stress plot for copper at different temperatures (Fig. 7), it is seen that the curves are flat at the temperatures tested. Based on these observations, it can be said that, if there is a delay-time for slip of copper crystals, it cannot be detected in our present experiments and must be less than 10^{-4} sec.

Since the slip plane for zinc is the basal plane; the orientations of zinc specimens were so selected that their axes made small angles with the (0001) plane so as to facilitate slip under compression and avoid twinning.

It can be observed from Fig. 8 that the critical resolved shear-stress value for zinc at 25°C is 43 g per mm^2. Davidenkov and Federov[13] have shown that, at room temperature, the twinning resistance is markedly higher than slip resistance, by a factor of at least 4. Although small amounts of twins were observed on the specimens after preparation, examination of the same specimen after impact testing

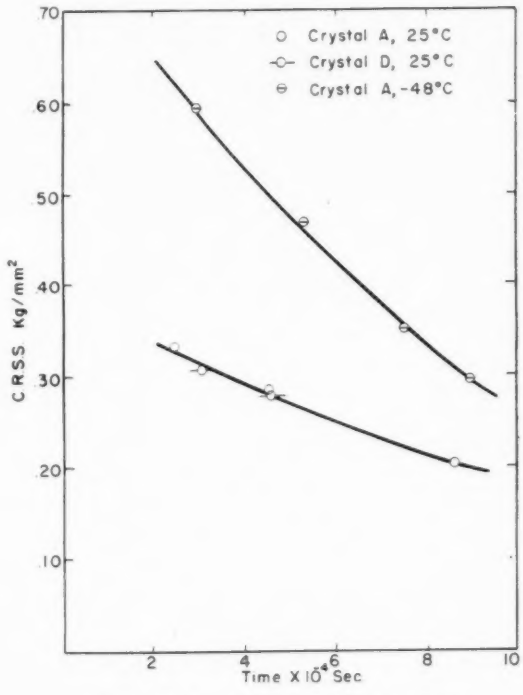

FIG. 9. Delay-time curves for beta-brass single crystals.

showed no detectable increase of twins; however, slip lines were now evident. It is thus believed that plastic deformation during the test occurred primarily by slip. The critical resolved shear stress for slip of zinc had been a matter of controversy in the literature. Miller and Milligan[14] concluded that the elastic range depends on the speed of testing; therefore, there is no definite critical shear stress for zinc. Harper and Cottrell,[15] using 99.99 wt. per cent pure zinc and a strain rate of 10^{-2} per sec in their investigation, obtained a value of 30 g per/mm^2. A corresponding value of 21 g per mm^2 was obtained at a strain rate of 10^{-5} per sec. Jillson[16] obtained a value of 18.4 g per mm^2 from "highly consistent data". The strain rate of testing by Jillson was such that a constant stress rate of 0.1 g per mm^2 per minute was maintained in the $\langle 10\bar{1}1 \rangle$ direction in the slip plane. The highest reported value, 94 g per mm^2, was obtained by Rosbaud and Schmid.[17] The scatter of the results reported in the literature might be partly due to the variance of the constraints imposed by the different experimental arrangements used in testing. However, in the present stage of our knowledge in this respect, the effects of a number of variables on the value of the critical resolved shear stress of zinc are not clear, and remain to be investigated.

A general trend of increase of the critical resolved

shear stress with decreasing strain duration can be observed from the strain time versus critical resolved shear-stress curves for zinc (Fig. 8). It is a well-known fact that zinc single crystals give brittle fractures on impacts of sufficient strength at low temperatures. All these observations point to the fact that there is a delay-time for slip in zinc single crystals.

The critical resolved shear stress of beta-brass single crystals at various temperatures was studied by Ardley and Cottrell.[18] At room temperature a value of approximately 0.21 to 0.25 kg per mm^2 was reported, and at −50°C it ranged from 0.27 to 0.30 kg per mm^2. Kramer and Maddin[6] reported a room temperature value of 325 p.s.i. (0.23 kg/mm^2). The values obtained in the present investigation compared favorably with these results. From data obtained at 25°C and −48°C (Fig. 9) it was observed that there is a definite rise in the critical resolved shear stress at strain durations shorter than 10^{-3} sec. The rise of critical resolved shear stress at room temperature was of particular interest. If the brittle transitions exhibited by beta-brass bear a close relationship to a delay-time for slip, as pointed out by Kramer and Maddin,[6] the present data would indicate that, with a stress of proper magnitude applied with sufficient rapidity, it would be possible to cause brittle fracture even at room temperature. While this has not been reported to date, the possibility cannot be denied. It should be realized that, as far as observable brittle behavior at room temperature is concerned, impurities play an important role.

It appears that crystal orientation does not affect the results obtained. This is not entirely true for zinc crystals, because in this case deformation by twinning complicates the analysis. With the metal crystals tested, specimens with different orientations yielded consistent data at a given temperature. This shows that the delay-time for slip on the glide plane is independent of the direction of the applied stress.

For a given temperature, the increase of critical resolved shear stress at short strain durations over that obtained by static tests, can be attributed to the increasing difficulty to free the "locking points" in the crystals due to insufficient duration of stress application. Actual slip is, therefore, in a sense "delayed" under such circumstances. Sietz[19] referred this to an incubation time and concluded from Gallagher's work[20] that this incubation time is affected by the combination of *thermal fluctuation* and the stress applied. If the contribution of the thermal fluctuation to this incubation time should be comparable to that due to stress application, it would be extremely informative to perform experiments whereby the specimens were held at a given temperature for different lengths of time before impact. This would enable us to detect quantitatively the extent to which the incubation or "delay" time for the initiation of plastic flow is dependent on thermal fluctuation.

A possible explanation for the difference in the plastic behavior at short strain durations between BCC and FCC metals was pointed out by Cottrell.[18] He attributed the difference to the interstitial atoms in the lattice. In a body-centered cubic lattice, the interstitial atoms are near a cube edge, thus relieving the shear component as well as the edge component of a dislocation. In a face-centered cubic lattice, an interstitial atom produces only hydrostatic strain and a screw dislocation cannot be anchored.

As pointed out by Maddin,[21] this could be tested on BCC specimens in which screw dislocations were unanchored from the solute atoms, such as by static tension or compression. If these specimens were tested immediately after deformation by the technique used in the present investigation, no delay-time should be observed.

Clark and Wood[2] assumed that plastic deformation begins after a certain number of dislocations have separated from their atmosphere within a prescribed volume of the material. If this number is large enough, the time required to attain it should be statistically well defined. As suggested by Gibson,[22] the incubation time would be given by a relationship of the form

$$t = K \cdot e^{\frac{Q}{RT}}$$

where t represents the incubation time, Q is the activation energy for the slip process, K is a material constant, R is the gas constant and T is the absolute temperature. Thus a plot of the logarithm of the incubation time against the reciprocal of the absolute temperature would yield a straight line, the slope of which is Q/R, from which the energy of activation for slip can be calculated. Although data at several temperatures are needed to derive the value of such activation energy accurately, preliminary calculations using the available data would give indications as to their order of magnitude. After such calculations were made, it was found that for zinc single crystals, to attain a critical shear-stress value of between 0.10 and 0.17 kg/mm^2, the activation energy varied from 100 cal/mol to 250 cal/mol, and for beta-brass single crystals, to attain a critical shear-stress value of between 2.8 and 3.5 kg/mm^2, the activation energy is

VOL. 4 1956

between 1000 and 2000 cal/mol. It should be borne in mind that the activation energy values obtained for zinc cannot be applied for slip at room temperature because the characteristics of the delay-time curve at room temperature and that at lower temperatures are entirely different for this metal. Due to the scarcity of data, it is realized that the values of activation energies for slip derived are far from being conclusive. The values are reported here to stimulate programs of research of similar nature, considering the fact that such an activation energy for slip cannot otherwise be easily obtained.

ACKNOWLEDGMENT

The authors would like to acknowledge the assistance of the Watertown Arsenal in the sponsorship of this research. They also appreciate the helpful discussions with Dr. R. Maddin, who kindly read the first draft of this paper. Part of the experimental work was carried out by Mr. H. Green. Single crystals used were prepared by Mr. V. E. Straughn, and the elastic constant measurements were done by members of the Physics Department at Horizons Incorporated.

This work was sponsored by Watertown Arsenal, Watertown, Massachusetts, U.S.A. under contract No. DA-36-034-ORD-871-RD.

REFERENCES

1. D. S. Clark and D. S. Wood, *A.S.T.M.*, **49,** 717 (1949).
2. D. S. Wood and D. S. Clark, *Trans. Amer. Soc. Metals*, **43,** 571 (1951).
3. D. S. Wood and D. S. Clark, *Trans. Amer. Soc. Metals*, **44,** 726 (1952).
4. T. Vreeland, jr., D. S. Wood, and D. S. Clark, *Trans. Amer. Soc. Metals*, **45,** 620 (1953).
5. J. A. Hendrickson, D. S. Wood, and D. S. Clark, *Trans. Amer. Soc. Metals*, **48,** 540 (1956).
6. I. R. Kramer and R. Maddin, *Trans. Amer. Inst. Min. Met. Eng.*, **194,** 197 (1952).
7. R. F. Miller, *Trans. Amer. Inst. Min. Met. Eng.*, **118,** 176 (1936).
8. J. S. Rhinehart, *Phys. Rev.*, **59,** 308 (1941).
9. G. Reinacher and E. Scheil, *Metallkunde*, **39,** No. 8, 231 (1948).
10. W. R. Hibbard, jr., *Trans. Amer. Inst. Min. Met. Eng.*, **175,** 66 (1948).
11. G. Sachs and J. Wurtz, *Z. ange. Physik*, **62,** 473 (1930).
12. F. D. Rosi, *Trans. Amer. Inst. Min. Met. Eng.*, **200,** 1009 (1954).
13. N. N. Davidenkov, A. F. Kolesnikov, and K. N. Federov, *J. Exptl. Theo. Phys.* (U.S.S.R.), **3,** 350 (1933).
14. R. D. Miller and W. E. Milligan, *Trans. Amer. Inst. Min. Met. Eng.*, **124,** 229 (1937).
15. S. Harper and A. H. Cottrell, *Proc. Phys. Soc.* (*London*), **63,** 331 (1950).
16. D. C. Jillson, *Trans. Amer. Inst. Min. Met. Eng.*, **188,** 1129 (1950).
17. P. Rosbaud and E. Schmid, *Z. Phys.*, **32,** 197 (1925).
18. G. W. Ardley and A. H. Cottrell, *Proc. Roy. Soc.*, **A219,** 328 (1953).
19. F. Sietz, *Phys. Rev.*, **88,** 722 (1952).
20. E. J. Gallagher, *Phys. Rev.*, **88,** 721 (1952).
21. R. Maddin, Private Communication.
22. J. Gibson, *Proc. Inst. Mech. Eng.* (*London*), **1B,** 536 (1953).

INTERPENETRATING "BANDS" IN TRANSFORMED INDIUM-THALLIUM ALLOYS*

Z. S. BASINSKI† and J. W. CHRISTIAN‡

The crystallography of interpenetrating "main bands" observed in polycrystalline indium-thallium alloys after the cubic-tetragonal transformation is discussed. Experimental confirmation of the predicted twinning pattern for the case of a set of parallel bands crossed by a single interface has been obtained. Ciné-photography shows that interpenetrating bands are probably not the result of growth from a common nucleus, but are merely a consequence of the ease with which one set of bands can accommodate the shear strain produced by another set. Bilby's theory of surface dislocations provides a convenient description of the transformation patterns.

"BANDES D'INTERPÉNÉTRATION" DANS DES ALLIAGES TRANSFORMÉS D'INDIUM-THALLIUM

L'étude cristallographique des "bandes principales d'interpénétration" qui ont été observées après la transformation cubique tétragonale dans des alliages polycristallins d'indium-thallium, est discutée. Une confirmation expérimentale a été obtenue de la structure de maclage prévue pour le cas d'une série de bandes parallèles traversées par une seule interface. Un enregistrement cinématographique montre que les "bandes d'interpénétration" ne sont probablement pas le résultat d'une croissance à partir d'un germe ordinaire, mais plutôt une conséquence de la facilité avec laquelle une série de bandes s'accomode à la déformation de cisaillement produite par une autre série. La théorie de Bilby sur les dislocations en surface fournit une description satisfaisante des structures de transformation.

SICH DURCHDRINGENDE "BÄNDER" IN UMGEWANDTELTEN INDIUM-THALLIUM-LEGIERUNGEN

Die Kristallographie von sich durchdringenden "Hauptbändern" (main bands), die in vielkristallinen Indium-Thallium-Legierungen nach der Umwandlung kubisch-tetragonal beobachtet werden, wird diskutiert. Die vorausgesagte Zwillingsstruktur für den Fall, dass eine Schar paralleler Bänder von einer einzelnen Grenzfläche gekreuzt wird, wurde experimentell bestätigt. Kinematographische Aufnahmen zeigen, dass sich durchdringende Bänder wahrscheinlich nicht das Ergebnis eines Wachstums aus einem gemeinsamen Keim heraus darstellen, sondern lediglich eine Folge davon sind, dass es leicht möglich ist, durch eine Schar von Bändern die von einer anderen Schar hervorgerufenen Scherungen auszugleichen. Die Theorie der "flächenhaften Versetzungen" (surface dislocations) von Bilby ergibt eine geeignete Beschreibung der Umwandlungsstruktur.

VOL. 4 1956

1. INTRODUCTION

Rather complex microstructures are observed in polycrystalline indium-thallium alloys after transformation of an originally flat specimen from the high-temperature cubic structure to the low-temperature tetragonal structure. The tetragonal phase consists of parallel sets of martensitic plates or "main bands," each of which is finely twinned and has a {110} habit plane. Bowles, Barrett, and Guttman[1] first observed that sets of main bands on {110} planes at 60° intersected each other, whilst those on planes at 90° did not, and this result has been confirmed for the analogous transformation in copper-manganese alloys.[2] According to the now generally accepted crystallography,[1, 2, 3, 4] the sets of interpenetrating bands may contain a single common orientation; the others have no common orientation. This has recently lead Geisler[4] to suggest that the interpenetrating bands arise from a single nucleus. A similar suggestion was made previously by Bowles *et al.*, and was based on their proposed two-shear mechanism of transformation. The habit plane, or "first" shear plane, of one set of bands is parallel to a twinning plane, or "second" shear plane, of alternate bands of the other set.§ It was, therefore, suggested that this second shear in the foremost of an advancing set of bands is sometimes able to penetrate the cubic matrix, and thus nucleate another set. Only alternate bands of the second set could be formed in this way; the material between was considered to be competitively transformed by the two sets.

The complete pole figure from a single set of main

* Received November 18, 1955.

† Division of Pure Physics, National Research Council, Ottawa, formerly of Inorganic Chemistry Laboratory, Oxford, England.

‡ Inorganic Chemistry Laboratory, Oxford, England.

§ The paper by Bowles *et al.* possibly gives a rather more physical meaning to the terms "first" and "second" than is now thought likely. As emphasized recently by Frank,[5] by Bowles and Mackenzie,[6] and by ourselves,[3] the resolution of the total strain into homogeneous and "invisible" components does not imply a corresponding resolution of the atom movements. The terms "first" and "second" have significance only in specifying the order of the mathematical factorization.

bands was determined by Bowles *et al.*, and the crystallography of the various types of transformation in well-annealed single crystals has also been investigated recently. In a paper on the single-crystal work,[3] we suggested that the formation of interpenetrating bands could be regarded as equivalent to the motion of a number of "X" interfaces, and we published a photomicrograph supporting this view. More detailed examination, however, shows that the actual twinning pattern must be slightly more complex, since the arrangement we described would contain some untransformed cubic regions. In the present paper we discuss the crystallography of interpenetrating bands. The predictions of the next section were made in the same way as those previously described for single-crystal transformations; they have been verified experimentally. The mode of formation of sets of interpenetrating bands has also been studied by ciné-photography. These results are relevant to a further discussion of the theory of this transformation.

2. PROPOSED TWINNING PATTERN IN INTERPENETRATING BANDS

Experiments on single crystals have shown that a single tetragonal orientation may be produced continuously from a cubic crystal by the motion of an "X" interface. A different type of double-interface transformation is also possible, and leads to a twinned tetragonal region. This transformation, described in Section 6 of reference (3) will, for convenience, be called an X' transformation in the present paper. Fig. 1 shows a hypothetical situation in which X and X' interfaces have a common portion OO'. The lines XOB and AOO' are the traces of an X interface transformation in which a single tetragonal region of orientation (a) is ultimately produced. The lines $ZO'C$ and $OO'Y$ are the traces of an X' interface, leading ultimately to tetragonal twins of orientations (b) and (a). Each of the twinned regions in the diagram contains two tetragonal orientations in the volume ratio 2:1; these orientations and their relative proportions are indicated by small letters and shading respectively. The actual orientations were enumerated in the previous paper, and need not be repeated. The portions of the crystal on each side of any of these interfaces have been given a macroscopic plastic shear of amount $2\varepsilon = \frac{2}{3}(c/a - 1)$ relative to each other, and an originally flat cubic surface would show sharp tilts along the lines $AOO'Y$, XOB, and $ZO'C$. The shears along XOB and $ZO'C$ are necessarily in the same sense, as may be seen by considering the progressive change in the proportion of orientation (b) on proceeding from the region AOB through

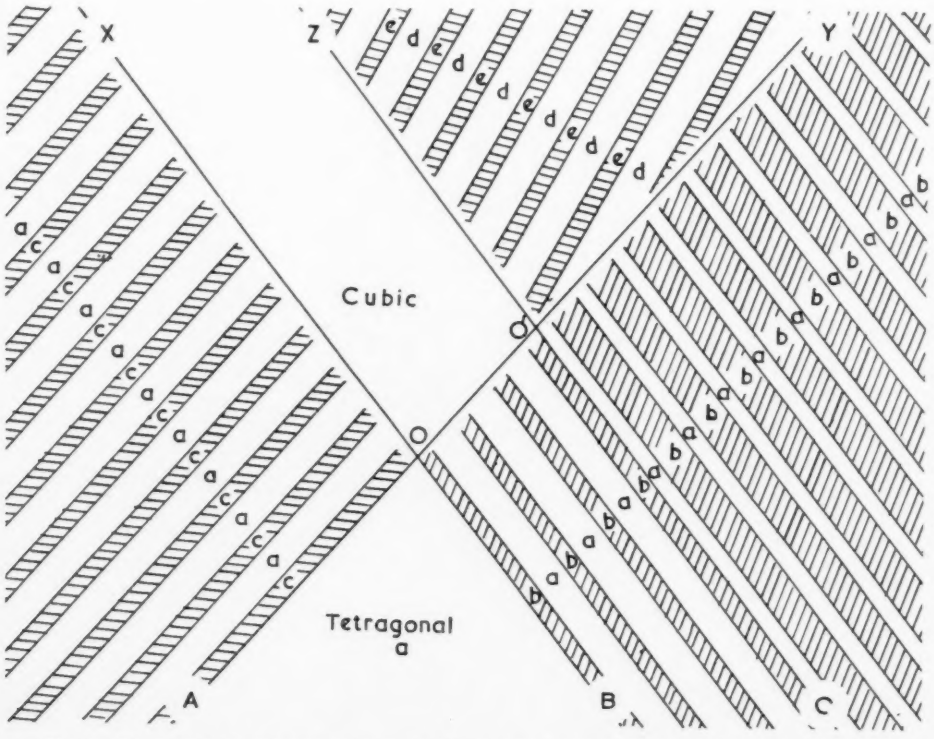

FIG. 1. Hypothetical twinning pattern resulting from a combination of X and X' interfaces.

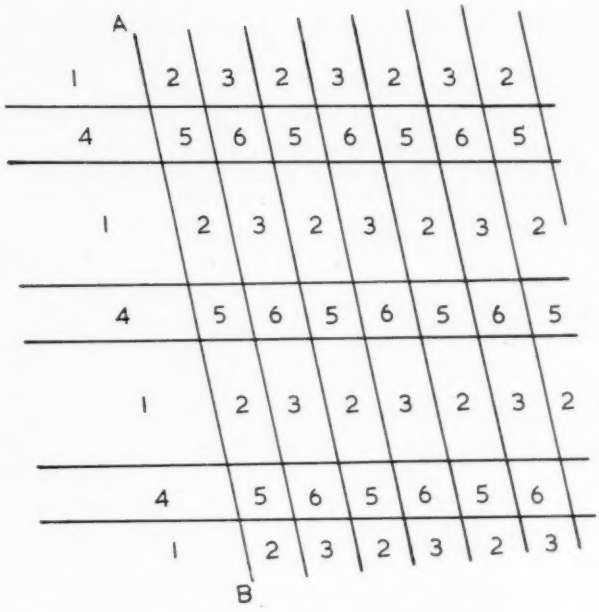

FIG. 2. "Penetration" of a set of main bands by three bands of another set.
Orientation 1 = $XOO'Z$ of Figure 1
2 = AOX of Figure 1
3 = $ZO'Y$ of Figure 1
4 = $BOO'C$ of Figure 1
5 = AOB of Figure 1
6 = $CO'Y$ of Figure 1

$BOO'C$ to $CO'Y$. Now, let the remaining cubic region be consumed by the motion of XOB and/or $ZO'C$. These two interfaces will thus amalgamate to form a single interface, and the twinned region $BOO'C$ will also be eliminated. The tilt in the surface across the combined interface will now correspond to a 4ε shear, whilst that across AOY is unchanged. The 4ε shear is characteristic of the boundary between adjacent main bands, and the orientations (*a*), (*c*), (*d*), and (*e*) represent four of the eight possible orientations in a single set of main bands.

The above virtual process may be extended by arranging a sequence of interfaces of the types $\cdots XX'X'XXX'X'XXX'X'X\cdots$ along a common line AY, and consuming the cubic regions as above. This gives a set of parallel main bands crossed by a single interface corresponding to a macroscopic shear of 2ε; this situation has actually been observed. In an identical manner, another interface, parallel to the first, but with opposite direction of shear, could be introduced. The structure then consists of a single main band crossing a parallel set. The twinning pattern obtained by the above process is not unique. A "λ" or a "V" interface could be substituted for any of the X interfaces without changing the argument. Thus a set of twins lying on a plane at 90° can be substituted for any set described in the above case.

Suppose now that one set of main bands does not extend beyond some limiting surface. A possible configuration is shown in Fig. 2, where part of the specimen is assumed to be still cubic. The set of bands on the right of the line AB has been penetrated by three bands of another set. The whole volume is divided into prismatic regions of repeating orientation patterns, indicated by numbers; the key gives the relation between these regions and those of Fig. 1. The dividing surfaces parallel to AB (except for AB itself) represent 4ε macroscopic shears, the others 2ε shears. If the cubic regions 1 now transform by formation of the complementary bands of the second set, the 1/4 boundaries become 4ε shears. This additional macroscopic shear, necessary to convert the cubic regions to tetragonal regions, can be accommodated in the regions 2, but the twins in regions 3 lie on the plane at 60° to that of the required shear. There is thus no way in which the 3/6 boundary can be changed to a 4ε shear.

Considerations of macroscopic accommodation thus lead to the conclusion that only alternate bands of any set are able to penetrate another set. In order to avoid large stresses caused by the sudden cessation of the shear, the transition must be accommodated by gradual tapering of the bands which penetrate. This process is closely analogous to the manner in which a set of parallel tetragonal twins may be merged into a

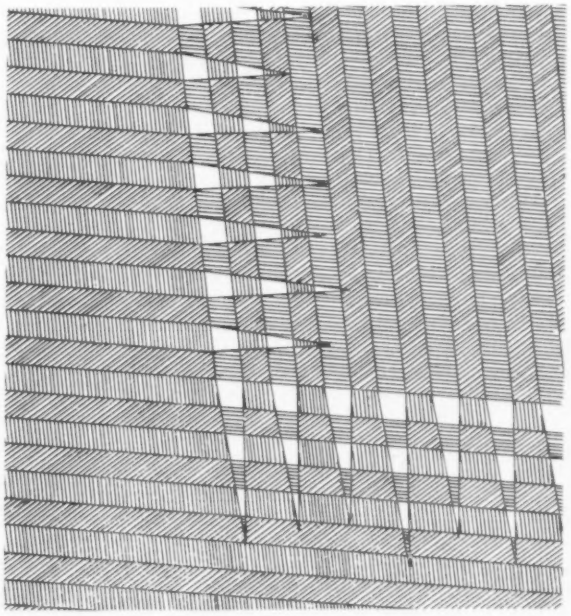

FIG. 3. Suggested twinning pattern for interpenetrating bands.

VOL. 4 1956

single tetragonal crystal: as shown previously,[7] the tapering may be described as a "distributed" shear. The possible configuration for two sets of interpenetrating bands is thus of the general type shown in Fig. 3, where the traces of the twins or sub-bands are indicated. The bands meet along two lines, and alternate bands of each set penetrate a limited distance into the other set. The bands which penetrate may have twin traces parallel to the plane of the pene trated bands and an orientation in common with them; those which do not, may have twin traces parallel to twin traces in the other set of bands. The tapering bands contain some single tetragonal regions.

FIG. 4. A single interface crossing a set of main bands. Specimen electropolished and etched after transformation. Polarized light ×45
Regions numbered as for Fig. 2.

3. EXPERIMENTAL WORK

Conditions similar to those in polycrystalline specimens were obtained by transforming mishandled single crystals and specimens containing a few large crystals; the transfo rmation patterns were then a fairly coarse scale. Fig. 4 shows a transformation on pattern in one such specimen; in order to show the directions of all the twin markings, the surface has been electropolished and then etched. This configuration corresponds clearly to the situation described above, in which a set of main bands is crossed by a single interface, and the twins in regions 2 and 6 are parallel to the boundaries of these regions with the 5 region, as expected. Laue photographs of the four marked areas were taken, using a simplified version of the precision micro-beam camera described by Cahn.[8] For greater accuracy in the relative orientations, the areas 5 and 3 were also photographed on the same film. All orientations of the tetragonal lattice agreed to within 20′ with those predicted from the above hypothesis. Intensities of Laue spots, as judged visually, were also in the expected proportions. Fig. 21 and 22 of reference (3) showed a single main band, i.e. two interfaces, crossing a set of main bands, and are also consistent with the previous discussion. Sets of tapering intersecting bands often occur [see, for example, Fig. 10 of reference (1)] and, so far as can be judged, these are all in agreement with Fig. 3.

Figs. 5–9 illustrate the formation of a set of interpenetrating bands. As previously described, a single set of bands spreads progressively on a macroscopic scale, but some bands continually form ahead of the

FIG. 5

FIG. 6

FIG. 7

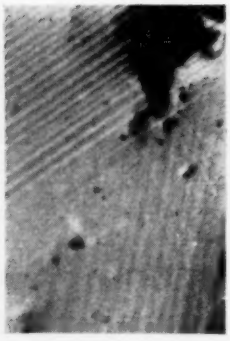

FIG. 8

FIG. 9

FIGS. 5–9. The formation of a set of interpenetrating bands in a polycrystalline indium-thallium alloy.
Oblique illumination ×30
Interval between frames, 1 sec

main group. These bands also show lengthwise growth, but diffuse regions are formed first and then change to sharp bands, and the ends often appear to form before the centers. It thus seems probable that this observation results from a delay in breaking through the surface, rather than a true rate of growth. These effects are all shown by the second set of bands in Figs. 5–9. The set of vertical bands in Fig. 5 continues to spread in Figs. 6 and 7. In Fig. 6, however, a second set of bands appears, and this grows in the succeeding frames, encroaching on the first set. Interpenetration of this kind, in which a growing set of main bands spreads into an already formed tetragonal region, has been observed on a large number of occasions. It follows that the formation of interpenetrating bands is not necessarily, or even usually, the result of growth from a common nucleus, in the ways suggested by Geisler or Bowles *et al.*

4. THEORIES OF THE TRANSFORMATION

Phenomenological theories of martensitic transformations aim at predicting the orientation relations, the habit plane, and the observed macroscopic distortion from a knowledge only of the structures and lattice parameters of the two phases. It is assumed that there is negligible mixing of the atoms during the structural change, so that the atoms defining some Bravais lattice of the parent structure move in a regular manner to the points of a Bravais lattice of the final structure. If neither structure has a basis, these atomic movements accomplish the whole transformation, which may be regarded as a homogeneous deformation of one structure into another. A structure with a basis may be divided into sets of atoms on interpenetrating Bravais lattices; the net atomic movements are then formally specified by giving each such lattice the same homogeneous deformation, and, in addition, translating the lattices with respect to each other. The inhomogeneous movements are sometimes called shuffles.

Any two *lattices* may be homogeneously deformed into one another in an infinity of different ways, but, except in special cases, the production of a macroscopic volume of product would involve an extremely high strain-energy. This strain-energy can only be avoided if the macroscopic, or shape deformation[9] associated with the lattice change approximates to an invariant plane strain, so that the transformed region may remain in contact with the matrix along an undistorted, unrotated plane (the habit plane). The shape deformation may be adjusted to the required type by combining the lattice deformation with a lattice invariant deformation, e.g. slip on a series of parallel planes, or by combining two different lattice deformations which alternate on a fine scale. In either case, the atom movements are such that the equivalent lattice deformation is homogeneous only over a small region; the lattices in adjacent regions either have the same orientation, giving a single crystal, or are twins of each other, as in the indium-thallium and similar transformations. In any such region, the lattice deformation may be factorized mathematically into two imaginary successive stages, of which the first is the same for all regions, and gives the shape deformation, and the second is opposite for adjacent regions in the sense that the net shape deformation is zero. This factorization gives the two components of the "two-strain" or "two-shear" theories of martensitic transformations, of which that due to Bowles *et al.*[1] is a particular example.

The above description is fundamental to almost all recent theories and is repeated here to emphasize the true nature of the two-strain or two-shear theories, which have given rise to some misunderstanding. These theories are not concerned with the detailed mechanism of transformation, and only specify the relations between initial and final atomic positions. They are concerned with mechanism in a general sense, in so far as they regard the macroscopic homogeneous distortion as automatically associated with the structural change, in contrast to the views expressed by A. H. Geisler.[10] Criticism of these theories on the grounds that they imply successive movements of planes of atoms is therefore invalid; no such interpretation is now intended.

In all theories, the inhomogeneous component of the lattice strain is assumed to be a simple shear. The homogeneous component, as already stated, approximates to an invariant plane strain. Some theories allow a small uniform dilatation, or a small uniaxial expansion in addition; for details see reference (9). The crystallographic significance of the habit plane is thus analogous to the composition or K_1 plane of a mechanical twin, and twinning may, indeed, be regarded as a particular type of martensitic reaction. When a martensite plate is produced in a surrounding matrix, the change of shape of the transformed region can only be accommodated by deformation of the matrix or possibly of the plate itself. The stresses then force the plate to adopt a lenticular shape, and the habit plane is not readily distinguishable. It is important to realize that this does not invalidate the above theories, as has been claimed,[4,10] but is rather to be regarded as an additional complication, the effects of which can be avoided in certain

VOL. 4 1956

circumstances. Exactly the same behavior is shown by mechanical twins, but the significance of the twinning plane is not in question.

There are two ways of avoiding the lenticular shape. The most effective is the production of single interface transformations in single crystals; and the observation of plane interfaces is strong supporting evidence for the assumptions of the phenomenological theories.[11] The second possibility arises in transformations in which plates with opposite macroscopic shape deformations may share a common habit plane.[1,2,12,13] A set of parallel plates, with opposite tilts and nearly plane interfaces, may then be formed, as this system is practically self-accommodating. This is the situation in polycrystalline indium-thallium alloys.

Single and double interface transformations in indium-thallium alloys were first reported by Burkart and Read.[14] These workers did not consider the crystallography of the various modes of transformation, or the elimination of accommodation stresses, but detailed attention was given to the theory of the transformation. Using the method developed by Wechsler, Liebermann, and Read,[15] they showed that the habit plane differs from a $\{110\}_c$ plane by $\sim 26'$, assuming the inhomogeneous part of the lattice strain to be a shear on the $\{101\}_t$ planes. This treatment thus corrects the approximate two-shear theory of Bowles *et al.*[1] in which terms of the order ε^2 were ignored.

In discussing their analysis, Burkart and Read criticize the Bowles theory, and show that successive movements of planes of atoms are not required. As indicated above, however, the theory may be regarded as purely phenomenological, and the treatment is then a very close approximation to the exact theory of Burkart and Read. If the invariant plane-strain condition is rigorously satisfied, the deviation of the habit plane from a rational $\{110\}$ plane is so small as to be negligible; the rotation of $\sim 26'$ would almost certainly be achieved by having interfaces, parallel to $\{110\}$, containing steps of atomic height.

There is an interesting formal difference between the exact theory and the approximate two-shear treatment, in as much as the latter is a degenerate case, having a smaller multiplicity of solutions. Thus, in Burkart and Read's analysis, there are twenty-four variants of the habit plane, and each variant corresponds to a pair of twin-related tetragonal orientations. There are four such habit-plane variants grouped round each cubic $\{110\}$ plane, two of them giving a macroscopic distortion of one sign, and the other two opposite distortions. In the approximate solution, these two pairs coalesce to give the two main bands having a common $\{110\}$ habit-plane interface. For the lattice parameters used by Burkart and Read, the habit-plane indices are of the form $\{1, 0.993, 0.013\}$. The relation between the two theories for a single set of main bands may be represented as shown in diagram at foot of page.

The twin orientations (a) and (b) correspond to the specific variant used in the analysis of Wechsler, Liebermann, and Read.[15] The exact theory shows that orientation (a) differs infinitesimally from one of the tetragonal orientations in the plate with habit plane $(1, 0.993, \overline{0.013})$; in the two-shear theory, these form the orientation common to the main bands parallel to (101) and (110). In the approximate theory, there are thus only thirty-six tetragonal orientations, while according to Burkart and Read's theory there are really forty-eight.

The experimental results show that single main bands often contain two sets of twins, and that interpenetration occurs. They do not, of course, provide a basis for

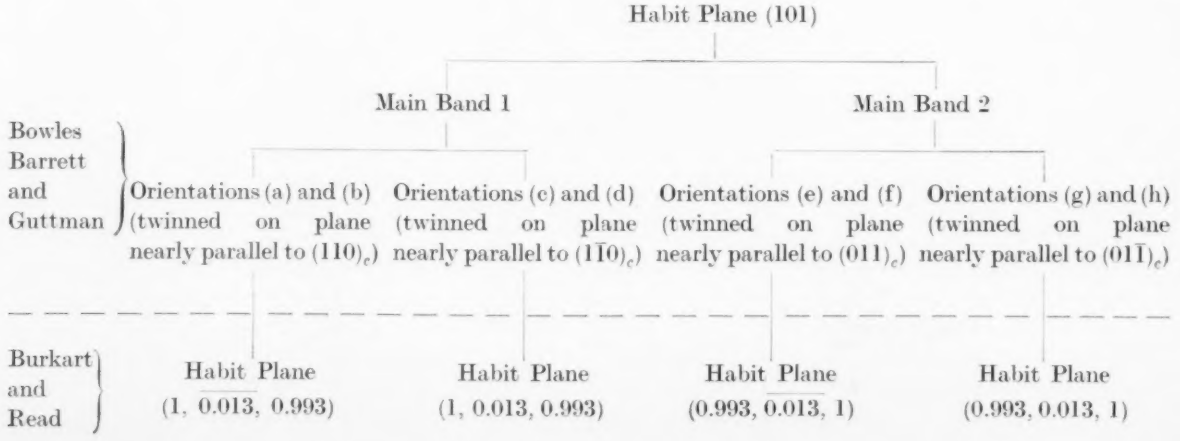
Habit Plane (101)
Main Band 1
Main Band 2
Bowles Barrett and Guttman
Orientations (a) and (b) (twinned on plane nearly parallel to $(110)_c$)
Orientations (c) and (d) (twinned on plane nearly parallel to $(1\bar{1}0)_c$)
Orientations (e) and (f) (twinned on plane nearly parallel to $(011)_c$)
Orientations (g) and (h) (twinned on plane nearly parallel to $(01\bar{1})_c$)
Burkart and Read
Habit Plane $(1, \overline{0.013}, 0.993)$
Habit Plane $(1, 0.013, 0.993)$
Habit Plane $(0.993, \overline{0.013}, 1)$
Habit Plane $(0.993, 0.013, 1)$

deciding whether or not the exact relations are valid, since the angle between the habit planes would in any case be unobservable. The observations reported in this paper on the formation of interpenetrating bands are, however, of interest in supporting the general phenomenological theory, since the avoidance of long-range stresses is once again shown to be the factor which governs the transformation patterns. Interpenetrating bands evidently arise not by growth from a common nucleus, but because of the geometrical possibility of shearing a fully formed set of bands on another {110} plane, at 60° to the habit plane, without introducing long-range stress. This shear is then able to accommodate the formation of a further set of bands. The reversibility and small hysteresis in this transformation are almost certainly due to the ease with which complex transformation patterns can be arranged to accommodate all the transformation strains, even in polycrystals. Plastic deformation of the matrix, which occurs, for example, in the transformations in steels and cobalt, is not then required.

Burkart and Read made one observation which we have been unable to duplicate in our experiments; namely, that single crystals sometimes transform by "X" interfaces on {110} planes at 90° to each other. The method of analysis used here and in our previous paper[3] shows that this type of interface is most improbable, since the systems of shears are not mutually compatible.

VOL. 4 1956

5. SURFACE DISLOCATIONS

In conclusion, we wish to point out that the theory of "surface dislocations," recently developed by Bilby, Bullough, and Smith, seems to be readily applicable to the transformation patterns in indium-thallium alloys. Bilby[16] treats the most general type of internal boundary, which separates two different lattices, and movement of which produces a plastic strain. In some cases, it may be possible to define individual arrays of line dislocations which will produce the required interface, as for a tilt boundary, but it is a useful formal concept to consider the boundary as a whole with its dislocation content smoothed out. When treated in this way, the boundary is called a surface dislocation, since it separates volumes of different plastic strain, in contrast to a line dislocation, which separates surfaces of different slip. Frank[17] showed how the total dislocation content of a general grain boundary is defined in a reference lattice by the lattice relations and the orientation of the boundary. The corresponding theory for a general surface dislocation has been developed by extending Nye's analysis of the geometrical properties of volume distributions of dislocations.[18] In particular the dislocation content of the surface is specified by a tensor, β_{ij}, defined in a given reference lattice, and this may be regarded as the formal analogue of the Burgers vector.

Bilby has given a formula by which the dislocation tensor may be calculated, at least for small deformations, from the normal to the interface, and the two opposite deformations which generate the actual lattices from the median reference lattice. The representation has the advantage that all the components of β_{ij} are zero for two lattices which are related by an invariant plane strain and joined along the invariant plane.* A fully coherent boundary between two lattices is thus assigned zero net dislocation content.

The boundary in a martensitic transformation usually connects lattices which are not related by an invariant plane strain, but, as explained above, the macroscopic shape deformation does approximate to such a strain. If the martensite plate is a single crystal, the dislocation tensor of the surface dislocation which represents the interface is thus zero. The smoothed-out density of dislocations in this case must, of course, include the slip disclocations responsible for the lattice invariant strain. When the product is a stack of fine twins, it is not immediately obvious that the surface dislocation concept can be used. Presumably, however, the difficulty can be avoided in the same way; the twinned region may be represented macroscopically by a single lattice having a large "unit cell" which encompasses at least two twin related regions. An alternative description of the present phenomenological theories of martensitic transformation is, in fact, that a large unit cell of the parent structure is converted into a correspondingly large unit cell of the product by a homogeneous deformation.[9] In the surface dislocation description, it will be immaterial whether this large unit cell contains regions which have slipped relative to each other, or regions which have slipped homogeneously to give twins. It should be noted that if the shape deformation is not exactly an invariant plane strain, as in some recent theories, the surface dislocation tensor will not vanish, but will specify the residual content of line dislocations necessary to accommodate the changes in length in the habit plane.

An extension of the above argument leads to the possibility of representing boundaries between two

* This result was obtained by Bilby[19] in the early development of his theory, but has not yet been published. It may readily be derived if one substitutes $a_{ij} = d_i u_j$ where d_i are the components of any vector, into the formula for β_{ij} (equation 10 of reference 16).

sets of different twins as surface dislocations. In particular, the arrays which occur in double interface transformations in indium-thallium alloys may be regarded as separated by surface dislocations which represent simple shears. Surfaces of discontinuity may meet in the interior of the crystal; this situation is called by Bilby a "surface node" by analogy with the familiar node of line dislocations. The fundamental compatibility condition (equation 11 of reference 16) is just the assumption used in analyzing the indium-thallium twinning patterns. An X-interface transformation may thus be regarded formally as a mobile surface node, which moves under the influence of stress or free-energy driving forces. In a similar manner, a set of interpenetrating bands consists of a network of surface dislocations meeting at surface nodes. In a λ transformation,[3] the region of distributed shear, produced by tapering the twin boundaries, seems to be equivalent to an extended surface dislocation. It will thus be seen that the various types of transformation form a reasonably consistent scheme when regarded in this way.

ACKNOWLEDGMENTS

We wish to acknowledge stimulating correspondence with the late Dr. A. H. Geisler. Thanks are also due to Dr. B. A. Bilby for discussions on surface dislocations, and to Dr. W. Hume-Rothery, O.B.E., F.R.S., for his interest. Dr. R. W. Cahn kindly supplied details of his simplified microbeam camera. Financial support was received from a grant to this laboratory for general research purposes by the British Non-Ferrous Metals Research Association.

REFERENCES

1. J. S. Bowles, C. S. Barrett, and L. Guttman, *Trans. Amer. Inst. Min. Met. Eng.*, **188**, 1478 (1950).
2. Z. S. Basinski and J. W. Christian, *J. Inst. Metals.*, **80**, 659 (1951–52).
3. Z. S. Basinski and J. W. Christian, *Acta Met.*, **2**, 148 (1954).
4. A. H. Geisler, *Acta Met.*, **2**, 639 (1954).
5. F. C. Frank, *Acta Met.*, **1**, 15 (1953).
6. J. S. Bowles and J. K. Mackenzie, *Acta Met.*, **2**, 129 (1954).
7. Z. S. Basinski and J. W. Christian, *Acta Met.*, **2**, 101 (1954).
8. R. W. Cahn, *J. Sci. Instrum.*, **30**, 201 (1953).
9. B. A. Bilby and J. W. Christian, Symposium on the Mechanism of Phase Transformations (The Institute of Metals), 1955.
10. A. H. Geisler, *Acta Met.*, **1**, 260 (1953).
11. Z. S. Basinski and J. W. Christian, *Acta Met.*, **1**, 759 (1953).
12. A. B. Greninger, *Trans. Amer. Inst. Min. Met. Eng.*, **133**, 204 (1939).
13. D. Hull and R. D. Garwood, Symposium on the Mechanism of Phase Transformations in Metals (The Institute of Metals), 1955.
14. M. W. Burkart and T. A. Read, *Trans. Amer. Inst. Min. Met. Eng.*, **197**, 1516 (1953).
15. M. S. Wechsler, D. S. Liebermann, and T. A. Read, *ibid.*, **197**, 1503 (1953).
16. B. A. Bilby, Report of Bristol Conference on Defects in Crystalline Solids, 1954 (The Physical Society).
17. F. C. Frank, Plastic Deformation of Crystalline Solids (Pittsburgh Conference, 1950), p. 150.
18. J. F. Nye, *Acta Met.*, **1**, 153 (1953).

VOL 4 195

THE SHAPES OF GLIDE PLANES IN BENT ZINC CRYSTALS*

B. A. BILBY† and E. SMITH‡

Experiments are described which show that, within the experimental error, the glide surfaces in uniformly bent zinc single crystals intersect the plane of bending in involutes of circles. The observation that "river-patterns" on the cleavage surfaces of zinc crystals often begin along the line of mosaic boundaries formed during the growth of the crystals is also reported.

LES FORMES DES PLANS DE GLISSEMENT DANS LES MONOCRISTAUX DE ZINC COURBÉS

Des expériences sont décrites qui montrent que, dans les limites d'erreurs expérimentales, les surfaces de glissement dans des monocristaux de zinc uniformément courbés, coupent le plan de courbure suivant des développées de cercle. On signale également le fait que les "river-patterns" sur les surfaces de clivage de cristaux de zinc commencent souvent le long des frontières mosaïques formées au cours de la croissance des cristaux.

DIE FORM DER GLEITEBENEN IN GEBOGENEN ZINK-KRISTALLEN

Es werden Experimente beschrieben, die zeigen, dass in gleichmässig gebogenen Zink-Einkristallen die Gleitflächen innerhalb der experimentellen Fehler die Biegungsebene in Kreisevolventen schneiden. Ausserdem wird über die Beobachtung berichtet, dass "Flussfiguren" (river patterns) auf Spaltflächen von Zink-kristallen häufig entlang der Spur von Mosaikgrenzen, die während des Kristallwachstums gebildet wurden, beginnen.

VOL. 4 1956

1. INTRODUCTION

In view of the paper by Gilman[1] which has just appeared in *Acta Metallurgica*, it seems desirable to report at once on some similar experiments which have been carried out independently at Sheffield. An account of preliminary experiments of this kind was first given by one of us (B. A. B.) at a colloquium at the University of Birmingham in March 1955.

The object of our experiments was to test the prediction[2] that in uniform plane bending, under conditions of single glide, the glide planes intersect the plane of bending in involutes of circles. This was done by examining the shape of the (0001) planes of single crystals of zinc bent at room temperature and subsequently cleft in liquid nitrogen.

2. EXPERIMENTAL DETAILS

Cylindrical crystals, 6 mm in diameter, were grown from zinc rod of 99.99% purity by the modified Bridgman method, using a vertical travelling furnace. The orientation of the crystals was controlled by using a seed. The position of the basal plane in each crystal was identified either by observation of slip lines which occasionally appeared during growth, or by cleaving a small piece from one end by reversed bending. The crystal was then turned so that, as it lay horizontally, a vertical plane through the axis was perpendicular to the basal plane, as judged by eye, and a line was scribed on the upper surface. Together with the specimen axis, this line defined the plane of bending. The crystals were then bent at room temperature round cylindrical formers of different radii, and about half an hour later were cleft in liquid nitrogen by applying a reverse bending moment. There was, apparently, no macroscopic deformation during this cleavage process. The cleavage surfaces were untwisted, and could be generated by the motion of a straight line parallel to the axis of bending, suggesting that plane bending had indeed occurred. The broken pieces were then mounted in a projection lantern and a shadow of the cleavage surface and the bent crystal thrown on to a screen; the magnification was about $20\times$. A record of the shape of a section through the centre of the specimen by the plane of bending was thus obtained. The light-beam was adjusted by eye so that it was parallel to the axis of bending, and in tracing contours of the cleavage surfaces the process was always repeated after rotation of the crystal through 180°, and the mean of the contours taken. From the agreement between these contours, and from the general shape of the cleavage surfaces described above, it appeared to be unnecessary to have a $\langle 11\bar{2}0 \rangle$ direction in the plane of bending, and the orientation was not controlled to ensure this. It was found that there was sometimes a slight discrepancy in the images of the cleavage faces of two matching pieces

* Received October 7, 1955.

† Department of Metallurgy, University of Sheffield.

‡ Formerly, Department of Metallurgy, University of Sheffield; now at A.E.I. Research Laboratory, Aldermaston, Berks.

near the outer edge. This was ascribed to deformation of the finely tapered acute wedge of that piece having a concave cleavage surface. The following measurements were therefore made only on images of pieces whose cleavage surface was convex. In all, the shapes of ten cleavage surfaces were examined using pieces from three long crystals A, B, C. Formers of diameter 0.953 cm (pieces $A1$, $A3$, $A4$, $B1$, $B2$, $C1$, $C2$, $C3$), 1.91 cm (piece $A5$), and 2.56 cm (piece $A6$) were used. The orientations of all the crystals were such that $\chi_0 \simeq 45°$, and during the bending no aural evidence of twinning was observed, although, of course, twins were visible after fracture on the cleavage surfaces, appearing with characteristic asymmetry (Bilby and Bullough[3]). After the cleavage surface and the bent cylindrical surfaces had been traced, a circle was fitted to the outline of the inner cylindrical surface. This was usually of radius R, about twenty times that of the former used for bending. For pieces $A3$, $A5$, $A6$, and $C3$, however, the image showed that circles of slightly different radius were required. The values of R are given in Table 1. Using the centre of this circle as origin, radii were drawn at intervals of 5° and a number of r, θ values corresponding to points on the cleavage surface obtained. The angle χ (in Nye's notation) was also obtained directly at positions along the trace of the cleavage surface by drawing tangents or normals to this trace and measuring the angles they made with the radius vector.

3. RESULTS

The theory predicts that along any glide surface $r \sin \chi = a$, where a is a constant equal to the radius of the generating circle of the system of involutes. Accordingly, $r \sin \chi$ was first computed for all the cleavage surfaces, using the χ values on each estimated by drawing tangents or normals. The mean values, together with the standard deviations σ, are given in Table 1. It is clear from this table that $r \sin \chi$ is approximately constant along the cleavage surface,

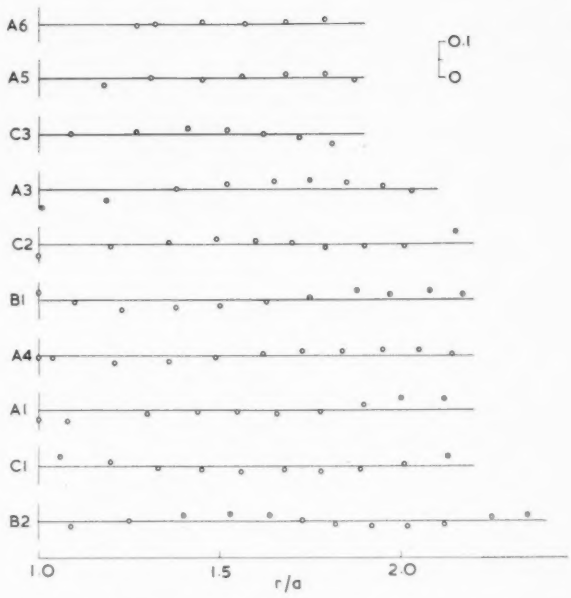

FIG. 1. Values of $\theta + f$ plotted against r/a for the ten cleavage surfaces. $\theta + f$ is plotted as ordinate, using the vertical scale indicated. The horizontal line for each test piece corresponds to the mean value $\bar{B}$ given in Table 1.

and also that, except for $A5$, $A6$, and perhaps $C3$, the crystals have been bent until the inner surface is approximately the generating circle estimated from the r, χ measurements. It is not possible, however, to draw normals or tangents to the trace of the cleavage surface with great accuracy, and an alternative method of assessing the results was therefore adopted. The (r, θ) equation of the involute may be written

$$\theta + f(r/a) = B$$

where B is a constant determining the origin of θ, and

$$f(r/a) = [(r/a)^2 - 1]^{\frac{1}{2}} - \sec^{-1}(r/a).$$

Thus, if a is chosen correctly, the quantity $\theta + f$ calculated from the measured r, θ values should be a constant, independent of θ. Fig. 1 shows $\theta + f$

TABLE 1

Crystal	$A1$	$A3$	$A4$	$A5$	$A6$	$B1$	$B2$	$C1$	$C2$	$C3$
Mean value of $r \sin \chi = a$	10.0	10.4	9.8	16.1	22.5	9.7	8.9	9.3	9.7	13.5
σ	0.2	1.0	0.6	1.0	1.0	0.7	0.8	0.8	0.7	1.8
R	9.5	10.5	9.5	18.7	27.4	9.5	9.5	9.5	9.5	15.9
a_F	9.5	10.4	9.5	15.8	21.5	9.5	8.9	9.3	9.5	14.7
$\bar{B}$	0.759	0.715	0.800	0.580	0.502	0.822	0.981	0.774	0.781	0.544

The values of a and R are those on the enlarged tracing and are in centimetres.

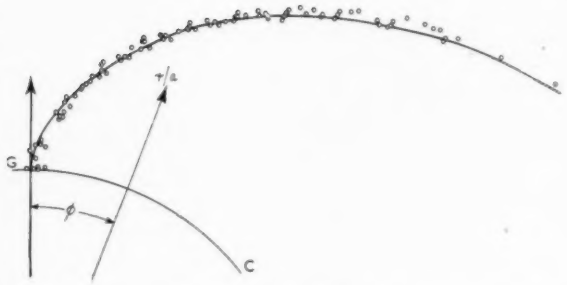

FIG. 2. Experimental results from all test pieces assembled on a master graph. *GC* is the generating circle, and the full curve is the theoretical involute on which all the experimental points should lie.

plotted against r/a for the ten cleavage surfaces. The initial a value for each testpiece was taken to be the smaller of the quantities a and R in Table 1. In some cases, however, a was subsequently adjusted to make $f + \theta$ more nearly constant; the final a values (a_F) are shown in row 4 of Table 1. The results are all assembled on a master graph in Fig. 2, where the values of r/a are plotted against the angle $\phi = B - \theta$ for each testpiece, together with the involute on which all the experimental points should lie. For each piece, B was taken to be the mean of the values of $\theta + f$; these mean values $\bar{B}$ are given in line 5 of Table 1.

4. DISCUSSION

The above experiments show that, within the experimental error, the predicted shape of the glide planes in uniform plane bending under conditions of single glide is observed in uniformly bent zinc crystals. This is in accord with Gilman's conclusion.[1] The latter's experiments and method of analysis of the results differ, however, in some details from the present ones. In so far as the deviation from the theoretical curve is systematic, it appears to be in the opposite sense to that indicated in Gilman's Fig. 7. This would be more marked had we not used a mean value of B, but had weighted the inner points more heavily. It is perhaps worth noting that in his Fig. 7 the experimental (and indeed also the theoretical traces of the glide planes do not appear to intersect the inner surface at 90°, although the latter is stated to be the generating circle. We have observed a similar discrepancy in some of our experimental curves; the results are, however, rather uncertain in this region.

Gilman[1] has also shown that polygon boundaries are very easily revealed on cleavage surfaces of zinc crystals, and it seems appropriate to report another observation of interest on small-angle boundaries. We have observed that new steps in the "river-patterns" on the cleavage surfaces frequently begin along the line of mosaic boundaries formed during the growth of the crystals. The phenomenon is quite general and is illustrated in Fig. 3, where the conditions have been adjusted to show clearly the relative tilt of the different regions of the cleavage surface. This effect is probably due to a tendency for the cleavage crack to continue moving in the same mean plane, and is consistent with the hypothesis[4, 5] that a crack passing through a screw dislocation becomes stepped. It will be discussed in more detail elsewhere.*

FIG. 3. "River pattern" markings on the cleavage surface of a zinc crystal beginning along the line of a mosaic boundary formed during the growth of the crystal. ×170.

5. ACKNOWLEDGMENTS

One of us (E. S.) wishes to thank the Department of Scientific and Industrial Research for financial support during the period of this research. The other author (B. A. B.) is indebted to the Royal Society for the award of the Sorby Research Fellowship.

6. REFERENCES

1. J. J. GILMAN, *Acta Met.*, **3**, 277 (1955).
2. J. F. NYE, *Acta Met.*, **1**, 153 (1953).
3. B. A. BILBY and R. BULLOUGH, *Phil. Mag.*, **45**, 631 (1954).
4. J. C. FISHER, Reported at the Conference on Mechanical Effects of Dislocations in Crystals, Birmingham 1954.
5. P. L. PRATT, Reported at the Conference on Mechanical Effects of Dislocations in Crystals, Birmingham 1954.
6. B. W. MOTT, *Research*, **8**, 307 (1955).

* It has recently come to our notice that this effect is just discernible in Fig. 2a of a review article.[6] No comment, however, is there made upon it.

VOL. 4 1956

THE EFFECT OF COLD WORK ON LOCAL ORDER*

P. S. RUDMAN† and B. L. AVERBACH‡

The local order in a polycrystalline 85 Cu–15 Au (atomic per cent) alloy has been measured in the annealed and in the severely cold-worked state by an X-ray method. The working was accomplished by abrasion, and it is shown that about 50% of the short-range order is destroyed by severe plastic deformation. This result also leads to the conclusion that slip occurred on about one-third of all the available {111} planes in this instance. An attempt was made to calculate the energy associated with the randomization.

L'EFFET DE L'ÉCROUISSAGE SUR L'ORDRE LOCAL

Dans un alliage polycristallin de composition atomique 85% Cu et 15% Au, l'ordre local a été mesuré par une méthode de rayons X après recuit et écrouissage poussé. L'écruissage a été effectué par abrasion et il est démontré qu'environ 50% de l'ordre à petite distance a été détruit par l'importante déformation plastique. Ce résultat peut aussi conduire à la conclusion que le glissement se produit sur environ un tiers de tous les plans {111} disponibles. Un effort a été fait pour calculer l'énergie associée au passage à l'état désordonné.

DER EINFLUSS EINER KALTBEARBEITUNG AUF DIE NAHORDNUNG

Mit einer Röntgenmethode wurde die Nahordnung in einer Cu-Au-Legierung (85 At. % Cu, 15 At. % Au) im ausgeglühten Zustand und nach einer starken Kaltbearbeitung untersucht. Die Kaltbearbeitung wurde durch Schmirgeln vorgenommen. Es hat sich gezeigt, dass dabei ungefähr 50% der Nahordnung durch starke plastische Verformung zerstört wird. Dieses Ergebnis lässt zudem darauf schliessen, dass im vorliegenden Fall auf etwa einem Drittel aller vorhandenen {111}-Ebenen Gleiten stattgefunden hat. Es wurde versucht, die Energie, die zur Herstellung einer regellosen Verteilung erforderlich ist, zu berechnen.

1. INTRODUCTION

The effects of cold work on solid solutions with long-range order have been known for some time, but there are apparently no direct observations of the effect of cold work on short-range order. Broom[1] has observed that, in general, the increase in electrical resistivity of alloys on plastic deformation is greater than that of pure metals. He cautions, however, against the conclusion that the effect is due to the added disordering of local order in the alloys, because the effect of local order on resistivity is unknown (but probably small) and the effect of cold work on local order is unknown. Aarts and Jarvis[2] have sought to explain their resistivity-deformation results for the alloy AgAu in terms of local-order changes, but Cottrell[3] has given a more probable explanation in terms of the separation of half dislocations. Local order as a strength factor in solid solutions has been treated by Fisher[4], and this concept implies that cold work destroys local order.

2. EXPERIMENTAL RESULTS

Local (short-range) order introduces a modulation of the diffuse X-ray scattering. For a power pattern, this scattering is given in electron units by[5]

$$I = m_A m_B N (f_A - f_B)^2 \left\{ 1 + \sum_{i=1}^{\infty} C_i \alpha_i \frac{\sin Sr_i}{Sr_i} \right\} \qquad (1)$$

where m_A = atomic fraction of A atoms,

N = number of atoms,

f_A = atomic scattering factor of an A atom,

C_i = ith neighbor co-ordination number

$$S = \frac{4\pi \sin \theta}{\lambda},$$

r_i = center-to-center distance between ith neighbors,

α_i = short-range order parameter,

$$= 1 - \frac{P_{AB}{}^i}{m_A m_B C_i N},$$

$P_{AB}{}^i$ = total number of AB bonds for ith neighbors,

$m_A m_B N (f_A - f_B)^2$ = Laue monotonic diffuse scattering from a perfectly random binary solution.

* This work was performed under the sponsorship of the U.S. Atomic Energy Commission under Contract AT(30–1)–1002, and represents a portion of the dissertation presented by P. S. Rudman for the degree of Sc.D. at the Massachusetts Institute of Technology. Received October 10, 1955.

† Present address: Westinghouse Research Laboratory, East Pittsburgh, Pennsylvania.

‡ Department of Metallurgy, Massachusetts Institute of Technology, Cambridge, Massachusetts.

The observed diffuse scattering also includes Compton-modified and temperature-diffuse contributions which must be subtracted before the values of α_i can be determined. However, the *change* in α_i as a result of plastic deformation can be obtained by taking the difference in diffuse scattering (in electron units) between an annealed and a cold-worked sample, since

$$I \text{ (annealed)} - I \text{ (cold-worked)} = \delta I$$

$$= m_A m_B (f_A - f_B)^2 \sum_{i=1}^{\infty} C_i(\delta\alpha_i) \frac{\sin Sr_i}{Sr_i} \quad (2)$$

where: $\delta\alpha_i = \alpha_i$ (annealed) $- \alpha_i$ (cold-worked).
It is also possible to evaluate the short-range order coefficient for each sample directly, using methods already described.[6]

The experimental technique was similar to that used previously,[6] except that Cu$K\alpha$ radiation, obtained with a LiF monochromator plus a Fe-Ni dalanced filter, was used with a recording spectrometer. The sample consisted of a fine-grained polycrystalline slab of 85 Cu–15 Au (atomic per cent) alloy, which was first annealed for ten hours at 250°C. The face of the sample was abraded roughly with emery paper, in order to introduce cold working. Although the cold-worked layer was shallow, the absorption coefficient was sufficiently high so that only the surface layers diffracted. This method of cold work did not seem to introduce any preferred orientation.

Values of α_i and $\delta\alpha_i$ were evaluated by a Fourier transform method.[7] The size-effect coefficients were small and were not evaluated. The diffuse scattering from the annealed and the cold-worked samples is shown in Fig. 1, and Fig. 2 shows a transform of the difference in intensity between the two samples. The area under the peak centered about r_1 is proportional to $\delta\alpha_1$; the higher-order interactions are unresolved because of the difficulty in obtaining data at sufficiently high scattering angles.

The difference transform gave the result: α_1 (annealed) $- \alpha_1$ (cold-worked) $= -0.08$. The direct transform of each sample gave: α_1 (annealed) $= -0.12$, α_1 (cold-worked) -0.06. The average value of $\delta\alpha_1$ was taken as -0.07, and the relative change in short-range order $\delta\alpha_1/\alpha_1 \approx 7/12$. It is evident that the severe plastic deformation has made the solution more random and reduced the local order by about 50%.

3. DISCUSSION

Let us first consider the relationship between $\delta\alpha_1$ and the fraction of slipped planes. Slip of only a few interatomic distances destroys the local order across

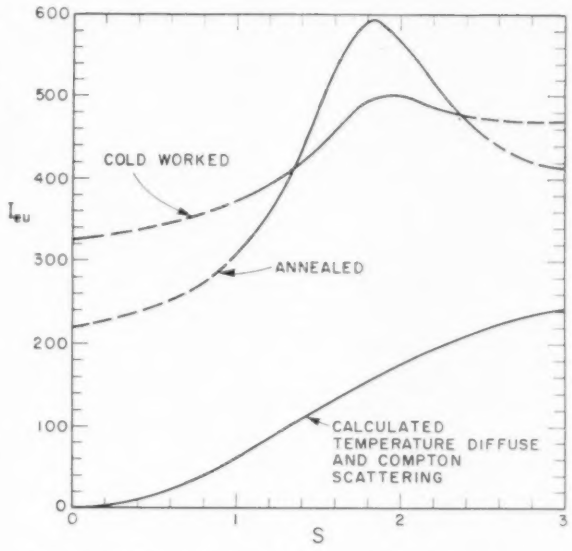

FIG. 1. Diffuse scattering from a 0.85 Cu-0.15 Au alloy in the annealed and cold-worked states.

the slip plane. If it is assumed that only the {111} planes are active, then slip on all of the planes in any two intersecting {111} planes is sufficient to make the solution completely random. Since there are four {111} planes, the fraction of slipped planes, $X = \frac{1}{2}\frac{\delta\alpha_1}{\alpha_1}$. From the data obtained in this work, $X = (1/2)(7/12) \approx 1/3$. That is, slip has occurred on approximately one-third of the possible slip planes in this severely deformed material. It would be difficult to detect such fine slip by metallographic methods.

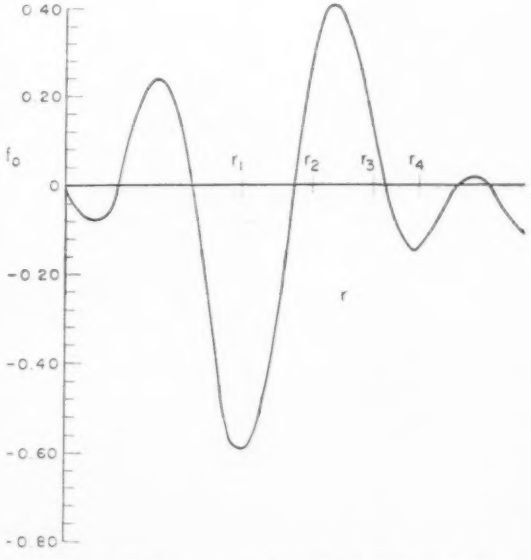

FIG. 2. Difference transform for 0.85 Cu-0.15 Au.

VOL. 4 1956

It is possible to estimate the change in enthalpy associated with the randomization of the alloy, using the quasi-chemical approximation for the heat of mixing. In this theory, the heat of mixing, H^M, is given by $H^M = P_{AB}v$, where $v = E_{AB} - \frac{1}{2}(E_{AA} + E_{BB})$. It is easily shown that the change in relative enthalpy per mol. (δH^M) which occurs as a result of a change in local order is given by

$$\delta H^M = m_A m_B C_1 N_0 v(\delta\alpha_1) \qquad (3)$$

where N_0 = Avogadro's number,

C_1 = number of nearest neighbors.

For example, in the case of the Au-Ag system, the value of $N_0 v$ has been evaluated as -250 cal/mol.[8] Extrapolating the data of Norman and Warren,[9] $\alpha_1 = -0.07$ (for a 62 Au atomic per cent alloy); thus, after severe deformation, $\delta\alpha_1 \approx -0.03$, and $\delta H^M \approx 0.1$ cal/g. The energy stored in filings of such an alloy has been recently measured to be 0.46 cal/g,[10] and it is evident that the energy associated with the randomization of the alloy is not negligible.

ACKNOWLEDGMENTS

The authors are grateful to Mr. David Chipman for his assistance, and to the Atomic Energy Commission for the support of this work.

REFERENCES

1. T. Broom, Lattice Defects and the Electrical Resistivity of Metals, *Phil. Mag.*, **3**, 26 (1954).
2. W. H. Aarts and R. K. Jarvis, The Change in Resistivity on Plastic Deformation of Ag-Cu and Ag-Au Alloys, *Acta Met.*, **2**, 87 (1954).
3. A. H. Cottrell, Interactions of Dislocations and Solute Atoms, *Relation of Properties to Microstructure*, ASM (1954).
4. J. C. Fisher, On the Strength of Solid Solution Alloys, *Acta Met.*, **2**, 9 (1954).
5. B. E. Warren, B. L. Averbach, and B. W. Roberts, Atomic Size Effect in X-ray Scattering by Alloys, *J. Appl. Phys.*, **22**, 1493 (1951).
6. P. S. Rudman and B. L. Averbach, X-ray Measurements of Local Atomic Arrangements in Al-Zn and Al-Ag Solid Solutions, *Acta Met.*, **2**, 576 (1954).
7. P. A. Flinn, B. L. Averbach, and P. S. Rudman, The Interpretation of Diffuse X-ray Scattering from Powder Patterns, *Acta Cryst.*, **7**, 153 (1954).
8. B. L. Averbach, P. A. Flinn, and Morris Cohen, Solid Solution Formation in the Gold-nickel System, *Acta Met.* **2**, 92 (1954).
9. N. Norman and B. E. Warren, X-ray Measurements of Short Range Order in Ag-Au, *J. Appl. Phys.*, **22**, 483 (1951).
10. B. L. Averbach, M. B. Bever, M. F. Comerford, and J. S. Ll. Leach. To be published.

PLASTIC DEFORMATION OF GERMANIUM IN COMPRESSION*

J. R. PATEL† and B. H. ALEXANDER‡

The effect of temperature, orientation, impurity content, and annealing on the compressive stress-strain characteristics of germanium single crystals has been investigated. It may be said that the deformation characteristics resemble in a general way the plastic behavior of face-centered cubic metals. The strain-hardening coefficient decreases very rapidly as the temperature is increased, but does not fall to zero as the melting-point is approached. Prolonged annealing of deformed samples at elevated temperatures does not markedly decrease the density of dislocations as revealed by etch pits. On samples oriented for single slip, double slip occurs from almost the start of deformation; the active slip planes are of the primary and critical type. Dislocations have been shown to lie along slip lines in germanium, and the variation of dislocation density as a function of strain has been established by a direct count of the etch-pit density.

LA DÉFORMATION PLASTIQUE DU GERMANIUM SOUMIS À LA COMPRESSION

Les auteurs étudient l'influence de la température, de l'orientation, de la teneur en impureté et du recuit sur les caractéristiques tension-déformation de monocristaux de germanium déformés plastiquement en compression. On peut dire qu'en général les caractéristiques de cette déformation ressemblent au comportement plastique des métaux cubiques à faces centrées. Le coefficient de consolidation par déformation décroît très rapidement lorsque la température augmente, sans toutefois s'annuler aux environs du point de fusion. Un traitement prolongé à température élevée d'échantillons déformés ne diminue pas sensiblement la densité des dislocations révélées par les piqûres de corrosion. Les échantillons orientés en vue d'un glissement simple se déforment cependant par glissement double quasi dès le début de la déformation; les plans de glissement effectif sont des types primaire et cubique. On a pu montrer que dans le germanium les dislocations se disposent selon les lignes de glissement et la variation de leur densité en fonction du degré de déformation a été établie par dénombrement de la densité des piqûres de corrosion.

PLASTISCHE VERFORMUNG VON GERMANIUM IM DRUCKVERSUCH

Es wurde der Einfluss von Temperatur, Orientierung, Verunreinigungsgehalt und Glühbehandlung auf die Druck-Verfestigungskurven von Germanium-Einkristallen untersucht. Man kann sagen, dass die Verformungs-Erscheinungen in ihren allgemeinen Zügen dem plastischen Verhalten kubisch-flächenzentrierter Metalle ähnlich sind. Der Verfestigungskoeffizient wird mit steigender Temperatur sehr rasch kleiner, sinkt aber bei Annäherung an den Schmelzpunkt nicht bis auf Null. Längeres Tempern verformter Proben bei erhöhten Temperaturen führt nicht zu einer merklichen Abnahme der durch Ätzgrübchen angezeigten Versetzungsdichte. Bei für Einfachgleitung orientierten Proben tritt meist von Beginn der Vorformung an Doppelgleitung auf; die aktiven Gleitebenen sind die primäre und die "kritische" Ebene. Es hat sich gezeigt, dass die Versetzungen entlang von Gleitlinien im Germanium liegen. Die Änderung der Versetzungsdichte als Funktion der Vorformung wurde durch direktes Auszählen der Ätzgrübchendichte festgestellt.

VOL. 4 1956

Little was known about the deformation of crystals with a diamond-cubic lattice until the work of Gallagher[1] and Graf and his co-workers[2] demonstrated the remarkable extent to which germanium and silicon can be plastically deformed at elevated temperatures. Indeed, the extremely brittle behavior of these covalently bonded materials at room temperature provides no indication of their excellent plastic properties at high temperature. Both these elements possess the diamond-cubic type of lattice which can be visualized as two interpenetrating face-centered cubic lattices. It is reasonable, therefore, to expect that the geometry of slip in germanium should resemble that in face-centered cubic metals. It has been determined that plastic deformation in germanium occurs above 400°C by glide on {111} planes.[1] More recently the slip direction has been found to be [110].[3] As in the case of face-centered metals, straight well-developed slip bands can be observed on suitably prepared surfaces of deformed germanium.

Prominent in germanium are two important phenomena, intimately connected with the deformation process, that are not readily observed in most metals where plastic deformation has been widely studied.

1. The ease with which dislocations[4] are revealed

* Received July 1, 1955; revised version November 18, 1955. This work was carried out by the authors at Sylvania Electric Products, Inc., Electronics Division, Ipswich, Mass.

† Now at Raytheon Manufacturing Company, Research Division, Waltham, Mass.

‡ Now at CBS-Hytron, Lowell, Mass.

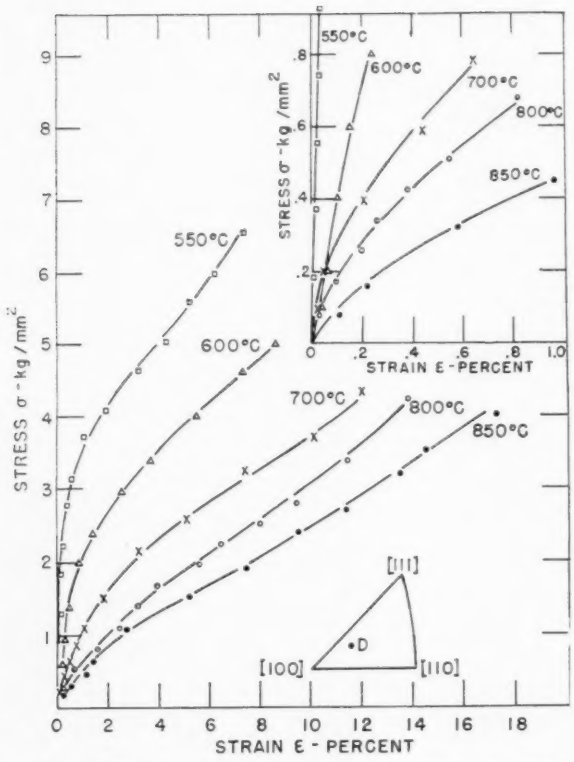

FIG. 1. Stress-strain curves of germanium single crystals in compression as a function of temperature.

on certain crystallographic faces by proper metallographic techniques provides a powerful tool for a study of the deformation process. Combined with the metallographic observations of slip lines, this provides a straightforward visual method of verifying, at least qualitatively, the correctness of dislocation multiplication mechanisms proposed to account for the large amount of slip that occurs on glide planes. One is also able to obtain a correlation between strain and dislocation density by direct visual observation rather than by the indirect means necessary in other systems.[5]

2. Germanium exhibits a pronounced delay-time of plastic flow.[1] This behavior has been found in some body-centered cubic metals, but is of extremely short duration, ranging from milliseconds to a few seconds.[6] The delay-time in germanium, however, has been found to be as large as twenty minutes at 400°C. This very pronounced delay-time and the consequent ease with which observations can be made on this system makes this an ideal material for the study of this little-understood phenomenon at elevated temperatures.

The present study is concerned primarily with the stress-strain characteristics of germanium single crystals in compression, and the effect of such variables as temperature, orientation, impurity content, annealing, and polycrystallinity on the deformation behavior.

EXPERIMENTAL PROCEDURE

High-purity single crystals of germanium were grown by the Czochralski technique and oriented by the Laue back-reflection method in the desired direction. Samples measuring 8.5 mm × 3.5 mm × 3.5 mm were then cut from the oriented bulk crystal. The specimen ends were ground parallel and placed between two refractory cylindrical blocks for compression. The blocks were enclosed in a hollow graphite cylinder. Heating of the graphite was accomplished by a high-frequency induction unit. The temperature was measured by a thermocouple embedded in the graphite cylinder and controlled within ±3°C during the experiments. The whole assembly was enclosed in a vycor tube under an inert atmosphere of argon, and load was applied by a simple lever system. The resulting deformation was read on a dial gage. The apparatus was designed to obtain primarily the plastic stress-strain characteristics of germanium. No attempt was made to determine the elastic portion of the stress-strain curve. The curves were obtained by the load-unload technique, i.e. the specimen was allowed to deform 15 sec after the application of the load and the load removed before the strain was measured. That the dial gage actually recorded the true length-change of the specimen was verified for two specimens by measuring with a micrometer the final length of the specimen at intermediate points; and after the conclusion of the run, both measurements agreed very closely.

For observations of slip bands, the specimens were mechanically polished with No. 600 silicon carbide grit followed by an etch with CP-4*. This yielded surfaces that were not quite flat, but were adequate for observing slip bands.

UNIAXIAL COMPRESSION OF GERMANIUM SINGLE CRYSTALS

Effect of Temperature

The influence of temperature on the stress-strain characteristics of germanium was investigated at a series of temperatures on samples with the same stress-axis orientation. The results of compressive tests at 550°C, 600°C, 700°C, 800°C, and 850°C are plotted in Fig. 1. The inset in Fig. 1 shows the

* 120 cm³ concentrated HF; 200 cm³ concentrated HNO_3; 120 cm³ stock solution (2 cm³ Br in 100 cm³ glacial acetic acid).

initial portions of the curves on a magnified scale. The strain readings were taken after the load was removed; hence, the experimental points even on the linear portions of the curves represent plastic strain only. While the nature of the equipment precluded any precise determination of the yield stress of these crystals, the present data indicates that the yield stress is not sharply defined, at least for this temperature range. The stresses required to cause a plastic strain of 0.01% vary from about 350 g/mm² at 550°C to 75 g/mm² at 800°C.

The stress necessary to continue glide as indicated by the slope of the stress-strain curve is also strongly affected by temperature. Fig. 2 shows the slope of the stress-strain curve at about 5 per cent strain versus the temperature of test relative to the melting-point. A relative temperature scale is used in order to compare the behavior in germanium with that of two other metals—aluminum[7] and molybdenum.[8] For both aluminum and molybdenum the hardening coefficient decreases rapidly at relatively low temperatures and reaches a value essentially zero well before the melting temperature is reached. This behavior is common to most metals, because at high temperatures of test a recovery or annealing process is superimposed on the basic deformation process. The annealing cancels out the hardening due to deformation and causes the material to deform at a constant stress. On the other hand, the strain-hardening coefficient for germanium exhibits very different behavior. The hardening coefficient in this case also decreases rapidly as the temperature rises and seems to depend only slightly on temperature as the melting-point is approached; the values for $d\sigma/d\varepsilon$, however, show no tendency to fall to zero and would, in fact, be higher still if the instantaneous values of stress-strain were recorded. The extreme sharp rise in the strain-hardening curve of germanium at low temperatures indicates that enormously high stresses would be required to continue glide in these crystals at room temperature.

It was mentioned above that the results in Fig. 1 were not obtained as instantanous stress versus strain. In fact, in all cases the specimens were allowed to deform for 15 sec after the application of the load and the strain reading recorded after the load was removed (load-unload technique). To show the effect of time of stressing on the stress-strain characteristics, two runs were made at a constant temperature of 600°C, one where the time of stressing was 7 sec, and the other where the time was 15 sec. The results are plotted in Fig. 3. The general nature of the curves is unchanged, except that the shorter-time curve is

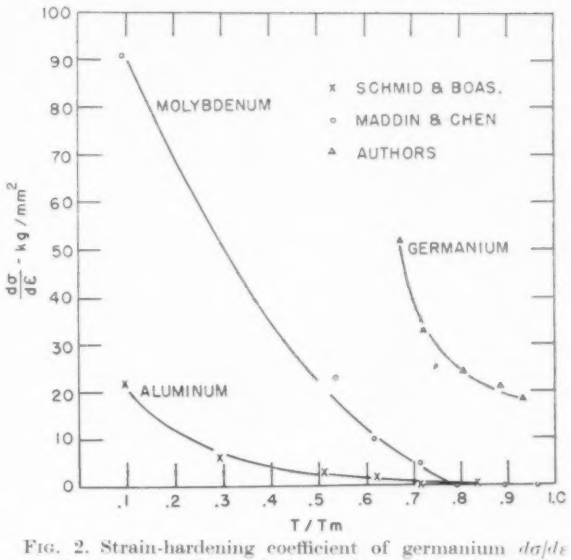

FIG. 2. Strain-hardening coefficient of germanium $d\sigma/d\varepsilon$ versus temperature of test relative to the melting-point T/T_m, as compared to aluminum and molybdenum.

displaced upward and has slightly steeper slope $d\sigma/d\varepsilon = 38$ kg/mm² as compared to $d\sigma/d\varepsilon = 33$ kg/mm² for the longer-time 15-sec curve.

Another factor, that may possibly influence the results in Fig. 1, is the appreciable delay-time of plastic yielding observed in this material.[1] To obtain a quantitative idea of the effect of this phenomena, strain-versus-time experiments were

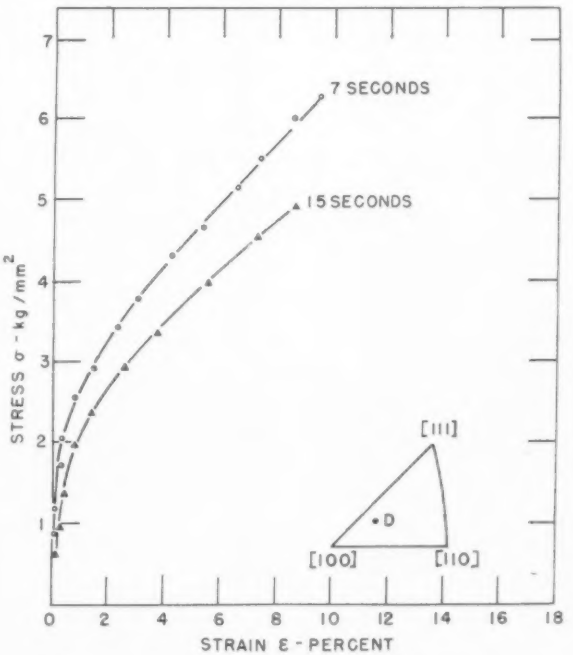

FIG. 3. Influence of time of application of load on the stress-strain characteristics at 600°C.

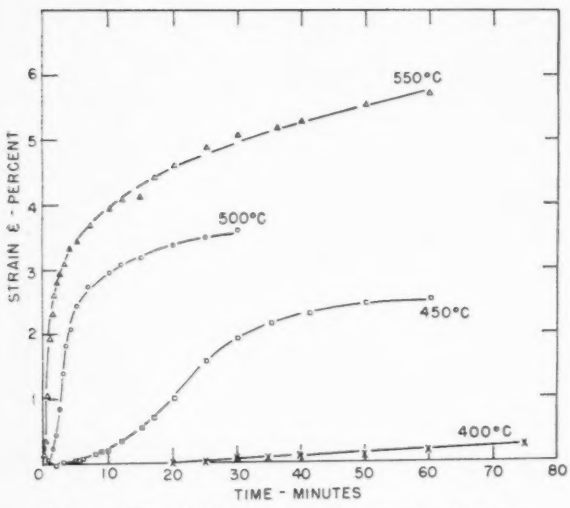

FIG. 4. Percent strain versus time as a function of temperature at a uniaxial compressive stress of 4.3 kg/mm².

made at four different temperatures, 550°C, 500°C, 450°C, and 400°C. In each case a constant load corresponding to an initial stress of 4.3 kg/mm² was applied to the specimens and maintained throughout the run; the resulting deformation was followed as a function of time. Fig. 4 shows the results plotted as strain versus time. While an appreciable time delay of 20 min is observed at 400°C, no delay is observable at 550°C. It is evident then that, at stress levels of 4 kg/mm² and above, the delay effect is negligible on the stress-strain curve at 550°C. Thus, the comparison of the slopes of the curves in Fig. 2 can be considered as valid. It should be mentioned here that these results are somewhat at variance with the delay-times observed by Gallagher[1] on bent samples of germanium. With approximately the same stress level as used in the compression experiments, Gallagher has found an appreciable delay-time of plastic deformation in the temperature range 500°C to 600°C; this difference in temperature at which the phenomena is observed may be due to the different loading conditions.

Influence of Orientation

The stress-strain curves of single crystals oriented in different directions are shown in Fig. 5. In this instance the temperature of test was fixed at 600°C. The [111] orientation strain hardens the most, followed by the [100] and [110] directions. This behavior has also been observed on aluminum[9] and more recently in silver and copper.[10] In all cases, crystals with initial orientations near a [111] or [100] showed a high hardening, whereas a lower hardening was observed in the [110] direction. The initial portions of the curves below about 0.2% strain do not seem to vary appreciably for the different orientations shown in Fig. 5. Above this value the [111] and [100] curves harden appreciably, whereas the [110] and curve *D* harden less rapidly before starting to rise again at about 6 to 8% strain. Since the stress in these specimens was calculated on the original cross-section area, the increase in the slope of the *C* and *D* curves may be attributed to the "barreling" effect or the increase in cross-section area that becomes prominent in these specimens after a strain of approximately 5 to 6%. This results in an apparent higher stress than is actually the case if the true cross-sectional area is used. Samples of orientation *A* and *C* were interrupted at various values of strain for an examination of slip-plane traces on the specimen surfaces. Fig. 6 shows the appearance of slip lines at different strains for: (a) a sample oriented near the [111], and (b) a [110] sample. For strains below 0.2%, one slip system essentially predominates, and there is little difference between the slip patterns for strains less than 0.2%. It is seen, however, that at larger strains the [111] sample shows a definite coarsening of one set

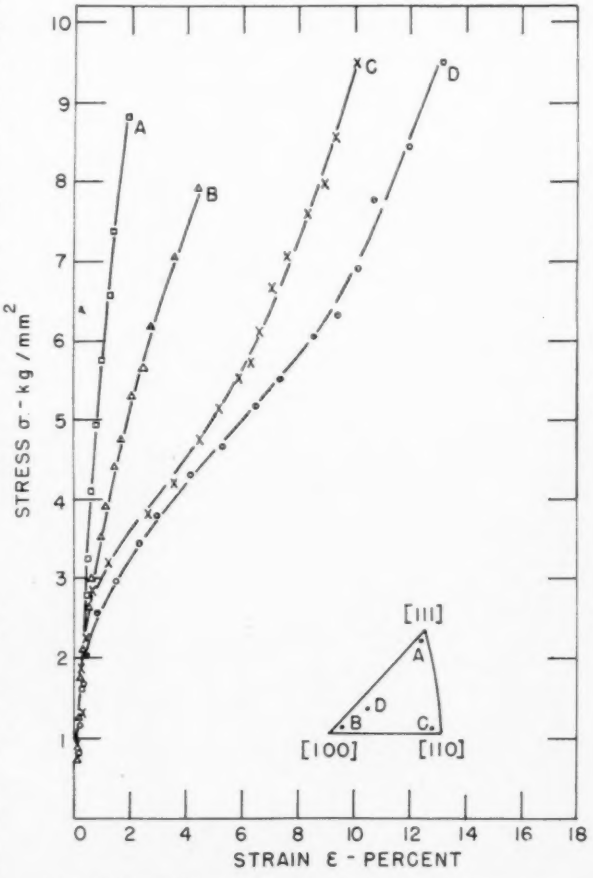

FIG. 5. Orientation dependence of stress-strain curves at constant temperature $T = 600°C$.

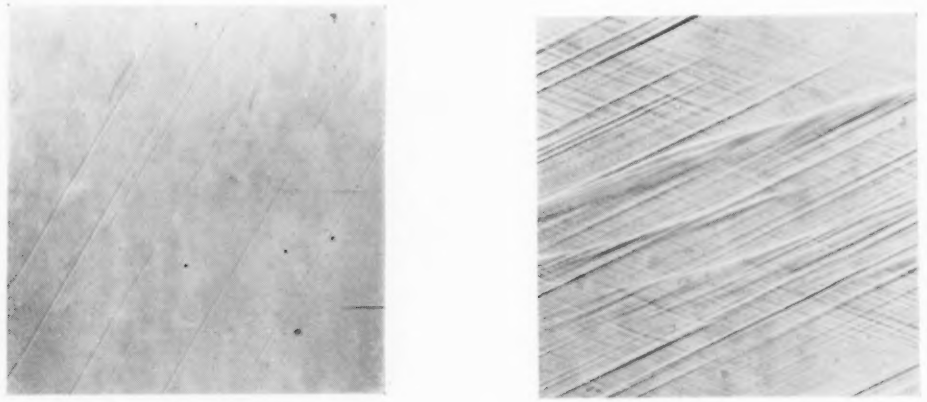

$\varepsilon = 0.06$ per cent

$\varepsilon = 3.2$ per cent

(a)

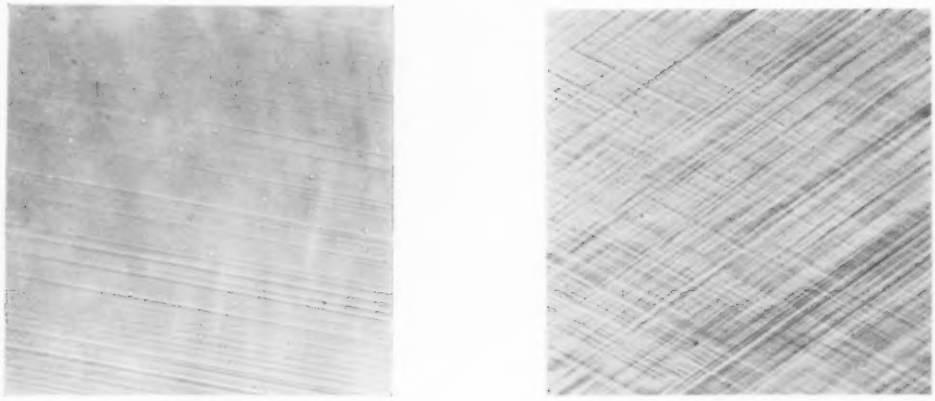

$\varepsilon = 0.22$ per cent

$\varepsilon = 7$ per cent

(b)

FIG. 6. Appearance of slip bands on samples deformed at 600°C; (a) orientation near [111], (b) orientation near [110]. All magnifications, 100×.

of slip bands, whereas in the [110] sample no such coarsening is evident, although slip on the second slip system is very pronounced. This difference in slip-band formation may be related to the different strain-hardening behavior. Coarsening of primary slip bands has also been noticed in copper[10] crystals oriented near the [111].

Microscopic examination of crystals of orientation *A* deformed at 800°C to 14% strain show what appear to be fine kink bands, Fig. 7, of the type observed in single crystals of copper[10] and aluminum.[11] The pronounced "barreling" effect in this sample attests to the constraints imposed by the end refractory plates. As commonly believed, the kink bands may in this case be attributed to relief of lattice bending caused by the inhibiting effect of the end constraints.

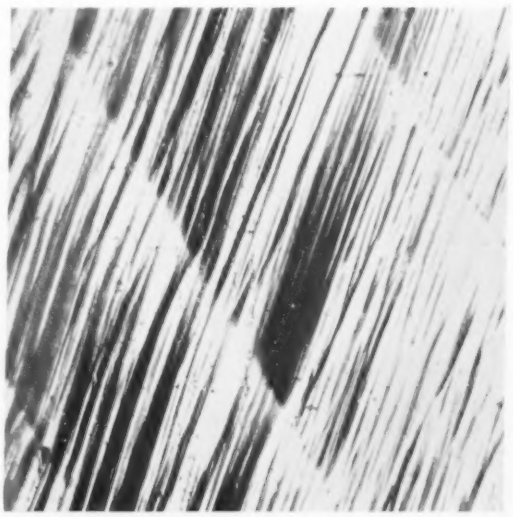

FIG. 7. Sample of orientation *D* showing fine kink bands, deformed 14% at 800°C, 100×.

Compression of Polycrystalline Germanium

Stress-strain experiments were made on a number of polycrystalline samples at a temperature of 600°C.

VOL. 4 1956

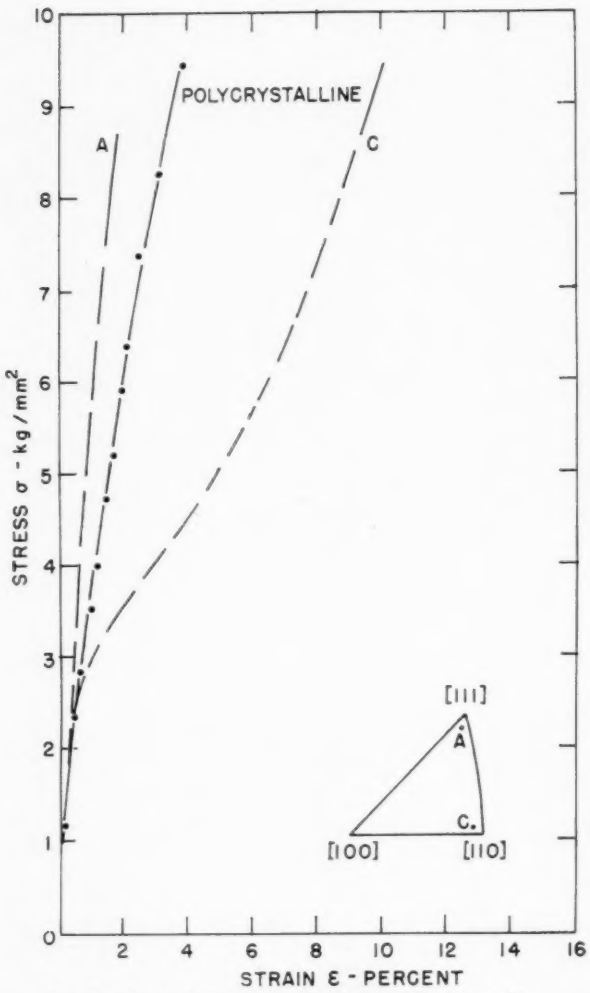

FIG. 8. Stress-strain curve of polycrystalline sample at 600°C.

The results on a sample with an average grain size of 0.15 mm is shown in Fig. 8. The curves for the [111] and [110] single-crystal samples are shown dashed for comparison. An analogous behavior is observed in polycrystalline cubic metals,[12] where the stress-strain curve in tension is observed to lie between the extreme tensile curves of single crystals of different orientations. The appearance of slip lines in different grains and across a twin boundary is shown in Fig. 9. It is evident from the slip pattern that certain favorably oriented grains have been deformed more extensively than others. The slip lines are discontinuous at grain boundaries, but are continuous though deflected at a twin boundary.

Effect of Annealing

The course of annealing was followed by a metallographic examination of the etch pattern of dislocations on {111} faces of deformed samples. For a sample deformed at 600°C to 1.5% strain, a metallographic examination after deformation and also after a subsequent anneal at 800°C for 30 min showed practically identical patterns of etch pits with perhaps a very slight decrease in the dislocation density of the annealed specimen. Similar observations on a sample deformed at 800°C yielded about the same results. From the metallographic evidence it is reasonable to conclude that any softening as manifested by a decrease in dislocation density does not occur to any significant extent in germanium during stress-strain experiments at elevated temperatures. While the reduction in the total number of dislocations is negligible and contributes little to the thermal softening process, any dispersion of piled-up groups of dislocations formed during the deformation process will lower the mean internal stress and contribute to softening. According to Mott,[13] it is the large stress field around the piled-up groups that are responsible for strain-hardening. Dispersal of these packed groups is achieved by a process that involves "climb" or the motion of dislocations out of their slip planes. Since this process occurs by the diffusion of vacancies or interstitial atoms to dislocations, it will occur only at temperatures where these can diffuse readily. The extremely low self-diffusion coefficient of germanium[14] makes this annealing process very slow when compared to metals. Vogel,[15] however, has found that polygonization seems to occur when samples are deformed in bending at high temperatures.

Prolonged heating at temperatures approaching the melting-point of germanium produces some noticeable

FIG. 9. Appearance of slip lines on polycrystalline germanium, 100×.

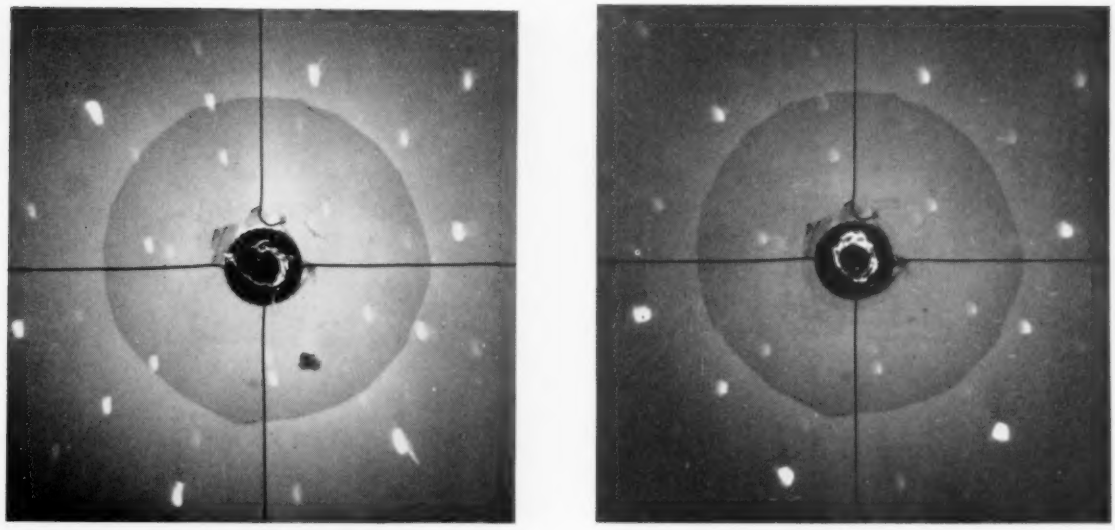

(a) (b)

FIG. 10. X-ray photograms (a) after deformation at 600°C and (b) annealed at 900°C for 16 h.

effects. A specimen deformed at 600°C to about 1.5% strain was heated in a vacuum for sixteen hours at 900°C. Metallographic examination of the specimen revealed that straight rows of etch pits that fell along slip lines in the deformed sample tended to break up and to become curved after annealing. The density of etch pits after annealing also decreased by about a factor of 5. The back-reflection Laue pattern after deformation shows asterism, Fig. 10, whereas for the X-ray pattern after annealing the asterism is markedly decreased.

Effects of Impurities

A single crystal of germanium was drawn from a melt of zone-purified germanium. During the growing process the pulling was interrupted to introduce an impurity, in this case antimony, into the melt, and the pulling operation was resumed. Specimens of the same orientation were cut from the undoped and doped portions of the crystal. Antimony is a donor-type impurity in germanium, and its concentration may be measured by suitable electrical measurements. Electrical resistivity and Hall measurements revealed that the undoped portion was 40 ohm cm n-type, corresponding to an impurity concentration of 1 part in 10^9 (10^{-7}%), while the doped region was 0.06 ohm cm n-type, with an impurity concentration of 1.4 parts in 10^7 (1.4×10^{-4}%). Stress-strain experiments on both samples at 550°C showed no effect of impurity addition on the behavior of the stress-straincurve.

DETERMINATION OF SLIP PLANES

The orientations of the samples for which slip planes were determined are shown in Fig. 11. Orientation D is the same as that of the specimens for which the stress-strain curves were determined as a function of temperature (Fig. 1). This particular orientation was chosen since it lies well within a region favoring single slip. It is noticed, however, in the early stages of the deformation process, that extensive double slip had occurred well before the specimen axis had rotated into a position favoring double slip.

The active slip planes were determined by plotting the traces of slip planes observed on two orthogonal faces on a stereographic net. In both cases the slip planes were found to be (in conventional terminology) of the primary and critical type (Fig. 11). While premature cross and conjugate slip is observed widely in

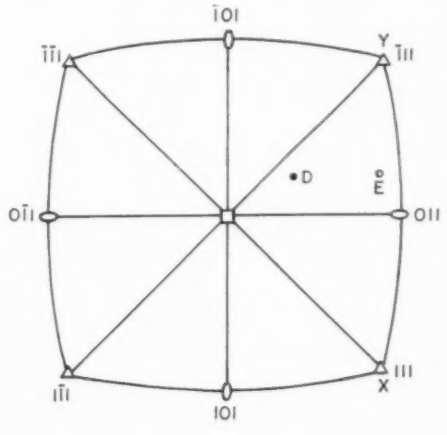

FIG. 11. Stereographic projection showing the planes on which slip occurs for sample of orientation D and E.

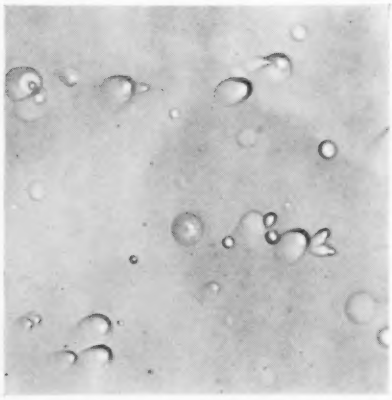

(a)

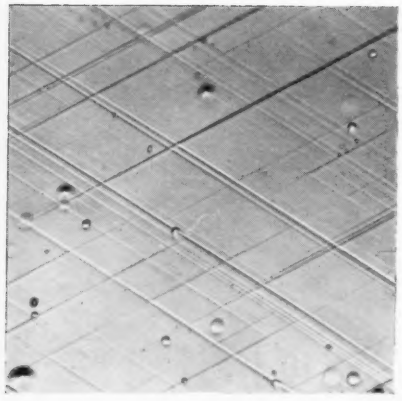

(b)

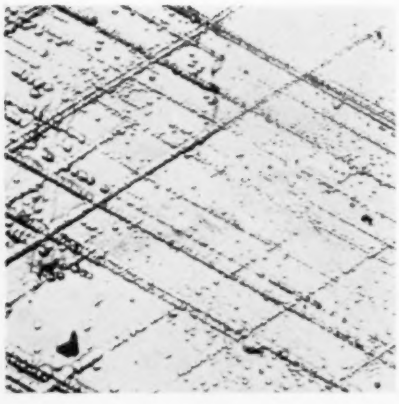

(c)

FIG. 12. Appearance of etch pits at slip lines on {111} face of germanium deformed 0.5% at 600°C, (a) before deformation, $\rho = 5 \times 10^3/cm^2$, (b) appearance of slip bands after deformation at 600°C, (c) etched to reveal dislocations $\rho = 1.6 \times 10^6/cm^2$; all magnifications 100×.

metal crystals under normal test conditions, slip on the critical plane is observed only when the specimen axis is initially in the position of symmetry or has rotated into the symmetry position. Rotation of the axis for these specimens was not sufficient to cause them to assume the symmetry position. It is possible that the geometrical shape of the specimens might result in a larger resolved shear stress on the critical plane than on the primary slip plane. For a sample of orientation *D* (Fig. 11), resolved shear stresses on the primary and critical plane have been analyzed. It was found that the resolved shear stress on the primary slip plane is larger than that on the critical by about the same factor as for a cylindrical specimen.

DISLOCATIONS AT SLIP LINES IN GERMANIUM

The large amount of slip that occurs on active slip bands requires the passage of dislocations in numbers many times larger than are normally present in well-annealed crystals. To account for this, Frank and Read[16] have suggested a mechanism for the multiplication of dislocations during plastic flow. That dislocations indeed multiply during the deformation process is shown in qualitative manner by the photographs in Fig. 12. Fig. 12(a) shows a {111} surface of a germanium specimen ground and etched in CP-4. The dark pits on the surface have been shown to be due to dislocations whose singular lines extend into the body of the crystal. The dislocation density as revealed by counting is $5.2 \times 10^3/cm^2$. Fig. 12(b) shows the same surface after the specimen was deformed to a strain of 0.5% at 550°C. It is noticed that there is extensive slip on two slip systems. Fig. 12(c) shows the same deformed surface after further etching in CP-4. The pattern of the etch pits follows the same pattern as the slip lines in Fig. 12(b), the density as revealed by counting at higher magnification being $1.6 \times 10^6/cm^2$. It is seen that etch pits fall along the slip markings. In view of the original low density of etch pits, this is certainly indication of the operation of a multiplication mechanism or source. Examination at higher magnification reveals that at this level of strain, 0.5%, the regions between the straight rows of etch pits are virtually undeformed, although some scattered etch pits that were not present originally are to be found in some of these areas. With increasing deformation, however, these regions become clustered with etch pits, and it is impossible to detect any of the regular lineage pattern that is evident at low values of strain. An example of this can be seen in Fig. 13(d), where a sample has been

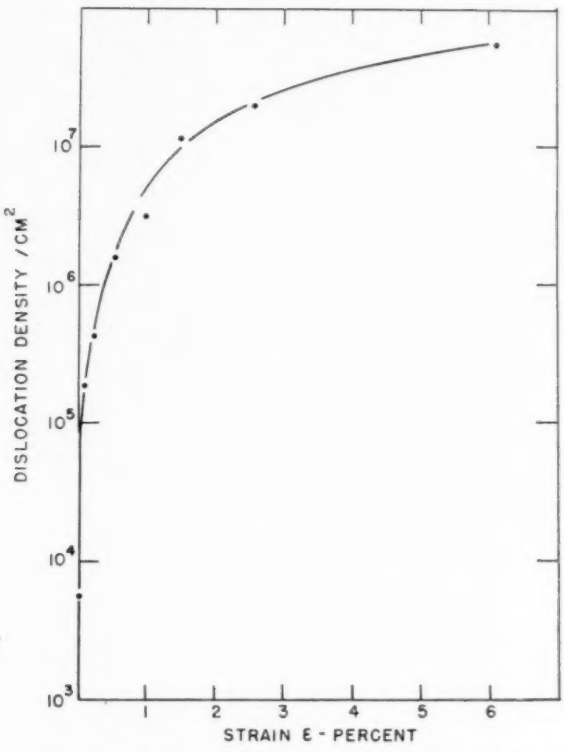

FIG. 14. Dislocation density ρ as a function of strain.

Fig. 11, were cut from a single crystal so that {111} faces formed two parallel longitudinal sides of the specimen. The density of dislocations in the as-grown condition as revealed by counting etch pits was about $6 \times 10^3/\text{cm}^2$. The samples were compressed to strains varying from 0.1% to 6% strain at 600°C. The {111} faces of the specimens were then ground and etched in CP-4. The appearance of the etch pits for strains of 0.09, 0.96, 2.5, and 6.1 % is shown in Fig. 13. Except for the sample deformed 6%, counting of the etch pits was relatively easy. Fig. 14 shows the plot of dislocation density (ρ) as a function of strain. Some uncertainty is introduced in the data around 6% strain because of the difficulty of resolving individual etch pits after heavy deformation. The density increases relatively rapidly at small strains; with 1% strain the density has increased by approximately three orders of magnitude from 5×10^3 to 2×10^6.

If the change in dislocation density with strain $d\rho/d\varepsilon$ is plotted as a function of strain, Fig. 15, it is seen that a maximum occurs between 2 to 3% strain, after which $d\rho/d\varepsilon$ decreases and seems to flatten out at higher strains. Fig. 15 would seem to indicate that two competing processes operate, one involving the generation of dislocations within the crystal, and the other the migration of dislocations out of the crystal. For equal increments of strain, the number of dislocations passing out of the crystal should be the same. It is reasonable to expect that relatively few sources are available early in the deformation process, and that most of the dislocations generated from these pass out of the crystal to give the observed strain. Consequently, the number of dislocations trapped in the crystal is relatively small. As deformation proceeds and more sources become active, many more dislocations are generated than leave the crystal. Finally, at higher strains, back-stresses set up by the dislocations and the obstruction offered by other dislocations will tend to neutralize the sources and thus slow down the generation of dislocations.

CONCLUSIONS

1. In compressing germanium single crystals at high temperature, the strain-hardening coefficient decreases very rapidly as the temperature is increased, but does not tend to zero as the melting-point is approached. The extremely sharp rise in the strain-hardening curve of germanium at lower temperatures indicates that enormously high stresses would be required to initiate glide in these crystals at room temperature, and most likely fracture would occur first.

2. The orientation-dependence of the stress-strain curves is similar to that observed for metals. The [111] orientation hardens the most, followed by the [100] and [110] orientations.

3. For polycrystalline germanium, the stress-strain curve is observed to lie between the extreme compression curves of single crystals of different

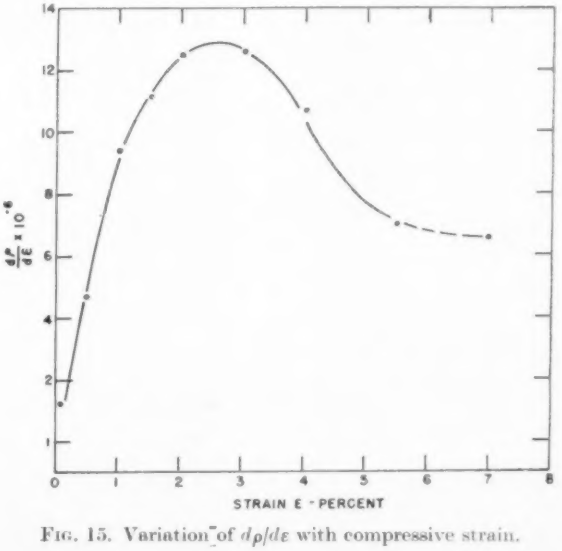

FIG. 15. Variation of $d\rho/d\varepsilon$ with compressive strain.

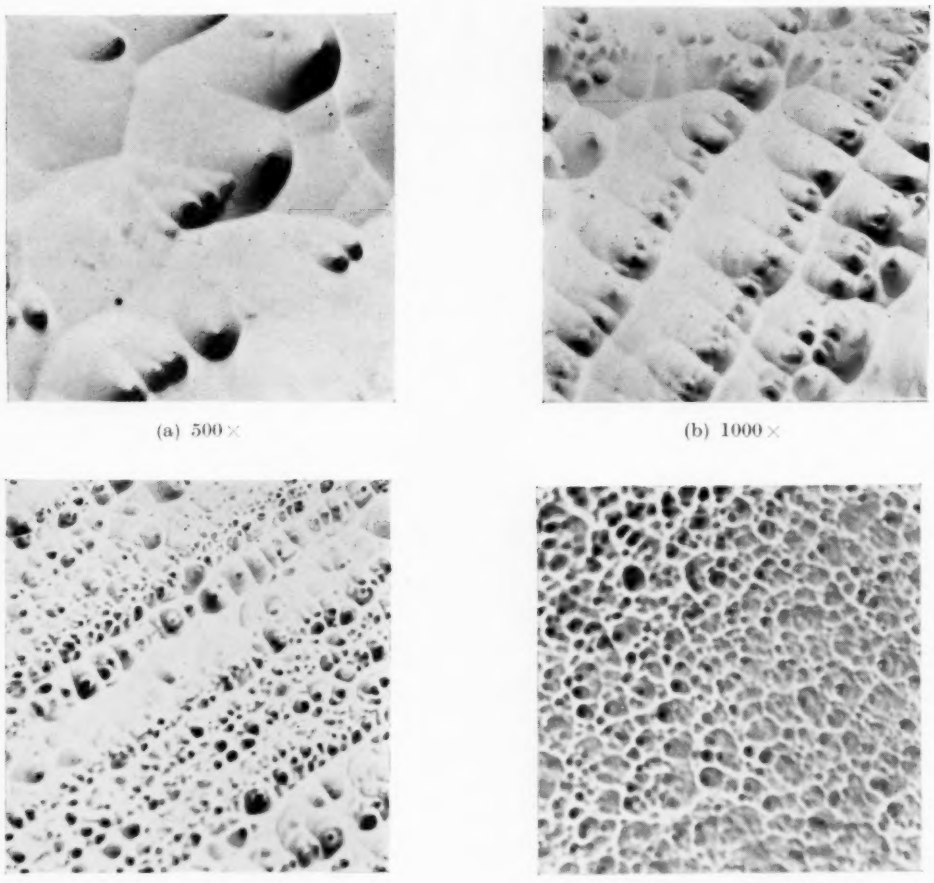

(a) 500× (b) 1000×

(c) 1000× (d) 2000×

FIG. 13. Appearance of etch pits at dislocations at various strains; (a) $\varepsilon = 0.09\%$, 500×, (b) $\varepsilon = 0.98\%$, 1000×, (c) $\varepsilon = 2.55\%$, 1000×, and (d) $\varepsilon = 6.1\%$, 2000×.

deformed to 6% strain and photographed at a magnification of 2000×.

The number of dislocations n that can be packed into a slip plane of length L can be estimated by a consideration of the back stresses from generated dislocations necessary to neutralize a source activated by an applied shear stress τ. Using a general method developed by Eshelby, Frank, and Nabarro,[17] Cottrell[18] has shown that

$$n = \pi L \tau K / Gb \qquad (1)$$

where K is a constant close to unity, G the shear modulus is 4×10^{11} dynes/cm^2, b is Burger's vector, and τ is the applied shear stress, in this case 2.3 kg/mm^2, acting on the primary slip plane. From the above, $n = 6 \times 10^4$ lines/cm. Counting the etch pits along the slip lines shows an average value $n = 2.5 \times 10^3$ lines/cm. On the other hand, in heavily cold-worked cubic metals, the number of trapped dislocations[19] per centimeter of the slip plane is about 10^6. The observed value of linear density is consistent with the density of 1.6×10^6/cm^2, obtained by counting on an area, but is an order of magnitude lower than the predicted value. Since, in this specimen, slip has not been confined to a single system, the estimate from equation (1) may be in error. However, a general observation that can be made on dislocation densities obtained by direct counting is that they are a good deal lower than the present theoretical estimates for most metals. Recent X-ray[20] evidence also shows that the observed dislocation density of heavily worked metals is generally less than the accepted value of 10^{12}/cm^2; the estimate for annealed metals was also found to be less than the usually accepted value of 10^8/cm^2.

VARIATION OF DISLOCATION DENSITY WITH APPLIED STRAIN

To determine dislocation density as a function of strain, identically oriented samples of orientation E,

orientation. The same behavior is observed in tension in polycrystalline cubic metals.

4. Annealing a previously compressed sample for 30 min at 800°C shows a very slight decrease in dislocation density. On heating for much longer times and at a higher temperature (16 h at 900°C), more significant changes are observed. The density of dislocations decreases by a factor of 5 and the straight rows of etch pits that fall along slip lines become curved after annealing.

5. Increasing the impurity concentration by a factor of 700 over an initial impurity content of $1 \times 10^{-7}\%$ does not seem to affect the stress-strain behavior at elevated temperature.

6. For orientations near the [100]–[111] and [111]–[110] boundaries, slip takes place on planes of the primary and critical type from almost the beginning of deformation, even through the specimens are oriented in a region favoring single slip.

7. Dislocations have been shown to lie along slip lines in germanium. The linear dislocation density obtained by counting etch pits along a slip line has been shown to be an order of magnitude lower than the calculated value.

8. Dislocation density has been determined as a function of strain by direct visual examination. Initially, the density ρ increases by three orders of magnitude from $5 \times 10^3/\text{cm}^2$ to $2 \times 10^6/\text{cm}^2$ for a strain of 1%. A plot of $d\rho/d\varepsilon$ versus ε shows that $d\rho/d\varepsilon$ passes through a maximum between 2 to 3% strain.

VOL. 4 1956

ACKNOWLEDGMENTS

The authors are indebted to R. Yannoulos for effective aid in the various experimental phases of this work, and to C. C. Wang of Sylvania and S. A. Kulin of the Lincoln Laboratories for helpful discussion of the results. This work was sponsored by the Electronics Division, Sylvania Electric Products, Inc.

REFERENCES

1. C. J. Gallagher, *Phys. Rev.*, **88,** 721 (1952).
2. L. Graf, H. R. LaCour, and K. Seiler, *Z. Metallkunde*, **44,** 113 (1953).
3. E. S. Greiner, *Trans. Amer. Inst. Min. Met. Eng.*, **203,** 203 (1955).
4. F. L. Vogel, W. G. Pfann, H. E. Corey, and E. E. Thomas, *Phys. Rev.*, **90,** 489 (1953).
5. A. H. Cottrell and A. T. Churchman, *J. Iron and Steel Institute*, **162,** 271 (1949).
6. D. S. Wood and D. S. Clark, *Trans. Amer. Soc. Met. Eng.*, **43,** 571 (1951).
7. E. Schmid and W. Boas, *Plasticity of Crystals*, p. 156.
8. R. Maddin and N. K. Chen, *Trans. Amer. Inst. Min. Met. Eng.*, **200,** 280 (1954).
9. N. K. Chen and C. H. Mathewson, *Trans. Amer. Inst. Min. Met. Eng.*, **191,** 653 (1951).
10. F. D. Rosi, *Trans. Amer. Inst. Min. Met. Eng.*, **200,** 1009 (1954).
11. R. W. K. Honeycombe, *J. Inst. Metals*, **80,** 45 (1951).
12. E. Schmid, *Phys. Z.*, **31,** 892 (1930).
13. N. F. Mott, *Proc. Roy. Soc.*, **A220,** 10 (1953).
14. W. M. Portnoy, H. Letaw, jr., and L. Slifkin, *Bul. Amer. Phys. Soc.*, **30,** No. 2, 13 (1955).
15. F. L. Vogel, *Acta Met.*, **3,** 95 (1955).
16. F. C. Frank and W. T. Read, *Phys. Rev.*, **79,** 722 (1950).
17. J. D. Eshelby, F. C. Frank, and F. R. N. Nabarro, *Phil. Mag.*, **42,** 351 (1951).
18. A. H. Cottrell, *Dislocations and Plastic Flow in Crystals*, p. 107.
19. A. F. Brown, *Advances in Physics*, **1,** No. 4, p. 472 (1952).
20. P. Gay, P. B. Hirsch, and A. Kelley, *Acta Met.*, **1,** 315 (1952).

THERMODYNAMICS OF IRON-CARBON MELTS*

E. T. TURKDOGAN, L. E. LEAKE,† and C. R. MASSON‡

Iron-carbon melts over the range from medium carbon content to saturation, have been equilibrated with methane-hydrogen mixtures at 1300°, 1400°, and 1500°C. The free energy of formation of methane determined is in agreement with existing data. The value of $\Delta\bar{H}_C$ over the entire composition range was estimated to be about 4400 cal/mole. The relationship between the activity coefficient and the atom fraction of carbon does not obey a particular solution law; the plot of a_C against N_C, however, gives a simple curve which is practically linear from about $N_C = 0.12$ to saturation. Choosing an infinitely dilute solution as the standard state, i.e. $\gamma'_C \to 1.0$ when $N_C \to 0$, the variation of the activity coefficient of carbon with concentration may be expressed as $\log \gamma'_C = 5.0 N_C$ when $N_C < 0.045$, and the free energy of solution of graphite in iron has been found to be $\Delta G^\circ = 4400 - 3.49T$ cal/g atom. An attempt has been made to calculate the effect of carbon on the activity coefficient of oxygen dissolved in molten iron from 0 to 5.0% carbon.

THERMODYNAMIQUE DES BAINS FONDUS Fe–C

Des bains fondus Fe–C avec des teneurs en C allant de valeurs moyennes à la saturation, ont été mis en équilibre avec des mélanges méthane-hydrogène à 1300°, 1400° et 1500°C. L'énergie libre de formation du méthane a été trouvée en accord avec les données connues. La valeur $\Delta\bar{H}_C$ dans le domaine de teneurs utilisées, a été estimée à environ 4.400 cal/mole. La relation entre le coefficient d'activité et la teneur en atomes de carbone n'obéit pas à une loi particulière; le diagramme de a_C en fonction de N_C donne une courbe simple qui est pratiquement linéaire de $N_C = 0{,}12$ environ jusqu'à la saturation. Si l'on choisit comme état de référence une solution infiniment diluée, c.à.d. $\gamma'_C \to 1.0$ pour $N_C \to 0$ la variation du coefficient d'activité du carbone avec la concentration peut s'exprimer: $\log \gamma'_C = 50 N_C$ pour $N_C < 0.045$, et l'énergie libre de dissolution du graphite dans le fer a été trouvée égalè à $\Delta G^\circ = 4.400 - 3.49T$ cal/atome gramme. On a tenté de calculer l'action du carbone sur le coefficient d'activité de l'oxygène dissous dans du fer fondu pour des teneurs allant de 0 à 5% de carbone.

THERMODYNAMIK VON EISEN-KOHLENSTOFF-SCHMELZEN

Eisen-Kohlenstoff-Schmelzen im Bereich zwischen mittlerem Kohlenstoffgehalt und der Sättigung wurden bei 1300°, 1400° und 1500°C mit Methan-Wasserstoff-Mischungen ins Gleichgewicht gebracht. Die freie Bildungsenergie von Methan, die bestimmt wurde, ist in Übereinstimmung mit vorliegenden Daten. Der Wert für $\Delta\bar{H}_C$ im gesamten Konzentrationsbereich wurde auf etwa 4400 cal/Mol geschätzt. Die Beziehung zwischen dem Aktivitätskoeffizienten und der Atomkonzentration des Kohlenstoffs gehorcht keinem spetiellen Lösungs-Gesetz; im Diagramm ergibt sich jedoch für a'_C in Abhängigkeit von N_C eine einfache Kurve, die von etwa $N_C = 0{,}12$ bis zur Sättigung praktisch linear ist. Wählt man als Normalzustand eine unendlich verdünnte Lösung, d.h. $\gamma'_C \to 1{,}0$ für $N_C \to 0$, so kann die Änderung des Aktivitätskoeffizienten von Kohlenstoff mit der Konzentration für $N_C < 0{,}045$ ausgedrückt werden durch $\log \gamma'_C = 5{,}0 N_C$; die freie Lösungsenergie von Graphit in Eisen wurde zu $\Delta G^\circ = 4400 - 3{,}49T$ cal/g-Atom bestimmt. Es wurde versucht, den Einfluss von Kohlenstoff auf den Aktivitätskoeffizienten von in geschmolzenem Eisen gelöstem Sauerstoff zwischen 0 und 5,0% Kohlenstoff zu berechnen.

1. INTRODUCTION

The iron-carbon binary alloys form one of the systems of importance in ferrous metallurgy. During recent years some interest has been given to the thermodynamic properties of these alloys. The activity of carbon in molten iron was first investigated by Marshall and Chipman.[1] Later an attempt was made by Chipman[2] to calculate carbon activity at medium- and high-carbon concentrations by assuming the validity of the approximate solution law proposed by Darken and Smith[3] for γ-iron-carbon alloys up to about 1.5% carbon. Temkin and Shvartsman[4] suggested that, because the number of sites available for carbon atoms in iron-carbon binary melts is one-fourth the number of iron atoms, the activity coefficient of carbon is given by

$$\gamma_C = \frac{1}{1 - 5N_C} \qquad (1)$$

where γ_C and N_C are the activity coefficient and the atom fraction of carbon. There is, however, no justification for this very simple relationship between γ_C and N_C. Darken and Gurry[5] assumed that log γ_C was directly proportional to $(1 - N_C)^2$; after evaluating the proportionality factor from the only

* Received May 31, 1955; revised version November 16, 1955.

† The British Iron and Steel Research Association, 140 Battersea Park Road, London, S.W.11, England.

‡ Present address: National Research Council of Canada, Halifax, N.S.

available data (on one or two points in the iron-carbon system), they were able to calculate the activity of iron and carbon for any temperature and composition.

The most reliable data so far available on the thermodynamics of iron-carbon binary melts are those presented by Richardson and Dennis,[6] who equilibrated iron-carbon melts with carbon monoxide-carbon dioxide mixtures at 1560°, 1660°, and 1760°C. These authors found that the relative partial molal heat of solution of graphite in molten iron was 6400 cal/mole, and independent of temperature and composition when $N_C < 0.025$. They were also able to calculate the partial molal entropy of solution of carbon for the composition range 0.01–0.025 N_C.

Sanbongi and Ohtani[7] have recently measured, in a high-temperature concentration cell, the electromotive force between two iron-carbon melts acting as electrodes in contact with a carbide slag electrolyte. Their results, although not consistent amongst themselves, provide the only data on the activity of carbon at medium and high concentrations.

It is clear from the foregoing brief review that a number of speculations have in the past been made to calculate certain thermodynamic properties of iron-carbon melts. It was therefore decided to measure directly the activity of carbon from medium concentrations up to saturation at various temperatures.

VOL. 4 1956

2. EXPERIMENTAL

2.1. *General*

The experimental scheme was essentially that of equilibrating methane-hydrogen mixtures with iron-carbon melts, measuring the concentration of methane in the gas phase, quenching the melt, and analyzing for carbon. The apparatus was virtually a closed system in which a solenoid-operated glass pump[8] continuously circulated the gas mixture through a horizontally disposed tube furnace.

An infra-red gas concentration recorder, adapted for methane, was connected in circuit with the pump and furnace system. This recorder proved to be sufficiently accurate to eliminate entirely the need for manual analysis of the gas system, and provided a convenient means of checking the progress of each experiment; establishment of equilibrium was readily identified by a constant reading of methane concentration.

On leaving the furnace system, the gas stream entered an ice-trap surrounded by solid carbon dioxide contained in a Dewar flask.

To compensate for possible changes of gas pressure occurring within the equilibrium apparatus, the circulating gas stream was isolated from the hydrogen supply line by a pressure-compensating device consisting of an arrangement of "blow-off" valves containing di-butyl phthalate. With this device the total gas pressure in the reaction chamber was maintained at a level slightly above atmospheric pressure.

The gas-flow rate in the circulating system was measured with a capillary flowmeter in series with the circulating pump. This pump was provided with a variable speed control so that the rate of circulations could be adjusted to any desired value.

2.2. *Furnace System and Temperature Control*

A platinum-wound resistance furnace, equipped with a recrystallized, impermeable alumina reaction tube, 2-in. diameter, was employed. Electrical power to the furnace was controlled by a variable autotransformer coupled to a stabilized voltage source.

At a given setting of the autotransformer, the temperature of the furnace could be maintained constant to within ±5°C of the required value, measurements being taken with a platinum/13% rhodium-platinum thermocouple.

The lime crucibles, in which the melts were held, were fashioned from cylindrical blocks by drilling a central ½-in.-diam. hole. The blocks were prepared by compressing slightly moistened powdered analytical reagent-grade calcium carbonate in a suitable mold. They were then dried and fired to 1600°C. The crucibles, which were externally ¾ in. in diameter and height, were carried on alumina boats which rested upon two alumina tubes, each ¼ in. in diameter, lying side by side along the bottom of the reaction tube. This arrangement served to protect the reaction tube against possible thermal strains on introducing the cold charge and facilitated the rapid withdrawal of the melt prior to quenching.

In the experiments where furnace temperatures above 1400°C were involved, the alumina boats were lined with a thick layer of pure zirconium-oxide powder in which the lime crucibles were embedded; direct contact between lime and alumina being impracticable at such temperatures.

2.3. *Procedure*

The furnace was adjusted to the required temperature, and the entire system flushed with pure dried argon. An iron-carbon charge, of pre-adjusted composition and approximately 5 g in weight, was slowly introduced into the hot zone of the reaction tube. The charge was allowed to melt and remain in argon for about one hour; this was considered a

reasonable period of time for the melt to attain homogeneity.

The flow of argon was then stopped, and purified and dried hydrogen was flushed through the apparatus. The hydrogen flow was then directed to the pressure-compensating bubblers, the circulating system checked for continuity, and the circulating pump set in motion. Throughout all the experiments, the rate of gas circulation was maintained as closely as possible at 250 cm^3/min.

Equilibrium between the gas phase and the melt was considered to be established when the methane reading traced on the recorder chart levelled out to a constant value. The time taken to reach state of equilibrium depended upon the experimental conditions, and varied from four to ten hours. An additional period of two hours was allowed to elapse, to check the constancy of the methane concentration.

The circulating pump was then stopped and the reaction chamber flushed with argon. Finally, the melt was withdrawn rapidly, dropped into a vessel of water, and analyzed for carbon.

2.4. *Materials*

Iron-carbon mixtures of the required composition were obtained by additions of electrolytic-pure iron powder to a master alloy prepared from B.I.S.R.A. AG iron and spectrographically pure graphite. The carbon content of the master alloy was 5.37%, and the impurities present were 0.01% S, 0.001% P, 0.002% Si, 0.005% Mn, 0.01% Ni, 0.006% Cu, 0.001% Cr, and 0.001% Al.

2.5. *Gas Analysis*

The methane/hydrogen ratio was measured with an infra-red gas concentration recorder (Infra Red Development Co. Ltd.). The instrument was calibrated against a prepared gas mixture of known methane content. Reproducibility was found to be accurate within 1% of the true value.

2.6. *Carbon Analysis*

Carbon determinations were carried out by the combustion method, agreement between duplicates being within $\pm 0.02\%$.

3. RESULTS

3.1. *Side Reactions*

Calculations based on the thermodynamic data on the free energies of formation of alumina[9] and aluminum carbide[10] indicated that if the water-vapor partial pressure in the system were that of ice at liquid-oxygen temperature, about 10^{-20} atm of methane (the remainder of the gas being hydrogen) would be sufficient to form aluminum carbide from alumina at high temperatures. On the other hand, if the partial pressure of water vapor in the reaction chamber was adjusted to that of ice at 0°C or above, oxidation of methane took place. Calculations and a few experiments showed that an ice trap kept at the temperature of solid carbon dioxide gave the optimum water-vapor pressure which prevented the reduction of alumina, and consequently, the formation of aluminum carbide, and yet was too low to oxidize the small percentage of methane.

3.2. *Establishment of Equilibrium*

In all experiments, the state of equilibrium between the melt and the gas phase was approached from zero methane level by the method described. As indicated by the methane recording charts for melts C7 and C9, given in Figs. 1a and 1b, the establishment of equilibrium could easily be estimated.

3.3. *Free Energy of Formation of Methane*

The free energy of formation of methane is known quite accurately up to 1300°K,[11] and, as pointed out by Richardson,[10] the available data can be extrapolated safely to much higher temperatures. Use has therefore been made of these data to check the reliability of the present experimental technique by measuring the methane/hydrogen ratios in equilibrium with spectrographically pure β-graphite at various temperatures. The experimental results, together with those taken from "Selected Values,"[11] are given in Table 1.

All the available data on the free energy of formation of methane, from its elements in their standard states,

TABLE 1. $p_{CH_4}/(p_{H_2})^2$ in equilibrium with β-graphite

No.	Temperature in °K	$p_{CH_4}/(p_{H_2})^2 \times 10^4$ in atm	
		Present work	Selected values[11]
	900	—	3250
	1000	—	982.8
	1100	—	367.7
	1200	—	160.7
	1300	—	79.2
	1400	—	43.3
	1500	—	25.6
A1	1473	31.0 ± 0.5	—
B5	1573	19.5 ± 0.5	—
C13	1673	12.6 ± 0.5	—
D4	1773	8.2 ± 0.1	—

VOL.
4
1956

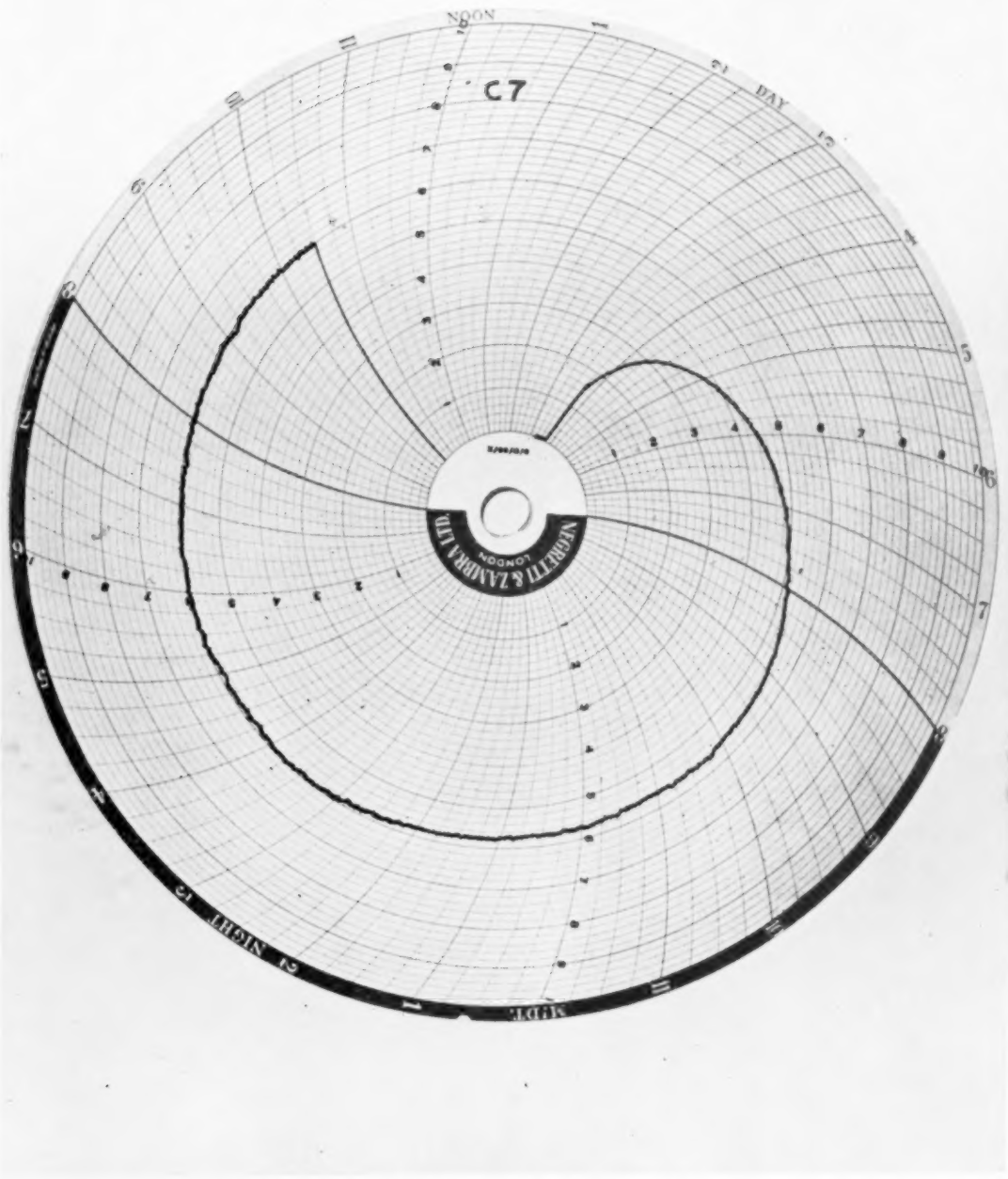

FIG. 1(a). Infra-red gas analyzer methane recording chart.

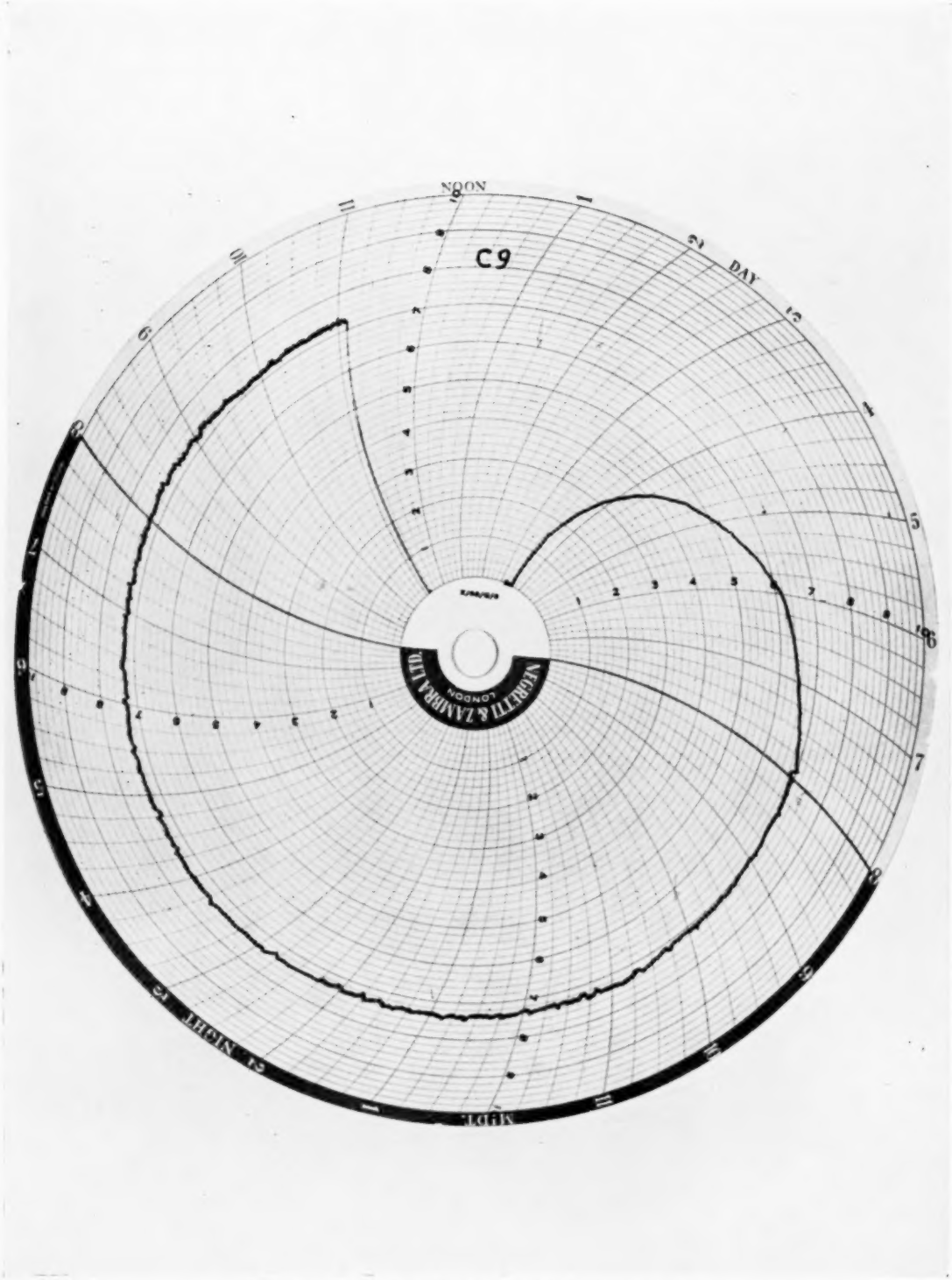

Fig. 1(b). Infra-red gas analyzer methane recording chart.

are given in Fig. 2, from which the following expression may be derived

$$\Delta G^0 = -21{,}550 + 26.16T \text{ cal.} \quad (2)$$

for the reaction

$$2H_2(g) + C(\beta\text{-gr.}) = CH_4(g). \quad (3)$$

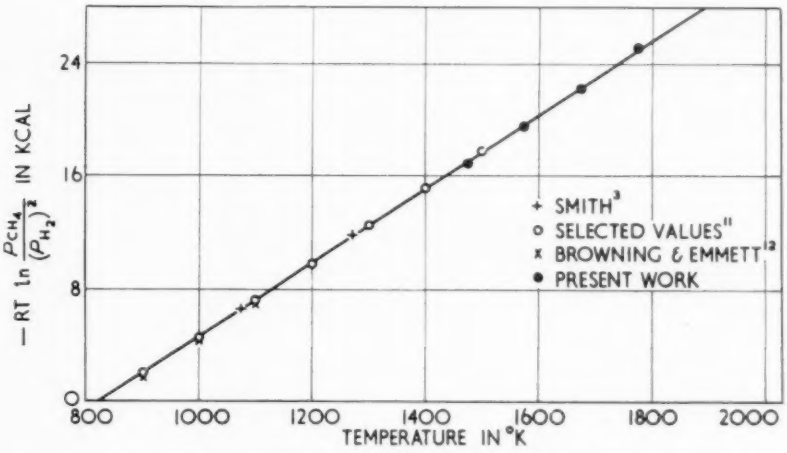

FIG. 2. Free energy of formation of methane, from its elements in their standard states, as a function of temperature.

Equation (2) was first given by Richardson,[10] who pointed out that the ΔG^0 vs. T relationship could be represented by this linear equation from about 500° to 2273°K. The close agreement between the authors' results and those of the previous workers, recorded in Fig. 2, indicates the reliability of the method employed in the present experimental work.

The results of Browning and Emmett[12] were obtained by equilibrating methane/hydrogen mixtures with carbon formed by decomposing pure Fe_3C. As pointed out by these authors, the carbon used in their experiments was thermodynamically unstable with respect to β-graphite, and consequently no weight was given to these results in drawing the line in Fig. 2.

3.4. *Activity of Carbon*

Iron-carbon melts have been equilibrated with methane-hydrogen mixtures at 1300°, 1400°, and 1500°c over a range of carbon concentration. The results are given in Table 2. Choosing β-graphite as the standard state for dissolved carbon, activity is given by the ratio of $p_{CH_4}/(p_{H_2})^2$ in equilibrium with an iron-carbon melt to that in equilibrium with β-graphite; the latter used are those determined experimentally. The activities thus calculated are included in the last column of Table 2.

The composition of melts saturated with graphite are calculated from the following equation, which is based on reliable data discussed elsewhere.[13]

$$\text{At saturation} \quad \log N_C = -\frac{560}{T} - 0.375 \quad (4)$$

where N_C is the atom fraction of carbon.

The range of composition for the liquid phase is rather limited at 1400°, and particularly so at 1300°C. At 1300°C, γ-solid solution crystallizes from melts containing less than about 3.0% carbon, and at 1400°C the separation of the solid phase takes place when the melt contains less than about 2.0% carbon, and therefore in alloys C1 to C6, which lie within a two-phase region, the activity of carbon remains constant within experimental error. A visual examination of these samples after quenching indicated the presence of some solid phase along with the liquid at the working temperature.

It should be pointed out that, due to the experimental difficulties involved, only a few experiments could be conducted at 1500°C. It was observed that at this and higher temperatures, the recrystallized alumina tubes developed a few very small pin-holes within about two days of continuous use. Although the leakage of gas was very small and would not have interfered with the experiments, had the gas phase been continuously swept out of the reaction chamber, in the closed system employed, this leakage could not be tolerated. For the four successful experiments carried out at 1500°C, two new tubes had to be used; in fact, for the entire experiments five tubes were consumed. In view of the difficulty of obtaining recrystallized alumina tubes of the right dimensions, no further experiments could have been carried out. Another limitation imposed on experiments at higher

VOL. 4 1956

temperatures and lower carbon concentrations was that under these conditions the equilibrium methane/hydrogen ratios were too low to be measured and recorded by the infra-red gas analyzer available. The limitations to the use of carbon monoxide-carbon dioxide mixtures are of the reverse order; for example, as pointed out by Richardson and Dennis,[6] at 1560°C $(p_{CO})^2/p_{CO_2}$ in equilibrium with more than 1.0% carbon cannot be metered into the reaction chamber with sufficient accuracy nor can such high carbon monoxide/carbon dioxide ratios be measured by any of the commercially available instruments. In spite of these limitations, however, the experimental results recorded in Table 2 cover a fair range of composition and temperature and justify drawing some conclusions.

Table 2. Iron-carbon melts in equilibrium with methane-hydrogen mixtures

No.	$\frac{p_{CH_4}}{(p_{H_2})^2} \times 10^4$ in atm	C%	N_C	a_C
	Melts at 1300°C			
B1	12.0	2.62	0.111	0.615
2	12.0	3.05	0.128	0.615
3	14.0	3.40	0.141	0.718
4	16.0	3.66	0.150	0.820
5*	19.5	4.674†	0.1858†	1.0
	Melts at 1400°C			
C1	4.8	1.52	0.067	0.381
2	5.0	1.64	0.072	0.397
3	4.7	1.90	0.083	0.373
4	4.6	2.02	0.087	0.365
5	5.3	2.04	0.088	0.421
6	5.3	2.12	0.092	0.421
7	6.0	2.63	0.112	0.476
8	6.5	2.68	0.114	0.516
9	7.3	3.11	0.130	0.579
10	8.0	3.22	0.134	0.635
11	8.7	3.29	0.137	0.690
12	10.2	3.87	0.158	0.809
13*	12.6	4.955†	0.1951†	1.0
	Melts at 1500°C			
D1	4.9	3.75	0.154	0.598
2	6.2	3.80	0.155	0.756
3	6.5	3.99	0.162	0.793
4*	8.2	5.213†	0.2038†	1.0

* Experiments with pure β-graphite.
† Carbon concentrations calculated (see text).

4. DISCUSSION

4.1. *Approximate Solution Law*

From the thermodynamic considerations, Darken and Smith[3] derived the following approximate expression by means of which the activity of carbon a_C, may be related to the composition of (γ) iron-carbon alloys containing up to 0.07 atom fraction of carbon:

$$\ln (a_C N_{Fe}/N_C) = (13 - 12\theta)\, N_C/N_{Fe} - I \qquad (5)$$

where the term θ is defined by

$$\theta = e^{-\Delta E/RT} \qquad (6)$$

where ΔE is the energy required to bring two dissolved carbon atoms, with no adjacent interstitial carbons, into nearest-neighbor sites. The constant I in equation (5) is equal to $\ln \gamma_C$ at infinite dilution. The experimental results of Smith agreed well with expression (5), and the value of ΔE was found to be 1500 cal for the temperature-range 800° to 1000°C.

Richardson and Dennis[6] treated their results in a similar manner, and found that a plot of $\log (a_C N_{Fe}/N_C)$ against N_C/N_{Fe} gave a straight line for melts at 1560°C; from the slope of the line, ΔE was found to be 3600 cal.

Although the approximation involved in the derivation of equation (5) is small in dilute solutions, and not detectable by the experimental results, it is, however, doubtful whether such a solution law could satisfactorily be applied to more concentrated solutions. In Fig. 3, $\log (a_C N_{Fe}/N_C)$ is plotted against N_C/N_{Fe} from the present results and from those of Richardson and Dennis. As pointed out by Richardson and Dennis, their experiments at 1660° and 1760°C using magnesia boats were not satisfactory; these results are therefore not included in Fig. 3. It is to be noted that the slopes of the lines for 1300°, 1400°, and probably also for 1500°C are practically zero from saturation down to about 0.14 atom fraction of carbon. This indicates that, if equation (5) still be applied, $\Delta E \leqslant 0$.

Although there is a wide gap between the points at high- and low-carbon concentrations, it is clear from Fig. 3 that, at a given temperature, the value of ΔE is very small near the saturation point but increases as the solution becomes dilute with respect to carbon.

The data given Sanbongi and Ohtani do not compare well with the above observations; the activities they measured (β-graphite being the standard state) are lower than those of the authors by about 0.1. Their results for 1445°, 1485°, and 1550°C also indicate that $\Delta \overline{H}_C$ is very high, and varies appreciably with temperature, which is not regarded as likely within such a narrow range of temperature.

4.2. *Relative Partial Molal Quantities*

It may be observed from the relationship in Fig. 3 that the values of $\log (a_C N_{Fe}/N_C)$ from saturation down to about $N_C = 0.14$ can be calculated from equation (4), which gives the temperature dependence

of graphite solubility in iron, where $a_C = 1.0$ by the definition of the standard state. The following results are obtained:

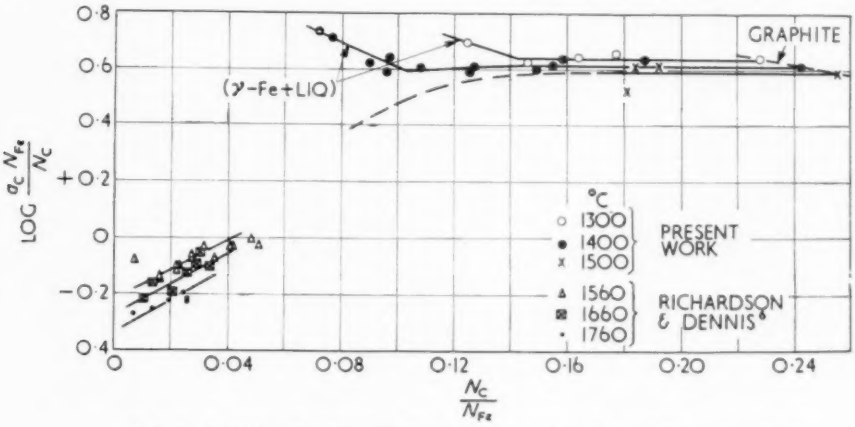

FIG. 3. Activity of carbon related to composition at various temperatures.

TABLE 3. Calculated data

°C	N_C saturation	log $(a_C N_{Fe}/N_C)$ from $N_C = 0.14$ to saturation
1300	0.1858 ± 0.0013	0.642 ± 0.03
1400	0.1951 ± 0.0018	0.616 ± 0.05
1500	0.2038 ± 0.0026	0.592 ± 0.07

The limits of uncertainty given in Table 3 are estimated from the data used to derive equation (4), which has recently been published elsewhere.[13] From the values in the third column of Table 3, the relative partial molal heat of solution of carbon, $\Delta\bar{H}_C$ is calculated, and found to be 3200 ± 300 cal/mole. The scatter of the points about the horizontal lines drawn through the saturation points in Fig. 3 increases the limit of uncertainty, giving a total uncertainty of ± 1200 cal/mole. Richardson and Dennis showed that in dilute solutions, i.e. $N_C < 0.025$, $\Delta\bar{H}_C$ is equal to 6400 ± 2000 cal/mole.

As indicated by the dotted curve (I) in Fig. 4a, $\Delta\bar{H}_C$ decreases as carbon increases from 0.025 to about 0.14 N_C and then remains unchanged. Combination of this curve with the activity values, taken from the curves in Fig. 3, make it possible to calculate the partial molal entropy of solution of carbon, $\Delta\bar{S}_C$; these values are plotted in Fig. 4b. The limits of uncertainty in the values of $\Delta\bar{H}_C$ are fairly large, and it therefore seems more justified to assume an intermediate value for $\Delta\bar{H}_C$ which is independent of composition. The horizontal line (II) in Fig. 4a corresponds to the lowest value of $\Delta\bar{H}_C$ given by Richardson and Dennis and to the highest calculated from the authors' results. Taking $\Delta\bar{H}_C$ equal to 4400 cal/mole and independent of composition, $\Delta\bar{S}_C$ has been calculated from the original experimental result and plotted against the atom fraction of carbon in Fig. 4c, where the points lie fairly close to a smooth curve.

4.3. *Activities of Carbon and Iron*

It is not yet clear whether $\Delta\bar{H}_C$ varies with the concentration of carbon in a manner similar to that of curve I in Fig. 4a or $\Delta\bar{H}_C$ remains constant at

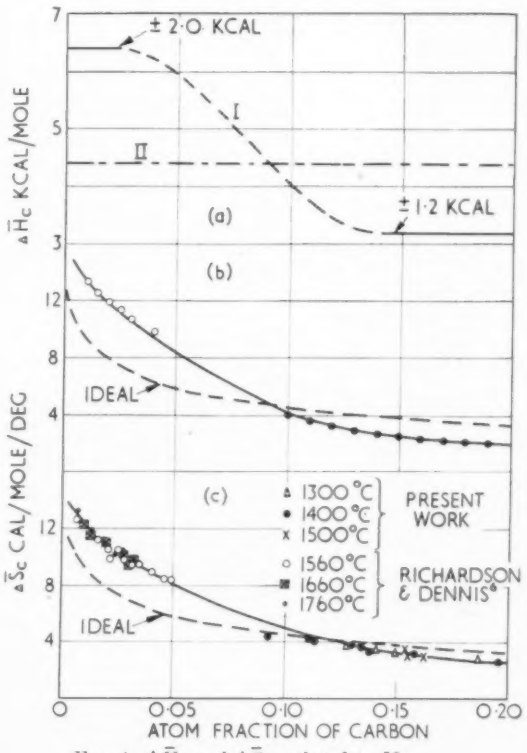

FIG. 4. $\Delta\bar{H}_C$ and $\Delta\bar{S}_C$ related to N_C.

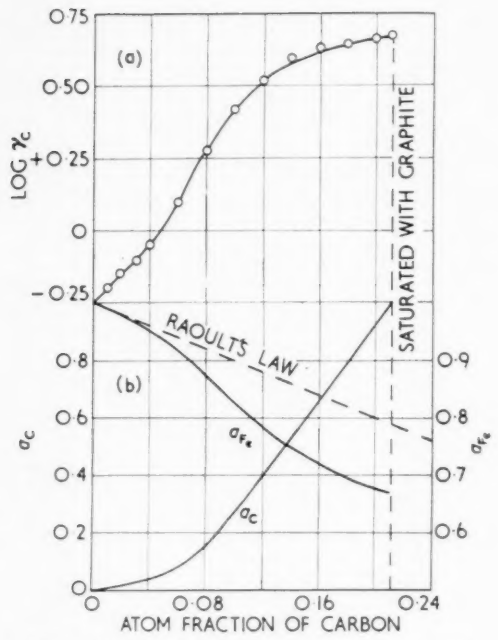

FIG. 5. Relationship between log γ_C, a_C, a_{Fe} and composition for melts at 1600°C.

about 4400 cal/mole over the entire composition range. Assuming, for the purpose of subsequent calculations, that $\Delta\bar{H}_C$ is equal to 4400 cal/mole and independent of temperature and composition within the limits of accuracy of the data, the activity of carbon may be calculated for any temperature and up to carbon saturation from the relationship in Fig. 4c. The results of the computations are given in Table 4.

TABLE 4. Activities of carbon and iron

N_C	$\Delta\bar{S}_C$ cal/mole/deg	log γ_C at 1600°C	log γ'_C at any temp.	a_C at 1600°C	a_{Fe} at 1600°C
		Standard states			
		β-graphite	Infinitely dilute sol.	β-graphite	pure liquid
0	∞	−0.250	0	0	1.0
0.01	12.4	−0.197	0.053	0.00635	0.989
0.02	10.8	−0.149	0.101	0.0141	0.978
0.03	9.8	−0.106	0.144	0.0235	0.965
0.04	9.0	−0.056	0.194	0.0352	0.951
0.06	7.5	0.095	0.345	0.0746	0.916
0.08	6.1	0.277	0.527	0.151	0.873
0.10	5.0	0.420	0.670	0.263	0.825
0.12	4.2	0.516	0.766	0.394	0.783
0.14	3.5	0.602	0.852	0.560	0.747
0.16	3.1	0.632	0.882	0.686	0.718
0.18	2.8	0.646	0.896	0.796	0.696
0.20	2.5	0.666	0.916	0.927	0.677
0.2118*	2.35	0.674	0.924	1.0	0.668

* Melt saturated with graphite at 1600°.

The activity of iron (pure liquid iron being the standard state) was calculated by means of the Gibbs-Duhem equation.

In Fig. 5a the values of log γ_C (standard state being β graphite), given in Table 4, are plotted against composition for melts at 1600°C. Activities are given in Fig. 5b for melts at 1600°C. It is interesting to note that although the log γ_C vs. N_C relationship is a high-order function, a plot of a_C against N_C gives a much simpler curve which becomes linear from about $N_C = 0.12$ to the limit of solubility.

4.4. *The Free Energy of Solution of Carbon in Iron*

It should be noted that the curve in Fig. 5a can be taken as linear when $N_C < 0.045$ and, on extrapolation to zero carbon content, log γ_C^0 becomes −0.25 for 1600°C. The standard state of carbon can now be converted, if required, from β graphite to an infinitely dilute solution by the following expression:

$$\log \gamma'_C = \log \gamma_C - \log \gamma_C^0 \qquad (6)$$

where γ_C and γ_C^0 are the activity coefficients at any carbon concentration and at infinite dilution, respectively, when β graphite is the standard state, and γ'_C is the activity coefficient at any carbon concentration when the standard state is an infinitely dilute solution in which activity is equal to the atom fraction. The values of γ'_C, given in Table 4, become independent of temperature as a result of the assumption that $\Delta\bar{H}_C$, which is taken as equal to 4400 cal/mole, does not vary with composition. In dilute solutions, the following expression may represent the relationship between log γ'_C and N_C:—

$$\log \gamma'_C = 5.0\, N_C \quad \text{when} \quad N_C < 0.045 \qquad (8)$$

The free energy of solution of graphite in liquid iron may be calculated from $\Delta\bar{H}_C = 4400$ cal/mole and log $\gamma_C^0 = -0.25$ at 1600°C to give

$$C(\beta\text{-gr.}) = [C] \qquad (9)$$

$$\Delta G^0 = 4400 - 3.49T \qquad (10)$$

If weight percentage of carbon is to be used instead of atom fraction, then equations (8) and (10) become:

$$\log f_C^C = 0.233[C\%] \quad \text{when} \quad C < 1.0\% \qquad (11)$$

and

$$\Delta G^0 = 4400 - 9.59T \qquad (12)$$

To avoid confusion of various activity coefficient terms, f will be used when activity coefficient is related to composition in weight per cent and, when composition is represented in terms of atom fractions, γ will be employed.

The factor 0.233 in equation (11) agrees well with

that derived previously by Turkdogan *et al.*,[14] i.e. $\log f_C^C = 0.22\ [C\%]$, from the data of Richardson and Dennis[6] by the well-known method of extrapolating the equilibrium ratio, i.e. $(p_{CO})^2/p_{CO_2}\ [C\%]$, to zero carbon concentration.

4.5. *Carbon-Oxygen Interaction*

Phragmen and Kalling[15] have investigated the carbon-oxygen reaction by equilibrating pure iron melts, containing less than 0.1% carbon, with carbon monoxide-carbon dioxide mixtures of known compositions at 1550° and 1700°C; the metal samples were analyzed for carbon and oxygen. The following attempt may be made to compare their results with those of the present findings. Combination of equation (12) and the free energy of formation of carbon monoxide from graphite and carbon dioxide[10] yields

$$[C] + CO_2(g) = 2CO(g), \tag{13}$$

$$\Delta G^0 = 36{,}100 - 31.66T, \tag{14}$$

and

$$\log K = -\frac{7890}{T} + 6.921. \tag{15}$$

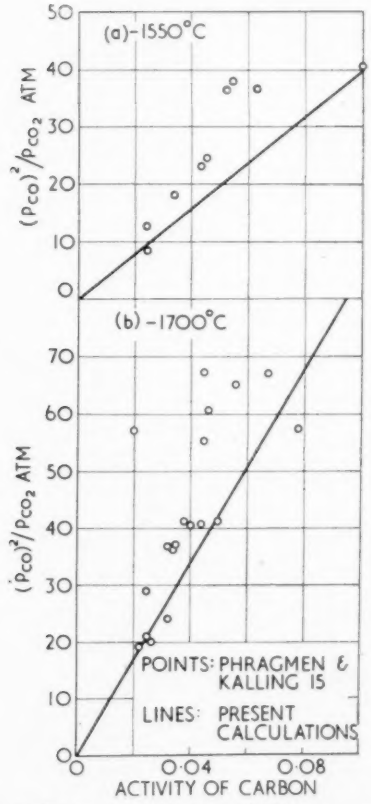

FIG. 6. Ratio $(p_{CO})^2/p_{CO_2}$ related to carbon activity per cent; standard state of dissolved carbon is infinitely dilute solution, i.e. activity coefficient → 1.0 when carbon concentration → zero.

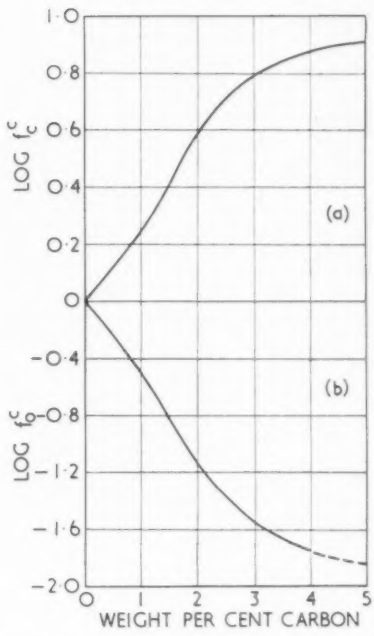

FIG. 7. Activity coefficient of carbon in Fe–C binary melts, f_C^C, and effect of carbon on activity coefficient of oxygen in Fe–C–O ternary melts, f_0^C, are related to weight per cent of carbon.

In iron-carbon-oxygen melts containing very little carbon, the concentration of oxygen is high and its effect on the activity coefficient of carbon becomes noticeable . It has recently been shown that[14]

$$\log f_0^C = -0.485\,[C\%] \quad \text{when} \quad C < 1\% \tag{16}$$

where f_0^C represents the activity coefficient factor of oxygen in iron-carbon-oxygen melts. The factor f_C^0, the effect of oxygen on the activity coefficient of carbon, can be calculated from equation (16) by the method introduced by Wagner,[16] and the following is obtained:

$$\log f_C^0 = -0.364\,[O\%]. \tag{17}$$

(Details of this calculation are given elsewhere).[17, 18]

The thermodynamic considerations[16] indicate that in very dilute solutions the following expression may be written

$$\log f_C = \log f_C^C + \log f_C^0, \tag{18}$$

i.e.

$$\log f_C = 0.233[C\%] - 0.364\,[O\%]. \tag{19}$$

The activity of carbon in the melts of Phragmen and Kalling[15] has been calculated by equation (19) and, in Figs. 6a and 6b $(p_{CO})^2/p_{CO_2}$ ratios for 1550° and 1700°C, respectively, are plotted against the activity of carbon. The straight lines drawn are those calculated from equation (15), which give the equilibrium

constant of reaction (13). Considering the accumulated errors, resulting from the use of data from several sources, involved in the calculations of a_C and equation (15), the distribution of the points about the lines in Fig. 6 is very satisfactory.

At the time the relationship between log f_0^C and concentration of carbon in iron-carbon-oxygen melts was evaluated,[14] the values of f_C^C were known only up to 1.0% carbon; the present results now permit the evaluation of f_0^C up to about 5.0% carbon. (For the details of the method see a recent paper by Turkdogan *et al.*)[14] In Figs. 7a and 7b, log f_C^C and log f_0^C are plotted against the weight per cent of carbon. It should be noted that log f_C^C is numerically the same as log γ'_C which is given in Table 4 for concentrations in atom fraction.

ACKNOWLEDGMENT

The authors wish to express their thanks to Dr. J. Pearson for the interest he has shown in this work. One of the authors (C. R. M.) wishes to thank the British Iron and Steel Research Association for hospitality extended during part of this work.

REFERENCES

1. S. Marshall and J. Chipman, *Trans. Amer. Soc. Metals*, **30**, 695–741 (1942).
2. J. Chipman, *Disc. Faraday Soc.*, **4**, 23–49 (1948).
3. R. P. Smith, *J. Amer. Chem. Soc.*, **68**, 1163–1175 (1946).
4. M. I. Temkin and L. A. Shvartsman, *Zh. fiz. Khim.*, **23**, 6, 755–760 (1949).
5. L. S. Darken and R. W. Gurry, *Physical Chemistry of Metals*, p. 413, McGraw-Hill Publishing Co. Ltd., New York, 1953.
6. F. D. Richardson and W. E. Dennis, *Trans. Faraday Soc.*, **49**, 171–180 (1953).
7. K. Sanbongi and M. Ohtani, *Sci. Rep. Res. Insts. Tôhoku Univ.*, **A5**, No. 3, 263–270 (1953).
8. L. E. Leake, *J. sci. instrum.*, **30**, 434 (1953).
9. F. D. Richardson and J. H. E. Jeffes, *J. Iron Steel Inst.*, **160**, 261–270 (1948).
10. F. D. Richardson, *ibid*, **175**, 33–51 (1953).
11. *Selected Values of Chemical Thermodynamic Properties: Series III, et seq.*, U.S. Department of Commerce, National Bureau of Standards (1947).
12. L. C. Browning and P. H. Emmett: *J. Amer. Chem. Soc.*, **73**, 581–583 (1951).
13. E. T. Turkdogan and L. E. Leake, *J. Iron Steel Inst.*, **179**, 39–43 (1955).
14. E. T. Turkdogan, L. S. Davis, L. E. Leake, and C. G. Stevens, *J. Iron Steel Inst.*, **181**, 123–128 (1955).
15. G. Phragmen and B. Kalling, *Jernkontorests Annaler*, **123**, No. 5, 199–218 (1939).
16. C. Wagner, *Thermodynamics of Alloys*, p. 53, Addison-Wesley Press Inc., Mass. (1952).
17. N. A. Gokcen and J. Chipman, *Trans. Amer. Inst. Min. Met. Eng.*, **194**, 171–181, (1952); *J. Metals*, Feb. 1952.
18. J. Pearson and E. T. Turkdogan, *J. Iron Steel Inst.*, **176**, 19–23 (1954).

VOL
4
195

THE STRUCTURE OF LITHIUM-MAGNESIUM SOLID SOLUTIONS—I*

Measurements on the Bragg Reflections

F. H. HERBSTEIN† and B. L. AVERBACH‡

Lattice parameters have been measured at 20°C and −183°C for seven BCC Li-Mg alloys. There is a strong negative deviation from Vegard's law and a minimum in the parameter-composition curve at 65 atomic per cent Li. Two measurements have been made on martensitic FCC Li-Mg alloys at −183°C, and a negative deviation from Vegard's law is also indicated for these alloys. In the HCP solid solutions of Li in Mg, both the a and c axes decrease with increasing Li content, while the c/a ratio decreases from 1.6235 for pure Mg to 1.608 at 18.4 atomic per cent Li (the $\alpha/\alpha + \beta$ phase boundary).

The presence of local static displacements of the atoms from the sites of the average lattice has been demonstrated from measurements of the Bragg intensities at 295°K and 90°K. These intensity measurements have also been used to derive values of the Debye characteristic temperature for five BCC alloys.

LA STRUCTURE DES SOLUTIONS SOLIDES LITHIUM-MAGNESIUM—I

Mesures sur les réflexions de Bragg

Les paramètres du réseau ont été mesurés à 20°C et −183°C pour sept alliages Li-Mg à structure cubique centrée. On constate une forte déviation négative à la loi de Végard et l'existence d'un minimum dans la courbe paramètre-composition pour une concentration atomique de 65% en Li. Deux mesures sur des alliages martensitiques Li-Mg (structure cubique à faces centrées) ont été effectuées à −183°C et un écart négatif à la loi de Végard a également été trouvé. Dans les solutions solides à structure hexagonale compacte de Li dans Mg, les deux axes a et c décroissent lorsque la teneur en Li croît, tandis que le rapport c/a décroit de 1,6235 pour le magnésium pur à 1,608 pour une concentration atomique de 18,4% de Li (frontière $\alpha/\alpha + \beta$).

L'existence d'écarts statistiques locaux d'atomes hors des sites du réseau moyen a été démontrée par des mesures d'intensité de réflexion de Bragg à 295°K et 90°K. Ces mesures d'intensité ont été utilisées pour déduire les valeurs de la température caractéristique de Debye pour cinq alliages à structure cubique centrée.

DIE STRUKTUR VON LITHIUM-MAGNESIUM-MISCHKRISTALLEN—I

Messungen an den Bragg-Reflexen

An sieben kubisch-raumzentrierten Li-Mg-Legierungen wurden die Gitterkonstanten bei 20°C und −183°C gemessen. Dabei ergibt sich eine starke negative Abweichung vom Vegardschen Gesetz und ein Minimum in der Gitterkonstanten-Konzentrations-Kurve bei 65 Atom-Prozent Li. Zwei Messungen wurden an martensitischen, kubisch-flächenzentrierten Li-Mg-Legierungen bei −183°C gemacht und auch bei diesen ergaben sich Anzeichen für eine negative Abweichung von Vegardschen Gesetz. In den hexagonal dichtest gepackten Mischkristallen von Li in Mg nehmen sowohl die a-als auch die c-Achse mit wachsendem Li-Gehalt ab, während das Achsenverhältnis c/a von 1,6235 für reines Mg auf 1,608 bei 18,4 Atomprozent Li (Phasengrenze $\alpha/(\alpha + \beta)$) zurückgeht. Auf Grund von Messungen der Bragg-Intensitäten bei 295°K und 90°K wurde das Vorliegen von statischen, lokalen Verrückungen der Atome aus den Plätzen des mittleren Kristallgitters heraus nachgewiesen. Die Intensitätsmessungen wurden weiterhin dazu verwendet, Werte für die Debye-Temperaturen von fünf kubischraumzentrierten Legierungen abzuleiten.

VOL. 4 1956

1. INTRODUCTION

In solid solutions of transition and Group 1B metals, ion-core repulsion plays an important role in determining the properties of the alloys. The Au-Ni,[1, 2, 3] Au-Cu,[4, 5] and Co-Pt[6, 7] solutions are examples of this type which have been investigated recently by thermodynamic and X-ray methods. These solutions show a marked size effect in that the atoms are displaced from the sites of the average lattice because of the close packing of atoms of disparate sizes. In addition, X-ray and thermodynamic data cannot be correlated in terms of nearest-neighbor binding forces alone and it appears necessary to introduce other forces arising from changes in electron energy levels.

The Li-Mg system was chosen for this investigation because the ion cores are small, and the effects of overlap should be negligible. The constituent atoms are also relatively simple and unusual electronic effects would not be expected. In Part I of this investigation the lattice parameters of seven BCC alloys (β phase) were measured at 295 and 90°K. The parameters of two alloys were also measured at 90°K after transformation to the martensitic FCC phase. The lattice parameters of two HCP alloys (α phase) were measured at 295°K. The lattice parameters of the BCC alloys exhibit a minimum value at 65 atomic per cent lithium, and this was taken to

* Received October 3, 1955. This work was sponsored by the U.S. Atomic Energy Commission under Contract AT(30-1)-1002.

† Present address: National Physical Laboratory, Pretoria, South Africa.

‡ Department of Metallurgy, Massachusetts Institute of Technology, Cambridge, Massachusetts.

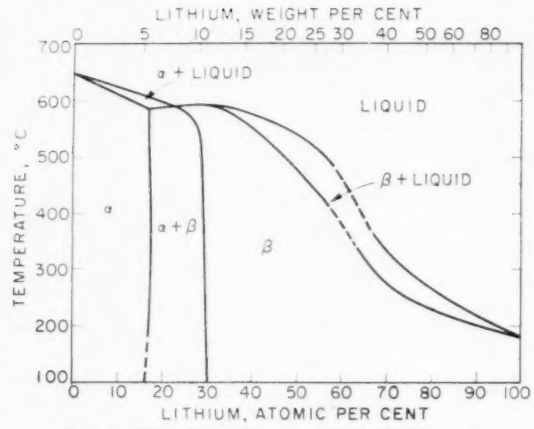

FIG. 1. The phase diagram of the Li-Mg system according to Freeth and Raynor.[12]

indicate that the Li-Mg interatomic distance is less than the average of the atomic diameters of the pure metals. A preference for unlike nearest neighbors would thus be expected in these alloys; diffuse X-ray scattering measurements showed that such a short-range order exists, and these data are described in Part II.[8]

The displacements of the atoms from the sites of the average lattice can be detected by two types of X-ray measurements. The static displacements affect the integrated intensities of the Bragg reflections in the same manner as the dynamic displacements produced by thermal vibrations.[9, 10, 11] The static displacements are, however, independent of temperature and can be derived from X-ray intensity measurements at two temperatures. Such measurements are described in this paper. On the other hand, atomic displacements also lead to a modulation of the diffuse scattering distinguishable from that associated with short-range order,[2, 5] and these measurements are presented in Part II; both sets of data are correlated in the latter paper.

The dynamic displacements arising from thermal vibration are related to the Debye temperature, and X-ray Debye temperatures are presented here for several BCC alloys.

2. PREVIOUS WORK ON THE Li-Mg SYSTEM

The phase diagram of the Li-Mg system had been determined by a number of workers; the most recent results are those of Freeth and Raynor,[12] which are shown in Fig. 1. BCC Li can dissolve about 70 atomic per cent magnesium and HCP Mg can dissolve about 18 atomic per cent Li. There is no superlattice formation in this system,[13] and this has been confirmed by our present results. A complex ordered structure with the atomic ratio Li_3Mg_5 has been reported[13] for alloys heavily contaminated with interstitial impurities (oxygen and nitrogen), but this structure appears improbable for the pure alloys.[14] Previous workers have reported lattice parameters for a number of alloys[13, 15, 16, 17] while resistivity measurements have been made over a wide range of compositions and temperatures.[15, 18] Pressure-volume relationships at room temperature and the variation of resistivity with composition have also been measured.[18] The occurrence of a martensitic transformation at low temperatures has been demonstrated in alloys of high Li content.[19]

3. EXPERIMENTAL METHODS

(i) *Materials.* The alloys used in this work were supplied by the Dow Chemical Company, who also provided analytical data for some of these alloys; the remaining alloys were analyzed here for magnesium. The weight percentage of sodium was less than 0.03 in all cases, and the amounts of other impurities were correspondingly small.

(ii) *Lattice-parameter measurements.* The lattice parameters of the alloys at room temperature were measured with a recording spectrometer and a Bradley-Jay type powder camera. Measurements at 90°K were made with the spectrometer, the specimens being cooled by a continuous stream of liquid nitrogen. For the alloys with high Li content, spectrometer measurements were unreliable because of the low absorption coefficient of the samples, and the parameters of the alloys with 81 and 89 atomic per cent Li were measured in a 114.6-mm North American Philips powder camera, modified to permit the specimen to be bathed in liquid nitrogen.* Specimen temperatures were measured with a copper-constantan thermocouple. Cu$K\alpha$ radiation (Ni-filtered) was used for all these measurements, the wavelengths of the α_1 and α_2 lines being taken to be 1.54050 Å and 1.54434 Å respectively.[20] The cell dimensions of the cubic alloys were determined in the usual manner by extrapolating the (linear) plot of a against $\sin^2\theta$ to $\theta = 90°$. For the HCP alloys, the computational procedure suggested by Archard[21] was used. For the room-temperature measurements the temperature during the experiments was noted and an approximate allowance for thermal expansion made. The values of the lattice parameters are given in Tables 1, 2, and 3. The maximum discrepancy of the individual values from the mean values is ± 0.001 Å.

(iii) *Thermal and static displacements of the atoms.* The dynamic and static displacements of the atoms

* The modifications to this camera were designed by Dr. E. H. Jacobsen; we are grateful to Prof. B. E. Warren for loaning it to us for this work.

TABLE 1. Lattice parameters of the BCC (β-phase) Li-Mg alloys

Atomic per cent Li	a at 20°C		a at −183°C	
	Film (Å)	Spectrometer (Å)	Film (Å)	Spectrometer (Å)
30	3.517	3.519	—	3.502
40	3.505	3.504	—	3.483
49	3.499	3.499	—	3.477
57	3.492	3.495	—	3.473
68	3.492	3.494	—	3.468
81	3.497	—	3.472	—
89	3.500	—	3.474	—
100	3.510*	—	3.483*	—

* Reference (22).

TABLE 2. Lattice parameters of the FCC Li-Mg alloys (martensitic phase) at −183°C

Film measurement

Atomic per cent Li	a (Å)
81	4.378
89	4.377
100	4.379*

* Reference (22).

TABLE 3. Lattice parameters of HCP Mg-Li alloys at 20°C 19 cm Bradley-Jay powder camera

Atomic per cent Li	a (Å)	c (Å)	c/a
0	3.2095	5.2106	1.6235
10.2	3.1982	5.1714	1.6170
12.5	3.1927	5.1474	1.6122
18.4	3.1918	5.1319	1.6078

from the average lattice sites are given for a disordered body-centered cubic Li-Mg alloy by:

$$pF(hkl) = 2\left\{m_{\mathrm{Mg}} f_{\mathrm{Mg}} \exp\left[-\frac{8\pi^2}{3}(\overline{u_T^2} + \overline{u_S^2})_{\mathrm{Mg}} \times \frac{\sin^2\theta}{\lambda^2}\right] + m_{\mathrm{Li}} f_{\mathrm{Li}} \exp\left[-\frac{8\pi^2}{3}(\overline{u_T^2} + \overline{u_S^2})_{\mathrm{Li}} \frac{\sin^2\theta}{\lambda^2}\right]\right\} \quad (1)$$

where F(hkl) is the measured structure factor on an arbitrary scale, p is the conversion factor to the absolute scale, m_{Mg},m_{Li} are the atomic fractions of Mg and Li in the alloy, f_{Mg},f_{Li} are the theoretical atomic scattering factors, $\overline{u_T^2}$, $\overline{u_S^2}$ are the respective mean-square amplitudes of thermal and static displacements of the atoms from the sites of the average lattice, θ is the Bragg angle, and λ is the wavelength.

The Hartree atomic scattering factor (Viervoll and Ogrim)[22] were used for f_{Mg} and f_{Li}. Since the angular dependence of the unitary scattering factors (f/Z), where Z is the atomic number, for Mg and Li are closely similar, and on assuming equal displacements for the atoms, equation (1) can be rewritten:

$$pF(hkl) = 2\bar{f}\exp\left[-\frac{8\pi^2}{3}(\overline{u_T^2} + \overline{u_S^2})\frac{\sin^2\theta}{\lambda^2}\right] = 2\bar{f}\exp\left(-\overline{B}\frac{\sin^2\theta}{\lambda^2}\right) \quad (2)$$

where $\bar{f}$ is a weighted mean atomic scattering factor and $\overline{u_T^2}$ and $\overline{u_S^2}$ are mean thermal and static atomic displacements. The mean thermal displacement can be defined by

$$\overline{u_T^2} = \frac{3}{8\pi^2}\overline{B}_T = \frac{9h^2T\left\{\phi(\chi) + \frac{\chi}{4}\right\}}{4\pi^2\overline{m}k\Theta_M^2} \quad (3)$$

where h is Planck's constant, k is Boltzmann's constant, T is the temperature, Θ_M the Debye temperature, $\overline{m}$ is the weighted mean atomic mass, $\chi = \frac{\Theta_M}{T}$, and $\phi(\chi)$ is the Debye integral. The total mean-square displacement ($\overline{u_T^2} + \overline{u_S^2}$) can be obtained from the slope of a plot of $\ln \frac{2\bar{f}}{F_{(hkl)}}$ vs. $\sin^2\theta/\lambda^2$.

The thermal displacements of the atoms can be determined separately from a comparison of intensities measured at two temperatures. If it is assumed that u_S is independent of temperature, then

$$\frac{F_{T_1}(hkl)}{F_{T_2}(hkl)} = \exp\left[-(\overline{B}_{T_1} - \overline{B}_{T_2})\frac{\sin^2\theta}{\lambda^2}\right] \quad (4)$$

The Debye temperature of the alloy can be determined from an obvious extension of equation (3), using the value of ($\overline{B}_{T_1} - \overline{B}_{T_2}$) obtained from equation (4), since this quantity includes only the effects of thermal vibration. The values of $\overline{u_{T_1}^2}$ and $\overline{u_{T_2}^2}$ are now calculated from equation (3) and used to obtain the value of $\overline{u_S^2}$. Thus by making measurements at two temperatures, the thermal and the static displacements of the atoms from the sites of the average lattice can be measured.

The experimental procedures were as follows. Compressed-powder briquettes were prepared of all the β-phase alloys except those with 81 and 89 atomic per cent Li, which were too corrosible to be powdered. Only the alloy with 30 atomic per cent Li could be powdered in air without excessive decomposition; the other compositions were filed under kerosene and the briquette surfaces were protected by a film of

VOL. 4 1956

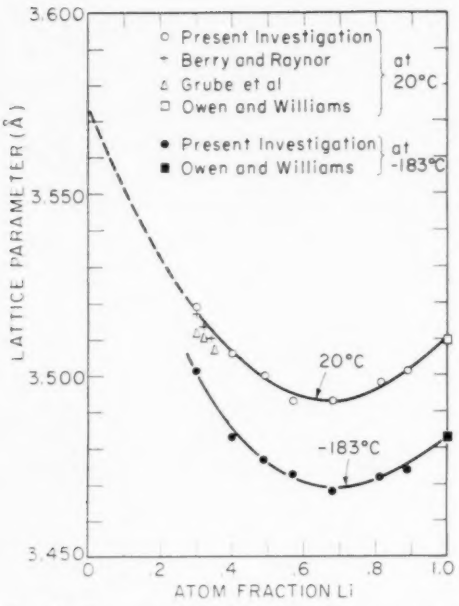

FIG. 2. The variation of the lattice parameter of the BCC (β-phase) alloys with composition. Measurements are in Ångstroms, and were corrected to 20°C and −183°C. The line through the experimental points at 20°C represents the equation

$$a = 0.1736 m_{Li}^2 - 0.2359 m_{Li} + 3.5732.$$

light oil. All briquettes were checked by back-reflection photographs for freedom from cold work, excessive grain size, and preferred orientation.

The intensity measurements were made with an automatic Gieger-counter spectrometer using Cu$K\alpha$ radiation. The specimens were rotated in their own planes during the measurements at room temperature, but not at liquid-nitrogen temperature. Equal incidence and reflection angles were used in order to avoid differential absorption corrections. Intensities were corrected for Lorentz, polarization, and multiplicity factors and converted to structure factors on an arbitary scale. While the reproducibility of a given structure factor was ± 2 per cent, the individual values deviated from a smooth curve by ± 6–8 per cent on occasion. These errors were ascribed to grain-size and preferred-orientation effects in the compressed briquettes. In addition, the (110) reflection was sometimes 15–20 per cent below the curve, but this was probably by extinction.

4. RESULTS

(i) *The Lattice Parameters*

(a) *The BCC alloys.* The lattice parameters of the BCC alloys at 20°C and −183°C are compared with the data of previous investigators[13, 23] in Fig. 2; The agreement among the various values is good. The values of a at 20°C were fitted, by the method of least squares, to the quadratic equation:

$$a = 0.1736\, m_{Li}^2 - 0.02359\, m_{Li} + 3.5732. \quad (5)$$

The maximum deviation of the measured values from the calculated curve was 0.0020 Å. From this relation, the lattice parameter of the hypothetical BCC Mg was found to be 3.573 Å, and the radius of BCC Mg is 1.547 Å. The radius of BCC Mg obtained from that of HCP Mg by applying Pauling's relation[24, 25] is 1.563 Å, which is larger than the extrapolated value. As the usual error in applying Pauling's relation is 0.01 Å or less, this suggests that the equation above does not apply accurately in the hypothetical region of Mg-rich BCC alloys.

The lattice parameter vs. composition curve is a striking one, the appearance of a minimum* being quite uncommon. The magnesium atom (in the hypothetical BCC form) is about 4% larger in diameter than the Li atom, yet the addition of up to 35 atomic per cent Mg reduces rather than increases the lattice parameter of the solid solution. This situation is not changed by cooling the alloys to −183°C. Minima in the curves of lattice parameter against composition have also been found in the Ti-Ta[26] and Ta-Nb systems.[27] In both systems an almost complete series of BCC solid solutions is formed. Among FCC systems the only reported example is the Ag-Au system.[28] The depths of the minima below the parameter of the smaller of the components have the values 0.009 Å and 0.003 Å in these three systems. These values are all smaller than that found in the Li-Mg system, where the parameter of the alloy with 65 atomic per cent Li is 0.017 Å less than that of pure Li. The negative deviations from Vegard's law shown by the BCC Li-Mg alloys are also rather larger than the deviations found in other systems. This can be seen from the following lists of maximum deviations of the cell edge from the linear relationship with composition. Li-Mg 0.05 Å, Cu-Pd 0.015 Å, Cu-Au 0.024 Å, Cu-Ni 0.008 Å, Au-Ag 0.006 Å.

(b) *The FCC (martensitic) alloys.* The martensitic transformation from BCC to FCC in Li-Mg alloys proceeds to a considerable extent above liquid-nitrogen temperature only for alloys with greater than about 80 atomic per cent Li. The parameters of the FCC alloys containing 81 and 89 atomic per cent Li were measured, but these results (Table 2) are of lower accuracy than those for the BCC alloys because the high-angle lines exhibited marked broadening.

* The term minimum is taken to mean that the parameters of some of the alloys are smaller than that of the smaller of the components.

Within the accuracy of the measurements (±0.003 Å) the lattice parameters of the FCC Li-Mg alloys do not differ from that of FCC Li. It appears that the FCC alloys also show a marked negative deviation from Vegard's law, although the presence of a minimum is not evident in these restricted data.

(c) *The HCP (α-phase) alloys.* The lattice parameters of the HCP (α-phase) alloys of Li in Mg have been measured previously by Hofmann[16] and Busk.[17] In this investigation the lattice parameters of three alloys, as well as that of pure Mg, were measured. These data and the results of other investigations are compared in Figs. 2, 3, and 4. The agreement is generally good, with the present results agreeing more closely with those of Hofmann than with the results of Busk. Addition of Li to Mg reduces both the c and a dimensions of the unit cell, the former decreasing relatively faster than the latter. Thus the c/a ratio decreases from 1.6235 for pure Mg to 1.608 at the $\alpha/(\alpha+\beta)$ phase boundary at about 18.4 atomic per cent Li.

The variations of the lattice parameters with composition in solid solutions in Mg have been explained in some detail by Jones,[29] by considering the effect of alloying on Brillouin-zone overlaps. After correction is made for atomic-size effects in the manner suggested by Jones, the variation in the cell-size of Mg-Li alloys with electron concentration is linear. This result is in accordance with Jones's general thesis, but the details of the variation do not support his detailed assumptions regarding the Brillouin-zone structure of Mg.

(ii) *Static and Dynamic Atomic Displacements in BCC Alloys.*

The experimental values of the Debye factors, $\bar{B}$ (exptl) for the BCC Li-Mg alloys are listed in Table 4. These values for 295 and 90°K were obtained by a comparison for each diffraction line of the experimental structure factors, $\bar{f}\exp\left(\frac{-\bar{B}\sin^2\theta}{\lambda^2}\right)$, with the theoretical values of $\bar{f}$ calculated for stationary atoms (the usual tabulated values of f). B (exptl) thus includes the effects of static and dynamic displacements. However, the quantity $(B_{295}-B_{90})$ involves only the thermal displacements, and this can be calculated in two ways: (1) from the difference of B (exptl) determined at each temperature, or (2) from the ratio of intensities at the two temperatures as indicated in equation (4). The latter method eliminates to some extent the errors arising from large grain sizes and preferred orientations in the specimen. Both sets of values are listed in Table 5; the mean was was obtained by giving the second set of values

TABLE 4. Experimental values of the Debye factors for BCC Li-Mg alloys at 295°K and 90°K

Atomic per cent Li	At 295°K			At 90°K		
	B (exptl) (Å²)	B (thermal) (Å²)	B' (distortion) (Å²)	B (exptl) (Å²)	B (thermal) (Å²)	B' (distortion) (Å²)
30	2.00	1.68	0.32	0.88	0.65	0.23
40	2.10	1.80	0.30	0.87	0.62	0.25
49	1.93	1.60	0.33	1.06	0.66	0.40
57	1.89	1.87	0.02	0.78	0.75	0.03

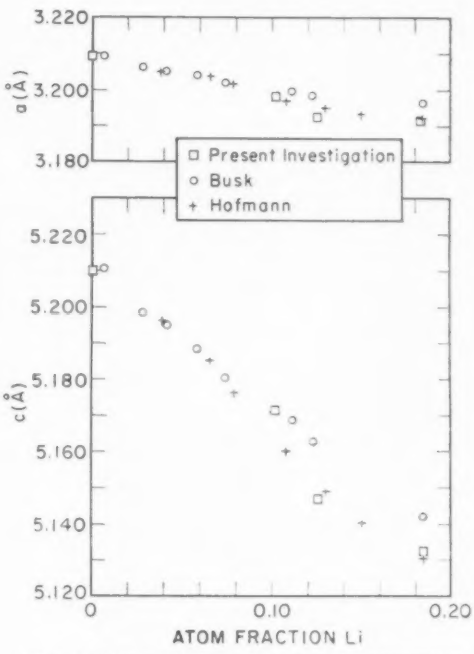

FIG. 3. The variation of the a and c parameters with composition for the HCP alloys of Li in Mg.

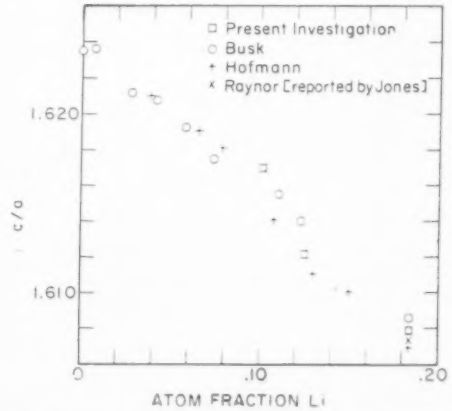

FIG. 4. The variation of the c/a ratio with composition for the HCP alloys of Li in Mg.

TABLE 5. Comparison of the values of $(B_{295} - B_{90})$ obtained two methods of calculation, and Debye temperatures for BCC Li-Mg alloys

Atomic per cent Li	$(B_{295} - B_{90})$			Debye temperature Θ_M
	From B (exptl) at each temperature (Å²)	Direct comparison of intensities at two temperatures (Å²)	Mean value (Å²)	(°K)
30	1.12	0.98	1.02	333
40	1.23	1.00	1.08	339
49	0.99	0.87	0.95	384
57	1.11	1.13	1.12	366

double weight. Values of the Debye temperature of the alloys have been calculated from the mean values of $(B_{295} - B_{90})$, and these are also listed in Table 5. No independent values of Debye temperature are available from other sources for a check on these values. The values of B (thermal) at 295°K and 90°K were calculated from equation (3), using these values of the Debye temperature, and are listed in Table 4. In every instance the measured value of the Debye factor is larger than can be accounted for in terms of the lattice vibration alone, and it is inferred that these additional contributions arise from local static displacements of the atoms from the sites of the average lattice. Evidence of local static displacements in other solid solutions, and the results of previous workers in this field, are summarized elsewhere.[9]

No great accuracy attaches to the individual values of B' (distortion) listed in Table 4. Because of the corrosibility of the alloys, it was not possible to prepare really satisfactory powder specimens, and hence the measured values of B (exptl) are not very accurate. For the measurements at 295°K it was possible to compensate partly for the deficiencies in specimen preparation by rotating the briquettes in their own planes, and those values of B (exptl) are accurate to about $\pm 5\%$. However, at 90°K the specimens were stationary, and these results are only accurate to within $\pm 10\%$. Since the values of both Θ_M and B (distortion) are obtained by difference, individual values cannot be expected to be very reliable. Nevertheless, the qualitative existence of the static displacements is clear, while in quantitative terms they correlate approximately with the results of the size-effect diffuse scattering described in Part II.

5. DISCUSSION

The negative deviation from Vegard's law for the BCC alloys, and particularly the minimum in the lattice parameters, is in contradiction to the predictions of a simple elastic model of solid solutions.[30] On the basis of this model, a positive deviation would be expected, since the larger atom (Mg) has the smaller compressibility.[18]

TABLE 6. Magnitudes of the RMS dynamic and static displacements in Li-Mg alloys

Atomic per cent Li	RMS dynamic displacements		RMS static displacement (Å)
	300°K (Å)	90°K (Å)	
30	0.25	0.16	0.10
40	0.26	0.15	0.10
49	0.25	0.16	0.11
57	0.27	0.17	0.03

The indications of a similar negative deviation from Vegard's law in the FCC (martensitic) alloys, suggests that it is a consequence of the nature of the component atoms rather than a result of the crystal structure of the alloys. The most immediate explanation for the reduction in the mean atomic volume of the solid solution on the addition of Mg, even though the Mg atom is larger than the Li atom, is the occurrence of Li-Mg distances in the solid solution, which are shorter than the average of the radii of Li and Mg atoms. This suggestion is examined in more detail in Part II.

The presence of local static displacements of the atoms from the sites of the average solid-solution lattice indicates that the Li and Mg atoms do not have equal sizes in solid solution. The magnitudes of the local static displacements are compared in Table 6 with the RMS dynamic displacements at 295°K and 90°K due to the thermal vibrations of the lattice.

6. ACKNOWLEDGMENTS

The authors are greatful to the Atomic Energy Commission for their sponsorship of this research, and to the Dow Chemical Company, and particularly to Dr. R. S. Busk, for their assistance in furnishing the alloys and analyses. The assistance of Robert Goss in the experimental phases of this investigation is also gratefully acknowledged.

REFERENCES

1. L. L. SIEGLE, M. COHEN, and B. L. AVERBACH. *Trans. Amer. Inst. Min. Met. Eng.*, 1320 (1952).
2. P. A. FLINN, B. L. AVERBACH, and M. COHEN, *Acta Met.*, **1**, 664 (1953).
3. B. L. AVERBACH, P. A. FLINN, and M. COHEN, *Acta Met.*, **2**, 92 (1954).
4. R. A. ORIANI, *Acta Met.*, **2**, 608 (1954).
5. B. E. WARREN and B. L. AVERBACH, *Modern Research Techniques in Physical Metallurgy*, A.S.M. Cleveland, p. 95 (1953).
6. R. A. ORIANI, *Acta Met.*, **1**, 144 (1953).
7. P. S. RUDMAN, ScD Thesis (1955). Metallurgy Department, M.I.T.
8. F. H. HERBSTEIN and B. L. AVERBACH, *Acta Met.*, **4**, 414 (1956).

9. F. H. HERBSTEIN, B. B. SORIE, and B. L. AVERBACH, *Acta Cryst.* (in press).
10. K. HUANG, *Proc. Roy. Soc.*, **A190,** 102 (1947).
11. R. A. COYLE and B. GALE, *Acta Cryst.*, **8,** 105 (1955).
12. W. E. FREETH and G. V. RAYNOR, *J. Inst. Metals*, **1954,** 575.
13. R. L. P. BERRY and G. V. RAYNOR, *Nature*, **171,** 1079 (1953).
14. F. H. HERBSTEIN and B. L. AVERBACH *Acta Cryst.* **9,** 91 (1956).
15. G. GRUBE, H. VON ZEPPELIN, and H. BUMM, *Z. Elecktrochem.*, **40,** 160 (1934).
16. W. HOFMANN, *Z. Metallk.*, **28,** 160 (1936).
17. R. S. BUSK, *Trans. Amer. Inst. Min. Met. Eng.*, **188,** 1460 (1950).
18. P. W. BRIDGMAN, *Proc. Amer. Acad. Arts Sci.*, **83,** 151 (1955).
19. C. S. BARRETT and O. R. TRANTZ, *Trans. Amer. Inst. Min. Met. Eng.*, **175,** 579 (1948).
20. W. L. BRAGG, *J. Sci. Instrum.*, **24,** 27 (1947).
21. G. D. ARCHARD, *Acta Cryst.*, **6,** 813 (1953).
22. VIERVOLL and H. OGRIM, *Acta Cryst.*, **2,** 277 (1948).
23. E. A. OWEN and R. G. WILLIAMS, *Proc. Phys. Soc.*, **A67,** 895 (1954).
24. L. PAULING, *J. Amer. Chem. Soc.*, **69,** 542 (1947).
25. J. THEWLIS, *J. Amer. Chem. Soc.*, **74,** 2279 (1953).
26. D. S. SUMMERS-SMITH, *J. Inst. Metals*, **81,** 73 (1952).
27. M. HANSEN, E. L. KAMEN, H. D. KESSLER, and D. J. MCPHERSON, *Trans. Amer. Inst. Min. Met. Eng.*, **191,** 881 (1951).
28. G. SACHS and J. WEERTS, *Z. Phys.*, **60,** 481 (1930).
29. H. JONES, *Phil. Mag.* (*Ser.* 7), **41,** 663 (1950).
30. B. J. PINES, *J. Exptl Theor. Phys. U.S.S.R.*, **3,** 309 (1940).

VOL.
4
1956

THE STRUCTURE OF LITHIUM-MAGNESIUM SOLID SOLUTIONS—II*

Measurements of Diffuse X-ray Scattering

F. H. HERBSTEIN† and B. L. AVERBACH‡

Diffuse X-ray scattering data from BCC solutions of Li-Mg alloys indicate a preference for unlike nearest neighbors, and the short-range order coefficients have been measured as a function of composition. Size-effect coefficients have also been determined, and these indicate that individual atoms are displaced from the average lattice sites. The lattice parameter minimum at 65 atomic per cent Li coupled with the variation of the size-effect coefficients with composition suggests that the Li-Mg interatomic distance is shorter than the average of the distances between like atoms, and the interatomic distances have been calculated. The hexagonal solid solutions appear to be almost random with no size effects.

LA STRUCTURE DES SOLUTIONS SOLIDES DE LITHIUM MAGNESIUM—II

Mesures de diffusion anormale des rayons X.

Les résultats de diffusion anormale de rayons X sur des solutions cubiques centrées d'alliages Li-Mg indiquent, pour un atome, une préférence marquée à s'entourer de premiers voisins différents de lui-même; les coefficients d'ordre à petite distance ont été mesurés en fonction de la composition. Les coefficients d'effet de taille ont également été déterminés: ils indiquent que les atomes individuels sont déplacés de leur position réticulaire moyenne. La comparaison du paramètre réticulaire, minimum pour une concentration atomique de 65% en Li, et des coefficients précédents, laisse supposer que la distance interatomique Li-Mg est moindre que la distance moyenne entre atomes identiques. Ces distances interatomiques sont d'ailleurs calculées. La structure des solutions solides hexagonales semble presque complètement résulter du hasard sans qu'aucun effet de taille n'intervienne.

DIE STRUKTUR VON LITHIUM-MAGNESIUM-MISCHKRISTALLEN—II

Messungen der diffusen Röntgenstreuung

Die Ergebnisse der diffusen Röntgenstreuung von kubischraumzentrierten Li-Mg-Legierungen zeigen eine Bevorzugung ungleichartiger nächster Nachbarn an. Die Nahordnungs-Koeffizienten wurden in Abhängigkeit von der Zusammensetzung gemessen. Ausserdem wurden Koeffizienten für den Grösseneffekt bestimmt. Diese zeigen Verrückungen einzelner Atome gegenüber den mittleren Gitterplätzen an. Das Minimum der Gitterkonstanten bei 65 Atom-Prozent Li zusammen mit der Variation der Grössen-Effekt-Koeffizienten mit der Konzentration deuten darauf hin, dass der Atomabstand Li-Mg kleiner ist als der Mittelwert der Abstände zwischen gleichartigen Atomen; die Atomabstände wurden berechnet. Bei den hexagonalen Mischkristallen scheint vorwiegend eine statistische Verteilung ohne Grössen-Effekt vorzuliegen.

1. INTRODUCTION

The lithium-magnesium system is an example of the extensive formation of solid solutions between atoms with small ion cores. Measurements of lattice parameters reported in Part I[1] of this series indicated that the Li-Mg distances in the BCC alloys are shorter than the mean of the interatomic distances between like atoms. Measurements of Bragg intensities indicated that there were appreciable static displacements of atoms from the sites of the average lattice.

In the present investigation the nearest-neighbor short-range order coefficients α_1, and the size effect coefficients β_1, were derived from measurements of diffuse X-ray scattering for seven BCC alloys at 295 and 93°K. Similar data were also obtained for two compositions in the HCP region. The local-order coefficients indicate a preference for unlike nearest neighbors in the BCC alloys, and the size-effect coefficients provide an independent confirmation of the displacements from the average lattice sites.

2. EXPERIMENTAL METHODS

2.1. *Diffuse scattering measurements.* The experimental procedures for measuring the diffuse scattering were essentially identical to those used in previous work in this laboratory.[2, 3] Geiger-counter spectrometer measurements were made on all samples, using the reflection method, with monochromatic Co$K\alpha$ radiation from a curved CaF_2 crystal focused

* Received October 3, 1955; revised version January 3, 1956. This work was sponsored by the U.S. Atomic Energy Commission under Contract AT(30-1)-1002.

† Present address: National Physical Laboratory, Pretoria, South Africa.

‡ Department of Metallurgy, Massachusetts Institute of Technology, Cambridge, Massachusetts.

on the specimen held in an evacuated chamber. For low-temperature measurements the specimen holder was cooled with a continuous stream of liquid N_2. Measurement of the specimen temperature with a calibrated thermocouple showed it to be at $93 \pm 5°K$, and it remained constant during the duration of a run (about four hours). The diffuse scattering measurements were put on an absolute scale by comparison with the independent scattering from a block of lucite, measured under identical experimental conditions.

This reflection spectrometer method has two drawbacks, (i) low resolving powder, (ii) inaccuracy at low scattering angles, and these measurements were therefore supplemented by transmission photography using samples normal and at 45° to the incident beam. The photographs were photometered, and these data were normalized with respect to the spectrometer measurements. A typical record of the experimental results is shown in Fig. 1.

The X-ray unit was run at 40 kV and 10 mA for most measurements. The fluorite monochromating crystal removed the $\lambda/2$ harmonic from the beam, but not the $\lambda/3$ harmonic. However, the latter was so weak that it did not affect the diffuse scattering pattern, although the $\lambda/3$ reflection from the (110) planes of the sample was observed as a small "pip" on the diffuse scattering curve. In this region the true shape of the curve was obtained by repeating the measurements with the tube run at 22 kV.

The spectrometer samples were taken from the same materials described in Part I and were in the form of plates 0.125 in. thick. This represents infinite thickness for all samples except the alloy with 89% Li, for which about 0.3% of the radiation was transmitted at normal incidence. All samples were checked by Laue photography for small grain size and randomness of orientation before use. It was found the alloys with more then 50% Li corrode (both oxide and nitride are formed) immediately on exposure to air. The procedure was therefore adopted of cleaning off the surface under toluene, and then transferring the sample to the specimen chamber while it was still wet with toluene. The toluene was removed during the evacuation of the specimen chamber. Examination after a run showed the surface to be still free of oxide; in addition, any oxide lines were immediately apparent on the scattering pattern, and no difficulty was experienced in interpolating through the few extra lines found in practice. Because of the high reactivity of the alloys, the diffuse scattering was not recorded at temperature, but was measured for samples quenched from 200°C.

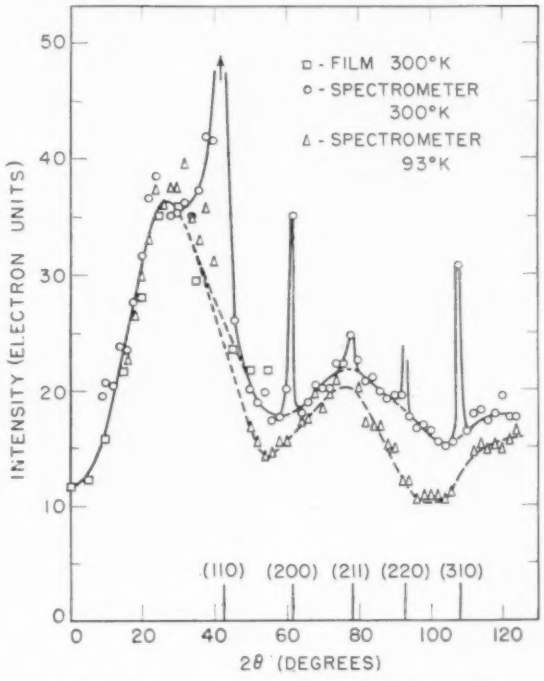

FIG. 1. Diffuse-scattering measurements for a 49 atomic per cent Li alloy, including film and spectrometer measurements at 295°K and spectrometer measurements at 93°K, with intensities in electron units.

Measurements were made at intervals of 2 degrees in 2θ with intermediate points measured where necessary. Approximately 1000 counts were recorded at each point. The standard deviation of the results due to statistical fluctuations was thus about 3%. Duplicate measurements were made on samples of the 40, 50, and 90% alloys, and the curves agreed within 7–8%. The major contribution to this discrepancy probably came from grain size and preferred-orientation effects.

2.2. *Corrections to the diffuse scattering.* The Compton modified contribution to the diffuse scattering was calculated, using the usual Compton-Raman formula.[4] The contribution arising from the thermal motion of the atoms was computed on the assumption of independent vibration of the atoms, with identical amplitudes of vibration for each atom. The temperature diffuse scattering for a polycrystalline sample is then:

$$\frac{I_T}{N} = [m_{\mathrm{Li}} f_{\mathrm{Li}}^2 + m_{\mathrm{Mg}} f_{\mathrm{Mg}}^2][1 - \exp(-2M)] \quad (1)$$

where N is the number of atoms in the atom, m_{Li} and m_{Mg} are the atomic fractions, f_{Li} and f_{Mg} are the respective atomic scattering factors, and M is the exponential factor defined by James.[4] Although the

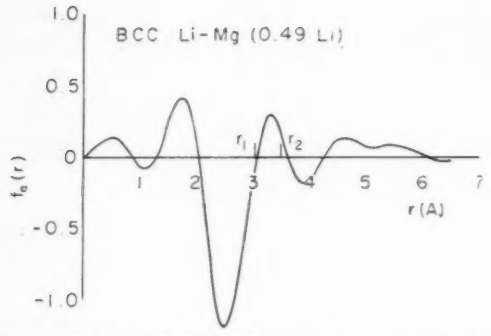

FIG. 2. The modified Fourier transform ($a^2 = 0.1$) of the corrected diffuse scattering shown in Fig. 1. The negative peak about r_1 is characteristic of the presence of short-range order. The displacement of this peak to smaller values of r indicates that β_1 is positive.

temperature diffuse correction is approximate, the final calculation of the short-range order and size-effect coefficients was performed by means of a Fourier analysis, which helps to isolate these effects from the others. As a result, the order and size coefficients could be determined with considerably more confidence than would be expected on the basis of these corrections.

2.3. *The analysis of the diffuse scattering curves.* In terms of local-order and atomic-size effects, the corrected diffuse scattering in a powder pattern is:[5]

$$I = Nm_A m_B (f_B - f_A)^2 \left\{1 + \sum_{i=1}^{i=\infty} \left[c_i \alpha_i \frac{\sin Sr_i}{Sr_i} + c_i \beta_i \left(\cos Sr_i - \frac{\sin Sr_i}{Sr_i}\right)\right]\right\} \qquad (2)$$

where I is the diffuse scattering in electron units, c_i is the number of atoms in the ith shell, r_i is the distance from a given atom to its ith shell of neighbors, $S = \frac{4\pi \sin\theta}{\lambda}$, and the other symbols have been defined previously.

The local atomic arrangement is described in terms of the short-range order coefficients, α_i, where

$$\alpha_i = 1 - \frac{c_i p_i^A}{c_i m_A} \qquad (3)$$

and p_i^A is the probability of finding an A atom in the ith shell about a B atom. The quantity $c_i p_i^A$ is thus the actual number of A atoms in the ith shell about a B atom, while $c_i m_A$ is the random number of A atoms in the ith shell about a B atom. The coefficients β_i depend on the local displacements of the atomic centers from the sites of the ideal lattice.

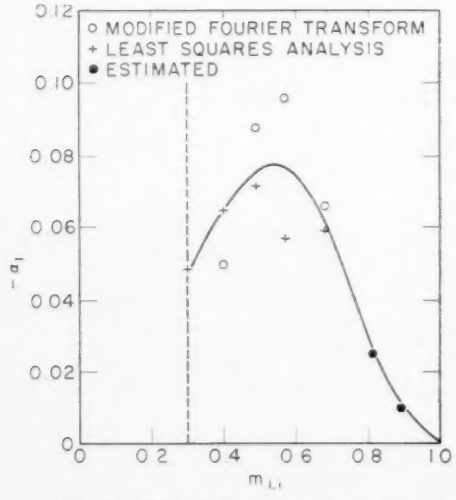

FIG. 3. The variation of α_1 with composition for the BCC alloys.

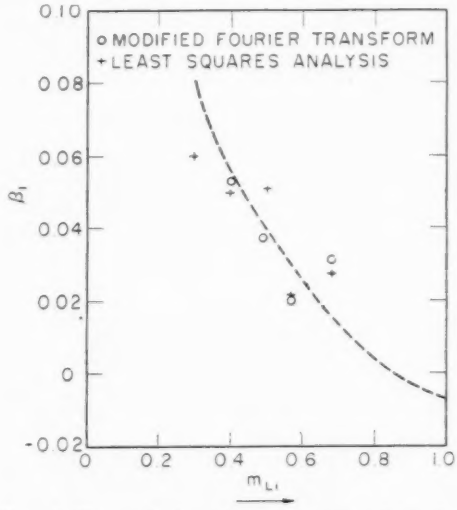

FIG. 4. The variation of β_1 with composition for the BCC alloys. The circles give the experimental points, while the dotted line gives the values of β_1 calculated on the assumption that the Li and Mg atoms retain the sizes characteristic of the pure metals while the Li-Mg distances are contracted.

The diffuse-scattering curves were first analyzed by the modified Fourier transform method,[6] in which the diffraction effects are reduced by the use of a damping factor of the form exp $(-a^2S^2)$. A typical transform is shown in Fig. 2. The transform has the negative peak characteristic of negative values of α_1: the displacement of this peak from the symmetrical position about r_1 is the evidence for the presence of a size effect. Quantitative analyses of the transforms for alloys with 40, 49, 57, and 68 atomic per cent Li were made, with the results shown in Figs. 3 and 4. Since the transforms showed that α_i and β_i were generally small for $i > 1$, an analysis of the curves by the method of least squares was also possible, and these results are also given in Figs. 3 and 4. The transform

of the alloy with 30 atomic per cent Li was not suitable for detailed analysis because of interference arising from a positive peak at r_2: this was probably due to the influence of the β_1 coefficient and to a small but appreciable value of α_2. It proved impossible to effect a separation of these two contributions to the transform, and reliance was placed mainly on the least-squares values of α_1 and β_1. There are also indications of small positive values for α_2 in the 40 and 49 atomic per cent Li alloys.

The modulations in the diffuse-scattering curves for the alloys with 12, 15, 81, and 89 atomic per cent Li were too small for either method of analysis to be practicable, and values of α_1 were estimated for these alloys from the shape of the diffuse intensity curves. The shape of the curves indicated that the size effect was negligibly small for these alloys.

The measured values of α_1 and β_1 were checked by calculating the diffuse-scattering curves from equation (2) and comparing these with the observed curves. An example is given in Fig. 5. The agreement, while not exact, was satisfactory in all cases and indicates that the diffuse scattering from the local atomic arrangements can be accounted for to a first approximation by the values of nearest-neighbor short-range order and size-effect parameters given in Figs. 3 and 4. Part of the discrepancy between the observed and the calculated curves may be ascribed to the inadequacy of the correction for the temperature-diffuse scattering.

From a comparison of the values of α_1 derived by the various methods of analysis of the experimental curves, it is considered that the mean values of α_1 are accurate to within about ± 0.01; the values of β_1 are probably accurate to within ± 0.005.

3. DISCUSSION OF RESULTS

A. *The BCC Alloys*

3.1. *The short-range order coefficients.* All of the BCC alloys exhibit a preference for unlike nearest neighbors (i.e. $\alpha_1 < 0$). The short-range order is most pronounced at the equiatomic composition (Fig. 3) in agreement with the predictions of the quasi-chemical theories which assume that chemical bonding factors are responsible for the preference for unlike neighbors. Even at the equiatomic composition, however, the preference for unlike neighbors is small. The present results indicate that an atom has 4.3 unlike nearest neighbors on the average in comparison to 4.0 in a random and 8.0 in an ordered solution. Comparable data for other BCC alloys are not available. In FCC alloys which do not order there are 6.2 unlike nearest neighbors in AuNi[2] and 6.5 in AuAg compared to 6.0 in the random solution.[7] In CuAu there are 6.8 unlike neighbors at 500°C (the critical temperature is 420°C), compared to 8.0 in the layered ordered structure.[7]

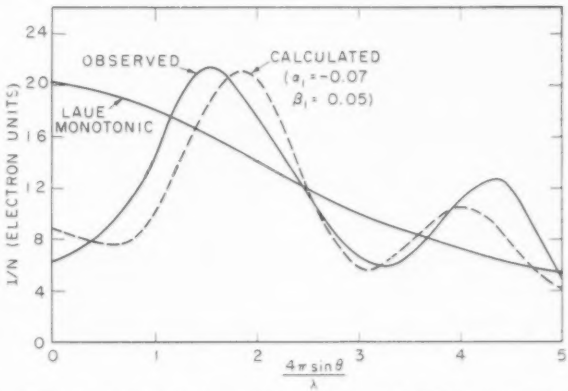

FIG. 5. A comparison of the observed diffuse-scattering curve for 49 atomic per cent Li alloy with the curve calculated using values of α_1 and β_1 from the least-squares analysis.

3.2. *Atomic displacements.* The displacements of the atoms from the sites of the average lattice are described by the parameters β_i, where

$$\beta_i = \left(\frac{1}{\eta - 1}\right)\left[-\left(\frac{m_A}{m_B} + \alpha_i\right)\varepsilon^i_{AA} + \left(\frac{m_B}{m_A} + \alpha_i\right)\eta\varepsilon^i_{BB}\right] \tag{4}$$

$$\eta = f_B/f_A, \qquad \varepsilon^i_{AA} = \frac{r^i_{AA} - r_i}{r_i}, \qquad \varepsilon^i_{BB} = \frac{r^i_{BB} - r_i}{r_i}$$

and r_i is the average radius of the ith shell as calculated from the lattice parameter, r^i_{AA} is the distance between an A atom and another in the ith shell, and similarly for r^i_{BB}.

The present measurements show that only β_1 is significant, and its variation with composition is shown in Fig. 4. Equation (4) may be recast in the form:

$$\varepsilon^1_{\mathrm{MgMg}} = D\,\varepsilon^1_{\mathrm{LiLi}} + E \tag{5}$$

where D and E as well as $\varepsilon^1_{\mathrm{MgMg}}$ and $\varepsilon^1_{\mathrm{LiLi}}$ are functions of composition. The existence of nonzero values of β_1 is unambiguous evidence for the displacement of atoms from the average sites, but more detailed information cannot be obtained without an additional relation between $\varepsilon^1_{\mathrm{MgMg}}$ and $\varepsilon^1_{\mathrm{LiLi}}$.

In the Au-Ni system the variation of β_1 with composition was linear, and it was assumed that $\varepsilon_{AA} = am_B$ and $\varepsilon_{BB} = bm_A$, where a and b are constants determined from the experimental data (8). The Au-Ni lattice parameters, however, were also almost linear with composition. The presence of a

VOL. 4 1956

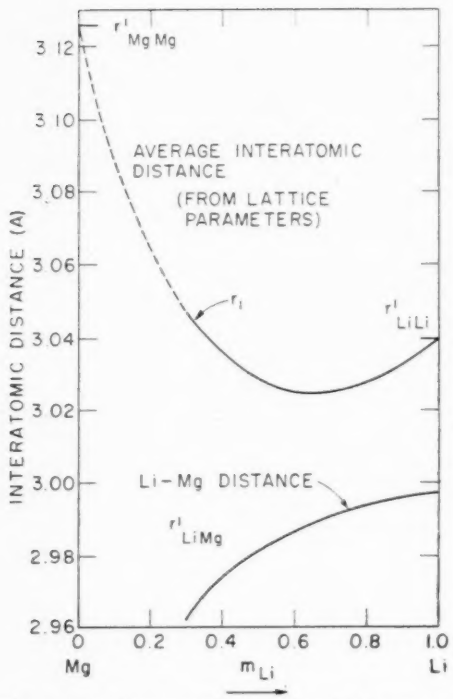

FIG. 6. The distance between Li and Mg atoms, calculated on the assumption that the Li and Mg atoms retain the radii characteristic of the pure metals while the Li-Mg distances contract.

minimum in the curve of lattice parameter vs. composition in BCC Li-Mg alloys (see Part I) suggests, however, that the distance between unlike atoms is less than the mean atomic diameter, and that the deviations from Vegard's law are due to a contraction of this kind rather than to variations in the radii of the atoms due to elastic forces.

Values of β_1 were therefore calculated on the assumption that both Li and Mg retain the radii characteristic of the pure metals. The Mg atom was considered to be in a hypothetical BCC state, and its radius was calculated from that of the HCP Mg, using Pauling's relation.[9, 10] The resultant variation of β_1 with composition (Fig. 4) is in fair agreement with the results. The value of r_1 is now (5):

$$r_1 = m_A[1 - m_B(1 - \alpha_1)]\, r^1_{AA} + 2m_A m_B(1 - \alpha_1) r^1_{AB} + m_B[1 - m_A(1 - \alpha_1)] r^1_{BB} \qquad (6)$$

where r_1 is the average nearest-neighbor distance obtained from the lattice parameter, $r^1_{\mathrm{LiLi}} = 3.040$ Å, and $r^1_{\mathrm{MgMg}} = 3.126$ Å, and the resulting variation of r^1_{LiMg} is shown in Fig. 6.

These results are in marked contrast to those for the Au-Ni alloys. In the latter system, values of β_1 calculated from the original sizes of the atoms were about four times the observed values, and the data were consistent with elastic changes in the interatomic distances independent of the identity of the nearest neighbors, i.e. $r_{AB} \approx \frac{1}{2}(r_{AA} + r_{BB})$. In the Li-Mg system, however, the data are consistent with the assumption that the Li-Li and Mg-Mg distances retain their original sizes, but that the Li-Mg distance is shorter than the average.

B. *The α-phase (HCP) Alloys*

Diffuse-scattering measurements were made on two α-phase alloys with 10 and 12.5 atomic per cent Li respectively, and these showed only very weak modulations. From these it was estimated that $\alpha_1 = -0.01$. The atomic arrangement in these alloys thus differs very little from random. In this respect the dilute HCP alloys are similar to the *dilute* BCC alloys, were the measured values of α_1 are also small.

C. *Deviations from Vegard's Law and the Short-range Order Coefficients of the BCC Alloys*

In Part I it has been pointed out that the presence of a negative deviation from Vegard's law in this system is in contradiction to the prediction of a simple elastic model of solid solutions.[11] Deviations from Vegard's law have been considered recently from another point of view by Fourner,[12] who attempted to relate these deviations to the degree of short-range order in the system. Fournet assumes a quasi-chemical model of a solid solution in which the internal energy can be represented as the sum of interaction energies between pairs of atoms, all other contributions to the internal energy being neglected. All of the atoms are taken to be at the lattice points (thus neglecting the size effects shown to be present here), and the effects of thermal agitation are neglected. The principal innovation of the theory is to consider explicitly the potential energy of a pair of atoms as a function of the distance between them. Taking into account first and second neighbors only, the function, $W(r) = W_{AA}(r) + W_{BB}(r) - 2W_{AB}(r)$, is minimized in order to find the interatomic distance at which the solid solution is stable. It is shown finally that the variation of lattice parameter with composition can be represented by

$$a - a_A = m_B(a_B - a_A) \times \left[1 + \frac{m_A}{m_A + Cm_B}(C + F - 1)\right] \qquad (7)$$

where a is the lattice parameter of a solid solution of composition m_A, m_B, and a_A, a_B are the lattice parameters of the pure metals A and B, with $a_B > a_A$;

$$C = \left(\frac{a}{\beta}\right)_B \Big/ \left(\frac{a}{\beta}\right)_A ; \quad \beta = \text{compressibility}.$$

When $(C + F - 1)$ is zero, equation (7) yields the expression for Vegard's law; when $F = 0$, the expression is applicable to an ideal solid solution with a random arrangement of the atoms for which $W(r) = 0$. Usually the sign of the deviation from Vegard's law is determined by the value of C; when $C < 1$, negative deviations are found, while the deviations are positive when $C > 1$. A value of $C = 7.3$ was estimated for these alloys, using the compressibility of hypothetical BCC Mg obtained by extrapolating the variation of compressibility with composition for the BCC Li-Mg alloys to $m_{Li} = 0$.[13] The value obtained is $\beta = 1.3 \times 10^{-12}$ cm²/dyne, compared to the value $\beta = 3.02 \times 10^{-12}$ cm²/dyne for HCP Mg.

The factor F is a correcting factor to allow for the departure of the solid solution from randomness. The observed variation of parameter with composition can be reproduced exactly by using the relationship, $F = -9.1 - 17.4m_{Mg}$.

The values of the short-range order coefficients were calculated (following Fournet) from F as follows:

$$F = \frac{\sum_i k_i c_i W'(r_i)}{2\alpha_A(r_B - r_A)} \qquad (8)$$

where $\sum_i$ represents a summation over pairs of atoms and is taken over the first two sets of neighbors; $k_i = r_i/r_1$, where r_i is the distance between ith neighbours, c_i is the number of atoms in the ith co-ordination shell, r_A and r_B are the nearest-neighbor distances in pure A and pure B;

$$\alpha_A{}^* = 4.5\left(\frac{r_2}{\beta}\right)_A ; \text{ and } W'(r_i) = \frac{\partial W(r_i)}{\partial r} = \frac{W(r_1) - W(r_2)}{r_1 - r_2} .$$

It is assumed that $W'(r_i)$ does not vary with r and that $W(r_2) = 0$. The latter approximation is justified by the experimental fact for Li-Mg alloys that the short-range order coefficient, α_2, is small. $W(r_1)$ can be found from (7) and (8), and this is then related to the short-range order coefficient by the equation,

$$\alpha_1 = (e^{-W(r_1)/kT} - 1)m_A m_B. \qquad (9)$$

The values of the short-range order coefficients corresponding to a temperature of 500°K were calculated, using these values of F, and are shown in Fig. 7. These computed values of α_1 are about

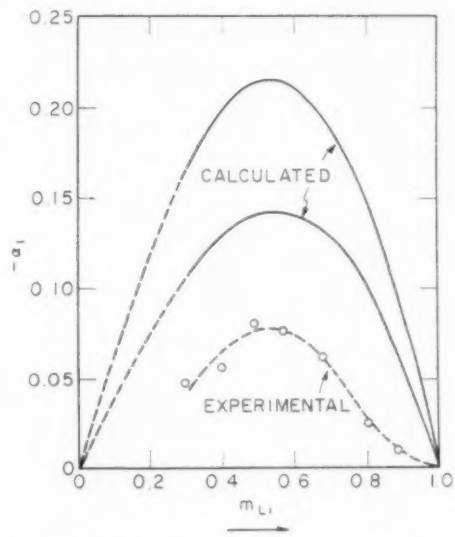

FIG. 7. A comparison of the short-range order coefficients α_1 calculated from Fournet's theory with the measured values. The upper curve was calculated using the compressibility estimated for hypothetical BCC Mg with $F = -9.1 - 17.4m_{Mg}$. The middle curve was obtained using the measured compressibility of HCP Mg with $F = -4.8 - 5.5m_{Mg}$. The experimental points are mean values taken from Fig. 3.

$2\frac{1}{2}$ times as large as the observed values, the discrepancy being well outside the limits of experimental error. Even if the value of β for HCP Mg is used in estimating C, the short-range order coefficients are still considerably larger than the observed values; these values of α_1 are also shown in Fig. 7. Thus values of F which reproduce the observed variation of lattice parameter with composition result in values of α_1 which are much too large; conversely, values of F which reproduce the observed variation of α_1 with composition ($F \approx -3.4$) give positive and not negative deviations from Vegard's law. From these results it is clear that Fournet's model of the solid solution is too simple to account for the observed variations of a and α_1 with composition in the β-phase alloys. This simple model neglects the displacements from the average lattice sites demonstrated experimentally by the values of β_1 in this paper and by the measurements in Part I, and also disregards the entropy arising from the thermal displacements which are sizable. The inclusion of a second-neighbor interaction energy, $W(r_2)$, in the calculation would also decrease the discrepancy in Fig. 7; this effect is small, however, since α_2 is almost zero.

D. *Correlation of the Data*

Both the Bragg intensity measurements in Part I and the values of β_1 obtained from diffuse-scattering data in this paper indicate that there are static

* α_A should not be confused with the symbol for the short-range order parameter αi.

VOL. 4 1956

displacements of the atoms from the average lattice sites. The minimum in the lattice parameters in the BCC alloys suggests that these displacements are due mainly to a shortening of the Li-Mg distances, rather than to changes in the atomic radii. As a matter of fact, the values of β_1 are consistent with an approximate model in which the Li and Mg atoms retain their original sizes and the Li-Mg distance is shortened by about 0.1 Å.

The contraction of the Li-Mg distance leads to the conclusion that there is a strong chemical bonding between unlike atoms, and according to the quasi-chemical theory this should result in a preference for unlike neighbors. This was observed, and all of the data are qualitatively compatible, but the theoretical basis for a quantitative correlation is lacking.

4. SUMMARY

The present measurements show that in the BCC alloys there is a definite, although not large, preference for unlike neighbors in the solid solutions. The variation of lattice parameter with composition shows a comparatively large negative deviation from Vegard's law, and there is a minimum in the curve at $m_{\mathrm{Li}} = 0.65$. The presence of a minimum in the curve of a against m_{Li}, coupled with the preference for unlike neighbors in the solid solution, and the variation of the size-effect parameters with composition, suggests that the Li-Mg interatomic distances are shortened relative to the sum of the atomic radii. The HCP α-solid solutions of Li in Mg show only slight deviations from randomness, and there appears to be a small preference for unlike neighbors.

An attempt was made to correlate the short-range order coefficients and the negative deviations from Vegard's law using Fournet's theory, but the agreement was poor.

5. ACKNOWLEDGMENTS

The authors are grateful to the Atomic Energy Commission for their sponsorship of the research, and to the Dow Chemical Company, and particularly to Dr R. S. Busk, for their assistance in furnishing the alloys and the analyses. The assistance of Robert Goss in the experimental phases of this investigation is also gratefully acknowledged.

REFERENCES

1. F. H. Herbstein and B. L. Averbach, *Acta Met.*, **4**, 407 (1956)
2. P. A. Flinn, B. L. Averbach, and M. Cohen, *Acta Met.*, **1**, 664 (1953).
3. P. S. Rudman and B. L. Averbach, *Acta Met.*, **2**, 576 (1954).
4. R. W. James, *The Optical Principles of the Diffraction of X-rays*, Bell, London, 1950; also A. H. Compton and S. K. Allison, *X-rays in Theory and Practice*, Van Nostrand, New York (1935).
5. B. E. Warren, B. L. Averbach, and B. W. Roberts, *J. Appl. Phys.*, **22**, 1493 (1951).
6. P. A. Flinn, B. L. Averbach, and P. S. Rudman, *Acta Cryst.*, **7**, 153 (1954).
7. B. E. Warren and B. L. Averbach, *Modern Research Techniques in Physical Metallurgy*, A.S.M. Cleveland, p. 95 (1953).
8. B. L. Averbach, P. A. Flinn, and M. Cohen, *Acta Met.*, **2**, 92 (1954).
9. L. Pauling, *J. Amer. Chem. Soc.*, **69**, 542 (1947).
10. J. Thewlis, *J. Amer. Chem. Soc.*, **74**, 2279 (1953).
11. B. J. Pines, *J. Exptl. Theor. Phys.*, U.S.S.R., **3**, 309 (1940).
12. G. Fournet, *J. Phys. Radium*, **14**, 374 (1953).
13. P. W. Bridgman, *Proc. Amer. Acad. Arts Sci.*, **83**, 151 (1955).

MAGNETICALLY INDUCED GRAIN-BOUNDARY MOTION IN BISMUTH*

W. W. MULLINS†

The various free energies which a magnetic field generates in the grains of a Bi polycrystal give rise to calculable forces on the grain boundaries. These forces produce a strong preferred orientation in a Bi sample undergoing grain-growth. The study of single boundaries driven by the known magnetic forces has permitted the estimation of an upper limit to the boundary free energy. In a number of samples the boundaries exhibit a type of sticking that does not seem to be due to impurities. A new hypothesis is considered which explains this variation of mobility in terms of changes in the concentration of vacancies at the grain boundaries.

MOUVEMENT DE LIMITE DE GRAINS INDUITE MAGNETIQUEMENT DANS LE BISMUTH

Les énergies libres variables obtenues par un champ magnétique dans les grains d'un polycristal de Bi donnent lieu à des forces calculables dans les limites des grains. Ces forces produisent une orientation préférentielle marquée dans un échantillon de Bi au cours d'un grossissement de grain. L'étude du mouvement de frontières individualles sous des forces magnétiques connues a permis l'estimation d'une limite supérieure pour l'énergie libre de la frontière. Dans certains échantillons, les frontières montrent un comportement qui ne semble pas être dû aux impuretés. Une hypothèse nouvelle est considérée qui explique cette variation de mobilité en termes de modifications dans la concentration des lacunes aux joints.

MAGNETISCH INDUZIERTE KORNGRENZEN-WANDERUNG IN WISMUT

Die unterschiedlichen Werte der freien Energie, die ein magnetisches Feld in den Körnern eines Bi-Vielkristalls hervorruft, verursachen Kräfte auf die Korngrenzen, die man berechnen kann. Diese Kräfte führen in einer Bi-Probe, in der Kornwachstum stattfindet, zur Ausbildung einer ausgeprägten Vorzugsorientierung. Die Untersuchung einzelner, durch die bekannten magnetischen Kräfte angetriebener Korngrenzen, erlaubte, eine obere Grenze für die freie Energie der Korngrenzen abzuschätzen. Bei einer Anzahl von Proben zeigte sich, dass die Korngrenzen festgehalten wurden und zwar in einer Weise, die nicht auf Verunreinigungen zurückzugehen scheint. Eine neue Hypothese, die diese Änderung der Beweglichkeit mit Hilfe von Veränderungen der Leerstellenkonzentration an den Korngrenzen erklärt, wird erörtert.

VOL. 4 1956

INTRODUCTION

From the macroscopic point of view, a grain boundary is an internal surface, in a single-phase material, across which there is a discontinuity of crystal orientation. It shares in common with interphase surfaces the property of a free energy per unit area. At high temperatures it is able to move under driving forces by invading one crystal and enlarging the other in its wake. These two properties of free energy and mobility have been effectively used to explain the structure and the dynamic features of the boundaries in a metal polycrystal. Thus, because of its free energy, a mobile boundary will always tend to diminish its area when subject to no other driving force. This determines the angles of intersection of boundaries according to their free energies or tensions,[1] and implies the motion of curved boundaries toward their centers of curvature.[2] The importance of the latter as the elementary process operating in normal growth has been recognized and emphasized by Harker and Parker,[3] Smith,[1, 4] and Burke.[5] If the polycrystal is strained, the boundaries will invade the metal of high strain energy, thereby enlarging the low-energy crystals behind it.[2] The study of boundary motion under these two types of driving forces, surface and strain-free energy, has recently been reviewed by several authors.[6]

In the atomistic approach to grain boundaries, one attempts to deduce their properties (free energy, mobility, etc.) from an atomic model. Low-angle boundaries ($\leq 10°$) may be represented as suitable arrays of widely spaced dislocations. By the application of elasticity theory, Reed and Schockley[7] have calculated the energy of such boundaries, and their motion under an applied shear stress has been predicted. The experiments of Dunn[8] and of Aust and Chalmers[9] on boundary energies, and of Washburn and Parker[10] on the stress-induced migration of boundaries, confirm the theoretical predictions.

* Received September 18, 1955.

† Westinghouse Research Laboratories, East Pittsburgh, Pennsylvania.

For higher-angle grain boundaries ($\geq 10°$), which predominate in a random polycrystal, the dislocation representation loses its uniqueness and its amenability to treatment by elasticity theory. In this case we turn to the experimental observation that intersection angles in such a polycrystal show that most of the boundaries have roughly equal free energies.[1] This suggests that a high-angle boundary has a disorganized liquid-like structure which is rather insensitive to the crystal orientations. Its motion, in contrast to that of simple low-angle boundaries, is an activated process in which the atoms of each crystal require a surplus of free energy to surmount and cross the energy barrier of the boundary.

The underlying objective in the work reported here has been to find some artificial way of exerting a known force on grain boundaries. Study of the response of the boundaries to this artificial driving force would permit the deduction of grain-boundary properties. A method employing the action of a strong magnetic field on hot polycrystalline bismuth seemed the most promising. The results that have been obtained by this method, in addition to those that may be obtained with a modification of present technique, promise much information about grain boundaries.

Goetz[11] has investigated the orienting effect of a magnetic field on Bi during its solidification. More recently, and more closely related to the work reported in this paper, is the investigation by Smoluchowski and Turner[12] of the preferred orientation produced by annealing an iron-cobalt alloy in a magnetic field. The details of this effect, however, are rather different from those occurring in Bi, due in part to the role played by magnetostriction in the iron-cobalt alloys.

BOUNDARY DRIVING FORCES

A driving force occurs when a free-energy change accompanies boundary displacements. Dividing the energy change by the displacement and the boundary area, we obtain the force per unit area or pressure, on the boundary. For example, a piece of a boundary whose radii of curvature on perpendicular sections are R_1 and R_2, will lose area and hence free energy as it moves toward its nearest center of curvature. This area loss is easily calculated,[13] and results in a pressure

$$p = \sigma\left(\frac{1}{R_1} + \frac{1}{R_2}\right) = \sigma K \qquad (1)$$

where K is the mean curvature at the point in question and σ is the free energy per unit area.

To obtain an artificial driving pressure, one needs to create conditions that cause a free-energy change to accompany boundary displacements. Two methods by which this may be done are to influence the free energy of the boundaries themselves or to influence the free energy of the crystals only.

A. *Gradient Method*

The first method depends upon establishing, in a polycrystal, a gradient of a quantity Q upon which the boundary free energy depends (e.g., Q = temperature, hydrostatic pressure, concentration of solute). Since a boundary can then lower its free energy by moving in the direction of appropriate change in Q, a driving pressure results. The calculation of this pressure is complicated by irreversible effects in the cases of the concentration and temperature gradients. Suzuki[14] has investigated the effect of a temperature gradient on boundaries. The author has tried the case of the pressure gradient, but was unable to obtain centrifugal fields large enough to move grain boundaries.

B. *Volume Free-energy Method*

1. *General account.* The pressure induced by the gradient method depends on the properties of the boundary. Let us now consider the second method in which the induced pressure is independent of the boundary properties and derives only from the fact that a boundary is an abrupt change of crystal orientation. Evidently one needs a single-phase polycrystal whose grains are anisotropic in a property that will allow a directed physical agent to generate various free energies in them, depending on their orientation. Grain boundaries will then experience pressures driving them from crystals in which the free energy is lower into those in which it is higher. These conditions are provided: by the action of a magnetic field on a polycrystal of a substance anisotropic in permeability; by the action of an electrostatic field on a polycrystal of an insulator anisotropic in dielectric constant; and by the application of a stress to a polycrystal of a substance anisotropic in elastic constants. We shall discuss at length the magnetic pressures utilized in the experiments and shall present the electrostatic and elastic stress cases only briefly in the Appendix.

2. *Magnetic pressures.* Consider a bicrystal of a substance that is anisotropic in magnetic susceptibility. Let $f_1 < f_2$ be the magnetic free energies per unit volume respectively induced in the two crystals by a uniform field H. Let a little cylinder of boundary with base dS and length dL (see Fig. 1) invade

crystal 2. Then, if f_1 and f_2 are independent of the boundary shape and position, the reversible change of free energy in this displacement determines the boundary pressure by $pdSdL = -(f_1 - f_2)dSdL$, or $p = f_2 - f_1$. This is a true pressure acting everywhere normal to the boundary.

As stated, this result is valid only if f_1 and f_2 are independent of the crystal shapes and sizes. The condition for this to be the case can be shown[15] to be $k \ll 1$. Then the density of magnetic free energy becomes $f = -\frac{1}{2}\,\boldsymbol{H}\cdot[k]\cdot\boldsymbol{H} = -\frac{1}{2}k_H H^2$, where $k_H = \dfrac{\boldsymbol{H}\cdot[k]\cdot\boldsymbol{H}}{H^2}$ is the susceptibility in the direction of the field. By substitution, we find the pressure on the boundary of a bicrystal situated in a uniform applied field H to be

$$p = f_2 - f_1 = \tfrac{1}{2}H^2(k_{H_1} - k_{H_2}) \qquad (2)$$

where k_{H_1} is the susceptibility of crystal 1 along the field, and similarly for k_{H_2}. Thus we see that when $k \ll 1$, p depends only on the strength of the field and its orientation with respect to the two crystals. Notice also that the direction of p remains the same when the sense of the field is reversed.

If $k \gtrsim 1$, the demagnetizing fields are comparable to the applied field, and the description of energies and boundary pressures becomes tractable only when the sample has a simple shape. For example, the bicrystal shown in Fig. 2 has its ends and its boundary parallel to the magnet pole pieces. The surplus of induced south poles on the boundary, arising from the discontinuity of H given by $\mu_1 H_1 = \mu_2 H_2$ provides a simple picture of the pressure exerted by the field tending to increase the crystal of largest μ. We shall defer the discussion of the pressure on such a boundary to the analogous cases of the electrostatic and elastic fields considered in the Appendix.

Let us see what form equation (2) assumes for the case of Bi which is magnetically uniaxial with $k \ll 1$. Suppose $k_\perp$ and $k_\parallel$ are the susceptibilities parallel and perpendicular to the trigonal or c axis, respectively. Take the field direction as the polar axis and θ as the polar angle of the c axis. Then by elementary crystal physics $k_H = \dfrac{\boldsymbol{H}\cdot[k]\cdot\boldsymbol{H}}{H^2} = k_1 + \Delta k\,\cos^2\theta$, where $\Delta k = k_\perp - k_\parallel$. Substituting this expression into equation (2), we find the pressure on a boundary between two Bi crystals whose c axes make angles θ_1 and θ_2 with the field to be given by

$$p = \tfrac{1}{2}H^2(k_{H_1} - k_{H_2}) = \frac{\Delta k}{2}H^2\,(\cos^2\theta_1 - \cos^2\theta_2). \qquad (3)$$

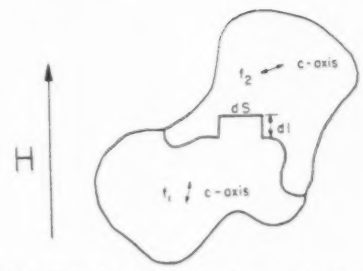

FIG. 1. Bi bicrystal of arbitrary shape with free energies $f_1 < f_2$. Boundary is urged into crystal 2.

When $\theta_1 = 0$, $\theta_2 = \pi/2$, a maximum pressure of $\frac{1}{2}\Delta k H^2$ results, whereas, to have a vanishing pressure, the crystal orientations need not be identical but only $\theta_1 = \theta_2$. The dependence of p on the field through H^2 gives a premium to high fields. To form an estimate of a possible boundary pressure for Bi, take $H = 80{,}000$ gauss (easily obtained in a Bitter magnet) and $\Delta k = 1.8 \times 10^{-6}$, then $p_{\max} \sim 5800$ dynes/cm^2. It follows from equation (1) that this pressure is comparable to that operating on a boundary with a radius of curvature of $\sim$1 mm (assuming $\sigma \sim 300$ ergs/cm^2). Since such pressures produce normal grain-growth, the magnetic field may be expected to have a large effect.

To understand the production of a preferred orientation, assume that we have a Bi polycrystal in which the orientations and sizes of the crystals are purely random. Consider the group of grains of orientation between θ and $\theta + d\theta$. The average magnetic pressure on the faces of these grains, taken $+$ if it tends to expand and $-$ if it tends to shrink the grain, is easily found by using equation (3) and the assumption of randomness to be $\bar{p}\theta = \frac{1}{2}\Delta k H^2 (\cos^2\theta - \frac{1}{3})$. Therefore, the magnetic pressures tend initially to expand grains of $\theta < \cos^{-1} 1/\sqrt{3} \simeq 55°$ and to shrink grains of $\theta > 55°$. This leads to a development of a preferred orientation with a greater volume of crystals whose c axes form small angles with the field.

MOBILITY

Smoluchowski[16] and Turnbull[17] have shown that a driving pressure p, acting on a grain boundary,

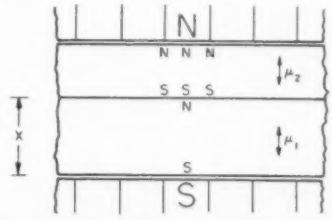

Fig. 2. Diamagnetic bicrystal with $\mu_1 > \mu_2$. Field urges boundary upward.

will move it at a speed S given by

$$S = \frac{p\alpha}{kT} A e^{-g/kT} \tag{4}$$

where g is the Gibbs free energy of activation of the elementary process that enables atoms to surmount and cross the boundary, A is a constant, α is the product of the area/atom and the boundary thickness, or approximately $3a^3$, where a is the lattice constant. Equation (4) is valid in the usual case that $p\alpha/kT \ll 1$. For example, in our case, $p < 10^4$ dynes/cm^2, $T \sim 500$°K, so that

$$\frac{p\alpha}{kT} \leq \frac{3(3 \cdot 10^{-8})^3\, 10^4}{1.36 \times 10^{-16} \times 500} = 10^{-5}$$

It is a simple consequence of the derivation of equation (4) that, during the time in which the driven boundary progresses one lattice spacing, an atom flanking the boundary will cross over an average of $\sim kT/p\alpha$ or 10^5 times under the conditions stated above. Hence, the progressive motion of the boundary can have very little influence on its structure.

Rewriting equation (4), we have $S = pM$, where $M = \frac{B}{T} e^{-g/kT}$ is defined as the mobility, or speed per unit pressure. It is seen to have the usual activation dependence on the temperature and otherwise depends on the details of the diffusion process. Of course, any progressive change in the state of the boundary (its density, concentration of solute) could destroy the proportionality of speed to pressure by continuously affecting the value of M.

Using equation (1), we have for normal grain-growth $S = pM = K\sigma M$. Isothermal grain-growth has been studied,[18] partly for the purpose of obtaining information on such questions of boundary migration as the constancy of M and the activation energy of migration. Analysis of the results in terms of single boundary motion is extremely difficult, however, due to such factors as the dependence of M on orientation and the complicated geometrical evolution of the system. It is hoped that the study of single Bi boundaries driven by a known magnetic pressure will help illuminate some of the central problems concerning mobility: the orientation and temperature-dependence of M; why M is so low in a casting; why grain-growth slows down and stops before it is theoretically complete; what is the cause of the sample size limitation discovered by Beck.[18] A hypothesis that might explain some of these phenomena and account for the results of the magnetic experiments will be discussed later.

PLAN AND PREPARATION OF EXPERIMENTS

General Account

It was planned to measure the boundary tension by grooving a circular V notch around each sample. Under conditions of ideal grain growth, one of the shrinking boundaries would become trapped across the area constriction of the notch. The imposition of the field was expected to bulge out this hung boundary until the restoring effect of its tension just balanced the magnetic pressure. The tension could be calculated from the measurement of the boundary's curvature, the crystal orientations, and the value of the field.

Cast boundaries were ruled out for such experiments, because it was found that they would not move when under pressures (exerted by their tension and curvature) comparable to those obtainable by magnetic means. Furthermore, it was found that in recrystallized metal, boundaries which had come to rest after undergoing grain-growth were unaffected by the imposition of the field. It was concluded that the magnetic pressures should be imposed on boundaries of proven mobility, i.e. those undergoing grain-growth.

Therefore, the plan of the experiment was: (1) to fabricate notched samples from extruded rods of the zone purified Bi; (2) to anneal them to start grain-growth (the furnace was inside the Bitter magnet); (3) to turn the magnetic field on while the boundaries were still mobile; (4) to leave it on until all boundary motion had ceased; (5) to remove and examine the samples, ensuring that no further boundary motion occur. The details of these experiments are described shortly.

Reasons for Selecting Bi

The important prerequisites of a material whose boundaries are to be studied by the magnetic method are: (1) magnetically anisotropic with the differences of principal susceptibilities large, while no susceptibility exceeds $\sim 10^{-2}$; (2) retention of the first prerequisite at temperatures of good grain-boundary mobility, which preferably should be ~200–500°C; (3) negligible secondary effects of magnetostriction and anisotropy of thermal expansion.

Bismuth seemed to be the best prospect. It is uniaxial in its diamagnetic properties[19] with $\Delta k = 1.76 \times 10^{-6}$ at 250°C and 2.30×10^{-6} at 200°C,

which were the two temperatures employed. Kapitza[20] has verified that $[k]$ is independent of H up to 250,000 gauss. From another investigation of Bi by Kapitza,[21] we conclude that the energies associated with magnetostriction at 10^5 gauss are less than 1% of the magnetic free energies, and may be neglected.

Bismuth melts at 271.3°C. Its grain boundaries behave in the usual way with, however, a greater sensitivity to trace impurities and a greater tendency to exaggerated growth than is the case for many metals. Any strain resulting from the anisotropy of thermal expansion coefficient ($\sim 4 \times 10^{-6}$) would diminish during isothermal annealing, and should certainly be relaxed on boundaries spanning the sample.

Preparation of Samples

The Bi, obtained from Cerro DePasco, was melted in a graphite boat and subjected to a reducing atmosphere of hydrogen. It was then sealed off in a glass tube and refined by zone melting.[22] Approximately twenty zones, produced three at a time by small resistance furnaces, were passed along the metal. The ratio of the length of a liquid zone to that of the entire rod was 0.1. 20% of the zone-processed metal, comprising the end presumed to be dirty, was rejected. The remainder, cast into a cylindrical ingot 1 in. in diameter, was extruded at 250°C to a $\frac{5}{16}$-in. rod. These rods were sectioned into $\frac{1}{2}$-in. lengths with a fine jeweler's saw, which was also used to cut the circular grooves around the sample. A layer of Bi approximately 0.020 in. thick, comprising the metal distorted by sawing, was removed with HNO_3.

Analysis of Samples

After treatment in the field, the Bi samples were prepared for metallographic examination by sectioning them (usually in the plane of their cylindrical axis) with a fine jeweler's saw. The orientation of individual grains was determined from back-reflection Laue photographs. The preferred orientation of the polycrystalline samples consisted in a clustering of crystallite c axes about a single direction, with approximate isotropy in the perpendicular plane. The extent of this clustering was determined by measuring the sample's magnetic anisotropy, in the plane containing the preferred direction, by means of a torsion balance.[23] The difference of principal susceptibilities so obtained was always divided by the maximum susceptibility difference of a single crystal of the same mass to obtain a figure called the fractional anisotropy (FA). This figure can be visualized as the fraction of the samples' crystallites, otherwise randomly oriented, that should have their c axes parallel in order to give the observed anisotropy.

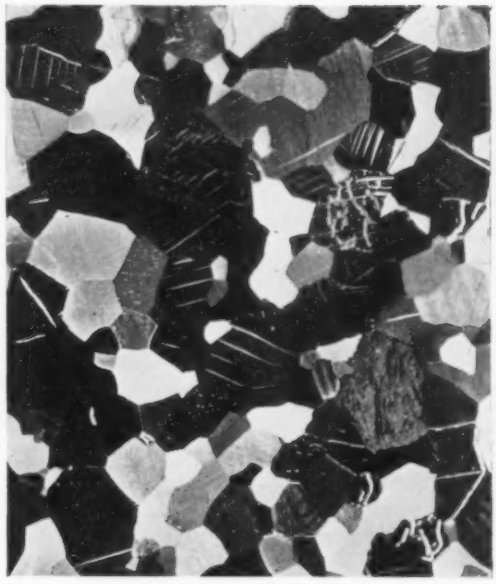

FIG. 3. Bi as extruded. ×12

Grain Orientation and Growth Characteristics (No Magnetic Field)

Purification by zone melting was found to greatly increase the mobility of Bi boundaries. Thus, before zone refining, grains of the extruded rod (having an average diameter 0.4 mm, as shown in Fig. 3) grew to ultimate sizes typified by Fig. 4, whereas, after zone refining, the larger ultimate grain size is shown in Fig. 5. Similarly, 0.38 of the zone-refined samples, when annealed, developed boundaries on their notches (Fig. 5), whereas this never occurred in samples of the original metal. Finally, extrusion and annealing of the impurity-rich ends of the zone-refined Bi charges gave an ultimate grain size much smaller than that of the original metal.

Zone melting concentrated 0.02% Ag and 0.03% Cu in the end of the Bi charge toward which the liquid zones moved, leaving the remainder with only 0.001% metallic impurities, according to spectroscopic analysis. It was not determined whether Ag, Cu, or some other concomitantly removed impurity or inclusion was the detriment to grain-growth.

The Bi rod had a preferred alignment of c axes

VOL. 4 1956

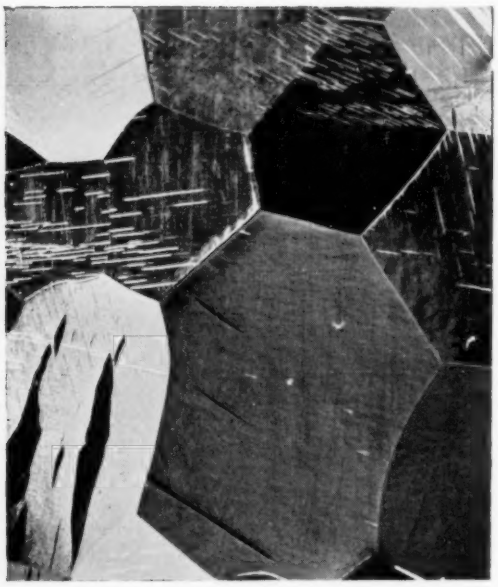

FIG. 4. Ultimate grain size prior to zone melting. ×12

along the extrusion direction which increased with lower extrusion temperatures. Magnetic measurement of this alignment for extrusion temperatures of 250°C and 80°C gave FA = 0.12 and 0.30 respectively.

MAGNETIC EXPERIMENTS

Equipment

The Naval Research Laboratory, Washington, D.C., kindly made available their air-core Bitter magnet to supply the strong fields requisite to the experiment. Steady fields of 70,000 to 80,000 gauss may be obtained in the central portion of the solenoid hole, $1\frac{1}{8}$ in. in diameter. A slender resistance furnace closed at one end and half-filled with silicone oil was situated vertically in the magnet. The samples, fastened to a long holder, were positioned under the oil, which promoted uniformity of temperature and prevented excessive oxidation of the Bi. An electronic controller, of the proportional type, maintained the temperature variation within 1°C.

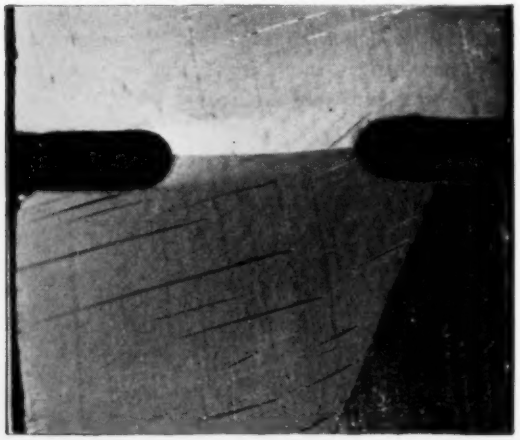

FIG. 5. Ultimate grain size after zone melting. ×12

Procedure

The principal variables of the experiments were time, temperature, and magnetic field. To ensure good boundary mobility, the temperature used was 250°C. The field strengths were 50,000 and 80,000 gauss. Various intervals of time were tried between the commencement of grain-growth upon plunging the samples into the hot oil, and the imposition of the magnetic field. This annealing, prior to switching on the field, will be termed preannealing. Preanneal times of 0 min, 4 min, 15 min, and 30 min were employed. One half-hour of additional annealing with the field proved sufficient to complete all boundary motion.

Results and Interpretation

The results are organized to emphasize three main points: the general nature of the effects produced by the magnetic pressures; the estimation of an upper limit to the boundary free energy in Bi; the phenomenon of the sticking of the grain boundaries.

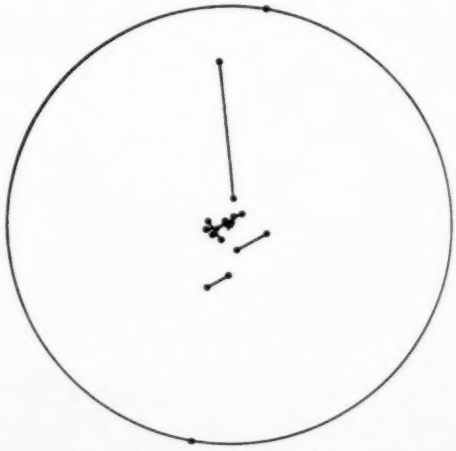

FIG. 6. Stereographic projection of the *c* axes of crystal pairs flanking hung boundaries. Pole axis (+) coincides with cylindrical axis of samples and with magnetic field. Treatment: Temp. = 250°C, 15 min preanneal with $H = 0$, then $H = 77{,}600$ gauss for ~half-hour.

1. *General nature of effect.* Table 1 and the polar projections of Figs. 6–8 summarize the results of the various preanneal treatments at 77,600 gauss and 250°C. When no preanneal is given, the induced anisotropy is the largest and, correspondingly, the average pressure on the hung boundaries is the

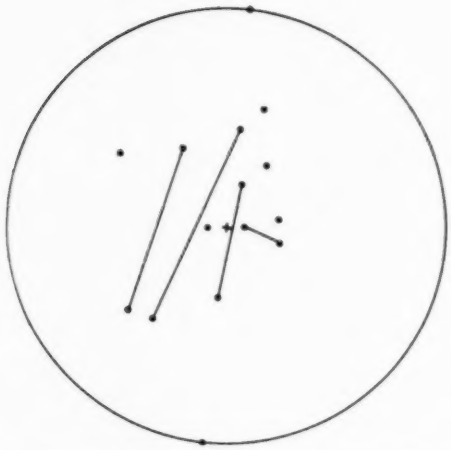

FIG. 7. Stereographic projection of the c axes of crystal pairs flanking hung boundaries and some large crystals. Pole axis coincides with cylindrical axis of samples.
Treatment: Temp. = 250°C, annealed for half-half-hour without field.

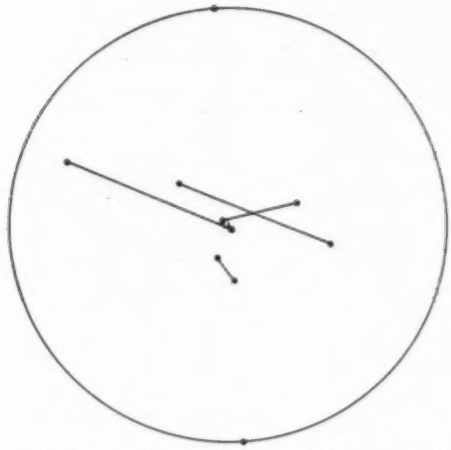

FIG. 8. Stereographic projection of the c axes of crystal pairs flanking hung boundaries. Pole axis (+) coincides with cylindrical axis of samples and with magnetic field.
Treatment: Temp. = 250°C; 30 min preanneal with $H = 0$, then $H = 77{,}600$ gauss for half-hour.

smallest. Presumably there are many grains having mobile boundaries and having c axes parallel to the field in the original sample (~2000 grains). These grains are encouraged to grow, impinge on each other, and result in a highly oriented sample having many low-energy boundaries with weak magnetic pressures (see the crooked boundaries of Fig. 9). Thus, as Table 1 shows, growth stops with more grains per sample than would occur in an anneal with no field.

Consider next the group of samples preannealed 15 min prior to the imposition of the field (77,600 gauss). Here growth has proceeded until there are ~20 grains per sample when the field is switched on. A crystal of favourable orientation may be expected to sweep out each half of the sample. These crystals would then form a low-force boundary where they meet at the notch. This picture is confirmed by the high fraction of hung boundaries (0.89) and by the low number of grains per sample obtained in this treatment. Also, the polar diagram of Fig. 6 shows the marked alignment of crystals flanking the hung boundaries. (The corresponding diagram of samples annealed with no field is shown in Fig. 7.)

The grains of the 30-min preanneal group have nearly grown to completion (~6 grains per sample) prior to the imposition of the field. The small average number of grains in each half of the sample reduces the chances of one of them having its c axis nearly parallel to the field. This fact, combined with some probable sticking (reduced mobility due to impurity trapping or other causes discussed shortly), explains the reduced fraction of hung boundaries, the greater average pressure on them, and the diminished clustering in the polar plot of Fig. 8.

Finally, the 4-min preanneal samples, while sharing the qualitative features of the other groups, seem to have a lower anisotropy and higher average hung-boundary pressure than the trend of Table 1 would indicate. This diminished effect of the field may be due to a kind of growth competition between the larger number of favorable grains present after 4 min than after 15 min preannealing. This kind of competition, which is less pronounced in the 0-min preanneal group, is consistent with the

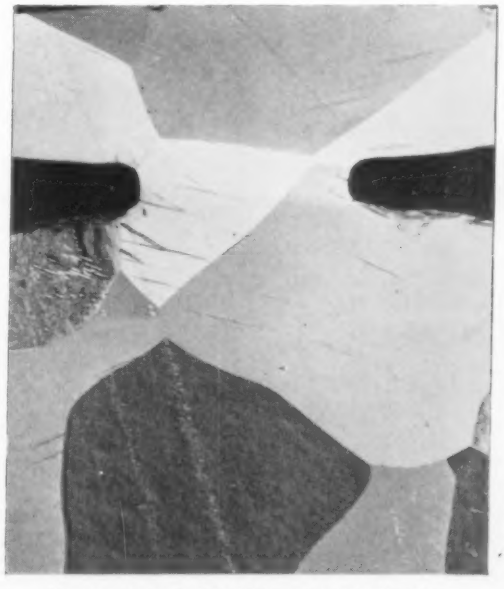

FIG. 9. Annealed half-hour at 250°C with $H = 77{,}600$ gauss. ×12

VOL. 4 1956

TABLE I

		No field	Number of minutes preannealed			
			0	4	15	30
Number of samples	In tota	16	9	33	9	6
	With single hung boundaries	6	3	8	7	4
	With double hung boundaries	1	0	6	1	0
Fraction of samples with any hung boundaries		0.38	0.33	0.43	0.89	0.66
Fractional magnetic anisotropy	of crystals flanking hung boundaries	0.25 ± 0.05	0.92	0.74	0.81	0.65
	of samples without hung boundaries	0.25 ± 0.05	0.87	0.81	0.59	0.3
Average magnetic pressure on the hung boundaries		—	0.03	0.26	0.15	0.40
Average number of grains per sample	in samples with hung boundaries	3.7	5.0	3.6	2.5	3.2
	in samples without hung boundaries	7.2	17.0	4.6	4.5	4.5

All temperatures are 250°C. All fields are 77,600 gauss Maximum magnetic pressure is 5280 dynes/cm².

explanation of some other results discussed shortly.

Nineteen of the fifty-seven samples treated in the field developed single hung boundaries (as in Fig. 5). Only three of these boundaries were strongly curved (Fig. 10), the remaining sixteen were all straight ($R \geq 0.8$ cm). This is not surprising in twelve of the straight cases, since analysis showed the magnetic pressure on these boundaries had been less than 0.10 maximum. (Maximum magnetic pressure at 250°C and 77,600 gauss is 5280 dynes/cm².) The other four straight boundaries (all from the 4-min preanneal group) appeared, however, to have stuck, for they had large pressures of 0.11, 0.18, 0.33, and 0.81 maximum. Additional instances of sticking are provided by the pairs of so-called double hung boundaries (see Fig. 12) occurring in three samples of the 4-min preanneal group. In these three cases, the parallel pairs of hung boundaries have resisted substantial pressures tending to drive them together. These pressures were 0.44 and 0.39, 0.37 and 0.01, 0.01 and 0.23 maximum, respectively.

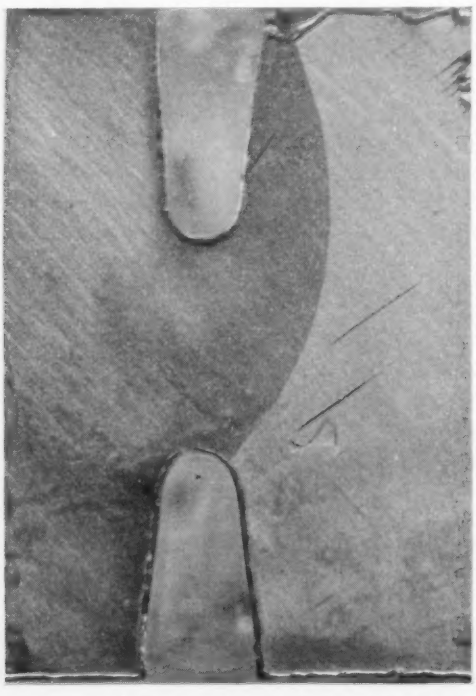

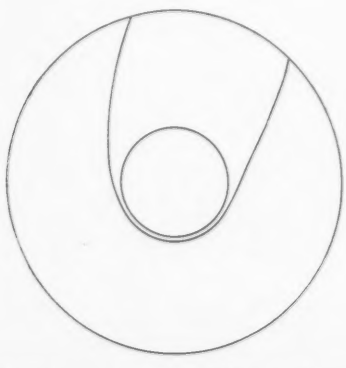

FIG. 10. Magnetic pressure of 4480 dynes per cm² (→) on boundary $T = 250$°C. ×12

Let us emphasize that a boundary never gets stuck while straightening out across the notch (at least, not until $R \gtrsim 0.8$ cm). This is true even when there is no field so that the driving force decreases to zero as the boundary straightens. Instead, the difficulty arises in trying to drive a boundary through the notch so that it bulges into the other crystal. Before we try to explain this type of sticking, let us examine the strongly curved boundaries.

2. *Estimation of boundary tension.* Each of the three curved boundaries, typified in the longitudinal section shown in Fig. 10, was bent in the direction favored by the magnetic pressure. It is evident, however, from the drawing of the end view at the notch shown in Fig. 10 that the boundary was not held up by the notch over its entire perimeter (true of all three curved boundaries).

Despite the appearance, it is believed that the boundary was not driven off of the notch from a hung condition. The reasons are as follows: many other hung boundaries with large pressures remained straight; the boundary in question is not bowed out into a hemisphere symmetrically meeting the notch at right angles, as it should be for ideal escape; the assumption that the center stuck, leaving only one sharply curved side to be forced off the notch, requires a boundary tension ($\sim$80 ergs/cm^2) lower than is consistent with the large induced anisotropy effect; furthermore, such heterogeneous sticking is inconsistent with the uniform curvature of the boundary.

It is proposed that the three curved boundaries were each laid down by the type of process depicted in Fig. 11. In this case, the boundary was never entirely on the notch and the bulge was produced and maintained by the action of the magnetic pressure during the last stages of grain-growth. Since we have seen that free boundaries are able to flatten out or decrease their area, it is inferred that the three strongly curved boundaries were prevented

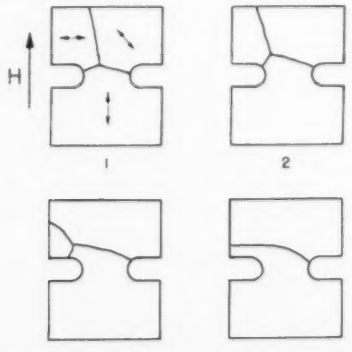

FIG. 11. Proposed origin of the strongly curved boundaries.

FIG. 12. Annealed at 250°C, $H = 0$ for 4 min, then $H = 77{,}600$ gauss for half-hour. $\times 12$

from doing so by the magnetic pressure on them. The resistance our boundaries have shown to bowing out, however, indicates that the three boundaries might not have a curvature as large as that of the equilibrium shape. Therefore, only an upper limit to the free energy may be obtained by: measuring their mean curvature K at any point; determining the pressure from equation (3); and then using the relation $\sigma \leq p/K$. Measurement of the sample of Fig. 10 gives $K = 6.9 \pm 1.6$ cm^{-1}, $p = 4480$ dynes /cm^2, so that $\sigma \leq 640 \pm 110$ ergs/cm^2. Similar measurements on the other curved boundary that was analyzed gave $K = 4.0 \pm 1.2$ cm^{-1}, $p = 1313$ dynes/cm^2, so that $\sigma \leq 330 \pm 90$ ergs/cm^2. The major source of error is in the determination of the radius of curvature on the section perpendicular to the photograph.

3. *Boundary sticking.* As we have seen, the notch seems to act as a barrier that prevents boundaries from being driven through it or that even prohibits double boundaries from being driven together. Let us rule out some possible explanations of this effect, then consider a hypothesis implying these results.

First, the stuck boundaries were not intrinsically of poor mobility, e.g. due to an orientation effect, for they must have been rather mobile to straighten out. Secondly, we are virtually certain that the stuck boundaries in the 4-min preanneal group did not hang up and stick prior to switching on the field, because no hung boundaries, single or double,

VOL. 4 1956

ever occurred after only 4-min annealing out of the field. Thirdly, the assumption of a very high free energy to explain the difficulty of bending the boundaries, neither accounts for the difficulty of collapsing the double boundaries nor is it consistent with the ease of producing strong preferred orientations in the 15-min preanneal group. Finally, it seems most unlikely that impurities would always choose to inhibit a strongly driven boundary just as it flattens across the notch.

Let us discuss a hypothesis, considered by C. S. Smith and the author, which may account for these sticking phenomena in terms of an intrinsic mechanism that would operate in a pure metal. Suppose that a grain boundary in equilibrium with a pure metal crystal had a low mobility. Assume that a boundary must have a concentration of vacancies* greater than it has at equilibrium in order to have the good mobility ordinarily observed in grain-growth (thus the more "porous" boundary would permit larger fluxes of atoms to cross it). Suppose further that diffusion of these vacancies along such a boundary is very rapid. During grain-growth, the source of new vacancies for the boundary would be defects in the recently worked crystal lattice and possibly the vacancies of the disappearing grain-boundary material itself. The boundaries would transfer vacancies from the interior sources to the surface, moving readily while thus oversupplied. When the excess vacancy supply was exhausted, and diffusion had cleared the boundaries' excess vacancies to the surface, the low equilibrium mobility would result.

The coefficients of diffusion of the vacancies in the lattice and in the boundary should be large enough (roughly 10^5 or 10^6 times that of self-diffusion) for excess vacancies present in the notched portion of the treated samples to diffuse to the nearby surface in a few minutes; just about one-tenth of the time that would be required by vacancies present in the bulk of the sample. This could account for the poor mobility of boundaries located near the notches compared with those in the bulk. Notice, however, that while straightening out, a boundary might be able to maintain its mobility by retaining some of the vacancies liberated from its diminishing area.

It is quite possible that excess vacancies in the lattice condense as micropores. If small enough, these could be absorbed and diffused to the surface by a moving boundary. The resulting spasmodic changes of mobility might account for the jerky nature of boundary motion.

In ordinary samples, weakly driven or slowly moving boundaries are certain to become trapped by impurities. Thus, Beck[18] finds the limiting grain size in thick sheets to be roughly constant and dependent on the state of purity. For sheets thinner than this constant diameter, however, he finds that grain-growth stops at grain sizes proportional to the sheet thickness, even though strong curvatures are present. We call this the intrinsic range, and believe the limiting size to be controlled by the diffusion of vacancies to the surface. In fact, if we denote by c the sheet thickness and by t the time required until the loss of vacancies stops grain-growth, we have from diffusion theory $t \sim c^2$. If we assume the boundary geometry, for a fixed ratio of c to grain size, differs by only a scale factor in the sheets of various thicknesses, we have boundary speeds $\sim$ curvatures $\sim 1/c$. Therefore, the distances moved by the boundaries before stopping $\sim t \times 1/c = c$. Thus the boundaries stop at a definite ratio of sheet thickness to grain size, which is the observed behavior.

That the enhanced curvature of the boundary of a large grain among small ones is an insufficient cause for exaggerated grain-growth is seen by observing that, in thin enough sheets, boundaries of the same curvature have stopped moving (the sample-size effect). According to the proposed hypothesis, however, boundaries of a few enlarged grains might collect the vacancies from all of the rest of the boundary material which they consume, thereby maintaining their mobility. Thus the rate of supply of excess vacancies would be $\sim$speed of large boundary $\times$ amount of consumed boundary material in unit area $\sim 1/c^2$ is also proportional to the rate of loss of excess vacancies, so that a steady balance is possible.

To check on the partitioning of excess vacancies, assume that the ratio of their concentration in the boundary to that of the crystal is constant for small variations and equal to 10^4, and that the boundary width is 10^{-7} cm. We see that the boundaries could retain 0.10 of a slight excess of vacancies provided the grain size were $10^{-7} \times 10^4 \times 10 = 0.01$ cm. Hence, for small grain sizes, disappearing grain boundaries may be an important source of excess vacancies.

Let us note a few more points consistent with the hypothesis. The ability of boundaries to absorb and transfer vacancies from the interior of a compacted metallic mass is shown by the work of

* Although boundary vacancies will undoubtedly be ill defined and rather smeared out, the term will be used for convenience. If preferred, one may think in terms of densities.

Alexander and Balluffi.[24] They noticed a great increase in the rate of disappearance of small voids when these were intersected by grain boundaries.

The low mobility of cast boundaries would follow not only from impurity trapping, but also from the absence of excess vacancies assumed to be produced by cold work, and by disappearing boundary material. In a recently reported case,[25] a bicrystal was cast so that the boundary ran parallel to and very near one edge, then curved in a 90° arc and intersected the edge at right angles. Upon annealing, the line of contact of the boundary with the edge of the sample moved slowly at first, then faster. Perhaps, after the sharp curvature started the motion, the considerable amount of disappearing boundary material furnished enough excess vacancies to raise the boundary mobility.

Dunn[26] has reported difficulty in obtaining large grains by the strain anneal technique in very thin (0.005 in.) sheets of silicon iron. This may be due to the propinquity of the surface, which rapidly drains the excess vacancies.

FUTURE WORK

We shall briefly discuss some planned work designed to illuminate the sticking phenomena and to test the vacancy hypothesis.

The disadvantage of the frequent occurrence of low-magnetic-force boundaries may be overcome by starting with a long single crystal of unfavorable magnetic orientation which has been slightly deformed at one end. Annealing it in the field will result in the selection, from the recrystallized end, of a mobile high-force boundary which will be driven along the sample as it consumes the unfavorable grain. Such a technique permits a knowledge of the history of the moving boundary unobscured by its relation to other boundaries. If the vacancy hypothesis is correct, this driven boundary will stop at positions and with shapes depending on the sample diameter and the condition of the metal. For comparison, a boundary can also be driven into a highly oriented polycrystal instead of a single crystal. The disappearing boundary material in this case might facilitate the advance of the moving boundary.

ACKNOWLEDGMENTS

Gratitude is expressed to the Naval Research Laboratory, Washington, D.C., for their willingness to provide their Bitter magnet, which made this work possible. Especially helpful and obliging at that laboratory were Dr. R. L. Dolecek and A. H. Mister. The author is indebted to many members of The Institute for the Study of Metals for help and advice, especially to Betty Nielsen for the metallography. It is a particular pleasure to acknowledge numerous profitable and encouraging discussions with Professor Cyril S. Smith.

Appendix

Consider a polycrystalline insulator which is anisotropic in dielectric constant, situated in an electric field. The slow neutralization of the internal electric field by conduction may be partially avoided by using alternating current, since the direction of the pressure is independent of the polarity of the field. If the electric susceptibility $k < 1$, the discussion is the same as in the magnetic case. For $k > 1$ we take the symmetrical case of a bicrystal disposed between condenser plates in the manner of Fig. 2. Assume the two crystals have different principal axes (of susceptibilities k_1 and k_2) perpendicular to the plates. The free energy as a function of boundary position x is found by integrating $\frac{1}{8\pi} \boldsymbol{E} \cdot \boldsymbol{D} dv$ over the system. Differentiation with respect to x for constant charge gives the boundary pressure. If, instead, the potential is constant, the pressure depends on the boundary position, and is larger the closer the boundary is to one end. The limiting pressure is easily found to be

$$p = \frac{1}{8\pi} \left(\frac{V}{300d} \right)^2 \frac{k_1}{k_2} (k_1 - k_2) \tag{5}$$

Here V is the condenser potential in practical volts and d is the spacing between the plates.

In order to obtain a large pressure, one looks for a substance with large $k_1/k_2(k_1 - k_2)$, very high resistance, high breakdown strength, and absence of stress complications due to electrostriction. To estimate a possible pressure for sulfur, take $k_2 = 3.9$, $k_1 = 4.7$ (room temperature values in rhombic S), and $V/d = 10^5$ volts/cm. Equation (5) gives $p = 6150$ dynes/cm^2. Although this is a large pressure, the grain structure of sulfur was examined and found to be bizarre and complicated by sluggish phase changes. It is possible that other materials, such as organic crystals, may be more suitable.

Consider now a bicrystal shaped again as in Fig. 2, between the plates of a mechanical press. Suppose the material is elastically anisotropic and that the two crystals have Young's moduli Y_1 and Y_2 respectively along the axis of compression. By considering the elastic strain energy, and the work done by the fixed stress τ due to changes in the sample length when the boundary shifts its position, one easily finds the boundary pressure to be

$$p = \frac{\tau^2}{2} \left(\frac{1}{Y_2} - \frac{1}{Y_1} \right). \tag{6}$$

VOL. 4 1956

Once again p is directed independently of the sign of τ, and, in accordance with LeChatelier's principle, urges the boundary in the direction that increases the volume of the crystal of greater longitudinal compliance, thereby tending to reduce the applied stress.

Consider as an example, a zinc bicrystal with one c axis parallel and the other perpendicular to the axis of compression. The small resolved shear stress on the slip planes should permit τ to be $\simeq 15 \times$ critical shear stress $= 1.75 \times 10^8$ dynes/cm^2. Taking $1/Y_2 = 13.2 \times 10^{-13}$, $1/Y_1 = 1.75 \times 10^{-13}$ (room temperature values). Equation (6) gives $p = 23{,}000$ dynes/cm^2. Such stress-pressures might be expected to play some role in the development of preferred orientations in worked materials, although the phenomena of plastic deformation and recrystallization usually supervene.

The stress-pressures discussed above are similar to those occurring in the experiments of Parker and Washburn.[10] Here a low-angle boundary, because of its special tilt-type structure, tends to relieve an appropriately applied shear stress by moving along the sample.

REFERENCES

1. C. S. Smith *Trans. Amer. Inst. Min. Met. Eng.* **175,** 15 (1948).
2. P. A. Beck Chapter in *Metal Interfaces*, ASM, Cleveland, p. 208 (1952).
3. D. Harker and E. Parker *Trans. Amer. Inst. Min. Met. Eng.* **34,** 156 (1945).
4. C. S. Smith Chapter in *Metal Interfaces*, ASM, Cleveland, p. 65 (1952).
5. J. E. Burke *Trans. Amer. Inst. Min. Met. Eng.* **180,** 73 (1949).
6. R. L. Fullman Chapter in *Metal Interfaces*, ASM, Cleveland, p. 179 (1952). J. E. Burke Chapter in *Atom Movements*, ASM, Cleveland, p. 209 (1951). P. A. Beck Chapter in *Metal Interfaces*, ASM, Cleveland, p. 208 (1952). E. S. Machlin *J. Metals* **5,** 437 (1953).
7. W. T. Read and W. Shockley *Phys. Rev.* **78,** 275 (1950).
8. C. G. Dunn, F. W. Daniels, and M. J. Bolton *Trans. Amer. Inst. Min. Met. Eng.* **188,** 1245 (1950).
9. K. T. Aust and B. Chalmers *Proc. Roy. Soc.* **201A,** p. 210 (1950).
10. J. Washburn and E. R. Parker *J. Metals* **4,** p. 1076 (1952).
11. A. Goetz *Phys. Rev.* **35,** p. 193 (1950).
12. R. Smoluchowski and R. W. Turner *J. Appl. Phys.* **20,** No. 8, p. 745 (1949).
13. N. K. Adam *The Physics and Chemistry of Surfaces*, Third Edition, Oxford University Press, London (1941).
14. H. Suzuki *J. Phys. Soc.*, Japan **6,** p. 522 (1951).
15. J. A. Stratton *Electromagnetic Theory*, First Edition, McGraw-Hill, New York (1941).
16. R. Smoluchowski *Phys. Rev.* **83,** p. 69 (1951).
17. D. Turnbull *J. Metals* **3,** p. 661 (1951).
18. P. A. Beck, J. C. Kremer, L. J. Demer, and M. L. Holzwoth, *Trans. Amer. Inst. Min. Met. Eng.* **175,** 372 (1948).
19. A. Goetz and A. Focke *Phys. Rev.* **45,** p. 170 (1934).
20. P. Kapitza *Proc. Roy. Soc.* (*London*) **A131,** p. 224 (1931).
21. P. Kapitza *Proc. Roy. Soc.* (*London*) **A135,** p. 556 (1932).
22. W. G. Pfann *J. Metals* **4,** p. 747 (1952).
23. J. W. Stout and M. Griffel *J. Chem. Phys.* **18,** p. 1449 (1950).
24. B. H. Alexander and R. Ballufi *J. Metals* **188** (10), p. 1219 (1950).
25. K. T. Aust, N. K. Chen, and E. Harrison work in progress at the Johns Hopkins University, Baltimore, Maryland.
26. C. G. Dunn U.S. Patent 2,700,006 (Serial No. 378,311), patented January 18, 1955.

THE EVOLUTION OF THE ENERGY STORED BY A GOLD-SILVER ALLOY COLD-WORKED AT −195°C AND AT ROOM TEMPERATURE*

PETER GREENFIELD† AND M. B. BEVER†

The energy stored in an 82.6 gold–17.4 silver (by weight) alloy, cold-worked at −195°C and at room temperature, has been measured by tin-solution calorimetry. The effect of annealing upon the energy content retained by samples deformed at these temperatures has been investigated. The stored energy in samples worked at −195°C is shown to anneal out in two distinct stages, while after working at room temperature the stored energy is evolved in only one stage. The results are discussed in terms of the types of lattice imperfections produced by cold working.

L'EVOLUTION DE L'ENERGIE ENMAGASINEE DANS UN ALLIAGE Au-Ag ECROUI A −195°C ET A TEMPERATURE AMBIANTE

L'énergie enmagasinée dans un alliage Au-Ag (82,6% Au, 17,4% Ag en poids) écroui à −195°C et à température ambiante a été mesurée au calorimétre à solution d'étain. L'effet du recuit sur la quantité d'énergie enmagasinée par les échantillons déformés à ces températures a été étudié. L'énergie accumulée par des échantillons déformés à −195°C se restaure en 2 étapes distinctes, tandis qu'après écrouissage à la température ambiante, l'énergie retenue est restaurée en une étape. Les résultats sont discutés en termes de types d'imperfections de réseaux produits par l'écrouissage.

DIE ABGABE DER IN EINER GOLD-SILBER-LEGIERUNG INFOLGE KALTBEARBEITUNG BEI −195°C UND BEI RAUMTEMPERATUR GESPEICHERTEN ENERGIE

Die in einer Legierung mit 82,6% Au und 17,4% Ag (Gewichtsprozente) durch Kaltbearbeitung bei −195°C und bei Raumtemperatur gespeicherte Energie wurde mit Hilfe eines Zinn-Lösungs-Kalorimeters gemessen. Weiterhin wurde an bei den genannten Temperaturen verformten Proben der Einfluss von Wärmebahandlungen auf den zurückbleibenden Energieinhalt untersucht. Es wird gezeigt, dass in Proben, die bei −195°C bearbeitet wurden, die gespeicherte Energie in zwei getrennten Erholungsstufen frei wird, während sie nach Bearbeitung bei Raumtemperatur in nur einer Stufe abgegeben wird. Die Ergebnisse werden auf Grund der verschiedenen Typen von Gitterfehlern, die bei der Kaltbearbeitung entstehen, diskutiert.

VOL. 4 1956

INTRODUCTION

The plastic deformation of metals below room temperature and the annealing of metals cold-worked in this range have attracted increasing attention in recent years. These processes have been investigated principally by measuring changes in electrical resistance and mechanical properties. Molenaar and Aarts[1] used such changes to examine the effects produced by working samples of copper, silver, and aluminum at the temperature of liquid air. The stress-strain curve of these samples remained unaffected by annealing for a few minutes at room temperature, but their electrical resistance decreased abruptly. Blewitt *et al.*[2] found that such recovery in electrical resistance of copper deformed at −195°C took place at temperatures as low as −79°C. Observations by Manintveld[3] suggested that the recovery in electrical resistance of deformed copper, silver, and gold occurred in two sharply defined stages near −100°C and 0°C. Eggleston's[4] results on copper were also resolvable into two low-temperature recovery stages, which were, however, far broader than those of Manintveld.

The recovery of electrical resistance at low temperature has been attributed to the rearrangement of vacancies, vacancy pairs, or interstitials generated by plastic flow.[5] Point defects of this type are considered as immobile at the temperature of liquid air,[5] but as possessing sufficient mobility at room temperature and even at −79°C to form aggregates large enough to reduce conduction electron scattering from the level produced by the isolated defects existing at low temperatures. The work of Manintveld would indicate the presence of two distinct types of point defect with different activation energies.

Work on samples irradiated at low temperatures with high-energy particles supports the interpretation of low-temperature recovery in electrical resistance as a process involving point defects. Changes in resistance induced by irradiation have been reviewed by Broom.[6] An investigation by

* Received November 21, 1955. This investigation was sponsored by the U.S. Atomic Energy Commission under Contract AT(30-1)-1002.

† Department of Metallurgy, Massachusetts Institute of Technology.

Overhauser[7] of the energy stored by irradiating copper shows that the energy is released over a wide temperature range below room temperature.

Recovery of the mechanical properties in deformed metals requires annealing at temperatures higher than those required for the recovery of electrical resistance. Most mechanical properties are little affected by point defects, but are markedly affected by line imperfections. Apparently line imperfections play a major part in the recovery at higher temperatures. Dorn and co-workers[8] concluded from observations of the resoftening in aluminum that at least two types of imperfections were involved in the recovery above room temperature. This distinction was based on the ease with which the imperfections were eliminated by annealing.

No information has been published on the evolution of the stored energy during annealing of samples deformed below room temperature. In the present work, the energy stored during deformation of an 82.6 Au–17.4 Ag (by weight) alloy at —195°C was measured by tin-solution calorimetry, and the evolution of this energy during annealing in the range from —130°C to 420°C was also investigated. For comparison, similar measurements were made on samples annealed after deformation at room temperature and —79°C.

EXPERIMENTAL PROCEDURES

Cold working. It was necessary to carry out the plastic deformation by a process which could be used at room temperature and at —195°C. Drilling appeared to meet this requirement best. This process performed under controlled conditions is related to orthogonal cutting, especially if the cutting face of the drill is in a radial position. In both processes the material is subjected to heavy shear. It has already been shown that orthogonal cutting and drilling yield reproducible values of stored energy.[9, 10]

A gold-silver alloy block was clamped rigidly to a thermally insulating base secured to the platform of a drill press. The torque exerted by the drill was measured by a strain ring assembly,[11] and in this way, the total energy expended was found. For drilling at —195°C, the alloy block, clamping jig, and most of the drill were immersed in liquid nitrogen. For drilling at room temperature, carbon tetrachloride served as cutting fluid. When water was substituted for carbon tetrachloride in one run, the same value of stored energy was found.

Three successive samples were drilled from each alloy block with straight-fluted drills of increasing diameter. The fourth and final cut was made with a twist drill; since it was difficult to keep the long chip submerged under liquid nitrogen, these samples were used for annealing at room temperature or above, along with other samples produced with straight fluted drills. The measured values of the stored energy showed no systematic effects of the type of drill used or the drill size.

Annealing. Samples worked at —195°C which were to be annealed below room temperature, had to be kept below the intended annealing temperature. After drilling, the sample was transferred under liquid nitrogen to a glass tube immersed in and containing liquid nitrogen. For annealing, the tube was then suspended in a constant-temperature bath; the nitrogen boiled off rapidly and the tube was sealed with glass-wool. A solution of 75% petroleum ether and 25% methyl cyclohexane, with an admixture of an appropriate amount of liquid nitrogen, was used at —130°C. A constant temperature of —79°C was maintained with a mixture of dry ice and acetone. Both media provided a temperature stability of ±1°C for at least one hour.

For annealing above room temperature, the samples were sealed in evacuated glass tubes and immersed in a liquid of constant-boiling temperature contained in a flask fitted with a reflux condenser. The liquids used and their boiling temperatures were water (100°C), carbitol (195°C), and benzophenone (306°C); these temperatures are not values taken from the literature, but the boiling temperatures actually observed. For annealing at 420°C, a salt bath with automatic temperature control was used.

Calorimetry. The energy contents were determined by tin-solution calorimetry. In this, the heat effect produced by adding the worked sample from a starting temperature such as —195°C to a bath of tin at 240°C is compared with that produced by the addition of a fully annealed sample. The difference in these heat effects, adjusted for the change in composition of the solution,[12] yields directly the difference in energy contents at the initial temperature of the two samples, that is the stored energy. It is important to keep the heat effects as small as possible so that the stored energy is the difference between two small values. For this reason, an alloy of such composition was used that the heat evolved upon its dissolution in tin balanced the heat absorbed in raising its temperature to that of the tin.

In earlier investigations, a 75 Au–25 Ag (by weight) alloy was used.[9, 13] This gave nearly

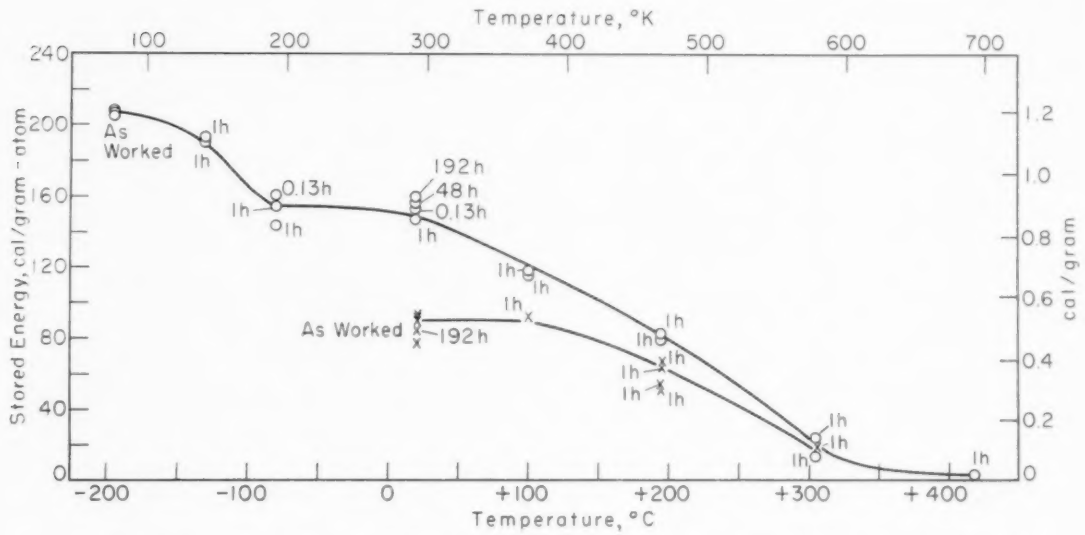

FIG. 1. The energy stored in samples of 82.6 Au–17.4 Ag alloy cold worked at two temperatures as a function of subsequent annealing treatment

perfect thermal balance when added from 0°C to tin at 240°C. In the present work, samples were added from —195°C and a larger heat of dissolution was required. By increasing the gold content of the alloy to 82.6 weight per cent, nearly perfect thermal balance was restored. For this reason, all samples, including those worked at room temperature and at —79°C. and the annealed samples, were also added from —195°C.

The technique of transferring the chips of alloy from the drill press to the calorimeter has been described.[10] Any rise in temperature and condensation of moisture on the specimen were prevented by keeping it at all times immersed in liquid nitrogen. Any ice condensed into the bath was removed by rinsing the sample in fresh liquid nitrogen. After the sample was placed in the addition arm of the calorimeter, the liquid nitrogen was pumped off, while the temperature of the sample was kept at —195°C by a bath of liquid nitrogen surrounding the arm. From this point on, the procedure and calculations were similar to those described elsewhere.[13]

Tensile tests. Strip for tensile specimens was prepared by rolling and annealing at 500°C for one hour, to obtain fully softened material The gage length of the specimens was 2.5 cm and the cross-section was 0.4 × 0.025 cm. The tests were carried out at room temperature and at —195°C in equipment which permitted immersion of the specimen in liquid nitrogen In one run at —195°C, the load was removed during the test and the specimen allowed to recover at room temperature for about ten minutes, before again cooling to —195°C and continuing the deformation.

X-ray diffraction. Material annealed at room temperature and above was examined by an X-ray back-reflection technique in order to follow the progress of recrystallization.

EXPERIMENTAL RESULTS

Stored-energy measurements. The values of the stored energy retained in samples of the 82.6 Au–17.4 Ag (by weight) alloy after various cold-working and annealing treatments are listed in Table 1. Most of these results are also shown in Fig. 1, with the time of annealing indicated for each sample.

The evolution of energy stored in samples worked at —195°C took place in two clearly defined stages. The first of these, which lies between —195°C and —79°C, involved a reduction in stored energy of about 50 cal/gram-atom, equal to approximately one-quarter of the total energy stored during working at —195°C. The lower limit of the second stage was near room temperature. After annealing for one hour at 100°C, 195°C, and 306°C, progressively less stored energy remained, and after annealing for one hour at 420°C the sample contained no stored energy.

In contrast to deformation at —195°C, the evolution of energy stored in samples worked at room temperature involved only one stage. This began at approximately 100°C and was almost complete at 306°C.

The stored-energy values obtained were independent of time of annealing at temperatures ranging from —130 to 22°C for the annealing periods used.

VOL. 4 1956

TABLE 1. The stored energy in samples of 82.6 Au–17.4 Ag alloy as a function of the conditions of cold work and annealing

Calorimetric run no.	Temperature of working, °C	Temperature of anneal, °C	Time of anneal, h	Stored energy cal/gram-atom
104	−195	—	—	205
101	−195	—	—	206
106	−195	—	—	207
161	−195	−130	1	190
160	−195	−130	1	192
122	−195	−79	0.13	160
117	−195	−79	1	143
118	−195	−79	1	155
114	−195	22	0.13	153
107*	−195	22	1	147
108*	−195	22	48	157
119	−195	22	192	160
114	−195	100	1	118
116*	−195	100	1	116
119*	−195	195	1	80
116*	−195	195	1	82
120	−195	306	1	24
120	−195	306	1	13
182	−195	420	1	1
126	−79	22	1	142
126	−79	100	1	119
112	R.T.	—	—	93
113*	R.T.	—	—	76
114	R.T.	—	—	93
156*	R.T.	—	—	94
116*	R.T.	22	192	86
123	R.T.	100	1	94
158	R.T.	195	1	52
158	R.T.	195	1	67
162*	R.T.	195	1	52
162*	R.T.	195	1	66
156*	R.T.	306	1	20

Note: Samples marked by * were cut with a twist drill, all others with straight-fluted drills.

Work not reported in detail here indicated that the stored energy retained after annealing treatments for one and two hours at 100°C and above was a function of the time of annealing.

One to two hours elapsed before samples worked at −195°C, but not intended for annealing, could be added to the calorimeter. Although no attempt was made to vary the holding time systematically at −195°C, slight variations in time imposed by the experimental conditions had no effect on the stored energy. Each of the values of the energy stored during drilling at −195°C (runs 101, 104, 106) represented a separate drilling operation and calorimetric run; their scatter was much smaller than that normally expected.

Samples worked at −195°C were annealed at −79°C for periods ranging from 0.13 to 1 hr and at 22°C from 0.13 to 192 hr. The variations in stored energy were independent of the time of annealing for these periods. Annealing at −79°C reduced the stored energy to the same value as annealing at room temperature.

An average value of 88 cal/gram-atom was obtained for the energy stored during drilling at room temperature. This figure is smaller than that obtained by working at −195°C and annealing at room temperature. The value of 88 cal/gram-atom was independent of holding time at temperature over periods ranging from 1 to 192 hr. The value was also independent of the coolant used during drilling. When in one instance water was substituted for carbon tetrachloride, a stored energy of 94 cal/gram-atom was found; this is within the experimental limits of accuracy of the values obtained with carbon tetrachloride. As the stored energy did not change with two such widely different lubricants, it may be concluded that the differences in stored energy produced by cutting under carbon tetrachloride (or water) at room temperature and under liquid nitrogen constitute primarily a temperature effect.

As shown in Fig. 1, the second stage of energy evolution in samples worked at −195°C begins at a lower temperature than the energy evolution from samples worked at room temperature. In spite of this, the energy retained by the former still exceeds that of the latter after annealing for one hour at temperatures as high as 200°C.

One experiment, not included in Fig. 1, was carried out by drilling at −79°C under a mixture of acetone and dry ice. This sample could not be cleaned at this temperature, but had to be heated to room temperature. It was divided into two parts, one of which was annealed for one hour at room temperature and the other at 100°C. The stored-energy values were similar to those obtained for material drilled at −195°C and annealed at room temperature or 100°C, respectively.

Energy expended during cold-working. Only about 1 per cent of the energy expended in drilling was retained in the samples. The energy expended at −195°C and −79°C was approximately twice the amount required at room temperature. Deformation with the twist drill required less energy than with the straight-fluted drills.

Tensile tests. Fig. 2 shows true stress-true strain curves for the alloy at room temperature and at

—195°C. Test 1 was uninterrupted, but in test 2, the stress was removed at *A*, and the specimen was held at room temperature for ten minutes before continuing the test at —195°C. This failed to produce any discontinuity in the stress-strain curve. The size effect resulting from the small thickness of the specimens should be kept in mind in considering absolute values of the true stress.

X-ray diffraction. X-ray back reflection photographs suggest that recrystallization is complete after annealing for one hour at 306°C. An annealing time of one hour at 195°C produced some line sharpening, but higher temperatures are necessary for recrystallization.

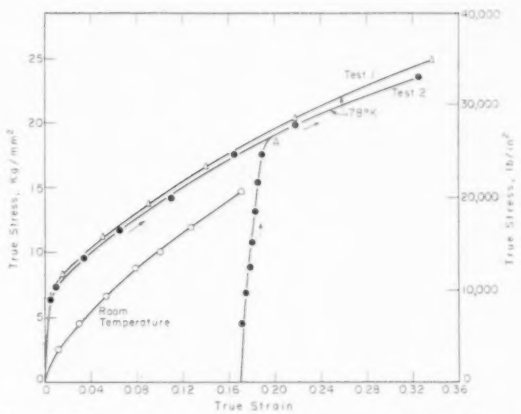

FIG. 2. True stress–true strain curves for 82.6 Au–17.4 Ag alloy at two temperatures.

DISCUSSION OF RESULTS

The most interesting feature of the experimental results is the presence of two distinct stages in which the energy evolves from samples deformed at —195°C. The low-temperature stage, complete at —79°C, is analogous to the recovery of electrical resistance in the experiments of Molenaar and Aarts[1] and of Blewitt *et al.*[2] According to the interpretation of these experiments by Seitz,[5] point defects produced by plastic flow form aggregates upon annealing, reducing the electrical resistance. Also, the energy associated with a given number of vacancies must decrease on clustering. Point defects, on the other hand, have little effect on the tensile properties, and consequently the stress-strain curve (Fig. 2) remains unaltered by room-temperature recovery of specimens worked in tension at —195°C. The low-temperature stage of energy evolution, as Fig. 1 shows, is complete after annealing for only 0.13 hr at —79°C, and is apparently readily activated.

The 50 cal/gram-atom evolved in the low-temperature stage cannot be ascribed unambiguously to the elimination of point defects from the samples. Stroh[14] has expressed the stored energy of cold work predominantly in terms of interaction energies between dislocations. Regrouping of dislocations into more stable patterns lowers the interaction energy of a network of dislocations. Such redistribution could take place at low temperatures through glide rather than by climb mechanisms requiring diffusion.[15] A mechanism of this kind would also lead to a reduction in the stored energy; the low-temperature stage shown in Fig. 1 may, therefore, be composed of several parts.

Observations by Manintveld[3] and Eggleston[4] show that recovery in electrical resistance takes place in two stages below room temperature. This suggests the annealing of more than one type of lattice defect, each of which should be associated with a characteristic stored energy. Observations of this kind are compatible with the present results. Small changes in energy produced by different recovery mechanisms, operating at slightly different temperatures, could perhaps be observed separately in a nonisothermal annealing calorimeter, but they may have been masked in the present work.

The stored energy evolved from samples cold-worked at —195°C on annealing below room temperature is approximately 50 cal/gram-atom. If this energy is attributed entirely to the rearrangement of vacancies, their number can be estimated. The energy associated with a single vacancy in gold-silver alloys may be estimated to be of the order of 1.0 eV from published values for gold and silver.[16, 17] The energy change during low-temperature annealing associated with the regrouping of vacancies (by formation of clusters or migration to dislocations) may be assumed to be one-half or more of the sum of the energies of formation of all the single vacancies involved.[5] On this basis, the fraction of vacancies to atoms in the 82.6 Au–17.4 Ag alloy cold-worked at —195°C ranges between 2 and 4×10^{-3}. It should be emphasized that this figure is probably too high, as the measured change in stored energy (50 cal/gram-atom) is unlikely to be associated entirely with the regrouping of vacancies.

Samples worked at —195°C and annealed at room temperature contain almost twice the amount of stored energy as samples worked at room temperature. Probably much of this excess is attributable to the formation of different patterns of dislocations. In an investigation by Kelly and Roberts,[18] deformation of aluminum at the temperature of liquid nitrogen produced a subgrain size half that obtained by a similar working process at room

VOL. 4 1956

temperature; also, the subgrains formed at low temperature did not grow during annealing at room temperature. The excess energy found in the present work can similarly be attributed to the greater volume of subgrain walls produced by the low-temperature deformation process. If the energy per unit area of subgrain boundary produced at the two temperatures is assumed to be equal, the corresponding two stored-energy values are in the same ratio as the subgrain sizes; hence the subgrain size of the gold-silver alloy deformed at —195°C is almost one-half that of the alloy deformed at room temperature, similar to the effect observed in aluminum.

An alternative explanation is possible for part of the excess of the stored energy found in the samples worked at —195°C and annealed at room temperature over the energy in samples worked at room temperature. Local regions in the latter undoubtedly have reached temperatures above room temperature as a result of the cold-working process. These regions may have suffered a reduction in stored energy by annealing.

Material deformed at —79°C and annealed for one hour at 22°C and 100°C gave stored-energy values similar to those obtained in samples worked at —195°C and annealed at 22°C and 110°C. Point defects formed by deformation at —79°C would anneal out immediately, but apparently a pattern of line defects is formed at this temperature similar to that produced by deformation at —195°C.

Samples worked at —195°C and annealed for one hour at 100°C, 195°C, and 306°C show a progressive decrease in stored energy. This is similar to the behavior of samples worked at room temperature, but in their case the decrease in stored energy starts at a slightly higher temperature. The X-ray back-reflection photographs of material worked at the two temperatures suggest that recrystallization takes place during annealing for one hour at temperatures between 200°C and 300°C. Annealing below 200°C does not involve recrystallization.

The annealing curves above room temperature (Fig. 1) are similar to that for a 75 Au–25 Ag (by weight) alloy cold-worked by filing at room temperature. The annealing behavior of this alloy was recently investigated by a combination of calorimetric and diffuse X-ray scattering techniques.[19] This investigation has shown that annealing below 250°C for periods of one hour had only a small effect upon the initial subgrain size, but higher temperatures resulted in a sharp increase. The local strains decreased moderately in one-hour anneals up to about 250°C, and were completely eliminated after one hour at 300°C. In the present investigation the high-temperature stage can, therefore, be interpreted as a combination of recovery, involving relief of local strain together with slight subgrain growth, and recrystallization. The recovery process may be expected to become more important if the initial subgrain size is smaller or the local strain greater, as would be the case in material deformed at —195°C. It may be for this reason that the decrease in stored energy begins at a lower temperature in samples deformed at —195°C than in those deformed at room temperature.

Norman and Warren[20] have shown that short-range order exists in alloys of silver and gold. Severe deformation produced by filing a 75 Au–25 Ag (by weight) alloy reduces the short-range order parameter by 50 per cent.[19] Application of the quasi-chemical theory to these results yielded an energy associated with the change in short-range order having a maximum value of 21 cal/gram-atom. On annealing, no change in the short-range order parameter occurred during recovery, but the parameter returned to its original value of —0.06 during recrystallization. For the 82.6 Au–17.4 Ag (by weight) alloy used in the present work, a short-range order parameter of —0.045 can be obtained by extrapolation of the value of —0.08 for a 64.6 Au–35.4 Ag alloy[20] and the value of —0.06 for a 75 Au–25 Ag alloy.[19] If deformation by drilling at room temperature affects the short-range order to the same extent as filing, the short-range order parameter is again reduced by 50 per cent. On this basis, the quasi-chemical theory indicates a contribution of short-range order to the energy of cold work by an amount of approximately 14 cal/gram-atom. This energy may be expected to be evolved during recrystallization.

ACKNOWLEDGMENTS

The authors express their appreciation of the support of this investigation by the U.S. Atomic Energy Commission under Contract No. AT(30-1)-1002. They are also grateful to Mr. Benjamin Howell for his assistance in the experimental work. Thanks are due Dr. J. S. L. Leach for advice.

REFERENCES

1. J. Molenaar and W. H. Aarts *Nature* **166,** 690 (1950).
2. T. H. Blewitt, W. Taylor and R. R. Coltman *Phys. Rev.* **82,** 769 (1951).
3. J. A. Manintveld *Nature* **169,** 623 (1952).
4. R. R. Eggleston *J. Appl. Phys.* **23,** 1400 (1952).
5. F. Seitz *Advances in Physics* **1,** 43 (1952).
6. T. Broom *Advances in Physics* **3,** 26 (1954).

7. A. W. OVERHAUSER *Phys. Rev.* **94,** 1551 (1954).
8. T. V. CHERIAN, P. PIETROKOWSKY, and J. E. DORN *Trans. Amer. Inst. Min. Met. Eng.* **185,** 948 (1949).
9. M. B. BEVER, E. R. MARSHALL, and L. B. TICKNOR *J. Appl. Phys.* **24,** 1176 (1953).
10. J. S. L. LEACH, E. G. LOEWEN, and M. B. BEVER *J. Appl. Phys.* **26,** 728 (1955).
11. E. G. LOEWEN and M. C. SHAW *Instruments* **23,** 560 (1950).
12. L. B. TICKNOR and M. B. BEVER *Trans. Amer. Inst. Min. Met. Eng.* **194,** 941 (1952).
13. M. B. BEVER and L. B. TICKNOR *Acta Met.* **1,** 116 (1953).
14. A. N. STROH *Proc. Roy. Soc.* [A] **218,** 391 (1953).
15. A. S. NOWICK *Acta Met.* **3,** 312 (1955).
16. J. W. KAUFFMAN and J. S. KOEHLER *Phys. Rev.* **97,** 555 (1955).
17. F. G. FUMI *Phil. Mag.* [7] **46,** 1007 (1955).
18. A. KELLY and W. T. ROBERTS *Acta Met.* **3,** 96 (1955).
19. B. L. AVERBACH, M. B. BEVER, M. F. COMERFORD, and J. S. L. LEACH to be published in *Acta Met.*
20. N. NORMAN and B. E. WARREN *J. Appl. Phys.* **22,** 483 (1951).

VOL.
4
1956

Retained Austenite in Slow-cooled Low-carbon Steels*

On a number of occasions, the possible existence of an austenitic film between ferrite grain boundaries in iron-carbon systems was suspected.[1–5] But there was no direct evidence reported concerning the presence of such a structure in low-carbon steels at room temperatures. However, during the course of an investigation on the constituents in low-carbon steels, using the electron microscope, an austenitic

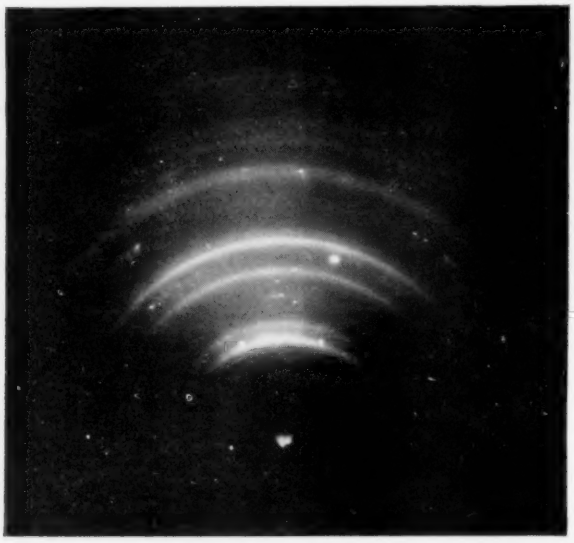

FIG. 1. Reflection electron-diffraction pattern from low-carbon steel surface etched with Nital, showing spotty α-Fe and diffuse γ-Fe rings.

diffraction pattern was found to occur from a slow-cooled sample. In view of the metallurgical background of the sample, it was surprising that the austenitic structure was present in the system at room temperatures. In order to confirm this effect, several more samples of low-carbon steels having a carbon content of about 0·05% were examined by electron diffraction. Identical patterns as the one shown in Fig. 1 were obtained for all the samples after etching with Nital. Analyses of the diffuse rings indicated the presence of a face-centered cubic structure having a mean unit cell dimension of 3.63 Å, comparable to that of austenite. The spotty rings were diffracted from the body-centered cubic α-Fe with a unit cell dimension of about 2.86 Å.

After the austenitic diffraction pattern was obtained, Formvar replicas were dry-stripped from the sample

FIG. 2. Electron micrograph of Formvar replica dry-stripped from low-carbon steel surface etched with Nital, showing protruding austenitic structure as ferrite grain-boundary film.

FIG. 3. Electron micrograph of Formvar replica dry-stripped from low-carbon steel surface etched with Nital, showing protruding austenitic film as ferrite grain boundaries and massive cementite surrounded by austenitic structure.

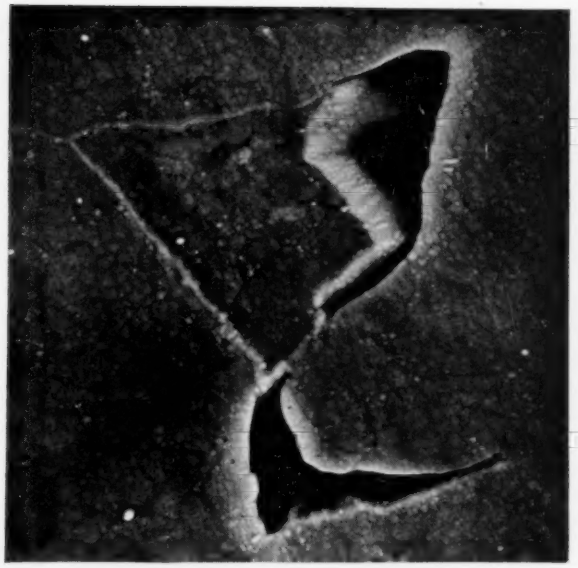

FIG. 4. Electron micrograph of Formvar replica dry-stripped from low-carbon steel surface successively etched with Nital and chromic acid, showing protruding austenitic film as ferrite grain boundaries and dark receding massive cementite surrounded by light protruding austenitic structure, as well as dark fine sub-grain veins in ferrite.

VOL. 4 1956

surface for microscopic examination. The electron micrograph of the replica showed fairly good contrast for the determination of the protruding structure responsible for the austenitic diffraction pattern. The light network in Fig. 2 was observed as the major protruding structure, and is believed to be responsible for the austenitic diffraction pattern. This indicates that the ferrite grains are surrounded by thin austenitic boundary films. Large protruding areas were also observed. However, they were not believed to be entirely austenitic, but more or less likely to be cementite, judging from the ordinary light microscope examination. In order to determine whether both structures were present, the same sample was electrolytically etched in chromic-acid solution for a short duration. Formvar replicas of the surface then revealed the separation of the presumed austenitic structure from cementite as the electrolytic etching removes the carbide or cementite but leaves the austenitic structure almost unattacked. Fig. 4 shows clearly the effect that the massive dark receding area of cementite is enveloped by the light areas of the presumed austenitic structure, which extends out continuously as the light austenitic films between the ferrite grains, as mentioned before. It is interesting to note that numerous dark subgrain veins are present throughout the ferrite grains. It is not known whether these veins are where the high carbon concentration was. Future investigations are planned. The research program is currently supported in part by a grant from the Graduate School of the University of Minnesota. It is hoped that more detailed information will be reported in the near future.

C. C. HSIAO

University of Minnesota,
Institute of Technology,
Minneapolis 14, *Minnesota.*

References

1. E. O. HALL, *Proc. Phys. Soc.* **B64,** 747 (1951).
2. A. L. TSOU, J. NUTTING, and J. W. MENTER, *J. Iron and Steel Inst.* **172,** Part II (1952).
3. J. NUTTING and A. L. TSOU, *Proc. Phys. Soc.* **65B** (1952).
4. E. W. WILLIAMS and H. O'NEILL, *J. Iron and Steel Inst.* **117,** Part II (1954).
5. L. COLOMBIER, *Metals Progress* **87,** No. 2, 116 (1955).

* Received February 6, 1956.

Creep of Sodium Chloride and Sodium Bromide at High Temperature*

In discussing results of a previous measurement of the steady-state creep rate of silver bromide single crystals,[1] it was suggested that they were interpretable in terms of the hypothesis that creep rate is related to the coefficient of self-diffusion. Since the diffusion coefficient of Br^- in AgBr is unknown, and it is the more slowly diffusing ion which could be expected to control the creep rate, the measurements have now been repeated on sodium bromide. A careful study of the diffusion of the Br^- ion in NaBr has recently been made by Schamp and Katz.[2] For comparison, the creep rate of sodium chloride was also measured and the results are included.

The apparatus in which a compressive load is applied to the crystal at high temperature is similar to that previously described.[1] It was modified so that the strain is measured by an optical lever arrangement, which is essentially frictionless, instead of by a dial-gage, which introduced an uncertainty in the stress due to friction in the gage. A serious problem was encountered in the corrosion of the stainless-steel apparatus near the melting-point of the alkali halide crystals. The corrosion was sufficiently retarded by silver-plating the apparatus, followed by a flash rhodium plating. The sodium bromide crystals were grown by the Czochralski method of withdrawal from the melt, using reagent-grade salt. The sodium chloride crystals were natural rock-salt. Creep specimens in the form of rectangular parallelepipeds were prepared by cleavage followed by light etching. The height of the specimens was between 5 and 11 mm. The cross-sections were usually not square, the smaller

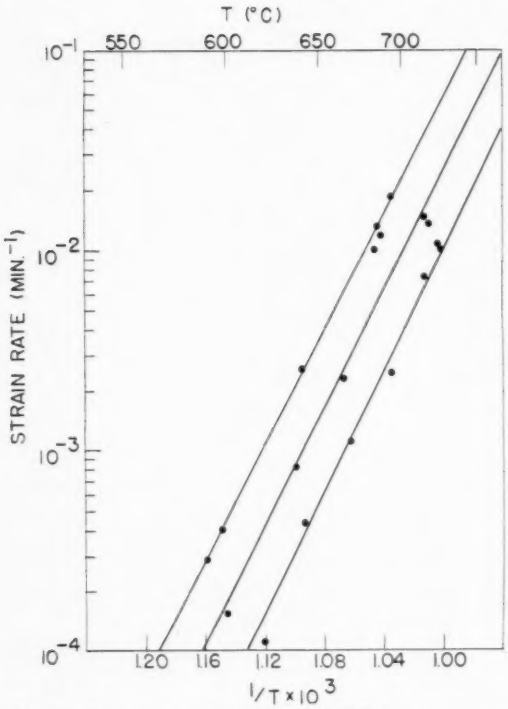

FIG. 1. Steady-state creep rate of NaBr at stresses of 60, 80, and 100 g/mm².

dimension being about one-half to one-fifth of the height. No dependence of the results on dimensions or shape was noticed.

The crystals were set in the apparatus between platens made by casting discs of alundum cement $\frac{1}{8}$ in. thick, which were then fired and polished smooth and parallel. Between these discs and the crystal were pieces of platinum foil. Since the axis of compression was an [001] axis, the preferred slip systems,[3] an [011] plane and (0$\bar{1}$1) direction, were also those of maximum resolved shear stress. The shape of the specimens after deformation indicated that slip had occurred on these systems.

Measurements of the creep rate were made down to temperatures about 200° below the melting-point, at stresses of 60, 80, and 100 g/mm². In this range there was a transient phase of creep during which the strain was of the order of 5 to 15%, followed by a phase in which the rate was approximately constant. As the transient creep was more quickly exhausted at higher temperature, for each stress σ the steady-state creep rate $\dot{\epsilon}$ was obtained at the highest temperature. The temperature was then changed and the rate measured at the same stress. The results for eight specimens of NaBr and eight specimens of NaCl are shown in Figs. 1 and 2, respectively. The temperature dependence is clearly exponential, indicating an activated process.

The lines drawn in the figures are described by the formula

$$\dot{\epsilon} = C \exp\{-(Q - B\sigma^{\frac{1}{2}})/RT\}.$$

$\sigma^{\frac{1}{2}}$ is used because it seemed to be preferred in the results on AgBr, although in the present experiments another stress dependence is not definitely precluded. The values of the parameters are

for NaBr $Q = 82.4$ kg-cal/mol

$B = 1.60$ (kg-cal/mol)/(g/mm²)$^{\frac{1}{2}}$

$C = 15.4 \times 10^{12}$ min^{-1}

and for NaCl $Q = 82.4$ kg-cal/mol

$B = 1.60$ (kg-cal/mol)/(g/mm²)$^{\frac{1}{2}}$

$C = 4.6 \times 10^{12}$ min^{-1}.

It is interesting that the data for both salts can be fit, using the same activation energy and stress dependence.

The fact that the activation energy for steady-state creep is about the same for NaCl and NaBr seems to exclude the assumption that these rates are controlled by the diffusion process in this range of stress, since the activation energy for the diffusion of Br^- in NaBr is[2] 47 kg-cal/mol and that for Cl^- in NaCl has been reported[4] to be 62 kg-cal/mol. These are appreciably different, and considerably smaller than the activation

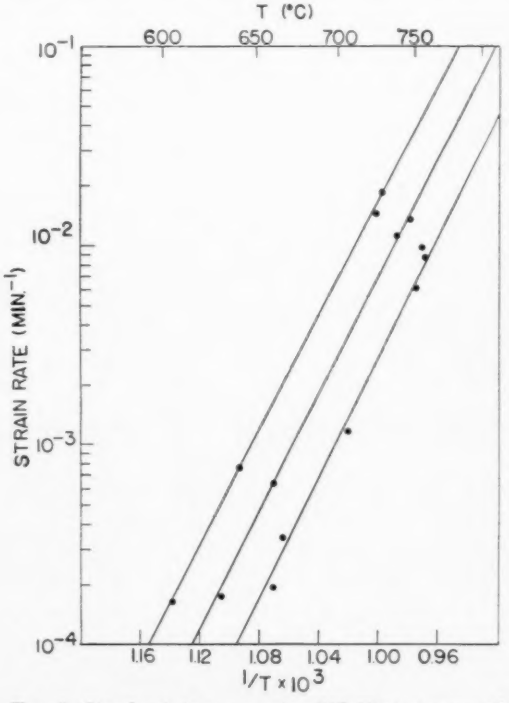

FIG. 2. Steady-state creep rate of NaCl at stresses of 60, 80, and 100 g/mm².

energy for the creep rate, which varies between 66 and 70 kg-cal/mol in this range. In the previous work on AgBr, however, there appeared to be two distinct regimes of behaviour, at low and at high stress. The high-stress regime was attributed to a limitation of dislocation climb by diffusion of vacancies, whereas it was supposed that at lower stresses the limitation was the inhibition of the motion of dislocations on the slip plane. It is possible that if the present results were extended to higher stresses, a similar break in the behavior would be found. Unfortunately, this extension presents difficulties, because at higher stresses the total amount of transient strain, before the onset of the steady-state, becomes very large, so that the specimen is too distorted geometrically to give reliable values for the steady-state rate.

A further comparison of the creep rates of NaBr and NaCl can be made by extrapolating to the values at the melting-points. Although the pre-exponential factors differ by a factor of more than three, at a stress of 100 g/mm² the creep rates at the melting-point would differ by less than 20%. If the data previously obtained at low-stress levels in AgBr crystals with [001] axis are also fit to the same formula, the parameters are for AgBr

$$Q = 81.5 \text{ kg-cal/mol}$$
$$B = 1.95 \text{ (kg-cal/mol)/(g/mm}^2)^{\frac{1}{2}}$$
$$C = 1.1 \times 10^{20} \text{ min}^{-1}.$$

The activation energy is about the same, the stress dependence is somewhat greater, and the pre-exponential factor is many orders of magnitude greater. The value for AgBr at its melting-point and at 60 g/mm², however, is the same as the values for the alkali halides at their melting-points. Thus from this point of view all of these values fall into line.

These considerations suggest expressing the creep rate by the "universal" formula

$$\dot{\epsilon} = A \exp\{(Q - E)/RT_m\} \exp\{-(Q - E(\sigma/\sigma_e)^{\frac{1}{2}})/RT\}$$

where $Q = 82$ kg-cal/mol

$E = 16$ kg-cal/mol

$A = 1.5 \times 10^{-1}$ min^{-1}.

T_m is the melting temperature and σ_e is 100 g/mm² for NaBr and NaCl and 60 g/mm² for AgBr. The question whether σ_e can be identified with the yield stress cannot be answered from available data. There is not good agreement among reported values.[3] Stepanow[5] gives a value of 70 g/mm² for the elastic limit of AgCl at room temperature and states that the value for NaCl is similar. The temperature dependence is also uncertain. For the present purpose σ_e can be taken as a parameter characteristic of the material.

The appearance of T_m can be explained by an argument of Zener.[6] The rate process is proportional to $\exp\{-\Delta G/RT\}$, where ΔG is the increment of Gibbs free energy. Since $\Delta G = \Delta H - T\Delta S$, and since ΔH must be identified with the measured heat of activation H, one has $\exp\{\Delta S/R\} \exp\{-H/RT\}$. If it is assumed that the major part of ΔG is expended in straining the lattice, its temperature coefficient will be about the same as that of the elastic modulus μ. Then

$$\Delta S = \beta(H/T_m),$$

where $$\beta = -d(\ln \mu)/d(T/T_m).$$

Thus one has here

$$\dot{\epsilon} = A \exp\{\beta H/RT_m\} \exp\{-H/RT\}$$

with $H(\sigma) = Q - E(\sigma/\sigma_e)^{\frac{1}{2}}$

$\beta = 1$.

We have put $H(\sigma_e)$ in the entropy term, but this will not make much difference in the narrow-stress range. Now, β for NaCl can be calculated independently from data on the temperature dependence of the elastic constants:[7] β is about 1 for NaCl; actually it is found to be 1.2 or 0.8, depending on whether the shear or tensile modulus is used, compared with values around 0.3 for most metals. No data are available for the other crystals, but assuming $\beta = 1$, the following activation entropies ΔS are calculated: 61 (NaCl), 64 (NaBr), 95 (AgBr) cal/mol-deg.

R. W. Christy

Department of Physics,
Dartmouth College,
Hanover, New Hampshire

References

1. R. W. Christy *Acta Met.* **2,** 284 (1954).
2. H. W. Schamp and E. Katz *Phys. Rev.* **94,** 828 (1954).
3. E. Schmid and W. Boas *Plasticity of Crystals,* London, F. A. Hughes and Co. (1950) Ch. VII.
4. M. Chemla *C. R. Acad. Sci. (Paris)* **234,** 2601 (1952).
5. A. W. Stepanow *Phys. Z. Sowjet.* **8,** 25 (1935).
6. C. Zener *Imperfections in Nearly Perfect Crystals.* New York, John Wiley and Sons (1952) p. 289.
7. W. C. Overton and R. T. Swim *Phys. Rev.* **84,** 758 (1951).

* Received March 1, 1956.

Orientierungsänderungen in aus der Schmelze gezogenen Metallkristallen*

Es wurden Aluminium- und Zink-Kristalldrähte (Durchmesser 0,2—1,0 mm) nach dem Czochralski-Verfahren[1] hergestellt. Die Kristalle wurden entweder in Luft oder in einem Schutzgas gezogen;

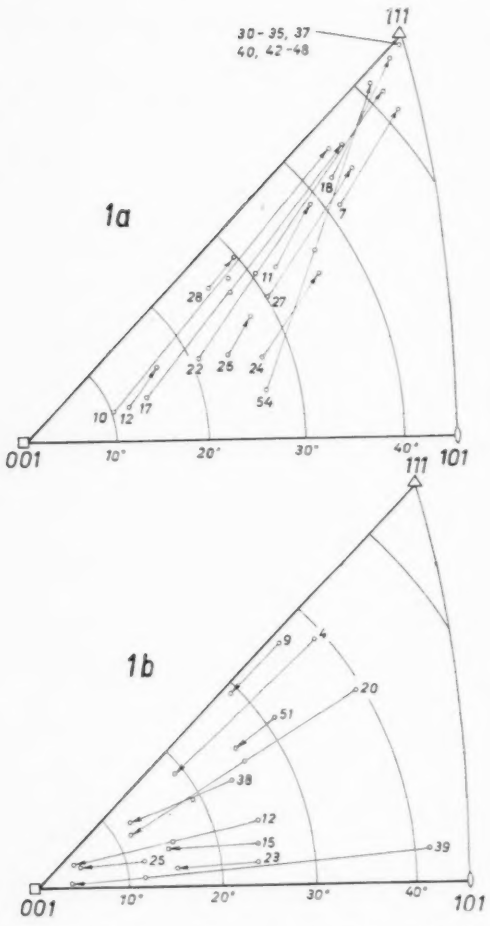

Abb. 1. Orientierungsänderungen von einigen der laufend numerierten Al-Kristallproben in stereographischer Projektion.

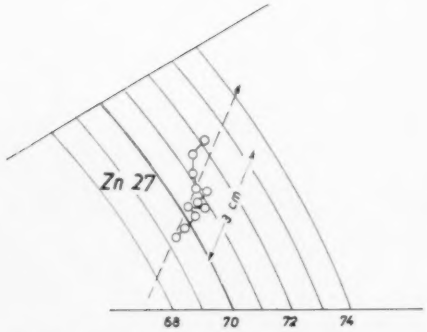

Abb. 2. Beispiel für die Orientierungsänderung entlang einer Zn-Probe in stereographischer Projektion (Ausschnitt); die Messpunkte entsprechen den alle 3 mm aufgenommenen Röntgenaufnahmen.

eine besondere Kühlung der Proben über der Schmelzoberfläche fand nicht statt, so daß also der Temperaturgradient im Wachstumsgebiet für alle Versuche als annähernd konstant gelten konnte. Der Reinheitsgrad der verwendeten Metalle betrug mindestens 99,99 v.H.

Bei der Verwendung verschieden orientierter Impfkristalle konnte festgestellt werden, daß sich die Kristallorientierung während der Herstellung entlang der proben ändert.[2]

Abb. 1 enthält in stereographischer Projektion Beispiele für die Art dieser Änderungen, wie sie an einer größeren Zahl von Aluminium-Proben gefunden wurden. (Das jeweilige Pfeilende gibt die Ausgangs-, die Pfeilspitze die Endorientierung der verschieden langen Proben an.) Die Übergänge von einer Orientierung zur nächsten scheinen unter den vorliegenden Versuchsbedingungen kontinuierlich vor sich zu gehen, wie sich an Hand einer entsprechenden Reihe von Drehkristallaufnahmen zeigte. Die Richtung der Orientierungsänderung ist kristallographisch im wesentlichen durch ein Umfallen der Drahtachse gekennzeichnet und zwar entweder in Richtung auf die Raumdiagonale (Abb. 1a) oder die Würfelkante (Abb. 1b), wodurch dichtest, bzw. zweitdichtest belegte Netzebenen parallel zur Schmelzoberfläche zu liegen kommen; eine ähnliche Bevorzugung der Flächendiagonale wurde nicht beobachtet. In Ergänzung und Übereinstimmung mit diesen Befunden steht die Tatsache, daß in Kristallen, in denen einmal eine Raumdiagonale parallel zur Drahtachse liegt, diese Orientierung im weiteren Verlauf des Wachstums beibehalten wird (siehe in Abb. 1a Proben Nr. 30–35, 37 usw.). Hingegen konnte bisher noch nicht vorausgesagt werden, ob sich in einem Kristall beliebig vorgegebener Orientierung—unmittelbare Nachbarschaft von [001] oder [111] ausgeschlossen—diese gemäß Abb. 1a oder Abb. 1b ändern würde. Von Einfluß auf das Ausmaß dieser Orientierungsänderung ist die Ziehgeschwindigkeit: Unterhalb von 60 cm/h konnten Änderungen von 3°/cm registriert werden, mit einer Steigerung der Ziehgeschwindigkeit gingen die Orientierungsänderungen stark zurück und betrugen bei 120 cm/h weniger als 1°/cm und schließlich bei 250 cm/h nur noch etwa 10°/cm. Noch höhere Geschwindigkeiten lieferten bereits in der Mehrzahl der Fälle keine Einkristalle.

Auch bei Zink konnten ähnliche Orientierungsänderungen gefunden werden; Abb. 2 bringt als Beispiel hiezu Meßpunkte, die entlang einer Probe alle 3mm aufgenommen wurden. Hier scheinen sowohl die hexagonale Achse als auch beide digonalen Nebenachsen als bevorzugte Endlagen der Drahtachse

ausgebildet zu werden. Dies bedeutet, daß auch im Falle des hexagonalen Zink wiederum besonders dicht belegte Netzebenen parallel zur Schmelzoberfläche eingedreht werden (vgl. hiezu auch[3] für Ionenkristalle).

II Physikalisches Institut S. MARINELLI
der Universität Wien F. BLAHA

References

1. J. CZOCHRALSKI *Z. Phys. Chem.* **92,** 219 (1917).
2. A.G. HOYEM u. E.P.T. TYNDALL *Phys. Rev.* **33,** 81 (1929).
3. A. C. MENZIES u. J. SKINNER *Disc Faraday Soc.* **5,** 306 (1949).

* Received March 1, 1956.

Thermodynamic Properties of Solid Solutions*

The detailed work by Dr Herasymenko[1] shows repeated anomalies in the relative partial molar entropy of mixing of cadmium in its solid solution in silver, which may be interpreted as repeated tendencies to ordering. In our own unpublished work on the α solid solutions of the ternary systems copper–zinc–gallium and copper–zinc–germanium we have observed anomalies which may be similarly explained. This work has led us to a reinvestigation of the primary solid solution of zinc in copper, which is now in progress. It is possible that such anomalies may be small in copper-zinc alloys and that we have observed, in copper–zinc–germanium in particular, an intensification of these effects. The form of such anomalies has been predicted by a consideration of the idealized types of partial molar entropy curves for binary and ternary systems.[2]

Department of Metallurgy, D. W. WAKEMAN
University of Sheffield, B. B. ARGENT
Sheffield, England

References

1. P. HERASYMENKO *Acta Met.* **4** (1) (1956).
2. F. H. M. VIDEIRA and P. B. ARGENT, unpublished work.

* Received February 2, 1956.

Slip in Germanium*

The plastic behavior of germanium at elevated temperatures was first reported by Gallagher,[1] and more recently Treuting[2] has investigated the tensile deformation of antimony-doped single-crystal germanium. Using X-ray techniques to establish the slip direction, he encountered some difficulty due to the unpredicted action of more than one slip system. In the present note the results of a metallographic investigation are described; a slip-trace analysis has confirmed the slip plane and direction as {111}, ⟨110⟩. "Unpredicted" secondary slips (also on {111} planes) and "bands of secondary slip" were observed too.

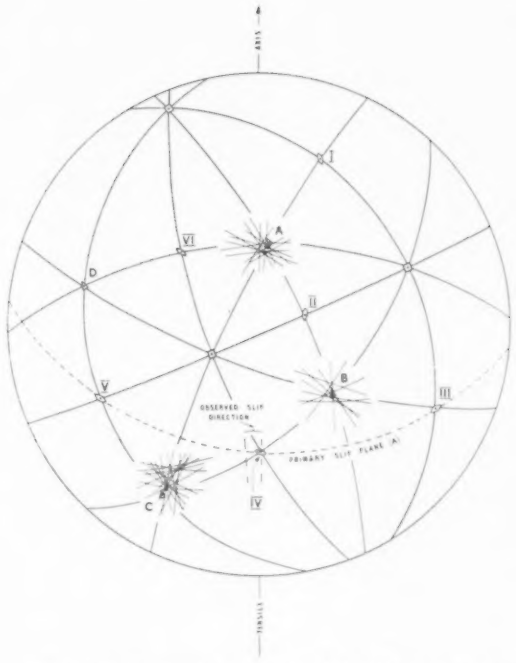

FIG. 1. Stereographic analysis of the slip traces on germanium single crystal

A high-resistivity (~60 ohm cm) germanium single crystal was prepared from zone-refined germanium by the pulling technique.[3] From this a dumbbell-shaped tensile specimen with cylindrical gage-length approximately 2 mm diameter and 11 mm long was made by careful grinding with a diamond wheel. Before deformation, the specimen was heavily etched in fast C.P.4[4] to remove the worked layer, this treatment producing at the same time a highly polished surface suitable for metallographic examination. Tensile deformation was carried out at 700°C in an atmosphere of dry, oxygen-free forming gas (N_2, 10% H_2). After periods of up to an hour at this temperature the specimen surface remained clean and photogenic. Orientations were checked by the standard back-reflection Laue technique. Metallographic examination at all points around the cylindrical gage-length was made possible by a special jig.

Four different sets of slip traces were observed when the specimen had been extended only 8%. Three of these sets were sufficiently well developed over the whole azimuth range for trace analyses to be made. In Fig. 1 the trace-normal intersections for each of these sets are superposed on the stereographic

FIG. 2. A "band of secondary slip" (×300).

projection obtained from a Laue photograph. It is seen that they correspond with {111} poles, i.e. the slip planes are {111}'s, as stated by previous workers.[1,2]

One set of slip traces (*A*) predominated; they could be seen clearly over the length of the crystal, and it was possible to establish the slip direction as follows: viewing around the crystal there were two azimuthal positions where the distinctness of the slip lines reached a definite minimum. These, of course, were positions at right angles to the slip direction. Four determinations were made; the band in Fig. 1 indicates the estimated accuracy of the measurements.

It is seen that the 110-pole labelled IV falls within band. Since there is no other close-packed direction in the vicinity, we can safely conclude that this is the slip direction. On this basis the maximum resolved shear-stress factors for the four {111} planes have been computed (Table 1). It is seen that the combination *A*, IV, the system on which slip predominated, was the most highly stressed. The frequency of slips on the other systems was noticed to be roughly in accord with the shear-stress factors. However, one would not expect any slip on these three at all. Calculation shows and observation confirmed that after 8% extension the stress axis had not reached the 111-100 symmetry line. "Bands of secondary slip",[5] i.e. bands approximately parallel to the primary slip plane containing slip on a second system but very few slips on the primary system, were observed. This suggests that slip on the nonprimary system occurred from the start of deformation. An example of a band of secondary slip is shown in Fig. 2. Slip on all three nonprimary systems can be seen in this area.

TABLE 1.

Slip system	$\sin\chi\cos\lambda$
A, IV	0.48
B, I	0.40
C, VI	0.41
D, I	0.18

Radar Research Establishment, W. BARDSLEY
Great Malvern, England R. L. BELL

Acknowledgment is made to the Controller, H.B.M.S.O., for permission to publish this letter.

References

1. C. S. GALLAGHER *Phys. Rev.* **88,** 721 (1952).
2. R. G. TREUTING *J. Metals* p. 1027, (1955).
3. G. K. TEAL and J. B. LITTLE *Phys. Rev.* **78,** 647, (1950).
4. R. D. HEIDENREICH U. S .Patent No. 2,5916,414, November 25, 1952.
5. R. W. K. HONEYCOMBE *J. Inst. Metals* **80,** 45, (1951–52).

* Received February 2, 1956.

SOME CURRENT PAPERS IN OTHER JOURNALS

Acta Crystallographica, Vol. 9

Part 5, May 1956:

The crystal and molecular structure of succinimide $C_4H_5O_2N$. R. Mason.

Étude théorique et expérimentale du facteur de température et de l'extinction dans la blende. André Authier.

The thermal expansion of sodium chloride and some other alkali halides at high temperatures. H. F. Fischmeister.

The structures of some ferric chloride–graphite compounds. J. M. Cowley and James A. Ibers.

A simplified calculation for the elastic constants of arbitrarily oriented single crystals. David S. Lieberman and Stanley Zirinsky.

An X-ray study of α-keratin. I. A general diffraction theory for convoluted chain structures and an approximate theory for coiled-coils. A. R. Lang.

An X-ray study of α-keratin. II. Diffractometer measurements of the complete diffraction pattern of canadian porcupine quill. A. R. Lang.

The crystal structure of the deuterides of ytterbium and europium. William L. Korst and James C. Warf.

La statistique des fonctions complexes: application à la cristallographie. E. F. Bertaut.

Crystalline forms of bovine pancreatic ribonuclease: techniques of preparation, unit cells, and space groups. Murray Vernon King, Beatrice S. Magdoff, Myra Burt Adelman and David Harker.

Local atomic displacements in solid solutions. F. H. Herbstein, B. S. Borie, jr., and B. L. Averbach.

Structure et valences de $VCeO_4$. A. Durif.

Joint note on the β-uranium structure. Charles W. Tucker, jr., Peter Senio, J. Thewlis and H. Steeple.

A note on celsian. P. Gay.

Part 6, June 1956 (partial contents):

The thermal expansion and phase transitions of WO_3. C. Rosen, E. Banks and B. Post.

The thermal expansion of cubic sodium tungsten bronzes. C. Rosen, B. Post and E. Banks.

The measurement of growth and deformation faulting in hexagonal cobalt. T. R. Anantharaman and J. W. Christian.

Über die Verfeinerung der Kristallstrukturbestimmung einiger Vertreter des Rutiltyps: TiO_2, SnO_2, GeO_2 und MgF_2. Werner H. Baur.

A comparison of various commercially available X-ray films.

X-ray study of the allotropic modifications of calcium metal. H. Melsert, T. J. Tiedema and W. G. Burgers.

Structure de $GeUO_4$. A. Durif.

The crystal structures of Nb_3Au and V_3Au. Elizabeth A. Wood and Bernd T. Matthias.

Comments on a method of structure determination. J. D. Dunitz and L. E. Orgel.

Eine empirische Sn-Streukurve. Werner H. Baur.

Archiv für das Eisenhüttenwesen

Heft 4, April 1956:

Reaktionen zwischen Eisenbad und Phosphatschlacke. Oskar Peter und Wilhelm vor dem Esche und Willy Oelsen.

Der Angriff eisengesättigter Zinkschmelzen auf kupferhaltiges Eisen. Dietrich Horstmann.

Bestimmung des Wasserstoffs in Lichtbogenöfen-Stählen. Werner Geller, Karl Bungardt, und Peter Hammerschmid.

Beobachtungen zur Graphitbildung im untereutektischen Gußeisen. Adalbert Wittmoser und Eduard Houdremont.

Oxydation von Karbidlegierungen für Hochtemperaturzwecke. Josef Hinnüber, Otto Rüdiger, und Willi Kinna.

Eigenspannungen durch Wärmebehandlung von instabilen austenitischen Manganstählen. Hans Bühler und Elmar Herrmann.

Die Zeitgesetze eutektoidischer Umwandlungen. Bernhard Ilschner

Ein Beitrag zum System Eisen-Stickstoff. Wolfgang Pitsch und Eduard Houdremont.

Berechnung der Druckverhältnisse beim Pressen von Pulvern. Karl Torkar.

Heft 5, Mai 1956:

Gütevorausbestimmung an Gußeisen- und Stahlschmelzen durch optische Temperaturmessungen. Kurt Orths.

Die Hemmwirkung von Aluminium in Feuerverzinkungsbädern auf die Bildung der Eisen-Zink-Legierungsschichten Dietrich Horstmann.

Die spektroskopische Bestimmung des Phosphors im Stahl. Hans Krempl und Fritz Bertram.

Anforderungen an die Werkstoffe für Gasturbinen. Boris Haas.

Ein Beitrag zur Frage der Ätzspannungen in Eisenwerkstoffen. Viktor Hauk, Hermann Möller und Friedhelm Brasse.

Potentialbildende Vorgänge an austenitischen Chrom-Nickel-Stählen in destilliertem Wasser und in neutralen Halogensalzlösungen. Carl Carius.

Berechnung von Diffusionsvorgängen bei veränderlicher Temperatur. Bernhard Ilschner.

Das Zustandsschaubild Eisenoxydul-Aluminiumoxyd. Wilhelm Anton Fischer und Alfred Hoffmann.

Ermittlung der Mengen und Kosten bei der Erzeugungsplanung eines gemischten Eisenhüttenwerkes. Wilhelm Bauer.

Journal of the Institute of Metals, Vol. 84

March, Part 7, 1955–56:

Symposium on the final forming and shaping of wrought non-ferrous metals (concluded).

Research into some metal-forming and shaping operations. W. Johnson.

Cold roll-forming and manipulation of light-guage sections. E. Griffin.

Stretch-forming of non-ferrous metals. R. D. Edwards.

Bending and allied forming operations. T. G. Perry.

The hot forming of magnesium alloys. R. G. Wilkinson.

Metallurgical research and development for nuclear power. H. K. Hardy.

Metallurgical research in nuclear power production. J. G. Ball.

Selection of canning materials for reactors cooled by sodium/potassium and carbon dioxide. A. B. McIntosh and K. Q. Bagley.

April, Part 8, 1955–56:

New and improved metallurgical techniques. Twenty-sixth autumn lecture. C. Sykes.

Some metallographic observations on the fatigue failure of bare and clad aluminium-copper-magnesium alloy sheet. J. J. Sebistry and J. O. Edwards.

A graphical solution of the cold-rolling problem, when tensions are applied to the strip. G. Lianis and Hugh Ford.

The constitution of the titanium-tin system in the region 0–25 atomic per cent. tin. (Mrs) M. K. McQuillan.

The constitutional diagram of the system chromium-beryllium from 0 to 70 atomic per cent beryllium. A. R. Edwards and S. T. M. Johnstone.

Slip-band extrusion. E. A. Calnan and Betty E. Williams.

May, Part 9, 1955–56:

Experiments on the semi-continuous casting of bronze. E. C. Ellwood, J. C. Prytherch, and E. F. Phelps.

The porosity and permeability of hot-compacted copper powder. G. Arthur.

The solid solubilities of tin, indium, and cadmium in aluminium. L. E. Samuels.

VOL. 4 1956

The criterion for the cleavage fracture of zinc single crystals. A. Deruyttère and G. B. Greenough.
The lattice spacings of nickel-copper and palladium-silver alloys. B. R. Coles.
A note on the plotting of accurate large-scale stereographic projections. J. W. Christian.

June, Part 10, 1955–56:
The influence of mould variables and inhibitors on mould reaction in aluminium–10% magnesium alloy. Marjorie Whitaker. With an appendix on the effect of moulding and casting variables on mould reaction in aluminium–5% magnesium alloy. J. Lund.
Structural changes during the fatigue of some aluminium alloys. T. Broom, J. H. Molineux, and V. N. Whittaker.
The mechanical properties of binary and ternary magnesium alloys containing lithium. W. R. D. Jones.
The structure and growth of oxide layers formed on beryllium. I. S. Kerr and H. Wilman.
Applications of the phenomenological theories of martensite. I.—Geometrical treatment. II.—Related types of martensitic transformation. J. W. Christian.

July, Part 11, 1955–56:
The history of magnesium. Presidential address. Major C. J. P. Ball.
The stress-corrosion of certain aluminium alloys. H. K. Farmery and U. R. Evans.
The phase sections at 500°C. and 350°C. of aluminium-rich aluminium-copper-lithium alloys. H. K. Hardy and (Miss) J. M. Silcock.
Trace-element effects in some precipitation-hardening Aluminium alloys. H. K. Hardy.
The dissociation pressures in the zirconium-oxygen system at 1000°C. O. Kubaschewski and W. A. Dench.
The routine determination of the hydrogen content of aluminium and aluminium alloys by the hot-extraction method. C. E. Ransley and D. E. J. Talbot.
A recording camera for metallography with polarized light. B. R. Butcher and I. A. McDonald.

La Metallurgia Italiana, Vol. XLVIII

March 1956:
Electromagnetic stirring. Application to the desulphurization. J. Duflot and M. Porcheray.
Comparative evaluation of ladle bricks. F. Gottardi and A. Palazzi.
About first stages of zinc surface oxidation (0001). G. P. Bolognesi.
On the mechanical and magnetic relaxation of α iron. A. Ferro and G. Montalenti.

April 1956:
Separation from oversaturated mixed crystals. F. Bollenrath.
One million tons steel produced by blowing oxygen in pig iron. R. Rinesch.
Scale breakdown by means of explosives at the N.2 blast furnace of ILVA-works in Piombino. D. Camici.

THE KINETICS OF GRAIN BOUNDARY NUCLEATED REACTIONS*

JOHN W. CAHN†

Rate laws are derived for transformations in which the new phase nucleates on grain boundary surface, grain edges, or grain corners, and in which the new phase grows with constant radial velocity. Time-dependent and time-independent nucleation rates are treated. At high nucleation rates (relative to growth rates and grain sizes) the rate law assumes a form independent of the nucleation rate, and the half-time of the transformation becomes approximately 0.1 D/G, where D is the grain diameter and G the radial growth velocity, independently of which sites are responsible for nucleation. At low nucleation rates the rate law approaches that given by randomly distributed nucleation sites. The conditions which determine which type of site will produce the most nuclei, and hence determine the form of the rate law, are discussed.

LA CINETIQUE DES REACTIONS DE GERMINATION AUX FRONTIERES INTERGRANULAIRES

Des lois de vitesse de germination sont établies pour des transformations au cours desquelles la nouvelle phase apparait aux surfaces intergranulaires aux bords et aux coins de grains, et croit à vitesse radiale constante. On étudiée également les vitesse de germination influencées ou non par le facteur temps. Pour des vitesses de germination élevées (comparativement aux vitesses de crossiance et aux dimensions des grains) la loi est indépendante de la vitesse de germination et la demi-durée de transformation est approximativement 0,1 D/G, avec D = diamètre du grain et G = vitesse radiale de croissance, quelque soient les endroits où s'effectue la germination.

Pour des vitesses de germination faibles, la loi se rapproche de celle valable lorsque la germination s'effectue à partir de sites distribués au hasard. L'auteur discute encore les conditions déterminant les types de sites de nucléation donnant lieu au plus grand nombre de germes, et par suite la forme de la loi de la vitesse de croissance.

DIE KINETIK VON REAKTIONEN MIT KEIMBILDUNG AN DEN KORNGRENZEN

Für Umwandlungen, bei denen die neue Phase an Korngrenzflächen, Kanten oder Ecken von Körnern entsteht und bei denen die neue Phase mit konstanter Radialgeschwindigkeit wächst, werden Gesetzmässigkeiten für die Umwandlungsgeschwindigkeit abgeleitet. Dabei werden zeitabhängige und zeitunabhängige Keimbildungsgeschwindigkeiten behandelt. Bei hohen Keimbildungsgeschwindigkeiten (im Vergleich zur Wachstumsgeschwindigkeit und der Korngrösse) nimmt die Gesetzmässigkeit der Umwandlungsgeschwindigkeit eine von der Keimbildungsgeschwindigkeit unabhängige Form an und die Halbwertszeit der Umwandlung wird—unabhängig davon, an welchen Stellen die Keimbildung erfolgt—näherungsweise 0,1 D/G, wobie D der Korndurchmesser und G die radiale Wachstumsgeschwindigkeit sind. Bei kleinen Wachstumsgeschwindigkeiten nähert sich die Gesetzmässigkeit der Umwandlungsgeschwindigkeit derjenigen für regellose Verteilung der Keimbildungsstellen. Schliesslich werden die Bedingungen diskutiert, die dafür massgebend sind, an welcher Art von Keimbildungsstellen die meisten Keime entstehen und die somit den Verlauf der Umwandlungsgeschwindigkeit bestimmen.

VOL. 4 1956

It has recently been suggested by Clemm and Fisher[1] that the nucleation energy at a junction of grain boundaries could be less than at a plane boundary, and that these junctions might be favored sites for nucleation. However, there are two factors opposing this purely energetic consideration. One factor results from the ease with which these sites can transform, and might lead to a situation where these sites lie wholly in transformed material at a time early in the reaction and, hence, be no longer available to nucleation. The other factor, affecting the nucleation rate, is the number of atoms associated with each type of nucleation site. This will be least for corners (junctions of 4 grains), and will be progressively greater as, one considers edges (junctions of 3 grains), grain boundary surfaces, and the interior of grains. It is the purpose of this paper to explore the suggestion of Clemm and Fisher, by deriving the rate laws associated with reactions nucleating at such sites, developing the limits under which a particular site is favored, and examining some of the characteristics of such a reaction.

In a polycrystalline material, nucleation is assumed to occur with characteristic frequencies on four types of sites. We shall designate the homogeneous nucleation frequency per unit volume as I_v, the specific grain boundary nucleation frequency per unit area as I_s, the specific edge nucleation frequency per unit length as I_e, the specific corner nucleation frequency

* Received November 18, 1955.

† General Electric Research Laboratory, Schenectady, New York.

per corner as I_c. We should also like to define nucleation frequencies per unit volume for each type of site, $\dot{N}_v$, $\dot{N}_s$, $\dot{N}_e$, $\dot{N}_c$. If S, L, C are respectively the boundary area, edge length, grain corner number (all per unit volume), then $\dot{N}_v = I_v$; $\dot{N}_s = I_s S$; $\dot{N}_e = I_e L$; $\dot{N}_c = I_c C$. The total rate of nucleation per unit volume $\dot{N} = \dot{N}_v + \dot{N}_s + \dot{N}_e + \dot{N}_c$.

In order to compare expressions containing S, L, and C, it will be necessary to express them approximately in terms of a grain diameter. If we assume that all grains are equally large tetrakaidecahedra arranged so that they fill space [a body-centered-cubic array oriented so that the square faces are in (100) planes, and hexagonal faces in (111) planes] and call the distance between square faces D, then the edge length will be $D/2\sqrt{2}$. The number of grains per unit volume are $2/D^3$, and

$$\begin{aligned} S &= 3.35D^{-1}, \\ L &= 8.5D^{-2}, \\ C &= 12.0D^{-3}. \end{aligned} \tag{1}$$

While the actual numerical constants in equations (1) are to be taken as approximate, the functional dependence on D is assumed to be exact.

DERIVATION OF THE RATE LAWS

Nucleation and growth reactions fall into two broad classes. The first, termed "discontinuous," will be treated in this report. In this class of reactions, the transformation product which nucleates and grows has the same average composition as the untransformed material, and, except for a short distance from the advancing interface, the untransformed material has the original composition. One can assume that, after a time, steady-state conditions are achieved in which both the growth rate and the specific nucleation rate are independent of time. This assumption will be treated first. In the last section we shall treat the case where, for some reason, steady-state conditions are not achieved in the nucleation rate during a significant part of the reaction time.

The other class, to be discussed more fully in a subsequent paper, is where the transformation product is of a different composition and the untransformed material is gradually changing composition. Here the nucleation rate in the untransformed material may be a strong function of time and distance from a growing transformed region, because the nucleation rate is a strong function of composition. In the case of grain boundary nucleated reactions (and incidentally, for reactions which nucleate on dislocations), the high diffusivity in a boundary could be expected to affect further nucleation drastically for considerable distance from a growing particle.

Johnson and Mehl[2] derived the rate law for grain boundary nucleation by assuming that the transformation product could not grow across grain boundaries. It will be necessary to examine this assumption in detail. At high nucleation rates many nuclei per grain will form and the reaction will be substantially complete when Gt is of the order of the grain diameter. At low nucleation rates the reaction is far from complete at that time. If one assumes that the transformation product cannot grow across boundaries, then the fraction transformed will be equal to the fraction of the grains in which a nucleus has formed, with a correction for that fraction of the untransformed volume which is in grains which are in the process of transforming. This correction becomes a constant fraction of the untransformed volume at time greater than the time it takes a nucleus starting at time 0 to consume its grain, that is, at $t > D/G$. (This is true whether the nucleation rate is high or low, except that when it is high, at $t = D/G$ the reaction is close to completion.) Indeed, Johnson and Mehl's analysis at $t > D/G$ reduces to

$$1 - X = (1 + K)e^{-\pi D^2 I_s t},$$

where K is the constant* which denotes the fraction of the untransformed material which is in grains in the process of transforming. One predicts, therefore, that where grain boundaries are not crossed by the growing transformed material, and where K is small, a plot of log log $(1/1 - x)$ vs. log t would rapidly approach slope unity whenever $t > D/G$.

An alternate assumption, and one which will be treated here, is that grain boundaries offer no resistance to a growing nodule. It is believed that this assumption is a better approximation to the true situation. Wherever grain boundaries stop a nodule, nucleation on the other side appears to be greatly enhanced, and this situation should be better approximated as

---

*$K = 4\pi b \left[\int_0^1 e^{+4\pi b x} (1 - x)^3 \, dx + 3\int_0^1 \int_{1-x}^1 e^{4\pi b x} y^2 w(x, y) \, dy \, dx + 3\int_1^2 \int_0^{x-1} e^{4\pi b x} y^2 w(x, y) \, dy \, dx \right]$ when $Gt > D$,

where $b = \dfrac{I_s D^3}{8G}$; x and y are dummy variables;

and $w = \left[\dfrac{(1 + y)^2 - x^2}{4y}\right] \exp\left\{4\pi b \left[2(1 - y - x) + (1 + y - x \log y + (1 + y) \log \dfrac{1 + y + x}{1 + y - x} + x \log \dfrac{(1 + y)^2 - x^2}{4}\right]\right\}$

K is a function of b only. For small b, K is proportional to b.

continued growth and not as the relatively rare phenomenon of original nucleation.

In the study of pearlite, for instance, where the parameter b is small, a plot of log log $(1/1 - x)$ vs. log time usually results in a slope of 4 or more, which is the slope one would expect from randomly distributed nodules growing with no restriction to their final size except impingement with one another. The occurrence of a slope of more than 4 appears to be due to transient effects in nucleation.

The derivation of the rate laws center around the problem of impingement. The newly formed grain is assumed to grow at constant radial velocity until it impinges on another growing grain. It then stops growing along the area of contact. It will be convenient to use a device used by Avrami,[3] and Johnson and Mehl called extended volume fraction X_e. This is the sum of the volumes of all grains, divided by the total volume, assuming that the grains never stop growing and that new grains keep nucleating at the same rate in transformed as well as untransformed material. X_e can exceed unity. If nucleation is randomly distributed, then the actual volume fraction X is rigorously given by

$$X = 1 - e^{-X_e}$$

It will be necessary to define an extended area fraction and an extended line fraction. The extended area fraction Y_e is the sum of all areas of intersection of the extended grains with a plane divided by the total area of the plane. If these intersections are randomly distributed on the plane, the actual area fraction

$$Y = 1 - e^{-Y_e}$$

The extended line fraction Z_e is the sum of all lengths of a line intercepted by extended grains divided by the length of the line. If these interceptions are randomly distributed on the line, the actual line fraction

$$Z = 1 - e^{-Z_e}$$

It will be assumed that only one kind of site is active in nucleating. The case where more than one type of site is important will be discussed later.

For the case of grain boundary and grain edge nucleated reactions, two types of impingement will be treated separately. The first type is impingement among nodules originating from the same plane or edge. For example, if this occurs early in the reaction, the individual nodules would cease growing parallel to the plane or edge, further growth only occurring perpendicular to the edge or plane. An expression is derived for the total volume of the nodules originating from a plane or edge, assuming that these are only impinging with nodules originating from the same plane or edges. One next considers a random distribution of planes or edges each giving rise to a certain transformed volume, and considers impingement among these volumes.

For the case of corner nucleation, it is just assumed that the corners are randomly distributed, and limited in number.

Grain Boundary Nucleation

Consider a plane boundary B of infinite extent having a specific nucleation rate I_s. Consider an arbitrary plane A parallel to B at a distance y from B. A nodule starting to grow at B at time τ with growth rate G will have a circular intersection with A whose radius at time t is

$$\begin{aligned} &[G^2(t-\tau)^2 - y^2]^{1/2} && \text{when } G(t-\tau) > y \\ &0 && G(t-\tau) < y\,. \end{aligned}$$

The extended area fraction due to all nodules starting at a time between τ and $\tau + d\tau$ is

$$\begin{aligned} dY_e &= \pi I_s\, d\tau [G^2(t-\tau)^2 - y^2] && G(t-\tau) > y \\ &= 0 && G(t-\tau) < y, \end{aligned}$$

and

$$Y_e = \int_0^t dY_e = \pi I_s \int_0^{t-y/G} [G^2(t-\tau)^2 - y^2]\, d\tau.$$

Letting $x = y/Gt$

$$\begin{aligned} Y_e &= \pi I_s G^2 t^3 \left[\frac{1-x^3}{3} - x^2(1-x)\right] && x < 1 \\ &= 0 && x > 1 \end{aligned}$$

Since these circular intersections will be randomly distributed on A

$$Y = 1 - e^{-Y_e}.$$

The volume occupied by nodules originating from a unit area of B is then

$$V_0 = 2\int_0^\infty Y\, dy$$

$$= 2Gt \int_0^1 1 - e^{-\pi I_s G^2 t^3 \left[\frac{1-x^3}{3} - x^2(1-x)\right]}\, dx.$$

The extended volume fraction due to a boundary area S per unit volume

$$X_e = SV_0 = b_s^{-1/3} f_s(a_s),$$

where

$$a_s = (I_s G^2)^{1/3}\, t \qquad b_s = \frac{I_s}{8S^3 G} = \frac{\dot{N}_s}{8S^4 G} \qquad (2)$$

$$f_s(a_s) = a_s \int_0^1 1 - e^{-\pi a_s^3 \left[\frac{1-x^3}{3} - x^2(1-x)\right]}\, dx$$

VOL. 4 1956

and if this boundary area is assumed randomly distributed in the specimen

$$X = 1 - \exp\left[-b_s^{-1/3} f_s(a_s)\right] \qquad (3)$$

$f_s(a_s)$ was evaluated numerically, using Simpson's rule.

Grain Edge Nucleation

Consider a straight-line edge E of infinite extent having a specific nucleation rate I_e. Consider an arbitrary line F parallel to E at a distance r. A nodule starting to grow at time τ from E will intercept on F a length

$$\begin{aligned} &2[G^2(t-\tau)^2 - r^2]^{1/2} && \text{when } G(t-\tau) > r, \\ &0 && G(t-\tau) < r. \end{aligned}$$

The extended length fraction at time t due to nodules starting at a time between τ and $\tau + d\tau$ is

$$\begin{aligned} dZ_e &= 2I_e\, d\tau\, [G^2(t-\tau)^2 - r^2]^{1/2} && G(t-\tau) > r, \\ &= 0 && G(t-\tau) < r. \end{aligned}$$

Integrating with respect to t and substituting x for r/Gt, we get

$$\begin{aligned} Z_e &= I_e G t^2 \left[\sqrt{1-x^2} - x^2 \log \frac{1+\sqrt{1-x^2}}{x}\right] && x < 1, \\ &= 0 && x > 1. \end{aligned}$$

The volume occupied by nodules originating from a unit length of E is

$$V_0 = \int_0^\infty 2\pi r Z\, dr = 2\pi G^2 t^2 \int_0^1 x(1 - e^{-Z_e})\, dx. \qquad (4)$$

Randomly distributing an edge length L in a unit volume will give

$$X = 1 - \exp\left[-b_e^{-1} f_e(a_e)\right]$$

where

$$a_e = \sqrt{I_e} G \cdot t \qquad b_e = \frac{I_e}{2\pi G L} = \frac{\dot{N}_e}{2\pi G L^2} \qquad (5)$$

$$f_e(a_e) = a_e^2 \int_0^1 x \left\{1 - e^{-a_e^2\left[(1-x^2)^{1/2} - x^2 \log \frac{1+\sqrt{1-x^2}}{x}\right]}\right\} dx$$

$f_e(a_e)$ was evaluated, using Simpson's rule.

Corner Nucleation

Here there is no problem about impingement between nodules starting from the same corner. The first nucleus is the only one which will determine how much volume will contribute to the extended volume. If the specific nucleation rate per corner is I_c, then the fraction of corners nucleating for the first time at a time between t and $t + dt$ is $e^{-I_c t}\, dt$. The extended volume fraction at time t is therefore

$$X_e = C \int_0^t \frac{4\pi}{3} G^3 (t-\tau)^3 \exp(-I_c \tau)\, d\tau$$

and $$= b_c^{-3} f_c(a_c) \qquad (6)$$

$$X = 1 - \exp\left[-b_c^{-3} f_c(a_c)\right]$$

where $a_c = I_c t$

and $$b_c = \left(\frac{3}{4\pi C}\right)^{1/3} \frac{I_c}{G} = \left(\frac{3}{4\pi C^4}\right)^{1/3} \frac{N_c}{G}$$

$$f_c(a_c) = a_c^3 - 3a_c^2 + 6a_c - 6\,(1 - e^{-a_c}),$$

which is the same as the expression derived and tabulated by Avrami for a limited number of randomly distributed nucleation sites.[4] The three functions $f(a)$ are tabulated in Table 1.

DISCUSSION

It will be noticed that all of the above rate laws can be plotted as log log $(1/1 - X)$ vs. log t to give characteristic master curves, Figs. 1–3, in which two parameters are undetermined as additive scale factors. Thus, instead of a family of curves obtained by Johnson and Mehl, a single curve is obtained. The parameters of Johnson and Mehl are related to the parameters a and b in the following way: The b's are equivalent to Johnson and Mehl's shape factor λ, in that they can both be expressed as $\dot{N}D^4/G$ times a geometrical constant. The a's are respectively proportional to $b_s^{1/3}Z$, $b_e^{1/2}Z$, and $b_c Z$. All curves have slope 4 when a is small and approach the equation

$$X = 1 - e^{-\pi/3 \dot{N} G^3 t^4}$$

which is identical with that obtained for randomly placed nucleation sites. In the vicinity of $a = 1$, the curves change slope. This change of slope is due to a process which we shall call site saturation. In the case of corner nucleation it occurs because there are only a limited number of corners. In the case of grain boundary and edge nucleation it occurs because the nucleation sites are not randomly distributed, but are in the vicinity of other nucleation sites. Hence, they have a greater probability of being transformed. Therefore, the fraction of boundary area or edge length transformed is larger than the volume fraction transformed, and the nucleation rate which is proportional to the untransformed area or length drops off faster than the untransformed volume. In the limit of $a \gg 1$, nucleation is so small compared to the untransformed volume fraction that the curves can be

approximated by ones derived on the assumption that all nucleation occurred everywhere at time zero.

For small values of the parameter b, the increase in probability for a boundary to be transformed compared to the rest of the material is small and the site saturation will not occur until the sample is almost completely transformed. It will occur early in the reaction if b is large. Substituting the approximate values of S, L, and C into the expressions for b, we get

$$b_s = 9.9 \times 10^{-4} \frac{\dot{N}_s D^4}{G}$$

$$b_e = 2.2 \times 10^{-3} \frac{\dot{N}_e D^4}{G}$$

$$b_c = 4{\cdot}9 \times 10^{-2} \frac{\dot{N}_c D^4}{G}.$$

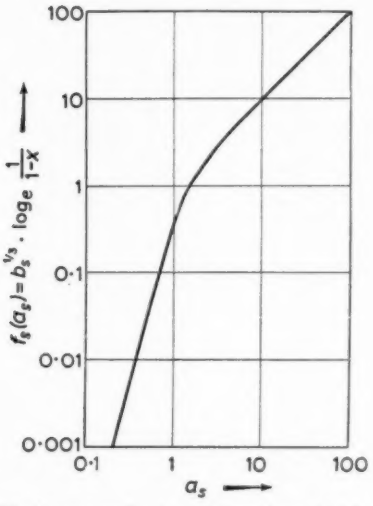

FIG. 1. Master curve for transformations which nucleate on grain boundary surfaces.

The requirement that site saturation occurs early in the reaction can be obtained from the Figs. 1–3 by finding a value of b for which the reaction would bend in the vicinity of half reaction. From this, one gets that whenever

$$\dot{N}_s > 6 \times 10^3 \, G/D^4,$$

$$\dot{N}_e > 10^3 \, G/D^4, \qquad (7)$$

or

$$\dot{N}_c > 2.5 \times 10^2 \, G/D^4$$

site saturation can be expected to occur early in the reaction.

The time at which saturation occurs is

$$t = (I_s G^2)^{-1/3},$$

$$= (I_e G)^{-1/2},$$

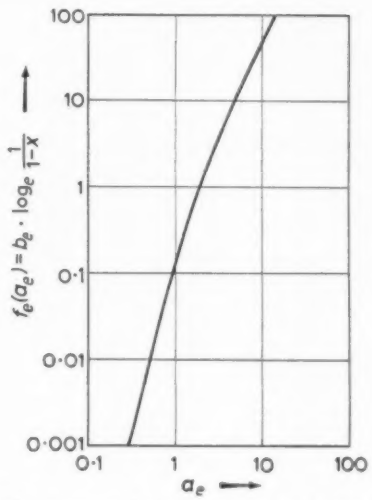

FIG. 2. Master curve for transformations which nucleate on grain edges.

or

$$= I_c^{-1},$$

which is independent of grain size.

At very large values of b the sites would saturate very early in the reaction, and further nucleation would cease. For a grain boundary nucleated reaction the transformed region would occupy an ever-thickening slab of material with the original boundary at its center. The rate law would then be of the form

$$X = 1 - e^{-2SGt}$$

which is what equation (3) approaches. Similarly, one would expect that for edge-nucleated reactions

$$X = 1 - e^{-\pi LG^2t^2}$$

which is the limit of equation (5) for large values of b.

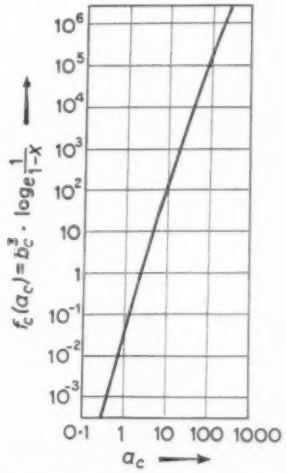

FIG. 3. Master curve for transformations which nucleate on grain corners.

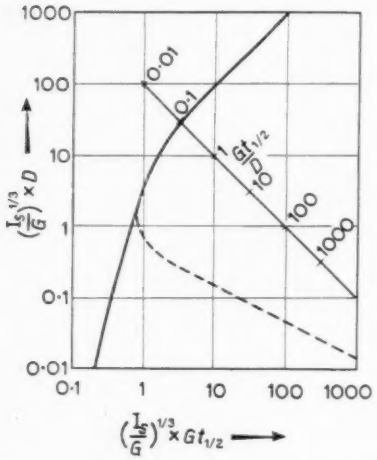

FIG. 4. Theoretical curves for half-times of transformations which nucleate on grain boundary surfaces.
This Paper ————
Johnson and Mehl - - - - - -

For corner nucleation equation (6) becomes

$$X = 1 - e^{-\frac{4\pi}{3} CG^3 t^3}$$

which is what one expects for a limited number of sites which nucleate at an early time.

The range from 1% reaction to 99% reaction is quite short, only a factor of 500 on the log $(1/1 - x)$ scale, or 2.7 cycles on the log log $(1/1 - x)$ scale. Since this is the limit of observation, most kinetic observations will be entirely in the straight-line extremes of Figs 1–3. Saturation will usually occur before 1% reaction, or not till after 99% reaction. Only in those reactions where parameter b is such that the inequalities (7) are close to being equalities, will the transition to saturation be observable. Even then, especially for corner nucleation, the kinetic data will not curve much in the observed range, but will appear to give a fairly straight line of intermediate slope.

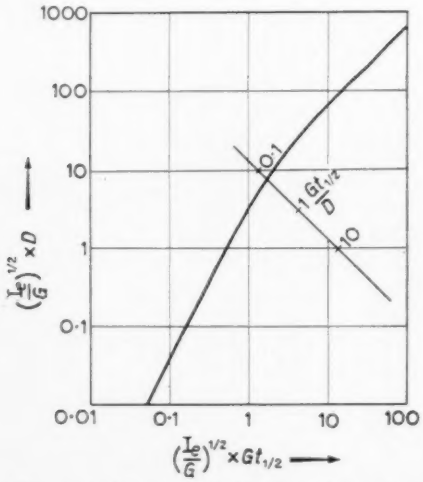

FIG. 5 Theoretical curve for half-times of transformations which nucleate on grain edges.

The Half-time of a Reaction and Its Dependence on Grain Size

The time required for a reaction to reach a certain stage of completion is a convenient parameter for cataloging the speed of a reaction. The relationships involving the half-time will be discussed here, but they can be generalized to the time for any fraction completion by substituting for ln 2, ln $(1/1 - X)$, where X is the desired fraction.

Substituting 0.5 for X, and $a' = a(t_{1/2})$, where $t_{1/2}$ is the half-time, into equations (3), (5), and (6), we get upon rearrangement

$$b_s^{1/3} = \frac{f_s(a'_s)}{\ln 2} ,$$

$$b_e = \frac{f_e(a'_e)}{\ln 2} ,$$

$$b_c^3 = \frac{f_c(a'_c)}{\ln 2} .$$

These equations may be used to find the relationship between the I's, G, D, and $t_{1/2}$, for the various types of nucleation sites.

Of particular interest is the relationship between $t_{1/2}$ and grain size, keeping the I's and G fixed (constant temperature).

Substituting the approximate expressions for

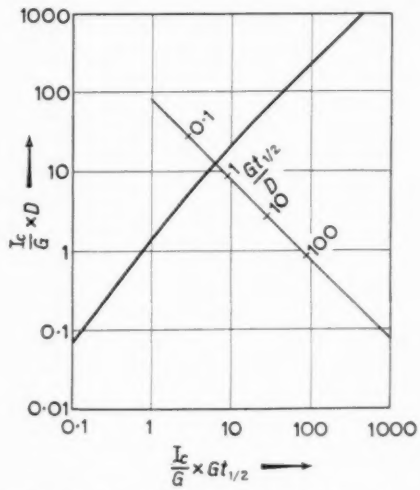

FIG. 6 Theoretical curve for half-times of transformations which nucleate on grain corners.

S, L, C into the b's and rearranging, we obtain

$$\left(\frac{I_s}{G}\right)^{1/3} D = 9.7\, f_s(a_s'),$$

$$\left(\frac{I_e}{G}\right)^{1/2} D = 8.8\,[f_e(a_e')]^{1/2}, \tag{8}$$

$$\left(\frac{I_c}{G}\right) \quad D = 4.18\,[f_c(a_c')]^{1/3},$$

since

$$\left(\frac{I_s}{G}\right)^{1/3} Gt_{1/2} = a_s'$$

$$\left(\frac{I_e}{G}\right)^{1/2} Gt_{1/2} = a_e'$$

$$\left(\frac{I_c}{G}\right) \quad Gt_{1/2} = a_c'$$

a plot of a_s against $9.7\, f_s(a_s)$; a_e against $8.8\,[fe(a_e)]^{1/2}$; or a_c against $4.18\,[f_c(a_c)]^{1/3}$ is a plot of D against $Gt_{1/2}$, for the various types of nucleation, with D and $Gt_{1/2}$ plotted in the same units and G/I to the appropriate power as the scale factor. This is plotted in Figs. 4–6 on a double log plot. The scale factor is now an additive constant. Since it is the same additive constant, the only permissible translation for the master curves, if IG is unknown, is along a 45° line. Also, points having a certain value of $(Gt_{1/2}/D)$ are constrained to lie on a certain 45° line. A $(Gt_{1/2}/D)$ axis is therefore indicated.

Figs. 4–6 can be used to obtain relationships between $Gt_{1/2}$, D, and I/G, or any of their combinations, if the type of site responsible for nucleation is known. A knowledge of the parameter b for example is sufficient to determine the value of $Gt_{1/2}/D$ and the parameter a'. An experimentally determined relationship among these parameters can be used to determine what type of site is responsible for nucleation. For comparison, the curve obtained from Johnson and Mehl's equations is also plotted (Fig. 4—dotted curve). The agreement is very good along the upper portion ($\pm 4\%$). However, one sees immediately that one consequence of the assumption that the transformation product cannot cross a grain boundary is that, at small enough grain size, the reaction rate decreases as the grain size decreases. This is apparent if one considers the consequences of that assumption. At sufficiently small grain size the time for half-reaction will be that required for half of the grains to obtain at least one nucleus. However, the area available for each grain to receive a nucleus decreases as the square of its diameter, and the half-time should increase with the inverse diameter squared.* At sufficiently large grain diameter, the grains have no trouble nucleating, and the half-time is the time required for the growing transformation product to consume half of its grain, which varies directly as the diameter.

The following conclusions can be drawn from the curves: (1) If, and only if, site saturation occurs, $Gt_{1/2}$ is approximately equal to $0.1D$. This corresponds to the upper portion of the curves, and is independent of the type of nucleating site. (2) $t_{1/2}$ can never be appreciably less than $0.1\,D/G$ for any reaction where nucleation occurs only on boundaries or intersections of boundaries. (3) At sufficiently low values of the parameter, $b = (\dot{N}D^4/G)$, the half-time is given approximately by $(\dot{N}G^3)^{-1/4}$, if the transformation product can cross boundaries. This is the same result one would expect for homogeneous nucleation.

Since the I's are independent of grain size, substitution into $(\dot{N}G^3)^{-1/4}$ leads to the result that $t_{1/2}$ is proportional to the $D^{1/4}$ for boundary nucleation, $D^{1/2}$ for surface nucleation, $D^{3/4}$ for corner nucleation, as well as D^1 for site saturation and D^3 for homogeneous nucleation.

Rates if More Than One Type of Site is Active

Whenever more than one type of site is active, the impingement problem is considerably more complicated. Certain limits can be discussed, however. Until one type of site begins to saturate, the rate law can be approximated by

$$X = 1 - e^{-\frac{\pi}{3}\dot{N}G^3t^4} \tag{9}$$

where $\dot{N}$ is the sum of all the $\dot{N}$'s.

Because of the geometry, when the boundaries saturate, the edges and corners saturate too, regardless of their specific nucleation rate. When the edges saturate, the corners saturate too, while the boundaries can continue to nucleate. When corners saturate, both edges and boundaries can continue to nucleate. The saturation of a type of site limits all further nucleation on sites of "lower dimensionality".†

*Another way of looking at it is that, when the grains become sufficiently small, the volume nucleation rate will increase as the surface area or as $1/D$, while the amount of transformation per nucleus will decrease as D^3. The over-all rate will decrease as D^2, and the half-time will increase as $1/D^2$.

For grain-edge and grain-corner nucleation the half-times will similarly depend on D^{-1} and D^0 instead of $D^{1/2}$ and $D^{3/4}$.

†For convenience, we shall refer to the dimensionality of a site as being 0 for corners, 1 for edges, 2 for boundaries, 3 for homogeneous nucleation. It is intended only as a notation, and what follows does not hold for nucleation on other types of sites to which a dimensionality can be assigned, such as vacancies, dislocation, etc.

VOL. 4 1956

What occurs when a site saturates depends therefore on the type of site as well as the relative values of the $\dot{N}$'s. The important site initially is the one whose $\dot{N}$ is the largest. From the inequalities (7) one can see that only sites of lower dimension than this site can saturate at an earlier time. If they do, they cease nucleating, and their effect on the rate law is one of changing $\dot{N}$ in equation (9) to a lower value. When the type of site with the largest contribution to $\dot{N}$ saturates, the rate law is approximated by adding the extended volumes of sites, of higher dimensionality only, to the extended volume of the site whose $\dot{N}$ is largest. If the $\dot{N}$'s are much smaller, these sites will never contribute much. If they are of comparable magnitude, the reaction rate will eventually be dominated by the new mode. The final stage will be dominated by the mode of highest dimensionality where the inequalities (7) hold.

The half-time will be of the order of $0.1\,D/G$ whenever one or more types of sites saturate early. If none saturate, it will be given approximately by $(\dot{N}G^3)^{-1/4}$. Therefore the half-time will depend on grain size in a way characteristic of the mode which contributes most to the volume nucleation.

NUCLEATION RATES

It was noted in the last section that it is necessary to know something about the relative nucleation rates for the various types of sites in order to determine which rate law the system will follow. It is also necessary to know something about the nucleation rate relative to G/D^4 in order to determine whether a site will saturate.

We will assume that the specific nucleation rates are given by equations of the form

$$I = \nu\rho \exp -\left(\frac{\Delta F^* + \Delta F_A}{kT}\right) \qquad (10)$$

where ν is a frequency factor, ρ the density of sites, ΔF^* is the minimum free energy required to form a nucleus, and ΔF_A is the free energy of activation for a nucleus to continue to grow. If δ is an effective grain boundary thickness and n the number of atoms per unit volume, ρ approximately equals $n(\delta/D)^{3-j}$. ν and ΔF_A can be assumed to be the same for all sites.

The volume nucleation rate for each site is then approximately

$$\dot{N}_j = \nu n \left(\frac{\delta}{D}\right)^{3-j} \exp -\left(\frac{\Delta F_j^* + \Delta F_A}{kT}\right) \qquad (11)$$

where j is the dimensionality of the site. This can be assumed to include homogeneous nucleation, although

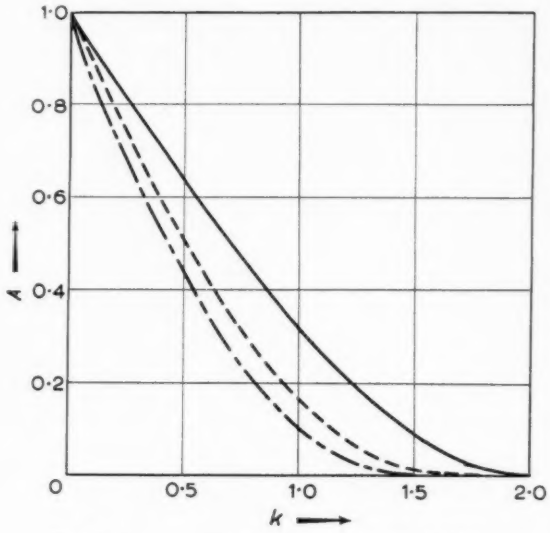

FIG. 7. ———— Grain boundary nucleation
– – – – – – Grain edge nucleation
— – — – Grain corner nucleation
Relative nucleation energies.

ΔF_A could be expected to differ from that of the other types of sites.

The calculation of nucleation rate is critically dependent on the assumption one has to make to calculate ΔF^*. However, to illustrate the relationships obtained, we shall use the calculations of Clemm and Fisher,[1] who assumed no strain energy, and a surface energy which was independent of orientation and curvature. One can express their value of ΔF_j^* as $\Delta F_j^* = A_j \Delta F_0^*$, where ΔF_0^* is the homogeneous nucleation energy and the parameter A_j which is a function of the ratio K of boundary energy to nucleus surface energy only. Fig. 7 is a plot of A_j versus this ratio. It will be noted that A decreases monotonically as one goes to nucleation sites of lower dimensionality. The exponential term in equation (11) favors sites of lower dimensionality. The degree to which this occurs is a function of ΔF_0^* as well as the differences in the A's for the various sites.

Opposing the energy consideration is the density of sites effect, which is $(\delta/D)^{\Delta j}$, and which favors sites of higher dimensionality. The ratio of these two opposing factors

$$R = \frac{\log_e D/\delta}{\Delta F_0^*/kT}$$

is a useful function. Forming the ratio of nucleation rates on sites of dimensionality i and j, we get that

$$\frac{\dot{N}_i}{\dot{N}_j} = (D/\delta)^{i-j} \exp -\frac{(A_i - A_j)\,\Delta F_0^*}{kT}$$

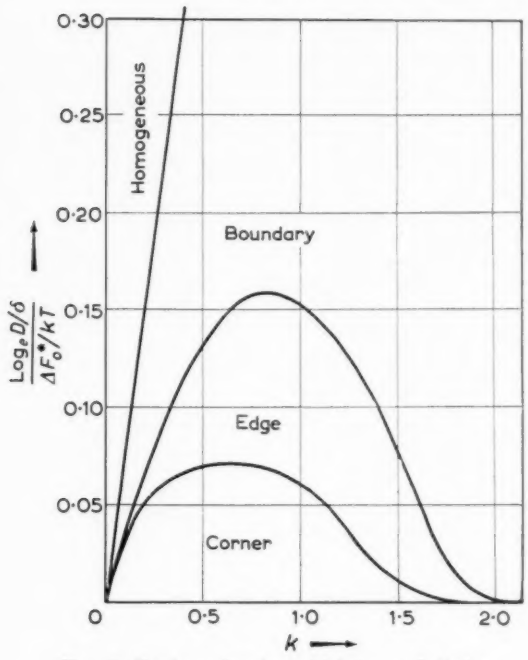

FIG. 8. Regions showing which type of site has the highest initial nucleation rate.

and $$\frac{kT}{\Delta F_0^*}\log_e\frac{\dot{N}_i}{\dot{N}_j} = (i-j)\,R - (A_i - A_j)$$

The requirement that $\dot{N}_i$ is greater than $\dot{N}_j$ is then that

$$(i-j)\,R < A_i - A_j$$

or

$$R < \frac{A_i - A_j}{i-j}\; i > j$$

$$R > \frac{A_i - A_j}{j-i}\; j > i\ .$$

If an interval of R can be found where these inequalities hold for all j, then in this interval, sites j will contribute most to the nucleation rate. For the A's determined from Fisher and Clemm, the sites which will have the highest nucleation rate are

the corners	when $R < A_e - A_c$
the edges	when $A_e - A_c < R < A_s - A_e$
the boundaries	when $A_s - A_e < R < 1 - A_s$

and homogeneous nucleation will predominate when $R > 1 - A_s$. Fig. 8 is a plot of these regions.

It is quite conceivable that in an actual system some sites will exist which will never contribute significantly to N. If, for example,

$$A_e > \frac{A_s + A_c}{2}$$

edge nucleation would never predominate, and the area marked edge in Fig. 8 would be absent.

Fig. 8 is not a plot of nucleation rates. It will be useful to sketch in several constant nucleation rate curves. If we assume $\nu n \exp(-\Delta F_A)/(kT) = 10^{30}$ cm^{-3} sec^{-1}, $D = 10^{-2}$ cm, $\delta = 10^{-8}$ cm, we can obtain four curves (Fig. 9). The lowest figure is that for $\dot{N} = 1$ cm^{-3} sec^{-1}, which can be taken as a lower limit of nucleation rate, the next three curves are those which obey the inequalities (7). The curves for saturation of sites of higher dimensionalities are continued into regions of lower dimensionality, since, after saturation of the lower site, the higher sites will continue to nucleate and will saturate too if R is large enough. From Fig. 9 it is apparent that under certain conditions one might never see nucleation of sites of lower dimensionality, because the undercooling required to get appreciable nucleation might place the reaction at a value of R where a higher mode of nucleation predominates.

In order to estimate what to expect as a function of undercooling, let us express ΔF_0^* in terms of a reduced temperature. $\theta = T/T_{eq}$, where T_{eq} is the equilibrium temperature. ΔF_0^* is then approximately

$$\Delta F_0^* = \frac{16\pi}{3}\,\frac{\gamma^3}{(\Delta H)^2\,kT_{eq}}\,\frac{1}{(1-\theta)^2\theta}$$

where ΔH is the heat of the reaction, and γ is the nucleus surface energy. Then

$$R = \frac{3(\Delta H)^2\,kT_{eq}\log D/\delta}{16\pi\gamma^3}\cdot\theta(1-\theta)^2$$

and the maximum R

$$R_{max} = \frac{(\Delta H)^2\,kT_{eq}\log D/\delta}{36\pi\gamma^3} \text{ at } \theta = 1/3.$$

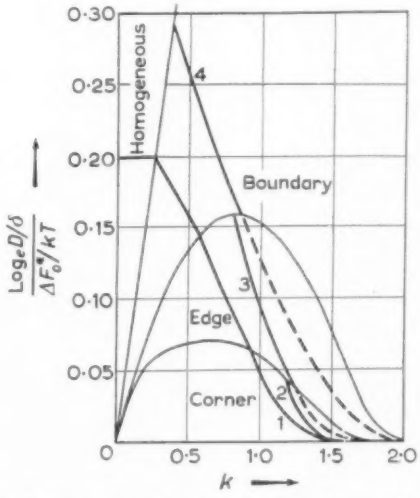

FIG. 9. Typical example showing conditions for barely detectable nucleation 1; nucleation sufficiently rapid for corner saturation 2; edge saturation 3, boundary surface saturation 4.

VOL. 4 1956

R rises initially as the undercooling squared reaches $\frac{1}{2}R_{max}$ at $\theta = \frac{2}{3}$, and has a very long plateau. If R_{max} is small for certain values of K, only modes of lower dimensionality will ever predominate. If R_{max} is large, R in the regions of interest in Figs. 8 and 9 can be taken as proportional to undercooling squared.

MORE GENERAL RATE LAWS

For the pearlite reaction it has been established that the nucleation rate is not constant, but a function of time.[5, 6] This may be due to the fact that it takes a finite time to establish a steady-state nucleation rate,[7] or as in the case of eutectoids it might be due to the fact that two phases have to be nucleated, the second nucleating in the changing environment of the first growing by itself, or nucleating on an ever-increasing surface of the first.[8]

Hull, Colton, and Mehl[6] have derived the rate law for homogeneous nucleation, when the nucleation rate can be expressed as a power series of time.

It is fairly simple to generalize the derivations of the rate laws given here to include a time-dependent nucleation rate I as well as the prior existence of nuclei, which instantaneously start growing at time 0. Let us call the number of such nuclei per unit area of boundaries J_s, per unit length of edges J_e, and the fraction of corners which have these nuclei J_c. Then as before we will assume that only one type of site is active.

The derivations lead to

$$X_s = 1 - \exp\left\{-2SGt\left[1 - \int_0^1 \exp\left(-\pi G^2 t^2 \times \left\{J_s(1-x^2) + \int_0^{t(1-x)} I_s\left[\left(1-\frac{\tau}{t}\right)^2 - x^2\right] d\tau\right\}\right) dx\right]\right\} \quad (12)$$

for grain boundary nucleation;

$$X_e = 1 - \exp\left\{-\pi L G^2 t^2\left[1 - 2\int_0^1 y \times \exp\left(-2Gt\left\{J_e(1-y^2)^{1/2} + \int_0^{t(1-y)} \times I_e\left[\left(1-\frac{\tau}{t}\right)^2 - y^2\right]^{1/2} d\tau\right\}\right) dy\right]\right\} \quad (13)$$

for edge nucleation; and

$$X_c = 1 - \exp\left\{\frac{4\pi}{3} C G^3 t^3\left[J_c - \left(1-J_c\right)\int_0^t \times I_c\left(1-\frac{\tau}{t}\right)^3 \times \exp\left(-\int_0^\tau I_c\, dt\right) d\tau\right]\right\} \quad (14)$$

for corner nucleation.

Similarly, one can derive an expression for homogeneous nucleation, using J_v for the number of nuclei present at time zero. This leads to

$$X_v = 1 - \exp\left\{-\frac{4\pi}{3} G^3 t^3\left[J_v \times \int_0^t I_v\left(1-\frac{\tau}{t}\right)^3 d\tau\right]\right\} \quad (15)$$

At high nucleation rates and long times, equation (12) reduces to

$$X = 1 - e^{-2SGt}$$

and equation (13) reduces to

$$X = 1 - e^{-\pi L G^2 t^2}$$

Since

$$I_e \exp\left\{-\int_0^t I_e\, dt\right\} = \frac{d}{dt}\left[\exp\left\{-\int_0^t I_e\, dt\right\}\right]$$

at high nucleation rate and long times, equation (14) reduces to

$$X = 1 - e^{-\frac{4\pi}{3} C G^3 t^3}$$

These limits are identical with those previously derived for constant nucleation rate. Site saturation exists and leads to a rate law which is independent of the nucleation rate, whether constant or not.

At the other extreme, far from saturation, equations (12), (13), and (14) reduce to equation (15). This is accomplished by expanding the exponentials in the integrand into a power series and interchanging the order of integration.

Far from saturation, then, the nucleation rate does not enter as an average as has often been assumed, but as a third moment about the time t. In other words, the nuclei are weighted according to the cube of the length of time they have been in existence.

The determination of the nucleation rate from a rate law is therefore a very complicated problem. Even for equation (15), which has a simple solution mathematically,

$$\dot{N} = -\frac{1}{8\pi G^3}\frac{\partial^4 \log(1-X)}{\partial t^4},$$

it is unlikely that kinetic data can be obtained with sufficient accuracy to make this solution useful.

If the nucleation rate follows an expression of the type

$$I_j = B_j t^n$$

it is possible to integrate equations (12–15). A plot of log log $(1/1-x)$ against log t would be similar to those of Figs. 1–3, except that the initial part of the

curve would have slope $4 + n$. The parameters a and b would become of the form

$$a_s = (B_s G^2)^{1/(3+n)} \cdot t$$

$$b_s = \frac{B_s}{S^{3+n} G^{1+n}}$$

$$a_e = (B_e G)^{2/(2+n)} \cdot t$$

$$b_e = \frac{B_e}{L^{1+n/2} G^{1+n}}$$

$$a_c = B_c^{1/(1+n)} \cdot t$$

$$b_c = \frac{B_c}{C^{(1+n)/3} G^{1+n}}$$

The half-time at saturation would be independent of the nucleation rate, while the expected half-time at low nucleation rates would be

$$t_{1/2} = \left[\frac{(n+1)(n+2)(n+3)(n+4)}{8\pi}\right]^{1/4+n} \left(\frac{1}{KG^3}\right)^{1/4+n}$$

where $K = B_s S$, $B_e L$, or $B_c C$ respectively for grain boundary, edge, or corner nucleation. The dependence of $t_{1/2}$ on grain size far from saturation would then be

$$t_{1/2} \propto D^{3-j/4+n},$$

where j is the dimensionality of the site.

REFERENCES

1. P. J. Clemm and J. C. Fisher *Acta Met.* **3,** 70–73 (1955).
2. W. A. Johnson and R. F. Mehl *Trans. Amer. Inst. Min. Met. Eng.* **135,** 416–442 (1939).
3. M. Avrami *J. Chem. Phys.* **7,** 1103–1112 (1939); **8,** 212–224 (1940); **9,** 177–184 (1941).
4. J. E. Burke and D. Turnbull *Progress in Metal Physics* **3,** 226 (1952).
5. E. Scheil and A. Langeweise *Arch. Eisenhüttenw* **11,** 93 (1937).
6. F. C. Hull, R. A. Colton, and R. F. Mehl *Trans. Amer. Inst. Min. Met. Eng.* **150,** 185–207 (1942).
7. D. Turnbull *Trans. Amer. Inst. Min. Met. Eng.* **175,** 774 (1948).
8. J. C. Fisher, from *ASM Symposium on Thermodynamics in Physical Metallurgy*, p. 201–241.

VOL.
4
1956

THE SURFACE TENSIONS OF LIQUID-METAL SOLUTIONS*

J. W. TAYLOR†

Two analytical methods are presented for the calculation of the surface tensions of binary liquid-alloy mixtures. Calculated surface tension-composition relationships are compared with the corresponding experimental values for ten binary systems.

For six simple eutectic systems the agreement is good. Three systems, showing intermediate phase formation in the solid state, exhibited considerable discrepancies between the calculated and experimental relationships. It is suggested that in these systems the surface has not the simple monolayer structure assumed in the analysis. In one system of peritectic form, the agreement was intermediate between the above two extremes.

It was not found possible to invert the analysis to calculate activity-composition relationships from surface tension data, although this is theoretically possible.

LES TENSIONS SUPERFICIELLES DE SOLUTION DE METAUX LIQUIDES

Deux méthodes analytiques sont présentées pour calculer des tensions superficielles dans les mélanges liquides d'alliages binaires.

Les relations entre les tensions superficielles calculées et la composition sont comparées avec les valeurs expérimentales correspondantes pour 10 systèmes binaires. Pour six systèmes eutectiques simples, l'accord est bon.

Trois systèmes montrant la formation de phases intermédiaires à l'état solide, présentent une divergence considérable entre les valeurs calculées et les valeurs expérimentales. Il est suggéré que dans ces systèmes la surface n'a pas la simple structure de monocouche supposée dans l'analyse. Dans un système de forme péritectique, l'accord est intermédiaire entre les deux extrêmes cités ci-dessus. Il n'a pas été possible d'appliquer cette analyse au calcul des relations activité—composition à partir des tensions superficielles, bien que ce soit théoriquement possible.

DIE OBERFLÄCHENSPANNUNG VON LÖSUNGEN FLÜSSIGER METALLE

Zur Berechnung der Oberflächenspannungen binärer Legierungsschmelzen werden zwei analytische Verfahren angegeben. Für zehn binäre Systeme werden dann die berechneten Beziehungen zwischen Oberflächenspannung und Zusammensetzung mit den entsprechenden experimentellen Werten verglichen.

Bei sechs einfachen eutektischen Systemen ist die Übereinstimmung gut. Dagegen zeigten sich bei drei Systemen, die im festen Zustand intermediäre Phasen bilden, beträchtliche Diskrepanzen zwischen den berechneten und den experimentell ermittelten Beziehungen. Es ist zu vermuten, dass in diesen Systemen die Oberfläche nicht die der Berechnung zugrunde gelegte einfache Struktur einer monoatomaren Schicht hat. Bei einem System mit Peritektikum lag die Übereinstimmung in der Mitte zwischen den beiden oben genannten Extremfällen.

Obwohl dies theoretisch möglich ist, ist es nicht gelungen, in umgekehrter Richtung aus den Daten über die Oberflächenspannung Beziehungen zwischen Aktivität und Zusammensetzung zu berechnen.

1. INTRODUCTION

Experimental surface tension-composition relationships exist for a number of binary liquid alloys,[1] but no satisfactory interpretation of such relationships, in terms of other physical parameters of the systems, has so far been proposed. Little is known also about the nature of the liquid surface and the effect which variations in interatomic forces, as for example on alloying, may have on this surface structure. The only serious attempt so far made to correlate surface tension-composition relationships and alloying behaviour was by Pelzel,[2] who determined the deviation of the experimental surface tensions of alloys from that predicted from a rule-of-mixture consideration of the alloy composition. On this basis, he concluded that systems with and without intermediate phase formation in the solid state differ in the order of magnitude of the deviations of the experimental surface tensions from those derived from the rule-of-mixture assumption. This treatment can only be regarded as over-simplified, ignoring as it does surface adsorption and activity considerations.

In this paper a more rigorous treatment of the problem is made, using as a basis the theoretical treatments of Schuchowitzky[3] and Guggenheim.[4]

2. THEORETICAL ANALYSIS

From a consideration of the total and free energies of a surface, defined as a monolayer at the boundary

* Received November 29, 1955.

† Metallurgy Division, Atomic Energy Research Establishment, Harwell, Berks, England.

between the bulk solution and the gas phase, Schuchowitzky[3] derived the general expression for the surface tension of a solution:

$$\sigma = \Sigma n_i(\lambda_i - \mu_i) \quad (1)$$

where σ = surface tension of the solution, n_i = number of moles of component i per unit area, λ_i = chemical potential of component i in the surface layer in the sense defined by Butler,[5] and μ_i = chemical potential of component i in the bulk solution.

He has simplified expression (1) in the case of a binary solution by applying the standard relationship between chemical potential of a component in the bulk phase and its activity and by assuming that a corresponding relationship exists for the component in the surface layer. Furthermore, he assumed that the area per molecule of component in the surface layer of the solution is equal to that in the pure component; the pure components are taken as standard states in relation to the thermodynamic activities. Thus, the final relationships derived by Schuchowitzky for the surface tension of a binary solution are:

$$\sigma = \sigma_1 + n_{01}\, RT \ln b_1/a_1 \quad (2)$$

and

$$\sigma = \sigma_2 + n_{01}\, RT \ln b_2/a_2 \quad (3)$$

where σ = surface tension, n_0 = specific number of moles in the surface layer, T = absolute temperature, b = activity of the component in the surface layer, a = activity of the component in the bulk solution. Subscripts 1 and 2 refer to the components of the binary system.

The relationship between the activities in the surface layer and in the bulk solution is given as:

$$b_1/b_2^{\gamma} = a_1/a_2^{\gamma} \exp([\sigma_2 - \sigma_1]/n_{01}RT) \quad (4)$$

where λ = displacement coefficient = A_1/A_2, where A = molar surface area of the component.

Guggenheim's statistical-mechanical treatment has been presented in detail elsewhere.[4, 6] It involves the setting up of a grand partition coefficient for the surface, which is again defined as a monolayer at the liquid-vapor interface. The surface tension of the liquid is related to the partition coefficient thus:

$$\sigma A = kT \ln \Xi \quad (5)$$

where σ = surface tension, A = surface area, k = Boltzmann constant, T = absolute temperature, Ξ = grand partition coefficient for the surface.

On the basis of a quasi-crystalline model for the structure of a liquid, the partition function for the surface of a binary solution is derived for the general case, and is subsequently evaluated for regular solutions, as defined by Guggenheim.[4] The final expression for the surface tension of such a binary solution is given as:

$$\exp(\sigma a/-kT) = (1 - x)\exp(\sigma_1 a/-kT) \times \exp(mx^2 w/kT) + x\exp(\sigma_2 a/-kT) \times \exp(m[1 - x]^2 w/kT) \quad (6)$$

where σ = surface tension, a = average area per molecule in the surface layer, k = Boltzmann constant, T = absolute temperature, x = mole fraction of component 2, m = fraction of the co-ordination number corresponding to the number of bonds between the surface layer and the layer below, w = interchange energy of a bond between components 1 and 2. Subscripts 1 and 2 refer to the components of the binary solution.

3. EVALUATION OF THEORETICAL TREATMENTS

In applying the first theoretical analysis, expressions (4) and (2) or (3) were employed. In addition, it was assumed that the functional relationship between (b_1/b_2^{γ}) and b_1 was the same as that between (a_1/a_2^{γ}) and a_1, so that from a knowledge of the latter, established by independent experimental study, appropriate values of b_1 could be deduced. Initially it was also assumed that the displacement coefficient, $\lambda = A_1/A_2$ was independent of composition, i.e. that there was a linear relationship between specific volume and composition. The following specimen calculation for the Bi-Sn system illustrates the type of calculation employed:

Expressions:

$$\sigma = \sigma_{Bi} + n_{Bi}\, RT \ln \frac{b_{Bi}}{a_{Bi}} \quad (2^1)$$

$$\frac{b_{Bi}}{b_{Sn}^{\gamma}} = \frac{a_{Bi}}{a_{Sn}^{\gamma}} \exp \frac{\sigma_{Sn} - \sigma_{Bi}}{n_{Bi}RT} \quad (4^1)$$

Temperature $T = 608°K$

Surface tension of Bi = 371 dynes/cm.

Surface tension of Sn = 560 dynes/cm.

Molar surface area of Bi = $A_{Bi} = 6.95 \times 10^8$ cm^2.

Molar surface area of Sn = $A_{Sn} = 6.00 \times 10^8$ cm^2.

Coefficient of displacement = 1.16.

The activity-composition data was that from Seltz and Dunkerley.[7]

$$\exp \frac{\sigma_{Sn} - \sigma_{Bi}}{n_{Bi}RT} = \exp \frac{189}{72.8} = 13.30$$

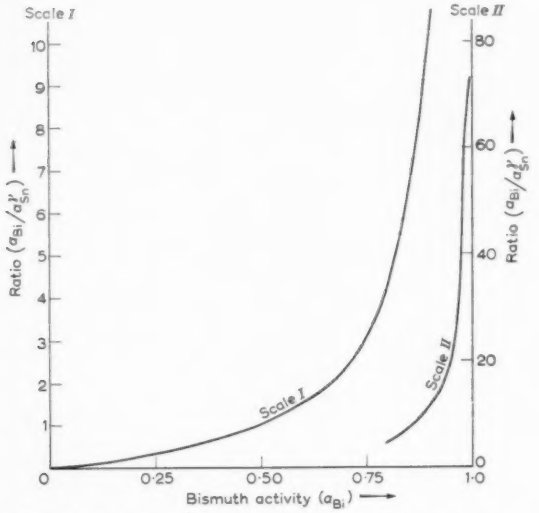

FIG. 1. Relationship (a_{Bi}/a_{Sn}^{γ})–(a_{Bi}) for Bi-Sn system.

The functional relationship between (a_{Bi}/a_{Sn}^{γ}) and a_{Bi} is shown in Fig. 1, using two scales, one for a_{Bi}=0–0.9 and one for a_{Bi} = 0.8–0.975; the activity-composition relationships are also shown.

(i) For composition

$N_{Bi} = 0.796$, $N_{Sn} = 0.204$

$a_{Bi} = 0.804$ and $a_{Bi}/a_{Sn}^{\gamma} = 4.40$ (from Fig. 1).

From (4[1]) $b_{Bi}/b_{Sn}^{\gamma} = 4.40 \times 13.30 = 58.50$.

From Fig. 1, $b_{Bi} = 0.98$.

Substituting the appropriate values in expression (2[1])

$$\sigma = \frac{371 + 8.315 \times 10^7 \times 608}{6.95 \times 10^8} \ln \frac{0.98}{0.804}$$

$$= 386 \text{ dynes/cm}.$$

In evaluating the surface tensions of regular solutions from expression (6), a value of $m = \frac{1}{4}$ was used, this being the value appropriate to a close-packed structure, while a was taken as the average molecular area at any composition based on the values for the two pure components; w, the interchange energy, was calculated from the heat of mixing data for the alloy in question.

4. COMPARISON OF THEORETICAL AND EXPERIMENTAL RELATIONSHIPS

The following binary alloy systems were used in comparing the experimental surface tension-composition relationships with those obtained from the two methods of analysis, viz. Bi-Sn, Bi-Pb, Pb-Sn, Pb-Sb, Cd-Sn, Al-Zn, Al-Mg, Sb-Zn, and Cd-Sb. The first six

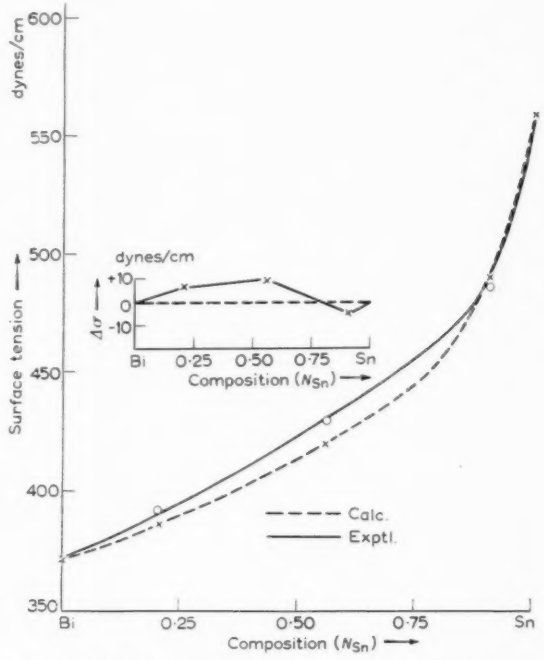

FIG. 2. Surface tension-composition relationships for Bi-Sn system.

of these systems are of simple eutectic type, while the remaining four form stable intermediate phases in the solid state.

The experimental surface tension-composition relationships are those reported as follows: Bi-Sn and Bi-Pb by Sauerwald,[8] Pb-Sn by Bircumshaw,[9] Cd-Sn by Kuznetsov *et al.*;[10] Sn-Zn, Al-Zn, and Al-Mg by Pelzel,[2] Sb-Zn, Cd-Sb, and Pb-Sb by Matuyama,[11] and Pb-Sb and Cd-Sb by Greenaway.[12] The corresponding thermodynamic data employed were

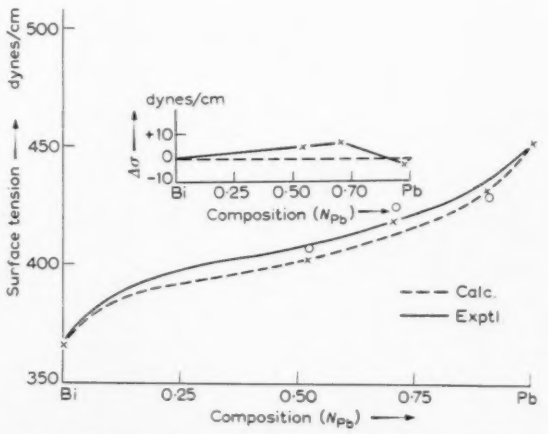

FIG. 3. Surface tension-composition relationships for Bi-Pb system.

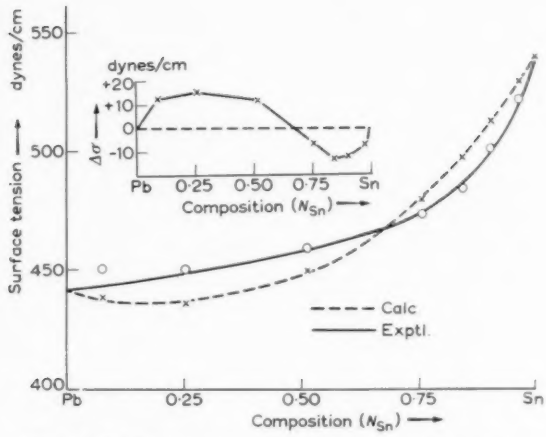

FIG. 4. Surface tension-composition relationships for Pb-Sn system.

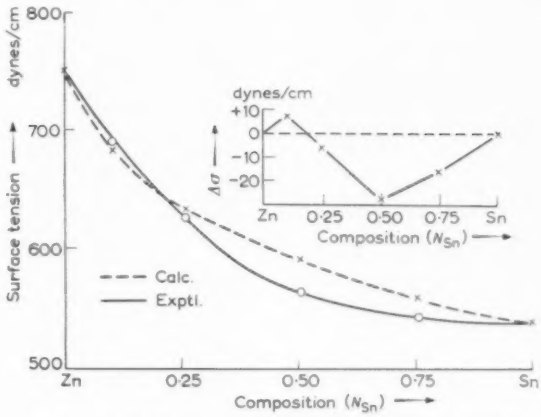

FIG. 7. Surface tension-composition relationships for Zn-Sn system.

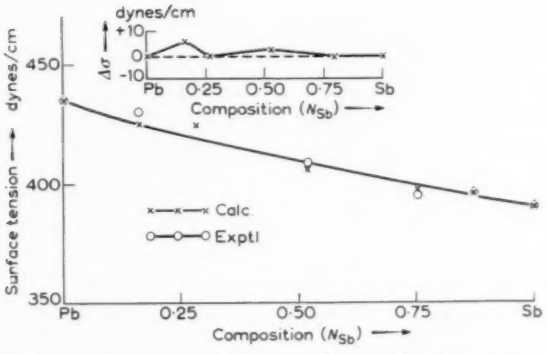

FIG. 5. Surface tension-composition relationships for Pb-Sb system.

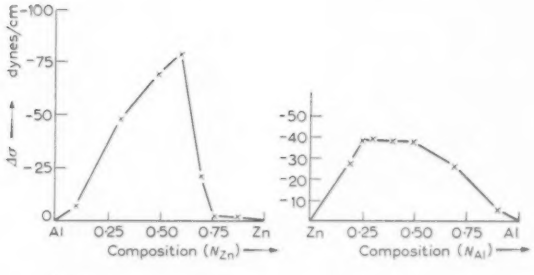

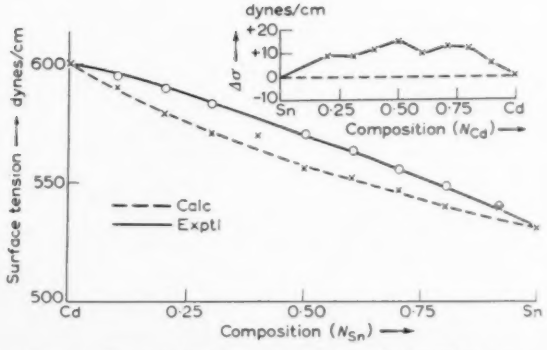

FIG. 6. Surface tension-composition relationships for Cd-Sn system.

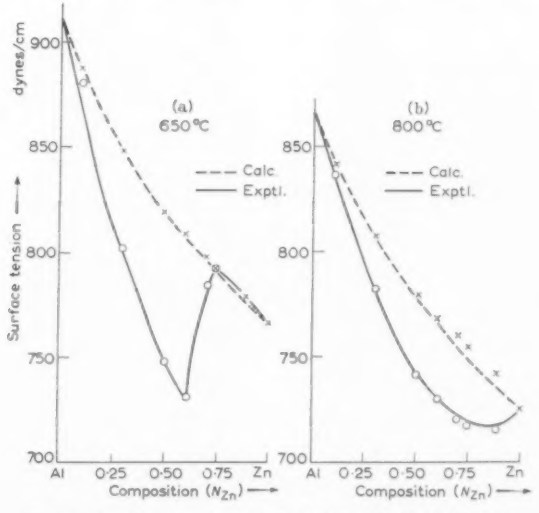

FIG. 8. Surface tension-composition relationships for Al-Zn system.

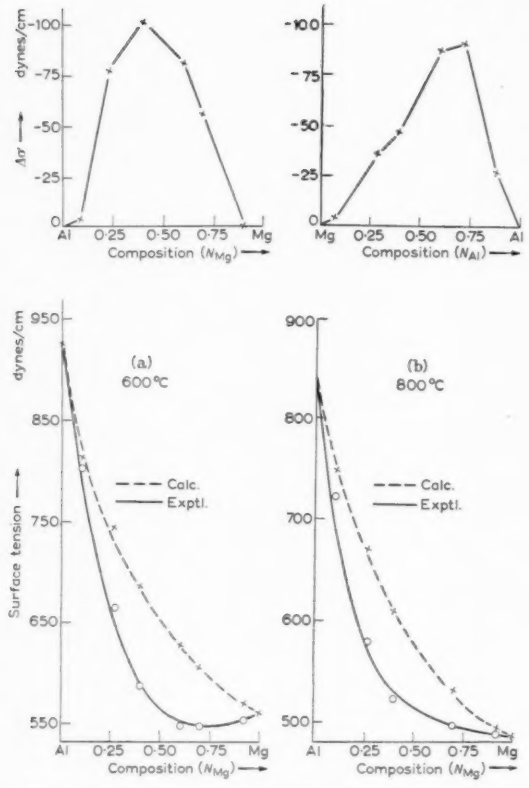

FIG. 9. Surface tension-composition relationships for Al-Mg system.

those reported by Seltz and Dunkerley[7] for Bi-Sn, by Seltz[13] for Bi-Pb, Cd-Sb, and Sb-Zn, by Jellinek and Wannow[14] for Cd-Zn and Sn-Zn, by Seltz and DeWitt[15] for Pb-Sb, by Schneider and Stoll for Al-Zn[16] and for Al-Mg.[17]

The experimental relationships are compared with the corresponding ones calculated by equations (2) and (4) in Figs. 2 to 11. Included in each figure is the relationship between $\Delta\sigma$ and composition, where $\Delta\sigma$ is the difference between the experimental and callated surface tensions. Relationships at two different temperatures are given in the case of the Al-Zn and Al-Mg systems, Figs. 8(a) and 8(b), and 9(a) and 9(b), respectively, while in the case of the Cd-Sb system the experimental relationships obtained by two separate studies, i.e. by Matuyama[11] and Greenaway,[12] are given for comparison, Fig. 11(a) and 11(b), respectively.

The surface tension values, calculated by expression (6) for regular solutions, are presented in Table 1; the corresponding experimental values and those obtained from expressions (2) and (4) are included for ease of comparison.

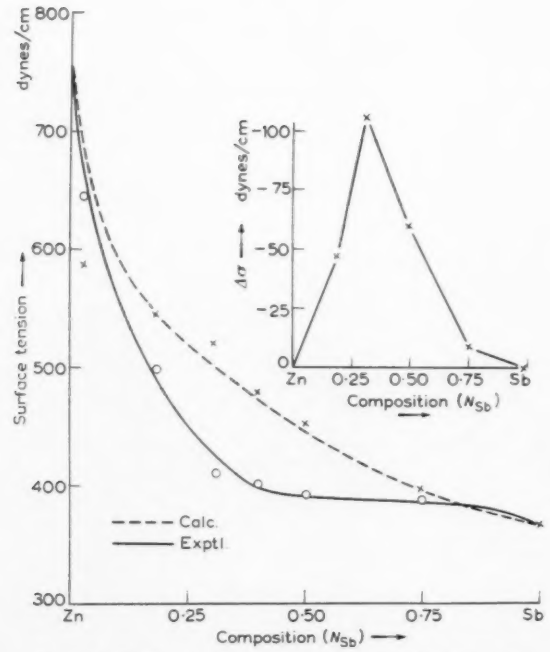

FIG. 10. Surface tension-composition relationships for Zn-Sb system.

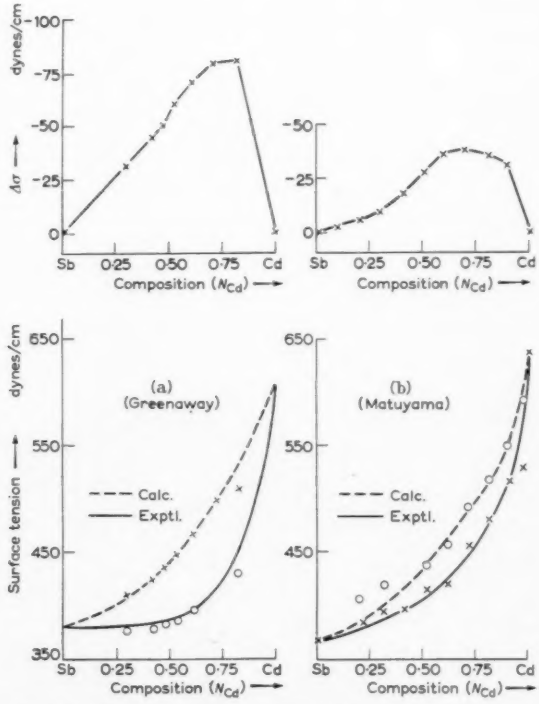

FIG. 11. Surface tension-composition relationships for Sb-Cd system.

TABLE 1. Comparison of calculated and experimental relationships for regular solutions

System	Composition (at. %)	Surface tension (dynes/cm)		
		Equation (24)	Equations (15) and (19)	Experimental
Bi-Sn (608°K)	100 Bi —	371	371	371
	79.6 Bi 20.4 Sn	385	386	392
	44.0 Bi 56.0 Sn	426	420	430
	9.1 Bi 90.9 Sn	510	490	486
	— 100 Sn	560	560	560
Bi-Pb (700°K)	100 Bi —	365	365	365
	48.4 Bi 51.6 Pb	410	402	407
	29.9 Bi 70.1 Pb	427	418	425
	10.0 Bi 90.0 Pb	460	430	428
	— 100 Pb	452	452	452
Pb-Sn (623°K)	100 Pb —	441	441	441
	92.6 Pb 7.4 Sn	428	438	450
	74.7 Pb 25.3 Sn	437	435	450
	48.9 Pb 51.1 Sn	470	447	459
	24.4 Pb 75.6 Sn	490	480	473
	15.9 Pb 84.1 Sn	502	498	485
	3.7 Pb 96.3 Sn	515	513	501
	— 100 Sn	541	541	541
Al-Zn (1073°K)	100 Al —	865	865	865
	90 Al 10 Zn	790	841	836
	70 Al 30 Zn	795	807	782
	50 Al 50 Zn	755	778	741
	40 Al 60 Zn	735	768	730
	30 Al 70 Zn	735	760	721
	25 Al 75 Zn	700	755	717
	10.3 Al 89.7 Zn	660	742	715
	100 Zn	725	725	725
Cd-Sb (753°K)	100 Cd —	607	607	607
	82.4 Cd 17.6 Sb	564	511	430
	72.0 Cd 28.0 Sb	525	499	420
	61.4 Cd 38.6 Sb	506	468	397
	53.2 Cd 46.8 Sb	503	447	386
	48.0 Cd 52.0 Sb	504	434	384
	42.7 Cd 57.3 Sb	490	424	379
	— 100 Sb	380	380	380

5. DISCUSSION OF RESULTS

To avoid undue confusion in the discussion, the comparison of the experimental and calculated surface-tension relationships will be made mainly with reference to the first method of analysis. This appears to give more consistent results on evaluation and is more generally applicable than the second analytical method. Although the latter has a more exact theoretical basis, much of this accuracy is lost in the simplifications which have to be introduced to obtain a form suitable for evaluation. However, the data contained in Table 1 indicate that the trends shown by the two analytical methods are essentially similar, with the possible exception of the Al-Zn system (discussed later); the discrimination in favor of one method is therefore not unreasonable.

In the six simple eutectic systems Bi-Sn (Fig. 2), Bi-Pb (Fig. 3), Pb-Sn (Fig. 4), Pb-Sb (Fig. 5), Cd-Sn (Fig. 6), and Sn-Zn (Fig. 7), the agreement between the calculated and experimental relationships is good, the maximum deviation between the two values being within the range $\pm$(5–30) dynes/cm. In these systems the coefficient of displacement, γ, covers the range 1.04 (Bi-Pb) to 1.42 (Sn-Zn), while the thermodynamic activity values indicate that the liquid solutions are far from ideal. Thus in the Bi-Pb and Pb-Sb systems there are negative departures for ideality (maximum deviations 10% and 5% respectively), while the Bi-Sn, Cd-Sn, and Sn-Zn systems show positive deviations (maximum values 3%, 9%, and 8% respectively). The agreement between experiment and calculation is particularly striking in the case of the Bi-Sn system, where the coefficient of displacement is quite large, 1.16, and the difference in the surface tensions of the two pure components is also large, i.e. 190 dynes/cm.

In the Sn-Zn system (Fig. 7) the agreement between the experimental and calculated surface-tension relationships is not so exact as in the previous five cases; in fact, the difference-composition relationship shows a maximum deviation between experiment and calculation at the equi-atomic composition. A possible reason for this greater discrepancy is discussed below.

In the remaining four systems, all of which form intermediate phases in the solid state, the agreement between the experimental and calculated relationships is poor, the experimental values being consistently lower than the corresponding calculated ones. The following points may be stressed in each individual system. The coefficient of displacement for the Al-Zn system (Fig. 8) is 0.89, and the activity of the alloys deviates in a strongly positive manner from ideal behavior. The experimental surface-tension-composition relationship at 650°C, Fig. 8(a), shows a sharp inversion and maximum between $N_{Zn} = 0.6$ and 0.8; the complete disappearance of this effect at 800°C, Fig. 8(b), makes the validity of this effect suspect. For this reason, only the experimental relationship at 800°C is used in the comparison with calculated surface tensions. Under these conditions the maximum difference between the calculated and experimental figures is 40 dynes/cm; this compares with the range $\pm$(5–30) dynes/cm for the eutectic systems in which the coefficients of displacement deviate more strongly from unity, but in which the activity deviations are smaller. In the Al-Mg system (Fig. 9) the coefficient of displacement has a value of 1.24 and there is a slight but

VOL. 4 1956

definite deviation of the activity coefficient from ideality. However, in spite of these relatively minor deviations of the system from ideal behavior, the calculated surface tension-composition relationship deviates strongly from the experimental one. At 600°C, Fig. 9(a), the experimental value is smaller by 100 dynes/cm at $N_{Mg} = 0.4$; at 800°C this figure is still essentially the same, i.e. 90 dynes/cm. In the Zn-Sb system the displacement coefficient is high, 1.92, and the activity coefficient shows a strong negative deviation from ideality. The discrepancy between the calculated and experimental relationships is correspondingly great, showing a maximum of 110 dynes/cm. The Cd-Sb system (Fig. 11) has similar characteristics to those of Zn-Sb. The displacement coefficient, 0.69, deviates considerably from the ideal value, while the activity coefficient is again less than unity, although to a smaller extent than for Zn-Sb. Once more the experimental surface tensions are much lower than those obtained by calculation, the maximum difference being 96 dynes/cm for Greenaway's results (Fig.11a), and 50 dynes/cm for Matuyama's values (Fig. 11b).

The binary systems Al-Zn, Al-Mg, Zn-Sb, and Cd-Sb, and to a lesser extent the Sn-Zn system, show a distinct tendency for the experimental surface-tension values to be lower than the corresponding calculated ones. Furthermore, these systems show deviations of the displacement and activity coefficients from ideality which are no greater than those shown by the eutectic systems in which the agreement calculated and experimental values is good. These deviations are usually greatest in the composition regions in which intermetallic phase formation occurs in the solid state, e.g. Figs. 9 and 10.

Before considering this difference in behavior of the two sets of alloys systems, it is relevant to refer to an assumption in the original analysis which might possibly affect this result. It has been assumed throughout that the displacement coefficient γ (equation 4) is independent of composition, i.e. that the surface area per atom of each component of the system is independent of composition. While the atomic volume-composition relationships for the systems Sn-Zn, Al-Mg, and Cd-Sb (density values are not known for the complete Sb-Zn system) are approximately linear, this is not so for the Al-Zn system,[18] which exhibits a pronounced maximum value at the equi-atomic composition. Although the observed disparity in the two surface tension relationships might have arisen from this fact, the results in Table 2 suggest that this is not the case. Here, for a number of compositions, surface tensions have been calculated on the basis of a displacement coefficient which was derived from the partial molar areas of each component at a given composition; corresponding values assuming a constant coefficient and experimental values are given for comparison. From Table 2 it is apparent that the composition dependence of the displacement coefficient is not able to account for the observed disparity between the calculated and experimental surface energies in the Al-Zn system.

TABLE 2. Calculated and experimental surface tensions for Al-Zn system at 800°C

Alloy composition N_{Zn}	Alloy composition N_{Al}	Surface tension (dynes/cm) Calculated $\gamma = f(N_{Zn})$	Calculated γ	Calculated $\gamma =$ const.	Calculated γ	Experimental
0.3	0.7	787	0.86	807	0.89	782
0.5	0.5	770	0.58	778	0.89	741
0.6	0.4	764	0.52	768	0.89	730
0.7	0.3	762	0.47	760	0.89	721

In comparing the five systems which showed the marked deviation of experimental and calculated relationships, the systems Sn-Zn and Al-Zn appear to occupy a somewhat intermediate position as regards the maximum deviation reached, i.e. 20 dynes/cm and 40 dynes/cm, respectively, compared with the 90–100 dynes/cm in the other three systems. These two systems show positive deviations of the activity coefficient from ideal behavior, the tendency being stronger in the Al-Zn system than in the Sn-Zn system. This positive deviation of the activity coefficient is synonymous with a tendency for the two components to separate, i.e. bonds of the *A-A* and *B-B* type are stronger than those of the *A-B* form. The Al-Zn system is of the peritectic type, with no tendency to form a stable intermetallic phase in the solid state, while the Sn-Zn system is of simple eutectic form. In the foregoing analysis employing equations (2) and (4), the assumption was made that the functional relationship between (b_1/b_2^{γ}) and b_1 was the same as that between (a_1/a_2^{γ}) and a_1. In systems showing tendencies to immiscibility, it may be that this assumption is no longer true. In fact, the surface layer may tend to a state more ideal than the bulk of the solutions as a result of the repulsive tendency between the two component atoms and the reduced coordination bonding of atoms at the surface. This is equivalent to saying that

$$b_1 \rightarrow x_1' \quad \text{and} \quad b_2 \rightarrow x_2'$$

where

x_1' = mole fraction of component 1 in the surface layer

x_2' = mole fraction of component 2 in the surface layer

Thus the surface tension-composition relationships were recalculated for these two systems on the basis that the surface layer was ideal. The results are

TABLE 3. Calculated surface tensions of Sn-Zn and Al-Zn systems assuming surface layer ideal

Alloy composition		Surface tension (dynes/cm)		
		Ideal layer	Nonideal layer	Experimental
N_{Zn}	N_{Sn} (700°C)			
0.9	0.1	661	683	691
0.75	0.25	618	636	629
0.50	0.50	579	592	564
0.25	0.75	553	560	544
N_{Zn}	N_{Al} (800°C)			
0.1	0.9	743	841	836
0.3	0.7	689	807	782
0.5	0.5	666	778	741
0.6	0.4	663	768	730
0.7	0.3	665	760	721
0.897	0.103	672	742	715

VOL. 4 1956

presented in Table 3. For the Sn-Zn system, the introduction of this modification has corrected the calculated surface tensions in the proper direction to give closer agreement with experiment; at $N_{Zn} = 0.9$ the corrected value is now considerably below the corresponding experimental point. In the Al-Zn system the assumption of an ideal surface layer has again lowered the calculated surface tensions, but the corrected values are now much lower than the corresponding experimental points. However, it does appear that, on the basis of the analysis contained in equations (2) and (4), the assumption of a surface layer more ideal than the bulk solution can account for the observed discrepancies between calculation and experiment in the Al-Zn and Sn-Zn systems. It is interesting to note from Table 1 that the Al-Zn system is the only one in which the two calculated relationships differ in trend relative to the experimental relationship. Thus the surface tensions calculated by expression (6) for the Al-Zn system are in much closer agreement with the experimental points than is the case for the alternative analysis.

In the remaining three systems, i.e. Al-Mg, Zn-Sb, and Cd-Sb, any assumption of an ideal component to the surface layer will only worsen the observed disparity between the calculated and the theoretical relationships. For the Cd-Sb system, Table 1, both calculated relationships indicate strong disagreements with the experimental one. In seeking an explanation for this discrepancy, it might be stated naively that, in systems showing strong A-B interaction in the solid state, a similar tendency in the liquid reduced the surface tension below that to be expected on the basis of the two calculations employed. More accurately, this discrepancy may imply that in these systems the surface layer is no longer a monolayer and that a form of short-range order or interaction exists at the surface which is not considered in either analysis and which effectively lowers the surface tension of the alloy. Thus, in any analysis designed to explain the surface-tension relationship for this type of system, it may be necessary to consider a more complicated surface model made up of a number of layers between which there is some degree of interaction.

The close agreement between the calculated and experimental surface tension-composition relationships for simple eutectic systems suggested that the analysis by expressions (2) and (4) might be inverted so as to yield activity-composition relationships calculable from experimental surface tension-composition relationships. While the calculation can be formulated in a quite rigorous manner, the final functional relationship between surface tension and activity is incapable of solution.

6. CONCLUSIONS

It has been found possible to account for the observed surface tension-composition relationships of six eutectic systems (Bi-Sn, Bi-Pb, Pb-Sn, Pb-Sb, Cd-Sn, and Sn-Zn), using two independent methods of analysis. The agreement between the calculated and the experimental relationships is quite close.

In the case of the three systems Al-Mg, Sb-Zn, and Cd-Sb, which form stable intermediate phases in the solid state, the agreement between the calculated and the experimental surface tension relationships is poor. This may be the result of an oversimplified model of the surface employed in the analysis. It may be necessary in such systems to consider a surface region composed of a number of layers between which some degree of interaction exists.

The Al-Zn system appeared to form an intermediate stage between the above two classes. One method of analysis gave good agreement with experiment in this case. On the basis of the other analytical method, the surface layer in this, and possibly also in the Sn-Zn system, may tend to a more ideal state than exists in the bulk of the liquid, a fact in keeping with the

positive deviations of their activity coefficients from ideality.

It was not found possible to invert the one method of analysis and deduce activity-composition relationships from surface tension-composition relationships, for eutectic systems, although this is theoretically possible.

The present methods of analysis will be of value in predicting surface tension-composition relationships at least for the simpler binary liquid systems. They could also be of value in predicting the surface energy of similar solid alloys, especially if used in conjunction with a method of estimating the surface-tension change on melting.[19]

ACKNOWLEDGMENTS

The author thanks Dr. J. Woodrow for mathematical assistance and helpful suggestions and Dr. H. M. Finniston for discussion during the preparation of the paper, which is published by kind permission of the Director, A.E.R.E., Harwell.

REFERENCES

1. J. W. Taylor *Atomic Energy Research Establishment Report* M/TN 24 (1954).
2. E. Pelzel *Berg-und Huttenmannische Monatshefte,* **93,** 248 (1948); *ibid.* **94,** 10 (1949).
3. A. Schuchowitzky *Acta Physicochimica U.R.S.S.* **19,** 176 and 508 (1944).
4. E. A. Guggenheim *Mixtures,* O.U.P. (1952).
5. J. A. V. Butler *Proc. Roy. Soc.* **135A,** 348 (1932).
6. E. A. Guggenheim *Trans. Farad. Soc.* **41,** 150 (1945).
7. H. Seltz and F. J. Dunkerley *J. Amer. Chem. Soc.,* **64,** 1392 (1942).
8. F. Sauerwald *Z. f. anorg. Chemie* **162,** 301 (1927).
9. L. L. Bircumshaw *Phil. Mag.* **17** (7th Series) 181 (1934).
10. V. A. Kuznetsov, V. P. Kochergin, M. V. Tishchenko, and E. G. Pozdnysheva *Dok. Akad. Nauk.* **92** (6), 1197 (1953).
11. Y. Matuyama *Sci. Rep. Tohoku Univ.* **16,** 555 (1927).
12. H. T. Greenaway *J. Inst. Met.* **74** (3), 133 (1948).
13. H. Seltz *Trans. Electrochem. Soc.* **77,** 233 (1940).
14. K. Jellinck and H. A. Wannow *Z. f. Elektrochem.* **41** (6), 346 (1935).
15. H. Seltz and B. J. DeWitt *J. Amer. Chem. Soc.* **61,** 2594 (1939).
16. A. Schneider and E. K. Stoll *Z. f. Elektrochem.* **47,** 527 (1941).
17. A. Schneider and E. K. Stoll *ibid.* **47,** 519 (1941).
18. E. Pelzel and H. Schneider *Z. f. Metkde.* **35,** 124 (1943).
19. J. W. Taylor *Atomic Energy Research Establishment Report* M/TN 30, 1955.

VOL
4
195

A DISLOCATION-ATTRACTION MODEL FOR THE FIRST STAGE OF TEMPERING*

B. S. LEMENT† and MORRIS COHEN‡

A dislocation-attraction model governing the flow of carbon atoms is proposed to account for the kinetics of the first stage of tempering in steel. It is predicted that the time exponent of the isothermal reaction should be 1/3, and the activation energy for the reaction should equal that for diffusion of carbon in martensite. On the basis of previous kinetic data, a good check of the theoretical time exponent is obtained; however, it appears that the activation energy for diffusion of carbon is about 50% higher in martensite than in α-ferrite. The slower rate of carbon diffusion in martensite is explained by the availability of paths of lower barrier energy in the b.c.c. ferrite than in the b.c.t. martensite.

UN MODELE D'ATTRACTION PAR LES DISLOCATIONS VALABLE POUR LA PREMIERE ETAPE DU REVENU

Un modèle d'attraction par les dislocations régissant le mouvement d'atomes de carbone est proposé pour expliquer la cinétique du glissement dans la première étape du revenu de l'acier. Il est prédit que l'exposant du temps de la réaction isotherme serait 1/3 et que l'énergie d'activation pour la réaction égalerait celle de la diffusion du carbone dans la martensite.

Sur la base de données cinétiques antérieures, on obtient une bonne confirmation de l'exposant pour le temps; cependant il apparaît que l'énergie d'activation pour la diffusion du carbone est dans la martensite d'environ 50% supérieure à celle caractérisant la ferrite α.

La vitesse réduite de diffusion du carbone dans la martensite est expliquée par l'existence de seuils énergétiques plus faibles dans la ferrite cubique centrée que dans la martensite quadratique.

EIN MODELL MIT VERSETZUNGS-ANZIEHUNG FÜR DIE ERSTE ANLASSSTUFE

Zur Erklärung der Kinetik der ersten Anlasstufe von Stahl wird ein Modell vorgeschlagen, bei dem die Anziehung durch Versetzungen für die Wanderung der Kohlenstoffatome massgebend ist. Daraus werden die Voraussagen abgeleitet, dass bei der isothermen Reaktion der Exponent der Zeit 1/3 betragen und die Aktivierungsenergie der Reaktion gleich derjenigen der Kohlenstoff-Diffusion im Martensit sein soll. Mit Hilfe früherer kinetischer Daten lässt sich der theoretische Zeit-Exponent gut nachprüfen. Hingegen scheint die Aktivierungsenergie der Kohlenstoff-Diffusion im Martensit um 50% grösser zu sein als im α-Ferrit. Die geringere Diffusionsgeschwindigkeit des Kohlenstoffs im Martensit wird dadurch erklärt, dass im kubisch-innenzentrierten Ferrit Diffusionswege mit niedrigerer Energieschwelle als im tetragonal-innenzentrierten Martensit vorhanden sind.

VOL. 4 1956

1. INTRODUCTION

The first stage of tempering in plain carbon or low-alloy steels consists of the formation of both h.c.p. ε-carbide (approximately 8.2% carbon) and b.c.t. low-carbon martensite (approximately 0.3% carbon) at the expense of the primary martensite present in the as-hardened condition. According to observations with the electron microscope,[1] the ε-carbide forms at subboundaries that are present in the primary martensite. On the basis of X-ray diffraction evidence,[2, 3] the first stage may be considered as a discontinuous reaction in that the primary martensite decreases in amount, but does not appear to change significantly in carbon content. Although the general nature of the first stage seems established, there is still some uncertainty regarding the kinetics and mechanism of this reaction.

According to Roberts *et al.*,[3] the precision-length data obtained for five high-purity iron-carbon alloys and two commercial steels varying in carbon content from 0.6 to 1.4% can be represented by the following empirical equation, up to at least 50% transformation:

$$\ln\left(\frac{1}{1-f}\right) = \frac{Kt^n}{n} \qquad (1)$$

where f = fraction transformed,
K = rate constant,
t = time,
n = time exponent.

Experimentally, $n \cong 0.30$, and the temperature dependence of K corresponds to an activation energy $Q_K \cong 8000$ cal/mol. Therefore, the activation energy for the reaction based on time^{-1} is $Q_R = Q_K/n \cong 27{,}000$ cal /mol.

In an attempt to account for the experimental value of n, Roberts postulated that the reaction is growth-controlled and essentially discontinuous in nature. Nuclei of ε-carbide are considered to be present in the

* *Received October* 27, 1955.

† Division of Industrial Cooperation, Massachusetts Institute of Technology, Cambridge, Massachusetts, U.S.A.

‡ Department of Metallurgy, Massachusetts Institute of Technology, Cambridge, Massachusetts, U.S.A.

as-hardened primary martensite or to form so rapidly on tempering as to negate nucleation as a factor in the kinetics. With this model, the controlling feature of the reaction is diffusion of carbon atoms along a relatively steep concentration gradient in the primary martensite, thus making possible growth on a plane front of an aggregate β which consists of ε-carbide and low-carbon martensite. A kinetic equation for the reaction was derived having the same form as (1), with $n = 1/2$ and K proportional to $D^{1/2}$, where D represents the diffusion coefficient for carbon in martensite. Accepting the theoretical value of $n = 1/2$ and the experimental value of $Q \cong 8000$ cal/mol, Roberts concluded that $Q_R = Q_D \cong 16{,}000$ cal/mol. This seemed in line with the supposition that the activation energy for diffusion of carbon in martensite Q_D should be approximately the same as that in α-ferrite (18,000 cal/mol) because of the close similarity in lattice structure, However, no explanation was given for the discrepancy between $n = 1/2$ as called for by the theory, and $n \cong 0.30$ as found experimentally. Furthermore, it was not evident why a discontinuous rather than a continuous reaction should occur under the conditions of diffusion that were set up.

In view of these objections, it appeared that a satisfactory model for the first stage of tempering was not yet available. Accordingly, a further attempt to solve this problem was considered worthwhile; and as an initial step, it was decided to make a more critical analysis of the precision-length data of Roberts in order to determine the reliability of the empirical equation (1) obtained for the kinetics. As will be shown, this analysis resulted in greater confidence that the experimental values of $n \cong 0.30$ and $Q_R \cong 27{,}000$ cal/mol are actually representative of the kinetics of the first-stage reaction.

The acceptance of $n \cong 0.30$ posed a dilemma, because the lowest possible value of n should be 1/2 if regular diffusion of carbon atoms is the basic mechanism involved. As shown by Zener,[4] $n = 1/2$ holds for the case of growth of a plane front with solute atoms being supplied by flowing down a concentration or activity gradient, the number of nuclei being constant. In order for n to be less than 1/2, a negative rate of nucleation (dissolving of nuclei) would have to be postulated. However, if a mechanism other than regular diffusion of carbon atoms were operative, $n \cong 0.30$ might be possible even with an essentially zero rate of nucleation. Since dislocation-attraction of carbon atoms had proved successful in accounting for the kinetics of strain-aging of α-ferrite,[5] an attempt was made to apply this concept to the first stage of tempering.

2. ANALYSIS OF ROBERTS'S DATA

In order to obtain equation (1), one assumes a rate equation of the following differential form:

$$\frac{df}{dt} = K\,(1 - f)t^{n-1} \tag{2}$$

The fraction untransformed, $(1 - f)$, represents an impingement factor which is commonly used to correct for one or more of the following effects; (a) collision of two advancing reaction products, thus stopping further growth along the area of their contact, (b) depletion of the untransformed matrix in solute content due to competing regions of growth of the reaction products, and (c) a decrease in either the volume or surface area of the untransformed matrix regions which supply solute atoms, such as when a film-like grain-boundary product grows toward the center of a grain on a more or less spherical front of decreasing radius. Since, in the general case, the simple $(1 - f)$ factor should be considered as only approximately correct for impingement, it seemed essential to ascertain the effect of other impingement factors on the time-exponent and activation energy of the first-stage reaction based on Roberts's data.

By assuming an impingement factor of the general form $(1 - f)^i$, the integrated form of equation (2) becomes

$$\int_0^f \frac{df}{(1 - f)^i} = \frac{Kt^n}{n} \tag{3}$$

$$\ln \int_0^f \frac{df}{(1 - f)^i} = \ln \frac{K}{n} + n \ln t \tag{3a}$$

For values of the impingement exponent i varying from 0 to $+2$, a plot of the left side of equation (3a) vs. ln t, using Roberts's data, gives a straight-line relationship over the range from zero to $f = 0.5 \pm 0.1$. With higher or lower values of i, the transformation range of the straight-line relationship decreases. On this basis, the most probable value of i may be taken to lie between 0 and $+2$.

The slope of the above linear relationship is equal to the time exponent n, and depends on i only to a small extent. Accepting Roberts's experimental value of 0.30 which corresponds to $i = 1$, n increases from 0.28 to 0.32 as i changes from 0 to $+2$. Taking also into account Roberts's experimental deviation of ± 0.02, the probable value of n can be considered as 0.30 ± 0.04, which is significantly different from the previously adopted theoretical value of 1/2.[3]

For straight-line relationships of equation (3a), the fractional changes in n and Q_K with variation in i can be shown to be equal. This means that the activation

energy of the reaction $Q_R = Q_K/n$ is independent of the particular impingement factor adopted. A precise evaluation of Q_R and its probable error was made on the basis of the dislocation-attraction model which is discussed next.

3. DISLOCATION-ATTRACTION MODEL

It is postulated that the first-stage reaction is controlled by attraction of carbon atoms to edge dislocations situated at the interface between ε-carbide and the martensitic matrix. Inasmuch as X-ray evidence[6] suggests that these phases are at least partially coherent, a series of edge dislocations would presumably be located at the interface. Nuclei of ε-carbide are assumed to be initially present at subboundaries in the martensite,[1] and the reaction is taken to be growth-controlled, just as in the Roberts's model. The ε-carbide is believed to grow in the form of platelets or films, the thickness of which increases as carbon atoms arrive at the interface. If the state of coherency is continued, the conditions for attraction of further carbon atoms are self-perpetuating. As the reaction proceeds, a region of depleted carbon content adjoining the ε-carbide is extended at the expense of the original primary martensite in a manner that simulates a discontinuous reaction. Two geometrical situations will be considered: (1) growth of a plane front, and (2) inward growth of a spherical shell. A schematic drawing illustrating growth of a plane front is shown in Fig. 1, as a basis for introducing the treatment of the problem. The edge dislocations at the interface

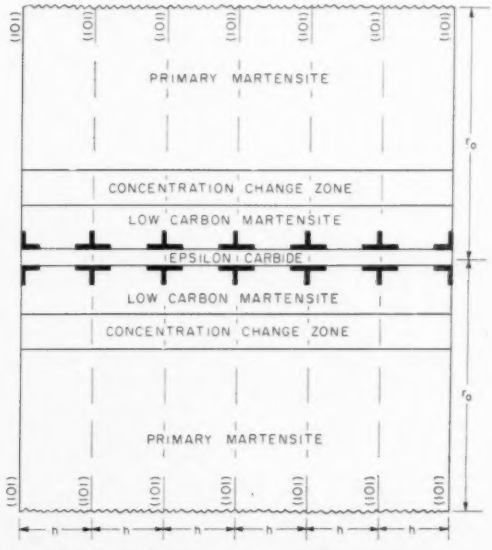

FIG. 1. Schematic diagram illustrating first stage reaction taking place on a plane front.

are assumed to be separated by a constant distance h. The inward growth of a spherical-shell front is taken up next, providing a geometric case that corresponds more closely to the actual precipitation process.[1]

4. KINETICS BASED ON GROWTH OF A PLANE FRONT

According to Cottrell,[7] the average velocity of a carbon atom attracted to a single-edge dislocation is given by the negative of the product of the mobility $B = D/kT$, and the gradient of the interaction energy dE/dx. For a direction perpendicular to the plane of misfit, it can be shown that the interaction energy $E = -A/x$, where A is the interaction energy constant (3×10^{-20} erg-cm). It seems reasonable to assume that carbon atoms in martensite would be attracted perpendicularly to the coherent interfacial plane set up by ε-carbide formation with about the same force as for a single-edge dislocation, provided that the dislocations in the interface are spaced far enough apart. Defining x as the initial distance from the interface to carbon atoms which just reach the interface in time t, the following equation for the velocity v of carbon atoms should hold during the first-stage reaction:

$$v = -\frac{dx}{dt} = -\left(\frac{D}{kT}\right)\frac{dE}{dx} = -\frac{DA}{kTx^2} \tag{4}$$

If, as an approximation, the interface is assumed not to move,

$$x = \left(\frac{3\,DA}{kT}\right)^{1/3} t^{1/3} \tag{5}$$

The fraction transformed may be defined as x/r_0, the parameter r_0 being equal to half the separation between the carbide plane fronts, which are considered equally spaced and parallel in this hypothetical case. Thus

$$f = \frac{1}{r_0}\left(\frac{3DA}{kT}\right)^{1/3} t^{1/3} \tag{6}$$

Changing to the differential form and inserting the general impingement factor $(1-f)^i$, the impingement being essentially of the type (b) on p. 470:

$$\frac{df}{dt} = \frac{1}{3r_0}\left(\frac{3DA}{kT}\right)^{1/3} (1-f)^i\, t^{-2/3} \tag{7}$$

$$\int_0^f \frac{df}{(1-f)^i} = \frac{1}{r_0}\left(\frac{3DA}{kT}\right)^{1/3} t^{1/3} \tag{8}$$

A comparison with equation (3) reveals that $n = 1/3$ and

$$K = \frac{1}{3r_0}\left(\frac{3DA}{kT}\right)^{1/3} \tag{9}$$

Thus the dislocation model results in a time-exponent

of 1/3, which is in good agreement with the probable value $n = 0.30 \pm 0.04$ determined from the preceding analysis of Roberts's kinetic data. The theoretical time-exponent in the case of strain-aging[5] equals 2/3, which is a geometrical consequence of the assumption that depletion of carbon atoms occurs throughout what can be approximated as a cylindrical volume surrounding each dislocation line situated at random. By assuming a row of dislocations situated in the same plane as the basic pattern of the first-stage reaction, the geometry of carbon-flow is changed from two-dimensional to one-dimensional and the time exponent is therefore 50% lower. The expression derived for the rate-constant (K in equation 9) indicates that the activation energy of the reaction $Q_R \cong Q_D$, the activation energy for diffusion of carbon in martensite. The value of Q_D will be determined later.

5. INWARD GROWTH OF A SPHERICAL-SHELL FRONT

Actually, the ε-carbide forms as thin shells at the boundaries of martensitic subgrains, instead of along parallel fronts. Assuming spherical subgrains of radius r_0, it is possible to derive explicitly a particular function for the integral in equation (8). Under these conditions, $x = r_0 - r$, where r represents the radius of the core of untransformed primary martensite, assuming a discontinuous reaction:*

$$f = 1 - \frac{r^3}{r_0^3} \tag{10}$$

$$\frac{df}{dr} = -\frac{3r^2}{r_0^3} = -\frac{3(1-f)^{2/3}}{r_0} \tag{11}$$

$$\int_0^f \frac{df}{3(1-f)^{2/3}} = \frac{(r_0 - r)}{r_0} \tag{12}$$

Thus the spherical case corresponds to an impingement factor of $3(1-f)^{2/3}$, with the impingement being of of the type (c) on p. 470. Since $x = r_0 - r$, the use of equation (5) gives the following equation for the kinetics of the reaction:

$$1 - (1-f)^{1/3} = \frac{1}{r_0}\left(\frac{3DA}{kT}\right)^{1/3} t^{1/3} \tag{13}$$

6. DETERMINATION OF Q_D AND r_0

Combining equation (13) and the diffusion equation (14) gives equation (15), which represents the temperature dependence of K:

$$D = D_0 \exp - (Q_D/RT) \tag{14}$$

$$(\log K + n \log T) = \log\left[\frac{1}{r_0}\left(\frac{3D_0A}{k}\right)^n\right] - \frac{nQ_D}{2.3R}\left(\frac{1}{T}\right) \tag{15}$$

Thus a plot of $(\log K + n \log T)$ vs. $1/T$ should enable determination of both Q_D, the activation energy for diffusion of carbon in martensite, and r_0, the half-spacing of ε-carbide fronts or subgrain radius. Using Roberts's individual values of rate-constant K determined for seven alloys as a function of five tempering temperatures on the basis that the time-exponent $= 0.30$, both average values and probable errors of K and $\log K$ were computed. By plotting the left-hand side of equation (15) vs. $1/T$, Fig. 2 was obtained. The average slope of this plot corresponds to $Q_D = 26{,}000$ cal/mol. Considering the probable errors in the average $\log K$ values and in n, the uncertainty in Q_D amounts to about 12%, or $Q_D = 26{,}000 \pm 3000$ cal/mol.

* As will be discussed later, the first-stage reaction is approximately discontinuous.

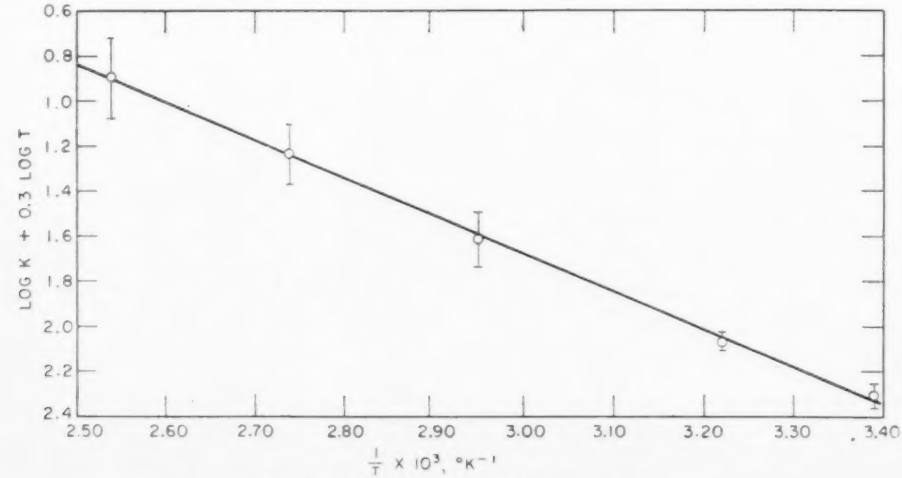

FIG. 2. Plot of $\log K + 0.3 \log T$ vs. $1/T$.

Extrapolating the plot of Fig. 2 to $1/T = 0$ gives an intercept of 3.33, which is the value of the first term of the right-hand side of equation (15). Taking the value $D_0 = 2 \times 10^{-2}$ cited by Wert[8] for diffusion of an interstitial element, gives $r_0 \cong 500$ Å. This is in excellent agreement with electron microscopic measurements[1] according to which the radius of a subgrain of martensite equals 500 to 1000 Å.

7. EFFECTIVE RANGE OF EDGE DISLOCATIONS

In the dislocation-attraction model presented here, it is tacitly assumed that the edge dislocations in a row do not mutually interact to a significant extent. The validity of this assumption will now be discussed on the basis of the similarity between a coherent boundary separating two different phases and a low-angle grain boundary in a single phase. Cottrell[7] has shown that for a distance away from a grain boundary in a single phase equal to the average spacing h between edge dislocations at this boundary, the field is essentially the same as for a single isolated dislocation; whereas for distances greater than h, the stress-field falls off steeply as an exponential function due to mutual interaction between dislocations.

It is possible to determine the approximate magnitude of h on the assumption that the ε-carbide and low-carbon martensitic phases are coherent. Jack[6] has suggested that the coherency planes are probably $(101)_\varepsilon$ and $(101)_M$, because the spacings of these planes are approximately equal. A comparison of these two phases is shown below:

Phase	Approximate carbon content (%)	Lattice	Lattice parameters (Å)		Spacing of (101) coherency planes (Å)	References
			a	c		
ε-carbide	8.2	h.c.p.	2.74	4.35	2.09	(6, 9)
Low-carbon martensite	0.3	b.c.t.	2.86	2.90	2.04	(10)

If registry exists between these two sets of planes, this might require the presence of a row of edge dislocations which are equally spaced along the interface of the lattices. Under such conditions, the martensitic phase would supply the extra rows of atoms and the $(101)_M$ planes would be spaced 0.05 ± 0.01 Å closer together than the $(101)_\varepsilon$ planes. It follows that the separation of the edge dislocations is about 80 Å, and there are approximately forty coherent planes between dislocations.

In order to determine whether this value of h is large enough to be significant from the standpoint of the first-stage reaction, it is necessary to calculate how much transformation would correspond to depletion of carbon atoms initially present in the primary martensite within a distance h of the ε-carbide interface This calculation can be carried out as follows, using values of the subgrain radius r_0 from 500 to 1000 Å.

$$f = 1 - \left(\frac{r_0 - h}{r_0}\right)^3 = 0.2 \text{ to } 0.4 \qquad (16)$$

The value of 20 to 40% transformation obtained is in relatively good agreement with the fact that $n = 0.30 \pm 0.04$ has been found experimentally to hold up to at least 50% transformation. Thus, mutual interaction of edge dislocations is probably not an important factor during the first half of transformation.

8. DISLOCATION-ATTRACTION vs. REGULAR DIFFUSION

In order to justify the hypothesis that dislocation-attraction is mainly responsible for the movement of carbon atoms to the ε-carbide interface, thereby neglecting regular diffusion that occurs due to a concentration gradient, the relative magnitudes of these two processes will now be compared. Assuming that dislocation attraction is operating alone, the following differential equation should hold for the variation of carbon concentration C with time t at any distance x from a plane ε-carbide interface:

$$\frac{\partial C}{\partial t} = -\frac{\partial (vC)}{\partial x} = BA \frac{\partial}{\partial x}\left(\frac{C}{x^2}\right) \qquad (17)$$

The solution of this equation has the following form:

$$\frac{(C - C_e)}{(C_p - C_e)} = \frac{x^2}{(x^3 + 3BAt)^{2/3}} \qquad (18)$$

where C_p = carbon concentration of primary martensite,
C_e = carbon concentration of low-carbon martensite adjacent to ε-carbide.

The number of carbon atoms per unit area arriving at the ε-carbide interface in time t due to dislocation-attraction is proportional to the area A_1 between the curve representing equation (18) and the straight line corresponding to $C = C_p$. This area has the following time dependence:

$$A_1 = \int_0^t (vC)_{x=0}\, dt = (C_p - C_e)\,(3BA)^{1/3}\, t^{1/3} \qquad (19)$$

If regular diffusion were occurring alone, the following equations should apply:

$$\frac{\partial C}{\partial t} = D\frac{\partial^2 C}{\partial x^2} \tag{20}$$

$$\frac{(C - C_e)}{(C_p - C_e)} = \text{erf}\,\frac{x}{2(Dt)^{1/2}} \tag{21}$$

$$A_2 = \int_0 D\left(\frac{\partial C}{\partial x}\right)_{x=2} dt = \frac{2(C_p - C_e)}{\pi^{1/2}} D^{1/2} t^{1/2} \tag{22}$$

where A_2 is proportional to the number of carbon atoms arriving at $x = 0$ in time t. Since $B = D/kT$, the ratio A_2/A_1 is given by the following:

$$\frac{A_2}{A_1} = \frac{2}{\pi^{1/2}}\left(\frac{kT}{3A}\right)^{1/3}(Dt)^{1/6} \tag{23}$$

For an intermediate tempering temperature of 340°K, the value of $D = 0.02 \exp(26{,}000/340R) = 4 \times 10^{-19}$ cm²/sec can be substituted in equation (23) to determine the time that gives a ratio of unity. The result is that about 6.5×10^6 sec at 340°K are required for regular diffusion occurring alone to furnish as many carbon atoms to the ε-carbide interface as dislocation-attraction occurring alone. In shorter times, the dislocation-attraction is more important. Since about 60% transformation occurs in this time at 340°K, dislocation-attraction can be considered to play a dominant role at least during the first half of transformation.[3]

Actually, both dislocation-attraction and regular diffusion would be expected to occur simultaneously, and then the following differential equation applies:

$$\frac{\partial C}{\partial t} = BA\frac{\partial}{\partial x}\left(\frac{C}{x^2}\right) + D\frac{\partial^2 C}{\partial x^2} \tag{24}$$

The complex nature of equation (24) makes it difficult to obtain an exact solution. However, it is found* that for times corresponding to $A_2/A_1 \leq 1$, equation (18), which represents dislocation-attraction acting alone, may be considered as a first-approximation solution. It can also be shown* that the following equation is a second-approximation solution:

$$\frac{C - C_e}{C_p - C_e} \cong \frac{x^2}{(x^3 + 3BAt)^{2/3}} + \frac{D}{BA}\left[\frac{3x^2}{7(x^3 + 3BAt)^{1/3}} - \frac{2x^2}{(x^3 + 3BAt)^{2/3}} + \frac{3x^6}{(x^3 + 3BAt)^{5/3}} - \frac{10x^9}{(x^3 + 3BAt^{8/3}}\right] \tag{25}$$

The number of carbon atoms arriving at $x = 0$ in time t is proportional to

$$A_3 = \int_0^t BA\left(\frac{C}{x^2}\right)_{x=0} dt + \int_0 D\left(\frac{\partial C}{\partial x}\right)_{x=0} dt. \tag{26}$$

Since $\partial C/\partial x_{x=0}$ must be zero in order for $C/x^2)_{x=0}$ to be finite, the second term in equation (26) equals zero. Substituting equation (25) in (26), the ratio of A_3/A_1 can be obtained to a second approximation:

$$\frac{A_3}{A_1} \cong 1 + \frac{9}{14}\left(\frac{kT}{3A}\right)^{2/3}(Dt)^{1/3} \tag{27}$$

After 10^6 sec at 340°K, which corresponds to about 50% transformation, $A_3/A_1 \cong 1.3$. Thus, treating the kinetics of the first-stage reaction in terms of dislocation-attraction alone seems to be a good approximation over the same range that the time exponent n of the reaction is found to be constant.

Beyond about 50% transformation, n would be expected to increase from the value of 1/3 for dislocation-attraction acting alone and eventually approach the value of 1/2 for regular diffusion acting alone. However, since n is actually observed to decrease rather than increase beyond about 50% transformation, other conditions may come into play. One possibility is the restricted range of dislocation-attraction due to the mutual interaction effect. Since mutual interaction may effectively limit dislocation-attraction to a distance of about 80 Å, the reaction would tend to slow down after the available carbon atoms are removed from a region corresponding to this distance.

9. DISCONTINUOUS NATURE OF FIRST-STAGE REACTION

If the first-stage reaction were truly discontinuous, a "low-carbon" martensitic region of constant carbon content would be separated from the primary martensite by a concentration gradient of infinite slope at any time during the course of the reaction. Based on X-ray intensity measurements, the first-stage reaction seems to be only approximately discontinuous, since some variation in the carbon content of both the "low-carbon" and primary martensitic regions apparently exists. In order to determine whether the proposed dislocation-attraction model is consistent with the X-ray evidence, it is necessary to examine the attendant variation in carbon content during the course of the reaction.

The carbon-concentration vs. distance curves for times of 10^4 and 10^6 sec at 340°K, which correspond to about 20 and 50% transformation respectively, are plotted in Fig. 3 and 4 for dislocation-attraction occurring alone (equation 18), for regular diffusion occurring alone (equation 21), and for both occurring

* Solutions were worked out by Dr. Carl Wagner, Department of Metallurgy, M.I.T., and Dr. Philip Franklin, Department of Mathematics, M.I.T.

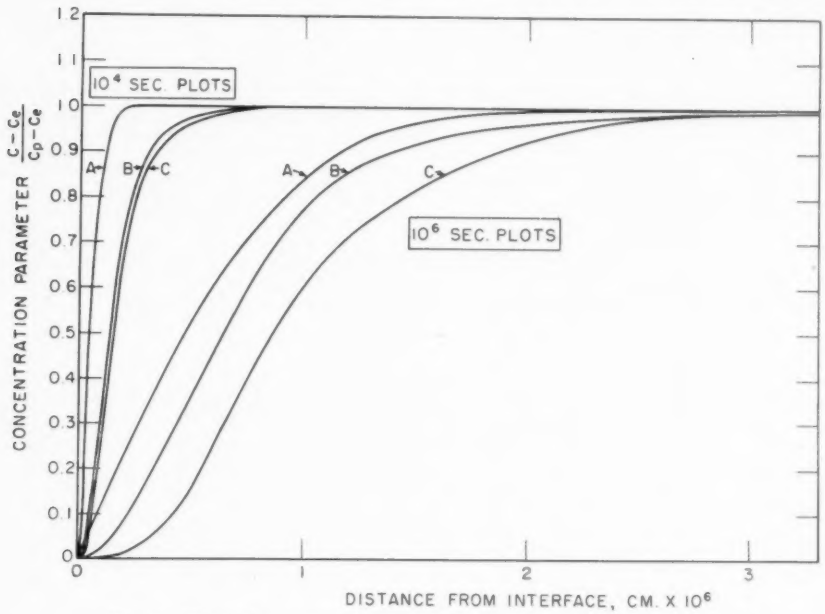

FIG. 3. Plots of concentration vs. distance for 10^4 and 10^6 sec at 340°K.
A—Regular diffusion. B—Dislocation attraction. C—Dislocation attraction plus regular diffusion.

simultaneously (equation 25). The distance over which a region corresponding to "low-carbon" martensite would contribute to X-ray intensity measurements is larger with dislocation-attraction operative than without it. If, for example, "low-carbon" martensite is considered to exist over the concentration range $(C - C_e)/(C_p - C_e) = 0$ to 0.2, which is in line with the accuracy of the X-ray measurements, the corresponding distances after 10^6 sec at 340°K are about 2×10^{-7} cm for regular diffusion, 3.5×10^{-7} cm for dislocation-attraction, and 5×10^{-7} cm for dislocation-attraction plus regular diffusion. On this basis, dislocation-attraction plus regular diffusion gives the best approximation to a discontinuous reaction. An even better approximation to a discontinuous reaction would presumably result if the restricted range of dislocation-attraction and the spherical-shell geometry were taken into consideration.

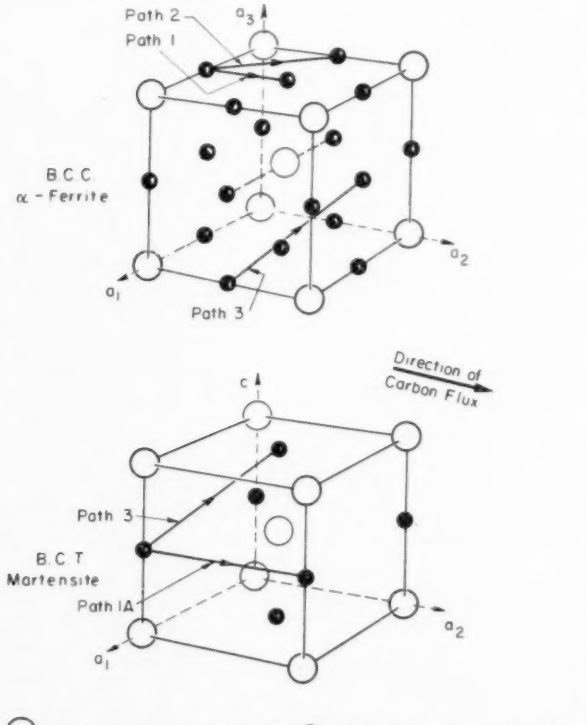

FIG. 4. Interstitial diffusion paths for carbon atoms in α-ferrite and martensite.

10. COMPARISON OF CARBON DIFFUSION IN MARTENSITE AND FERRITE

If the experimental value of activation energy for the reaction (26,000 cal/mol) is actually equal to that for diffusion of carbon in martensite, it follows that diffusion in martensite should be slower than in ferrite, provided that the values of D_0 are about the same in the two phases. Although actual diffusion experiments have not been carried out, a consideration of the available interstitial sites for carbon atoms in b.c.t. martensite and in b.c.c. ferrite indicates that it is reasonable to assume slower diffusion in b.c.t. martensite.

In b.c.c. ferrite, the available sites are the centers of the cube edges and faces, a total of six sites per unit cell. In b.c.t. martensite, the available sites are the

centers of the c-edges and the centres of the a–a faces, a total of two sites per unit cell. Diffusion of carbon atoms involves jumps from one neighboring interstitial site to another. Each advance that contributes to the net flow of carbon consists of a jump with a component in the diffusion direction. Because the b.c.t. and b.c.c. lattices are quite similar, it is possible to classify the principal jump-paths on the basis of the particular initial and final positions involved. These paths are listed below and are illustrated in Fig. 4.

Type of Path	*Examples*
1	Center of edge to center of face, or vice versa.
2	Center of edge to center of perpendicular edge, or center of face to center of perpendicular face.
3	Center of edge to center of perpendicular face, or vice versa.

For the b.c.c. lattice, it seems logical to assume that jumps of carbon atoms along type-1 paths require the lowest activation energy as compared with jumps along paths 2 and 3. Thus almost all of the jumps would be expected to occur directly along type-1 paths, and carbon atoms probably reach the final positions of paths 2 and 3 by making two and three successive jumps respectively along mutually perpendicular type-1 paths.

In the b.c.t. lattice, type-1 paths which result in an advance equal to one-half the lattice parameter are not available because of the preferred distribution of interstitial sites. The direct path of lowest activation energy would appear to be of type 1A, which is somewhat similar to two successive jumps along type-1 paths in the b.c.c. lattice, resulting in an advance equal to one lattice parameter. If the difference in path-length between types 1 and 1A were the only factor involved, the activation energies required for jumps along these paths would be the same. However, inasmuch as only alternate octahedral interstitial sites are stable positions for carbon atoms in the b.c.t. lattice, every other octahedral site must be a position of higher energy. It is likely that this circumstance would raise the level of the barrier energy in the diffusion process, and therefore the activation energy for carbon diffusion in martensite could be higher than in α-ferrite, which is in accord with the present analysis of the tempering data.

11. CONCLUSIONS

1. Analysis of the kinetics of the first stage of tempering based on precision-length data indicates that the time exponent of the reaction is 0.30 ± 0.04 and that the activation energy for the reaction is $26{,}000 \pm 3000$ cal/mol.

2. A dislocation-attraction model proposed for the first-stage reaction predicts that the time exponent is 1/3, that the activation energy for diffusion of carbon in martensite is 26,000 cal/mol, and that the radius of subgrains in martensite is about 1500 Å. The dislocations are presumed to lie in the partially coherent interface between the ε-carbide precipitate and the martensitic matrix.

3. The slower rate of diffusion of carbon in b.c.t. martensite than in b.c.c. ferrite can be attributed to the existence of paths of lower barrier energy for carbon jumps in the b.c.c. lattice than in the b.c.t. lattice.

4. The approximately discontinuous nature of the first-stage reaction as indicated by previous X-ray intensity measurements is explained by the shape of the carbon-concentration vs. distance curve that results from dislocation-attraction.

5. Because of the dominating effect of dislocation-attraction on carbon flow up to about 50% transformation, the role of regular diffusion due to concentration gradients can be neglected as a first approximation.

ACKNOWLEDGMENTS

The co-operation of Dr. Carl Wagner of the Department of Metallurgy, M.I.T., and Dr. Philip Franklin of the Department of Mathematics, M.I.T., in obtaining an approximate solution to equation (24) is gratefully acknowledged. The financial support of the Instrumentation Laboratory of M.I.T. made this work possible.

REFERENCES

1. B. S. Lement, B. L. Averbach, and M. Cohen Microstructural Changes on Tempering Iron-Carbon Alloys, *Trans. Amer. Soc. Metals* **46,** 851 (1954).
2. G. Kurdjumov and L. Lyssak Kinetics of the Primary Stage of Martensite Decomposition *J. Tech. Phys.* **19,** 525 (1949).
3. C. S. Roberts, B. L. Averbach, and M. Cohen The Mechanism and Kinetics of the First Stage of Tempering *Trans. Amer Soc. Metals* **45,** 576 (1953).
4. C. Zener Theory of Growth of Spherical Precipitates from Solid Solution *J. Appl. Phys.* **20,** 950 (1949).
5. S. Harper Precipitation of Carbon and Nitrogen in Cold-Worked Alpha-Iron *Phys. Rev.* **83,** 709 (1951).
6. K. H. Jack Structural Transformations in the Tempering of High-Carbon Martensitic Steels *J. Iron and Steel Inst.* **169,** 26 (1951).
7. A. H. Cottrell *Dislocations and Plastic Flow in Crystals* Oxford at the Clarendon Press (1953).
8. C. Wert *The Metallurgical Use of Anelasticity* ASM Seminar on Modern Research Techniques in Physical Metallurgy (1952) 225.
9. A. E. Nygren *The Decomposition of Martensite* Master's Thesis, M.I.T. (1951).
10. C. S. Roberts Effect of Carbon on the Volume Fractions and Lattice Parameters of Retained Austenite and Martensite *Trans. Amer. Inst. Min. Met. Eng.* **197,** 203 (1953).

X-RAY AND CALORIMETRIC INVESTIGATIONS OF COLD WORKING AND ANNEALING OF A GOLD-SILVER ALLOY*

B. L. AVERBACH,† M. B. BEVER,† M. F. COMERFORD,† and J. S. Ll. LEACH‡

Calorimetric and X-ray diffraction line-broadening measurements were carried out on samples of a 75Au–25Ag (weight per cent) alloy deformed by filing and annealed at various temperatures up to 500°C. Stored energy, hardness, subgrain size, local strain, and short-range order determinations were made. It appears that most of the stored energy is associated with the presence of subboundaries; a small fraction of the energy is attributable to a reduction in the short-range order and a negligible amount is stored in the local elastic distortions. The recovery process involves a substantial reduction of the local strains and a small increase in the subgrain size in this alloy. Recrystallization appears to involve a removal of the low-angle boundaries and the complete elimination of the local strains.

EXAMENS PAR RAYONS X ET CALORIMETRIQUES D'ALLIAGES OR-ARGENT ECROUIS ET REVENUS

Des mesures calorimétriques et d'élargissement de raies de lignes de diffraction de rayons X ont été effectuées sur des échantillons 75% Au–25% Ag (% en poids), alliage déformé à la lime et revenu à différentes températures jusqu'à 500°C. L'énergie accumulée, la dureté, la dimension des sous-grains, la déformation locale et l'ordre à petite distance ont été déterminés.

Il semble que la plus grosse partie de l'énergie accumulée est associée à la présence des limites de sous-grains. Une petite fraction de l'énergie est attribuable à la réduction de l'ordre à petite distance et une quantité négligeable est accumulée dans les distorsions élastiques locales.

Le procédé de restauration implique une réduction sensible des déformations locales et un petit accroissement de la dimension du sous-grain de cet alliage. Une recristallisation semble entrainer la supression des joints à petits angles et l'élimination complète des déformations locales.

RÖNTGENOGRAPHISCHE UND KALORIMETRISCHE UNTERSUCHUNGEN DER VORGÄNGE BEI KALTBEARBEITUNG UND ANLASSEN EINER GOLD-SILBER-LEGIERUNG

An Proben einer Legierung aus 75% Au und 25% Ag (Gewichtsprozente), die durch Feilen verformt und daraufhin bei verschiedenen Temperaturen bis herauf zu 500°C angelassen wurden, wurden kalorimetrische Untersuchungen sowie Messungen über die Verbreiterung der Röntgenlinien durchgeführt. Im einzelnen wurden gespiecherte Energie, Härte, Subkorngrösse, lokale Verzerrungen und Nahordnung bestimmt. Der Hauptteil der gespeicherten Energie geht offenbar auf das Vorhandensein von Subkorngrenzen zurück; ein kleiner Bruchteil der Energie lässt sich der Verringerung der Nahordnung zuschreiben und ein vernachlässigbarer Anteil ist in den lokalen elastischen Verzerrungen aufgespeichert. Der Erholungsvorgang ruft in dieser Legierung ein starkes Zurückgehen der lokalen Verzerrungen und eine geringe Zunahme der Subkorngrösse hervor. Die Rekristallisation scheint zum Verschwinden der Kleinwinkel-Korngrenzen und zum vollständigen Abbau der lokalen Verzerrungen zu führen.

VOL. 4 1956

INTRODUCTION

Calorimetric and X-ray diffraction measurements were used to investigate the changes which occur on annealing a heavily deformed gold-silver alloy. Although each type of measurements has been previously applied separately to various metals, a combination of the techniques was expected to give some insight into the mechanism by which energy is stored in cold-worked metals and to provide information on the changes which occur during recovery and recrystallization.

Cold-worked samples were prepared by filing and these were then annealed at various temperatures up to 500°C. The X-ray diffraction line broadening was observed for each sample, and the stored energy was determined by tin-solution calorimetry. Later it was realized that the short-range order in these samples had been affected by the plastic deformation and annealing treatments. Additional samples were then produced by procedures identical with those used for the original set, and short-range order parameters were determined from diffuse X-ray measurements.

The samples represent the entire annealing range from the heavily cold-worked to the fully recrystallized and annealed condition, but caution should be exercised before assuming that the exact sequence of events observed in this alloy is necessarily the same for other metals and alloys.

* This work was sponsored by the U.S. Atomic Energy Commission under Contract AT(30-1)-1002. *Received November 9, 1955.*

† Department of Metallurgy, Massachusetts Institute of Technology, Cambridge, Massachusetts.

‡ Present address: Murex Welding Processes, Ltd., Waltham Cross, Herts, England.

EXPERIMENTAL PROCEDURES

Preparation of the Cold-worked Powder

The powders were prepared with a fine file from a block of gold-silver alloy, containing 75 per cent gold by weight. The powder was passed over a magnet to remove iron; after this treatment there was still about 0.2 per cent iron left in the material, presumably by mechanical admixture, but this did not interfere with the calorimetric or X-ray measurements. Large filings were removed and the powder was divided into three size groups: +200 mesh, 200 to 325 mesh, and −325 mesh. About 20 per cent by weight of the sample fell into the first size-range, and the balance was about equally divided between the two other size-ranges. The specific surface area of the powder used in the experimental work as determined by a krypton adsorption technique was 2040 cm^2/gm. (This measurement was carried out by Mr. S. R. Mitchell under the supervision of Professor R. T. J. Charles.)

The powders were compressed into briquettes measuring approximately $1 \times \frac{1}{2} \times \frac{1}{8}$ in. with the finest powders at the face which was to be used for the X-ray measurements. The fine powders favored the production of smooth diffraction rings. The overall size distribution of the sample, however, was kept close to that of the original filings. The briquettes were stored in a refrigerator at approximately −10°C until they were annealed or measured.

Annealing

The briquettes were sealed in evacuated Pyrex tubes and annealed for one hour at the temperatures indicated. (Two samples were also annealed at 500°C for two hours.) The earliest samples and all samples annealed at 500°C were heated in a temperature-controlled furnace; the remaining samples were heated in liquids boiling in a flask provided with a reflux condenser. The liquids and their boiling-points were: cumene (150°C), carbitol (195°C), benzophenone (306°C), and carbazole (345°C). The temperatures stated are the boiling-points which were actually observed and not those reported for ideal standard samples. In a few instances two samples were annealed at a given temperature. Both were used for the calorimetry, but only one was used for diffraction measurements.

X-ray Line Broadening Measurements

X-ray diffraction line shapes were obtained by using either a Philips recording spectrometer and filtered Co$K\alpha$ radiation or a hand spectrometer with Cu$K\alpha$ radiation monochromated by diffraction from a LiF crystal. The diffraction lines were obtained at a low rate of travel ($\frac{1}{8}$ deg per minute) with the recording spectrometer, and at small intervals in 2θ on the hand spectrometer, and care was taken to include all of the line above the background. A correction for instrumental broadening was made by measuring the diffraction contours for well-annealed aluminum single crystals. Since the lattice parameter of the gold-silver alloy is almost identical with that of aluminum, it was possible to use each diffraction line from the aluminum crystal as representing only the instrumental broadening.

Each diffraction peak was expressed in terms of a Fourier series and then analyzed by the method of Warren and Averbach.[1, 2, 3] This analysis expresses the broadening function as a cosine Fourier series, in which coefficients, $A_n(l)$, describe the cold-worked material. The coefficients include the effects of particle size and distortion in the following form:

$$A_n(l) = A_n{}^P A_n{}^D(l) \tag{1}$$

where: $A_n{}^P$ = particle-size coefficient,

$A_n{}^D(l)$ = distortion coefficient.

These effects can be separated if more than one order (l) of each line is measured, since only the distortion coefficient is a function of the order of the reflection. As (l) approaches zero,

$$A_n{}^D(l) = \exp\left(-2\pi^2 l_0{}^2 \langle \Delta L^2 \rangle / a^2\right) \tag{2}$$

where: $l_0{}^2 = h^2 + k^2 + l^2$,

ΔL = change in length of a column of crystals of length, L,

a = lattice parameter.

Equation (1) becomes:

$$\ln A_L(l_0) = \ln A_L{}^P - 2\pi^2 l_0{}^2 \langle \Delta L^2 \rangle / a^2 \tag{3}$$

For different orders of a particular set of planes (hkl), a plot of $\ln A_L(l_0)$ vs. $l_0{}^2$ should give a curve which approaches a straight line at $l_0 = 0$. Thus even if the exponential expansion involved in equation (2) is not justified at large values of $\langle \Delta L^2 \rangle$, it is still valid at $l_0{}^2 = 0$. Experimentally it appears that the separation afforded by equation (3) can be carried out in the cases of the first two orders of the (111) and (200) lines.

Williamson and Smallman[4] have recently criticized the separation of particle-size and distortion coefficients described above on the basis that it is not valid for the case where the strains have an arbitrary distribution. They chose a Cauchy distribution of strains for their illustrative case; this requires that the mean-square strain in the crystal be infinite (i.e. $\left\langle \left(\frac{\Delta L}{L} \right)^2 \right\rangle$ is infinite), and in this case the separation

does break down. However, such a case is physically impossible.

In this work, the diffraction contours were determined for the pairs (111),(222) and (200),(400) and the particle sizes and distortions were determined from equation (3). The strain, $\varepsilon = \Delta L/L$, was obtained as a function of the gage length, L. This strain rises smoothly as the gage length is reduced and tends to approach a constant value as L approaches the spacing of the diffraction plane. These maximum values at small distances, L, were reported as the local strain, and represent the root-mean-square local strains, averaged over distances of a few ångströms, for columns of cells normal to the diffraction planes. The particle sizes represent the average lengths of a column of crystals normal to the diffraction planes which lie within a particle. A particle boundary is thus any surface which destroys the diffraction-phase relationship; this includes grain boundaries, subgrain boundaries, and inclusion interfaces. Since the particle sizes measured by X-ray methods were much smaller than the grain sizes, it was assumed that the X-ray particle sizes were primarily associated with the presence of subgrain boundaries.

It is also possible to detect the presence of large numbers of stacking faults by the relative shift in the positions of diffraction lines.[5] The shifts observed here were, however, within the experimental error and much smaller than those observed for alpha-brass. It was concluded, therefore, that the stacking-fault concentration was low.

Short-range Order Measurements

The short-range order was determined from measurements of diffuse X-ray scattering, using a reflection-spectrometer method described elsewhere.[3, 6, 7] Geiger-counter spectrometer readings were made with monochromatic Co$K\alpha$ radiation from a curved fluorite crystal focused on the specimen held in an evacuated chamber. The X-ray unit was run at 20 kV and 22 mA for all of these measurements. The diffuse scattering measurements were put on an absolute scale by comparison with the independent scattering from a block of lucite, measured under identical experimental conditions. The fluorite monochromator removed the $\lambda/2$ harmonic from the beam, and the $\lambda/3$ harmonic was not excited at the voltage used.

The Compton modified contribution to the diffuse scattering was calculated in the manner described by James.[8] The temperature diffuse scattering was computed on the assumption of independent vibration of the atoms with identical amplitudes for each atom.[9] Although the temperature diffuse correction is approximate, the final calculation of the short-range order and size-effect coefficients was performed by means of a Fourier analysis, which helps to isolate these coefficients from extraneous effects. Consequently, the order and size-effect coefficients were of considerably greater accuracy than would be expected on the basis of the accuracy of the corrections.

The nearest-neighbor short-range order was expressed in terms of the coefficient, α_1, which is determined directly as the coefficient in the Fourier transform. This coefficient is defined as

$$\alpha_1 = 1 - \frac{p_1^A}{X_A}$$

where p_1^A = probability of finding an A atom as a nearest neighbor for a B atom,

X_A = atomic fraction of A atoms.

In principle, it is also possible to obtain values for the coefficients, α_2, α_3, etc., from powder data, but in practice the resolution of the powder method is too low to give anything beyond the first-neighbor coefficient. The size-effect coefficient, β_1, which arises from a difference in the atomic sizes in solution,[10] was found to be quite small, indicating that the gold and silver atoms have almost the same sizes in solid solution. The short-range order coefficient, α_1, was found to be negative for this alloy, indicating a preference for unlike nearest-neighbors, and the data were consistent with those of Norman and Warren[11] for other gold-silver compositions.

Calorimetric Measurements

The samples used for the line-broadening measurements were also used for calorimetric determinations of the stored energy. Each briquette was broken into small pieces, which were shaken up in a tube to round off sharp corners and to remove any particles likely to be knocked off easily. The lumps were then separated from the powder, weighed, and added to the calorimeter. Addition of lump specimens rather than powder facilitated the manipulation and insured that the total weight of the samples reached the bath. The additions usually weighed 4–6 g.

The stored energy of the powders was determined, using a tin-solution calorimetry technique which has been described elsewhere.[12, 13] The success of this technique depends on the small heat effect associated with the dissolution in liquid tin of some alloys, such as a 75 per cent gold-silver alloy added from 0°C to tin at 240°C. This permits the determination of small energy contents, such as that due to cold-work, from

VOL. 4 1956

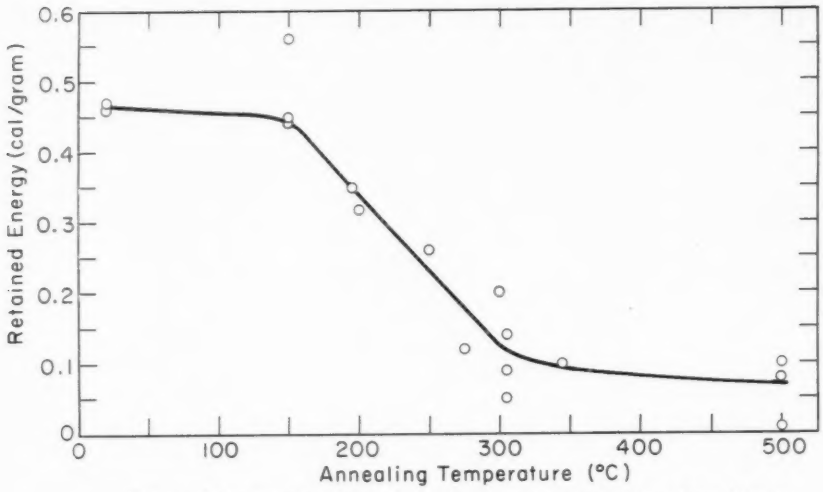

FIG. 1. Calorimetric values of stored energy in 75Au–25Ag alloy filings.

the difference in the heat effects associated with the dissolution of the sample in question and an annealed standard of the same alloy.

In this investigation, the accuracy of the calorimetric measurements was adversely affected by the use of powders, even though they were in briquetted form. The dissolution of the samples in the calorimeter was accompanied by the evolution of gas which raised the pressure from the usual working level of 0.02 microns to as much as 10 microns. Also, the powder samples required 3–4 min for complete dissolution compared to 1 min for the annealed strip which was used as a standard. These undesirable features in the behavior of the powder samples were probably caused by surface contamination. Although this interfered with the best accuracy of which the calorimetric method is capable, the data were still sufficiently accurate to indicate the main features of the annealing processes.

Hardness Measurements

Hardness measurements were made by means of a Bergsman microhardness tester, using a load of 10 g. A number of impressions was made with a Vickers diamond, avoiding grain boundaries and pores as far as possible, and these were collected in a distribution

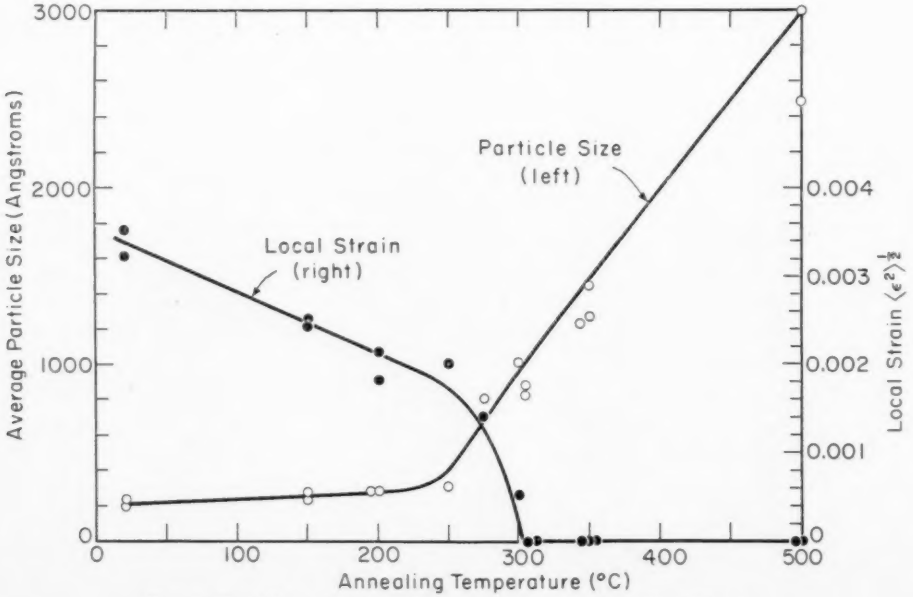

FIG. 2. Particle sizes and local strains in 75Au–25Ag alloy filings.

curve for each sample. The value which appeared most frequently was assumed to represent the most probable hardness, and this was expressed as a diamond-pyramid-hardness (DPH) number. Although the absolute values of these hardness readings are probably quite uncertain, the observed trend of hardness vs. annealing temperature was considered significant.

DISCUSSION OF EXPERIMENTAL RESULTS

The calorimetric data on stored energy are listed in Table 1, and the line-broadening X-ray data are summarized in Table 2. The mean values for strain and particle size in Table 2 were weighted with the multiplicity for each direction. Although an attempt was made to obtain both X-ray and calorimetric data on all samples, a few calorimetric runs were unsuccessful However, the scatter in the data was sufficiently small to warrant a correlation in terms of average values taken from a smoothed plot vs. annealing temperature, as shown in Figs. 1 and 2.

It is apparent that the stored energy drops on annealing for one hour in the range 150–300°C, although there may be a smaller decrease on annealing at lower temperatures The particle size in the as-filed condition was approximately 200 Å; it increased to about 300 Å on annealing at temperatures up to 250°C, but increased sharply on annealing at higher temperatures The local strains decreased to about half their original value in the annealing range up to 250°C and dropped to zero on annealing at 300°C. The hardness values are shown in Fig. 3, and the conjugate decrease in hardness as well as the changes in back-reflection photograms suggested that visible recrystallization took place rapidly in the temperature range 250–300°C. Annealing treatments below 250°C

TABLE 1. Stored energy in 75Au–25Ag alloy filings

Sample	Treatment (°C, 1 hour)	Retained energy (cal/gram)
3	As-filed	0.46
4	As-filed	0.47
1a	150	0.45
17a	150	0.45
17b	150	0.56
19a	195	0.35
5a	200	0.32
6a	250	0.26
10a	275	0.12
7a	300	0.20
21a	304	0.05
16a	306	0.09
16b	306	0.14
20a	345	0.10
12a	500	0.10
18a	500 (2 hours)	0.10
18b	500 (2 hours)	0.01

TABLE 2. Local strains and particle sizes in 75Au–25Ag alloy filings

Sample	Treatment (°C, 1 hour)	Strains (10^{-3})			Particle sizes (Å)		
		[111]	[200]	Weighted mean	[111]	[200]	Weighted mean
3	As-filed	2.6	4.6	3.5	260	170	220
4	As-filed	2.3	4.4	3.2	240	170	210
1a	150	2.1	3.1	2.5	290	200	250
8a	150	2.2	3.0	2.5	280	190	240
19a	195	1.6	2.0	1.8	320	230	280
5a	200	1.6	2.8	2.1	300	210	260
6a	250	1.5	2.6	2.0	330	260	300
10a	275	0.6	2.4	1.4	830	730	790
7a	300	0	1.2	0.5	1050	960	1010
21a	304	0	0	0	900	720	860
15a	305	0	0	0	980	710	820
20a	345	0	0	0	1230	1230	1230
9a	350	0	0	0	1550	1300	1440
13a	350	0	0	0	1300	1200	1260
11a	500	0	0	0	3000	3000	3000
12a	500	0	0	0	2700	2200	2480

VOL. 4 1956

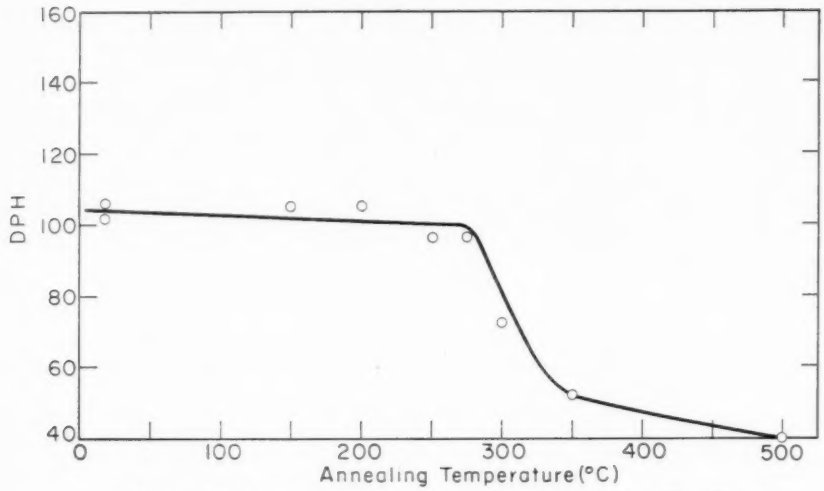

FIG. 3. Hardness vs. annealing temperature 75Au–25Ag alloy filings.

appeared to correspond to the recovery process, whereas above 250°C there was apparent recrystallization. These data suggest that the recovery process involves the relief of local strains along with some subgrain growth. On recrystallization, all of the local strain disappears, and regions with large subgrains are formed.

Since the local elastic strains measured by the X-ray technique represent the averages for columns of crystals throughout the irradiated volume taken over a gage-length of the order of the interplanar spacing, it is possible to calculate the stored elastic energy associated with these distortions. Table 3 lists the elastic energies calculated from the smoothed strain values in Fig. 2, and it is evident that these energies are insignificant in comparison with the measured stored energies. It thus appears that relatively little energy is stored in the form of elastic distortions in these deformed filings.

The diffuse X-ray measurements indicated that the short-range order in this alloy was reduced by the severe plastic deformation of filing, and the measured nearest-neighbor short-range order parameter, α_1, is listed as a function of annealing temperature in Fig. 4. It appears that filing reduces the short-range order by about 50 per cent, and a similar result was obtained by Rudman for a copper-gold alloy.[15] On annealing, there appears to be no increase in the short-range order during recovery (up to 200°C), but the coefficient, α_1, returns to its equilibrium value, —0.06, after recrystallization occurs.

A small size-effect parameter, β_1, was also derived from the Fourier transforms used to evaluate α_1, and the values of β_1 are listed in Fig. 4. The presence of a size-effect coefficient indicates that the gold and silver atoms have different sizes in solid solution [10, 6], and although the effect is small (with $\beta_1 = 0.004$), it is probably sufficient to account for the minimum observed in the lattice parameters of gold-silver alloys at about 50 atomic per cent.[16]

The energy associated with the reduction in short-range order as a result of the deformation may be estimated if the quasi-chemical theory for solid

TABLE 3. Elastic stored energy in 75Au–25Ag alloy filings

Treatment (°C, 1 hour)	Average strain (10^{-3})	Elastic energy (cal/gm) $W = \frac{3}{2}E\varepsilon^2$
As-filed	3.3	0.016
150	2.5	0.009
200	2.1	0.006
250	2.0	0.006
275	1.4	0.003
300	0.2	0.0001
350	0	0
500	0	0

$E = 9.9 \times 10^6$ p.s.i. $= 0.68 \times 10^{12}$ dynes/c $\times 10^3$m$^2 = 0.95$ cal/gm[14] $\rho = 17.1$ gm/cm^3

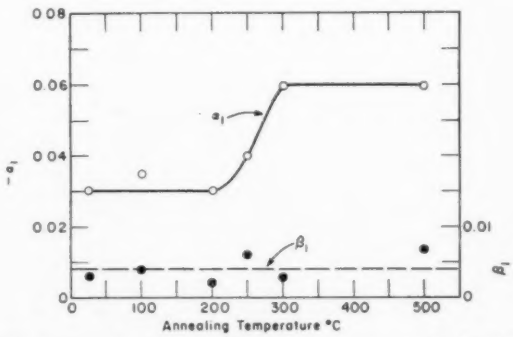

FIG. 4. Short-range order coefficients, α_1, and size-effect coefficients, β_1, in cold-worked and annealed filings of 75Au–25Ag alloy.

TABLE 4. Energy stored in subgrain boundaries 75Au–25Ag alloy filings

Annealing Temperature 1 hour (°C)	Total interface area per gram 10^4(cm)^2	Reduction of stored energy (cal/gm)				Specific interfacial energy (ergs/cm^2)
		Measured	Elastic	Local order	Interface	
As-filed	5.56	0.46	0.016	0.13	0.31	240
150	4.67	0.45	0.009	0.13	0.31	280
200	4.33	0.34	0.006	0.13	0.20	190
250	3.33	0.23	0.006	0.09	0.13	163
275	1.67	0.18	0.003	0.04	0.14	350
300	1.24	0.13	0.0001	0	0.13	440
350	0.78	0.09	0	0	0.09	480
500	0.39	0.08	0	0	0.08	860

solution formation is assumed to be valid. Gold-silver alloys may apparently be treated this way,[16] since the atoms have similar sizes and no unusual electronic effects are expected. Rudman[15] has recently shown that the change in internal energy, δH^M, associated with a change in short-range order is given by

$$\delta H^M = X_A X_B Z N_0 v(\delta\alpha_1) \qquad (4)$$

where X_A, X_B = atomic fractions of components A, B,

Z = number of nearest neighbors,

N_0 = Avogadro's number,

$v = E_{AB} - \frac{1}{2}(E_{AA} + E_{BB})$ = interaction energy,

$\delta\alpha_1 = \alpha_1$ (annealed) $- \alpha_1$ (cold-worked)

Taking $(N_0 v)$ as -250 calories per gram atom,[17] the contribution arising from the change in short-range order to the stored energy was calculated from Fig. 4. in accordance with equation (4), and the resultant energies are listed in Table 4. The energy associated with the reduction in short-range order has a maximum value of about 0.10 calories per gram, and it represents a small but significant contribution to the stored energy.

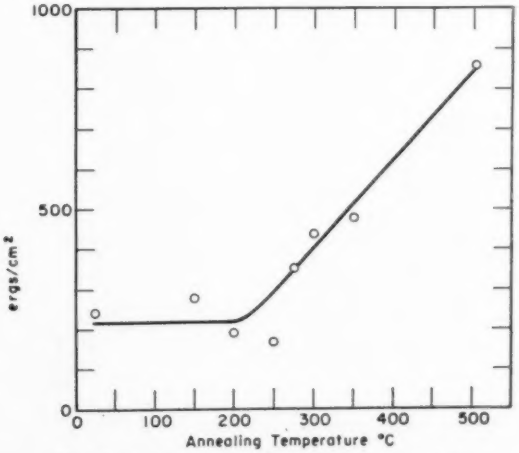

FIG. 5. Average specific interfacial energy in 75Au–25Ag filings.

Since the stored energy cannot be explained on the basis of elastic energy or changes in short-range order alone, an attempt was made to calculate the specific surface energy of the interfaces formed during deformation and annealing. Since the average particle sizes, $\bar{L}$, correspond to the average intercepts for the particles taken in four {111} and three {200} directions, it was assumed that they were equivalent to the average random intercept length. The total interfacial area per gram is then $S/(V\rho) = 2/(\bar{L}\rho)$, where S = total interfacial area, V = volume, and ρ = density. The specific surface energy, γ, was computed, and the results are shown in Fig. 5.

It is interesting to note that the specific surface energy is about 250 ergs/cm^2 in the cold-worked and recovered region, but rises when recrystallization starts and reaches a value near 900 ergs/cm^2. The latter value is that expected for a random grain boundary, whereas the low-energy boundary region is representative of a material which contains numerous small-angle boundaries.

These results suggest that low-angle boundaries are introduced during deformation and that they change little during the recovery process, even though the subgrain size may increase somewhat. Recrystallization appears to involve the growth of high-energy boundaries at the expense of a large area of low-angle boundaries. It is interesting to note, however, that substantial strain relief occurs during recovery, and it appears that the driving force for recrystallization is the interfacial energy available from the elimination of subboundaries, and not the stored elastic energy.

SUMMARY AND CONCLUSION

The findings of this investigation indicate that the energy stored in filings of a 75Au–25Ag (weight per cent) alloy is released during the recovery and

recrystallization processes. The combined X-ray and calorimetric measurements suggest that most of the stored energy is associated with the presence of low-energy boundaries introduced during the deformation, and the average specific interfacial energy for these boundaries has been calculated. Even though the total stored energy decreases and the average subgrain size increases on annealing, the interrelation is such that the specific interfacial energy is relatively constant during the recovery stages (up to 250°C), and increases to the random grain-boundary value after recrystallization.

The contributions to the stored energy arising from the elastic energy were shown to be negligible and those from the reduction in short-range order were shown to be significant, but small in comparison with the calorimetric values. A substantial relief of the local strains occurs during the recovery process. In the case of a heavily cold-worked alloy, the recovery process thus seems to involve the reduction of local strains and a slow subgrain growth, whereas on recrystallization the strains disappear completely and the low-energy boundaries are eliminated, and the equilibrium short-range order is restored.

ACKNOWLEDGMENTS

The authors wish to acknowledge the financial assistance of the U.S. Atomic Energy Commission. They are indebted to Professor B. E. Warren for many helpful discussions, and to Dr. David Chipman, D. A. Hay, and L. R. Rubin for their assistance. B. Howell and N. Hanson also assisted in the experimental phases of the program.

REFERENCES

1. B. E. Warren and B. L. Averbach *J. App. Phys.* **21,** 595 (1950).
2. B. E. Warren and B. L. Averbach *J. App. Phys.* **23,** 497 (1952).
3. B. E. Warren and B. L. Averbach *Modern Research Techniques in Physical Metallurgy,* ASM 95, Cleveland (1953).
4. G. K. Williamson and R. E. Smallman *Acta Cryst.* **7,** 574 (1954).
5. B. E. Warren and B. L. Averbach *J. App. Phys.* **23,** 1059 (1952).
6. P. A. Flinn, B. L. Averbach, and M. Cohen *Acta Met.* **1,** 664 (1953).
7. P. S. Rudman and B. L. Averbach *Acta Met.* **2,** 576 (1954).
8. R. W. James *The Optical Principles of the Diffraction of X-Rays.* Bell (1950) London.
9. F. H. Herbstein and B. L. Averbach. Submitted to Acta Met.
10. B. E. Warren, B. L. Averbach, and B. W. Roberts *J. App. Phys.* **22,** 1493 (1951).
11. N. Norman and B. E. Warren *J. App. Phys.* **22,** 483 (1951).
12. L. B. Ticknor and M. B. Bever. *Trans. Amer. Inst. Min. Met. Eng.* **194,** 941 (1952).
13. M. B. Bever and L. B. Ticknor *Acta Met.* **1,** 116 (1953).
14. P. A. Clarkin and F. X. Spinelli. S.B. Thesis, Department of Metallurgy, Massachusetts Institute of Technology (1952).
15. P. S. Rudman and B. L. Averbach. Submitted to Acta Met.
16. G. Sachs and J. Weerts *Z. Physik* **60,** 481 (1930).
17. B. L. Averbach, P. A. Flinn, and M. Cohen *Acta Met.* **2,** 92 (1954).

VOL
4
195

EASY GLIDE OF CUBIC METAL CRYSTALS*

J. GARSTONE,† R. W. K. HONEYCOMBE,‡ and G. GREETHAM‡

The structural features associated with easy glide in high-purity aluminum crystals have been studied by microscopic and X-ray methods. The temperature dependence of the phenonemon has been examined on identically oriented crystals over the range −196°C to 200°C, while the influence of specimen-length has been studied at room temperature.

An examination of the orientation dependence of the stress-strain curves of copper single crystals confirms the results of Rosi in so far as easy glide ends at a value of the resolved shear stress σ_0 such that $\sigma_0 - \tau_c$ (critical resolved shear stress) is constant. However, it is shown that the length of the easy-glide range varies because of the existence of a size factor, demonstrated by experiments on crystals of identical orientation, but of different sizes. The effect of thin electro-deposits and, in particular, of alloying additions on the extent of easy glide, has been investigated.

The view is advanced that easy glide ends as a result of secondary slip arising prematurely in the vicinity of dislocation pile-ups. Examination of this model gives the result that τ_c/σ_0 is constant, in accord with the experimental results. The value of τ_c determines the extent of easy glide, and from this follows an explanation of the temperature dependence. Variation in the length of the slip path and consequently of the number of pile-ups, is put forward as an explanation of the orientation dependence of the phenomenon.

GLISSEMENT FACILE DE CRISTAUX CUBIQUES METALLIQUES

Les traits structuraux de cristaux d'aluminium de haute pureté, associés ou glissement facile, ont été étudiés par des méthodes de rayons X et microscopiques.

L'effet de la température sur le phénomène a été examiné sur des cristaux identiquement orientés pour le domaine de −196°C jusqu'à 200°C, tandis que l'influence de la longueur de l'échantillon a été étudiée à la température ambiante.

Un examen de l'effet de l'orientation sur les courbes tension-déformation de monocristaux de cuivre confirme les résultats de Rosi dans la mesure où le glissement facile se termine à une valeur de la tension de cisaillement résolue σ_0 telle que $\sigma_0 - \tau_c$ (tension critique de cisaillement résolue soit constant. Il est cependant démontré (par des expériences sur des cristaux d'orientations identiques mais de tailles différentes) que la longueur du domaine du glissement facile varie, à cause de l'existence d'un facteur de taille. L'effet de fins dépôts électrolytiques et, en particulier, d'additions d'alliages sur l'ampleur du glissement facile a été étudié.

L'hypothèse est émise que le glissement facile se termine avec l'apparition prématurée d'un glissement secondaire aux environs d'empilements de dislocations. L'examen de ce modèle donne le résultat que τ_c/σ_0 est constant en accord avec les résultats expérimentaux. La valeur de τ_c détermine l'étendue du glissement facile et de ceci résulte l'explication de l'influence de la température. Une variation de la longueur de glissement et, par conséquent, du nombre d'empilements est avancée pour expliquer l'influence de l'orientation sur le phénomène.

"EASY GLIDE" IN KUBISCHEN METALLKRISTALLEN

An Reinstaluminium-Kristallen wurden die mit easy glide zusammenhängenden strukturellen Veränderungen (Gleitlinien, Knickbänder usw.) mikroskopisch und röntgenographisch untersucht. Ausserdem wurde an Kristallen gleicher Orientierung die Temperaturabhängigkeit dieses Verfestigungsbereichs zwischen −196°C und 200°C verfolgt, während eine Untersuchung über den Einfluss der Probenlänge bei Raumtemperatur erfolgte.

Eine Nachprüfung der Orientierungsabhängigkeit der Verfestigungskurve von Kupfer-Einkristallen bestätigt insoweit die Ergebnisse von Rosi, als der easy-glide-Bereich bei einem Schubspannungswert σ_0 endigt, für den $\sigma_0 - \tau_c$ (kritische Schubspannung) konstant ist. Es wird jedoch gezeigt, dass die Variation der Länge des easy-glide-Bereichs auf die Existenz eines Grössen-Effektes zurückgeht, der durch Experimente an Kristallen mit gleicher Orientierung aber verschiedenem Querschnitt nachgewiesen wird. Weiterhin wurde der Einfluss dünner elektrolytisch abgeschiedener Schichten und insbesondere von Zulegierungen auf die Ausdehnung des easy-glide-Bereichs untersucht.

Die Autoren sind der Auffassung, dass das Ende des easy glide von sekundärer Gleitung herrührt, die in der Nähe von Versetzungsaufstauungen vorzeitig einsetzt. Eine Nachprüfung dieses Modells führt in Übereinstimmung mit den experimentellen Ergebnissen zu dem Resultat, dass τ_c/σ_0 konstant ist. Der Wert von τ_c bestimmt somit die Ausdehnung des easy glide-Bereichs, woraus auch eine Erklärung der Temperaturabhängigkeit folgt. Die Orientierungsabhängigkeit der Erscheinung wird damit erklärt, dass sich mit der Orientierung die Länge des Gleitwegs und somit auch die Zahl der Aufstauungen ändert.

* Received November 10, 1955.

† Atomic Energy Research Establishment, Harwell, formerly Metallurgy Department, University of Sheffield, England.
‡ Metallurgy Department, University of Sheffield, England.

VOL. 4 1956

1. INTRODUCTION

Hexagonal metal crystals to a first approximation give linear shear-stress strain curves up to large plastic strains. The rate of strain hardening is much less than in comparable cubic metal crystals where the stress-strain curves are normally approximately parabolic. However, it has been known for some time that exceptions to this behavior occur; notably, Von Goler and Sachs[1] showed that 70/30 brass crystals exhibited very low hardening from the yield-point to as much as 20% plastic strain. More recently, Maddin, Mathewson and Hibbard[2] have shown that this stage of little or no hardening ceases when slip on more than one system begins.

In recent years it has become clear that linear hardening can occur in pure metal crystals regardless of their crystal structure, provided slip on a single system takes place and is uninterrupted by the occurrence of inhomogeneities. Masing[3] considered that the parabolic stress-strain behavior of cubic metal crystals arose from the formation of deformation bands and slip on other systems. This opinion was partly based on experimental work carried out on aluminum crystals by Masing and Raffelsiefer,[4] who found that crystals with orientations near [100] or [111] hardened parabolically, whereas crystals near [110] gave initially a linear hardening curve followed by a more rapid hardening parabolic curve. Rosi and Mathewson[5] also found a linear law with aluminum crystals up to 2% elongation. Lücke and Lange[6] showed that the extent of this linear region in aluminum depended not only on the crystal orientation, but also on the purity of the material. Andrade and Henderson[7] found that gold and silver crystals behaved in a similar manner to aluminum, and the region of linear hardening, or "easy glide," as it is frequently called, became greater the lower the temperature of deformation. The range of easy glide was markedly restricted in silver crystals when these had a thin oxide film, and in general the presence of impurities in the metals had the same effect. Jaoul and Crussard,[8] working with aluminum crystals, found that the range of easy glide decreased as the purity was reduced from 99.995 to 99.8%.

Metallographic studies,[9, 10, 11, 12] principally on aluminum, have shown that deformation bands and unpredicted slip on other planes occur in the early stages of deformation in crystals which would be expected to deform on one set of planes. Rosi,[13] using both silver and copper single crystals, found that the end of the linear hardening was associated with the occurrence of sporadic multiple glide. Sawkill and Honeycombe[14] have suggested that the range of easy glide depends on the rotations occurring in kink bands, which determine when secondary slip occurs within them. As these rotations are larger the higher the temperature, the easy-glide range becomes shorter.

This paper is an attempt to assess the important variables in easy glide in both pure metals and in alloy crystals, and to propose a general explanation of the phenomenon. Results will be presented on aluminum crystals of identical orientation deformed at three different temperatures and examined by X-ray and microscopic methods. The role of crystal size and orientation has been investigated with copper crystals on which metallographic observations have also been made. The effects of electrodeposited films and of alloying additions to copper crystals have also been studied.

2. PREPARATION OF CRYSTALS

The aluminum crystals were prepared by a modification of the critical-strain method from 0.125-in. square wire (99.99% pure). Long lengths of the critically strained (2% elong.) wire were passed through a gradient furnace, the highest temperature being 600–630°C. In this way crystals up to 22 in. long were prepared and could be cut into a number of identical specimens (4 in. long). Copper crystals of similar cross-section (0.125 in.) were prepared from the melt, using a split graphite mold. The copper used in these experiments was OFHC, which was subsequently twice vacuum-melted in graphite which had previously been thoroughly heated to eliminate volatile bonding agents. Unless these precautions were taken, the critical resolved shear stress of the copper varied greatly from the characteristic low value (~40–60 g/mm^2).

For the investigation of the size effect, a special graphite mold was made which allowed the growth of three square-sectioned crystals from a common source, the dimensions of the specimens being 0.250, 0.188, and 0.125 in. square; the length in each case was four in. Identically oriented crystals of different sizes were also grown in separate molds from parts of the same seed crystal.

Prior to deformation, the aluminum crystals were polished in an ethyl alcohol (900 ml) perchloric acid (100 ml) electrolyte with a voltage across the cell of 27. The copper crystals were polished in aqueous orthophosphoric acid (1000 g/l.) at a voltage of approximately 1.8.

The crystals were carefully mounted, using a jig designed to avoid accidental bending and to ensure axial alignment. The ends of each crystal were held in steel cups by using Woods metal for the copper

crystals, and a special aluminum solder for the aluminum crystals. The copper crystals were deformed primarily in a Polanyi-type tensile machine, while the aluminum crystals were strained in a Hounsfield tensometer which was adapted to carry out tests both at −196°C and at 200°C, in addition to deformation at room temperature.

3. EXPERIMENTAL RESULTS WITH ALUMINUM CRYSTALS

The microstructural features associated with easy glide were most readily studied on aluminum crystals. Furthermore, the fact that very long crystals could be prepared by the strain-anneal method made it easy to eliminate the orientation variable by using identical specimens, and the effect of crystal length could be studied within wide limits.

FIG. 1. Aluminum crystal 04B 4.4% elongation at room temperature. Optical micrograph ×250.

(a) *Correlation of Structural Changes with Stress-strain Curves*

The work confirmed earlier investigations in so far as the occurrence of easy glide depended markedly on the orientation of the crystal. Crystals in which more than one slip system were predicted to operate from the earliest stages of deformation, in particular crystals near [100] and [111] and on the boundary between these poles, gave no region of easy glide and showed marked strain hardening from the beginning of the deformation. Large bands of secondary slip were observed, but kink bands were absent.

Particular attention was paid to those crystals the orientation of which fell well within the stereographic triangle and which gave regions of easy glide. The deformation was interrupted at a point near the end of the easy-glide region and the crystals were examined

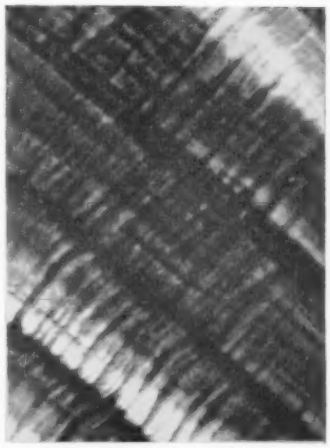

FIG. 2. Same as Fig. 1. X-ray micrograph ×20.

microscopically and by X-ray diffraction methods. A further examination was carried out at a later stage when the rate of hardening had increased considerably. It was established that both types of deformation band, bands of secondary slip, and kink bands were present during the region of easy glide. Figs. 1 and 2 show an optical micrograph and an X-ray micrograph from the same face of a crystal taken just after the end of easy glide (approx. 4.4% elongation); the latter reveals two sets of deformation bands, one parallel to the operative slip bands and the others normal to them. Optical examination did not show secondary slip in the regions of either type of deformation band. Little X-ray asterism was observed at this stage (Fig. 3).

After somewhat heavier deformations (~8–9% elongation) the stress-strain curve became parabolic and marked strain hardening had taken place. X-ray

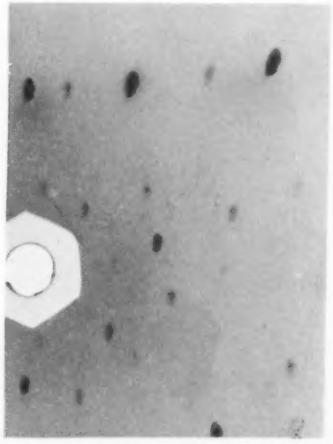

FIG. 3. Crystal 04B after 4.4% elongation. X-ray Laue photograph.

VOL. 4 1956

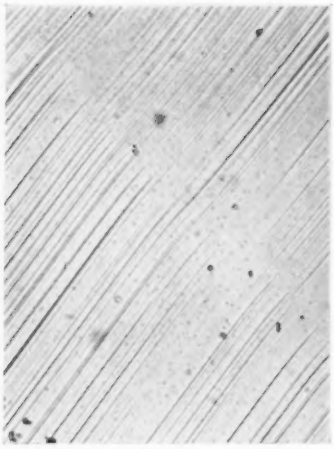

FIG. 4. Aluminum crystal 04B after 8.8% elongation at room temperature. Optical micrograph ×250.

micrographs confirmed that the crystals had become more heavily disoriented and that the major disorientations were associated with the kink bands rather than the bands of secondary slip. Fig. 5 is the X-ray micrograph after 8.8% elongation, which can be compared directly with Fig. 2 taken on the same crystal at the earlier stage. The X-ray asterisms were correspondingly more pronounced (Fig. 6; cf. Fig. 3). Microscopic examination did not reveal any marked evidence of slip other than on the primary system in crystals deformed at room temperature (Fig. 4) and −196°C, (Fig. 7); however, in crystals deformed at 200°C, the kink bands were more pronounced, and secondary slip was observed in them. The slip bands in these latter crystals were coarser and contained larger numbers of individual slip lamellae than those occurring after similar deformations at lower temperatures.

FIG. 5. Same as Fig. 4. X-ray micrograph ×20.

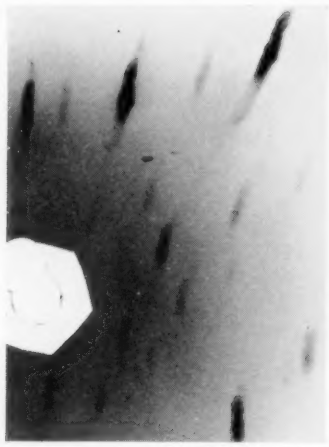

FIG. 6. Same as Fig. 4. X-ray Laue photograph.

(b) *Temperature Dependence of Easy Glide*

Crystals of identical orientation deformed at −196°C, room temperature, and 200°C, and were examined after approximately the same amount of deformation. The length of the easy-glide range increased as the temperature of testing fell; however, the rate of subsequent hardening increased with decreasing temperature. For example, crystals 18 a, b, and c (Fig. 10) showed this behavior quite clearly, the crystal deformed in liquid nitrogen giving an easy-glide range of approximately 10% shear strain.

For a given deformation, the extent of X-ray asterism increased with increasing temperature of test (Figs. 6 and 9). This was qualitatively correlated with the disorientations observed in the X-ray micrographs which resulted primarily from the formation of kink bands (Figs. 5 and 8). Microscopic observations showed clearly that the size and spacing of the kink

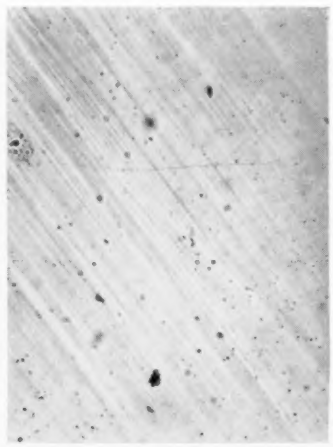

FIG. 7. Aluminum crystal 04A deformed to 8% elongation at −196°C. Optical micrograph ×250.

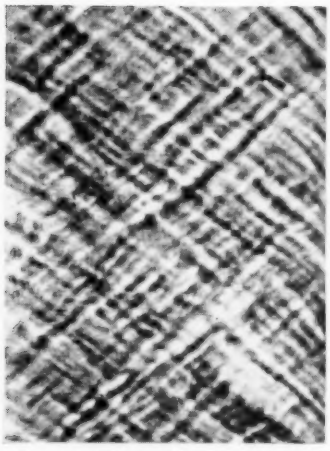

FIG. 8. Same as Fig. 7. X-ray micrograph ×20.

bands increased with the temperature. It seems that there is a correlation between the length of the easy-glide range and the disorientations introduced by the kink bands.

(c) *Influence of Specimen Length*

Two identically oriented crystals (17a, 17b), one 9 in. long, the other 3 in. long, which had received the same treatment, were deformed to the end of the easy-glide range. The load-extension curves are shown in Fig. 11. While the curves are not identical, the range of easy glide is similar in each case. An X-ray examination carried out after the easy-glide deformation was complete, revealed little difference in X-ray asterism between the two crystals. Furthermore, a survey of the length of the crystals revealed noticeable differences only within 1 mm of the grips.

X-ray micrographs revealed the presence of fine deformation bands throughout both crystals.

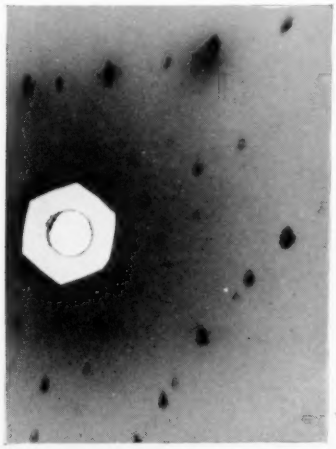

FIG. 9. Same as Fig. 7. X-ray Laue photograph.

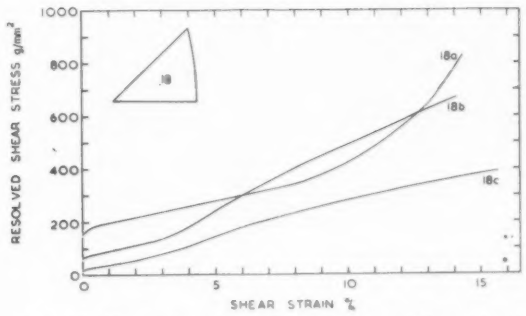

FIG. 10. Shear-stress/shear-strain curves of three identically oriented aluminum crystals. 18a, deformed at −196°C. 18b, deformed at room temperature. 18c, deformed at 200°C.

4. EXPERIMENTAL RESULTS WITH COPPER CRYSTALS

Rosi,[13] and Cupp and Chalmers[15] have published stress-strain curves on copper crystals of various orientations. Both the slope and length of the easy-glide part of the stress-strain curves vary with orientation. However, Rosi has shown that this part of the curve is associated with a constant increment of shear stress which is independent of crystal orientation. The present work, while confirming this observation, not only for copper but also dilute alloys, shows that variations in the easy-glide range can arise from the differences in the size and surface condition of the crystals tested.

(a) *Orientation Dependence of the Stress-strain Curve*

Fig. 12a shows the shear stress-shear strain curves for a number of copper crystals of different orientations (Fig. 12b), all of which would be expected to show linear hardening at the beginning of plastic deformation. These differ from Rosi's results in so far as the length of the easy-glide range is bigger by at least

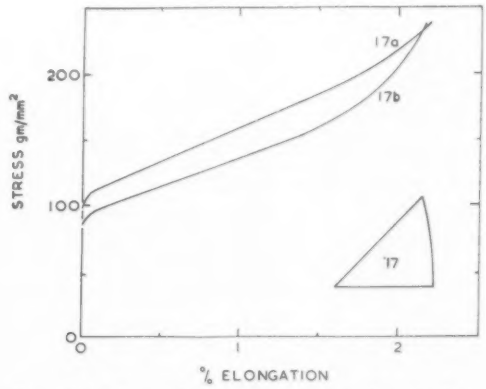

FIG. 11. Linear hardening of two identically oriented aluminum crystals of different lengths. 17a—3 in. long. 17b—9 in. long.

VOL. 4 1956

TABLE 1. Data on copper and copper-silver single crystals

Crystal	X_0	λ_0	τ_c (dev)	τ_c (ext)	σ_0 (ext)	$\sigma_0 - \tau_c$		σ_0/τ_c	
						dev.	ext.	dev.	ext.
Cu-49	63½°	34½°	64	86	142	78	56	2.22	1.65
Cu-50	56°	37°	58	58	138	80	80	2.38	2.38
Cu-51	56°	33½°	49	58	108	59	50	2.2	1.86
Cu-43	59°	35°	59	59	136	77	77	2.31	2.31
Cu-48	58°	37°	38	61	106	68	45	2.79	1.74
Cu-53	48°	42°	38	64	121	83	57	3.18	1.89
Cu-42	43°	49°	48	65	127	79	62	2.65	1.95
Cu-40	48°	43°	44	57	123	79	66	2.8	2.16
Cu-38	49°	41°	41	53	120	79	67	2.93	2.26
Cu-44	46°	46°	49	55	122	73	67	2.49	2.22
Cu-45	51°	39°	37	50	100	63	50	2.7	2
Cu-55	43°	48°	46	53	117	71	64	2.54	2.21
Cu-35	46°	49°	57	57	134	77	77	2.35	2.35
Cu-Ag alloys									
1B	47°	47°	595	595	1230	635	635		2.07
2C	48°	42°	232	232	485	253	253		2.09
3F	44°	50°	386	386	770	384	384		2.00

Note: In this table, X_0 is the angle between the specimen axis and the normal to the slip plane: λ_0 is the angle between the specimen axis and the slip direction; τ_c (dev) is the critical resolved shear stress determined by the first deviation from Hooke's law; τ_c (ext) is the critical resolved shear stress determined by extrapolation of the stress/strain curve to zero strain; σ_0 is the stress at which the extrapolated easy-glide range meets the extrapolation of the rapid-hardening part of the curve.

a factor of 2. However, they confirm that linear hardening ends at a value of the shear stress σ_0 such that $\sigma_0 - \tau_c$ is approximately constant, where τ_c is the critical resolved shear stress for glide. The essential results are tabulated in Table 1.

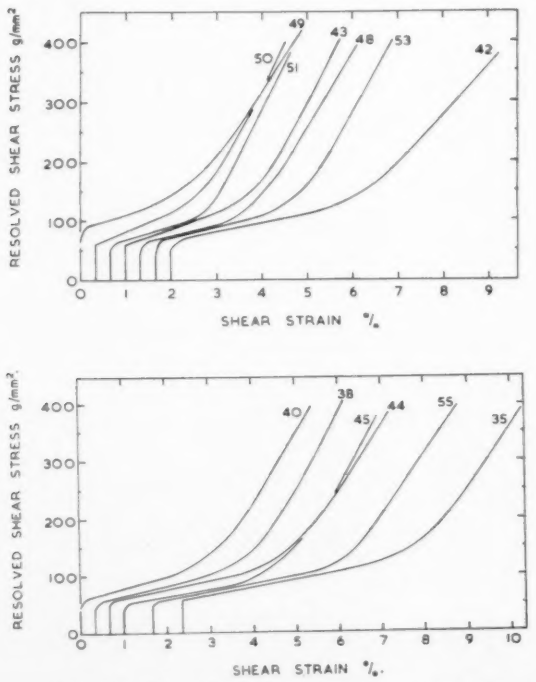

FIG. 12a. Shear-stress/shear-strain curves of copper crystals of various orientations.

The resolved critical shear stress for glide (τ_c) is not constant. The variation can in part be attributed to differences in purity of the crystals as grown, in part to structural differences due to mosaics, and in part to the difficulty of handling such fragile specimens. Added to this there is considerable uncertainty in determining τ_c precisely, as the curves change slope very gradually. Bearing these difficulties in mind, the degree of constancy of $\sigma_0 - \tau_c$ is quite surprising. The extent of easy glide is a maximum near [110] and decreases as the [100]-[111] boundary is approached.

(b) *Microstructure*

The crystals were electropolished prior to deformation, and many were examined under the microscope at various stages during the deformation.

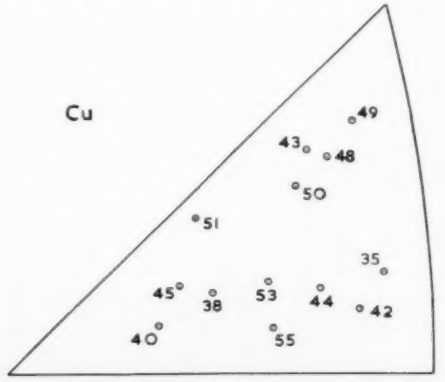

FIG. 12b. Orientations of copper crystals of Fig. 12a.

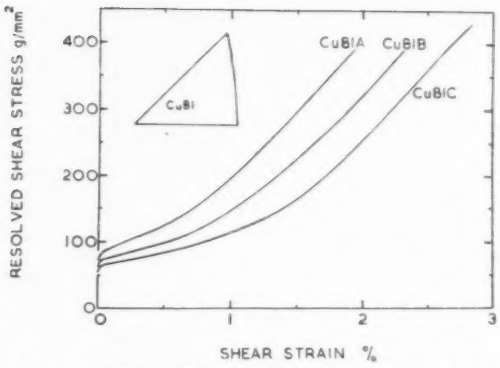

FIG. 13. Shear-stress/shear-strain curves of identically oriented copper crystals of different sizes. A, $\frac{3}{8}$ in. diam.; B, $\frac{1}{4}$ in. diam.; C, $\frac{3}{16}$ in. diam.

Slip on the predicted primary system occurred exclusively during the region of easy glide, but slip on secondary systems was detected in limited regions fairly soon after the end of easy glide. The first operative secondary plane was the cross-slip plane first identified by Maddin, Mathewson, and Hibbard;[2] however, at higher stresses the majority of the other {111} planes operate at least locally.

(c) *Crystal Size*

Comparison of the recent results[7, 13] on easy glide in copper, silver, and gold shows that there is a wide variation in the extent of linear hardening even with metals of comparable purity. As the various investigations have used different sizes and shapes of crystals, the existence of a size-effect was possible.

Copper crystals of three sizes $\frac{1}{8}$, $\frac{3}{16}$, and $\frac{1}{4}$ in. square of identical orientation were grown in a triple graphite mold, and each crystal was tested in a similar manner. Repeatedly it was found that the largest crystal gave the least easy glide; however, the smallest crystal did not always behave in the expected manner, due to the difficulty of removing it undamaged from the mold.

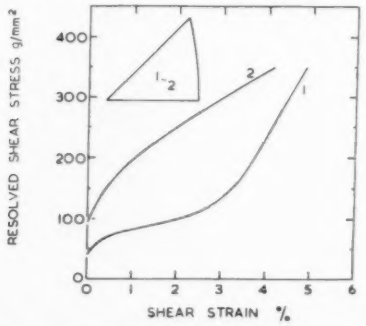

FIG. 14. Effect of surface coatings on the easy-glide range in two similarly oriented copper crystals
(1) unplated,
(2) nickel-chromium plated.

To overcome this trouble, three crystals of different sizes ($\frac{3}{16}$, $\frac{1}{4}$, and $\frac{3}{8}$ in. diam.) but of identical orientation were grown in separate molds from parts of the same seed crystal. The smallest crystal could be removed without damage from the single mold. Fig. 13 shows the shear stress-shear strain curves for three crystals of different sizes prepared in this way. It is clear that the amount of easy glide increases with decreasing crystal size. Furthermore, the easy-glide range ends at approximately the same resolved shear stress.

(d) *Electroplating of Crystals*

There is already some evidence that surface coatings will reduce the extent of easy glide, presumably by causing dislocation pile-ups below the surface. Andrade and Henderson[7] found that an oxide film on silver crystals would markedly reduce the linear part of the stress-strain curve.

A copper crystal was plated with 10,000 Å of Ni, but this did not eliminate easy glide, and slip appeared on the surface as in the case of unplated crystals. However, the further addition of 10,000 Å of chromium did result in the elimination of the linear hardening region (Fig. 14).

(e) *Alloying*

Particular attention has been paid to dilute alloys of silver in copper, but experiments give similar results for other alloying elements such as gold. Fig. 15 shows typical shear stress-shear strain curves for crystals of three alloys containing approximately 0.3, 0.6, and 1.0% by weight of silver.

The critical resolved shear stresses fall into three groups characterized by the average values 240, 450, and 600 g/mm². Furthermore, the stress-strain curves also fall into three families, the greatest range of easy glide being shown by the crystals with the highest silver content. Closer examination of the curves reveals that, as in the case of pure copper, the end of easy glide occurs at approximately twice the critical resolved shear stress for glide.

In the curves of Fig. 15 the slopes of the linear range are very similar. This arises from the fact that crystals fairly closely oriented to each other were chosen so that the effect of the alloying element could be more readily determined. The slope is clearly more a function of orientation than of composition.

Metallographic observations revealed that the end of easy glide in all crystals examined was associated with the localized occurrence of unpredicted secondary slip. Some secondary slip was observed prior to the end of easy glide, but this was usually associated with

VOL. 4 1956

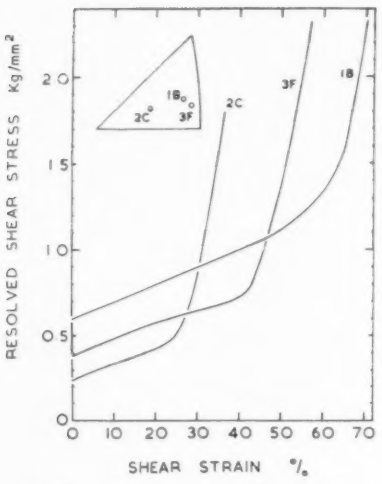

FIG. 15. Typical shear-stress/shear-strain curves of three dilute copper silver alloy crystals.
2C—0.3
3F—0.6
1B—1.0
} weight per cent silver.

surface defects such as pits or scratches, which would be expected to act as stress-raisers. The first operative secondary slip plane was again found to be the cross-slip plane, but in most crystals all the octahedral planes were found to operate locally sooner or later.

5. DISCUSSION

The general viewpoint on easy glide has been crystallized by Cottrell,[16] who distinguishes between laminar flow resulting in a linear stress-strain curve and the subsequent turbulent flow resulting in a more or less parabolic hardening curve. Koehler[22] has interpreted the linear region as that in which exhaustion of the Frank-Read sources takes place, while he postulates that the more rapid hardening is due to the interaction of dislocation pile-ups. However, it is widely agreed, and the present experiments confirm, that the end of easy glide is in fact characterized by the occurrence of unpredicted slip on other octahedral planes. The possibility of sporadic unpredicted slip within the region of easy glide cannot nevertheless be excluded. The transition from laminar to turbulent flow can be understood in terms of the interaction of dislocations on different planes which give rise to increased hardening by virtue of the generation of jogs and subsequent interstitial and vacancy formation. However, an important question yet to be answered is: What decides when this transition takes place? The effect of such variables as temperature, orientation, purity, size of specimen, and effect of surface films on the extent of easy glide must all be explained.

As the secondary slip operates at macroscopic resolved shear stresses below those which would be expected to produce slip on the secondary planes, stress concentrators must exist locally to raise the shear stress sufficiently to cause glide. Pile-ups of dislocations seem to be the most likely stress concentrators in a deformed single crystal.

Stroh[17] has shown that the stress at a point $(r\theta)$ from the head of a dislocation pile-up is:

$$\frac{Pij}{\sigma_0}\left(\frac{r}{n}\right)^{\frac{1}{2}} = f(\theta)$$

where Pij is the local stress, σ_0 the applied shear stress, n the number of dislocations in the pile-up, and r the distance from it measured in units of

$$\frac{\mu b}{4\pi(1-\nu)\sigma_0}.$$

$f(\theta)$ determines which plane is the first to operate in the secondary system.

A Frank-Read source on any system near a pile-up will operate when the local stress Pij reaches a critical value $\mu b/l$, which is approximately τ_c the critical shear stress, so the above expression becomes:

$$\frac{\tau_c}{\sigma_0}\left(\frac{r}{n}\right)^{\frac{1}{2}} = K \qquad (1)$$

The distribution of dislocation sources in the crystal will determine the distance (L) of the source from the head of the pile-up.

Now

$$r = \frac{L}{\dfrac{\mu b}{4\pi(1-\nu)\sigma_0}} = K_2\sigma_0 \qquad (2)$$

Eshelby, Frank, and Nabarro[18] have shown that

$$n = \frac{\sigma_0\pi\ d(1-\nu)}{\mu b} = K_3\sigma_0 \qquad (3)$$

where d is the length of the pile-up.

Substituting values of r and n in (1).

$$\frac{\tau_c}{\sigma_0} = \text{constant}$$

This means that secondary slip starts and consequently easy glide ends when the resolved shear stress on the primary system reaches a given multiple of the critical resolved shear stress τ_c. In the present experiments, the ratio has been found to be approximately 2 both for pure copper and the dilute alloys with silver. The longer easy-glide ranges in the alloys can be explained simply as necessary for the local stress to build up to

a value approaching that of the critical resolved shear stress so markedly increased by alloying. Other factors being equal, the present theory indicates that the critical resolved shear stress τ_c determines the extent of easy glide.

As Rosi has pointed out, the results on the effect of impurities on easy glide have not been unambiguous. When a finely dispersed second phase is present, the pile-ups would occur in the vicinity of the small particles and at an early stage of the deformation, thus leading to rapid hardening. Carlsen and Honeycombe[19] have shown in aluminum 3.3% copper single crystals that linear hardening only occurs in the super-saturated solid solution, and ordinary parabolic hardening occurs when a finely dispersed second phase is present.

As the temperature of deformation is lowered, τ_c increases, so again an increase in the extent of easy glide would be expected. This is confirmed by the experiments of Andrade and Henderson[7] and those described above. Lowering the temperature also reduces the amount of slip per slip band. At elevated temperatures, the slip bands will be coarser and the stresses around the pile-ups should lead earlier to the occurrence of secondary slip. The above experiments on aluminum have confirmed this view: secondary slip is observed in kink bands at a much earlier stage at 200°C than during deformation at —196°C.

Having established that easy glide ends when a given stress is reached, an explanation of the orientation dependence of easy glide can be sought in evaluating the slope σ/a of the stress-strain curve. This is a minimum for orientations near [110], and increases as the [100]-[111] boundary is approached, i.e. as the tension axis rotates towards the primary slip direction. The salient feature of this transition is that the slip plane becomes elongated, so that the length of the slip direction increases. If the view of Mott[20] is followed that, during easy glide, dislocations pass out of the crystal, then the change in slope of the stress-strain curve with orientation is now explained, since it would be more difficult for dislocations to escape if the slip path is increased. This is well supported by the present experiments, which show that large crystals harden more rapidly than small crystals of identical orientation. Furthermore, plotting σ/a against the length of the slip direction for copper crystals of different orientation does, in fact, give an approximately linear correlation (Fig. 16).

The effect of surface films is also evidence in support of the above argument, since such films would tend to retain dislocations within the crystal, thereby reducing the easy-glide range. These effects would be expected

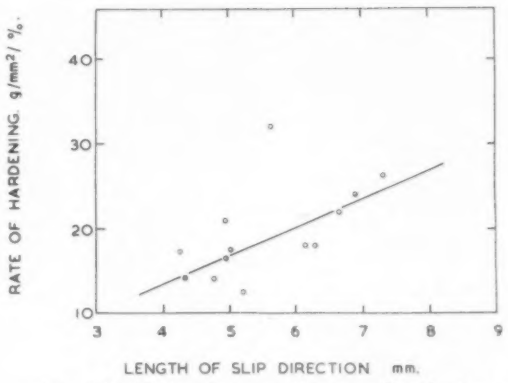

FIG. 16. Relation between the rate of hardening σ/a and the length of the slip direction.

to be particularly pronounced with small crystals; this is, in fact, what Andrade and Henderson found.

One final point which needs some discussion is the question of where the pile-ups occur in the deformed crystals. In aluminum the obvious sites of secondary slip are primarily the deformation bands, as the above experiments have indicated. These bands are less pronounced, but closer spaced at lower temperatures; this means that secondary slip will occur at a later stage, for the critical pile-ups will require more deformation to form them. At higher temperatures (200°C) the distortions in the bands are heavier for a given deformation, and secondary slip occurs at a correspondingly earlier stage.

Of course, it could be postulated that kink bands are initiated by local secondary slip and, as they develop, cause further secondary slip. However, it is felt that deformation bands must play a significant role, as it is only when pile-ups are spaced at fairly large distances that the specimen size could be expected to make a substantial difference.

It is doubtful whether the above considerations apply to the behavior of certain highly alloyed crystals, e.g. 70/30 brass, although the early observations of easy glide were made on this material. Here, the linear region of the curve is almost parallel to the strain axis and the lack of hardening appears to be related to the occurrence of a yield phenomenon. Piercy, Cahn, and Cottrell[21] have recently shown that in brass crystals, slip propagates through the specimen in the linear zone. Furthermore, slip in brass crystals is much coarser and more grouped than in crystals of copper and its dilute alloys.

ACKNOWLEDGMENTS

One of us (G. G.) is indebted to the Department for Scientific and Industrial Research for a studentship. We gratefully acknowledge the helpful comments of our colleagues at all stages of the work.

VOL. 4 1956

REFERENCES

1. F. von Göler and G. Sachs *Z. Physik.* **55,** 581 (1929).
2. R. Maddin, C. H. Mathewson, and W. R. Hibbard *Trans. Amer. Inst. Min. Met. Eng.* **175,** 86 (1948); *ibid.* **185,** 527 (1950).
3. G. Masing *Lehrbuch der allgemeinen Metallkunde* Berlin, Springer-Verlag (1950).
4. G. Masing and J. Raffelsiefer *Z. Metallkunde* **41,** 65 (1950).
5. F. D. Rosi and C. H. Mathewson *Trans. Amer. Inst. Min. Met. Eng.* **188,** 1159 (1950).
6. K. Lücke and H. Lange *Z. Metallkunde* **43,** 55 (1952).
7. E. N. da C. Andrade and C. Henderson *Phil. Trans.* **A244,** 177 (1951).
8. B. Jaoul and C. Crussard *Comp. Rend.* **234,** 700 (1952).
9. R. W. Cahn *J. Inst. Metals* **79,** 448 (1951).
10. R. K. Chen and C. H. Mathewson *J. Metals* **3,** 653 (1951).
11. R. W. K. Honeycombe *J. Inst. Metals* **80,** 49 (1951).
12. E. A. Calnan *Acta. Cryst.* **5,** 557 (1952).
13. F. D. Rosi *J. Metals* **6,** 1009 (1954).
14. J. Sawkill and R. W. K. Honeycombe *Acta Met.* **2,** 854 (1954).
15. C. R. Cupp and B. Chalmers *Acta Met.* **2,** 803 (1954).
16. A. H. Cottrell *Prog. in Metal Physics* **4,** 205 (1953).
17. A. N. Stroh *Proc. Roy. Soc.* **A223,** 404 (1954).
18. J. D. Eshelby, F. C. Frank, and F. R. N. Nabarro *Phil. Mag.* **42,** 351 (1951).
19. K. M. Carlsen and R. W. K. Honeycombe *J. Inst. Metals* **83,** 449 (1955).
20. N. F. Mott *Phil. Mag.* **44,** 742 (1953).
21. G. R. Piercy, R. W. Cahn, and A. H. Cottrell *Acta Met.* **3,** 331 (1955).
22. J. S. Koehler *Phys. Rev.* **86,** 52 (1952).

KINETICS OF PRECIPITATION IN SMALL LEAD-TIN SPHERES*

W. DeSORBO AND D. TURNBULL†

The precipitation reaction in very small crystal spheres of Pb-Sn alloy that may be freer than large specimens of grosser structural imperfections, has been followed by a calorimetric technique. In all cases studied the precipitation energy evolved isothermally is 1/10 to 1/400 of the values evolved by bulk-polycrystalline specimens having the same composition. After cold working and a short homogenization treatment, the precipitation energy evolved by the spheres is several orders of magnitude larger than the energy released in the as-cast and homogenized state or after prolonged homogenization.

For polycrystalline samples it is shown that the time τ required for the isothermal half-completion of the precipitation is a function of the homogenization time and temperature and the deformation history prior to homogenization. These results demonstrate the decisive role of gross imperfections in some cellular precipitation processes.

CINETIQUE DE PRECIPITATION DANS DES PETITES SPHERES PLOMB-ETAIN

La réaction de précipitation dans de très petites sphères cristallines en alliage Pb-Sn qui peuvent contenir moins d'imperfections structurales importantes que des échantillons plus larges, a été suivie au moyen d'une technique calorimétrique.

Dans tous les cas étudiés, l'énergie de précipitation développée d'une façon isotherme est 1/10 jusqu'à 1/400 des valeurs développées par des échantillons polycristallins massifs ayant la même composition.

Après écrouissage et un court traitement d'homogénéisation, l'énergie de précipitation développée par les sphères est de plusieurs ordres de grandeur supérieure à celle libérée dans l'état coulé et homogénéisé ou après un long traitement d'homogénéisation.

Pour des échantillons polycristallins, il est démontré que le temps τ nécessaire pour la demi-précipitation isotherme est une fonction du temps, de la température d'homogénéisation ainsi que de l'hérédité de déformation avant l'homogénéisation. Ces résultats démontrent le rôle décisif des grandes imperfections dans quelques processus de précipitation cellulaire.

AUSSCHEIDUNGSKINETIK IN KLEINEN BLEI-ZINN-KUGELN

Mit einem kalorimetrischen Verfahren wurde die Ausscheidung in sehr kleinen Kristallkugeln einer Pb-Sn-Legierung, die weniger grobe Fehlstellen enthalten dürften als grosse Kristalle, verfolgt. In allen untersuchten Fällen beträgt die isotherm entwickelte Ausscheidungswärme 1/10 bis 1/400 der Werte von grossen Vielkristallproben gleicher Zusammensetzung. Nach Kaltbearbeitung und einer kurzen Homogenisierungsbehandlung ist die von den Kugeln entwickelte Ausscheidungswärme um mehrere Grössenordnungen grösser als die freiwerdende Energie im homogenisierten Gusszustand oder nach ausgedehntem Homogenisieren.

An polykristallinen Proben wird gezeigt, dass die Zeit τ, in der die isotherme Ausscheidung zur Hälfte abläuft, eine Funktion der Homogenisierungsdauer und -temperatur sowie der Verformungsgeschichte vor der Homogenisierung ist. Durch diese Ergebnisse wird die entscheidende Rolle, die grobe Fehlstellen bei einigen "zellartigen" Ausscheidungen (cellular precipitation) spielen, nachgewiesen.

VOL. 4 1956

INTRODUCTION

It has been shown[1] that the precipitation of tin (β) from bulk polycrystalline α-lead-tin solid solutions is accomplished by the growth of cells ("cellular precipitation") consisting of tin lamellae interspersed in a depleted α solid solution. Tiedema and Burgers[2] observed that tin precipitation occurred in the same way in large single crystals of α-lead-tin. A reorientation of the solid solution accompanies the growth of cells in all cases. It was established[1] that all of the cell nuclei form at structural singularities (usually —though not always—in the vicinity of grain boundaries) in the earliest stages of precipitation. Also, there is strong evidence[3, 3a] that the tin drains from solution by diffusion along the cell boundary, which sweeps the solid solution in cell growth, rather than by lattice diffusion. Therefore, it was suggested[3] that the rate of cellular precipitation should be much less in structurally perfect single crystals than in ordinary solid-solution specimens. Although structurally-perfect α-lead-tin crystals were not available, small cast spheres of the alloy should be comparatively free of grosser imperfections such as grain boundaries and inclusions. Therefore, we have investigated, with a calorimetric technique, the precipitation of tin from very small spherical crystals of α-lead-tin alloy. Also, the same calorimetic method has been used to investigate the influence of homogenization time and temperature on precipitation in ordinary bulk specimens.

* Presented in part before the American Physical Society Meeting, Baltimore, Maryland, March 17–19, 1955 [*Phys. Rev.* **98**, 1554 (1955)]. Received December 5, 1955.

† General Electric Research Laboratory, Schenectady, New York

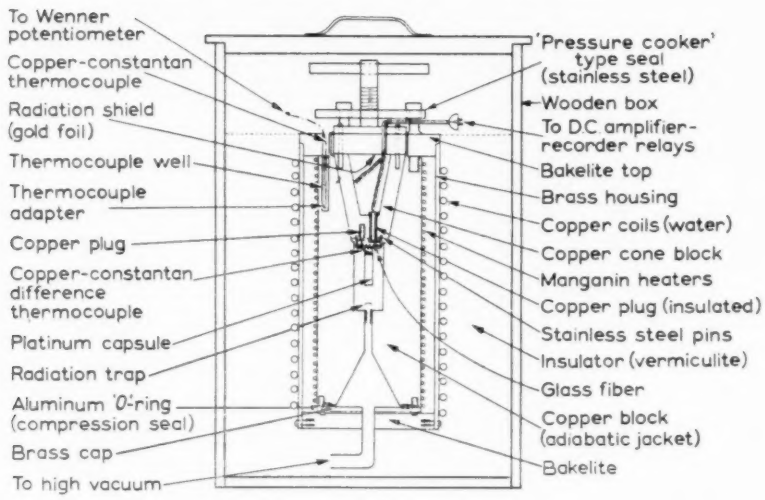

(a)

FIG. 1(a). The adiabatic micro-calorimeter.

EXPERIMENTAL

Calorimeter

The adiabatic micro-calorimeter used in this investigation has been described earlier by Overhauser[4] (see Fig. 1a). The unit has a fast adiabatic jacket, making it useful for the measurement of precipitation energies arising from solid-phase transformations that have incubation times longer than 2 to 5 min.

The calorimeter container used in this work consisted of a short length (about 1 in.) of platinum tubing (0.187 in. o.d. $\times$ 0.010 or 0.006 in. wall-thickness obtained from the American Platinum Works). Lead-tin alloy samples, usually weighing approximately 1 g or less, were sealed in the container by cold welding both ends of the platinum tube.* The second and final cold-weld was accomplished after the sample in the platinum tubing had been degassed for approximately an hour at 100°C under a vacuum of better than 10^{-5} mm Hg. Just prior to this final second weld, there was introduced approximately 1 mm of helium exchange gas which, during the experiment, helped to serve as an effective heat-exchange medium. A copper-constantan difference thermocouple junction was soldered† to one end of the cold-weld of the platinum container. The diameter of each thermocouple wire was 0.002 in., and each segment was about 4 in. in length (coil) between the platinum container and bottom of the copper cone. A small platinum wire hook, soldered† to this same end of the container (i.e. top end where the difference thermocouple junction was also located) provided a means for suspending the calorimeter from the bottom of the copper cone. The platinum hook hung from a short length of small glass fiber stretched between two metal screws attached to the bottom of the copper cone (see Fig. 1a).

Adiabatic conditions better than 10^{-3} °C between the platinum calorimeter capsule and the copper cone (and the adiabatic jacket were maintained semi-automatically throughout the experiment.‡ That is, as the alloy sample released energy, which raised the temperature of the platinum container and sample, the temperature of the adiabatic jacket and copper cone was increased externally at the same rate such that a temperature differential dT maintained between the platinum container and the environment temperature was less than 10^{-3} °C at all times during an experiment. The temperature rise ΔT (of the calorimeter containing the sample and of the copper block, and cone) measured from the start of the precipitation reaction to the end of the transformation was measured by means of a strain-free copper-constantan thermocouple (described by Giauque *et al.*[5] The μV readings of this thermocouple were read with a high-precision Wenner potentiometer and recorded at time-intervals of a minute during the more rapid stage

* By this technique we have been able to homogenize the sample for days without any oxidation or other contamination of the alloy; also any number of experiments could be tried or repeated on the same sample.

† The solder was the same composition as the alloy sample inside the calorimeter container. In some cases the junction was spot-welded to the platinum capsule.

‡ This condition of adiabaticity was readily accomplished by having the small μV response (of the difference thermocouple due to the small dT existing between the platinum container and copper cone) amplified by a d.c. amplifier (Liston-Becker, Model 14). This amplified signal was then fed to a Brown recorder which, being equipped with a rotary mercury switch, controlled the "on" and "off" time of the heating circuit to the block heaters.

of the transformation. The galvanometer-telescope system was arranged to provide a sensitivity of approximately 200 mm/μV. The temperature rise ΔT due to the precipitation energy evolved could be measured to better than 10^{-3} °C.

Preparation of Alloys

The alloy samples were made from the same stock and in the same manner as those prepared earlier by Turnbull and Treaftis.[1] All samples reported were analyzed for tin to ± 1 part in 100. The powder samples consisted of small spheres of the alloy prepared from wire specimens by a metallizing gun technique. In order to minimize any effects of possible surface oxidation that might arise during this processing, the powder used in some experiments was heated to the molten state and then dropped through a dry-hydrogen atmosphere, solidified, and then sealed in the platinum container.*

Homogenization

The design of the calorimeter provided a unique and simple way for homogenizing the sample while the latter was held in position in the apparatus (see Fig. 1b). The copper block holding the sample container was placed in a hollow copper cone (spun from $\frac{1}{16}$-in. copper). The whole assembly was clamped in place directly over a cylindrical nichrome-wound furnace such that the suspended platinum container was inside the heating chamber of the furnace. The copper block (in position over the furnace) was kept at a constant temperature by means of water-cooled copper coils (brazed to the outer edge of the cone). The same water (thermostated) that circulated through these copper coils also circulated through the coils wound around the outside of the adiabatic jacket of the calorimeter, thereby helping to maintain essentially identical temperatures between this latter unit and the spun-copper cone.

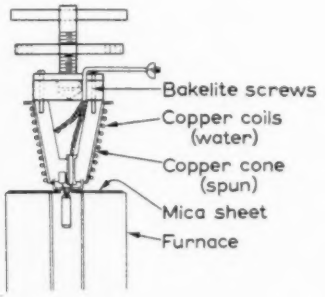

(b)

FIG. 1(b). Homogenization of sample.

The samples were homogenized in most cases at approximately 50° higher than the equilibrium homogenization temperatures for a specified time, ranging from 15 min to several days. This homogenization temperature was lower in some experiments dealing with cold-worked samples and higher in some experiments where long annealing times were tried.

Procedure

The precipitation reaction in the alloy was initiated by removing the copper cone from the water-cooled jacket (above the furnace) and immediately quenching the platinum capsule (only) into dry-ethyl alcohol followed by a direct quench into dry-ethyl ether. A "Jones" electrical plug connector fixed permanently in place at the top of the cone (accommodating the two thermocouple leads) was connected to the cable going to the amplifier and potentiometer recorder. When the recorder indicated that the platinum capsule was slightly higher in temperature than the cone, the latter was assembled and clamped vacuum-tight by a compression seal (see Fig. 1a) to the adiabatic jacket. Evacuation of the apparatus could then be started. The temperature-time measurements of the block were started after adiabatic conditions of 10^{-3} °C or better were attained, and also after a vacuum of better than 10^{-5} mm Hg was evident. This entire operation of removing the copper cone (and platinum calorimeter from the furnace) to the time of the first temperature-time measurement would take on the average from 2–5 min. Maintaining the temperature of the massive cone and large calorimeter block almost identical during the homogenization of the sample, as mentioned above, was important in permitting a study of the reaction at such a short time after its initiation (quenching time).

The characteristics of the calorimeter are such that the energy evolved by the sample is, to a good approximation, directly proportional to the rise in temperature ΔT of the calorimeter block (and cone). The proportionality factor is represented by the product of the sum of the mean heat capacities† and the product of the sum of the number of gram-atoms of each component making up the calorimeter container and sample.‡ For reactions where the incubation times are greater

* For further details on this heat-treating process of purifying powder samples, see Cech and Turnbull.[6]

† Sources of the various heat-capacity data used are listed under ref. 7.

‡ The Kopp-Neumann rule has been assumed in the calculations of the heat capacity of these alloys containing relatively small amounts of tin. The weight of the fine copper and constantan leads was taken as one half of the total weight. This correction amounted to less than 0.1% of the final result.

VOL. 4 1956

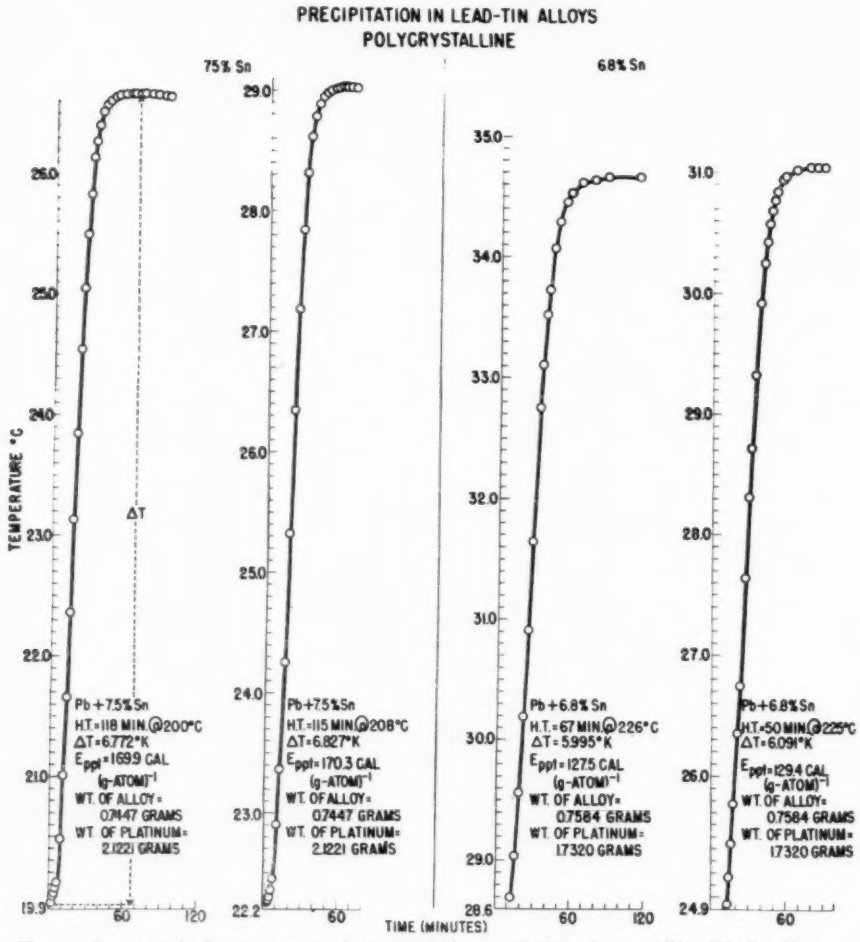

FIG. 2. Some typical temperature-time curves for two bulk-polycrystalline Pb-Sn alloys.

than 2–5 min, the adiabatic rise in temperature, ΔT, (of the platinum container plus the sample) due to the energy released during the transformation can be determined to a precision of better than 10^{-3} °C. For the weight of the alloy samples used (approximately 1 g or less) and for the weight of the small platinum capsule used (less than 2.5 g), the maximum ΔT encountered in this work amounted to about 7–8°C (for bulk polycrystalline samples).*

RESULTS AND DISCUSSION

A. Powder Specimens

1. *Preliminary results on bulk specimens.* Prior to the experiments on the lead-tin alloy powdered specimens, several studies on the precipitation energies of some bulk polycrystalline Pb-Sn alloys were carried out. Typical temperature-time curves during the precipitation reaction for polycrystalline Pb-Sn alloy are presented in Fig. 2. Results of two determinations are presented for each alloy shown. In each case the samples were homogenized at 200–225°C prior to quenching. A comparison of the results showing energy release for each of the two determinations of a given sample represents the approximate precision of the apparatus. The results obtained for the 7.5% and 6.8% (by weight) alloys are in good agreement with those reported earlier by Nyström[8] (see Fig. 3); especially when one considers the various factors (see below) that can influence this value. Nyström's results have been taken from smooth curves drawn through his data presented in ref. 8. (A "Gerber" variable scale facilitated reading the data from the small graphs.)

2. *Results on powders of various compositions.* The calorimetric data and other pertinent information of each experiment for the various Pb-Sn alloys

* In one study on a bulk polycrystalline sample (7.5% Sn a platinum capsule was used having roughly half the wall thickness (0.006 in.). In this case ΔT came out to be ~11°C (see Table 3, sample C).

TABLE 1. Precipitation energy in lead-tin alloy powders

Run No.		Homogenization		T_i°K	T_f°K	E cal (g-atom)$^{-1}$
		Time (min)	Temp. °C			
	(a) 5.4% Sn, $X_0 = 0.091$					
1	Slds → $H_1 \rightarrow Q$	963	200	293.14	293.51	8.8
2	$H_2 \rightarrow Q$	990	204	295.81	296.03	5.0
3	C.W. → $H_1 \rightarrow Q$	32	218	296.04	297.53	36.5
4	$H_2 \rightarrow Q$	65	212	294.51	294.93	10.1
5	$H_3 \rightarrow Q$	164	207	293.22	293.35	2.9
6	$H_4 \rightarrow Q$	1000	208	290.40	290.43	0.3
7	$H \rightarrow Q \rightarrow$ C.W.	948	210	295.56	296.10	13.0
8	$H \rightarrow W \rightarrow Q$	992	206	295.86	297.56	41.5
Nyström's[8] value for energy of precipitation (E_N) (bulk-polycrystalline Pb-Sn 5.4% Sn) $\cong$ 135 cal (g-atom)$^{-1}$ (extrapolated) $T_m = 295$°K						
	(b) 7.1% Sn, $X_0 = 0.118$					
1	Slds → $H_1 \rightarrow Q$	70	190	295.77	296.45	15.6
2	C.W. → $H_1 \rightarrow Q$	202	186	296.66	299.45	63.8
3	$H_2 \rightarrow Q$	74	206	296.72	298.88	49.6
4	$H_3 \rightarrow Q$	2477	200	295.69	297.11	32.5
Energy of precipitation (E_N) (bulk-polycrystalline Pb-Sn—7.1% Sn) $\cong$ 140 cal (g-atom)$^{-1}$ (interpolated) $T_m = 297$°K						
1	C.W. → $H_1 \rightarrow Q$	24	208	277.36	278.21	8.0
2	$H_2 \rightarrow Q$	122	200	275.96	276.70	5.1
3	$H_3 \rightarrow Q$	49	200	278.32	279.13	5.2
4	C.W. → $H_1 \rightarrow Q$	94	200	274.89	275.78	10.5
Energy of precipitation (E_N) (bulk-polycrystalline Pb-Sn—7.1% Sn) $\cong$ 160 cal (g-atom)$^{-1}$ (interpolated) $T_m = 277$°K						
	(c) 7.7% Sn, $X_0 = 0.127$					
1	Slds → $H_1 \rightarrow Q$	3926	200	289.33	289.62	4.5
2	$H_2 \rightarrow Q$	1259	200	296.23	296.50	4.3
3	$H \rightarrow W \rightarrow Q$	987	200	295.49	298.04	40.2
4	$H_1 \rightarrow Q$	104	220	293.18	294.23	16.5
5	$H_2 \rightarrow Q$	1037	210	295.46	296.05	9.5
6	$H \rightarrow W \rightarrow Q$	1103	202	293.30	296.70	53.7
7	$H_1 \rightarrow Q$	1000	205	292.50	294.70	34.7
8	$H_2 \rightarrow Q$	5421	198	293.83	294.94	17.5
9	$H_3 \rightarrow Q$	987	230	293.13	293.21	1.2
Energy of precipitation (E_N) (bulk-polycrystalline Pb-Sn—7.7% Sn) $\cong$ 150 cal (g-atom)$^{-1}$ (interpolated) $T_m = 294$°K						

Slds → H → Q = Sample solidified, sealed in calorimeter capsule, homogenized, and then quenched.
H → Q = After completion of previous precipitation reaction, the sealed capsule containing sample was re-homogenized and then quenched.
C.W. → H → Q = After completion of previous precipitation reaction, the sealed capsule containing sample was cold-worked by hammering, re-homogenized, and then quenched.
H → Q → C.W. = After completion of previous precipitation reaction, the sealed capsule containing sample was re-homogenized, quenched, and then cold worked by hammering.
H → W → Q = After completion of previous precipitation reaction, the sealed capsule containing sample was re-homogenized, worked by hammering, and then quenched.

examined are summarized in Tables 1, 2, and 3. In the first column are presented the experimental run number for a given Pb-Sn alloy carried out successively upon the completion of the reaction of the previous run. The second column gives information on the sequence used in homogenizing, quenching, and cold-working the specimen. The symbols and their meanings used to describe the procedure are listed as footnotes at the bottom of Table 1. The same symbols are used in the subsequent tables. The third column gives the pertinent information on the duration (minutes) of the homogenization treatment as well as the temperature maintained during this heat treatment. "T_i°K" represents the temperature of the calorimeter block (and platinum container) at the time t_i in minutes after the sample had been quenched ($t = 0$). Time t_i was taken as that time when the proper adiabatic conditions ($T_{\text{block}} - T_{\text{container}} < 1 \times 10^{-3}$ °C) and a vacuum of better than 10^{-5} mm of Hg were first attained. In every experiment, t_i varied from 2 to 5 min, with $t = 0$ referring to quenching time. T_f°K represents the temperature of the calorimeter block (and sample) at the time (t) when the time-rate of change of temperature (dT/dt) was approximately equal to the time-rate of change of temperature that might be caused by the presence of background "noise" and/or slight thermals due to the difference thermocouple. This dT/dt amounted to less than 10^{-3} °C/min. Energy (E) released by the alloy in cal (g-atom)$^{-1}$ is tabulated in the last column.

VOL. 4 1956

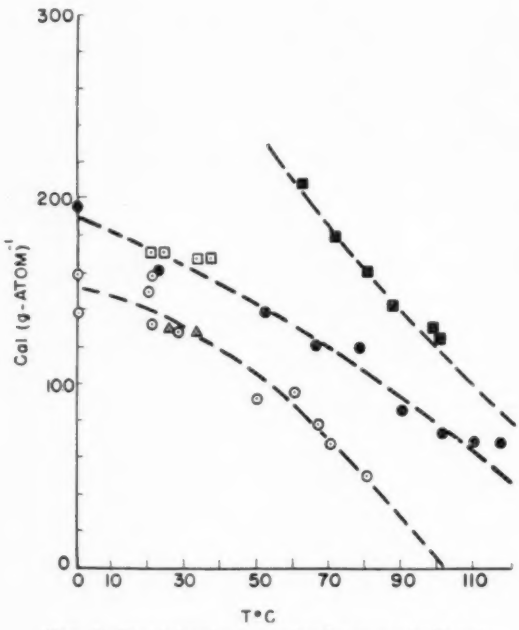

FIG. 3. Precipitation energies for some bulk-polycrystalline Pb-Sn alloys.
Nyström's data.
■ 12% Sn
● 9% Sn
○ 6% Sn
This research.
△ 6.8% Sn
⊡ 7.5% Sn

In Table 1(a) are presented the results obtained in studying the precipitation reaction of a lead-tin alloy powder specimen containing 5.4% (weight) Sn. This specimen consisted of small divided (spherical) particles whose dimensions were less than 40 microns.* Prior to sealing this alloy in the platinum container, the specimen had been purified by dropping the particles through a hydrogen atmosphere at elevated temperatures (as described above). The results for the first run No. 1 are those obtained for the sample after it was solidified and after the physical geometry of the specimen was reduced to small spheres (see above). The second run represents the results after the precipitation reaction had been completed in run 1. The sample (sealed in the platinum container) was annealed for 990 min at 204°C. In the third successive experiment, the capsule containing the powder was cold worked by hammering,† then homogenized at 218°C for 32 min. It is probable that the sample recrystallizes before or during homogenization, so that the effect of the treatment is to introduce grain boundaries. We shall refer to these specimens as C.W. $+ H_n$, where n denotes the number of homogenization treatments following cold work. The evolution of energy during precipitation in specimen C.W. $+ H_1$ has increased severalfold over that obtained prior to cold-working (run 2). The remaining runs (4–8) repeat the energy determinations by successively annealing the sample (4–6) and then modifying the procedure (7–8) by working the sample; in one case immediately after quenching and in another just prior to quenching. In run No. 8, the specimen has been homogenized, worked by hammering, and then quenched. The energy of precipitation following this procedure was the highest observed in the small-particle precipitation. The minimum precipitation energy released is that obtained in run 6. After homogenizing for 1000 min at 200°C, the precipitation energy amounts to only 0.3 cal (g-atom)$^{-1}$, a value that is approximately 1/400 of the value obtained for the evolution of energy in a bulk-polycrystalline sample of the same concentration (Nyström's data, ref. cited).

Temperature-time curves of some typical runs for this 5.4% Sn powder sample are presented in Fig. 4. Shown in the same graph is a typical temperature vs. time curve obtained on an empty capsule. These very small values of dT/dt, not due to the precipitation reaction, were corrected for in evaluating E, the energy of precipitation. This correction amounted to less than 1% of the total energy (depending on the absolute value of E).

For the above series of runs the precipitation energy evolved by the spheres cold worked‡ and homogenized once is several orders of magnitude larger than the energy released prior to the deformation. Also, significant is that for each successive homogenization treatment after the first cold-work, the energies evolved decrease, although the time-interval between the quenching time and the time of the first measurements was kept approximately the same. The precipitation energies released by the powder for each of the eight runs are all significantly smaller than the energy values reported for the polycrystalline alloy[8] having the same composition.

Precipitation energies obtained for a powdered Pb-Sn alloy (containing 7.1% Sn) under various conditions of times of homogenization, cold work, etc.,

* Microscopic examination established that all but a small fraction of the particles were single crystals. The particle diameters ranged from 10 to 40 microns. This work was done by Miss D. Kontoleon.

† A separate experiment carried out on a cold-worked empty platinum capsule indicated that the energy of cold work released at the temperatures of interest in this report was negligible when compared with the energy of precipitation of the alloys.

‡ In this series of experiments, as well as in the subsequent ones, no attempt has been made to evaluate the "amount" of cold work imparted to a given sample.

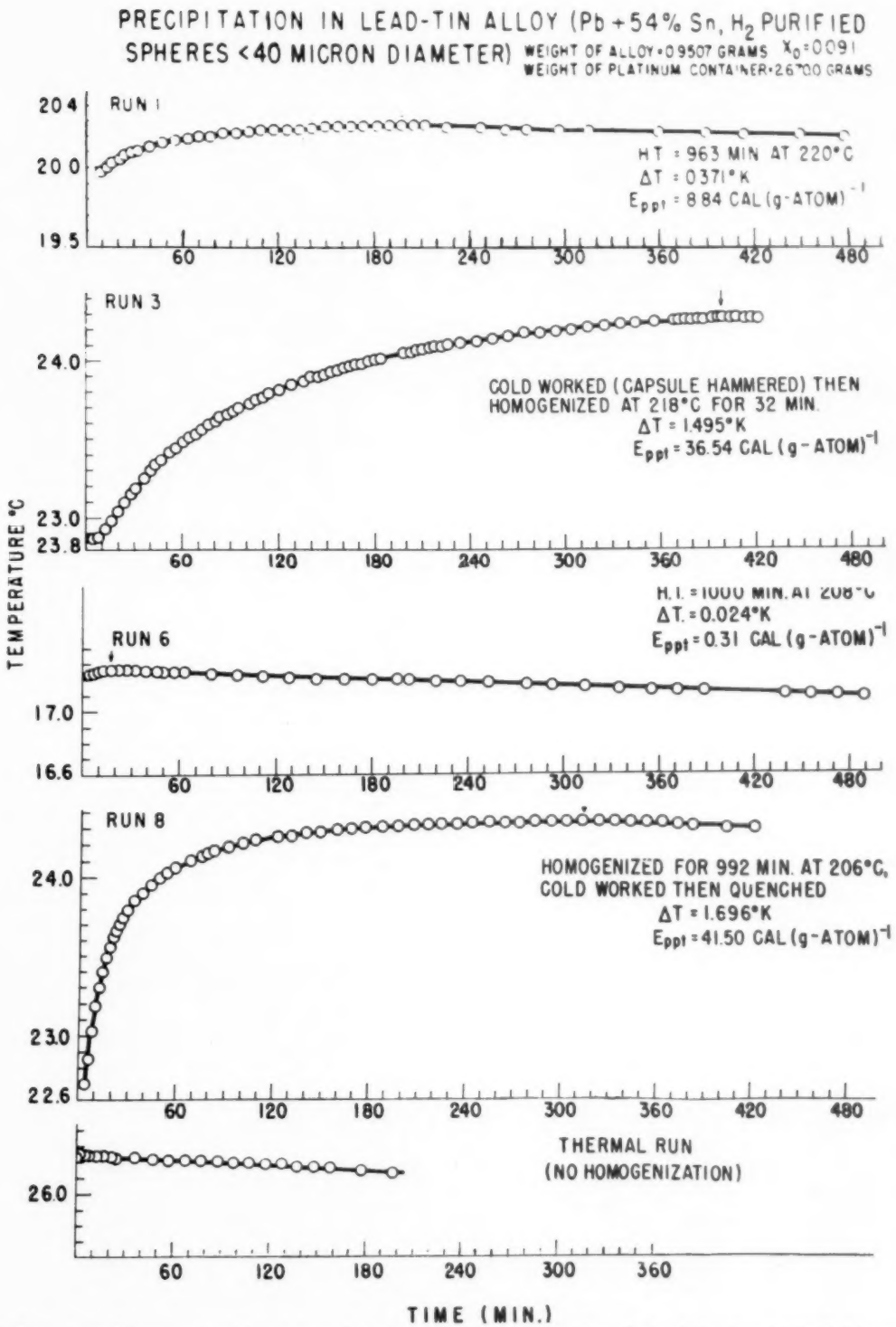
PRECIPITATION IN LEAD-TIN ALLOY (Pb + 5.4% Sn, H_2 PURIFIED
SPHERES < 40 MICRON DIAMETER) WEIGHT OF ALLOY = 0.9507 GRAMS X_0 = 0.091
WEIGHT OF PLATINUM CONTAINER = 26.700 GRAMS
RUN 1
HT = 963 MIN AT 220°C
ΔT = 0.371°K
E_{ppt} = 8.84 CAL (g-ATOM)$^{-1}$
RUN 3
COLD WORKED (CAPSULE HAMMERED) THEN
HOMOGENIZED AT 218°C FOR 32 MIN.
ΔT = 1.495°K
E_{ppt} = 36.54 CAL (g-ATOM)$^{-1}$
H.T. = 1000 MIN. AT 208°C
ΔT = 0.024°K
E_{ppt} = 0.31 CAL (g-ATOM)$^{-1}$
RUN 6
RUN 8
HOMOGENIZED FOR 992 MIN. AT 206°C,
COLD WORKED THEN QUENCHED
ΔT = 1.696°K
E_{ppt} = 41.50 CAL (g-ATOM)$^{-1}$
THERMAL RUN
(NO HOMOGENIZATION)
TEMPERATURE °C
TIME (MIN.)

FIG. 4. Some typical temperature-time curves during the precipitation reaction of a lead-tin alloy (5.4% Sn) (powder).

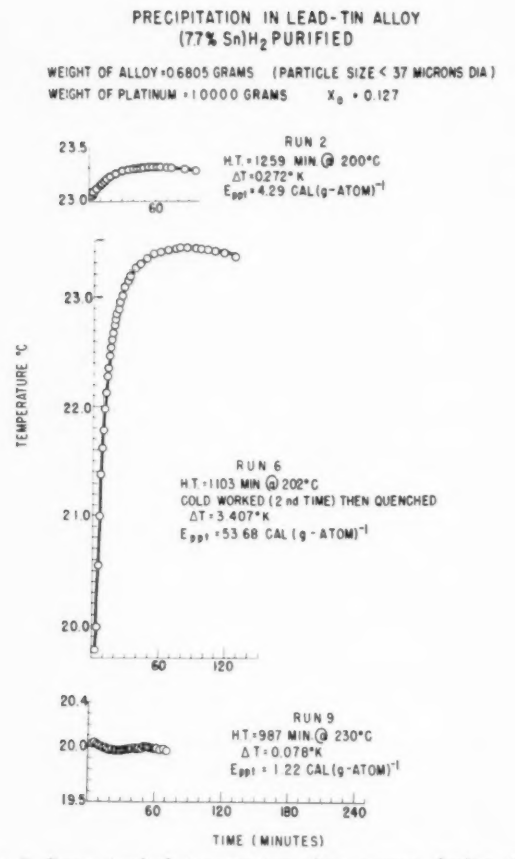
PRECIPITATION IN LEAD-TIN ALLOY
(7.7% Sn) H_2 PURIFIED
WEIGHT OF ALLOY = 0.6805 GRAMS (PARTICLE SIZE < 37 MICRONS DIA.)
WEIGHT OF PLATINUM = 1.0000 GRAMS X_0 = 0.127
RUN 2
H.T. = 1259 MIN. @ 200°C
ΔT = 0.272° K
E_{ppt} = 4.29 CAL (g-ATOM)$^{-1}$
RUN 6
H.T. = 1103 MIN @ 202°C
COLD WORKED (2 nd TIME) THEN QUENCHED
ΔT = 3.407° K
E_{ppt} = 53.68 CAL (g-ATOM)$^{-1}$
RUN 9
H.T. = 987 MIN. @ 230°C
ΔT = 0.076° K
E_{ppt} = 1.22 CAL (g-ATOM)$^{-1}$
TEMPERATURE °C
TIME (MINUTES)

FIG. 5. Some typical temperature-time curves during the precipitation reaction of a lead-tin alloy (7.7% Sn) (powder).

are tabulated in Table 1(b). The effect of cold work, followed by homogenization, on the precipitation energy of a second sample of the same alloy at lower temperatures is also shown in the same table. In both studies, cold-working the sample before homogenization enhances the value of the precipitation energy released, while successive homogenization tends to decrease this value.

A summary of the precipitation energies and other pertinent information of a Pb-Sn powdered alloy sample containing 7.7% Sn is presented in Table 1(c). Three typical temperature-time graphs for this specimen are shown in Fig. 5. In the study of this alloy, a total of nine successive experiments under various conditions of homogenization and cold work, etc., were carried out to determine the evolution of energy during the transformation of the alloy to the α and β phases. Two complete cycles are presented, long-annealing times, cold work, annealing, second cold work, followed by more annealing. Again, as in the two above samples, annealing the alloy decreases the value of the precipitation energy, while deforming the sample either prior to or after homogenizing increases this evolution of heat. In all cases these transformation energies for the powder specimen were less than the values reported by Nyström for the corresponding alloys in the bulk polycrystalline state. Deforming the particles increases the energy of precipitation by an appreciable amount. However, this value is still significantly smaller than the precipitation energy for the bulk-polycrystalline sample. This fact is illustrated in Fig. 6, where temperature-time curves are compared for a polycrystalline sample (7.5% Sn) and a powder sample (7.7% Sn). Two experiments were carried out on the powder sample; in the first, the sample had been cold worked prior to the transformation, while in the second, the sample had been annealed for a considerable time before being studied.

3. *Effect of coalescence of powders.* In order to investigate the possibility that the very low precipitation rate in powders is due to some unforseen composition effect, we have measured the rate of precipitation in a bulk-polycrystalline specimen made by *coalescence** of a powder on which we had rate measurements. The comparisons of the rates of precipitation and energy released in the two types of specimens (containing 7.7 weight per cent of tin) are shown in Fig. 7 and Table 2. The total precipitation energy released by the coalesced powder is about the same as that obtained for an ordinary bulk-specimen of the same composition and about thirty-seven times greater than the energy release of the powder before coalescence. Thus, it seems very unlikely that the results on powders can be explained by some unknown chemical difference from bulk-specimens. Rather, these results strengthen the hypothesis that the rate of precipitation in powders is very small because they are relatively free of the grain boundaries and inclusions that normally lead to nucleation in bulk-specimens.

4. *X-ray diffraction results.* In the calorimetric technique, the sample usually has been at the reaction temperature 2 to 5 min before the first measurement can be made. It is, of course, possible that most of the precipitation in the powders occurred in this early period. Although this possibility seemed very remote, because a negligible amount of tin has precipitated after 2 to 5 min in bulk-specimens having the compositions of the powder, it can only be eliminated by some property measurement on the powders, which

* The sample was melted in a quartz tube in a dry-hydrogen atmosphere. The particles coalesced only upon prolonged heating at a dull-red heat.

VOL. 4 1956

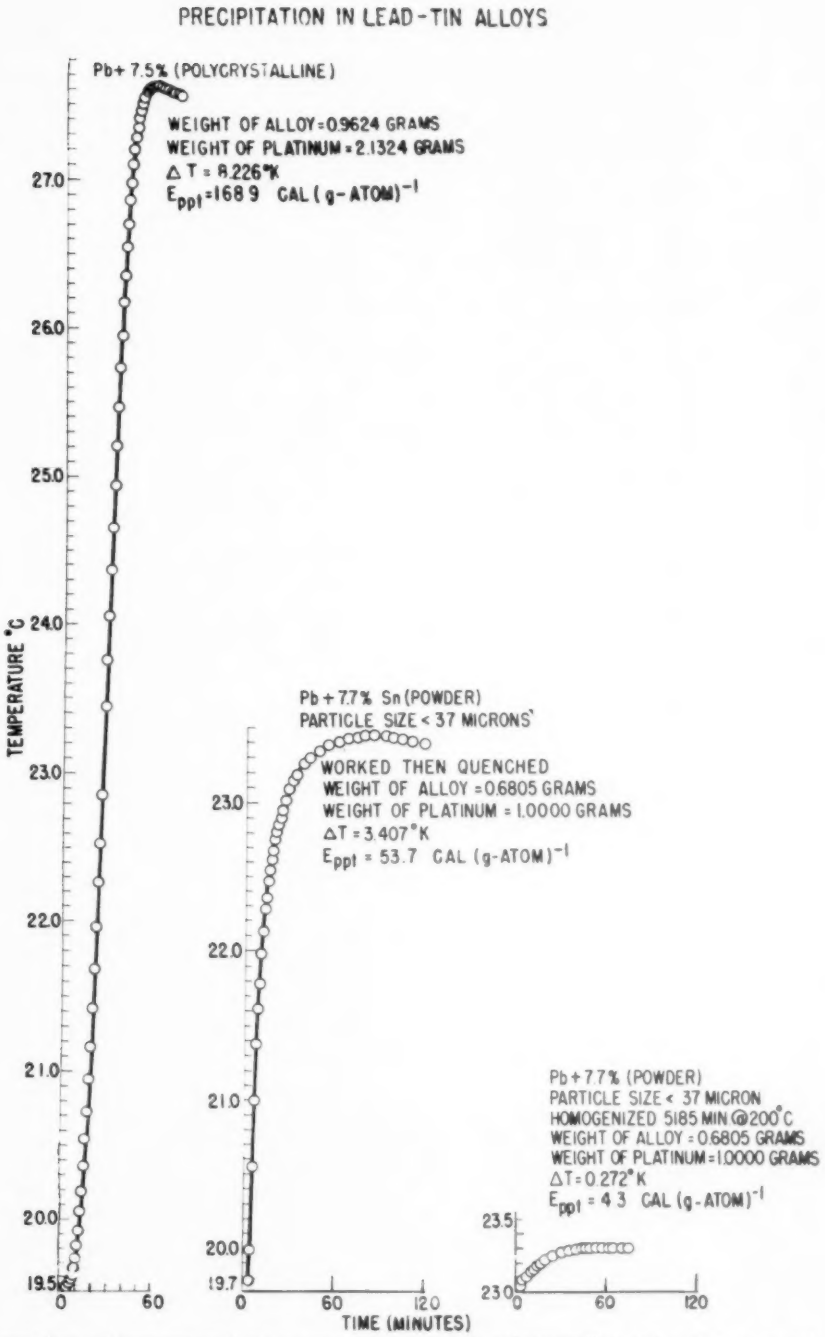

FIG. 6. A comparison of temperature-time curves between a bulk-polycrystalline and a powder sample of Pb-Sn.

TABLE 2. Precipitation energies in lead-tin alloy powder (7.7% Sn) before and after coalescing

Run No.		Homogenization		T_i°K	T_f°K	E cal (g-atom)$^{-1}$
		Time (min)	Temp. °C			
		(Before coalescing)				
1	Slds → H_1 → Q	34	174	300.80	301.48	8.9
2	H_2 → Q	34	180	301.54	301.89	4.6
		(After coalescing)				
1	Coalesced → H_1 → Q	32	180	299.45	311.37	172.6
2	H_2 → Q	1260	210	299.23	311.50	169.0

indicates that the tin is still in solution after the calorimetric measurement. Therefore, X-ray diffraction patterns were obtained on a powder sample A (7.7 weight per cent tin) that released a negligible amount of energy in the calorimeter and on an identical sample $A_{c.w.}$, that had been worked at room temperature in order to induce precipitation.

The weights of the specimens were identical and a constant amount of copper powder was added to each for calibration and lattice-parameter measurement. Each sample was exposed to X-rays for a 16-h period.* The intensities of comparable copper lines on the Debye-Scherrer patterns of the two specimens were identical within the observational error. The pattern for the cold-worked powder $A_{c.w.}$ showed a strong (211) tin line, but this line was barely detectable on the pattern for sample A. Further evidence that the tin remained in solution in sample A was obtained from lattice-parameter measurements. a_0 for A was 4.929 Å compared with $a_0 = 4.940$ Å for $A_{c.w.}$ and $a_0 = 4.9506$ Å for pure lead. If the lattice parameter varies linearly with tin content these observations are consistent with the interpretation that a negligible amount of tin had precipitated from sample A and about 55% of the thermodynamic excess of tin had precipitated from specimen $A_{c.w.}$. The amount of tin precipitated from the worked powder is in fair agreement with that (ca. 60%) deduced from earlier kinetic measurements, precipitated during the "fast" reaction.[1]

Thus, the X-ray diffraction measurements seem to establish quite conclusively that all but a negligible part of the tin-content of the unworked powder was in solid solution after the calorimetric measurements were completed.

5. *The kinetic law.* The kinetics of precipitation have been described[1] by a kinetic law $X = f(t)$, where X is the fraction of the sample precipitated isothermally in time t. It was found that the kinetic law for the "fast" reaction in bulk specimens is:

$$X = 1 - e^{-bt^n} \tag{1}$$

where b is a temperature-dependent constant and n was approximately 3.0 for all temperatures and concentrations investigated.

Following Nyström,[8] we shall assume that X_t is directly proportional to the total energy released at time t. That is:

$$X_t = \frac{T_t - T_0}{T_f - T_0} \tag{2}$$

where T_0 is the temperature at the beginning of the reaction (time is measured from the instant of quenching)

T_f = final temperature,

T_t = temperature at time t.

It is presumed that the small but definite energy released by the powder was due to precipitation in the small fraction of the particles that may have contained grain boundaries or inclusions. The apparent fraction of precipitation was calculated for the powder samples, using equation (2). The dependence of X, so calculated, on time is shown for a number of runs in Fig. 8. There seems to be no systematic and easily interpreted relation between X and t. If the results are described by equation (1), n varies from 0.8 to 2.0 for the various runs.

6. *Concluding remarks about the powder results.* In all of the above-mentioned studies, then, the values of the precipitation energy evolved isothermally by the lead-tin alloys in powder form (that are freer of grosser imperfections) seem to be decidedly smaller, by factors ranging from about 1/10 to 1/400 of the transformation energies, than the values obtained for the bulk-polycrystalline specimens having the same composition. After some grain boundaries are introduced into the particles, by working (hammering)

* This work was done by Mrs. A. S. Cooper.

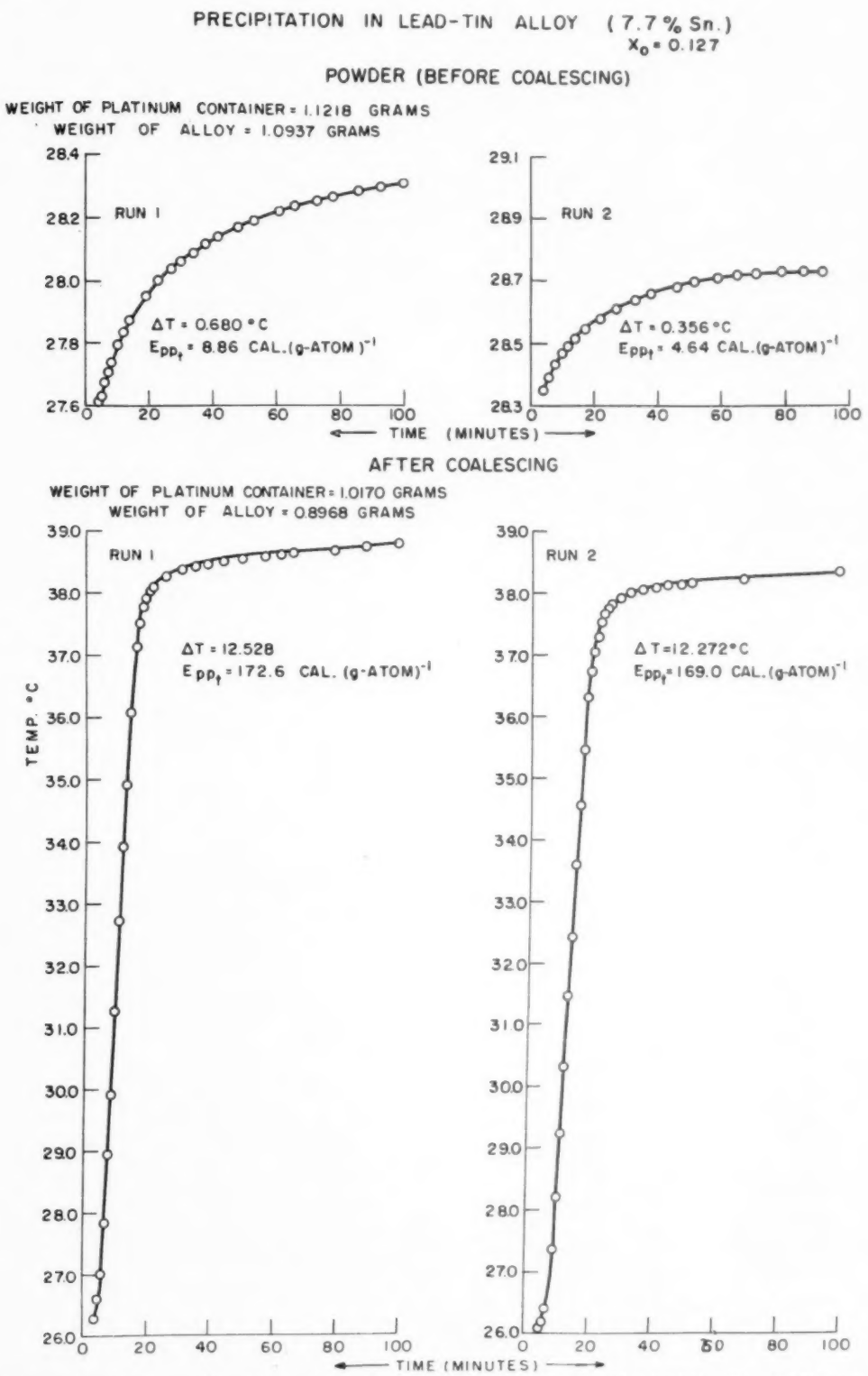

FIG. 7. A comparison of temperature-time curves during precipitation reaction of a lead-tin alloy (7.7%) powder both *before* and after coalescing.

VOL. 4 1956

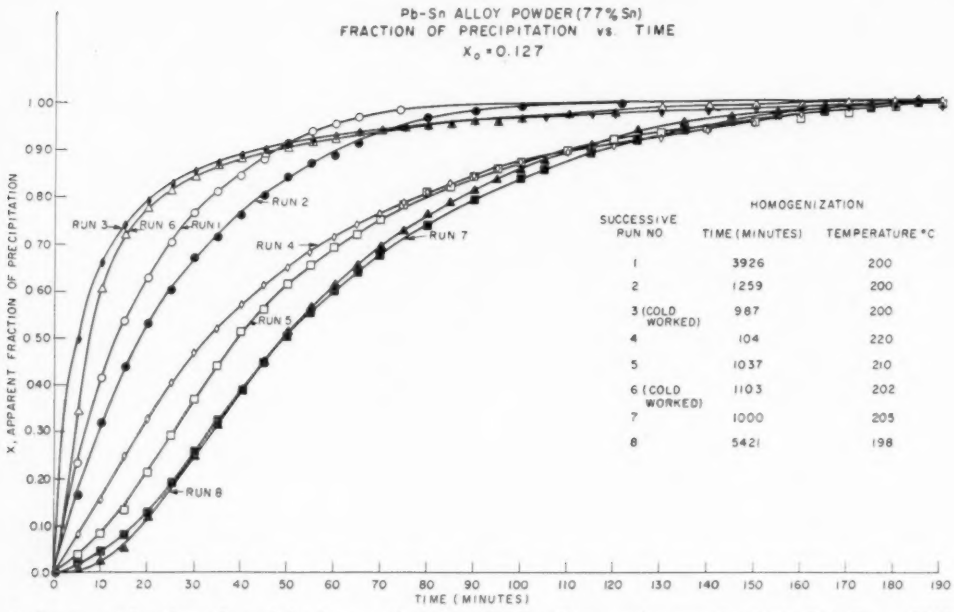

FIG. 8. Apparent fraction of precipitation vs. time for a Pb-Sn alloy powder sample (7.7% Sn), $T_{av} = 294°K$.

and recrystallizing (in the homogenization treatment), the energy values are significantly increased. However, in none of these samples were precipitation energies as large as those evolved by the same sample in the bulk-polycrystalline state. In considering even the qualitative aspects of this comparison, it should be pointed out that (a) the method of cold-working the powder was not an efficient one, (i.e. in all probability not all the particles became deformed, since we cold worked the sample by hammering the platinum wall of the container); (b) many of the grain boundaries produced by recrystallization annealed out during the homogenization treatment (especially in cases where we cold worked the capsule prior to the heat treatment). In general, for a given alloy powder, the precipitation energies would be greater if the sample were cold worked immediately *after* being homogenized rather than before. Also, the rates of precipitation of the reaction would be greater while the "half life," τ, would be smaller for the former sequence of operations (see below). In cases where the sample was "heavily" worked *after* homogenization, the energy of transformation was still at most one-half to one-third of the value obtained for the same composition of bulk-polycrystalline alloy.

B. *Bulk-polycrystalline Specimens of Pb-Sn Alloy*

1. *The precipitation energy.* An investigation was made to determine the effect of homogenization time and temperature on the rate of precipitation in a bulk-alloy containing 7.5 weight per cent (atom fraction = 0.124) tin. The experimental conditions and the total energy E evolved in each experiment on three different experiments are summarized in Table 3. In general, the E values are fairly constant and agree fairly well with Nyström's results. However, there are some minor trends. Thus, E appears to decrease very slightly after each homogenization. Also, E is definitely larger (by 7 to 10%) in the first experiment after the specimen has been worked and recrystallized.

2. *The kinetic law.* $X = f(t)$, for the various runs, was calculated, using equation (2). The relationships are shown in Fig. 9. Of course, the experiments are not strictly isothermal. However, the temperature coefficient of the precipitation rate is not large (see reference 1) for the temperature range used; therefore we tested the agreement of the data with equation (1). We found that the data were described by (1) within experimental error, and the constants b and n are given in Table 3. In general, $n \cong 3$ in good agreement with Nyström's[8] calorimetric and Turnbull and Treaftis's[1] resistometric results. However, n appeared to be significantly larger than 3 (ca: 3.5) whenever the specimen had been worked at the homogenization temperature just before quenching.

3. *Effect of homogenization time and temperature on precipitation rate.* Since the results are described fairly well by equation (1), with n approximately 3,

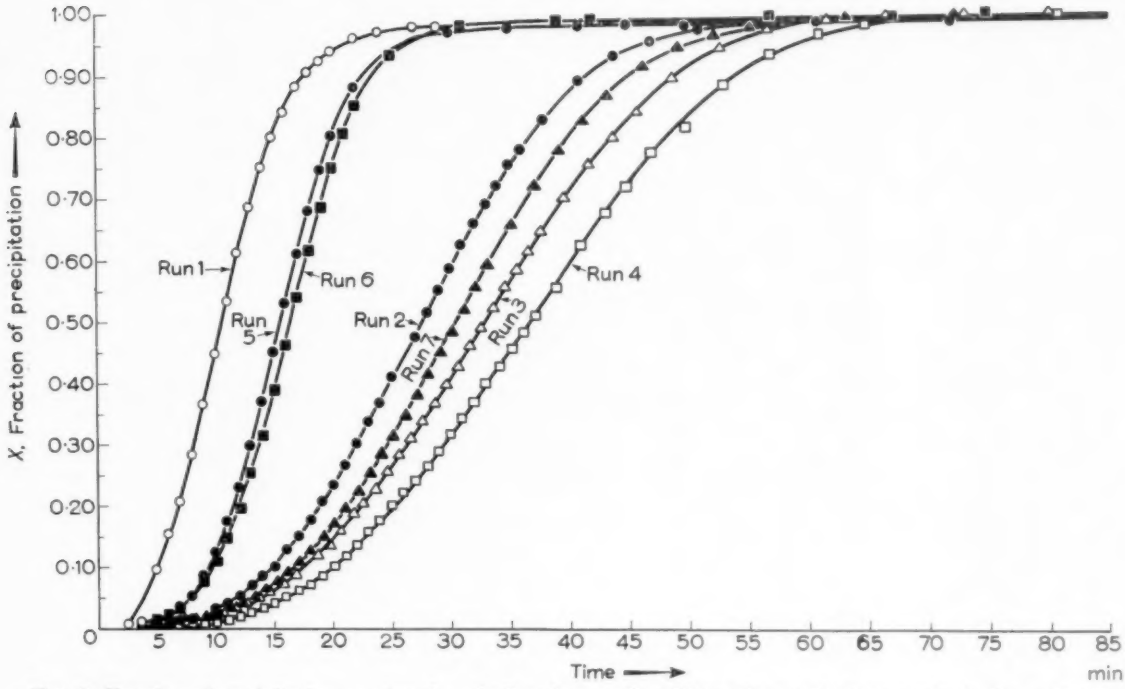

FIG. 9. Fraction of precipitation vs. time for a bulk polycrystalline Pb-Sn alloy (7.5% Sn) sample *A*, $T_{av} = 296°K$.

Successive run no.	Homogenization Time (min)	Homogenization Temperature °C
1	64	203
2	998	245
3	8240	242
4	2437	244
5 (cold worked)	32	180
6	64	175
7	999	245

the reciprocal of the time $\tau_{1/2}$ for half-completion of the precipitation is directly proportional to the precipitation rate (see reference 1) at any constant fraction of precipitation. The $\tau_{1/2}$ values found in the various experiments are also listed in Table 3. It is observed that $\tau_{1/2}$ *increases markedly with increasing homogenization time and temperature*. Thus, $\tau_{1/2}$ is increased by $3\frac{1}{2}$ times in sample *A* by homogenizing it for nearly 200 h at 240–245°C. However, $\tau_{1/2}$ is immediately decreased by a factor greater than 2 when the specimen is worked at the homogenization temperature just before quenching.

These results are consistent with the idea that some of the crystal imperfections that initiate nucleation are annealed out of the specimen by prolonged heating at high temperatures. More specifically, since nuclei form preferentially at grain boundaries, the decrease in specific grain boundary area that might be effected by the annealing would account for the observations. Then working the specimen either during or before homogenization leads to recrystallization which refines the grain size and hence increases the number of potential nucleation sites. Thus, it appears that prolonged annealing of a bulk-specimen can decrease the number N of nuclei by a factor of 10 or more, since $1/\tau_{1/2}$ varies as $N^{1/3}$.[1]

This variation of $\tau_{1/2}$ with specimen history (i.e. grain-boundary area) supports the explanation of Turnbull and Treaftis[1] for the differences between their precipitation rates and those of Borelius *et al.*[9] for the same composition and temperature. Our results on samples in the "Slds → H → Q" state, where the homogenization time and temperature is not large, agree with those of Borelius *et al.* However, the values of $\tau_{1/2}$ for a specimen homogenized more than an hour at temperatures 200–220°C are in agreement with the results of Turnbull and Treaftis; and for very long annealing times ($t > 1000$ min) at temperatures $> 225°C$, $\tau_{1/2}$ was substantially larger than obtained by Turnbull and Treaftis.

A plot of $\tau_{1/2}$ vs. log t_H (where t_H represents *total* homogenization time) is presented in Fig. 10. In run 1 the sample was in the "Slds → H → Q" state. In each successive run 2 and 3, the sample was homogenized and then quenched; while in run 4 the sample was homogenized, worked, and then quenched. In run 5

VOL. 4 1956

TABLE 3. Precipitation energy in lead-tin alloy (Pb + 7.5% Sn, polycrystalline) $X_0 = 0.124$

Run No.		Homogenization		T_i°K	T_f°K	E cal (g-atom)$^{-1}$	n	$-\log b$	$\tau_{1/2}$ (min)
		Time (min)	Temp.						
				Sample A					
1	Slds → H_1 → Q	64	203	289.54	297.82	169.6	2.52	2.75	10.4
2	H_2 → Q	988	245	292.71	300.93	168 9	2.97	4.60	27.7
3	H_3 → Q	8240	242	297.95	305.96	164.9	2.93	4.61	32.9
4	H_4 → Q	2437	244	291.12	299.23	166.4	3.05	4.96	36.9
5	H → W → Q	32	180	290.38	299.49	181.3	3.69	4.59	16.0
6	H_1 → Q	64	175	292.86	301.77	177.4	3.54	4.49	16.3
7	H_2 → Q	999	245	288.28	296.79	169.1	3.09	4.76	30.1
	E_N (bulk polycrystalline) ≅ 145 cal (g-atom)$^{-1}$, T_m = 296°K (interpolated) (ref. 8)								
				Sample B					
1	H_3 → Q*	118	200	293.10	299.88	169.9	3.00	3.88	17.5
2	H_4 → Q	130	208	295.42	302.25	170.3	2.88	4.85	18.8
3	H_5 → Q	143	210	292.49	299.23	168.9	3.10	4.31	21.5
4	C.W. → H_1 → Q	81	200	288.14	295.34	178.3	3.29	4.28	20.8
5	H_2 → Q	3996	200	291.32	298.21	171.9	2.92	4.29	27.1
	E_N (bulk polycrystalline) ≅ 145 cal (g-atom)$^{-1}$, T_m = 295°K (interpolated) (ref. 8)								
				Sample C					
1	Slds → H_1 → Q	107	208	294.87	306.34	165.3	3.05	3.30	11.0
2	H_2 → Q	1146	200	301.15	312.49	164.0	2.91	3.79	18.0
3	H_3 → Q	14437	197	298.59	309.94	163.8	3.13	4.50	24 5
4	C.W. → H_1 → Q	31	185	290.21	302.84	181.6	3.57	4.67	18.0
5	H_2 → Q	2489	248	295.00	306.77	169.5	2.75	3.83	21.9
	E_N (bulk polycrystalline) ≅ 135 cal (g-atom)$^{-1}$, T_m = 302°K (interpolated) (ref. 8)								

* Sample had been previously homogenized after solidification.

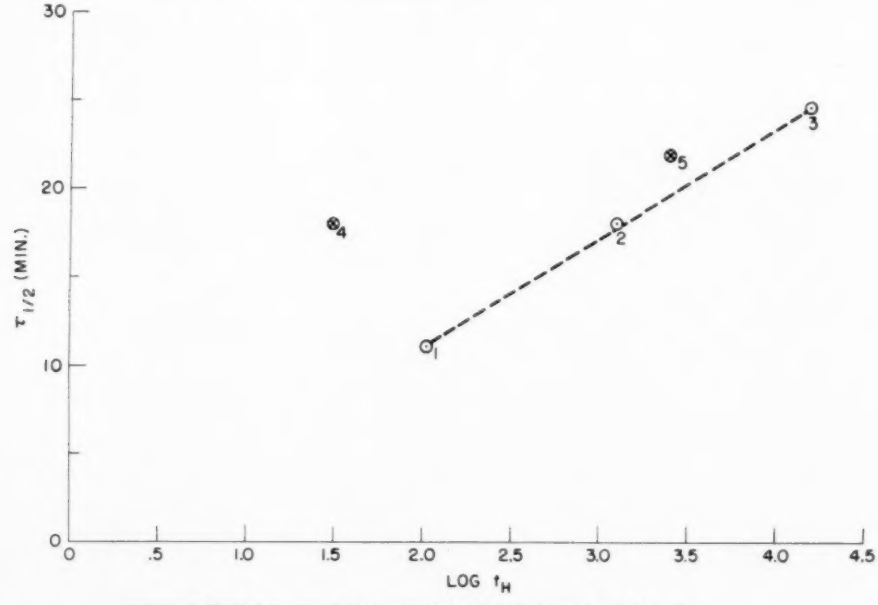

FIG. 10. "Half-life" of the precipitation reaction for a bulk-polycrystalline Pb-Sn alloy (7.5%) as a function of homogenization time.

Successive run no.		Homogenization Total time (min)	Temp. °C
○ 1	Slds → H → Q	107	208
○ 2	H → Q	1253	200
○ 3	H → Q	15,690	197
⊗ 4	H → W → Q	31	185
⊗ 5	H → Q	2520	248

the temperature-time curve was taken after the sample had been homogenized and quenched (H → Q).

Summary of Results

1. A new calorimetric technique has been applied to the study of kinetics of precipitations in Pb-Sn alloys. The precision of the measurements amount to better than 2% (room temperature) when comparing results on bulk-polycrystalline samples.

2. Precipitation energies in powder samples, consisting largely of single-crystal particles, have been found to be 1/10 to 1/400 of the values reported for bulk-polycrystalline alloys of the same composition.

3. The precipitation energy released by a powder specimen of Pb-Sn alloy could be enhanced by factors of up to approximately 100 by deforming the specimen.

4. The total precipitation energy in bulk-polycrystalline Pb-Sn alloys is influenced to only a small extent (~5%) by continued homogenization or by deformation.

5. Upon prolonged homogenization, the total precipitation energy released by powders worked and recrystallized falls to a negligible value. This result indicates that all the grain boundaries produced by recrystallization are annealed out of the small particles.

6. The time $\tau_{1/2}$ for half-completion of precipitation in bulk-polycrystalline alloy increases with increasing homogenization time and temperature. Recrystallization of the specimen decreases $\tau_{1/2}$ considerably.

7. It is probable that the nuclei for cellular precipitation in large specimens form at grain boundaries or within inclusions that may retain solid solutions with an orientation different from the matrix (e.g. as may have been the case in Tiedema and Burgers's experiments with single crystals).

VOL. 4 1956

ACKNOWLEDGMENTS

The authors are pleased to acknowledge the assistance of Mrs. E. L. Fontanella in the calorimetric measurements and of H. N. Treaftis in the preparation of the many alloy samples. J. B. Newkirk gave helpful advice in connection with the X-ray diffraction measurements.

We are grateful to Professors J. S. Koehler and Frederick Seitz of the University of Illinois for the loan of the calorimeter and to Professor A. W. Overhauser of Cornell University for helpful advice concerning its operation.

REFERENCES

1. D. TURNBULL and H. N. TREAFTIS *Acta Met.* **3,** 43 (1955).
2. T. J. TIEDEMA and W. G. BURGERS *Appl. Sci. Res.* **4A,** 243 (1954).
3. D. TURNBULL *Acta Met.* **3,** 55 (1955).

3a. D. TURNBULL, Physical Society Report of Conference on Defects in Crystalline Solids p. 203 (1954).

4. A. W. OVERHAUSER, Ninth Annual Calorimetry Conference, General Electric Research Laboratory, September 17–18, 1954.
5. W. F. GIAUQUE, R. M. BUFFINGTON, and W. SCHULZE *J. Amer. Chem. Soc.* **49,** 2343 (1927).
6. R. E. CECH and D. TURNBULL, *Trans. Amer. Inst. Min. Met. Eng.* **206,** 124 (1956).
7. Pt: C. A. SHIFFMAN *The Heat Capacities of the Elements Below Room Temperature,* General Electric Research Laboratory, October (1952).
   Pb: P. F. MEADS, W. R. FORSYTHE, and W. F. GIAUQUE *J. Amer. Chem. Soc.* **63,** 1902 (1941).
   Sn: F. LANGE *Z. phys. Chem.* **110,** 350 (1924).
   Cu: W. F. GIAUQUE and P. F. MEADS *J. Amer. Chem. Soc.* **63,** 1897 (1941).
   Constantan *Handbook of Chemistry and Physics,* 33rd Edition (1951–1952).
8. J. NYSTRÖM *Ark. Fys.* **1,** No. 18, 359 (1949).
9. G. BORELIUS, F. LARRIS, and E. OHLSSON *Arkiv Matematik, Astronomi och Fysik* **31A,** No. 10 (1944).

FOURIER ANALYSIS OF X-RAY DIFFRACTION PROFILES OBTAINED FROM TANTALUM FILINGS*

F. R. L. SCHOENING†

A Fourier analysis of the diffraction profiles obtained from spectrographically pure tantalum filings gave the following dimensions for the coherently reflecting domains: 170 Å and 100 Å for a hydrogen-free sample in the [110] and [100] directions respectively, and 160 Å and 95 Å for a sample containing 6·5 atomic per cent hydrogen. The influence of the dissolved hydrogen on the line profiles is discussed. The variation of the r.m.s. displacement with distance suggests a nonuniform distribution of hydrogen in the crystal lattice.

ANALYSE DE FOURIER DES PROFILS DE RAIES DE DIFFRACTION DES RAYONS X OBTENUES SUR DES LIMAILLES DE TANTALE

L'analyse de Fourier des profils de raies de diffraction obtenues à partir de limailles de tantale spectrographiquement pur ont fourni les dimensions suivantes pour les domaines cohérents: 170 Å et 100 Å pour un échantillon exempt d'hydrogène, dans les directions respectives [110] et [100], et 160 Å et 95 Å pour un échantillon contenant 65% d'hydrogène.

L'influence de l'hydrogène dissous sur les profils de raies est discutée. La variation de la moyenne des carrés réduite avec la distance suggère une distribution non uniforme de l'hydrogène dans le réseau cristallin.

FOURIER ANALYSE DER RÖNTGENREFLEXE VON TANTAL FEILSPÄNEN

Die Fourier Analyse der Röntgenreflexe von spektroskopisch reinen Tantal Feilspänen ergab die folgenden Grössen für die kohärent streuenden Bereiche: Für ein Wasserstoff freies Präperat 170 Å in der [110] Richtung und 100 Å in der [100] Richtung, für ein Präperat, welches 6,5 Atomprozente Wasserstoff enthält, 160 Å und 95 Å. Der Einfluss des gelösten Wasserstoffs auf die Linienformen wird besprochen. Die Veränderung der Wurzel aus dem mittleren Verschiebungsquadrat mit der Entfernung deuted darauf hin, dass der Wasserstoff ungleichförmig im Kristallgitter verteilt ist.

The shapes of the X-ray-diffraction profiles obtained from filings of degassed and of hydrogenated tantalum rods were investigated by Fourier analysis, following the technique developed by Warren and Averbach.[1, 2] Tantalum readily absorbs hydrogen, whereby an interstitial solid solution is formed which has the b.c.c. structure of tantalum up to 12 atomic per cent hydrogen according to Hägg,[3] or up to at least 34 atomic per cent according to Horn and Ziegler.[4] A shift of the diffraction lines shows that the tantalum lattice is expanded by the absorption of hydrogen. The influence of the hydrogen charge on the shapes of the diffraction lines obtained from the cold-worked metal is discussed in the following.

EXPERIMENTAL

The hydrogen-free sample was prepared from a spectrographically pure tantalum rod, supplied by Johnson and Matthey, which was degassed at 2600°C for half an hour in a vacuum of 10^{-4} mm Hg. The rod was mechanically filed in liquid oxygen, and from the filings, which passed a 325-mesh sieve, a suitable briquette was pressed.

The sample charged with hydrogen was prepared by degassing a second rod at 800°C in a vacuum better than 10^{-5} mm Hg, and then connecting the specimen tube to a measured amount of purified hydrogen. The specimen was kept in the hydrogen atmosphere for forty hours at 600°C, for seven hours at 500°C, and for sixty-five hours at 400°C. By observing the change in gas volume, it was found that the specimen had taken up 6.5 atomic per cent hydrogen.‡ After twenty-three days the rod was filed in liquid oxygen, and a briquette was pressed.

Annealed specimens were prepared by filing one hydrogen-free rod in liquid oxygen and another in air. The filings were annealed for one hour at 1140°C, pressed into briquettes, and again annealed for one hour at 1140°C. In both cases a vacuum which was better than 10^{-5} mm Hg was maintained during the heating process. Both annealed specimens showed very weak reflexions at $d = 2.36$ Å, which, according

* Received December 21, 1955: revised January 16, 1956.

† National Physical Laboratory, Council for Scientific and Industrial Research, South Africa.

‡ The author is indebted to Mr. A. J. Eve of the National Chemical Research Laboratory of the C.S.I.R. for carrying out this experiment.

to the ASTM card index, is the spacing of the strongest TaH line. Owing to the faintness of the reflexion, it is not known whether this impurity was already present before the samples were annealed.

Using Cu$K\alpha$ radiation, the X-ray measurements were made on a Norelco diffractometer fitted with current and voltage stabilizers, specimen spinner, and curved quartz monochromator. The diffraction pattern was recorded from $2\theta = 14°$ to $2\theta = 149°$ by setting the goniometer manually at intervals of 2θ ranging from 1° to 0.01°. The minimum number of counts taken at any setting was 1600.

FOURIER ANALYSIS OF THE LINE PROFILES

For the purpose of evaluating the Fourier coefficients, the corrected counting rates were plotted against 2θ. For every reflexion, two diagrams were drawn, one of these being an enlarged plot of the foot of the profile from the background level to an intensity value of about 3 counts/sec. For this diagram the unit of the Lipson and Beevers strips was made to correspond to 0.05 counts/sec as compared to a statistical error of about ± 0.03 counts/sec for a background point. The second diagram represented the more intense part of the profile, plotted on a convenient scale. By this treatment it was endeavoured to include as much of the tails of the profiles as was experimentally possible.

The interval from the low- to the high-angle termination of a profile was divided into equal parts numbered from −60 to +60, with the zero point at the center of the $K\alpha_1$ reflexion. For the sharp reflexions, the zero points were fixed by inspection. For a broadened profile, the overlapping of the α_1 and α_2 reflexions and the presence of line shifts made it necessary to locate the zero point in the following manner: It was assumed that the diffraction broadening is symmetrical and that any line shift displaces the profile bodily. A provisional zero point was taken by inspection, and the absolute values $C_n = (A_n'^2 + B_n'^2)^{\frac{1}{2}}$ of the complex Fourier coefficients were evaluated. The C_n values calculated in this way for a slightly misplaced zero point are equal to the A_n values for the correct zero point, because C_n is independent of the position of the zero point and $C_n = A_n$ for symmetrical diffraction broadening. The amount of mislocation c of the zero point is given by $\tan(2\pi nc/120) = B_n'/A_n'$.

The conversion of the number n to a length L, representing a distance in the crystal lattice perpendicular to the reflecting planes, was done by using the relation $L = \frac{1}{4}n\lambda\,(\sin\theta' - \sin\theta'')^{-1}$ where θ' and θ'' are the angle values at $\frac{1}{4}$ and $\frac{3}{4}$ of the Fourier interval.

Following the method of Warren and Averbach,[1]

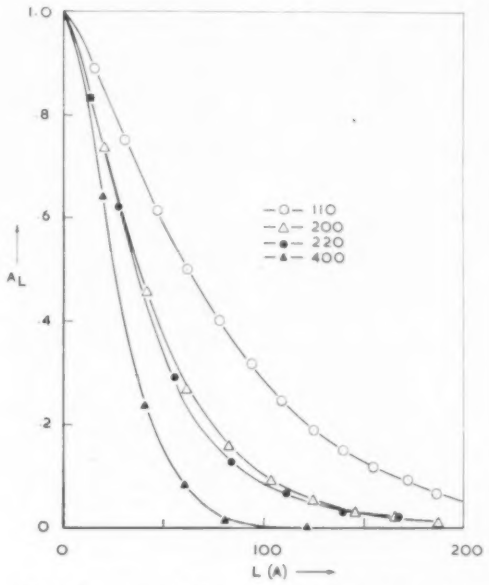

FIG. 1(a). Fourier coefficients obtained from filings of hydrogen-free tantalum.

the Fourier coefficients shown in Fig. 1 were separated into their strain and particle-size components by plotting $\ln A_L$ versus $(h^2 + k^2 + l^2)$, as shown in Fig. 2. Assuming a Gaussian strain distribution, the particle-size contribution to the Fourier coefficients was evaluated and is shown in Fig. 3.

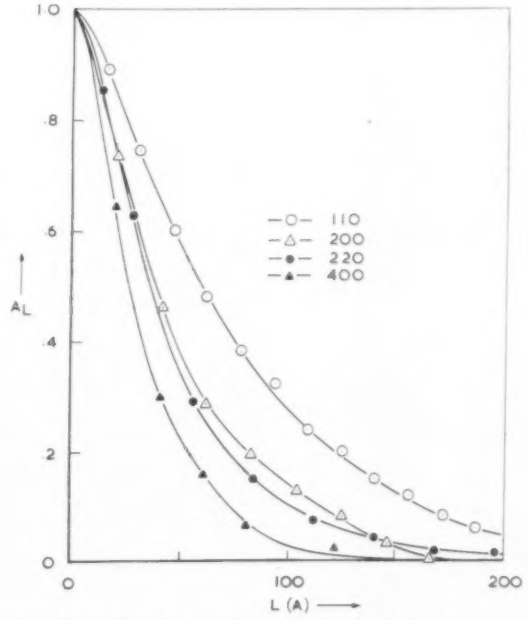

FIG. 1(b). Fourier coefficients obtained from filings of tantalum containing 6.5 atomic per cent hydrogen.
The Fourier intervals were chosen so that $C_L = A_L$ and $B_L = 0$.

VOL. 4 1956

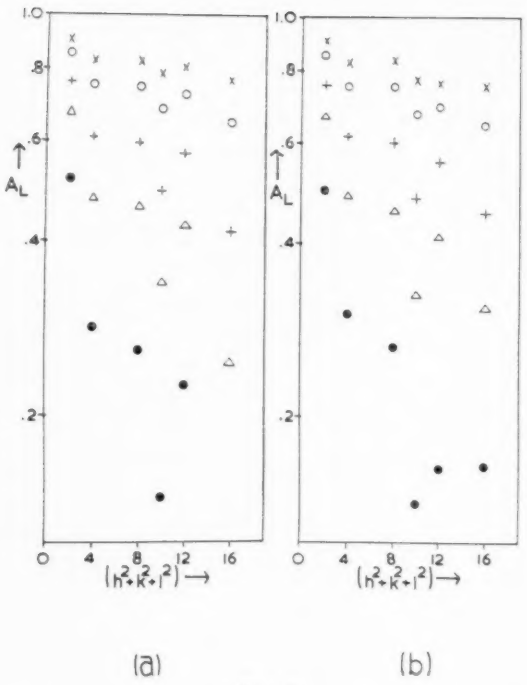

FIG. 2.
(a) ln A_L of the hydrogen-free specimen plotted against $(h^2 + k^2 + l^2)$.
(b) ln A_L of the hydrogenated specimen plotted against $(h^2 + k^2 + l^2)$.
The L values are: × 15 Å, ○ 20 Å, + 30 Å, △ 40 Å, ● 60 Å.

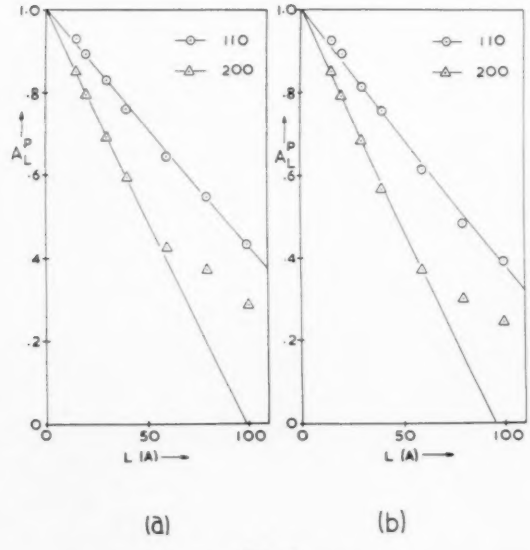

FIG. 3.
(a) The particle-size contribution A_L^P of the hydrogen-free sample plotted against L.
(b) The particle-size contribution A_L^P of the hydrogenated sample plotted against L.

DISCUSSION OF THE RESULTS

The scatter of the points plotted in Fig. 2 makes it impossible to draw smooth curves for constant L values, which indicates that tantalum is elastically anisotropic. From the slopes of the curves shown in Fig. 3 the following average dimensions $\bar{L}$ of the coherently reflecting domains were calculated:

Ta (degassed),

$$\bar{L}_{100} = 100\,\text{Å},\ \bar{L}_{110} = 170\,\text{Å}.$$

Ta + 6.5 atomic per cent H,

$$\bar{L}_{100} = 95\,\text{Å},\ \bar{L}_{110} = 160\,\text{Å}.$$

Within the error of experiment, the average sizes of the domains are the same for the two samples.

Huang's[5] theory of X-ray diffraction from a solid solution containing elastic distortions distributed at random, predicts diffuse scattering around reciprocal lattice points, an artificial temperature factor, a shift of the diffraction lines, and no broadening of the Bragg reflexions. Because of the relatively small distortion produced by a hydrogen atom, diffuse scattering and an artificial temperature factor could not be expected and were also not observed. A significant difference between the two cold-worked samples could be detected neither by a statistical significance test of thirty-eight background points nor by a comparison of integrated intensities. The observed shift of the diffraction lines from the cold-worked, hydrogenated sample with respect to the lines from the cold-worked, hydrogen-free sample amounts to an isotropic expansion of 0.3%. Referring to Huang's theory, only deviations from the randomness of the hydrogen distribution can be expected to broaden the diffraction profiles. The r.m.s. displacements shown in Fig. 4 were obtained from the broadening of the profiles and, therefore, do not contain the isotropic expansion originating from that part of the hydrogen charge which is distributed at random. Displacements of the value of $0.003L$ should be added to the data shown in Fig. 4 for the hydrogenated sample when the total effect of the hydrogen is considered.

The r.m.s. value of the displacements of unit cells L Ångstrom units apart is plotted in Fig. 4. For increasing values of L, the curves for the hydrogenated sample drop below those for the degassed sample. For small L values, the curves tend to be the same. If these are real effects, they indicate:

(i) Less unit cells are distorted in the hydrogenated sample than in the hydrogen-free sample, and

(ii) the distortion of the affected unit cells in the hydrogenated sample is bigger.

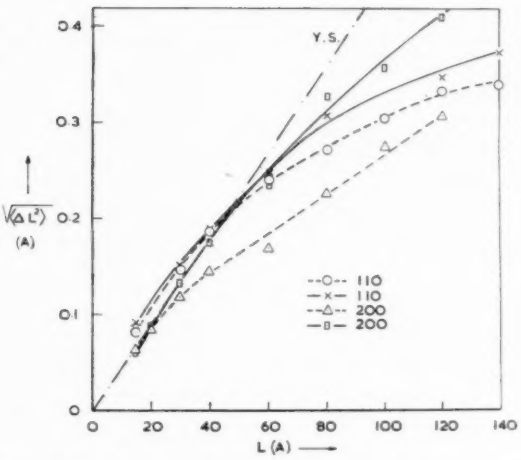

FIG. 4. The r.m.s. value of displacements of unit cells L Ångstrom units apart, drawn in full lines for the hydrogen-free sample and in broken lines for the hydrogenated sample.

The latter follows because the r.m.s. values for the two samples are the same for small values of L. A diffusion of hydrogen atoms from compressed regions of the lattice to extended regions can account for this observation if the boundaries of the reflecting domains are not shifted by the diffusion process. The compression and extension will increase and will be concentrated in regions of changed hydrogen content. It must be remembered that, for the hydrogenated sample, compressions and extensions were measured with respect to an undistorted but uniformly expanded tantalum lattice.

The initial slopes of the curves in Fig. 4 represent the r.m.s. strains, and can be compared to a yield-strain obtained from values given by Bechthold[6] and shown as a straight line in the figure.

ACKNOWLEDGMENTS

In conclusion, the author wishes to thank Dr. J. N. van Niekerk for his continued interest and encouragement throughout the work, and Mr. F. T. Wybenga for his help with the experiments and calculations.

This paper is published by permission of the South African Council for Scientific and Industrial Research.

REFERENCES

1. B. E. WARREN and B. L. AVERBACH *J. Appl. Phys.* **21,** 595 (1950).
2. B. E. WARREN *Acta Cryst.* **8,** 483 (1955).
3. G. HÄGG *Z. Phys. Chem.* **11,** 433 (1931).
4. F. H. HORN and W. T. ZIEGLER *J. Amer. Chem. Soc.* **69,** 2762 (1947).
5. K. HUANG *Proc. Roy. Soc.* **A190,** 102 (1947).
6. J. H. BECHTHOLD *Acta Met.* **3,** 249 (1955).

VOL. 4 1956

THE PINNING OF DISLOCATIONS BY X-IRRADIATION OF ALKALI HALIDE CRYSTALS*

R. B. GORDON† and A. S. NOWICK‡

A study is made of the effect of X-irradiation on the room-temperature elastic modulus (s_{11}^{-1}) of NaCl crystals. The modulus is observed to be unchanged by irradiation for well-annealed crystals, but may increase by as much as 7% when cold-worked crystals are irradiated. It is demonstrated that the modulus change on irradiation corresponds exactly to the elimination of the modulus decrease due to oscillating dislocation loops through the creation of pinning points along the dislocations. A quantitative theory is developed for the variation of modulus with X-ray dose. This theory assumes that vacancies, released within the volume of the crystal through the action of the radiation, migrate to dislocations and contribute to the formation of pinning points. The theory appears to be in good agreement with experiment and makes possible a calculation of the density of dislocations and the mean length of the free dislocation loops prior to irradiation.

LE BLOCAGE DES DISLOCATIONS PAR IRRADIATION X DES CRISTAUX d'HALOGENURES ALCALINS

L'effet d'une irradiation X sur le module d'élasticité (s_{11}^{-1}) de cristaux NaCl à température ambiante est étudiée. Les observations montrent que le module reste inchangé par l'irradiation pour des cristaux bien revenus, mais peut augmenter jusqu'à 7% de sa valeur quand des cristaux écrouis sont irradiés.

Il est démontré que la variation du module lors de l'irradiation correspond exactement à l'élimination de la décroissance du module due aux anneaux de dislocation oscillants, lors de la création de points d'ancrage le long des dislocations. Une théorie quantitative est développée pour la variation du module avec la dose des rayons X. Cette théorie admet que les lacunes, libérées dans le volume du cristal sous l'action de la radiation, migrent aux dislocations et contribuent à la formation de points d'ancrage.

La théories semble être en bon accord avec l'expérience et rend possible un calcul de la densité des dislocations et la longueur moyenne des anneaux libres de dislocations avant l'irradiation.

VERANKERUNG VON VERSETZUNGEN DURCH RÖNTGENBESTRAHLUNG VON ALKALI-HALOGENID-KRISTALLEN

Von den Autoren wurde an NaCl-Kristallen eine Untersuchung über den Einfluss von Röntgen-Bestrahlung auf den bei Raumtemperatur gemessenen Elastizitätsmodul (s_{11}^{-1}) vorgenommen. Dabei wurde beobachtet, dass der Modul gut ausgeglühter Kristalle bei Bestrahlung unverändert, dass er jedoch um 7% ansteigen kann, wenn kaltbearbeitete Kristalle bestrahlt werden. Wie gezeigt wird, entspricht die Moduländerung infolge der Bestrahlung genau dem Abbau der von schwingenden Versetzungsschleifen herrührenden Modulabnahme, die dadurch rückgängig gemacht wird, dass entlang der Versetzungen Verankerungspunkte erzeugt werden. Für die Veränderung des Moduls mit der Röntgendosis wurde eine quantitative Theorie entwickelt. Dabei ist angenommen, dass Leerstellen, die durch die Bestrahlungswirkung im Kristallinnern freigeworden sind, zu den Versetzungen wandern und dort zur Bildung von Verankerungsstellen beitragen. Die Theorie scheint in guter Übereinstimmung mit den Experimenten zu stehen. Sie ermöglicht eine Berechnung der Versetzungsdichte und der mittleren freien Länge der Versetzungsschleifen vor der Bestrahlung.

1. INTRODUCTION

Irradiation of an alkali halide crystal with X-rays usually results in the formation of visible color within the crystal, related to the creation of certain optical absorption bands. The most prominent of these bands is the "*F* band" which is due to the presence of so-called "*F* centers" generated in the crystal during the irradiation. It is now known[1] that an *F* center consists of an electron trapped at a negative-ion vacancy.§ The number of *F* centers formed in

* This research was supported by the U.S. Air Force through the Office of Scientific Research of the Air Research and Development Command. Paper received December 19, 1955.

† School of Mines, Columbia University, New York, N.Y.; formerly at Yale University.

‡ Hammond Metallurgical Laboratory, Yale University, New Haven, Conn.

§ In an ionic crystal a negative-ion vacancy carries an effective positive charge. Thus, when an electron is released into the conduction band by absorption of ionizing radiation in the crystal, it may be attracted to the vacancy where it can fall into a series of bound states. Absorption of light in the *F* band occurs when this trapped electron is raised from the ground state to the first excited state. When a colored crystal is illuminated with light in the *F* band, the color slowly fades ("optical bleaching") because electrons raised to an excited state can be thermally released into the conduction band at room temperature. Other color centers may also be formed during irradiation. Among these are, for example, the V-type centers consisting of holes trapped at positive-ion vacancies or simple clusters of vacancies. Such centers, which give rise to absorption bands in the ultra-violet, will not be of primary interest here.

alkali halide crystals by X-irradiation is far greater than that which can be accounted for in terms of the free vacancies originally present in the unirradiated crystals.[1] Thus, additional vacancies must be generated during the irradiation. Because a change in number and distribution of vacancies is produced by X-irradiation, it follows that a study of the change in mechanical properties resulting from irradiation with X-rays provides a unique method for obtaining information concerning the interaction between point defects and dislocations.

It has been known for many years that irradiation of alkali halides with X-rays produces marked changes in various mechanical properties of the irradiated crystals. Early experiments by Kusnetzow and Sementzow[2] and by Podaschewsky[3] have shown that the yield-strength of irradiated rock-salt is greater than the breaking strength of unirradiated specimens. Substantial increases in hardness of the alkali halides have also been observed to result from X-irradiation by Li[4] and by Westervelt.[5] These radiation-induced hardening effects are permanent; they are not reversed by optical bleaching. Recent experiments[6] have shown that for unfiltered radiation the hardness increase occurs only in the thin layer of the crystal close to the irradiated surface.

Frankl[7] discovered that irradiation has a marked effect on the internal friction properties of rock-salt, viz. that the amplitude-dependent part of the damping is almost eliminated by a brief irradiation. He found that this effects occurs throughout the entire volume of the crystals studied (in contrast to the hardness increase), and further observed that the amplitude dependence of the damping is not restored by optical bleaching of the crystal. In addition to the changes in decrement, Frankl also noted an increase in the elastic modulus (measured at low-strain amplitudes) of about 0.1% in some irradiated crystals.

According to Frankl, the observed suppression of the damping occurs because positive-ion vacancies which are freed during the irradiation, can pin down the dislocation segments responsible for the damping. (A positive-ion vacancy may be freed from a vacancy pair which dissociates when the negative-ion vacancy of the pair becomes an F center.) In considering this mechanism, Seitz[1] has suggested that it is more likely that the pinning is due to clusters of vacancies of both signs which condense near dislocations during irradiation at room temperature.

Unfortunately, the three mechanical properties which have been investigated in greatest detail—yield-strength, hardness, and internal friction—are relatively difficult to relate quantitatively to the dislocation distribution. The effect of dislocations on the elastic moduli, on the other hand, is predicted by a quantitative theory. If N is the density of dislocation lines (in lines/cm^2 or total line-length per unit volume) which are pinned down at regular intervals to form segments of length l, then, according to Mott[8] and Friedel,[9] the movement of these segments in phase with an applied stress results in a *lowering* of the shear modulus of an isotropic material by an amount $\Delta\mu$ given by

$$\frac{\Delta\mu}{\mu} = \frac{Nl^2}{\xi'} \tag{1}$$

where ξ' is a slowly varying function of l having a magnitude near unity. In view of the simplicity of this result, elastic-modulus measurements would appear to provide an excellent means for the investigation of the pinning of dislocations by point defects. The present investigation is directed primarily toward a detailed study of the increase in dynamic modulus which results from X-irradiation of alkali halide crystals. In some of the experiments, internal friction is also measured simultaneously with the dynamic modulus.

2. EXPERIMENTAL METHODS

Modulus Measurements

The modulus measurements are made by the dynamic method, using the three-part composite piezoelectric resonator described by Marx.[10] Two identical quartz crystals are used in this resonator, one which serves to drive the resonator in forced vibration, and the other (the gage crystal) which indicates the resulting amplitude of vibration by means of the voltage developed across its electrodes. The driving crystal is excited by an a.c. signal taken from a variable-frequency oscillator. The specimen, whose length lies in a ⟨100⟩ direction, is thus driven in the fundamental longitudinal mode. From the measured resonant frequency of the composite resonator, the resonant frequency on the specimen alone, f_s, may be calculated. The elastic constant s_{11} of the specimen crystal is related to the frequency f_s by means of the relation

$$f_s = \frac{1}{2L_s}\sqrt{\frac{1}{\rho s_{11}}} \tag{2}$$

where L_s is the length and ρ the density of the specimen. (The quantity $s_{11}{}^{-1}$ may be regarded as the appropriate elastic modulus.) Thus, the relationship between a change in f_s and the corresponding change in elastic constant is

$$2\Delta f_s/f_s = -\Delta s_{11}/s_{11}. \tag{3}$$

The advantage of using the three-part resonator is that its resonant frequency, decrement (ratio of the energy-loss per cycle to the total stored vibrational energy), and maximum strain amplitude of vibration, can all be measured simultaneously. The decrement can be obtained with equal ease regardless of whether the damping is amplitude-dependent or not. From the measured decrement of the composite resonator, the decrement Δ_s of the specimen alone may be obtained. Furthermore, the maximum strain-amplitude in the specimen ϵ_s may be calculated from the voltage developed across the gage crystal. All of the measurements to be described were made with specimens which had a resonant frequency very nearly equal to 85 kc, and which matched the resonant frequency of the quartz crystals to better than 5%.

The frequency of the signal generated by the variable-frequency oscillator can be determined with a precision of better than 1 part in 10^5 by comparison with a quartz-controlled secondary standard. This standard oscillator is in turn monitored by comparison with a reference-frequency broadcast by radio station WWV. The precision attainable in measuring the resonant frequency of the composite resonator depends on two conditions. First, the total decrement of the resonator must be small so that the maximum of the resonance response curve can be found with precision. If the decrement of the specimen is of the order of 10^{-3} or less, its resonant frequency can be determined to within at least 1 part in 10^5 with the present equipment. Second, the composite resonator must be in thermal equilibrium. If the resonator is kept at the ambient temperature, as in the present experiments, its temperature must be measured and appropriate corrections to the observed resonant frequency made for departure of the temperature from that selected as the reference temperature. In the present case, the temperature of the resonator was measured by means of a small thermocouple mounted immediately adjacent to the specimen (the temperature coefficient of the resonant frequency of the specimen is substantially greater than that of the quartz). The practical limit of error in temperature measurement by this method is ± 0.01°C, which corresponds to an uncertainty in resonant frequency of about ± 0.2 parts in 10^5.

Resonant-frequency measurements as a function of temperature were found to fall on a straight line. When the time-rate of change of temperature was less than 0.03°C/min, the data fell on the same straight line regardless of whether the temperature was increasing or decreasing; when the temperature was changing more rapidly, it did not. Accordingly, the resonator was considered to be in thermal equilibrium with the thermocouple whenever the rate of change of temperature was less than 0.03°C/min. In order to make the necessary temperature corrections to the observed resonant frequencies, the temperature coefficient of the resonant frequency of the composite resonator was actually measured for every specimen used.

Specimens

Almost all the experiments were carried out with crystals obtained from the Harshaw Chemical Company. The specimens used were free of mechanical defects and lineage structure, as revealed by the flatness of their cleavage planes. NaCl crystals were used in most of the experimental work. The spectroscopic analyses of Harshaw rock-salt made in a number of different laboratories are reported by Duerig and Markham.[11] These crystals generally carry a small amount of divalent impurity such as calcium along with traces of trivalent impurities such as iron.

The natural rock-salt used in some of the experiments was obtained from the Brush Mineral Collection, Yale University, and originated in the Stassfurt deposits. This material had a pronounced lineage structure, making it difficult to cleave into bars suitable for modulus measurements.

Bars of the various alkali halides used were supplied by Harshaw cleaved to the same cross-section as the quartz bars used to make up the composite resonator (0.22 in.^{2}), and were further cleaved to the proper length (about 1.03 in.) to match the frequency of the quartz driver-gage assembly. It was found possible to cleave with an accuracy of about ± 0.003 in. in most cases. Final adjustment of the length was made by grinding the ends of the bars on metallographic polishing paper.

Specimens to be cold-worked were cut oversize by the correct amount and the ends coated with collodion. The plastic deformation was accomplished by compressing the bars lengthwise in a toolmaker's vise. The collodion coating prevents the ends of the bars from splitting during heavy deformation.

Irradiation

The X-rays used for irradiation were obtained from a copper target Coolidge-type tube containing beryllium windows and operating at 39 kV accelerating potential and a tube current of 10 mA. Unfortunately, the power supply for the X-ray tube did not include a voltage regulator, so that normal fluctuations of the voltage taken from the mains resulted in about a 10% fluctuation in the operating conditions of the tube over periods of the order of tens of minutes.

Since the size of the X-ray beam was too small to irradiate the specimen uniformly over its length, the composite resonator was mounted so that it could be translated vertically in front of the tube. The translational motion was obtained from a cam follower running on a motor-driven cam. The cam was cut so that the resonator moved up and down with a constant velocity, its period being about 15 sec. In this way the specimen could be irradiated uniformly without removing it from the composite resonator.

The resonator assembly was mounted in a light-tight, air-tight box containing a drying agent. X-rays were admitted through an aluminum-foil window. It was demonstrated that the presence of this window in no way influenced the formation of color centers in the specimen upon irradiation.

It was not possible to make resonant-frequency measurements during the course of irradiation because of the changing capacitance between the leads to the resonator and the light-tight box during the translation of the resonator. This capacitance change caused erratic readings on the vacuum-tube voltmeter connected to the gage electrodes. It was therefore necessary to turn off the X-rays and stop the translation of the resonator before each reading. Measurements of resonant frequency showed that the irradiation slightly perturbed the thermal equilibrium of the resonator, but that equilibrium was generally restored within a minute or two after the X-rays were turned off.

In order to irradiate a specimen at low temperature it was necessary to remove it from the resonator. The specimen was surrounded on three sides by coolant by placing it in a re-entrant cavity formed on the side of the copper box containing the coolant. This box had a volume of about one quart, and the cavity projected into the box about one inch. The coolant used was either liquid air or crushed dry ice. Radiation was admitted through an aluminum-foil window placed over the mouth of the cavity, the window serving to exclude both light and moisture.

For bleaching experiments a 4.5-amp carbon arc lamp was used as the light-source. A pair of glass condenser lenses and a water-cell heat-filter were included in the optical path. For bleaching at room temperature the specimen remained attached to the composite resonator, and the aluminum window of the dry box was replaced by a lucite one. No window was used to protect the crystal in the low-temperature box during illumination at low temperature; all water-vapor condensed at the mouth of the re-entrant cavity leaving the specimen completely dry.

3. EXPERIMENTAL RESULTS

General Character of the Radiation Effects

The effect of X-irradiation is to increase the modulus and to decrease the internal friction of NaCl crystals. The magnitude of the total change in modulus or in damping produced by irradiation is sensitive to the history of the individual specimen under investigation. Regardless of magnitude, however, both these properties respond to irradiation in the manner shown in Fig. 1. Here the modulus change is reported in terms of the change Δf_s in the resonant frequency of the specimen, and the internal friction as the decrement Δ_s. The resonant frequency generally decreases with increasing strain amplitude of vibration.* The frequency measurements reported in Fig. 1 (and throughout the rest of this paper), however, are measured at *low-strain amplitudes* where frequency is independent of amplitude. Fig. 1 shows that at the beginning of irradiation the changes in frequency and decrement are very rapid, but with larger X-ray doses the rate of change decreases, and eventually "saturation" values are reached. The decrement at large strain amplitudes is decreased by irradiation to the same final value as the decrement observed at small strain amplitudes, i.e. the damping becomes independent of strain amplitude, as was observed by Frankl.

The frequency and decrement changes resulting from X-irradiation are permanent at room temperature; after irradiation to saturation, neither of these quantities shows any tendency to return to its preirradiation value. Illuminating a crystal with white light after irradiation likewise has no effect on either the frequency or the decrement, in spite of the fact that such illumination bleaches out all of the coloration in the crystal.

The effects of irradiation on both the frequency and the damping represent changes throughout the volume of the crystal (in contrast to the hardness increase[6] which occurs only in a thin layer near the surface where soft X-rays are heavily absorbed). This is evident in the case of the damping merely from the fact that irradiation on one face of the specimen destroys all of the amplitude-dependent part of the damping. That the modulus increase is a volume effect is demonstrated by irradiating a crystal on one face until the frequency change is nearly complete, and then irradiating on the reverse face. For one of the NaCl specimens (No. 4) it was found, for example, that Δf_s after irradiating on one face for

* These changes are usually small compared to the change in frequency (at a given amplitude) produced by irradiation.

VOL. 4 1956

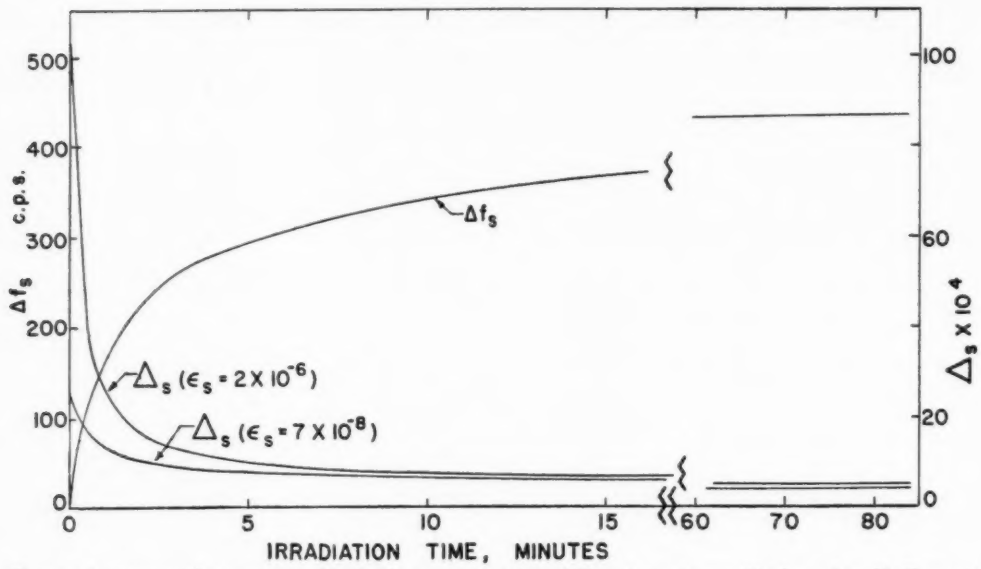

FIG. 1. Changes in resonant frequency, and in the decrement at two different strain amplitudes, of an NaCl crystal (No. 5) exposed to 39 kV X-rays. Experimental points were taken at time-intervals in geometric progression (viz. at 0.5, 1, 2, ··· min) and lie on the curves shown to within the thickness of the pen line.

50 min was 175 c.p.s., while irradiation on the back face to saturation produced an additional change of only 10 c.p.s. Further irradiation with higher-energy X-rays has no additional effect on the modulus, after saturation has been achieved with lower-energy radiation.

Additional evidence on this point is supplied by an experiment in which a crystal was irradiated through a thin NaCl filter. The filter crystal, 0.030 cm thick, was interposed in the X-ray beam in front of the specimen, and the resonant frequency and decrement measured as a function of dose. The filter is thick enough to absorb a substantial fraction of the incident X-ray intensity (particularly in the long-wavelength region). Nevertheless, the modulus and damping curves so obtained are completely equivalent to those obtained without a filter. This result shows that the changes in modulus and damping are produced throughout the volume of the crystal by the more penetrating (short wavelength) X-rays.

It is known that X-irradiation increases the length[12] and decreases the density[13] of rock-salt crystals, so that some question may arise as to whether the changes in resonant frequency observed in these experiments can be wholly attributed to modulus changes. First it should be noted that, for the present radiation dosages, the density and dimensional changes are most probably confined to the layer less than 0.01 cm thick at the front of the crystal, where the majority of the incident radiant energy is absorbed,[6] whereas the resonant-frequency change resulting from irradiation has been shown to be a volume effect. Second, the magnitude of the dimensional and density changes produced by the relatively short irradiations used in these experiments are too small to account for changes in resonant frequency of the magnitudes found here. For example, the increase in length of about 2 parts in 10^5 found by Sakaguchi and Suita[12] in irradiated NaCl would cause a resonant-frequency change of only 1 c.p.s. at 85 kc, which is within the experimental error of the present measurements. It is concluded that the resonant-frequency changes observed upon irradiation must be due entirely to changes in modulus.

The modulus and damping changes resulting from irradiation have been measured in specimens of NaCl from four different lots of Harshaw crystals and from one natural crystal. The nature of the radiation effects produced in all these crystals was found to be the same; only the magnitude of the effects differed from crystal to crystal.

Effects of Deformation and Recovery

A crystal which has been annealed at 500°C for 1 h and subsequently handled with care is characterized by a decrement which is almost amplitude-independent and by a modulus which is unaffected by X-irradiation. Curve *A* in Fig. 2 shows the decrement of a carefully annealed crystal as a function of strain amplitude.

Crystals quenched from temperatures of the order of 500°C show a somewhat higher decrement than the annealed crystals (equivalent to Curve *B*, Fig. 2),

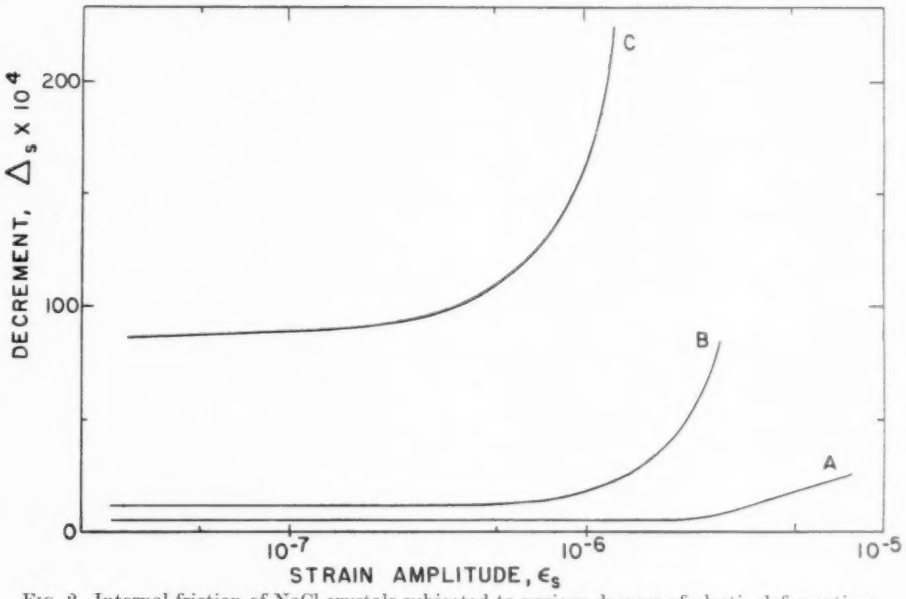

FIG. 2. Internal friction of NaCl crystals subjected to various degrees of plastic deformation. (A) fully annealed; (B) compressed 0.04%; (C) compressed 2.3%.

and a small modulus increase upon irradiation. In the as-received condition the modulus-change upon irradiation and the damping prior to irradiation are again higher than in the annealed condition. Table 1 lists some of the changes in resonant frequency produced by irradiation.

When one of the specimens used for modulus measurements is compressed in the direction of its length, slip takes place on two sets of the {110} planes. Both the decrement and modulus of the crystal are changed as a result of such deformation. Curve *B* in Fig. 2 shows the decrement as a function of strain amplitude observed after a carefully annealed crystal has been compressed 0.04%, while Curve *C* corresponds to this same crystal after a compression of 2.3%.

TABLE 1. Total change in resonant frequency produced in various NaCl crystals by X-irradiation

Crystal number	Treatment	Recovery time (min)	Recovery temperature (°C)	Total Δf_s (c.p.s.)
1	annealed	—	—	0
1	quenched from 500°C	—	—	34
1	(as received)	—	—	175
8	deformed 4.07%	150	100	123
7	deformed 4.40	150	100	129
9	deformed 2.00	5760	20	212
5	deformed 2.14	180	20	434
6	deformed 4.20	1700	20	720
12	deformed 3.08	1936	20	1945
10	deformed 4.08	1440	20	2150
13	deformed 3.24	119	20	2870

It is evident that the internal friction is increased markedly by small deformations and that the strain amplitude at which the decrement becomes dependent on the amplitude of vibration is simultaneously decreased. This behavior is similar to that of deformed metal crystals.[14, 15]

The elastic modulus of the compressed crystals is lowered as a result of the deformation. This change is not conveniently observed by direct measurement, because of the dimensional changes that accompany the deformation; it becomes apparent, however, from the fact that the modulus increases spontaneously with time after deformation. Correspondingly, internal friction decreases on standing at room temperature. Similar changes in modulus and damping following plastic deformation have also been observed in deformed metals,[16] and are collectively known as the Köster effect, after their discoverer. The course of the recovery of the Köster effect is such that over a large time-interval the modulus increase is approximately linear with the logarithm of time after deformation, as is shown in Fig. 3. The decrement at large strain amplitudes decreases with time more rapidly than that at small amplitudes, while both decrement curves have the inverted *S* shape characteristic of a recovery phenomenon involving a broad spectrum of recovery times.

Exposure of the deformed crystals to X-rays increases the modulus and decreases the damping in the same way as it does in the as-received and quenched crystals, but the magnitude of the effects produced is

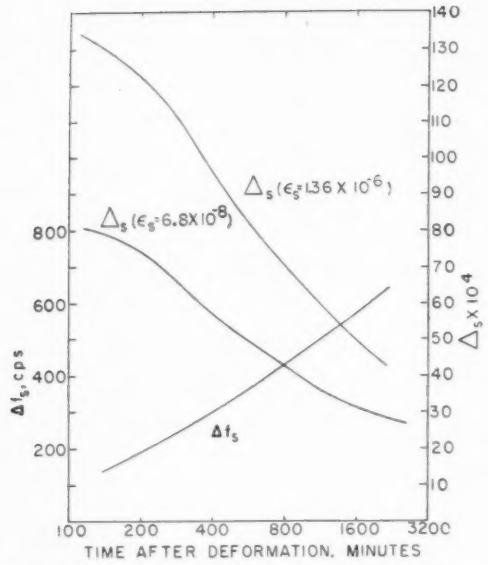

FIG. 3. Spontaneous recovery of the resonant frequency (measured from an arbitrary reference frequency) and decrement of a plastically deformed NaCl crystal (No. 6) at room temperature. The crystal was compressed 4.2% at zero time.

very much greater. The total changes in the resonant frequency of a number of crystals subjected to different deformation and recovery treatments prior to irradiation are listed in Table 1. It should be noted that the largest changes reported correspond to modulus changes of nearly 7%. It is evident from the data presented in the table that the total modulus change produced by irradiation is greater, the greater the prior deformation and the less the prior recovery time. In addition to the amount of deformation and the recovery time, the modulus change observed in any particular crystal apparently depends on other factors, such as the rate at which the crystal was deformed and/or the particular configuration of slip planes which happened to be active during the deformation (varying amounts of double slip were seen in all the crystals).

The data on crystals 7 and 8 presented in Table 1 show that recovery at 100°C prior to irradiation substantially reduces the modulus effect produced by the irradiation. It has also been shown that no modulus effect is observed when carefully annealed crystals are irradiated. These observations suggest that *irradiation can only raise the modulus in crystals where the modulus has been previously lowered by deformation and not allowed to recover fully.* In other words, the sum of the modulus increases resulting from recovery and irradiation should be the same in crystals which have been deformed the same amount, provided that care is taken to deform the crystals in exactly the same manner.

An experimental test of the above hypothesis was carried out as follows. Two crystals (Nos. 12 and 13) were carefully deformed by nearly the same amounts and then allowed to recover for different lengths of time before exposure to X-rays. The resulting resonant-frequency changes on recovery and on irradiation are shown in Fig. 4 and in Table 2. The X-irradiation was

TABLE 2. Comparison of frequency changes in two similarly deformed crystals

Crystal No.	12	13
Per cent deformation	3.08	3.24
Recovery time at 20°C (min)	2936	119
Δf_s in recovery (c.p.s.)	1007	193
Δf_s on irradiation (c.p.s.)	1931	2872
Total Δf_s	2938	3065
Corrected to 3.08% deformation	2938	2950

for two hours in both cases. The total changes in resonant frequency of the two crystals agree to within 4%. Even better agreement is obtained if a correction is made for the small difference in initial deformation of the two crystals, assuming a linear dependence of Δf_s on per cent deformation. This correction is made in the last line of Table 2 as well as in the plotted data for crystal No. 13 in Fig. 4. The excellent agreement obtained for the total modulus change of the two crystals, after correction, is undoubtedly somewhat fortuitous in view of the difficulty in deforming two different specimens in exactly the same way.

The manner in which the modulus changes with X-ray dosage has been demonstrated thus far only in Fig. 1. It is now of interest to compare such modulus vs. dose curves for crystals subjected to different prior treatments. For this purpose it is convenient to define the *modulus defect*, Φ, as

$$\Phi = \frac{M^\infty - M}{M^\infty} = 2\frac{f_s^\infty - f_s}{f_s^\infty} \qquad (4)$$

where M^∞ and f_s^∞ are the "saturation values" of the modulus $M = s_{11}^{-1}$, and of the resonant frequency f_s, of the specimen attained after prolonged irradiation. The quantity Φ_0 will represent the modulus defect at the start of irradiation. The relation between the modulus vs. dose curves for specimens deformed different amounts is shown in Fig. 5, where the relative modulus defect, Φ/Φ_0, is plotted against the logarithm of the irradiation time. It is seen that during the major part of the modulus change these curves are straight lines; also, within experimental error, curves for the different crystals differ from one another only

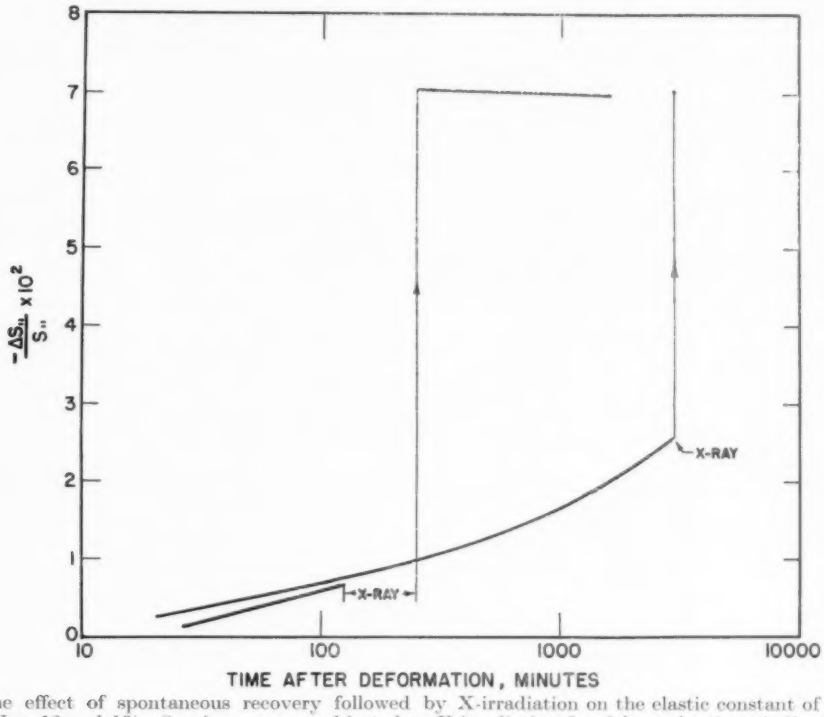

FIG. 4. The effect of spontaneous recovery followed by X-irradiation on the elastic constant of two crystals (Nos. 12 and 13). Specimens were subjected to X-irradiation for 2 h at the times indicated.

VOL. 4 1956

in such a way that they can be shifted into coincidence by a translation along the log-time axis.

Effect of Irradiation Temperature

Crystal No. 9 was irradiated at a temperature of 42°C instead of room temperature. As is evident from Fig. 5, irradiation at this slightly elevated temperature does not change the form of the modulus defect vs. dose curve.

Measurements *at room temperature* were also made on crystals irradiated at low temperatures. In view of the fact that Frankl[7] reported a decrease in damping for crystals irradiated at a low temperature and warmed in the dark, but not for crystals irradiated and optically bleached at low temperature, it seemed desirable to carry out similar experiments on the modulus changes. Accordingly, some of the crystals were subjected to strong illumination after low-temperature irradiation, while the others were warmed up to room temperature in the dark. The results of these experiments are given in Table 3. In this Table, Δf_s (obs) is the total change in resonant frequency

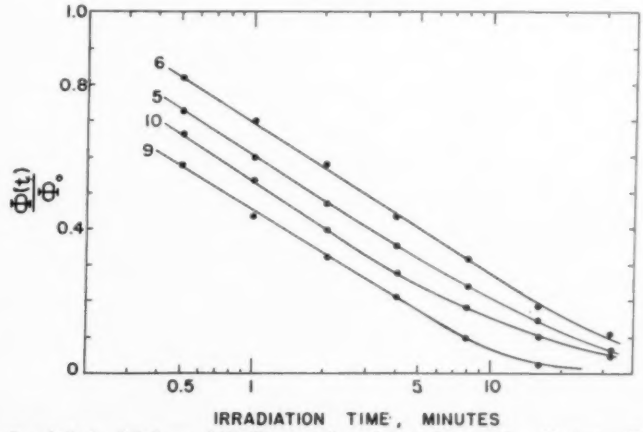

FIG. 5. Relative modulus defect of deformed NaCl crystals subjected to X-irradiation. Each curve is numbered with the identification number of the crystal measured. Data for crystal No. 4 superimposes on that for crystal No. 9.

TABLE 3. Change in resonant frequency, measured at room temperature, resulting from 1-h irradiations at various temperatures. (All crystals deformed approximately 1.5% and allowed to recover about 800 min before irradiation)

Crystal No.	Irradiation temperature (°K)	Illumination	Δf_s (obs)	Δf_s (corr)
18	298	none	235	241
19	180	none	250	256
20	180	at 180°K	403	310
21	78	none	261	266
22	78	at 78°K	187	214
23	78	during warm-up	45	48

upon irradiation, obtained by direct measurement; the Δf_s (corr) values are obtained by correcting the observed values to a standard deformation of 1.50%, under the assumption of a direct proportionality between the total frequency change and the amount of deformation. This correction is generally quite small.

In view of the difficulty in obtaining exactly the same modulus change in two different crystals, even for the same per cent deformation, it cannot be claimed that there are any significant differences between the modulus changes observed for crystals Nos. 18–22. It should be noted that, in contrast to the results reported by Frankl, there is no substantial difference between a crystal irradiated at liquid-nitrogen temperature and then warmed up in the dark (No. 21) and one irradiated and strongly illuminated at liquid-nitrogen temperature before warming (No. 22). The smaller modulus change in specimen No. 23 must, however, be regarded as significantly different. This crystal was irradiated in the usual way, but during illumination with the arc lamp the water-cell heat-filter was removed and the liquid air in the low-temperature box allowed to boil away. In this way the crystal was slowly warmed up to a temperature somewhat less than room temperature over the course of an hour while it was simultaneously subjected to strong illumination.

It was observed that very much less color is produced by the same X-ray dose when a crystal is arribiated at 78°K instead of at 180°K or room temperature. Furthermore, the color produced at either 180°K or 78°K cannot be bleached appreciably at the temperature of irradiation even under prolonged exposure to strong illumination. Among the crystals listed in Table 3, bleaching was effected only on crystal No. 23.

Other Alkali Halides

In addition to the work on NaCl, modulus and damping measurements were also made during irradiation of KCl and LiF crystals. The observed response of the modulus and damping of KCl to X-irradiation was similar in all respects to that of NaCl. The decrement of plastically deformed LiF, however, is substantially less than that of NaCl and KCl, while the response of both its modulus and damping to X-irradiation is much slower. The resulting damping change is also small, as is to be expected in view of the fact that plastic deformation produces only a small increase in damping. Nevertheless, the magnitude of the modulus change upon irradiation seems to be comparable with that observed in both NaCl and KCl.

4. DISCUSSION

The modulus measurements on cold-worked crystals show clearly that the modulus increase produced by irradiating NaCl crystals with X-rays corresponds exactly to the elimination of the modulus decrease (Köster effect) produced by plastic deformation. The Köster effect is known to be due to the presence of mobile dislocation loops produced during deformation,[7] i.e. to the effect described by equation (1). The radiation-induced modulus increase must then result from the restraint of the motion of these dislocation loops, either through regrouping of the loops in the dislocation network into more stable configurations or by the pinning down of the loops at a finite number of points by the products of irradiation. Since X-irradiation does not result in any appreciable gross heating of the crystal structure, it is difficult to see how the irradiation can produce a regrouping of dislocations. Consequently the modulus increase may be most reasonably ascribed to the formation of pinning points along dislocation loops; it may be that these pinning points are vacancies or clusters of vacancies located along the dislocations.

An attempt will now be made to calculate the shape of the curves of modulus vs. radiation dose with the aid of a number of simplifying assumptions. Let ϕ be the fractional decrease in modulus (i.e. the modulus defect) in any given element of volume of the crystal due to the oscillating dislocation loops. Correspondingly, Φ will designate the modulus defect of the crystal, resulting from the dislocations. (This definition is then consistent with equation 4.) Let P represent the total number of pinning points per unit volume created by irradiation, n be the number of pinning points per unit length of dislocation line (assumed for simplicity to be equally spaced), N be the total length of dislocation line per unit volume, and x represent depth below the irradiated surface. Since the number of pinning points is, presumably,

a function of both dose (measured by the time of irradiation, t) and depth, we write $P(t,x)$. The linear density of pinning points as a function of dose and depth is

$$n(t,x) = n_0 + P(t,x)/N \tag{5}$$

where n_0 is the number of pinning points per unit length of dislocation line present before irradiation. Presumably the number n_0 represents, primarily, points where three dislocation lines intersect. Since n varies with both t and x, the modulus defect ϕ of an element of volume of the crystal will depend on both t and x. The modulus defect for the whole crystal, $\Phi(t)$, observed at any time t will then be the average of the modulus defect in each layer of the crystal, providing that $\phi \ll 1$ everywhere. Thus

$$\Phi(t) = \frac{1}{b}\int_0^b \phi(t,x)\,dx \tag{6}$$

where b is the thickness of the crystal in the direction of the incident radiation.

In order to express $\phi\,(t,x)$ in terms of $n(t,x)$ we may make use of the theory of the decrease in modulus due to dislocation loops devised by Mott and Friedel. Since $n = l^{-1}$, equation (1) becomes

$$\Delta\mu/\mu = N/n^2\xi'$$

which, as discussed in the appendix, may be written as

$$\phi = -\frac{\Delta s_{11}}{s_{11}} = \frac{N}{n^2\xi} \tag{7}$$

where ξ is a slowly-varying function of n whose value is about 2.5. Substituting equations (5) and (7) into (6), we obtain,

$$\Phi(t) = N\int_0^b \frac{dx}{b\xi\,(n_0 + P(t,x)/N)^2} \tag{8}$$

if ξ is taken as essentially constant. Correspondingly, Φ_0, the value of Φ prior to irradiation, is given by

$$\Phi_0 = N/\xi n_0^2. \tag{8a}$$

To carry the calculation further requires the introduction of more detailed assumptions about $P(t,x)$. The following two assumptions will be considered.

Assumption I: The number of pinning points created by the irradiation is assumed to be proportional to the number of F centers created. Now, it is known from optical measurements[6] that, at all depths in the crystal, the number of F centers per unit volume increases nearly linearly with irradiation time in the range of X-ray dosage required to bring the modulus increase very close to saturation.* Thus it is possible to introduce the simplification that

$$P(t,x) = f(x)\cdot t \tag{9}$$

where $f(x)$ gives the dependence of the rate of coloring on depth. It was also observed in the optical measurements[6] that the initial rate of formation of F centers is essentially the same in annealed crystals as in crystals deformed various amounts before irradiation. Consequently, $f(x)$ may be taken to be essentially the same in all the crystals which are being considered here. Equation (8) combined with (8a) then becomes

$$\frac{\Phi(t)}{\Phi_0} = \frac{1}{b}\int_0^b \frac{dx}{(1 + tf(x)/Nn_0)^2} \tag{10}$$

Thus the relative modulus defect, $\Phi(t)/\Phi_0$, depends on irradiation time and on the previous history of the crystal only through variable t/Nn_0. It is therefore anticipated that curves of Φ/Φ_0 vs. log (irradiation time) for different crystals should differ from each other only by a translation along the log-time axis (i.e. by a change in time scale). As shown in Fig. 5, this prediction is indeed verified within experimental error† for crystals subjected to varying amounts of deformation and recovery.

If the constant C is arbitrarily defined as the change in time scale required to bring all of the Φ/Φ_0 vs. log-time curves into coincidence with the curve for crystal No. 6, the quantity C will be proportional to $(Nn_0)^{-1}$. Utilizing this result and equation (8a), we can evaluate quantities proportional to N and n_0 for each crystal in terms of the known quantities C and Φ_0. Thus,

$$\left.\begin{aligned} N &\approx \Phi_0^{1/3}\,C^{-2/3} \\ l_0 = n_0^{-1} &\approx (C\Phi_0)^{1/3} \end{aligned}\right\} \tag{11}$$

Values of these quantities are given in Table 4 under the heading "Assumption I" for a number of crystals having different mechanical histories.

Assumption II: The fact that optical measurements show an initial rate of formation of F centers which is essentially independent of the state of deformation or anneal of the specimen implies that F centers are not formed at dislocations during irradiation‡. The

* In the optical measurements (reference 6) direct irradiation was used, in contrast to the present experiments in which the specimen was translated in front of the X-ray beam. Consequently a 10-min irradiation in the present experiments is equivalent to only 2 min in the optical experiments.

† It should be noted that the experimental error in determining $\Phi(t)$ is largest when $\Phi(t)$ approaches zero, because of the difficulty in determining the exact saturation value of the modulus.

‡ The interpretation of these optical data is presented in greater detail elsewhere.[6]

VOL. 4 1956

modulus increase resulting from X-irradiation is supposed to arise, however, from the pinning of dislocations by the action of the absorbed radiation. It is therefore conceivable that the modulus increase is due to *direct* interaction between the products of the irradiation (excitons and/or free electrons and holes) and dislocations, even though F centers are not primarily formed in this way. If this were the case, the density of pinning points P created by the irradiation would not be proportional to the number of F centers (as in Assumption I) but rather to the density of dislocation lines N. We may therefore state, for Assumption II, that equation (9) still applies, except that $f(x)$ is no longer independent of the histories of the various specimens, but rather that it is proportional to N. The result obtained under Assumption I, that the curves of $\Phi(t)/\Phi_0$ vs. log (irradiation time) for crystals given different prior treatments are displaced from each other by translation along the log-time axis, is therefore still valid under Assumption II. However, the relative shift C of the curves is now proportional to n_0^{-1} and independent of N (since the proportionality of $f(x)$ to N cancels this quantity out of equation 10). Under these conditions, we obtain for Assumption II, in place of equations (11),

$$\left.\begin{aligned} N &\approx \Phi_0 C^{-2} \\ l_0 = n_0^{-1} &\approx C \end{aligned}\right\} \qquad (12)$$

Values of the quantity $\Phi_0 C^{-2}$ for various crystals are given in Table 4, under the heading "Assumption II," while the quantity C itself is already listed in an earlier column.

A choice between the two assumptions just discussed may be made on the basis of a comparison of numbers proportional to N and l_0 calculated in terms of these assumptions. For example, when the quantities $\Phi_0^{1/3} C^{-2/3}$ for different crystals are compared, one finds that interpretation of the data in terms of Assumption I leads to the conclusion that N increases roughly in proportion to the amount of deformation and decreases somewhat as recovery is allowed to proceed. The values of $(C\Phi_0)^{1/3}$ show that l_0 is very nearly the same in all cases except one, viz. that of crystal No. 10. This crystal was evidently either deformed at a substantially different rate or else was very different in its history prior to deformation. Its large decrement (15×10^{-3} as against a value of 4×10^{-3} for crystal No. 6) as well as its large Φ_0-value are consistent with the large value of l_0.

On the other hand, interpretation of the data in terms of Assumption II leads to numerical values which are difficult to reconcile with the prior treatments received by the various crystals. A comparison of $\Phi_0 C^{-2}$ for crystals Nos. 5 and 9 shows that N is required to decrease by a factor greater than 10 during recovery from 180 min to 5760 min for specimens deformed very nearly the same amount. It is difficult to reconcile such a large decrease in N as the result of this recovery with the fact that such recovery does not greatly affect other properties of the material (such as X-ray line broadening) which are sensitive to dislocation density. The large difference in values of $\Phi_0 C^{-2}$ for crystals No. 6 and 10 is also difficult to explain, since the deformations and recovery times of these two crystals are very nearly the same. Finally, according to Assumption II, N would vary much faster than linearly with the amount of deformation. This result also does not seem reasonable. In general, then, it is seen that Assumption I leads to the most satisfactory agreement between the calculated numbers proportional to N and l_0 and the histories of the specimens.

Evaluation of the integral in equation (10) requires knowledge of the form of $f(x)$. In terms of Assumption I, $f(x)$ should have the same form as the variation in the density of F centers with depth below the irradiated surface. This variation has been determined experimentally and found to be roughly proportional to the rate of absorption of X-ray energy at each depth in the crystal.[18] The functional form of this depth dependence is rather complex, but under the conditions of irradiation used in the present experiments,

TABLE 4. Analysis of the modulus changes in cold-worked NaCl crystals

Crystal No.	Def. %	Room temperature recovery (min)	$\Phi_0 \times 10^2$	C	Assumption I		Assumption II	$N\beta^{2/3}$ (cm$^{-2}\times 10^{-8}$)	$l_0\beta^{-1/3}$ (cm$\times 10^6$)
					$\Phi_0^{1/3}C^{-2/3}$	$(C\Phi_0)^{1/3}$	$\Phi_0/C^2 \times 10^3$		
6	4.20	1700	1.68	1.00	0.258	0.256	16.8	32.0	3.61
10	4.08	1440	5.02	2.47	0.201	0.505	8.22	25.0	7.04
5	2.14	180	1.01	1.65	0.154	0.255	3.68	19.2	3.61
9	2.00	5760	0.495	3.79	0.068	0.265	0.343	8.5	3.75
4	(as received)		0.413	3.79	0.067	0.250	0.287	8.3	3.53

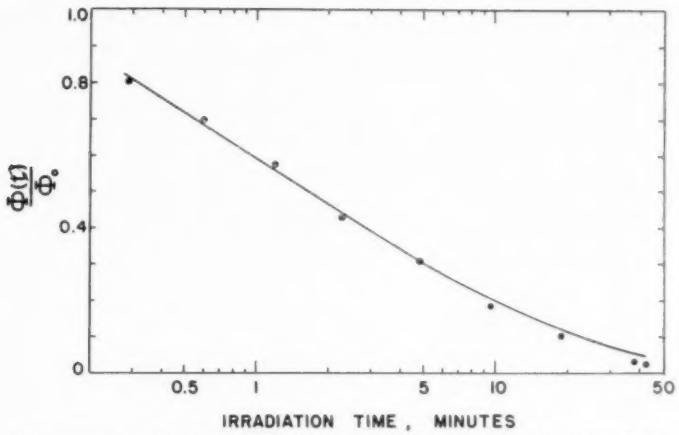

FIG. 6. Comparison of calculated and observed relative modulus defect for crystal No. 6. Curve, calculated. Points, experimental.

may be roughly approximated over a substantial range of depths by an exponential. Hence we write

$$f(x) \cong Ae^{-\gamma x} \tag{13}$$

where γ is the effective absorption coefficient of X-rays in the crystal. Making this substitution in equation (10), the integration may be carried out to obtain

$$\frac{\Phi(t)}{\Phi_0} = \frac{1}{\gamma b}\left\{\frac{1}{1+Kt} - \frac{1}{1+Kte^{-\gamma b}} + \ln\frac{1+Kte^{-\gamma b}}{(1+Kt)e^{-\gamma b}}\right\} \tag{14}$$

where $K = A/Nn_0$. The expression on the right-hand side of equation (14) has the property that, in a plot of $\Phi(t)/\Phi_0$ vs. log (irradiation time), the factor γ determines the shape of the curve while K only determines its position along the log-time axis. The best fit of equation (14) to the data of Fig. 5 is obtained with $\gamma = 9.5$ cm^{-1}. Fig. 6 shows the theoretical expression fitted to data for crystal No. 6, using this value of γ and $K = 1.76$ min^{-1}. Values of K for the other crystals are proportional to the values of C given in Table 4.

The value of γ obtained by means of this analysis agrees, within experimental error, with a rough value obtained from optical measurements on similarly irradiated crystals. It is also equal to the absorption coefficient of NaCl for X-rays of wavelength 0.55 Å. This wavelength falls close to that for maximum intensity in the continuous spectrum of the X-rays used.

Assumption I may be expressed by the statement that β F centers are formed for each pinning point created by irradiation. Then, according to the assumptions of equations (9) and (13), the number of F centers generated per unit volume per unit time at depth x is $Be^{-\gamma x}$, where $B = \beta A$. The quantity B may be obtained from optical data on the rate of formation of F centers at a given depth in a rock-salt crystal irradiated in the same way as the modulus specimens. From such data[6] B is found to be 1.5×10^{15} cm^{-3} sec^{-1}. The definition of K and equation (8a) provide two equations in N and n_0, which when solved for these quantities give

$$\left.\begin{aligned} N &= (B^2\xi\Phi_0/\beta^2K^2)^{1/3} \\ l_0 = n_0^{-1} &= (B\xi K\Phi_0/B)^{1/3} \end{aligned}\right\} \tag{15}$$

Since all the quantities on the right-hand sides of the above equations are known, except β, the quantities $N\beta^{2/3}$ and $l_0\beta^{-1/3}$ may be determined from the experimental results. Values for these quantities are displayed in the final columns of Table 4, calculated with $\xi = 2.5$ (see Appendix).

Comparison of the values of $N\beta^{2/3}$ and $l_0\beta^{-1/3}$ presented in Table 4 for crystals Nos. 5 and 9 suggests that the annealing out of the modulus defect produced by cold-working results from a decrease in N, and that l_0 remains about constant. This result is in contrast to the suggestion previously advanced,[17] according to which this recovery effect is the result of rearrangement of the dislocation network generated by deformation into a more stable configuration, i.e. that recovery results from a decrease in l rather than a decrease in N. Further experiments along these lines would be most desirable.

Values for β, the number of F centers per pinning point, which fall in the range from 1 to 100, would appear to be reasonable. For crystal No. 6 (deformed 4%) N values of 3×10^9 and 1×10^8 cm^{-2} and l_0 values of 100 and 500 atomic distances correspond to $\beta = 1$ and 100 respectively. A comparison of these results with Harper's estimates of dislocation densities

VOL. 4 1956

in lightly cold-worked iron,[19] favors values of β near unity; on the other hand, to obtain a reasonable value for N for the as-received crystal (No. 4, Table 4) would require a relatively high value for β.

Since Assumption II above has been ruled out, the results of the preceding analysis support the hypothesis already developed on the basis of optical data,[6] viz. that vacancies are not generated at dislocations during short-time X-irradiation, except in a layer of the specimen less than 0.01 cm thick adjacent to the irradiated surface (the region of "slow-type" coloring). This thin layer near the surface does not appreciably influence the observed modulus defect which derives from the entire volume of the crystal, as demonstrated in these experiments.

If vacancies which produce the pinning of dislocations during irradiation are not generated at dislocations, what then is their source? According to Frankl and to Seitz,[1] positive-ion vacancies, liberated from vacancy pairs (or larger aggregates) when the negative-ion vacancy of a pair becomes an F center, may migrate to the dislocation lines, where they may act as pinning points either individually or after condensation into clusters. It appears that the jump-frequency of positive-ion vacancies in NaCl at room temperature is great enough to allow vacancies liberated in this way to reach dislocations.*

Since the above mechanism of dislocation pinning involves vacancy diffusion, no modulus change is to be expected when irradiation and modulus measurement are *both* conducted at low temperatures. If, as in the present experiments, a crystal is irradiated at low temperature and warmed up without first bleaching out the color centers, the usual modulus change may still be observed at room temperature. This is due to the fact that dissociation of vacancy pairs will have occurred during irradiation at the low temperature, leaving the positive-ion vacancies free to migrate to dislocations during the warm-up period. This explanation accounts for the results of the low-temperature experiments on crystals Nos. 19 and 21 (Table 3). Since there is no appreciable bleaching of F centers formed at 78°K or 180°K during illumination at the temperature of irradiation, it is no surprise that the same modulus change is obtained even when the specimens are illuminated before warm-up (crystals Nos. 20 and 22). Only in the case of illumination *during* slow warm-up (crystal No. 23) is the room-temperature modulus change substantially reduced. This result may be explained if it is assumed that during warm-up the bleaching process takes place before the positive-ion vacancies become mobile. When an electron is released from a negative-ion vacancy by the action of light quanta, this vacancy regains its net charge and is then electrostatically attracted to the positive-ion vacancy with which it was originally associated. Thus, as soon as the specimen reaches the temperature range in which vacancy mobility begins, recombination will take place. The fact that there is a small change in modulus in crystal No. 23 shows that recombination is not complete, i.e. some vacancies escape and produce pinning. On the other hand, when warm-up is in the dark, there is no electrostatic attraction, so that positive-ion vacancies are free to migrate when the temperature becomes sufficiently high.

The decrease in damping due to irradiation seems to be due to the same cause as the increase in elastic modulus, i.e. to dislocation pinning. In view of the fact that substantial bleaching does not take place at liquid-nitrogen temperature, it is difficult to see why the damping was not suppressed in Frankl's experiment in which a specimen was first irradiated and illuminated at 78°K, then warmed to room temperature. Since Frankl illuminated his crystal with an ordinary incandescent lamp placed close to the specimen,[20] it is suggested that the light-source employed by Frankl warmed the crystal up to the range of temperatures where a substantial amount of bleaching could take place.

5. CONCLUSIONS

1. Pinning points on dislocations are created during X-irradiation of an alkali halide crystal at room temperature through the release of vacancies within the volume of the crystal and the migration of these vacancies to dislocations.

2. Relatively few pinning points are produced in a crystal irradiated at 78°K and slowly warmed up under strong bleaching illumination. Under these conditions vacancies of opposite sign, which were originally dissociated through the action of the radiation, may recombine.

3. The dislocation density calculated from curves of modulus vs. irradiation time is of the order of 10^8–10^9 cm^{-2} for a crystal deformed 4%; the corresponding mean length of free dislocation segment is of the order of 100 atom distances. Upon recovery at room temperature, there appears to be a substantial decrease in dislocation density.

4. The pinning of dislocations by vacancies is by no means restricted to ionic crystals. Recent experiments show that excess vacancies produced in metals by

* Positive-ion vacancies have a significantly lower activation energy for migration than negative-ion vacancies in most alkali halides.[1]

neutron irradiation[21] and by quenching from elevated temperatures[22] also result in dislocation pinning.

ACKNOWLEDGMENTS

One of the authors (R. B. G.) received partial financial support during the course of this work from fellowships of the General Electric Company and the Dow Chemical Company. The basic equipment for the measurement of elastic constants was purchased through the Higgins Fund.

This paper represents part of a dissertation submitted by R. B. Gordon in partial fulfillment of the requirements for the degree of Doctor of Engineering in the School of Engineering at Yale University.

Appendix

The factor ξ' which appears in equation (1) is given by[9]

$$\xi' = \frac{3}{\zeta\pi} \ln\left(\frac{r_1}{r_0}\right)$$

where $\zeta = 1$ for a screw dislocation and $\zeta = 1 + \nu$ for an edge dislocation, ν being Poisson's ratio. This result applies to an isotropic medium. The quantities r_0 and r_1 are the radii of the inner and outer surfaces, respectively, of the doubly connected region used in calculating the stress field around a dislocation line. Since in the case of a short segment of dislocation of length l the calculation of the stress field should only be carried out to a distance of about l from the dislocation line, r_1 may be taken as approximately equal to l. The value to be taken for r_0 is somewhat more uncertain, but according to Cottrell[23] should be chosen to be several times the Burgers vector, i.e. about 10^{-7} cm. In a real crystal the dislocation network will be made up of segments having partly a screw character and partly an edge character; nevertheless, ζ will still be of the order of unity, since $\nu \cong 0.3$. Because it is but a slowly varying function of l, ξ' is taken to be a constant in the present calculations. In the specimens being considered, l has values ranging between 10^{-5} and 10^{-6}, so that ξ' will be approximately equal to 3.

The elastic modulus which is measured in the present case is $s_{11}{}^{-1}$, whereas the shear modulus μ on the {110} slip planes is given by

$$\mu^{-1} = \tfrac{1}{2}s_{44} + s_{11} - s_{12}$$

It is this shear modulus which properly belongs in equation (1) if an attempt is to be made to introduce anisotropy. Even though it is known that the motion of dislocation loops does not affect the cubical compressibility $3(s_{11} + 2s_{12})$, there is not enough information about the effect of dislocation motion on the compliance constant s_{44} to make possible a calculation of the relation between a change in μ and a change in the measured compliance s_{11}. Detailed analysis of the atomic forces which surround the dislocation loops would be required to obtain this information.

Instead, it seems desirable to adhere to an isotropic approximation. The measured modulus $s_{11}{}^{-1}$ corresponds to Young's modulus, Y, and

$$\frac{\Delta Y}{Y} = \left(1 - \frac{\mu}{\mu + 3k}\right)\frac{\Delta\mu}{\mu}$$

where k is the bulk modulus. Thus, by analogy to equation (1),

$$-\frac{\Delta s_{11}}{s_{11}} = \frac{Nl^2}{\xi}$$

where

$$\xi = \left(1 - \frac{\mu}{\mu + 3k}\right)\xi'$$

Using the measured values of s_{11}, s_{12}, and s_{44} to obtain values for μ and k, it is found that $\xi \cong 2.5$.

REFERENCES

1. F. SEITZ *Rev. Mod. Phys.* **26,** 7 (1954)
2. W. D. KUSNETZOW and W. A. SEMENTZOW *Z. Exper. Theor. Physik* (Russ.) **2,** 199 (1932)
3. M. N. PODASCHEWSKY *Phys. Z. Sowjet.* **8,** 81 (1935)
4. YIN-YUAN LI *Acta Met.* **1,** 455 (1953)
5. D. R. WESTERVELT *Acta Met.* **1,** 755 (1953)
6. R. B. GORDON and A. S. NOWICK *Phys. Rev.*, **101,** 977 (1956)
7. D. R. FRANKL *Phys. Rev.* **92,** 573 (1953)
8. N. F. MOTT *Phil. Mag.* **43,** 1151 (1952)
9. J. FRIEDEL *Phil. Mag.* **44,** 444 (1953)
10. J. MARX *Rev. Sci. Instrum.* **22,** 503 (1951)
11. W. H. DUERIG and J. J. MARKHAM *Phys. Rev.* **88,** 1043 (1952)
12. K. SAKAGUCHI and T. SUITA *Tech. Repts. Osaka Univ.* **2,** 177 (1952)
13. ESTERMANN, LEIVO, and STERN *Phys. Rev.* **75,** 627 (1949)
14. T. A. READ *Trans. Amer. Inst. Min. Met. Eng.* **143,** 30 (1941)
15. J. WEERTMAN and J. S. KOEHLER *J. Appl. Phys.* **24,** 624 (1953)
16. A. S. NOWICK *J. Appl. Phys.* **25,** 1129 (1954)
17. A. S. NOWICK *Acta Met.* **3,** 312 (1955)
18. MADOR, WALLIS, WILLIAMS, and HERMAN *Phys. Rev.* **96,** 617 (1954)
19. S. HARPER *Phys. Rev.* **83,** 709 (1951)
20. D. R. FRANKL, private communication.
21. D. O. THOMPSON, D. K. HOLMES, and T. H. BLEWITT *J. Appl. Phys.* **26,** 1188 (1955)
22. R. MADDIN and A. H. COTTRELL *Phil. Mag.* **46,** 735 (1955)
23. A. H. COTTRELL *Dislocations and Plastic Flow in Crystals* (Oxford Univ. Press, London, 1953)

VOL. 4 1956

CRYSTAL STRUCTURES OF LITHIUM-MAGNESIUM ALLOYS AT LOW TEMPERATURES*

C. S. BARRETT†

The crystal structures of Li-rich Li-Mg alloys uniquely offer the possibility of testing theories of the influence of valence-electron concentration on hexagonal axial ratio in the range 1.0–1.16 electrons per atom. The body-centered cubic phase at 78°K has $a_0 = 3.475$ Å for Li + 13·4 atomic per cent Mg and 3.474 for 19.7 atomic per cent Mg, and the face-centered cubic phase at 78°K resulting from cold work has $a_0 = 4.381$ and 4.375 Å respectively for the same compositions. The phase appearing on simple cooling was fully accounted for as close-packed hexagonal with stacking faults and with a and c lattice dimensions at 78°K as follows, respectively, for the atomic per cent Mg compositions listed: 4.6%, 3.099, 5.074 Å; 8.8%, 3.098, 5.063; 12.5%, 3.110, 5.079 and 3.107, 5.073; 13.4%, 3.098, 5.073 and 3.098, 5.073; 16.3%, 3.104, 5.083. Distortion of c/a to less than 1.633 by stresses, proposed by Goodenough, was observed in none of the alloys; the mean axial ratio was 1.6356. Difficulties of developing a quantitative theory are pointed out.

STRUCTURES CRISTALLINES DES ALLIAGES LITHIUM-MAGNESIUM AUX BASSES TEMPERATURES

Les structures cristallines des alliages Li-Mg riches en Li offrent la possibilité de vérifier les théories de l'influence de la concentration en électrons de valence sur le rapport des axes hexagonaux dans le domaine de 1,0 à 1,16 électrons par atome. Pour la phase cubique centrée à 78°K, $a_0 = 3{,}475$ Å pour Li + 13,4% at. Mg et $a_0 = 3{,}474$ pour 19,7% at. Mg.

La phase cubique à faces centrées à 78°K résultant d'un écrouissage a des axes respectifs de $a_0 = 4{,}381$ et 4,375 Å pour les mêmes compositions.

La phase apparaissant au cours du simple refroidissement a été trouvée hexagonale compacte avec des défauts d'empilement et des dimensions a et c qui, à 78°K, sont les suivantes pour les différentes compositions: 4,6%, 3,099, 5,074 Å; 8,8%, 3,098, 5,063; 12,5%, 3,110, 5,079 et 3,107, 5,073; 13,4%, 3,098, 5,073 et 3,098, 5,073; 16,3%, 3,104, 5,083.

La distorsion de c/a jusqu'à moins de 1,633 par tension, proposée par Goodenough, n'a été observée dans aucun des alliages étudiés; le rapport d'axes moyen est 1,6356. Les difficultés de développer une théorie quantitative sont exposées.

KRISTALLSTRUKTUREN VON LITHIUM-MAGNESIUM-LEGIERUNGEN BEI TIEFEN TEMPERATUREN

Die Kristallstrukturen der Li-reichen Li-Mg-Legierungen bieten eine einzigartige Möglichkeit zur Nachprüfung von Theorien über den Einfluss der Valenzelektronenkonzentration auf das hexagonale Achsenverhältnis im Bereich zwischen 1,0 und 1,16 Elektronen pro Atom. Die kubisch-raumzentrierte Phase hat bei 78°K für Li + 13,4 Atomprozent Mg die Gitterkonstante $a_0 = 3{,}475$ Å und für 19,7 Atomprozent Mg $a_0 = 3{,}474$ Å. Die kubisch-flächenzentrierte Phase, die bei Kaltverformung entsteht, weist für dieselben Zusammensetzungen Werte von $a_0 = 4{,}381$ bezw. 4,375 Å auf. Die Struktur der bei einfachem Abkühlen auftretenden Phase wurde genau bestimmt; sie ist hexagonal dichtest gepackt mit eingelagerten Stapelfehlern und hat bei 78°K für die angegebenen Mg-Atomprozentgehalte die folgenden Gitterkonstanten a und c: 4,6%, 3,099, 5,074 Å; 8,8%, 3,098, 5,063; 12,5%, 3,110, 5,079 und 3,107, 5,073; 13,4%, 3,098, 5,073 und 3,098, 5,073; 16,3%, 3,104, 5,083. Bei keiner der Legierungen wurde beobachtet, dass c/a, wie von Goodenough vorgeschlagen, durch Spannungen auf weniger als 1,633 gestaucht wird; das mittlere Achsenverhältnis betrug 1,6356. Abschliessend wird auf die der Entwicklung einer quantitativen Theorie entgegenstehenden Schwierigkirten hingewiesen.

1. INTRODUCTION

A method of computing lattice constants from powder-diffraction patterns of hexagonal crystals that contain many stacking faults is proposed which makes use of current knowledge of the effects of faults on diffraction lines. Since unit-cell axial ratios in hexagonal alloys have lately become the subject of theoretical investigations aimed at prediction of the ratios and interpretation of them in terms of Brillouin zone concepts, it is of particular importance to obtain observed ratios in the range of electron concentration between 1 and about 1.14 valence electrons per atom. The only known alloy system covering this range is the Li-rich Li-Mg solid solution, in which a portion of the material transforms to faulted close-packed hexagonal structure from body-centered cubic on cooling to low temperatures, and to faulted face-centered cubic during deformation at low temperatures.[1–3] Patterns from these alloys (both from the

* *Received December* 27, 1955.

† Institute for the Study of Metals, The University of Chicago, Chicago, Illinois.

current and the earlier investigations) were analyzed, with the results reported herein.

Preparation of Samples

The Li-Mg samples were prepared from C.P. electrolytic magnesium of 99.88% purity from Dow Chemical Co., and C.P.-grade lithium of purity estimated spectrographically as 99.9%. Each sample was cut, weighed, and sealed in an iron capsule with a tight-fitting screw-cap while in a dry box filled with an argon atmosphere; after melting (with several inversions of the capsule) and quenching, each alloy was homogenized 20 hr at 180–200°C, then cut from the surrounding iron on a lathe, pounded into a recess in the specimen holder of the X-ray instrument, scraped flat and clean, and then annealed under oil (15 min at 130–140°C) to produce a strain-free fine-grained state. The holder was then fastened into the vacuum chamber of the cryostat, while the specimen was covered with a slight film of octoil to limit tarnishing. Additional samples were prepared without homogenizing and strain-relief annealing; the results with these are perhaps less reliable as to the absolute value of the parameters, but are worth reporting.

Experimental Methods

The specimens were mounted in a recess in a copper block that was surrounded by radiation shields and centered in an evacuated cryostat mounted on a precision X-ray spectrometer, the details of which are given elsewhere.[4] Filtered copper (or occasionally cobalt) characteristic radiation from a current- and voltage- stabilized X-ray tube entered and left the cryostat through plastic windows and slits in the radiation shields, and were recorded automatically by a Geiger counter connected conventionally to a recorder.

A stainless-steel rod entered the cryostat through a ball-and-socket joint and sylphon bellows. The end of the rod was shaped and sharpened so that it could be used to cut off an oxide layer from the specimen, to cold-work the specimen to a depth of the order of a millimeter, or to rub the surface of the specimen smooth in preparation for X-raying.

Nelson-Riley extrapolation was used for lattice-constant determinations, and probable errors were estimated from the uncertainties encountered in making the extrapolation.

The Transformations of Li-Mg Alloys

The ordinary BCC phase in these alloys transforms on cooling to liquid-nitrogen temperature (78°K) provided the magnesium content does not exceed about 40 weight per cent, according to the earlier studies.[2] This is confirmed in the present series, since the 35.2% alloy transformed and the 45.2% alloy did not. Both 35.2 and 45.2% magnesium alloys transformed to FCC when cold-worked at 78°K. A 54.5% alloy that had not been homogenized or annealed failed to transform on cooling to liquid-nitrogen or liquid-helium temperatures or on cold working at 78°K or at 37°K, but did contain some FCC material after cold working at 4°K. The FCC phase was retained unchanged in amount as this specimen warmed up to at least 230°K, but had reverted fully to the BCC phase by the time the temperature had reached 20°C, about as expected from earlier results.

Lattice Constants of the BCC and FCC Phases

An alloy of Li + 35.2% Mg (13.4 atomic per cent) cold worked and X-rayed at liquid-nitrogen temperature gave lattice constants for BCC and FCC phases as follows:

$$a_{\mathrm{BCC}} = 3.475 \pm 0.002\ \text{Å}$$

$$a_{\mathrm{FCC}} = 4.381 \pm 0.003\ \text{Å at } 78°\text{K},$$

the unit-cell volumes being $V_{\mathrm{BCC}} = 41.96\ \text{Å}^3$ $V_{\mathrm{FCC}} = 84.08$, the volume per atom changing less than the error of the measurements during the transformation.

An alloy of Li + 46.2% Mg (19.7 atomic per cent) cold worked and X-rayed at liquid-nitrogen temperature gave

$$a_{\mathrm{BCC}} = 3.474 \pm 0.002\ \text{Å}$$

$$a_{\mathrm{FCC}} = 4.375 \pm 0.003\ \text{Å at } 78°\text{K},$$

$$V_{\mathrm{BCC}} = 41.93\ \text{Å}^3, \qquad V_{\mathrm{FCC}} = 83.74\ \text{Å}^3,$$

again a change of volume per atom less than the experimental error. The wavelength of CuKα used throughout the work was 1.54178 Å.

Lattice Constants of the CPH Phase

The Nelson-Riley plot for the BCC phase was used as the plot for correcting the remaining lines of the patterns. It was found that all lines appearing with appreciable intensity in the simply-cooled specimens could be given indices appropriate to a close-packed hexagonal structure. The strength and sharpness of the hexagonal 002, 110, 112, and sometimes 004 peaks relative to the others suggested that the hexagonal phase contained numerous stacking faults, and this was confirmed by the breadth, the asymmetry, and the shifted position of the hexagonal 100 and 101 peaks. The axial ratio of the CPH phase was determined from peaks that were unwidened and unshifted

VOL. 4 1956

by the faults, namely, 110 and 112, omitting 002, since this was too close to BCC 110 for good resolution, and using the 002 and the very weak 004 peaks as separate approximate checks on the determinations. (This procedure had led to lattice constants different from those originally proposed[2, 3] for lithium, but takes account of the effects of faults on the pattern to aid in its interpretation.)

An objection may be anticipated with regard to the present method of interpreting the patterns from alloys that have simply been cooled: if an alloy contained an appreciable amount of FCC phase in addition to the CPH, and if 220 and 311 FCC lines fell exactly on the 110 and 112 CPH lines, respectively, the FCC component would tend to make the CPH lines appear to be in the position for $c/a = 1.633$ and could mislead the investigator regarding the hexagonal axial ratio. The answer to this objection is that there is no evidence of any well-developed FCC phase in the cooled alloys, since the FCC 200 line is absent in these samples when they are not cold worked (although this line appears strongly after cold working); therefore it can be assumed that no appreciable FCC component is altering the position of the CPH lines on which the c/a ratio is based. The method was tested by cold working a CPH alloy of Cu-Ga of accurately known c/a ratio, and was found to be reliable.

The alloy of 35.2% Mg (13.4 atomic per cent) gave, in one run at 78°K,

$$a = 3.098, \quad c = 5.073\,\text{Å}, \quad c/a = 1.6375$$

Table 1 lists the observed spacings as corrected by Nelson-Riley interpolation from BCC peaks using $a_{BCC} = 3.475\,\text{Å}$, and gives in the last column the spacings calculated for the above lattice constants.

The same alloy on a second run gave the same values (though the accuracy was not such as to lead one to expect this):

$$a = 3.098, \quad c = 5.073\,\text{Å}, \quad c/a = 1.6375.$$

The volume of the unit cell was 42.16 Å^3, greater than the calculated volume of the BCC cell by slightly more than estimated errors.

TABLE 1. Diffraction data for hexagonal phase in Li-35.2% Mg alloy cooled to 78°K, compared with calculated values for $a = 3.098$, $c = 5.073$ Å

HKL	I_{obs}	d_{obs}	d_{calc}
100	M	2.653	2.683
002	S	2.531	2.536
101	M	2.320	2.371
110	S	1.549	1.549
112	M	1.322	1.322
004	vw	1.267	1.268

Data read from the charts of the earlier experiments[2] and corrected by an interpolation on a Nelson-Riley plot through the BCC data of the same chart, yielded the following results for 78°K:

Li—14.5% Mg (4.5 atomic per cent):

$a = 3.099, \quad c = 5.074\,\text{Å}, \quad c/a = 1.638$

Li — 25.27% Mg (8.8 atomic per cent) at 78°K:

$a = 3.098, \quad c = 5.063\,\text{Å}, \quad c/a = 1.634$

Li — 33.3% Mg (12.5 atomic per cent):

$a = 3.110, \quad c = 5.079\,\text{Å}, \quad c/a\ 1.633$

$a = 3.107, \quad c = 5.073\,\text{Å}, \quad c/a = 1.633$

Li — 40.6% Mg (16.3 atomic per cent):

$a = 3.104, \quad c = 5.083\,\text{Å}, \quad c/a = 1.637$

The probable error in the above values, unless noted otherwise, is estimated to be ± 0.001 to 0.003 in values of a, ± 0.002 to 0.005 in c, and ± 0.002 in c/a.

For comparison, we quote values for lithium we have obtained by the same methods[4] at 78°K:

$a_{BCC} = 3.491 \pm 0.002\,\text{Å} \quad V_{BCC} = 42.54\,\text{Å}^3$

$a_{CPH} = 3.111 \pm 0.001\,\text{Å} \quad c_{CPH} = 5.093 \pm 0.009$

$V_{CPH} = 42.69\,\text{Å} \quad c/a = 1.637 \pm 0.002.$

The c/a ratios for lithium and all the alloys are very close to the ideal value 1.633 for close-packed spheres, as might be anticipated from the presence of many faults in the structure. In fact, the deviations from 1.633 cannot be regarded as significant when judged by usual statistical methods. Using the "t test" for the significance of the deviation from 1.633 for the results of the seven alloy determinations (without regard to the sign of the deviation), one finds $t = 2.10$, which is less than the value $t = 2.44$ required in the significance test at the 5% level. Thus more than 5% of the times such seven determinations are made, mean deviations of at least this much would be expected in a normal distribution having a mean at 1.633. The mean of the seven alloy determinations is 1.6356, and is within estimated experimental error of the value for lithium. The value for CPH sodium[4] by the same method is 1.634 at 5°K.

Discussion

Current interest in these results lies in their relation to the electron theory of alloy phases, and to the question of whether distortion of a CPH unit cell from the ideal value of 1.633 can be viewed as the result of a distorting force arising from the interaction of the

Fermi surface with the Brillouin zone boundaries. It has been proposed by Goodenough[5] that distortion would result even in the absence of Brillouin zone overlap, when the Fermi surface approaches a Brillouin zone boundary. If one assumes a spherical Fermi surface, it would touch the Brillouin zone "A" face (which stands parallel to the c axis) when the electron concentration has increased to the value $\frac{2\pi}{9}\frac{c}{a} = 1.14$, for a unit cell with $c/a = 1.633$. As the electron concentration approaches this value, the "A" zone faces should, on this theory, be forced toward the center of the zone and the a crystal dimension enlarged; there should be no compensating effect at the "B" zone face (normal to the "A" face) since the "B" face is not reached until a considerably higher concentration is reached (1.36 electrons per atom, under the same assumptions, for $c/a = 1.633$). Thus the theory predicts a distortion of the axial ratio c/a to values less than 1.633 for electron concentrations somewhat less than those at which overlap into the next zone occurs.

McClure[6] recently re-examined this theory and the parent theory of Jones from which it developed, and concluded that basic modifications of them are needed. He pointed out that the local distortions of the lattice around solute atoms in alloys are neglected by earlier theories and that if these are considered there should be no Brillouin-zone effects, the lattice-distorting stress arising from adding electrons being cancelled by the change in stress due to the electrons already present. He notes, also, that other contributions to the stress might be expected from causes that have not been treated in the theory: "changes in the energy of the bottom of the band, Coulomb, exchange, and correlation energies, and energy of lattice vibrations."

Although McClure concluded that a different mechanism than that postulated by Jones and Goodenough must be operating to change the axial ratios in alloys, nevertheless his revised approach led qualitatively to the same conclusions as the older theories as to the relation of the band structure to the change in axial ratios for the one metal he examined. Detailed calculations covering Li-Mg alloys have not yet been made, either for conditions of overlap or approaching overlap, and calculations taking stacking faults into consideration are also missing. Just as faults widen some diffraction lines, they presumably would effectively blur the zone boundaries and therefore alter any effects based on overlap or approach to the boundaries. An added uncertainty stems from a lack of knowledge of the variation of effective mass of electrons moving in different crystallographic directions.

When alloy phases of CPH structure are surveyed,[7] it is seen that most of them exhibit marked variations of axial ratio with composition. Above the electron concentration of about 1.36 many CPH phases have a rapid drop in c/a with increasing concentration, which Raynor and Massalski attribute[8] to the effect of "A" face overlap, as Jones[9] did for ϵ-brass. Below this concentration the data are few at present, and the present results alone are available below 1.16; these, for electron concentrations from 1.0 to 1.163, indicate no distortion of c/a to less than 1.633 in any of the alloys (a distortion expected on Goodenough's theory) and a minor increase, hardly of statistical significance, to larger values than 1.633.

VOL. 4 1956

ACKNOWLEDGMENTS

We are indebted to T. B. Massalski and M. Cohen for helpful discussions and continued interest. The X-ray spectrometer has been furnished by the Physics Department of the University of Chicago; the cryostat was designed by E. Long, L. Meyer, C. B. Walker, and the author, and was constructed under the skilled supervision of T. J. O'Donnell and J. Getzholtz. Chemical analyses were carried out by Miss M. Batchelder; Y. Baskin assisted in the laboratory. This work was supported in part by Contract N6ori-02004 with the Office of Naval Research.

REFERENCES

1. C. S. Barrett *Phys. Rev.* **72,** 245 (1947).
2. C. S. Barrett and O. R. Trautz *Trans. Amer. Inst. Min. Met. Eng.* **175,** 579 (1948).
3. C. S. Barrett in *Phase Transformations in Solids*, Wiley, N.Y. (1950).
4. C. S. Barrett X-Ray Study of the Alkali Metals at Low Temperatures *Acta Cryst.*, in press.
5. J. B. Goodenough *Phys. Rev.* **89,** 282 (1953).
6. J. W. McClure *Phys. Rev.* **98,** 449 (1955).
7. T. B. Massalski in 1955 *ASM Symposium on Alloy Phases*, ASM, in press.
8. G. V. Raynor and T. B. Massalski *Acta Met.* **3,** 480 (1955).
9. H. Jones *Proc. Roy. Soc.* **A147,** 400 (1934); *Phil Mag.* **41,** 633 (1950).

ELASTIC AND PLASTIC BEHAVIOR OF THE FERRITE LATTICE IN A LOW-ALLOY STEEL*

H. C. VACHER, R. LISS, AND R. W. MEBS†

A specimen of normalized NE-9420 steel was loaded and unloaded in cycles at progressively higher loads. The first four cycles were alternately in tension and compression. The remaining eight were in tension. Lattice-strain measurements by the X-ray back-reflection method were made in seventeen directions with the specimen in the loaded and unloaded conditions. Analysis of the lattice compliances (strain-stress ratio) indicated that a transverse compressive stress and a shear stress were superposed on the axial stress. The following values gave the best agreement with the experimental results: Young's modulus 32×10^6 lb/in.^{2}, Poisson's ratio 0.41, transverse stress 13% of axial stress, and shear stress 26% of axial stress. The lattice elastic limit for negative compliances was higher than for positive compliances. Analysis of residual strains after plastic deformation indicated a compressive strain in the loading direction. The change in lattice spacing on release of load from the plastic range could be predicted from the lattice compliance, thus indicating that loading stresses can be computed for stresses exceeding the elastic limit.

COMPORTEMENTS ELASTIQUE ET PLASTIQUE DE RESEAU DE LA FERRITE DANS UN ACIER FAIBLEMENT ALLIE

Un échantillon dè l'acier normalizé NE 9420 a été soumis à des cycles de mise en charge pour des charges de plus en plus diverses.

Les quatre premiers cycles ont été effectués alternativement en tension et compression; les huit derniers, uniquement en tension.

Les mesures de déformation du réseau par la méthode des rayons X en retour ont été faites dans 17 directions avec et sans charge sur l'échantillon.

L'analyse des coefficients réticulaires (rapport déformation-tension) a montré qu'une tension de compression transverse et une tension de cisaillement étaient superposées à la tension axiale.

Les valeurs suivantes ont fourni le meilleur accord avec l'expérience:

Module de Young 32×10^6 livres/pouces^2

Rapport de Poisson 0,41

Tension transverse 13% de la tension axiale

Tension de cisaillement 26% de la tension axiale.

La limite élastique réticulaire pour des coefficients négatifs est plus élevée que pour des coefficients positifs.

L'analyse des tensions résiduelles après déformation plastique a montré une déformation de compression dans la direction de la charge.

La modification du paramètre réticulaire après libération de charge du domaine plastique a pu être prédite à partir du coefficient d'élasticité réticulaire.

Ce qui montre que les tensions de charge peuvent être assimilées à des tensions dépassant la limite élastique.

ELASTISCHES UND PLASTISCHES VERHALTEN DES FERRIT-GITTERS IN EINEM SCHWACH LEGIERTEN STAHL

Eine Probe aus normalisiertem Stahl NE-9420 wurde unter laufender Erhöhung der Last wechselweise be- und entlastet. Die ersten vier Wechsel fanden alternierend unter Zug und Kompression statt, die restlichen acht unter Zug. Mit dem Röntgenrückstrahlverfahren wurden an der Probe im belasteten und entlasteten Zustand in 17 Richtungen Messungen der Gitterverzerrungen angestellt. Eine genaue Analyse de "Gitter-Nachgiebigkeiten" (lattice compliances – Verhältnis Dehnung zu Spannung) zeigte, dass der Achsialspannung eine quergerichtete Druckspannung und eine Schubspannung überlagert sind. Die beste Übereinstimmung mit den experimentellen Ergebnissen gaben folgende Werte: Elastizitätsmodul 32×10^6 lb/in^2, Poisson-Zahl 0,41, Querspannung 13% der Achsialspannung, Schubspannung 26% der Achsialspannung. Die Elastizitätsgrenze des Gitters lag für negative Nachgiebigkeiten höher als für positive. Die Analyse der nach plastischer Verformung zurückbleibenden Verzerrungen zeigt eine Kompression in der Belastungsrichtung an. Die Änderungen im Gitterabstand bei der Entlastung aus dem plastischen Bereich konnten mit Hilfe dur Gitter-Nachgiebigkeiten richtig vorausgesagt werden, woraus hervorgeht, dass es möglich ist, die Lastspannungen, auch wenn sie oberhalb des elastischen Bereichs liegen, au berechnen.

* Received September 3, 1955; in revised form, January 3, 1956.

† National Bureau of Standards, Washington 25, D.C.

VOL. 4 1956

1. INTRODUCTION

For the past thirty years X-ray diffraction measurements of lattice strains have been used for the determination of stresses in metals. Recent reviews[1, 2, 3, 4] indicate that the relationship, as ordinarily interpreted, between lattice-strain measurements and body stresses (the type of stresses most important to the engineer) probably is an oversimplification and in some cases can lead to erroneous conclusions. It has also been apparent, however, that further investigations of lattice strains would give a better understanding of the stress distribution in polycrystalline metals.

There is general agreement that lattice-strain measurements can be used to compute body stresses in the surface of annealed material up to the beginning of plastic deformation determined by mechanical methods. Hyler and Jackson[4] and others point out that X-ray strain measurements do not agree with mechanical strain measurements in the plastic range under load or after release of load. Examination of data in two cases[5, 6] indicated that for specimens in tension the upper limit of the range of stress in which the equation

$$\left(\frac{\partial d/d}{\sigma_L}\right)_{\rho,\phi} = C \qquad (1)$$

was applicable depended on whether the measurements were made perpendicular or inclined to the surface. The upper-limit stress may also be referred to as the elastic limit stress. The compliance C corresponds to $1/E$ when ρ and ϕ are zero and σ_L is equal to σ_1.

The following symbols are used in this paper:

$\partial d/d$ Fractional change in lattice spacing taken as a measurement of lattice strain,
σ_L Stress in direction of loading,
ρ Angle between loading direction and direction of strain measurement,
ϕ Angle between surface normal and the plane, including the directions of loading and strain measurement,
C Lattice compliance (7),
E Young's modulus of elasticity,
D_W Diameter of the tungsten-222α_1 ring from cobalt radiation,
F Difference in radii of the tungsten-222α_1 and ferrite-310α_1 rings at a certain location in the rings,
θ Diffraction angle,
ϵ Strain,
ϵ_L Strain component in direction of loading,
ν Poisson's ratio,
K_T Proportionality constant, assuming that $\sigma_T = K_T \sigma_L$,
σ_T Transverse stress perpendicular to loading direction,
K_τ Proportionality constant, assuming $\tau = K_\tau \sigma_L$,
τ Shear stress in plane perpendicular to loading direction,
ϵ_D The fractional change in lattice spacing on release of load,
ϵ_A Strain under load,
ϵ_R Measured residual lattice strain,
σ_1 Maximum principal stress,
ϵ_{RL} Residual strain component in direction of loading.

For loads in excess of the range of equation (1), there is disagreement[1] on whether or not lattice strains remain constant or decrease with increases in the loading stress. This disagreement might be the result of different types of loading. Wood[5, 8] showed that on application of tensile loads, the lattice strains in fine-grain iron increased up to the elastic limit and then remained constant.

Many investigators have reported compressive stresses in the surface in the direction of extension (longitudinal) after removing tensile loads that exceeded the range of equation (1). Several investigators, particularly Wood[5] and Greenough[3, 9] have shown that in such cases different values of residual strain were obtained with different wavelengths of X-rays, and concluded that the apparent compressive body stresses were the result of a complex system of textural stresses[10] rather than body stresses caused by nonuniform plastic deformation. Certain results obtained by Greenough,[9] however, showed that residual lattice strains decreased after removal of a layer of 0.008 in. This indicated that deviations from the average textural stress across the cross-section were not random. More recently, Bateman[11] confirmed the findings of Wood and Greenough with respect to lattice strains varying with wavelength, but disagreed with Greenough that the effect resulted from the anisotropy of the elastic limit of individual crystals.

Wood[5, 8] reported a residual transverse compressive stress in addition to a residual longitudinal compressive stress in iron after tensile loading. The transverse stresses varied from 60% to 110% of the longitudinal stresses. Wood and Dewsnap[8] reported a transverse tensile component that was about equal to the longitudinal component under loads corresponding to elongations of 9.4% and 14.3%; however, for elongations of 21.2% to 31.5%

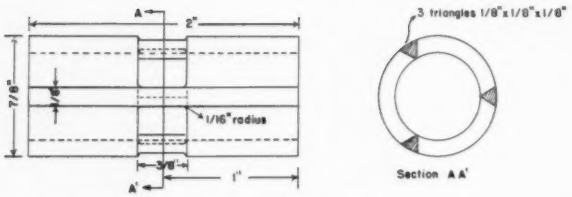

FIG. 1. Specimen

this transverse tensile stress was negligible. Greenough[9] also reported a residual transverse component that was about 20% of the longitudinal compressive component after a 6% elongation. It was not indicated whether or not an apparent transverse component was present in the elastic range. It should be remembered that in tensile loading the average transverse body stress must be zero, so that the apparent transverse tensile component reported is not a body stress.

The foregoing review shows a need for information on:

1. The directionality of the elastic limits.
2. Whether or not the lattice strain remains constant for loads in the plastic range.
3. Whether or not lattice strains indicate an apparent transverse stress in the elastic range for the condition of uniaxial loading.
4. The nature of the residual strains observed after plastic deformation, and the mechanism of their formation.

In order to obtain information on these items, lattice strain measurements were made in seventeen directions in a low-alloy steel specimen under a series of progressively higher loads. After each increase the load was released and the lattice strain was measured in the seventeen directions. From these measurements, a distribution of body stresses and elastic constants was derived on the basis of well-known elastic theory for homogeneous media, that provided lattice compliances which deviated least from the measured values. Also, the stress limits of the lattice compliances were determined, and a system of body stresses and elastic constants was derived from the residual strains that developed after a 45,500 lb/in.^{2} loading stress.

2. EXPERIMENTAL METHOD

The specimen was machined from 1-in. diameter bar stock of NE-9420 steel. This low-alloy structural steel had a ferrite grain-size corresponding to ASTM No. 9 and fine pearlite in the normalized condition. Its composition and tensile properties in the normalized condition are listed in Table 1. Measurement of the relative intensities of diffraction lines from

TABLE 1. Chemical composition and tensile properties of specimen material as normalized

Chemical composition	Per cent	Tensile properties
Carbon	0.21	Yield strength (0.2% offset) 52,000 lb/in.^{2}
Manganese	0.91	Tensile strength 75,000 lb/in.^{2}
Silicon	0.48	Elongation 37.5%
Nickel	0.33	Reduction of area 67%
Chromium	0.34	
Molybdenum	0.11	
Sulfur	0.031	
Phosphorus	0.020	

both the longitudinal and transverse sections showed no measurable degree of preferred orientation.

The specimen was a hollow cylinder, 7/8 in. outside diameter, 2 in. long, and 1/8 in. wall thickness, with portions machined away to leave a reduced section consisting of three symmetrically spaced legs (Fig. 1). The legs were identical within close tolerance, each being 3/8 in. long and having a triangular cross-section 1/8 in. on a side. The specimen was welded to two supports for a previously calibrated loading rod placed axially within the specimen (Fig. 2). A nut was threaded on to the loading rod so that a clockwise turn applied a compressive load and, by supplying backing for the nut, a counter-clockwise turn applied a tensile load. The nut and the far end of the loading rod made contact with the specimen supports through spherical surfaces in

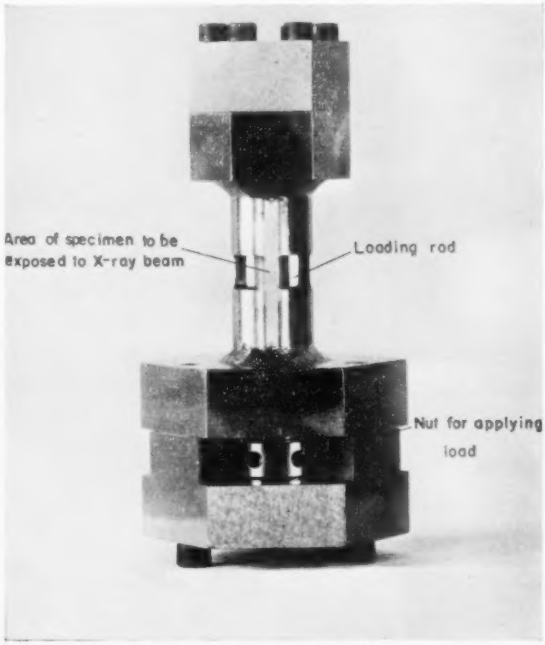

FIG. 2. Specimen and loading jig.

order that the load might be distributed equally and axially on the three legs. Between the threaded and reduced portions of the loading rod there was a length of hexagonal cross-section. This fitted a hexagonal hole in the specimen support in order to prevent twisting of the specimen when the loading nut was turned. After completion of the strain measurements, it was found that the fit was not sufficiently close to prevent a shear stress from being superposed on the axial load. This will be discussed after presenting the results.

After normalizing the specimen in a vacuum, the load was applied by slowly turning the nut on the loading rod until the strain indicator gave the desired reading, based on the previous calibration of the loading rod. Lattice-spacing measurements were made before loading, under load, and after release of each load. In order to determine the lattice compliance over a large elastic stress range, the first four cycles were alternately in tension and compression. The remaining eight cycles were in tension at progressively higher loads.

The principles involved in making conventional lattice-strain measurements were described in a previous paper.[6] Only details that affect the accuracy of the measurements will be described in this paper.

The X-ray patterns for strain measurement were obtained by using tungsten as a calibrating powder. The specimen was translated about 5 mm in the 2-h exposure, keeping the film-to-specimen distance and the angle between the collimated beam and specimen surface constant within a close tolerance. Translating the specimen increased the number of crystals contributing to the diffraction rings, thereby making them less spotty and easier to measure.

Two types of measurements were made, D_W and F, and used to compute $-\tan 2\theta$, according to the equation

$$-\tan 2\theta = -\tan 2\theta_W \left(1 - \frac{2F}{D_W}\right) . \qquad (2)$$

An experimentally determined value of 0.4362 was used for $-\tan 2\theta_W$. The relation of $-\tan 2\theta$ to strain is given in the following equation:

$$\epsilon = \frac{\partial d}{d} = -\cot\theta\ \partial\theta$$
$$= -\left[\frac{(1 - 2\sin^2\theta)^2}{2\tan\theta}\right] \Delta \tan 2\theta . \qquad (3)$$

The term in brackets is equal to 0.0760 when θ is 80° 30′, that is, for the strain-free condition. The change in the bracketed term is approximately 1% for the range of $\Delta \tan 2\theta$ encountered in lattice-strain measurement; therefore the error introduced by using the value 0.0760 for all patterns is well within the precision of measurement.[6] The diameter of the tungsten ring D_W was measured with a graduated scale and vernier at four locations, spaced 45° apart, and the average value for each pattern was used with corresponding F values.

The F measurements were made with a photomicrometer[12] that had been modified so that small differences in the radii of two concentric rings could be measured conveniently. The modified instrument had two concentric scanning arcs of light, each 15° and 0.25 mm wide, whose radii of curvature corresponded closely to the iron and tungsten rings that were to be measured. After mounting the patterns in the photomicrometer, measurements of F were made by determining the positions of the iron and tungsten rings, each with its appropriate scanning arc, the other being blocked by a shutter. These positions were determined by readings on a dial indicator corresponding to the minimum light transmission as the film was translated past the scanning arc. In order to improve the precision of the value for $-\tan 2\theta$ in equation (2), three independent patterns were obtained for each condition of loading and angle of incidence, and the average of measurements on all three were used to compute $-\tan 2\theta$. This average value was reproducible to 10^{-4} in terms of strain and was less than the deviations from systematic trends in the data.

For this investigation four positions of the incident beam were used, and are identified as A, B, C, and D. The projections of these positions along with projections of corresponding possible directions of strain measurement are shown in Fig. 3. Of the possible

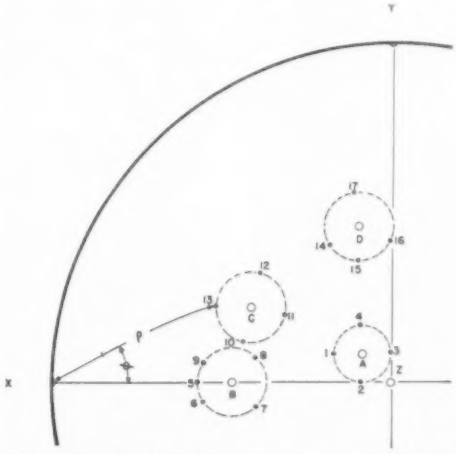

FIG. 3. Stereographic chart showing positions of X-ray beam and directions of strain measurement. X and Z are the directions of loading and surface-normal respectively.

TABLE 2. Angular co-ordinates of X-ray beam and of directions of strain measurements

X-ray beam			Strain measurement		
Position	ρ	ϕ	Direction	ρ	ϕ
	degrees	degrees		degrees	degrees
			1	72	10
			2	80	0
A	80.5	9.5	3	90	10
			4	80	19
			5	31	0
			6	33	−10
B	40.0	0	7	47	−10
			8	47	10
			9	33	10
			10	43.5	17
			11	56	24.5
C	47.5	29.0	12	52	40
			13	38	33
			14	72	45
			15	80	40
D	80.5	49.5	16	89	45
			17	80	59

directions of measurement, seventeen were chosen, and are identified in Fig. 3 by numbers. Actually, the measurements included directions within a 15° arc centered at these locations, because a 15° scanning arc was used in measuring F. The orientations of the primary beam and the directions of strain measurement are given in Table 2.

3. RESULTS

Typical results are shown in Fig. 4, where the values of −tan 2θ obtained under load and after release of load are plotted as a function of the applied stress. The −tan 2θ value for the no-load condition was plotted on the abscissa value corresponding to the previous load. The strain-free value is the average of those obtained for the normalized condition and for the first four no-load conditions in the elastic range. This average value was considered a better strain-free value than the value for the normalized condition because the latter value was in general slightly lower than the average value for the first four no-load conditions. This suggests that textural stresses were initially present and were removed by stressing in the elastic range.

Inspection showed that the −tan 2θ values for the compressive loads, the strain-free value, and certain values for the tensile loads, indicate lattice strains proportional to the loading stress. Using the zero-strain zero-load point as a pivot, lines were drawn through as many of the strain values at low

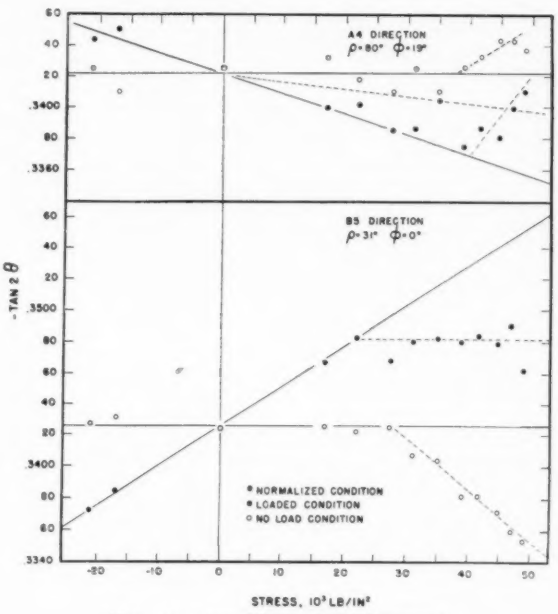

FIG. 4. −tan 2θ vs. stress diagrams for directions $A4$ and $B5$.

stresses and the high-strain values at high stresses as was consistent with the graphs. The slopes of the best lines representing the linear range for the seventeen directions of strain measurement, expressed as ϵ/σ_L, are listed in Table 3.

Further inspection of the −tan 2θ vs. stress diagrams showed that, at the intermediate and high-tensile loads, deviations from the lattice compliances appeared to be of two types. Deviations from lines

TABLE 3. Measured and computed values for lattice compliance

Direction	ϵ/σ_L measured in.²/lb	ϵ/σ_L computed in.²/lb	Difference
	($\times 10^{-9}$)	($\times 10^{-9}$)	($\times 10^{-9}$)
$A1$	−8.7	−8.6	−0.1
$A2$	−10.8	−10.2	−0.6
$A3$	−9.7	−11.7	2.0
$A4$	−10.5	−12.1	1.6
$B5$	19.6	22.0	−2.4
$B6$	21.2	22.4	−1.2
$B7$	13.1	11.7	1.4
$B8$	9.0	7.5	1.5
$B9$	17.3	18.6	1.3
$C10$	9.7	8.8	0.9
$C11$	−7.9	−5.1	−2.8
$C12$	−4.3	−3.2	−1.1
$C13$	4.1	9.8	−5.7
$D14$	−13.3	−14.9	1.6
$D15$	−16.6	−15.2	−1.4
$D16$	−11.4	−14.5	3.1
$D17$	−15.7	−17.9	2.2

with positive slopes, $B5$, $B6$, $B7$, $B8$, $B9$, $C10$, and $C13$, tended to lie on a line parallel to zero strain The deviations from the lines with negative slopes tended to be within a triangular area for intermediate loads and on a line with a positive slope for high loads. This tendency was most marked in the $A1$ and $A4$ diagrams. The deviations of the no-load values from zero strain tended to lie on lines having slopes opposite in sign to those of the corresponding lattice compliance lines.

4. INTERPRETATION OF RESULTS

In order to determine whether or not the lattice compliances conformed to what would be expected for uniaxial loading, ϵ/σ_L values were plotted on a stereographic projection showing the directions of strain measurement. These values are proportional to the strain-ratio according to the following equation:

$$\frac{\sigma_L}{\epsilon} = \frac{1}{E} \cdot \frac{\epsilon}{\epsilon_L}. \tag{4}$$

Lines of equal strain-ratio were computed on the basis of the following equation:

$$\frac{\epsilon}{\epsilon_L} = \cos^2 \rho - \nu \sin^2 \rho \tag{5}$$

assuming $\nu = 0.3$. Inspection of this projection showed that the ϵ/σ_L values were not proportional to the strain-ratio values for the axially loaded condition. This was particularly noticeable for the C and D positions.

The deviations of the measured lattice compliances from those corresponding to a uniaxial loading condition seemed to indicate the presence of shear and transverse stresses superposed on the loading stress. There was evidence that such a shear stress was present. After the 48,600 lb/in.^{2} tensile stress it was observed that the legs of the specimen were inclined about 3° to the axis of the specimen. This twist caused the legs to be slightly S-shaped, thereby showing that bending stresses were present at the ends of the legs in addition to the shear stress in the straight portion where the strain measurements were made. The twist developed because of the loose fit of the loading rod in the specimen support, as described in Section 2. These observations indicate that the twisting action was present at the lower loadings and caused deviations from the axially loaded condition.

In order to correlate the measured ϵ/σ_L values with a corresponding series of computed values based on the assumption that the strains were in a homogeneous medium, the following equation was derived:

$$\frac{\epsilon}{\sigma_L} = \frac{1}{E}\Big\{(\cos^2 \rho - \nu \sin^2 \rho) + K_T[(1+\nu)\sin^2 \rho \sin^2 \phi - \nu] + 2K_\tau (1+\nu) \sin \rho \cos \rho \sin \phi\Big\}. \tag{6}$$

Although the system of loading apparently precludes the presence of a transverse component, in deriving equation (6) a shear stress and an apparent transverse stress were taken to be proportional to the loading stress. In this case the shear plane was perpendicular to the loading stress. The four constants, E, ν, K_T, and K_τ in equation (6) can be computed from the measured values of ϵ/σ_L and the corresponding angular co-ordinates ρ and ϕ. One way this could be done would be by the solution of simultaneous equations, and averaging the resultant values. Such would be extremely lengthy and laborious, even with the use of a computing machine. A more direct approach is to assume various values for these constants, substitute in equation (6) for each of the seventeen strain directions, and by successive estimates arrive at the set of appropriate values which closely satisfy the measured ϵ/σ_L values. This method gave the values 32×10^6 lb/in.^{2}, 0.41, —0.13, and —0.26 for E, ν, K_T, and K_τ respectively. On the basis of these values, ϵ/σ_L was computed for each direction, and listed in Table 3 for comparison with the measured values. The correlation between the measured and computed values is good, thus showing that the fractional changes in the 310-spacing per unit stress in the elastic range conform to an ellipsoid defined by E and ν. The values 32×10^6 lb/in.^{2} and 0.41 obtained for E and ν are in good agreement with the values 31.3×10^6 lb/in.^{2} and 0.37 obtained by Möller and Martin.[13]

Möller and Martin,[13] Greenough,[2, 3] and Hershey[14] showed that values for E and ν could be computed from an equation similar to equation (6), but it would contain an additional constant. This constant would be related to the elastic anisotropy of the ferrite crystal. If the ferrite crystal deformed anisotropically in a polycrystalline body, then different values for E and ν should be obtained for changes in the lattice spacings of the 310- and 211-planes. Differences in strain values for different crystallographic planes[2, 3] have been reported, but it is a moot question whether or not the difference is entirely caused by the anisotropic strains in the

VOL. 4 1956

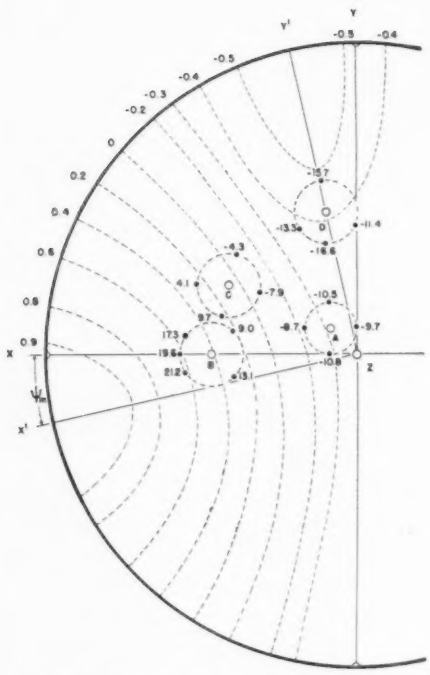

FIG. 5. Stereographic chart showing distribution of values for lattice compliance. The lines of equal strain-ratio are for the condition of transverse and shear stresses superposed on the axial loading stress, $\nu = 0.41$, $K_T = -0.13$, and $K_\tau = -0.26$. Values for compliance $\times 10^9$ are plotted adjacent to directions of strain measurement.

iron crystal in a polycrystalline body. Recent work in this laboratory[15] has indicated that the difference in strain values from measurements of the spacing of the 310- and 211-planes is indeed small. On the basis of this discussion it is concluded that the ellipsoid of strain is essentially the same in all of the ferrite crystals. This implies that there are steep stress-gradients in the vicinity of the boundaries of the ferrite crystals because of the elastic anisotropy of the individual crystals.

The value for K_T indicates that the apparent transverse stress in the elastic range is compressive and is 13% of σ_L. Wood[8] reported an apparent transverse tensile stress in a fine-grained iron specimen that was under load in the plastic range. Inasmuch as these apparent transverse stresses cannot be related to the system of loading, they cannot be considered as body stresses, but rather as an indication of textural stresses. Perhaps the apparent transverse component will be explained when more is known about the changes in the interplanar spacing of planes, other than the 310, that result from applied stresses.

The shear stress is 26% of σ_L, and probably results from the manner of loading, as has been pointed out. The effect of the apparent transverse and shear stresses on lines of equal strain-ratio is shown in Fig. (5). It can be seen that the shear stress has rotated the maximum principal stress $-12°$ from the loading stress, and that the apparent transverse stress introduces asymmetry in the plane perpendicular to the maximum principal stress.

The $-\tan 2\theta$ vs. stress diagrams show a distinct difference between the type of divergence in $-\tan 2\theta$ values from compliance lines having positive slopes and those having negative slopes. For positive ϵ/σ_L values, the $-\tan 2\theta$ values tend to remain constant with an increase in σ_L, beginning at an average stress of 21,000 lb/in.^{2}, whereas for negative ϵ/σ_L slopes they tend to increase with an increase in σ_L, beginning at an average stress of 40,000 lb/in.^{2} A difference in elastic limits for lattice compliances was indicated in previous work in this laboratory[6] and in the results of Wood.[5]

Smith and Wood[16] showed that plastic deformation did not affect the lattice compliance. This implies that the change in lattice spacing that occurs on release of the loading stress is proportional to the loading stress even though the elastic limit might have been exceeded. For the condition in which the elastic limit had been exceeded, the change in lattice spacing on release of load is equivalent to the difference in $\Delta \tan 2\theta$, expressed as strain, obtained for the loaded and unloaded conditions as indicated in Fig. 4, that is,

$$\epsilon_D = \epsilon_A - \epsilon_R \,. \tag{7}$$

Values for ϵ_D were plotted against the loading stress for each of the seventeen directions of strain measurement, and the appropriate lattice-compliance lines were drawn, using the computed values in Table 3. The agreement of ϵ_D with the computed lattice compliance was good within a fair tolerance for all directions. Fig. 6 is typical of the diagrams obtained in this treatment of the data. The elongation of the specimen for the highest load was approximately 1.6%. The agreement of ϵ_D with the lattice compliance indicates that the magnitude and directions of the principal stresses can be computed for a certain loading condition from the change in lattice spacing on release of load, even though the elastic limit has been exceeded.

It is of interest to determine the residual stress system giving rise to the residual strains measured. This cannot be done with a high degree of accuracy, because of the large deviations in the no-load values from a systematic trend dependent on previous

loading stress. The deviations from a recognizable trend, however, are sufficiently small in some directions to permit a fair estimation of the residual strain. The no-load values at the intersection of the abscissa, 45,500 lb/in.^{2}, were converted to strain, Table 4, and used to compute the constants ν, K_T, and K_τ in a manner similar to that used in computing values from the lattice compliances. The values obtained were $\nu = 0.31$, $K_T = 0$, and $K_\tau = 0.18$. The positive sign of K_τ indicates a clockwise rotation of σ_1 from σ_L. This is opposite to the loaded condition. The absence of a transverse component is contrary to the findings of Wood[5, 8] and Greenough.[9]

Using the values 0.31 and 0.18 for ν and K_τ and the measured values obtained after releasing the loading stress of 44,600 lb/in.^{2}, values for ϵ_{RL} for each direction of strain measurement were computed and listed in Table 4. There is considerable variation in the ϵ_{RL} values, the average being -4.6×10^{-4}, with a probable error of $\pm 54\%$. On the basis of $E = 32 \times 10^6$ lb/in.^{2}, the average ϵ_{RL} value is equivalent to a 15,000 lb/in.^{2} compressive stress with a superposed shear stress of 2700 lb/in.^{2}

A satisfactory explanation for the balancing of the residual compressive stress indicated by the foregoing results has been an enigma since its discovery by Smith and Wood.[16] The prevailing opinion is that this stress is textural in nature, being balanced by opposite stresses in adjacent crystals of different orientations. From results given above, this explanation is not satisfactory, because the strains were measured in many directions and thus represent a large number of crystals of different orientations. It is probable that if the lattice strain were measured in a sufficient number of directions to include all of the ferrite crystals, the values would conform to an ellipsoid. If the strain-ellipsoid is approximately the same in all ferrite crystals, as was concluded for the lattice compliances, then the residual lattice strains cannot be balanced entirely by the stresses in adjacent crystals.

A more satisfactory explanation is the assumption that the apparent residual body stresses indicated by lattice-strain measurements are balanced by opposite stresses in material that does not scatter X-rays coherently, that is, in a highly distorted crystal lattice, such as is found at grain boundaries. Such an explanation implies that the residual strains measured by X-ray diffraction would be essentially the same in the interior as at the surface. There is evidence to support this implication. Recent work[15] has indicated that the lattice strains measured on sections cut from specimens that had been plastically deformed under uniaxial loading were representative of the stresses in the surface before sectioning.

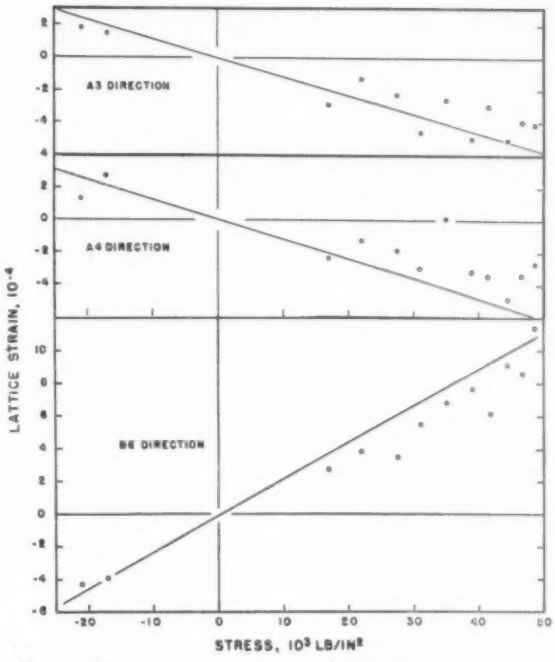

FIG. 6. The agreement of the change in lattice spacing that occurs on release of loading stress (open circles) with the computed lattice compliance, directions $A3$, $A4$, and $B6$.

TABLE 4. Estimated and measured residual lattice strains and computed values for the residual strain in the direction of loading

	ϵ_R (estimated for 45,500 lb/in.^{2} loading stress)	ϵ_R (measured after 44,600 lb/in.^{2} loading stress)	Calculated (ϵ_{RL})
	($\times 10^{-4}$)	($\times 10^{-4}$)	($\times 10^{-4}$)
$A1$	1.6	1.3	−7.9
$A2$	2.3	1.7	−6.2
$A3$	2.0	2.0	−6.4
$A4$	1.4	1.6	−6.5
$B5$	−4.4	−4.1	−6.3
$B6$	−5.2	−4.6	−8.1
$B7$	—	−0.3	−1.2
$B8$	—	−1.9	−4.9
$B9$	−4.0	−2.7	−4.2
$C10$	—	−2.7	−6.0
$C11$	—	0.4	2.1
$C12$	—	−1.7	−5.1
$C13$	−4.6	−3.8	−6.0
$D14$	—	−0.4	4.5
$D15$	1.5	0.5	−2.3
$D16$	—	0.9	−3.1
$D17$	1.6	2.1	−10.0
		Average	−4.6
		P.E.	±54%

5. CONCLUSIONS

Lattice-strain measurements made under load and after release of load have indicated the values 32×10^6 lb/in.^{2} and 0.41 for Young's modulus and Poisson's ratio, and that an apparent transverse compressive stress of 13% and a shear stress of 26% were superposed on the loading stress.

The lattice elastic limit for positive compliances was approximately 21,000 lb/in.^{2} an d40,000 lb/sq. in. for negative compliances. The lattice elastic limits appear to depend primarily on the sign of the lattice compliance.

The change in lattice spacing on release of load from the plastic range could be predicted from the lattice compliance, thus indicating that loading stresses can be computed for stresses exceeding the elastic limit.

Calculations of the residual strain in the direction of loading after a loading stress of 44,600 lb/in.^{2} gave an average value of -4.6×10^{-4}.

ACKNOWLEDGMENT

The authors wish to express their appreciation to Mr. John A. Bennett for suggesting the problem and for many helpful discussions during the progress of the work. They also wish to extend their thanks to Dr. Julius Lieblein of the NBS Statistical Engineering Laboratory for evaluating the precision of the X-ray measurements, and to Mr. W. L. Schlarman of the NBS Instrument Shop for helpful suggestions in the design of the specimen and accessories. Many painstaking measurements of diffraction patterns were made by Miss Ruth E. Dowden and Mr. Spencer Williams. The work was supported in part by the Wright Air Development Center.

6. REFERENCES

1. C. S. Barrett *The Structure of Metals* p. 333 (2nd ed., McGraw-Hill Book Co., New York, N.Y., 1952).
2. G. B. Greenough Quantitative X-ray Diffraction Observations on Strained Metal Aggregates, p. 176 *Progress in Metal Physics, Vol.* 3, 1952, edited by Bruce Chalmers.
3. G. B. Greenough Residual Stresses Associated with Lattice Strains, p. 285 (*Residual Stresses in Metals and Metal Construction*, edited by William R. Osgood, Reinhold Publishing Corp., 1954).
4. W. S. Hyler and L. R. Jackson Precautions to be Used in the Measurement and Interpretation of Residual Stresses by X-ray Technique, p. 297 (*Residual Stresses in Metals and Metal Construction* edited by William R. Osgood, Reinhold Publishing Corp., 1954).
5. W. A. Wood The Behavior of the Lattice of Polycrystalline Iron in Tension *Proc. Roy. Soc.* **192,** 218 (1947-48).
6. John A. Bennett and Herbert C. Vacher Calibration of X-ray measurement of strain, *J. Res. Nat. Bur. Stand.* **40,** 285 (1948).
7. C. Zwikker *Physical Properties of Solid Materials, Systematic Relations* p. 72, Interscience Pub., Inc., 1954.
8. W. A. Wood and N. Dewsnap Atomic displacements associated with elasticity in plastically deformed metals *J. Inst. Metals.* **77,** 65-78 (1950).
9. G. B. Greenough Macroscopic surface stresses produced by plastic deformation. *J. Iron and Steel Inst., London* **169,** 235 (1951).
10. C. W. MacGregor The Significance of Residual Stresses p. 103 (*Residual Stresses in Metals and Metal Construction* edited by William R. Osgood, Reinhold Publishing Corp., 1954).
11. Catherine M. Bateman Residual lattice strains in plastically deformed aluminum *Acta Met.* **2,** 451 (1954).
12. John A. Bennett Instrument for measurement of X-ray diffraction patterns *Rev. Sci. Instrum.* **20,** 908 (1949).
13. H. Möller and G. Martin Elastic anisotropy and X-ray stress measurement *Mitt. K.-Wilh.-Inst. Eisenforschg.* **21,** 261-269 (1939).
14. A. V. Hershey The elasticity of an isotropic aggregate of anisotropic cubic crystals *J. App. Mechanics* 21, Sept. 1954, p. 236-240.
15. C. J. Newton and H. C. Vacher Residual lattice strains in sectioned bars of plastically deformed iron. AIME Tech. Note 281E *J. Metals* **7,** 1193 (1955).
16. S. L. Smith and W. A. Wood A stress-strain curve for the atomic lattice of iron *Proc. Roy. Soc.* **A178.** 93-106, (1941).

VOL
4
195

INITIAL OXIDATION RATE OF METALS AND THE LOGARITHMIC EQUATION*

HERBERT H. UHLIG†

The logarithmic oxidation equation $y = k_0 \ln (t/\tau + 1)$ is derived assuming control of the rate by electron flow from metal to oxide. Electron flow during oxidation, in turn, is a function of a changing less-positive or a more-negative space charge in the oxide extending up to several thousand ångström units from the metal surface, where increasing numbers of trapped electrons at lattice defect sites account for the changing space charge. The space charge is composed of two parts: (1) a uniform-charge density layer next to the metal and (2) a diffuse-charge density layer beyond the uniform layer. Oxidation follows the logarithmic equation during formation of both space-charge layers, but not afterward, with a higher oxidation rate accompanying formation of the diffuse layer. It is shown that under some circumstances the particular distribution of negative charge in the diffuse layer may lead to the cubic oxidation equation. Experimental conditions, especially impurities present in the oxide and its heat treatment, probably determine which electric-charge distribution is favored. For oxidation beyond the space-charge layer, either the linear equation is obeyed, with control of the rate still focused at the metal-oxide interface, or, more frequently, the parabolic equation is obeyed with control centered in diffusion and migration processes in the oxide, in accord with Wagner's theory.

From oxidation data for copper, the density of trapped electrons in the uniform charge density Cu_2O layer at 150° is calculated to be 1.3×10^{15}, which decreases to 6×10^{13} at 250°C. The number of available sites for trapped electrons in the diffuse layer is calculated correspondingly to be 1.0×10^{14} and 2.6×10^{12} respectively. The thickness of the uniform charge density layer varies from 360 Å at 150° to 1630 Å at 250°C.

The Rideal-Jones empirical relation $\Delta E = \phi - 3.6$, where ΔE is the activation energy for oxidation and ϕ the metal-work function, both in electron volts, and which has been shown to hold for carbon, tungsten, and platinum, is shown herewith to apply to nickel, tantalum, and titanium, and more approximately to copper and iron. This relation is derived theoretically from the same fundamental assumptions used in deriving the logarithmic oxidation equation.

LA VITESSE D'OXYDATION INITIALE DES METAUX ET L'EQUATION LOGARITHMIQUE

L'équation logarithmique d'oxydation $y = k_0 \ln (t/\tau + 1)$ est établie en supposant que la vitesse est contrôlée par le flux d'électrons passant du métal à l'oxyde. Au cours de l'oxydation, ce flux d'électrons est, à son tour, fonction de la variation de la charge, moins positive ou plus négative, de la couche d'oxyde s'étendant sur une épaisseur pouvant atteindre plusieurs milliers d'angströms à partir de la surface métallique et où le nombre croissant d'électrons retenus par les défauts réticularies justifie les variations de charge spatiale. La charge spatiale est composée de deux parties: (1) une couche à densité de charge uniforme, près du métal et, sous celle-ci (2) une couche à densité de charge variable. L'oxydation obéit à l'équation logarithmique pendant la formation de ces deux couches, mais plus ultérieurement car un accroissement de la vitesse d'oxydation accompagne la formation de la couche à charge variable. On montre que, sous certaines conditions, la distribution particulière des charges négatives de cette dernière répond à l'équation cubique d'oxydation.

Les conditions expérimentales, en particulier les impureté présentes dans l'oxyde et son traitement thermique, déterminent probablement quelle sera la distribution des charges électriques/ L'oxydation sous la couche à charge spatiale, obéit soit à l'équation linéaire avec contrôle de la vitesse à l'interface métal-oxyde, ou plus généralement à l'équation parabolique avec contrôle des procédés de diffusion et et migration dans l'oxyde, selon la théorie de Wagner.

Par les données expérimentales d'oxydation du cuivre, on a pu calculer la densité des électrons immobilisés dans la couche de Cu_2O à densité de charge uniforme: $1{,}3 \times 10^{15}$ à 150°C, 6×10^{13} à 250°C. Le nombre de places possibles pour l'ancrage des électrons dans la couche à densité de charge variable a été également calculée: pour les mêmes températures, on obtient respectivement $1{,}0 \times 10^{14}$ et $2{,}6 \times 10^{11}$. L'épaisseur de la couche à densitè de charge uniforme varie entre 360 Å à 150°C et 1630 Å à 250°C.

La relation empirique de Rideal-Hones: $E = \phi - 3{,}6$, où E est l'énergie d'activation de l'oxydation et ϕ la fonction de travail du métal, toutes deux exprimées en électrons-volts, qui s'applique bien au carbone, tungstène et platine, est valable également, comme on le montre, pour le nickel, pour le tantale et le titane et moyennant certaines approximations, pour le cuivre et le fer. Cette relation est également déduite théoriquement en utilisant les mêmes hypothèses fondamentales que pour l'étsblissement de l'équation logarithmique d'oxydation.

ANFÄNGLICHE OXYDATIONSGESCHWINDIGKEIT VON METALLEN UND DIE LOGARITHMISCHE GLEICHUNG

Die logarithmische Oxydationsgleichung $y = k_0 \ln (t/\tau + 1)$ wird unter der Annahme abgeleitet, dass die Geschwindigkeit durch den Elektronenstrom vom Metall zum Oxyd bestimmt wird. Der Elektronen-

*Received January 3, 1956.

†Corrosion Laboratory, Department of Metallurgy, Massachusetts Institute of Technology, Cambridge, Massachusetts

VOL. 4 1956

strom bei der Oxydation ist seinerseits eine Funktion einer sich ändernden, von positivem Ladungsunterschuss oder negativem Ladungsüberschuss herrührenden Raumladung im Oxyd, die sich vom Metall aus bis zu einer Dicke von mehreren tausend Angström erstreckt. Sie kommt durch eine zunehmende Anzahl eingefangener Elektronen an Gitterfehlstellen zustande. Die Raumladung setzt sich aus zwei Anteilen zusammen: (1) Eine Schicht mit einheitlicher Ladungsdichte unmittelbar am Metall und (2) eine Schicht mit diffuser Ladungsdichte jenseits der ersteren. Während der Bildung beider Raumladungs-schichten folgt die Oxydation der logarithmischen Gleichung, wobie der Bildung der diffusen Schicht eine höhere Oxydationsgeschwindigkeit entspricht. Danach gilt die logarithmische Gleichung nicht mehr. Es wird gezeigt, dass unter gewissen Umständen die spezielle Verteilung der negativen Ladung in der diffusen Schicht zur kubischen Oxydationsgleichung führen kann. Welche elektrische Ladungsverteilung begünstigt ist, wird wahrscheinlich durch die experimentellen Bedingungen, insbesondere die im Oxyd enthaltenen Verunreinigungen und dessen Wärmebehandlung, bestimmt. Jenseits der Raumladungs-schicht folgt die Oxydation entweder der linearen Gleichung, wobei der geschwindigkeitsbestimmende Vorgang noch an der Grenzfläche Metall-Oxyd lokalisiert ist oder, was häufiger der Fall ist, sie gehorcht in Übereinstimmung mit der Theorie von Wagner der parabolischen Gleichung mit Diffusion und Wanderungsvorgängen im Oxyd als massgebenden Prozessen.

Aus Daten über die Oxydation von Kupfer errechnet sich die Dichte der eingefangenen Elektronen in der Cu_2-Schicht mit einheitlicher Ladungsdichte zu $1{,}3 \times 10^{15}$ bei 150°C; für 250°C nimmt sie auf 6×10^{13} ab. Die Anzahl der möglichen Plätze für eingefangene Elektronen in der diffusen Schicht wird in entsprechender Weise zu $1{,}0 \times 10^{14}$ bzw. $2{,}6 \times 10^{12}$ berechnet. Die Dicke der Schicht mit einheitlicher Ladungsdichte variiert zwischen 360 Å bei 150° und 1630 Å bei 250°C.

Es zeigt sich, dass die empirische Beziehung von Rideal-Jones $\Delta E = \phi - 3{,}6$, in der ΔE die Aktivierungsenergie der Oxydation und ϕ die Austrittsarbeit des Metalls—beide in Elektronenvolt gemessen—bedeuten und deren Gültigkeit sich für Kohlenstoff, Wolfram und Platin erwiesen hat, auch auf Nickel, Tantal und Titan sowie näherungsweise auch auf Kupfer und Eisen anwendbar ist. Theoretisch wurde diese Beziehung unter denselben grundlegenden Annahmen abgeleitet, die auch bei der Ableitung der logarithmischen Oxydationsgleichung verwendet wurden.

Whenever the oxidation rate of a metal is controlled by diffusion of ions (or lattice vacancies) and by migration of electrons (or positive holes) through the oxide film, the familiar parabolic equation applies:

$$y^2 = k_1 t + C \tag{1}$$

where y is the thickness of the film, t is time, and k_1 and C are constants. (C may sometimes be zero). Wagner[1] established the fundamental reaction kinetics for this equation and was able to calculate the rate-constant k, and its dependence on oxygen partial pressure, from independent physical chemical properties of oxide and metal.

However, oxidation in the lower-temperature range or when thin films are formed is found to follow the so-called logarithmic equation:

$$y = k_0 \ln\left(\frac{t}{\tau} + 1\right) \tag{2}$$

where k_0 and τ are constants. For $t \gg \tau$, this equation is approximated by:

$$y = k_0 \ln t - k_0 \ln \tau \tag{3}$$

and y becomes linear plotted with logarithm of t.

When the logarithmic equation was first announced in 1922 by Tammann and Köster[2] on empirical grounds, its validity was questioned. However, careful measurements since then have established beyond doubt that for oxidation of many metals under specific conditions of temperature and time, this equation and no other describes the facts. The logarithmic equation, for example, has been shown to apply to oxidation of copper,[2, 3, 4, 5, 6] zinc,[2, 7] cadmium,[2] lead,[2] tin,[2] manganese,[2] iron,[2,8,9,10,11] nickel,[2, 12, 13] aluminum,[3, 14] titanium,[15] and tantalum.[16]

Several attempts have been made to describe a mechanism of diffusion through oxides resulting in the logarithmic equation, such as by assumed specialized flaw-paths or zones of loose structure in oxides,[17] or by diffusion blocks and leakage paths in the oxide,[11, 18] or by an assumed ion-concentration gradient or polarization.[19]* Mott[20] contributed an

* Vernon, Calnan, Clews, and Nurse[10] believe that the logarithmic equation, as found to apply to thin-film oxidation of iron, expresses oxygen diffusion through the oxide to the metal surface, whereas the parabolic equation, when it applies, corresponds to diffusion of iron ions through the oxide from metal to gas. They base their opinion on observed greater weight-gain of iron specimens when oxidized in the logarithmic rate region than corresponds to oxygen in the isolated oxide film, in contrast to correspondence of weight-gain and oxygen in the oxide in the parabolic region. Their observations, however, can be explained by surface oxidation of carbon contained in their iron (0.09% C), occurring parallel with the oxidation of iron, the carbon oxidation products being retained by the iron oxides perhaps as carbonates. For higher temperatures and thicker oxide films where the parabolic equation holds, carbonates are not stable and, hence, are not expected to be retained by the film. Oxidation of carbon also explains the delayed appearance of interference colors which they report. In this connection, the effect of carbon probably enters as a factor in the thinning (by reduction) of oxide films on iron during vacuum treatment reported by Davies, Evans, and Agar.[11] A pertinent reference in this regard is the work of V. Holm.[21]

analysis of electronic and ionic processes in thin insulating oxide films of stoichiometric composition on metals which led to a logarithmic equation. He employed the tunnel effect of quantum mechanics to express rate of electron flow from metal to oxide, which he assumed controlled the oxidation process. This special model accounted, however, for oxide films only in the order of 40 Å, whereas the general logarithmic equation in practice holds for films as thick as 10,000 Å, and also his derivation predicted a temperature-independent k_0, contrary to what is observed. Subsequently, Mott and Cabrera[22, 23] hypothesized an alternative rate-control by diffusion of metal ions rather than escape of electrons, assuming that negatively charged oxygen ions when adsorbed on the oxide surface create an electric field within the oxide which induces migration of positive ions to the oxide surface. They showed that under conditions where migration velocity of positive ions is proportional to field strength, a parabolic oxidation equation results, but for thinner films for which the migration velocity is proportional to an exponential power of the field strength and rate of escape of metal ions into the oxide becomes controlling, an equation of the type $1/y = C - k \ln t$ is derived (the inverse logarithmic equation). This also led to the situation where, below a critical temperature, a limiting oxide film-thickness could be expected. But the logarithmic equation (2) observed experimentally did not result from these particular assumptions.

Campbell and Thomas[24] expressed the opinion that initial deviations from the parabolic equation of oxidation for copper are caused by a space-charge layer in the oxide, about 10^4 Å thick as determined by electrical capacitance. Tylecote[6] confirmed that the logarithmic equation holds for films less than about 10^5 Å thick, whereas the parabolic equation applies to thicker films. Later discussion in the present paper bears out that the logarithmic equation is related to conditions applying to formation of the space-charge layer, and that the mechanism of oxidation changes for thicker oxide films.

Oxidation Control at the Metal-oxide Interface

It is perhaps obvious that an acceptable mechanism of thin-film oxidation of metals should first establish the actual rate-controlling process. A detailed examination of reaction-rate data provides evidence that the rate is controlled largely by processes at the metal-oxide interface rather than by reactions at the oxide-oxygen interface, or by diffusion through the oxide. This evidence comes from the effect on the oxidation rate of:

(1) *Crystal orientation*, one crystal face oxidizing at a rate appreciably different from any other crystal face.[3, 8, 25] Lustman,[8] and Mehl and McCandless[26] pointed out that these differences cannot be ascribed to differing diffusion rates through oxides specifically oriented on metal crystal faces, because the oxides of iron and copper at low temperatures are cubic, and diffusion through cubic lattices is isotropic. Differing degree of sintering or differing recrystallization of oxide as a function of crystal face is also not an acceptable explanation, because Mehl, McCandless, and Rhines[27] found that oxides grown on single crystals of copper remain single crystals even after they have developed into thick scales, precluding the possibility of any sintering or recrystallization.

(2) *Lattice transformation*. The activation energy for oxidation of iron in $CO_2 + H_2O$ undergoes a discontinuity at the transformation temperature of iron from α (b.c.c.) to γ (f.c.c.) lattice.[28] A similar discontinuity was found for a 10.6% chromium-iron alloy,[29] heated in oxygen under conditions where thin films are formed.

(3) *Curie temperature*. The activation energies for oxidation of several chromium-iron alloys in oxygen are higher above the Curie temperatures than below.[29] This relation is also found to hold for nickel.[12] Tammann and Siebel[30] furthermore found discontinuities in the oxidation rates of iron-nickel alloys at the Curie temperatures. All these observations show that magnetic transitions in metals at the Curie temperature can affect the oxidation rate.

The overall evidence for control of rate at the metal-oxide interface applies whenever thin films are formed. For thicker films, of course, where diffusion through the oxide is controlling, factors of grain orientation, lattice transformation, and magnetic change are no longer important.

Control by Electron Emission

Mott[22, 23] favored slow escape of metal ions from the metal into the oxide lattice as the controlling step in several reactions producing relatively thin films, and electron emission as controlling in insulator-type films below 40 Å thick. Convincing evidence is available to show that actually electron flow from metal to oxide is the slow step for several

metals, and therefore dominates the reaction process in formation of films as thick as several thousand Ångströms. This evidence in part comes from the empirical relation first proposed by Rideal and Wansbrough-Jones.[31] They showed that for oxidation of platinum, carbon, and tungsten the following relation holds:

$$\Delta E = \phi_0 - K \tag{4}$$

where ΔE is the observed activation energy for oxidation, and ϕ_0 is the work-function of metal or carbon. The term K is a constant equal to 3.6 eV (83 kcal), and was expressed by Rideal and Wansbrough-Jones as the sum of $\phi_a + \phi_\epsilon$, where ϕ_a is the energy of adsorption and ϕ_ϵ is the electron affinity of the adsorbed oxygen molecule. In other words, for these elements, each of whose oxides at elevated temperatures is volatile, the activation energy for oxidation is related directly to the energy necessary to transfer an electron from metal to oxygen.

According to equation (4), metals with work function less than 3.6 eV (e.g. Na and Ca) possess an activation energy for oxidation equal to zero (it cannot be negative), and the metal oxidizes initially as rapidly as oxygen comes into contact. For metals of higher work function, on the other hand (e.g. Ni, Pt, W), the activation energy is positive, the reaction is delayed, and more oxygen reaches the metal surface than can react. This means that oxygen is able to adsorb (chemisorb) on the metal, for which it has a certain affinity, remaining there a measurable time before metal atoms leave their lattice to initiate an oxide lattice.

It is of interest to note that the measured value of K in equation (4) (3.6 eV) approximates the electron affinity of the oxygen atom (3.4 eV).[32] The small difference of about 0.2 eV (4600 cal) is possibly accounted for by the sum of energy changes associated with adsorption and dissociation of molecular oxygen on the metal surface. In other words, the slow process of oxidation of carbon, Pt, and W can be interpreted as the transformation of physically adsorbed molecular oxygen, in which only weak Van der Waals binding forces apply, to chemisorbed atomic oxygen with the metal acting as electron donor and oxygen as electron acceptor. Accordingly, equation (4) indicates that both rates of physical adsorption of oxygen on the metal surface and volatilization of the metal-oxygen ion complex, at the high temperatures presently considered, are rapid compared to chemisorption of oxygen. This conclusion is in agreement with previous expressions to the effect that chemisorption is often (but not always) a slow process requiring an activation energy.[33, 34] It also agrees with previous proposals that the process of physical adsorption precedes chemisorption.[35, 36]

TABLE 1. Relation between activation energy for oxidation and work function: $\Delta E = \phi_0 - K$

	ΔE (eV)	ϕ_0 (eV)	K (eV)
Pt	2.74	6.35*	3.61
W	0.87	4.48*	3.61
C	0.52	4.31*	3.79
Ni	0.90†	4.50[37]	3.60
Ta	0.55[16]	4.12[38]	3.57
Ti	0.56[15]	3.95[37]	3.39

* These values employed by Rideal and Wansbrough-Jones are close to mean values given by H. Michaelson based on a review of the literature, with the exception of platinum, where the value in Table 1, employing photoelectric data of DuBridge (1928) is 1.06 V higher.

† H. H. Uhlig and J. J. Pickett, unpublished data.

It is significant that the Rideal-Jones relation can be applied also to some metals having nonvolatile oxides under conditions where the oxide films are thin and the logarithmic equation is obeyed. The data are summarized in Table 1, and provide evidence that for such metals oxidation continues to be controlled by electron flow from the metal. Presumably, the energy gained by the electron entering the oxide is almost exactly compensated for by the electron leaving the oxide again at the oxide-air interface to enter the oxygen atom, now adsorbed not on the metal, but on the oxide. The negatively charged oxygen ions eventually enter lattice positions in the oxide in accord with the Wagner mechanism of oxidation and tarnish. Therefore, ΔE is again given essentially by the difference of the metal-work function and the electron affinity of oxygen. From the above considerations, equation (4) can be expected to hold whenever electron escape from the metal controls, and when the work function of the oxide has approximately the same value at the metal-oxide and oxide-environment interfaces.

The observed relation between work function and activation energy clarifies why the rate of oxidation should vary with crystal face, since the work function also varies with crystal face.[39, 40, 41] Furthermore, the work function of γ-iron differs from that of α-iron, in accord with change of activation energy for oxidation above and below the transition temperature. Houdremont and Rüdiger[42] reported a higher work function for γ- than for α-iron, but Wahlin[43] reported the reverse, namely, a higher value for α- than for γ-iron*.

* The activation energy for oxidation is higher above the α-γ transition temperature.

Along the same lines, values of work function ϕ_0 for nickel above the Curie temperature (350°C) are higher than values below the Curie temperature,[44] corresponding to an observed activation energy for oxidation of nickel in oxygen above the Curie temperature that is 1150 cal/mole, or 0.05 eV greater than the value below the Curie temperature.[12] These correlations point toward the important part played by electron flow from the metal in the initial oxidation process, and focus the necessity of attention on various factors affecting electron emission during oxide growth.

Space-charge Effects

If at equilibrium, an oxide has greater electron affinity or higher work function than the metal in contact from which it forms, the oxide will tend to acquire excess negative charge, and the metal, in turn, will acquire an equal positive charge, resulting in an electrical double layer. Similarly, if the electron affinities are reversed, the oxide will lose electrons to the metal. The amount of charge eventually transferred across the boundary in either event will set up a field compensating exactly for the differences in electron affinity of the two phases. Or, stated another way, when contact is made between a metal and a semiconductor, all the electronic energy levels of the semiconductor are altered relative to those of the metal by the amount of the contact potential difference.

For two dissimilar metals in contact, the electric charge constituting the double layer is confined to a very small region of atomic dimensions at the interface. In semiconducting oxides, on the other hand, with filled energy levels and relatively few electrons excited into the conduction band, excess charge associates itself mainly at lattice imperfections, such as occur at impurity centers or at lattice vacancies. Negative charge of this kind exists as so-called bound or "trapped" electrons[45] Similarly, bound or trapped electron-deficient sites or positive holes may exist. In view of the restricted number of sites for trapped electrons or positive holes, the space charge in oxides extends over a greater volume than in the case of metals. Volta or contact potential measurements for oxidized copper and zinc, as described later, indicate that the space charge may extend into the oxide film for several thousand ångstroms. When the oxidation rate, therefore, is controlled by electron flow from the metal, an increasing negative space charge (or decreasing positive space charge) obviously enters as an important factor in establishing the rate of electron flow, tending in general to slow down escape of electrons as the oxide grows, and, therefore, simultaneously slowing down escape of metal ions and the oxidation process itself.

Volta Potential Measurements and the Initial Oxidation Reaction

The oxidation process, of course, is not an equilibrium situation, but rather a dynamic building-up of oxide through interaction of the metal and oxide with molecular oxygen. The various steps in the initial process appear to be:

(1) Rapid physical adsorption of molecular oxygen on the metal,
(2) Dissociation of molecular oxygen into chemisorbed atomic oxygen,
(3) Sublimation of the metal-oxygen complex to initiate an oxide lattice,
(4) Vaporization of metal ions and electrons into the oxide to form additional oxide,
(5) Formation of lattice vacancies by oxygen, or combination of interstitial metal ions with oxygen at the oxide-air interface. (We shall not treat the relatively few known cases where oxygen diffuses to the metal-oxide interface.)

If step 4 controls, in accord with present considerations, the rate of escape of ions is given by the expression $K' \exp(-W/kT)$, where W is the heat of sublimation of the ions from the metal into the oxide at the metal-oxide interface, k is Boltzmann's constant, T is the absolute temperature, and K' is a constant. Electrons can be assumed to evaporate simultaneously at a rate equal to $K'' \exp(-e\phi/kT)$, where ϕ is the work function of the metal as modified by the oxide in contact. When electron emission is the slower process and therefore the controlling factor in the formation of oxide, as has been discussed, and since the exponential terms and not K' and K'' in the above rate expressions are usually dominant, it follows that ϕ in this instance must be greater than W.

This state of affairs leads to an initial positive space charge in the oxide when a metal is first oxidized because of the rapid escape of positive metal ions. Their rate of escape almost immediately is established by the slower electron flow from metal to oxide. As the oxide grows, a decrease of positive space charge occurs because a portion of the electrons escaping into the oxide become trapped at oxide lattice imperfections. Eventually, the oxide may acquire an overall negative charge, depending on the final equilibrium state of electric charge.

VOL. 4 1956

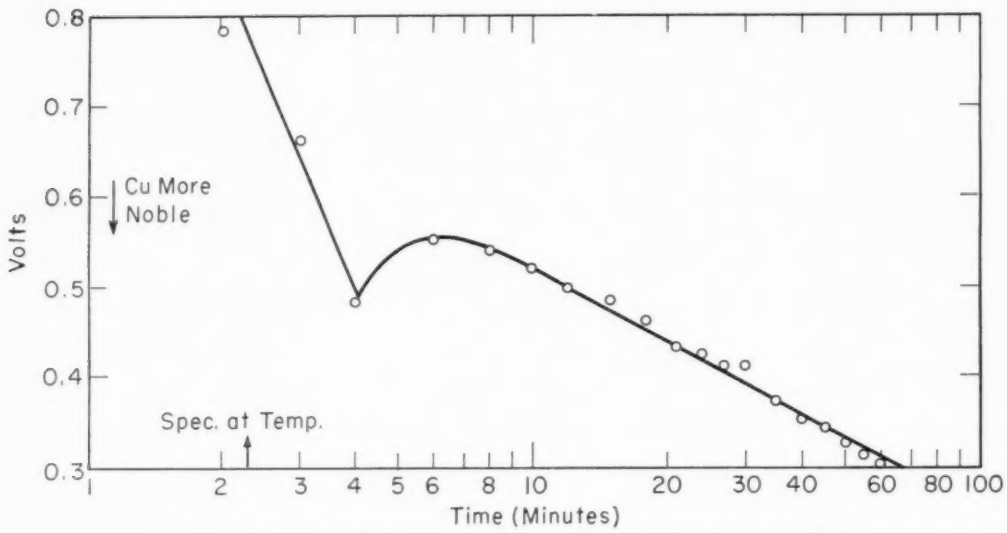

FIG. 1. Volta potential of copper oxidizing in air vs. silver. Both at 225°C.

As oxidation continues, rates of escape of ions and of electrons approach each other, and some factor other than electron flow assumes control of the rate, particularly after the oxide grows to a thickness corresponding to equilibrium electric charge distribution at the metal-oxide interface (or when the Fermi levels in metal and oxide become identical). Thicker oxides forming beyond the boundaries of the space-charge layer are electrically neutral. If escape of electrons and ions should continue to control the rate at this stage, as is possible, the oxidation rate would become constant, leading to the so-called linear equation, ($y = k_2 t + C_3$). But the constant oxidation rate in this instance would be preceded by an initially more rapid and gradually decreasing rate. Gulbransen and Wysong[46] found aluminum to behave somewhat along these lines, which may confirm that this type of oxidation control is sometimes found. Aluminum when oxidized in low-pressure oxygen below 450°C followed the parabolic equation, and above 450°C followed the linear equation. Whether one equation or another is obeyed probably depends on the defect structure of the oxide under the particular conditions of any given experiment. That is, factors become important which determine whether sites continue to be available, as the oxide grows, for trapping of electrons or positive holes, and which establish whether control of the rate remains at the metal-oxide interface or is transferred to diffusion and conduction processes in the oxide. Also, patterns of crack formation in the oxide may play a role in accord with the conventional explanation of mechanism applied to the linear equation. Nevertheless, it is apparent that the linear equation, as described above, may also hold for metals covered by a continuous protective oxide film *free of cracks*. Such protective films have, in fact, been observed when magnesium, which follows the linear equation, oxidizes initially.[47, 48] Also, the black crustaceous MgO found by Leontis and Rhines[47] next to the metal surface, over which white MgO forms, may be visible evidence of the space-charge layer, as well as evidence, as they suggest, of a nonstoichiometric composition.

Evidence for the trend of space charge with oxide growth is provided by contact or Volta potential measurements of metals undergoing oxidation in air at elevated temperatures. Typical potentials of copper oxidized in air at 225°C and of zinc at 200°C are given in Figs. 1 and 2. These measurements

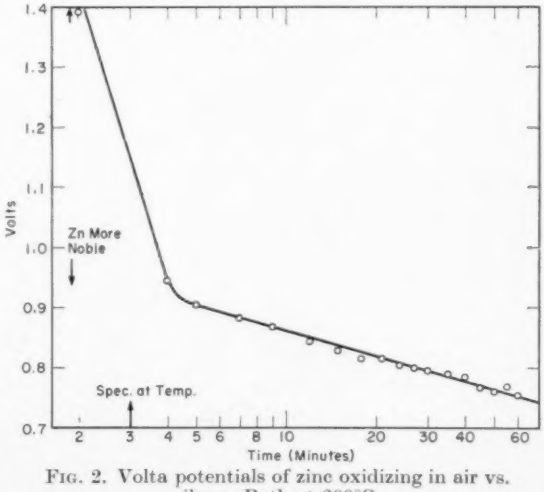

FIG. 2. Volta potentials of zinc oxidizing in air vs. silver. Both at 200°C.

were made employing the vibrating condenser method.[49, 50] A silver electrode as reference was heated electrically to the same temperature as the copper or zinc electrodes, all of the same size (1 × 1 in.) the temperature of the electrodes being measured and controlled automatically by means of embedded thermocouples. The initial oxidation process for copper results in a Volta potential 0.5–0.7 V more active than silver, and for zinc about 1.5 V more active than silver, corresponding to buildup of a positive space charge in the metal oxides. As the metals oxidize further, these potentials become first rapidly more noble (more like Ag), indicating that the positive space charge is being neutralized, followed by a less rapid and prolonged trend in the noble direction.

Similar conclusions may be derived from Volta potential measurements reported by Hirschberg and Lange.[51] They heated zinc surfaces between 20 and 407°C for 20 min at each temperature, and measured Volta potentials of such surfaces (presumably at room temperature rather than at elevated temperature, as above) with respect to zinc. At lower temperatures of oxidation and hence for the thinner films, the sign of Volta potential corresponded to a positive space charge in the oxide, but for higher temperatures and thicker oxide films the sign reversed.

VOL. 4 1956

Volta potential measurements of metals undergoing oxidation are not easily reproducible, so that quantitative features of Figs. 1 and 2 should not assume great weight. Qualitatively, however, the trend of effects can be reproduced from one run to the next. These measurements are being continued at various temperatures and for various metals, and will be reported elsewhere. In all instances observed so far, the sign of Volta potential after an initial period of oxidation corresponds to decreasing positive space charge or increasing negative charge. Interpretation of Volta potential measurements as described above assumes that electric charge at the air-oxide interface remains essentially constant, which is a reasonable assumption for constant partial pressure of oxygen; and that major change of potential is accounted for by changing electric charge in the thin oxide films.

The potential at the metal-oxide interface set up by changing space charge in the oxide layer alters, of course, the work necessary to carry a positive ion or electron across the interface, and, hence, influences their rate of escape into the oxide. It is this approach to the oxidation process that is explored next.

Calculation of Oxidation Rate

We shall consider first that excess charge in the growing oxide film of total thickness y is uniformly distributed throughout the oxide volume. This corresponds to an oxide with uniform defect or impurity density at which electrons or positive holes are bound. When a film of this kind reaches a supposed thickness l, we shall further assume that the total negative charge in the film creates a field at the metal surface compensating exactly for the positive field. The positive field results from excess metal ions of positive charge escaping into the oxide, or, alternatively, results from the electron "sink" at lattice vacancies formed at the outer oxide surface. Therefore, when the hypothetical film thickness becomes l, the electric field at the metal surface reaches the equilibrium value or zero (Fermi levels in oxide and metal are equal), corresponding to an order of film thickness beyond which the space charge can exert either a constant or a negligible effect on electron escape and rate of oxide growth. If n is the density of trapped electrons in the oxide, and $-e$ is the charge on the electron, the potential V at the metal-oxide interface is given by Poisson's relation:

$$\frac{d^2V}{dy^2} = \frac{4\pi ne}{\epsilon} \tag{5}$$

where ϵ is the dielectric constant of the oxide, and the term y is the *total* oxide thickness at any given time. Then integrating (5), we have:

$$\frac{dV}{dy} = \frac{4\pi ne}{\epsilon} y + C_1 . \tag{6}$$

Since the field dV/dy equals zero at the metal surface when the assumed thickness of the constant charge density film is l, it follows that

$$C = \frac{-4\pi nel}{\epsilon}$$

and

$$V = \frac{-4\pi ne}{\epsilon}\left(ly - \frac{y^2}{2}\right) + C_2 . \tag{7}$$

Now, the potential at the metal surface is $-(\phi - v)$ for the condition that the oxide-film thickness y approaches zero, where $e\phi$ is the energy required to remove an electron from the metal and place it in the oxide at the metal-oxide interface, and v is the apparent positive potential at the metal surface created by the growing oxide. The term v, in general, is numerically equal to the potential difference between the metal-oxide interface and the oxide-oxygen interface for metal-oxide systems in which lattice

diffusion of oxygen ions toward the metal is negligible. As will be shown later, v is approximated by the electron affinity of oxygen adsorbed on the oxide; it is, therefore, a constant independent of oxide thickness and, like the work function, it is substantially independent of temperature. Then $C_2 = -(\phi - v)$.

For values of y much smaller than l, the term $y^2/2$ can be neglected. Hence, from equation (7), the potential affecting escape of an electron from the metal surface in contact with an oxide of increasing uniform negative space charge is approximated by:

$$V = \frac{-4\pi ne}{\epsilon} ly - (\phi - v) . \tag{8}$$

Rate of oxide growth dy/dt is proportional to rate of escape of positive ions, which in turn is controlled by rate of electron escape. Electron current across the contact of a metal and a semi-conducting oxide is found to follow an equation of the type:[52]

$$i = A' \exp \frac{-e\phi}{kT} \left(\exp \frac{ev'}{kT} - 1 \right) \tag{9}$$

where A' is a constant, ϕ is the work function of the metal modified by contact with the oxide, and v' is the applied voltage across the metal-oxide interface. The above equation satisfactorily describes the observation that log i for a rectifying contact is linear with v' over a limited range of applied voltage. Since in our present considerations, v' is found to be in the order of volts, the term exp (ev'/kT) is much greater than unity (at 1 volt, 25°C, $(ev'/kT) = 39$), and, hence, equation (9) simplifies to

$$i = A' \exp \frac{-e(\phi - v')}{kT} \tag{10}$$

This equation neglects the reverse electron current from oxide to metal and considers as important only current leaving the metal.* A simplification of this kind is justified by the high positive field at the metal surface when a metal first oxidizes and whenever the oxide film is relatively thin. Then since the rate of film growth is proportional to electron flow, $(dy/dt) = \beta i$, where β is a constant, and employing equation (8) for the actual potential at the metal surface, i.e. substituting $v - (4\pi ne/\epsilon)ly$ for v', we have:

$$\frac{dy}{dt} = A \exp \frac{-e\phi + ev - \dfrac{4\pi ne^2 ly}{\epsilon}}{kT} \tag{11}$$

where A now replaces $A'\beta$. This equation implies that the effective applied voltage v across the metal-oxide surface is decreased by the accumulating negative charge in the oxide as the oxide grows. Integrating on the condition that when $y = 0$, $t = 0$:

$$y = \frac{\epsilon kT}{4\pi ne^2 l} \ln \left[\left(\frac{4\pi ne^2 lA}{\epsilon kT} \exp \frac{-e(\phi - v)}{kT} \right) t + 1 \right] \tag{12}$$

which is the same form as the logarithmic equation observed experimentally, namely:

$$y = k_0 \ln \left(\frac{t}{\tau} + 1 \right) \tag{13}$$

where $k_0 = \dfrac{\epsilon kT}{4\pi ne^2 l}$

and $\tau = \dfrac{\epsilon kT}{4\pi ne^2 lA} \exp \dfrac{e(\phi - v)}{kT} = \dfrac{k_0}{A} \exp \dfrac{e(\phi - v)}{kT}$.

The above equation (12) applies only to a limited film thickness adjacent to the metal. At the stage of oxidation where the existing interface electric field and oxide structure are no longer conducive to filling all available sites for trapped charge in the oxide, the available sites become only partially occupied. Hence, the excess charge density in oxide further removed from the metal is no longer saturated and uniform, but is influenced by the potential existing at any point in the film. On this premise, nonuniform charge density becomes a property of films that are thicker than those considered above. The situation is similar to the diffuse double layer at metal surfaces in contact with electrolytes, as described by Gouy,[53] Chapman,[54] and Stern.[55] For oxide films still thicker than the diffuse barrier layer, the space charge disappears, and the oxide becomes electrically neutral.

When the charge density in the oxide depends on potential V, the density of positive charge in accord with the derivation of Mott and Gurney[56] can be expressed by $n_1 \exp(-eV/kT)$, and the corresponding density of negative charge by $n_2 \exp(eV/kT)$ where n_1 and n_2 respectively represent the density of lattice sites at which positive and negative charge may attach itself. The excess negative charge density n is the difference of these expressions, and assuming $n_1 = n_2 = n_0$

$$n = n_0 \left(\exp \frac{eV}{kT} - \exp \frac{-eV}{kT} \right) . \tag{14}$$

* Equation (10) applies in theory only to electron current leaving the metal and entering the oxide when this is the direction of easy flow or forward direction, as is the case when copper oxidizes. Oxidation of zinc, to the contrary, corresponds to electron flow in the blocking direction, but even here current-voltage data for rectifying contacts indicate that an equation applies of the same form as (9) but with values of A' and ϕ differing from corresponding values for current flow in the forward direction. See Ref. 52, p. 84–85.

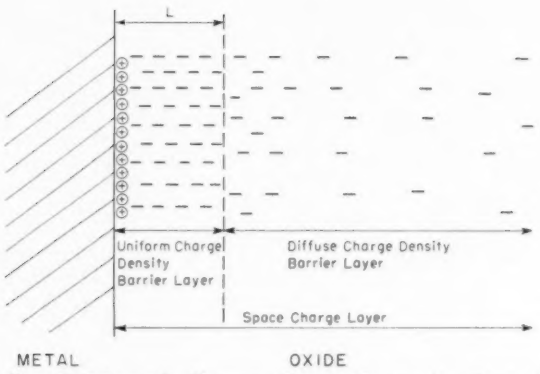

FIG. 3. Schematic diagram of trapped negative charge in uniform and diffuse barrier layers. Positive charge may be localized as shown, or distributed throughout a larger volume of oxide.

If the energy eV is small compared with kT, the exponential terms can be expanded, neglecting higher-power terms than the first, whereupon

$$n = \frac{2n_0eV}{kT} \quad . \tag{15}$$

Substituting this expression for n into the Poisson equation and assuming the potential to be zero when the field is zero, and $V = C'_1$ at $Y = 0$, where Y marks the distance into the diffuse-charge density layer:

$$V = C'_1 \exp \frac{-2Y}{x_0} \quad \text{and} \quad n = \frac{2n_0eC'_1}{kT} \exp \frac{-2Y}{x_0}$$

where x_0 is equal to $\left(\frac{\epsilon kT}{2\pi n_0 e^2}\right)^{\frac{1}{2}}$, and C'_1 is the potential at the oxide-oxygen interface corresponding to the oxide thickness L marking a transition between uniform and diffuse charge density. The density of negative charge n obviously falls off rapidly with distance Y into the oxide (Fig. 3). If we now consider the potential at the metal-oxide interface produced by the diffuse space charge, potential V must become more negative with increased *total* thickness of oxide y, following an equation identical with the above, except for sign of the exponent and where C'_1 is replaced by C_0 equal to the potential at the oxide-metal interface when $y = 0$. If we assume for simplicity that $y = 0$ when the thickness of oxide is L corresponding to a transition from uniform to diffuse charge density, then from equation (8):

$$C_0 = \frac{-4\pi nelL}{\epsilon} - (\phi - v) \, . \tag{16}$$

The oxidation rate as before is proportional to the number of electrons escaping from the metal into the oxide per unit time. From equations (10) and (16), and the relation: $V = C_0 \exp(2y/x_0)$, the oxidation rate is given by the following expression:

$$\frac{dy}{dt} = A \exp \frac{C_0 e \exp \frac{2y}{x_0}}{kT} \, . \tag{17}$$

Furthermore, on the condition that $y \ll (x_0/2)$, the term $\exp(2y/x_0)$ can be expanded and approximated by $1 + (2y/x_0)$. As will be shown later, n_0 for Cu_2O at 225°C equals 4.9×10^{12}, $\epsilon = 10.5$, and $(x_0/2)$, therefore, equals 16,000 Å. This thickness is measured not from the metal surface, but from the point at which the oxide grows beyond uniform density of negative charge; it is appreciably larger than values of oxide thickness y with which we are presently concerned, and on this basis, expansion of the exponential term is justified. Integrating on the condition that when $y = 0$, $t = 0$,

$$y = \frac{x_0}{2}\left(\frac{kT}{-C_0e}\right) \ln \left[\left(\frac{2A}{x_0} \frac{(-C_0e)}{kT} \exp \frac{C_0e}{kT}\right) t + 1\right] \tag{18}$$

which again is of logarithmic type: $y = k'_0 \ln\left(\frac{t}{\tau'} + 1\right)$

where $k'_0 = \frac{x_0}{2}\left(\frac{kT}{-C_0e}\right)$

and $\tau' = \frac{x_0}{2A}\left(\frac{kT}{-C_0e}\right) \exp \frac{-C_0e}{kT} = \frac{k'_0}{A} \exp \frac{-C_0e}{kT}$.

We obtain, therefore, two logarithmic equations; the first, equation (12), expressing the thickness of oxide y as a function of time during build-up of space charge having uniform charge density, and the second, equation (18), corresponding to build-up of oxide having diffuse space charge. These two equations indicate that a change of oxidation rate should occur at the transition from the first-type space charge to that of the second. Data in the literature support this conclusion, discontinuous changes in the logarithmic oxidation rate having been observed for several metals, including copper[2, 3, 6], iron,[2, 8] and zinc.[7] Recent data for copper were obtained for the temperature range 150–250°C by MacNairn.[57] Fig. 4 is a plot of his results at 225°C; the data at other temperatures show a similar linear relation between y and $\log t$, and an increase of the slope to a higher value at a critical thickness of oxide. Specimens of OFHC copper measuring $1 \times 1 \times \frac{3}{8}$ in. were heated in oxygen, using a resistance winding cemented to one face. A thermocouple was embedded in the metal specimen, both for measuring temperature and regulating it automatically. The specimen, with

VOL. 4 1956

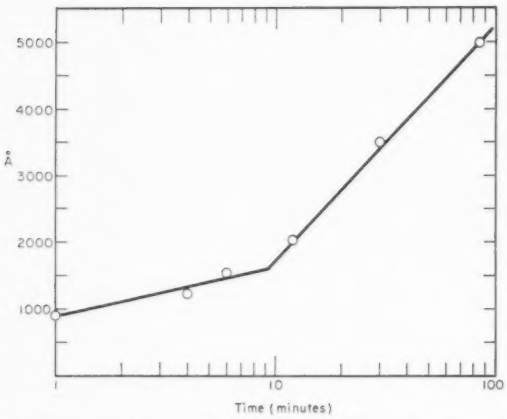

FIG. 4. Thickness of oxide film on copper as a function of time at 225°C in oxygen. Filed surface.

surface prepared using a clean No. 4 file, was introduced into an all-glass chamber containing flowing purified N_2, and the temperature brought up to the required value, using low-voltage a.c. current. Oxygen was then admitted, and the time of oxidation measured from this point, after which the specimen was cooled in N_2. Thickness of the Cu_2O film was determined by cathodic reduction in 0.1 N KCl, employing a small constant d.c. current.

Observed values for k_0, k'_0, τ, and τ' are summarized in Table 2. Values of τ were obtained by extrapolating the first slope to $y = 0$, and for τ' by noting the time at which change of slope occurs. In each instance, the observed value of k'_0 is consistently higher than k_0. Values of τ, inherently subject to large experimental error, vary from 0.03 to 0.3 min, averaging 0.12 min, and for τ' vary from 6 to 14 min, averaging 11 min. Thickness of oxide L at which a change of slope occurs and which is equivalent, according to the foregoing theory, to thickness of that portion of the barrier layer having constant charge density, increases by a factor of 4.5, going from 150°C to 250°C. Lustman and Mehl's[3] oxidation measurements on single crystals of copper scatter appreciably, but show similarly that k'_0 is consistently greater than k_0, with values generally of the same order of magnitude as data of Table 2

TABLE 2. Oxidation rate constants for copper (MacNairn)

Temp	k_0	k'_0	τ	τ'	L (value of y at change of slope)
150°C	90 Å	280 Å	0.3 min	13 min	360 Å
175°	155	520	0.1	14	750
225°	310	1630	0.06	10	1540
250°	290	2440	0.03	6	1630

for overlapping temperatures. Their values for τ and τ' vary from 0.02 to 0.8 min and from 8 to 80 min, respectively, within the temperature range 80° to 155°C. The significance of these terms will be discussed shortly.

The Cubic Equation

It is of interest to note that if the density of negative charge n in the diffuse barrier layer falls off, not as described in deriving equation (18), but in accord with the Boltzmann expression:

$$n = n_0 \exp \frac{Ve}{kT} \tag{19}$$

then upon substituting into the Poisson equation, the solution for potential V is of the type:[58]

$$V = \frac{-2kT}{e} \ln \left(\frac{y}{x_0} + 1 \right) \tag{20}$$

where, as before, $x_0 = \left(\frac{\epsilon kT}{2\pi n_0 e^2} \right)^{\frac{1}{2}}$. The above solution assumes that the field (dV/dy) tends toward zero as y approaches infinity, and $V = 0$ at $y = 0$. If instead we place the condition that at the metal surface $V = C_0$ when $y = 0$, where C_0 is the potential at the metal surface for critical thickness of uniform barrier layer L, then

$$V = \frac{-2kT}{e} \ln \left(\frac{y}{x_0} + \exp \frac{-C_0 e}{2kT} \right). \tag{21}$$

The sign of the potential is such that V becomes more negative the greater the oxide thickness y. Substituting into equation (10) for electron current from metal to oxide, which is proportional to oxidation rate, we obtain:

$$\frac{dy}{dt} = A \exp \frac{eV}{kT} \tag{22}$$

or

$$\frac{dy}{dt} = A \exp \ln \left(\frac{y}{x_0} + \exp \frac{-C_0 e}{2kT} \right)^{-2}. \tag{23}$$

Integrated on the condition that $y = 0$, $t = 0$, we obtain an equation of the cubic form:

$$\left(y + x_0 \exp \frac{-C_0 e}{2kT} \right)^3 = \frac{3A}{x_0^{2/3}} t + x_0^{1/3} \exp \frac{-3C_0 e}{2kT}. \tag{23a}$$

The cubic oxidation equation has been shown to hold approximately within certain ranges of temperature for oxidation of copper,[24, 59, 60] nickel,[61] titanium,[62] and tantalum.[62] One is led to the conclusion, therefore, that charge distribution in the

barrier layer may follow more than a single pattern, depending on experimental conditions, and that the particular pattern followed becomes apparent through the oxidation behavior of the metal.

A cubic-rate equation has been derived by Mott,[63, 23] employing the premise that diffusion of cation vacancies is rate-controlling where the number of vacancies is proportional to number of negative ions per unit surface area and to a linear field set up by the ions. Engell, Hauffe, and Ilschner[61] derived a similar equation based on migration of positive holes and diffusion of lattice vacancies. The present derivation is based on electron flow from the metal as the controlling step in the oxidation process, and, hence, differs basically from both derivations of Mott, and of Engell *et al.* Further experimental work is needed, including effect of grain orientation, of Curie temperature, and of lattice transformation on constants of the cubic equation in order to decide whether the rate for any given metal is controlled by processes of diffusion and conduction in semiconductors, or by electron flow from metal to oxide at the stage where deviations from the logarithmic equation become marked. For thicker films, where the parabolic equation takes over, it is clear through the work of Wagner[1] that ion-diffusion and electric-conduction processes become dominant.

Derivation of the Rideal-Jones Relation

From equation (11), taking the logarithm of both sides, we have:

$$\ln \frac{dy}{dt} = \frac{-e(\phi - v)}{kT} - \frac{4\pi n e^2 l}{\epsilon k T}\, y + \ln A. \qquad (24)$$

Also, from the relation $y = k_0 \ln\left(\frac{t}{\tau} + 1\right)$, we have:

$$\ln \frac{dy}{dt} = \ln k_0 - \ln (t + \tau). \qquad (25)$$

Comparing (24) and (25), and remembering that $k_0 = \frac{\epsilon k T}{4\pi n e^2 l}$,

$$\ln k_0 = \frac{-e(\phi - v)}{kT} + \ln \tau + \ln A. \qquad (26)$$

The constant A is essentially temperature-independent. Since $\left(\frac{dy}{dt}\right)_{t=0} = \frac{k_0}{\tau}$, the term τ is the time necessary to oxidize the metal to thickness k_0 at the initial oxidation rate. It was found by Tammann and Köster[2] to be strictly independent of temperature, based on their oxidation data for a variety of metals. Although it is conceivable that τ may actually vary slightly with temperature for some metals and not at all for others, precision of present-day data, including values in Table 2, are not adequate to imply a conclusion different from that of Tammann's. Therefore, $\frac{d \ln \tau}{d1/T}$ may be considered negligible or zero, and:

$$\frac{d \ln k_0}{d1/T} = \frac{-e(\phi - v)}{k} = \frac{-e(\Delta E)}{k} \qquad (27)$$

where ΔE is the activation energy for oxidation in electron volts from the Arrhenius relation $k_0 = \text{const}\ \exp(-e\Delta E/kT)$, ϕ is the work function of the metal modified by contact with the oxide, and v is a constant positive potential in the oxide at the metal sufrace (approximated by the electron affinity of the oxygen atom). If X_1 and X_2 are work functions of the oxide at the metal-oxide and oxide-oxygen interfaces, respectively, it follows that

$$\Delta E = \phi_0 - X_1 + [X_2 - (\phi_a + \phi_\epsilon)] \qquad (28)$$

where ϕ_0 is the work function of the metal, ϕ_ϵ is the electron affinity of oxygen, and ϕ_a is a small additive energy introduced by adsorption of oxygen on the oxide. If $X_1 = X_2$,

$$\Delta E = \phi_0 - (\phi_a + \phi_\epsilon) = \phi_0 - K \qquad (29)$$

which is the Rideal-Jones relation as applied to oxidation of metals forming thin, nonvolatile oxides, and is the empirical expression originally proposed for W, Pt, and C, which form volatile oxides.

If the work function of the oxide at the metal interface X_1 is less than the work function X_2 at the oxygen interface, then K will be larger than the value calculated from equation (29) above. This may be the situation for both Cu and Fe. Values of $\phi_0 - \Delta E$ or of K for Cu are $4.5 - 0.28 = 4.3$ eV, and for Fe are $4.4 - 0.30 = 4.1$ eV, where the activation energy for Cu is taken from MacNairn's data, and for iron from Davies, Evans, and Agar's[11] data.* The work functions are from Michaelson.[38]

* Since the logarithmic equation applies to the oxidation of iron over the temperature range considered, the activation energy is obtained from the slope of log weight gain, at t = constant, vs. $1/T$. This follows from the proportionality between thickness of oxide y and weight gain, and the fact that $\ln y = \ln k_0 + \ln \ln \left(\frac{t}{\tau} + 1\right)$. Hence, since τ is a constant and t is held constant, $\frac{d \ln y}{d \frac{1}{T}} = \frac{d \ln k_0}{d \frac{1}{T}} = \frac{-e\Delta E}{k}$ where k is Boltzmann's constant. Data in Fig. 13 of Davies, Evans, and Agar's paper[11] show that essentially the same activation energy is calculated for various times of oxidation (15 min to 8 h) in the logarithmic range, with the exception of the 15- and 30-min runs where experimental error is perhaps greatest.

VOL. 4 1956

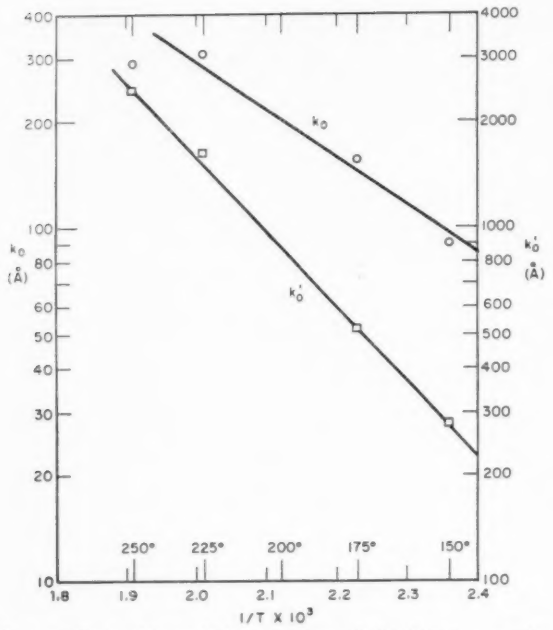

FIG. 5. Plots of k_0 and k'_0 vs. reciprocal absolute temperature for copper oxidized in oxygen. Filed surfaces.

These values of K are larger than 3.6 eV, the average value for elements listed in Table 2. When more precise data are available both for metal-work functions and for activation energies of oxidation, more definite conclusions will be possible than are now warranted.

Using a derivation similar to that given above, it can also be shown that

$$\frac{d \ln k'_0}{d1/T} = \frac{C_0 e}{k} \tag{30}$$

where C_0 is given by equation (16), and k'_0 is the second and steeper slope obtained by plotting y vs. $\ln t$.

DISCUSSION

In accord with equations (27) and (30), plots of $\log k_0$ and $\log k'_0$, using data of Table 2, vs. $1/T$ provide means for calculating $(\phi - v)$ and $-C_0$, respectively. From slopes of data so plotted in Fig. 5, these values are 0.28 eV and 0.42 eV, respectively. Since $C_0 = \dfrac{-4\pi nelL}{\epsilon} - (\phi - v)$ (equation 16), we know all terms of this equation except the product nl, for which we can solve. On the basis that $\epsilon = 10.5$ and observed L at 225°C = 1540 Å (Table 2), $nl = 5.3 \times 10^{10}$. Also, from the relation $k_0 = \dfrac{\epsilon kT}{4\pi ne^2 l}$ and employing the observed value for k_0 at 225°C equal to 310 Å, we obtain $nl = 8.1 \times 10^{10}$, which is in reasonable agreement with the value calculated from C_0 and $(\phi - v)$. We can next calculate a value for n_0 from the relation given in equation (18) that $k'_0 = \dfrac{x_0}{2}\left(\dfrac{kT}{-C_0 e}\right)$, and from the observed value of $k'_0 = 1630$ Å, where $x_0 = \left(\dfrac{\epsilon kT}{2\pi n_0 e^2}\right)^{\frac{1}{2}}$. The corresponding value for n_0 is 4.9×10^{12}, which is the density of available sites for trapped electric charge in the diffuse space charge layer. This density is equivalent to about one lattice site for every 5×10^9 molecules of Cu_2O.

We have next to check how density n_0 compares with density n of trapped electrons in the uniform space charge layer. Since only the product nl is known from experiment, an estimate of l must be made through equation (7), substituting $V = -\phi$ at $y = l$ and $C_2 = -(\phi - v)$. It follows that $v = \dfrac{4\pi nel^2}{2\epsilon}$. Since the value of v is the same order as K (equation (29)) or the same order as the modified electron affinity of oxygen equal to 3.6 eV, we find, substituting 6.7×10^{10} for the average value of nl, in accord with the foregoing calculations, that $l = 6.2 \times 10^{-4}$ cm. This value for l represents the theoretical maximum thickness of the uniform charge density barrier layer (the diffuse barrier layer may be considerably thicker). It is larger than the observed thickness of uniform barrier layer L by a factor of about 40, and should be approximately comparable with the thickness of the "blocking" layer next to the copper surface in the Cu-Cu_2O rectifier. The thickness of the blocking layer is estimated from capacitance measurements to be about 10^{-4} cm.[64] which is not far from the above calculated value for l.

Knowing the value for l, the value for n, therefore, equals $\dfrac{6.7 \times 10^{10}}{6.2 \times 10^{-4}}$, or 1.08×10^{14}. Accordingly, the actual density of trapped charge in the Cu_2O layer of thickness L next to the metal appears to be larger than the density (4.9×10^{12}) of available sites for trapped charge in the diffuse space charge layer farther away from the metal surface.

This relative difference in density persists, although absolute densities increase, if correction is made for the larger absolute surface compared to the geometrical surface of a filed copper surface. Assuming a roughness factor of 3, comparable with published values of 3.8,[65] and 2.5[66] for abraded metal

surfaces, film-thickness values such as those in Fig. 4 would be decreased to one-third the given values, and both n_0 and n would increase by a factor of 9, making the densities approximately 5×10^{13} and 10^{15}, respectively. Values of l and L correspondingly would be reduced by one-third.

Values for n, l, and n_0 calculated from MacNairn's data at several temperatures and not corrected for roughness factor are given in Table 3. Values of nl are averages of values obtained from observed k_0 and L, with the exception of 250°C, where only the value obtained from L was used. This procedure was followed because the value for k_0 at 250°C falls off the line in Fig. 5. If the value for k_0 were included, the corresponding calculated value for nl is 0.9×10^{11} compared with 0.5×10^{11} given in Table 3. It is evident that for cuprous oxide in contact with copper, n_0 decreases with temperature (fewer sites for trapped charge in the diffuse barrier layer as the temperature increases). This is also true of n, the actual charge density in the uniform space charge layer. Accordingly, the equilibrium:

Bound hole + free electron $\leftrightharpoons$ trapped electron

is displaced to the left as the temperature increases. The observed increase of l with temperature parallels extension of the space charge to greater distances into the oxide the higher the temperature. This trend is also reflected by increased observed thickness L for the uniform barrier layer (Table 2).

Brattain[67] calculated the density of holes in Cu_2O as function of temperature from conductivity of the oxide and mobility of carriers. He found that a limiting upper density, equal to the density of electron acceptors minus density of acceptors occupied by electrons from higher-lying donor levels, occurs in the range 100°C or higher and that the limiting density is 10^{15} for OFHC copper and 10^{14} for Chile copper. These values are reasonably comparable with the calculated density of charge n or density of defect sites for bound electrons n_0 in Table 3. His calculations, however, show that the density of holes does not decrease with temperature, but instead is relatively insensitive to temperature in the region of 100°C or higher, and that below 100°C the density increases with temperature.

TABLE 3. Numerical evaluation of terms in logarithmic oxidation-rate equations

Temperature	nl (cm)$^{-2}$	n_0	n	l (cm)
150°C	2.3×10^{11}	1.0×10^{14}	1.3×10^{15}	1.8×10^{-4}
175°C	1.3×10^{11}	3.5×10^{13}	3.8×10^{14}	3.3×10^{-4}
225°C	0.67×10^{11}	4.9×10^{12}	1.1×10^{14}	6.2×10^{-4}
250°C	0.50×10^{11}	2.6×10^{12}	0.60×10^{14}	8.4×10^{-4}

The value for A in equation (11) can be calculated from the relation following equation (13), $\tau = \frac{k_0}{A} \exp \frac{e(\phi - v)}{kT}$. At 225°C, for example, $\tau = 3.6$ sec, $k_0 = 310$ Å, $(\phi - v) = 0.28$ V. Therefore, $A = (0.86 \times 10^{-6}) \exp 6.53 = 5.9 \times 10^{-4}$ cm/sec. It will be remembered that $A = A'\beta$, where β expresses the relation between electric current and rate of oxide growth, and whose value for density of $Cu_2O = 6$ is 1.23×10^{-4} cm^3/coulomb. The value for A' in equation (10), accordingly, equals $\frac{5.9 \times 10^{-4}}{1.23 \times 10^{-4}} = 4.8$ amp/cm^2. The average value for A' for all temperatures of Table 2 is 2.2 amp/cm^2. Similarly, the average value of A' from the relation $\tau' = \frac{k'_0}{A} \exp \frac{-C_0 e}{kT}$ averaging all values of τ' and $k'_0 \exp \frac{-C_0 e}{kT}$ is equal to 3.5 amp/cm^2. These two values are the same order of magnitude. These average values of A', if corrected for a roughness factor of 3, would be one-third the given values.

The ratio τ'/τ as derived from equations (12) and (18) is equal to the expression $(k'_0/k_0) \exp (-C_0 e/kT - e(\phi - v)/kT)$. The exponential factor is a constant at any given temperature, since $-C_0$ and $(\phi - v)$ are constants equal to 0.42 and 0.28 V, respectively. At 225°C, for example, $\tau'/\tau = (1630/310) \exp 3.3 = 143$. The observed ratio is $10.0/0.06 = 167$, which is of the same order of magnitude. The average of calculated ratios for τ'/τ for all temperatures is 153, corresponding to an observed average (Table 2) of 138, showing that the agreement of theory with experiment is good.

The described dependence of oxidation rate on work function of the metal and on properties of semiconducting oxides in contact, immediately suggests several reasons for experimental hurdles usually encountered in reproducing thin-film oxidation behavior. Despite refined techniques for metal-surface preparation and gas purification, it is extremely difficult to avoid the trace impurities which greatly affect the metal-work function, and also the number of sites available for trapped charge in oxide films. The major influence of trace impurities in semiconducting germanium and silicon has only recently been fully appreciated in connection with the use of these substances for rectifiers and for transistors. Added to the marked effect of impurities, often present

VOL. 4 1956

in amounts below detection by common analytical techniques, is the appreciable effect of thermal treatment on the density of lattice imperfections in semiconductors. It is little wonder that various investigators have reported difficulty in reproducing oxidation data at low temperatures; Vernon, Akeroyd, and Stroud[7] reported such difficulties in their study of zinc, Leontis and Rhines[47] in their study of magnesium, and Brasunas and Uhlig[29] in their studies of Cr-Fe alloys. A full appreciation of the various factors entering thin-film oxidation should help such studies in the future.

Acknowledgments

Support of this research by the Office of Naval Research on Contract No. N5ori-07815, and also by The Research Corporation, is gratefully acknowledged. Reproduction in whole or in part is permitted for any purpose by the United States Government. Appreciation is expressed to T. B. Smith and to J. MacNairn for assistance in the Volta-potential and oxidation-rate measurements.

REFERENCES

1. C. Wagner *Z. phys. Chem.* **21B,** 25 (1933); **32B,** 447 (1936); **40B,** 455 (1938).
2. G. Tammann and W. Köster *Z. Anorg. Allg. Chem.* **123,** 196 (1922).
3. B. Lustman and R. Mehl *Trans. Amer. Inst. Min. Met. Eng.* **143,** 246 (1941).
4. A. H. White and L. Germer *Trans. Electrochem. Soc.* **81,** 305 (1942).
5. H. H. Uhlig and A. Brenner *Acta Met.* **3,** 108 (1955).
6. R. Tylecote *J. Inst. Metals* **78,** 327 (1950).
7. W. Vernon, E. Akeroyd, and E. Stroud *J. Inst. Metals* **65,** 301 (1939).
8. B. Lustman *Trans. Electrochem. Soc.* **81,** 359 (1942).
9. A. Winterbottom *J. Iron and Steel Inst.* **165,** 9 (1950).
10. W. Vernon, E. Calnan, C. Clews, and T. Nurse *Proc. Roy. Soc.* **216A,** 375 (1953).
11. D. Davies, U. Evans, and J. Agar *Proc. Roy. Soc.* **225A,** 443 (1954).
12. H. H. Uhlig and J. J. Pickett unpublished data.
13. W. Scheuble *Z. Physik.* **135,** 125 (1953).
14. A. Steinheil *Ann. Physik.* **19,** 455 (1934).
15. J. Waber, G. Sturdy, and E. Wise *J. Amer. Chem. Soc.* **75,** 2269 (1953).
16. J. Waber, G. Sturdy, E. Wise, and C. Tipton *J. Electrochem. Soc.* **99,** 121 (1952).
17. U. R. Evans *Trans. Electrochem. Soc.* **83,** 335 (1943).
18. U. R. Evans *Nature* **157,** 732 (1946).
19. H. Miley *Trans. Electrochem. Soc.* **81,** 391 (1942); O. Hamilton and H. Miley *ibid.* **81,** 413 (1942).
20. N. Mott *Trans. Faraday Soc.* **35,** 1175 (1939).
21. V. Holm *J. Res. Nat. Bur. Stds.* **28,** 569 (1942).
22. N. Mott *Trans. Faraday Soc.* **43,** 429 (1947).
23. N. Cabrera and N. Mott *Reports on Prog. in Physics* **12,** 163 (1949).
24. W. Campbell and U. Thomas *Trans. Electrochem. Soc.* **91,** 623 (1947).
25. A. Gwathmey *Corrosion Handbook,* p. 33–35, edited by H. H. Uhlig, John Wiley and Sons, Inc., New York, 1948.
26. R. Mehl and E. McCandless *Trans. Amer. Inst. Min. Met. Eng.* **125,** 531 (1937).
27. R. Mehl, E. McCandless, and F. Rhines *Nature* **134,** 1009 (1934).
28. K. Fischbeck and F. Salzer *Metallwirtschaft* **14,** 753 (1935).
29. H. H. Uhlig and A. S. Brasunas *J. Electrochem. Soc.* **97,** 448 (1950).
30. G. Tammann and G. Siebel *Z. anorg. allg. Chem.* **148,** 297 (1925).
31. E. Rideal and O. Wansbrough-Jones *Proc. Roy. Soc.* **123A,** 202 (1929).
32. *Oxidation Potentials,* W. M. Latimer, second edition, p. 18, Prentice-Hall, Inc., New York, 1952.
33. H. S. Taylor *J. Amer. Chem. Soc.* **53,** 578 (1931).
34. *Chemisorption,* B. Trapnell, Academic Press, New York, 1955.
35. J. Becker and C. Hartman *J. Phys. Chem.* **57,** 153 (1953).
36. G. Ehrlich *J. Phys. Chem.* **59,** 473 (1955).
37. K. Krishnan and S. Jain *Nature* **170,** 759 (1952).
38. H. Michaelson *J. Appl. Physics* **21,** 536 (1950).
39. R. Smoluchowski *Phys. Rev.* **60,** 661 (1941).
40. H. Farnsworth and R. Winch *Phys. Rev.* **58,** 812 (1940).
41. Also various papers on field emission microscope, e.g., E. W. Müller *Ergeb. der Exakten Naturwiss* **27,** 290–360 (1953); J. A. Becker *Bell Syst. Tech. J.* **30,** 907 (1951).
42. E. Houdremont and O. Rüdiger *Naturwiss.* **39,** 399 (1952).
43. H. Wahlin *Phys. Rev.* **61,** 509 (1942).
44. A. Cardwell *Phys. Rev.* **76,** 125 (1949).
45. N. Mott and R. Gurney *Electronic Processes in Ionic Crystals,* pp. 80–88, Oxford Press (1940).
46. E. Gulbransen and W. Wysong *J. Phys. Chem.* **51,** 1087 (1947).
47. T. Leontis and F. Rhines *Trans. Amer. Inst. Min. Met. Eng.* **166,** 265 (1946).
48. E. Gulbransen *Trans. Electrochem. Soc.* **87,** 589 (1945).
49. W. Zisman *Rev. Sci. Instrum.* **3,** 367 (1932).
50. H. H. Uhlig *J. Appl. Phys.* **22,** 1399 (1951).
51. R. Hirschberg and E. Lange *Naturwissenschaften* **39,** 187 (1952).
52. *Crystal Rectifiers,* H. Torrey and C. Whitmer, p. 22, 80–84, McGraw-Hill, New York, 1948.
53. G. Gouy *J. de Physique* **9,** 457 (1910).
54. D. Chapman *Phil. Mag.* **25,** 475 (1913).
55. O. Stern *Z. Elektrochem.* **30,** 508 (1924).
56. Ref. 45, p. 176.
57. J. MacNairn and H. H. Uhlig unpublished data.
58. Ref. 45, p. 170.
59. T. Rhodin *J. Amer. Chem. Soc.* **72,** 5102 (1950).
60. R. Tylecote *J. Inst. Metals* **81,** 681 (1953).
61. H. Engell, K. Hauffe, and B. Ilschner *Z. Elektrochem.* **58,** 478 (1954).
62. J. T. Waber *J. Chem. Physics* **20,** 734 (1952).
63. N. Mott *Trans. Faraday Soc.* **36,** 472 (1940).
64. Ref. 45, page 178.
65. R. Powers and N. Hackerman *J. Electrochem. Soc.* **100,** 314 (1953).
66. O. Erbacher, *Z. Physik. Chem.* **163,** 215 (1933); *Chemiker Z.* **62,** 601 (1938).
67. W. Brattain *Rev. Modern Physics* **23,** 203 (1951).

L'Interaction Elastique d'Atoms en Solution Solide*

Dans un article datant de quelques années,[1] j'avais donné une théorie générale des énergies d'interaction entre un champ de contrainte et un défaut (dislocations, atomes étrangers, lacunes, etc.). Cette théorie permettait de distinguer deux cas: celui où le défaut a une même constante élastique que la matrice (ce qui constitue une généralisation de l'effet Cottrell) et celui où le module du défaut est différent, ce qui introduit un terme d'interaction supplémentaire. Appliquée au cas de deux atomes étrangers en solution solide dans un métal, cette théorie dans sa forme primitive, prévoyait que, lorsque ces atomes étrangers constituent des "points plus durs" que la matrice, ils devaient en général s'attirer mutuellement.

Récemment, Eshelby[2] vient de reprendre le calcul de ce cas, et a trouvé un résultat qualitativement différent: des points durs devraient se repousser mutuellement. Eshelby n'a pas cherché quelle était l'origine de ce désaccord.

En regardant la question de près, on constate deux différences entre la théorie d'Eshelby et la mienne.

1°—Eshelby s'est cantonné au domaine de l'élasticité linéaire, alors que j'avais pensé que, dans les fortes déformations au voisinage d'atomes étrangers, il fallait tenir compte des termes du second ordre. Ces termes n'ont pas d'importance dans le cas de l'effet Cottrell (interactions entre dislocations et atomes étrangers) qui est un effet du premier ordre; mais entre deux atomes dissous l'interaction est du second ordre et le fait de négliger les écarts à l'élasticité linéaire conduit en réalité à négliger des termes qui sont du même ordre que l'effet lui-même.

2°—Mais même en négligeant ces termes du second ordre, on voit que le signe de l'energie d'interaction est différent dans les deux théories.

Il est aisé de trouver l'origine de ce désaccord en remontant les deux calculs pas à pas: les calculs se déroulent de façon tout-à-fait parallèle, sauf en ce qui concerne une des hypothèses de départ: j'avais considéré un *champ de contrainte* uniforme dans un petit volume entourant un atome dissous, alors qu'Eshelby y suppose un *champ de déformation* uniforme.

Sans entrer dans le détail des calculs, on peut illustrer cette différence de point de vue de façon intuitive: les calculs d'Eshelby et les miens sont d'accord pour démontrer que l'introduction d'atomes plus durs augmente le module moyen d'une masse métallique, ce qui semble assez normal. Il en résulte que pour une *déformation imposée* la variation d'énergie due à l'introduction de ces atomes durs est positive, alors que pour des *contraintes imposées* sur une surface externe, cette variation est négative.

Ceci étant, considérons une masse, supposée infinie, d'un métal A dans laquelle se trouve un atome d'un autre métal B, soit B_1, en insertion ou en substitution. Prenons un 2ème atome de métal B soit B_2 et cherchons à l'introduire dans la masse. Pour cela pratiquons une coupure en forme de petite sphère dans le métal A et introduisons y l'atome B_2. Pour être correct, il faut que la petite sphère ait un rayon au moins aussi grand que celui de l'écran électronique qui s'établit autour d'un atome étranger; s'il s'agit d'une solution solide d'insertion cela conduira à enlever un petit nombre n d'atomes A, d'inserér en leur milieu l'atome B_2, puis de réintroduire le tout dans la cavité; s'il s'agit d'une solution solide de substitution, on retirera de la cavité n atomes, on en enlèvera un que l'on remplacera par l'atmoe B_2, puis on réintroduira dans la cavité $(n-1)$ atomes A plus l'atome B_2.

Plaçons nous dans le cas où le petit volume réinséré a un module plus élevé que le métal A: c'est ce que j'ai appelé plus haut un point dur.

Si on considère que l'acte de la réinsertion de ce petit volume impose un *déplacement* aux parois de celle-ci, il est évident d'après les considérations générales exposées plus haut que le supplément d'énergie dû à la présence de l'atome B_1 sera positif. C'est l'hypothèse que fait Eshelby.

Si au contraire on considére que cette réinsertion produit essentiellement une *contrainte* imposée sur la paroi de la cavité, ce supplément sera négatif. C'est ce que j'avais supposé dans ma théorie basée toute entière sur les contraintes.

La réalité doit être entre les deux, et dépend de façon complexe des forces interatomiques locales, question encore mal connue et discutée, comme l'a montré récemment Oriani dans ce même journal.[3] Intuitivement et qualitativement, la solution réelle doit être plus proche de celle d'Eshelby que de la mienne, mais s'en écartera d'autant plus que les atomes en jeu sont plus compressibles.

VOL. 4 1956

D'ailleurs, il s'agit là de termes qui décroissent comme l'inverse de la 6ème puissance de la distance entre atomes étrangers; ils ne se manifestent que lorsque les atomes sont très proches; et à ce moment, comme ils sont du second ordre, ils se trouvent faibles vis à vis des termes électroniques, de sorte qu'en pratique cette interaction élastique n'a probablement pas grande influence. La question est donc plutôt académique.

C. CRUSSARD

Institut de Recherches de la Siderargie
Saint-Germain-en-Laye, France

References

1. C. CRUSSARD Diffusion et Interaction des impuretés et des défauts de structure dans les métaux *Métaux et Corrosion* n° 301, 203 (1950).
2. ESHELBY *Acta Met.* **3,** 487 (1955).
3. ORIANI *Acta Met.* **4,** 15 (1956).

* Received February 25, 1956.

Geometrical Effects Observed in the Ti (solid)-Al (liquid) Diffusion Couple due to Compound Formation*

During an investigation of diffusion occurring between titanium and aluminum and their alloys, an unexpected geometrical effect has been observed in the "diffusion" zone.

The materials used were titanium (100 A and 75 A), titanium steel (RCA-110-AT), and superpurity aluminum. The titanium specimens, $10 \times 5 \times 3.14$ mm, were first abraded using 0-grade emery paper, etched in an aqueous solution containing 1.5% hydrofluoric acid and 3% nitric acid at 60°C for about 3 min, rinsed in water and acetone, and then dried. The titanium specimens were then immersed in molten aluminum and heated *in vacuo* at 800 ± 5°C for various periods of time. After cooling, metallographic sections of the titanium enclosed by the solidified aluminum were prepared and scanned microscopically to determine the growth of the "diffusion" zone. In addition, X-ray diffraction, microhardness measurements, and spectrographic analysis were used to identify the constituents.

Figs. 1, 2, and 3 show typical patterns produced by the above procedure and illustrate how the apparent diffusion zone appears to grow perpendicular to the surface of the titanium so that no diffusion occurs at the corners. A preliminary investigation has led to the conclusion that the "diffusion" zone (dark-grey) consists of an aluminum matrix containing $TiAl_3$, whereas the areas at the corners (light-grey) consist of aluminum only. Microhardness measurements

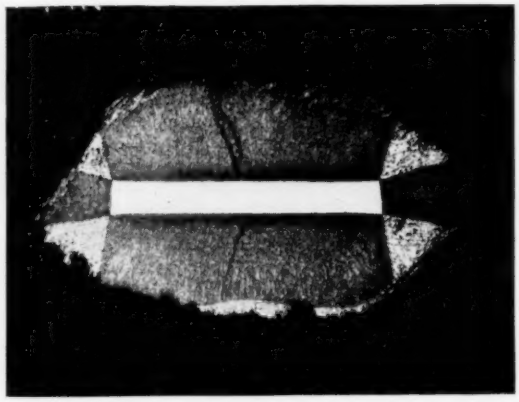

FIG. 1.

indicate that there is slight diffusion of aluminum into solid titanium, as there is some evidence that a thin diffusion layer, which does not thicken with time, exists at the interface.

Fig. 1 shows a typical diffusion pattern produced by heating titanium (white area) in aluminum at 800 ± 5°C for $2\frac{1}{2}$ hr. The dark grey area consists of $TiAl_3$ and Al, whilst the areas at the corners (light-grey) consist of aluminum. This section was taken parallel to the length of the specimen. Fig. 2 shows a section taken perpendicular to the length, and was obtained by heating at 850 ± 5°C for 5 hr. Microhardness measurements of an enlarged view of a corner are illustrated in Fig. 3.

A survey of the literature shows that a similar phenomenon has been observed previously in the Fe-Zn (molten) system by Scheil and his coworkers,[1, 2, 3] and that the "cruciform" patterns obtained resemble those illustrated (Figs. 1–3). However, whereas the corner angles observed in the present work were always acute and thus resembled those produced during the high-temperature oxidation

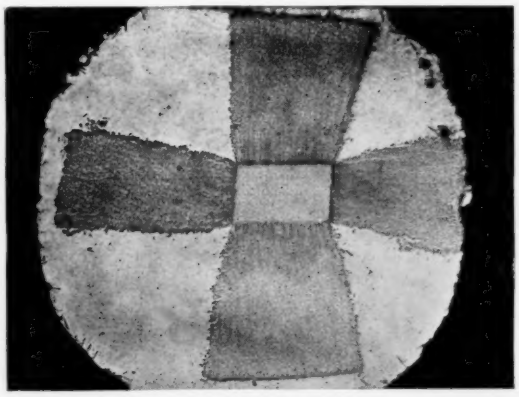

FIG. 2.

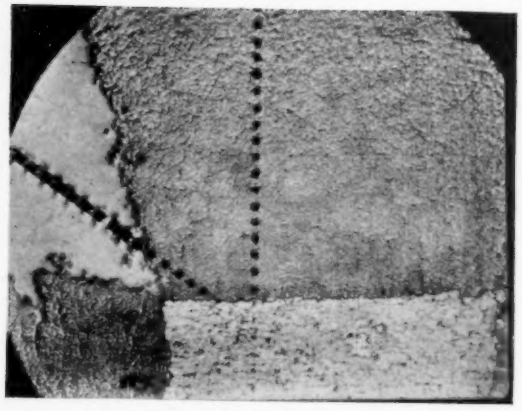

FIG. 3.

of titanium and tungsten carbide,[4, 5] the patterns obtained by Scheil showed the corners to be right angles.

Scheil points out that, with the Fe-Zn (molten) system, this pattern is only obtainable in a limited temperature range of about 450–520°C, and that the temperature is markedly affected by impurities in the iron and zinc. The mechanism of the process is considered to be due entirely to the formation and crystallization of $FeZn_7$, which forms layers pervious to molten zinc so that the formation and growth of the compound follow a linear law. At temperatures above and below the temperature range, $FeZn_3$ is produced as an impervious continuous layer resulting in a parabolic growth law.

It is considered from the results observed in the present work, that the mechanism for the formation of the "cruciform" patterns is due to the following three-stage process.

Firstly, titanium dissolves in the liquid aluminum at a rate which is very rapid compared to the rate of diffusion of aluminum into titanium. A saturated solution of Al-Ti is thus produced from which $TiAl_3$ precipitates as a loosely adherent layer around the titanium. Since this layer is pervious to the molten aluminum, $TiAl_3$ forms continuously at the Al-Ti interface, resulting in the initial layers being forced away from the titanium surface. Finally, the tensile stress in the continuous layer of $TiAl_3$ becomes sufficient to cause rupture at its weakest pionts, i.e. at the corners of the titanium.

The concurrent formation of $TiAl_3$ at the interface, rupture of the layer, and the decrease in dimensions of the titanium specimen result in a cruciform pattern in which the outer dimensions of the layer correspond to those of the titanium originally. This mechanism also accounts for the acute angles observed.

It would appear that the cruciform patterns obtained with Ti-Al (molten) and Fe-Zn (molten) are due to compound formation, producing layers which are pervious to the molten metals resulting in a linear growth law. However, whereas in the Fe-Zn (molten) system the patterns have been explained by Scheil as due to a process of crystallization only, it is considered necessary to postulate the above three-stage mechanism to account for the cruciform pattern obtained with the Ti-Al (molten) system.

Further work is being carried out on the kinetics of the process.

J. MACKOWIAC
L. L. SHREIR

Metallurgy Dept.
Battersea Polytechnic
London

1. E. SCHEIL *Z. Metall.* **27,** 76 (1935).
2. W. PUNGEL, E. SCHEIL, and R. STENKOFF *Arch. Eisenhütt.* **9,** 301 (1935).
3. E. SCHEIL and H. WURST *Z. Metall.* **29,** 224 (1937).
4. R. KIEFFER and F. KOLBL *Z. anorg. Chem.* **Z82,** 245 (1950)
5. R. KIEFFER and F. BENOSOVSKY *Z. Metallkunde* **42,** 97 (1951).

*Received March 26, 1956.

Gases in Rocksalt and the Joffé Effect*

1. *The Stress-strain Curve*

In this note we report preliminary results of experiments which indicate that gases can effect in a considerable way the mechanical properties of rocksalt single crystals.

A small block, cleaved from the interior of a freshly made and well-annealed rocksalt single crystal was divided into different parts. These were compressed in a Chevenard micro-tensile machine. It was observed that some difference existed between the mechanical behavior of the parts examined immediately after dividing the original block and those that had been exposed to dry air for a couple

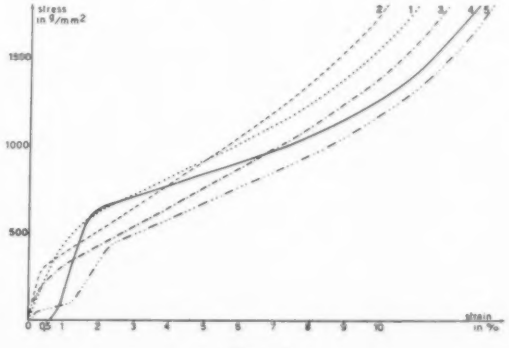

FIG. 1.

of weeks. This aging effect could only be due to adsorption of gases. In order to obtain more definite information, blocks, cleaved from neighboring regions of rocksalt single crystals, were heated at 300°C in an autoclave filled in turn with nitrogen, hydrogen, and argon at a pressure of 10 atm.

Stress-strain curves were made after each treatment. The results are summarized in Fig. 1. It was found that hydrogen and argon gave no observable effect; the stress-strain curves were identical with those obtained for crystals which had not been submitted to a gas treatment (curve 1).

Nitrogen, on the contrary, had a marked effect; the outer lamella cleaved from the block after a 48-hr. run were much harder than those from the interior part. Smaller blocks and longer runs gave curves marked 2 in the figure.

Heating at 650°C in oxygen at reduced pressure makes the crystals softer (curve 3). This effect is far more marked when the same treatment is applied in argon under reduced pressure or in a high vacuum (curves 4 and 5). In the latter cases the shape of the curves alters quickly when the crystals are exposed to air. After two or three hours it becomes comparable with curve 1: approaches it more and more closely. The reported examples show that the stress-strain curve of rocksalt is extremely sensitive to treatments consisting in adsorbing and (or) dissolving gases in the crystals or desorbing them.

2. *The Joffé Effect*

It has for long been known that rocksalt crystals can be heavily deformed under water or when the specimens are wetted. When this precaution is not taken, surface cracks develop after a certain amount of deformation and they spread very quickly through the crystals. The dissolving action of the water, by which incipient cracks are healed or removed, has mostly been accepted as the explanation of this Joffé effect.[1] We were able to show that such is not the case and that the water layer essentially prevents adsorption of gases on the surface features resulting from slip. In order to prove this, the following procedure was adopted. The surface layers of cleaved specimens were dissolved in alcohol; they were afterwards rinsed with ether. Some were allowed to dry in air and were deformed immediately afterwards in a small and rudimentary tensile machine. Surface cracks developed very quickly after a small amount of deformation.

Other samples were transferred immediately after rinsing into a small tank filled with ether or paraffin-oil. Under these liquids, which have no dissolving action at all, the specimens could be deformed as heavily as under water. This is consistent with the statement of Joffé[2] that crystals which had been wetted could be deformed without formation of surface cracks some days afterwards if they had been stored in a vacuum.

3. *Conclusion*

The reported experiments indicate that the stress-strain curves of rocksalt crystals are markedly affected by gases, especially nitrogen, which can, under certain circumstances, diffuse into the crystals. The layer containing the gas varies in thickness according to the previous history of the specimens and is much harder than the other parts of the crystals. This indicates that the gas molecules pin down the dislocations and prevent their movement in the considered layer; the resulting piling-up produces the surface cracks. That the adsorption is a rapid process is proved by the fact that screening from air during deformation has a major effect; this points towards open dislocations. The presence of a more or less developed hard layer may be responsible for the large discrepancies between theoretical considerations about the plasticity of rocksalt and the observed properties.[3] In order to check this, we are now examining the mechanical properties of fully degassed crystals in a gas-free surrounding.

This work is part of a research program CES sponsored by IRSIA (Brussels).

E. Aerts
W. Dekeyser

Laboratorium voor Kristalkunde
Rozier, 6
Gent/Belgium

References

1. A. Joffé *The Physics of Crystals* 1st ed., 2nd imp. McGraw-Hill Book Co. N.Y. p. 63 (1928).
2. A. Joffé *The Physics of Crystals* 1st ed., 2nd imp. McGraw-Hill Book Co. N.Y. p. 21 (1928).
3. H. R. Huntington, J. E. Dexter, and R. Thomson *Phys. Rev.* **100,** 1117 (1955).

* Received April 3, 1956.

Elektrische Leitfähigkeit und Suszeptibilität des Systems Titan-Aluminium*

Für das System Titan-Aluminium wurde nach den bisherigen Untersuchungen[1–4] angenommen, dass das Gebiet des homogenen α-Mischkristalls sich von 0 bis 25 Gewichts-% Aluminium erstreckt. Ähnliche Löslichkeitsverhältnisse wurden für das System Titan-Zinn festgestellt.[5, 6] Das homogene Gebiet erstreckt sich hier von 0 bis 20 Gewichts-% Zinn. Während aber im System Titan-Zinn alle α-Legierungen

verformbar sind, ist dies beim System Titan-Aluminium nicht mehr der Fall, wenn der Aluminium-Gehalt 7,5% übersteigt.[7] Dieser Unterschied in den mechanischen Eigenschaften veranlasste uns, das elektrische und magnetische Verhalten der α-Legierungen im System Titan-Aluminium zu untersuchen.

Als Ausgangsmaterialien dienten in unserem Laboratorium hergestelltes Jodid-Titan (Brinellhärte $HB_{30} < 90$ kg/mm²) und technisches, durch Magnesium-Reduktion gewonnenes Titan ($HB_{30} < 130$ kg/mm²) mit einem Eisengehalt $< 0{,}04\%$, ferner Aluminium mit einem Reinheitsgrad von 99,99%. Die Legierungen wurden im Lichtbogenofen mit Wolfram-Elektrode unter Argon (99,99%) erschmolzen und zur Homogenisierung zweimal umgeschmolzen. Die elektrische Leitfähigkeit wurde nach der Kompensationsmethode im Temperaturbereich von −190°C bis +1050°C gemessen. Die Messungen bei gewöhnlichen und höheren Temperaturen wurden teils im Vakuum ($<10^{-4}$ mm Hg), teils unter sehr reinem Argon durchgeführt. Bei den Tieftemperaturmessungen befanden sich die Proben in der entsprechenden Kältemischung. Die beim Aufheizen und Abkühlen gemessenen Werte stimmen im allgemeinen gut überein; in einigen Fällen wurden kleine Abweichungen gefunden, die aber 3% nicht überschreiten. Einige Proben wurden bei verschiedenen Temperaturen über 20h auf konstanter Temperatur gehalten. Die maximale Änderung der Leitfähigkeit, die dabei beobachtet wurde, betrug 2%.

Es kann daher angenommen werden, dass die gemessenen Werte praktisch die Gleichgewichtswerte darstellen. Zwischen den aus Jodidtitan und aus technischem Titan geschmolzenen Proben war kein wesentlicher Unterschied festzustellen.

Die Messungen der Suszeptibilität wurden nach der Zylindermethode und nur bei Raumtemperatur durchgeführt. Zur Eliminierung des störenden Einflusses der ferromagnetischen Verunreinigungen wurde das von Knappwost[8] angegebene verfahren benutzt.

Abb. 1 zeigt die Widerstand-Temperatur-Kurven für eine Reihe von Legierungen. Auffallend ist hier einmal das starke Ansteigen des spezifischen Widerstandes in der Gegend von 12% Aluminium und weiter, dass in dem Bereich von etwa 8–22% Aluminium der Temperaturkoeffizient des Widerstandes über ein mehr oder weniger grosses Temperaturintervall negativ ist.

Die Beziehungen des elektrischen Verhaltens zum Phasendiagramm lassen sich besser an Hand der Isothermen des spezifischen Widerstandes übersehen, von denen einige in Abb. 2 dargestellt sind. Man sieht sofort, dass diese Kurven mit dem bisher angenommenen Zustandsdiagramm unvereinbar sind. Die Abweichungen von dem für eine homogene Lösung zu erwartenden Verlauf beginnen etwas unterhalb der Konzentration, bei der die Anomalien im mechanischen Verhalten auftreten, was im Hinblick auf die grössere Empfindlichkeit der elektrischen Methode ohne weiteres plausibel ist.

Der Verlauf der spezifischen Suszeptibilität, der in Abb. 3 wiedergegeben ist, zeigt ebenfalls, dass die Annahme einer sich bis 25 Gewichts-% Aluminium erstreckenden homogenen Lösung kaum zu halten ist.

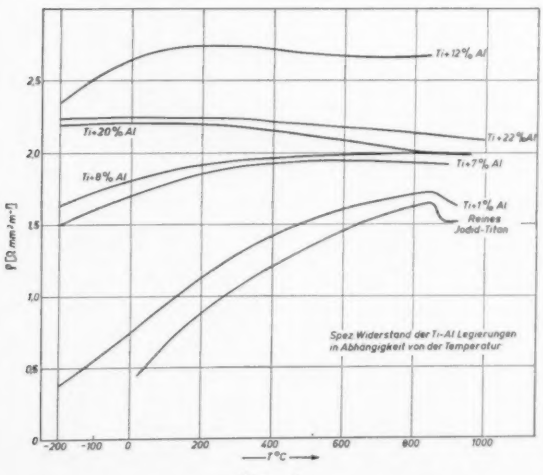

FIG. 1.

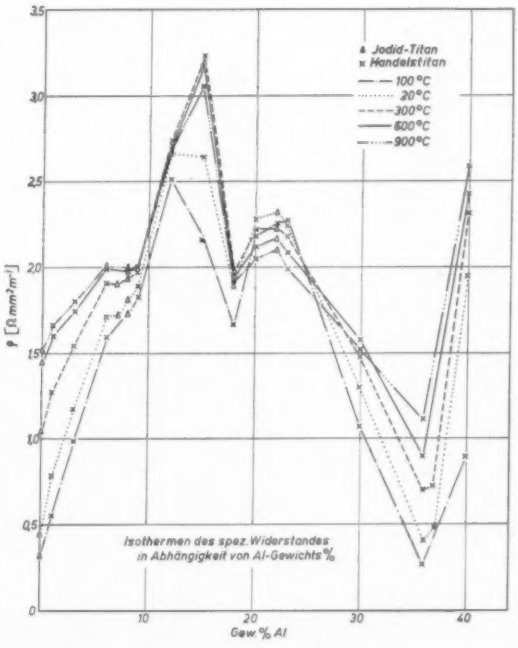

FIG. 2.

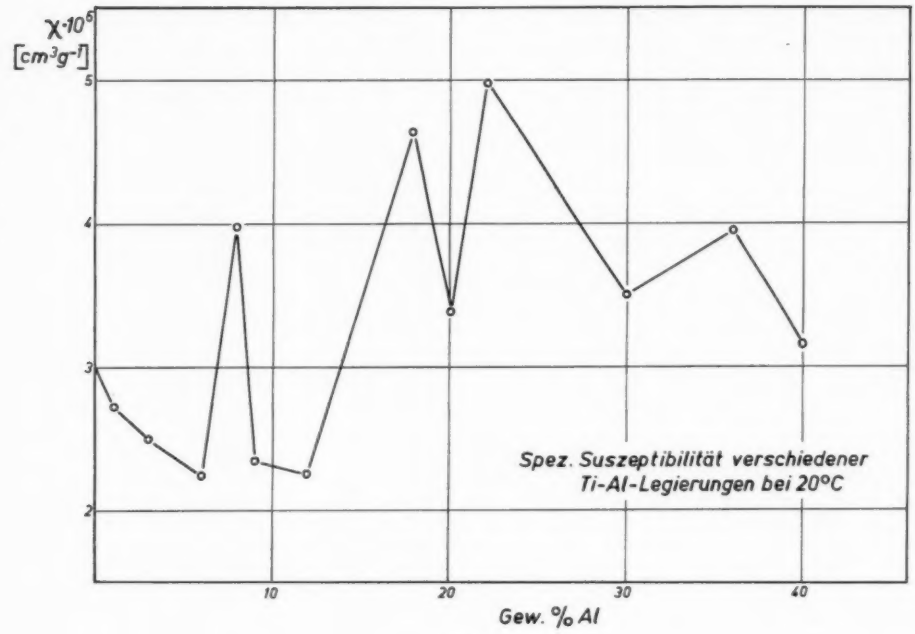

FIG. 3.

Man kann sich unschwer Phasendiagramme konstruieren, welche den mitgeteilten Ergebnissen Rechnung tragen. Dieselben würden jedoch ohne Heranziehen weiterer experimenteller Daten einen mehr oder weniger spekulativen Charakter besitzen. Wir ziehen es deshalb vor, diese Frage im Zusammenhang mit den Ergebnissen der zur Zeit laufenden metallographischen und röntgenographischen Untersuchungen zu diskutieren.

A. MÜNSTER
K. SAGEL
U. ZWICKER

Aus dem Metall-Laboratorium
der Metallgesellschaft A.G.
Frankfurt/Main

References

1. H. R. OGDEN, O. J. MAYKUTH, W. L. FINLAY, und R. J. JAFFEE *Trans. Amer. Inst. Min. Met. Eng.* **191,** 1150 (1951).
2. E. S. BUMPS, H. O. KESSLER, und M. HANSEN *Trans. Amer. Inst. Min. Met. Eng.* **194,** 609 (1952).
3. A. A. MCQUILLAN *J. Inst. Met.* **83,** 181 (1954).
4. W. ROSTOKER *J. Metals* **4,** 209 (1952).
5. H. W. WORNER *J. Inst. Met.* **81,** 521 (1952/53).
6. W. L. FINLAY, R. J. JAFFEE, R. W. PARCEL, und R. D. DURSTEIN *J. Metals* **6,** 25 (1954).
7. H. R. OGDEN, D. J. MAYKUTH, W. L. FINLAY, und R. J. JAFFEE *J. Metals* **5,** 267 (1953).
8. A. KNAPPWOST *Z. Elektrochemie* **59,** 561 (1951).

* Received March 9, 1956.

Note on the Heating Effect of Moving Dislocations*

In a recent paper,[1] Freudenthal and Weiner have proposed that thermal stresses produced during fatigue are severe enough to create microcracks; these stresses are due to highly localized "thermal flashes," associated with repeated and reversed slip processes, which in the extreme case may raise the temperature near the slip plane by some 200°C. The heating effect of dislocations moving along slip planes is in fact of importance in many aspects of plastic deformation. In this note the heating effect is calculated in a different manner, and some of the assumptions of Freudenthal and Weiner are discussed.

We take the dislocation to be a moving line-source of heat of strength

$$q = b\tau V \text{ erg cm}^{-1} \text{ sec}^{-1}$$

where b is its Burgers vector, V its velocity, and τ is the applied shear stress. The temperature at (x,y) is[2]

$$T = \frac{q}{2\pi K} e^{x/\Lambda} K_0(r/\Lambda),\ r^2 = x^2 + y^2.$$

x,y are rectangular co-ordinates centered on the dislocation, $y = 0$ is the slip-plane, and x is positive behind the dislocation. K is the heat conductivity and κ is the thermal diffusivity (K divided by the specific heat per unit volume). The Bessel function $K_0(z)$ has the asymptotic forms

$$K_0(z) \sim -\ln z, \qquad z \gg 1;$$

$$K_0(z) \sim \left(\frac{\pi}{2z}\right)^{\frac{1}{2}} e^{-z}, \quad z \ll 1.$$

The length

$$\Lambda = 2\kappa/V$$

fixes the scale of the temperature pattern. It will usually be many atomic distances, so that near the dislocation

$$T = \frac{b\tau V}{2\pi K} \ln \frac{\Lambda}{r}$$

(compare Seitz[3]). Even for fairly extreme values of the constants, T is of the order of only a fraction of a degree a few atomic distances from the dislocation.

The question now is, do the temperature fields of a succession of dislocations add up to give an appreciable rise? We can make an estimate in two extreme cases. Consider a procession of n equally-spaced dislocations spread over a distance λ. Then if $\Lambda \gg \lambda$ the maximum temperature will be about

$$T = \frac{q}{2\pi K} \sum_{\nu=1}^{n} \ln \frac{\Lambda\nu}{\lambda} \sim \frac{q}{2\pi K}\, n \ln \frac{n\Lambda}{\lambda}$$

and the temperature will be n times what it would be at a distance λ/n (inter-dislocation spacing) for a single dislocation.

If $\Lambda \ll \lambda$, the maximum temperature will be about

$$T = \frac{q}{2\pi K} \int_{\lambda/n}^{\lambda} \left(\frac{\pi\Lambda}{2r}\right) \frac{dr}{\lambda/n} \sim \frac{q}{2\pi K} \left(\frac{\pi\Lambda}{2\lambda}\right)^{\frac{1}{2}} n$$

which is identical with Freudenthal and Weiner's equation (5):

$$T = \frac{\tau}{mK} \left(\frac{\kappa\lambda}{\pi}\right)^{\frac{1}{2}}$$

where m is the spacing between successive dislocations in units of b. As before, there will be a temperature-rise about n times that due to a single dislocation, provided the factor $(\Lambda/\lambda)^{\frac{1}{2}}$ is not too unfavorable.

To determine the actual temperature rise, we have to estimate plausible values for V, λ, n, and decide if one of the approximations $\Lambda \gg \lambda$, $\Lambda \ll \lambda$ is appropriate. V has a maximum value of some fraction of the velocity of sound, say $\frac{1}{3}V_0 \sim 10^5$ cm/sec. It is commonly assumed that all the dislocations on one slip-plane come from the same Frank-Read source; if the sweeping velocity of the source is about the same as the velocity of the moving dislocations, the spacing between successive dislocations will be about l, the length of the Frank-Read source. In annealed material, $l \sim 10^{-4}$ cm, and, with $n = 500$, λ becomes about 10^{-1} cm. Thus, $\Lambda \ll \lambda$, and the second form of our equation is the most appropriate. Freudenthal and Weiner achieve a temperature rise of about 8°C on a slip-plane in aluminum, with 500 dislocations moving at $\frac{1}{3}V_0$ in a procession 10^{-4} cm in length; whereas our model suggests that this procession has an effective length of 10^{-1} cm, giving a temperature-rise of about half a degree. Similarly, for the hard light alloy, 24S-T, we would suggest a temperature-rise of about two degrees rather than fifty degrees.

This discrepancy, of course, arises from the differing values, in the two models, of the length λ of the procession of dislocations. We have considered the case in which dislocations move freely along the slip-plane with a spacing determined by their rate of emission from the Frank-Read source, whereas Freudenthal and Weiner consider a procession of dislocations uniformly separated by about five interatomic distances. Bunching of the dislocations in the slip-plane may occur because of retarding forces, but it is unlikely that the average spacing could reach the value suggested by Freudenthal and Weiner. Their distribution would require very high stresses to keep the dislocations together, and the stress around the array would then exceed the theoretical strength of the material. If the bunching was so severe that the distribution was similar to that of a static pile-up of n dislocations, the distance between first and last, λ, would be about n^2 times the distance between the leading pair,[4] as against n times this distance for Freudenthal and Weiner's equally spaced procession. We believe then that the value of λ for 500 dislocations, about 10^{-4} cm from the simple picture of the Frank-Read source, might be reduced to 10^{-2} cm if bunching should occur, but that the figure of 10^{-4} cm is too small.

The effect of stacking individual slip processes into nearby parallel slip-planes increases considerably the possible rise in temperature. Freudenthal and Weiner's equation 7 is the same as that, obtained by different arguments, by Cottrell[5] and before that by Orowan.[6] For a given shear stress, the rise in temperature varies linearly with the amount of glide on each plane and inversely with the spacing between the slip-planes, so that a large shear on many closely-packed planes could give an appreciable rise in temperature. For this magnified heating effect it is necessary that the nearby slip processes occur simultaneously, and Freudenthal and Weiner suggest that this is not highly probable. The microscopical evidence presented by Brown[7] and Forsyth[8] suggests that, during fatigue, slip only occurs simultaneously on planes a micron or more apart. the "striations" widening and intensifying during the test by the addition of individual slip processes one after the other. Furthermore, if displacements of 1500 Å were to occur on many planes 200 Å apart, as Freudenthal and Weiner suggest, the material would suffer the equivalent of a homogeneous shear of seven atomic

VOL. 4 1956

diameters on each atom plane; and this is clearly not achieved over large volumes of the material. The nearest approximation to this case is fine slip,[9] in which the displacement is about 50 Å on many slip-planes 200 Å apart. Here the maximum rise in temperature might be a few degrees if many of the slip processes occurred simultaneously.

It seems improbable then that there can be appreciable local heating near the glide-plane, except perhaps at very high rates of loading. The creation of cracks during normal reversed stressing may be explained by the pile-up of dislocations,[10] and the softening processes by the local generation of vacancies.[11]

J. D. Eshelby
P. L. Pratt
Department of Physical Metallurgy
Birmingham University, England

References

1. A. M. Freudenthal and J. H. Weiner *J. Appl. Phys.* **27,** 44 (1956).
2. H. S. Carslaw and J. C. Jaeger *Conduction of Heat in Solids* p. 224, Oxford (1947).
3. F. Seitz *Advances in Physics* **1,** 43 (1952).
4. J. D. Eshelby, F. C. Frank, and F. R. N. Nabarro *Phil. Mag.* **42,** 351 (1951).
5. A. H. Cottrell *Dislocations and Plastic Flow in Crystals* p. 6 Oxford (1953).
6. E. Orowan in *Principles of Rheological Measurement* p. 180 Nelson (1949).
7. A. F. Brown *Advances in Physics* **1,** 427 (1952).
8. P. J. E. Forsyth *J. Inst. Metals* **80,** 181 (1952/53); **82,** 449 (1953/54); P. J. E. Forsyth and C. A. Stubbington *R.A.E. Report Met.* 76 (1953), *Met.* 78 (1954).
9. D. Kuhlmann-Wilsdorf and H. Wilsdorf *Acta Met.* **4,** 394 (1953).
10. N. F. Mott *J. Phys. Soc. Japan* 10 (8), 650 (1955).
11. T. Broom and J. H. Molineux *J. Inst. Metals* **83,** 528 (1954/55).

* Received March 14, 1956.

Calorimetric Measurements of the Grain-boundary Energy in Zinc*

Although relative grain-boundary energies can be easily obtained, absolute values of these energies are more difficult to estimate. The values reported in the literature are all indirect in the sense that they have been obtained by comparing the energy of a grain boundary with that of an external surface, the surface energy of which is determined, e.g., from the dihedral angles formed between the solid and a liquid of known surface tension. This procedure, though correct in principle, seems not to be very accurate in practice. The present investigation is a direct measurement of the grain-boundary energy in zinc with an isothermal calorimetric method, practiced earlier.[1, 2]

The calorimetric apparatus used for the measurements was an electrically heated and regulated thermostat with a very large heat capacity,[3] The specimen was located in a central hole in the thermostat and a series of thermocouples, connected to a sensitive galvanometer, was arranged between the specimen and the wall of the thermostat in such a way that the deflection of the galvanometer was proportional to the rise in temperature of the specimen caused by evolution of heat due to the transformation. As the heat liberated during the grain enlargement of a metal is very small—at a grain size of 0.01 mm the total boundary energy is of the magnitude of 0.1 cal/mole—extreme precautions must be taken to reduce disturbing effects, which will be discussed in a later article. The zinc specimens used had the form of granules of a size of about 3 mm with the composition: As $< 0.000015\%$, Fe $< 006\%$, and Pb $< 0.05\%$. The granules were put into a thin-walled aluminum container fitting into the measuring cell. The junction of a Pt-PtRh peltiercouple was located at the center of the container for calibration purposes.

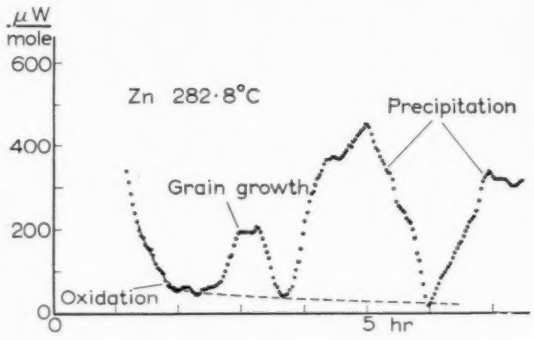

Fig. 1. Rate of evolution of energy- versus time-curve for a measurement at 282.8°C.

In Fig. 1 the rate of evolution of energy- versus time-curve for a measurement at 282.8°C is shown. Although the measurements were carried out in an atmosphere of argon, it was almost impossible to avoid a small oxidation effect of the specimens, due to rests of oxygen absorbed at the surface of the granules and the container. This oxidation effect gives an approximately exponential initial fall of the measuring curves. The effect of the grain growth in the specimen, from a size of the grains of somewhat less than 0.1 mm to about 1 mm, appears as a small evolution of heat with a maximum after about 3 hours, as shown Fig. 1. The form of the curve is bell-shaped, which may be expected for a coalescence-process. As the oxidation effect and the growth of the grains have different energies of activation, the temperatures of the measurements have been chosen so that the maximum of the latter effect does not occur until the rate of oxidation has diminished.

The integrated area of the grain-growth curve in Fig. 1 corresponds to an energy of 0.05 cal. By studying microscopically the grain structure before and after the evolution of heat, the decrease in grain-boundary area can be estimated from the average number of intercepts with the boundaries per unit length of random lines in sections of the samples.[4]

The results of the calorimetric measurements, which were carried out in the temperature range 280–285°C, are given in Table 1. Δa is the corresponding change in interfacial area obtained from microscopical examination. τ is the time for the maximum of the grain-growth curves. The values marked with an asterisk are the results of a microscopical determination of the maximum rate of decrease of the total grain-boundary area at constant temperature.

TABLE 1.

Temp. (°C)	τ (h)	Q (cal/mole)	Δa (cm²/mole)	$Q/\Delta a$ (erg/cm²)
278.4	7.0*			
281.1	4.2			
282.1	3.85			
282.8	3.08	0.088	2140	1720
283.6	2.25	0.068	1490	1920
283.6	2.0*			
285.8	1.22			
292.7	0.27*			

From the dependence on temperature of τ, Fig. 2, the average energy of activation for the anisotropic coalescence effect in zinc can be calculated. The apparent value was about 150,000 cal/mole. This high value may be due to an activation of more than one single atom in the unit process of coalescence, and/or to the disturbances in the metal caused by the anisotropy in the thermal expansion of zinc.

If the effect of strain is neglected, the energies in Table 1 observed during the grain growth must be ascribed to the decrease of the total boundary area. This gives a specific grain-boundary energy for zinc of 1800 erg/cm² within an accuracy of about 15%. Earlier there are only reported values of the interfacial energy for copper, 550 erg/cm² at 800–900°C, according to Fisher and Dunn,[5] and for silver, 300–400 erg/cm² at 900°C.[5, 6] These results are, however, grain-boundary free energies, while the calorimetric measurements give the total energy, including the entropy term, which must be taken into account, if the values are to be compared. A rough estimate of the importance of the entropy term on the grain-boundary structure may be obtained if, for the interfacial free energy of zinc, we take the value of the surface

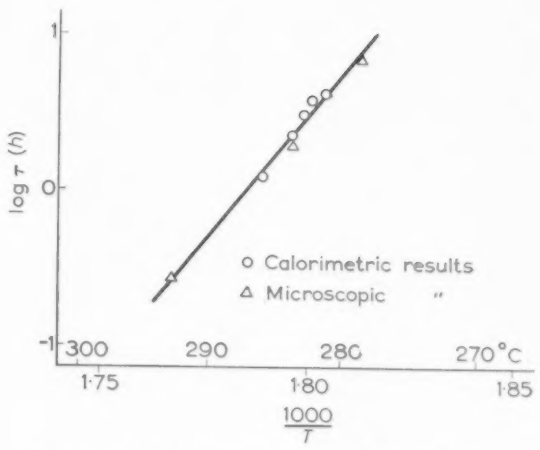

FIG. 2. Time for the maximum rate of grain growth versus the reciprocal of the temperature.

tension, which is about 820 dyne/cm at the melting-point,[7] and assume that the entropy term for a large-angle boundary approximately corresponds to the energy needed for melting a thin layer of metal along the grain boundaries. The breadth of the liquid zone thus obtained is about 12 Å.

The concentration of iron and lead in the zinc used is, though small, higher than the solid solubility of these metals at the measuring temperature. A certain evolution of heat due to the precipitation of iron and lead might thus be expected. This effect was also observed, and was found to occur during or immediately after the grain-growth phenomenon. This close connection between coalescence and precipitation is probably due to a concentration of the impurities along the boundaries on account of the grain growth, which increases the rate of nucleation and by that the rate of precipitation.

The results of this investigation will be given and discussed in more detail in a paper planned for publication in *Arkiv för Fysik*.

The work has been supported by a grant from the Swedish Council for Technical Research.

HANS U. ÅSTRÖM.

Department of Physics
Royal Institute of Technology
Stockholm, Sweden

References

1. H. U. ÅSTRÖM *Arkiv f. Fysik* **8,** 495 (1954).
2. H. U. ÅSTRÖM *ibid.* **10,** 197 (1956).
3. A. KELEN *Appl. Sci. Res.* **B4,** 309 (1955).
4. C. S. SMITH and L. GUTTMAN *J. Metals* **5,** 81 (1953).
5. J. C. FISHER and C. G. DUNN *Imperfections in Nearly Perfect Crystals*, New York and London 1952, p. 317.
6. A. P. GREENOUGH and R. KING *J. Inst. Metals* **79,** 415 (1951).
7. E. PELZEL *Berg- u. Hüttenm. Mh.* **93,** 248 (1948).

* Received April 13, 1956.

VOL. 4 1956

SOME CURRENT PAPERS IN OTHER JOURNALS

Acta Crystallographica, Vol. 9

Part 7, July 1956 (Partial contents):

The Crystal Structures and Lattice Parameters of High-Purity Scandium, Yttrium and the Rare Earth Metals. F. H. Spedding, A. H. Daane and K. W. Herrmann.

An Approximate Calculation of Attachment Energies for Ionic Crystals. P. Hartman.

On Order-Disorder Structures (OD-Structures). K. Dornberger-Schiff.

Neutron Diffraction Studies of Hafnium–Hydrogen and Titanium–Hydrogen Systems. S. S. Sidhu, LeRoy Heaton and D. D. Zauberis

On the unreliability of the "reliability index". Jerry Donohue and Kenneth N. Trueblood.

Note on the statistical approach to the phase problem. J. Gillis.

Independent measurement of the atomic scattering factor and the debye factor. Bernard Borie.

Part 8, August 1956:

Twinning properties of lattice planes. M. A. Jaswon and D. B. Dove.

The crystal structure of NbO_2F and TaO_2F. L. K. Frevel and H. W. Rinn.

The crystal structure of sulfamide. Kenneth N. Trueblood and Stanley W. Mayer.

A theory of phase determination for the four types of non-centrosymmetric space groups $1P222$, $2P22$, $3P_12$. J. Karle and H. Hauptman.

Estimates of the standard deviations of the observed structure factors and of the electron density from intensity data. James A. Ibers.

The crystal structure of histidine hydrochloride monohydrate. Jerry Donohue, L. R. Lavine and John S. Rollett.

On the crystal structure of 9DL-methyloctadecanoic acid. Sixten Abrahamsson.

The crystal and molecular structure of $Cl_2BC_2H_4BCl_2$. Emmett B. Moore, Jr. and William N. Lipscomb.

X-ray study of the alkali metals at low temperatures. C. S. Barrett.

The structure of anhydrous scandium phosphate. Rose C. L. Mooney.

Symmetry relations among coefficients of the anisotropic temperature factor. Henri A. Levy .

The θ' structure in aluminium copper alloys. J. M. Silcock and T. J. Heal.

A note on *cyclo*-(hexaglycyl). E. M. Cant.

Measurement of particle absorption by X-ray fluorescence. P. M. de Wolff.

Polymorphis in lead metaniobate. M. H. Francombe.

The structure of TiF_3. Stanley Siegel.

Lattice parameters of Zn_3As_2. H. Cole, F. W. Chambers and H. M. Dunn.

The crystal structure of mercury(II)oxide. Karin Aurivillius.

The structural crystallography of indium bismuthide. W. P. Binnie.

Archiv für das Eisenhüttenwesen

Heft 6, Juni, 1956:

Bestimmung der Oberflächenspannung an reinem und legiertem Eisen. Wilhelm vor dem Esche und Oskar Peter.

Mengenregelung mit Strömungsdrosseln. Michael Hansen.

Entwicklung eines Kalorimeters für Temperaturen bis 1100° und Bestimmung der Reaktionsenthalpie des Spinells $FeO \cdot Al_2O_3$ zwischen 800 und 1000°. Wilhelm Anton Fischer und Gert Lorenz.

Einfluß der Wärmebehandlung auf die Zerspanbarkeit von Einsatz- und Vergütungsstählen. Franz Wever, Hans-Joachim Wiester, Werner Strassburg, Herwart Opitz und Karl-Heinrich Fröhlich.

Stabilisierung des passiven Zustandes austenitischer Chrom-Nickel-Stähle durch anodische Polarisation in siedender 4*n*-Schwefelsäure. Carl Carius.

Untersuchungen über die Kinetik der Martensitbildung. Heinrich Beißwenger und Erich Scheil.

Die Ermittlung von Porengrößen nach dem Kapillardruck-Verfahren. Hermann Schenck und Josef Cloth.

La Metallurgia Italiana Vol. XLVIII

June 1956:

Ultrasonic Tests. E. Martin.

Common Determination of Copper and Lead in Copper-Base Alloys - Rapid Electrolytic Method. S. Bertoldi and A. Tartari.

Comparing Runner Bricks with Regard to their Behaviour in Use. F. Gottardi and A. Palazzi.

Protecting Ammonium Sulphate Crystallizers by Means of Inhibitors. G. Roberti, F. Gianni and G. Bombara.

July 1956:

On high temperature corrosion of metals by vanadium dioxide. Note 1. Researches on systems metal-vanadium-oxigen. V. Cirilli, A. Burdese and C. Brisi.

Extensometric measurements of dynamic deformations on a gun. A. Bray.

A particular case of hexogen inclusions in steel. R. Zoja.

New electrolytic reactives for stainless steels containing σ-phase. J. Bertetti.

August 1956:

On high temperature corrosion of metals by vanadium dioxide. Note 2. Behaviour of some metals (Fe, Co, Ni, Cr) and of their alloys. A. Burdese and C. Brisi.

Roentgenographic researches on the η-phase Cu-Sn. C. Goria.

Ageing of steel 16-25-6 and identification of precipitates. A. Ferro, S. Gallo and C. P. Galotto.

A QUANTITATIVE STUDY OF THE FORMATION OF AUSTENITE AND THE SOLUTION OF CEMENTITE AT DIFFERENT AUSTENITIZING TEMPERATURES FOR A 1.27% CARBON STEEL*

GÖRAN MOLINDER†

The course of transformation of a 1.27% carbon steel after rapid heating to temperatures above A_{c1} has been investigated quantitatively. The steel used for the investigation was soft-annealed, i.e. with a structure consisting of ferrite with rounded grains of cementite.

The quantitative microscopical measurements on etched specimens have been made, using lineal analysis.

The experimental results indicate that the small austenite volumes first formed at a certain austenitizing temperature have a low-carbon content close to the A_3-line. While the amount of austenite increases at increasing time, at austenitizing temperature its carbon content is also increased due to dissolution of cementite, and at the moment when the last part of ferrite disappears the austenitic matrix has a carbon content of 0.55–0.60% at all temperatures used for testing.

When the austenite formation has been completed, a slow dissolution of cementite takes place, and then after a relatively long time a state of equilibrium is attained.

A study of the increase of carbon content in the austenite as a function of time indicates that the factor determining how quickly the dissolution of the cementite takes place is not the speed of diffusion of carbon in the austenite, but the speed of disintegration of cementite at the phase boundary.

UNE ÉTUDE QUANTITATIVE DE LA FORMATION D'AUSTÉNITE ET DE LA DISSOLUTION DE CEMENTITE A DIVERSES TEMPERATURES D'AUSTÉNITISATION POUR UN ACIER A 1,27% DE CARBONE

La transformation d'un acier à 1.27% de carbone après chauffage rapide au-dessus du point A_{c1} a été étudiée quantitativement. L'acier utilisé a été recuit lentement, sa structure consistant en ferrite avec des grains arrondis de cémentite. Les mesures optiques quantitatives sur des échantillons attaqués ont été basées sur l'analyse linéaire.

Les résultats expérimentaux montrent que les petits volumes d'austénite initialement formés à une certaine température d'austénitisation ont une faible teneur en carbone près de la ligne A_3. Tandis que la quantité d'austénite augmente avec le temps d'austénitisation, le contenu en carbone augmente également comme résultat de la dissolution de cémentite et lorsque la dernière trace de ferrite disparait la matrice austénitique a une teneur de 0,55—0,60% de carbone à toutes les températures observées.

Lorsque la formation d'austénite est terminée, une dissolution lente de la cémentite prend place et un état d'équilibre est atteint après un temps relativement long.

Une étude de l'augmentation de la teneur en carbone dans l'austénite en fonction du temps montre que le facteur déterminant (avec quelle rapidité la dissolution de cémentite prend place) n'est pas la vitesse de diffusion du carbone dans l'austénite mais bien la vitesse de désintégration de la cémentite à la ligne de transformation.

EINE QUANTITATIVE UNTERSUCHUNG ÜBER DIE BILDUNG VON AUSTENIT UND DIE AUFLÖSUNG VON ZEMENTIT BEI VERSCHIEDENEN AUSTENITISIERUNGSTEMPERATUREN AN EINEM 1,27% IGEN KOHLENSTOFF-STAHL

Der Verlauf der Umwandlung eines 1,27% igen Kohlenstoff-Stahls nach rascher Erhitzung auf Temperaturen oberhalb A_{c1} wurde quantitative untersucht. Der verwendete Stahl war weichgeglüht, d.h. seine Struktur bestand aus Ferrit mit kugeligen Zementit-Körnern.

Die quantitativen mikroskopischen Messungen wurden an geätzten Proben vorgenommen.

Die experimentellen Ergebnisse zeigen, dass die bei einer bestimmten Austenitisierungs-Temperatur zuerst gebildeten kleinen Austenitbereiche einen niedrigen Kohlenstoffgehalt, nahe der A_3-Linie, haben. Bei der Austenitisierungstemperatur steigt dann—gleichlaufend mit der zeitlichen Mengenzunahme des Austenits—dessen Kohlenstoffgehalt infolge der Auflösung von Zementit an. Schliesslich hat in dem Augenblick, in dem der letzte Ferritrest verschwindet, das Austenitgitter bei allen untersuchten Temperaturen einen Kohlenstoffgehalt von 0,55 bis 0,60%.

Nach Abschluss der Austenitbildung findet ein langsames Auflösen von Zementit statt, und erst nach relativ langer Zeit wird ein Gleichgewichtszustand erreicht.

Eine Untersuchung über die Zunahme des Kohlenstoffgehalts im Austenit als Funktion der Zeit zeigt, dass die massgebende Grösse dafür, wie schnell die Auflösung des Zementits erfolgt, nicht die Diffusionsgeschwindigkeit des Kohlenstoffs im Austenit ist, sondern die Geschwindigkeit, mit der sich der Zementit an der Phasengrenze auflöst.

* Received December 22, 1955. † Munkfors Bruk, Uddeholms AB, Munkfors, Sweden.

VOL. 4 1956

INTRODUCTION

The method of lineal analysis has been introduced to metallographical measurements by Cohen and co-workers for the study of the martensite transformation,[1, 2] and has proved to be an accurate and relatively rapid method for quantitative microscopical investigations. The method has later been further developed by the author. The improvement consists mainly of a device for speed regulation, which has considerably increased the speed and usefulness of the method.[3]

Any comprehensive quantitative studies of the austenite formation from ferrite-cementite aggregates has not previously been made. The investigations published by Roberts and Mehl[4] in 1943 were indeed quantitative, but were entirely devoted to a study of the austenite formation, disregarding the influence of the carbides on the amount of matrix and on the composition of the austenite. The method used for quantitative determination of austenite content was counting of squares on a microphotograph. The steels investigated were technical carbon steels with carbon contents from 0.51 to 1.35% and with lamellar pearlite as main component in the structure.

Roberts and Mehl demonstrated the great influence of initial structure on the speed of formation of austenite. Thus, for the same steel, a finer pearlite gives a more rapid transformation than a coarser one. The same effect had previously been established by Hultgren[5] and also by Pomp and Wijkander.[6]

Several investigators have observed that, by heating a ferrite-carbide aggregate above A_{c1}, the transformation of the matrix to austenite occurs rapidly, while the dissolution of carbides in the austenite proceeds with great sluggishness. Even by 1929, Hultgren[5] showed that concentration gradients remained in the austenite a certain time after a carbide particle had been dissolved. By the austenitizing of lamellar pearlite this phenomenon can often be observed after etching ("pearlite ghosts," according to Bayertz[7]). Roberts and Mehl[4] are of the opinion that this phenomenon depends on the remaining carbon concentration gradients.

TEST MATERIAL

Cold-rolled strip steel 0.10 mm (0.004 in.) thick with the following analysis was used for examination

%C	%Si	%Mn	%Cr	%V
1.27	0.20	0.36	0.19	0.03

The material was annealed. The microstructure is shown in Fig. 1.

The amount of cementite has been determined

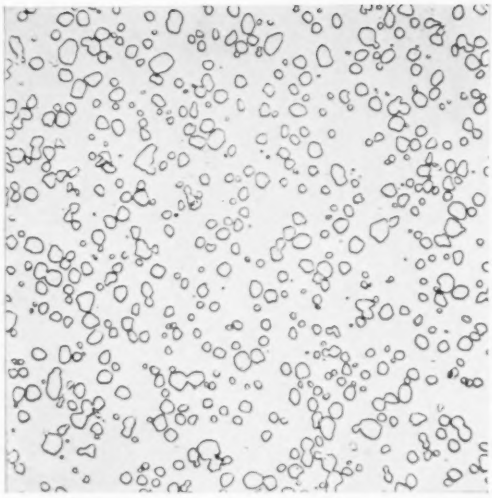

FIG. 1. Microstructure of test material at 1300× magnification. Electrolytically etched in a 10% CrO_3 solution in water.

to 18.4% ± 0.1%. The number of carbide particles on an area of the microsection of 10 μ × 10 μ is average 16.6.

The cementite has been isolated electrolytically in a 5% HCl-solution in water and has been analyzed with the following result:

%C	%Mn	%Cr	%V
6.67	1.24	0.80	0.15

This gives the following approximate analysis of the ferritic matrix:

0.05	0.15	0.05	low.

X-ray examination of the isolated carbide has shown it to be pure cementite with no trace of other carbides.

EXPERIMENTAL

(a) *Heat Treatment*

Specimens in the size 10 × 2 × 0.1 mm were cut from the above test material. One of the short sides of each specimen was welded to a 0.5-mm steel wire.

The austenitizing temperature was attained in a neutral salt bath when the austenitizing time was below 5 min. The specimen was quickly immersed in the bath and the time was measured by means of an electric chronometer connected in a series with the bath and the specimen. After a predetermined time in the salt bath, the specimen was very quickly quenched in 25°C brine.

A tube furnace with purified argon was used for heating times between 5 and 30 min. The time was then determined with an ordinary stop-watch.

When the heating times exceeded 30 min, the specimens were melted into evacuated quartz tubes in order to avoid decarburization. The tubes were broken immediately quenching took place.

(b) *Hardness Testing*

The specimens thus heat-treated were mounted into an iron fixture. Cross-sections were prepared.

The hardness was measured by means of a Bergsman's microhardness tester[8] with 200-g load, and the impressions were very carefully made in the center of the cross-section.

(c) *Microscopical Investigations*

In order to have the martensite areas, present after quenching (previously austenite), to appear in contrast to the rest of the matrix, all specimens were heated to 300°C for 5 min after hardness-testing. By etching in 1% nital, the martensite areas were darkly colored and a quantitative determination could be made (see Figs. 7, 8, and 9).

In order to determine the amount of carbide, the specimens were repolished and etched electrolytically in a 10% solution of chromic acid in water. It was found that an etching in 1% nital did not give reliable values of the carbide content, partly because of the carbide boundaries not being clear enough, and partly because of some carbide grains becoming visually too large. By electrolytical etching, lower figures were obtained than by etching in nital.

Measurements were made for each specimen by lineal analysis with five traverses of 1 mm each.

(d) *X-ray Investigation*

As a check on the carbon content in the matrix obtained by means of lineal analysis measurements, X-ray determination was made of the *c/a* ratio of the martensite after quenching. For this purpose, filings were taken from the test material. These filings were melted into evacuated quartz tubes which were heat-treated in the same way as were the micro specimens.

The filings were then used for lattice determination in a 57.5-mm Debye camera.

RESULTS

Fig. 2 shows the variation of the hardness with austenitizing time.

Fig. 3 shows the decrease of the amount of ferrite and the increase of the amount of austenite with time at the different austenitizing temperatures used (750°, 775°, 800°, 850°, and 900°). The percentages of ferrite or austenite do not reach 100%, as cementite is present in all specimens.

Fig. 4 shows the decrease of the amount of cementite with the austenitizing time. For all temperatures except 900° the moment is indicated when all ferrite has transformed.

Fig. 5, finally, shows the variation of the carbon content of the austenite with austenitizing time. These points and curves have been calculated from Figs. 3 and 4, assuming a carbon content of the ferrite of 0.04% and of the cementite of 6.67%. In the same figure the results of X-ray determination of the carbon content of the martensite have also been plotted.

When evaluating the results at shorter heating times, it must be borne in mind that the time at austenitizing temperature is calculated from the moment the specimen is immersed in the salt bath and connection of the circuit through the chronometer is made until the moment the specimen leaves the bath and the circuit is cut. The time of heating the specimen to the austenitizing temperature is therefore included in the time of contact, but the time taken in removing it from the salt bath to the quenching bath is excluded. The heating time and the time taken for removal are very short and do not affect the results unless the austenitizing time is shorter than about 1 sec. It is very difficult to determine accurately these two short time-intervals, but there are good reasons to believe that both are of the magnitude of 0.1 sec.

DISCUSSION

(a) *Mode of Transformation*

The course of transformation from the ferrite-cementite aggregate to austenite-cementite can schematically be divided into three periods.

Period 1: The initial structure remains untransformed. During this period embryo for austenite nuclei are formed.

Period 2: The ferrite transforms to austenite with simultaneous rapid dissolution of cementite. The speed at which the carbides are dissolved is so high that the carbon content of the austenite increases although the amount of austenite rapidly increases. During this period the hardness increases from 250 Vickers to about 850 Vickers.

Period 3: The cementite dissolves further in the austenite until the equilibrium carbon content at the austenitizing temperature is attained.

(b) *Period* 1.

Any fully developed period 1 has been observed only for the austenizing temperature of 750°. During this period a nucleation of austenite in ferrite is started. It is highly probable that the carbon content of the ferrite in contact with grains of cementite increases during this period and approaches the equilibrium content, according to Fig. 6.

VOL. 4 1956

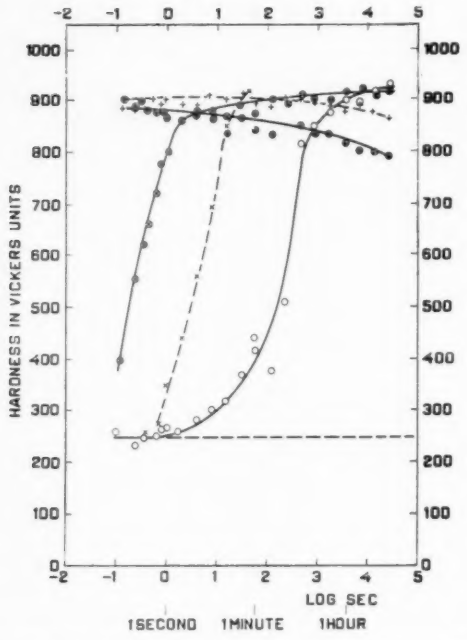

FIG. 2. Vickers hardness vs. logarithm of time at different austenitizing temperatures.
○ 750°C + 850°C
× 775°C ⊕ 900°C
⊗ 800°C

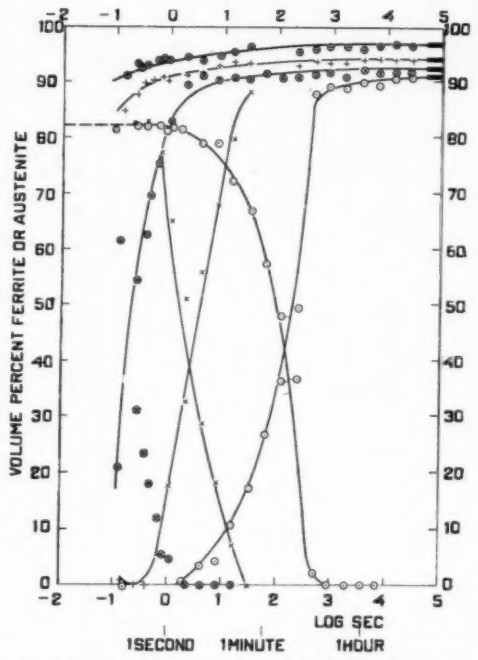

FIG. 3. Amount of austenite and ferrite in volume per cent vs. logarithm of time at different austenitizing temperatures.
○ 750°C + 850°C
× 775°C ⊕ 900°C
⊗ 800°C

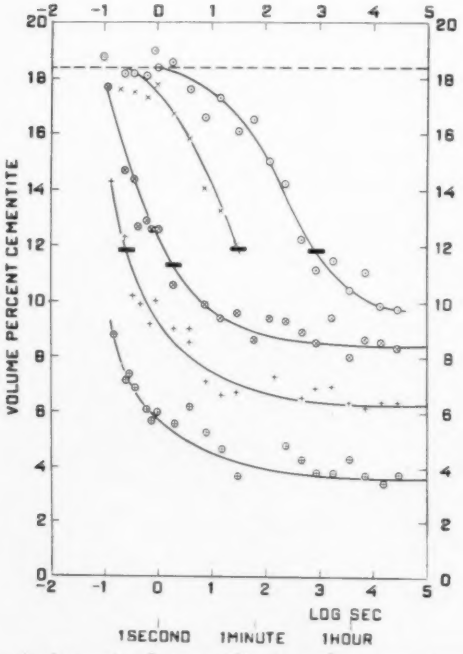

FIG. 4. Amount of cementite in volume per cent vs. logarithm of time at different austenitizing temperatures.
○ 750°C + 850°C
× 775°C ⊕ 900°C
⊗ 800°C
—indicates the time when the final residue of ferrite is dissolved.

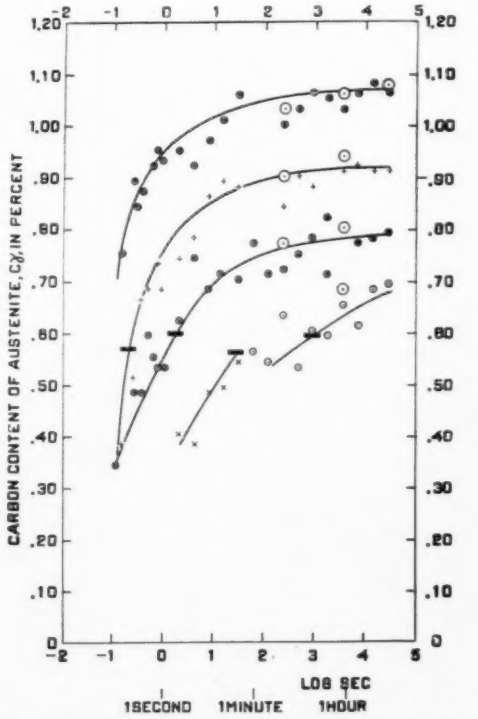

FIG. 5. Carbon content of austenite vs. logarithm of time at austenitizing temperature.
○ 750°C + 850°C
× 775°C ⊕ 900°C
⊗ 800°C
—indicates the time when the final residue of ferrite is dissolved.
⊙ X-ray determinations of carbon content.

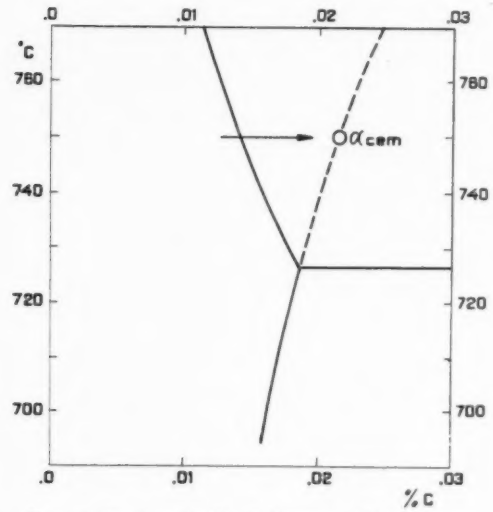

FIG. 6. Part of the Fe-C diagram. Lines drawn according to Dijkstra,[9] Stanley,[10] and Wert[11].

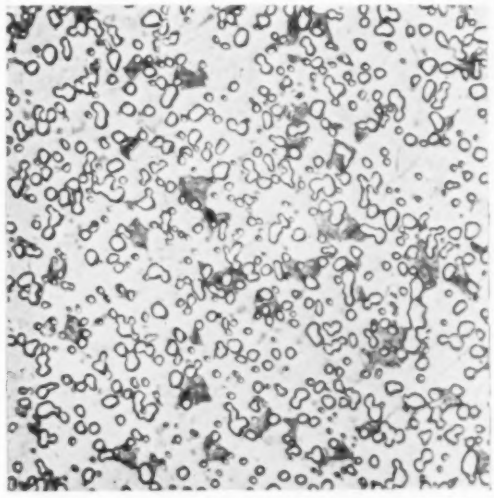

FIG. 8. Austenite formation after 8 sec at 750°C. Specimen reheated and etched, as in Fig. 7.

For the austenitizing temperatures 800°, 850°, and 900°C, the transformation to austenite has already begun or is even completed at the shortest measurable austenitizing times.

(c) *Period* 2.

Period 2 is observed to its full extent at 750° and 775° and almost completely at 800°. At 850° a small balance of ferrite is observed at the shortest austenitizing time tested. At 900°, period 2 is already completed in a time shorter than 0.1 sec.

The formation of austenite starts at least for the austenitizing temperatures 750° and 775° from cementite particles (see Figs. 7, 8, and 9). The small volumes of austenite first formed have a relatively low-carbon content, but the carbon content increases and when the remaining parts of ferrite disappear the austenite has a carbon content of 0.55–0.60% at all austenitizing temperatures tested (except possibly 900°).

The carbon content of the austenite volumes first formed can naturally not be lower than A_3 in the Fe-C diagram (Fig. 10). It is probable that, at least for 750, 775, and 800°C, it is very close to A_3. The lowest reasonably accurate figures of the carbon content of the austenite which can be calculated from the experimental results are

at 750°	about 0.55%,
at 775°	about 0.40%,
at 800°	about 0.35%.

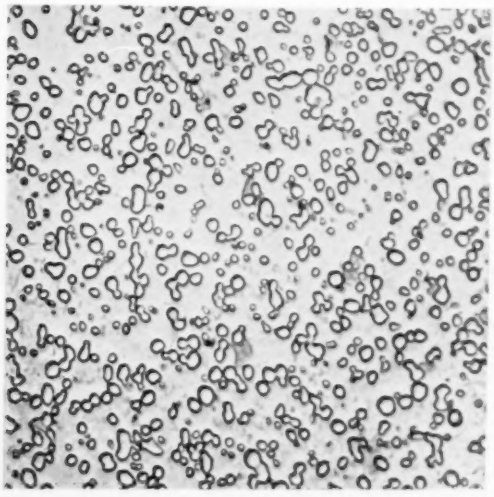

FIG. 7. Austenite formation after 1.9 sec at 750°. Specimen reheated after quenching 5 min at 300°C. Etched in 1% nital.

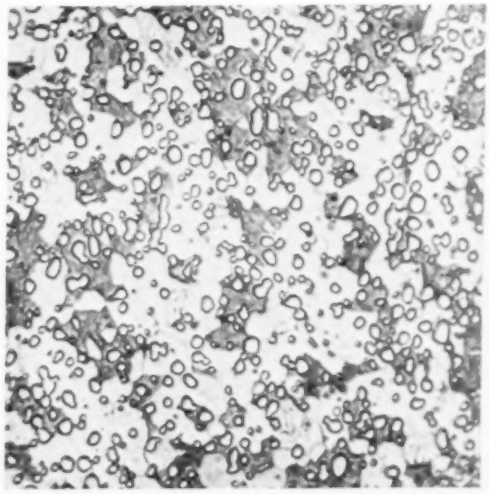

FIG. 9. Austenite formation after 1 min at 750°C. Specimen reheated and etched, as in Fig. 7.

VOL. 4 1956

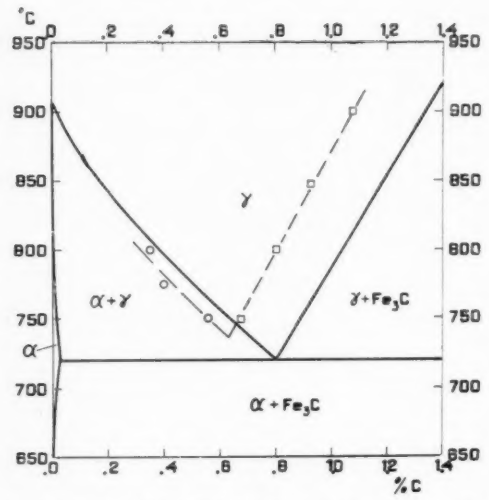

FIG. 10. Part of the Fe-C diagram. A_3, according to Mehl and Wells[12]. A_{cm}, according to Darken and Gurry[13]. α — region, according to Stanley[10].
○ Carbon content of austenite volumes first formed.
□ Ditto at equilibrium.

These figures have been plotted in Fig. 10. It is easily understood that the calculation of the carbon content becomes very inaccurate when small amounts of austenite have formed.

The question of whether the austenite first formed has a carbon content near A_3, even at higher austenitizing temperatures, cannot be answered with the experimental technique used.

(d) *Period* 3.

Period 3 starts when the remainder of ferrite disappears. The carbon content of the austenite is then 0.55–0.60%. At increasing time at the austenitizing temperature gradual dissolution of carbide in the austenite takes place and the carbon content of the austenite approaches the equilibrium value.

The rate of carbide solution is now very much slower than during period 2.

Table 1 shows the amounts of cementite which at different austenitizing temperatures, according to Fig. 4, can be considered to correspond to equilibrium. The corresponding carbon contents (Fig. 5) are also given in the table.

TABLE 1. Equilibrium figures of amount of cementite and carbon content in the austenite of different temperatures

Temperature (°C)	Amount of cementite (volume per cent)	Carbon content of austenite (weight per cent)
750	9.8	0.67
800	8.2	0.80
850	6.2	0.93
900	3.7	1.07

The figures from Table 1 are plotted in the Fe-C diagram (Fig. 10). Depending on the amounts of manganese and chromium in the test material, the A_{cm} line evidently has been displaced to lower carbon contents than for pure Fe-C alloys.

(e) *Some Thermodynamical Calculations*

Fig. 5, showing the variation of austenite-carbon content as a function of the logarithm of time, makes it possible to investigate whether the speed of dissolution of cementite during period 3 is determined by the rate of carbon diffusion or by any other factor. In order to investigate this question, a very approximate calculation has been made, assuming that the rate of carbon diffusion is the governing factor. Fig. 11 shows the carbon distribution in the austenite between two carbides under that assumption. The distribution curves have been drawn for two different austenitizing temperatures T_1 and T_2 ($T_2 > T_1$), but the same average carbon content c_γ in the austenite.

It is assumed that the amount of carbon passing per unit-time dm/dt through a certain spherical surface A around a spherical carbide grain (i.e. a surface just inside the phase boundary) is proportional to the increase in average carbon content of the austenite dc/dt. It is further assumed that at least near the phase boundary dc/dx is proportional to $A_{cm} - c_\gamma$.

Fick's first law

$$\frac{dm}{dt} = -DA\frac{dc}{dx} \tag{1}$$

can then be written

$$\frac{dc_\gamma}{dt} = -D \cdot K \cdot (A_{cm} - c_\gamma) \tag{2}$$

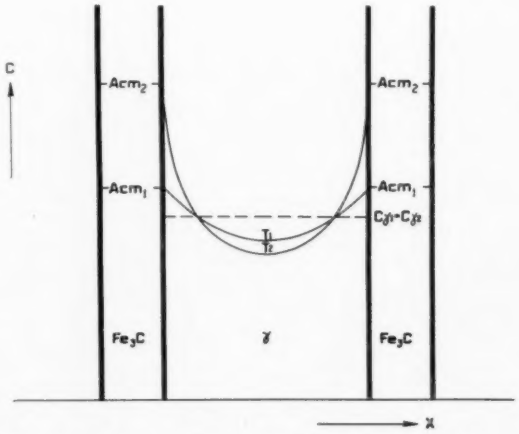

FIG. 11. Carbon distribution between two cementite grains during period 3 at two different austenitizing temperatures, T_1 and T_2 ($T_2 > T_1$), under the assumption that the rate of carbon diffusion determines the rate of cementite dissolution.

TRANSFORMATION KINETICS DURING CONTINUOUS COOLING*

JOHN W. CAHN†

It is shown that transformations which nucleate heterogeneously will quite often obey a rule of additivity and transform nonisothermally according to simple rate laws which can be calculated from isothermal transformation data.

CINÉTIQUE DE LA TRANSFORMATION PAR REFROIDISSEMENT CONTINU

L'auteur montre que des transformations à germination hétérogène obéiraient souvent à une règle d'additivité et se transformeraient anisothermiquement suivant des lois simples de vitesse que l'on peut calculer à partir des données de la transformation isotherme.

UMWANDLUNGSKINETIK BEI KONTINUIERLICHEM ABKÜHLEN

Es wird gezeigt, dass Umwandlungen mit heterogener Keimbildung häufig einer Additivitäts-Regel gehorchen und die nichtisotherme Umwandlung nach einfachen Geschwindigkeitsgesetzen abläuft, die man aus Daten der isothermen Umwandlung berechnen kann.

INTRODUCTION

The problem of transformation kinetics under nonisothermal conditions is of tremendous practical importance. It has not been extensively studied, using fundamental kinetic quantities. Part of the difficulty is that both the nucleation rate and growth rate of the transformation product are time-dependent if the temperature is time-dependent. However, it has been found that some transformations obey an additivity rule.[1] Avrami[2] has shown that for the case where the nucleation rate is proportional to the growth rate over a range of temperatures, the reaction is additive. This is a very special condition, and one would not expect to encounter such a system. Especially, for the case of the pearlite reaction, where, even isothermally, the nucleation rate is a function of time,[3] this condition would not hold. Yet, additivity has been demonstrated for this system.[4]

Many systems in which nucleation is heterogeneous exhibit the property that all nucleation occurs early in the reaction.[5, 6] This may be due to the fact that only a limited number of sites for nucleation exist, such as impurity particles or grain corners, or in case of grain surface or edge nucleation, that these sites can be consumed very early in the reaction. This is a general property of heterogeneous nucleation, and will be called site saturation. It has been shown for the case of grain-boundary surface, edge and corner nucleation, that the expected interval in undercooling from the initiation of nucleation to site saturation is small.[7] This is due to the large temperature coefficient of nucleation.

Many reactions where the nucleation is apparently homogeneous also are describable by the assumption that all nucleation occurred early in the reaction.[8] If the number of nuclei formed is also independent of temperature, what follows will hold equally well for these systems.

If all nucleation does occur at the beginning of the reaction, it will be shown that under certain conditions the reaction is isokinetic in the sense of Avrami, and that such a reaction would be additive. We then have here a condition which leads to the rule of additivity, and which one could often expect to find in real systems. It also becomes possible to estimate the deviations from additivity.

THE RULE OF ADDITIVITY

The rule of additivity can be stated as follows: given an isothermal TTT curve for the time τ, as a function of temperature, at which the reaction has reached a certain fraction of completion, x_0. Then, on continuous cooling, at that time t and temperature T, when the integral

$$\int \frac{dt}{\tau} = \int \frac{dT}{\tau\left(\frac{dT}{dt}\right)} = \int \frac{dx}{\tau\left(\frac{dx}{dt}\right)} \qquad (1)$$

quals unity, the fraction completed will be x_0. The rule has often been stated for the initiation of the reaction. This is a quantity difficult to define, since it depends on the method of observation. It is better to define the time for the initiation as the time for about 1% reaction. A sufficient condition of additivity has been described by Avrami. He found that for the "isokinetic" range, i.e. when the nucleation rate is proportional to the growth rate, that the reaction

* Received January 25, 1956.

† General Electric Research Laboratory, Schenectady, New York.

VOL. 4 1956

where K is a constant and D is the diffusion coefficient.

In order to be able to use the experimental results from Fig. 5, dc/dt has to be transformed in terms of $dc/(d \log t)$

$$\frac{dc_\gamma}{dt} = \frac{dc_\gamma}{d \log t} \cdot \frac{\log e}{t} \tag{3}$$

This gives

$$\log D = \log \frac{dc_\gamma}{d \log t} - \log t - \log (A_{cm} - c_\gamma) + K_1 \tag{4}$$

K_1 is a constant.

Using the curves in Fig. 5 over the variation of c_γ with $\log t$, $\log D - K_1$ has been calculated for the different austenitizing temperatures and is plotted as a function of $1000/T$ in Fig. 12.

The slope of the lines in Fig. 12 indicates an activation energy in the magnitude of 200,000 cal/mole. This figure is substantially higher than the activation energy for carbon diffusion in austenite, which is of the magnitude of 35,000 cal/mole. It is, therefore, evident that a factor other than the rate of carbon diffusion is the governing factor for rate of dissolution. This factor is probably the rate of disintegration of the cementite.

A consequence of this should be that, before equilibrium is attained, the rate of disintegration of the cementite is not sufficient to keep the carbon content of the austenite at the phase boundaries at the equilibrium value. Fig. 13, which might be compared with Fig. 11, shows schematically the possible carbon distribution.

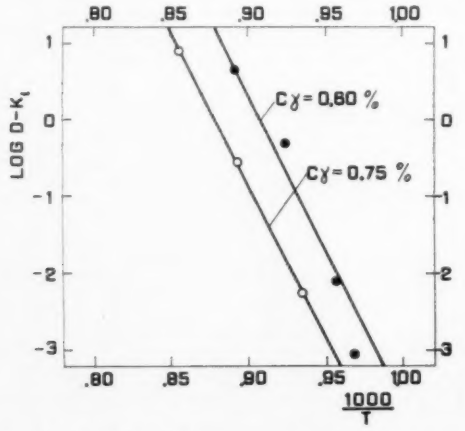

FIG. 12. Log $D - K_1$ vs. $1000/T$. The slope of the lines gives $Q = 190{,}000$ cal/mole.

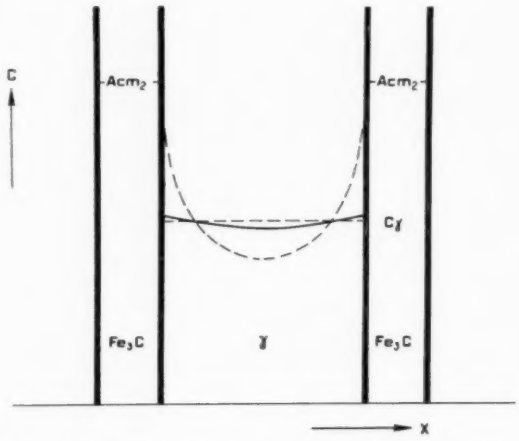

FIG. 13. Carbon distribution between two cementite grains during period 3 at two different austenitizing temperatures, T_1 and T_2 ($T_2 > T_1$), under the assumption that the rate of cementite dissolution is determined by (1) the rate of carbide disintegration (full line), (2) the rate of carbon diffusion (dotted curved line).

ACKNOWLEDGMENTS

The author wishes to thank Uddeholms Aktiebolag, Uddeholm, Sweden, for permission to publish this paper.

His thanks are also due to Bergsingeniör Erik Nygren, Sandviken, for helpful discussions; to Ingeniör Börje Winqvist, Munkfors, for building the instrument for lineal analysis; and to Mrs. Austra Jacobsons, Munkfors, for making the great number of lineal counts.

REFERENCES

1. HOWARD R. T. and COHEN M. *Metals Technology* **14,** T. P. 2215 (1947).
2. HARRIS W. J. and COHEN M. *Trans. Amer. Inst. Min. Met. Eng.* **180,** 384 (1949)
3. MOLINDER A. G. *Jernkontorets Ann* **139,** 174 (1955)
4. ROBERTS G. A. and MEHL R. F. *Trans. Amer. Soc. Metals.* **31,** 613 (1943)
5. HULTGREN A. *Trans. Amer. Soc. S.T.* **16,** 227 (1929).
6. POMP A. and WIJKANDER R. *Mitt. K.WI.* **8,** 55 (1926).
7. BAEYERTZ M. *Trans. Amer. Soc. Metals.* **30,** 755 (1942).
8. BERGSMAN E .B. *Jernkontorets Ann.* **128,** 81 (1944).
9. DIJKSTRA L. J. *Trans. Amer. Inst. Min. Met. Eng.* **185,** 252 (1949)
10. STANLEY J. K. *Trans. Amer. Inst. Min. Met. Eng.* **185,** 752 (1949).
11. WERT C. A. *Trans. Amer. Inst. Min. Met. Eng.* **188,** 1242 1950).
12. MEHL R. F. and WELLS C. *Trans. Amer. Inst. Min. Met. Eng.* **125,** 429 (1937)
13. DARKEN L. S. and GURRY R. W. *Trans. Amer. Inst. Min. Met. Eng.* **191,** 1015. (1951)

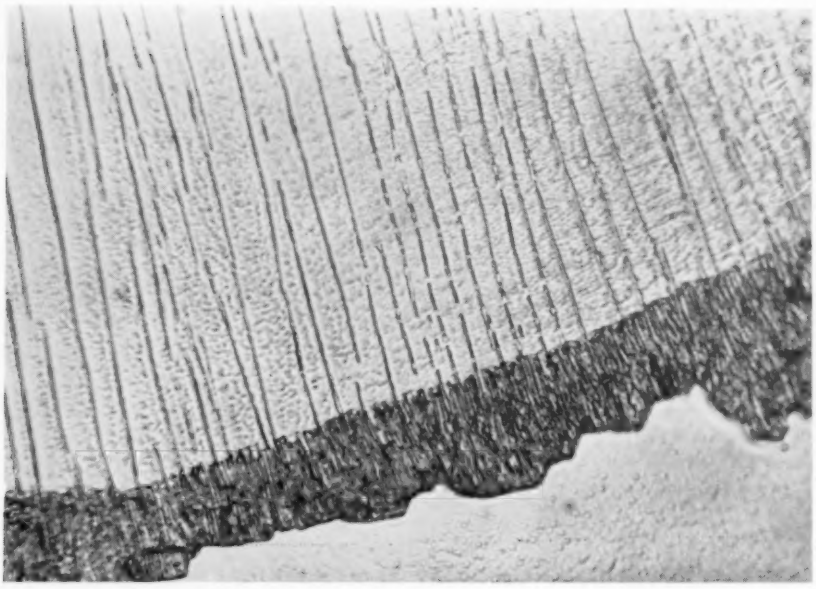

FIG. 1. Pb–6.8% Sn partially precipitated at 100°C, then quenched to room temperature for further precipitation.

would be additive. Under these conditions, he showed that the reaction would take the same course, except for the time scale, regardless of the temperature path.

It has been more generally assumed that a reaction is additive whenever the rate is a function only of the amount of transformation and the temperature

$$\frac{dx}{dt} = f(x, T). \tag{2}$$

Then $\tau = \int_0^{x_0} \frac{dx}{f(x, T)}$. Upon substitution into (1) and integrating to x_0, one can see that (1) becomes identically unity, showing that equation (2) is a sufficient condition for additivity.

The general isokinetic reaction will be defined as a reaction which can be written

$$x = F\left(\int h(T)\, dt\right) \tag{3}$$

where $h(T)$ is a function of temperature only, such as growth rate, nucleation rate, or diffusion constant. It will be convenient to consider x the independent variable, and write (3) as

$$\int h(T)\, dt = H(x). \tag{4}$$

Then

$$\frac{dx}{dt} = \left[\frac{dH(x)}{dx}\right]^{-1} \cdot h(T)$$

which satisfies condition (2), and such a reaction will be additive. It will be noted that a reaction involving two time-temperature parameters will in general not be additive. Nucleation and growth reactions in general involve an integrated nucleation parameter as well as an integrated growth parameter. However, if the nucleation sites saturate early in a reaction, and if the growth rate is a function of the instantaneous temperature only, the reaction will be additive.

The question of to what extent growth rate is a function of thermal history can be estimated by examining micrographs of a reaction started at one temperature and permitted to continue at another temperature. Fig. 1* is a micrograph of Pb–6.8 wt. per cent Sn held at 100°C for partial precipitation, quenched to room temperature and allowed to react further. The spacing characteristic of the room temperature appears immediately, and one would expect that the growth rate would likewise be that of the new temperature. On the other hand, Hull and Mehl[9] have published micrographs of similar experiments on pearlite in which the spacing changes over a finite distance. This may be due to a slack quench or it may be a real effect. If it is the latter, deviations from additivity could be expected to result. If the growth rate G under nonisothermal conditions can be described by $G = G_0\left(1 + \varepsilon \frac{dT}{dt}\right)$ where G_0 is the growth rate under isothermal conditions and ε is a constant, then for a constant cooling rate (1) leads to a value of

* I am indebted to Mr. H. N. Treaftis for the use of this micrograph.

$1/1 + \varepsilon \dfrac{dT}{dt}$ when the nonisothermal reaction has reached x_0 completion.

The deviation from the assumption of instantaneous site saturation can be estimated. We shall confine ourselves to point sites. The same arguments with slight modification will apply to other types of sites. The number of sites per unit volume nucleating at time between $\bar{t}$ and $\bar{t} + d\bar{t}$ is

$$IN \exp\left[-\int_0^{\bar{t}} I\, dt\right] d\bar{t}$$

where I is the fraction of the untransformed sites nucleating per unit time, and N is the number of sites per unit volume. The extended volume[2, 7] of these sites at time t is

$$\frac{4\pi}{3} IN \exp\left[-\int_0^{\bar{t}} I\, dt\right][R(t) - R(\bar{t})]^3\, d\bar{t} \qquad (5)$$

where

$$R(t) = \int_0^t G\, dt.$$

Then

$$-\ln(1-x) = \frac{4\pi}{3} N \int_0^t I e^{-\int_0^{\bar{t}} I\, dt} [R(t) - R(\bar{t})]^3\, d\bar{t}\,.$$

Integrating by parts results in

$$-\ln(1-x) = \frac{4\pi}{3} N [R(t)]^3 - 4\pi N \int_0^t \exp\left[\int_0^{\bar{t}} I\, dt\right] \times [R(t) - R(\bar{t})]^2\, G\, d\bar{t} \qquad (6)$$

The first term is the only term that remains for instantaneous saturation. The second term is the correction term. If saturation occurs relatively early in the reaction,

$$-\ln(1-x) = \frac{4\pi}{3} [R(t)]^3 \left\{1 - 3 \int_0^1 \exp\left[-\int_0^{\bar{t}} I\, dt\right] d\frac{R(\bar{t})}{R(t)}\right\}. \qquad (7)$$

The correction factor is of the order of the ratio of R at saturation to $R(t)$, and becomes less as the reaction proceeds. This is the correction term for deviations from instantaneous saturation, and applies to isothermal as well as nonisothermal reactions. When substituted into (1), the correction term will enter both into τ and dx/dt. If I is proportional to G, the correction term will vanish, as Avrami has shown, because there will only be a single time-temperature parameter. However, if I is sufficiently large, the correction terms will be small regardless of whether I is proportional to G. For the pearlite reaction in high carbon steels, the correction term will be small. For medium-carbon steels, if the bulk of the reaction occurs in the vicinity of the nose of the TTT curve, it will also be small, and will increase with decreasing cooling rate.[6] The method of Grange and Kiefer,[10] which requires neglecting part of $\int \dfrac{dt}{\tau}$ is a correction which has the correct sign, since the ratio of the nucleation rate to the growth rate increases with increasing undercooling. Its quantitative success is probably fortuitous.

Zener[11] has given a solution for growth of diffusion-controlled precipitations. In this case it is possible to show that the radius of a particle is proportional to $\left[\int_0^t D\, dt\right]^{1/2}$ and that his solution is a solution for a time-dependent diffusion coefficient D if Dt is replaced by the $\int D\, dt$, provided that the equilibrium concentrations are independent of temperature. This is a condition that is fairly often approached at large undercoolings, and if all nucleation occurs early in the reaction, such a reaction will also be additive. A change in the equilibrium compositions with temperature will produce deviations, not only because the same volume of precipitate may not correspond to the same fraction of completion, but also because a sudden change in the equilibrium concentrations will make the material close to the new phase, which previously had been close to equilibrium, suddenly undersaturated or supersaturated. Therefore, the additional restriction must be applied that the bulk of the reaction occur at temperatures where the composition of the equilibrium phases are relatively constant, in order that the rule for additivity hold.

THE EFFECT OF GRAIN SIZE

It must be noted that the proof, that equation (2) is sufficient for additivity, requires that the function F be the same function for the nonisothermal specimen and the isothermal specimen. For reactions where the nucleation sites saturate, this means that the quantity of nucleation sites must be the same for both specimens. For example, for grain-boundary nucleated reactions both specimens must have the same grain size. If isothermal data are available for a specimen which has a grain size different from a nonisothermal specimen, one has to modify the rule of additivity to

take differences in quantity of nucleation sites into account.

For discontinuous or cellular reactions which saturate[7]

$$\begin{aligned} x &= 1 - e^{-2SR(t)} \\ &= 1 - e^{-\pi L[R(t)]^2} \\ &= 1 - e^{-4\pi/3N[R(t)]^3} \end{aligned} \tag{8}$$

for transformations which nucleate on surfaces, edges, or points respectively. S is the area of nucleating sites per unit volume, L is the length of nucleating sites per unit volume, and N is the number of point sites per unit volume, and R is defined in equation (5). Differentiating with respect to time, one obtains upon substitution into (1) that when

$$\begin{aligned} \int \frac{dt}{\tau} &= \frac{S_i}{S_n} \\ &= \left(\frac{L_i}{L_n}\right)^{1/2} \\ &= \left(\frac{N_i}{N_n}\right)^{1/3} \end{aligned} \tag{9}$$

the amount of transformation is x_0. The subscript i refers to the isothermal specimen from which τ was obtained and the subscript n to the nonisothermal specimen. If these are grain-boundary nucleated reactions, the equations (9) all reduce to

$$\int \frac{dt}{\tau} = \frac{D_n}{D_i} \tag{10}$$

where D_n and D_i are the respective grain diameters.

THE NONISOTHERMAL RATE LAWS FOR ISOKINETIC REACTIONS

The amount of transformation expected from an isokinetic reaction for any temperature path can be calculated if $h(T)$ and the function F are known. This, however, is not always known. What is known often is τ, and one usually has some clues of the function F. From (4) we can write an expression for $h(T)$ in terms of τ:

$$h(T) = \frac{1}{\tau} H(x_0) \tag{11}$$

When this is substituted into (4), it gives an expression for $H(x)$ for nonisothermal reactions

$$H(x) = H(x_0) \cdot \int \frac{dt}{\tau} \tag{12}$$

For discontinuous or cellular transformations which saturate, where H is R, one obtains from (8)

$$\begin{aligned} H &= \frac{-\ln (1 - x)}{2S} \\ H &= \left(\frac{-\ln (1 - x)}{\pi L}\right)^{1/2} \\ H &= \left(\frac{-\ln (1 - x)}{\frac{4\pi}{3} N}\right) \end{aligned}$$

respectively for the three types of nucleation sites.

The amount of transformation can then be calculated from

$$\begin{aligned} \log (1 - x) &= \frac{S_n}{S_i} \log (1 - x_0) \int \frac{dt}{\tau} \\ \log (1 - x) &= \frac{L_n}{L_i} \log (1 - x_0) \left[\int \frac{dt}{\tau}\right]^2 \\ \log (1 - x) &= \frac{N_n}{N_i} \log (1 - x_0) \left[\int \frac{dt}{\tau}\right]^3 . \end{aligned} \tag{13}$$

For grain-boundary nucleated reactions the quantities S_n/S_i, L_n/L_i, and N_n/N_i are easily expressible in terms of the grain size.

ACKNOWLEDGMENTS

The author wishes to thank Dr. J. H. Hollomon for his advice and for some stimulating suggestions.

REFERENCES

1. J. H. Hollomon, L. D. Jaffe, and M. R. Norton *Trans. Amer. Inst. Min. Met. Eng.* **167,** 419 (1946).
2. M. Avrami *J. Chem. Phys.* **8,** 212 (1940).
3. F. C. Hull, R. A. Colton, and R. F. Mehl *Trans. Amer. Inst. Min. Met. Eng.* **150,** pp. 185-207 (1942).
4. H. Krainer *Archiv Eisenhuttenw.* **9,** 619 (1936).
5. D. Turnbull and H. N. Treaftis *Acta Met.* **3,** 43 (1955).
6. J. W. Cahn The kinetics of the pearlite reaction. Submitted to the *Journal of Metals.*
7. J. W. Cahn *Acta Met.* **4,** 449 (1956).
8. C. Wert *J. Appl. Phys.* **20,** 943 (1949).
9. F. C. Hull and R. F. Mehl *Trans. Amer. Soc. Metals* **30,** 381 (1942).
10. R. A. Grange and J. M. Kiefer *Trans. Amer. Soc. Metals* **29,** 85 (1941).
11. C. Zener *J. Appl. Phys.* **20,** 950 (1949).

VOL. 4 1956

A THEORY OF SURFACE TENSION OF SOLIDS—I*

APPLICATION TO METALS

ADAM S. SKAPSKI†

A theory is developed which allows one to calculate the surface tension of nonionic solids (metals and nonmetals) from the arrangement of their next neighbors, from the heat of fusion, and from the surface tension of the liquid at the melting-point.

Theoretically-calculated interface tension values of solid metals with their own liquids are compared with the interface tensions determined by D. Turnbull from undercooling of metal droplets. The agreement is satisfactory.

The temperature coefficient of the surface tension of solid metals is calculated from the theory; it is compared with that obtained from Strattons' electron theory in two cases in which Stratton's theoretical solid-surface tension values come closest to reality. The agreement is good.

Maximal and minimal surface tensions for solid gold, silver, and copper are calculated from the theory and compared with these obtained from the thin-foil and or wire-stretching method. The experimental figures, if their uncertainties are taken into consideration fall within the theoretically-predicted limits.

The tacit assumptions of the theory are critically discussed.

UNE THÉORIE DE LA TENSION SUPERFICIELLE DES SOLIDES—I APPLICATION AUX METAUX

L'auteur développe une théorie qui permet de calculer la tension superficielle des solides non-ioniques (métaux ou non) à partir de l'arrangement de leurs plus proches voisins, de la chaleur de fusion et de la tension superficielle du liquide au point de fusion.

Les valeurs théoriques de la tension interfaciale des phases solide et liquide d'un même métal sont comparées à celles déterminées par D. Turnbull à partir du refroidissement de gouttelettes métalliques. Une bonne concordance est observée.

Le coefficient de température de la tension superficielle des métaux solides est calculé par cette théorie et comparé à celui obtenu par la théorie électronique de Stratton dans les deux cas où cette dernière permet d'obtenir des valeurs de la tension superficielle des solides correspondant à la réalité et à nouveau, l'accord est satisfaisant.

Les tensions superficielles maximum et minimum, pour l'or, l'argent et le cuivre à l'état solide, sont déduites de la théorie et comparées à celles obtenues, par la méthode d'étirage d'une feuille mince et/ou d'un fil. Si l'on tient compte de leur imprécision, les figures expérimentales sont comprises entre les limites prévues théoriquement.

Enfin, les hypothéses tacites exigées par le théorie sont discutées d'un point de vue critique.

EINE THEORIE DER OBERFLÄCHENSPANNUNG VON FESTKÖRPERN—I ANWENDUNG AUF METALLE

Es wird eine Theorie entwickelt, die erlaubt, die Oberflächenspannung von Nichtionen-Festkörpern (Metalle und Nichtmetalle) aus der Anordnung der nächsten Nachbarn, der Schmelzwärme und der Oberflächenspannung der Schmelze am Schmelzpunkt, zu berechnen.

Theoretisch berechnete Werte der Grenzflächenspannung zwischen festen Metallen und ihren Schmelzen werden mit den von D. Turnbull beim Unterkühlen von Metalltröpfchen bestimmten Grenzflächenspannungen verglichen. Die Übereinstimmung ist zufriedenstellend.

Der Temperaturkoeffizient der Oberflächenspannung von festen Metallen wird aus der Theorie berechnet; er wird dann mit den Ergebnissen der Elektronentheorie von Stratton verglichen und zwar in zwei Fällen, in denen die Strattonschen theoretischen Werte für die Oberflächenspannung der Wirklichkeit am besten gerecht werden. Die Übereinstimmung ist gut.

Ferner werden mit der Theorie obere und untere Grenzwerte der Oberflächenspannung von festem Gold, Silber und Kupfer berechnet und diese mit experimentellen Werten verglichen. Letztere liegen, berücksichtigt man ihre Unsicherheit, innerhalb der theoretisch berechneten Grenzen.

Die stillschweigenden Annahmen, die die Theorie enthält, werden kritisch diskutiert.

Growing interest in grain boundaries focuses our attention on the numerical values of the surface tension of solids, since the knowledge of the latter leads to a better understanding of the interphase boundary phenomena. Unfortunately, the experimental data on the surface tension of solids are few and incomplete. On the other hand, we do not have any good theory of surface tension of nonionic solids;‡ and the best of the existing electron theories of surface tension of solid metals, that developed by R. Stratton,[1] gives numerical values which are

* Part of a research project supported by a National Science Foundation grant. Received June 2, 1955; revised version January 9, 1956.

† Physics Department, University of Vermont.

‡ Except for inert-gas crystals: R. SHUTTLEWORTH *Proc. Phys. Soc.* **62A**, 167 (1949).

obviously quantitatively incorrect, since they are consistently (and in most cases considerably) lower than the experimentally rather well-known surface tensions of liquid metals. In such a situation there is a need for a theory, preferably simple, which would be capable of at least approximative predictions of the numerical values of the surface tension of solids.

This paper presents a theory, based on the elementary next-neighbors approach, which has been designed to cover the nonionic solids, both metals and nonmetals. In the first part the general theory has been outlined and its predictions confronted with the existing experimental data for metals, including the solid/liquid interface tension. Nonmetallic solids will be dealt with in the second part.

NEXT-NEIGHBORS THEORY OF SURFACE TENSION OF SOLIDS

If we enlarge the surface of a condensed (solid or liquid) phase by A—which is the area occupied by N-Avogadro molecules (atoms) in one layer—the following thermodynamic relation holds:

$$\Delta F = \sigma_M = \Delta U - T\Delta S \tag{1}$$

Here $\sigma_M = \sigma A$ is the molar surface tension, i.e. the product of the specific surface tension (erg/cm²) and the molar area, ΔU is the change of internal energy, and $\Delta S = -(d\sigma_M/dT)$ the change of entropy (per mole) connected with the transfer of one molecule from the inside of the condensed phase to its surface.

In equilibrium, the kinetic energy of a molecule is the same in the bulk and in the surface. Thus, the term ΔU can be interpreted as the difference of the potential energy of the molecule in the bulk and in the surface. This difference can be expressed as a function of the heat of fusion in the following way.

If u is the energy (per mole) of interaction between the chosen molecule and its next neighbors—i.e. the work necessary to separate them to infinite distance—the difference in potential energy connected with bringing up one molecule from the bulk (where it is surrounded by Z_i next-neighbors) to the surface (where it is surrounded by Z_a next-neighbors) can be written as:

$$\Delta U = Z_i u - Z_a u \tag{2}$$

From (1) and (2) we shall have, at the melting temperature, for the solid:

$$\sigma_{MS} = (Z_i - Z'_A)u_s - T_M \Delta S'_s \tag{3a}$$

and for the liquid:

$$\sigma_{ML} = (Z_i - Z_A)u_L - T_m \Delta S_A \tag{3b}$$

While Z_i is always the same for the liquid and for the solid, as is well known from X-ray investigations in the neighborhood of the melting-point, the prime on Z'_a reminds us that the number of next-neighbors surrounding (on the sides and from below) the molecule situated in the surface depends, in a solid, on the crystal plane, and may be different from Z_a in the liquid state. The latter, since liquids always minimize their surface, corresponds to the most populated plane through the solid. If we choose such a crystal plane for the solid, we can, because of $Z'_a = Z_a$, obtain by subtraction of (3b) from (3a):

$$\sigma_{MS} - \sigma_{ML} = (Z_i - Z_A)(u_s - u_L) + T_m(\Delta S_L - \Delta S_s). \tag{4}$$

But since $(u_s - u_L)$ is the change of interaction energy (per mole) between the chosen molecule and one of its neighbors due to the melting process, we can obviously write

$$u_s - u_L = Q_f/Z_i$$

and thus obtain

$$\sigma_s = \frac{Z_i - Z_A}{Z_i}\frac{Q_f}{A_s} + \frac{A_L}{A_S}\sigma_L + \frac{T_m}{A_s}(\Delta S_L - \Delta S_s) \tag{5}$$

in which the molar surface tensions have been replaced by the respective products of specific surface tensions and molar areas.

Equation (5) can be brought into a more convenient form. Let us first note that the molar areas can be calculated from the formula

$$A = fN^{1/3}(M/\rho)^{2/3}$$

where f is the population density factor for a given crystal plane. Since f is the same in the plane of the densest population of the crystal and in the surface of its liquid, it follows that

$$A_L/A_S = (\rho_S/\rho_L)^{2/3}$$

and consequently

$$\sigma_S = \frac{Z_0}{Z_i}\frac{Q_f}{A_s} + \left(\frac{\rho_s}{\rho_L}\right)^{2/3}\sigma_L + \frac{T_m}{A_s}(\Delta S_L - \Delta S_s) \tag{6}$$

where $Z_0 = Z_i - Z_a$.

The second term on the right side of equation (6) accounts for the fact that the molar area of the liquid is different from that of the solid. The third term accounts for entropy changes.

In the first approximation, the third term can be safely neglected as small in comparison with the sum of the two others. We shall, however, attempt to estimate its numerical value.

VOL. 4 1956

The limits of ΔS_L have been calculated by this author[2] in a paper dealing with liquid metals. The comparison of these limits with experiment showed that

$$\Delta S_L = 3R \ln \left(\frac{Z_i}{Z_A}\right)^{1/2} - \frac{1}{2}\frac{R}{Z_i+1}\left[Z_0 \ln \frac{Z_0}{Z_i+1} + (Z_A+1)\ln\frac{Z_A+1}{Z_i+1}\right] \quad (7)$$

gives good agreement between theory and experiment. The evaluation of ΔS_s follows the line of reasoning given below.

The first term of equation (7) can be accepted for solids without any modification; it represents the entropy change due to the changed oscillation frequency in the surface, and depends only on Z_i and Z_a, which are the same in the liquid and in the solid.

The second term accounts for the disorder in the "interphase region" groups which include the virtual upper Z_0 sites ($Z_i + 1$ sites altogether). It has been calculated on the assumption of equivalence of all sites. Since these sites cannot actually be completely equivalent, it was anticipated that the calculated configurational entropy $\Delta S_{L\,\mathrm{conf}}$ must be too great and represents the upper theoretical limit. By comparison with experimental data, it was found that the actual configurational disorder amounts to one-half of the calculated one.

If the solid surface were absolutely static, we should have no configurational entropy term. But the surface of a solid at its melting-point is not "dead"; it is very much alive with thermal motion, as is evident from the self-diffusion in the surface. In our attempt to evaluate the entropy of this live surface, we shall assume that the layer of empty virtual sites forming an extension of the crystal lattice can be, through thermal motion, partly filled by the atoms of the first layer, with corresponding "surface holes" appearing in the first layer—and only in the first layer, in distinction from a liquid surface—until a statistical equilibrium has been reached. Such a live solid surface has the same total number of Z_a neighbors, and thus the ΔU term in our equation (1) remains unaffected. But it has an entropy greater than that of a "dead" surface. This increase in entropy can be expressed by a configurational term as follows.

Translating the above reasoning into the language of our "interphase region" groups, we have an exchange of atoms between the Z_0 sites (the virtual "upper" sites) and the $(Z_a - Z_0 + 1)$ sites (the "side" sites plus the site of the chosen atom), while the lower Z_0 sites remain permanently filled. This exchange contributes to the entropy increase a term equal to:

$$\Delta S_{s\,\mathrm{conf}} = -\frac{R}{Z_i+1}\left[Z_0 \ln \frac{Z_0}{Z_i - Z_0 + 1} + (Z_A - Z_0 + 1)\ln\frac{Z_A - Z_0 + 1}{Z_i - Z_0 + 1}\right] \quad (7a)$$

Taught by our experience with liquids, we shall assume that the lack of equivalence of the Z_0 and the $(Z_a - Z_0 + 1)$ sites is, in solids, also represented by the factor $\frac{1}{2}$ with the configurational entropy term. We shall thus have, for the temperature coefficient of the solid surface tension

$$\frac{d\sigma_s}{dT} = \frac{-\Delta S_s}{A_s} = -\frac{\Delta S_{\mathrm{osc}} + \frac{1}{2}\Delta S_{s\,\mathrm{conf}}}{A_s} \quad (7b)$$

It is interesting to compare the figures obtained from (7b) with those calculated from Stratton's theory for sodium and potassium for which Stratton's theoretical surface tension values come close to reality, although remaining somewhat too low. With $Z_i = 8$, $Z_a = 6$, $Z_0 = 2$, and $A_s = 1.12N^{1/3}(M/\rho_s)^{2/3}$, we get, for the 110-face (that of densest population in the c.b.c. system) from equation (7b), for sodium

$$\frac{d\sigma_s}{dT} = -\Delta S_s/A_s = (5.50/7.90) \times 10^{-1} = -0.070 \text{ erg/cm}^2\text{/degree}$$

while Stratton's theory gives -0.06 erg/cm²/degree,* and, from equation (7b), for potassium

$$\frac{d\sigma_s}{dT} = -\Delta S_s/A_s = (5{\cdot}50/12{\cdot}00) \times 10^{-1} = -0.046 \text{ erg/cm}^2\text{/degree},$$

while Stratton's theory gives -0.04 erg/cm²/degree.*

The agreement is satisfactory.

The complete equation for the calculation of the surface tension of a solid in its most densely populated planes ($Z'_a = Z_a$) is thus

$$\sigma_s = \frac{Z_0}{Z_i}\frac{Q_f}{A_s} + \left(\frac{\rho_s}{\rho_L}\right)^{2/3}\sigma_L + \frac{1}{2}\frac{T_m}{A_s}[\Delta S_{L\,\mathrm{conf}} - \Delta S_{s\,\mathrm{conf}}] \quad (6a)$$

To obtain the surface tension of the solid in any other plane in which $Z'_a \neq Z_a$, we have to proceed in the following way.

For nonmetallic liquids a relation between the

* Quoted after J. W. Taylor *Phil. Mag.* **46,** 875 (1955).

surface tension and the heat of vaporization L has been shown to exist[3]

$$\sigma_L A_L + T\Delta S_L = \frac{Z_i - Z_A}{Z_i} L \tag{8}$$

which has been deduced,[3] on the assumption that the number and configuration of next-neighbors in liquids is the same as it is in solids.* It is thus obvious that we can expect an analogous relation—with the heat of sublimation L_s substituted for that of evaporation—to hold for solids. We shall therefore have, for $Z'_a = Z_a$

$$\sigma_s A_s + T_m \Delta S_s = \frac{Z_i - Z_A}{Z_i} L_s \tag{8a}$$

and for any other plane in which $Z'_a \neq Z_a$

$$\sigma'_s A'_s + T_m \Delta S'_s = \frac{Z_i - Z'_A}{Z_i} L_s \tag{8b}$$

Dividing (8b) by (8a) and introducing $Z'_0 = Z_i - Z'_a$, we obtain, at the melting-point

$$\sigma'_s = \frac{Z'_0}{Z_0} \frac{A_s}{A'_s} \sigma_s + \frac{T_m}{A'_s} \left[\frac{Z'_0}{Z_0} \Delta S_s - \Delta S'_s \right] \tag{9}$$

which allows us to calculate the surface tension in any plane of the crystal from that in its most densely populated plane.

For metals, equation (8) was shown *not* to hold.[3] The main reason for that is, in this author's opinion, the following. Equation (8) has been obtained by expressing the energy of interaction of next-neighbors in terms of the heat of evaporation (sublimation), the latter being assumed to measure the work necessary to separate the molecules (atoms) from each other to infinite distance. In metals, however, the heat of evaporation (sublimation) includes more than mere work of separating of atoms to infinite distance; it also includes the change of the status of their outermost electrons. In the condensed phase, the electrons are free, while in the vapor phase they are bound by the atoms. If we knew what fraction of the heat of sublimation is used for the separation of atoms while preserving the same status of their electrons—we might call such an ideal heat of sublimation L_{id}—that is, if we knew the numerical relation between the terms of the following equation

$$L_{id} = L_s - \Delta E_{el}$$

where ΔE_{el} is the change of the energy of electrons connected with the sublimation, we could calculate the surface tension of the solid metal from a formula identical with equation (8a) or with equation (8b), except for L_{id} in place of L_s. But we have already obtained a much more convenient equation (6a), in which any actual difference of the energy of electrons is already included in the heat of fusion, and which gives the surface tension of a solid metal in its most populated plane. And for the calculation of the surface tension of the same metal in a plane with $Z'_a \neq Z_a$, we do not need to know L_{id} numerically, since it cancels out in the process of dividing equation (8b) by equation (8a), leading us again to equation (9), which is thus valid for both metallic and non-metallic solids.

The present theory is based on the concept of an ideal crystal without any inner lattice disorders or inner holes. But it can be shown by simple probability calculations that the influence of holes—because of their distribution between the inner- and the surface-neighbors groups—cannot be serious. For instance a 10% hole disorder would change the Z_0/Z_i ratio in c.f.c. metals by only a few per cent. Small amounts of impurities in solid solution should also have rather small effect, theoretically, unless they have a marked tendency to accumulate in the surface. Any gas, vapor, or liquid, which shows strong adsorption on the surface of the solid, thus creating additional "foreign surface-neighbors," is theoretically expected to decrease the ΔU in Equation (1). This may cause considerable lowering of the surface tension of the solid.

SURFACE TENSION OF A SOLID AND ITS INTERFACE TENSION WITH ITS OWN LIQUID AT MELTING-POINT

A simple relation between the surface tension of a solid and its interface tension with its own liquid (at the melting-point) can be deduced in—among other ways[4]—the following way.

In J. H. Poynting's and J. J. Thomson's classical theory of the plate detachment method of measuring the surface tension of liquids,[5] the pull per area required to detach a plate from the surface of a liquid is given by

$$P/A = g\rho_L X \tag{10a}$$

where

$$X^2 = 4\sigma_L / g\rho_L \tag{10b}$$

X being the height of the lower surface of the plate above the undisturbed level of the liquid, and g the gravity acceleration.

Accordingly, the work per area required to detach the plate is, by integration and substitution of (10b),

$$W/A = \int_0^x (P/A)\, dX = 2\sigma_L \tag{11}$$

* A factor 1/2 was unnecessarily used with Z_i and Z_a in the quoted paper; this factor eliminated itself in the final result.

VOL. 4 1956

The only condition for obtaining equation (11) is Poynting's and Thomson's assumption that the plate is completely wetted (contact angle zero) by the liquid. Therefore, equation (11) remains valid for a plate made of the solid phase of the measured liquid (at melting-point). In the latter case, the work per area needed to detach the plate can be also expressed by

$$W/A = \sigma_S + \sigma_L - \sigma_{SL} \tag{11a}$$

since the solid/liquid interface is replaced by the two new surfaces. From (11) and (11a) we get

$$\sigma_S = \sigma_{SL} + \sigma_L. \tag{12}$$

From equation (12) and from equation (6a) we obtain

$$\sigma_{SL} = \frac{Z_0}{Z_i}\frac{Q_f}{A_s} + \left[\left(\frac{\rho_s}{\rho_L}\right)^{2/3} - 1\right]\sigma_L + \frac{T_m}{A_s}\left[\Delta S_L - \Delta S_s\right] \tag{13}$$

which, for metals, gives the minimal interface tension, since the most densely populated planes are, in metals, those with minimal surface tension (111-face in the c.f.c. metals, 110-face in the c.b.c. metals).

It is natural to expect these minimal interface tensions to be primarily instrumental in controlling the growth of crystals from the nuclei in their melt. Now, interface tensions involved in nucleation have been determined by D. Turnbull[6] from a completely different theoretical approach by measuring the undercooling of metal droplets. If our next-neighbors theory is basically correct, Turnbull's interface tension values should thus be somewhat greater than, but rather close to, those calculated from equation (13).

For the purpose of numerical calculation, it is convenient to take advantage of an expansion and introduce the volume change $\Delta V/V_s$ at melting

$$\left(\frac{\rho_s}{\rho_L}\right)^{2/3} - 1 = \left(1 + \frac{\rho_s - \rho_L}{\rho_L}\right)^{2/3} - 1 \cong \frac{2}{3}\frac{\Delta V}{V_s}$$

The error caused by neglecting the higher powers of expansion is small and certainly smaller than the uncertainties involved in the density data at melting-point.

We accordingly obtain, after numerical substitutions, for the c.f.c. metals

$$\sigma_{SL} = \tfrac{1}{4}\frac{Q_f}{A_s} + \tfrac{2}{3}\frac{\Delta V}{V_s}\sigma_L + 0.3 \times 10^7 \frac{T_m}{A_s}$$

and for the c.b.c. metals

$$\sigma_{SL} = \tfrac{1}{4}\frac{Q_f}{A_s} + \tfrac{2}{3}\frac{\Delta V}{V_s}\sigma_L + 0.5 \times 10^7 \frac{T_m}{A_s}$$

The last term in these equations contributes less than 10%. The details of numerical calculations are given further in the text.

Table 1 gives the σ_{SL} calculated from the above equations for some metals, and the corresponding figures found by Turnbull.

In view of the sensitivity of our calculated values to densities ($\Delta V/V_s$) and the experimental errors in the latter, the agreement can be considered as satisfactory.

COMPARISON OF THEORETICAL AND EXPERIMENTAL SURFACE TENSIONS OF SOLID METALS

The experimental figures for the surface tension of solid metals can be obtained from two methods, which are briefly discussed below.

(a) *The Thin Foil and/or Wire Method*

Gold, silver, and copper have been investigated by this method. There is, however, some confusion as to the proper way of arriving at the final numerical

TABLE 1.

Metal	Q_f (kJ per g-at.)	ρ_s	$\Delta V/V_s$	Surface tensions in erg/cm^2		
				σ_L	Calculated σ_{SL}	Turnbull σ_{SL}
Na	2.65	0.95	0.027	200	15	20*
Li	3.5	0.53	0.015	400	27	30*
Pb	4.86	11.00	0.034	465	32	33
Ag	11.7	10.00	0.045	930	101	126
Au	13.1	18.46	0.052	1135	121	132
Cu	11.5	8.52	0.041	1240†	128	177
Pt	22.0	20.2	0.069	1820	236	240

* Quoted after J. W. Taylor *Phil Mag.* **46,** 857 (1955)
† Calculated from Libman's capillary constant 0.308 at m.p. with $\rho_L = 8.2$.[7]

values, and no complete agreement as to their interpretation.

The overwhelming opinion, shared by this author, is that the main effect measured in this method is due to the free surface energy, and that the mechanical surface stress plays a minor role. Even so, there is neither direct experimental evidence nor general theoretical agreement as to the crystal faces whose surface tension is, or is most likely to be, responsible for the measured effects.

In such a situation, the best one can do is to calculate from the next-neighbors theory the minimal and the maximal values of the solid surface tension (in the case of the three quoted metals that in the 111-face and that in the 100-face) and to confront them with the experimental data. The latter, again if the theory is basically correct, should fall within the theoretically predicted limits, or—if the mechanical surface stress does play a minor role—might slightly but not considerably exceed the upper theoretical limit.

(b) *The Undercooling Method*

Because of the simple relation given by equation (12), any method which can measure the interface tension of the solid with its own liquid can be used for the determination of the solid-surface tension. The undercooling method combined with the theory of nucleation can therefore be considered as a legitimate method for the solid-surface tension measurement. The values obtained represent, most likely, the minimal surface tensions of solids.

In Table 2 the experimental data based on the two quoted methods are compared with those calculated from our theory. A few remarks concerning numerical calculations are given below.

Densities ρ_S at melting-point were, in most cases, computed from room-temperature data through cubical coefficients of thermal expansion taken from Mott and Jones *Properties of Metals and Alloys*, 1936, Appendix II. The $\Delta V/V_s$ and Q_f values were taken from International Critical Tables.

For the c.b.c. metals, $Z_i = 8$, $Z_a = 6$, and hence $Z_0/Z_i = 1/4$. The surface-packing factor $f = 1.12$. The oscillation entropy term is $\Delta S_{\text{osc}} = 3.58 \times 10^7$ erg/degree. The configurational entropy term for the solid surface is $\Delta S_{L\,\text{conf}} = 4.84 \times 10^7$ erg/degree, and for the solid surface $\Delta S_{s\,\text{conf}} = 3.85 \times 10^7$ erg/degree. With the factor 1/2 introduced with the configurational entropy terms, we have $(\Delta S_L - \Delta S_s) = 0.50 \times 10^7$ erg/degree. All figures are for the 110-plane.

For the c.f.c. metals, $Z_i = 12$, $Z_a = 9$, and hence $Z_0/Z_i = 1/4$. The surface-packing factor $f = 1.09$. The oscillation entropy term is identical with that for the c.b.c. metals. The configurational entropy term for the liquid surface is $\Delta S_{L\,\text{conf}} = 4.48 \times 10^7$ erg/degree, and the configurational entropy term for the solid surface is $\Delta S_{s\,\text{conf}} = 3.90 \times 10^7$ erg/degree. With the factor 1/2 introduced with the configurational entropy terms we get $(\Delta S_L - \Delta S_s) = 0.30 \times 10^7$ erg/degree. All these figures refer to the 111-plane.

For the 100-plane of the c.f.c. metals (that of the maximal surface tension) $Z_i = 12$, $Z'_a = 8$, and hence $Z'_0/Z_i = 1/3$. The surface-packing factor is $f = 1.258$. The total entropy change for the solid surface $\Delta S'_{s100} = 7.02 \times 10^7$ erg/degree. Since the total entropy change for the solid 111 surface is $\Delta S_{s\,111} = 5.53 \times 10^7$ erg/degree, the numerical value of the term

$$\frac{T_m}{A'_s}\left(\frac{Z'_0}{Z_0}\Delta S_s - \Delta S'_s\right) = \frac{T_m}{A'_s}\ 0.35 \times 10^7 \text{ erg/degree},$$

The contribution of this term to the maximal surface-tension value of the c.f.c. metals is thus, for silver 8 erg/cm², for gold 9 erg/cm², for copper 12 erg/cm².

The entropy terms entering into our equations for the solid surface tension σ_S have been calculated and included into the figures listed in Table 2 mainly for the sake of completeness of the theoretical picture; in fact, for all practical purposes, the entropy terms could have been omitted from equation (6) and equation (9), at the present stage of the development of the theory.

CRITICAL DISCUSSION

The solid surface tensions obtained from undercooling lie all close to the minimal theoretical values. This is simply the consequence of the agreement shown in Table 1. Large σ_L values entering equation (12) tend to play down the relative discrepancies

TABLE 2. All surface tension values in erg/cm²

Metal	σ_S min theoretical	σ_S undercooling	σ_S* stretching	σ_S max theoretical
Sodium	215	220		
Lithium	427	430		
Lead	497	498		
Silver	1031	1056	1130 ± 60	1200
Gold	1256	1267	1350 ± 70	1460
Copper	1368	1417	1650 ± 80	1590
Platinum	2056	2060		

* Quoted after A. J. Shaler[8] with uncertainties amounting, according to Shaler, to about 5% in each case.

VOL. 4 1956

between the theoretical and the experimental σ_S figures.

As for the data obtained from the thin-foil and/or wire-stretching method, silver and gold fall within the predicted limits. The average σ_S of copper is greater than the maximal theoretical value by less than 4%. It is interesting to note that the Turnbull σ_{SL} value for copper is also greater than the theoretical σ_{SL} figure.*

In general, it seems fair to say that the confrontation of the theory with experimental data for metals is very encouraging, the more that, in its present stage of development, the theory contains the following tacit approximations.

(1) The interaction energy between the chosen atom and its Z_a neighbors is assumed to be the same as that between the chosen atom and its Z_i neighbors. This may not be quite true, and the situation may be somewhat different in liquids and in solids.

(2) The difference between the concentration (and hence the kinetic energy) of free electrons in the bulk and in the surface is assumed to be the same in solid and in liquid metals. This, again, may not be quite true.

It might be of interest to note, however, that corrections due to (1) and (2) would presumably work in opposite directions.

(3) The omission of farther-than-next neighbors introduces a systematic error. A. D. Crowell[9] has recently succeeded in accounting for this omission in a simple and general way. Crowell's correction results in substituting in our formulas $Z_0 + \frac{1}{2}$ for Z_0, and $Z_i + 1$ for Z_i. This raises the σ_{SL} values for metals by a few per cent, and somewhat narrows the gap between the theoretical and the Turnbull's σ_{SL} figures. In case of copper, in particular, one gets, with Crowell's correction, 134 erg/cm² instead of our 128 erg/cm². In the final σ_S values the effect of Crowell's correction is numerically insignificant.

The fact that the simple approach of the theory can nevertheless render some service is probably due to its basic assumptions which incorporate two main characteristic features of nonionic solids and liquids: (a) the similarity of their "neighborhood structure" (near the melting-point) as far as the next-neighbors—and only the next-neighbors—are concerned; (b) the steep falling off of the interaction potentials in the process of fusion with the distance, which again allows us to limit this interaction to the next-neighbors only and to interpret them in terms of the heat of fusion with reasonable approximation.

It may be added that interpreting the interaction energies in term of heat of fusion, and taking σ_L at the melting-point as the starting point, allows us to avoid many difficulties involved in the use of heat of evaporation and sublimation.

* (Added in proof) On the other hand, there is some doubt about the numerical value of the correction (for the presence of grain boundary tension) which brings the average σ_s stretching for copper up to the quoted high value. If Fisher's and Dunn's (Imperfections in Nearly Perfect Crystals, John Wiley & Sons, 1952, p. 123) evaluation of Udin, Shaler and Wulf data for copper is accepted instead, viz. $\sigma_s = 1435 \pm 80$ erg/cm², the theoretical average (σ_s min + σ_s max)/2 and the experimental average come quite close to each other for all the three metals.

ACKNOWLEDGMENTS

I wish to acknowledge my great indebtedness to Dr. Carl Benedicks, of Stockholm, whose anticipation of the role of interface tensions in metals many years ago first aroused my interest in the solid surface tension phenomena. I also wish to thank warmly D. Cyril Stanley Smith, of Chicago; his constructive criticism has contributed much to the clarification of some initially doubtful points of the theory. To my colleague Dr. N. L. Walbridge I owe thanks for discussions.

REFERENCES

1. R. Stratton *Phil. Mag.* **44,** 519 (1953); *ibidem* **44,** 1236 (1953).
2. A. Skapski *J. Chem. Phys.* **16,** 386 (1948).
3. A. Skapski *J. Chem. Phys.* **16,** 389 (1948).
4. R. Sill and A. Skapski *J. Chem. Phys.* **24,** 644 (1956)
5. T. H. Poynting and J. J. Thomson *Textbook of Physics,* London, 1913.
6. D. Turnbull *J. Chem. Phys.* **18,** 768 (1950); *ibid.* 769 (1950).
7. Earl E. Libman *Proc. Nat. Acad. Sci.* **13,** 588 (1927).
8. A. J. Shaler an article in *Structure and Properties of Solid Surfaces,* University of Chicago Press, p. 123 (1953).
9. *J. Chem. Phys.* (in print). Private communication.

A NEXT-NEIGHBORS THEORY OF MAXIMUM UNDERCOOLING*

ADAM S. SKAPSKI†

Considering the equilibrium between a small spherical crystal and its melt, as influenced by the interface curvature and the interface tension, and introducing the next-neighbors theory which he had developed, the author shows that the smallest crystal which exhibits the full "macro" interface tension has a radius $r = 3.5d$, where d is the distance between next neighbors.

Assuming that below $r = 3.5d$ the interface tension decreases very rapidly and the capillary influence on the melting equilibrium practically ceases to exist, the author arrives at a general relation between the absolute temperature of maximum undercooling and the melting-point T_m, which, for the c.f.c. and hex.c.p. systems is given by

$$T_{\text{max.und.}} = 0.81 T_m$$

The formula gives a surprisingly good agreement with the experimental figures for the c.f.c. and h.c.p. metals, and a reasonably good agreement for other metals and for water.

UNE THÉORIE DES PLUS PROCHES VOISINS APPLICABLE A LA SURFUSION MAXIMUM

Considérant que l'équilibre entre un petit cristal sphérique et son liquide est influencé par la courbure à l'interface et par la tension interfaciale, et introduisant la théorie des plus proches voisins qu'il a développée, l'auteur montre que le plus petit cristal qui présente la tension interfaciale macroscopique a un rayon $r = 3{,}5d$, où d est la distance entre plus proches voisins.

En admettant que en-dessous de $r = 3{,}5d$, la tension interfaciale décroît très rapidement et que l'influence capillaire sur l'équilibre de fusion disparaît pratiquement, l'auteur établit une relation générale entre la température absolue de la surfusion maximum et la température de fusion T_m, qui, pour les systèmes c.f.c. et h.c., est donnée par:

$$T_{\text{surf. max.}} = 0{,}81\ T_m$$

La formule est en accord surprenant avec les figures expérimentales pour les métaux c.f.c. et h.c. et la concordance est satisfaisante pour l'eau et les autres métaux.

THEORIE MIT WECHSELWIRKUNG NÄCHSTER NACHBARN FÜR DIE MAXIMALE UNTERKÜHLUNG

Berücksichtigt man, dass das Gleichgewicht zwischen einem kleinen kugelförmigen Kristall und seiner Schmelze von der Grenzflachenkrümmung und der Grenzflächenspannung abhängt, so zeigt sich bei Anwendung der vom Autor entwickelten, auf der Wechselwirkung nächster Nachbarn beruhenden Theorie, dass die kleinsten Kristalle mit der vollen "makroskopischen" Grenzflächenspannung einen Radius $r = 3{,}5d$ haben, wobei d der Abstand zwischen nächsten Nachbarn ist.

Unter der Annahme, dass unterhalb $r = 3{,}5d$ die Grenflächenspannung sehr rasch abnimmt und der Einfluss der Kapillarwirkung auf das Schmelz-Gleichgewicht praktisch verschwindet, gelangt der Autor zu einer allgemeinen Beziehung zwischen der absoluten Temperatur der maximalen Unterkühlung und dem Schmelzpunkt T_m, die für kubisch flächenzentrietre und hexagonal dichtest gepackte Systeme

$$T_{\text{max. und.}} = 0{,}81 T_m$$

lautet.

Die Formel gibt eine überraschend gute Übereinstimmung mit den experimentellen Zahlenwerten für die Metalle dieser beiden Strukturen und eine ziemlich gute Übereinstimmung für andere Metalle und Wasser.

INTRODUCTORY REMARKS

The assumptions of the next-neighbors approach, in which the present author has been interested for some time,[1, 2, 3] stem from two now generally recognized facts, namely: (a) that liquids show a short-range order which—at least at temperatures near the melting-point—is identical with that of their solids, (b) that the interaction forces between atoms and molecules decrease very steeply with their distance.‡

Basing on these two facts, the theory assumes that the heats of sublimation,[3] evaporation,[1, 4, 5] and fusion[3] can be interpreted in terms of interaction between the next neighbors only, the influence of the second-next neighbors being considered negligible. It also assumes that the entropy of an atom (molecule) in the liquid and in the solids is in part determined by the number of its next neighbors.[2, 3] Thus the theory tries to establish relationships between the characteristic features of groups of next neighbors and the properties of solids and liquids.

* Part of the research supported by a grant from the National Science Foundation. Received June 24, 1955; revised version January 9, 1956.

† Physics Department, University of Vermont

‡ For distance changes due to fusion, (b) is true also for metallic and ionic substances, because of the large contribution of short-range forces to this process.

VOL. 4 1956

In particular, the capillary properties of solids and liquids seem to be closely related to the characteristics of two sorts of groups of neighbors: the "surface" group and the "inner" group. The latter consists of Z_i next neighbors surrounding any chosen atom situated inside of the condensed (solid or liquid) phase. All Z_i neighbors are also inside of the condensed phase.

The Z_a "surface" neighbors which surround, on the sides and from below, the chosen atom after it has been transferred to the surface of the condensed phase, have average potential energies and entropies different from those of the inner group. It is from these differencies of energies and entropies that the surface tension of the condensed phase and its temperature coefficient can be calculated.[3]

Thus the whole next-neighbors approach to capillary properties is based on a clear-cut distinction between the inner and the surface group. In other words, the "shell" of the Z_i neighbors and the two layers of the Z_a neighbors cannot overlap. We shall see that this determines the dimensions of the smallest crystal which—from the point of view of the next-neighbors theory—has still the full "macro" surface (and interface) tension.

THE MINIMAL MELTING TEMPERATURE OF A SMALL CRYSTAL IN CAPILLARY EQUILIBRIUM WITH ITS LIQUID PHASE

The relation between the curvature $C = 1/r_1 + 1/r_2$, the interface tension of the solid with its own liquid σ_{SL} and the melting point T, is expressed by the well-known equation

$$T_m - T = \frac{T_m C \sigma_{SL}}{q_f \rho_s} \tag{1}$$

where T_m is the "normal" melting-point (at $C = 0$), q_f is the heat of fusion in erg/gram, and ρ_s is the density of the solid at melting-point. For an idealized small spherical crystal ($C = 2/r$) the above equation becomes

$$T = T_m - \frac{2T_m \sigma_{SL}}{q_f \rho_s} \frac{1}{r} \tag{2}$$

The interface tension σ_{SL} has been recently expressed from the next-neighbors theory,[3] in a fair agreement with the experimental evidence, by the equation

$$\sigma_{SL} = \frac{Z_0}{Z_i} \frac{Q_f}{A_s} + \frac{2}{3} \frac{\Delta V}{V_s} \sigma_L + \frac{T_m}{A_s} \left[\Delta S_L - \Delta S_s \right] \tag{3}$$

where $Z_0 = Z_i - Z_a$, $Q_f = Mq_f$ in erg/mole (per gram-atom), A_s is the surface area of the solid occupied by N Avogadro molecules (atoms) in one layer, $\Delta V/V_s$ is the relative volume change at melting, and ΔS_L and ΔS_s are the entropy surpluses in the surface of the liquid and of the solid, respectively. This equation yields the minimal σ_{SL}, the very one which is most likely to control the equilibrium of very small crystals with their melt.

One sees from equation (2) that the smaller is the radius of the crystal, the lower is the temperature at which the crystal coexists in equilibrium with its melt. In fact, equation (2) predicts a linear decrease of T with increasing $(1/r)$, provided the interface tension stays the same, that is, equal to its macroscopic value given by equation (3). In this prediction the changes in ρ_S and q_f are, of course, neglected, and equation (2) is assumed to hold down to, and below, the dimensions at which equation (3) holds.

But the validity of equation (3)—as it has been pointed out in the introductory remarks—is subject to the condition that the inner and the surface groups of next neighbours must not overlap. This condition is satisfied only down to (and including) $r = 3.5d$, where d is the distance between the next neighbours. The crystal of these dimensions consists namely of a central atom surrounded by one layer (shell) of its Z_i neighbors and by two farther layers of the Z_a neighbors. At $r < 3.5d$ the difference of the potential energy between the central atom and that situated in the very surface of the sphere will diminish, and so will the interface tension, which will no longer obey equation (3). The capillary influence on the melting-point will decrease, and the slope of the function $T = f(1/r)$ will begin to level off, rather quickly.

One might attempt to find, e.g. statistically, the exact form of the function $T = f(1/r)$ for $r < 3.5d$, and in this way arrive at the temperature at which the solid/liquid equilibrium ceases to be influenced by capillarity any more, that is the $T_{\min}$ below which the solidification of the whole system must occur (the lowest temperature of the solid/liquid equilibrium). If the theory is correct, the numerical value of the $T_{\min}$ should be equal to the absolute temperature of maximum undercooling.

But one should get a reasonably approximative value for $T_{\min}$ by substituting in equation (2) the σ_{SL} obtained from equation (3) and putting $r = 3.5d$. Such an approach implies that at $r = 3.5d$ the $T = f(1/r)$ line becomes parallel to the $(1/r)$ axis in a discontinuous manner. Provided the $T = f(1/r)$ function does actually level off quickly in the neighborhood of $r = 3.5d$, the latter approximation should work.

We thus express A_s and $r = 3.5d$ in terms of molar volume

$$A_s = fN^{1/3}(M/\rho_s)^{2/3} \tag{4a}$$

$$r = 3.5kN^{-1/3}(M/\rho_s)^{1/3} \tag{4b}$$

where f is the surface packing factor and k is a constant characteristic for the given crystal system. With (4a) and (4b) and with the substitution of σ_{SL} from equation (3) in equation (2), we obtain

$$T_{\min} = \left[1 - \frac{2Z_0}{3.5kf} - \frac{4N^{1/3}\left(\frac{\Delta V}{V_s}\right)\sigma_L}{10.5k\rho_s^{2/3}M^{1/3}q_f} - \frac{2(\Delta S_L - \Delta S_L)}{3.5kf\Delta S_f}\right] T_m \tag{5}$$

where $\Delta S_f = Q_f/T_m$ is the entropy of fusion.

If our assumptions are correct, equation (5) should be valid for all nonionic substances consisting of atoms or of not too elongated molecules. We shall solve it numerically for the c.f.c. and hex. close-packed lattices (for which f and k are the same) and confront the obtained $T_{\min}$ with the measured temperatures of maximum undercooling in metals.

For the two quoted crystal lattices $Z_0/Z_i = 1/4$; $f = 1.09$; $k = 1.122$; $(\Delta S_L - \Delta S_S) = 0.3 \times 10^7$ erg/deg.[3] After collecting the numerical and conversion factors, we get

$$T_{\min} = (0.883 - 0.68B - 0.033/\Delta S_f)T_m = AT_m \tag{6}$$

where the entropy of fusion is in cal/deg per mole (per gram-atom) and

$$B = \frac{\left(\frac{\Delta V}{V_S}\right)\sigma_L}{\rho_s^{2/3}M^{1/3}q_f}$$

with q_f in cal/gram.

The second and the third terms in the bracket of equation (6) vary slightly from metal to metal, but these variations do not affect the value of A to any significant degree, as it may be seen from Table 1.

TABLE 1.

Metal	$0.68B$	$0.033/\Delta S_f$	A
Lead	0.065	0.017	0.801
Silver	0.050	0.015	0.818
Gold	0.063	0.014	0.806
Copper	0.050	0.016	0.817
		Aver.	0.810

TABLE 2.

Metal	T_m	$T_{\min}$ calc.	$T_{\min}$ exper.	per cent error
Mercury	234	189	176	+7.4
Gallium	303	245	227	+7.9
Tin	505	409	400	+2.2
Bismuth	544	440	454	−3.1
Lead	600	486	520	−6.5
Antimony	904	732	769	−4.8
Germanium	1232	998	1005	−0.7
Silver	1234	1000	1007	−0.7
Gold	1336	1082	1106	−2.2
Copper	1356	1098	1120	−1.9
Manganese	1535	1243	1225	+1.5
Nickel	1728	1400	1409	−0.6
Cobalt	1768	1432	1438	−0.4
Iron	1808	1464	1513	−3.2
Palladium	1828	1480	1496	−1.1
Platinum	2047	1658	1667	−0.5
Water	273	221	234	−5.5

All the auxiliary data needed for computation have been taken from.[3]

Accepting the average from Table 1 for all metals of the two quoted lattice systems, we have

$$T_{\min} = 0.81T_m \tag{7}$$

The error in retaining $A = 0.81$ for other lattices can be estimated at less than 10% in the calculated $T_{\min}$.

In Table 2 the $T_{\min}$ values from equation (7) have been listed, together with the observed temperatures of maximum undercooling taken from Turnbull's paper.[6] The experimental figure for water was taken from Fisher, Hollomon, and Turnbull.[7]

The agreement between the calculated and the observed figures is surprisingly good for the c.f.c. metals (except for Pb, which gets out of line) and reasonably fair for other metals and even for water.

It is interesting that a correct general relationship between the temperature of maximum undercooling at the "normal" melting-point can be theoretically deduced from equilibrium conditions, if the latter take into consideration the capillary aspect of coexistence of the solid and the liquid phases. It seems also interesting to this author that theoretical figures reathr close to the experimental ones can be obtained by reasoning based on the next-neighbors theory.

REFERENCES

1. A. SKAPSKI *J. Chem. Phys.* **16,** 389 (1948).
2. A. SKAPSKI *J. Chem. Phys.* **16,** 386 (1948).
3. A. SKAPSKI *Acta Met.* (in print).
4. H. DUNKEN, H. KLAPPROTH, and K. L. WOLF *Koll. Z.* **91,** 232 (1941).
5. K. L. WOLF and R. GRAFE *Koll. Z.*, **98,** 257 (1942).
6. D. TURNBULL *J. Chem. Phys.* **18,** 769 (1950).
7. J. C. FISHER, J. H. HOLLOMON, and D. TURNBULL *Science* **109,** 168 (1949).

VOL. 4 1956

PRECIPITATE KINETICS AND STRUCTURE IN A Cu–2.4% Fe ALLOY*

J. M. DENNEY†

The kinetics of the isothermal precipitation of Fe from a supersaturated solid solution of Cu–2.4% Fe in the temperature range 550°C to 800°C have been obtained from measurements of the saturation magnetization of the specimens. The rate limiting process in the development of the coherent Fe precipitate is the diffusion of Fe in the Cu matrix, described in part by an activation energy of 1.65 ± 0.1 eV. X-ray diffraction studies indicate the precipitate forms coherently with the Cu matrix. The coherent f.c.c. Fe precipitate transforms during plastic deformation to a stable ferromagnetic body-centered structure (perhaps b.c.t. with $c/a = 1.1$). Transformation of the coherent precipitate to the ferromagnetic structure is never observed by thermal treatment alone in the range 4°K to 1073°K; but the precipitate transformation is readily accomplished by plastic deformation.

CINÉTIQUE ET STRUCTURE DE PRECIPITATION DANS UN ALLIAGE Cu–2,4% Fe

La cinétique de précipitation isotherme du Fer à partir d'une solution solide sursaturée de Cu–2,4% Fer dans le domaine de température 550°C à 800°C at été obtenu en mesurant la saturation magnétique des échantillons.

Le processus limitant la vitesse dans le développement du précipité cohérent de fer est la diffusion de Fe dans la matrice Cu, décrite en partie par une énergie d'activation de 1,65 ± 0,1 eV.

Les études de diffraction de rayons X montrent que le précipité est cohérent avec la matrice de cuivre. Le précipité cohérent cubique à faces centrées se transforme au cours de la déformation plastique en une structure stable cubique centreé et ferromagnétique (peut-être quadratique centré avec $c/a = 1,1$).

La transformation du précipité cohérent en une structure ferromagnétique n'est jamais obtenue par simple traitement thermique dans le domaine de 4°K à 1073°K; mais cette transformation s'effectue aisément pardéformation plastique.

AUSSCHEIDUNGSKINETIK UND STRUKTUR IN EINER Cu Fe-LEIGIERUNG MIT 2,4% Fe

Die Kinetik der isothermen Ausscheidung von Fe aus einem übersättigten Cu-Fe-Mischkristall mit 2,4% Fe wurde mit Hilfe von Messungen der Sättigungsmagnetisierung der Proben im Temperaturbereich zwischen 550° und 800°C verfolgt. Der geschwindigkeitsbegrenzende Prozess bei der Entwicklung der kohärenten Eisenausscheidungen ist die Diffusion des Fe im Cu-Gitter, die durch eine Aktivierungsenergie von 1,65 ± 0,1 eV zu beschreiben ist. Röntgenuntersuchungen zeigen, dass sich die Fe-Ausscheidungen in Kohärenz mit dem Cu-Gitter bilden. Bei plastischer Verformung wandeln sich die kohärenten kubisch-flächenzentrierten Fe-Ausscheidungen in eine stabile raumzentrierte Struktur (evtl. tetragonal-raumzentriert mit $c/a = 1,1$), die ferromagnetisch ist, um. Die Umwandlung der kohärenten Ausscheidungen in die ferromagnetische Struktur konnte allein infolge von Wärmebehandlungen im Temperaturbereich zwischen 4°K und 1073°K niemals beobachtet werden; durch plastische Verformung jedoch lassen sich die Ausscheidungen ohne weiteres umwandeln.

1. INTRODUCTION

The precipitation of Fe from Cu-rich solid solutions has been studied extensively in the past. The solubility of Fe in Cu was examined microscopically by Hanson and Ford,[1] and magnetically by Tammann and Olson.[2] Tammann[3] studied the magnetic properties and hardness of aged alloys. Studies of a series of Cu-rich Cu-Fe alloys by Bitter and Kaufman,[4] Gordon and Cohen,[5] and Smith[6] led to the realization that the initially paramagnetic Fe precipitate became ferromagnetic after cold working or extended aging at elevated temperature. Smith[7] was led to suggest that the paramagnetic precipitate might well be face-centered cubic and similarly oriented with respect to the Cu matrix; while the ferromagnetic precipitate could be identified with the more stable, body-centered cubic Fe structure. Hetherington and Reekie[8] studied the resistivity of cold-worked Cu-Fe alloys, and Hutchison and Reekie[9] studied the magnetization of Cu-Fe alloys to determine the solubility of Fe in Cu. More recently Cech and Turnbull[10] found that quenching to −196°C increased the magnetization of some aged Cu-Fe alloys, but only by a small fraction of the increase obtained by cold working.

* Received December 22, 1955

† This paper is based on studies begun at the Atomic Energy Research Department, North American Aviation, Downey, California, and completed at the General Electric Research Laboratory, Schenectady, New York. Present address: General Electric Research Laboratory.

In an effort to determine if Smith's suggestion regarding the precipitate structure was correct, the present study was undertaken. If the Fe precipitate can be assumed to be initially coherent with the Cu matrix, as Smith suggests, then it would appear that the homogeneous precipitation should proceed at a more rapid rate than heretofore indicated;[5] and that the kinetics previously observed were actually representing the growth of the ferromagnetic form of the precipitate indicated in part by the work of Hetherington and Reekie.[8] Moreover, Smith's suggestion regarding the precipitate structure might be directly determinable by X-ray diffraction analysis; in which case it becomes of significance to ask under what conditions the coherent precipitate would become unstable and transform.

While it has not been possible to provide definitive answers to these questions, it has been possible to provide additional evidence in support of the coherent precipitate and some information about its formation and stability.

2. SPECIMEN PREPARATION

The alloy specimens were prepared from Johnson-Matthey copper, more than 99.999% pure, and Johnson-Matthey iron, 99.997% pure. Finally divided iron chips were added to approximately 50 g of copper in a fused zircon crucible, after thoroughly cleaning the crucible and the metals. The crucible containing the metals was hung in a vertical vacuum furnace for melting and held at 1350°C for four hours under a pressure of 0.2 micron. The iron was observed to dissolve in the molten copper in approximately one hour. Stirring of the molten alloy was accomplished by maintaining a thermal gradient in the crucible, allowing the convection currents to provide mixing. Chemical analysis of the resulting ingot indicated a uniform composition throughout, and agreed with the weight analysis.

Specimen foils were prepared from the homogenized bulk material by cold rolling the alloy to 0.005-in. sheet. The individual specimens were die-cut to 0.395 by 0.089 in. from the sheet. Wire specimens were prepared by drawing a small piece of the ingot to 0.003-in. wire, followed by etching to remove the surface contamination.

3. EXPERIMENTAL METHODS

All specimens were solution-annealed *in vacuo* in a vertical furnace at 1060°C for two hours and quenched in iced brine. In order to determine the effectiveness of such a quench, six specimens were annealed and quenched in a modified Rosenhain apparatus.[11] The aging kinetics of these latter specimens were not found to be observably different than the kinetics of the specimens in small Vycor capsules. Therefore, in order to reduce the specimen-contamination to a minimum, all specimens were quenched in the small evacuated Vycor crucibles.

A modified Curie balance was employed to determine as accurately as possible the amount of ferromagnetic iron developed during a given specimen treatment. The Curie balance consisted of a Consolidated Engineering Corporation electromagnet which was fitted with wedge-shaped pole pieces, between which the specimen was hung from the pan of a microbalance. The vertical translational force on the ferromagnetic iron due to the field gradient, providing the iron is saturated, is given approximately by:

$$\bar{F} = mc\sigma \overline{\nabla} \mid \overline{H} \mid \qquad (1)$$

where $\bar{F}$ is the vertical force on the specimen, m is the mass, c is the concentration of the ferromagnetic phase, σ is the specific magnetization of the ferromagnetic phase, and $\overline{\nabla} \mid \overline{H} \mid$ is the field gradient. This relation and further considerations pertaining to the measurement are discussed in detail in the Appendix. The saturation magnetization of the specimens was determined from the force measurement accomplished with the Curie balance.

Hardness measurements were made with a Tukon hardness tester, using the 136° diamond braille and a 1.0-kg load. Diamond pyramid hardness was computed using the standard formula.

Cold working of the specimen foils was accomplished by compression in a large press. The specimens were mounted between etched copper foil, and the resulting sandwich pressed between two flat stellite blocks. Uniform reduction of 10% could be obtained in this manner.

4. PRECIPITATION KINETICS

It was found that no amount of thermal aging in the range 550°C to 800°C produced a ferromagnetic precipitate in a 2.4% Fe in Cu alloy. This result is in contradiction to the results previously reported.[4,5,6] The conclusion derived from this study regarding the ferromagnetic precipitate is that no thermal treatment below 800°C (even quenching into liquid helium) can transform the paramagnetic iron precipitate to the ferromagnetic form.

In order to determine the amount of transformed Fe precipitate by the saturation magnetization of the specimen, it was therefore necessary to cold-work and anneal the specimen. Accordingly, a 10% deformation was chosen, followed by a one-minute anneal at the

VOL. 4 1956

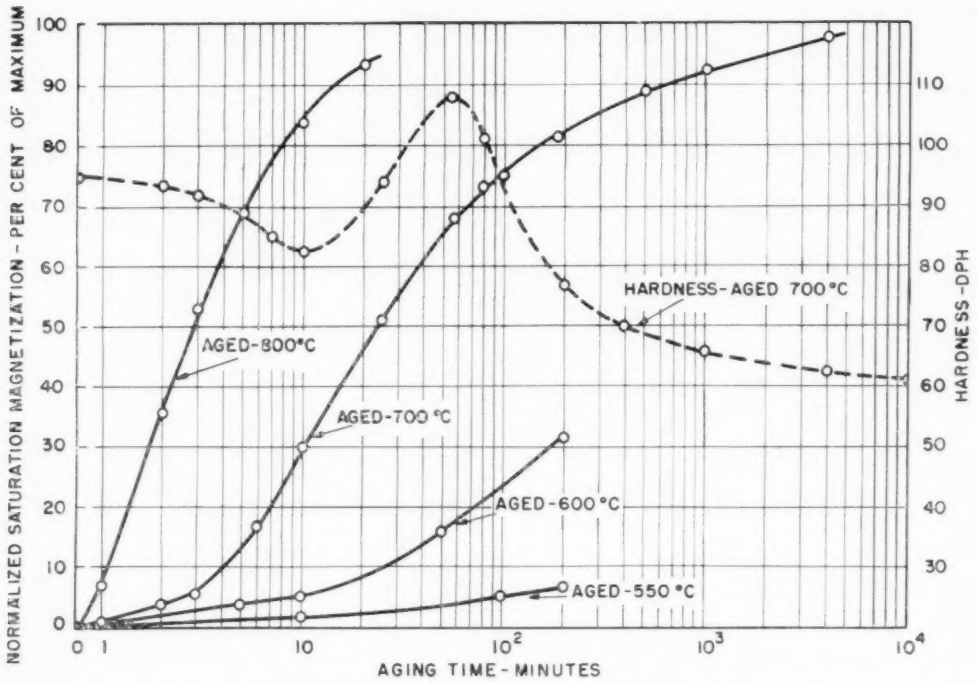
NORMALIZED SATURATION MAGNETIZATION - PER CENT OF MAXIMUM
HARDNESS - DPH
AGING TIME - MINUTES
HARDNESS - AGED 700 °C
AGED - 800 °C
AGED - 700 °C
AGED - 600 °C
AGED - 550 °C

FIG. 1. Precipitation kinetics of a Cu–2.4% Fe alloy. Saturation magnetization determined after aging, 10% deformation, and 1-min anneal at aging temperature (no anneal for 1-min aging).

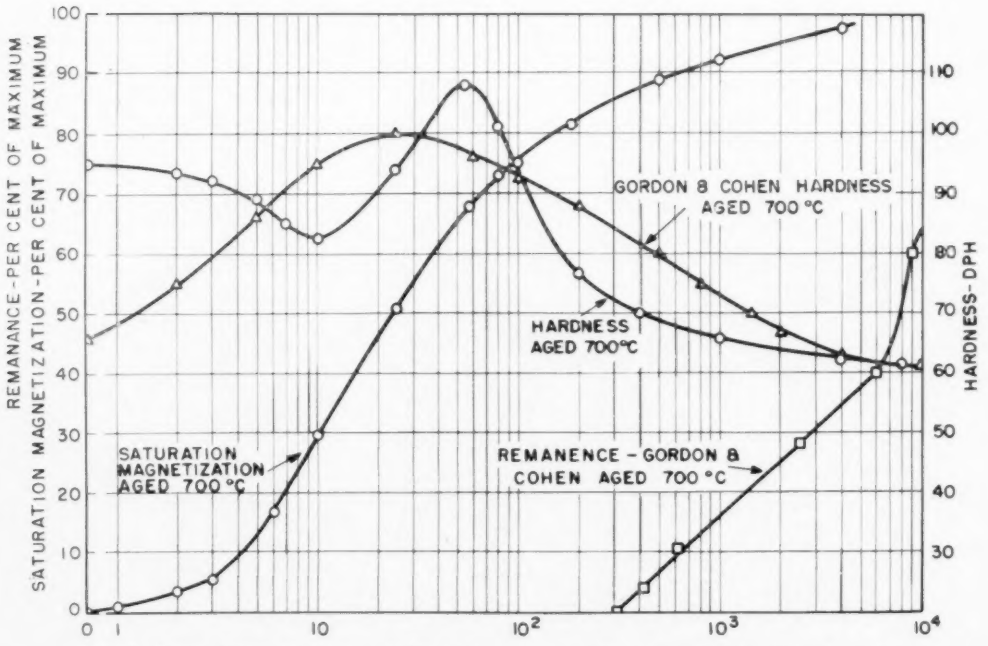
REMANANCE - PER CENT OF MAXIMUM
SATURATION MAGNETIZATION - PER CENT OF MAXIMUM
HARDNESS - DPH
GORDON & COHEN HARDNESS AGED 700 °C
HARDNESS AGED 700°C
SATURATION MAGNETIZATION AGED 700 °C
REMANENCE - GORDON & COHEN AGED 700 °C

FIG. 2. Precipitation kinetics at 700°C. Comparison of Gordon and Cohen[5] and results of this study.

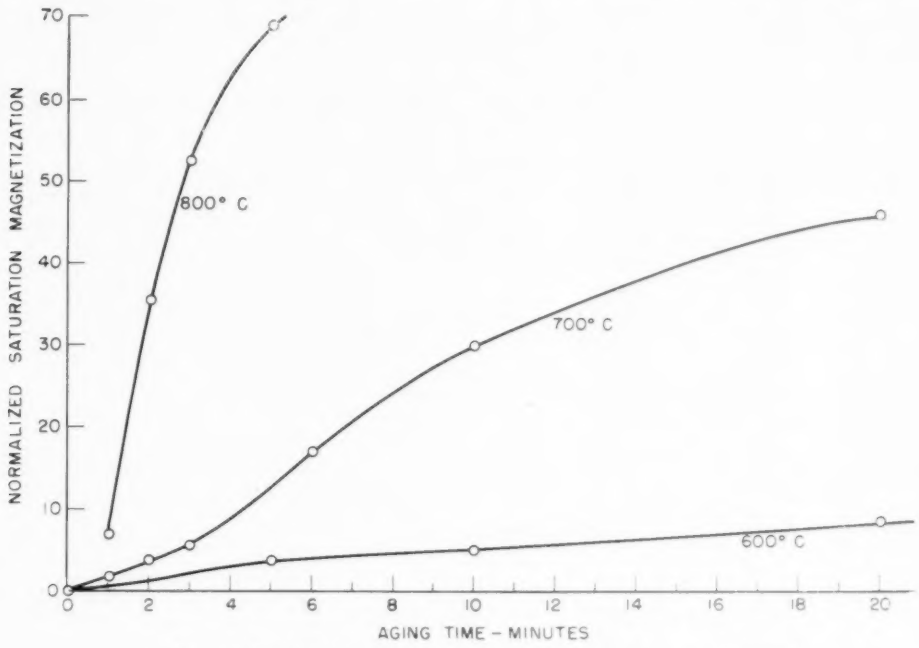

FIG. 3. Precipitation kinetics of Cu–2.4% Fe alloy, linear time-scale.

aging temperature (no anneal in the case of 1-minute aging). The aging kinetics determined in this manner (i.e. aging, cold working, and annealing) are shown in Fig. 1. It is to be noted that the aging kinetics obtained differ significantly from those reported by Gordon and Cohen[5] and Cech and Turnbull.[10] These are shown for an aging temperature of 700°C in Fig. 2. A possible explanation of the discrepancies will be discussed later.

The activation energy for the precipitate development, assuming a thermally activated growth process, may be calculated from Fig. 1. Both log time at constant per cent magnetization and log per cent magnetization at constant time are linear with reciprocal temperature and yield an activation energy of 1.65 ± 0.1 eV per atom. It appears reasonable to assume that 1.65 eV is the activation energy for the diffusion of Fe in the Cu matrix, since it is somewhat smaller than the activation energy for Cu self-diffusion (2.0 eV) as expected for the smaller Fe atom. Furthermore, the $t^{3/2}$ dependence of saturation magnetization on isothermal aging time, Fig. 3, for small aging time, is in agreement with the hypothesis of precipitate growth by diffusion of Fe. These considerations and the sigmoidal character of the curves of Fig. 3 indicate that the rate-limiting process in the precipitation is the diffusion of Fe in the Cu matrix. Presumably the precipitate nuclei are formed during the quench, or very rapidly in the aging process, in at most a few seconds. In view of a recent suggestion by Turnbull,[21] this rapidly terminating nucleation is not surprising, since the available dislocation sites for nucleation can quickly become "saturated" and other nucleation sites are not made available. Therefore, it is concluded that the isothermal-precipitate formation proceeds at a rate limited by the diffusion of iron to the nuclei, and which can be described in part with an activation energy of 1.65 eV.

Hardness measurements (DPH) made on specimens aged at 700°C, but not cold worked, are shown in Fig. 1. A comparison with the hardness measurements at 700°C of Gordon and Cohen is shown in Fig. 2. The hardness measurements of the present study are qualitatively explicable in terms of current theory. The initial hardness decrease, which occurs in the first 10 min at 700°C, can be attributed to a decrease in the strain hardening by the decrease of iron in supersaturated solid solution.[13] The hardness peak at one hour at 700°C and the following decrease are interpretable in terms of the Mott and Nabarro theory[14, 15, 16] of precipitation hardening.

5. PRECIPITATE STRUCTURE

Metallographic examination of some of the specimens aged at 700° showed a homogeneous plate-like precipitate which could be resolved after ten hours at 700°C (1500×), with a remarkably small amount of grain-boundary precipitate. As aging progressed, the precipitate coarsened, indicating preferential growth of the large precipitate particles at the expense of the

smaller ones. One specimen aged at 800°C for six months (2.64×10^5 min) developed a precipitate structure which had coarsened to the extent of resembling a Widmanstätten structure. The maximum platelet size in this specimen was estimated to be of the order of 10 microns in diameter.

Determination of the crystallographic structure of the precipitate and its relation to the parent lattice by X-ray diffraction techniques was not conclusively attained; however, further evidence in support of Smith's suggested structural relation[7] was obtained. Laue patterns of large crystals in the 0.005-in. foils showed sharp f.c.c. spots after quenching from 1060°C. After aging at 700°C for a few minutes, it was found that "streaks" had developed near the (111) and (200) Laue spots from these crystals. These streaks near the (111) and (200) grew in size and intensity (even though still quite faint) as aging progressed to a maximum intensity at approximately one hour at 700°C. Further aging at 700°C caused the streaks to decrease in intensity and finally disappear after approximately ten hours at 700°C. Continued aging, up to 1000 hours at 700°C, produced no further change in the Laue patterns.* No combination of thermal or mechanical treatment of the specimen foils was sufficient to develop additional Laue spots which could be taken as adequate evidence for the existence of another structure in addition to the f.c.c. parent lattice. Therefore, according to the Laue evidence, the precipitate initially forms coherently with the copper parent lattice as platelets on the {111} and {100}, perhaps simultaneously. Efforts to resolve the apparent lack of a unique habit plane for the platelet formation were not successful.

Some evidence for the determination of the structure of the transformed (ferromagnetic) precipitate was obtained using a 0.001-in. polycrystalline wire in a Debye-Scherrer camera. The results of this investigation are summarized in Table 1. Lattice parameters for the parent lattice were obtained by the method of least squares and Cohen's method.[17] Extension of the wire by 25% caused the appearance of very faint lines, which could be indexed as (110), (200), and (112) body-centered tetragonal lines. The lattice parameters for the b.c.t. lattice cell calculated on the basis of this indexing are $a_0 = 2.8$ Å, $c_0 = 3.1$ Å, $c/a = 1.1$. Annealing the wire at 700°C for one hour produced an increase in intensity of the body-centered lines and a small relative shift of the lines. The resulting parameter determination for a body-centered cubic structure yielded $a_0 = 2.86$ Å.

While the X-ray diffraction results are inadequate for the complete specification of the precipitate structure, the X-ray and kinetic evidence forms a basis for a suggested precipitate structure. Therefore, it is suggested that the Fe precipitate forms isothermally as coherent platelets on the parent (111) and (100) planes. These platelets grow at a rate limited by the thermal diffusion of Fe in parent solid solution, and never lose coherency with the parent lattice during growth. The Fe precipitate, however, can be made to lose coherency by cold working or by charged-particle irradiation[18]; whereupon the precipitate transforms to a ferromagnetic body-centered tetragonal structure with an axial ratio slightly greater than unity. The metastable Fe precipitate evidently transforms by a martensitic-type transformation, since the transformation is completed in less than 1 sec at temperatures as low as 80°K.

The Gordon and Cohen[5] and Cech and Turnbull[10] results can be explained on the basis of this suggested precipitate structure. The larger specimens used by Gordon and Cohen and by Cech and Turnbull cannot be quenched as rapidly as the 0.005-in. foil specimens; determined, in the limiting quench, by the thermal diffusivity and geometry of the alloy. The reduced cooling rate and the possibility of a higher impurity content, in at least one case[10] could conceivably

* Recent, more intensive, investigation of the precipitate structure in various copper-iron alloys by Laue methods by W. G. Martin and J. B. Newkirk at the General Electric Research Laboratory have further substantiated the findings herein reported.

TABLE 1. Summary of X-ray diffraction analysis of a Cu–2.4% Fe alloy

Treatment	Magnetic	Phase	Structure	Lattice parameter (Å)
quenched 1060°C, 6 hr,	Para-	Solid solution	f.c.c.	$a_0 = 3.6123$
aged 700°C, 24 hr.	Para-	Solid solution precipitate	f.c.c. f.c.c.	$a_0 = 3.6148$ $a_0 =$?
cold worked	Ferro-	Solid solution precipitate	f.c.c. b.c.t. (?)	$a_0 = 3.6148$ $c/a = 1.1 \pm 0.1$
annealed 700°C, 1 hr.	Ferro-	Solid solution precipitate	f.c.c. b.c.c.	$a_0 = 3.6152$ $a_0 = 2.86$

greatly increase the impurity contribution to the determination of precipitate structure. It is suggested that the previously reported results are due to the formation of noncoherent nuclei, perhaps impurities, which grew during subsequent aging. The interesting temperature effects observed by Cech and Turnbull do not appear to be completely explicable in terms of noncoherent nuclei, but may be due to impurities (principally C) which allow only a partial coherency between precipitate and the parent lattice. Thus the energy necessary to cause transformation of the precipitate could be reduced to the extent that quenching to 80°K would transform a fraction of the precipitate particles. None of the foil specimens of the present study exhibited a similar effect on quenching to temperatures as low as 4°K.

6. SUMMARY

The kinetics of the homogeneous isothermal precipitation of Fe from a supersaturated solid solution of Cu–2.4% Fe have been found to proceed as a diffusion-limited growth process characterized with an activation energy of 1.65 ± 0.1 eV. The paramagnetic Fe precipitate transforms to a ferromagnetic structure upon plastic deformation of the alloy, but cannot be transformed by any thermal treatment below 800°C. X-ray diffraction studies suggest that the paramagnetic Fe precipitate forms coherently with the parent Cu lattice on the {111} and {100} planes, transforming under plastic deformation to a ferromagnetic body-centered structure (probably tetragonal with $c/a \simeq 1.1$). The transformation of the metastable Fe precipitate occurs by an unknown martensitic mechanism in less than 1 sec at room temperature and below when initiated by plastic deformation.

7. ACKNOWLEDGMENTS

The writer is indebted to C. J. Meechan for assistance in specimen preparation, and to G. Collins for aid in some of the X-ray diffraction measurements. This paper is based, in part, on studies conducted for the Atomic Energy Commission.

Appendix

8. DETERMINATION OF THE AMOUNT OF FERROMAGNETIC PRECIPITATE

The saturation magnetization of the specimens was determined from the translational force due to a magnetic field gradient of 459.0 oersted/cm in a field of approximately 10 kilo-oersted. Providing the specimen is saturated, and homogeneously ferromagnetic, and in a medium of unit permeability, the force is:

$$\bar{F} = mc\sigma \overline{\nabla} \left| \overline{H} \right| , \tag{1}$$

where the symbols have been defined previously.

Equation (1), in this instance, must be corrected for the force due to the paramagnetic matrix surrounding the Fe-precipitate particles, the permeability of the matrix, and the effect of the size, geometry, and magnetic anisotropy of the Fe-precipitate particles.

The first two of these corrections are negligible in most cases: The permeability, μ, is related to the volume susceptibility, κ, by the relation:

$$\mu = 1 + 4\pi\kappa \tag{2}$$

Since κ is of the order of 10^{-5} e.m.u./cm^3 for the Cu matrix, the permeability is different from unity by of the order of 10^{-4}. The force due to the Cu matrix is given by:

$$\bar{F}_{\mathrm{Cu}} = m(1 - c)\chi \left| \overline{H} \right| \overline{\nabla} \left| \overline{H} \right| , \tag{3}$$

where χ is the gram susceptibility. Comparing equation (3) with equation (1), it is seen that for a fully developed precipitate ($c = 2.4$ at. per cent ferromagnetic Fe) the ratio of the forces due to the matrix and precipitate is $F_{\mathrm{Cu}}/F_{\mathrm{Fe}} \simeq 10^{-5}$. Thus the force due to the matrix is significant only in magnetization determinations involving less than 1% of the precipitate.

The effect of the precipitate size, shape, and anisotropy cannot be dispensed with so easily. Considering first the particle size, it can be shown[19, 20] that the particle magnetization at room temperature behaves as "superparamagnetic" for particles smaller than about 100 Å in diameter. The magnetization of particles smaller than 100 Å is temperature-dependent. From the observation that I_s for the cold-worked foils was not temperature-dependent between 80°K and 300°K, it may be concluded that the ferromagnetic particles are larger than 100 Å in diameter. (It is also probably not possible to transform these small particles to the body-centered structures.)

Body-centered cubic Fe particles larger than about 100 Å acquire approximately 0.9 of their total magnetization in a field of 10^4 oersted.[21] The exact value of the magnetization depends upon the particle shape, size, and distribution. The fractional magnetization calculated according to Stoner and Wohlfarth[21] was substantiated experimentally by determining the magnetization in a series of foils aged for six months at 800°C, followed by cold working and annealing. The amount of precipitated Fe was determined from the phase diagram, assuming the alloy had

VOL. 4 1956

reached equilibrium at 800°C. The ratio of the observed magnetization to the calculated total magnetization was 0.9. This fractional magnetization (0.9) was used in all determinations of the amount of precipitated Fe; however, an undetermined error is undoubtedly incurred with smaller particle sizes (~200 Å). This correction is important only for very short aging times (~1 min at 700°C) or small magnetizations, $I_s/I_{s\,\max} < 0.05$, and therefore may be neglected. In Fe the dependence of the coercive force on crystallographic direction amounts to a few hundred oersted, and therefore may be neglected in the present treatment.

The quantitative determination of the amount of precipitated Fe by magnetization measurements is therefore considered accurate within about 2% for magnetization ratios, $I_s/I_{s\,\max}$ above 0.10. For magnetization ratios below about 0.03 the data probably bear little relation to the amount of precipitated Fe, based on an estimate of the precipitate particle size.

REFERENCES

1. D. Hanson and G. W. Ford *J. Inst. Metals* **32,** 335 (1924).
2. G. Tammann and W. Olson *Z. anorg. chem.* **186,** 257 (1930).
3. G. Tammann *Z. Metallkunde* **22,** 365 (1930)
4. F. Bitter and A. R. Kaufmann *Phys. Rev.* **56,** 1044 (1939).
5. R. B. Gordon and M. Cohen Symposium, *Age Hardening of Metals* 161, American Society for Metals, Clevland (1940).
6. C. S. Smith *Phys. Rev.* **57,** 337 (1940)
7. C. S. Smith Discussion to paper by Gordon and Cohen, *ibid.* 186.
8. F. E. Hetherington and J. Reekie *J. Appl. Physics* **22,** 1293 (1951).
9. T. S. Hutchison and J. Reekie *Phys. Rev.* **83,** 854 (1951).
10. R. E. Cech and D. Turnbull *J. Metals,* 45, Jan. 1954.
11. A. Taylor *X-Ray Metallography* Wiley and Sons, Inc., N.Y., 141 (1949).
12. D. Turnbull *Imperfections,* A.S.M. Cleveland (1955).
13. A. H. Geisler Symposium, *Phase Transformations in Solids,* Wiley and Sons, Inc., N.Y., 476, 1951.
14. N. F. Mott and F. R. N. Nabarro *Proc. Phys. Soc.* **52,** 86 (1940); Report on Strength of Solids (London: Physical Society) **1,** (1948).
15. N. F. Mott *J. Inst. Metals* **72,** 367 (1946).
16. F. R. N. Nabarro *Proc. Phys. Soc.* **58,** 669 (1946).
17. M. U. Cohen *Rev. Sci. Instrum.* **6,** 68 (1935).
18. J. M. Denney *Phys. Rev.* **92,** 531 (1953).
19. L. Neel *Rev. Mod. Phys.* **25,** 293 (1953).
20. C. P. Bean Submitted to Journal of Applied Physics.
21. E. C. Stoner and E. P. Wohlfarth *Phil. Trans.* **240A,** 599 (1948).

VOL
4
195

THE INFLUENCE OF TEMPERATURE ON PRE-YIELD PLASTIC AND ANELASTIC MICROSTRAIN IN LOW-CARBON STEEL*

J. A. HENDRICKSON, D. S. WOOD, and D. S. CLARK†

Pre-yield plastic and anelastic microstrains in an annealed low-carbon steel have been measured as a function of time under rapidly applied constant tensile stress at temperatures of −23°F (−31°C), +76°F (+24°C), and +150°F (+66°C). The rates of pre-yield microstrain when stress is first applied are compared with the theoretical rates for the thermally activated release of dislocations from atmospheres of interstitial solute atoms. This comparison indicates limited agreement with theory in that the apparent activation energy for dislocation release is inversely proportional to the applied stress, as predicted by Fisher. However, the results obtained at +150°F (+66°C) do not correlate with those obtained at the two lower temperatures in the manner predicted. Also, the magnitudes of the activation energies required to fit the experimental measurements are almost two orders of magnitude lower than those predicted by previous dislocation theory. A modification of existing theory which might account for these discrepancies is discussed qualitatively.

The total amounts of pre-yield microstrain observed at +150°F (+66°C) are found to be several times larger than those at the two lower temperatures. This result also indicates that some modification of existing theories is required.

L'INFLUENCE DE LA TEMPÉRATURE SUR DES MICRODÉFORMATIONS "PRE-YIELD" PLASTIQUES ET NON ÉLASTIQUES D'UN ACIER A BAS CARBONE

Sur un acier revenu à bas carbone, les microdéformations "pre-yield" plastiques et non élastiques ont été mesurées en fonction du temps, sous des tensions de traction constantes, appliquées rapidement à des températures de −23°F (−31°C), +76°F (+24°C) et 150°F (+66°C).

Les vitesses de la microdéformation "pre-yield" quand la tension est initialement appliquée, sont comparées aux vitesses théoriques de la libération des dislocations, due à l'activation thermique à partir des atmosphères d'atomes interstitiels en solution.

Cette comparaison indique un accord limité avec la théorie en ce que l'énergie d'activation apparente pour la libération des dislocations est inversement proportionnelle à la tension appliquée, comme Fisher le prévoit; cependant les résultats obtenus à +150°F (+66°C) ne sont pas en accord avec ceux obtenus aux deux températures inférieures. D'autre part, les grandeurs des énergies d'activation nécessaires pour expliquer les mesures expérimentales sont à peu prés de deux ordres de grandeurs inférieures à celles prévues par la théorie des dislocations.

Une modification de la théorie existante qui pourrait tenir compte de ces différences est discutée qualitativement.

Les grandeurs totales des microdéformations "pre-yield" observées à +150°F (+66°C) sont trouvées plusieurs fois supérieures à celles obtenues aux deux températures inférieures. Ce résultat indique également qu'une modification des théories existantes est nécessaire.

DER EINFLUSS DER TEMPERATUR AUF DIE AUSGIEBIGEM FLIESSEN VORHERGEHENDE PLASTISCHE UND ANELASTISCHE MIKRODEHNUNG IN KOHLENSTOFFARMEM STAHL

An einem ausgeglühten Stahl mit niedrigem Kohlenstoffgehalt wurden unter konstanter, rasch aufgebrachter Zugspannung die vor dem ausgiebigen plastischen Fliessen auftretenden plastischen und anelastischen Mikrodehnungen bei den Temperaturen −31°C, +24°C und +66°C in Abhängigkeit von der Zeit gemessen. Die Geschwindigkeiten des Mikrofliessens beim ersten Aufbringen der Belastung werden verglichen mit den theoretischen Geschwindigkeiten für das thermisch aktivierte Losreissen der Versetzungen von Wolken aus gelösten Zwischengitter-Atomen. Dieser Vergleich lässt insofern in begrenztem Umfang eine Übereinstimmung mit der Theorie erkennen, als die sich für das Losreissen der Versetzungen ergebende Aktivierungsenergie entsprechend der Voraussage von Fisher umgekehrt proportional zur angelegten Spannung ist. Hingegen stehen die bei +66°C gewonnenen Ergebnisse nicht in der vorhergesehenen Weise mit den Messungen bei den beiden tieferen Temperaturen im Einklang. Ausserdem sind die zur Befriedigung experimentellen Messungen erforderlichen Werte der Aktivierungsenergie fast um zwei Grossenordnungen kleiner als die bisherigen versetzungstheoretischen Voraussagen. Eine Modifizierung der vorhandenen Theorie, die die aufgetretenen Diskrepanzen erklären kann, wird qualitativ diskutiert.

Die beobachteten Gesamtdehnungen des Mikroffliessens sind bei +66°C um ein Mehrfaches grösser als bei den zwei niedrigeren Temperaturen. Auch dieses Ergebnis weist auf die Notwendigkeit, die bisherige Theorie zu modifizieren, hin.

INTRODUCTION

The initiation of discontinuous yielding in metals which exhibit distinct yield points in their stress-strain relations is known to be preceded by small plastic and anelastic strain. The maximum value of this strain may be only a few per cent of the elastic strain at the upper yield point in the case of annealed low-carbon steels. Plastic and anelastic strain of

* Received January 16, 1956.

† California Institute of Technology, Pasadena, California.

VOL. 4 1956

the order of 10^{-6} in./in. may be detected at stresses of about one-half the upper yield stress by employing techniques for strain measurement of high sensitivity. Such strain has been studied by Roberts, Carruthers, and Averbach,[1] who employed resistance-sensitive wire strain gages to detect residual strain in plain carbon steels subjected to cycles of loading and unloading in tension. They found that the amount of this plastic microstrain increased with increasing applied stress.

Pre-yield plastic and anelastic microstrain in annealed low-carbon steel has been investigated as a function of time at room temperature under conditions of rapidly applied constant tensile stress by Vreeland, Wood, and Clark.[2, 3] This work shows that such strain takes place at relatively low rates (10^{-6} to 10^{-3} in./in./sec) during the delay time for the initiation of discontinuous yielding. The much larger strain associated with discontinuous yielding is found to begin after a total pre-yield microplastic strain of about 30×10^{-6} in./in. The pre-yield microstrain is clearly distinguished from the yield strain in tests at constant tensile stress exceeding the static upper yield stress by a marked increase in rate of extension of the specimen when discontinuous yielding begins. The pre-yield microstrain that occurs when the applied tensile stress is below the static upper yield stress is less than at stresses above the upper yield stress. The total equilibrium plastic microstrain for an annealed plain carbon steel of 0.12% carbon, having a static upper yield stress of 42,000 lb./in.^{2}, varies from about 3×10^{-6} in./in. at a stress of 25,000 lb./in.^{2} to about 30×10^{-6} in./in. at the upper yield stress.

Pre-yield plastic and anelastic microstrain has also been observed in ductile molybdenum[4] subjected to rapidly applied constant tensile stresses. A distinct yield point in the stress-strain relation and the phenomenon of delayed yielding in this material is very similar to that found in annealed low-carbon steel.

Vreeland, Wood, and Clark,[2, 3] have attributed these pre-yield plastic and anelastic microstrains to the generation of dislocation loops at Frank-Read sources.[5] The rate of such generation, and hence the microstrain rate, may be governed by the thermally activated release of the source dislocation from an "atmosphere" of interstitial solute atoms as proposed by Cottrell and Bilby.[6] The latter authors developed a relationship for the thermal activation energy as a function of the stress tending to release the dislocation. More recently, Fisher[7] has proposed an approximate relation based upon a considerably simpler derivation. Fisher's result is that the activation energy for the release of a dislocation from a Cottrell "atmosphere" is inversely proportional to the stress tending to move the dislocation.

The purpose of the present paper is to present the results of experimental measurements of the pre-yield plastic and anelastic microstrain in annealed low-carbon steel as a function of applied stress and temperature. The rates of pre-yield microstrain are compared with the rates predicted on the basis of thermally activated release of dislocations from "atmospheres."

MATERIAL AND TEST SPECIMENS

The material and the form of test specimens used in this investigation are the same as those employed for the previous studies,[2, 3] of pre-yield microstrain. The material is of the following analysis:

Carbon	0.12%
Manganese	0.43%
Phosphorus	0.019%
Sulfur	0.042%
Silicon	0.27%
Copper	0.23%
Tin	0.037%

The specimens have a thin flat gage section of $\frac{1}{2}$ in. $\times$ 0.100 in. and $\frac{1}{2}$ in. long. The heat treatment consisted of annealing at a temperature of 1680°F (915°C) for $2\frac{1}{2}$ hr in dry hydrogen, followed by a homogenizing treatment at 1300°F (704°C) for 22 hr. It has been shown[2] that there is essentially no change in the carbon content of the specimens during these treatments. Previous investigation[2] has shown that this material has an ASTM grain size of 6.7 and a Rockwell-B hardness of 54. Also, static tensile tests at +73°F (+23°C) showed that the upper yield stress is 42,000 lb /in.^{2} and the lower yield stress is 29,000 lb /in.^{2}

EQUIPMENT AND TEST PROCEDURE

The tests in this investigation were made by rapidly but smoothly applying a tensile load to the specimen within a period of about 10 msec, after which the load remained substantially constant. This was accomplished by means of a rapid load-testing machine of special design which has been described previously.[8]

The plastic and anelastic microstrain was determined by essentially the method described in a previous paper.[2] This method employs a strain-bar having a gage-section area almost the same as that of the specimen to which it is connected in series. The strain-bar is made of SAE-4130 steel, heat-treated to provide an elastic limit, sufficiently high so that it remains

elastic under the loads applied in this investigation. Two type A-7, SR-4 wire strain gages are bonded to the gage section of the strain-bar and electrically connected to the two type A-7 gages bonded to the specimen in such a way that the elastic strain of the strain-bar subtracts from the total strain of the specimen. This arrangement permits the use of the maximum sensitivity of the recording system without exceeding the total strain-recording capacity of the system.

The load acting on the specimen was measured by means of a dynamometer, described previously,[2] employing type AB-14, SR-4 wire strain gages. The load and microstrain were determined as functions of time during each test by recording the amplified signals of the dynamometer and strain gages with a suitable galvanometer-type oscillograph. The sensitivity of this system is such that the strain resolution is 10^{-6} in./in. or less. The load on the specimen was determined within an overall accuracy of 4%. The time resolution of the measurements depended upon the recording-paper speed employed. The latter was varied to suit the expected microstrain rates. At the highest recording rate employed, the time resolution is about 1 msec.

Several tests were performed to determine as nearly as possible whether or not the strain produced in the strain-bar by rapid load applications was truly elastic. This question is important, since any appreciable plastic and/or anelastic microstrain in the strain-bar would cause an apparent indication of less microstrain in the test specimen than the true value.

This check was made by performing rapid load tests in which the strain in the strain-bar alone and the signal from the dynamometer were recorded with the amplifiers set for maximum sensitivity. These sensitivity settings are such that a one-inch trace deflection corresponds to approximately 50×10^{-6} in./in. strain in the strain-bar and approximately 140-lb load. The records can be measured readily to within 0.02 in. or better. The loads used for these tests were in the range employed for the investigation of pre-yield strain, i.e. of the order of 1000 lb. The trace deflections from no-load to full load in such tests would be much more than the 4 in. maximum allowable trace deflection for the recording equipment. Therefore, the balancing controls of the amplifiers were set before the tests so that the signals were biased off the record by such an amount that when load was applied the traces would come onto the record. In this manner, plastic and anelastic microstrain which might occur in the strain-bar after the load had been applied could be investigated with the same high sensitivity as that employed in the pre-yield strain tests.

The recording system itself was checked under operating conditions of the above type by applying purely electrical input signals of the same magnitude as those encountered in the investigation of the strain-bar. This showed that the recording system itself does not introduce any detectable error when subjected to such large initial off-balance signals.

The rapid loading tests on the strain-bar showed that the ratio of the signal produced by the SR-4 gages on the strain-bar to the signal produced by the SR-4 gages on the dynamometer is constant with respect to time at load within the accuracy to which the record traces can be measured. The signals themselves are not constant with respect to time, because the rapid load-testing machine employed does not maintain an exactly constant load.

The results of these tests could mean that the dynamometer and strain-bar exhibit exactly equal plastic and/or anelastic microstrain effects. However, this seems very improbable for three reasons. First, the cross-sectional area of that portion of the dynamometer to which the SR-4 gages are cemented is twice the corresponding section of the strain-bar, so that the stress in the dynamometer is one-half the stress in the strain-bar. Second, the dynamometer and the strain-bar are made of the same steel (SAE-4130) but with different quench and temper treatments such that the hardness of the dynamometer and strain-bar are 40 Rc and 34 Rc respectively. Third, both dynamometer and strain-bar are subjected to stresses of less than one-half their yield stress. Therefore, as a result of these check tests, it is concluded that a plastic and/or anelastic microstrain greater than 10^{-6} in./in. is not produced in the strain-bar for loads in the range employed in this investigation.

The gage-section area of the strain-bar was deliberately made slightly smaller than the nominal gage-section area of the specimen so that the elastic strain of the strain-bar would always be slightly larger than the elastic strain of the specimen. The onset of microstrain in the specimen then caused a deflection of the strain trace on the test record in an opposite direction to that caused by the original elastic off-balance between the strain-bar and specimen. The inflection point caused by this change in direction of the strain trace is assumed to be time $t = 0$, i.e. it is assumed that a negligible amount of microstrain has occurred in the specimen up to this time. The microstrain, at any given time, is found

VOL. 4 1956

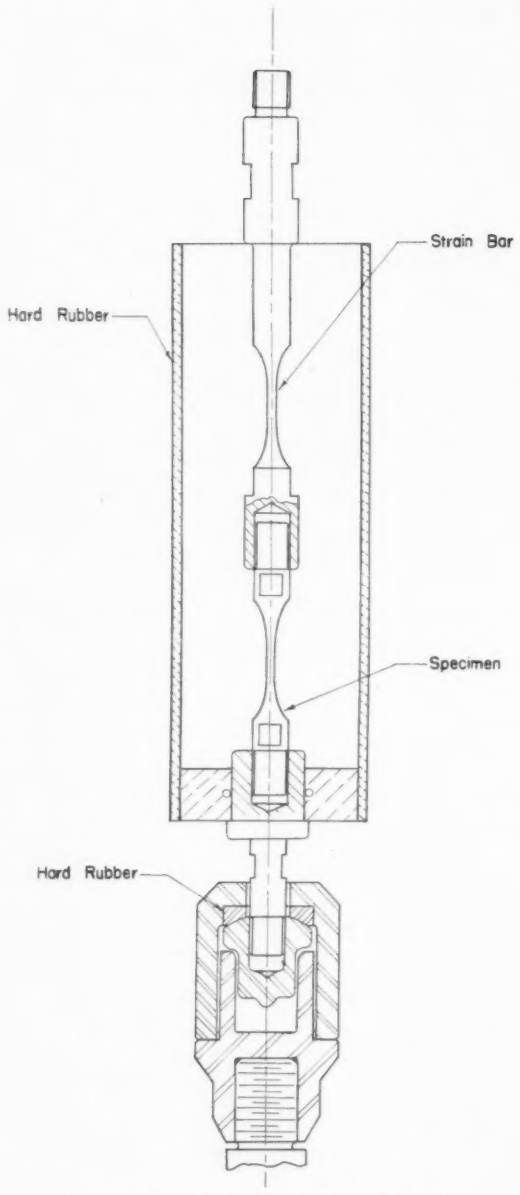

FIG. 1. Assembly of specimen, grips, and container for thermostatic bath.

by determining the relative deflection of the strain trace, at that time, from this inflection point. A correction was applied to the measured microstrain to account for small changes in the elastic off-balance strain associated with small load changes which are produced by the rapid load-testing machine.

Tests for the determination of pre-yield microstrain were conducted at temperatures of −23°F(−31°C), +76°F (24°C), and +150°F (66°C). The initial plans also included tests at −100°F (−74°C). However, reliable measurements of pre-yield microstrain could not be obtained at this temperature due to failure of the strain-gage bonding cement (Duco). The tests at temperatures of −23°F and +150°F were made while the specimen and strain-bar were immersed in suitable thermostatic baths. The bath was held in a hard rubber container around the specimen while attached to the grips of the machine. This container is shown in the assembly drawing given in Fig. 1, which also shows the insulated specimen grips and the strain-bar. The tests at 76°F were conducted without a thermostatic bath.

The temperature of the specimens was determined by means of copper-constantan thermocouples held in contact with the specimen gage-length by "Scotch" electrical tape. The output of the thermocouples was measured with a Leeds and Northrup portable precision potentiometer. Temperatures were determined to about ±1°F, and variations during a test and from test to test were within a range of variation of ±2°F.

EXPERIMENTAL RESULTS

A typical test record is shown in Fig. 2. This record for a test at +76°F (+24°C), indicates the initial elastic off-balance strain between the specimen and strain-bar, and shows the general manner in which the pre-yield microstrain varies with time at nearly constant stress. The pre-yield plastic and anelastic microstrain is shown as a function of time for various stress levels in Figs. 3, 4, and 5 at temperatures of −23°F (−31°C), +76°F (+24°C), and +150°F (+66°C) respectively. The significant test results are given in Table 1 for each test stress and temperature employed. The equilibrium microstrain is given for tests at stresses below the static upper yield stress. This is the total microstrain reached after a relatively long time at load when the microstrain rate has dropped to zero. The pre-yield microstrain is given for tests at stresses above the static upper yield stress. The latter values of microstrain are taken at the points of minimum slope of the microstrain vs. time curves. The delay-time for yielding is given for those tests in which yielding occurred. The values of the initial microstrain rates (slopes of the microstrain vs. time curves at time zero) are also given in the table. These rates may be in error by as much as 50% in some cases, due to the very small changes of strain which occur during the initial period of approximately constant strain rate. This error tends to be greatest for values obtained at relatively low stresses where the total plastic and anelastic microstrain is the least. The errors in initial microstrain rates for tests at the higher stress levels are probably considerably less than 50%. Similar results taken from the records

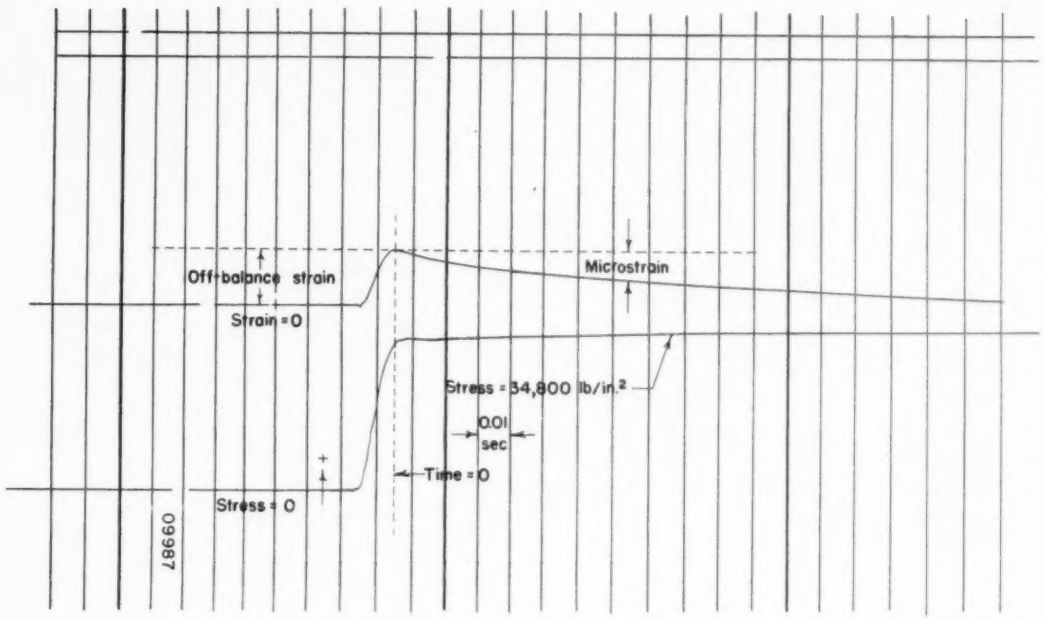

FIG. 2. Typical test record.

VOL. 4 1956

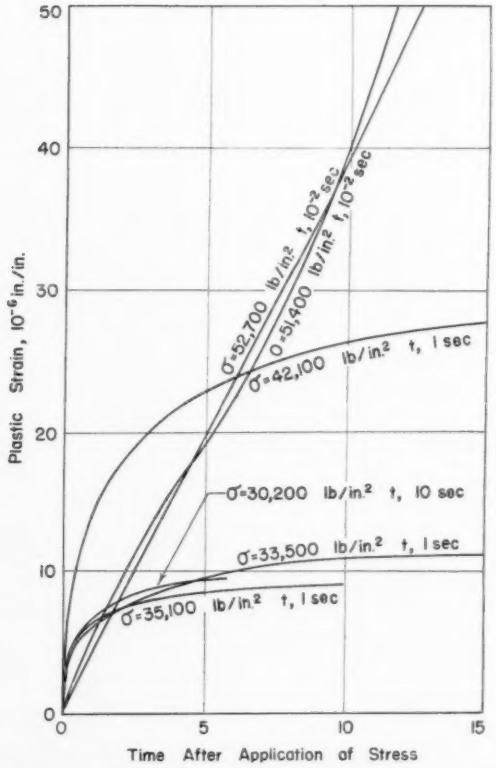
Plastic Strain, 10⁻⁶ in./in.
Time After Application of Stress
σ=52,700 lb/in.² t, 10⁻² sec
σ=51,400 lb/in.² t, 10⁻² sec
σ=42,100 lb/in.² t, 1 sec
σ=30,200 lb/in.² t, 10 sec
σ=33,500 lb/in.² t, 1 sec
σ=35,100 lb/in.² t, 1 sec

FIG. 3. Pre-yield plastic and anelastic microstrain vs. time at $-23°F$ ($-31°C$); σ and t values give the constant test-stress and time-scale multiplying factor respectively for each curve.

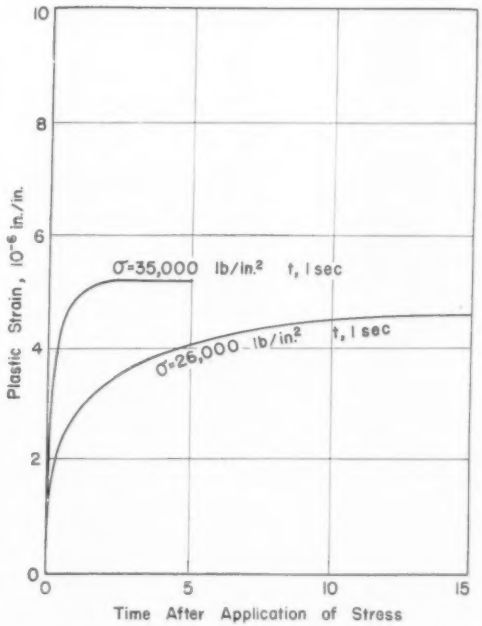

FIG. 4. Pre-yield plastic and anelastic microstrain vs. time at $+76°F$ ($+24°C$); σ and t values give the constant test-stress and time-scale multiplying factor respectively for each curve.

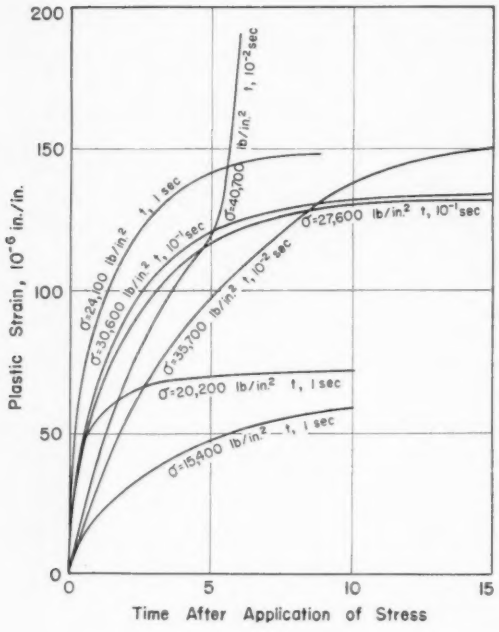
Plastic Strain, 10^{-6} in./in.
Time After Application of Stress
σ=24,100 lb/in.² t, 1 sec
σ=30,600 lb/in.² t, 10^{-1} sec
σ=40,700 lb/in.² t, 10^{-2} sec
σ=27,600 lb/in.² t, 10^{-1} sec
σ=35,700 lb/in.² t, 10^{-2} sec
σ=20,200 lb/in.² t, 1 sec
σ=15,400 lb/in.² t, 1 sec

FIG. 5. Pre-yield plastic and anelastic microstrain vs. time at +150°F (+66°C); σ and t values give the constant test-stress and time-scale multiplying factor respectively for each curve.

of tests made at +73°F (+23°C) in previous investigations [2, 3] are presented in Table 2.

DISCUSSION

Fisher[7] has proposed that the thermal activation energy W^* required for the release of a dislocation from an "atmosphere" of solute atoms is given by

$$W^* = \gamma_0^2 f(\gamma/\gamma_0)/b\tau \qquad (1)$$

where γ_0 is the energy per unit length of a dislocation which is free from absorbed solute atoms, γ is the energy in the presence of an "atmosphere," b is the magnitude of the Burgers vector, τ is the resolved shear stress acting on the dislocation, and

$$f(\gamma/\gamma_0) = \text{arc cos } \gamma/\gamma_0 - \gamma/\gamma_0 [1 - (\gamma/\gamma_0)^2]^{1/2} \qquad (2)$$
$$\approx 4\sqrt{2}/3 [1 - \gamma/\gamma_0]^{3/2} \quad \text{for} \quad \gamma/\gamma_0 = 1$$

TABLE 1. Results of measurements of pre-yield plastic and anelastic microstrain

Spec. No.	Temperature	Stress (10^3 lb/in.^{2})	Equilibrium microstrain (10^{-6} in./in.)	Pre-yield microstrain (10^{-6} in./in.)	Delay time (sec)	Initial microstrain rate (in./in./sec)
84	−23°F (−31°C)	30.2	9.5	—	No yield	4.5×10^{-6}
74	−23°F (−31°C)	33.5	11.2	—	No yield	8.0×10^{-6}
98	−23°F (−31°C)	35.1	9.0	—	No yield	1.8×10^{-5}
86	−23°F (−31°C)	42.1	28.0	—	No yield	1.0×10^{-4}
75	−23°F (−31°C)	51.4	—	20.0	0.16	5.3×10^{-4}
77	−23°F (−31°C)	52.2	—	45.0	0.17	4.6×10^{-4}
71	−23°F (−31°C)	52.7	—	40.0	0.20	3.9×10^{-4}
85	−23°F (−31°C)	63.4	—	—	0.015	3.3×10^{-3}
87	+76°F (+24°C)	26.0	4.65	—	No yield	5.6×10^{-6}
97	+76°F (+24°C)	29.8	3.30	—	No yield	1.4×10^{-5}
96	+76°F (+24°C)	35.0	5.20	—	No yield	6.5×10^{-5}
72	+76°F (+24°C)	40.5	19.0	—	No yield	3.8×10^{-4}
60	+76°F (+24°C)	49.6	—	—	0.014	2.1×10^{-3}
83	+150°F (+66°C)	15.4	60	—	No yield	4.3×10^{-5}
89	+150°F (+66°C)	20.2	72	—	No yield	2.0×10^{-4}
80	+150°F (+66°C)	24.1	148	—	No yield	2.4×10^{-4}
92	+150°F (+66°C)	27.6	132	—	No yield	1.2×10^{-3}
91	+150°F (+66°C)	30.6	134	—	No yield	1.2×10^{-3}
93	+150°F (+66°C)	34.8	—	—	No yield	1.5×10^{-3}
79	+150°F (+66°C)	35.7	158	—	No yield	2.8×10^{-3}
90	+150°F (+66°C)	40.7	—	120	0.05	3.8×10^{-3}

TABLE 2. Results of previous measurements of pre-yield plastic and anelastic microstrain[2, 3]

Spec. No.	Temperature	Stress (10^3 lb/in.^{2})	Equilibrium microstrain (10^{-6} in./in.)	Pre-yield microstrain (10^{-6} in./in.)	Delay time (sec)	Initial microstrain rate (in./in./sec)
19	+73°F (+23°C)	25.0	3.0	—	No yield	5.1×10^{-6}
18	+73°F (+23°C)	29.0	4.0	—	No yield	1.8×10^{-5}
20	+73°F (+23°C)	31.5	6.0	—	No yield	5.0×10^{-5}
21	+73°F (+23°C)	35.5	10.0	—	No yield	1.2×10^{-4}
17	+73°F (+23°C)	38.5	13.0	—	No yield	1.7×10^{-4}
16	+73°F (+23°C)	41.0	24.0	—	No yield	1.6×10^{-4}

The number of dislocations released per unit time, $\dot{n}$, is given by

$$\dot{n} \propto \exp[-W^*/kT] \tag{3}$$

where k is Boltzmann's constant, and T is the absolute temperature.

Assuming that the observed pre-yield plastic and anelastic microstrain is due to dislocations released from Cottrell atmospheres, the microstrain rate should be proportional to $\dot{n}$. The value of the resolved shear stress to be used in equation (1) is taken to be one-half the applied tensile stress, σ, when load is first applied. However, after some pre-yield microstrain has taken place, this may be an incorrect value because of back stresses caused by dislocations previously released and held up at obstacles such as grain boundaries. Under a constant applied stress the local resolved shear stress acting on the dislocations still to be released from atmospheres may decrease as the microstrain increases. This would then result in an increase of the activation energy, W^*, and, hence, a decrease in the microstrain rate as the total amount of microstrain increases during a given test. Just such behaviour is often observed experimentally, as may be seen in Figs. 3, 4, and 5.

Thus the initial pre-yield microstrain rate (the rate when load is first applied) may be related directly to the applied stress, while the microstrain rates at later times may not. Therefore, the initial microstrain rate, $\dot{\varepsilon}_{\mu_0}$, which is proportional to $\dot{n}$, may be expressed by the relation

$$\dot{\varepsilon}_{\mu_0} = C \exp[-2\gamma_0^2 f(\gamma/\gamma_0)/\sigma bkT], \tag{4}$$

or in the more convenient form

$$\ln \dot{\varepsilon}_{\mu_0} = C' - 2(\gamma_0^2/bk) f(\gamma/\gamma_0)(1/\sigma T), \tag{5}$$

where C and C' are undetermined constants.

Thus, according to equation (5), the dependence of the initial microstrain rate upon applied stress and temperature is contained entirely in the term $(1/\sigma T)$. Actually, the quantities γ_0 and γ depend slightly upon temperature through the temperature dependence of the shear modulus, as Fisher[7] has indicated. However, over the temperature range of the experiments reported here, this effect is negligible compared with experimental uncertainties.

The experimental results are compared with equation (5) in Fig. 6, in which the initial microstrain rate is plotted on a logarithmic scale as a function of the quantity $(1/\sigma T)$. The experimental points obtained at room temperatures and at $-23°$F ($-31°$C) lie on the same straight line, within experimental accuracy, in agreement with the form of equation (5). However, the results obtained at $+150°$F ($+66°$C) lie on a distinctly separate straight

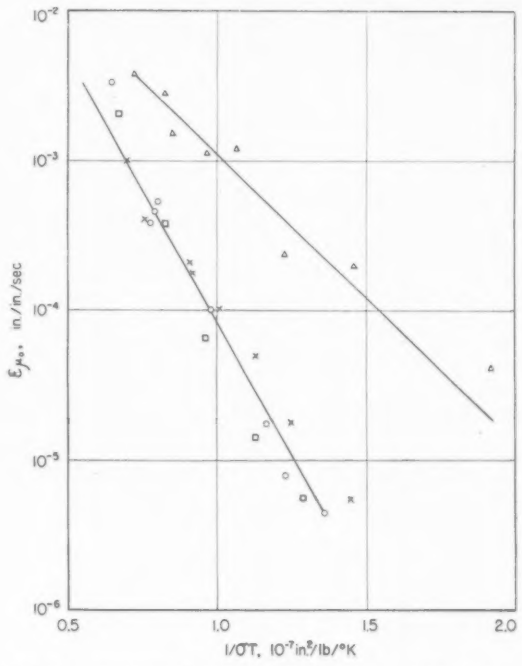

FIG. 6. Initial pre-yield microstrain rate, $\dot{\varepsilon}_{\mu_0}$, vs. reciprocal of the product of stress and temperature, $1/\sigma T$ for annealed 0.12% carbon steel.
○ $-23°$F (243°K) □ $+76°$F (298°K)
× $+73°$F (296°K) △ $+150°$F (339°K)

line. Thus, equation (5) describes the stress dependence of the initial microstrain rate correctly and the temperature dependence in the range from room temperature down to at least $-23°$F ($-31°$C). However, it fails to describe the temperature dependence properly in the range above room temperature.

The experimental results obtained at $+150°$F ($+66°$C) exhibit another distinct difference from the results obtained at lower temperatures. Namely, the total amount of pre-yield plastic and anelastic microstrain at any given stress level is much greater at $+150°$F ($+66°$C) than at room temperature and below. This may be seen in the values for equilibrium microstrain and pre-yield microstrain given in Table 1 and also by comparing the curves of microstrain vs. time given in Fig. 5 with those given in Figs. 3 and 4. On the other hand, the total amounts of pre-yield microstrain are about the same at the two lower temperatures for a given stress level.

This contrast between the results obtained at a temperature of $+150°$F ($+66°$C) and those obtained at room temperature and below is in disagreement with a dislocation theory previously proposed[3] to account for the total equilibrium plastic and anelastic microstrain. According to this theory, the total amount of pre-yield microstrain should only depend upon the

VOL. 4 1956

TABLE 3. Values of the binding energy ratio $(1 - \gamma/\gamma_0)$

Temperature	$(1 - \gamma/\gamma_0)$
−23°F (−31°C) +73°F (+23°C) +76°F (+24°C)	0.0018
+150°F (+66°C)	0.0012

applied stress and not upon temperature. (This assumes that the variation of the shear modulus with temperature is negligible as discussed previously.) Thus, the results obtained in the present investigation at −23°F (−31°C) and +76°F (+24°C) are in agreement with the previous theory, while those obtained at +150°F (+66°C) are not.

The present experimental results may be compared with dislocation theory in another respect by considering the slopes of the lines representing the data in Fig. 6. According to equation (5), these slopes are given by

$$S = -2(\gamma_0^2/bk)\, f(\gamma/\gamma_0). \tag{6}$$

The dislocation energy γ_0 in equation (6) is estimated by dislocation theory to be

$$\gamma_0 \approx Gb^2/2 \tag{7}$$

Thus all quantities in equation (6) are known except γ, the energy per unit length of a dislocation with a Cottrell atmosphere. Hence, equation (6) may be employed to calculate the numerical values of γ using the experimental values of S. For purposes of comparison with results obtained by Fisher,[7] values of the quantity $(1 - \gamma/\gamma_0)$ have been computed instead of γ itself. The results of these calculations are given in Table 3. Fisher[7] obtained the value $(1 - \gamma/\gamma_0) = 0.00373$ by comparing his theory with measurements of the delay time for yielding[9] in annealed specimens of the same steel as that employed in the present investigation. He also obtained an identical value from delay-time measurements[10] made on another annealed low-carbon steel.

This quantity, $(1 - \gamma/\gamma_0)$, is the ratio of the binding energy of a dislocation with an atmosphere to the total energy of a dislocation without an atmosphere. Cottrell[11] estimates the binding energy to be about 0.5 eV per atomic distance along the dislocation. The total energy of a dislocation without an atmosphere is generally estimated[12] to be of the order of 5 eV. Therefore, according to dislocation theory, the binding energy ratio should be

$$(1 - \gamma/\gamma_0) \approx 0.1$$

Thus, the values obtained as a result of the present investigation as well as those obtained by Fisher are significantly lower than the theoretical estimates.

A tentative explanation for this discrepancy in the binding energy is as follows. Cottrell and Bilby's[6] estimate is based upon the assumption that for every atomic length along the dislocation an interstitial solute atom occupies the position of maximum binding energy (directly below the center of the dislocation if it is an edge type). However, if the dislocation line does not happen to lie along certain special crystallographic directions in the slip plane, this condition may not be possible, because the solute atoms can occupy only certain interstitial sites in the lattice. Therefore, the distances of the interstitial atoms from the position of maximum binding energy (as determined from elasticity theory for a continuous medium) may vary from zero to about one-half the lattice parameter on either side of the dislocation. Thus, when the material is subjected to a stress which tends to move the dislocation, some of the solute atoms aid the first portion of the motion, while others oppose it. Also, the binding energy of a solute atom decreases rapidly as the distance of the atom from the position of maximum binding energy changes by amounts of the order of the lattice parameter. For these reasons it appears that the thermal activation energy required for the release of some of the dislocations from their atmospheres may be considerably less (at a given stress) than the value computed by Cottrell and Bilby.[6] A quantitative theory to account for these effects has not been formulated.

The above explanation of the low experimental values of activation energy for release of dislocations from atmospheres of solute atoms does not conflict with the fact that Harper's[13] measurements of the time for precipitation of carbon and nitrogen onto dislocations in iron are in agreement with Cottrell and Bilby's[6] theory. The time for precipitation depends upon the interaction of the solute atoms with the elastic stress field of the dislocation at relatively large distances from the center of the dislocation. This interaction is therefore independent of the details at the core of the dislocation. Furthermore, the precipitation times depend only upon the interaction between individual solute atoms and the dislocation, while the activation energy for the release of a dislocation from an atmosphere depends upon the simultaneous interaction with many solute atoms.

The reason that the apparent dislocation-atmosphere binding energy ratio obtained at +150°F (+66°C) in this investigation is less than the value obtained at room temperature and lower may be related to the effects discussed above. Namely,

it may be that, at +150°F (+66°C), the thermal energy of the interstitial atoms comprising the atmosphere is sufficient to render the atmosphere at the dislocation core more diffuse than at the lower temperatures. Thus, by the arguments given previously, the activation energy required for dislocation release would be less at a temperature of +150°F (+66°C) than at room temperature and below.

A second explanation which might be advanced for the microstrain rates observed at +150°F (+66°C) as compared with those observed at room temperature and below is that motion of additional dislocations is occurring by some mechanism other than by break-away from atmospheres. Such a mechanism might be the motion of dislocations with their atmospheres accompanying them by diffusion. No reliable theoretical method for estimating the order of magnitude of microstrain rates which might occur by this mechanism is known to the authors.

This latter argument might also be advanced to explain the experimental observation that the total amount of pre-yield plastic and anelastic microstrain is considerably greater at +150°F (+66°C) than at room temperature and below. However, this might also be interpreted to mean that dislocations released from atmospheres move several times farther, on the average, at +150°F (+66°C) than at room temperature and below, prior to the onset of macroscopic yielding.

VOL. 4 1956

SUMMARY AND CONCLUSIONS

The pre-yield plastic and anelastic microstrain resulting from a rapidly applied constant stress on annealed low-carbon steel has been investigated at three temperatures, −23°F (−31°C), +76°F (+24°C), and +150°F (+66°C). The results show that at the two lower temperatures the logarithm of the initial rate of microstrain is inversely proportional to the product of the applied stress and the absolute temperature. This is in agreement with Fisher's[7] relation for the thermally activated release of dislocations from atmospheres of interstitial solute atoms which predicts that the activation energy for such release is inversely proportional to the applied stress. At +150°F (+66°C) the initial microstrain rates also correspond to an activation energy which is inversely proportional to the applied stress, within experimental errors. However, at this temperature the value of the proportionality constant is different than at the lower temperatures. The quantitative application of Fisher's theory to the experimental results leads to values for the binding energy between a dislocation and an atmosphere of interstitial solute atoms. These values are almost two orders of magnitude less than the values estimated by Cottrell and Bilby[6] and Cottrell.[11] An hypothesis is presented which might account for this discrepancy. The activation energy for release of a dislocation from an atmosphere may be sensitive to the detailed arrangement of the solute atoms in the region of the core of the dislocation, and this arrangement may depend upon the crystallographic orientation of the dislocation. Such an hypothesis might also lead to a temperature dependence of the activation energy for release of a dislocation from the atmosphere. This might explain the differences observed in the initial microstrain rates at +150°F (+66°C) as compared with those at lower temperatures.

The total amounts of pre-yield plastic and anelastic microstrain were also determined experimentally. These are approximately the same at temperatures of −23°F (−31°C) and +76°F (+24°C) for a given applied stress. The result is in agreement with a previously proposed[3] dislocation model of a yield nucleus. However, the total pre-yield microstrain observed at +150°F (+66°C) is several times as great as that observed at the lower temperatures. This suggests that some additional mechanism for the motion of dislocations prior to macroscopic yielding is involved at a temperature of +150°F (+66°C), but not at room temperature and below.

ACKNOWLEDGMENTS

This investigation was conducted under the sponsorship of the Office of Naval Research, and appreciation is expressed to this agency for their support of this work. The progress of this work was greatly aided by many discussions with Professor T. Vreeland, Jr. of the California Institute of Technology.

REFERENCES

1. C. S. Roberts, R. C. Carruthers, and B. L. Averbach *Trans. Amer. Soc. Metals* **44,** 1150 (1952).
2. T. Vreeland Jr., D. S. Wood, and D. S. Clark *Trans. Amer. Soc. Metals* **45,** 620 (1953).
3. T. Vreeland Jr., D. S. Wood, and D. S. Clark *Acta Met.* **1,** 414 (1953).
4. J. A. Hendrickson, D. S. Wood, and D. S. Clark Submitted and accepted for publication in *Trans. Amer. Soc. Metals* **48** (1956).
5. F. C. Frank and W. T. Read *Phys. Rev.* **79,** 722 (1950).
6. A. H. Cottrell and B. A. Bilby *Proc. Phys. Soc. London, Sec. A.* **62,** Part 1, 49 (1949).
7. J. C. Fisher *Trans. Amer. Soc. Metals* **47,** 451 (1955).
8. D. S. Clark and D. S. Wood *Proc. Amer. Soc Test. Metals* **49,** 717 (1949).
9. D. S. Wood and D. S. Clark *Trans. Amer. Soc. Metals* **44,** 726 (1952).
10. D. S. Wood and D. S. Clark *Trans. Amer. Soc. Metals* **43,** 571 (1951).
11. A. H. Cottrell *Dislocation and Plastic Flow in Crystals* Oxford 134 (1953).
12. *Ibid.* 38.
13. S. Harper *Phys. Rev. Ser.* 2, **83,** 709 (1951).

THE RESISTIVITY-TEMPERATURE-CONCENTRATION RELATIONSHIPS IN β-PHASE TITANIUM-HYDROGEN ALLOYS*

S. L. AMES†‡ and A. D. McQUILLAN‡

An attempt has been made to test the tentative conclusion reached in earlier work on the resistivity/composition curves for β-phase titanium-niobium alloys that the extrapolated resistivity/temperature relationship for unalloyed β-titanium at temperatures below the α-β transformation temperature would have a form more to be expected from a semiconductor than from a pure metal. This has been done by means of similar studies of β-phase titanium-hydrogen alloys in which resistivity measurements were made over a temperature range of 400–904°C and at compositions up to TiH. The form of the resistivity/composition curves has precluded their direct extrapolation to zero hydrogen content except at temperatures only just below the transformation temperature, but a more detailed analysis of the experimental results has provided some basis for a not unreasonable extrapolation of the resistivity/composition isotherms at lower temperatures, and the results thus obtained agree qualitatively with those of the earlier work. The validity of the various assumptions made is discussed. The present results indicate that at 480°C, below the transformation temperature, the resistivity of β-titanium would have fallen only 2% below the value of the resistivity immediately above the transformation temperature, and not by the 40% to be expected of a normal metal.

LES RELATIONS RÉSISTIVITÉ-TEMPÉRATURE-CONCENTRATION DANS LES ALLIAGES Ti-H EN PHASE β

On a tenté de vérifier la conclusion d'un travail antérieur sur les courbes résistivité-composition de la phase β dans des alliages titane-niobium d'après lesquelles la relation résistivité-température extrapolée au titane-β non allié à des températures inférieures à celle de la transformation α-β correspondrait plutôt à semi-conducteur qu'à un métal pur. Ce travail a été réalisé grâce à des études similaires d'alliages Ti-H en phase β pour lesquels des mesures de résistivité ont été effectuées dans un domaine de températures allant de 400 à 904°C, et pour des compositions allant jusqu'à TiH.

La forme des courbes résistivité-composition n'a pas permis l'extrapolation au cas du titane pur sauf à des températures se situant un peu en-dessous de la température de transformation. Mais une analyse détaillée des résultats expérimentaux a fourni les bases d'une extrapolation raisonnable des isothermes résistivité-composition à des températures plus basses et les résultats obtenus sont qualitativement en accord avec ceux des travaux antérieurs. La validité des hypothèses adoptées est discutée.

Les résultats actuels montrent qu'à 480°C, en dessous de la température de transformation, la résistivité du titane β tomberait à 2% seulement de la valeur obtenue un peu au-dessus de la température de transformation et non à 40% ainsi qu'on devrait s'y attendre pour un métal normal.

DER ZUSAMMENHANG ZWISCHEN WIDERSTAND, TEMPERATUR UND KONZENTRATION IN DER β-PHASE VON TITAN-WASSERSTOFF-LEGIERUNGEN

Es wurde versucht, die in einer früheren Arbeit über die Wider-stands-Konzentrations-Kurven von β-Titan-Niob-Legierungen geäusserte Auffassung zu prüfen, wonach die extrapolierte Temperaturabhängigkeit des Widerstandes von unlegiertem Titan unterhalb der Temperatur der α-β-Umwandlung eher die für einen Halbleiter zu erwartende Form hat, als diejenige eines reinen Metalls. Diesem Zweck dienten ähnliche Untersuchungen an β-Titan-Wasserstoff-Legierungen, an denen Widerstandsmessungen im Temperaturbereich zwischen 400° und 904°C bei Konzentrationen bis zu TiH durchgeführt wurden. Die Form der Widerstand-Konzentrations-Kurven liess eine direkte Extrapolation auf den Wasserstoffgehalt Null ausser für Temperaturen unmittelbar unterhalb der Umwandlungstemperatur nicht zu. Erst eine eingehendere Analyse der experimentellen Ergebnisse schuf die Möglichkeit für eine sinnvolle Extrapolation der Widerstand-Konzentrations-Isothermen bei niedrigeren Temperaturen, deren Resultate qualitativ mit denjenigen der früheren Arbeit übereinstimmen. Die Gültigkeit der verschiedenen dabei verwendeten Annahmen wird diskutiert. Aus den vorliegenden Ergebnissen geht hervor, dass bei 480°C, unterhalb der Umwandlungstemperatur, der Widerstand von β-Titan nur um 2% unter dem Widerstandswert unmittelbar über der Umwandlungstemperatur liegt und nicht um 40%, wie man es für ein normales Metall zu erwarten hat.

INTRODUCTION

In an earlier paper,[1] the authors have communicated results obtained during an investigation of the effects of niobium in the resistivity/temperature relationship of β-titanium which would suggest that the restivity of β-titanium, if it could exist below the transformation temperature, would not decrease with temperature towards zero resistivity at the absolute zero of temperature in the manner expected of a pure metal. Rather, it would appear that at

* Received February 16, 1956.

† Now at Research Department, Imperial Chemical Industries Ltd. (Metals Division), Birmingham.

‡ Department of Physical Metallurgy, University of Birmingham, England.

low temperatures the resistivity of β-titanium would increase with decreasing temperature in the manner of a semiconducting material. This tentative and surprising conclusion depended for its validity on a number of assumptions, the most important of which were first that the electrical properties of titanium-rich alloys could be simply related to the properties of pure titanium, and secondly that titanium-rich β-phase alloys retained in the metastable β form by quenching from a high temperature were truly homogeneous body-centered cubic structures free from ω phase of the type described by a number of workers.[2, 3, 4] It is desirable, therefore, that the extrapolated resistivity/temperature relationship for pure β-titanium at low temperatures should be checked by an investigation on another binary system of titanium, preferably with an element which has an electronic structure very different from that of niobium. This has now been done, using hydrogen as the addition element.

From the experimental point of view, hydrogen is a particularly convenient alloying addition to titanium for this type of work, since the absorption of hydrogen by titanium is a readily reversible process at temperatures above a few hundred degrees centrigrade, and the composition of the resistivity specimen may, therefore, be continuously varied after it has been mounted in the apparatus, merely by changing the hydrogen pressure within the system. A knowledge of the hydrogen pressure in equilibrium with the hydrogen dissolved in the specimen, and of the specimen temperature, enables the concentration of hydrogen in solution in the titanium to be uniquely defined. The necessary hydrogen-equilibrium-pressure / hydrogen-concentration / temperature relationships in the system titanium-hydrogen have previously been given by McQuillan,[5] and a few confirmatory experiments were sufficient to establish the fact that the relationships were valid for the sample of titanium used in the present investigation. Once the resistivity and temperature of the specimen, and the hydrogen pressure within the apparatus, had been measured, it was possible, therefore, to derive the resistivity/concentration/temperature relationship in the β-phase field of the titanium-hydrogen system.

The use of hydrogen as the addition element, however, imposes some limitations on the scope of the work. The addition of hydrogen to titanium, as can be seen from the constitutional diagram presented in Fig. 1, stabilizes the β phase, but unlike the β solid solutions in systems of titanium with the transition elements which are of the same general form, it is not possible to retain the hydrogen-bearing β phase at

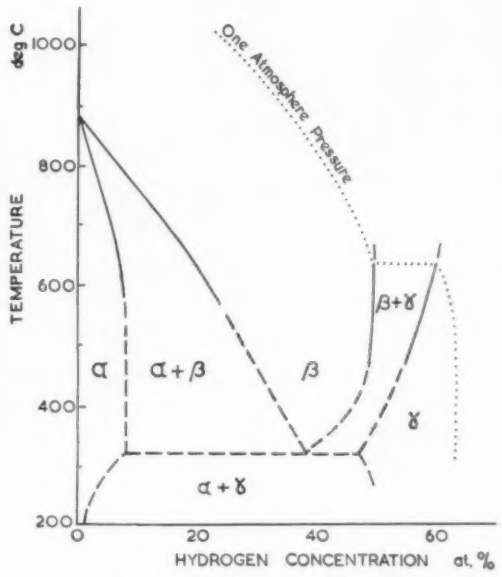

FIG. 1. The constitutional diagram of the titanium-hydrogen system after McQuillan.[5]

room temperature in a metastable condition by rapid cooling from the β-phase field. As may be seen in Fig. 1, at temperatures below the transformation temperature of titanium (882.5°C), the range of hydrogen concentrations over which the β phase can exist diminishes progressively with decreasing temperature until the eutectoid temperature is reached at about 300°C. Below the eutectoid horizontal the stable phases are the α-solid solution and a hydride phase. Since it is necessary, in work in which extrapolation plays a large part, to have an accurate knowledge of the change in resistivity of β-phase alloys over a range of compositions, it was considered that there was little point in obtaining results at a temperature much below 450°C, at which temperature the β phase is stable only over the composition range 31 to 48 at. per cent hydrogen. The fact that the apparatus was constructed mainly of glass and silica, and is, therefore, incapable of withstanding internal pressures greater than one atmosphere, further limited the range of temperature and composition over which the β phase could be investigated to that in which the hydrogen equilibrium pressure did not exceed 760 mm of mercury.

Hydrogen forms an interstitial solution in β-titanium. Nothing is at present known of the mode of electronic bonding between the hydrogen and the metal atoms with which they are associated, but it would seem unlikely that the hydrogen atoms would be completely ionized. It is much more probable that some form of weak bonding takes place

VOL. 4 1956

and that the interstitial proton is almost wholly shielded by an associated electron. It is not possible, therefore, to predict at the outset the effect of dissolved hydrogen on the resistivity of β-titanium, although it would be expected, on very general principles, that the presence of an almost completely shielded proton in the metal lattice would not give rise to much scattering of the conduction electrons and that additions of hydrogen would consequently not cause a marked increase in resistivity of the metal. As will be shown below, this prediction appears to be substantially correct. It is, however, unnecessary for our present purpose to understand in detail the electronic structure of titanium-hydrogen solutions. It is sufficient to know that the modification of the electronic structure of titanium brought about by the introduction of hydrogen atoms into interstitial sites in the titanium is likely to be very different from that produced by the substitution of the more complex niobium atoms for titanium atoms in the metal. In fact, one of the main advantages of using hydrogen as an addition element is that, should the form of the extrapolated resistivity/temperature curve of β-titanium obtained from the present work resemble that deduced from the results of the titanium-niobium investigation, the great dissimilarity between the two systems would enhance our belief in the validity of our conclusions.

EXPERIMENTAL PROCEDURE

The apparatus used in this investigation was a modified form of that used in the previous investigation of titanium-niobium alloys.[1] The modifications consisted of the addition of a vacuum tap which permitted the silica tube in which the specimen was situated to be isolated from the pumping system, a means of generating pure hydrogen within the apparatus, and manometers for measuring the hydrogen pressure in the closed system. The pure hydrogen was produced by heating hydrogen-saturated titanium chips in a side tube attached to the system. This method of preparation has the advantage that the hydrogen so produced is of very high purity and also that any desired pressure of the hydrogen generated can be obtained by control of the temperature in the hydrogen generator. The pressure within the apparatus was measured with either a dibutyl phthalate (density 1.045 g/cm^3 at 20°C) or a mercury manometer, so that pressures within the range 0.2 to 760 mm of mercury could be accurately determined. In order that readings should be independent of atmospheric pressure, one arm of each manometer was continuously evacuated.

Only a single titanium specimen was used for the whole range of hydrogen concentrations studied, since its hydrogen content could be continuously varied by increasing the amount of hydrogen in the closed system surrounding the specimen, equilibrium between gaseous hydrogen and hydrogen dissolved in the titanium being established almost instantaneously at temperatures above 500°C. The specimen, which was in the form of a rod 2-mm diameter and 4-cm length, was fabricated from a piece of iodide-refined titanium specially selected for its high purity (as evidenced by the fact that the α-β transformation occurred within a temperature interval of only 2°C). The current and potential leads to the specimen were made from titanium in order to eliminate the possibility of contamination of the specimen from this source at high temperatures. The current leads served the additional purpose of clamping the specimen to two rods of molybdenum which acted as electrical conductors, and also positioned the specimen rigidly within the silica tube and prevented it from coming into contact with the walls. Molybdenum was chosen for the current-carrying supports because of its high rigidity at elevated temperatures and also because it does not absorb hydrogen.

The resistance of the specimen was measured using a double-balance bridge of conventional design. By determining accurately the specific resistivity of the unalloyed titanium before mounting the specimen in the apparatus, it was possible to relate subsequent changes in the specimen resistance to changes in resistivity. In doing this, however, no account could be taken of the unknown dilation of the specimen with changes in temperature and hydrogen concentration, and values quoted for the resistivity of β-phase alloys at high temperatures and hydrogen concentrations will, therefore, be slightly in error because of these effects.

In the earlier resistivity work, the silica sheath in which the specimen assembly was inserted was continuously evacuated during the whole course of a high-temperature experiment. Since hydrogen can be readily pumped out of titanium at elevated temperatures, however, it was necessary for the present work to close the system after the preliminary evacuation, and much greater care had to be taken to ensure that before closing the system the internal surfaces of the system were degassed to such an extent that no significant quantity of contaminating gas was liberated during the experiments. In addition to the silica specimen tube, which could be outgassed fairly simply by heating to 900°C, the system necessarily

VOL
4
195

included such features as vacuum taps and manometers, which present more formidable problems. The only way, in fact, in which a sufficient degree of outgassing could be achieved was by holding the whole system at a pressure of at least 10^{-6} mm of mercury for a period of two weeks. Filling of the manometers, which was carried out after this treatment, was done by distilling the liquids into the manometer tubes in order to remove from them any dissolved air which might otherwise be liberated during subsequent use. During the degassing treatment, the vacuum taps were turned periodically in their sockets to allow air dissolved or entrapped in the silicone-tap grease to be pumped away. These precautionary measures were judged to have been satisfactory when, on closing the system after evacuation to a pressure of 10^{-6} mm of mercury, the gas pressure in the apparatus did not rise beyond 10^{-4} mm of mercury in the course of several days.

Since, as already mentioned, hydrogen can be easily removed from solution in titanium by exposing the heated metal to a high vacuum, there are many advantages in first producing a specimen containing the maximum amount of hydrogen required in the projected experiments and subsequently reducing the hydrogen concentration to the series of required levels by pumping away known amounts of hydrogen. This simplified the experimental procedure and had the further advantage that it reduced the number of times that the vacuum taps within the enclosed system had to be turned, and thus reduced the chances of specimen contamination due to gases liberated from the disturbed vacuum-tap grease. Furthermore, since the tap connecting the system to the pump was opened only to remove hydrogen, any gases liberated during the operation would tend to be carried out of the system in the hydrogen stream.

Titanium hydride (the γ phase in Fig. 1) is extremely friable, and the presence of appreciable amounts of this phase in the specimen or in the titanium current and potential contacts renders them particularly liable to fracture by accidental mechanical shock. Once hydrogen had been introduced into the specimen and contacts, therefore, their temperature was never allowed to fall sufficiently for the material to enter a phase field in which titanium hydride is stable. In order, however, to reduce the amount of contamination suffered by the specimen during the course of the whole investigation, the specimen temperature was kept as low as possible within the limits imposed by this consideration during the times when no measurements were being taken.

By observing the above-mentioned precautions, the amount of contamination suffered by the specimen was small. It was possible to estimate its extent by comparing the resistivity-temperature curve of the original hydrogen-free metal with the similar curve obtained after the major experiments had been completed and all traces of hydrogen had been removed from the material. No change had occurred in the resistance of the specimen at any temperature other than that immediately above the transformation temperature. Although, in its final condition, the specimen exhibited a sharp decrease in resistance on passing through the normal transformation temperature, the resistance-temperature curve was not exactly reproduced at temperatures immediately above this point. In its final condition, therefore, the great part of the material of the specimen appeared to transform at the expected temperature, but the rounding of the initially sharp discontinuity in the resistance-temperature curve on the side of the transformation indicates that an oxygen-contaminated layer must be present on the specimen, causing this part of the specimen to transform from the α to the β form at a higher temperature than the pure metal. The occurrence of superficial contamination on this scale was not unexpected, and had been largely offset by choosing a thick specimen, on the resistance of which surface contamination would have relatively little effect except at temperatures immediately above the $\beta/(\alpha+\beta)$ boundary. If, therefore, all results obtained at temperatures within 20°C of the $\beta/(\alpha+\beta)$ boundary are rejected, no appreciable error would seem to have been introduced into the results by the small surface contamination of the specimen.

Since the pressure of the gaseous hydrogen which is in equilibrium with that dissolved in the specimen varies with specimen temperature, the quantity of free hydrogen present in the apparatus is also temperature-dependent, and will be greater at high temperatures, where the equilibrium pressure is high, than at lower temperatures. The total amount of dissolved and free hydrogen present in the apparatus during any one resistivity/temperature investigation is, however, a constant, and the fraction of the total hydrogen which is in solution in the metal must, therefore, decrease progressively with increasing specimen temperature. Consequently, the resistivity/temperature curve obtained directly from an experimental run does not represent the relationship for constant concentration in the specimen. By measuring the hydrogen pressure within the apparatus simultaneously with specimen resistance and temperature, however, it is possible to relate the measured resistance

VOL. 4 1956

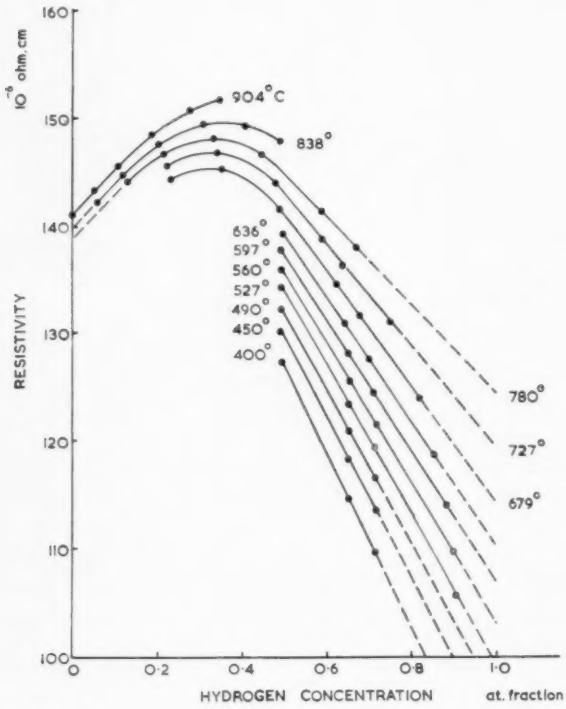

FIG. 2. Resistivity/concentration isothermal curves of β-phase titanium-hydrogen alloys. The broken lines represent linear extrapolation of the curves towards pure titanium and towards the hypothetical saturated alloy having a composition corresponding to the formula TiH. The isothermal temperatures are given in degrees centigrade, and the hydrogen concentrations in this and subsequent figures are expressed in terms of the ratio of the number of hydrogen atoms in solution per titanium atom.

of the specimen to its hydrogen concentration by making use of the known pressure/concentration/temperature relationships for the β phase in the hydrogen-titanium system.[5] This is done by reading off from the families of smooth curves representing the hydrogen concentration/temperature relationships and the resistivity/temperature relationships, hydrogen concentration and resistivity values corresponding to any particular temperature. Resistivity/composition isothermals can then be plotted.

DISCUSSION OF RESULTS

The family of isothermal curves for β-phase titanium-hydrogen alloys, constructed as described in the previous section, are shown in Fig. 2. In order to obtain the desired information on the probable form of the resistivity/temperature curve of pure β-titanium in the temperature range below the α-β transformation, it is necessary to be able to extrapolate the isothermal resistivity/concentration curves of Fig. 2 to zero hydrogen concentration. Since these are markedly curved at least over part of the concentration range in which they have been determined, no simple extrapolation to zero hydrogen concentration is possible, and it is necessary, therefore, first to develop a theoretical interpretation of their form.

The Form of the Resistivity/Composition Curves

The effect of the addition of small quantities of hydrogen on the electrical resistivity of β-titanium can be considered to be due to a combination of two separable factors:—

1. Scattering of the conduction electrons due to the introduction of additional scattering centers.
2. Possible changes in the electronic structure of the titanium as a result of the presence of the interstitial hydrogen.

Ignoring, for the moment, possible changes in the electronic nature of titanium on the addition of hydrogen, the solution of a small quantity of hydrogen in titanium can be regarded as the introduction of a random arrangement of new scattering centers, and will, therefore, increase the resistivity of the material. Since the hydrogen atoms occupy interstitial sites in the metal lattice, the contribution of dissolved hydrogen atoms to the resistivity of the solid solution will not obey the parabolic law characteristic of substitutional solid solutions, but will be directly proportional to the amount of hydrogen in the metal. That this appears to be the case can be seen in the 904°C isotherm of Fig. 3, in which the resistivity of β-titanium is seen to increase linearly with increasing hydrogen concentration up to about $TiH_{0.2}$.

The experimental results show, however, that at hydrogen concentrations greater than $TiH_{0.5}$, further additions of hydrogen give rise to a rapid decrease in resistivity. This fact can be accounted for as follows. The hydrogen pressure/concentration curves of McQuillan for the β phase in the hydrogen-titanium system[5] show that the hydrogen equilibrium

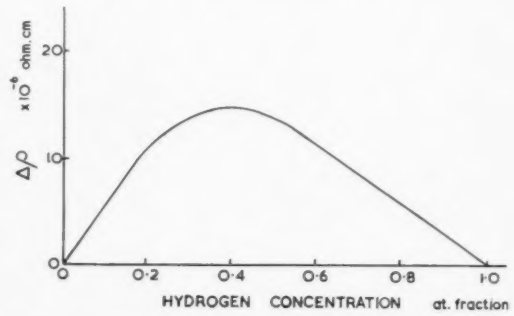

FIG. 3. The postulated contribution of solid-solution scattering to the resistivity of β-phase titanium-hydrogen alloys at 780°C.

pressure increases very rapidly for small increases in hydrogen concentration as the hydrogen concentration approaches the limit of solubility of hydrogen in β-titanium. From the form of these isothermal curves it would seem that, even in the absence of the hydride phase, the β phase would be unable to take into solution more than 50 at. per cent hydrogen. If, following Hägg,[6] it is assumed that a dissolved hydrogen atom will occupy a tetrahedral interstice in the body-centered cubic titanium lattice, then there are six interstices available for occupation by hydrogen for each titanium atom in the metal. Since it would appear that no further hydrogen can be dissolved in β-titanium once the composition has reached the value corresponding to the formula TiH, it must be assumed that at saturation only one of the six possible interstices is occupied, and the presence of a hydrogen atom in a particular interstice renders the remaining five adjacent inoperative. A hydrogen atom in solution in β titanium must, therefore, exert a repulsive force on other dissolved hydrogen atoms if these approach within a distance of about one atomic spacing. When the metal is saturated with hydrogen, this repulsive force between adjacent hydrogen atoms will, in all probability, bring about an ordering of the hydrogen atoms on the available sites, and the lattice would, in this condition, have perfect periodicity; the hydrogen would thus make no contribution to the resistivity due to solid-solution scattering. In the absence of electronic effects in the titanium due to the presence of dissolved hydrogen, therefore, the resistivity of the β-phase solution of composition TiH would be expected to be almost equal to that of the pure metal.

The linearity of the resistivity/concentration curves at the hydrogen-rich end can be considered in terms analogous to those used in discussing the dilute titanium-hydrogen alloys. If a small quantity of hydrogen is removed from the ordered, saturated β-phase solution, the periodicity of the lattice will be destroyed by the presence of vacant interstitial sites previously occupied by hydrogen atoms. There is no reason to suppose that the vacant sites produced by the removal of a small part of the total hydrogen content of the material would not be arranged in a random manner throughout the metal, and it would be expected, therefore, that reduction in hydrogen concentration below TiH would bring about an increase in the resistivity of the β-phase solution. Again, since the scattering centers are interstitial, the increase in resistivity will increase linearly with the number of vacant sites, that is to say, the increase in resistivity will be proportional to the amount by which the atomic fraction of hydrogen in the material is less than unity. The rate of increase in resistivity of the saturated hydrogen solid solution when hydrogen is removed will not in general be equal to the rate of increase in resistivity of pure β-titanium when small quantities of hydrogen are dissolved in the metal, since the degree of scattering produced by a hydrogen atom will be different from, and probably greater than, that due to a vacant interstitial site in an otherwise hydrogen-saturated solution. In the absence of effects due to electronic changes in the metal atoms, the basic shape of the resistivity/concentration curves can therefore be considered to result from the combination of two straight lines of opposite, but not equal, slope.

The form of the family of curves presented in Fig. 2, especially that of the 780°C isotherm which covers the widest composition range, conforms well with this requirement and suggests that the superimposed effect due to electronic changes in the metal brought about by the introduction of hydrogen into it varies linearly with hydrogen concentration.* Furthermore, the linear nature of the two branches of the curves permits simple extrapolation in all cases in which a sufficiently great proportion of either branch can be determined experimentally. Thus the 838° and 780°C isotherms can be extrapolated to zero hydrogen content, and those at 780°C and below to the composition TiH. When these extrapolations are carried out it becomes apparent that a large electronic change must indeed take place in the metal on the addition of hydrogen, since at any given temperature the resistivity of the β-solid solution of composition equivalent to TiH is appreciably less than that of pure β-titanium. This is particularly clear from the 780°C isothermal, the only one in which extrapolation in both directions is possible.

At the present stage of our knowledge of the electronic structure of β-titanium little can be said about the nature of the electronic changes which occur when hydrogen is dissolved in the metal. Immediately above the transformation temperature the resistivity of β-titanium is an order of magnitude greater than would be expected of a normal metal at this temperature. Furthermore, the temperature coefficient of the resistivity of β-titanium at this temperature is abnormally low, and the increase in resistivity with temperature due to thermal scattering must therefore be almost completely compensated for by a decrease in resistivity with increasing

* The absence of sudden changes in resistivity at any hydrogen concentration suggests that no effects which might have arisen from minor Brillouin zone overlaps are present.

VOL. 4 1956

temperature brought about by a thermally activated process which increases the number of effective conduction electrons in the metal. Since β-phase titanium-hydrogen alloys having hydrogen contents in the region of the composition TiH exhibit a lower resistivity and a much higher temperature coefficient than β-titanium, it would appear that the addition of hydrogen to β-titanium destroys the anomalous electrical behavior exhibited by the metal at low temperatures. Furthermore, it would appear from the form of the family of curves presented in Fig. 2, that the disappearance of abnormal electrical resistivity effects in β-phase titanium-hydrogen alloys is proportional to the amount of dissolved hydrogen, and that the transition from abnormal to normal conduction is a gradual process which takes place over the whole range of compositions from Ti to TiH.

The Resistivity of β-Titanium

The linear extrapolation of the resistivity/concentration curves, in accordance with the earlier discussion, gives values for the resistivity of unalloyed β-titanium only down to 780°C, since at lower temperatures no experimental data are available at sufficiently low hydrogen concentrations to indicate the slope of the titanium-rich part of the curve. Thus from these results it is only possible to extend the resistivity/temperature curve of β-titanium from 882.5° to 780°C, which is insufficient to provide a satisfactory check on the findings of the earlier work on titanium-niobium. The most interesting aspect of the results on titanium-niobium alloys, however, was the implication that at lower temperatures the resistivity/temperature curve would not fall as for a normal metal, but instead rise again with decreasing temperature below 200°C.

The present results can be made to yield no direct information on this point; but if the conclusion that the effect of the electronic-structure change is a linear function of hydrogen content is accepted and it is assumed, furthermore, that the resistivity contribution of solid-solution scattering is substantially independent of temperature, it is possible to construct an approximation to the low-hydrogen section of the resistivity isothermals at temperatures below 780°C from the experimentally determined sections at higher hydrogen concentrations. The contribution of changes in the number of scattering centers alone as a function of hydrogen content is first determined by subtracting from the resistivity values given by the 780°C isotherm the resistivity contribution due to the electronic effect alone. The latter is obtained for each hydrogen concentration by drawing a straight line between the extrapolated values of the resistivity for unalloyed β-titanium and for the alloy of composition TiH at this temperature. On the assumption that effects due to the presence of additional scattering centers are unlikely to be very strongly temperature-dependent, the resultant contribution, $\Delta\rho$, due to solid-solution scattering alone, plotted against hydrogen concentration in Fig. 3, can be considered to be representative of all temperatures, and the subtraction of $\Delta\rho$ from the experimentally determined resistivity isotherms for lower temperatures should therefore yield the resistivity contribution due to electronic changes as a function of hydrogen concentration for these temperatures. If the various assumptions made are valid, this relationship should be linear, and it is, in fact, found to be so, although the significance of this result is less striking than it might otherwise seem, since it arises, over much of the hydrogen concentration range, from the difference between two linear functions. Nevertheless, at hydrogen concentrations of about 50 at. per cent, where the functions subtracted are not linear, the linear nature of the resistivity-difference/hydrogen-concentration relationship persists, and some support is thus obtained for the assumptions made.

For any temperature, once the resistivity contribution due to electronic changes has been determined as a function of hydrogen content for the composition range over which experimental resistivity measurements have been made, the linear nature of the relationship permits extrapolation to zero hydrogen content. The resistivity value thus obtained is that which unalloyed β-titanium would have at the temperature concerned if it in fact existed at this temperature.

The resistivity values obtained for β-titanium obtained from the series of isothermals given in Fig. 2 both by direct extrapolation and by the indirect method outlined above are plotted against temperature in Fig. 4, which also includes the experimentally determined resistivity/temperature curve for the sample of titanium studied at temperatures above that of the α-β transformation. The probable form of the resistivity/temperature curve for the β form of titanium at temperatures below the transformation temperature can therefore be dotted in.

Direct comparison between these results and those obtained in the work on titanium-niobium alloys[1] is not possible, since no satisfactory method of extrapolating the S-shaped isothermal resistivity/composition curves in β-phase titanium-niobium alloys to zero niobium content was found. Broadly,

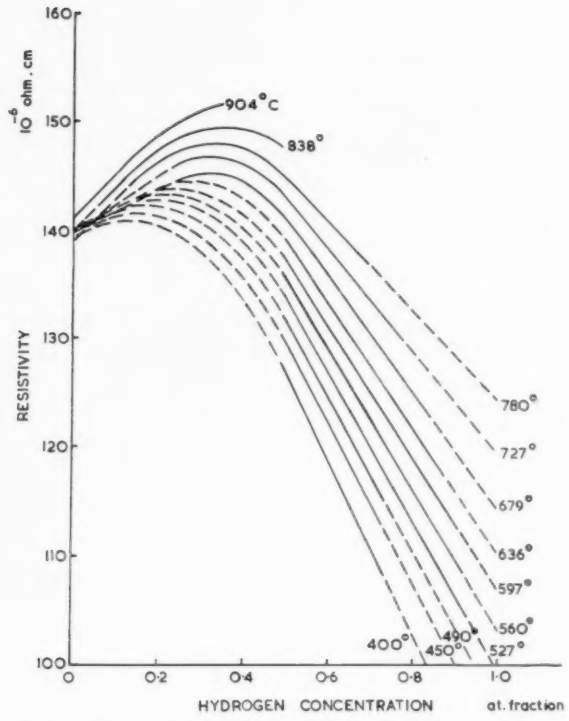

FIG. 4. The complete family of resistivity/concentration/temperature curves of β-phase titanium-hydrogen alloys including extrapolated values for the resistivity of β-phase alloys of low-hydrogen concentration obtained by making use of the scattering relationship shown in Fig. 3.

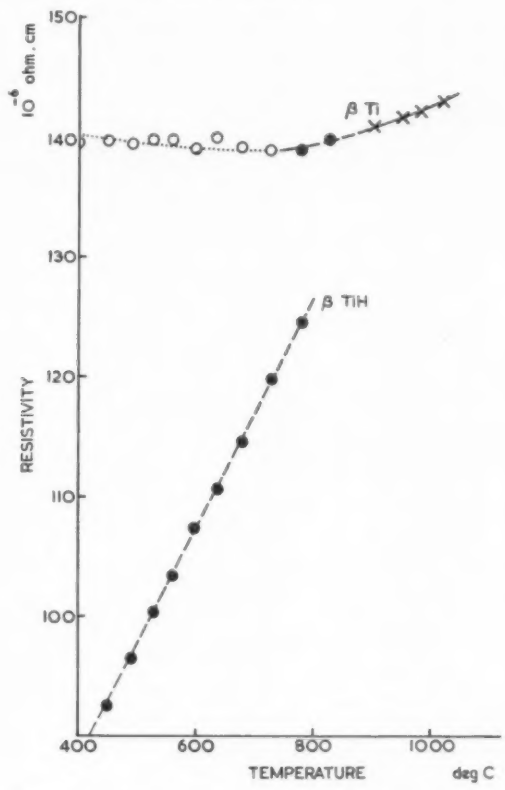

FIG. 5. The resistivity/temperature curves of pure β-titanium and the hypothetical saturated β-phase alloy having a composition corresponding to the formula TiH.
× Experimentally determined values.
● Values obtained by direct extrapolation of experimental curves.
○ Values obtained by indirect extrapolation.

however, the earlier results indicated that the resistivity of β-titanium would not decrease very markedly from the transformation temperature down to 200°C and that below this temperature it would increase rapidly with decreasing temperature. The results obtained in the present work are, therefore, consistent with those obtained in the earlier work in that the extrapolated resistivity decreases only by a few per cent of its value at the transformation temperature between that temperature and 400°C. The forms of the low-temperature resistivity/temperature curve of β-titanium derived from two such dissimilar systems as the titanium-niobium and titanium-hydrogen systems are, therefore, in general agreement. The only alternative to accepting the validity of the extrapolated resistivity/temperature curve for β-titanium shown in Fig. 5 is to assume that the effect of adding relatively small amounts of either niobium or hydrogen to β-titanium at temperatures in the neighborhood of 400°C is to cause its resistivity to increase by a very large amount, whereas the addition of the same amount of these elements to titanium above the transformation temperature has been shown to give rise only to comparatively small resistivity changes. The authors feel that the first assumption is most likely to prove to be correct. It should, however, be stressed that there is no suggestion that β-titanium, if it could exist below the transformation temperature, would actually be a semiconductor, but only that its resistivity would not approach a zero value at the absolute temperature. If the metal were a semiconductor, very small amounts of addition elements would serve to destroy the semiconducting properties of the material, and since this has been shown not to be the case, the anomalous electrical behavior of β-titanium cannot be attributed to the existence of a simple energy gap in the conduction band of electrons. In this respect, its behavior is perhaps more akin to that of α-manganese[7] than to that of a true semiconductor.

At the present state of our knowledge of the physical properties of β-titanium and β-phase titanium-rich alloys it does not seem possible to form

VOL. 4 1956

any clear picture of the way in which the electronic structure of these materials differs from the accepted picture of metallic electronic structures. There is, therefore, a need for much further work on this problem, and it is hoped that when, in the future, results obtained by examining other physical properties of titanium-rich alloys become available, the cause of the anomalous behavior of β-titanium will be clarified.

REFERENCES

1. S. L. Ames and A. D. McQuillan *Acta Met.* **2,** 831 (1954).
2. P. D. Frost, W. M. Parris, L. L. Hirsch, J. R. Doig, and C. M. Schwarz *Trans. Amer. Soc. Metals* **46,** 231 and 1056 (1954).
3. J. M. Silcock, M. H. Davies, and K. H. Hardy *Nature* **175,** 731 (1955).
4. F. R. Brotzen, E. L. Harmon, and A. R. Triano *Trans. Amer. Inst. Min. Met. Eng.* **203,** 413 (1955).
5. A. D. McQuillan *Proc. Roy. Soc.* **A204,** 309 (1950).
6. G. Hägg *Z. Phys. Chem. B.* **12,** 33 (1931).
7. G. Grube and H. Speidel *Z. Elektrochem.* **46,** 233 (1940).

VOL
4
195

AN X-RAY INVESTIGATION OF THE STRUCTURE OF LIQUID MERCURY AND LIQUID MERCURY-THALLIUM ALLOYS*

R. E. SMALLMAN† and B. R. T. FROST†

Intensity and atomic-distribution curves have been determined for pure mercury and four liquid mercury-thallium alloys at a constant temperature of 17°C ± 1°. The intensity curves, obtained using a Geiger-counter diffractometer, display highest and sharpest peaks on the first interference maxima for the alloys corresponding to the compound composition together with a significant alteration in interatomic distances.

Fourier inversion of the intensity data to give atomic and electronic distribution functions was performed. The values of co-ordination number and closest distance of approach for the five liquids are in agreement with the indications of the intensity curves alone. In general, the diffraction data imply that there is a more orderly atomic arrangement in the liquid at a compound composition than at other compositions.

ÉTUDE AUX RAYONS X DE LA STRUCTURE DU MERCURE LIQUIDE ET DES ALLIAGES LIQUIDES MERCURE-THALLIUM

Les courbes d'intensité et de distribution atomique ont été déterminées pour le mercure pur et quatre alliages mercure-thallium à la température constante de 17°C ± 1°. Les courbes d'intensité, obtenues à l'aide d'un diffractomètre à compteur de Geiger, révèlent des pics plus élevés et plus étroits sur les premiers maxima d'interférence dans le cas d'alliages dont la teneur élémentaire est équiproportionnelle à celle du composé définie.

En même temps, une variation importante des distances interatomiques est observée.

On a effectué l'inversion de Fourier des intensités pour obtenir les fonctions de distribution atomique et électronique. Les valeurs du nombre de coordination et de la plus courte distance d'approche pour les cinq liquides sont seulement en accord avec les courbes d'intensité.

En général, les données de diffraction suggèrent l'existence dans le liquide d'un arrangement atomique plus ordonné pour la composition correspondant à la combinaison intermétallique, que pour les autres.

EINE RÖNTGENUNTERSUCHUNG ÜBER DIE STRUKTUR VON FLÜSSIGEM QUECKSILBER UND FLÜSSIGEN QUECKSILVER-THALLIUM-LEGIERUNGEN

An reinem Quecksilber und vier flüssigen Quecksilber-Thallium-Legierungen wurden bei konstanter Temperatur von 17°C ± 1° Intensitätsund Atomverteilungs-Kurven bestimmt. Die Intensitätskurven, die unter Verwendung eines Zählrohr-Goniometers gewonnen wurden, weisenzusammen mit einer ausgeprägten Änderung der Atomabstände—die höchsten und schärfsten Spitzen bei denersten Interferenz-Maxima der Legierungen, die der Verbindungszusammensetzung entsprechen, auf. Ausserdem wurde eine Fourier-Analyse der Intensitätsdaten, aus der man die Atom- und Elektronenverteilungsfunktionen erhält, durchgeführt. Die Werte der Koordinationszahl und die kürzesten Abstände zwischen den Atomen stimmen für die fünf Flüssigkeiten mit den Ergebnissen überein, die aus den Intensitätskurven allein schon zu entnehmen sind. Ganz allgemein geht aus den Beugungsdaten hervor, dass im flüssigen Zustand bei Zusammensetzungen, die einer Verbindung entsprechen, eine geordnetere Atomverteilung vorliegt als bei anderen Zusammensetzungen.

VOL. 4 1956

1. INTRODUCTION

Much evidence exists to indicate that intermetallic compounds retain some of their solid state characteristics on melting, particularly where there is a high electrochemical factor between the two components.[1] This has a marked effect on physical properties, e.g. electrical conductivity shows a minimum at the compound composition. Further evidence about the nature of such liquids may be expected to be gained from X-ray diffraction. Accordingly, as the first phase of an X-ray study of liquid-alloy systems containing intermetallic compounds, the system mercury-thallium was examined. The reasons for this choice were as follows:

(i) The system contains an intermetallic compound Hg_5Tl_2 (see Fig. 1).

(ii) Reliable thermodynamic data on this system have been published.[2, 3, 4]

(iii) In the region of interest (0–40% Tl) the alloys are all liquid at room temperature. In particular, the melting point of Hg_5Tl_2 (14.5°C) is convenient for making measurements at room temperature.

(iv) Mercury and thallium are adjacent in the Periodic Table, so that their scattering factors for X-rays are almost identical, and analysis may proceed as for a monotomic liquid.

(v) Two previous X-ray investigations of this

* Received February 16, 1956.

† Metallurgy Division. Atomic Energy Research Establishment Harwell, England.

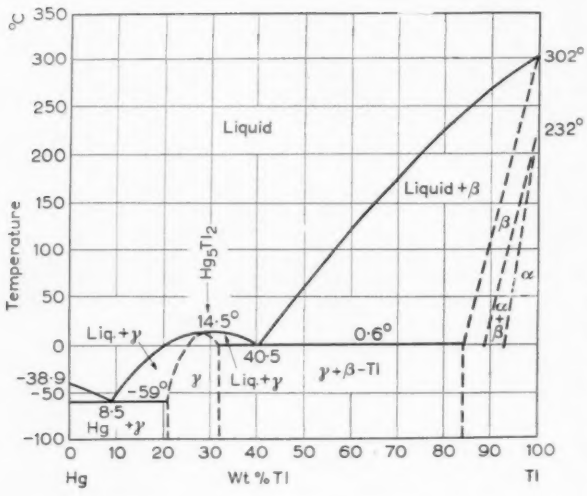

FIG. 1. Equilibrium diagram of the system mercury-thallium from Hansen.

system have been made, one showing a double maximum on the first intensity peak[5] and one showing a single maximum.[6]

2. EXPERIMENTAL

A. (a) *Method.* Previous work has shown it is important to obtain precise intensity data up to large diffraction angles. The error of the most refined photographic measurements is not much less than $\pm 5\%$, and errors of the order of 10% and more are common at low intensity levels. This places an intolerably low limit on the precision with which Fourier inversion of data to give the radial distribution function can be computed. To increase the precision in the present work, a bent crystal monochromator was used in conjunction with Bragg-Brentano focusing and a Geiger-counter detector giving an estimated accuracy of 1 or 2% in intensity.

(b) *The specimen holder.* This consisted of a mild-steel plate $1\frac{1}{2} \times 1\frac{1}{2} \times \frac{1}{4}$ in., in which was milled a channel $1 \times 1\frac{1}{4} \times \frac{3}{32}$ in. Cellophane, 0.001 in. thick, reinforced by mica, held the liquid while the cell was mounted vertically on the axis of a diffractometer. Water-cooling coils were soldered to the back of the rectangular cell to maintain the liquid at a constant temperature of 17 ± 1°C.

(c) *Preparation of specimens*—The alloys of mercury thallium were made from Johnson Matthey triply distilled mercury and spectroscopically pure thallium. Oxidation of the thallium was prevented by weighing and handling in a dry-box containing an atmosphere of pure argon. Estimation of the thallium content was made by freezing the alloy and comparing the temperature of freezing with the equilibrium diagram, Fig. 1. Two alloys near the composition corresponding to the compound Hg_5Tl_2 with estimated thallium contents of 34% and 30% thallium respectively, and the low thallium (8.5%) and high thallium (40%) eutectic alloys were prepared.

B. *Procedure.* Copper $K\alpha$ radiation generated at 50 kV peak and monochromatized by a lithium fluoride crystal (to minimize harmonics) was used throughout at 30 mA. Measurements every $\frac{1}{4}$° were made at specific angular settings of the Geiger counter to avoid distortion introduced by the use of a counting-rate meter. The focused reflected beam entered the counter through a slit subtending an angle of 20 min of arc in χ at the center of the diffractometer, the radius of which was 8.6 cm. The count was recorded on a scaling unit, not for a constant time but for a standard monochromatic X-ray output from the X-ray set as measured on a second monitoring counter, and was corrected for losses in both counters. Frequent checks on the stability of the monitoring were made.

3. INTERPRETATION

(a) *X-ray theory.* Two methods are available for analyzing experimentally determined intensity data: the radial and electronic distribution methods. The radial distribution function is derived from Debye's work[7] to give the Zernike-Prins formula*

$$4\pi r^2\rho(r) = 4\pi r^2\rho_0 + \frac{2r}{\pi}\int_0^\infty S\left(\frac{I}{Nf^2} - 1\right)\sin Sr\, dS \quad (1)$$

for monatomic liquids. Here $\rho(r)$ is the number of atoms per unit volume at a distance r from a reference atom, and $4\pi r^2\rho(r)$ is the number of atoms contained in a spherical shell of radius r and thickness dr, $S = 4\pi \sin\theta/\lambda$, ρ_0 is the average density of the liquid in atoms per unit volume, and I/N is the coherent scattered intensity in electron units. In recent years it has been pointed out by Finbak[8] that in atomic-distribution analysis undue weight is assigned to experimental intensities at higher angles because of the presence, in the $S \cdot i(S)$, i.e. $S\left(\frac{I}{Nf^2} - 1\right)$ function, of the factor $1/f^2$, which increases rapidly with angle. Thus, small errors in the intensities at high angles, which is the region where experimental inaccuracy is largest, have a large influence on the integration. Finbak defined an electronic radial distribution function, $\sigma(r)$, in terms of the probability $\sigma(r)\, dr$ of one electron in an atomic system being found at a distance between r and $r + dr$ from another electron.

* A simple derivation of this formula is given in the review by Gingrich.[12]

The difference between the actual distribution of electrons in the sample and the mean density is given by

$$\text{const. } r\int_0^\infty S(I - Nf^2)\sin rS\, dS \qquad (2)$$

which differs from the corresponding atomic distribution function by the omission of a $1/f^2$ term.

If, in a liquid consisting of two kinds of atom, the coherent scattering of both is very nearly the same, e.g. mercury and thallium, or if the coherent scattering of one is negligibly small, the analysis of the data may proceed essentially as in the case of a monatomic liquid without serious error. However, when the liquid alloy contains atoms of widely different scattering power, the different contributions of each kind of atom must be taken into account.

(b) *Analysis of results.* Before the function $4\pi r^2\rho(r)$ can be determined, it is necessary to evaluate the integral $\int_0^\infty S\left(\frac{I}{Nf^2} - 1\right)\sin rS\, dS$. In practice, however, there is a limit of range of S values over which diffraction data can be obtained; for the experiments described this is $S \sim 1A^{-1}$ to $7A^{-1}$. Thus, unless some form for $i(S)$ is assumed in the range $0 < S_{\min}$ and $S_{\max} < S < \infty$, the integration cannot be carried out. The extrapolation of the range to zero is relatively sound, since the function $Si(S)$ tends rapidly to zero without fluctuation in sign. The possible error obtained by analyzing the data from the 30% thallium alloy with and without this low-angle extrapolation was found to be relatively small (see Fig. 5).

The elimination of the finite upper limit is much more difficult to deal with, since any extrapolation is unsound due to rapid fluctuation in the $Si(S)$ curve. If the series is terminated at $S = S_{\max}$, the effect is to introduce subsidiary maxima to the distribution, which appear at approximately $2\pi/S_{\max}$ on either side of the main peaks. These subsidiary details are noticeable in the distribution curves given later (see, for example, Fig. 3 for mercury). Such false detail may be minimized by multiplying the integral of equation (1) by a modifying function. Discussion of suitable modification functions has recently been made by Waser and Shoemaker,[9] but the "arbitrary temperature factor," exp $(-a \cdot S^2)$, first introduced by Bragg and West,[10] appears to be the most suitable.

The Geiger-counter intensity results, after subtracting the cellophane scattering intensity, are corrected for absorption in the cellophane window and for polarization[11] of the X-ray beam both by monochromator and sample. The resulting intensity versus $\sin\theta/\lambda$ curve is then corrected for incoherent scattering and matched at high diffraction angles to give the intensity scale in electron units. The standard procedure described in detail by Warren[11] and Gingrich[12] was adopted for this conversion.

4. RESULTS

(a) *The intensity function.* Fig. 2 shows the intensity versus $\sin\theta/\lambda$ curves for the five mercury-rich liquids expressed in electron units. The diffraction pattern in all cases consists of three diffuse bands of decreasing intensity. The three peaks for pure mercury occur at $\sin\theta/\lambda$ values, equal to 0.188, 0.36, and 0.53, which compare well with recent values obtained by neutron diffraction:[13] (0.194, 0.361, and 0.523), and by X-rays[14]: (0.185, 0.365, and 0.530). The position of the first of the bands for each of the liquids examined is shown in Table 1. It is not possible to obtain an absolute value of the interatomic distance directly from the intensity curve, but nevertheless it is possible to bracket it.

The interatomic distance d_B given in Table 1 is that corresponding to the first peak calculated using the Bragg law. However, since there is no regularly repeating lattice in the liquid, this law cannot strictly apply. In the extreme case of only two diffracting centers, the diffraction maxima occur[15] when $(n + \frac{1}{4})\lambda = 2d\sin\theta$ or $\lambda = \frac{8}{5}d_E\sin\theta$, where d_E is the distance between diffracting centers. Thus, for a real liquid the correct lattice distance will be intermediate between d_B and d_E. The addition of the larger thallium atom to mercury increases the d value, but the change does not obey a linear composition-size relationship, since for mercury $d_B = 2.66$ and for thallium[16] $d_B = 2.78$.

The intensity values obtained for the five liquids are of interest, as the results were determined at a constant temperature. Thus, although the liquids have the same thermal energy, the peak intensity values are significantly different, varying from 6200 e.u. for the low-temperature thallium eutectic to 9600 e.u. for the compound composition. The half-peak width of the first diffuse intensity band is also different,

TABLE 1. Calculated limits of interatomic distance for the five mercury-rich liquids

Liquid	$\sin\theta/\lambda$	d_B Å	d_E Å
Hg	0.188	2.66	3.33
Hg/8.5 Tl	0.188	2.66	3.33
Hg/30 Tl	0.184	2.71	3.39
Hg/34 Tl	0.184	2.71	3.39
Hg/40 Tl	0.186	2.69	3.36

VOL. 4 1956

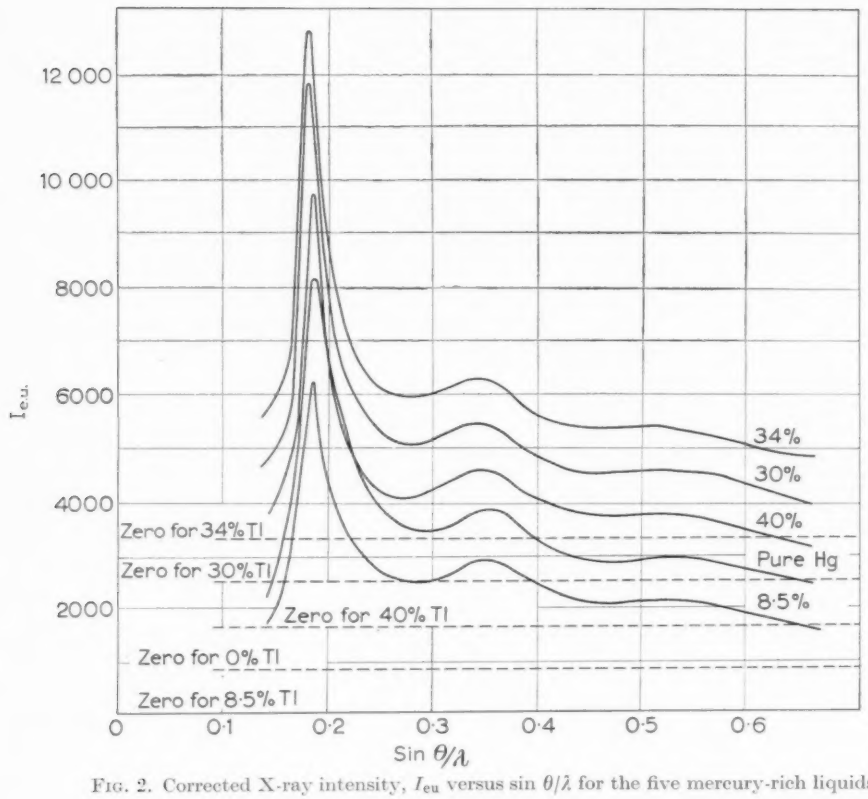

FIG. 2. Corrected X-ray intensity, I_{eu} versus sin θ/λ for the five mercury-rich liquids.

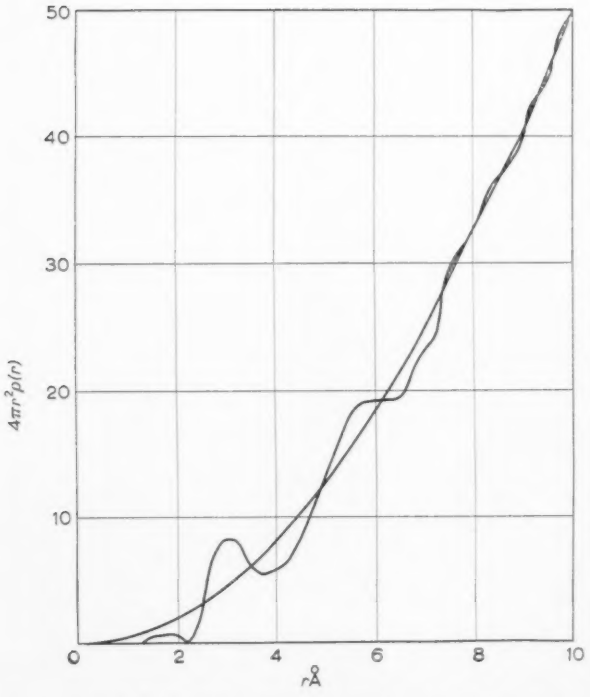

FIG. 3. Radial distribution curve for pure mercury.

being more than 50% wider for the pure mercury and low-thallium-content eutectic than for the liquid of the compound composition. The variations both in width and intensity appear to depend on the temperature above the melting-point; thus, an 8.5% thallium alloy, which has the lowest melting-point, gives the lowest intensity and widest peak, while a 30%–34% alloy gives a high intensity and a narrow peak.

(b) *Radial distribution analysis.* The radial distribution function $4\pi r^2\rho(r)$ is such that $\rho(r)$ gives the number of atoms between r and $r + dr$ and is greater than $4\pi r^2\rho_0$ at regions where the density is greater than average. The existence of oscillations in this function indicates a tendency for the atoms to arrange themselves so that certain interatomic distances are preferred.

The resulting radial-distribution curves calculated from equation (1) for the five liquids examined, for r up to 10 Å, are shown in Figs. 3 to 5. The continuous smooth curve is the average atomic distribution $4\pi r^2\rho_0$, where ρ_0 is the average atomic density. Many of the distribution curves exhibit small subsidiary maxima which in the past have been analyzed as true interatomic distances. Those appearing at distances about 2 Å or smaller are

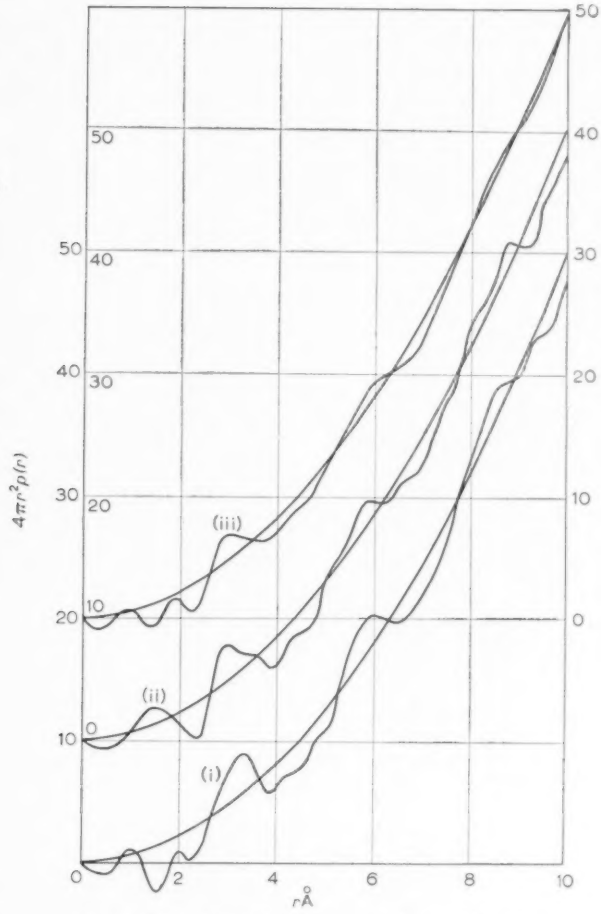

FIG. 4. Radial distribution curves for (i) 34% Tl, (ii) 40% Tl, (iii) 8.5% Tl alloys.

obviously spurious, since distances much less than the atomic diameter cannot occur. Those occurring at larger values of r can easily be distinguished from the true interatomic distances and are due to one or more of the radial distribution analysis errors already discussed.

For pure mercury (Fig. 3) the area under the first peak at 3.1 Å is 8.2 atoms. This represents the co-ordination number of the first shell of close neighbors. For the 8.5% thallium alloy the first peak, also at 3.1 Å, is not so well defined, but a smaller co-ordination number of approximately 7 atoms is indicated. Of the three remaining radial distribution curves, the 34% thallium alloy has a co-ordination number of 9.1 at a distance of 3.3 Å, but the 30% and 40% thallium liquids both exhibit double maxima.

The occurrence of double maxima for the liquid with the compound composition might be indicative of some tendency for molecular association, the molecule containing two close but distinctly separate interatomic distances. However, the absence of a double maximum for the 34% thallium alloy for which the intensity function is similar, together with the presence of the false peaks referred to above, suggests this might be spurious detail introduced by the Fourier inversion process. This suggestion is strengthened by the reappearance of the double peak on the 40% thallium distribution curve. To minimize the spurious detail in the distribution curve for the 30% thallium alloy, the modification function exponential ($-aS^2$) has been applied (Fig. 5iii). The value of a was taken to be 0.03, so that $M(S_{\max})$ had a negligibly small value of 0.1. The result is an extremely well-defined distribution curve with a minimum of false detail. The co-ordination number of the first shell at 3.25 Å is 9. The succeeding shells at 5.8 Å and 8.5 Å are not sufficiently sharp to warrant being assigned co-ordination numbers.

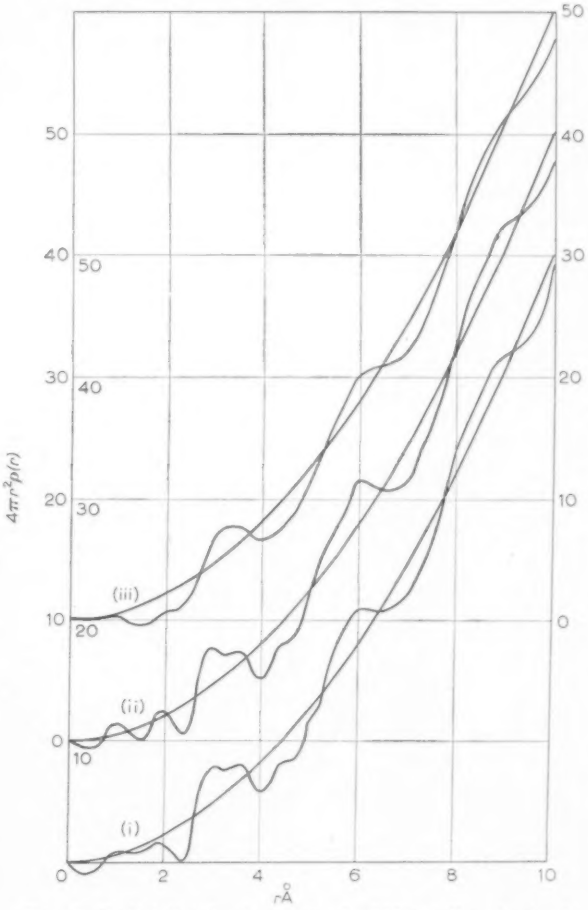

FIG. 5. Radial distribution curves for 30% Tl alloy obtained
(i) from measured intensity data.
(ii) using extrapolated intensity data in region 0 to $\sin\theta/\lambda = 0.14$.
(iii) using artificial temperature factor exp $(-aS^2)$ applied to curve (i).

VOL. 4 1956

(c) *Electronic distribution analysis*—This method of analysis has been applied to the three liquid alloys, 30%, 34%, and 40% thallium, and the resulting distribution curves shown in Fig. 6(i, ii, iii). The positions of the first four shells are well defined with a minimum of spurious detail. The closest distance of approach for both the alloys near the compound composition is larger than for the eutectic alloy in agreement with the interatomic distance from intensity functions themselves.

The application of the electronic distribution analysis is not in general considered worthwhile (although it has been of use in settling long-standing arguments as to the significance of subsidiary maxima) since more information can be determined from the atomic distribution curves.

5. DISCUSSION

Intensity and atomic-distribution functions have been determined for pure mercury and four mercury-thallium alloys at a constant temperature of 17°C. Many of the previously published intensity curves[17, 18] for mercury appear to be in error, since the occurrence of a diffraction peak at $\sin\theta/\lambda$ between 0.1 and 0.15 is suspect.[13] There is also some discrepancy between the older work reported by Sauerwald[19] and Hendus[20] and the more recent work of Jennings [21] and Vineyard,[13] Sauerwald quotes a twelve-fold co-ordination, while Hendus obtains a value of 10; with six atoms at 3 Å and four atoms at 3.47 Å. Jennings obtained a value of 8.6, while Vineyard reports a value of 8.3. The present work is in good agreement with these latter results obtained by X-ray and neutron diffraction, a value of 8.2 being obtained.

The intensity functions for the four alloys show no evidence of a division of the first interference maximum into two closely separated maxima; a result which supports the later work of Sauerwald.[6] This is not surprising, since Hg_5Tl_2 is a size-factor type of compound of face-centered cubic structure ($a = 4.66$ Å) having a low heat of formation (2.5 kcal/mole). Thermodynamic measurements of Hg-Tl liquid alloys by both the vapor-pressure and e.m.f. methods show a negative deviation from Raoult's law, implying an attraction for unlike atoms; however, this is not so marked as, for example, in the magnesium-lead or gold-tin systems. From an examination of the latter system, Hendus[16] has reported a double interference peak at the liquid composition AuSn, and associates the smaller d value of the doublet with the intense (012) line ($d = 2.20$ Å) of the nickel arsenide solid-compound structure, which he interprets as evidence for gold-tin aggregation in the liquid state.

The difference in the diffracted intensity magnitude for the four mercury-thallium liquids indicates that there are considerable differences in the structures of the liquids studied, although they were all examined at the same temperature. Since thallium has approximately the same scattering factor as mercury, the intensity functions for the five liquids should, other factors being equal, be similar. Consideration of the differences in size between the mercury and thallium atoms would lead to a regular and gradual variation in the intensity functions. However, since the intensity scattered is low for a liquid corresponding

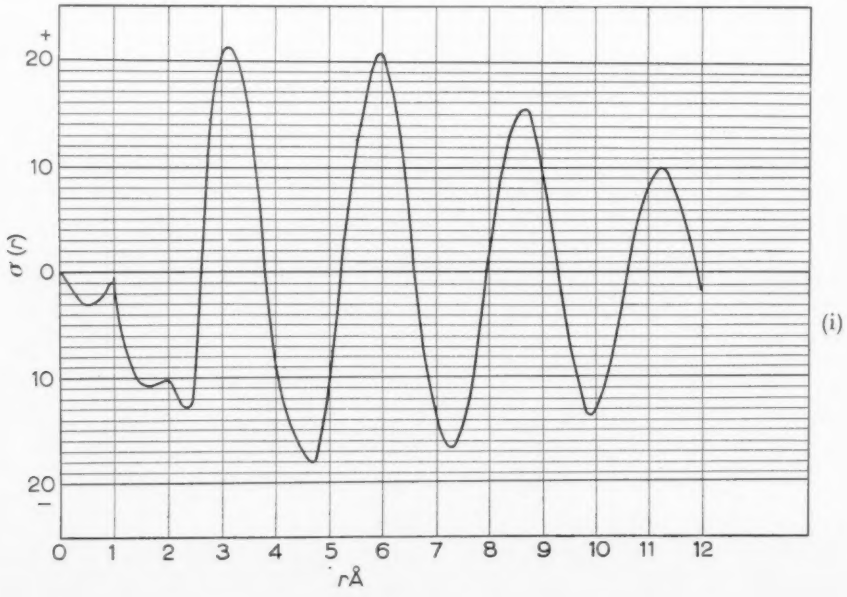

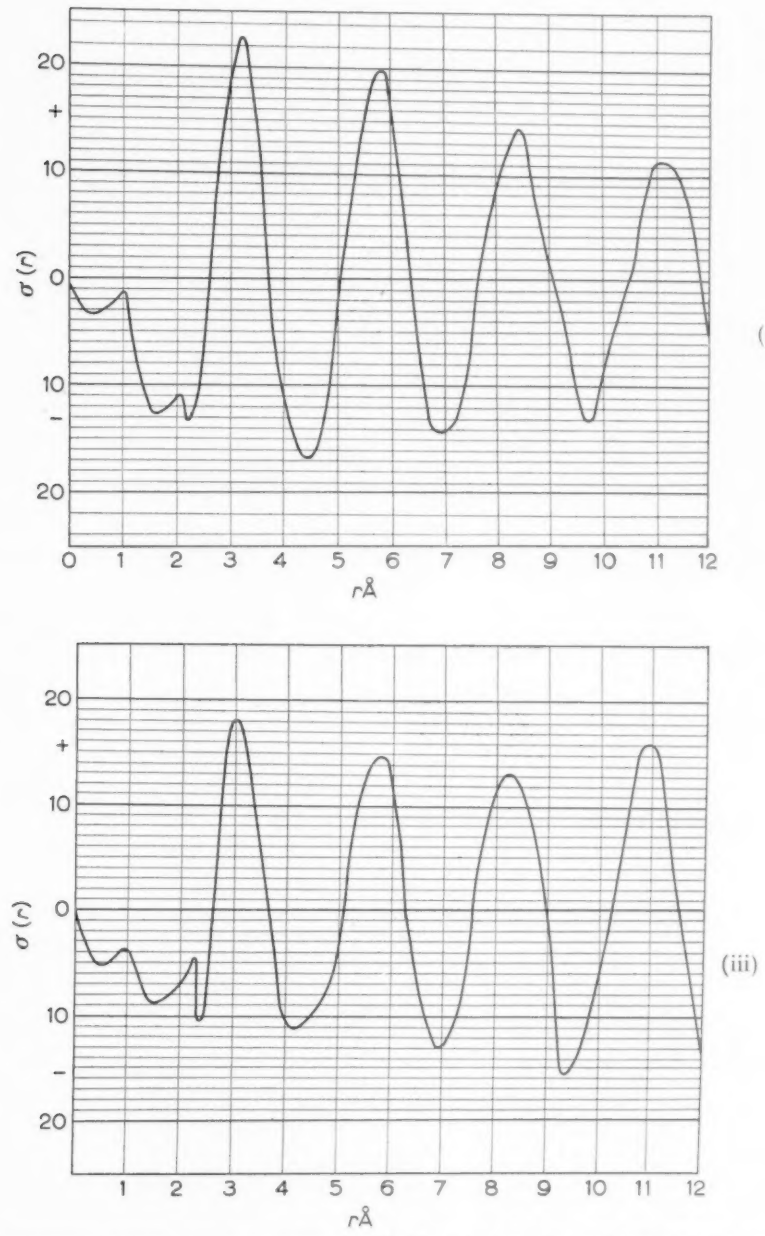

FIG. 6. Electronic distribution curves for (i) 30% Tl, (ii) 34% Tl, and (iii) 40% Tl alloys.

to the eutectic composition and high for that of the compound composition, it appears that the structure of the liquid is influenced by the corresponding solid. The different values of the co-ordination number observed for the liquids substantiate this, and it appears that at a given temperature the liquid structure will be more ordered at a composition corresponding to a compound in the solid state than at a eutectic where the melting-point is lower. In terms of a dislocation model of liquids, this implies that at the melting-point the density of dislocations is a minimum for the liquid state ($\sim 10^{13}$ lines/cm^2) and increases with rise in temperature.

The characteristic interatomic distances, for the four alloys, taken from the radial distribution functions cannot be accounted for on a simple statistical mixture of mercury and thallium atoms. From the radial distribution curves of Hendus, the interatomic distance for thallium is 3.25 Å, and since that for mercury is 3.1 Å, the 8.5%, 30%, and 40% alloys

should have the values of 3.11, 3.14, and 3.16 respectively. The results obtained from the 8.5% and 40% alloys could be in agreement with such a random mixing, since the accuracy in estimating the interatomic distance is not expected to be better than 0.05 Å. However, the value of 3.3 Å obtained for the liquid alloy of the compound composition is significantly larger than either of the eutectics or pure metals. This larger value would be consistent with an aggregation of Hg_5Tl_2 molecules continually forming and breaking up in a matrix of disordered mercury and thallium atoms, since the closest distance of approach in this structure is about 3.3 Å. This may, therefore, indicate that the tendency for aggregation at 2 to 3° above the melting-point is not great enough to lead to appearance of a discrete peak characteristic of the compound, but is sufficient to cause an appreciable movement of the diffraction peak.

ACKNOWLEDGMENTS

We wish to thank Dr. H. M. Finniston for consistent encouragement during the course of this work. Thanks are also due to Miss J. Hume-Rothery, who assisted in the experiments while on vacation study, and to Dr. Howlett and Mr. Crouch of Theoretical Physics Division for help with the numerical integration.

REFERENCES

1. B. R. T. Frost *A.E.R.E. Report M/TN* 21.
2. J. H. Hildebrand and E. D. Eastman *J. Amer. Chem. Soc.* **37,** 2452 (1915).
3. T. W. Richards and F. Daniels *J. Amer. Chem. Soc.* **41,** 1732 (1919).
4. G. N. Lewis and M. Randall *J. Amer. Chem. Soc.* **43,** 233 (1921).
5. F. Sauerwald and W. Teske *Zeits. Anorg. Chem.* **210,** 247 (1933).
6. F. Sauerwald and E. Osswald *Zeits. Anorg. Chem.* **257,** 195, 1948.
7. P. Debye *Amm. Phys.* **46,** 809 (1915).
8. C. Finbak *Acta. Chem. Scand.* **3,** 1272 (1949).
9. J. Waser and V. Shoemaker *Rev. Mod. Phys.* **25,** 671 (1953).
10. W. L. Bragg and J. West *Phil. Mag.* **10,** 823 (1930).
11. B. E. Warren *J. App. Phys.* **4,** 236 (1936).
12. N. Gingrich *Rev. Mod. Phys.* **15,** 90, (1943).
13. G. H. Vineyard *J. Chem. Phys.* **22,** 1665 (1954).
14. R. E. Jennings (see *Acta Cryst.* **5,** 1 (1952), Figure 3).
15. A. H. Compton and S. K. Allison, X-Rays in Theory and Experiment.
16. H. Hendus, *f. Naturforsch.* **29,** 505 (1947).
17. R. N. Boyd and H. R. Wakeham *J. Chem. Phys.* **7,** 958 (1939).
18. J. A. Campbell and J. N. Hildebrand *J. Chem. Phys.* **11,** 330 (1943).
19. F. Sauerwald *Zeits. f. Metal* **41,** 97 (1950).
20. H. Hendus *Zeits. f. Naturforsch* **3,** 416 (1948).
21. R. E. Jennings Private communication.

VOL
4
195

THE EFFECT OF ADDITION ELEMENTS ON THE ELECTRICAL RESISTIVITY OF α-TITANIUM*

S. L. AMES†‡ and A. D. McQUILLAN†

As part of a study of the effect of alloying elements on the anomalous electrical resistivity of metallic titanium, resistivity measurements at temperatures up to about 800°C have been made on a series of solid solutions based on the hexagonal α modification of titanium. The addition elements, though limited in number and concentration range by the very restricted solubility of many elements in α-titanium and by difficulties in fabricating suitable specimens, have been selected to represent a series of different valencies, and one interstitial element, oxygen, has been included. The results have indicated that the metallic elements, from the point of view of their effect on the resistivity of α-titanium, can be grouped into two classes—transition metals and others. Oxygen differs from the nontransition metals only in its effect on the temperature at which the anomalous resistivity behavior begins. The significance of the results is discussed, and it is concluded that the findings cannot be finally interpreted until information on other electron-dependent properties of titanium alloys becomes available.

L'EFFET D'ÉLÉMENTS D'ADDITION SUR LA RÉSISTIVITÉ ÉLECTRIQUE DU TITANE α

Dans le cadre d'une étude de l'influence d'éléments d'alliage sur la résistivité électrique anormale du titane métallique, des mesures de résistivité ont été effectuées à des températures allant jusqu'à 800°C sur une série de solutions solides dans le cas de la forme α hexagonale du titane.

Les éléments d'addition, bien que limités en nombre et en concentration par la solubilité réduite de beaucoup d'éléments dans le titane α et par les difficultés de préparation, ont été choisis avec des valences différentes et un élément interstitiel, l'oxygène, a été inclus. Les résultats ont montré qu'en ce qui concerne leur influence sur la résistivité de titane α, les éléments métalliques peuvent être groupés en deux classes—lés métaux de transition et les autres. L'oxygène diffère des métaux de la 2e classe par son effet sur la température pour laquelle le comportement anormal de la résistivité commence; La signification des résultats est discutée et l'on conclut qu'ils ne peuvent être interprétés complètement sans information complémentaire sur les propriétés électroniques des alliages de titane.

DER EINFLUSS VON LEGIERUNGSZUSÄTZEN AUF DEN ELEKTRISCHEN WIDERSTAND VON α-TITAN

Als Teil einer Untersuchung über den Einfluss von Legierungszusätzen auf den anomalen elektrischen Widerstand von metallischem Titan wurden an einer Reihe von Mischkristallen mit der Struktur der hexagonalen α-Modifikation des Titans bei Temperaturen bis zu etwa 800°C Widerstandsmessungen durchgeführt. Die Auswahl der Zusatzelemente erfolgte unter dem Gesichtspunkt, eine Reihe von verschiedenen Wertigkeiten zu erfassen, obohl wegen der sehr gewingen Löslichkeit vieler Elemente im α-Titan und der Schwierigkeit, brauchbare Proben herzustellen, die Zahl und der Konzentrationsbereich der verwendbaren Elemente beschränkt ist. Zusätzlich wurde Sauerstoff, ein Element, das auf Zwischengitterplätzen eingebaut wird, verwendet. Die Ergebnisse zeigten, dass man die metallischen Elemente hinsichtlich ihres Einflusses auf den Widerstand des α-Titans in zwei Gruppen einteilen kann, in die Übergangsmetalle und die übrigen Metalle. Sauerstoff unterscheidet sich von den Nicht-Übergangsmetallen nur in seinem Einfluss auf die Temperatur, bei der das anomale Widestandsverhalten beginnt. Aus der Diskussion über die Bedeutung der Ergebnisse ergibt sich, dass dass Versuchsmaterial nicht endgültig erklärt werden kann, bevor weitere Kenntnisse über andere Eigenshaften von Titan-Legierungen, die ebenfalls von der Elektronenstruktur abhängen, verfügbar sind.

INTRODUCTION

The form of the resistivity/temperature curve of the low-temperature, hexagonal close-packed, α form of titanium has been determined by a number of previous workers.[1, 2, 3, 4] From 20° to approximately 400°C, the resistivity of titanium was found to be a linear function of temperature, as would be expected of a pure metal at temperatures higher than the Debye temperature of the material. Above 400°C, however, the rate of change of resistivity ρ with temperature T decreased progressively as the temperature of the allotropic transformation (882.5°C)[5] was approached. This may be seen from Fig. 1, in which the resistivity temperature curve for the titanium used in the work described in this paper is presented. The quantity $d\rho/dT$ falls from 178×10^{-9} ohm/deg C at 400°C to a very low value immediately below the α-β transformation temperature. Any theoretical explanation for the form of the resistivity-temperature

* Received February 16, 1956.

† Department of Physical Metallurgy, University of Birmingham, England.

‡ Now at Research Department, Imperial Chemical Industries Ltd. (Metals Division), Birmingham.

VOL. 4 1956

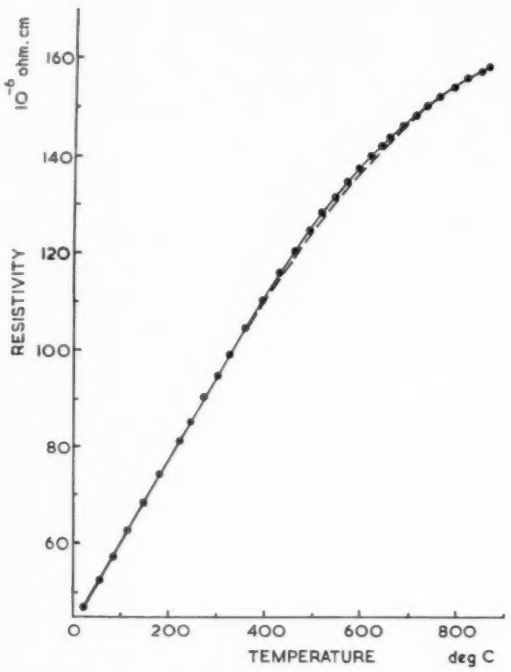

FIG. 1. Resistivity/temperature curve of α-titanium. The broken line represents the curve of best fit using an equation of the form

$$\rho = a + bT - pe^{-q/T}$$

curve of α-titanium must, therefore, account for both the deviation of the curve from linearity at high temperatures and for the high value of $d\rho/dT$ at room temperature.

The resistivity of a metal is dependent upon the number of electrons available for conduction and upon the amount of scattering suffered by them during interaction with the thermally vibrating metal atoms. The Debye temperature of α-titanium is not abnormally low[6] and the high resistivity of the metal at room temperature cannot therefore be attributed to an excessive elastic scattering of the conduction electrons by lattice atoms having thermal vibrations of large amplitude. This can be illustrated by the fact that when the resistivity of α-titanium is reduced to the value it would have if the metal atoms were in a standard state of thermal vibration, the reduced resistivity $M\rho\theta^2/T$ (where M is the atomic weight, θ the Debye temperature, and T the temperature at which the resistivity ρ has been measured) is still very high compared with most other metals.

As has been suggested by Mott,[7] the scattering of conduction electrons in a metal will be enhanced if an interaction between them and a partially filled d band can occur. This type of interaction will, however, only be important if there is a high density of vacant electronic energy states at the top of the d band. In titanium, which as a free atom contains only two $3d$ electrons, it would be expected that the $3d$ band in the metallic state would extend over a wide range of energies and the density of energy levels at the top of the filled portion of the band would consequently be quite low. Studies of the soft X-ray spectrum of titanium metal[8] tend to confirm this supposition, although a measurement of the electronic specific heat of the metal by Friedberg *et al.*[9] would seem to support the assumption of a fairly high density of states at the top of the d band in titanium. It would seem, therefore, that the high resistivity of the metal at room temperature can only be attributed to the existence of sub-bands within the $3d$ band as suggested by Goldman[10] and Kriessman and Callen[11] or to a small effective number or mass of conduction electrons brought about by the existence of a zone of forbidden energy levels immediately above the Fermi level of these electrons in titanium.

The lack of any accepted explanation of the high resistivity of titanium at temperatures below 400°C is a severe disadvantage when we come to consider possible reasons for the deviation of the resistivity/temperature curve from linearity above that temperature. The fact, however, that the extent of the deviation from a linear resistivity-temperature relationship increases rapidly with increasing temperature suggests strongly that a thermally-activated process involving the conduction electrons is taking place. The possibility of the existence of such a process is strengthened by the fact that a straight line is obtained if the magnitude of the difference $\Delta\rho$ between the actual resistivity and the value which it would have been expected to attain at the same temperature had the resistivity continued to increase linearly with increasing temperature above 400°C is plotted logarithmically as a function of the reciprocal of the absolute temperature (see Fig. 2).

At the present stage of our knowledge of the electronic structure of metallic titanium it is impossible to attempt a purely theoretical interpretation of the form of the resistivity/temperature curve. It may be mentioned at this point, however, that the resistivity/temperature curves of both zirconium[12, 13] and hafnium[14] are similar in form to that of titanium, and hence this type of electrical behavior is common to at least three of the Group IVA elements. It is likely, therefore, that a study of the electrical properties of titanium and its alloys will throw some light upon the question of the electronic structure of the transition elements in the earlier part of the long periods of the Periodic Table. In particular, observation of the effect on the electrical properties

VOL
4
195

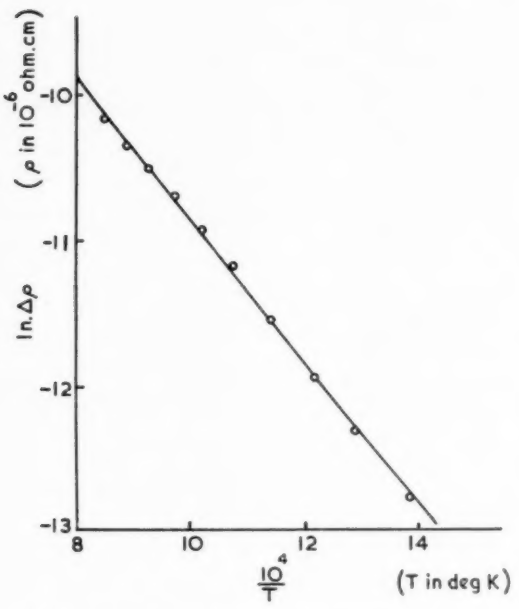

FIG. 2. Relationship between the logarithm of the extent of the deviation, $\Delta\rho$, of the resistivity of α-titanium from linearity at high temperatures and reciprocal of the absolute temperature.

of deliberate electronic changes brought about by the addition of alloying elements of different electronic structure, is likely to provide useful information, and it was for this reason that the resistivity/temperature relationships in dilute α phase titanium-rich alloys described in the present paper were examined.

An attempt was made, when selecting alloying elements to be added to titanium to form α-phase solid solutions, to include among them elements having as many different types of electronic structure as possible. Metals of valency one, three, and four were represented by copper, aluminum, and tin. No element of valency two was used because of the difficulty of preparing homogeneous alloys of titanium with these metals and also because no reliable data were available on the solid-solubility limit of any of them in α-titanium. The negligibly small solubility of the transition elements between chromium and iron in α-titanium prevented any of these metals being used as alloying additions. Niobium, which lies in the adjacent group of the periodic table to titanium, does, however, show a small range of solubility in α-titanium, and one alloy of this system was, therefore, examined. Zirconium, which belongs to the same group of elements as titanium, is completely miscible with it in the α form, and has, furthermore, a resistivity/temperature curve closely similar in form to that of α-titanium, appeared likely to be a particularly interesting alloying element, and a number of titanium-zirconium alloys were therefore examined. All the foregoing addition elements form substitutional solid solutions with titanium, and it was felt that an alloy containing an interstitial addition element should be included in this survey. Oxygen, nitrogen, and carbon all give rise to interstitial solutions in titanium, but unfortunately all produce marked embrittlement of the material. Since rod-shaped specimens were required for the resistivity work, fabrication difficulties limited the study of interstitial alloys to a very low concentration range. A titanium-oxygen alloy containing 1.5 at. per cent oxygen was eventually chosen as a representative of this class of alloy. The range of alloys studied is given in Table 1.

TABLE I.

Addition element	Composition or composition range studied (at. per cent)
Aluminum	0–8
Tin	0–8
Zirconium	0–50
Copper	1.0
Niobium	1.0
Oxygen	1.5

EXPERIMENTAL METHODS

The methods used for the production of alloy specimens and in the determination of the resistivity/temperature curves have been described in detail in an earlier paper.[4] Only a brief summary of the important features of the methods need, therefore, be given here.

Iodide-refined titanium having an α-β transformation range (as determined by the hydrogen pressure method[2] of 879° to 884°C and a hardness of 80 V.H.N., was used for the preparation of the alloys. The aluminum, tin, and copper were all 99.99% pure, the niobium as supplied by Johnson Matthey Ltd. was spectroscopically pure, while the zirconium, which was iodide-refined metal, contained about 2.5% hafnium. The oxygen alloy was prepared by adding spectroscopically pure titanium dioxide in which the only appreciable impurity could have been a slight trace of titanium nitride.

Alloy ingots were prepared by melting the component metals in an arc furnace under an argon atmosphere at reduced pressure and were subsequently hot-forged into rods 6 mm in diameter. Homogenizing treatments of about 2 days duration were carried out under vacuum at 1000°C, or, in cases in which this temperature lay within a two-phase region, at the highest temperature at which the alloy

VOL. 4 1956

was able to exist in the α-phase condition. The homogenized materials were reduced to rods of 2.0-mm diameter suitable for resistivity specimens by cold-swaging and were then vacuum stress-annealed at the highest possible temperature below 1000°C in the α-phase region.

In all the materials used in this work, the axial ratio of the close-packed hexagonal cell of the α phase is less than the value for ideal close packing ($c/a = 1.587$ for pure titanium[15]). The possibility therefore arises that some degree of anisotropy of the electrical resistivity may exist in these materials, and hence the resistivity of a particular specimen may depend to an unknown extent on the amount of preferred orientation present in the polycrystalline specimens. It was for this reason that a standard method for specimen fabrication and annealing was adopted so that the degree of preferred orientation in each specimen could be reproduced at a later date should this prove to be of interest. In the present work no attempt has been made to estimate the magnitude of the anisotropy effects.

Resistance measurements were made, using a double-balance bridge, titanium potential and current leads being used to avoid contamination of the heated alloys. For high-temperature measurements, the specimen was enclosed in a continuously evacuated silica sheath in which the pressure was approximately 10^{-6} mm of mercury. A diagrammatic representation of the apparatus has been presented in the earlier paper.[4]

The room-temperature resistivity of the alloy specimens was computed from measurement of the specimen resistance between accurately spaced knife-edged potential contacts. The results are accurate to within 1%, the rather large error in this quantity being due to difficulties in measuring the cross-sectional diameter of the rods because of the presence of a slight surface rumpling due either to thermal etching effects produced during the final annealing treatment or to the existence of anisotropic effects in the thermal expansion and contraction during the final thermal cycle of the stress-relief anneal. The specimen resistance was measured at intervals of 20°C from room temperature to the upper limit of the α-phase region, or to 1000°C if the α phase was stable above this temperature. The specimen temperature was maintained within ±0.1°C during the course of each individual measurement, and changes in the resistance of a single specimen with temperature could be given, therefore, to an accuracy of at least 0.1%. In order to detect spurious resistance changes brought about by contamination of the specimen or electrical faults in the apparatus, the resistance measurements were taken in a random sequence of temperatures.

EXPERIMENTAL RESULTS

Experimentally determined resistivity/temperature curves for the series of α-phase titanium-rich alloys studied are presented in Figs. 3 to 6. The effect of adding the substitutional elements aluminum, tin, zirconium, copper, and niobium to titanium is, in all cases, to increase the magnitude of the high-temperature deviation of the resistivity/temperature curve from linearity. Oxygen, the interstitial alloying element, is exceptional and reduces the extent of the deviation from linearity. The increase in deviation produced by the substitutional elements is quite marked, with the exception of that due to zirconium, which is much less effective than the other metallic elements. In cases in which the low-temperature part of the resistivity/temperature curve is linear (i.e. all the alloys studied except those containing more than 5 at. per cent aluminum and tin) it has been possible to obtain a numerical estimate of the extent of the curve's departure from a linear relationship at higher temperatures, and hence to plot it logarithmically as a function of the reciprocal of the absolute temperature. The relationship between the two quantities has proved to be linear in every instance, and the

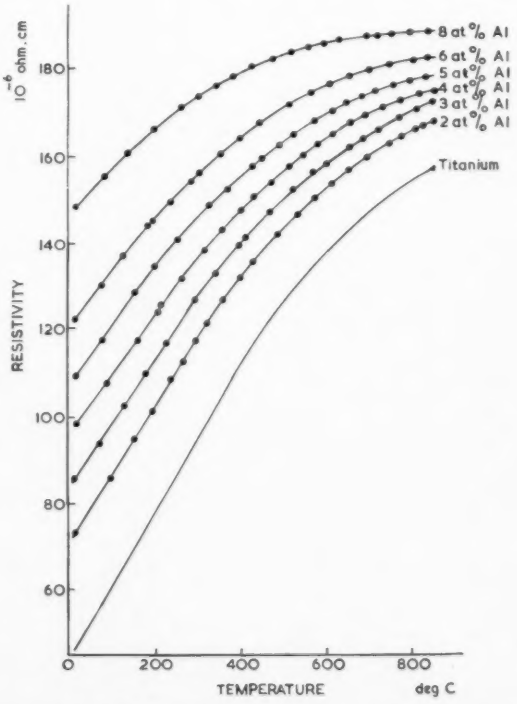

FIG. 3. Resistivity/temperature curves of a series of α-phase titanium-aluminum alloys.

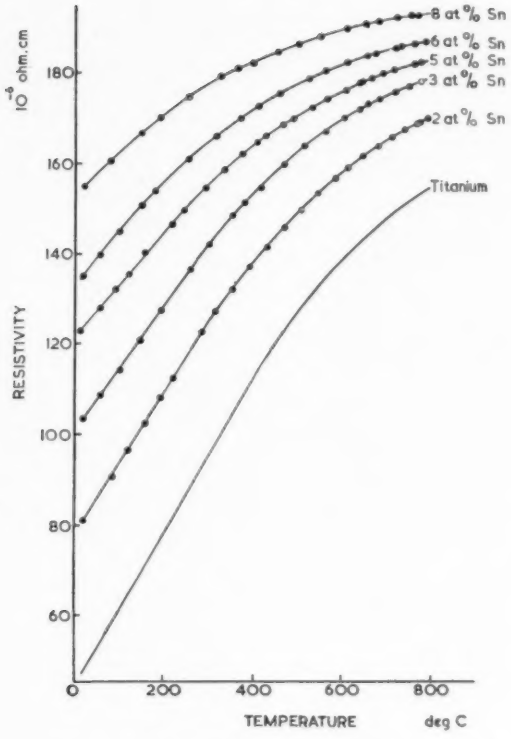

FIG. 4. Resistivity/temperature curves of a series of α-phase titanium-tin alloys.

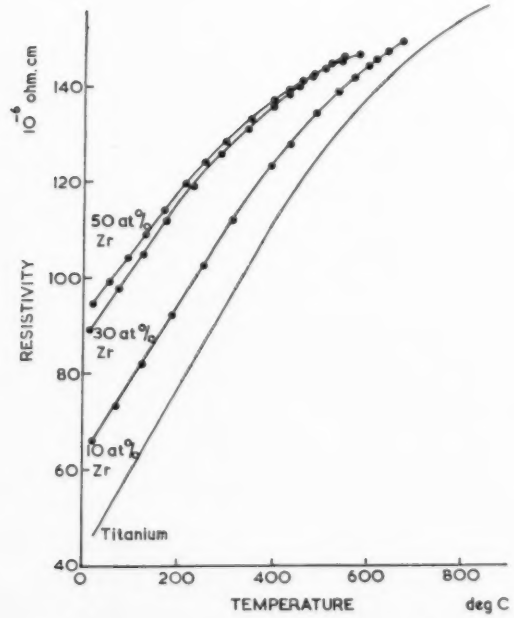

FIG. 5. Resistivity/temperature curves of a series of titanium-zirconium alloys.

experimentally determined resistivity/temperature curves of the alloys concerned may, therefore, be expressed analytically in the form of the equation

$$\rho = a + bT - pe^{-q}/T \qquad (1)$$

where a, b, p, and q are constants for any particular alloy over the temperature range considered in this paper. It is very probable that this type of relationship would be equally valid for titanium-aluminum and titanium-tin alloys of higher concentration than 5 at. per cent, but unfortunately the form of equation (1) is such that no accurate deduction of the value

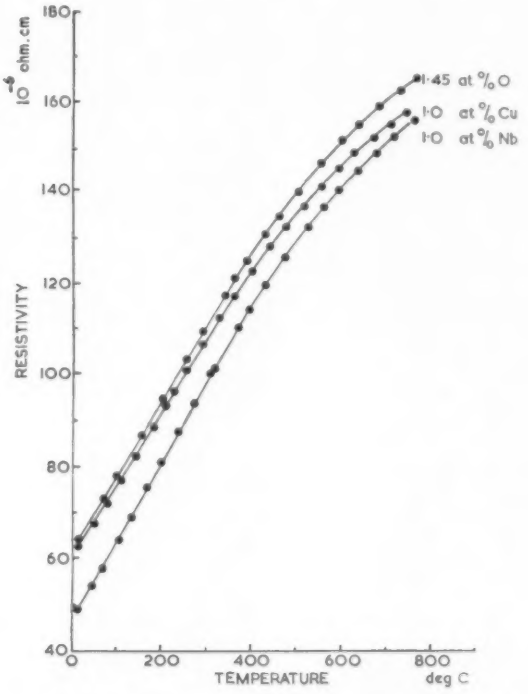

FIG. 6. Resistivity/temperature curves of α-phase titanium-oxygen, -copper, and -niobium alloys.

of the constants in the equation can be obtained by a direct substitution of the experimental results in it. No quantitative analysis of the form of the curves for higher tin and aluminum alloys has, therefore, been possible.

DISCUSSION OF RESULTS

In Fig. 7 the resistivities of the various α-phase alloys at room temperature have been plotted as a function of alloy composition. It is immediately apparent that the increase in resistivity of α-titanium on alloying bears little or no relationship to the usually accepted valency of the added element, as it does in certain simple nontransition metals.[7] It would seem

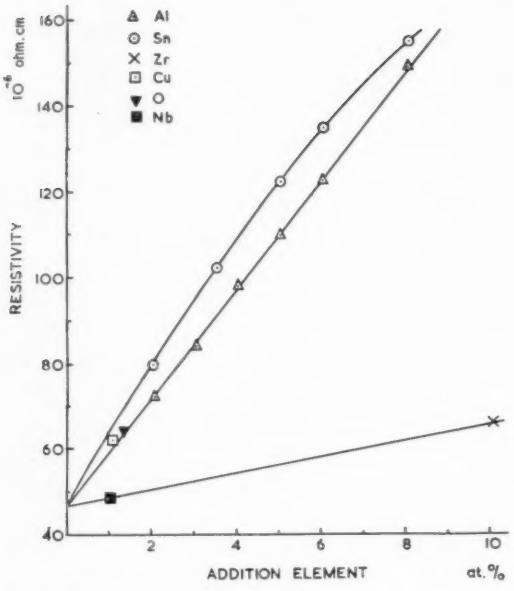

FIG. 7. The effect of various addition elements on the resistivity of α-titanium at room temperature.

from the results shown in Fig. 7 that solute elements which lie close to titanium in the Periodic Table (i.e. zirconium and niobium) bring about only a relatively small increase in the resistivity of α-titanium, whereas a wide selection of nontransition elements including oxygen appear to have a much greater and, surprisingly, an almost equal effect.

The rate at which the resistivity of α-titanium solid solutions increases with addition element concentration at room temperature is very large compared with that for dilute solid solutions based on the more normal metals, such as copper and aluminum. Even the effect of zirconium and niobium on the resistivity of α-titanium, though very much less than that of the other elements studied, is much greater than the normal effect of solute additions. The result is not entirely unexpected, since, in a metal such as titanium, which exhibits a remarkably high resistivity at moderately low temperature, the high resistivity must be due to either a small number of conduction electrons or a low effective mass of such electrons. In either case, the presence of randomly distributed solute atoms on the metal lattice would be expected to lead to a pronounced increase in the resistivity of the material. That the abnormally high value of $d\rho/dc$ in titanium-rich alloys is not due to any special electronic effect introduced when the alloying elements are added to the metal, can be illustrated by the fact that the relative increase in resistivity due to alloying, $(1/\rho_\alpha)(d\rho/dc)$, (where ρ_α is the resistivity of α-titanium) is of the same order of magnitude as that found in copper-, gold- or aluminum-rich alloys. The existence of a strong interaction between the conduction electrons and the metal atoms in titanium is consistent with the supraconducting behavior of the metal[14, 15] if the Fröhlich-Bardeen theory of that phenomenon is accepted.

The deviation from linearity of the resistivity/temperature curves of α-phase titanium-rich alloys at elevated temperatures is always towards a lower resistivity, and it would seem, therefore, that as the temperature is raised, the strong electron-atom interaction which exists at low temperatures begins to weaken. The exponential term in equation (1) suggests that the conduction electrons are being excited over an energy gap which, if the coefficient q is assumed to be the quotient of an activation energy and Boltzmann's constant, is of the order of 0.5 eV wide for the titanium alloys under examination. This point is put forward with some reserve, and it may later prove to have been an over-simplified interpretation of the form of the experimental curves.

It is interesting to consider systematically the effect of changes in the concentration of addition elements on the values of the coefficients p and q in the exponential term of equation (1). Figs. 8 and 9 show p and q as functions of alloy composition. The forms of the p/concentration and q/concentration curves for each individual addition element are very similar and suggest that the two quantities p and q are closely interrelated. A plot of p against q given in Fig. 10 indicates that, with the exception of the points derived from the titanium-zirconium alloys, all other points lie on a single smooth curve irrespective of the nature or concentration of the addition element, a fact which

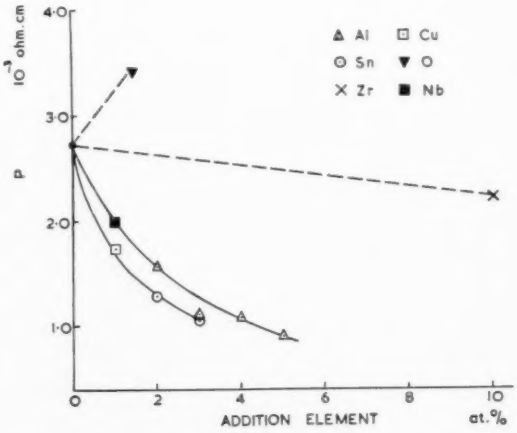

FIG. 8. The variations of the quantity p in equation (1) as a function of addition element concentration for the titanium-rich α-phase alloys investigated in the present work.

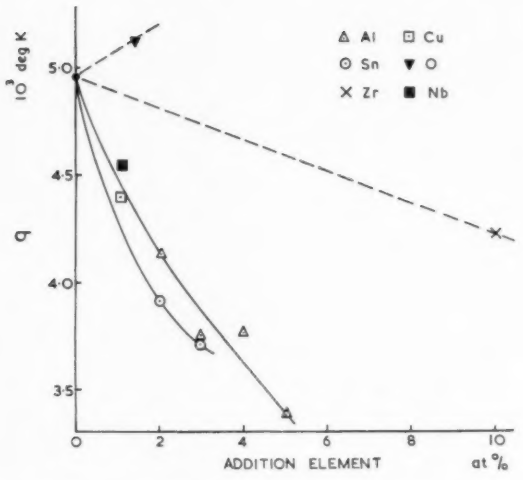

FIG. 9 The variation of the quantity q in equation (1) as a function of addition element concentration for the same alloys as those indicated in Fig. 8.

strongly suggests that the interrelationship between p and q is a consequence of a particular electronic effect existing in pure titanium metal and that alloying additions do not alter the fundamental character of the phenomenon.

With the exception of zirconium, which does not give rise to values of p and q lying on the p/q curve common to the other addition elements, none of the metals added to titanium show anomalies of the type observed in titanium in their own resistivity/temperature curves. It would be expected, therefore, that if complete solid solubility between α-titanium and these elements were possible, increasing addition-element concentrations should bring about a gradual decrease in the importance of the exponential term in equation (1) which would eventually become zero for the pure addition element. Unfortunately, elements other than those of Group IVA have only limited solubility in α-titanium, and the point cannot be checked experimentally. In the case of zirconium, with which titanium is completely mutually soluble, the argument does not apply, because the resistivity/temperature curve of pure α-zirconium has the same form as that of α-titanium, and hence can also be described in terms of equation (1). Values of p and q for pure α-zirconium have not been obtained by us, because zirconium metal satisfactorily free from both hafnium and oxygen was not available, but it would be expected that these quantities for pure α zirconium would not necessarily be numerically equal to those obtained for α-titanium. The p/q relationship for titanium-zirconium alloys must, therefore, change continuously from that of pure titanium to that of pure zirconium. The points plotted for titanium-zirconium alloys in Fig. 10 suggest that this is indeed the case, since they lie on a separate curve which intersects the curve common to all other alloys at the point corresponding to pure titanium.

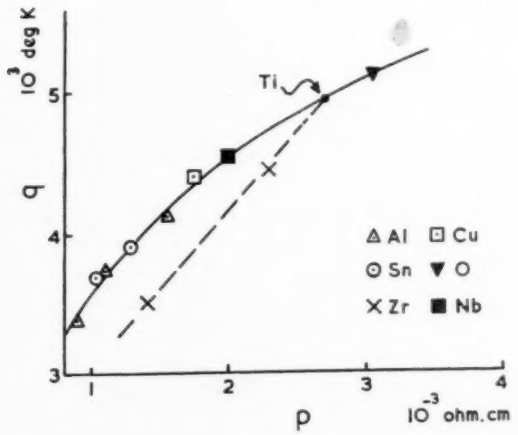

FIG. 10. Interrelationship between p and the corresponding value of q in equation (1) for the titanium-rich alloys considered in Figs. 8 and 9.

CONCLUSION

It does not appear possible, at the present stage of our knowledge of the electronic structure of titanium, to put forward a satisfactory theoretical explanation of the effects observed in this work. No simple interpretation of the results in terms of Brillouin-zone effects have so far met with any success, and it is felt that the anomalous electrical behavior of titanium and titanium-rich alloys must, therefore, be connected in some way with the configuration of the d-electrons in the metal. In view of the mathematical difficulties experienced in attempting to obtain a direct quantum mechanical solution of the problem of the electronic structure of titanium,[18] it would seem that the only course at present open to us is to obtain more information on other properties of titanium and its alloys which are dependent, like the electrical resistivity, on the electronic structure of the material. When these become available, it may then be possible to formulate a number of possible solutions to the problem capable of direct check by either further experimental or theoretical investigation.

REFERENCES

1. J. H. DE BOER, W. G. BURGERS, and J. D. FAST *Proc. Acad. Sci. Amst.* **39**, 515 (1936).
2. A. D. McQUILLAN *J. Inst. Met.* **78**, 249 (1950–51).
3. J. L. WYATT *Trans. Amer. Inst. Min. Met. Eng.* **197**, 903 (1953).
4. S. L. AMES and A. D. McQUILLAN *Acta Met.* **2**, 831 (1954).
5. A. D. McQUILLAN *Proc. Roy. Soc.* **204**, 309 (1950).

VOL. 4 1956

6. C. W. KOTHEN and H. L. JOHNSON *J. Amer. Chem. Soc.* **75,** 3101 (1953).
7. N. F. MOTT and H. JONES *The Theory of the Properties of Metals and Alloys* O.U.P. (1936).
8. H. W. B. SKINNER, T. G. BULLEN, and J. E. JOHNSON *Phil. Mag.* **45,** 1070 (1954).
9. S. A. FRIEDBERG, I. ESTERMANN, and J. E. GOLDMAN *Phys. Rev.* **85,** 375 (1952).
10. J. E. GOLDMAN *Rev. Mod. Phys.* **25, 108** (1953).
11. C. J. KRIESSMAN and H. B. CALLEN *Phys. Rev.* **94,** 837 (1954).
12. H. K. ADENSTEDT *Trans. Amer. Soc. Metals* **44,** 949 (1952).
13. B. A. ROGERS and D. F. ATKINS *Trans Amer. Inst. Min. Met. Eng.* **203,** 1034 (1955).
14. J. D. FAST *J. Appl. Phys.* **23,** 350 (1952).
15. H. T. CLARK *Trans. Amer. Inst. Min. Met. Eng.* **185,** 588 (1949).
16. T. S. SMITH, W. B. GAGER, and J. G. DAUNT *Phys. Rev.* **89,** 654 (1953).
17. M. C. STEELE and R. A. HEIN *Phys. Rev.* **92,** 243 (1953).
18. B. SCHIFF *Proc. Phys. Soc.* **68,** 686 (1955).

VOL
4
195

INTERNAL FRICTION IN ALLOYS OF Mg AND Cd*

J. LULAY† and C. WERT‡

The internal friction of alloys of Mg and Cd has been studied in the range 8% to 30% Mg. An order peak is observed near room temperature for all alloys in this composition range. The behavior of the internal friction for this alloy system is quite different from that for Cu–Zn and Ag–Zn in the same composition range. This is thought to be caused by the difference in structure at the composition AB_3; $MgCd_3$ possesses long-range order at 20°C, whereas the 25% alloys of Zn in Cu and Zn in Ag do not. The effects observed in alloys of Mg and Cd are shown to be consistent with all facts known about the constitution diagram. They seem also to be consistent with data obtained for the kinetics of ordering of $MgCd_3$.

LE FROTTEMENT INTERNE D'ALLIAGES DE Mg ET Cd

Le frottement interne d'alliages de Mg et Cd a été étudié pour des concentrations de 8% à 30% de Mg. Un pic d'orde est observé à la température ordinaire pour tous les alliages de cette gamme. L'évolution du frottement interne pour ce système est tout-à-fait différente de celle observée sur Cu-Zn et Ag-Zn dans le même domaine de composition. On pense que cela est dû à la différence de structure à la composition AB_3; $MgCd_3$ présente un ordre à grande distance à 20°C, ce qui n'est pas le cas pour les alliages à 25% de Zn dans Cu et Ag. Les effets observés dans ces alliages Mg et Cd sont en accord avec tous les faits connus du diagramme d'état. Ils semblent également s'accorder avec les données de la cinétique d'ordre de $MgCd_3$.

INNERE REIBUNG IN Mg-Cd LEGIERUNGEN

Die innere Reibung von Mg-Cd Legierungen wurde im Bereich zwischen 8% und 30% Mg untersucht. Für alle Legierungen aus diesem Zusammensetzungsbereich wird in der Gegend der Raumtemperatur infolge des Einflusses der Ordnungsstruktur ein Dämpfungsmaximum beobachtet. Das Verhalten der inneren Reibung in diesem Legierungssystem unterscheidet sich stark von dem bei Cu-Zn und Ag-Zn im gleichen Konzentrationsbereich. Es wird angenommen, dass dies von der unterschiedlichen Struktur bei der Zusammensetzung AB_3 herrührt. In $MgCd_3$ Liegt bei 20°C Fernordnung vor, während dies bei 25% Zn in Cu bzw. Zn in Ag nicht der Fall ist. Es wird gezeigt, dass die in den Mg-Cd Legierungen beobachteten Effekte mit allen über dan Zustandsdiagramm bekannten Tatsachen übereinstimmen. Sie scheinen auch im Einklang zu stehen mit den Daten, die man aus derKinetik der Ordnungsvorgänge in $MgCd_3$ erhält.

VOL. 4 1956

1. INTRODUCTION

One of the most puzzling of all the internal friction effects presently under study is that caused by stress-induced ordering in certain substitutional alloys. This phenomenon, first seen by Zener in a 30% Zn-Cu alloy,[1] has been observed later in many other substitutional alloys. However, even with all the data so far available, it has been difficult to establish criteria for the existence and magnitude of the effect in terms of other facts known about a given alloy system. This is unfortunate, since it appears that proper understanding of the effect could lead to its successful use in the study of several physical and metallurgical processes occurring in these alloys.

The two alloy systems for which the damping effects have been studied most extensively are the systems Cu–Zn and Ag–Zn.[2, 3] Two pieces of information were obtained from these studies which are of interest here; these concern the magnitude of the damping and the activation energy for the process. (1) The magnitude of the effect goes up roughly as the square of the zinc concentration (at least up to 30 at. per cent zinc). (2) The process is an activated process with an activation energy close to that observed for diffusion in the alloy. The activation energy varies with alloy concentration; it decreases somewhat with increasing zinc concentration in each case.

The earliest explanation of the effect was that offered by Zener, who supposed that the damping had its origin in the microscopic rearrangement of atoms under the application of an external stress.[4] He chose nearest-neighbor pairs of like atoms as the smallest unit which would undergo rearrangement. Later, Nowick[2] and Le Claire and Lomer[6] have postulated more elaborate geometrical schemes for the process. They have, however, retained Zener's idea that the effect arises fundamentally from a microscopic rearrangement of atoms when the material is placed under stress.

If the explanations just referred to are reasonably correct, it is likely that the magnitude of the damping would be greatly influenced by the order occurring

* Received January 27, 1956. This work was sponsored by the Office of Ordnance Research, U.S. Army.

† Battelle Memorial Institute, Columbus, Ohio.
‡ University of Illinois, Urbana, Illinois.

naturally in the crystal. Two extreme cases will illustrate this point. The first is that which is characteristic of those alloys in which no rearrangement of atoms occurs under stress because such rearrangement produces no anelastic strain. There is then no damping arising from this source. This is apparently typical of such alloy systems as Cu–Ni or Ni–Cr. The second extreme is that of the highly-ordered alloys. In this case the damping is also low or absent completely. This is presumably so because the relatively small external stress is not sufficient to significantly change the naturally occurring high degree of order. This effect has been observed in MgCd and β-brass.[6,7]

The work of Le Claire and Lomer enables one to put these thoughts on a more quantitative basis. They presume that the relaxation arises from a lattice dilatation accompanying changes in the degree of order. They further express the damping of a given alloy in terms of a number of parameters, among which they include the short-range order parameter, σ. The expression they derive shows a rather complicated dependence for the damping on σ, but it does go to zero for certain values of σ (for example for $\sigma = 1$, as is the case for β-brass and for $\sigma = 1/3$, as for ordered Cu_3Au. These are the maximum values which σ can take for these compositions. They correspond to complete long-range order in these alloys).

We have made a further experimental study of the influence of ordering on the internal friction arising from this source. The alloys used were the Cd-rich alloys of Mg and Cd. This part of this alloy system was chosen because it contains both a region of normal solid solution and an ordered structure $MgCd_3$.† The specific aims of the experiment were these:

(1) To measure the damping of these alloys as a function of composition. The damping was expected to fall to zero for the composition $MgCd_3$. The variation of the damping with composition in this system can be compared directly with that in the systems Zu-Cu and Zn-Ag, which contain no ordered structure of composition AB_3.

(2) To observe how the activation energy for this process varies with alloy composition.

2. EXPERIMENTAL PROCEDURE

The operations necessary to carry out this investigation are conveniently *divided into three* groups. These are (1) the preparation of the specimens, (2) the making of the damping measurements, and (3) the chemical analysis of the specimens. These will be described briefly.†

The materials used in making up the alloys were high-purity Mg from the Dow Chemical Company and "Super-Purity" Cd from the New Jersey Zinc Company. The Mg was stated to be about 99.99% pure. The actual purity of the Cd is not known; the only impurity reported was a trace of Mg which was observed by spectroscopic means. Small ingots of the various alloys were made by melting together in vacuum small pieces of the constituent metals. The melting was done with the metals contained in a graphite crucible which had been sealed off in a Vycor tube. Mixing was aided by mechanical shaking of the molten metal.

Since the specimens were to be 15-cm lengths of 1-mm wire, some method had to be developed to reduce these ingots to that size. The alloy is too brittle for successful cold forming, so a casting method was developed. By this method, small pieces of the ingot were melted and cast in a Pyrex capillary tube in vacuum. Several wires of the same composition were made from each ingot.

The internal friction at frequencies close to 1 c.p.s. was measured for each specimen by the use of a torsional pendulum.[6] The region of interest for all alloys was around room temperature, so a pendulum was built for measurement both below and above room temperature. The low temperatures (down to −50°C) were obtained by circulating cold acetone through a double-walled jacket around the pendulum. Temperatures higher than 20°C were obtained by use of an electric heating coil wound on this jacket. A measurement was made by first cooling off the equipment to −50°C, then letting it slowly warm up to higher temperatures both by heat transfer to the room and by the use of the heating coil. Measurements were made at frequent intervals during this warm-up period.

Chemical analyses of the samples were made by the sulfate method described by Trumbore, Wallace, and Craig.[8] By this method, a known quantity of the alloy is completely converted to the sulfates of Mg and Cd. These sulfates are dried thoroughly. From a knowledge of the weight of the original alloy and that of the dehydrated sulfates, the composition of the alloy can readily be calculated. Several check analyses of mechanical mixtures of known portions of metallic Mg and Cd showed that the method as we used it was accurate to about 0.3 at. per cent Mg (this accuracy varies slightly over the range of alloys used). Since

† The critical temperature for this ordered structure is about 80°C.

† A full description of these operations can be found in a thesis by John Lulay, Univ. of Ill., 1955.

this accuracy was adequate, we did not develop the method further. To make sure that the analysis made for a given alloy was actually that of the material used for the damping measurement, the specimens themselves were analyzed. Each specimen was cut into three parts after the damping measurements were complete and each part was analyzed separately. The actual composition was taken as an average of these three determinations. The gross inhomogeneity over the length of the specimens was small—of the order of a few tenths atomic per cent.

3. RESULTS AND DISCUSSION

The internal friction when measured at 1 c.p.s. manifested itself in a peak (in temperature) which appeared near room temperature for all alloys examined. The temperature variation of the internal friction is given closely by the equation

$$Q^{-1} = \Delta M \{\tau\omega/(1 + \tau^2\omega^2)\} \quad (1)$$

in which

$$\tau = \tau_0 \exp(\Delta H/RT). \quad (2)$$

In the first of these equations, Q^{-1} is the internal friction, ΔM the magnitude of the relaxation strength, ω the angular frequency of the pendulum, and τ the relaxation time. The second expression gives τ in terms of the activation energy for the process, ΔH, and another constant of the material τ_0.

The data obtained in this study fit these equations rather well; an example is given in Fig. 1 for the alloy of 29.3 at. per cent Mg. The solid line is drawn according to equations (1) and (2), with ΔM chosen to be 0.26, and ΔH 19,000 cal/mol. The experimental

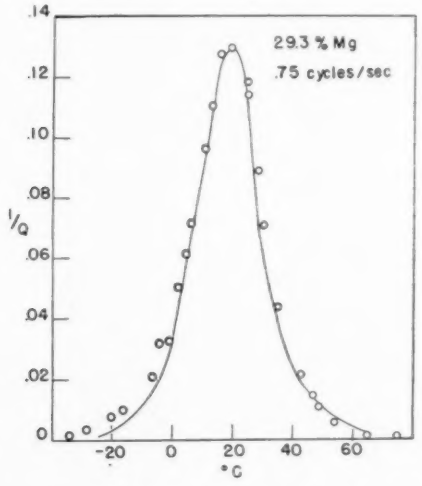

FIG. 1 The "order" peak for an alloy of 29.3 Mg. The solid line is plotted for a single relaxation time, according to equation (1). The adjustable parameter ΔM is fixed to give agreement with the experimental points at 20°C.

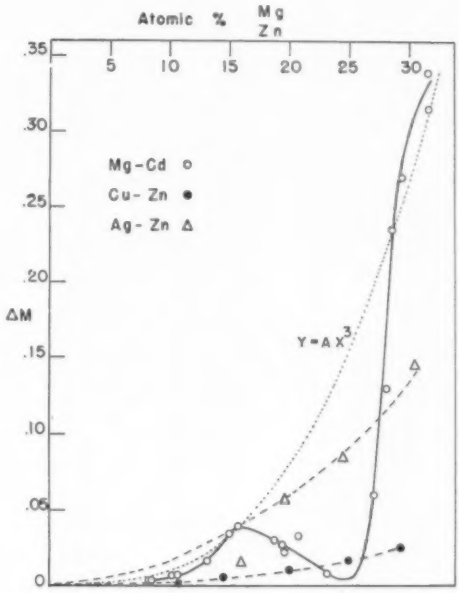

FIG. 2. ΔM vs. concentration for the systems Mg–Cd, Cu–Zn, and Ag–Zn.

data fit equation (1) rather well far down on the sides of the peak, showing that the relaxation is closely characterized by a single relaxation time. This is a general feature of this "order" peak.

The chief item of interest in this study was to see how the magnitude of the peak varies with composition. This behavior is presented in Fig. 2, where the magnitude of the relaxation ΔM is plotted as a function of Mg-content. This curve can be conveniently divided into several parts: (1) a slow increase from zero at 0% Mg to a maximum at 16% Mg, and (2) a more or less linear decrease to a low value at 25% Mg, and (3) a rather linear increase to a high value of ΔM at 32% Mg. Neglecting the dip at 25% Mg, the data fit fairly closely an analytical expression

$$Y = AX^3.$$

A comparison between ΔM for this system and ΔM for alloy systems which contain no ordered structures in this composition range is also given in Fig. 2. Here are plotted data for Ag–Zn and Cu–Zn. The dashed curves in each case are plotted according to the expression $Y = AX^2$, where A is adjusted for each to give the best fit.

The effect of the ordered composition $MgCd_3$ on the behavior of as a function of Mg-content is seen from these comparisons to be very pronounced. The following points can be made:

(1) For alloys up to 16% Mg, the variation of ΔM with concentration is normal as compared to the

VOL. 4 1956

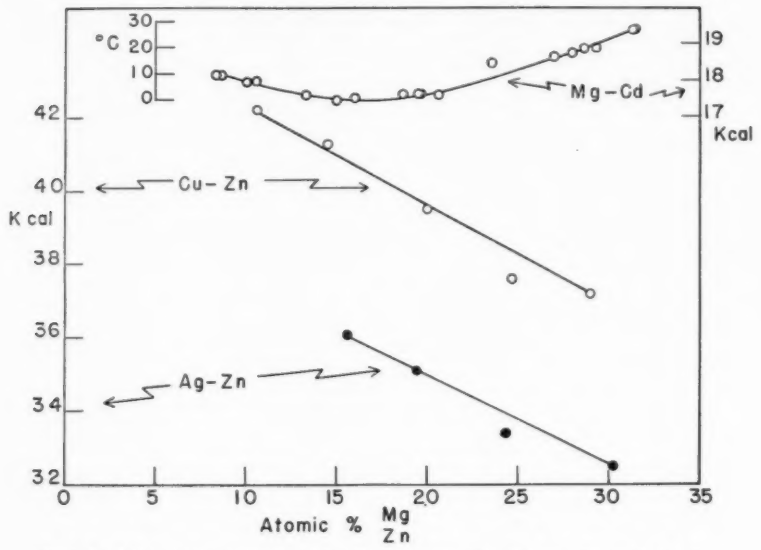

FIG. 3. ΔH in kilocalories/mol for the systems Mg–Cd, Cu–Zn and Ag–Zn.

other systems. This means that the Mg-Cd alloys in this region behave like normal solid solutions. This is in agreement with the observations of Edwards, Wallace, and Craig.[9]

(2) In the region between 16% and 25% Mg the alloy behaves like a two-phase region; i.e. like a mixture of $MgCd_3$ (ordered) and a solid solution of 16% Mg in Cd. This observation also agrees with the X-ray observations of Edwards, Wallace, and Craig.[9]

(3) At the composition $MgCd_3$, the damping is very low (perhaps zero). This is predicted by the expression of Le Claire and Lomer (for an AB_3 alloy with $\sigma = 1/3$).[5]

(4) Above 25% Mg, the alloy again behaves like a mixed phase region to about 32% Mg. There is no evidence from other sources to support this view.

The rate of relaxation is also an interesting feature. This rate is conveniently expressed as the temperature of the maximum of the peak for a given frequency of the pendulum. In Fig. 3 these data are plotted as a function of alloy composition for a frequency of about 0.75 c.p.s. The inset scale for the upper curve shows that for low-Mg content the peak has a maximum around 10°C. It decreases slowly to a minimum of 0°C at about 15% Mg then slowly increases to nearly 30°C at 32% Mg.

It is common to express the temperature dependence of such processes as this exponentially as with equation (2). The significant feature of the rate of the process is then the activation energy, ΔH. In the present experiment the activation energy can be obtained by the well-known method of measuring the shift in peak temperature with a change in frequency of the pendulum. For an alloy of 27% Mg, a value of ΔH so obtained was 18,000 $\pm$ 1000 cal/mol. A second method to measure this same value is the method of Wert and Marx;[10] it is based on their observation that ΔH is a linear function of the peak position (expressed in °K); the value of ΔH can be obtained from a measurement of the peak position at a single frequency. The values of ΔH so obtained for these alloys may be read off the same curve in Fig. 3, using the scale on the right. The single value obtained by the two-frequency method, 18 kcal for an alloy of 27% Mg, fits satisfactorily on the curve.

Since the values of ΔH for this same process in alloys of Cu–Zn and Ag–Zn are already known, comparisons can again readily be made. For this purpose, the data of Childs and Le Claire for Cu–Zn[3] and of Nowick for Ag–Zn[2] are also plotted in Fig. 3. These pieces of data both show a linear decrease of ΔH with alloy concentration for these solid solutions. For Mg–Cd the data also show a decrease below 15% Mg, where a solid solution also exists, but above this composition the data deviate from the "normal" behavior. We have no explanation for this effect at present.

It has been supposed for a number of years that the mechanism by which this ordering occurs is closely related to bulk diffusion. The evidence for this is good.[5, 11] Therefore, diffusion in Cd-rich alloys of this alloy system ought to occur with an activation energy of from 17,000 to 19,000 cal/mol. This should be the case at least for alloys containing less than 15% Mg. Above this composition range, in the two-phase region about $MgCd_3$, it is not clear that this

should be true, however, since in this region the internal friction and a tracer-penetration measurement might measure quite different averages of the movements of the atoms.

In some measurements of the specific heat of $MgCd_3$ by Coffer, Craig, Krier, and Wallace, some interesting observations were made.[12] Among them were these: below 180°K, the degree of order is practically frozen in, at about 180°K, there begins a process occurring over a period of many hours; this process can be attributed to changes in order occurring after temperature changes. It occurs more rapidly the higher the temperature; at 240°K it becomes so rapid that it is hidden by the instrumental transients of their equipment (which comes to equilibrium in about 30 min). They have concluded that the process is the onset of the breakup of the ordered lattice.

Since it is likely that the internal-friction phenomena reported in this paper are also caused by ordering in the lattice, it is quite possible that our measurements are simply related to these specific heat measurements. To show that this is so, we offer the following observations: The relaxation time τ at 180°K can be calculated to be about 1000 hours, at 240°K about 1 min. This means that significant atom movements would be expected to occur in about 1000 hours at 180°K and in about 1 min at 240°K. Hence, at temperatures just below 180°K. Coffer *et al.* would have to wait more than 2 months to see a significant change in the degree of order. On the other hand, at 240°K and above, the changes in lattice configuration occurring in 1 min or less ought to be masked by the half-hour recovery time of their apparatus, as indeed they are. It does appear then that the rates of the phenomena described in this paper and in theirs are quite compatible, and that both processes are related to some sort of local ordering in the alloy.

VOL. 4 1956

REFERENCES

1. C. ZENER *Trans. Amer. Inst. Min. Met. Eng.* **152,** 122 (1943).
2. A. S. NOWICK *Phys. Rev.* **88,** 925 (1952).
3. B. G. CHILDS and A. D. LE CLAIRE *Acta Met.* **2,** 718 (1954).
4. C. ZENER *Phys. Rev.* **71,** 34 (1947).
5. A. D. LE CLAIRE and W. M. LOMER *Acta Met.* **2,** 731 (1954).
6. C. WERT *Modern Research Techniques in Physical Metallurgy* ASM, p. 225 (1953).
7. R. ARTMAN *J. Appl. Phys.* **23,** 475 (1952).
8. F. A. TRUMBORE, W. E. WALLACE, and R. S. CRAIG *J. Amer. Chem. Soc.* **74,** 132 (1952).
9. D. A. EDWARDS, W. E. WALLACE, and R. S. CRAIG *J. Amer. Chem. Soc.* **74,** 5256 (1956).
10. C. WERT and J. MARX *Acta Met.* **1,** 113 (1953).
11. J. HINO, C. TOMIZUKA, and C. WERT *Internal Friction and Diffusion in* 31% *Alpha Brass.* In press.
12. L. W. COFFER, R. S. CRAIG, C. A. KRIER, and W. E. WALLACE *J. Amer. Chem. Soc.* **76,** 241 (1954).

SUBGRAIN AND ELECTRICAL RESISTIVITY STUDIES OF MOLYBDENUM SINGLE CRYSTALS*

K. T. AUST† and R. MADDIN‡

The electrical resistivity for single crystals of molybdenum after various amounts of bending at room temperature and after annealing isothermally at several temperatures was measured and correlated with metallographic and X-ray observations. Resistivity during room-temperature bending is found to increase slightly initially and is followed by a rapid rise coincident with crossing slip bands. Etch-pit density measurements are found to be proportional to the reciprocal of the bend radius, in agreement with the Cottrell relation.

ÉTUDES DE SOUS-GRAINS ET DE RÉSISTIVITÉ ÉLECTRIQUE DANS LES MONOCRISTAUX DE MOLYBDÈNE

La résistivité électrique de monocristaux de molybdène après divers degrés de flexion à la température ordinaire et revenus isothermes à des températures différentes a été mesurée et mise en relation avec des observations microscopiques et de rayons X. La résistivité pendant la flexion à la température ordinaire augmente d'abord légèrement puis d'une manière considérable lors de l'apparition de bandes de "cross-slip". La densité de piqûres de corrosion a été trouvée proportionnelle à l'inverse du rayon de courbure, en accord avec la relation de Cottrell.

UNTERSUCHUNGEN ÜBER SUBKÖRNER UND ELEKTRISCHEN WIDERSTAND AN MOLYBDÄN-EINKRISTALLEN

An Molybdän-Einkristallen wurde der elektrische Widerstand gemessen, nachdem die Kristalle bei Zimmertemperatur verschieden stark gebogen und danach bei verschiedenen Temperaturen isotherm angelassen worden waren. Die Ergebnisse wurden mit metallographischen und mit Röntgen-Beobachtungen verglichen. Es zeigt sich, dass der Widerstand mit dem Biegen bei Raumtemperatur zunächst langsam anwächst; sein darauf folgender starker Anstieg fällt mit dem Auftreten sich durchschneidender Gleitbänder zusammen. Das Auszählen von Ätzgrübchen ergibt, dass ihre Dichte umgekehrt proportional zum Biegeradius ist, was mit der Cottrellschen Beziehung in Einklang steht.

It is possible to obtain in deformed crystals a type of annealing phenomenon, called polygonization, which leads to discontinuous asterisms in the Laue X-ray patterns. Cahn[1] has observed polygonization in bent single crystals of zinc, magnesium, aluminum, and sodium chloride, after annealing near the melting-point. The break-up of the asterism into discrete spots is believed to be due to the alignment of the edge dislocations introduced by bending into the walls, perpendicular to the active slip direction. The existence of these dislocation walls was confirmed by Cahn[1] and by Dunn and Daniels.[2]

Mott[3] and Cottrell[4] conclude that the basic process in polygonization is the movement or climbing of edge dislocations out of their slip planes in order to change their grouping from a "horizontal" one to a "vertical" one. This process involves the migration of vacancies to or from the edges of the half-planes of the dislocations. Mott[3] and Seegar[5] have also suggested that the process of recovery, as well as polygonization, may be dependent on a dislocation climb process.

Calculations, e.g. Jongenburger,[6] have shown that electrical resistivity of metals is effected by the presence of point singularities, i.e. vacancies. It has also been suggested by Nabarro[7] that dislocations can act as sinks for vacancies. Hence, recovery of electrical resistivity might be expected if vacancies are annihilated by diffusing to dislocations. Since the process of the climbing of dislocations out of their slip planes involves the migration of vacancies to the edges of the half planes, it should be expected that polygonization (dislocation climb) would be accompanied by a decrease in the electrical resistivity attributed initially to the presence of vacancies.

It has not, as yet, been possible to calculate the resistivity due to groups of piled-up dislocations which are considered to be present in cold-worked metals.[8] If groups of piled-up dislocations contribute substantially to the resistivity, as is quite likely, it is to be expected that a decrease in resistivity may be accompanying an alteration of the piled-up arrays into configurations containing less strain-energy.

The present investigation was initiated to determine under what conditions polygonization or subgrain

* Received July 21, 1955; revised version March 6, 1956.
† The Johns Hopkins University. Now at the General Electric Research Laboratory, Schenectady, New York.
‡ The Johns Hopkins University. Now at The University of Pennsylvania, Philadelphia 4, Pa.

formation may occur in bent molybdenum single crystals. Electrical resistance measurements were conducted in order to obtain a quantitative measurement of the changes occurring during recovery and polygonization.

EXPERIMENTAL DETAILS

Single-crystal specimens of molybdenum were grown from sintered molybdenum rods of 99.9% purity, using the method described elsewhere.[9] The specimens were about 3 mm in diameter and 18 cm long, with single crystals approximately 2 cm to 5 cm in length occupying the entire center sections of each specimen. The specimens were electrolytically polished and then bent at room temperature, applying the same techniques described previously.[10] The radius of bend of the crystals was varied from 8 cm to 1.5 cm. The bent crystals were annealed in an argon atmosphere for periods of 1 hour to 25 hours at temperatures from 300°C to approximately 1600°C.

X-ray back-reflection Laue photograms were obtained from the crystals in the grown and bent conditions and after the various annealing treatments. The longitudinal specimen axis orientations for the initially unstrained crystals are shown in Fig. 1 in a unit stereographic triangle. Microscopic examination was conducted after etching the crystals in a sodium hydroxide and potassium ferricyanide solution, and also after electroetching in 5% oxalic acid at 4 V. The electroetch method was found to be more sensitive for revealing subgrains in molybdenum crystals. Several crystals were also examined after slight deformation at an elevated temperature (2000°C).

Electrical resistance measurements were made with a Leeds and Northrup Kelvin double bridge, after increasing amounts of bend and after the various annealing treatments. A jig was constructed for holding a bent crystal in an identical position for each resistance measurement, so that the distance between the potential leads was constant. A correction was made to take account of the increase in specimen length between the potential leads due to the bending. A current of 5 amp was passed through the specimen for a period of less than 10 sec. All resistance measurements were made at atmospheric temperature (21° to 26°C) and were corrected to 21°C. The sensitivity of the resistance measurements was 1×10^{-8} ohms and the accuracy was $\pm 1 \times 10^{-6}$ ohms. The resistivity values were accurate to $\pm 0.02 \times 10^{-6}$ ohm-cm, or $\pm 0.3\%$.

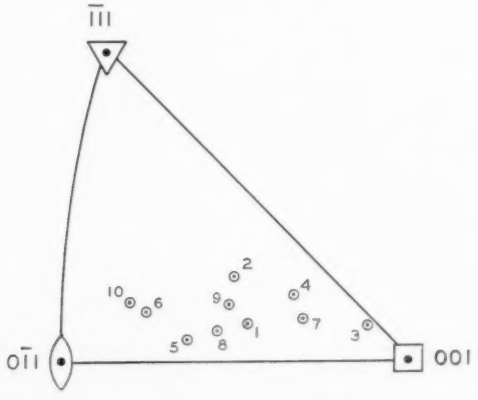

FIG. 1. Initial orientations of molybdenum crystals investigated.

EXPERIMENTAL RESULTS AND DISCUSSION

1. *High-temperature Deformation*

Subgrains were detected microscopically and by the split-up of Laue reflections in molybdenum single crystals subjected to a slight external stress during high-temperature annealing. Typical examples are shown in Figs. 2a and 2b, which were obtained from a crystal (*M*-1) deformed about 1% in tension at 2000°C, and from another crystal (*M*-2) deformed by bending to a 18-cm radius at the same temperature. The average size of the subgrains depicted in Fig. 2a is about 10 microns. Etch pits which are spaced in a nearly regular manner are visible at the sub-boundaries. It is also evident, particularly in the lower part of Fig. 2b, that the density of etch pits changes markedly when the direction of the sub-boundary changes. The etch pits are believed to occur at dislocations which are found at regularly spaced distances aligned in the sub-boundary. The average spacing of the etch pits in the sub-boundaries was 1×10^{-4} cm to 2×10^{-4} cm. From the dislocation relation $\theta = \lambda/h$, where θ = orientation difference, λ = interatomic spacing, and h = etch pit spacing, misorientations, θ, of 0.01° to 0.02° were calculated for the crystals deformed slightly at 2000°C.

Microscopic examination at ×1300 of the single-crystal section adjacent to a polycrystalline end revealed no apparent change of direction of a grain boundary where it meets a sub-boundary. This indicates that the "pull" of a sub-boundary at the junction is very much smaller than that of a grain boundary. Back-reflection Laue photograms revealed a breakup of each Laue reflection into discrete spots, similar to that observed by Chen and Maddin[11] for a single crystal of molybdenum bent at about 2400°C. The orientation-spread between the individual spots of a Laue reflection was less than 0.1°.

VOL. 4 1956

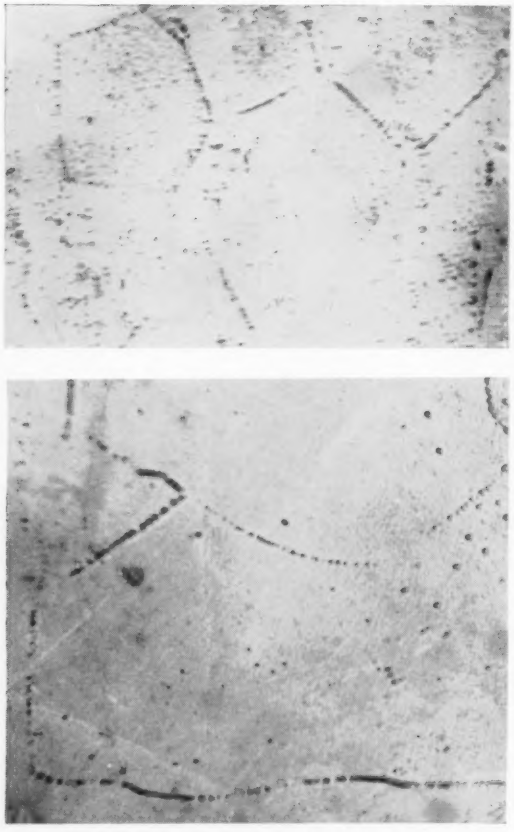

FIG. 2. Sub-boundaries in molybdenum single crystals—electrolytically polished and electroetched 15 sec in 5% oxalic acid solution. (a) Top: Crystal *M*-1 deformed in tension at 2000°C; ×400. (b) Bottom: Crystal *M*-2 deformed in bending at 2000°C; ×500.

2. *Bending at Room Temperature followed by Annealing*

In a previous investigation,[10] X-ray Laue patterns of molybdenum single crystals bent at room temperature revealed a breakup of Laue spots into high-intensity regions connected by diffuse areas. This phenomenon was interpreted in terms of crystallite fragmentation where the individual crystallites are connected by high-strain regions. In the present study, four single crystals (*M*-3, *M*-4, *M*-5, *M*-6) were bent from 8 cm to 1.5 cm at room temperature and annealed in an argon atmosphere for periods up to ten hours at temperatures from 300°C to 1400°C. No significant change was noted either in orientation or in the appearance of the Laue reflections after the above treatments. Microscopic examination after chemical and electroetching showed no evidence of subgrain formation or polygonization. It is possible, of course, that subgrains were present, but still too small in size and misorientation to be detected by conventional techniques. However, the failure to detect any structural changes even after ten hours at 1400°C, suggests that it is unlikely that sub-boundaries in molybdenum crystals form by an athermal process on plastic deformation.

Another crystal (*M*-7), which was bent to 2.3 cm at room temperature and then annealed for one hour at temperatures from 300°C to 1000°C, also showed no structural changes. This same crystal was then bent from 2.3 cm to 1.8 cm during an anneal at 1200°C. Microscopic examination revealed sub-boundaries, as shown in Fig. 3a, similar to those observed in an early stage of formation by Dunn and Daniels[2] in bent

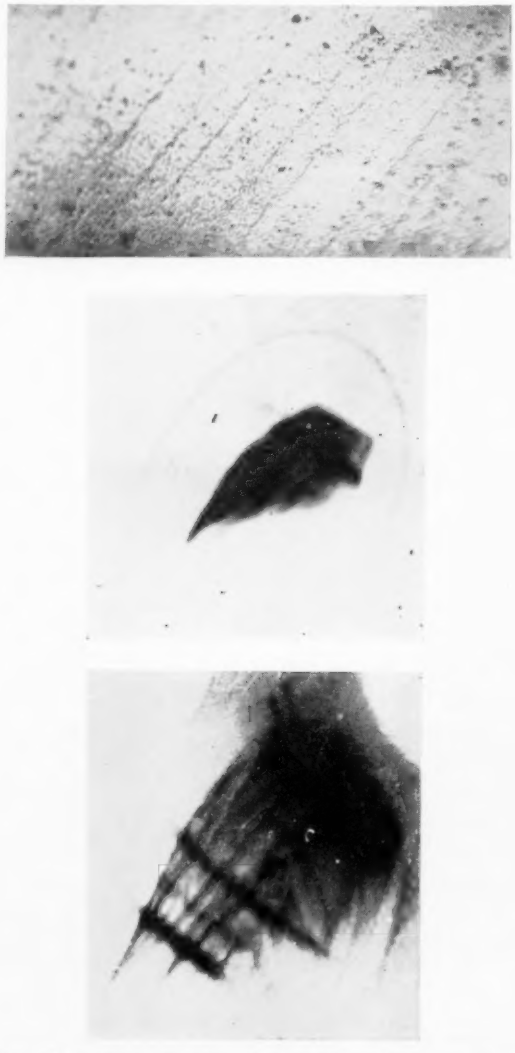

FIG. 3. (a) top: Sub-boundaries in molybdenum single crystal (*M*-7) after 1-hr anneal at 1500°C. Crystal was previously bent to 2.3 cm at room temperature, and then bent to 1.8 cm at 1200°C. Electrolytically polished and electroetched 15 sec in 5% oxalic acid solution. ×300. (b) Centre: Enlarged Laue spot of *M*-7 after bending to 2.3 cm at room temperature. (c) Bottom: Enlarged Laue spot of *M*-7 after an additional bending to 1.8 cm at 1200°C and annealed 1 hr at 1500°C.

and annealed silicon-iron crystals. Microscopic examination at ×1000 indicated that each sub-boundary in Fig. 3a consists of a discontinuous succession of etch pits similar to the walls of edge dislocations revealed in aluminum crystals by Cahn.[1] The average spacing of the etch pits in crystal *M*-7 was 0.5×10^{-4} cm, which corresponds to a misorientation θ of 0.04° when calculated from the dislocation relation $\theta = \lambda/h$. From the relationship,[2] $\theta = \dfrac{W \times 57.3}{R(\cos \phi)}$, where W is the average width of the subgrains, R is the radius of bend, and ϕ the boundary direction, the misorientation θ is calculated to be 0.08°. The latter value of misorientation is in reasonable agreement with the 0.04° value derived from the etch-pit spacing.

Enlarged Laue reflections from crystal *M*-7 are shown in Figs. 3b and 3c, after room-temperature bending and after the additional bending to 1.8 cm at 1200°C. The high-intensity regions of Fig. 3c appear to be arranged in a preferential manner suggesting crystallographic order to the formation of the subgrains. The X-ray photograms from crystal *M*-7 also revealed partial Debye rings of a textured aggregate after bending at 1200°C and after further one-hour anneals at 1400°C and 1500°C. The Debye arcs consisted of very small spots, reminiscent of polygonization, which became better developed and increased in size as the temperature was increased from 1200°C to 1500°C. This phenomenon may be interpreted in terms of subgrain growth, as was observed in bent silicon-iron crystals when annealed from 950°C to 1300°C.[2] The orientation difference between the individual spots in the X-ray patterns of crystal *M*-7 was less than 0.1°, which is consistent with the θ values calculated from microscopic observations.

Crystal *M*-7 was next bent a slight additional amount at room temperature in order to reveal slip traces. It was observed on microscopic examination that the sub-boundaries were approximately at right angles to the slip traces, as predicted by the dislocation mechanism of polygonization.[4] The nearly straight, parallel sub-boundaries found in crystal *M*-7 (Fig. 3a) differ in appearance from the irregular network of sub-boundaries observed in crystals after slight bending or tension at 2000°C (Figs. 2a and 2b). The nearly parallel or lamellar sub-boundaries may be described as polygonization. However, as the structure coarsens, it loses the characteristics of a polygonized one, not because the lamellar structure disappears, but possibly because larger units no longer have simple orientation relationships.[2]

3. *Etch-pit Densities*

Microscopic measurements of etch-pit densities were conducted on several crystals after electroetching in 5% oxalic acid solution. The excess density of edge dislocations of the same sign to produce a certain amount of strain in bending was calculated from the relation given by Cottrell:[4] $p = 1/rb$, where p is the number of dislocations per unit area parallel to the bend axis, r is the bend-radius at the neutral axis, and b is the Burgers vector of the dislocation. For molybdenum, b is the interatomic distance in the ⟨111⟩ direction. The results are summarized in Table 1.

The reasonable agreement between the measured etch-pit density and the dislocation density calculated from the Cottrell relation supports the belief that the etch pits are locations of intersections of dislocations with the surface. Good agreement between measured and calculated dislocation densities was also found by Hendrickson and Machlin[12] for bent and annealed silver crystals, and by Dunn and Hibbard,[13] who controlled the geometry of their silicon-iron crystals such that ⟨112⟩-edge dislocations were measured after electroetching.

4. *Increase of Electrical Resistivity due to Bending.*

The electrical resistivity at 21°C (ρ 21°) of molybdenum single crystals in the "as-grown" or unstrained condition was found to be $5.95\ (\pm 0.05) \times 10^{-6}$ ohm-cm. The effect of amount of bending at room temperature on the electrical resistivity (ρ 21°) of molybdenum crystals was measured. Increases of resistivity up to 15% were observed after bending to a radius of 2 cm. Fig. 4 shows the relationship between the per cent increase of resistivity and angle of bend over a 1.25-cm length for two molybdenum crystals (*M*-9 and *M*-10). A very rapid increase of resistivity is evident after about a 12° bend. Metallographic examination of the slip traces as a result of bending revealed one system of fairly straight slip bands after

Table 1

Crystal No.	Condition of crystal	Measured etch-pit density (cm^{-2})	Calculated dislocation density (cm^{-2})
M-7	bent from 2.3 cm to 1.8 cm at 1200°C and annealed 1 hr at 1500°C	1.4×10^7	2.0×10^7
M-10	bent to 2.1 cm at room temperature and annealed 12 hr at 1550°C	1.5×10^7	1.7×10^7
M-2	bent to 18 cm at 2000°C	1.8×10^6	2.1×10^6

VOL. 4 1956

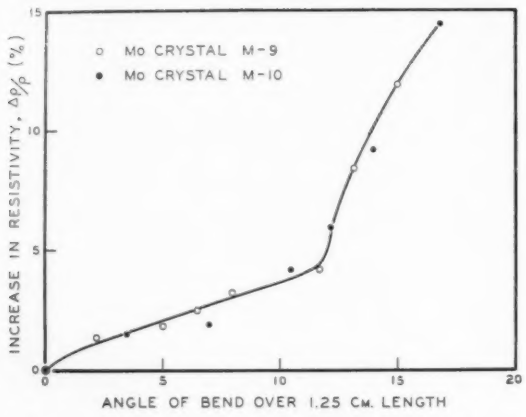

FIG. 4. Per cent increase in resistivity as a function of amount of bending at room temperature.

a 5° bend, and a slight forked nature of the bands after about 12°. After a 15° bend over 1.25 cm, the slip bands were very forked, i.e. intersecting, and similar to the slip bands previously observed in bent molybdenum crystals (Fig. 10 of reference 10). Load-deflection curves obtained for bent molybdenum crystals[10] also gave some indication of a behavior similar to that shown in the resistivity-angle of bend-curves of Fig. 4.

It is interesting to note, in this connection, that Masima and Sachs[14] found that the electrical resistivity of single crystals of alpha brass increased by only about 1% as slip began and then remained constant during almost the whole period when slip was confined to one system. However, a marked increase in resistivity was observed as a second-slip system became operative in alpha brass crystals. The rapid increase in resistivity coincident with intersection of slip bands observed in bent molybdenum crystals here, and in alpha-brass crystals,[11] may be understood if resistivity is appreciably affected by the presence of vacancies and piled-up groups of dislocations formed by crossing dislocations. Mott,[8] in specifically considering vacancies, has given diagrammatic stress-strain curves which are very similar to the resistivity-strain curves found for polycrystalline nickel by Broom.[15] The relatively high per cent increase in resistivity for bent molybdenum crystals (Fig. 4) and polycrystalline molybdenum and tungsten after >99% reduction of cross-section,[16] may be the result of a high concentration of frozen-in vacancies as well as piled-up groups of dislocations which can remain in the lattice when the deformation is carried out at room temperature.

5. *Recovery of Electrical Resistivity*

Several single-crystal specimens (*M*-5 to *M*-10 inclusive) were bent at room temperature to radii of 1.5 cm to 5 cm with resulting increases of resistivity of 15 to 7%. These crystals were given various annealing treatments, and the electrical resistivity measured at room temperature after each anneal. No recovery of resistivity, within $\pm 0.3\%$, was found after 90 hours at room temperature and after annealing for periods up to 10 hours at 1400°C. Also, no structural changes were evident after microscopic and X-ray examination.

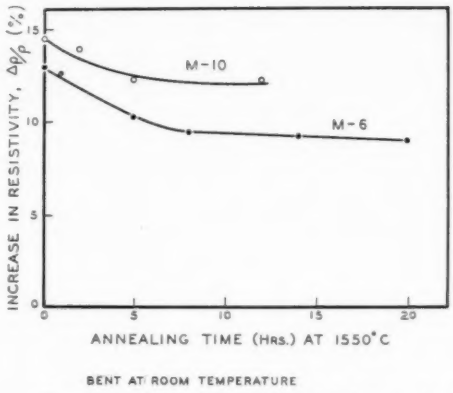

FIG. 5. Recovery data for molybdenum single crystals bent at room temperature.

Isothermal annealing at 1550 ± 30°C resulted in partial recovery of the total increase of resistivity due to bending, as shown for crystals *M*-6 and *M*-10 in Fig. 5. It should be noted that crystal *M*-6 was annealed for one-hour periods at temperatures from 300 to 1400°C, prior to the 1550°C treatment; crystal *M*-10 received no prior anneals (*M*-10 was bent to a smaller radius of curvature than *M*-6). This might explain the differences observed in the curves of Fig. 5. Microscopic and X-ray back-reflection studies indicated that the recovery of resistivity could not be attributed to a reduction in dislocation density, i.e. recrystallization. However, the X-ray photographs did reveal distinct structural changes occurring during recovery of resistivity. The Laue reflections of Fig. 6 were obtained from crystal *M*-6 after room-temperature bending and after 1 hour, 8 hours, and 20 hours annealing at 1550°C. A gradual alignment of the high-intensity regions in crystallographic manner is evident in Fig. 6 with increasing time of anneal, suggesting the occurrence of polygonization. Microscopic examination also indicated a partial alignment of etch pits into sub-boundaries, which is depicted in Fig. 7.

A calculation of the activation energy for recovery of electrical resistivity from the data at 1400°C and at 1550°C during the first 5 hours yields a value of between 3.5 and 7 eV. This can be compared with the activation energy of approximately 2.6 eV for

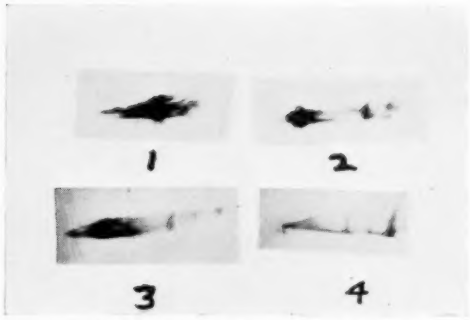

FIG. 6. Laue reflections from crystal M-6 after
(1) room-temperature bending,
(2) 1 hour at 1550°C,
(3) 8 hours at 1550°C,
(4) 20 hours at 1550°C.

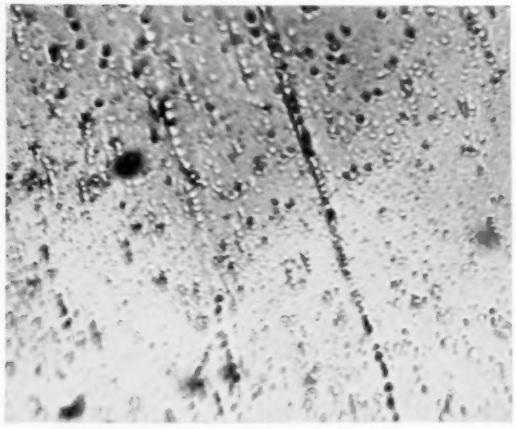

FIG. 7. Sub-boundaries revealed by alignment of etch pits in crystal M-10 after 12-hr anneal at 1550°C. Electrolytically polished and electroetched 15 sec in 5% oxalic acid. ×700.

the climbing of dislocations in bent and annealed silicon-iron crystals obtained by Dunn and Hibbard.[17] A higher activation energy might be expected for molybdenum in view of its much greater temperature of melting as compared with silicon-iron.

SUMMARY

Sub-boundaries which separate regions of misorientation of 0.01° to 0.02° were observed in molybdenum single crystals subjected to slight deformation by bending or tension at approximately 2000°C. No experimental evidence of polygonization, recovery of electrical resistivity, or recrystallization was found in crystals bent only at room temperature to radii from 8 cm to 1.5 cm and annealed for periods up to 10 hours at 1400°C. However, evidence of polygonization was observed in bent molybdenum crystals after isothermal annealing at approximately 1550°C for periods of 1 to 20 hours. A partial recovery of the total increase of resistivity due to bending was also found to occur during the annealing at 1550°C. An approximate calculation of the activation energy for the partial recovery of electrical resistivity produces a value of between 3.5 and 7 eV. These results are interpreted in terms of the suggestions of Mott and Seegar that the phenomena of recovery of electrical resistivity and polygonization are dependent on a dislocation climb process. Recovery of electrical resistivity may also be considered in terms of a realignment of piled-up groups of dislocations into configurations containing less strain-energy.

A relatively large increase of resistivity due to room-temperature bending of molybdenum single crystals was observed. The beginning of a rapid increase in resistivity was found to coincide with the initiation of intersecting slip bands. This result may be explained in terms of a high concentration of "frozen-in" vacancies and piled-up groups of dislocations formed by crossing dislocations. Good agreement was obtained between the experimentally measured area density of dislocations and that calculated using the Cottrell formula for the excess density as a function of the radius of curvature of the bent crystal. The experimental observations of subgrain formation in bent and annealed molybdenum crystals are consistent with the dislocation model of the structure of sub-boundaries, and with the dislocation mechanism of polygonization.

ACKNOWLEDGMENTS

The authors would like to acknowledge the helpful discussions of Drs. N. K. Chen, R. W. Cahn, and F. C. Miller. The research was sponsored at The Johns Hopkins University by the Office of Naval Research.

REFERENCES

1. R. W. CAHN *J. Inst. Metals* **76,** 121 (1949).
2. C. G. DUNN and F. W. DANIELS *Trans. Amer. Inst. Min. Met. Eng.* **191,** 147 (1951).
3. N. F. MOTT *Proc. Phys. Soc.* **B64,** 729 (1951); *Report of* 9th *Solvay Conference* (1952).
4. A. H. COTTRELL *Dislocations and Plastic Flow in Crystals* Oxford, Clarendon Press, 182 (1953).
5. A. SEEGAR *International Conference on Defects in Crystalline Solids* Univ. Bristol, July, 1954.
6. P. JONGENBURGER *Phys. Rev.* **90,** 710 (1953).
7. F. R. N. NABARRO *Report of the Conference on Strength of Solids* (*London: Physical Soc.*) 75 (1948).
8. N. F. MOTT *Phil. Mag.* **43,** 1151 (1952).
9. N. K. CHEN, R. MADDIN, and R. B. POND *Trans. Amer. Inst. Min. Met. Eng.* **191,** 461 (1951).
10. K. T. AUST, R. MADDIN, and N. K. CHEN *Trans. Amer. Inst. Min. Met. Eng.* **197,** 1477 (1953).
11. N. K. CHEN and R. MADDIN *Trans Amer. Inst. Min. Met. Eng.* **191,** 531 (1951).
12. A. A. HENDRICKSON and E. S. MACHLIN *Acta Met.* **3,** 64 (1955).
13. C. G. DUNN and W. R. HIBBARD JR. *Amer. Inst. Min. Met. Eng.* Research in Progress, Chicago, Feb. 1955.
14. M. MASIMA and G. SACHS *Zeit. Physik* **50,** 161 (1928); **51,** 321.
15. T. BROOM *Proc. Phys. Soc.* **B65,** 871 (1952).
16. W. GEISS and J. A. M. VAN LIEMPT *Zeit Physik* **41,** 867 (1927).
17. C. G. DUNN and W. R. HIBBARD JR. Private Communication.

VOL. 4 1956

THE FORMATION OF LOW-ENERGY INTERFACES DURING GRAIN GROWTH IN ALPHA AND ALPHA-BETA BRASSES*

HSUN HU† and CYRIL STANLEY SMITH‡

Measurements have been made of the relative areas of various types of interface observable in the microstructure of alpha-beta brasses. In alpha brass the ratio of twin-boundary area to that of grain boundary increases with grain size in accordance with the Fisher-Fullman concept of nucleation at grain corners. In alpha-beta brasses, interfaces across which the two phases are related in orientation are common and their fraction increases as the grain size of the duplex mixture increases, but this is a result of selective growth and not nucleation. These interfaces appear on microsections as straight lines similar in appearance to twins in the alpha phase, but they do not correspond to any particular orientation of the boundary plane with respect to the grains. They do, however, include the single close-packed direction common to both phases.

LA FORMATION D'INTERFACES DE BASSE ÉNERGIE PENDANT LA CROISSANCE DU GRAIN DANS LES LAITONS ALPHA et ALPHA-BETA

On a mesuré les surfaces relative de différents types d'interface, observables dans la microstructure des laitons alpha-bêta. Dans le laiton alpha, le rapport de la surface des joints de macle à celle des joints des grains augmente avec la dimension du grain en accord avec la conception de Fisher-Fullman sur la germination aux coins des grains. Dans les laitons alpha-bêta, les interfaces, à travers lesquelles les deux phases ont une orientation apparentée sont communes et leur nombre augmente avec la taille du grain de l'alliage. Ceci est un résultat de croissance sélective et non de germination.

Ces interfaces apparaissent sur des microsections comme des lignes droites semblables aux macles dans la phase alpha, mais ne correspondent pas à une orientation particulière du plan des joints par rapport aux grains eux-mêmes.

Cependant elles contiennent l'unique direction compacte commune aux deux phases.

DIE BILDUNG VON GRENZFLÄCHEN NIEDRIGER ENERGIE WÄHREND DES KORNWACHSTUMS IN α- UND α-β-MESSING

Die Autoren haben Messungen über die relative Grösse verschiedener Typen von Grenzflächen, die in der Mikrostruktur von α-β-Messing zu beobachten sind, angestellt. In α-Messing nimmt das Verhältnis zwischen der Fläche der Zwillingsgrenzen und derjenigen der Korngrenzen in Übereinstimmung mit dem Vorschlag von Fisher-Fullman, wonach die Keimbildung an den Ecken der Körner stattfindet, mit der Korngrösse zu. In α-β-Messing findet man häufig Grenzflächen, über die hinweg eine Orientierungsbeziehung zwischen den beiden Phasen besteht. Ihre Anzahl nimmt mit der Korngrösse der Mischphase zu, was auf selektives Wachstum und nicht auf die Keimbildung zurückzuführen ist. Im Schliffbild äussern sich diese Grenzflächen in ähnlicher Weise wie die Zwillinge in α-Messing als gerade Linien. Dies entspricht aber nicht einer speziellen Orientierung zwischen der Ebene der Grenzfläche und den Körnern. Lediglich die eine, dichtgepackte Richtung, die in beiden Phasen übereinstimmt, fällt mit der Grenzfläche zusammen.

INTRODUCTION

Various theories concerning the formation of annealing twins in single-phase face-centered cubic metals have been advanced. Maddin, Mathewson, and Hibbard[1] proposed the mechanical nucleation theory, which assumes that twin faults produced by the first movement of the atoms in a two-stage slip process may serve as nuclei for annealing twins in brass. However, as pointed out by Burke[2] and by Burgers, Meijs, and Tiedema,[3] the mechanical nucleation hypothesis cannot explain all of the observed phenomena. The growth-accident theory, which was first suggested by Carpenter and Tamura[4] in 1926 and was emphasized again by Burke[2] in 1950, assumes that during the migration of a grain boundary, when its advancing front corresponds approximately to an octahedral plane of the growing grain and encounters some kind of a discontinuity in the matrix, a twin will result, which under favorable conditions will grow to a visible twin. Burgers advanced the stimulation theory,[5, 6] which assumes that a "stimulated" crystal starts to grow at the moment when an already growing "stimulating' crystal comes into contact with a lattice region of the matrix that has a twin relationship with it.

The most widely accepted theory is that of Fullman and Fisher,[7] who proposed that annealing twins are formed by a typical nucleation process occurring whenever the appearance of material of twin orientation to a growing crystal will produce a sufficient

* Received March 13, 1956.

† Westinghouse Research Laboratories, Churchill Borough, Pennsylvania.

‡ Institute for the Study of Metals, University of Chicago.

lowering of the free energy of the grain boundaries locally involved. Since such nucleation is probable only when extremely small volumes are involved, it can occur only at the moment when a growing grain first touches a grain with which it has not previously made contact. In its simplest form this theory applies to the formation of twins during the growth of already recrystallized grains, though twins can also form by an analogous mechanism during recrystallization when a grain is growing into a highly strained or polygonized matrix. In the growth stage the number of new grain contacts which could give rise to twins will be directly proportional to the number of grain corners and, hence, grains that have disappeared. Assuming a constant shape distribution and no change in preferred orientation, then the number of twins will increase with grain size according to the following relationship:[8]

$$N = p \int_{A_1}^{A_2} A^{-1}\, dA = p\,(\log A_2 - \log A_1) \qquad (1)$$

where A is the average area of grain, N the change in number of twins in growing from a grain size A_1 to size A_2, and p the probability of forming a twin, i.e. the number of contacts necessary before a twin appears, divided by the number of corners per grain.

Although much attention has been paid to the formation of oriented interfaces during transformation in two-phase alloys, the formation of oriented low-energy interfaces during grain growth has not been studied. In the case of alpha-beta brass, the interfaces between the two phases can be insensitive to orientation, which results in a curved typical foam structure (Fig. 1), or they can have an obvious direction preference and be in appearance straight much like a twin (Fig. 2) in a manner strongly suggesting orientation-dependence of energy. The former structure is obtained by annealing a large-grained two-phase structure after deforming in a manner to give random orientations; the latter after extensive grain growth in an initially fine-grained two-phase structure.

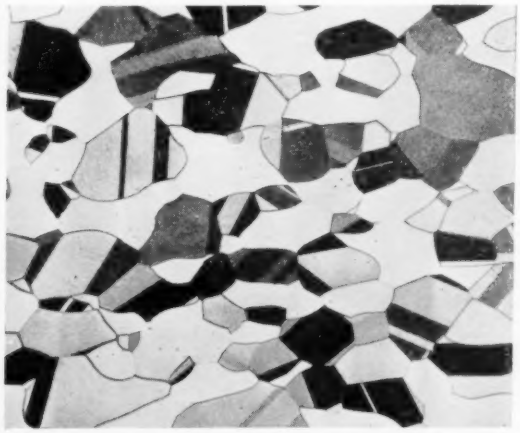

FIG. 1. Randomly oriented alpha and beta grains. Alloy with 61.57% copper, rolled 65% in alpha condition, annealed 700°C for 24 hours, quenched, cold rolled 50%, re-annealed 2 hours at 700°C, quenched. Light areas are beta phase. ×250.

This paper describes some quantitative studies of the various interfaces present in the microstructure of alpha and alpha-beta brasses carried out with a view to understanding their formation and movement.

PREPARATION OF ALLOYS

The material for study was made by casting alloys of the appropriate composition in graphite molds, followed by forging, homogenizing at 800°C, and quenching. The alloys contained less than 0.005% lead, less than 0.003% iron, with spectrographically detectable but unimportant amounts of Si, Ag, Ni, Sn, Mg, and Mn.

The alpha alloy (67.37% Cu) was cold-forged on a press and annealed at 600°C to give a relatively randomly oriented starting material of 0.18-mm grain size and about 1½ in. square. Pieces were machined from this to thicknesses of 1.533, 0.547, and 0.250 in., then rolled with reductions of 32, 68, and 91% respectively to final thickness between 0.14 and 0.17 in. Microsamples were cut from the strips and annealed in a salt bath held at a desired temperature (±3°C). Long anneals were completed, after an initial two hours in the salt bath, by quenching, sealing in helium in hard-glass capsules, and continuing at the same temperature in a laboratory-tube furnace.

After preliminary forging in the same way as the alpha alloy, the alpha-beta alloys (61.57 and 60.83% Cu) were annealed for 24 hours at 500°C or 72 hours at 460°C in order to obtain nearly homogeneous alpha. After cold rolling and annealing directly in a salt bath at higher temperatures, this gave rise to very fine dispersion of beta in alpha by simultaneous recrystallization and partial transformation. Other treatments can be inferred from the discussion later.

EXPERIMENTAL METHODS

The areas of the various kinds of interface in the samples were determined on plane metallographic sections, cut in a longitudinal direction, normal to the rolled surface.

As Smith and Guttman[9] have shown, the number of intersections of a random line of unit length with a two-dimensional feature in a three-dimensional structure is exactly equal to one-half the ratio of surface to volume, and the relative areas of two

kinds of interface are directly proportional to the numbers of intersections with them.

To minimize error due to anisotropy, a microscope stage with circular traverse was used. For linear integration measurement of volume fractions, the worm drive of the stage was provided with a light chopper which produced pulses in a photocell circuit arranged so that they could be channelled to separate counters which recorded the traverse across each phase separately. This stage will be described elsewhere.

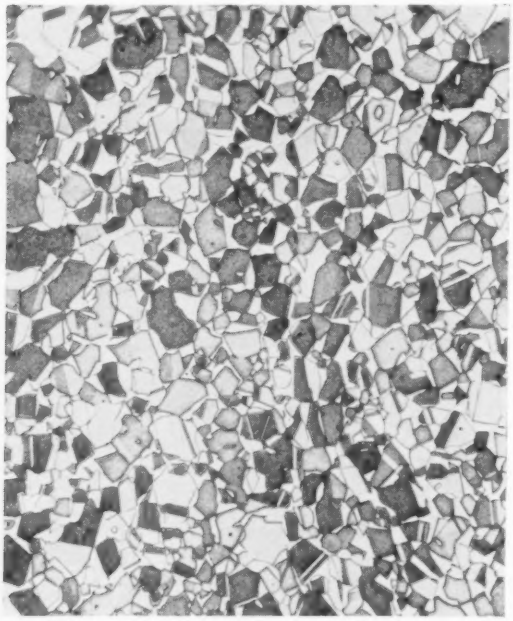

(a)

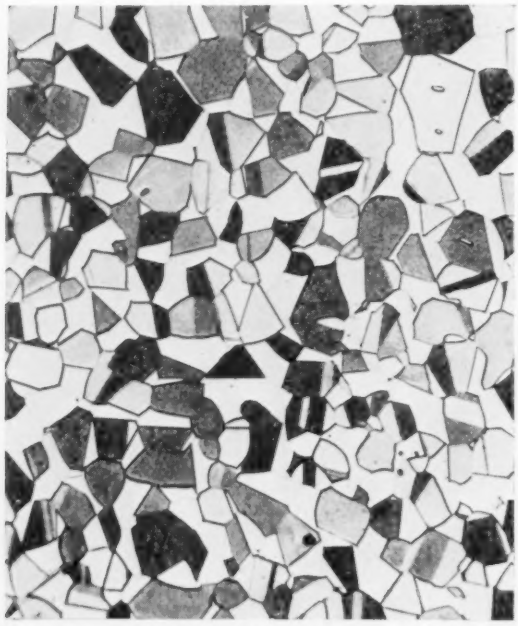

(b)

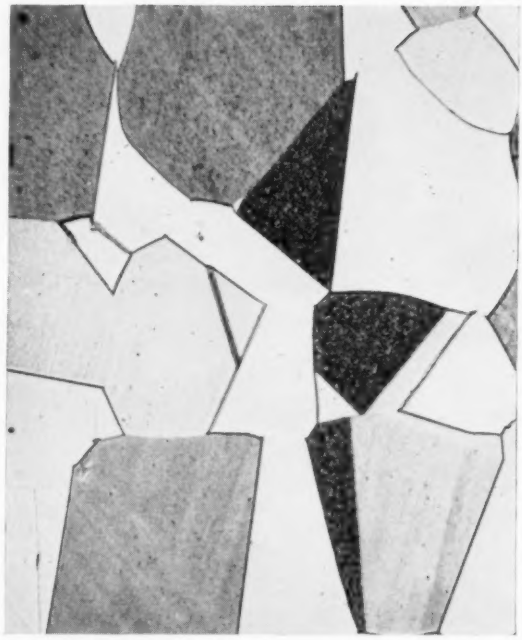

(c)

FIG. 2. Development of oriented plain alpha-beta interfaces during grain growth. Same alloy as Fig. 1, rolled 65% in alpha condition, then annealed at 700°C for (a), one minute (×500); (b), 2 hours (×250); and (c), 288 hours (×250). Light areas are beta phase.

The results are subject to metallographic uncertainty, for it is sometimes difficult to classify a boundary as to type, and, in fine structures, the section cannot be regarded as strictly two-dimensional or the boundaries as lines without width. With large-grained structures these difficulties decrease, but they are more than compensated by the statistical difficulty associated with a small number of grains. The results given are in general subject to about a 5% uncertainty.

TWINNING IN ALPHA BRASS

Data for twin formation in heavily rolled and annealed alpha brass (67.37% copper) are summarized in Table 1. The ratio of twin to grain-boundary area versus log average grain diameter is shown in Fig. 3. Variable results were obtained with lower reductions, the variation apparently being related to the recrystallization process, for reproducible data were obtained when samples were first recrystallized at a low temperature, and the resulting fine-grained material was used for growth studies at higher temperatures. With a given amount of reduction prior to annealing at or below 700°C,

TABLE 1.—Summary of boundary area measurements on alpha brass (67.37% Cu). Cold-rolled 91%, recrystallized at 500°C, 30 sec, and isothermally annealed as indicated

Specimen and heat treatment	L (Total length of traverse) (mm)	G_b (Total number of grain boundary intercepted)	T_b (Total number of twin boundary intercepted)	L/G_b (Average grain diameter) (mm)	T_b/G_b (Ratio of twin to grain-boundary area)
C-11 (500°C—30 sec)	9.500	2523	2016	0.0038	0.800
C-7 (500°C—1 min)	12.500	1967	1851	0.0064	0.941
C-8 (500°C—10 min)	12.500	1084	1092	0.0115	1.007
C-9 (500°C—2 h)	43.900	1212	1604	0.0362	1.323
C-10 (500°C—24 h)	62.500	777	1181	0.0805	1.520
C-2 (600°C—1 min)	25.346	1278	1697	0.0198	1.328
C-3 (600°C—10 min)	62.500	1066	1533	0.0586	1.438
C-4 (600°C—2 h)	125.000	996	1574	0.1255	1.580
C-6 (600°C—24 h)	150.000	784	1345	0.1913	1.716
C-5 (600°C—290 h)	300.000*	1122	1824	0.2674	1.626
C-11 (700°C—1 min)	126.446*	1958	3070	0.0646	1.568
C-12 (700°C—10 min)	125.000	736	1274	0.1698	1.731
C-13 (700°C—2 h)	250.000*	714	1118	0.3501	1.566
C-14 (700°C—24 h)	256.250*	548	929	0.4676	1.695
C-15 (800°C—15 sec)	62.500	885	1150	0.0706	1.299
C-16 (800°C—30 sec)	75.000	617	847	0.1216	1.373
C-17 (800°C—1 min)	137.500	771	1142	0.1783	1.481
C-18 (800°C—10 min)	112.500	283	467	0.3975	1.650
C-19 (800C—2h)	112.500	193	334	0.5829	1.731

* Sum of two individual measurements.

the ratio of twin-to-grain-boundary area depends only on the grain size and is independent on the combination of time and temperature used to produce it. The ratio becomes smaller for a given grain size as the initial rolling reduction decreases, but it increases approximately linearly with the logarithm of the average grain diameter, as expected from equation (1).

The difference between the results obtained at 800°C and the lower temperatures is probably a result of changing texture, as reported by Wilson and Brick,[10] although the grain size was too large for X-ray texture studies to be made to confirm this. The difference between these results and those of Hibbard, Liu, and Reiter,[11] who found a marked decrease in the number of twins per grain as the grain size increased, is supposedly also a result of textural changes.

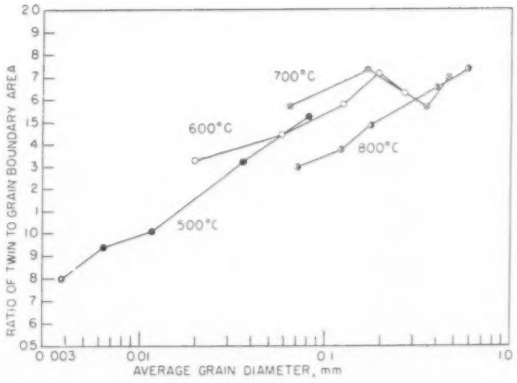

FIG. 3. The ratio of twin to grain-boundary area in annealed alpha brass (67.37% copper) cold rolled 91% and annealed at 500 to 800°C.

VOL. 4 1956

INTERFACES IN TWO-PHASE ALLOYS

In two-phase alloys there are six possible types of interface:

1. Incoherent interfaces between two grains of phase 1.
2. Twin-oriented interfaces between two parts of a single grain of phase 1.
3. Incoherent interfaces between two grains of phase 2.
4. Twin-oriented interfaces between two parts of a single grain of phase 2.
5. Incoherent duplex interfaces between phases 1 and 2.
6. Oriented duplex interfaces between phases 1 and 2.

Type 4 does not appear in alpha-beta brass. Sometimes there may be subdivisions of class 2 and 6 corresponding to different relative orientations of the crystals or of the boundary, and, of course, the behavior of boundaries of different types merges continuously into each other. For most purposes, the above six classes suffice.

If a grain is defined as a volume of matter in identical or crystallographically related orientation, then the grain size is the average linear distance between incoherent boundaries of any type. It may or may not include material of different phases.

Table 2 summarizes all data obtained with a brass containing 61.57% copper subjected to the various treatments indicated. The ratio of oriented two-phase interface area to that of incoherent boundary, (i.e. the number equivalent to the ratio of twin to grain-boundary areas in a single-phase alloy) is plotted in Fig. 4 as a function of the average grain diameter.

The difference between the samples of the various treatments is instructive. In order to obtain a two-phase structure of very small grain size the alloy had been previously rendered homogeneous alpha by long annealing at 500°C, then cold-rolled and plunged in a salt bath at 700°C. Recrystallization of alpha and precipitation of beta were simultaneous, and the presence of two phases prevented subsequent movement of grain boundaries except as a result of compositional diffusion. As growth progressed, the fraction of oriented alpha-beta interfaces increased markedly to about 0.4, but it did not increase thereafter—as indeed it could not in view of the limited volume of beta available. It was believed at one time that the increase in oriented boundaries was a result of *nucleation* of beta of the appropriate orientation in a way exactly analogous to the formation of an alpha twin, the driving force for nucleation being the decrease in surface free energy. Later, it was

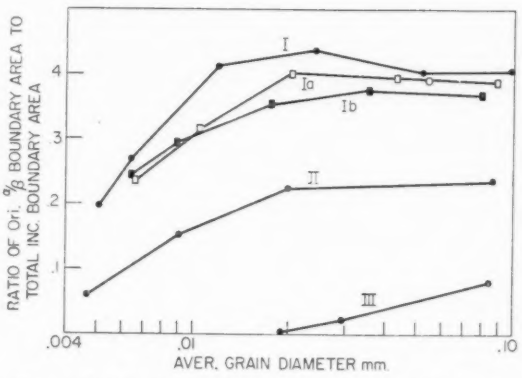

FIG. 4. Ratio of area of oriented plain alpha-beta interfaces to grain boundary area in alpha-beta brass 61.57% copper.
Curve I—rolled 65%, annealed at 700°C.
Curve Ia—rolled 65%, annealed at 700°C for 30 sec, transferred immediately to 675°C and held for times shown.
Curve Ib—rolled 65%, annealed at 700°C for 30 sec, transferred immediately to 640°C and held for times shown.
Curve II—rolled 65%, annealed at 700°C for 1 min, quenched, rolled 50%, then annealed at 700°C.
Curve III—rolled 65%, annealed at 700°C for 24 hours, quenched, rolled 50%, then annealed at 700°C.
On Curve I,—○ was measured on a section cut at about 40° from the rolling plane along the rolling direction.

observed that the initial sample was far from equilibrium and that the amount of beta phase was progressively increasing throughout the anneal (see column 2, Table 2) indicating that further relief of supersaturation was accompanying grain growth. Series Ia and Ib, in which the temperature was changed after the beginning of the anneal in order to decrease subsequent supersaturation, had a slight effect on the ratio. A very considerable effect resulted in Series II and III, in which cold rolling was used to break up orientation relations between the two phases after some annealing, followed by further annealing of the specimens at the same temperature.

It seems, therefore, that the increased fraction of oriented alpha-beta boundaries that appears after prolonged growth is mainly a result of a selective growth of those particles of beta oriented to the adjacent alpha in such a manner as to have a low-energy interface. Nucleation of new beta crystals occurs only in the early stages when considerable supersaturation exists, and it does not seem to occur either as a result of the slight composition differences that are caused by boundary curvature, or as a result of the decrease in interface energy that would accompany the replacement of an incoherent with an oriented interface.*

* This latter factor is sufficient in some alloy systems; for example, copper-silicon alloys, where the energetic factors are particularly favorable. The large-banded crystals of these alloys grow on annealing with continued formation of new bands always parallel to the old, and deformation does not cause spheroidization on subsequent annealing.

VOL. 4 1956

TABLE 2.—Summary of boundary area measurements on alpha-beta brass, 61.57% Cu

	Alpha-beta brass (61.57% Cu)			Area per unit volume of surface ($S/V = 2\,N/L$)							Ratio of area of surfaces				
	(1) Spec. number and heat treatment	(2) Vol % β	(3) Total number of counts	(4) Inc. α/α	(5) Inc. β/β	(6) Inc. α/β	(7) Ori. α/β	(8) Tw. Ori. α/α	(9) Total inc.	(10) Aver. gr. diameter	(11) Ori. α/β / (9)	(12) Ori. α/β / Inc. $\alpha/\beta+2$ Inc. β/β	(13) Ori. α/β / Inc. $\alpha/\beta+2$ Inc. α/α	(14) Tw. Ori. α/α / (9)	(15) Tw. Ori. α/α / Ori. α/β + Inc. $\alpha/\beta+2$ Inc. α'/α
Series I 65% rolled	(A) 700°C—30 sec	25.56	8,647	32.06	35.84	326.08	77.56	81.86	393.98	0.0051	0.197	0.195	0.199	0.208	0.175
	(B) 700°C—1 min	27.52	7,272	27.14	31.68	252.10	83.90	70.60	310.92	0.0064	0.270	0.266	0.274	0.227	0.181
	(C) 700°C—10 min	33.75	8,599	23.96	23.40	121.34	69.66	36.80	168.70	0.0119	0.413	0.414	0.412	0.218	0.154
	(D) 700°C—2 h	36.65	8,585	12.90	12.16	58.44	36.46	17.40	83.50	0.0240	0.437	0.441	0.433	0.208	0.144
	(E) 700°C—24 h	42.08	2,664	6.15	6.81	25.44	15.45	7.04	38.40	0.0521	0.402	0.396	0.391	0.183	0.132
	(*E*)* 700°C—24 h	41.70	2,567	5.76	6.70	24.94	14.77	6.51	37.40	0.0535	0.395	0.385	0 405	0.174	0.127
	(F) 700°C—288 h	41.43	2,123	2.95	3.43	13.28	7.99	3.23	19.66	0.1017	0.406	0.397	0.417	0.164	0.119
Series II 65% rolled, 700°C—1 min then 50% rolled	(BB) 700°C—1 min	33.56	7,094	78.08	39.36	310.64	25.68	113.76	428.08	0.0047	0.060	0.066	0.055	0.265	0.231
	(BC) 700°C—10 min	37.66	8,290	32.68	24.40	163.80	33.80	76.92	220.88	0.0091	0.153	0.159	0.147	0.348	0.293
	(BD) 700°C—2 h	40.21	4,037	18.68	14.44	67.32	22.64	38.40	100.44	0.0199	0.225	0.235	0.216	0.382	0.302
	(BF) 700°C—288 h	42.36	1,403	3.25	3.98	15.85	5.43	6.58	23.08	0.0867	0.235	0.228	0.243	0.285	0.237
Series III 65% rolled, 700°C—24 h then 50% rolled	(EB) 700°C—1 min	40.67	7,257	28.54	10.14	67.16	0.34	38.96	105.84	0.0189	0.003	0.004	0.003	0.368	0.313
	(ED) 700°C—2 h	40.99	4.760	13.08	7.54	47.36	1.48	25.74	67.98	0.0294	0.022	0.024	0.020	0.379	0.343
	(EF) 700°C—288 h	43.14	1.998	3.50	3.76	16.50	1.90	14.30	23.76	0.0842	0.080	0.079	0.081	0.602	0.563
Series Ia 65% rolled, 700°C—30 sec transfer immediately to 675°C	(IA) 675°C—1 min	26.46	8,111	25.60	31.68	244.75	71.31	59.25	302.03	0.0066	0.236	0.231	0.241	0.196	0.161
	(IB) 675°C—10 min	30.27	14,600	20.38	24.22	144.30	59.68	43.42	188.90	0.0106	0.316	0.310	0.322	0.230	0.177
	(IC) 675°C—2 h	32.96	4,877	16.96	12.06	69.47	39.63	20.64	98.49	0.0203	0.402	0.423	0.383	0.210	0.144
	(IF) 675°C—24 h	34.15	9,334	9.50	6.55	30.36	18.30	9.96	46.41	0.0431	0.394	0.421	0.371	0.215	0.147
	(ID) 675°C—288 h	35.21	2,228	4.62	3.58	14.30	8.74	4.40	22.50	0.0889	0.388	0.407	0.371	0.196	0.136
Series Ib 65% rolled, 700°C—30 sec transfer immediately to 640°C	(JA) 640°C—1 min	21.04	8,825	45.23	19.79	245.23	75.63	84.80	310.25	0.0064	0.244	0.266	0.225	0.273	0.206
	(JB) 640°C—10 min	21.37	6,420	38.61	16.53	168.59	65.87	52.80	223.73	0.0089	0.294	0.327	0.268	0.236	0.169
	(JC) 640°C—2 h	24.18	5,801	27.71	11.39	75.01	40.29	31.23	114.11	0.0175	0.353	0.412	0.309	0.274	0.183
	(JD) 640°C—24 h	25.03	5,806	16.46	5.05	35.30	21.26	14.82	56.81	0.0352	0.374	0.468	0.312	0.261	0.166
	(JE) 640°C—288 h	25.07	2,608	7.02	2.53	15.52	9.23	7.42	25.07	0.0798	0.368	0.448	0.312	0.296	0.191

Column (9) = (4) + (5) + (6)
Column (10) = $1/(9) \times 2$
* Measured on a section cut at about 40° from rolling plane along rolling direction
Equilibrium vol. fraction of β at 700°C = 45%
Equilibrium vol. fraction of β at 675°C = 35.5%
Equilibrium vol. fraction of β at 640°C = 26.5%

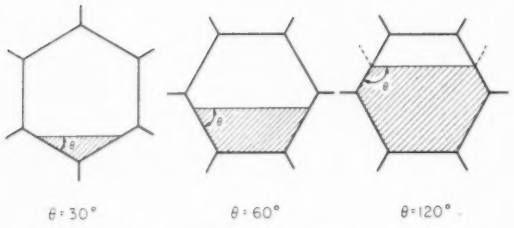

FIG. 5. Sketch illustrating relation between dihedral angle and volume fraction of a second phase.

The maximum fraction of oriented interface that can form is dependent on the volume fraction of the two phases. Surface-tension equilibrium requires the oriented interface to meet the grain boundary at an appropriate angle, and this angle cannot be reconciled with the topological features of the grain as a whole unless the correct number of corners are occupied in the second phase. Fig. 5 illustrates this. Assuming the ideal hexagonal grain, a phase with a dihedral angle of about 30° can conveniently be accommodated in one piece up to a sixth of the total volume. With an angle of about 60°, the volume fraction should not exceed one-half; if it does, then the total energy is actually less if low-energy interfaces are avoided, for the dihedral angle should be 120°. The typical microstructure of a brass with 55% beta shown in Fig. 6 confirms this. The structure consists chiefly of unrelated grains of the two phases.

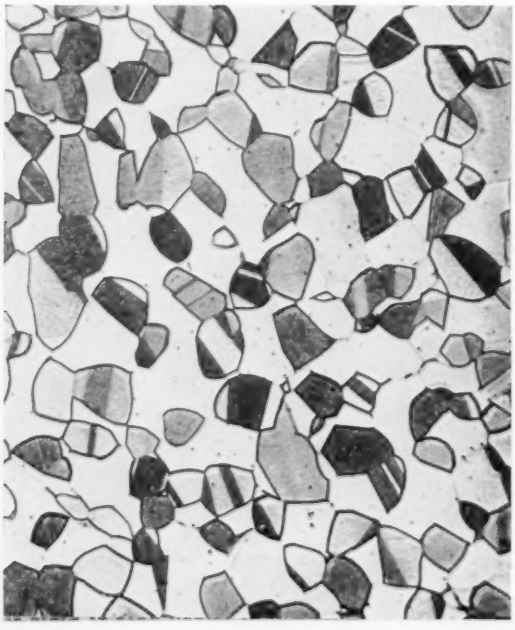

FIG. 6. Brass with 60.83% copper, annealed two hours 700°C. Contains 55% beta. Compare with Fig. 2(b). ×250. Light areas are beta phase.

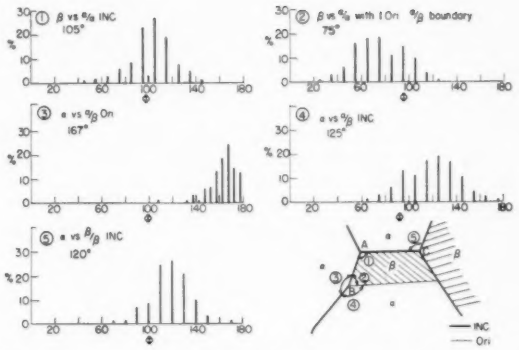

FIG. 7. Distribution of observed dihedral angles on large-grain alpha-beta brass. (Specimen shown in Fig. 2(c).)

INTERFACE ENERGY MEASUREMENTS

The statistical distribution of dihedral angles existing in a typical alpha-beta structure of large grain size is shown in Fig. 7. Treating these angles according to the rudimentary principles of surface-tension equilibrium and taking the incoherent alpha-grain-boundary energy as unity, they correspond to the following energies for the other interfaces:

$$\gamma_{\alpha\alpha}\ \text{(incoherent)} = 1.00\ \text{(Standard)}$$
$$\gamma_{\alpha\beta}\ \text{(incoherent)} = 0.85\ \text{(Point } B\text{)}$$
$$\text{or } 0.82\ \text{(Point } A\text{)}$$
$$\gamma_{\alpha\beta}\ \text{(oriented)} = 0.23\ \text{(Point } B\text{)}$$
$$\gamma_{\beta\beta}\ \text{(incoherent)} = 1.00\ \text{(Point } C\text{)}$$

The two values of the random alpha-beta interface are in good agreement with each other. The lower value previously reported[12] probably resulted from unwitting inclusion of some oriented interfaces.

RELATIVE ORIENTATION MEASUREMENTS

The metallographic studies described above were done on the basis of the visual appearance of the interfaces, it being assumed that a straight interface and a small angle with a grain boundary corresponded to a crystallographically oriented interface. X-ray examination of the relations gave unexpected results.

For orientation determinations, four comparatively large grains (0.20 to 0.30 mm diam.) were selected in the specimen that had been used for dihedral angle measurements. One of them is shown in Fig. 8. Back-reflection Laue patterns were obtained, using a fine-beam collimator (0.010 in. diam.) and a specimen holder which permitted exact location of the beam on a chosen microscopic feature. For each boundary to be studied, two exposures were made, one showing reflections from both alpha and beta crystals and the other registering only one (selected by painting over its surroundings with lead paint) to permit easy identification of spots.

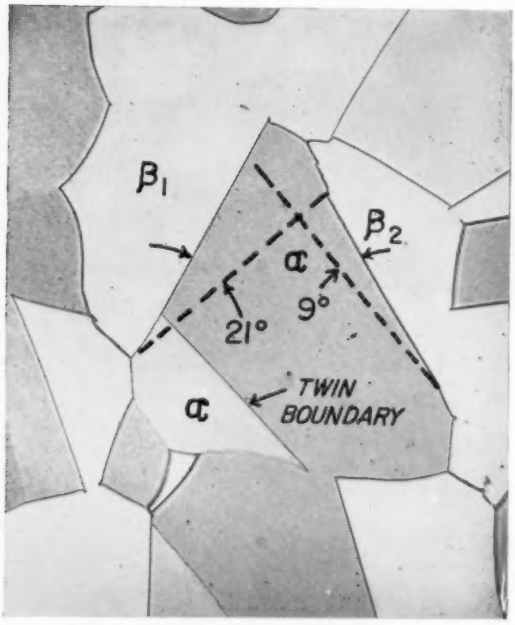

FIG. 8. Another area of specimen shown in Fig. 2(c), with grain parts whose orientations were measured. Dotted lines show predicted direction of ideal interface plane $(111)_\alpha$ $(110)_\beta$.

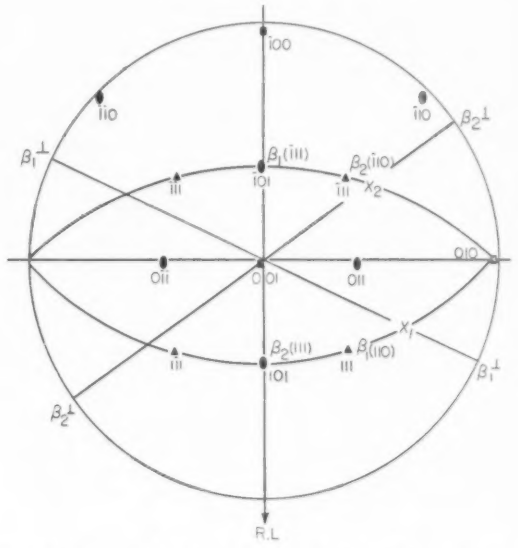

FIG. 9. Stereographic projection of grains shown in Fig. 8. $\beta_1\perp$ and $\beta_2\perp$ are trace normals of α/β_1 interface and α/β_2 interface respectively. Great circles are loci of the poles of planes containing [101] and [101] axes as zone axes; X_1 and X_2 indicate pole positions of α/β_1 and α/β_2 interfaces respectively.

The relative orientations of nine different beta crystals with respect to adjacent alpha crystals, with which they shared an apparently oriented interface and from which they had supposedly precipitated, were determined. In each of the nine cases it was found that the following relations held within two degrees:

$$(111)_\alpha \parallel (1\bar{1}0)_\beta$$
$$[1\bar{1}0]_\alpha \parallel [111]_\beta$$

This orientation relationship is identical with that found by previous investigators of the alpha-beta transformation in the copper-zinc system, regardless of whether the new phase is formed by precipitation on temperature change (see, for example, O. T. Marzke[13] by peritectic reactions[14] or by diffusion[15]). Measurements on the rather irregular outline of the needles formed on precipitating alpha from beta convinced Mehl and Marzke[16] that there was no simple low-index plane corresponding to the interface, despite the simple orientation of the grains themselves. The appearance of the microstructure of the present annealed polycrystalline alloys strongly suggested that a simple crystallographic plane was involved, for the similarity between the straight interfaces and twins was most striking. Measurements failed to confirm this, however.

The grains in the specimen referred to above were too small for sectioning in another direction in order to locate the plane exactly. However, in only one of the nine cases studied did the interface lie in the direction on the surface corresponding to the close-packed plane $(111)_\alpha$ or $(110)_\beta$. In one case, the angle on the surface differed by as much as 32°. When the directions in a single grain (Fig. 8) are plotted on stereographic projection (Fig. 9), it is seen that both of the interfaces have in common a close-packed direction, i.e. $[111]_\alpha$ and $[110]_\beta$, as a possible zone axis. The points of the intersection of the trace normals and the great circle lie exactly the correct angular distance from its corresponding (111) plane; in Fig. 9, point X_1 is 21° away from (111) and point X_2 is 9° away from $(\bar{1}11)$.

Fig. 10 is a microphotograph of a large beta grain in which alpha was precipitated by heat treatment without grain growth, as in the previous experiments. By measuring the trace of the interface on two sections cut at 90° to each other, the trace was completely identified as in the stereographic projection of Fig. 11. Again it will be seen that the plane of the interface (as marked X) does not coincide with any low-index plane in either lattice, but it does contain the (parallel) closest-packed directions of both lattices. This was also found to be true (within an error of 4°, which is believed to be due to nonplanar surfaces) of two other specimens whose orientations were similarly determined.

If the alpha-beta interface does not correspond to any particular lattice plane, how can the fact

VOL. 4 1956

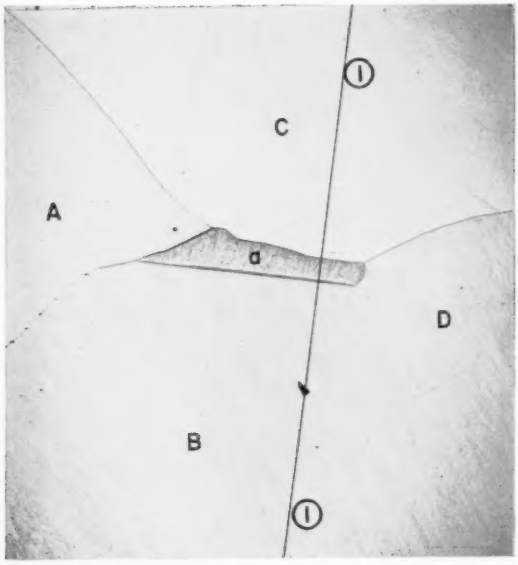

FIG. 10. Alpha phase precipitated in corner of beta grain by cooling. Alloy contained 57.22% copper, annealed for 45 min at 750°C, slowly cooled to 625°C, held 64 hours, quenched. Line indicates direction of second section giving traces plotted in Fig. 11. ×50

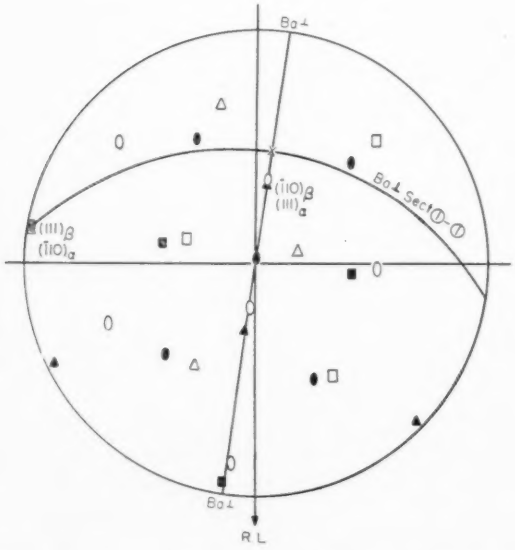

FIG. 11. Stereographic projection showing orientation of beta grain B (open figures) and alpha crystal a (solid figures) in Fig. 10. $Ba\perp$ is the trace normal of B/a interface, X indicates pole position of B/a interface.

that it is unmistakably flat be explained? It must be that its energy is relatively insensitive to orientation as long as it contains the close-packed directions, and that it is plane simply because this is the configuration of lowest possible area within a peripheral line established by the required dihedral angle in equilibrium with the grain boundary, which is of much higher energy. The fact that curvature is so rare in these interfaces suggests that they have a very high degree of mobility. Such high mobility may be a characteristic of any lattice interface with lines of perfect registery separated by unavoidable disorder, for lateral diffusion can never produce a tighter structure in such a boundary and only very few of the atoms need to change their neighbors as the boundary advances.

ACKNOWLEDGMENTS

The authors wish to thank Mr. K. K. Ikeuye and Mr. F. d'Heurle for preparation of the alloys used, and Mrs. Betty Nielsen for polishing and etching many microspecimens and taking their photomicrographs. The work was supported in part by a research contract from the Office of Ordnance Research (Contract No. DA-11-022-ORD-834) and the Office of Naval Research (Contract No. N-6ori-02004).

REFERENCES

1. R. MADDIN, C. H. MATHEWSON, and W. R. HIBBARD, JR. *Trans. Amer. Inst. Min. Met. Eng.* **185,** 655 (1949).
2. J. E. BURKE *Trans. Amer. Inst. Min. Met. Eng.* **188,** 1324 (1950).
3. W. G. BURGERS, J. C. MEIJS, and T. J. TIEDEMA *Acta Met.* **1,** 75 (1953).
4. H. C. H. CARPENTER and S. TAMURA *Proc. Roy. Soc.* **113A,** 161 (1926).
5. W. G. BURGERS *Proc. Kon. Ned. Akad. Wet.* **50,** 858 (1947).
6. W. G. BURGERS *Physica* **15,** 92 (1949).
7. R. L. FULLMAN and J. C. FISHER *J. Appl. Phys.* **22,** 1350 (1951).
8. C. S. SMITH, Discussion, *J. of Metals* 712 (May, 1955).
9. C. S. SMITH and L. GUTTMAN *Trans. Amer. Inst. Min. Met. Eng.* **197,** 81 (1953).
10. F. H. WILSON and R. M. BRICK *Trans. Amer. Inst. Min. Met. Eng.* **161,** 173 (1945).
11. W. R. HIBBARD, JR., Y. C. LIU, and S. F. REITER *Trans. Amer. Inst. Min. Met. Eng.* **185,** 635 (1949).
12. C. S. SMITH *Trans. Amer. Inst. Min. Met. Eng.* **175,** 15 (1948).
13. O. T. MARZKE *Trans. Amer. Inst. Min. Met. Eng.* **104,** 64 (1933).
14. A. B. GRENNINGER *Trans. Amer. Inst. Min. Met. Eng.* **124,** 379 (1937).
15. S. WOO, C. S. BARRETT, and R. F. MEHL *Trans. Amer. Inst. Min. Met. Eng.* **156,** 100 (1944).
16. R. F. MEHL and O. T. MARZKE *Trans. Amer. Inst. Min. Met. Eng.* **93,** 123 (1931).

GLIDE IN LEAD TELLURIDE*

W. A. RACHINGER†

The occurrence of ⟨100⟩ glide in lead telluride has been verified by means of prismatic punching. Rocksalt, which has the same crystal structure, glides in ⟨110⟩ directions. This may be explained in terms of the bonding energies of the compounds. At low bonding energies, as in PbTe, slip occurs by the movement of coupled partial dislocations of the type $\frac{1}{2}a[001]$. In ionic salts, however, these partials could not exist and perfect dislocations of the type $\frac{1}{2}a[110]$ are effective in producing slip.

GLISSEMENT DU TELLURURE DE PLOMB

L'existence du glissement ⟨100⟩ dans le tellurure de plomb a été vérifiée au moyen de poinçonnement prismatique. Le sel gemme qui a la même structure cristalline, glisse dans les directions ⟨110⟩. Ceci peut être expliqué au moyen des énergies de liaison des composés.

Pour les basses énergies de liaisonk comme dans le cas de Pb Te, le glissement résulte du mouvement de dislocations partielles couplées, du type $\frac{1}{2}a[001]$. Pour les sels ioniques cependant, des dislocations partielles ne pouvant exister, on doit attribuer le glissement aux dislocations parfaites du type $\frac{1}{2}a[110]$.

GLEITEN IN BLEI-TELLURID

In Blei-Tellurid wurde das Auftreten der Gleitrichtung ⟨100⟩ mit Hilfe des Prismen-Eindruck-Verfahrens (prismatic punching) verifiziert. Steinsalz, das dieselbe Kristallstruktur aufweist, gleitet in ⟨110⟩-Richtungen. Dies kann auf Grund von Verschiedenheiten in der Bindungsenergie dieser Verbindungen erklärt werden. Bei kleiner Bindungsenergie, wie in PbTl, erfolgt das Gleiten durch die Bewegung von gekoppelten Teilversetzungen vom Typ $\frac{1}{2}a[001]$. In Ionen-Kristallen können jedoch diese Teilversetzungen nicht existieren. Daher sind beim Gleiten vollständige Versetzungen vom Typ $\frac{1}{2}a[110]$ wirksam.

VOL.
4
1956

It has been reported[1] that lead sulfide deforms by glide in both the ⟨100⟩ and ⟨110⟩ directions. Sodium chloride, which has the same crystal structure, but is of a strongly ionic character, glides exclusively in ⟨110⟩. The occurrence of ⟨100⟩ glide in PbS is of interest, since it illustrates the dependence of glide direction on bonding energy, ⟨100⟩ glide being favored by low energies.

Of all the components having the NaCl type of crystal structure, lead telluride has the lowest heat of formation. Since tellurium is less electronegative than sulfur, PbTe would be expected to be of a more metallic nature than PbS. Thus, ⟨100⟩ glide should occur in PbTe. In order to investigate this, use was made of prismatic punching,[2] this being ideal for showing ⟨100⟩ glide even in the presence of other operative glide systems. In this method a thin single-crystal plate is indented on one surface. This causes a prism of material bounded by four sets of slip planes to move bodily through the crystal in the glide direction and produce a pyramidal bump on the opposite face. Since the glide direction is the line joining the indentation and the pyramidal bump, this direction may be readily determined by measuring the thickness of the crystal and the relative positions of the indentation and the bump. If the crystal face is perpendicular to the glide direction, the bump assumes the shape of a right pyramid, its base bounded by slip plane traces. Thus the occurrence of ⟨100⟩ glide in PbTe could be readily checked by indentation on a {100} face.

EXPERIMENTAL

Single crystals of PbTe, 3 mm in diameter, were grown in an evacuated silica system by cooling from the melt at 7°C per hour. Chemical analysis showed the composition to be 61.06 wt. per cent lead, 38.95 wt. per cent tellurium. Oscillating crystal and powder photographs revealed the compound to be of the NaCl structure with lattice parameter $a = 6.45$ Å. At room temperature the crystals were brittle and cleaved readily on {100} planes.

Single crystal slabs, approximately 0.5 mm thick, were prepared with both faces metallographically polished. In some cases the faces were {100} cleavage faces, in others they were random sections through the crystal. The usual technique of prismatic punching is to support the crystal slab, either around its periphery or on a soft backing, and indent its top surface with a conical indenter. Because of the brittleness of PbTe, appreciable deformation could

* Received March 9, 1956.

† Aeronautical Research Laboratories, Department of Supply, Melbourne, Australia.

be obtained by this method only at temperatures of 300°C and above. Measurements of the pyramidal bumps on both {100} and randomly cut surfaces indicated the glide direction to be ⟨100⟩ and the glide planes {110}

The glide elements at room temperature were determined by a modification of this method. Thin crystal slabs were set inside perspex blocks and an indenter was introduced through a fine hole in each block. In this way, the crystals, which were firmly supported and enclosed by the perspex matrix, could be indented without cleavage. Measurements on the pyramidal bumps showed the glide elements to be ⟨100⟩{100} at 20°C. The compound is known to be ordered and to have the NaCl structure at this temperature.

DISCUSSION

Studies of the geometry of plastic deformation in compounds having the CsCl structure[3] have shown that the glide direction is dependent on the bonding energy of the compound. Here is a similar situation with compounds of NaCl structure. NaCl, a typical ionic salt with a heat of formation of 98.2 kcal/mole, has glide elements ⟨110⟩{110}, whilst PbTe, which has a heat of formation of 16.6 kcal/mole and whose bonding is of a more metallic character, has been shown to glide on the ⟨100⟩{110} system. The change-over in glide direction may be explained in terms of bonding energies.

Consider dislocations in a NaCl structure, capable of slip on a $(1\bar{1}0)$ plane, having Burgers vectors equal to unit lattice vectors. These are $a[110]$, $a[111]$, and $a[001]$. Dissociations of these are possible.

(i) $a[110] \rightarrow \frac{1}{2}a[110] + \frac{1}{2}a[110]$

This dissociation would certainly take place, since it leads to a reduction in energy, the $\frac{1}{2}a[110]$ dislocations being perfect.

(ii) $a[111] \rightarrow a[110] + a[001]$

This reaction does not lead to a reduction in energy. However, $a[110]$ can dissociate as in (i), leading to a decrease in energy, thus

$$a[111] \rightarrow \tfrac{1}{2}a[110] + \tfrac{1}{2}a[110] + a[001]$$

(iii) $a[001] \rightarrow \frac{1}{2}a[001] + \frac{1}{2}a[001]$ + stacking fault.

This dissociation can take place only when the stacking-fault energy is sufficiently small, i.e. the bonding energy of the compound is not too high. The structure of the stacking fault can be readily seen by imagining the plane *DEFG* of Fig. 1 slipped through one interatomic distance $\frac{1}{2}a$ in the [001] direction.

Thus, the dislocations most likely to take part in a slip process are $\frac{1}{2}a[110]$ and those of the [001] type,

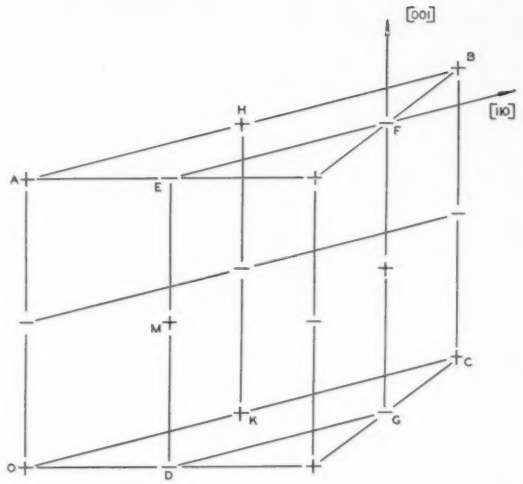

FIG. 1. One half of the unit cell of the NaCl structure, showing the two possible glide directions for plane *DEFG* slipping across plane *DABC*.

either $a[001]$ or coupled $\frac{1}{2}a[001]$ pairs. The dislocations, effective in causing slip in a given compound, are determined by the geometry of the slip process and the electrical interactions between ions in the neighbourhood of the dislocation.

Disregarding electrical interactions, the structure may be considered as simple cubic. Slip would occur in the [001] close-packed direction in preference to [110], since [001] glide involves rows of ions sliding in the grooves in the underlying layer (e.g. the line of atoms *DE* in Fig. 1 slides in the groove between *OA* and *HK*). [110] glide, on the other hand, necessitates the ion *E* "riding over" the ion *H*.

The effect of electrical interactions is best illustrated by two extreme cases.

(a) If the bonding energy is low, all [001] dislocations capable of glide on $(1\bar{1}0)$ would be of the extended type consisting of two $\frac{1}{2}a[001]$ dislocations connected by a stacking fault. Since the coupling distance between these is unlikely to be such that they both sit in their potential energy hollows simultaneously, the Peierls force for moving this coupled pair is likely to be lower than that for moving a $\frac{1}{2}a[110]$ dislocation.[4] Thus, [001] glide is to be expected.

(b) If the bonding energy is high, stacking faults cannot exist and consequently all [001] dislocations, if these exist, would be of the type $a[001]$. Since movement of these dislocations would involve bringing whole rows of like ions into nearest-neighbor positions (e.g. the ion at *M* would move into position *E* in the half-slipped configuration), it is unlikely that the dislocation would be mobile. Movement of $\frac{1}{2}a[110]$ dislocations does not necessitate like ions

being nearest neighbors. Thus, glide should be in the [110] direction.

In NaCl, case (b) applies, the electrical interactions over-riding any geometrical considerations and the compound glides in ⟨110⟩. In the weakly bound PbTe, case (a) is applicable, glide being in ⟨100⟩. PbS with a bonding energy intermediate between those of NaCl and PbTe is an interesting borderline case in which both ⟨100⟩ and ⟨110⟩ glide occurs.

ACKNOWLEDGMENTS

The author wishes to thank the Chief Scientist, Department of Supply, for permission to publish.

REFERENCES

1. E. Schmidt and W. Boas *Plasticity of Crystals*, F. A. Hughes and Co., London, 1950, 228.
2. A. Smakula and M. W. Klein *Phys. Rev.* **84**, 1013 (1951).
3. W. A. Rachinger and A. H. Cottrell *Acta Met.* **4**, 109 (1956).
4. A. H. Cottrell Private communication.

VOL.
4
1956

THERMAL AND FORCED DIFFUSION OF OXYGEN IN β-TITANIUM*

FERNAND CLAISSE† and H. PAUL KOENIG‡

This paper reports on a study of the diffusion coefficient and mobility under the influence of an electric field, of oxygen in solid solution in β-titanium. The experimental arrangement and the procedure followed is such as to yield a pair of values, one concerning diffusion and one concerning mobility in each experiment. This permits the judicious application of the Nernst-Einstein relationship relating the above-named coefficients to the charge carried by the migrating atom. A negative excess of 0.4 electron units is here found to be carried by the oxygen atoms.

The exponential variation of the diffusion coefficient with temperature is best expressed by the following equation:

$$D = 8.3 \times 10^{-2} \exp\left[-(31{,}200 \pm 2000)/RT\right]$$

The values in this equation are compared with theoretical and existing experimental values.

DIFFUSION DE L'OXYGÈNE DANS LE TITANE β

Cet article est relatif à une étude des coefficients de diffusion et de mobilité de l'oxygène en solution solide dans le titane β en présence d'un champ électrique. L'équipement et la méthode des essais sont tels que chaque expérience permet d'obtenir une couple de valeurs, l'une relative à la diffusion, l'autre à la mobilité. On peut ainsi appliquer judicieusement la relation de Nernst-Einstein, relative aux coefficients précités, à la détermination de la charge de l'atome diffusant. On trouve ainsi que la charge portée par les atomes d'oxygène est en excès de $-0{,}4$ unités de charge électronique.

La variation exponentielle du coefficient de diffusion avec la température s' exprime au mieux par l'équation suivante:

$$D = 8{,}3 \times 10^{-2} \exp.\left[-(31.200 \pm 2.000)/RT\right]$$

Les valeurs déduites de cette relation sont comparées avec les valeurs théoriques et expérimentales.

THERMISCHE UND ERZWUNGENE DIFFUSION VON SAUERSTOFF IN β-TITAN

In dieser Arbeit wird für Sauerstoff in fester Lösung in β-Titan der Diffusionskoeffizient und die Beweglichkeit unter dem Einfluss eines elektrischen Feldes untersucht. Versuchsanordnung und Versuchsführung sind so angelegt, dass jedes Experiment zwei Werte liefert, von denen sich das eine auf die Diffusion und das andere auf die Beweglichkeit bezieht. Dies erlaubt die richtige Anwendung der Nernst-Einsteinschen Beziehung, welche die obengenannten Koeffizienten mit der Ladung verknüpft, die das wandernde Atom trägt. Es ergibt sich, dass die Sauerstoffatome eine negative Ladung von 0,4 Elektronenladungen tragen.

Die Temperaturabhängigkeit des Diffusionskoeffizienten wird am besten durch die folgende Gleichung ausgedrückt:

$$D = 8{,}3 \times 10^{-2} \exp\left[-(31200 \pm 2000)/RT\right]$$

Die Zahlenwerte dieser Gleichung werden mit theoretischen und bestehenden experimentellen Werten verglichen.

INTRODUCTION

The knowledge of the state of gases in solid solution in metals is rather limited, and this is so even in those particular cases where known abnormal physical properties causing very interesting speculations should have been a stimulant to research. One of these cases is that of oxygen, which in solid titanium can form interstitial solutions having surprisingly high concentration, the saturation limit being 34 at. per cent, in the α phase.[1]

The subject of the present report is an experimentally obtained measurement of the charge associated with the oxygen atom in solid solution in β-titanium. A measure of the diffusion coefficient as a function of temperature is obtained as a byproduct.

Note should be made of the fact that these experiments were done on the β phase of the metal in order to bring the diffusion processes within a convenient laboratory time-scale, even though the solubility of oxygen here is not at all as spectacular as it is in the α phase.

The method used involves the experimental measurement of the forced migration of the oxygen atoms in solid titanium under the influence of an electric

* Received March 8, 1956. A joint contribution of the Department of Physics, Université Laval, and of the Quebec Department of Mines Research Laboratories. This work is in partial fulfillment of the requirements for the degree of Doctor of Science from the Graduate School of Université Laval.

† Quebec Department of Mines, Laboratories Branch, Research Division, Quebec, Canada. Published by permission of the Deputy Minister, Department of Mines, Quebec.

‡ Department of Physics, Université Laval, Quebec, Canada.

field. In experiments of this type, the diffusion is a true one, produced by thermal agitation, and the ensuing migration reflects the unidirectionality of the electrical field. Therefore, the well-known Nerst-Einstein relationship[2, 3] giving the mobility of the diffusing particle as a function of the charge carried and of the coefficient of diffusion, is applicable. Thus:

$$\frac{B}{D} = \frac{n\,e}{k\,T} \tag{1}$$

where B = mobility or speed of displacement of the atoms in a unit electric field.

D = diffusion coefficient.

n = number of unit electronic charges producing migration.

e = unit electronic charge.

k = Boltzmann constant.

T = absolute temperature.

This formula has been accurately verified in its original form for colloidal particles[4] and in the modified form given above for electrons in germanium.[5]

However, from the fact that diffusion coefficients usually vary to a great extent with grain shape, grain size, and purity of the metal, it is obvious that the use of mobilities and diffusion coefficients from two different sources may be the cause of serious errors in the ensuing computation of n. An example of such disquieting results is that of hydrogen in palladium, where the following values of n have been successively quoted: 0.001, 0.04, 0.4.[6, 7] Therefore, even though diffusion coefficients for oxygen in titanium have been reported recently,[8] we have chosen to complement our measurements of mobility by a parallel set of measurements of the diffusion coefficient, a pair of each values being obtained from a pair of independent simultaneous measurements in each experiment. Thus, perturbing influences on the value of n of such factors as grain size, purity of the metal, concentration of oxygen, variations in temperatures, etc., which effect both B and D equally, are eliminated.

The complete procedure consists in:

(a) The introduction of a very small quantity of oxygen at a point of a long pure titanium wire.

(b) The heating of the wire by an electric current in a high vacuum, thus modifying by diffusion the initial distribution of oxygen, till it sufficiently resembles the gaussian distribution given by equation (2).[7] This distribution is the starting-point of the experiment; it defines a time to which should be added the measured time of further controlled diffusion.

$$C = \frac{A}{2\sqrt{\pi Dt}} \exp\left(\frac{-x^2}{4\,Dt}\right) \tag{2}$$

where C = oxygen concentration at point x on the wire.

A = total quantity of oxygen dissolved; the expression is normalized.

D = diffusion coefficient.

t = total time.

The use of this formula assumes that the oxygen initially introduced in the wire is concentrated in a length which is small compared to that which will subsequently be used in the measurements. Care has been taken that this limitation be effectively complied with.

(c) The subsequent forcing of a statistically unidirectional migration by the use of direct current for heating the wire.

The spreading, with time, of the shape of the oxygen distribution along the wire will give values of D, while the migration towards one end of the wire will provide for values of B.

EXPERIMENTAL

The diffusion experiments were done on wires $\frac{1}{4}$ mm in diameter made of titanium-75A. A thin coating of copper, which was still present from the drawing process, was removed by dipping the wires into a solution of hydrogen peroxide in concentrated ammonia. Spectrographic and chemical analysis of the clean metal gave a purity of about 99.7% Ti, copper being the most important impurity.

A workable distribution of oxygen is obtained in the following way: a length of wire is held between two insulated brass vises $\frac{1}{2}$ mm apart. After the surrounding air has been replaced by pure oxygen, an alternating electrical current is passed through the wire, the unclamped part of which gets white hot and is maintained so for about 3 sec. A length of about 1 mm oxidizes, the degree of oxidation being much higher in the center of the gap. The oxygen is then dissolved into the wire by heating it at 1200°C for two hours in a vacuum of 10^{-6} mm Hg. This heat treatment causes a diffusion of the oxygen of such a type that the gaussian distribution referred to above is effectively obtained, with a central concentration limited to some 2 at. per cent. Most of the grain growth has also taken place, giving

VOL. 4 1956

crystals of some $\frac{1}{4}$ to $\frac{1}{2}$ mm in length with most grain boundaries running across the wire and somewhat perpendicular to its axis. This orientation is advantageous, since it decreases grain-boundary diffusion.

The curve giving the concentration of oxygen as a function of its position in the wire is subsequently obtained from an instrument which could be called a "resistometer."* This instrument registers as a continuous curve the mean resistance along the titanium wire, as measured between two contacts $\frac{1}{2}$ mm apart while these are moving along said wire. This movement is synchronized to that of the speedomax recorder chart, the ratio of the displacements being 7 : 1, so as to obtain an enlarged and more easily readable trace.

Now, it is known that oxygen in zirconium increases the resistivity linearly with concentration at least up to 10 at. per cent.[9] It has here been assumed that sufficient linearity, up to 2%, also exists for titanium. In fact, linearity up to 1% has been verified by Jaffee and Campbell.[10]

Before starting the experiment, two superficial markings involving small deformation of the wire are made at about 15 mm in both directions away from the region under observation. These markings have no appreciable influence on the resistance of the wire and on our consequent knowledge of the electric field prevailing in it, but are efficient in causing a sharp anomaly on the resistometer curve, thus forming reliable reference points.

The diffusion in each experiment is done by periods The curve of concentration of oxygen along the wire is traced before and after each period. The progress of diffusion, which can be characterized by the product Dt in the argument of the exponential equation (2), is measured by comparing, at each period, the observed distribution in the wire (resistometer curve, see Fig. 1) with gaussian curves of known Dt values. At the same time the center of gravity of the distribution is noted.

For each experiment the value of D is obtained by plotting Dt against t and measuring the slope of the best straight line drawn through the points. Similarly, the change in position of the center of gravity of the oxygen distribution relative to above explained markings was plotted as a function of time. Evidently the slope of the line thus obtained gives the mobility directly observed in the prevailing constant electric field.

As usual, the temperature of the wires was kept constant as much as possible by adjusting the current when necessary. It was found unnecessary to change the voltage by more than 2% to keep the temperature constant during a complete experiment. The temperature was measured periodically with a Leeds and Northrup optical pyrometer. In order to prevent a deposit of evaporated metal on the glass wall through which temperature readings were taken, a shield, operated from the outside by a magnet, was used. Brilliance temperatures were converted to absolute temperatures by the use of emissivity coefficients taken from Bradshaw's[11] tables.

The electric field was obtained to sufficient accuracy by measuring with a potentiometer, the voltage between two points on the wire, these being chosen in the region of uniform temperature in order to eliminate the effect of lower resistance of the cold ends.

RESULTS

To show the type of curves from which measurements of D and B were made, curves representing the progress of diffusion as a function of time at 1510°K, such as given by the resistometer, are reproduced in Fig. 1. Usually these graphs were obtained three times for each stage of the diffusion, the wire being rotated by 120° on its axis each time in order to eliminate surface effects from resistometer readings. As mentioned above, the value of Dt for each experimental distribution is obtained by choosing, from a sufficiently numerous set, the precalculated gaussian curve that will best fit the resistometer trace. The mean observed value from six observers was taken as the measure. The spread in the measures decided upon by these observers was accepted as the experimental error. The results are plotted as a function of time in Fig. 2. Similarly, Fig. 3 gives the displacements towards

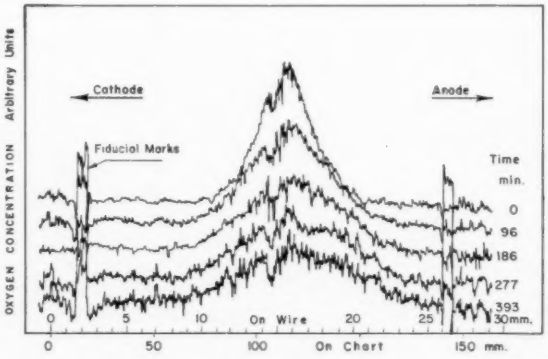

FIG. 1. Resistometer curves showing the progress of the diffusion and migration of oxygen towards the anode. Operating temperature 1510°K.

* To be described elsewhere.

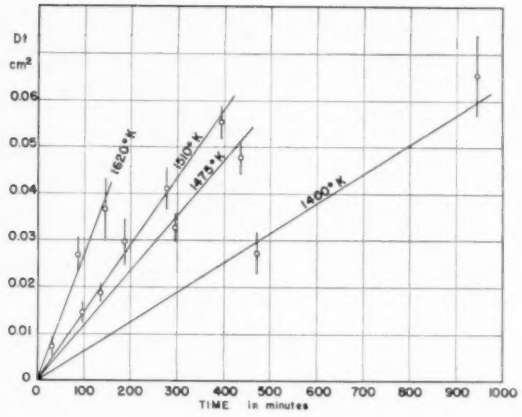

FIG. 2. Progress of diffusion as a function of time.
Since only the slope of these curves is used, they have been made to pass through the origin. Moreover, for all of them, the experimental point close to the origin has been omitted. Some curves have been omitted in order to simplify the drawing.

the positive end of the wire of the center of gravity of the distribution of oxygen, as a function of time.

The values of D calculated from the slopes of the straight lines of Fig. 2 are plotted in Fig. 4 on a logarithmic scale as a function of the inverse of the temperatures. The best straight line obtained by the method of least-squares obeys the relation:

$$D = 0.083 \exp\left[(-31{,}200 \pm 2000)/RT\right] \qquad (3)$$

Using Nernst-Einstein relationship and equation (3), curves of the values of log B as a function of the inverse of the absolute temperature for different values of n were drawn in Fig. 5. The curve that best fits the experimental points corresponds to $n = 0.4$.

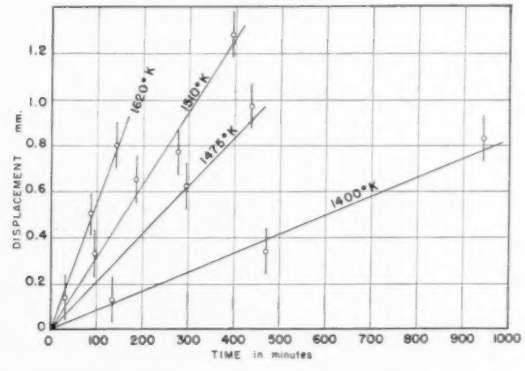

FIG. 3. Migration of the center of gravity of the oxygen distribution towards the positive end of the wire, as a function of time.
Since only the slope of these curves is used, they have been made to pass through the origin. Moreover, the point close to the origin has been omitted for clarity. Two curves are not shown.

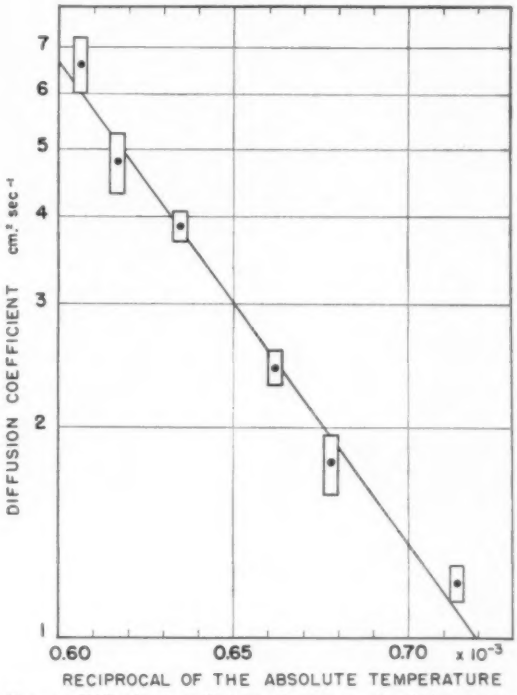

FIG. 4. Diffusion coefficient of oxygen in β-titanium as a function of the inverse of the absolute temperature.

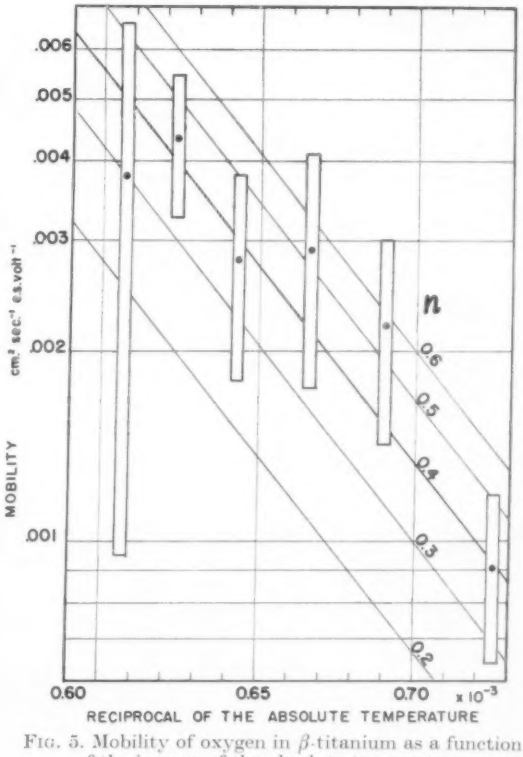

FIG. 5. Mobility of oxygen in β-titanium as a function of the inverse of the absolute temperature.
The slanted lines have the slope determined by the previously found diffusion coefficient. The heavy line ($n = 0.4$) fits the experimental mobility determinations best.

VOL. 4 1956

TABLE 1. Activation energy Q for diffusion of oxygen in b.c.c. metals

Metal	Q (kcal/g at.)	a_0 (Å)	Reference
Nb	27	3.28	Ang[12]
Ta	28	3.29	Ang[12]
Ta	29	3.29	Ke[13]
β—Ti	31.2	3.31	Present paper
β—Ti	48.2	3.31	Wasilewski and Kehl[8]

DISCUSSION

The first thing which can be observed in Fig. 2, which, we recall, shows the progress of diffusion as a function of time, is the interesting linearity; this in spite of the fact that the actual values of the concentrations locally measured vary at places by a large factor. This observation suggests that the coefficient of diffusion is relatively independent of concentration, at least in the range used here, which goes from 0 to 2 at. per cent. As in these experiments the concentration changes with time, if the coefficient of diffusion were strongly dependent upon concentration the value of D would also change with time and the relation between Dt and t would not be linear.

Our value of the activation energy, as computed by equation (3), is comparable to those in other metals where the crystal lattice and the crystallographic parameters are equivalent (Table 1). It is quite different from the value of 48,200 cal/g at. reported by Wasilewski and Kehl.[8]

A relation between the so-called "frequency factor" D_0 and the activation energy Q for pure intracrystalline diffusion has been proposed by Wert and Zener[14] and by Zener;[15] it can be written:

$$D_0 = \gamma a^2 \nu \exp\left(-\frac{\lambda \xi Q}{RT_f}\right)$$

with

$$\xi = -\frac{d\mu}{\mu_0}\frac{T_f}{dT}$$

where γ = constant, characteristic of the type of lattice,

a = lattice parameter,

ν = Debye frequency,

λ = constant, characteristic of the type of diffusion,

R = gas constant,

μ_0 = elastic modulus at 0°K,

μ = elastic modulus,

T_f = melting-point of the metal.

For diffusion of interstitial atoms in body-centered cubic lattices, γ and λ are respectively equal to 1/6 and 1.[16]

Unfortunately, because β-titanium is not stable below 882°C, no data on the temperature coefficient of μ is available. It is found, however, that the experimental values of D_0 and Q are consistent with equation (4) if ξ has a value of 0.54. Now, there is no great risk in stating this value with such precision. To compare it with experiment one would have to know the value of μ as a function of T for β-titanium, which, to our knowledge, is not in the literature. Moreover, if from the already known curve for α-titanium one tries to figure out what the curve should or could be for β-titanium, it is found that ξ could be almost anything between 0 and 1. But it lies between 0.2 and 0.6 for most metals for which data are available.

ACKNOWLEDGMENTS

Thanks are offered to Dr. Arthur Dubé, of Laval, for some interesting and relevant comments. One of us (F. C.) is also grateful to the Honourable W. M. Cottingham and to Dr. A. O. Dufresne, respectively Minister and Deputy Minister of the Quebec Department of Mines, for having provided the laboratory facilities as well as the financial support for the investigation.

REFERENCES

1. P. EHRLICH *Z. Anorg. Chem.* **247,** 53 (1941).
2. W. NERNST *Z. Phys. Chem.* **2,** 613 (1888).
3. A. EINSTEIN *Ann. Phys. Lpz.* (4) **17,** 549 (1905).
4. J. PERRIN *Les atomes* Félix Alcan, Paris (1924).
5. A. B. GIORDANO *et al. Phys. Rev.* **88,** 1386 (1952).
6. R. M. BARRER *Diffusion in and through Solids* Cambridge University Press (1941).
7. W. JOST *Diffusion in Solids, Liquids, Gases* Academic Press, New York (1952).
8. R. J. WASILEWSKI and G. L. KEHL *J. Inst. Met.* **83,** 94 (1954).
9. J. H. DEBOER and J. D. FAST *Rec. Trav. Chim.* **55,** 459 (1936).
10. R. I. JAFFEE and I. E. CAMPBELL *Trans. Amer. Ins. Min. Met. Eng.* **185,** 646 (1949).
11. F. J. BRADSHAW *Proc. Phys. Soc.* (London) **63B,** 375 (1950).
12. C. Y. ANG *Acta Metall.* **1,** 121 (1953).
13. T. KE *Phys. Rev.* **74,** 9 (1948).
14. C. WERT and C. ZENER *Phys. Rev.* **76,** 1169 (1949).
15. C. ZENER *J. Appl. Phys.* **22,** 372 (1951).
16. C. WERT *J. Appl. Phys.* **21,** 1196 (1950).

On the Mechanism of Intercrystalline Cracking*

In the January 1956 issue of *Acta Metallurgica*, R. D. Gifkins proposed a mechanism for the formation of intercrystalline cracks when boundary sliding occurs.[1] In his mechanism, tensile stresses are developed at suitably oriented jogs along the grain boundary, as a result of slip in the grains which does not completely pass through the boundaries. After sufficient dislocation pile-up at grain boundaries, these tensile stresses may exceed the fracture stress. If boundary sliding occurs concomitantly, the fractured surfaces at the jog are separated to produce intercrystalline cracks.

As a result of an experimental investigation conducted in the previous year,[2] we had come to a different conclusion about the mechanism of intercrystalline void formation, which, however, requires, as does Gifkins's, the existence of boundary sliding and boundary jogs. In particular, Gifkins calls upon dynamic slip in one of the bounding grains, which is partially accommodated by slip in the other bounding grain, to produce the grain boundary jogs. Further, he calls upon the piled-up dislocations at the boundary jog to produce the tensile stress that is supposed to produce the local fracture at the jog.

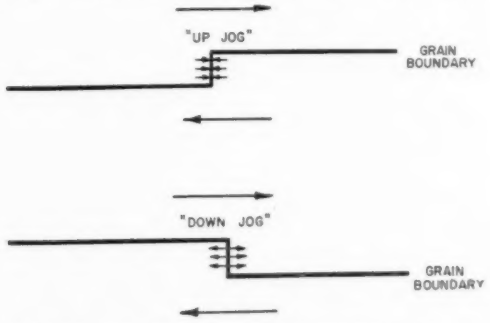

FIG. 1. Stresses induced by boundary sliding in the direction shown at jogs.

On the other hand, we believe that the boundary slip (inability of the grain boundary to maintain shear traction) at high temperature will lead to the formation of dilational stresses parallel to the boundary at regions where the boundary slip is impeded, such as at abrupt jogs along the boundary or at grain corners. The latter possibility was originally conceived by Zener[3] and recently experimentally demonstrated by Chang and Grant.[4] There are two possible directions to boundary jogs relative to a horizontal boundary. Namely, up or down as the boundary is traversed from left to right. If the top grain is sliding to the right relative to the bottom grain, then compressive stresses are produced across "up" jogs and tensile stresses are produced across "down" jogs. Fig. 1 illustrates this point. The magnitude of the stress developed across a jog depends upon the shear relaxation length between jogs and the boundary area of the jog itself. Thus, in our mechanism, the boundary sliding accomplished two necessary conditions for the production of intercrystalline cracks. It produces the tensile stresses that result in fracture across the jogged interface, and also it separates the fractured surfaces. Fig. 2 illustrates this sequence. In Gifkins's mechanism, on the other hand, boundary slip is required solely to separate the fractured surfaces.

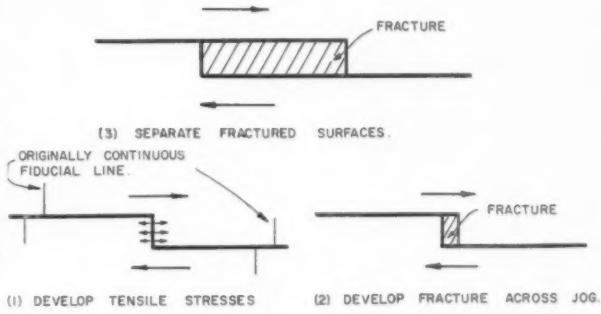

FIG. 2. Steps in the development of intercrystalline cracks due to increasing boundary slip, according to the mechanism by Chen and Machlin.[4]

The experimental evidence we have obtained relates to the necessity of having grain-boundary sliding in order to produce intercrystalline voids. Bicrystals were grown from 99.999% copper. Specimens were cut from one bicrystal so that the grain orientation relative to the boundary is constant for all specimens. For one series of such specimens, shear traction was applied parallel to the bicrystal boundary at 1200°F for 20 hours in a dead loading apparatus. For another series of such specimens, a tensile stress of 1000 p.s.i. was applied normal to

VOL. 4 1956

FIG. 3. Specimen subjected to shear parallel to grain boundary. Voids have developed along grain boundary. Conditions: 600 p.s.i., 482°C, 20 hours in H_2, as polished, ×150.

the boundary for 10 hours at 1200°F. For a third series of specimens, shear traction, applied as before parallel to the boundary, was succeeded by tensile stress, applied as above, normal to the boundary. The results of the tests were, that with shear alone some voids were found along the boundary. With tension alone, *no* voids were found at the boundary. With shear, followed by tension, many voids were found along the boundary. Both diamond polishing and etching techniques were used. Typical results are shown in Fig. 3.

It is apparent, therefore, that boundary shear is a necessary condition for the formation of intercrystalline voids (cracks). Unfortunately, our experiments were performed prior to a knowledge of Gifkins's mechanism, and do not serve to distinguish between his concepts and ours. We are now performing some simple experiments to so differentiate. In any case, it is apparent that grain-boundary sliding is a necessary prerequisite in order to obtain intercrystalline cracking.

School of Mines, C. W. CHEN
Columbia University, E. S. MACHLIN
New York 27, *N.Y.*

References

1. R. D. GIFKINS *Acta Met.* **4**, 1955.
2. C. W. CHEN and E. S. MACHLIN On the Mechanism of Intercrystalline Fracture, to be submitted to *A.S.M.*
3. C. ZENER The Micro-Mechanism of Fracture. Fracturing of Metals, *A.S.M.* (1947), p. 3.
4. H. C. CHANG and N. J. GRANT Mechanism of Intercrystalline Fracture *Journal of Metals* February, 1956.

* This research was supported by the United States Air Force through the Wright Air Development Center. Received April 25, 1956.

Au Sujet de la Mise en Evidence de la Polygonisation de l'Aluminium par la Methode des Rayons X et par la Micrographie*

Sous le même titre, M. de Beaulieu[1] a récemment comparé les importants résultats obtenus au laboratoire du Professeur Chaudron avec nos propres observations.[2]

D'après lui, les fragmentations des taches de diffraction X obtenues dans les deux cas ne correspondraient pas au même phénomène. Des monocristaux d'aluminium très pur faiblement déformés polygoniseraient uniquement vers 630°C.

Nous voudrions préciser exactement notre point de vue.

Il est d'abord certain que la méthode que nous avons proposée[3] possède une sensibilité supérieure à celle de Guinier-Tennevin.[4] M. de Beaulieu peut difficilement détector dans ses cristaux des sous-grains d'une taille inférieure au dixième de millimètre. Il lui est donc impossible de asvoir si, pour les traitements thermiques effectués à des températures inférieures à 630°, une sous-structrue plus fine n'est pas déjà présente. En fait, même dans des cristaux moins purs, nous avons trouvé des stries nettes dans les taches de diffraction enregistrées immédiatement après une déformation faible (quelques %) et nous avons pu suivre leur évolution après divers traitements thermiques.

Nos observations peuvent se résumer de la manière suivante.

1. En-dessous d'une certaine gamme de températures, les sous-grains formés directement à la température ordinaire (sans intervention du processus thermiquement activé de Cahn) ne semblent pas croitre d'une manière importante. La matrice élimine progressivement les courbures locales présentes à coté des sous-grains parfaits et plus ou moins continues. Ce mécanisme peut être probablement identifié à la diffusion et à la réorganisation des dislocations, c'est-à-dire à ce que l'on appelle généralement la "polygonisation."

2. Au-dessus de ces températures (variables suivant la pureté du métal, de la déformation, etc.), une croissance régulière de certains individus se développe avec conservation d'une haute perfection interne pour chacun des sous-grains. Dans les cas observés, cette étape se déroule dans une matrice déjà entièrement polygonisée et peut être caractérisée par un simple processus de croissance.

3. Par contre, au voisinage du point de fusion, une sous-structure à larges domaines moins parfaits se forme quelquefois (aussi bien dans le fer que dans l'aluminium). Cet état nous parait correspondre à ce que Crussard[5] a appelé "recristallisation in situ."

Il est probable due les observations de M. de Beaulieu se rapportent à cet état. Quoi qu'il en soit, nous n'avons jamais observé la formation de ces grands sous-grains imparfaits directement à partir de cristaux ne contenant pas au préalable une sous-structure à caractère parfait. Il importe de remarquer

qu'une telle observation requiert une technique à haute sensibilité.

Enfin le caractère stable de l'état polygonisé peut être clairement illustré par le fait queles monocristaux que nous avons examinés ne recristallisent pas à l'état solide.

Laboratoire de Cristallographie H. LAMBOT.
Université de Liège (Belgique)
et Centre National de Recherches
Metallurgiques (Liège)

REFERENCES

1. C. DE BEAULIEU *Acta Met.* **4,** 100 (1956).
2. H. LAMBOT, L. VASSAMILLET, et J. DEJACE *Acta Met.* **3,** 157 (1955).
3. H. LAMBOT, L. VASSAMILLET, et J. DEJACE *Acta Met.* **1,** 711 (1953).
4. A. GUINIER et J. TENNEVIN *Acta Cryst.* *2,* 133 (1949).
5. C. CRUSSARD *Rev. Metall.* **45,** 317 (1944).

* Received April 27, 1956.

Investigation of Pure Iron and Soft Steel with the Electron Microscope*

Introduction

The Research on pure metals is of great theoretical importance. The two most interesting subjects are the verification dislocation theory and the mechanism of slip. The advantage of using a pure metal is obvious, as no complications arise from precipitates and less complications from dissolved atoms. The iron investigated is of 99.99% purity. Samples were kindly put at our disposal by Prof. J. D. Fast of the Philips Physical Laboratory at Eindhoven. The scope of this research was to develop a method of etching, clearly showing the substructure of the crystallites and to see whether the same etch effect could be obtained on soft steel, Moreover, etched specimens were deformed to examine the effect of slip.

Experimental Method

After preliminary experiments, we decided to use an electrolytic polish etch, which has the advantage that no deformation results from preparation. A commercial apparatus, the Disa Electropol, was used with a bath on a perchloric-acid base (Electrolyte A-2), by which aluminum was etched beforehand.

The method of replication used is as follows. First, a negative silver replica is made by evaporation of silver in vaccum onto the specimen. This replica, of about 7-μ thickness, is easily removed from the specimen. A second positive replica is deposited on the first by evaporation of carbon in vacuum. After dissolving the silver in nitric acid, washing and drying of the carbon replica, the replica is shadowed with tungsten oxide, generally under an angle of 45°. The electron microscope used was that of the E.M. Division of the Technical Physics Department T.N.O. and T.H. at Delft. We thank Dr. J. B. le Poole for his kind help.

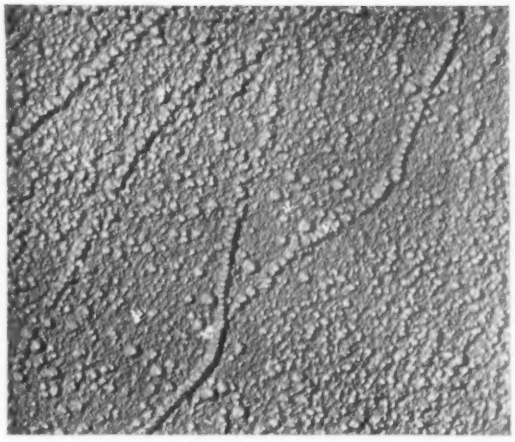

FIG. 1. Pure iron lightly etched. 8,000×.

Experimental Results

The method of etching used gives as a rule etch marks, which are protruding from the surface. The subboundaries in the ferrite crystallites form small dikes, and this makes it reasonable to suppose that, though generally etch pits mark the location of dislocations, the etch marks found in our case indicate the site of dislocations. A reason for the etch figures being hills rather than holes might be that there are still interstitial atoms present, which concentrate around the dislocations and lower the rate of attack, as Dr. J. Nutting of Cambridge, U.K., suggested to us.

Figs. 1 and 2 show the result of a light etching, that

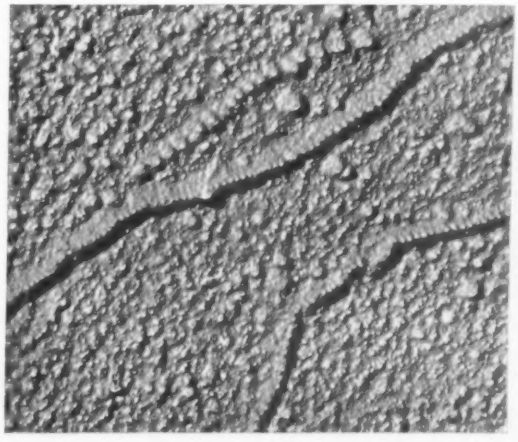

FIG. 2. Pure iron lightly etched. 16,000×.

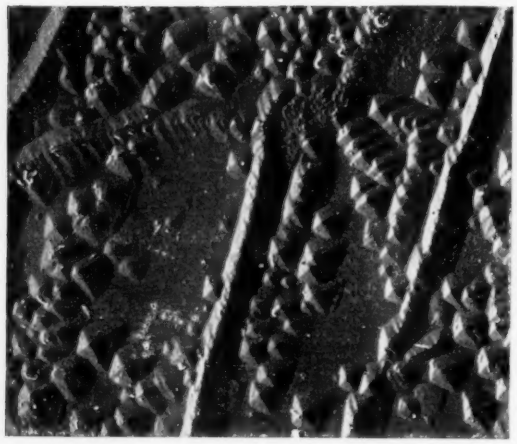

FIG. 3. Pure iron heavily etched. 16,000×.

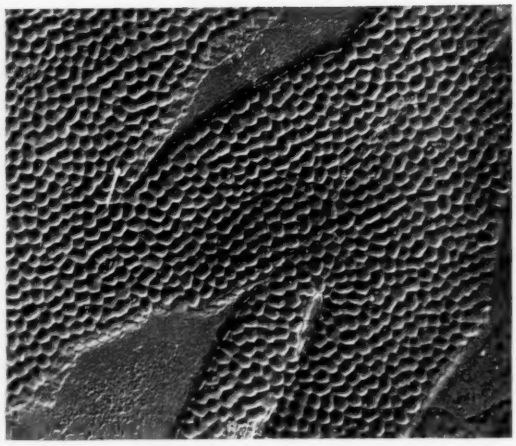

FIG. 6. Cementite in soft steel. 8,000×.

FIG. 4. Same as Fig. 3. Double subboundary. 16,000 ×.

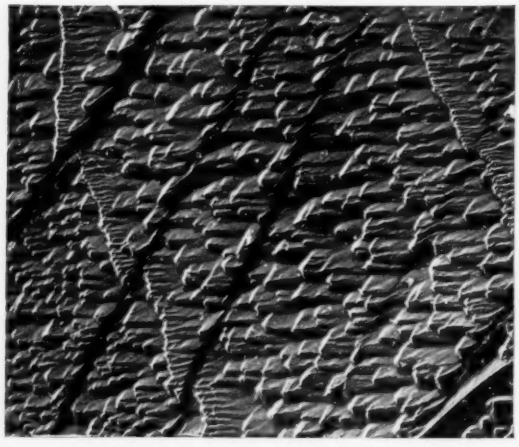

FIG. 7. Soft steel deformed after etching. 8,000×.

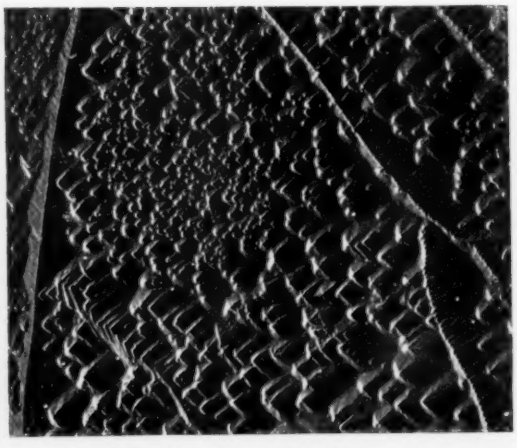

FIG. 5. Soft steel heavily etched. 8,000×.

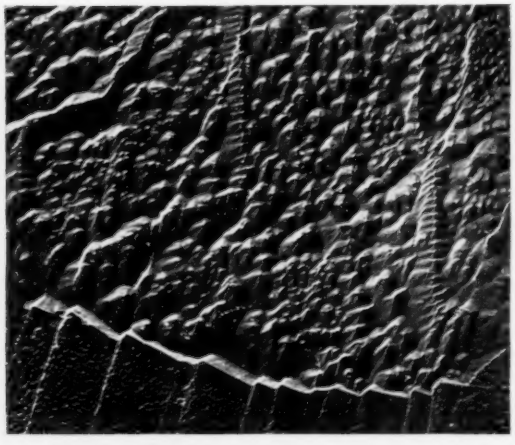

FIG. 8. Same as Fig. 7 at grain boundary. 8,000×.

results in rather rounded hills and subboundaries like a string of beads. Heavier etching gives etch figures in the form of small pyramids, while the grain boundaries show up as segmented dikes, as can be seen in Figs. 3 and 4. The subboundary in Fig. 4 shows a double array of dislocations that might be of theoretical interest. The rather regular orientation of the sides of the pyramids makes it clear that they approximate crystallographic planes. The determination of their orientations will be attempted in the near future. The same etch figures have been obtained on commercial soft steel (0.05% C and less than 0.1% of both Mn and Si). In both cases the number of dislocations is of the order of 10^9 per square cm. Fig. 5 demonstrates this fact, and Fig. 6 shows how this etch affects cementite, which develops shallow more or less spherical holes of rather constant size.

Some specimens of soft iron etched beforehand were deformed 6% under uniaxial pressure. The etch figures serve as markings to show how slip has taken place; in particular, the original subboundaries are very useful in this respect. Examples are given in Figs. 7 and 8. Fig. 8 shows how slip extends across a real grain boundary.

The resemblance of the etch figures with those found on germanium by Vogel, Pfann, and Lovell is remarkable, but it may be premature to try to draw conclusions as long as the orientation of the crystallites has not been determined. If this can be done, the method may be very useful.

F. van Wijk.
J. A. B. van Dijck.

Metals Research
Institute T.N.O.
Delft, the Netherlands

References

1. W. G. Pfann and L. C. Lovell *Acta Met.* **3**, 512 (1955).

* Received March 29, 1956.

VOL.
4
1956

SOME CURRENT PAPERS IN OTHER JOURNALS

Acta Crystallographica, Vol. 9

Part 9, September 1956:

Anisotropic Temperature Vibrations in Crystals. I. Direct Measurements of Debye Factors for Urea. R. E. GILBERT and K. LONSDALE.

Anisotropic Temperature Vibrations in Crystals. II. The Effect of Changes in Atomic Scattering Factors and Temperature Parameters on the Accuracy of the Determination of the Structure of Urea. H. J. GRENVILLE-WELLS.

The Morphology of Zircon and Potassium Dihydrogen Phosphate in Relation to the Crystal Structure. P. HARTMAN.

The Crystal Structure of Aluminum Phosphate and Gallium Phosphate, Low-Cristobalite Type. ROSE C. L. MOONEY.

A Note on the Debye-Waller Theory. M. BLACKMAN.

On the Systematic Absence of Magnetic Reflections of Neutron Diffraction. YIN-YUAN LI.

The Crystal Structure of the Silver Perchlorate-Dioxane Complex, $AgClO_4.3C_4H_8O_2$. RICHARD J. PROSEN and KENNETH N. TRUEBLOOD.

The Determination of the Anisotropic Thermal Motion of Atoms in Crystals. D. W. J. CRUICKSHANK.

The Analysis of the Anisotropic Thermal Motion of Molecules in Crystals. D. W. J. CRUICKSHANK.

Errors in Bond Lengths Due to Rotational Oscillations of Molecules. D. W. J. CRUICKSHANK.

The Crystal Structure of Dickite. R. E. NEWHAN and G. W. BRINDLEY.

Packing in Framework Structures. WILLIAM T. HOLSER.

Zur Kristallographie des Lävoglukosans.

Algèbre des facteurs de structure. E. F. BERTAUT.

Zur Deutung der diffusen Wärmewellenstreuung ausserhalb des mit Kristallreflexen belegten reziproken Bereiches. W. HOPPE.

Archiv für das Eisenhüttenwesen

Heft 7, Juli 1956:

Elektrolytische Isolierung intermetallischer Eisen-Zink-Verbindungen und Bestimmung der Löslichkeit einiger Metalle in diesen Verbindungen. DIETRICH HORSTMANN und HANNS MALISSA.

Coulometrische Titrierverfahren für die Bestimmung von Silizium und Phosphor in Eisen und Stahl. WALTER FUCHS nud O. VEISER.

Anlaßvorgänge im Martensit. WERNER JELLINGHAUS.

Gleichzeitige Ermittlung kleiner Kohlenstoff- und Stickstoffgehalte im α-Eisen durch Dämpfungsmessung. WOLFGANG WEPNER.

Intermetallische Phase mit α-Manganstruktur in einem austenitischen Chrom-Nickel-Molybdän-Stahl mit erhöhtem Titangehalt. WALTER KOCH und CHRISTA ILSCHNER-GENSCH.

Einwirkung von elektromagnetischer Strahlung und Korpuskularstrahlung auf die Eigenschaften von Festköpern. PAUL HÖLLER.

Der Einfluß einiger Begleitelemente des unlegierten Baustahls St 37 auf die Korrosion in verschiedenen Angriffsmitteln. FRANZ EISENSTECKEN und WOLFGANG STINNES.

Elektrochemische Untersuchungen über den Einfluß des Walz- und Glühzunders von Stahl auf die Korrosion und über den Beizvorgang. FRANZ WEVER und HANS-JÜRGEN ENGELL

Heft 8, August 1956:

Zur thermodynamischen Analyse. IV. Vermischungsentropie und Bildungsaffinität der Blei-Kadmium-Schmelzen aus kalorimetrischen Messungen. WILLY OELSEN, EBERHARD SCHÜRMANN, HANS-JOACHIM WEIGT und OLAF OELSEN.

Zur Schnellbestimmung des Eisens in der Schlacke. HERMANN-JOSEF KOPINECK.

Kinetik der Austenitbildung unlegierter und niedriglegierter untereutektoidischer Stähle. ADOLF ROSE und F. WERNER STRASSBURG.

Der Wüstitzerfall unterhalb 570° in Gegenwart von Eisen. WILHELM ANTON FISCHER, ALFRED HOFFMANN und RYUSUKE SHIMADA.

Prüfung von unlegierten Stählen im mehrachsigen Spannungszustand durch Innendruckversuche. Teil I. Bruchaussehen der Proben. ALFRED KRISCH.

Der magnetische Arbeitspunkt von Dauermagneten als Werkstoffkennzeichen und abnahmewert. HANS NEUMANN.

Journal of the Institute of Metals, Vol. 84

August, Part 12, 1955–56:

Ferroelectrics: The Dielectric Analogue of Ferromagnetics. WILLIS JACKSON.

Decomposition of the Beta Phase in a Copper-Gallium Eutectoid Alloy. CHESTER W. SPENCER and DAVID J. MACK.

The Cleavage Fracture of Copper-Plated Zinc Crystals. G. B. GREENOUGH and D. A. RYDER.

Electron-microscopic Observations on the Precipitation of the Theta Phase in an Aluminium-4% Copper Alloy. E. LANGER.

Sub-structure Formation in Slightly Bent Aluminium Single Crystals. J. H. LAMBOT.

Vol. 85

September, Part 1, 1956–57:

The Plastic Deformation of Aluminium and Aluminium Alloys. G. THOMAS and J. NUTTING.

The Refinement of Cast Grain-Size in Copper-Aluminium Alloys Containing 7–9 Per Cent Aluminium. J. P. DENNISON and E. V. TULL.

Some Observations on the Development of Face-Centred Cubic Rolling Textures. R. F. BRAYBROOK and E. A. CALNAN.

Observations on Grain-Boundary Migration in Aluminium Bicrystals. K. T. AUST, (Mrs.) E. H. HARRISON, and R. MADDIN.

The Attack of Unstressed Metals by Liquid Mercury. J. F. STRACHAN and N. L. HARRIS.

The Effect of High and Low Temperatures on the Notched-Bar Characteristics of a Cast, High-tensile Beta-Brass. A. R. BAILEY, R. MCDONALD, and L. E. SAMUELS.

The Constitution of Tin-Indium Alloys in the Range 0–30 Per Cent Indium. J. C. BLADE and E. C. ELLWOOD.

October, Part 2, 1956–57:

The Removal of Oxide from Aluminium by Brazing Fluxes. M. F. JORDAN and D. R. MILNER.

The Relation During Creep Between Grain-Boundary Sliding, Sub-crystal Size, and Extension. D. MCLEAN and M. H. FARMER.

The Nature of Mechanically Polished Metal Surfaces: The Surface Deformation Produced by the Abrasion and Polishing of 70 : 30 Brass. L. E. SAMUELS.

The System Uranium-Palladium. J. A. CATTERALL, J. D. GROGAN and R. J. PLEASANCE.

Some Experiments on the Determination of the Latent Heats of Transition of Titanium and Iron. T. H. SCHOFIELD.

The Behaviour of Interfaces in Lightly Worked Uranium During Recrystallization. P. E. MADSEN.

Calculation of the Contribution Made by Grain-Boundary Sliding to Total Tensile Elongation. H. BRUNNER and N. J. GRANT.

VOL
4
195

VOL.
4
1956